

Extraction of Single and Double Differential Cross-Sections on Argon for CC1 μ 2p0 π Event Topologies in the SBND

Emilio Peláez Cisneros

September 21, 2024

Abstract

The precise measurement of cross-sections for a variety of interactions is critical to the success of upcoming flagship neutrino experiments. Of special interest are neutrino interactions that leave the nucleus in a 2-particle 2-hole state (2p2h). This note will present cross-section measurements for the production of 2p2h states on Argon. Using SBND data collected from the **period** of operation, we select events corresponding to a charged-current ν_μ interaction that left the Argon nucleus in a 2p2h state. These interactions produce a topology with one muon and two protons in the final state (CC1 μ 2p0 π). This analysis targets both single differential and double differential cross-section measurements for CC1 μ 2p0 π event topologies in a variety of kinematic variables. Comparisons are made to a set of theoretical models that explore different cross-section modeling configurations. Code for this analysis is available on [GitHub](#).

Contents

1	Introduction and motivation	3
2	Generator analysis	3
2.1	Signal definition	3
2.2	Generators	3
2.3	Variables definition	4
2.4	Pre-FSI events	17
2.5	Double differential plots	20
2.6	Pure MEC events	31
3	SBND analysis	35
3.1	Fiducial volume	35
3.2	Signal definition	35
3.3	Purity and efficiency studies	38
3.4	Variable plots	39
3.5	Interaction and topology breakdown	42
3.6	Signal efficiency	47
3.7	Migration and response matrices	50
3.8	Systematics	57
3.9	Wiener-SVD unfolding	60
3.10	Closure test	62
3.11	Event rate uncertainties	65
3.12	Difference and resolution	68
4	Cross-section results	71
4.1	Cross-section uncertainties	74

5	Fake data studies	77
5.1	MEC 2x weight	77
5.2	QE 0.5x and MEC 1.5x weights	82
6	SBND Data	87
7	Appendices	90
7.1	Cross section systematics	90
7.2	Flux systematics	357
7.3	Statistical systematics	449
7.4	POT	453
7.5	Number of targets	457
7.6	Detector	461
7.7	Reinteraction	465
8	References	469

1 Introduction and motivation

2 Since many current and next generation neutrino oscillation experiments will utilize dense nuclear targets,
3 such as liquid argon (LAr), it is critical to characterize the impact of nuclear effects on neutrino cross-sections.
4 One area of interest are neutrino events that eject 2 nucleons from the nucleus, leaving it with 2 holes: known
5 as 2-particle 2-hole states (2p2h). The general picture is that the neutrino has a charged-current interaction
6 with a neutron in the nucleus, producing a proton with significant momentum; this proton interacts with
7 another proton, producing the 2p2h state. While the majority of 2p2h states are caused by Meson Exchange
8 Currents (MEC) [15], some nuclear effects, such as Short-Range Nucleon-Nucleon correlations (SRC) [10],
9 can also produce these states. In an accelerator-based liquid argon time projection chamber (LArTPC)
10 experiment, such as SBND, a charged-current (CC) muon neutrino (ν_μ) interaction that results in a 2p2h
11 state would have a final state topology of 1 muon, 2 protons, and no charged or neutral pions. While
12 there are existing measurements of CC1 μ 2p0 π events on argon, the analyses were statistically limited and
13 no cross-sections were extracted [1, 19]. There was a previous report with single differential cross-section
14 measurements from the MicroBooNE detector [20], but this document presents the first double differential
15 cross-section measurements of CC1 μ 2p0 π topologies on argon, using data collected from the period of SBND
16 operations.

17 2 Generator analysis

18 2.1 Signal definition

19 We choose charged-current muon neutrino interactions that result in one muon, two protons, no charged pions
20 with $P_\pi > 70$ MeV/c, no neutral pions or heavier mesons, and any number of neutrons. These interactions
21 are denoted as CC1 μ 2p0 π . We require the momentum of the muon and protons to be in the following ranges
22 (in MeV/c):

$$100 < P_P < 1200 \quad 300 < P_\mu < 1000 \quad (1)$$

23 2.2 Generators

24 The following generators are used to create events, which are then discriminated using the signal definition
25 above: NuWro, GiBUU, NEUT, GENIE G18, GENIE AR23. Information about these generators is
26 summarized in Table 1.

Name	Generator/Configuration
G18	GENIE v3.0.6 G18_10a_02_11a
AR23	G18 with SuSAv2 MEC model
NuWro	NuWro 19.02.1
NEUT	NEUT v5.4.0
GiBUU	GiBUU 2021

Table 1: Generator and configuration data.

27 The GENIE configurations we used are:

- 28 (i) GENIE G18 [2, 3]: This modern model configuration uses the local Fermi gas (LFG) model [9],
29 the Nieves CCQE scattering prescription [23], which includes Coulomb corrections for the outgoing
30 muon [11], and random phase approximation (RPA) corrections [22]. Additionally, it uses the
31 Nieves MEC model [25], the KuzminLyubushkin-Naumov Berger-Sehgal RES [6, 28, 16], Berger-Sehgal
32 COH [7] and Bodek-Yang DIS [29] scattering models with the PYTHIA [26] hadronization part, and
33 the hA2018 FSI model [4].
- 34 (ii) GENIE AR23: Same as the G18 model configuration but using the SuSAv2 MEC model.

35 The alternative event generators are:

- 36 (i) NuWro [12]: Includes the LFG model [9], the Llewellyn Smith model for QE events [18], the Nieves
37 model for MEC events [24], the AdlerRarita-Schwinger formalism to calculate the Δ resonance explicitly [13],
38 the Berger-Sehgal (BS) COH [7] scattering model, an intranuclear cascade model for FSI [24],
39 and a coupling to PYTHIA [26] for hadronization.
- 40 (ii) NEUT [14]: Corresponds to the combination of the LFG model [8, 9], the Nieves CCQE scattering
41 prescription [23], the Nieves MEC model using a lookup table [25], the Berger Sehgal RES [6, 13, 5]
42 and BS COH [7] scattering models, FSI with medium corrections for pions [2, 3], and PYTHIA [26]
43 purposes.
- 44 (iii) GiBUU [21]: Uses similar models to GENIE, but they are implemented in a coherent way by solving
45 the Boltzmann-Uehling-Uhlenbeck transport equation [21]. The modeling includes the LFG model [9],
46 a standard CCQE expression [17], an empirical MEC model, and a dedicated spin dependent resonance
47 amplitude calculation following the MAID analysis [21]. The DIS model is from PYTHIA [26]. GiBUU's
48 FSI treatment propagates the hadrons through the residual nucleus in a nuclear potential consistent
49 with the initial state.

50 2.3 Variables definition

51 Given the momentum vectors for the leading proton \vec{p}_L , recoil proton \vec{p}_R , and muon \vec{p}_μ , we define several
52 variables. First, we define the momenta and opening angle of each variable, denoted as $|\vec{p}|$ and $\cos(\theta_{\vec{p}})$, with
53 the appropriate index for each momentum vector. These variables are plotted in Figure 1.

54 We also define variables relating the multiple momentum vectors. First, the opening angle between the
55 protons in the lab frame, given by

$$\cos(\theta_{\vec{p}_L, \vec{p}_R}) = \frac{\vec{p}_L \cdot \vec{p}_R}{|\vec{p}_L| |\vec{p}_R|}. \quad (2)$$

56 Then, the opening angle between the total proton momentum ($\vec{p}_{\text{sum}} = \vec{p}_L + \vec{p}_R$) and the muon, given by

$$\cos(\theta_{\vec{p}_\mu, \vec{p}_{\text{sum}}}) = \frac{\vec{p}_\mu \cdot \vec{p}_{\text{sum}}}{|\vec{p}_\mu| |\vec{p}_{\text{sum}}|}. \quad (3)$$

57 The momentum transverse to the direction of the neutrino beam, which we denote $\delta\vec{P}_T$ and is given by

$$\delta\vec{P}_T = \vec{p}_T^\mu + \vec{p}_T^L + \vec{p}_T^R. \quad (4)$$

58 For the transverse momentum, we will be interested in its magnitude $|\delta\vec{P}_T|$. Finally, the angular orientation
59 of the transverse momentum with respect to the transverse muon is defined as

$$\delta\alpha_T = \cos^{-1} \left(\frac{-\vec{p}_T^\mu \cdot \delta\vec{P}_T}{|\vec{p}_T^\mu| |\delta\vec{P}_T|} \right). \quad (5)$$

60 We plot the differential cross sections of these variables for the given generators in Figure 2. We can also
61 see the cross section by event type for all variables and all generators in Figures 3 to 12.

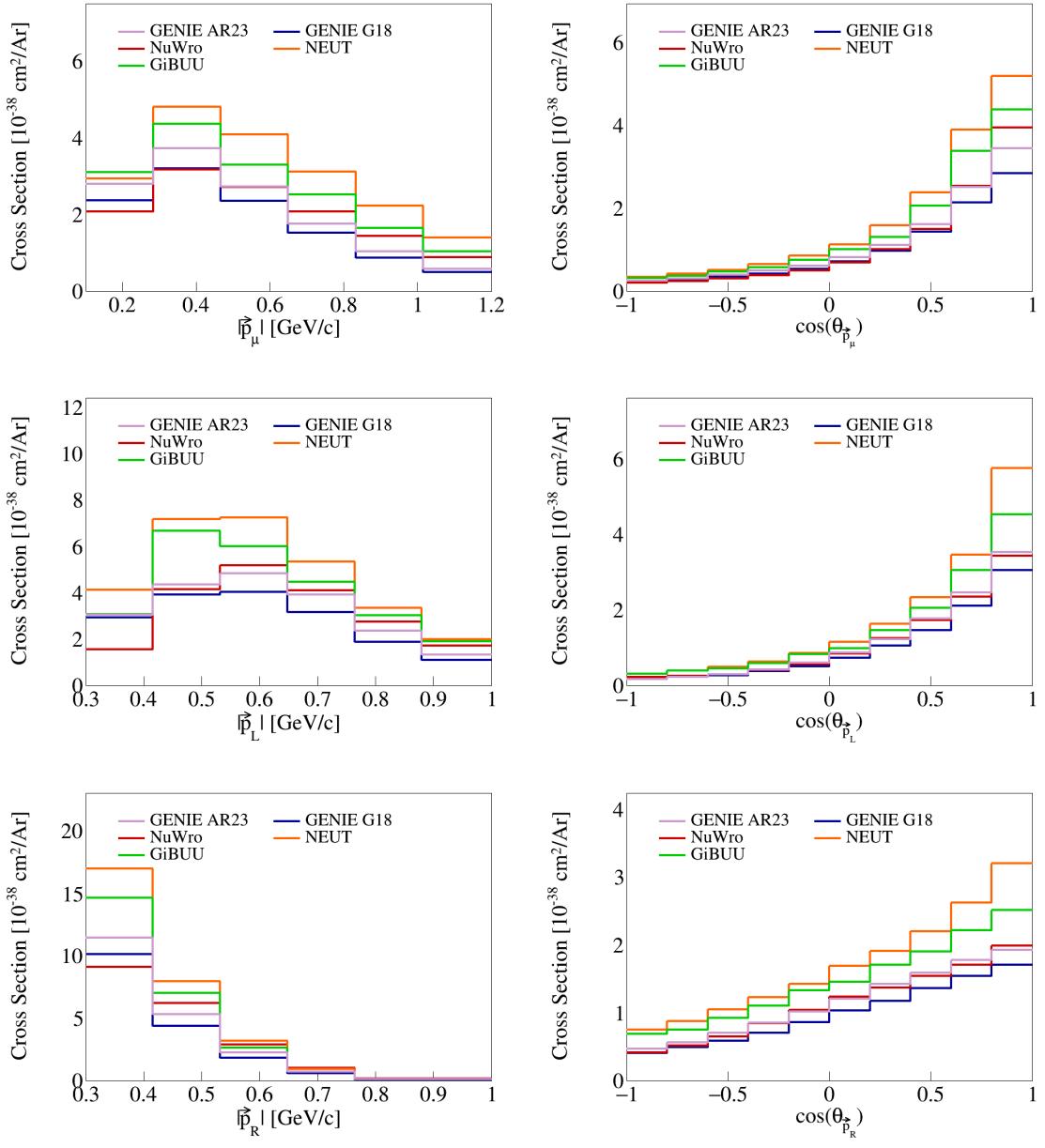


Figure 1: Cross sections for momenta and opening angles of individual particles.

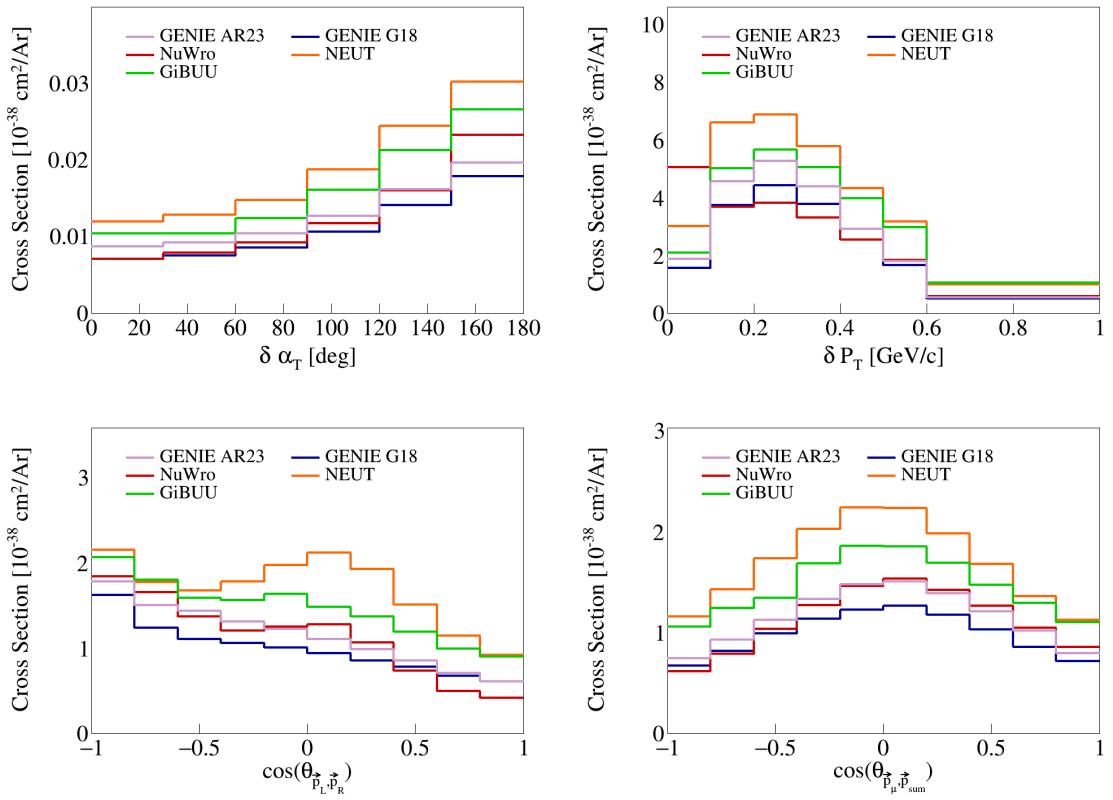


Figure 2: Cross sections for opening angles and transverse momentum.

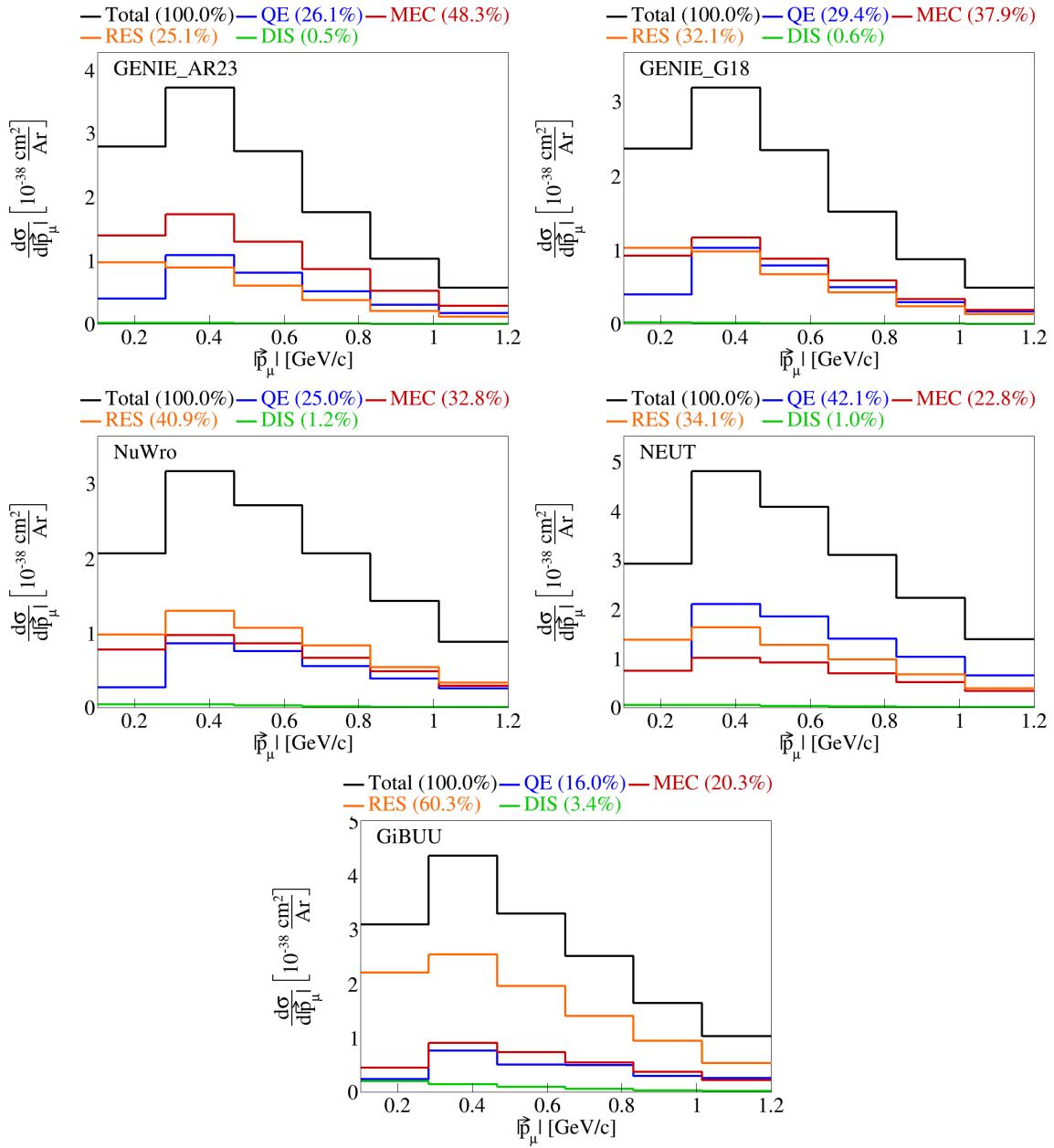


Figure 3: Event interaction breakdown for $|\vec{p}_\mu|$.

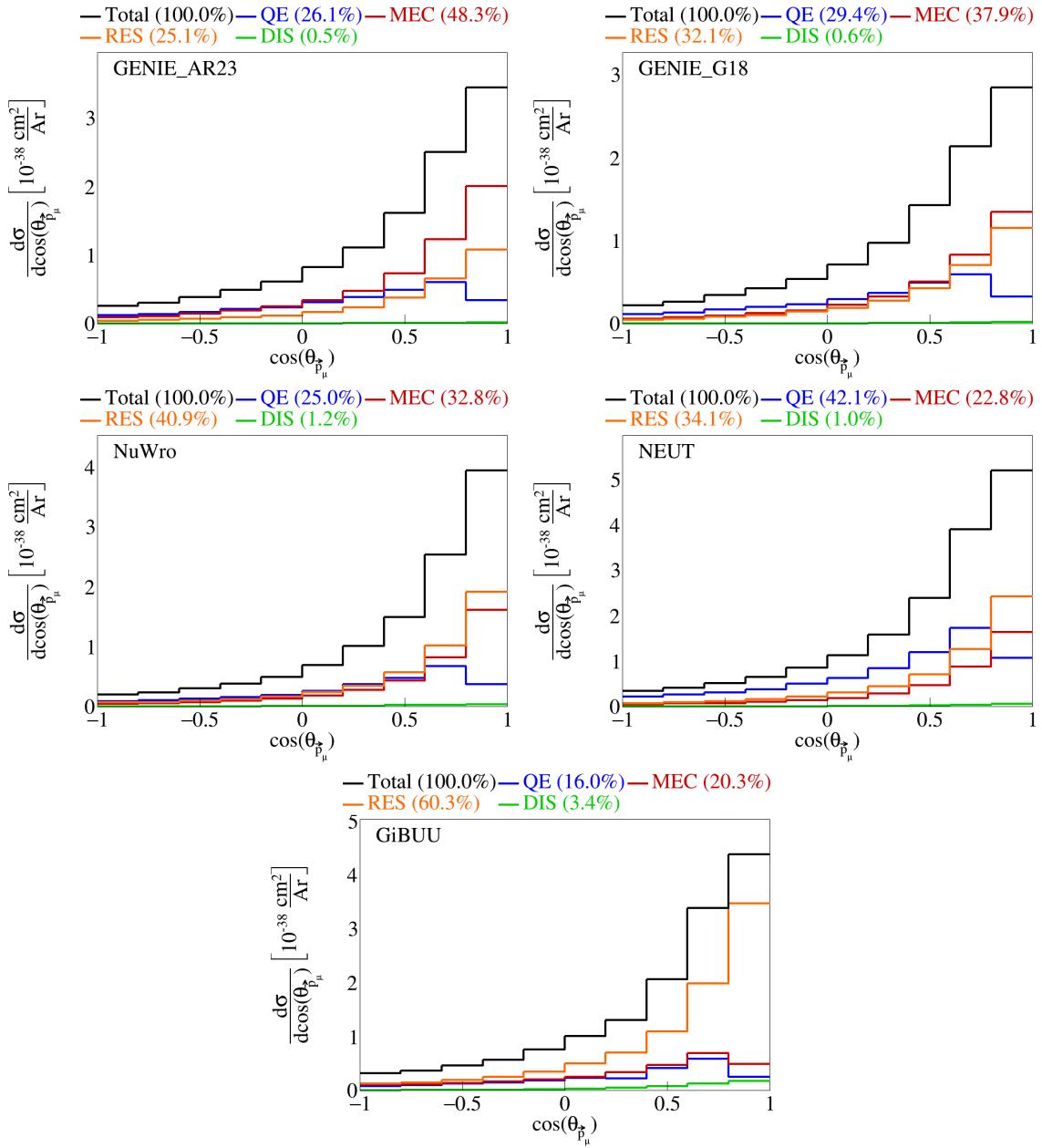


Figure 4: Event interaction breakdown for $\cos(\theta_{\vec{p}_\mu})$.

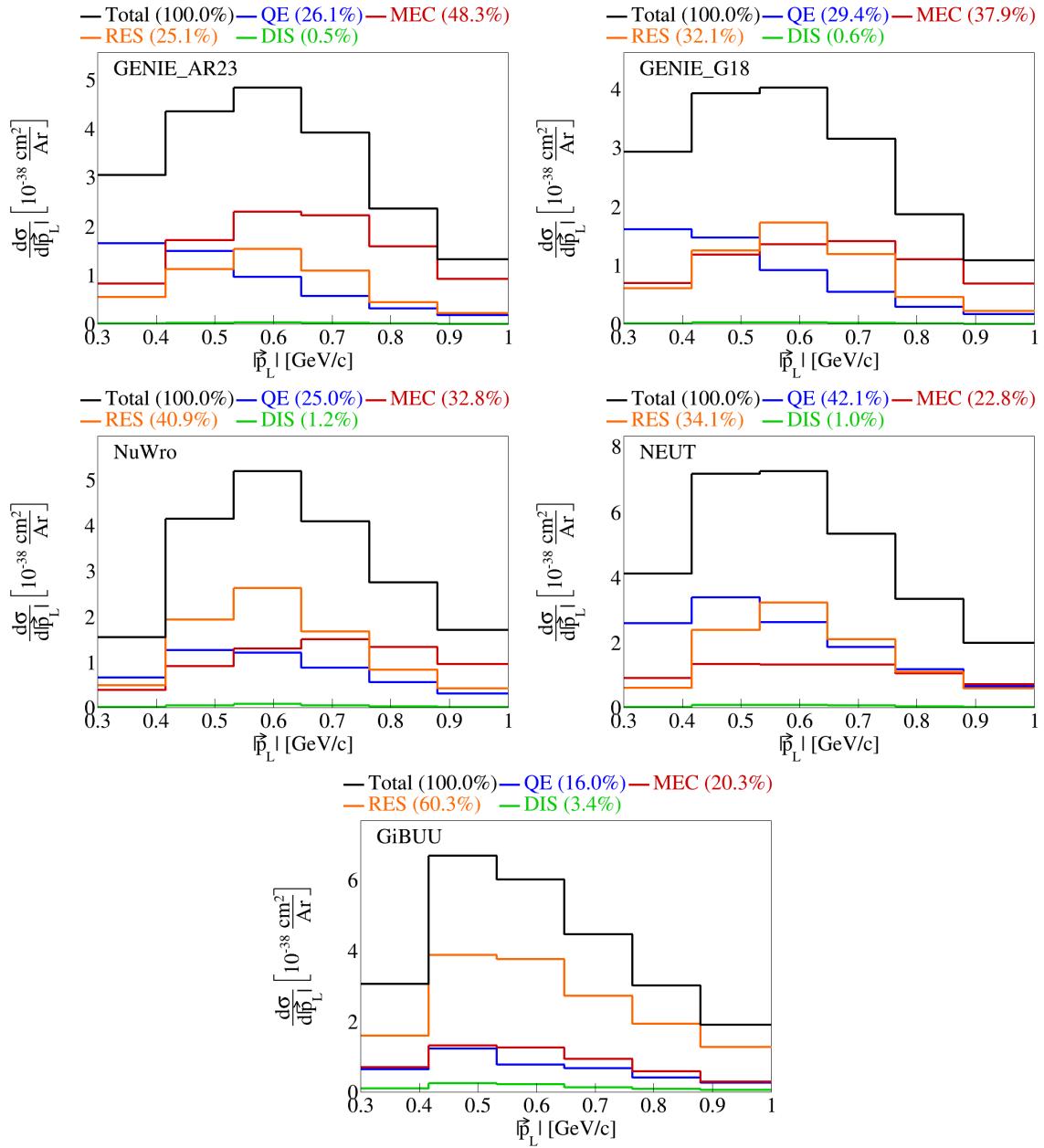


Figure 5: Event interaction breakdown for $|\vec{p}_L|$.

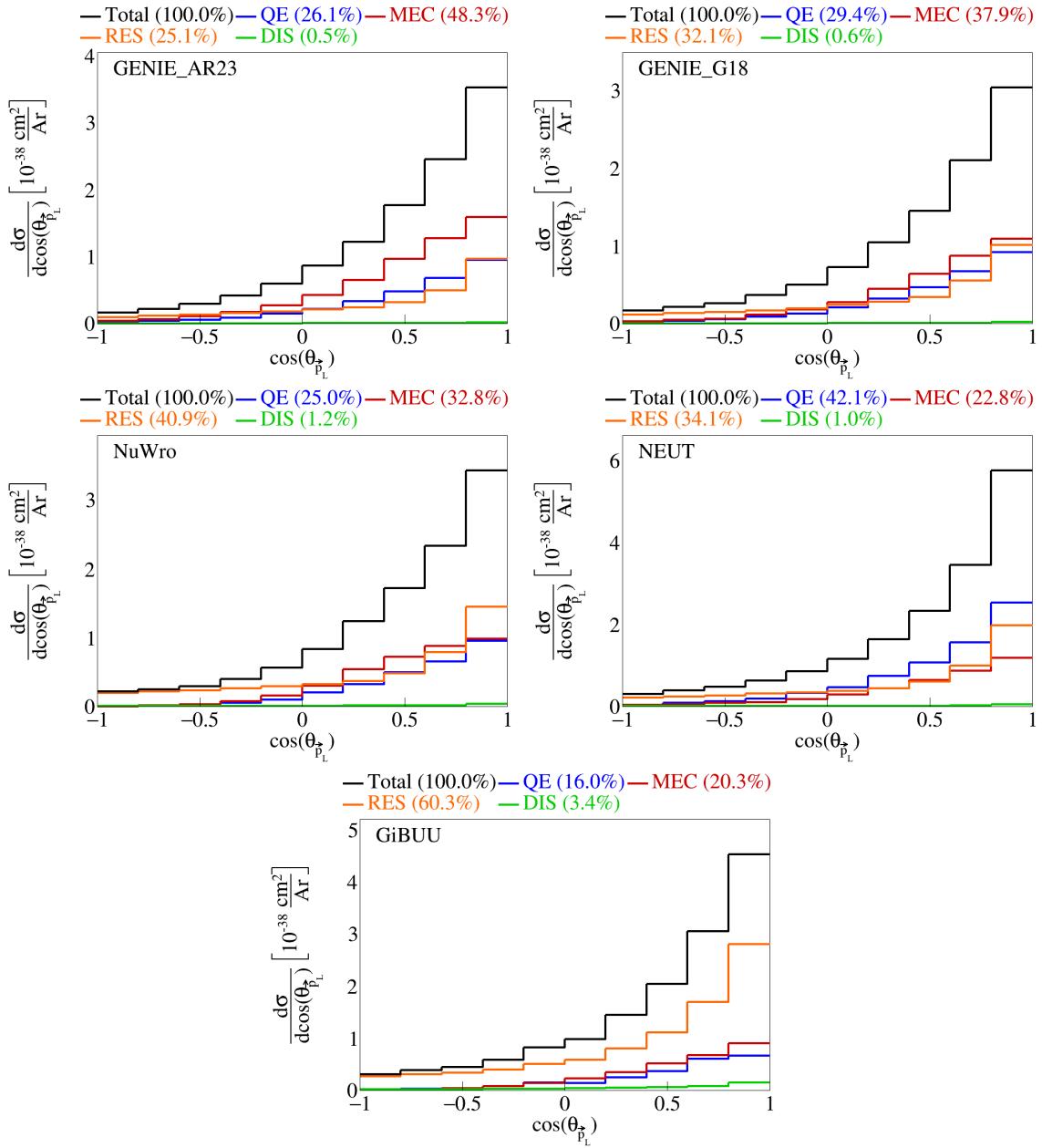


Figure 6: Event interaction breakdown for $\cos(\theta_{\vec{p}_L})$.

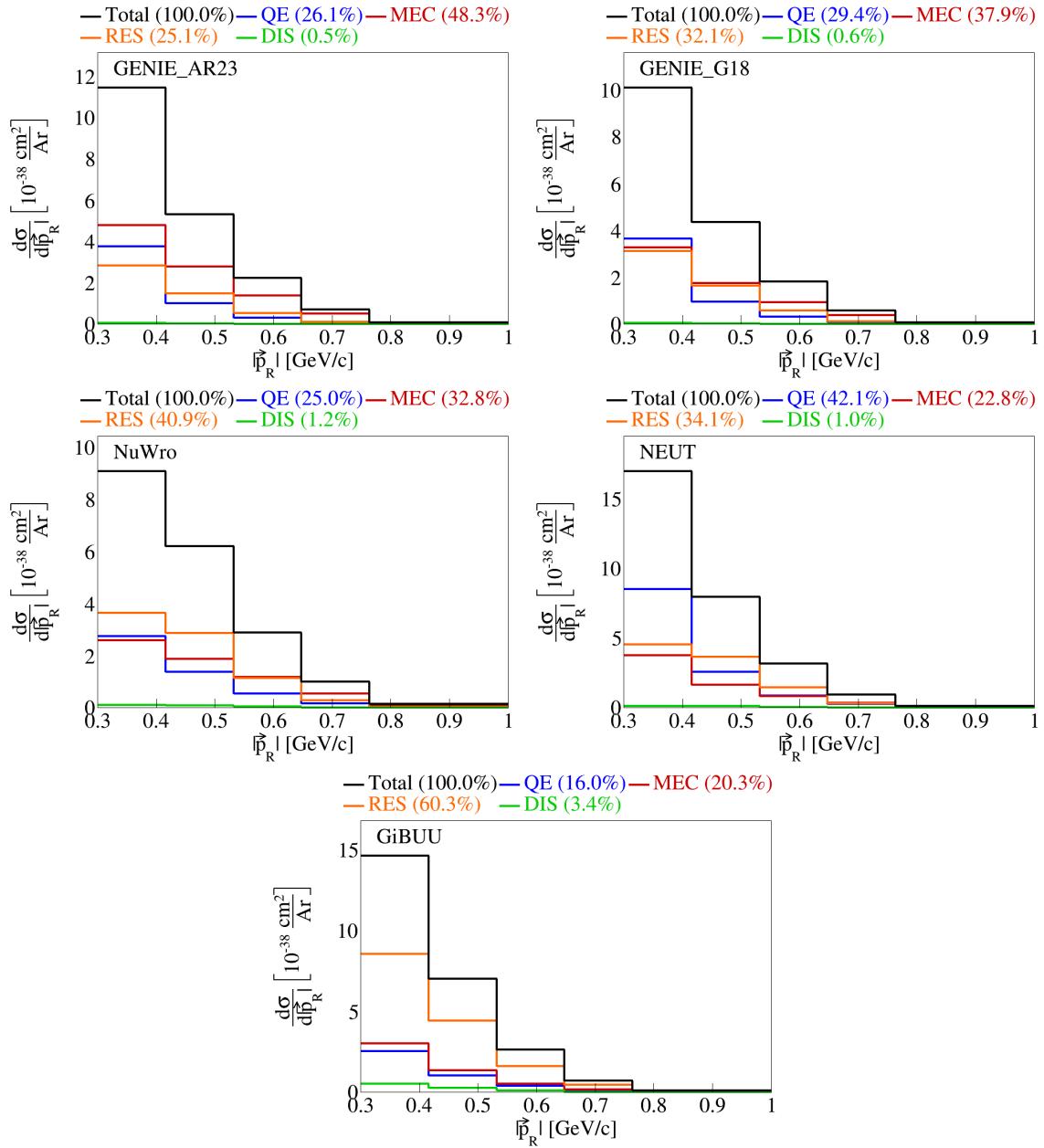


Figure 7: Event interaction breakdown for $|\vec{p}_R|$.

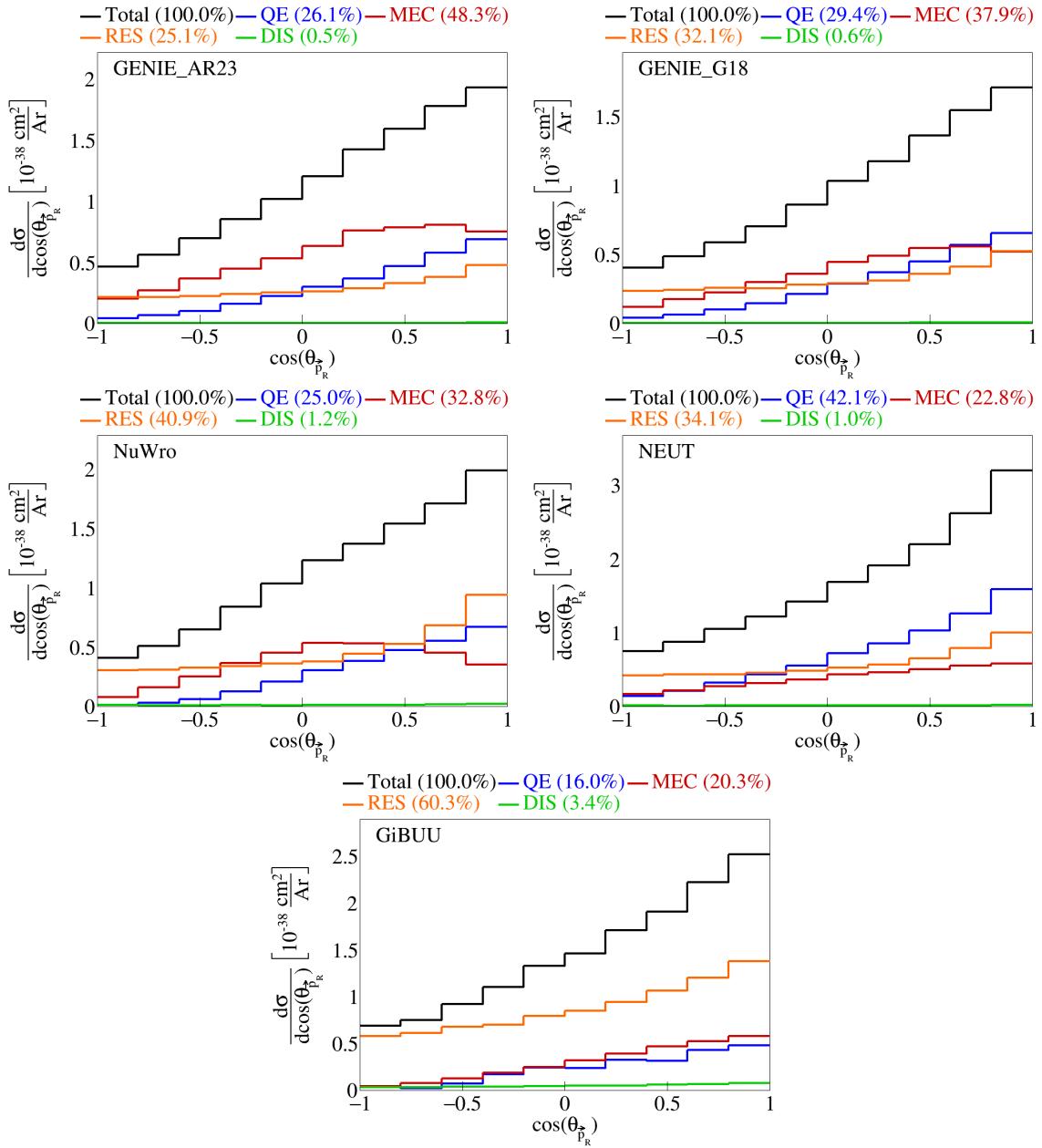


Figure 8: Event interaction breakdown for $\cos(\theta_{\vec{p}_R})$.

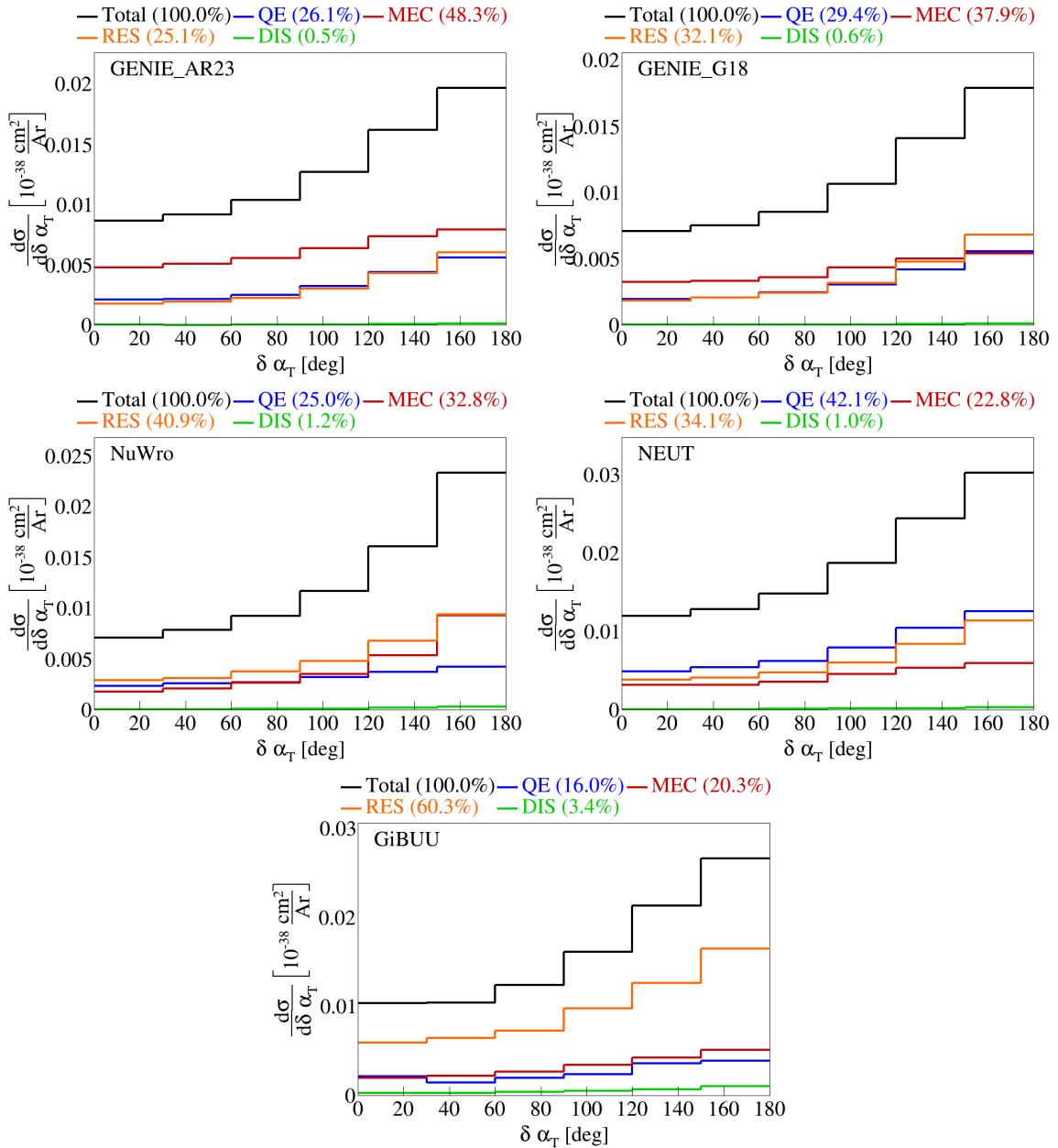


Figure 9: Event interaction breakdown for $\delta \alpha_T$.

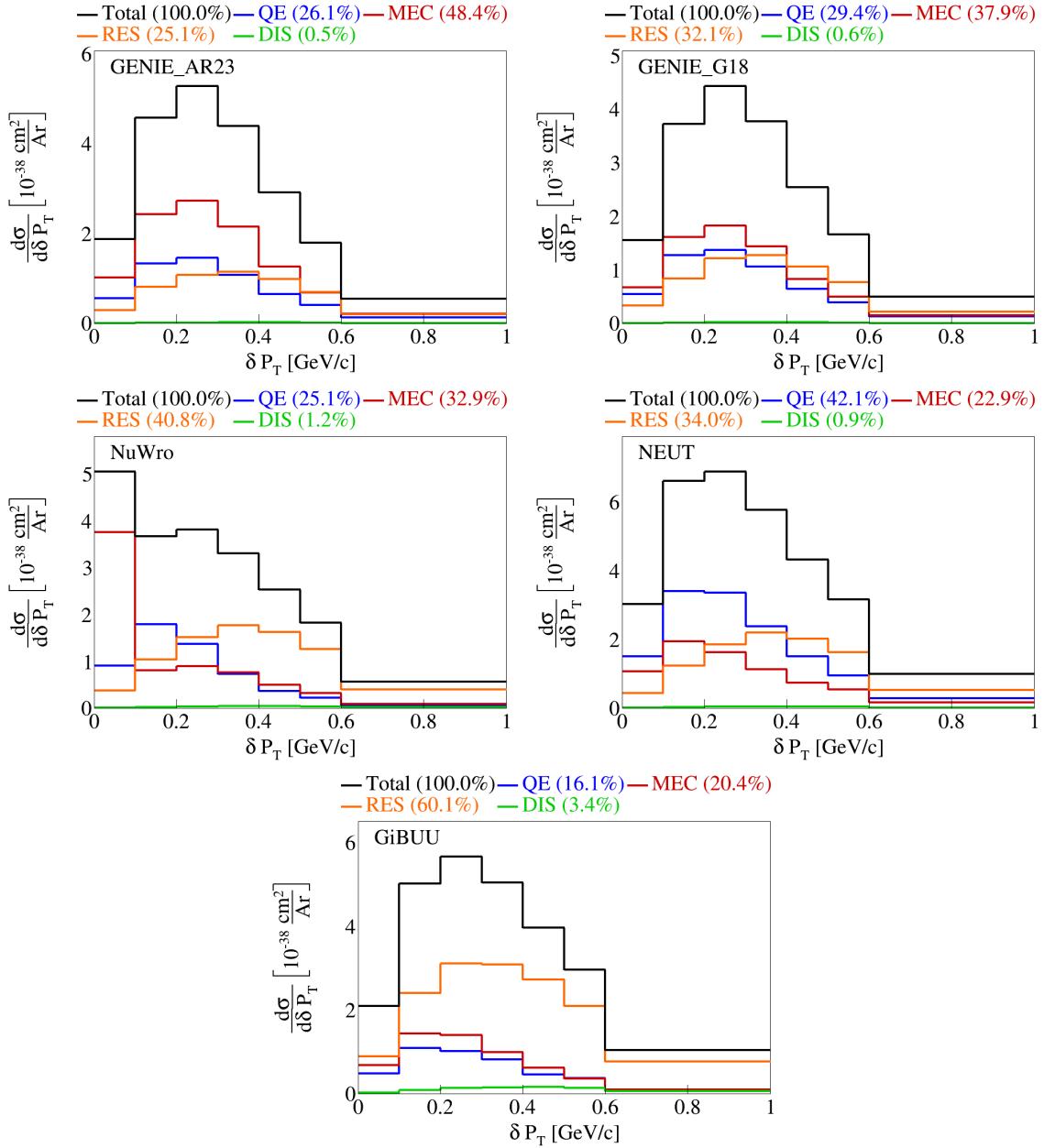


Figure 10: Event interaction breakdown for $|\delta \vec{P}_T|$.

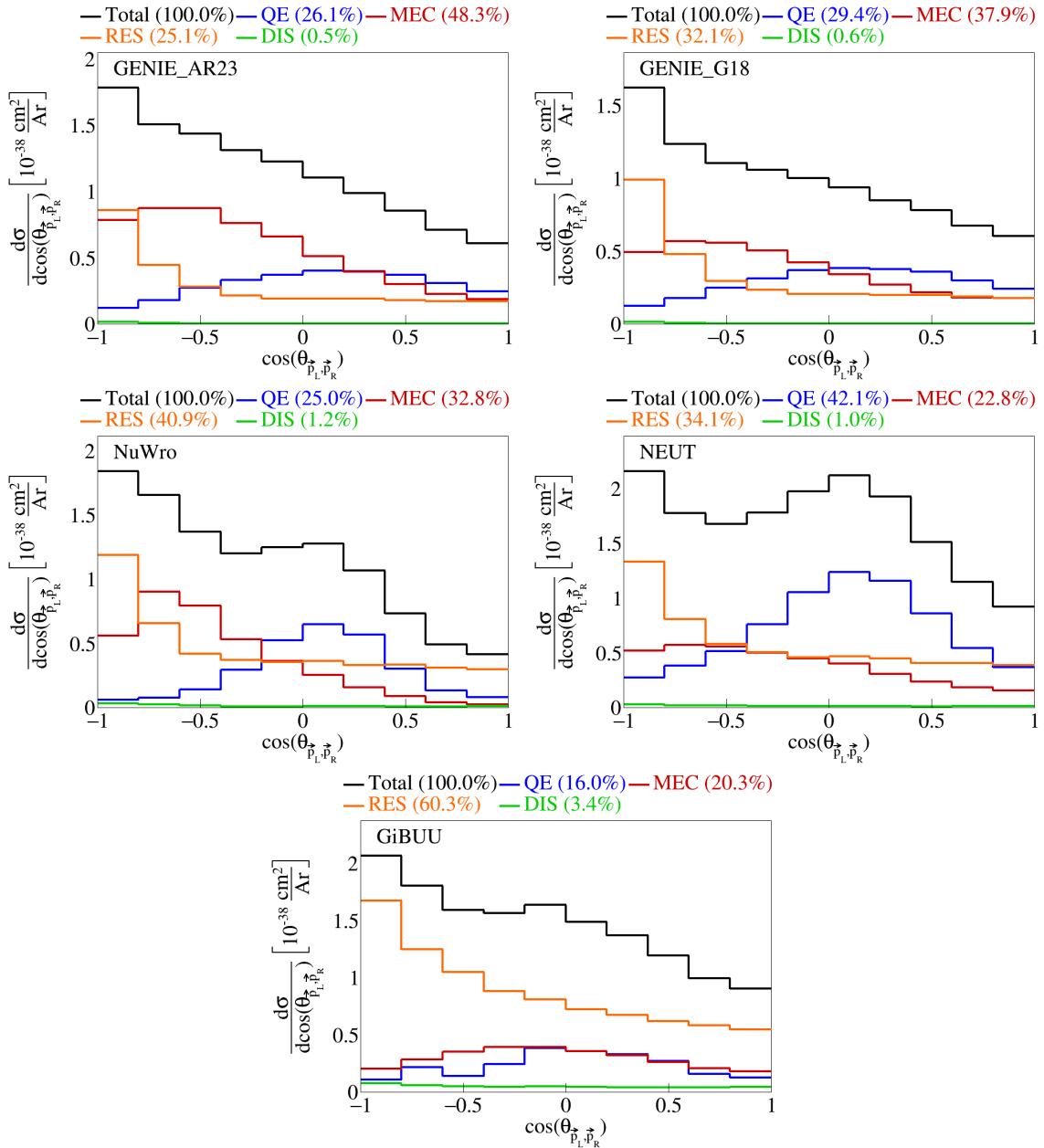


Figure 11: Event interaction breakdown for $\cos(\theta_{\vec{p}_L, \vec{p}_R})$.

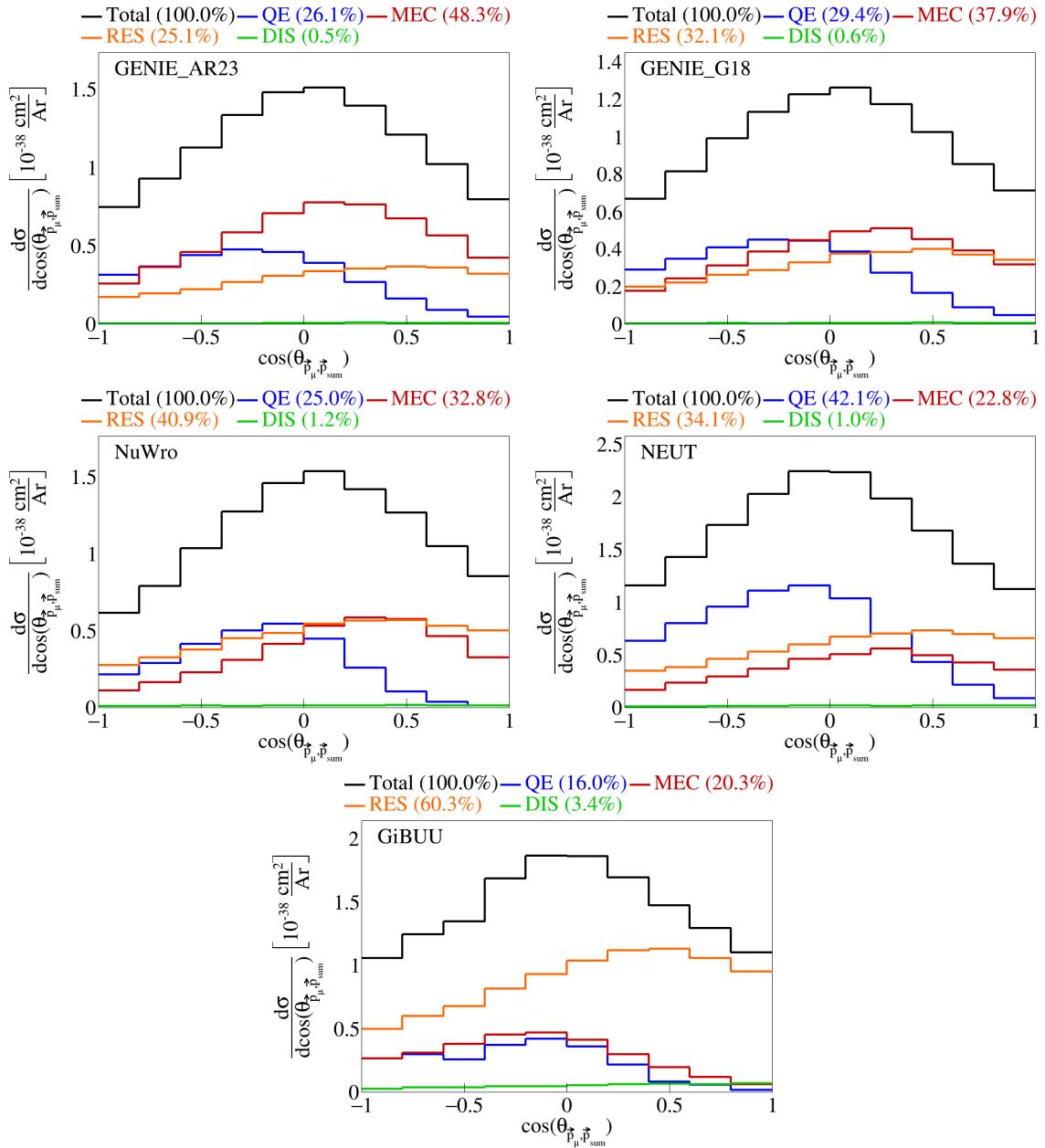


Figure 12: Event interaction breakdown for $\cos(\theta_{\vec{p}_\mu, \vec{p}_{\text{sum}}})$.

62 **2.4 Pre-FSI events**

63 To investigate why the percentage of MEC events for some generators is low, we performed event selection
64 before any final state interactions took place and plotted the interaction breakdown. For both GENIE tunes,
65 NEUT, and NuWro, we got 100% MEC events pre-FSI. For GiBUU, only 4.1% MEC versus 76.2% RES and
66 16% DIS events pre-FSI. The interaction breakdown for $|\vec{p}_\mu|$ for all the generators are shown in Figure 13.
67 Since GiBUU is the outlier, we checked the specific interaction mode for the resonance events. We got that
68 10 has 39.3%, 11 has 34.7%, 12 has 0.0136%, 13 has 26 %, and 27, 22, and 23 all have zero percent of the
69 resonance events.

70 We also checked the event interaction breakdown for GiBUU samples generated without final state
71 interactions, in which we found that 100% of the events are MEC, shown in Figure 14. Note that the
72 difference between these two GiBUU samples is that in the former, the samples were generated with final
73 state interactions, and then we look at the state before the final state interactions reportedly took place,
74 and in the latter the event generation was done without any final state interactions.

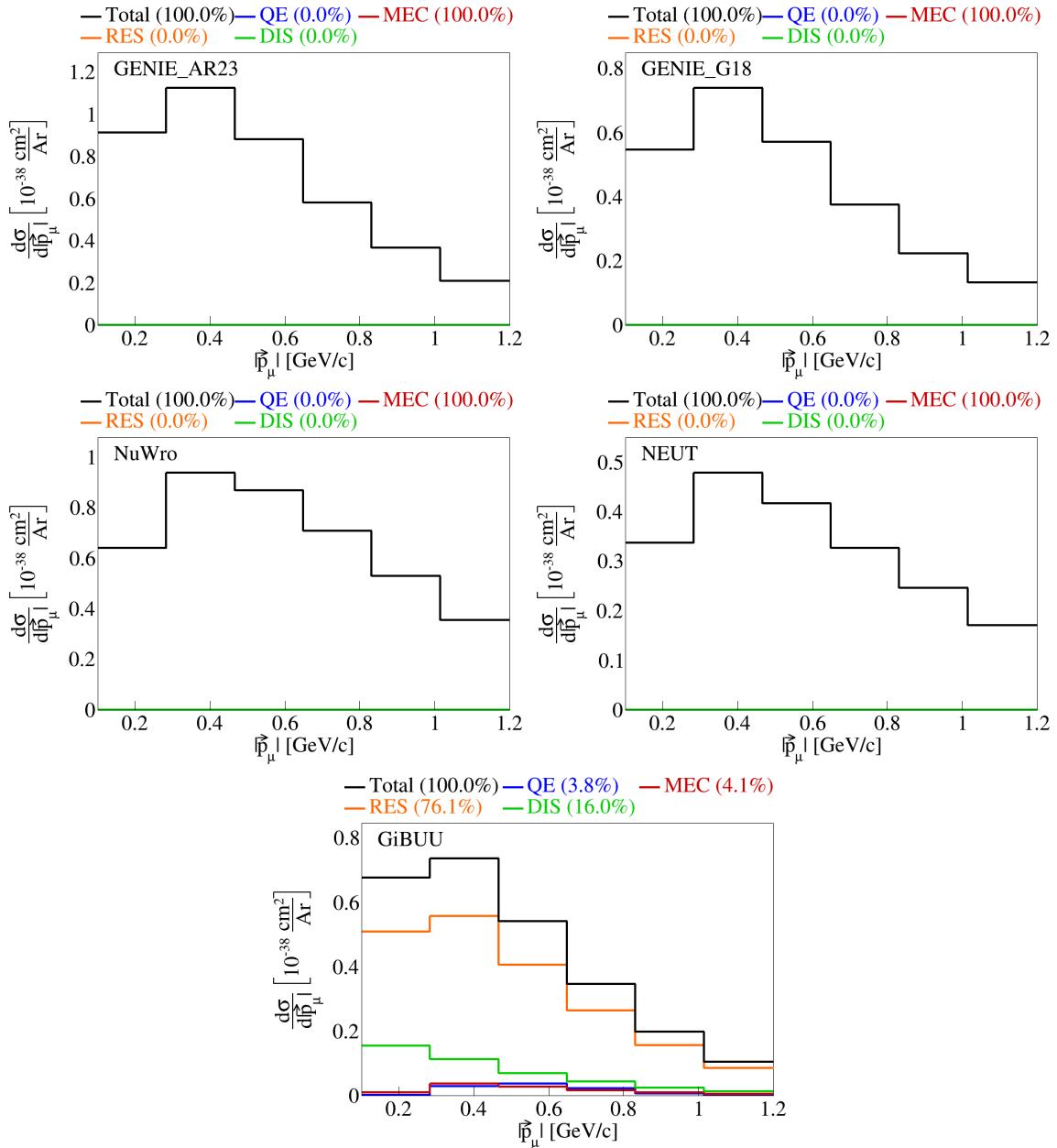


Figure 13: Event interaction breakdown of $|\vec{p}_\mu|$ before final state interactions.

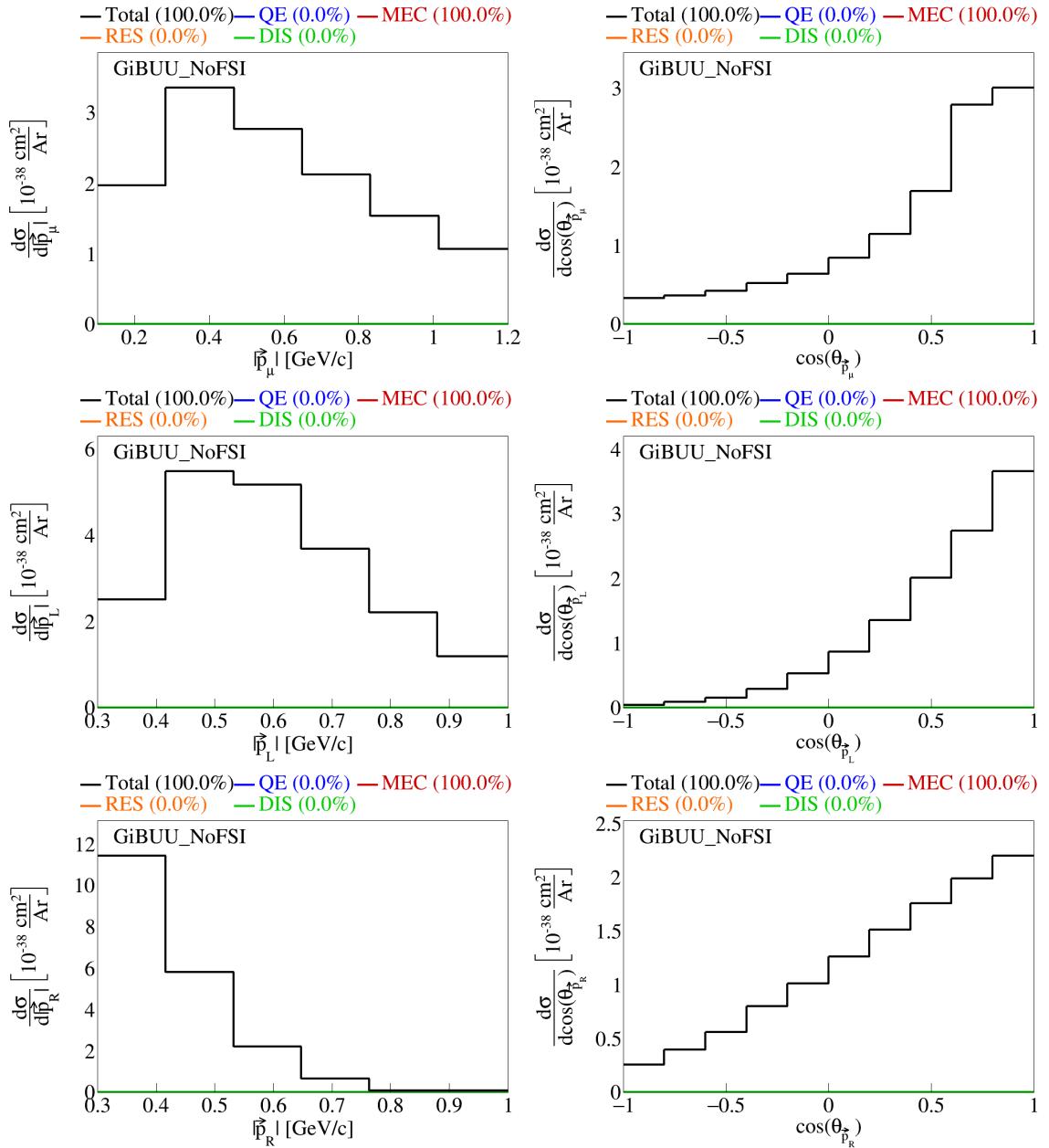


Figure 14: Event interaction breakdown for final events from GiBUU events with no FSI.

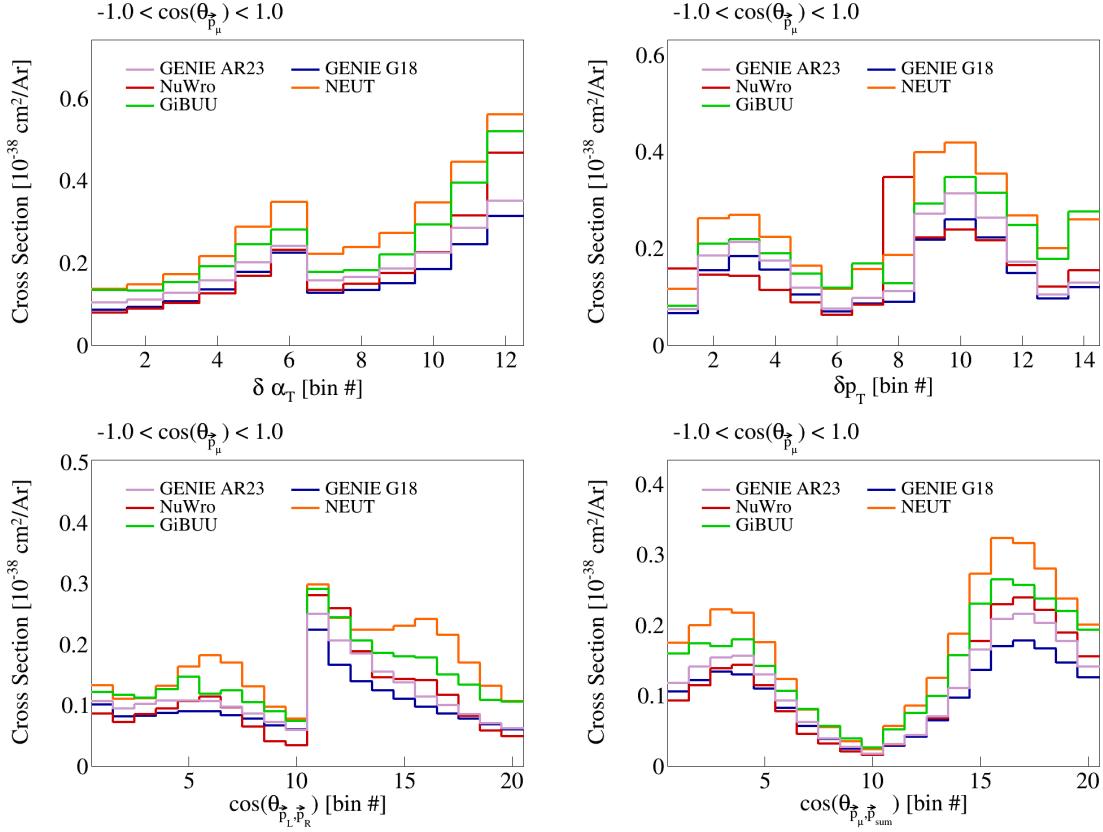


Figure 15: Double differential serial plots, all in $\cos(\theta_{\vec{p}_\mu})$.

75 2.5 Double differential plots

76 We define four double differential variables as δP_T , $\delta \alpha_T$, $\cos(\theta_{\vec{p}_L, \vec{p}_R})$, and $\cos(\theta_{\vec{p}_\mu, \vec{p}_{\text{sum}}})$ in $\cos(\theta_{\vec{p}_\mu})$. We have
 77 two bins for $\cos(\theta_{\vec{p}_\mu})$, the first one going from -1 to 0.5 and the second from 0.5 to 1 . Therefore, these are
 78 irregular bins, with the first covering a larger range than the first. These plots are shown in Figure 15. Note
 79 that, in these plots, the horizontal axis is defined by bin number of the double differential measurement, not
 80 the value of the variable. This is because we are representing both variables in a single axis, but we can slice
 81 the plots to get our usual horizontal axis in two slices of $\cos(\theta_{\vec{p}_\mu})$.

82 We slice the double differential plots into two plots each, so that we have the variable of interest in the
 83 horizontal axis instead of bin numbers, and each slice corresponds to one bin of $\cos(\theta_{\vec{p}_\mu})$. These plots are
 84 shown in Figure 16, and the plots broke down by interaction type are in Figures 17 to 20. In these plots,
 85 the bins contents have been reweighted appropriately, by dividing the content of each bin in the horizontal axis
 86 by the width of the bin for the variable in the horizontal axis multiplied by the width of the $\cos(\theta_{\vec{p}_\mu})$ slice.
 87 Note that the plots for the $0.5 < \cos(\theta_{\vec{p}_\mu}) < 1$ slice have more events in general, although they span a
 88 smaller phase space of $\cos(\theta_{\vec{p}_\mu})$, as it can be seen by the scale of the vertical axis. We plot the same double
 89 differential variables for the events before final state interactions. These are shown in Figure 21, and the
 90 corresponding interaction breakdown plots are in Figures 22 to 25.

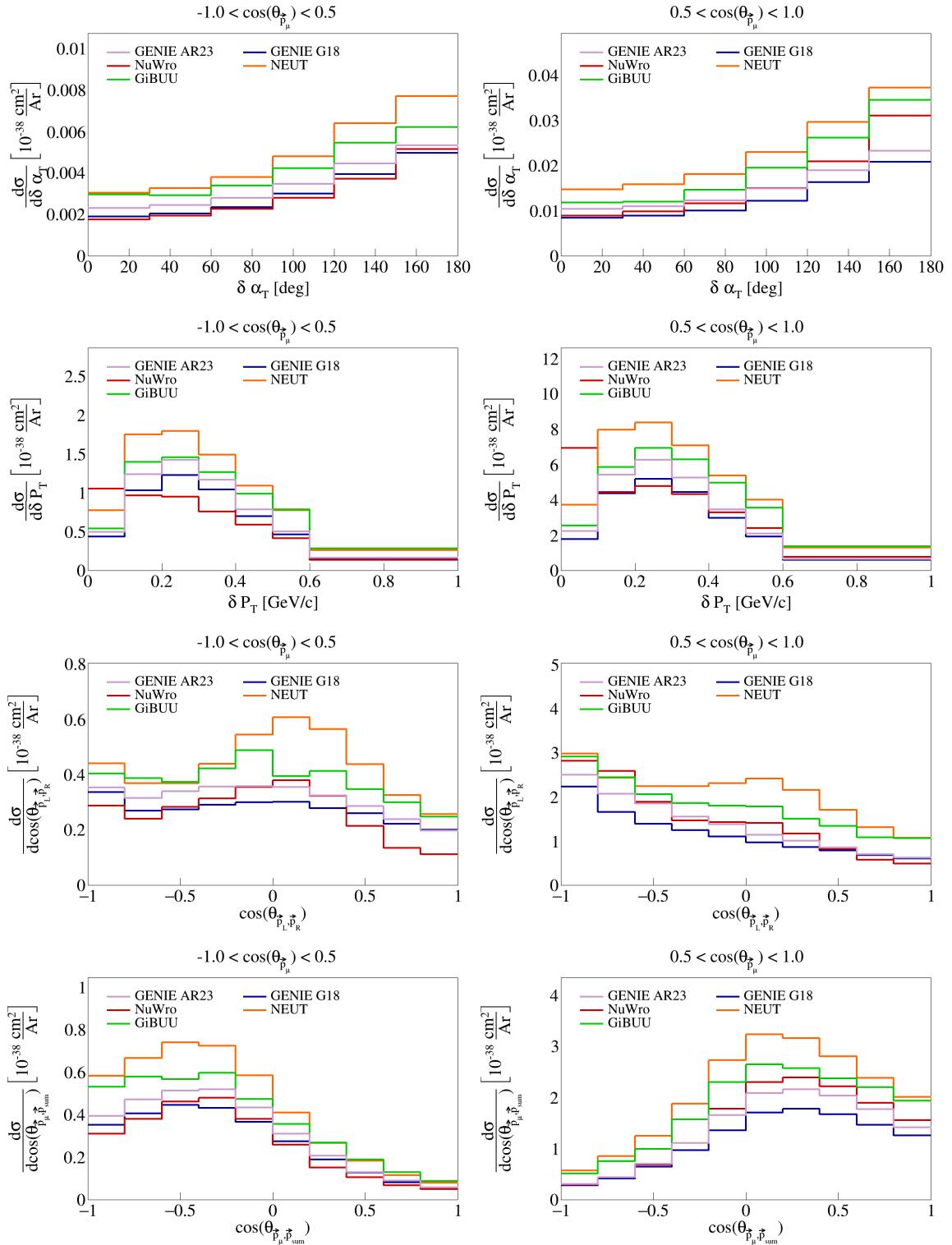


Figure 16: Sliced double differential plots.

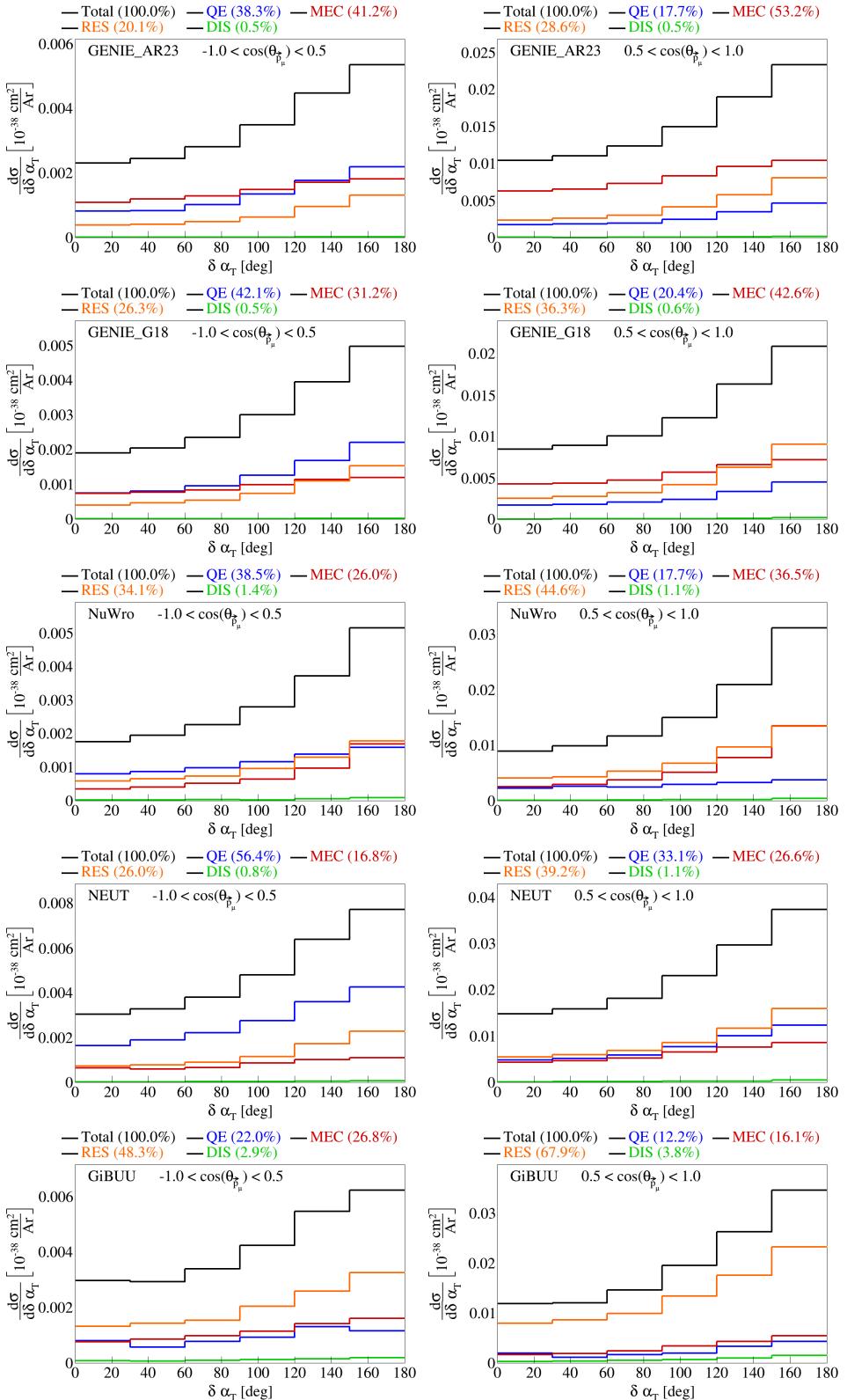


Figure 17: Interaction breakdown for sliced double differential plots for $\delta\alpha_T$ in $\cos(\theta_{\vec{p}_\mu})$.

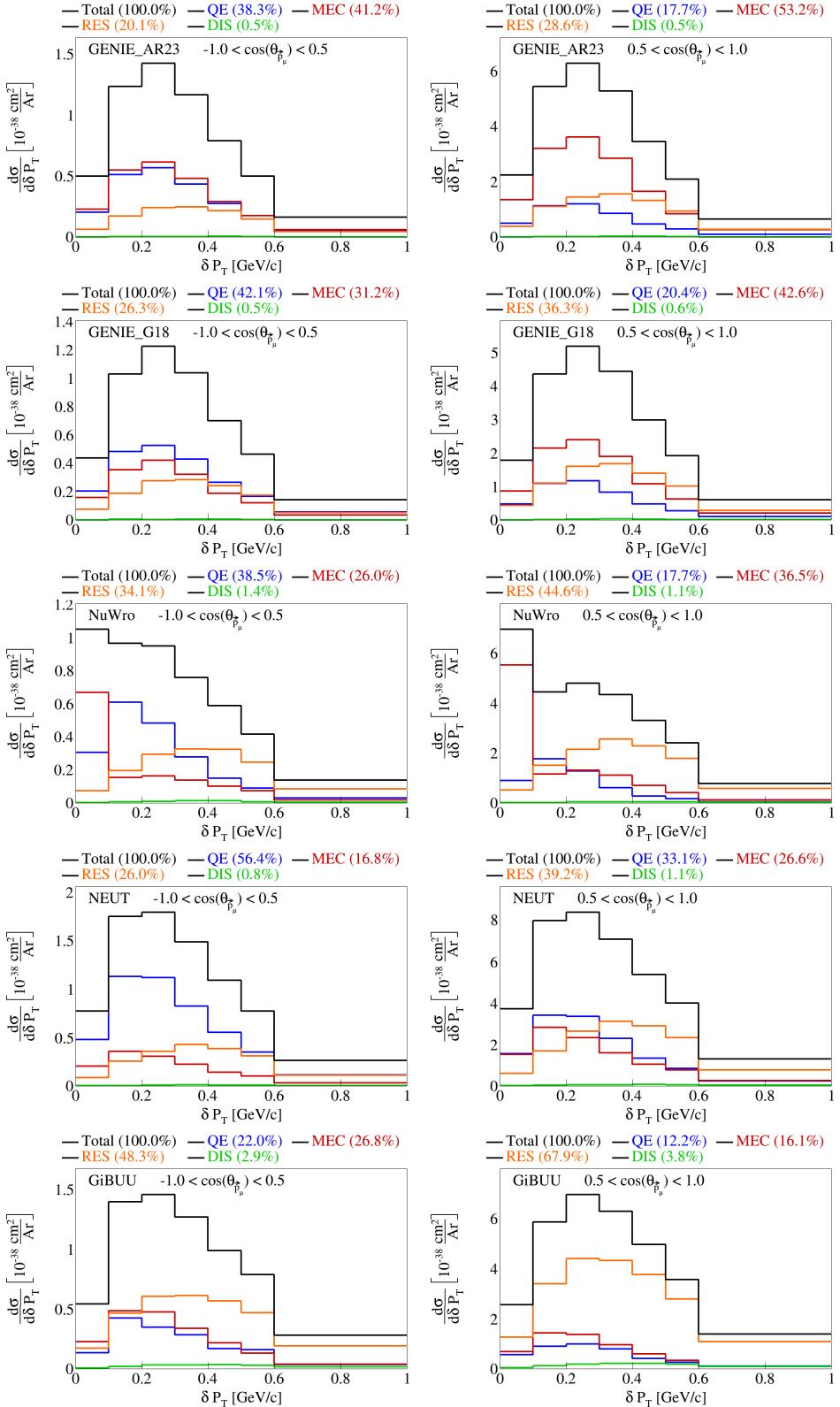


Figure 18: Interaction breakdown for sliced double differential plots for $|\delta\vec{P}_T|$ in $\cos(\theta_{\vec{p}_\mu})$.

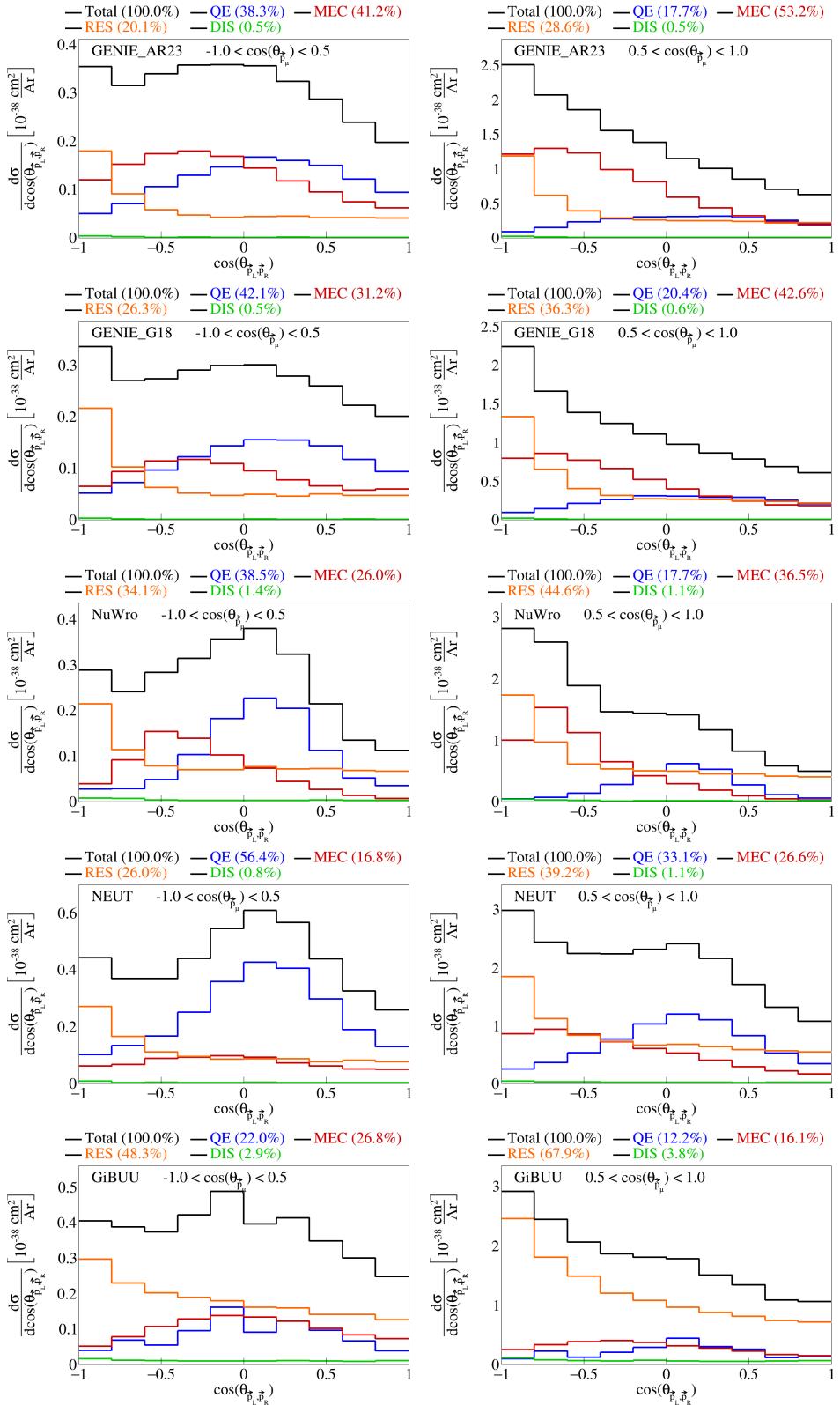


Figure 19: Interaction breakdown for sliced double differential plots for $\cos(\theta_{\vec{p}_L, \vec{p}_R})$ in $\cos(\theta_{\vec{p}_\mu})$.

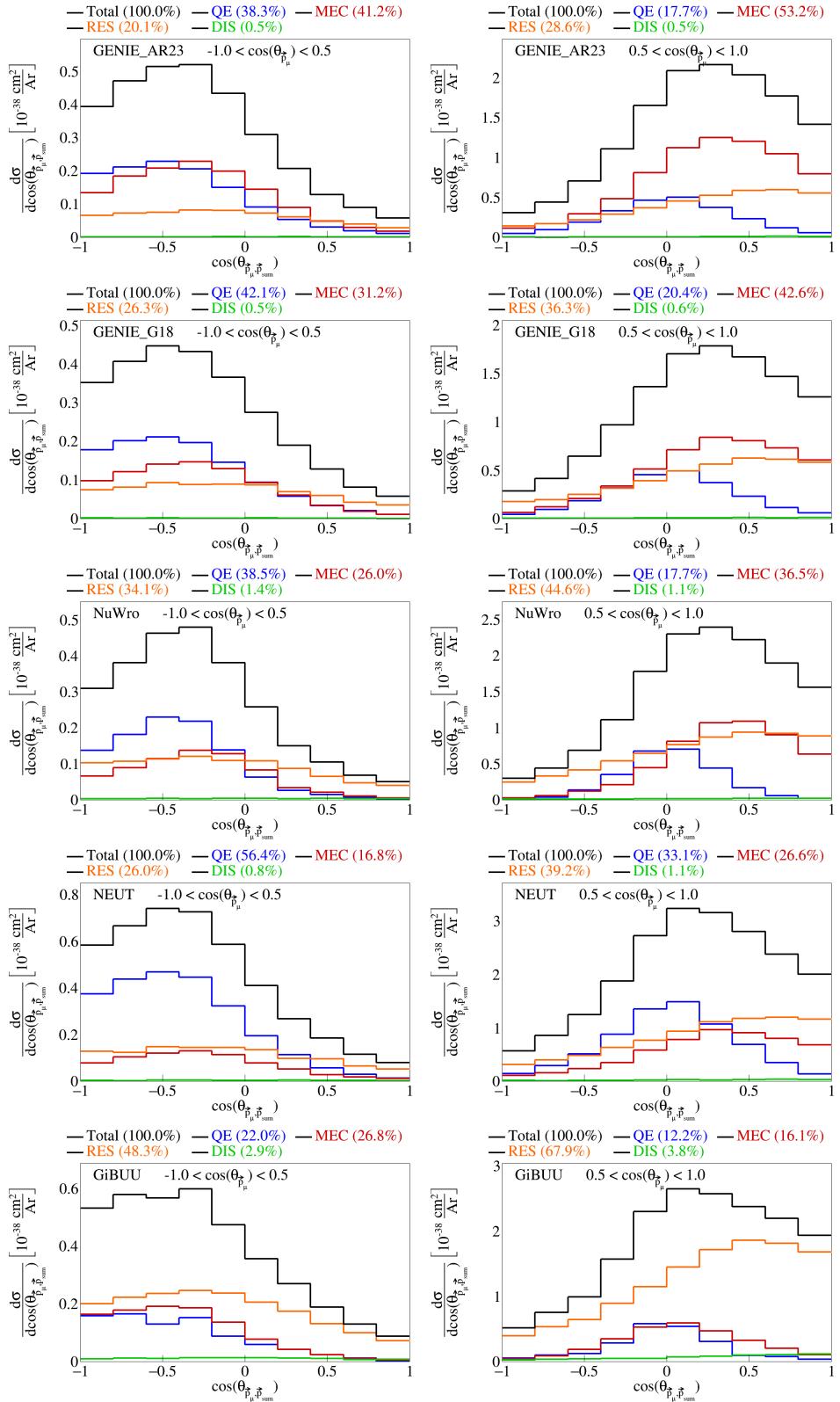


Figure 20: Interaction breakdown for sliced double differential plots for $\cos(\theta_{\vec{p}_\mu, \vec{p}_{\text{sum}}})$ in $\cos(\theta_{\vec{p}_\mu})$.

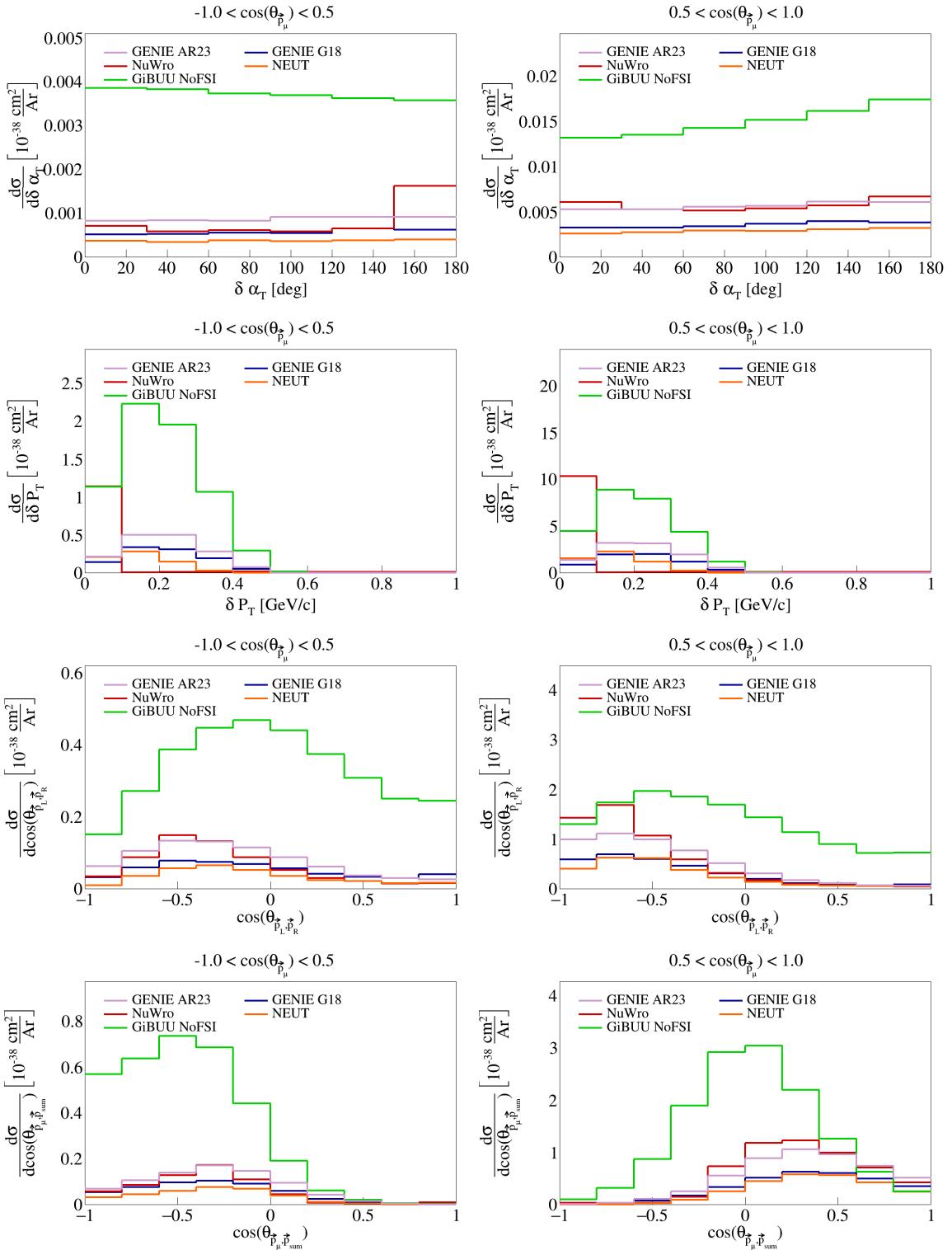


Figure 21: Sliced double differential plots for pre-FSI events.

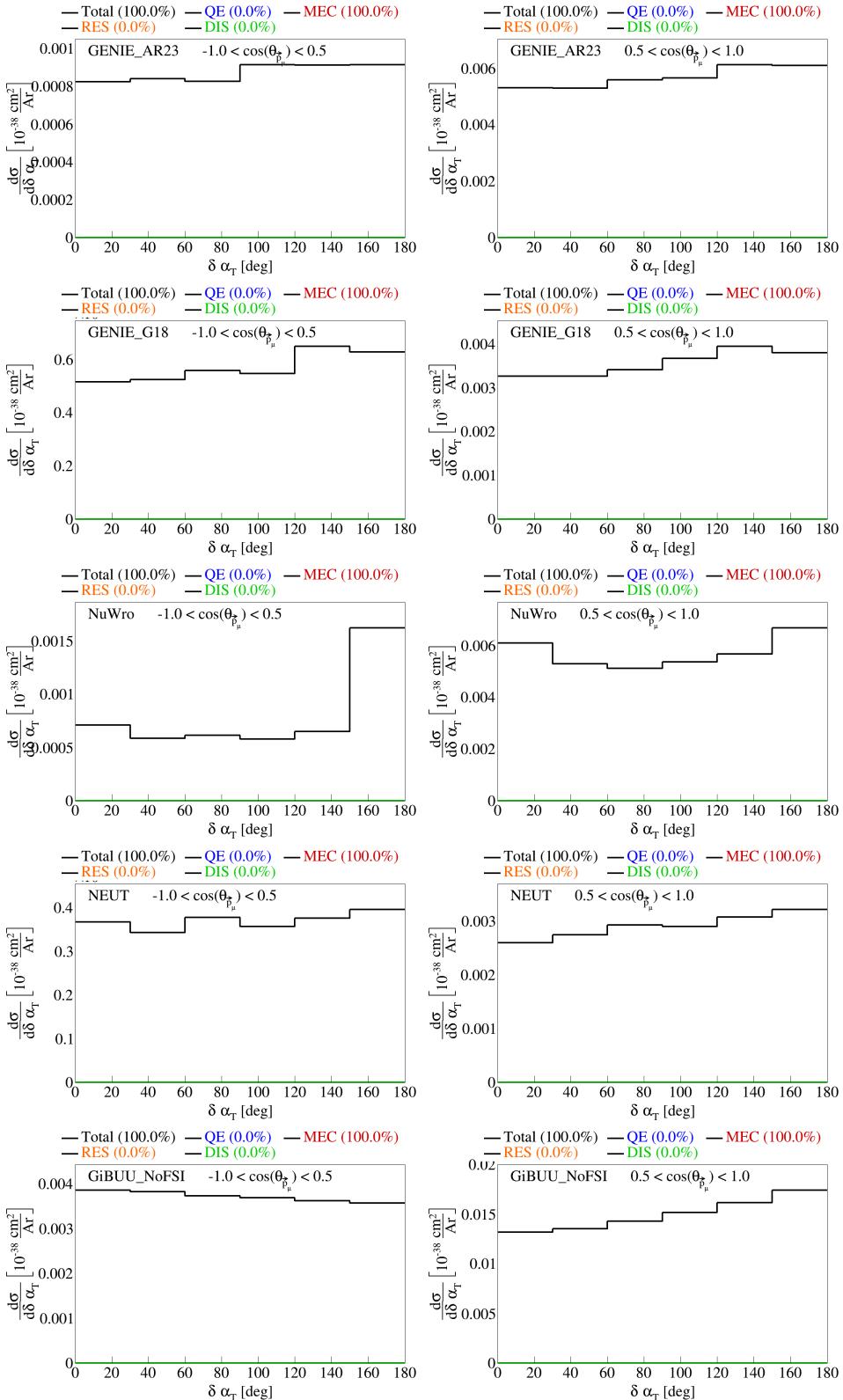


Figure 22: Interaction breakdown for sliced double differential plots for pre-FSI $\delta\alpha_T$ in $\cos(\theta_{\bar{p}_\mu})$.

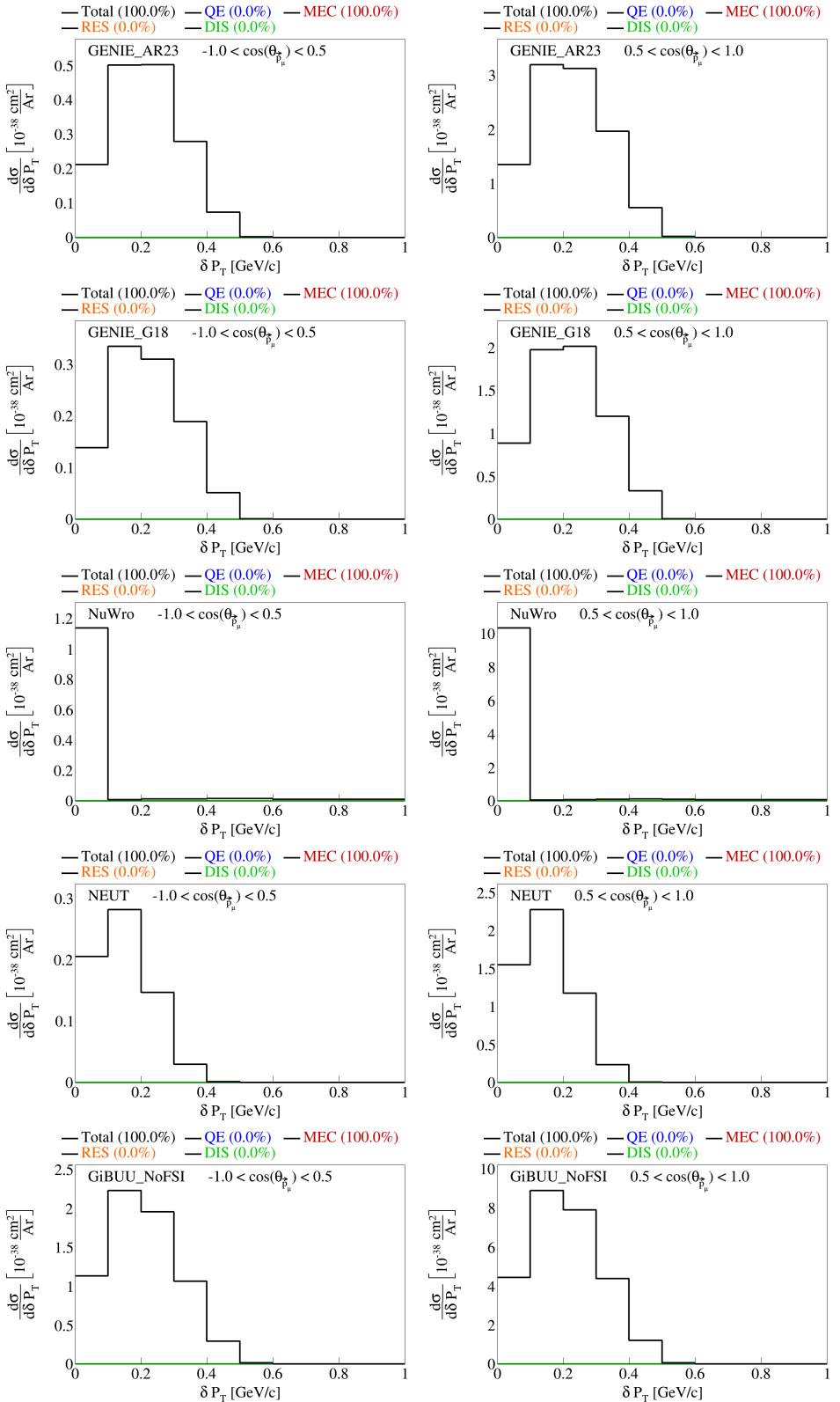


Figure 23: Interaction breakdown for sliced double differential plots for pre-FSI $|\delta\vec{P}_T|$ in $\cos(\theta_{\vec{p}_\mu})$.

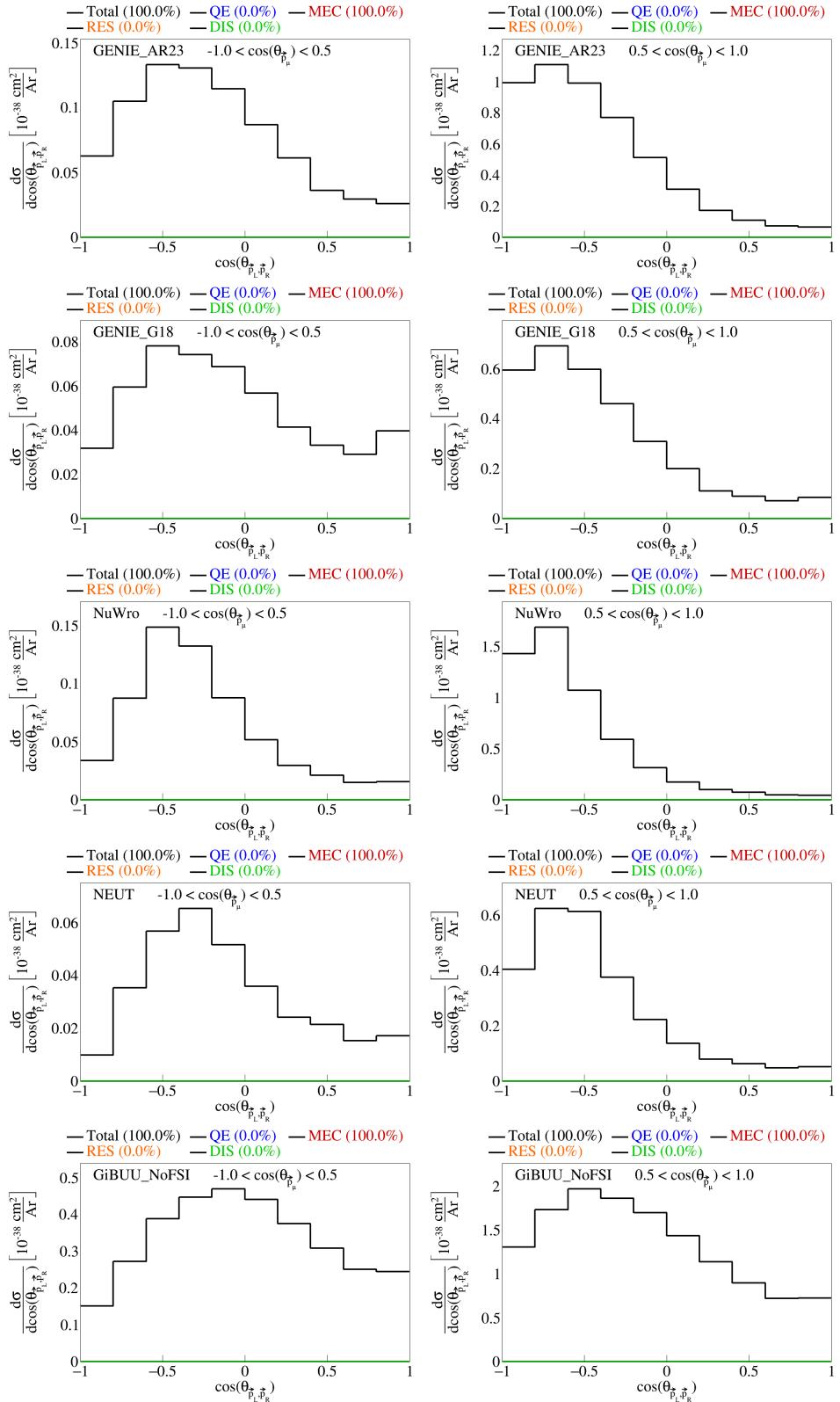


Figure 24: Interaction breakdown for sliced double differential plots for pre-FSI $\cos(\theta_{\vec{p}_L, \vec{p}_R})$ in $\cos(\theta_{\vec{p}_\mu})$.

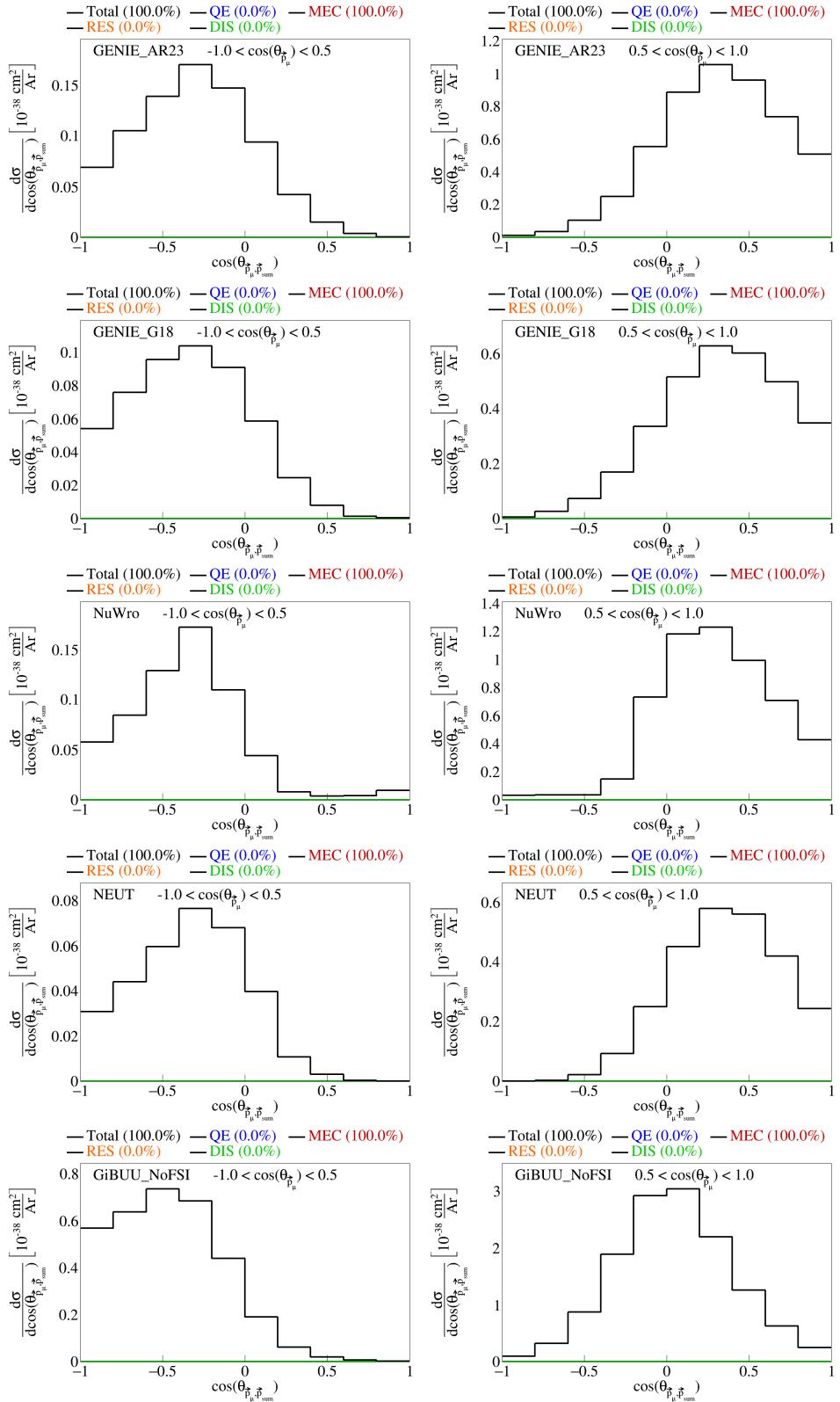


Figure 25: Interaction breakdown for sliced double differential plots for pre-FSI $\cos(\theta_{\vec{p}_\mu, \vec{p}_{\text{sum}}})$ in $\cos(\theta_{\vec{p}_\mu})$.

⁹¹ **2.6 Pure MEC events**

⁹² We also generated pure meson exchange current events using different configurations to get the MEC splines.
⁹³ These were all generated using different tunes of GENIE:AR23, G18 with Empirical MEC model, and G18
⁹⁴ with Nieves MEC model. The plots for the transverse kinematic variables are shown in Figures 26 and 27.
⁹⁵ The sliced double differential plots are shown in Figure 28.

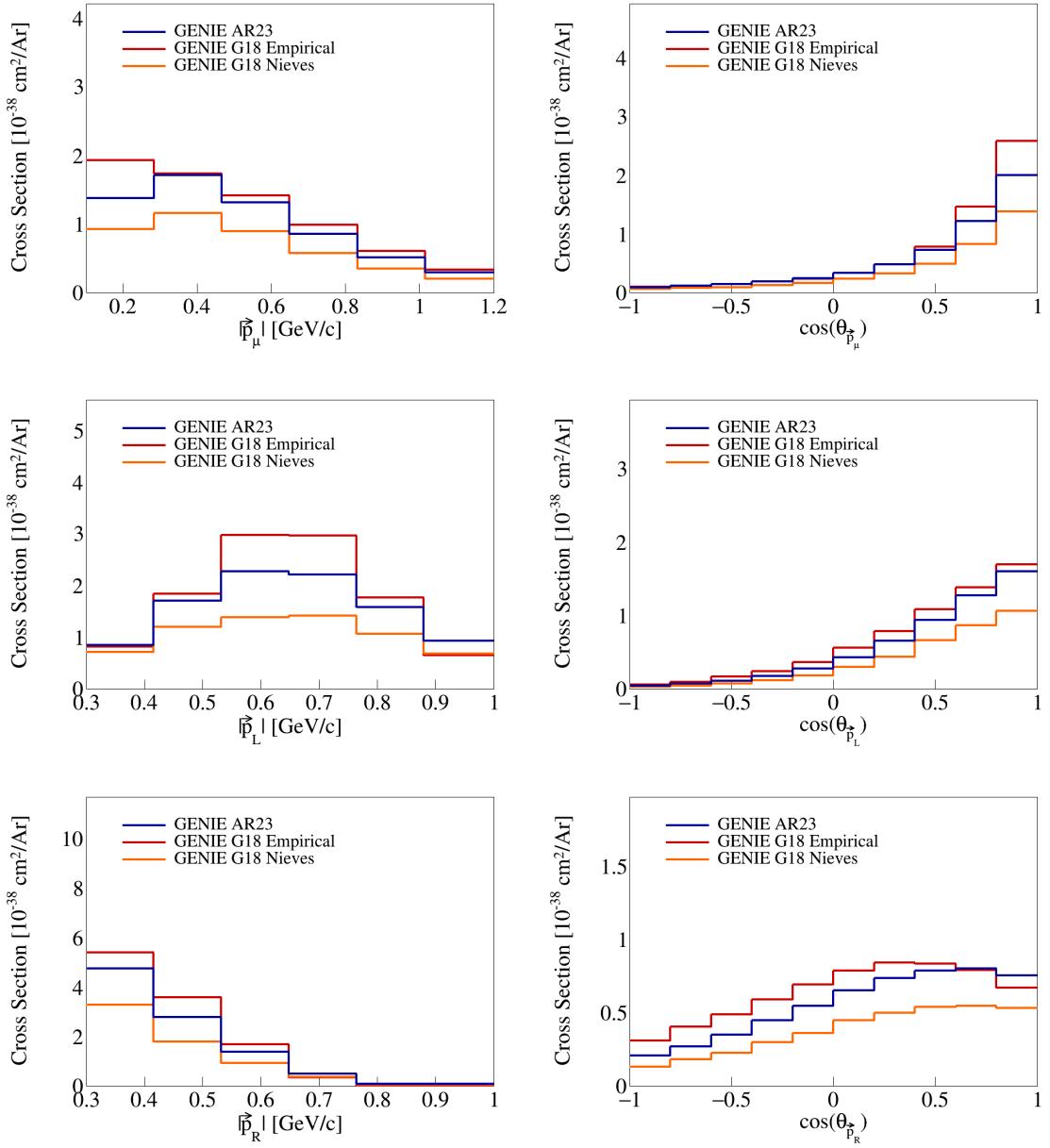


Figure 26: Momenta and opening angles of single particles for pure MEC events.

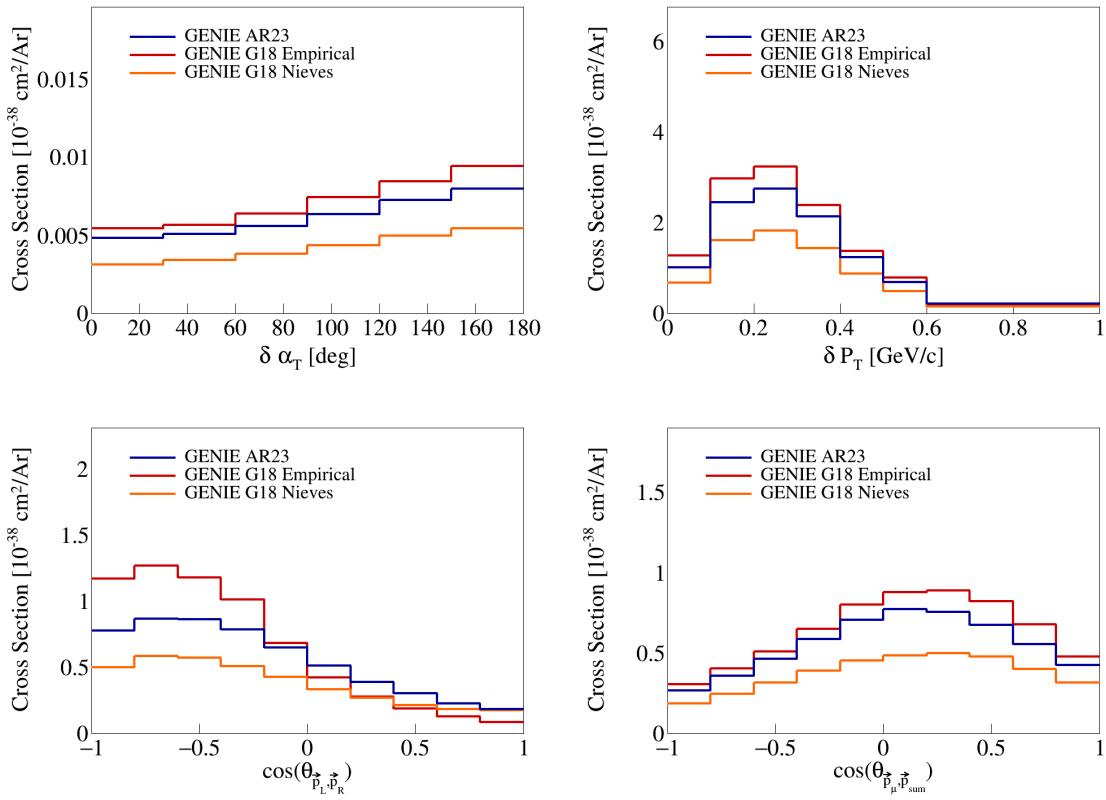


Figure 27: Transverse momentum and opening angles for pure MEC events.

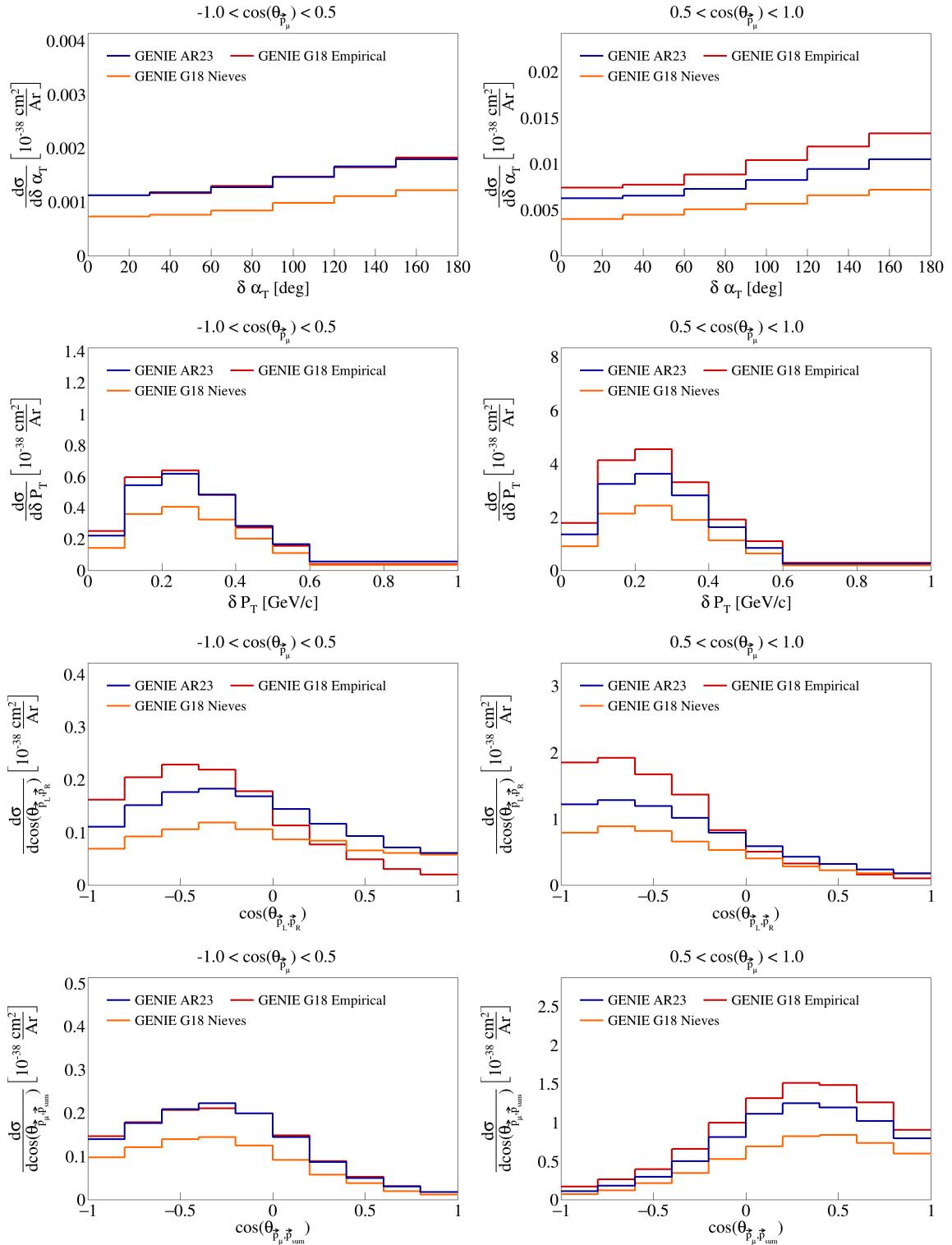


Figure 28: Sliced double differential plots for pure MEC events.

96 **3 SBND analysis**

97 The CAF files used for this analysis are available in the Fermilab gpvms at the path

98 `/pnfs/sbnd/persistent/users/twester/sbnd/v09_78_04/cv/*.flat.caf.root`

99 where the asterisk means that all the files in the directory with the extension `.flat.caf.root` will be used.

100 **3.1 Fiducial volume**

101 To perform the analysis of SBND data, we have to define the fiducial volume of the detector, which represents
102 a central part of the detector in which we will accept signals, as:

$$5 < |x| < 180 \quad |y| < 180 \quad 10 < z < 450 \quad (6)$$

103 where x , y , and z are the coordinates in the detector frame, all in centimeters.

104 **3.2 Signal definition**

105 To perform the analysis, we will be using the CAFAna framework. This allows us to perform cuts based
106 on the reconstructed and Monte Carlo data to discriminate events. To discriminate events based on their
107 Monte Carlo data and define our true signal, we perform a simple `TruthCut` that checks the following:

- 108 (i) That the neutrino interaction takes place in the fiducial volume.
- 109 (ii) That the neutrino is a muon neutrino.
- 110 (iii) That the interaction is a charged current interaction.
- 111 (iv) That there is only one muon in our allowed momentum range.
- 112 (v) That there are only two protons in our allowed momentum range.
- 113 (vi) That there are no charged/neutral pions in our defined momenta ranges.

114 Using the reconstructed event data, the cut we have to use is not a simple as in the Monte Carlo data
115 case. We now have to use a `Cut` that looks at different variables of the reconstructed event to determine if
116 it is a signal event. We perform the following cuts to define our reconstructed signal:

- 117 (i) Cosmic: that the event is not a cosmic event by Pandora's criteria, i.e., requiring `nu_score > 0.4` to
118 check how neutrino-like the event is, and `fmatch.score < 7` with $0 < fmatch.time < 1.8$ to check the
119 event comes from the beam.
- 120 (ii) Vertex in FV: that the reconstructed vertex for the neutrino interaction takes place in the fiducial
121 volume defined above.
- 122 (iii) One muon: that there is one muon track with $L_{\text{track}} > 50$ cm, starting point in the fiducial volume,
123 $\chi^2_\mu < 30$, $\chi^2_p > 60$, with momentum in our allowed range; if there are multiple candidate tracks, the
124 one with the longest track length is chosen.
- 125 (iv) Two protons: that there are two proton tracks with $\chi^2_p < 100$, full track in the fiducial volume, and
126 that these have momentum in our allowed range.
- 127 (v) No charged pions: that there are no other reconstructed tracks with momentum in the allowed range
128 for charged pions inside the fiducial volume.
- 129 (vi) No neutral pions: that there are no reconstructed particles with a positive `trackScore` less than 0.5
130 indicating a shower, so we do not allow any neutral pions.

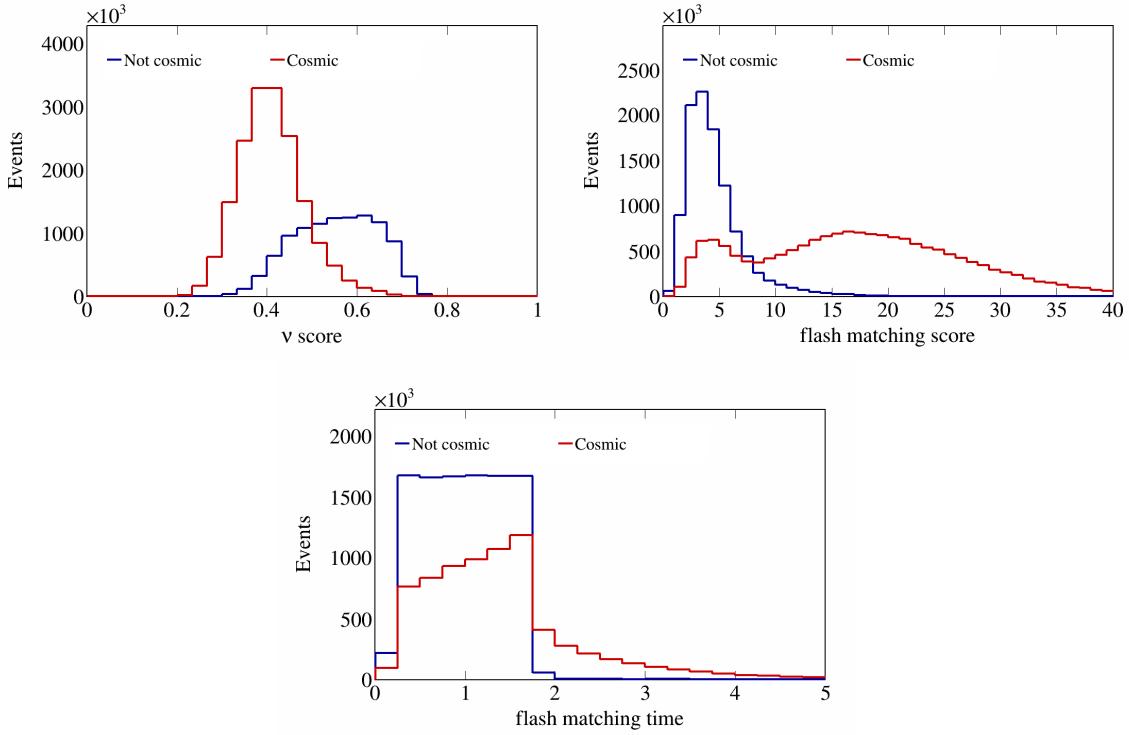


Figure 29: Cosmic cut variables before rejecting cosmic events.

Using these two cuts, we can perform a study of Monte Carlo data. Given the events that pass the reconstructes signal definition, we can look at the background and true signal events. In later sections, we also look at interaction type and topology breakdowns to get a better sense of the composition of our reconstructed signal. To get a better sense of what values the variables chosen to do the cuts take on for each true particle, we plot the flash matching score, time, and ν score in Figures 29, and the χ^2 values for muons and protons in Figure 30.

We use a one-bin histogram to get total counts of generated events, true signal events, all reconstructed events, and efficiency and purity data after each of the cuts described above is applied to the reconstructed events. These results are shown in Table 2. Counts are obtained using ROOT's command `Histo->Integral()` on the histograms generated. Global efficiency is defined as the ratio between events that pass the cut and reconstructed events, signal efficiency as the ratio between true events that pass the cut and all true signal events, and purity as the ratio between true signal events that pass the cut and all events that pass the cut. The numbers reported in this table are POT normalized to 6.79×10^{20} .

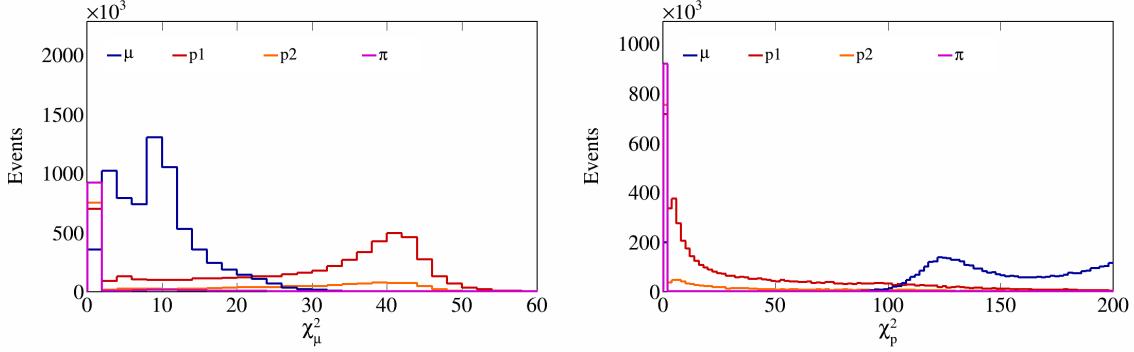


Figure 30: Muon and proton χ^2 values for all particles.

Cut	Number of events	Global efficiency	Signal efficiency	Purity
All	$1.3938 \cdot 10^7$	-	-	-
True signal events	272161	-	-	-
All reco events	$6.82359 \cdot 10^6$	100%	-	-
Cosmic cut	$5.88624 \cdot 10^6$	86.2632%	89.6205%	4.14377%
Vertex in FV cut	$3.29309 \cdot 10^6$	48.2603%	88.2885%	7.29671%
One muon cut	$2.23536 \cdot 10^6$	32.7593%	70.5202%	8.58603%
Two protons cut	146922	2.15315%	17.517%	32.4488%
No charged pions cut	67852.2	0.994377%	12.6665%	50.8065%
No neutral pions cut	54719.5	0.801917%	11.3094%	56.25%

Table 2: Global efficiency, selection efficiency, and purity for cuts made in signal definition.

¹⁴⁴ 3.3 Purity and efficiency studies

¹⁴⁵ Before performing the cross-section extraction, we performed a study of the purity and efficiency of the
¹⁴⁶ slice in the forward direction of the double differential variables. This way, we could ensure that we have
¹⁴⁷ the maximal possible signal contribution, while getting rid of most background events. This is achieved by
¹⁴⁸ maximizing the product of the efficiency and purity. The purity is defined as

$$\text{Purity} = \frac{\text{MC}_{\text{Reco}}^{CC1p0\pi}}{\text{MC}_{\text{Reco}}} \quad (7)$$

¹⁴⁹ and the efficiency is

$$\text{Efficiency} = \frac{\text{MC}_{\text{Reco}}^{CC1p0\pi}}{\text{MC}_{\text{True}}^{CC1p0\pi}} \quad (8)$$

¹⁵⁰ The efficiency, purity, and their product for each cut position in increments of 0.05 are shown in Figure 31.
¹⁵¹ Since we see no major improvement when moving away from 0.5, we maintain the cut at this position. We
¹⁵² do not move the cut to the apparent peak around 0.9 as this would increase the statistical uncertainties in
¹⁵³ the forward slice due to the low number of events that would remain there.

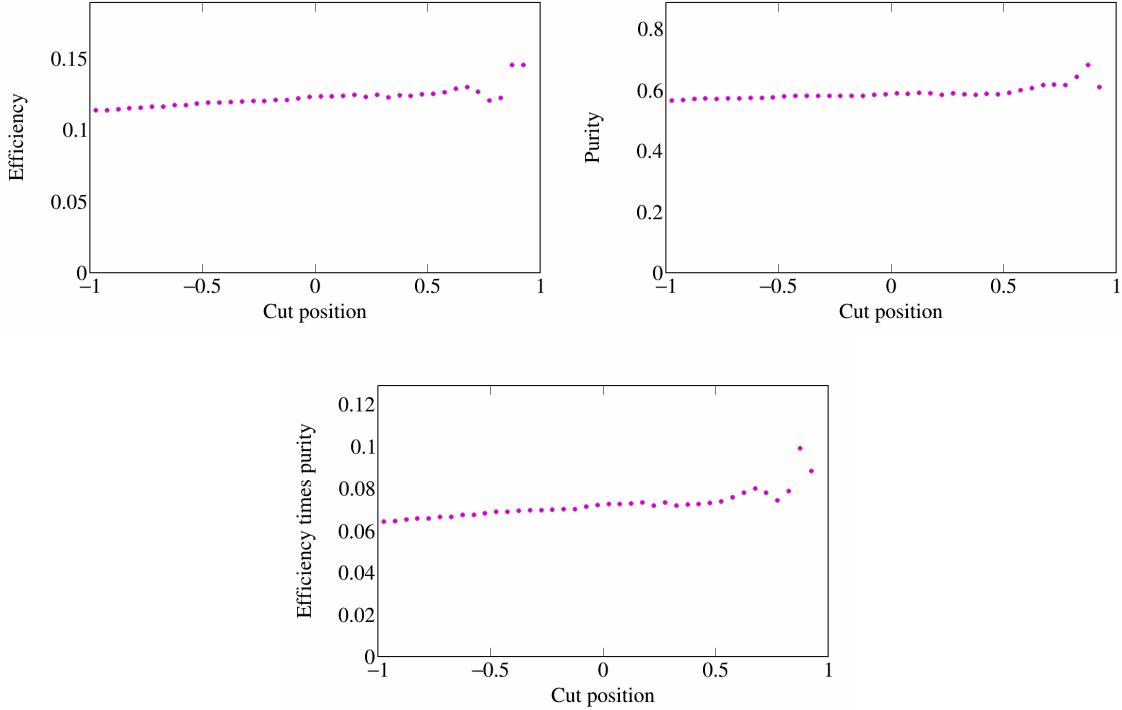


Figure 31: Efficiency and purity of the forward slice at different cut positions for double-differential variables.

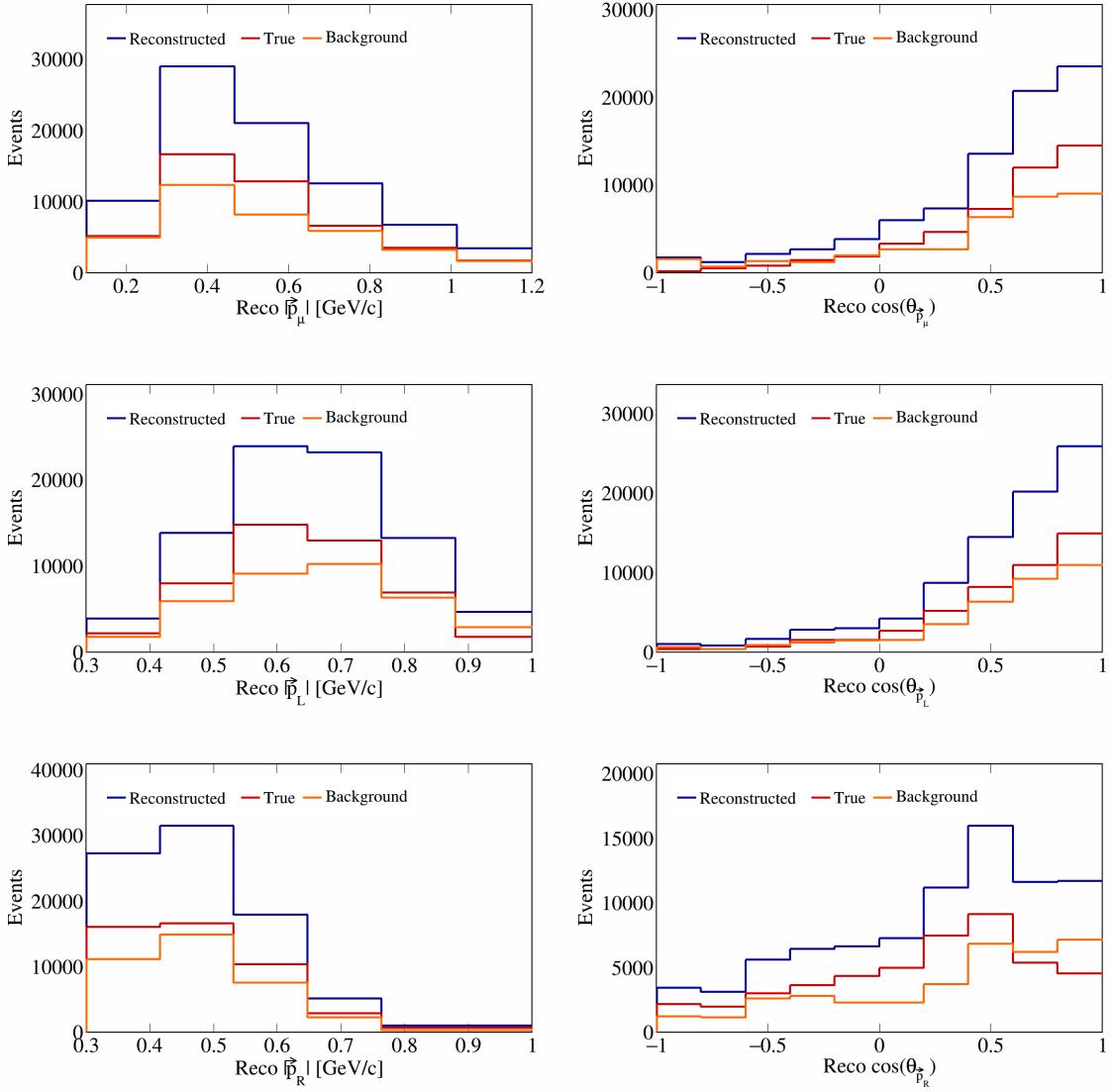


Figure 32: Momenta and opening angles for individual particles for SBND data.

154 3.4 Variable plots

155 Using all the variable definitions as we did when studying the event generators, and the signal definition
 156 based on the cuts described in the previous section, we can generate plots for SBND data. The reconstructed
 157 single differential variables corresponding to vector opening angles and magnitudes are shown in Figure 32.
 158 In these figures, three lines are shown, corresponding to: all reconstructed (all the reconstructed events that
 159 pass our signal definition), signal (reconstructed events that pass signal definition and are true signal events
 160 as determined by the TruthCut from our previous section), and background (reconstructed events that pass
 161 signal definition but are not true signal events) events. Similarly, the variables relating multiple vectors are
 162 shown in Figure 33, and double differential sliced variables are shown in Figure 34.

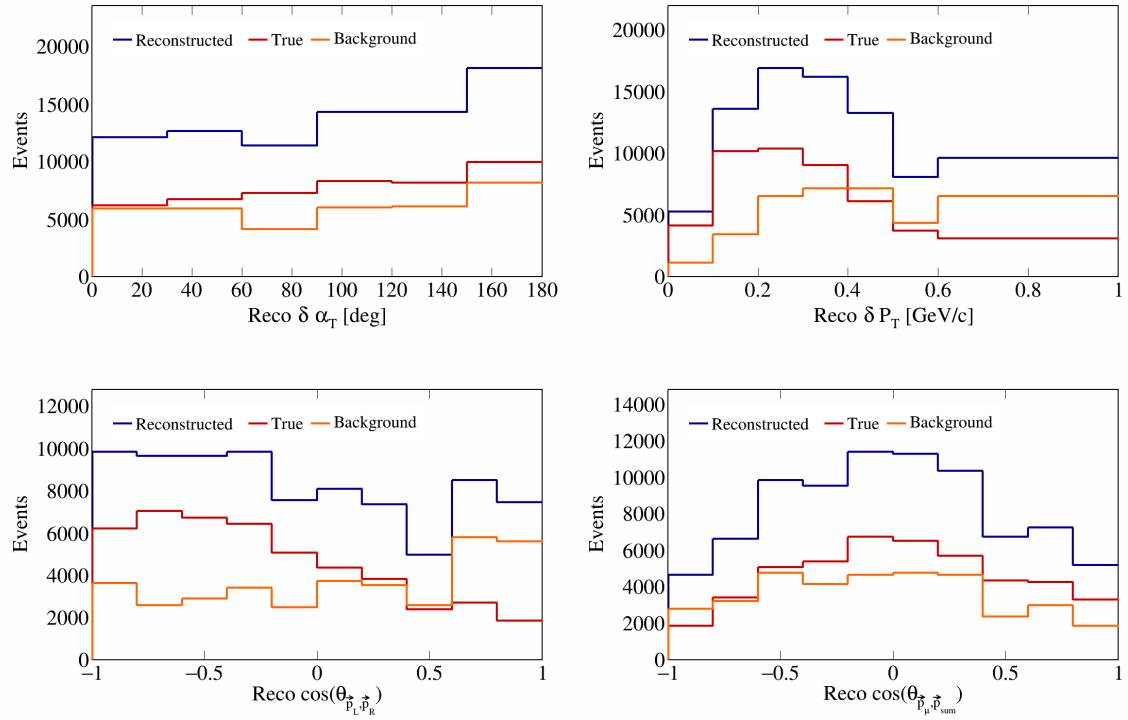


Figure 33: Transverse momentum and opening angles for SBND data.

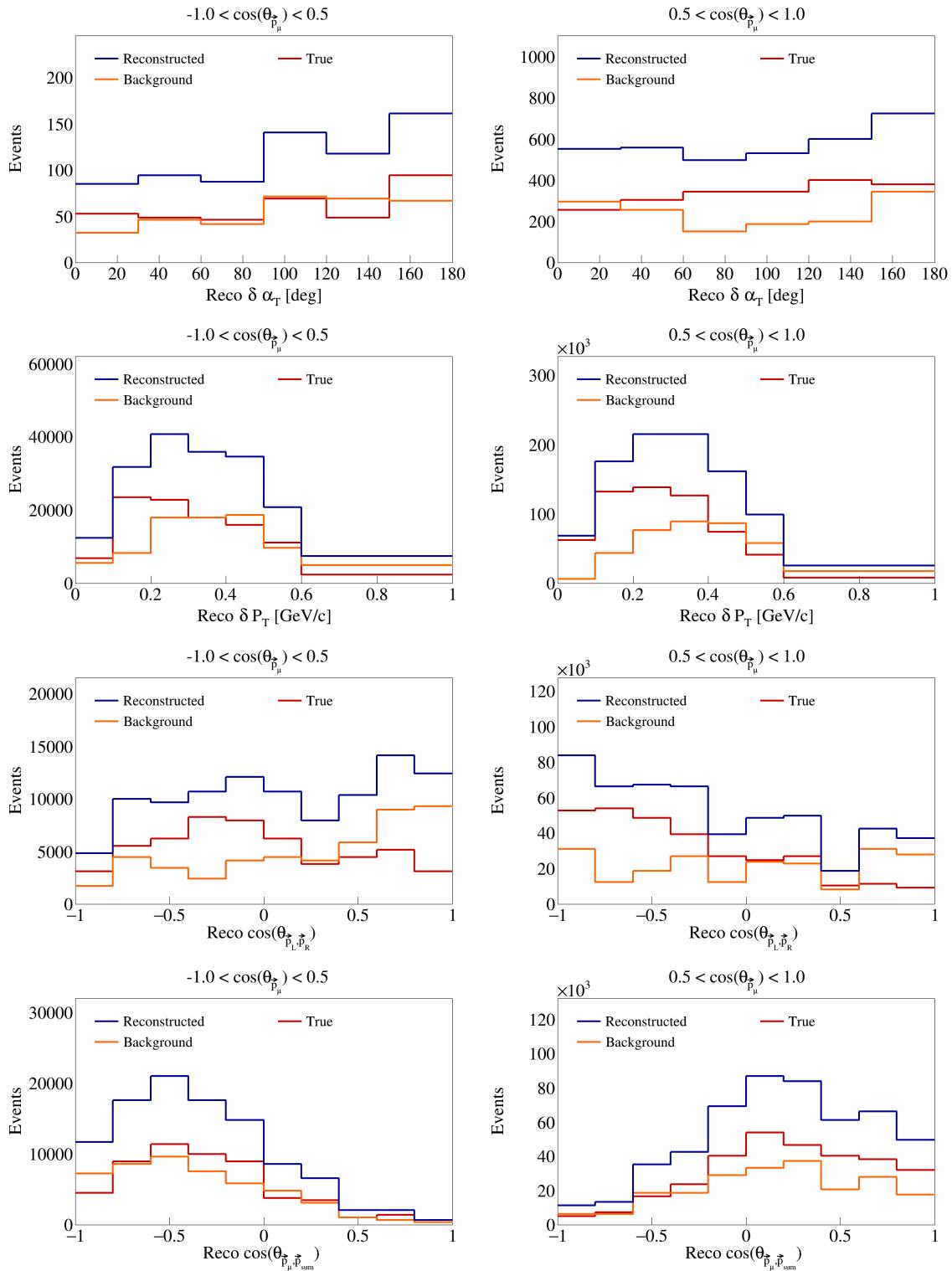


Figure 34: Sliced double differential plots for SBND events.

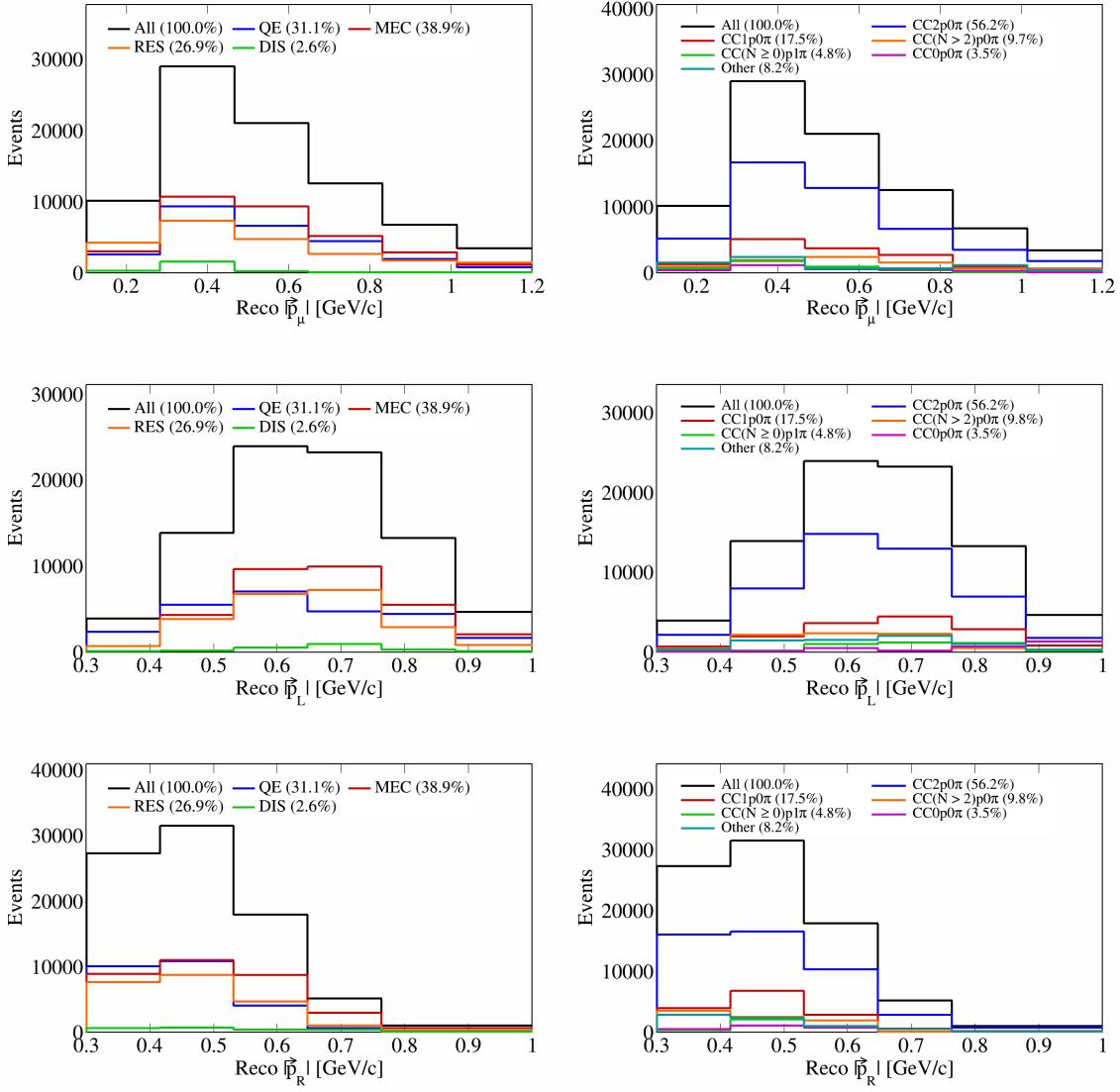


Figure 35: Interaction and topology breakdown for momenta of individual particles.

163 3.5 Interaction and topology breakdown

164 We perform an interaction and topology breakdown for the SBND data. For these breakdowns, we look at
 165 the reconstructed events that pass our signal definitions cuts and see what percentage of these are generated
 166 from different interaction modes and topologies. This helps us get a better idea of what our background
 167 signal is composed of. For the interaction breakdown, we look at quasielastic (QE), MEC (meson-exchange
 168 current), RES (resonance), and DIS (deep inelastic scattering) events. For the topology breakdown, we look
 169 at the number of protons, pions, and muons in the final state. The topologies we label are CC2p0 π (our
 170 signal definition), CC1p0 π , CC(N > 2)p0 π , CC(N ≥ 0)p1 π , and CC0p0 π . Any other event topology is
 171 labeled as “Other”. These breakdowns are shown in Figures 35 to 39.

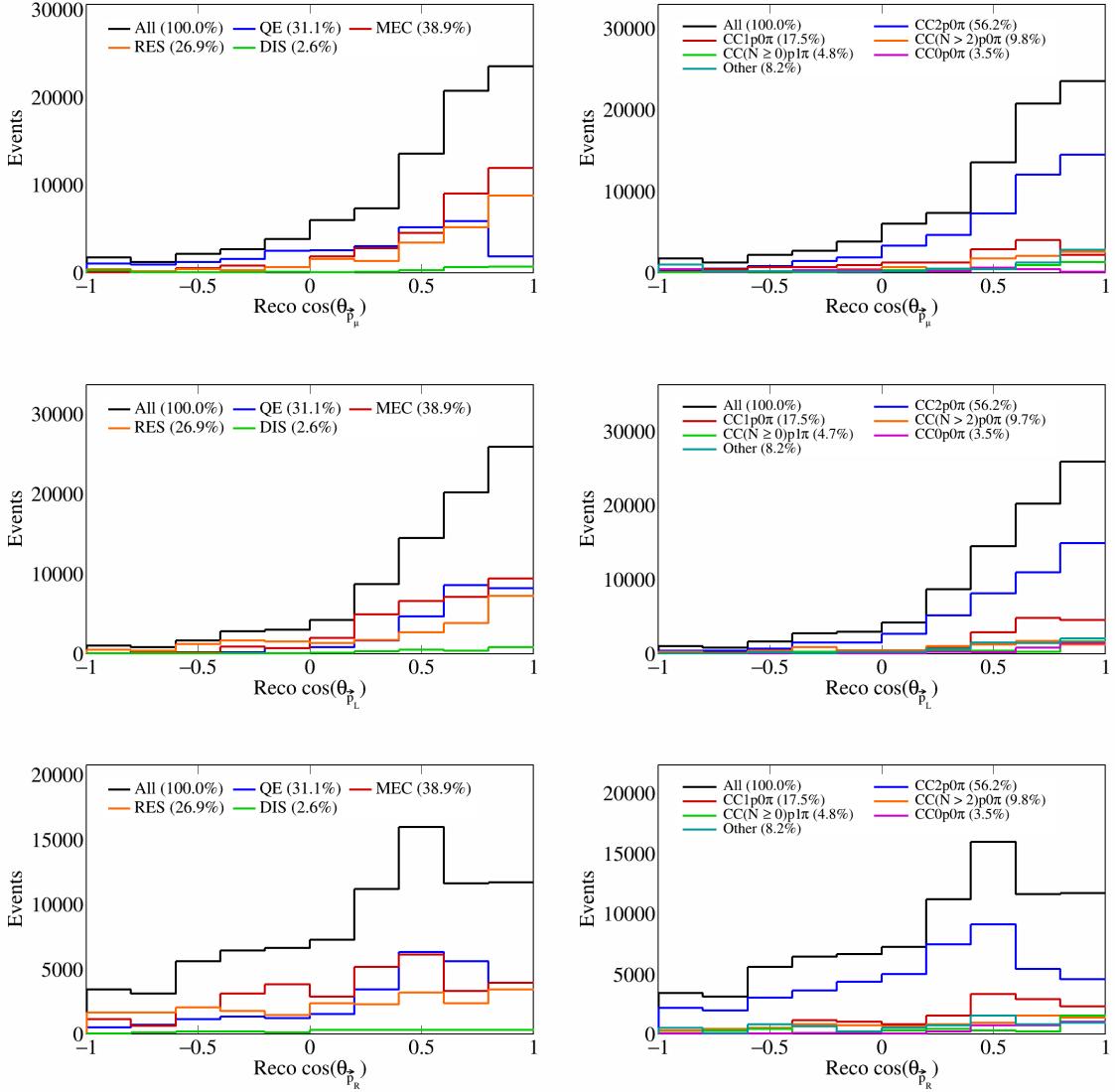


Figure 36: Interaction and topology breakdown for opening angles of individual particles.

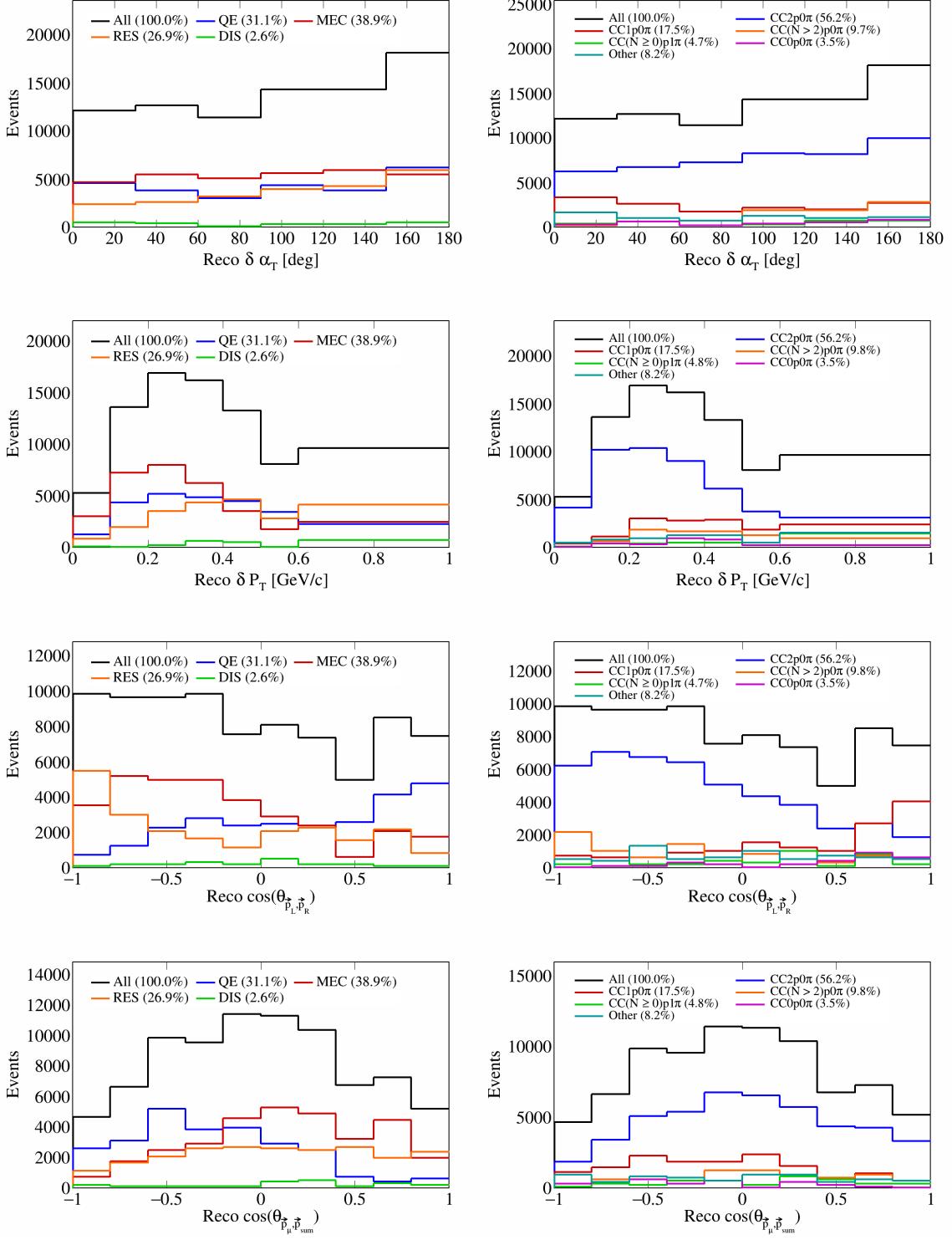


Figure 37: Interaction and topology breakdown for opening angles and transverse variables.

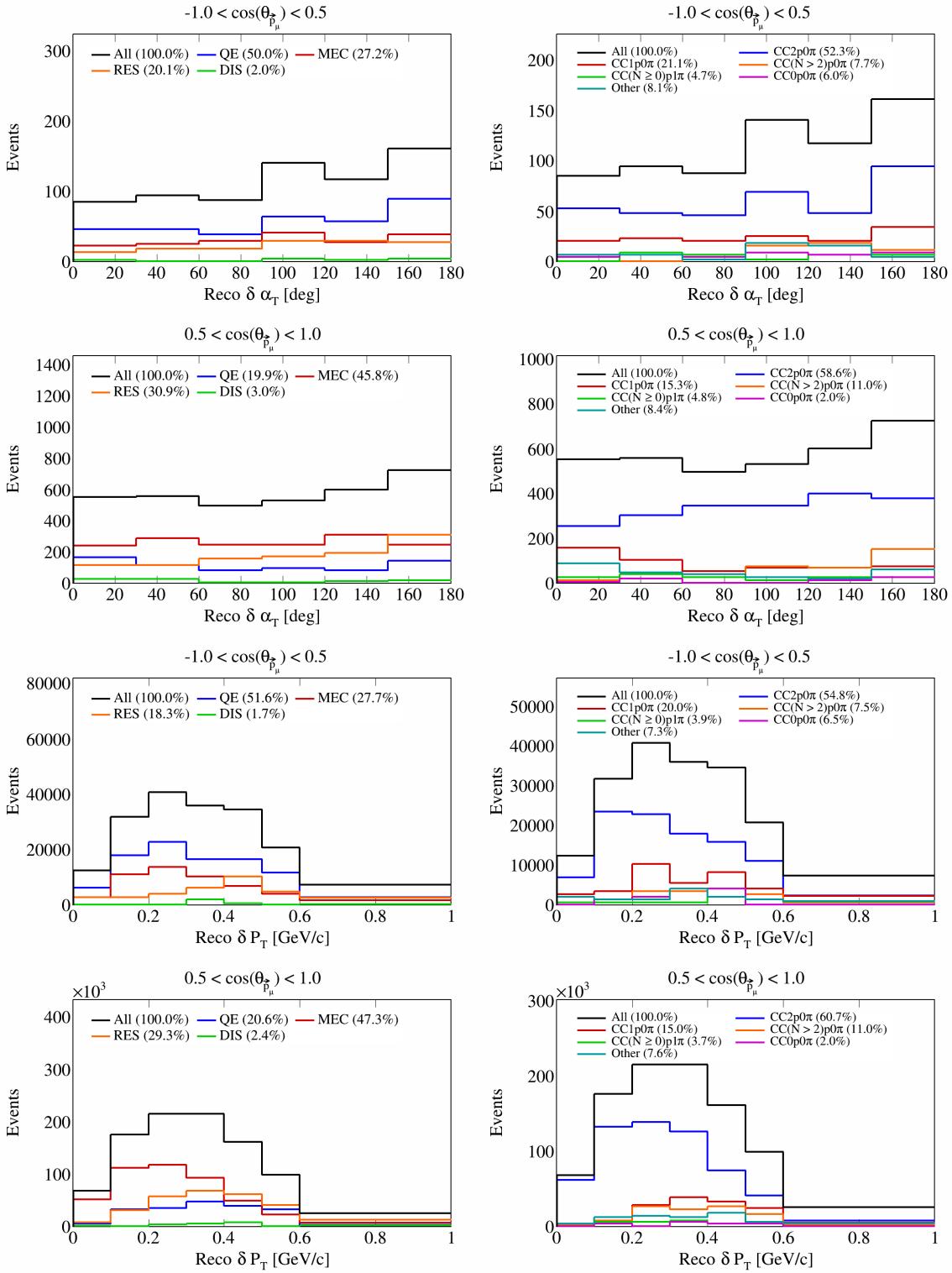


Figure 38: Interaction and topology breakdown for double differential transverse variables.

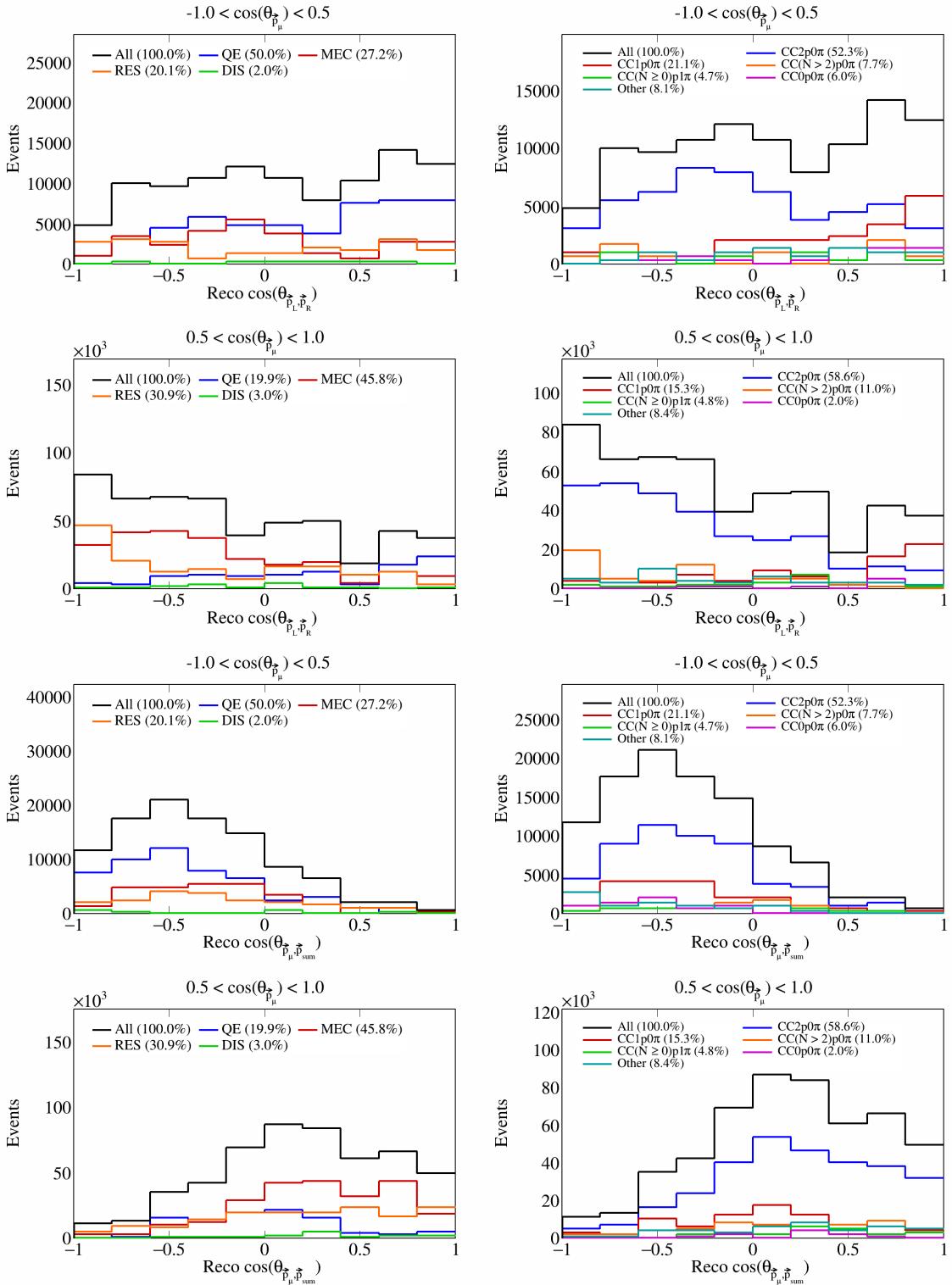


Figure 39: Interaction and topology breakdown for double differential opening angles.

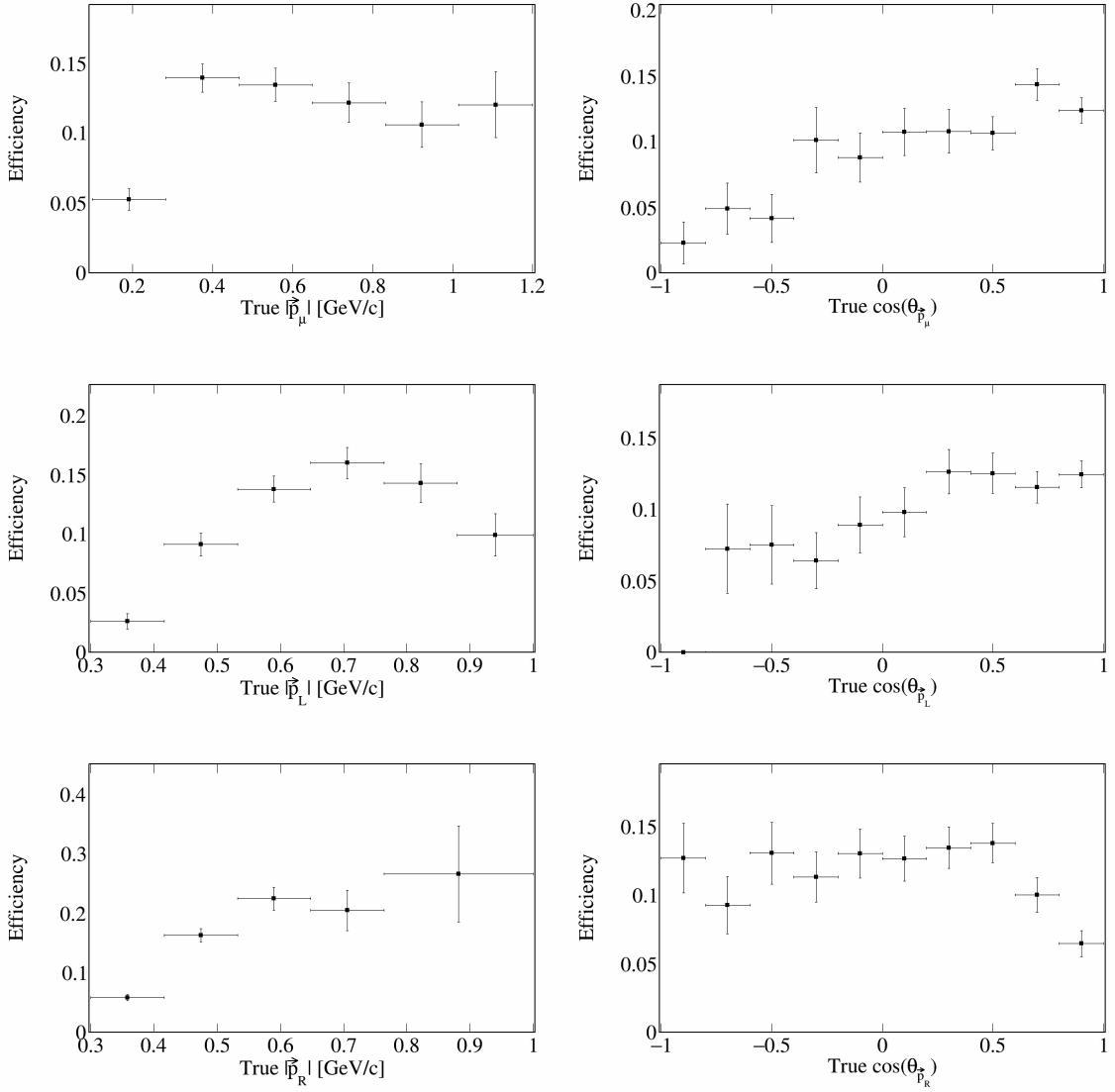


Figure 40: Signal efficiency plots for single differential vector directions and magnitudes.

172 3.6 Signal efficiency

173 Using the truth information about reconstructed events, we can also compute signal efficiency on a bin-by-
 174 bin basis. To be precise, signal definition on a bin i is defined as the ratio between the number of events
 175 generated in bin i and reconstructed in any bin over the number of events generated in bin i . These plots
 176 are shown in Figure 40 and Figure 41 for single-differential variables and Figure 42 for double differential
 177 variables.

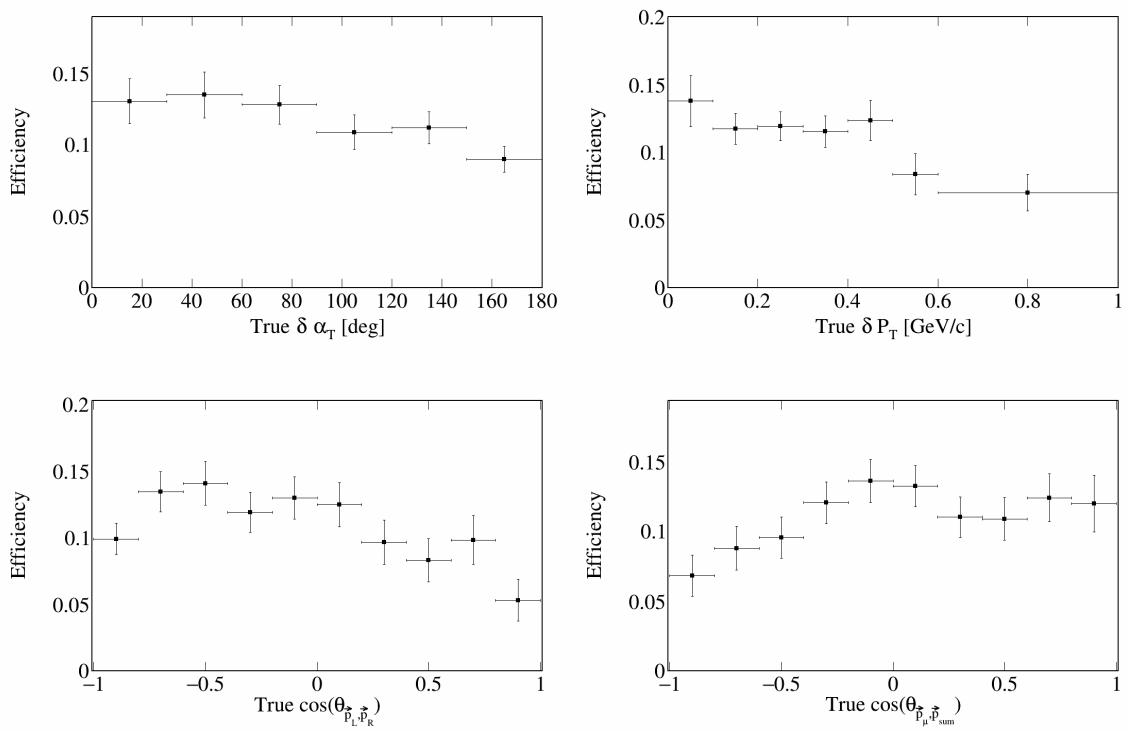


Figure 41: Signal efficiency plots for single differential vector opening angles and transverse momentum.

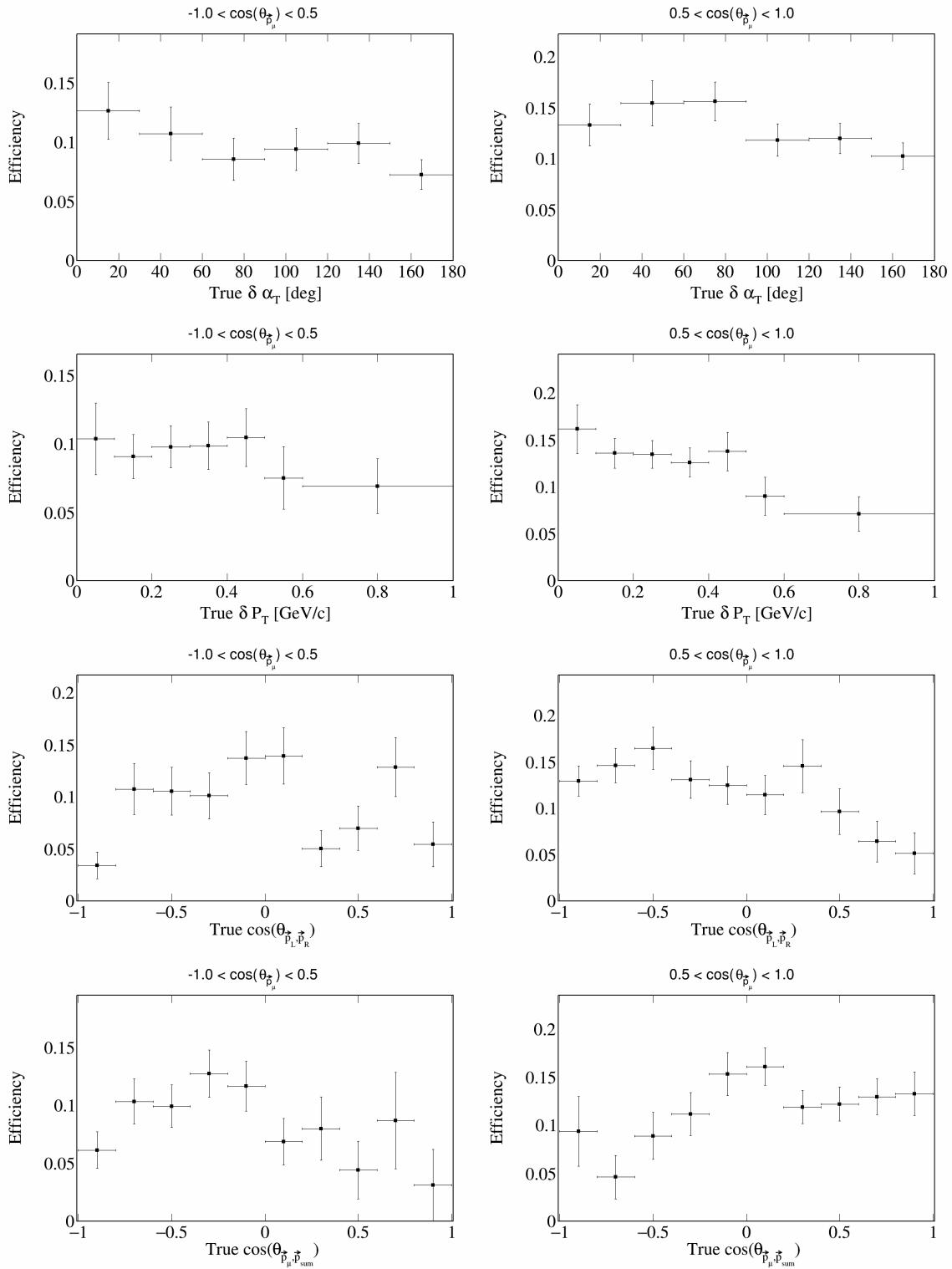


Figure 42: Signal efficiency plots for double differential variables.

¹⁷⁸ **3.7 Migration and response matrices**

¹⁷⁹ Further, we compute migration matrices which give us a measure of how reliable our reconstructed variables
¹⁸⁰ are. A given column in this matrix represents a bin of the truth variable, i.e., the value with which the
¹⁸¹ event was generated. Then, each row corresponds to a reconstructed bin of the same variable, and each cell
¹⁸² corresponds to the probability that an event generated with the truth value corresponding to the column gets
¹⁸³ reconstructed with the value corresponding to the row. For the migration matrix, we consider true signal
¹⁸⁴ events that were reconstructed and satisfy our signal definition in the denominator. Therefore, the values in
¹⁸⁵ each column must add up to 1. The migration matrices for the single differential variables are presented in
¹⁸⁶ Figure 43 and Figure 44. The migration matrices for the double differential variables (given in terms of the
¹⁸⁷ bin number) are presented in Figure 45.

¹⁸⁸ Response matrices are computed in a similar manner, but using the total number of generated events in the
¹⁸⁹ denominator when computing the ratios, i.e., without requiring the events to be successfully reconstructed.
¹⁹⁰ Therefore, for these matrices, the columns of the response matrices do not have to add up to 1. The response
¹⁹¹ matrices for single differential variables are presented in Figure 46 and Figure 47, and the double differential
¹⁹² response matrices are given in Figure 48. A mathematical definition of the response matrix is given in
¹⁹³ Equation (12).

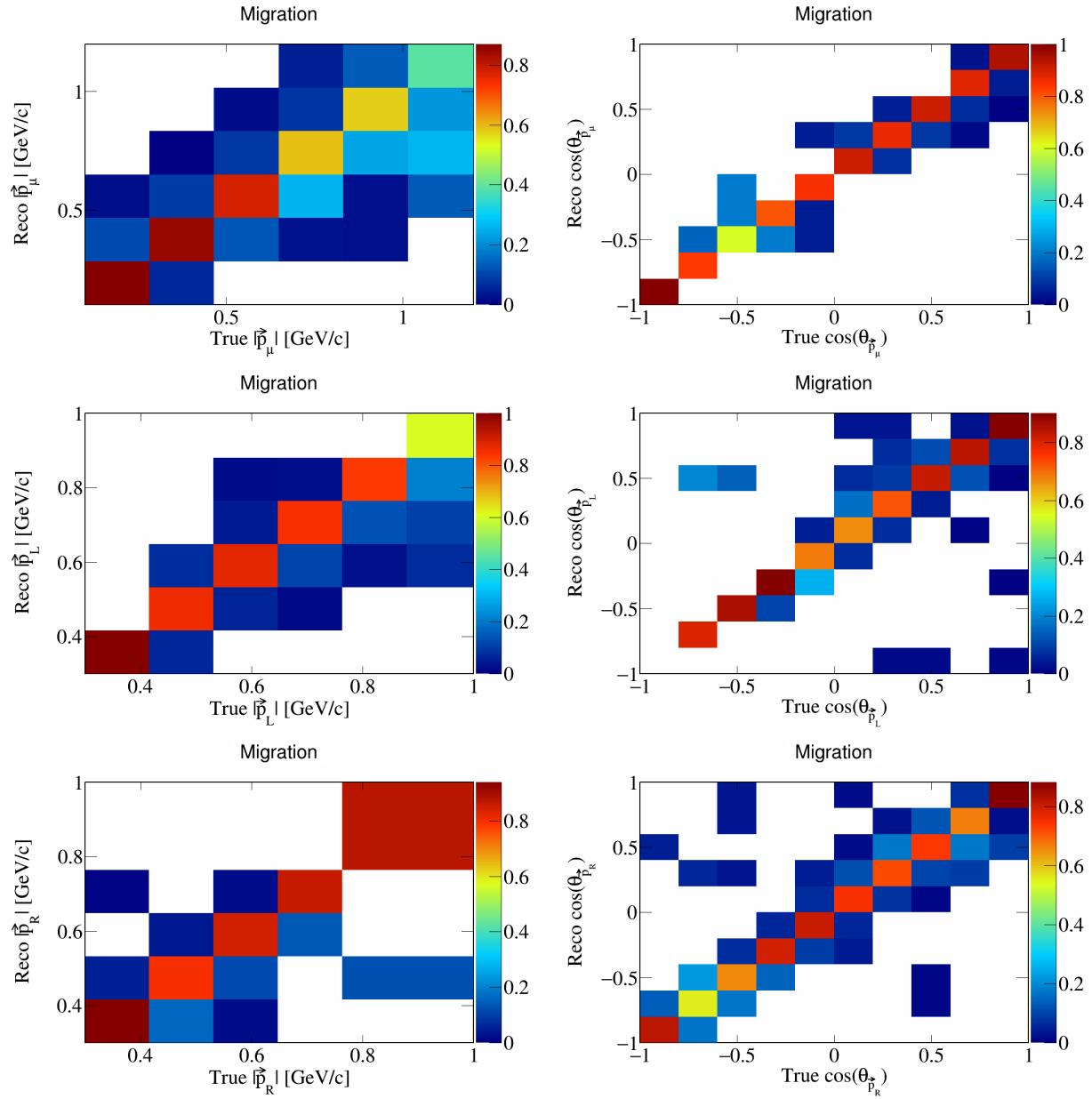


Figure 43: Migration matrices for single differential momenta and opening angles of individual particles.

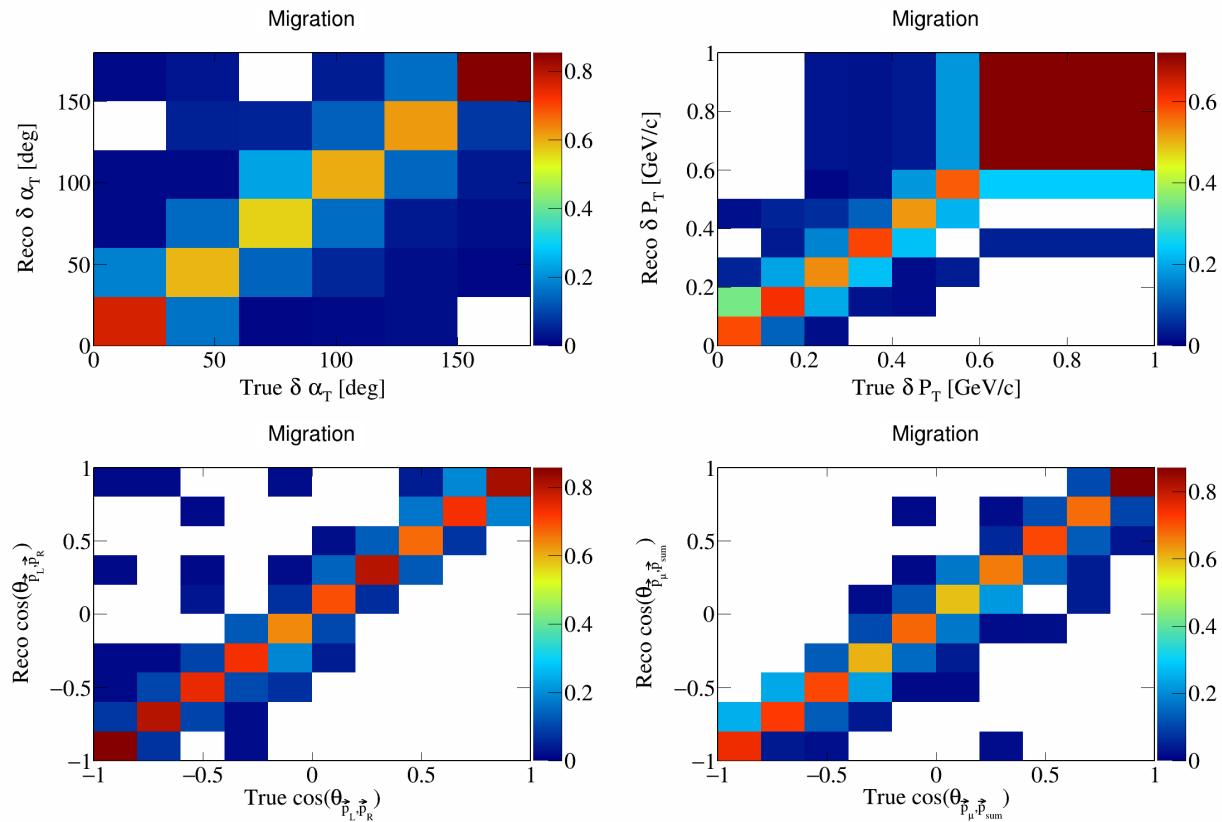


Figure 44: Migration matrices for single differential transverse momentum and opening angles.

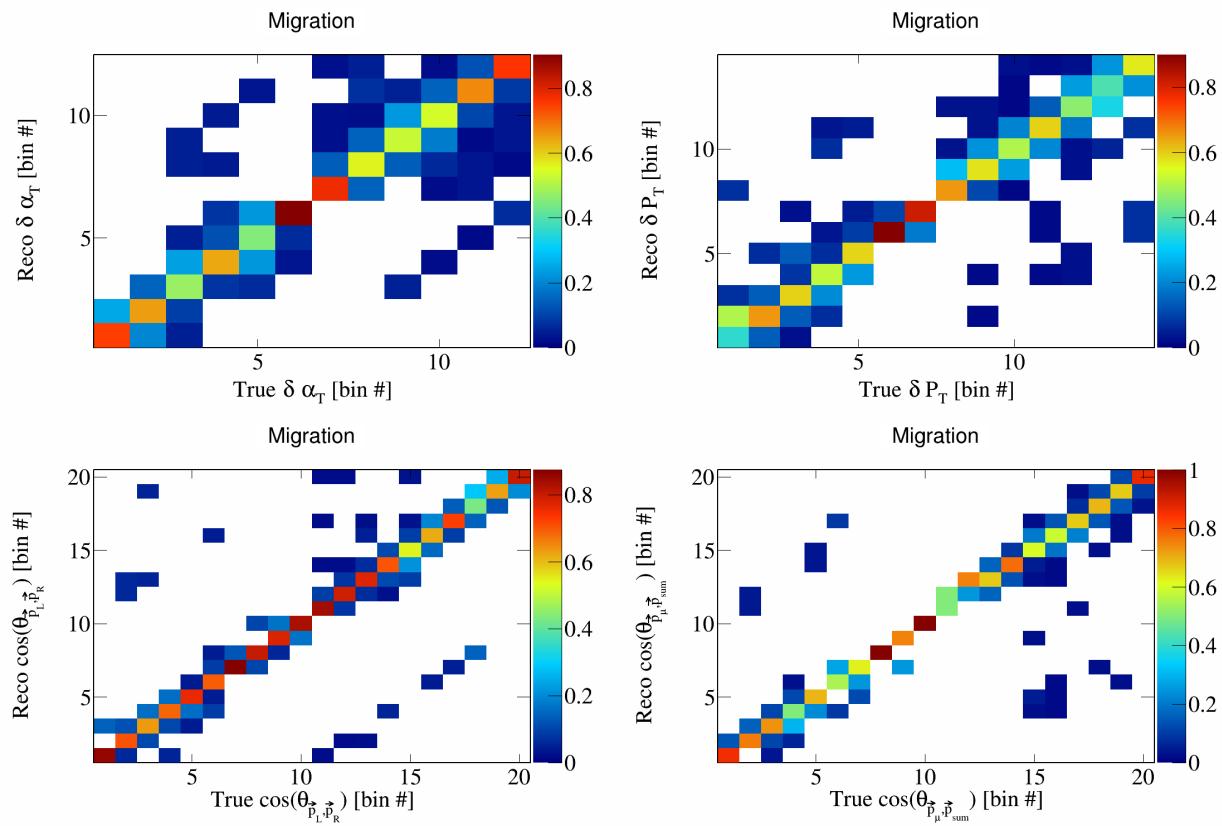


Figure 45: Migration matrices for double differential variables.

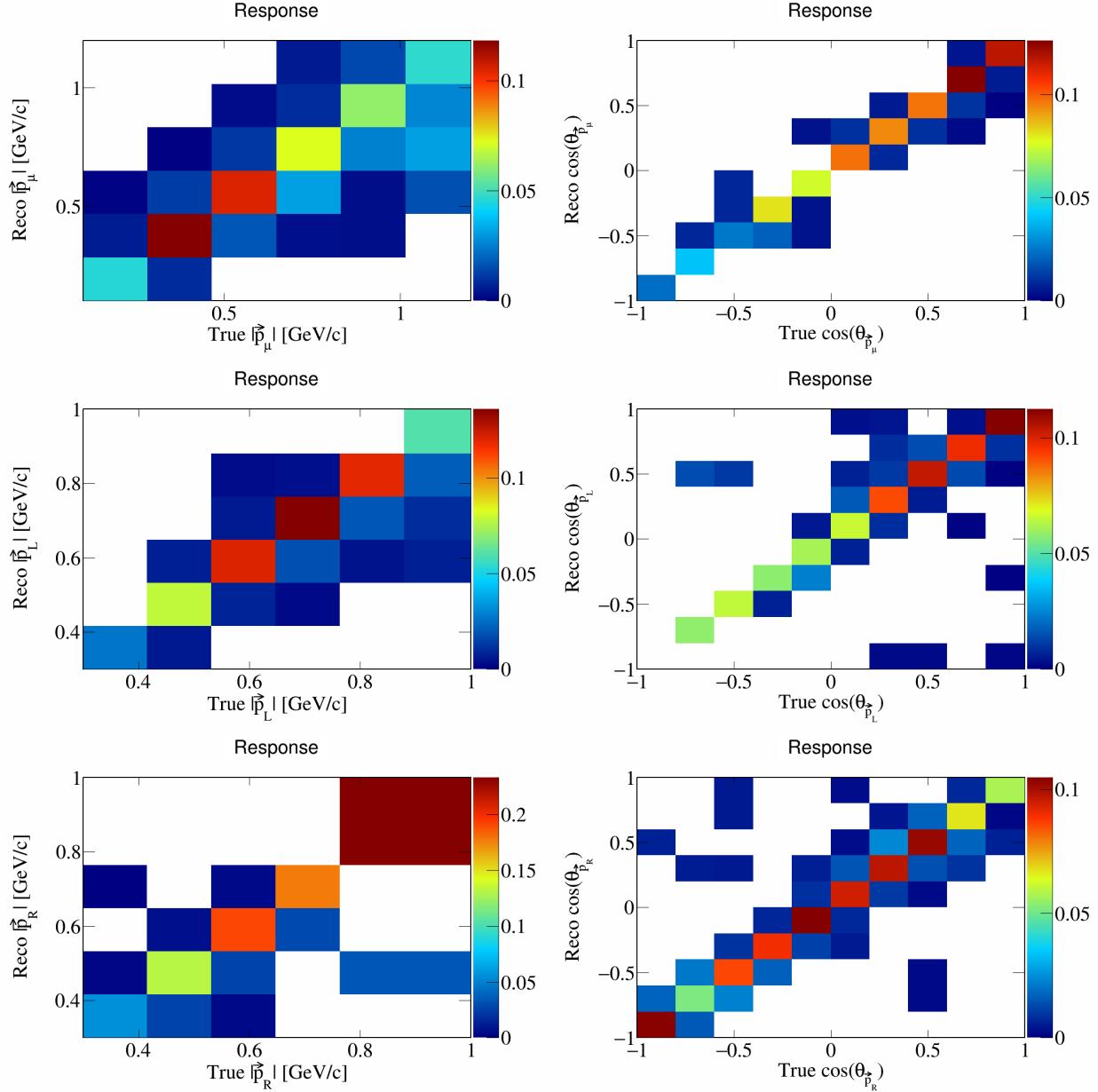


Figure 46: Response matrices for single differential momenta and opening angles of individual particles.

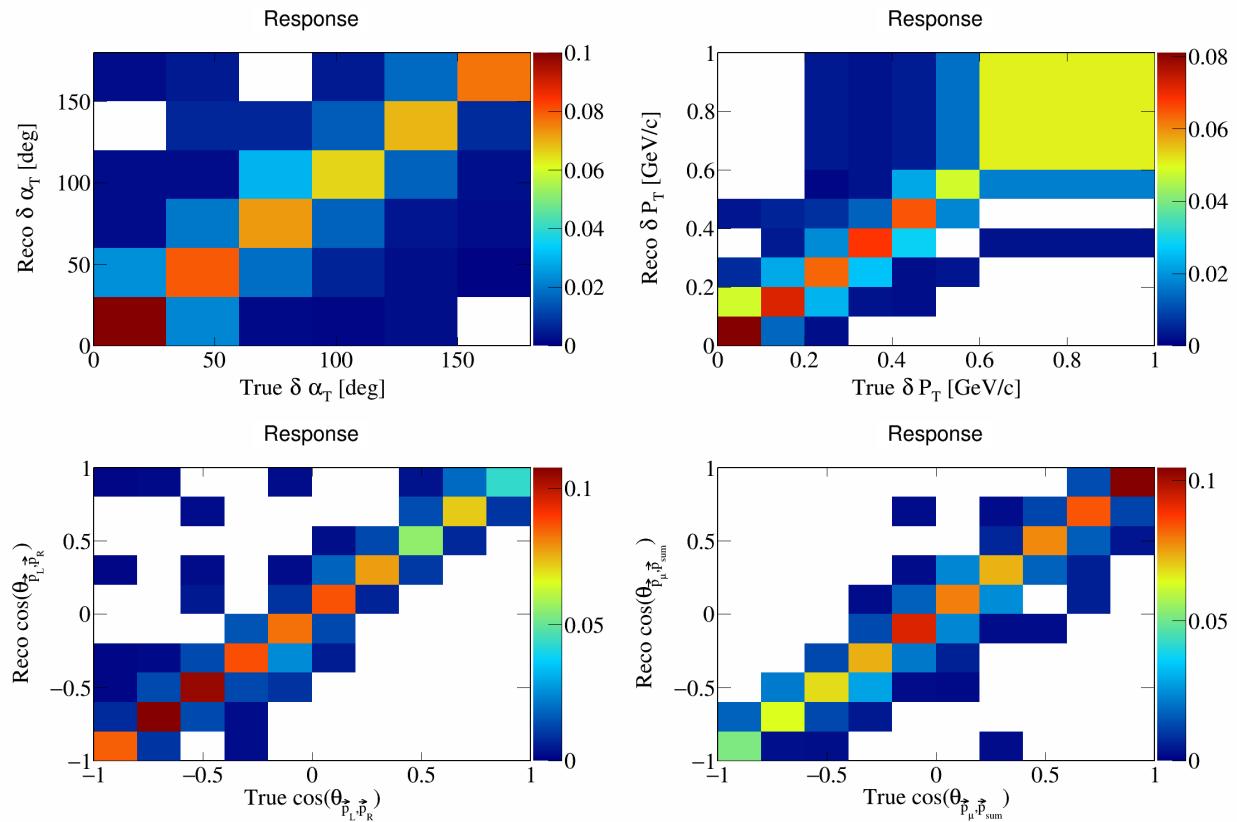


Figure 47: Response matrices for single differential transverse momentum and opening angles.

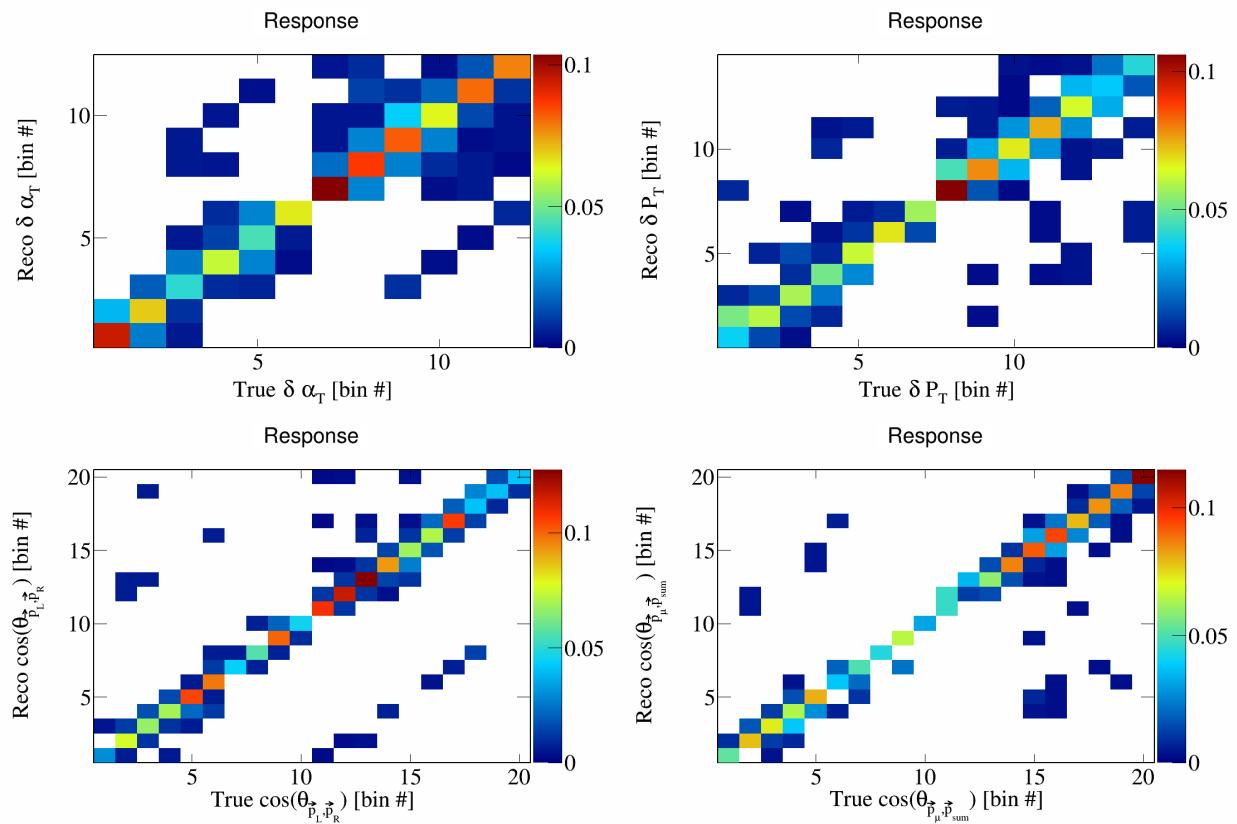


Figure 48: Response matrices for double differential variables.

194 **3.8 Systematics**

195 To include systematic uncertainties in our study, we first consider cross sectional systematics. These are
 196 variations in the cross section models used to generate the events. They can be of two types: multisigma and
 197 multisim. For the former, we consider a 1σ variation of the affected parameters, and in the latter we consider
 198 some number of universes, each with a random variation picked from a Gaussian distribution between 0σ
 199 and 1σ . These weights are already preloaded in the event data file, so we only have to load them into our
 200 script and use them to compute the relevant quantities. From these variations, we compute the covariance
 201 matrix as

$$E_{i,j} = \frac{1}{N_{\text{Univ}}} \sum_{s=1}^{N_{\text{Univ}}} (\tilde{\sigma}_i^{\text{Var},s} - \tilde{\sigma}_i^{\text{CV}})(\tilde{\sigma}_j^{\text{Var},s} - \tilde{\sigma}_j^{\text{CV}}) \quad (9)$$

202 where $\tilde{\sigma}_i^{\text{Var},s}$ represents the variation flux-integrated event rate of the variable in the i -th bin in the s -th
 203 universe, and $\tilde{\sigma}_i^{\text{CV}}$ is the central value (without any variation) of the flux-integrated event rate in the i -th
 204 bin. More formally,

$$\tilde{\sigma}_i = \frac{N^{\text{reco } i}}{\Phi_{\nu}^{\text{CV}} \times N_{\text{targets}}}, \quad (10)$$

205 where $N^{\text{reco } i}$ is the number of reconstructed events in bin i , Φ_{ν}^{CV} is the central value of the neutrino flux
 206 (which remains the same for each variation), and N_{targets} is the number of target Argon nuclei. Further, we
 207 have that $N^{\text{reco } i} = M_{i,j} \times S^{\text{true } j} + B^{\text{reco } i}$, where $M_{i,j}$ is the response matrix corresponding to the true bin j
 208 and reco bin i , $S^{\text{true } j}$ is the number of true signal events in bin j , and $B^{\text{reco } i}$ is the number of reconstructed
 209 background events in bin i . Therefore, we have that

$$\tilde{\sigma}_i = \frac{M_{i,j}^{\text{univ}} \times S^{\text{true } j \text{ CV}} + B^{\text{reco } i \text{ univ}}}{\Phi_{\nu}^{\text{CV}} \times N_{\text{targets}}}, \quad (11)$$

210 where

$$M_{i,j}^{\text{univ}} = \frac{RS^{\text{true } j, \text{ reco } i \text{ univ}}}{S^{\text{true } j \text{ CV}}}, \quad (12)$$

211 with $RS^{\text{true } j, \text{ reco } i \text{ univ}}$ being the number of signal events generated in bin j and reconstructed in bin i , and
 212 $S^{\text{true } j}$ being the number of signal events generated in bin j . For each variation, terms labeled with univ
 213 are modified according to the variation, and terms labeled with CV remain the same. When considering the
 214 cross-section variations, the response matrix is modified via the normalization to the true signal in a given
 215 universe as

$$M_{i,j}^{\text{univ}} = \frac{RS^{\text{true } j, \text{ reco } i \text{ univ}}}{S^{\text{true } j \text{ univ}}}. \quad (13)$$

216 Then, the fractional covariance matrix is defined as

$$F_{i,j} = \frac{E_{i,j}}{\tilde{\sigma}_i^{\text{CV}} \tilde{\sigma}_j^{\text{CV}}}. \quad (14)$$

217 And the correlation matrix is defined as

$$\rho_{i,j} = \frac{E_{i,j}}{\sqrt{E_{i,i} E_{j,j}}}. \quad (15)$$

218 In the case of a multisigma systematic, $N_{\text{Univ}} = 1$, and for a multisim systematic, this number varies but is
 219 usually 100 or 1000.

220 The plots for all the individual cross sectional systematics are shown in Appendix 7.1. Flux systematics
 221 are computed in the same way, but each universe varies a flux parameter. The corresponding plots for the
 222 individual flux systematics are shown in Appendix 7.2. We also consider statistical systematics. This are

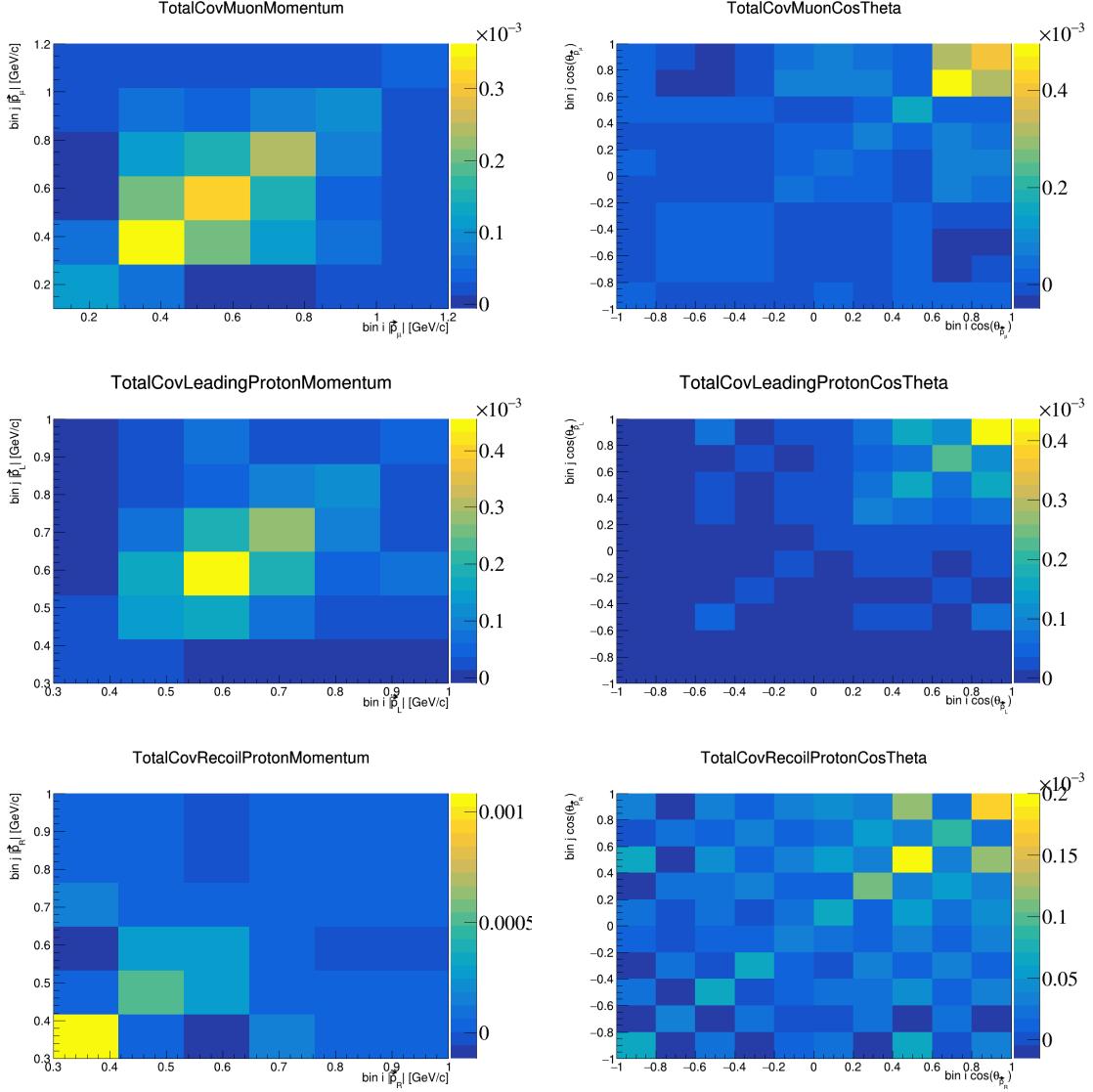


Figure 49: Total covariance matrices for momenta and opening angles of individual particles.

223 straightforward to compute, as the covariance matrix is given by the square root of the number of elements
 224 in the corresponding bin in the histogram. These statistical covariance matrices are shown in Appendix 7.3.
 225 For POT systematics, we consider a 2% variation in the number of protons on target and treat it as a 1σ
 226 variation. The corresponding plots are shown in Appendix 7.4. For number of target systematics, we likewise
 227 consider a 1% variation in the number of target nuclei and treat it as a 1σ variation. The corresponding
 228 plots are shown in Appendix 7.5. We consider detector variations across various universes, and these are
 229 shown in Appendix 7.6. We consider reinteraction systematics as a 2% flat variation, and these are shown
 230 in Appendix 7.7. The total covariance matrices for each variable are shown in Figures 49 to 51.

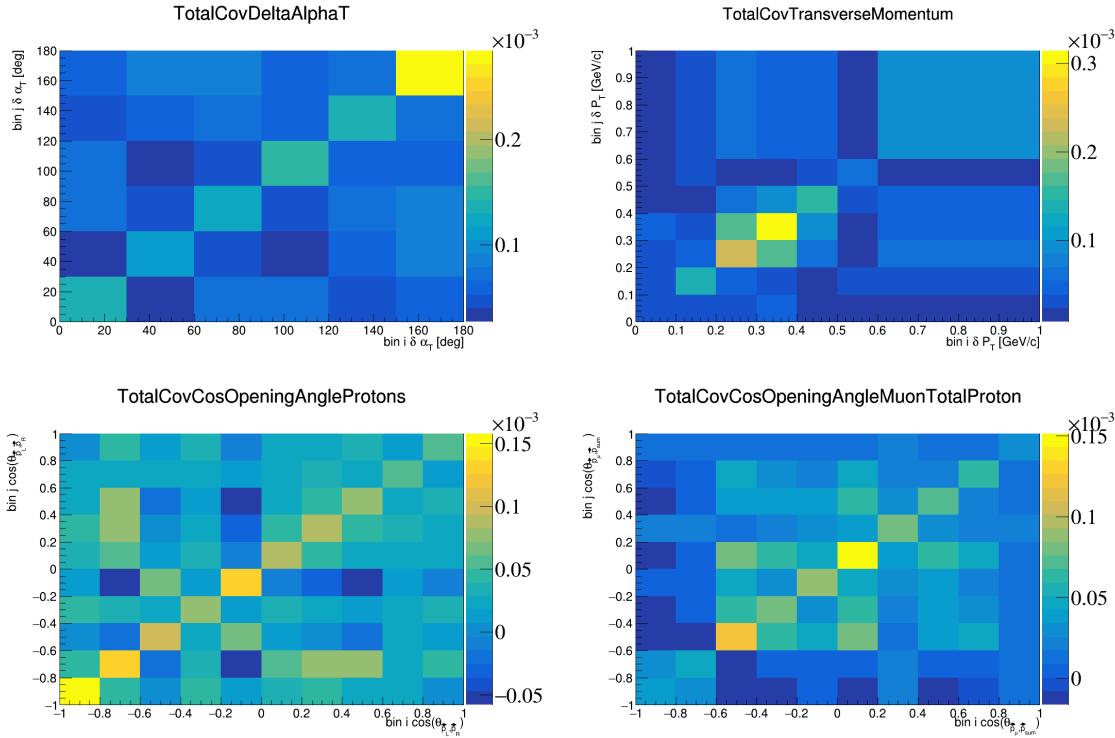


Figure 50: Total covariance matrices for transverse and opening angle variables.

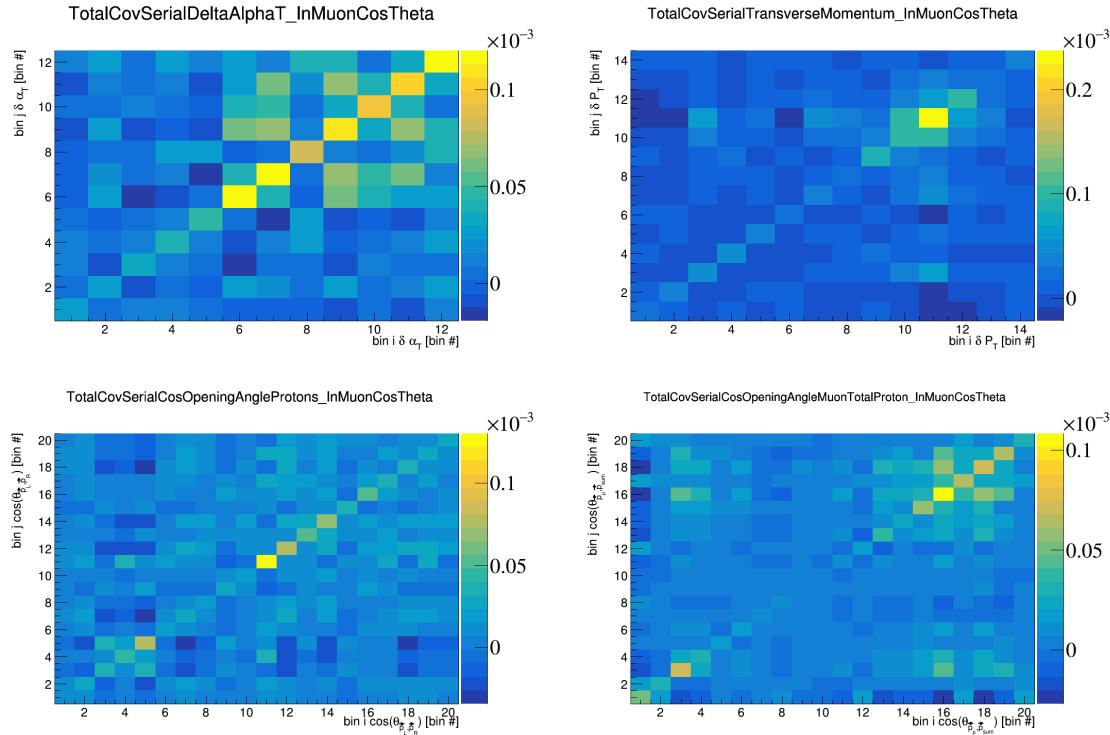


Figure 51: Total covariance matrices for double differential variables.

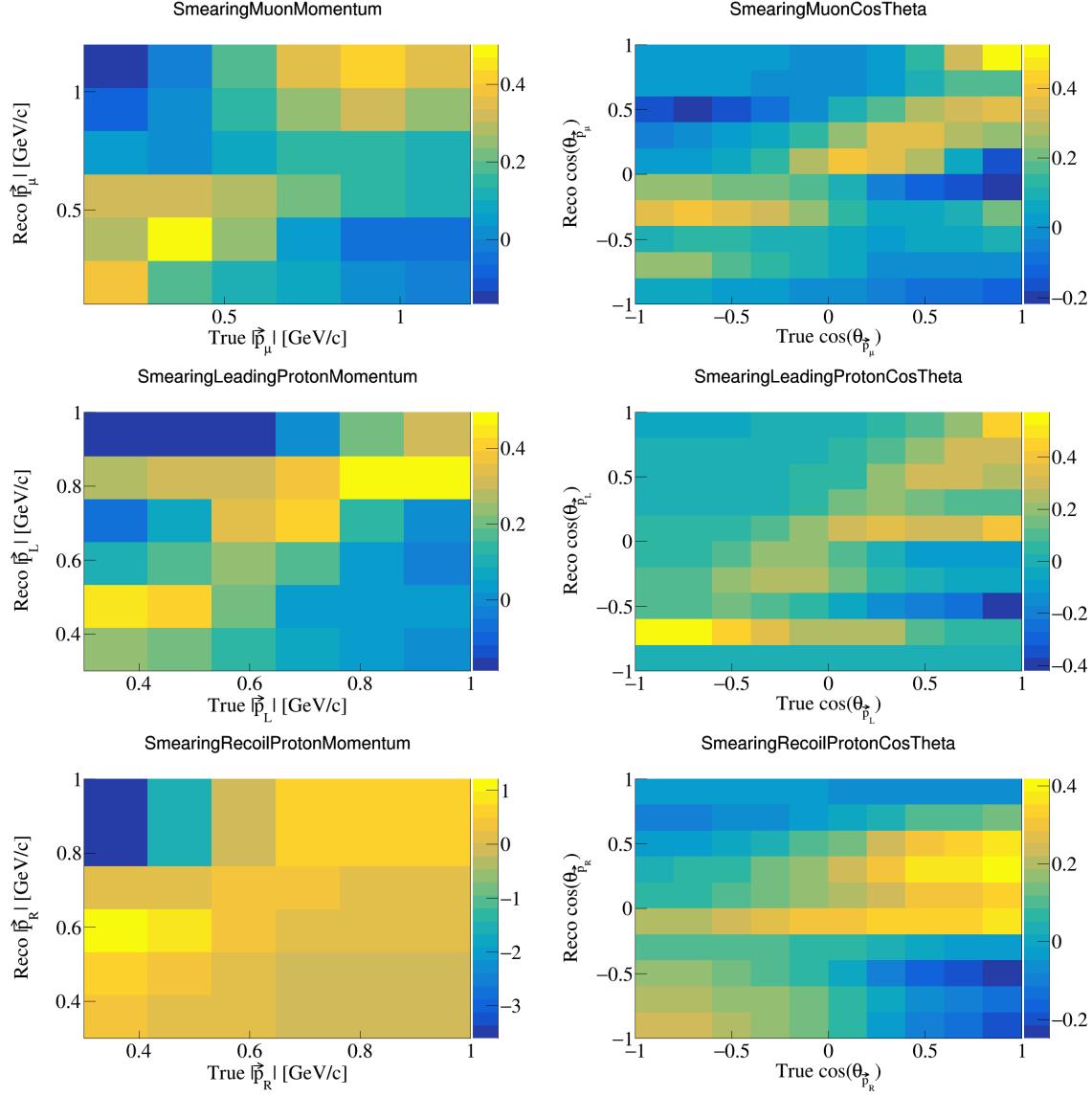


Figure 52: Additional smearing matrices for momenta and opening angles of individual vectors.

3.9 Wiener-SVD unfolding

We use the total covariance matrices obtained from all the systematics and shown in the previous section to unfold our data. We perform this unfolding following the Wiener-SVD method [27], which for a given variable takes as input a response matrix, true signal histogram, a reconstructed signal histogram, and the covariance matrix.

The output is the unfolded spectrum, a smearing matrix that can be used to smear true signal histograms, and a covariance rotation matrix to consider uncertainties in the regularized space as opposed to the true space. The additional smearing matrices obtained from the Wiener-SVD unfolding are shown in Figures 52 to 54.

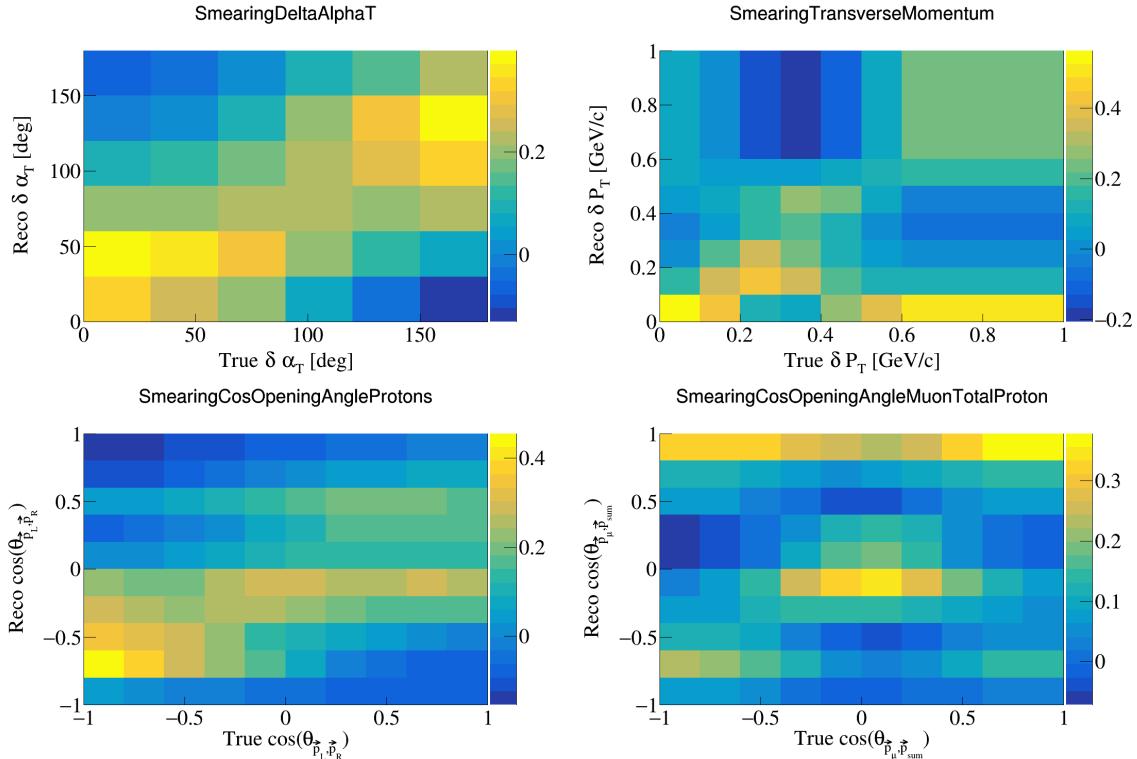


Figure 53: Additional smearing matrices for transverse and opening angle variables.

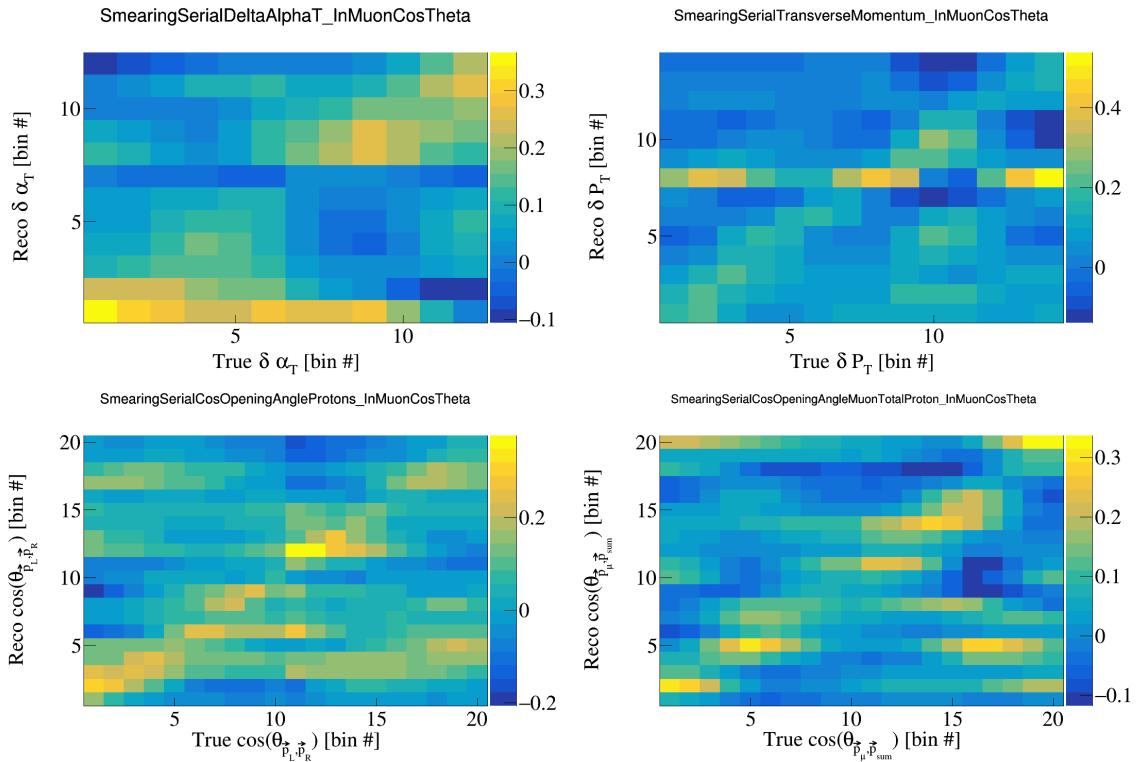


Figure 54: Additional smearing matrices for double differential variables.

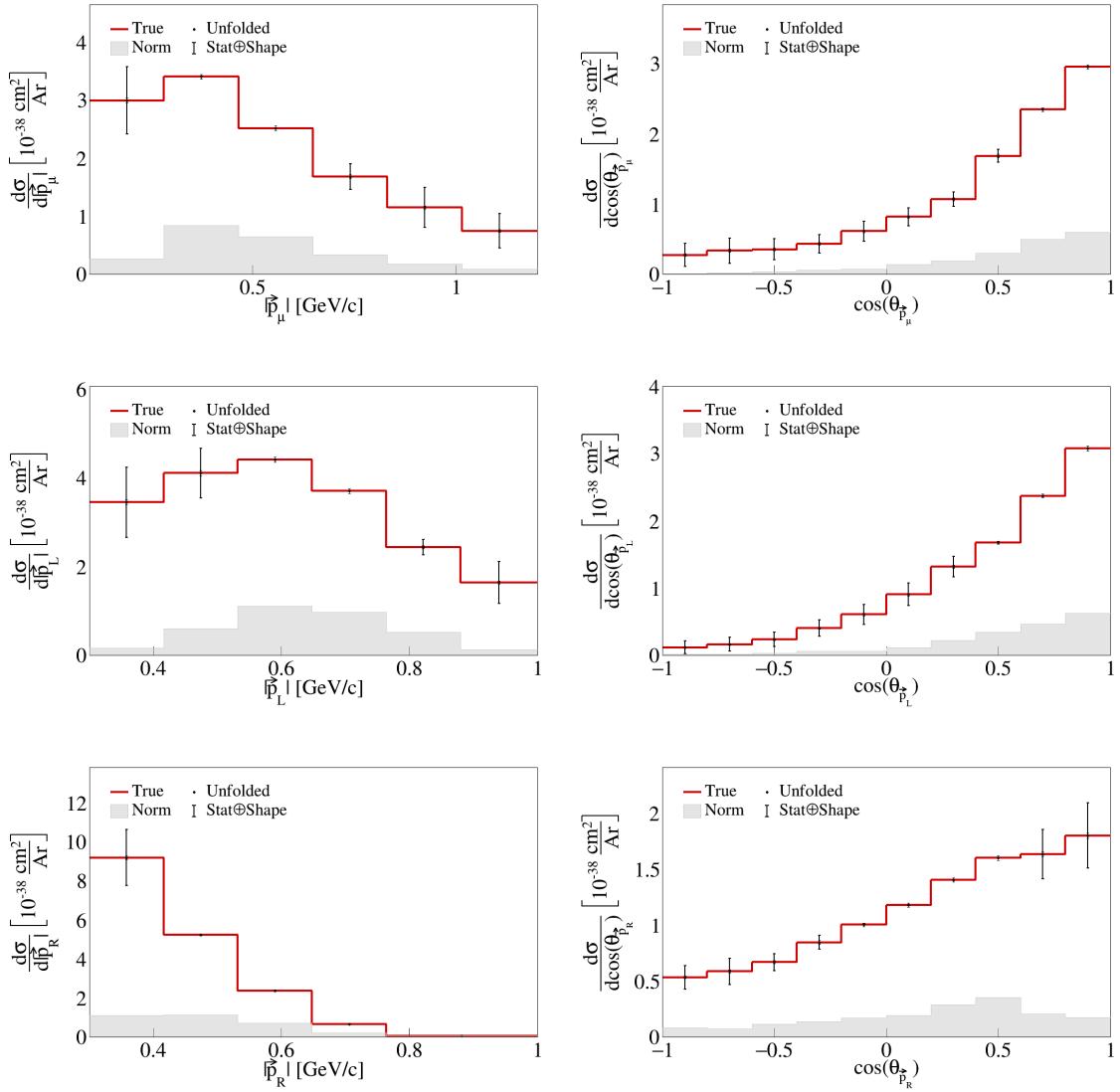


Figure 55: Closure test for momenta and opening angles of individual particles.

240 3.10 Closure test

241 To ensure that the unfolding techniques implemented work correctly, we use the true signal part of our Monte-
 242 Carlo data as our signal, and compare it to the unfolded cross-section obtained from our reconstructed signal
 243 to see that they are identical. The plots showing they are identical are in Figures 55 to 57.

244 The error bands for the unfolded spectra are given by the unfolded total covariance matrices, which
 245 are shown in a bin-by-bin basis in the Section 4.1. For the sliced double differential measurements, we
 246 make sure to divide by the slice and bin widths to obtain the correct error bands. In the single differential
 247 measurements, we only have to divide by the bin width.

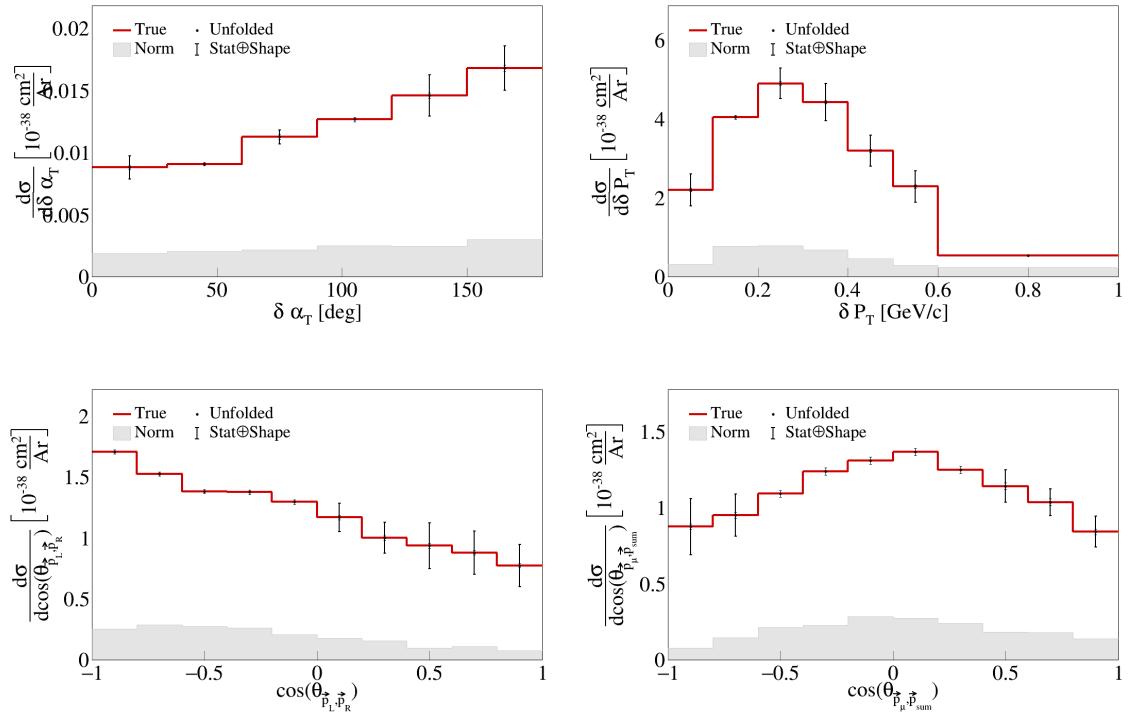


Figure 56: Closure test for transverse and opening angle variables.

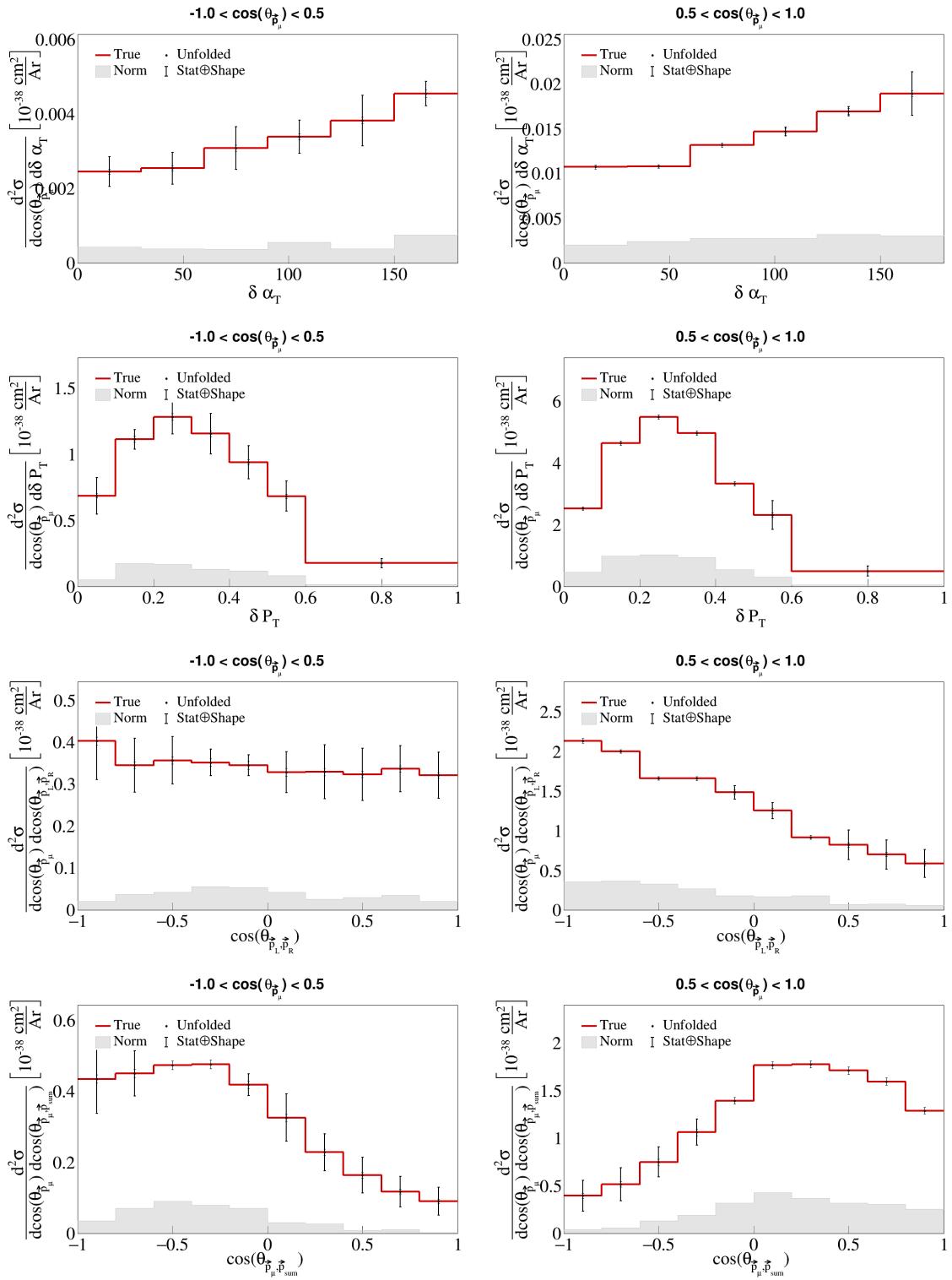


Figure 57: Closure test for double differential plots.

²⁴⁸ **3.11 Event rate uncertainties**

²⁴⁹ Figure 58 shows the single bin uncertainty breakdown using the event rates. We used the square root of
²⁵⁰ the relevant fractional covariance matrix for each of the outlined sources of uncertainty to obtain the figure.
²⁵¹ The bin by bin event rate uncertainties for all our variables are shown in Figures 59 to 61.

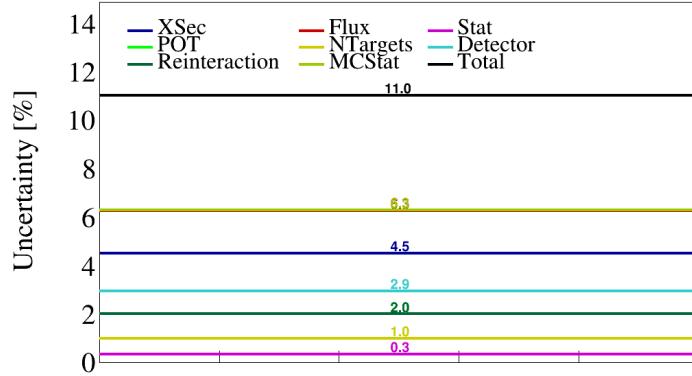


Figure 58: Fractional contribution of the sources of uncertainty using the event rates.

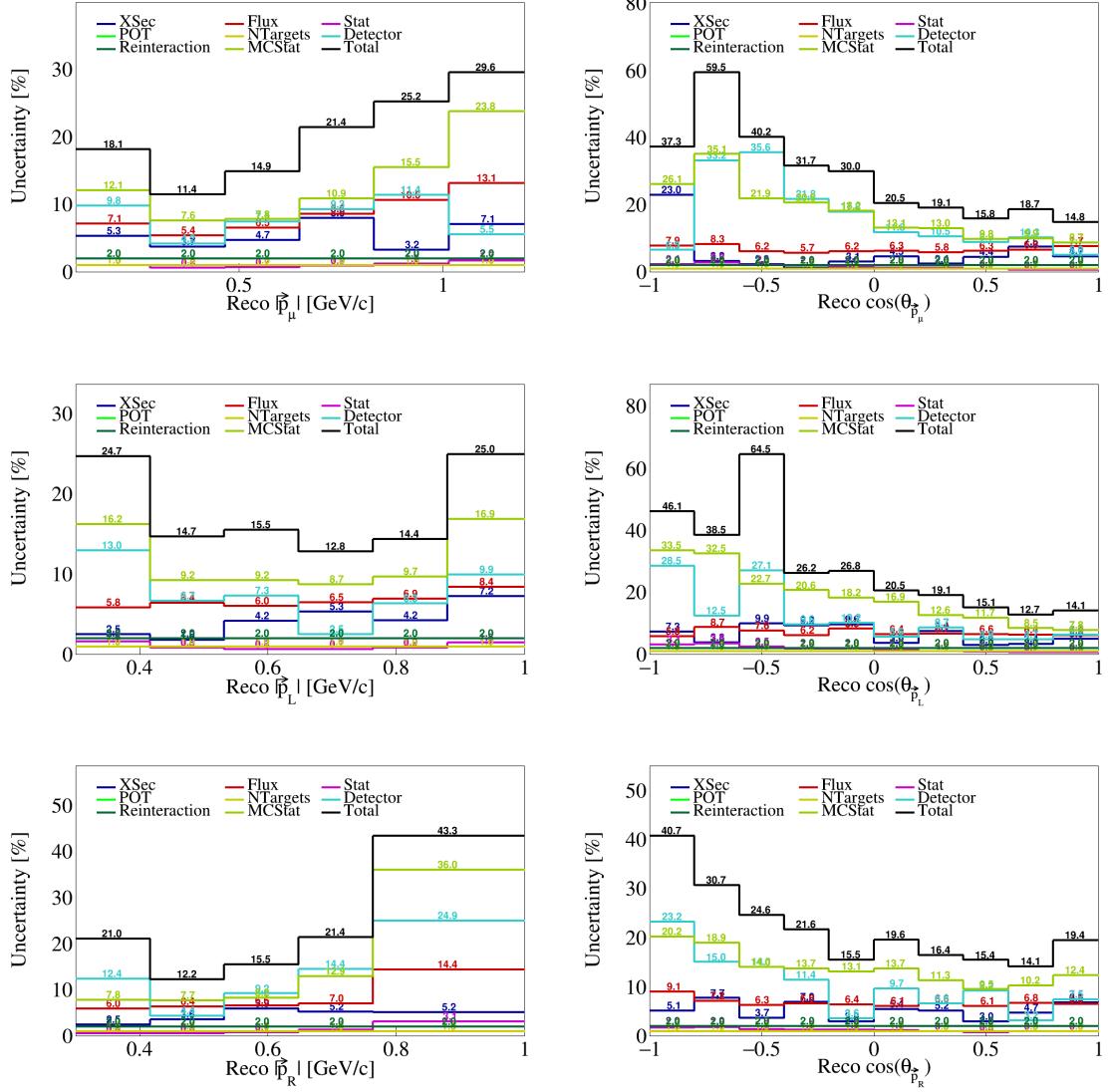


Figure 59: Bin by bin event rate uncertainties for momenta and opening angles of individual particles.

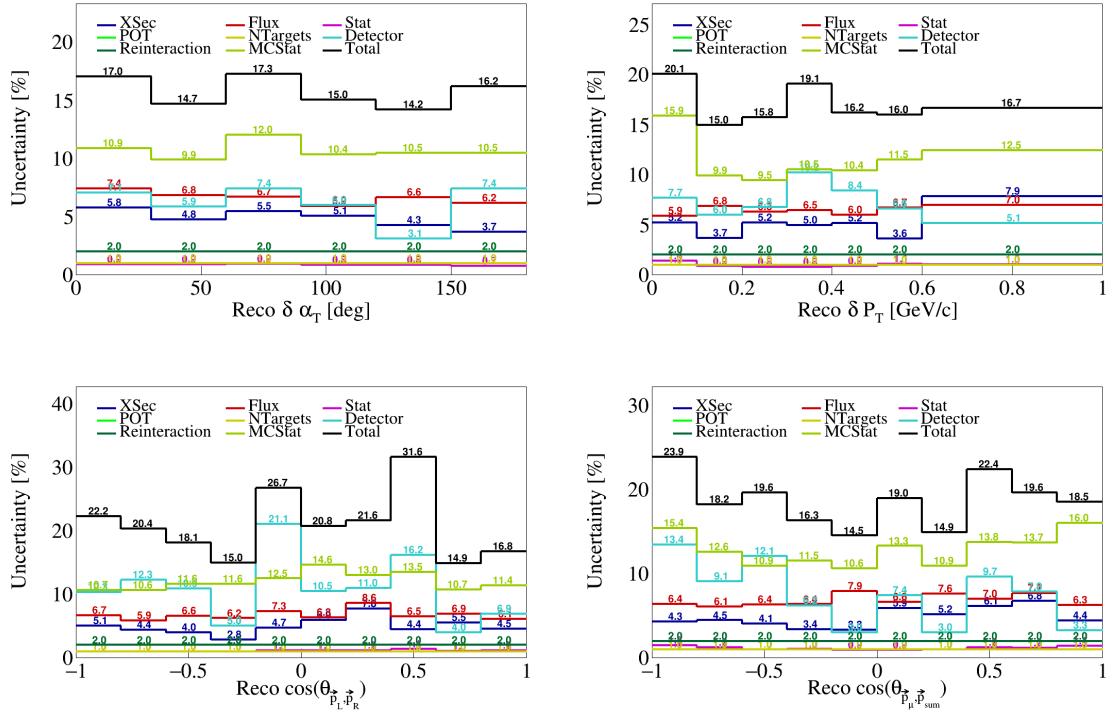


Figure 60: Bin by bin event rate uncertainties for transverse and opening angles variables.

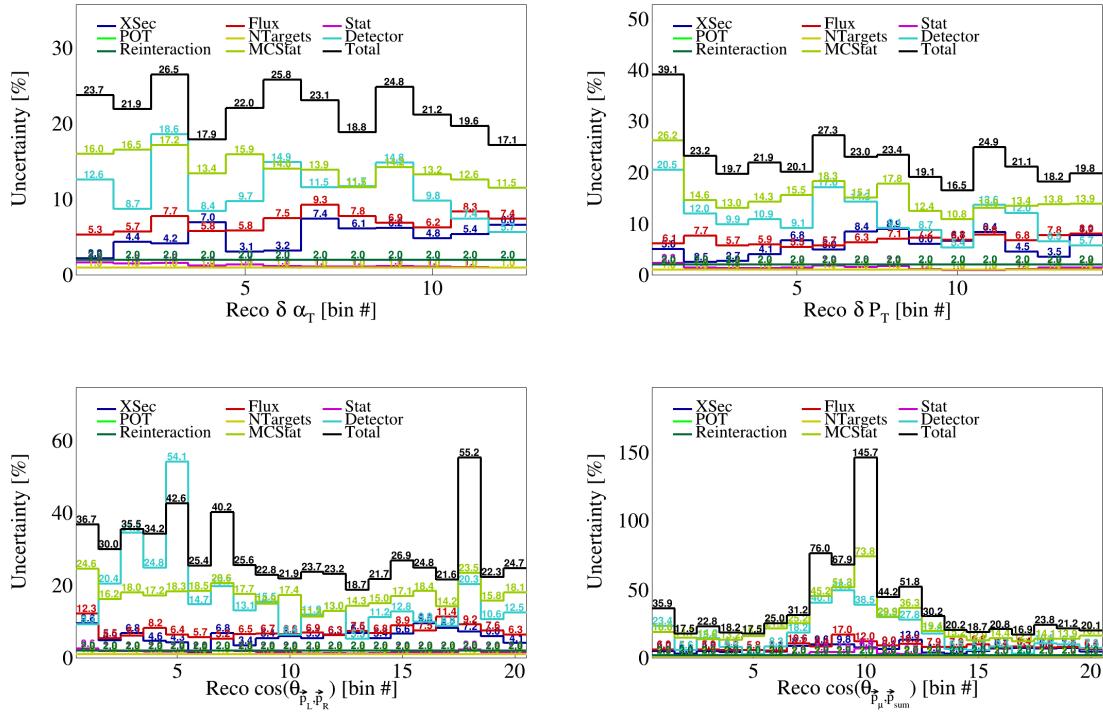


Figure 61: Bin by bin event rate uncertainties for double differential variables.

3.12 Difference and resolution

As a sanity check, we compute the difference and resolution between the reconstructed and the true values for each of our single-differential variables for events that satisfy our signal definition. The difference is defined as

$$x_{\text{Difference}} = x_{\text{reco}} - x_{\text{true}}, \quad (16)$$

while the resolution is defined as

$$x_{\text{Resolution}} = \frac{x_{\text{reco}} - x_{\text{true}}}{x_{\text{true}}}. \quad (17)$$

We expect both distributions to be centered around zero. The distributions are shown in Figures 62 to 64.

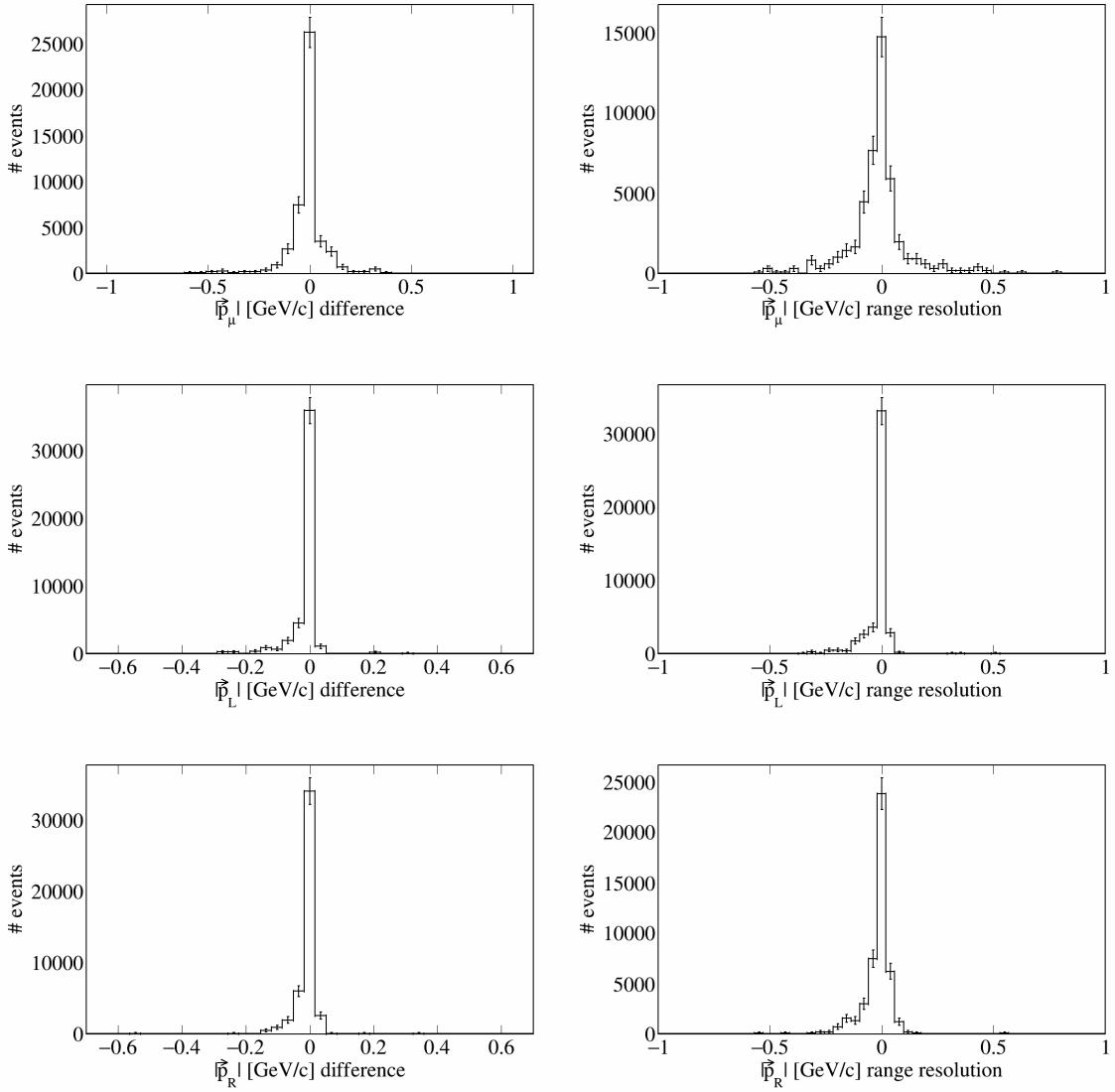


Figure 62: Difference and resolution plots for momenta of individual particles.

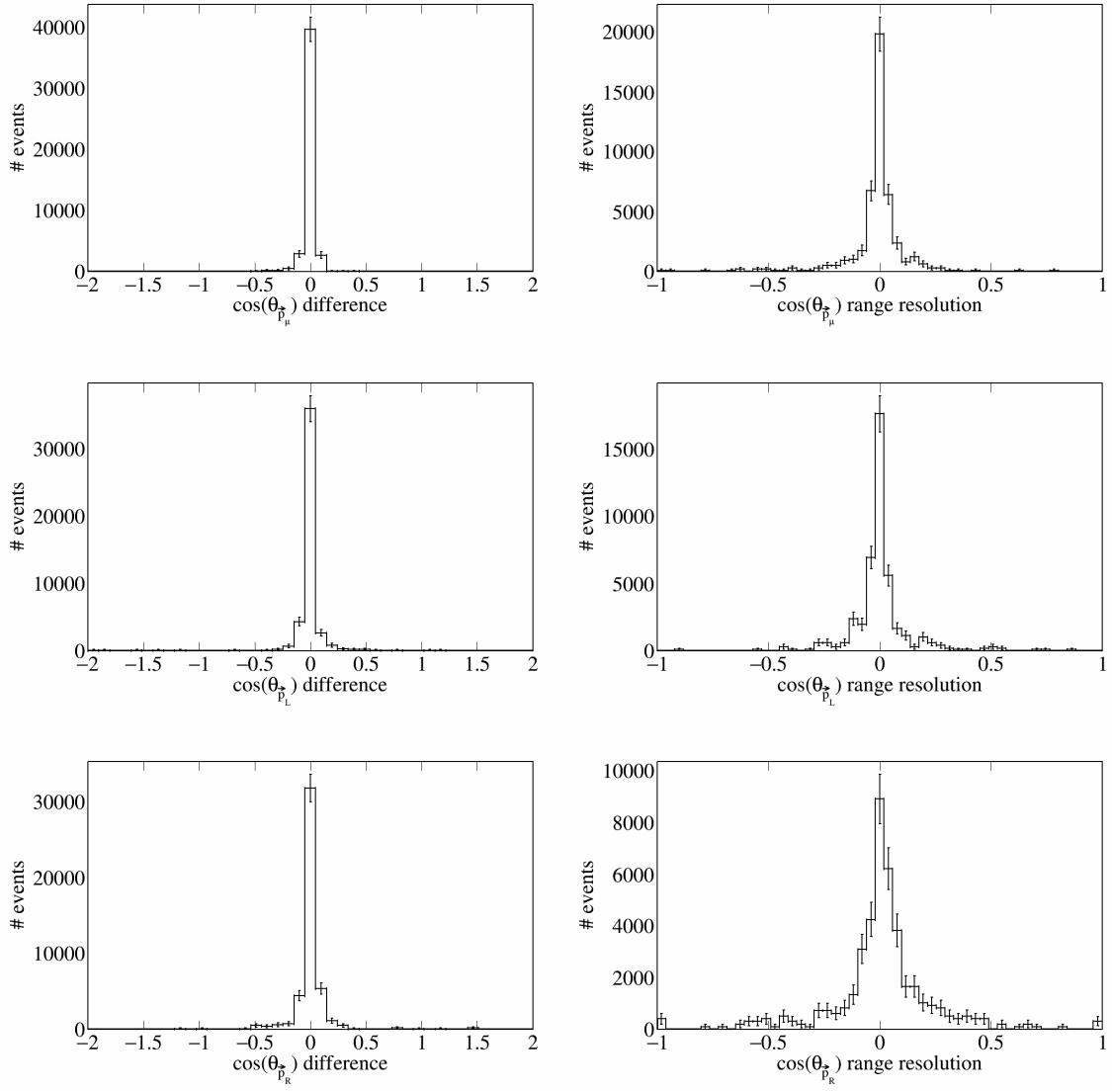


Figure 63: Difference and resolution plots for opening angles of individual particles.

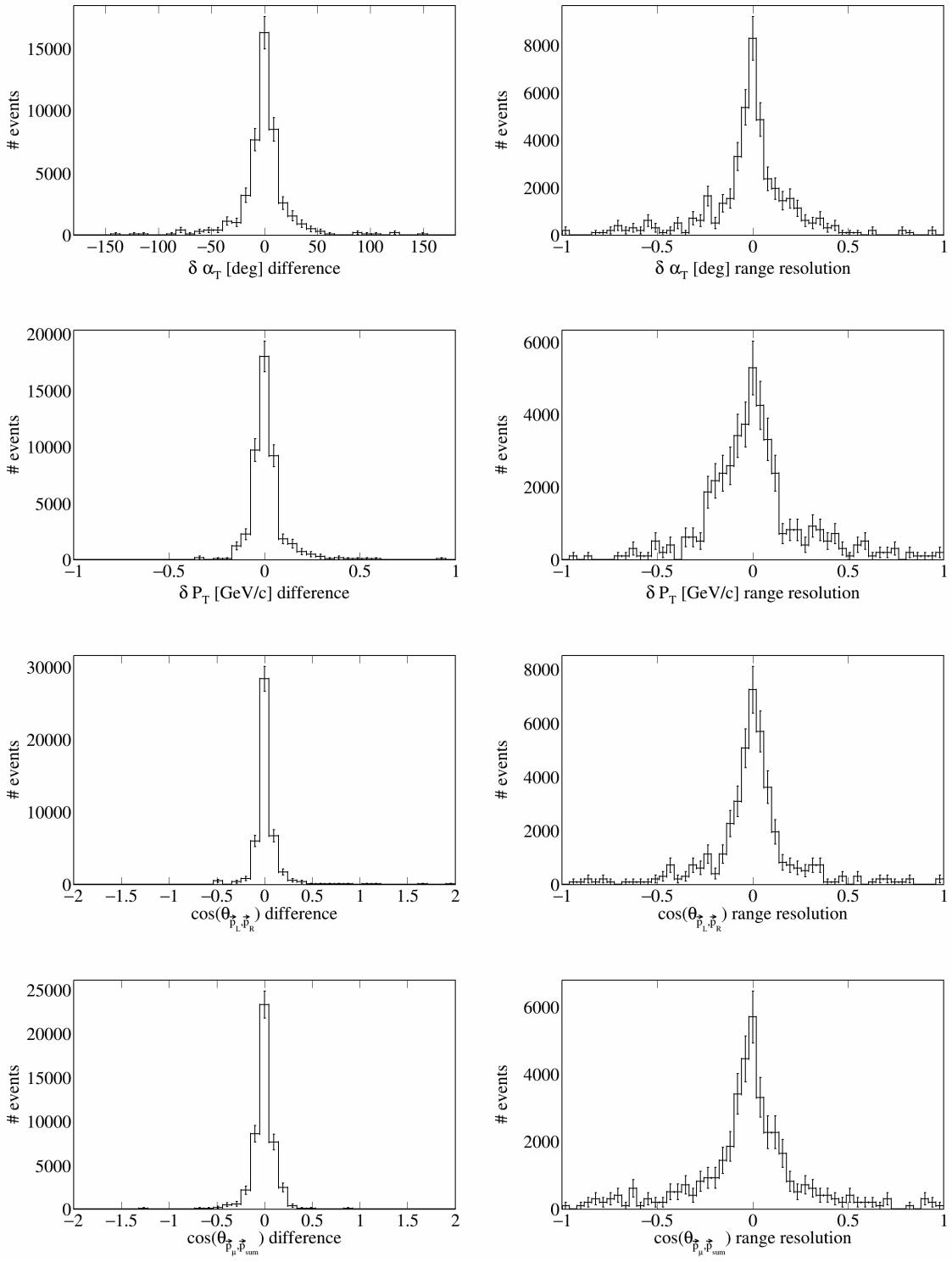


Figure 64: Difference and resolution plots for transverse and opening angle variables.

258 4 Cross-section results

259 We present the unfolded cross-sections obtained using the Wiener-SVD filter, and overlay it with the generators studied in the earlier sections of this document. The generator cross-sections are smeared using the
 260 additional smearing matrices, and the uncertainties are obtained using the unfolded total covariance matrix.
 261 The unfolded cross-sections are shown in Figures 65 to 67. Note that the “data points” shown are unfolded
 262 cross-sections of Monte-Carlo data from the SBND production, first results on real data are presented in the
 263 next section.
 264

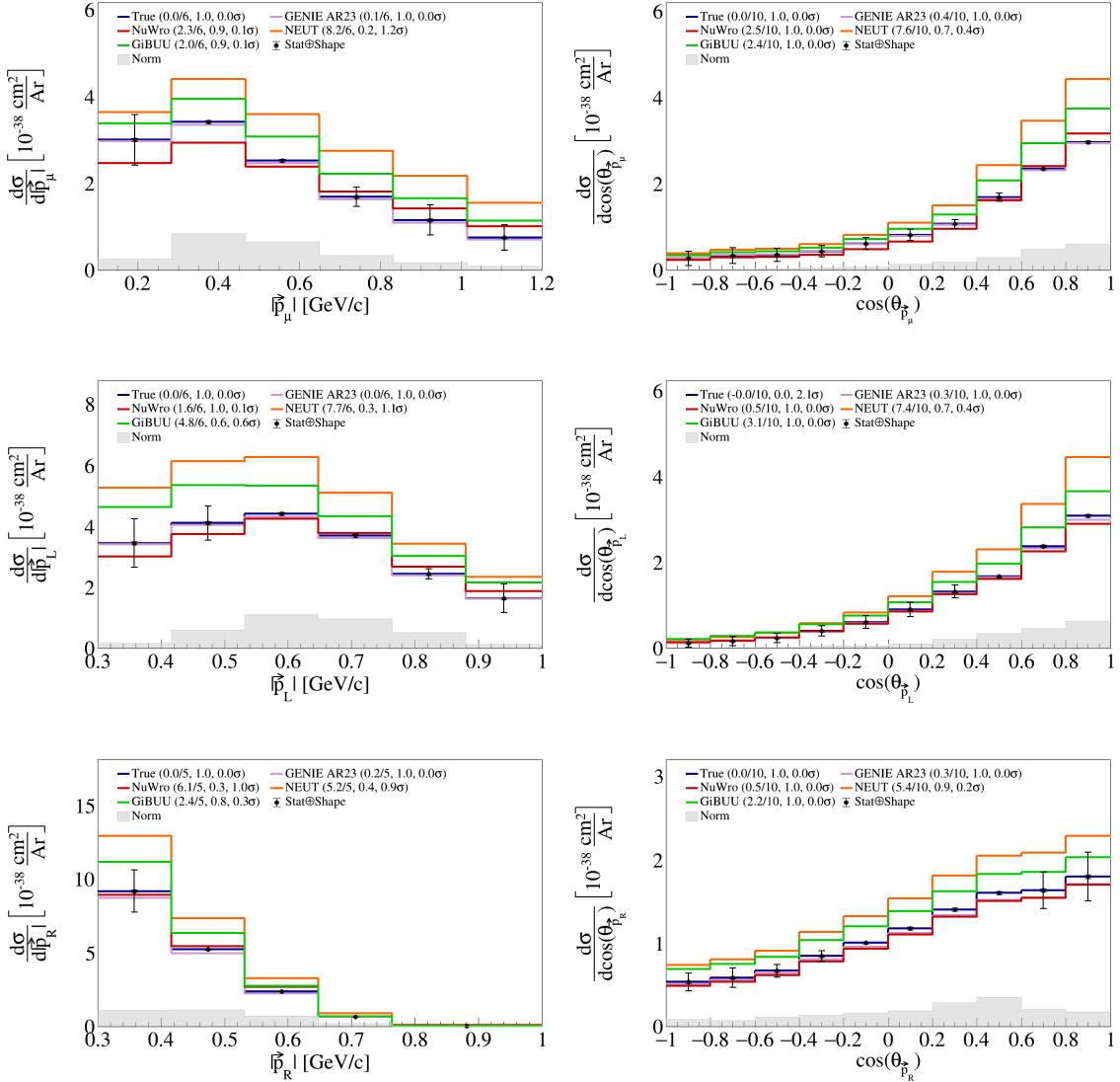


Figure 65: Cross-section results for momenta and opening angles of individual particles.

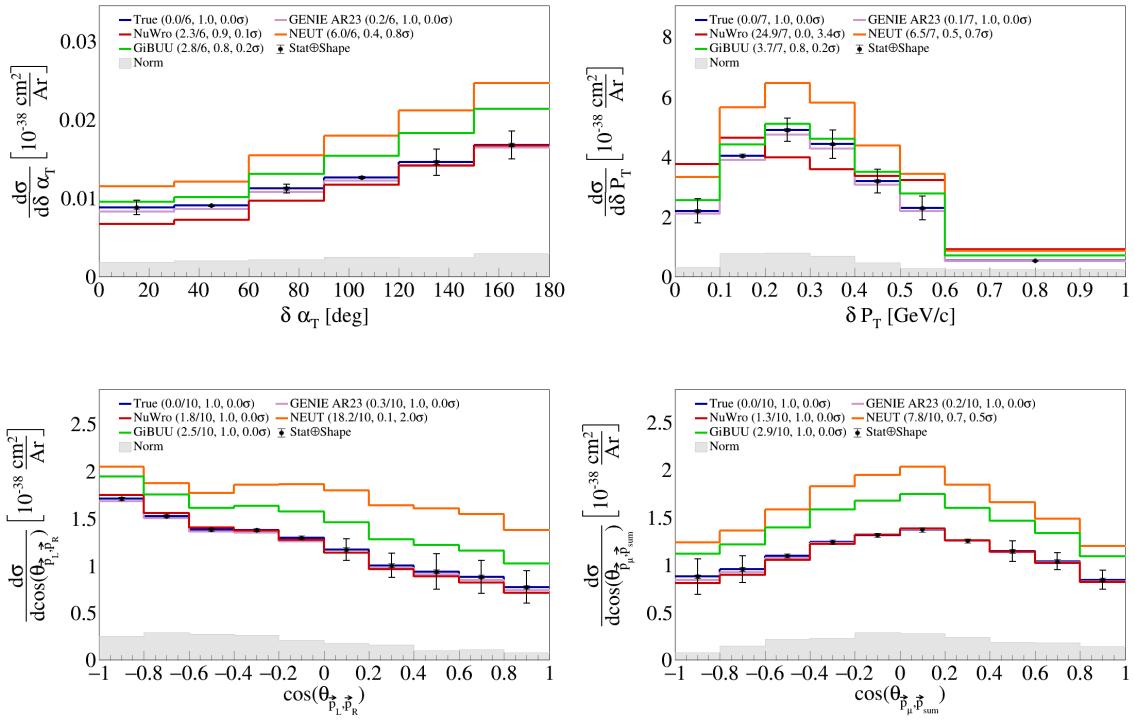


Figure 66: Cross-section results for transverse and opening angle variables.

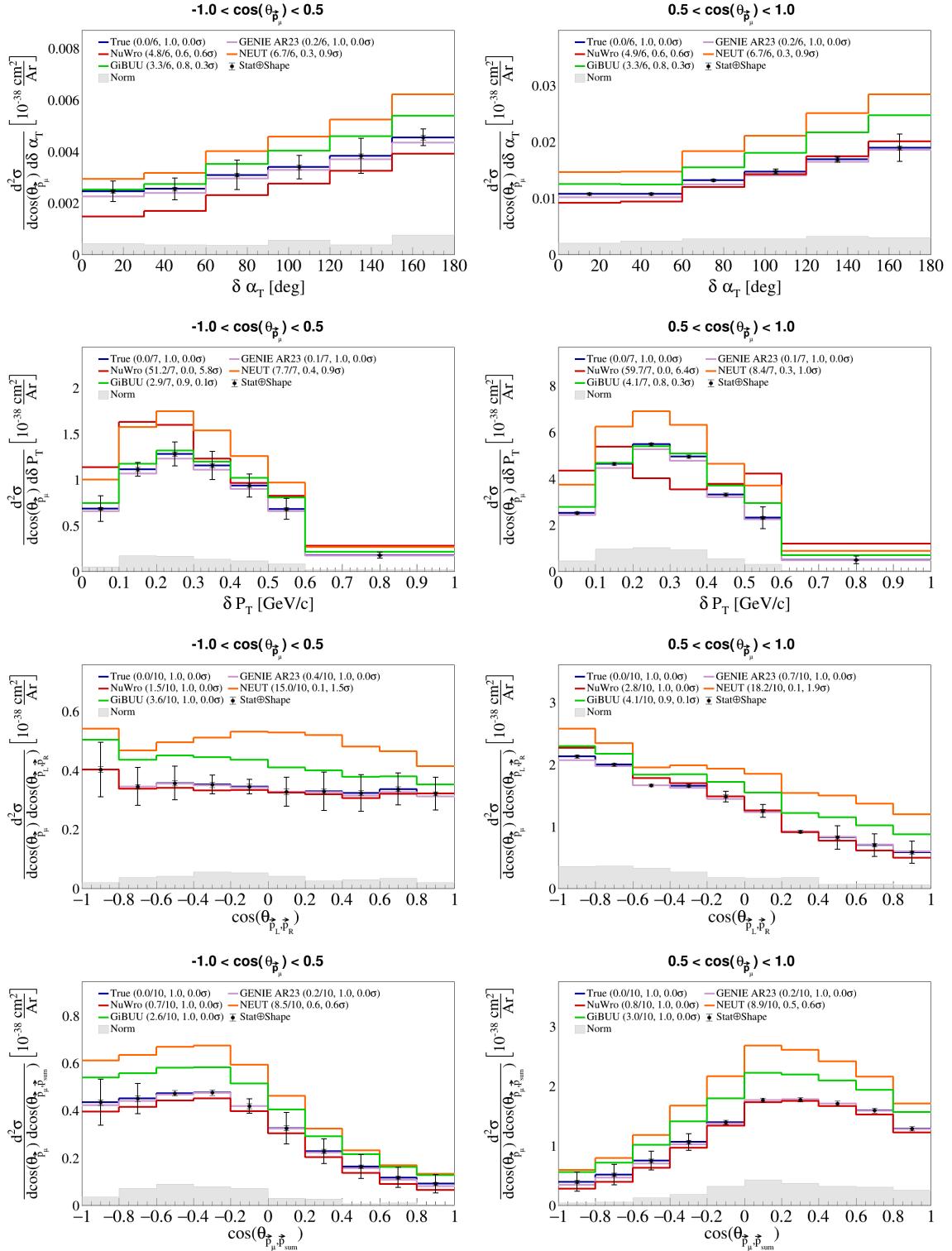


Figure 67: Cross-section results for sliced double differential variables.

265 **4.1 Cross-section uncertainties**

266 Figure 68 shows the single bin uncertainty breakdown using the cross sections. We used the unfolded
267 covariances obtained with the Wiener-SVD filter for each of the sources of uncertainty. The square root of the
268 corresponding fractional covariance matrix is normalized to the CV cross-section value for the uncertainties
269 to be obtained. The bin by bin cross section uncertainties for all our variables are shown in Figures 69 to 71.

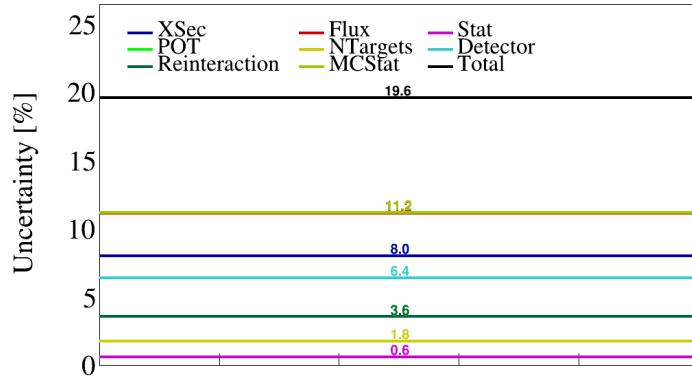


Figure 68: Fractional contribution for the sources of uncertainty using the cross sections.

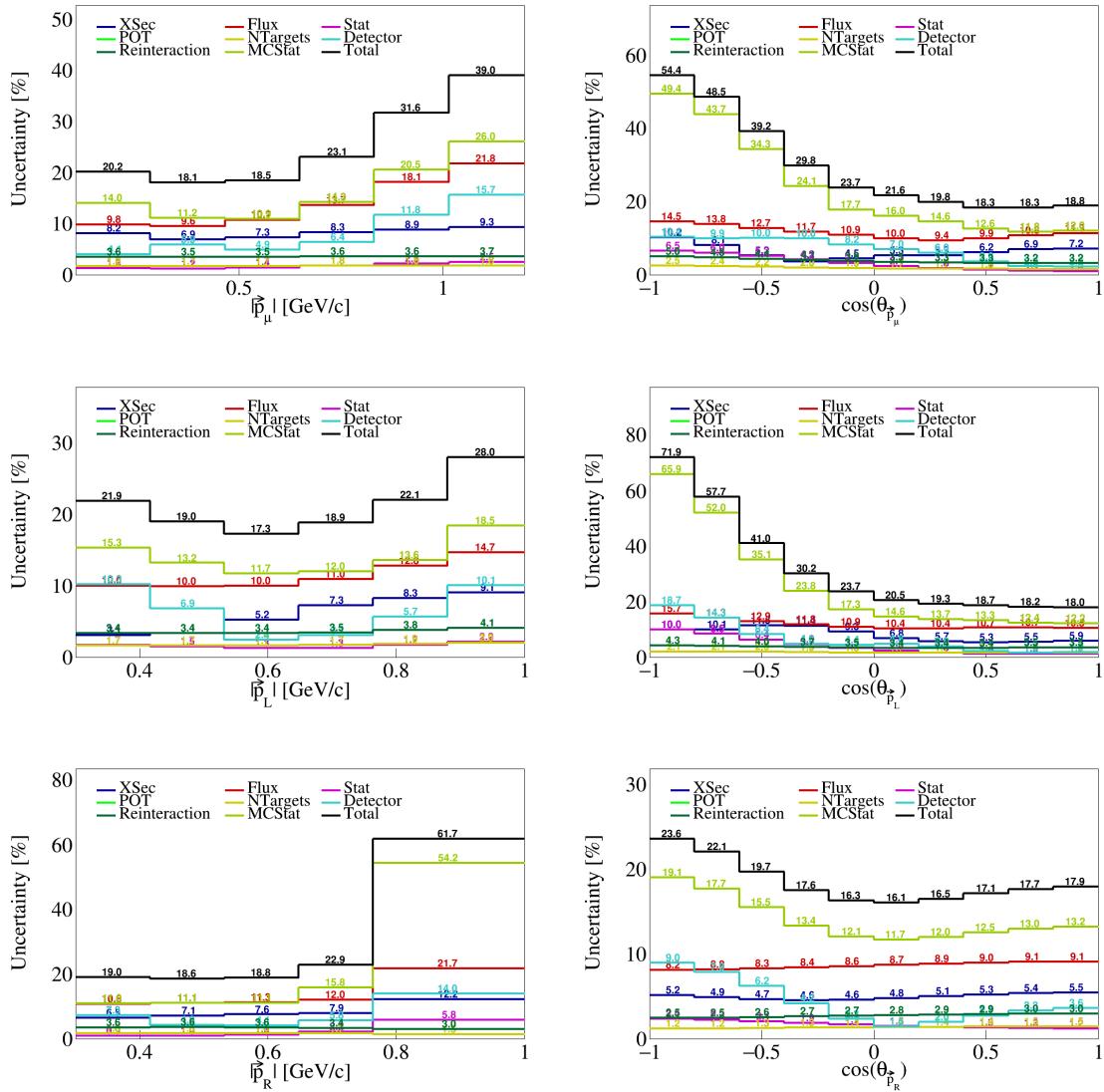


Figure 69: Bin by bin event cross-section uncertainties for momenta and opening angles of individual particles.

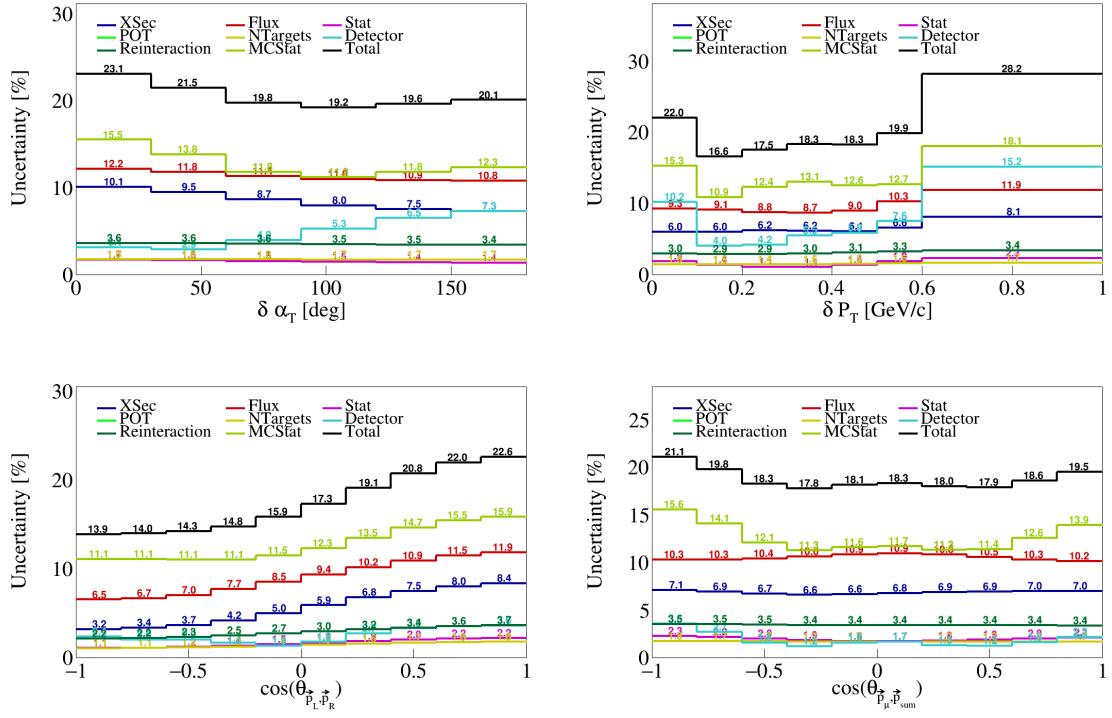


Figure 70: Bin by bin cross-section uncertainties for transverse and opening angles variables.

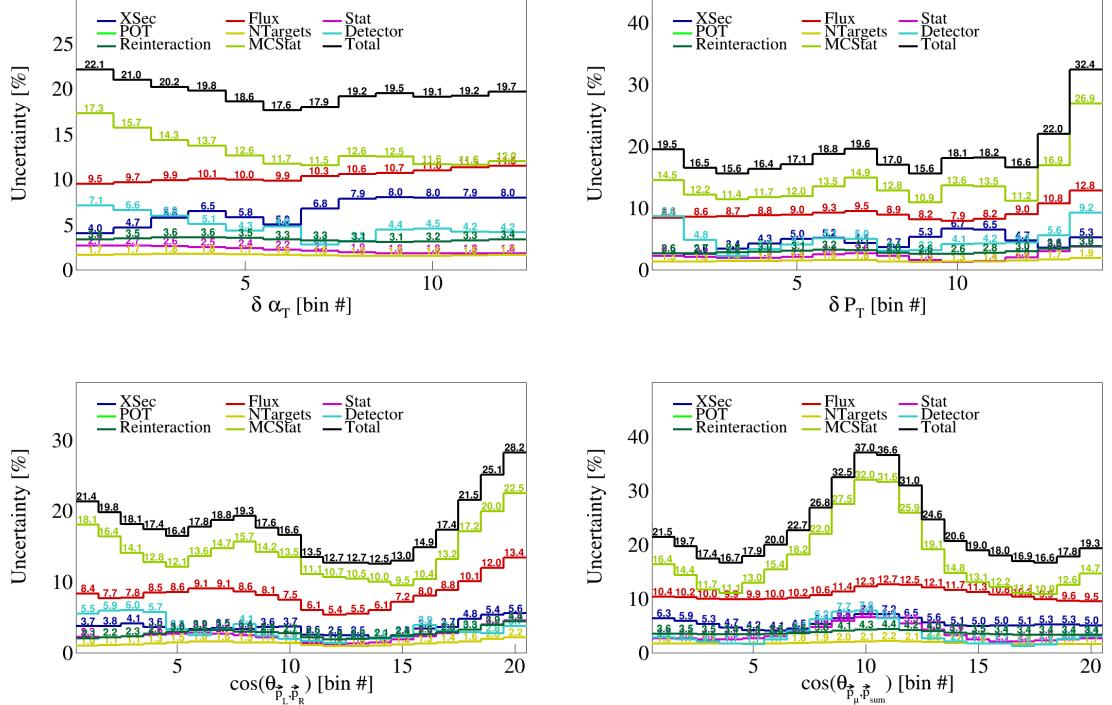


Figure 71: Bin by bin cross-section uncertainties for double differential variables.

270 **5 Fake data studies**

271 To test our unfolding procedure, we generate fake data by increasing the weight of certain events in our
272 Monte Carlo simulations. We give meson exchange current (MEC) events a weight of 2 in Section 5.1, and
273 quasi-elastic (QE) events a weight of 0.5 combined with a MEC weight of 1.5 in Section 5.2. We then unfold
274 these fake data using the nominal Monte-Carlo predictions from the GENIE AR23 generator. Therefore, the
275 input to the Wiener-SVD unfolding are: the response matrix constructed with the nominal predictions, the
276 true nominal signal, the reconstructed signal from the fake data (this is the only input that changes), and
277 the total covariance matrix, which in this case was the statistical covariance matrix for the fake data added
278 to the MC statistical and cross-section covariance matrices obtained with the nominal predictions.

279 After unfolding the fake data, we compare the unfolded fake data to the smeared fake signal and the
280 smeared nominal signal, using the additional smearing matrix obtained from the Wiener-SVD unfolding. We
281 then perform a χ^2 test to see if the unfolded fake data agrees with the smeared fake signal. Additionally, we
282 also report the p - and σ -values for the distributions. We expect to see good agreement between the smeared
283 fake signal and the unfolded fake data, while the smeared nominal signal should not agree with the unfolded
284 fake data. In other words, we expect below 1σ agreement between the smeared fake signal and unfolded fake
285 data.

286 **5.1 MEC 2x weight**

287 In this first fake data study, we give MEC events a weight of 2, while keeping all other events with a weight
288 of 1. We see that we are under 1σ agreement between the smeared fake signal and the unfolded fake data
289 for all our variables, while on or above 2.9σ with the smeared nominal signal, as expected. Therefore, we
290 can conclude that this fake data study was successful. The unfolded fake data along with the two smeared
291 signals is shown in Figures 72 to 75.

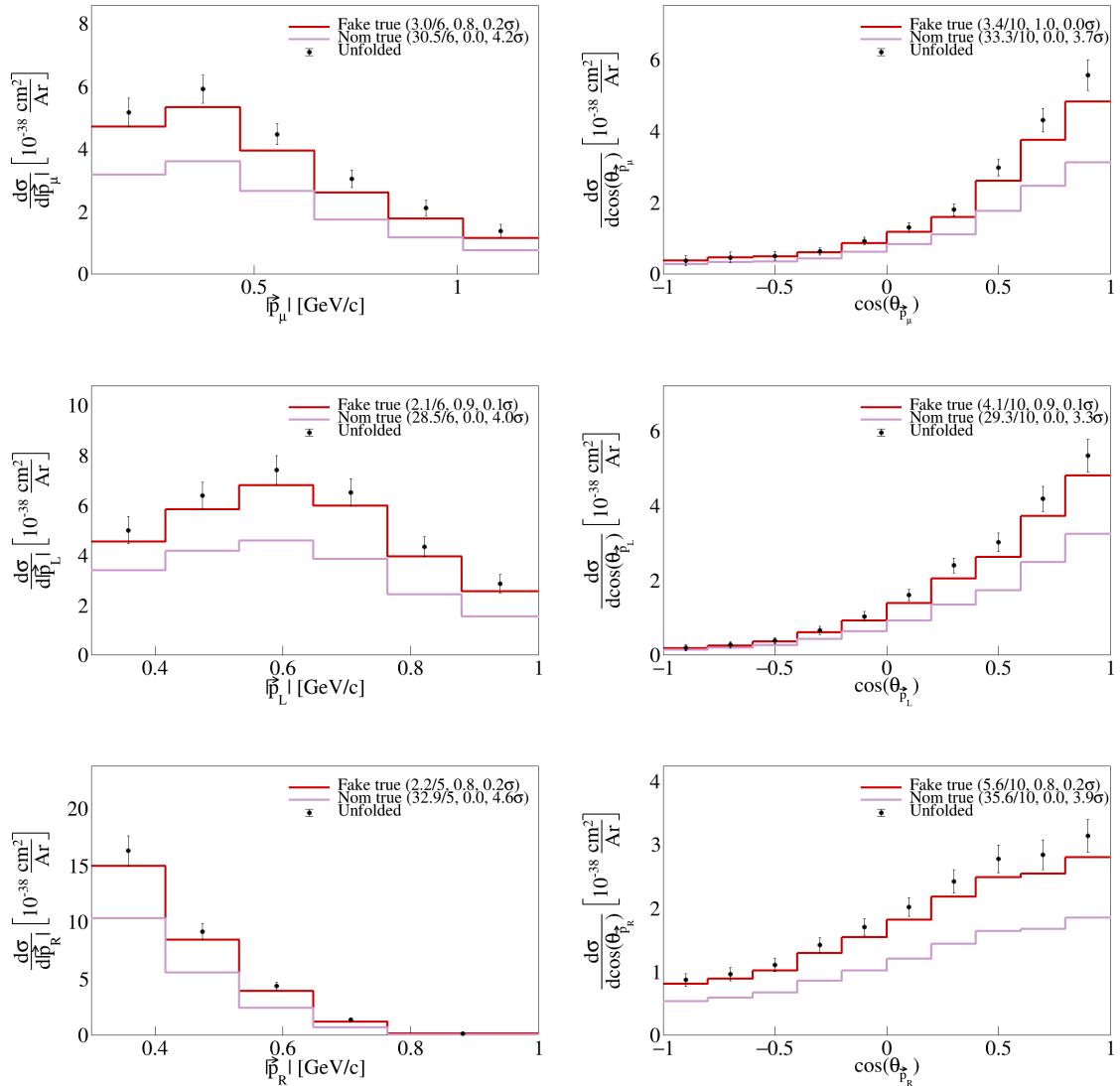


Figure 72: Unfolded 2x MEC fake data showing agreement with smeared fake signal data for single differential vector directions and magnitudes.

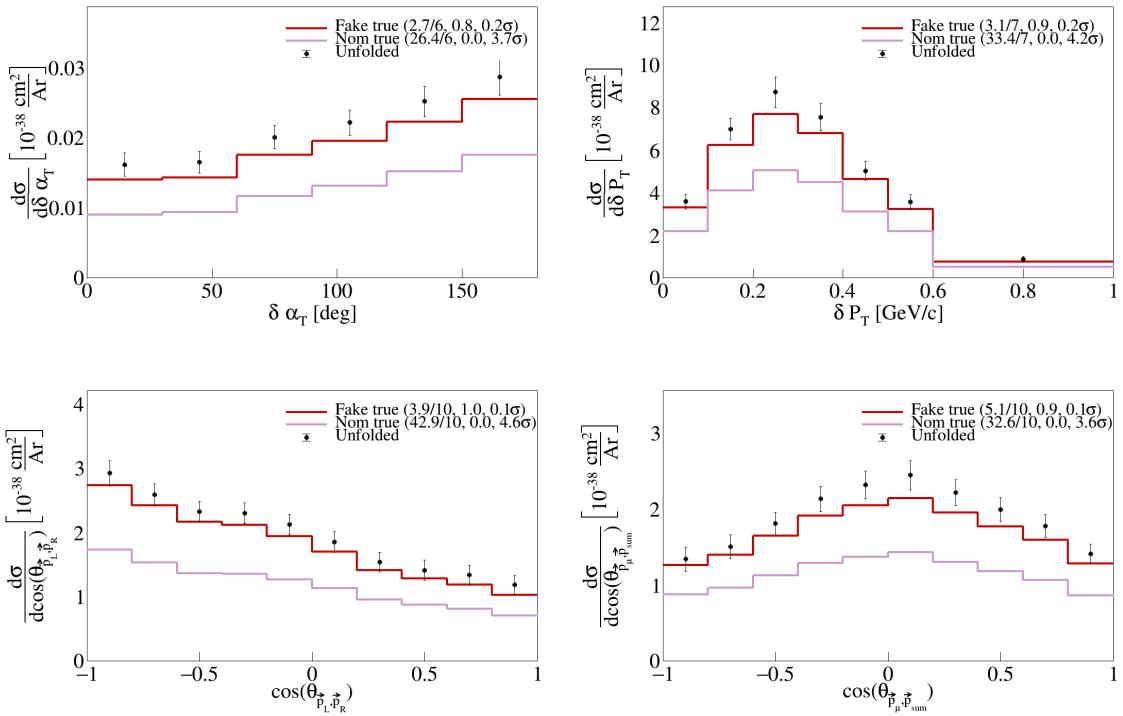


Figure 73: Unfolded 2x MEC fake data showing agreement with smeared fake signal data for single differential vector opening angles and transverse momentum.

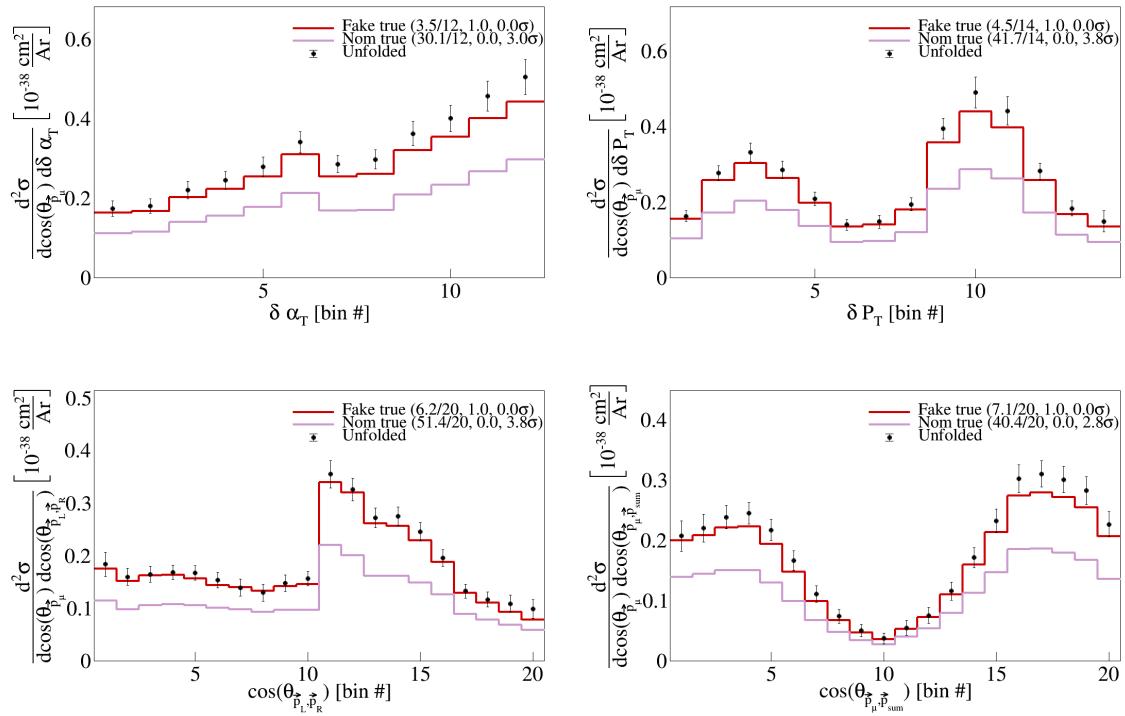


Figure 74: Unfolded 2x MEC fake data showing agreement with smeared fake signal data for serial double differential variables.

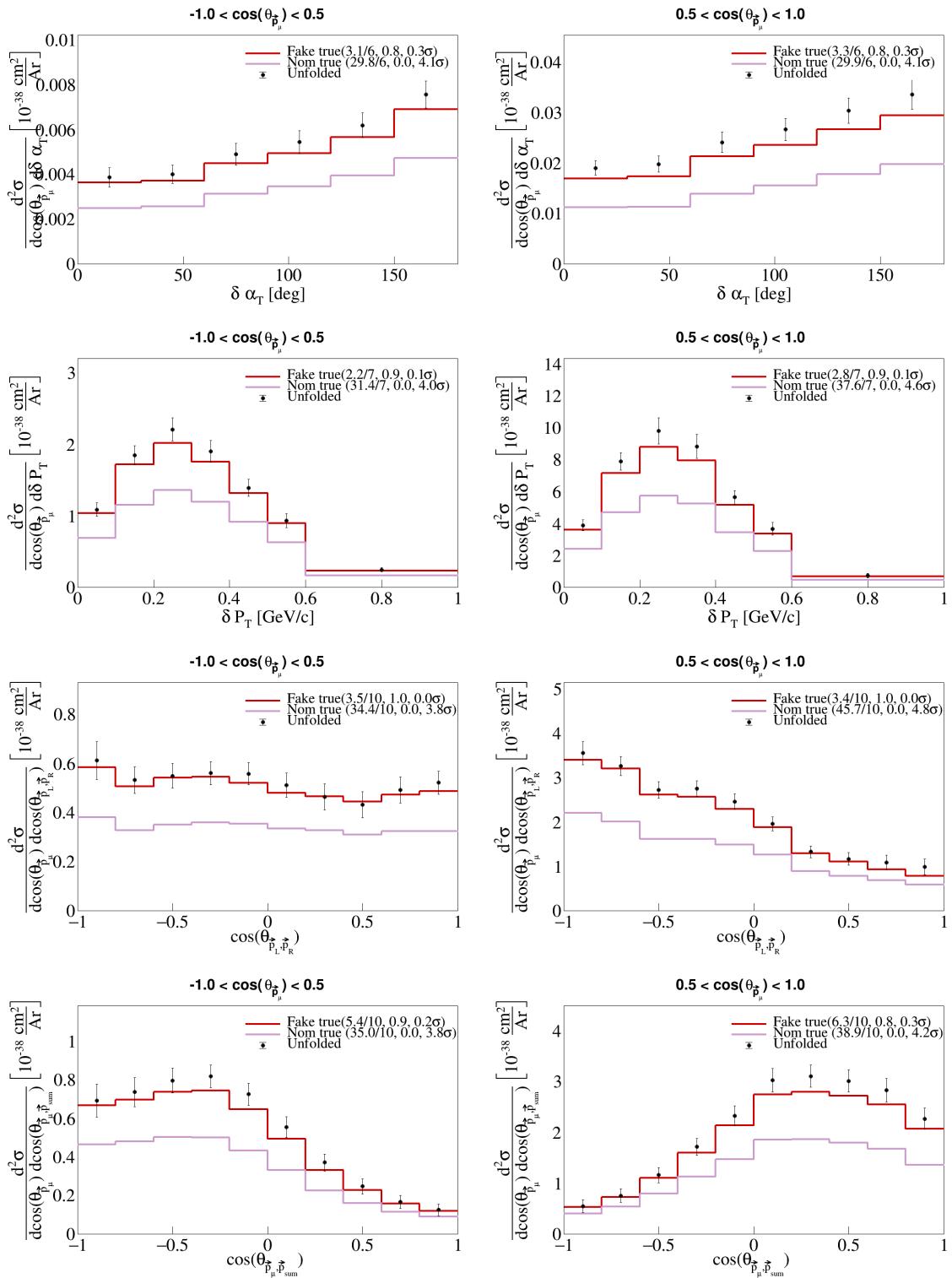


Figure 75: Unfolded 2x MEC fake data showing agreement with smeared fake signal data for sliced double differential variables.

292 **5.2 QE 0.5x and MEC 1.5x weights**

293 For this fake data study we give QE events a weight of 0.5 and MEC events a weight of 1.5, while keeping
294 all other events with a weight of 1. We see that we are under 1σ agreement between the smeared fake signal
295 and the unfolded fake data for all our variables, but contrary to the first study, we also see agreement with
296 the smeared nominal signal in many of our variables. The unfolded fake data for this study along with the
297 two smeared signals is shown in Figures 76 to 79.

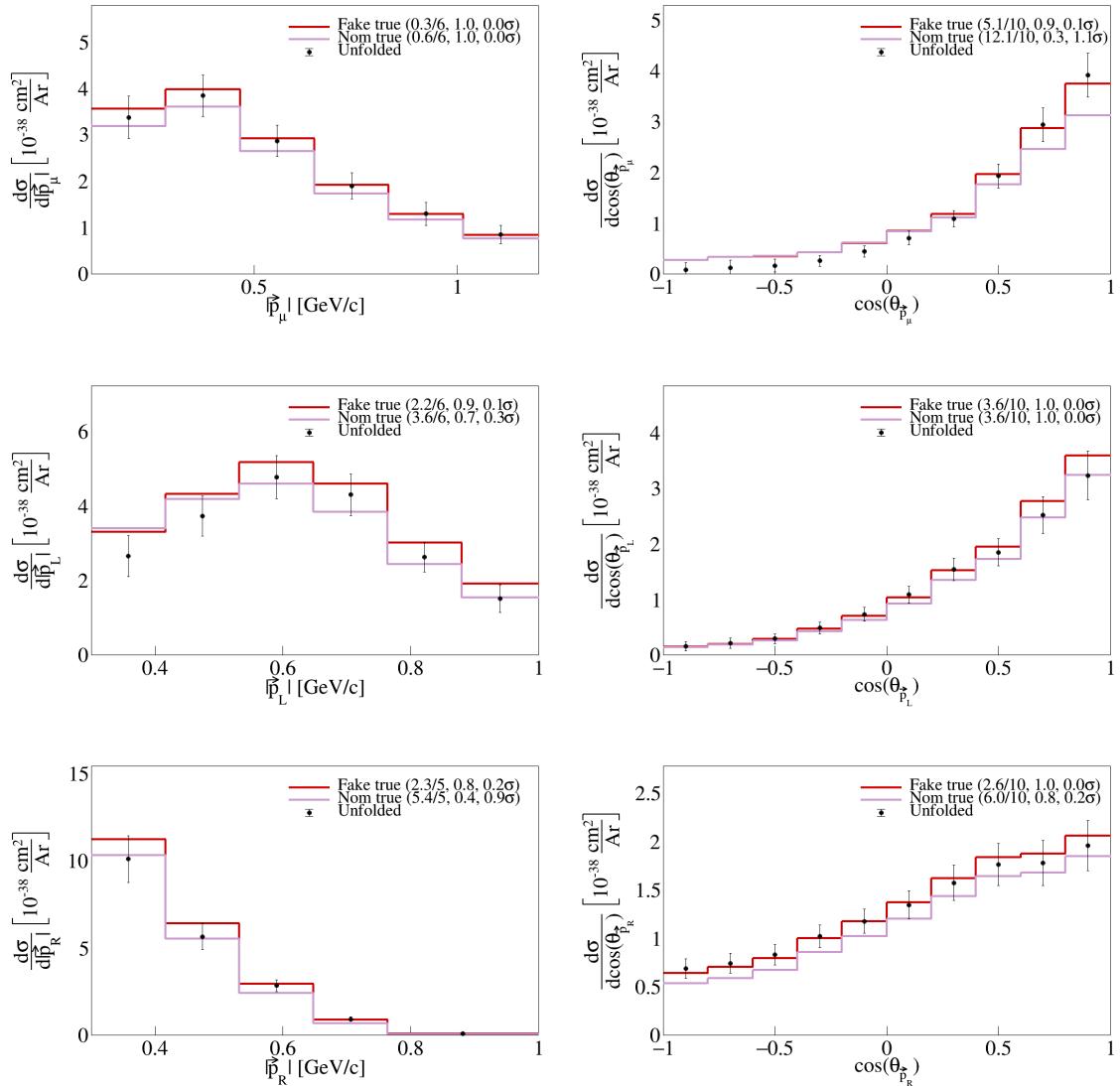


Figure 76: Unfolded combined weights fake data showing agreement with smeared fake signal data for single differential vector directions and magnitudes.

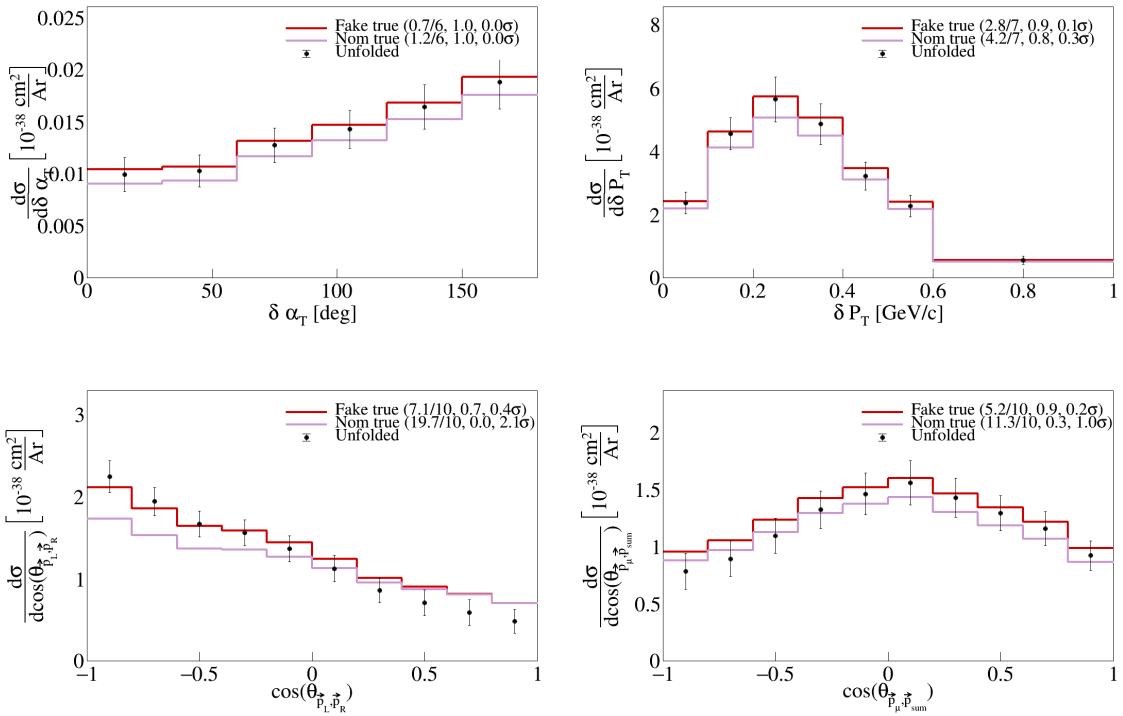


Figure 77: Unfolded combined weights fake data showing agreement with smeared fake signal data for single differential vector opening angles and transverse momentum.

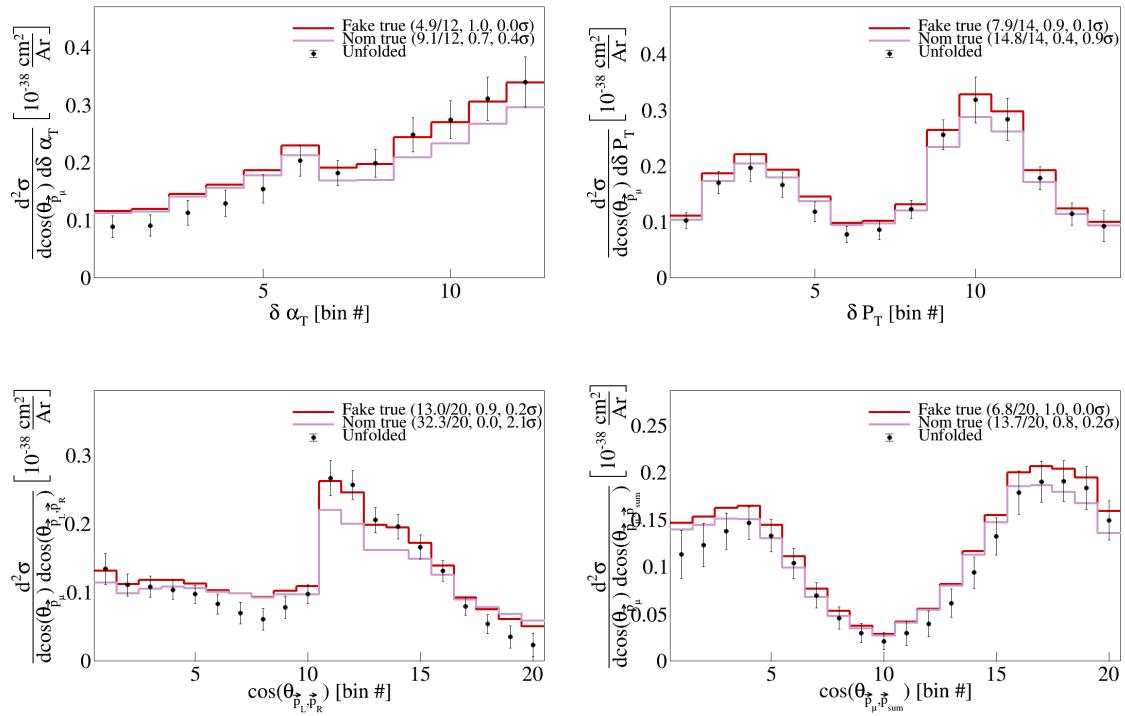


Figure 78: Unfolded combined weights fake data showing agreement with smeared fake signal data for serial double differential variables.

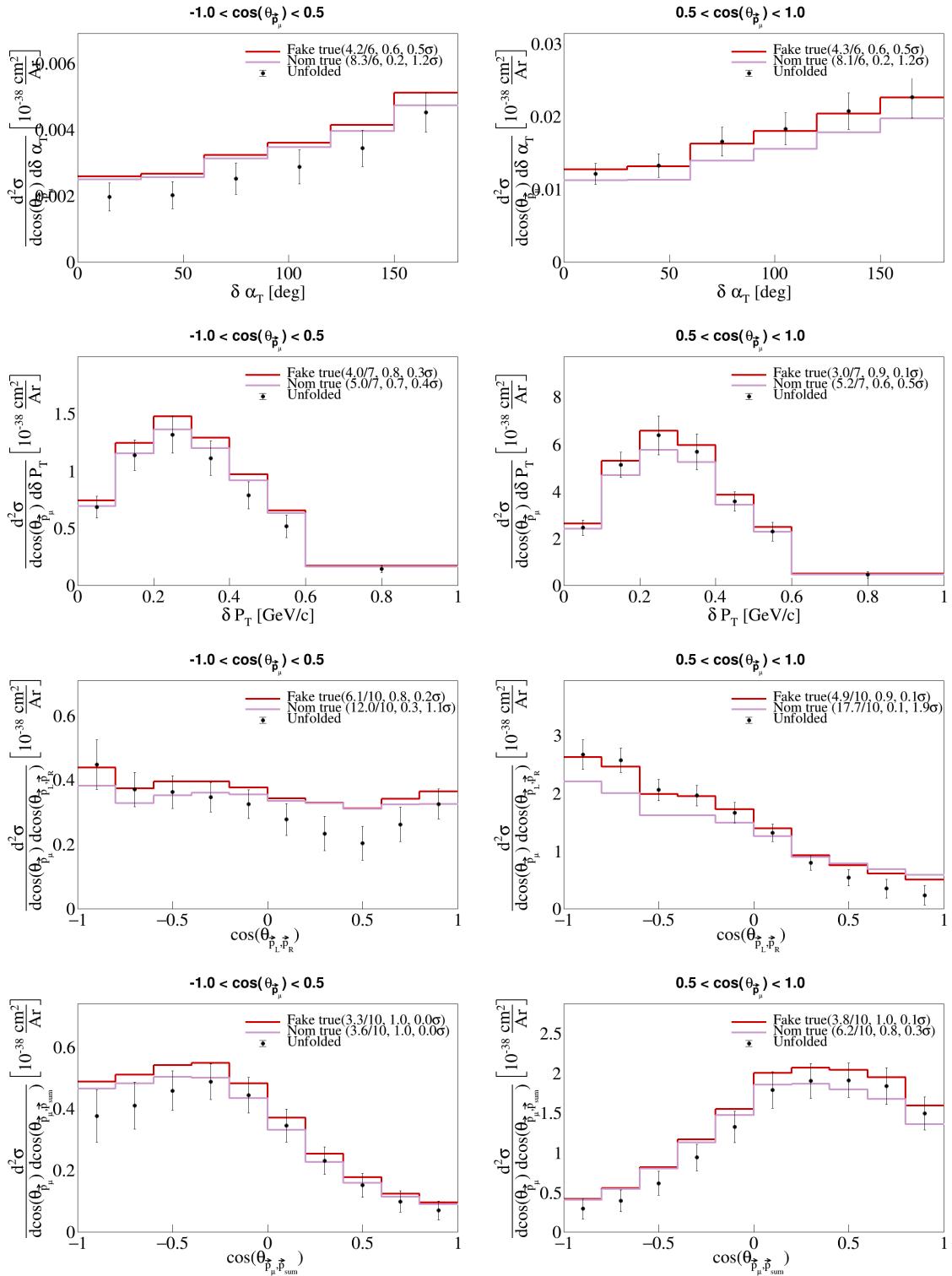


Figure 79: Unfolded combined weights fake data showing agreement with smeared fake signal data for sliced double differential variables.

298 6 SBND Data

299 Using the first available real data, we can perform initial comparisons between data and predictions. Since
 300 this first data does not have POT information yet, we only perform shape comparisons, i.e., we divide the
 301 event counts by the total number of events in the data. Further, the data does not have flash matching data
 302 necessary for our signal cuts. Therefore, we present some data before any cuts are applied (in neither the
 303 data nor the predictions), in Figure 80, which shows good agreement.

304 We show our usual variables in Figures 81 to 83, but these do not show the same agreement since we can
 305 not apply all the signal cuts, and the data is still low-statistics for signal events.

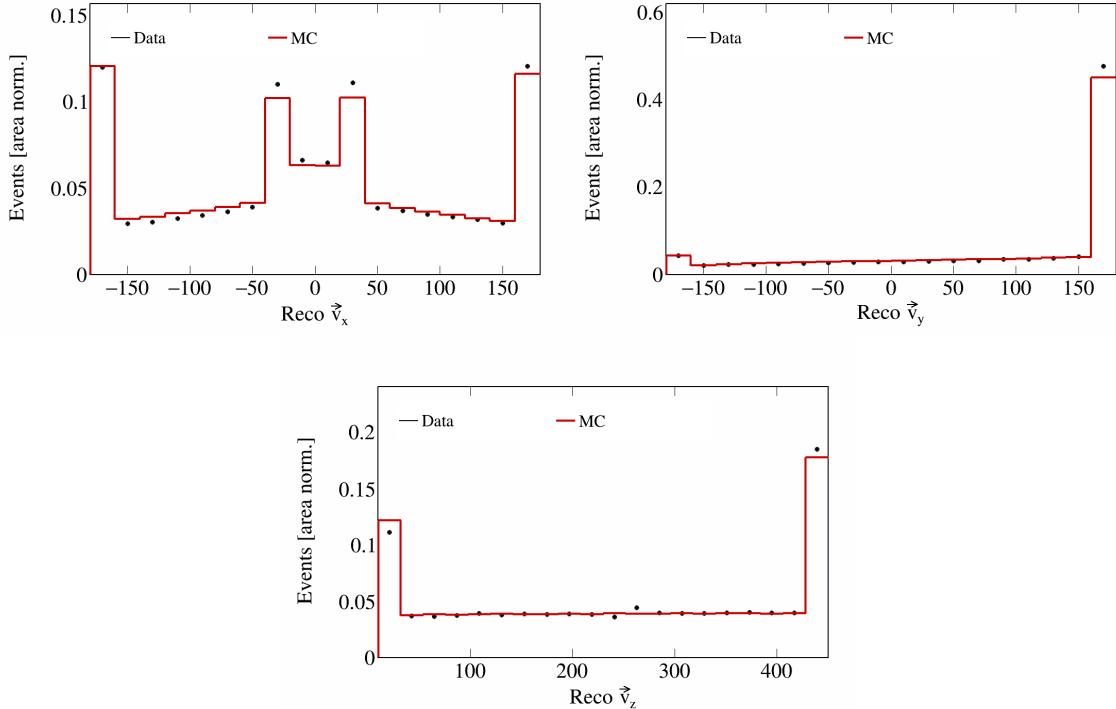


Figure 80: SBND data counts for vertex position before any cuts.

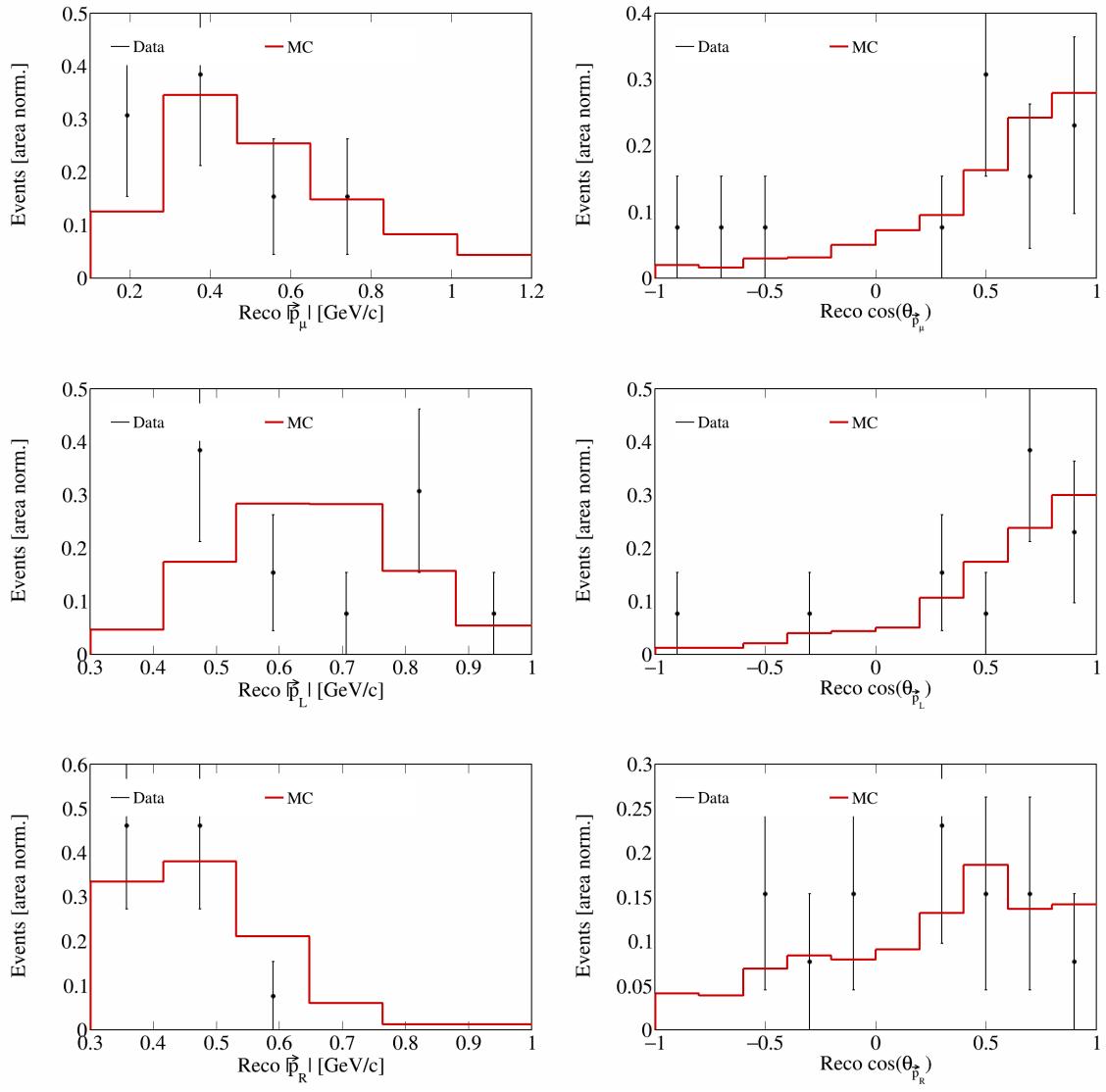


Figure 81: SBND data counts for momenta and opening angles of individual particles.

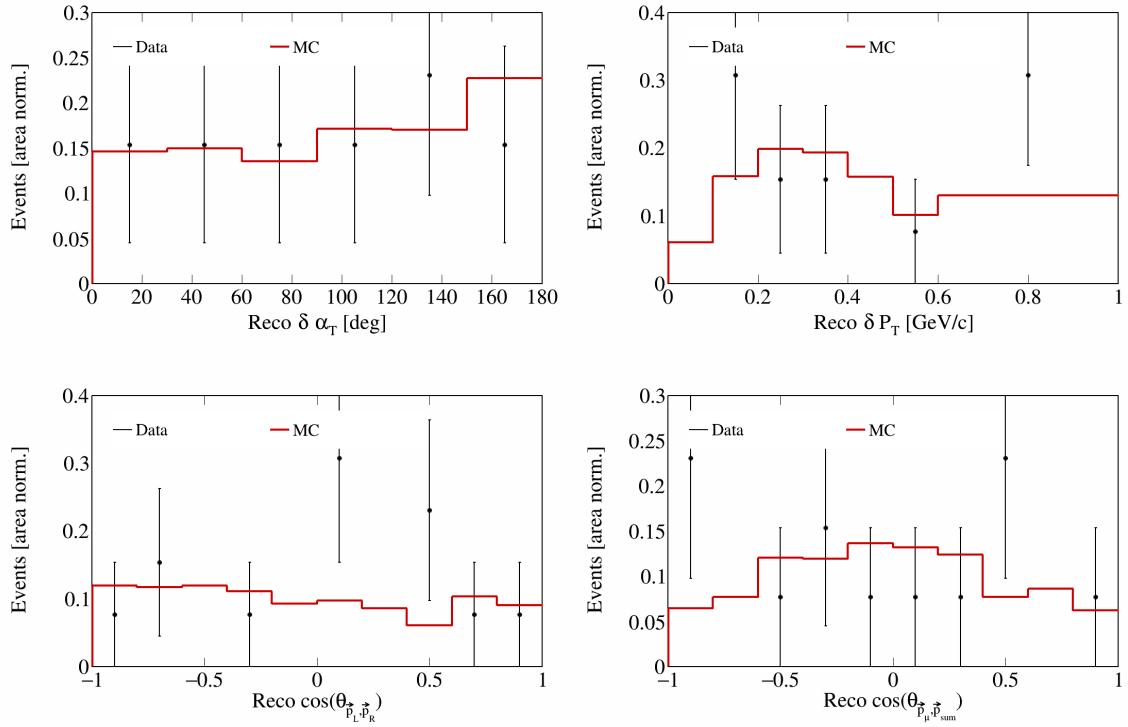


Figure 82: SBND data counts for transverse momentum and opening angles variables.

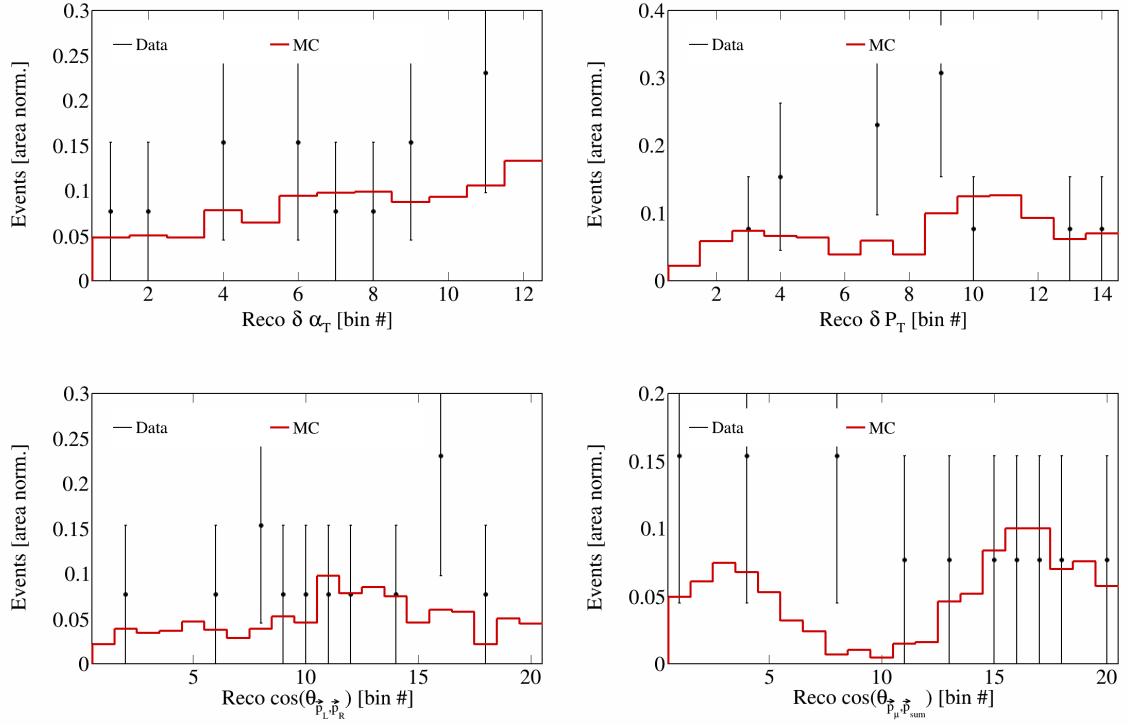


Figure 83: SBND data counts for serial double differential variables.

306 **7 Appendices**

307 **7.1 Cross section systematics**

308 In this appendix, the variations, covariance matrices, fractional covariance matrices, and correlation matrices
 309 are plotted for all of the cross section systematics and variables.

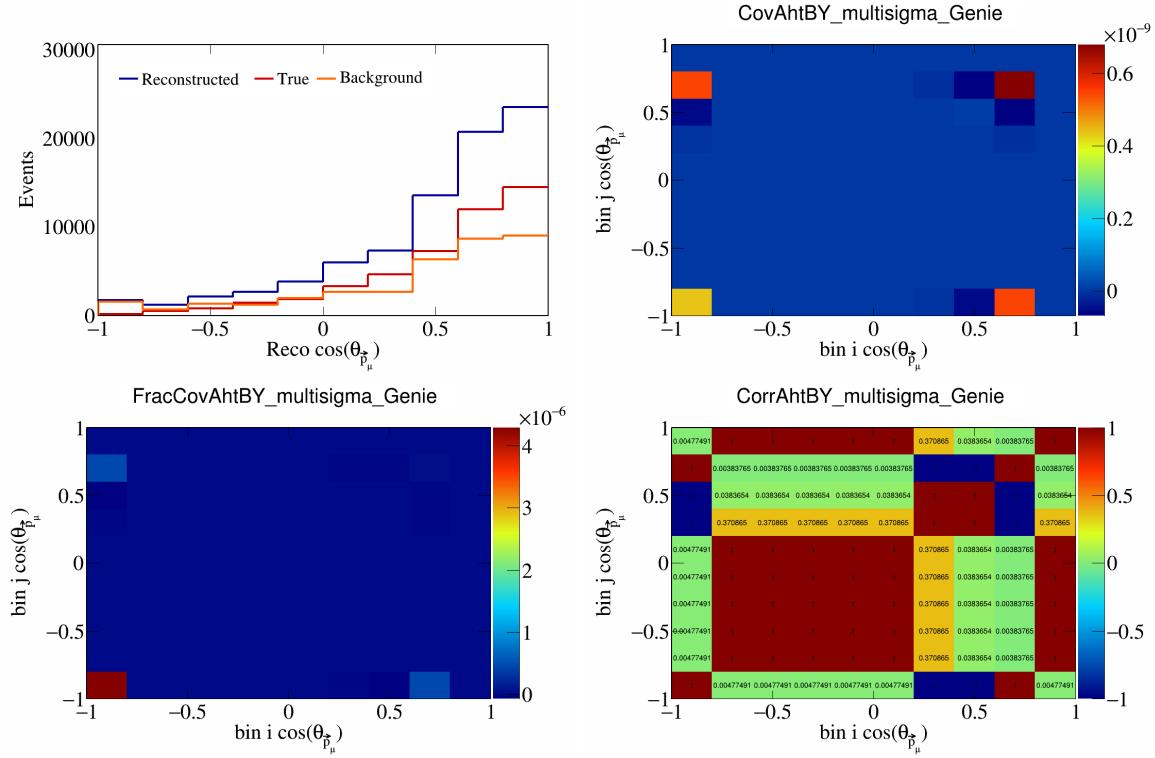


Figure 84: AhtBY variations for $\cos(\theta_{\vec{p}_\mu})$.

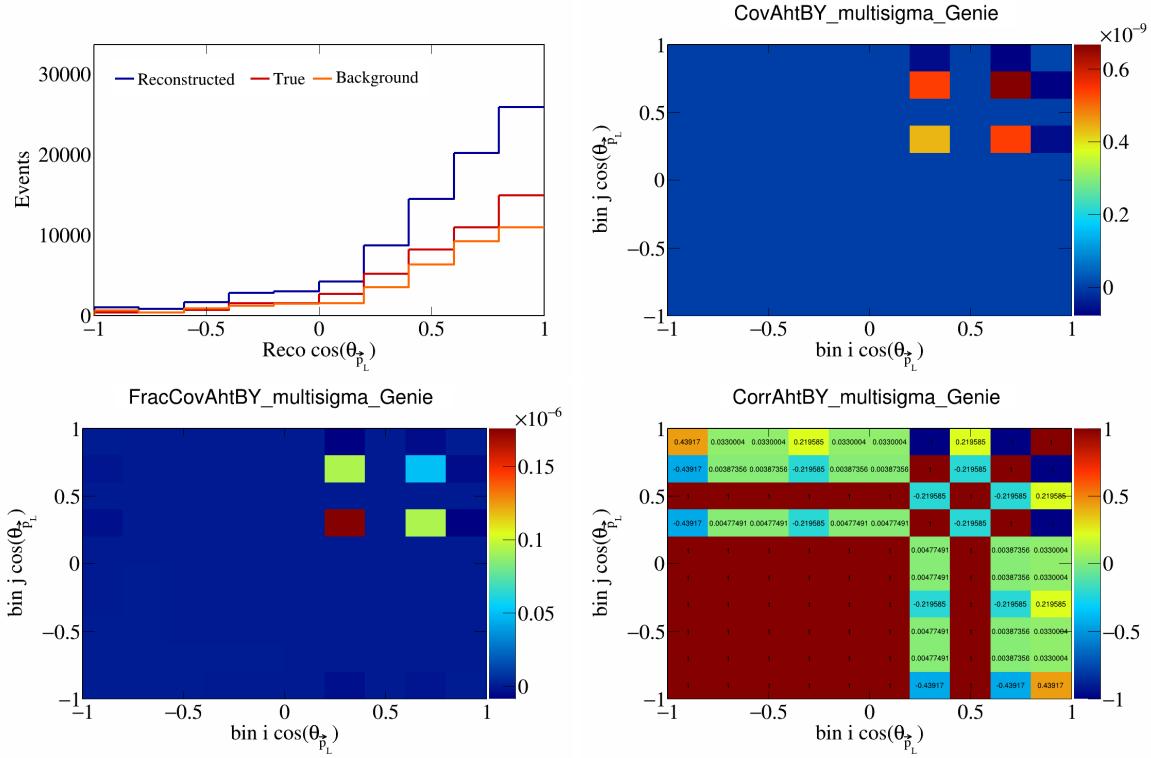


Figure 85: AhtBY variations for $\cos(\theta_{\vec{p}_L})$.

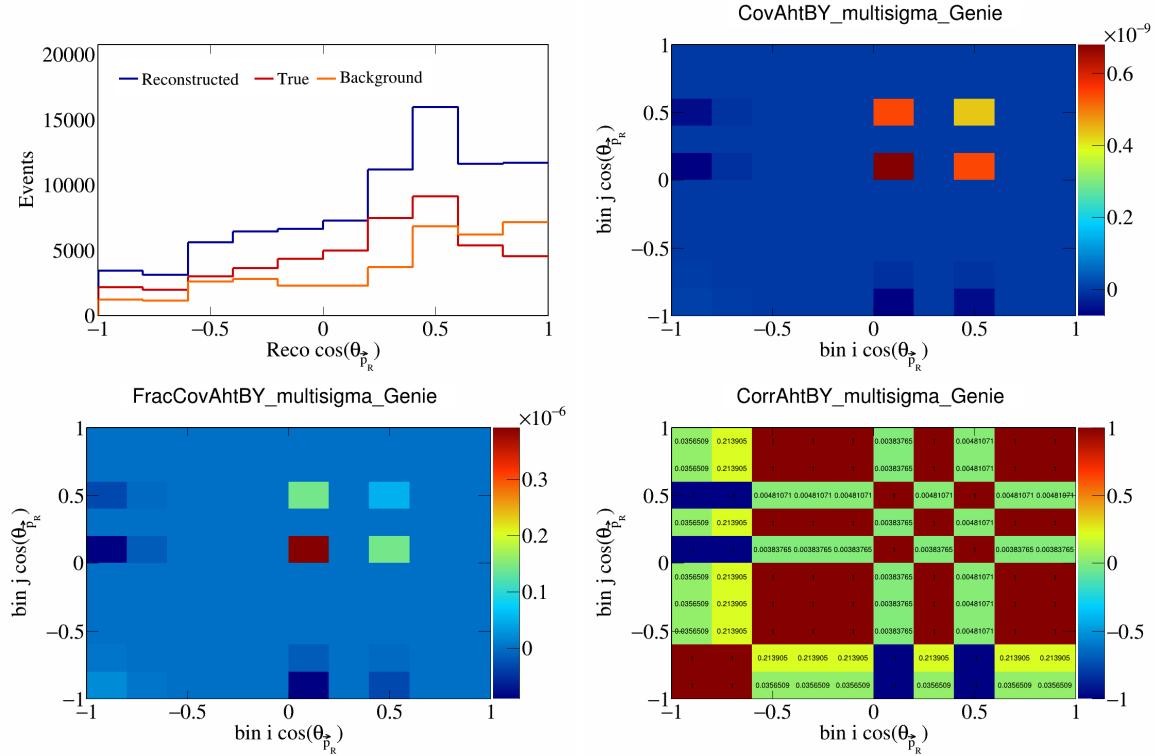


Figure 86: AhtBY variations for $\cos(\theta_{\vec{p}_R})$.

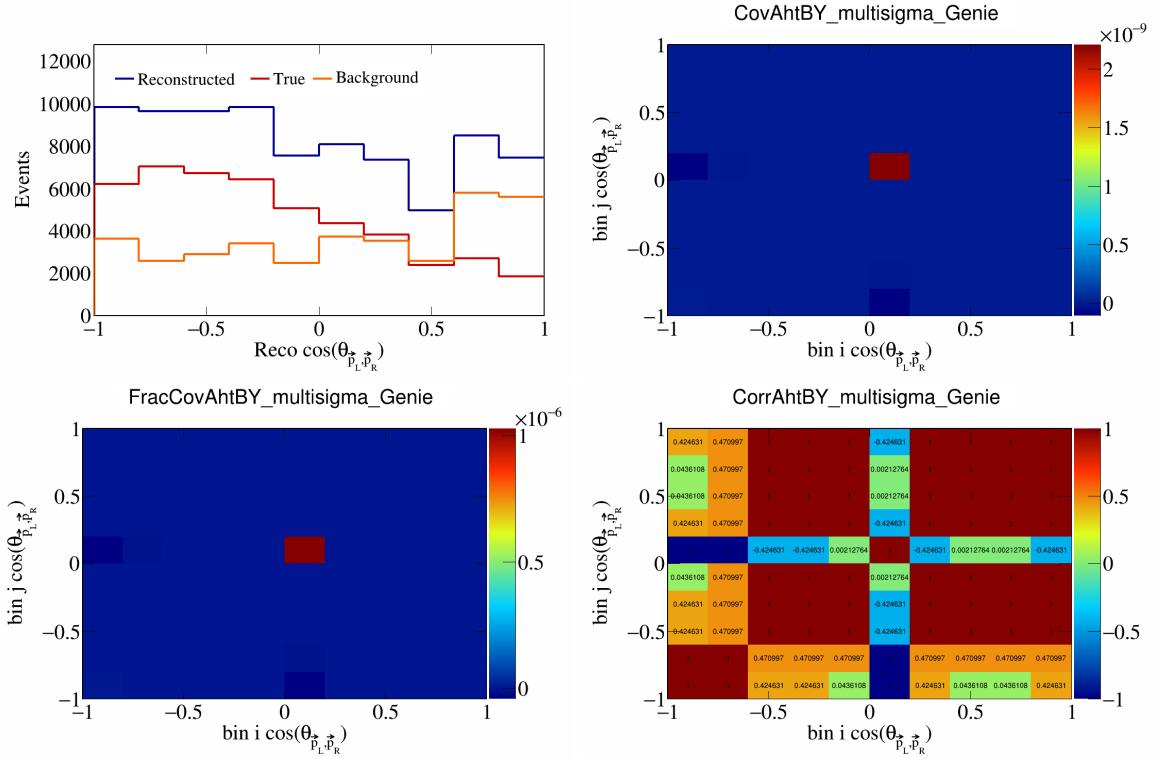


Figure 87: AhtBY variations for $\cos(\theta_{\vec{p}_L, \vec{p}_R})$.

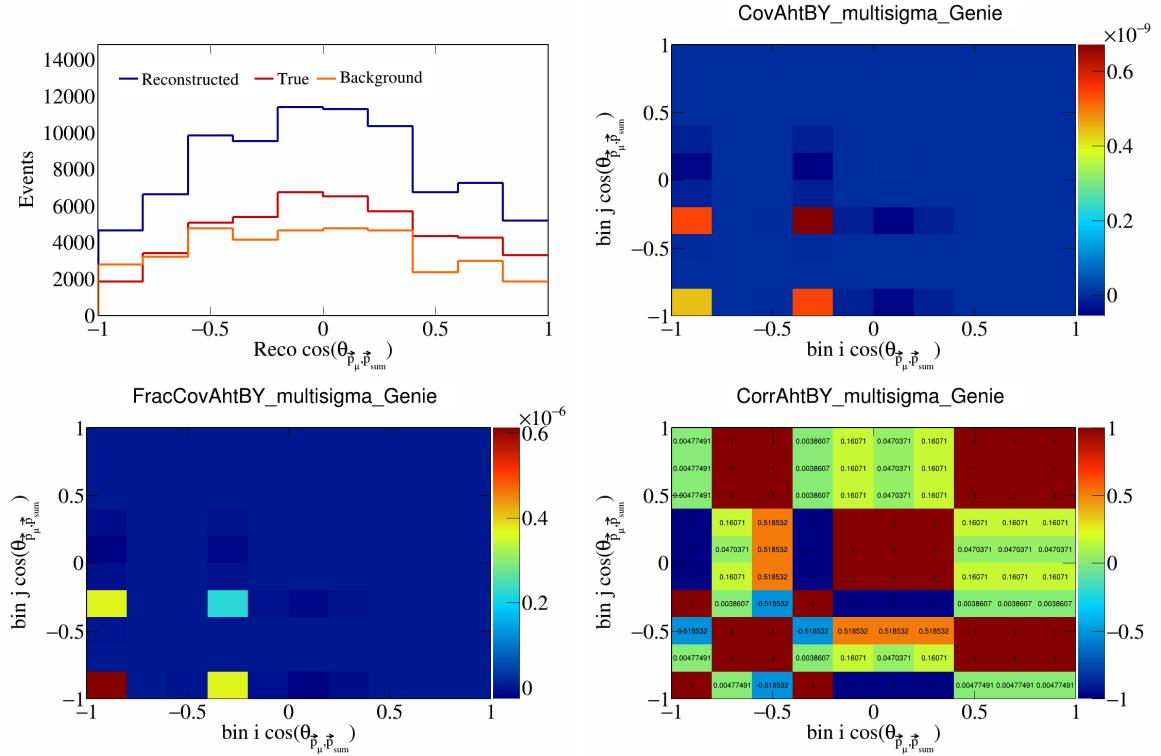


Figure 88: AhtBY variations for $\cos(\theta_{\vec{p}_\mu, \vec{p}_{\text{sum}}})$.

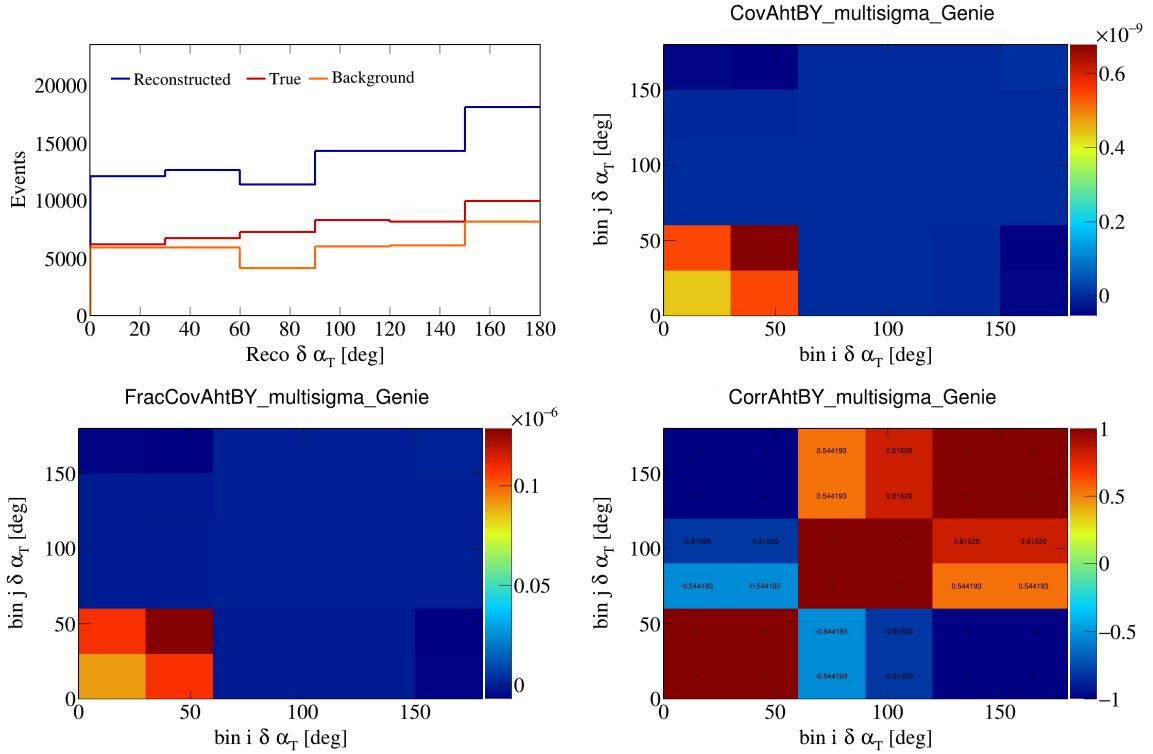


Figure 89: AhtBY variations for $\delta\alpha_T$.

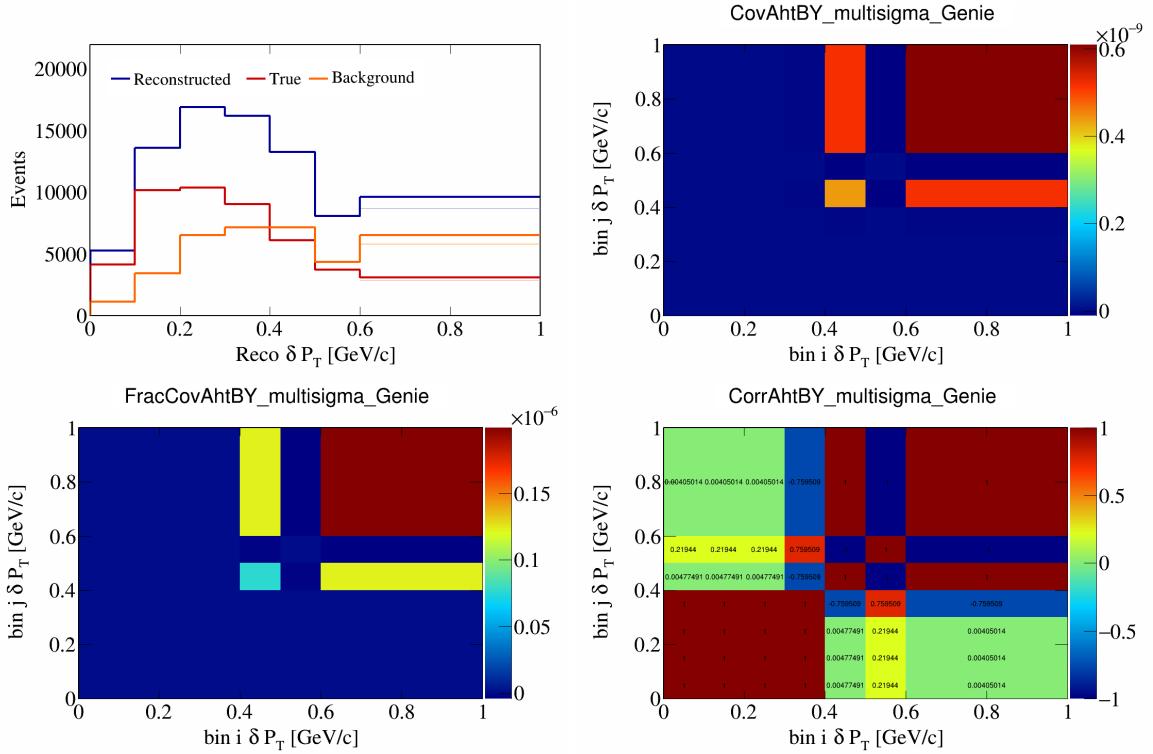


Figure 90: AhtBY variations for δP_T .

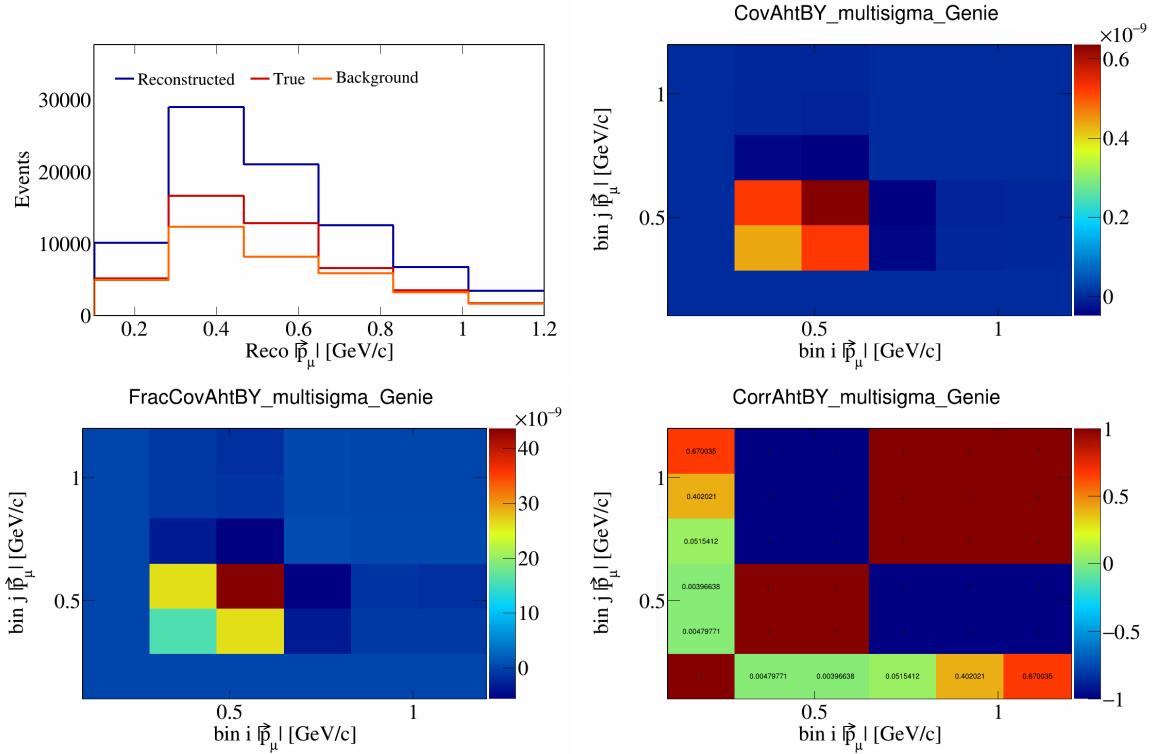


Figure 91: AhtBY variations for $|\vec{p}_\mu|$.

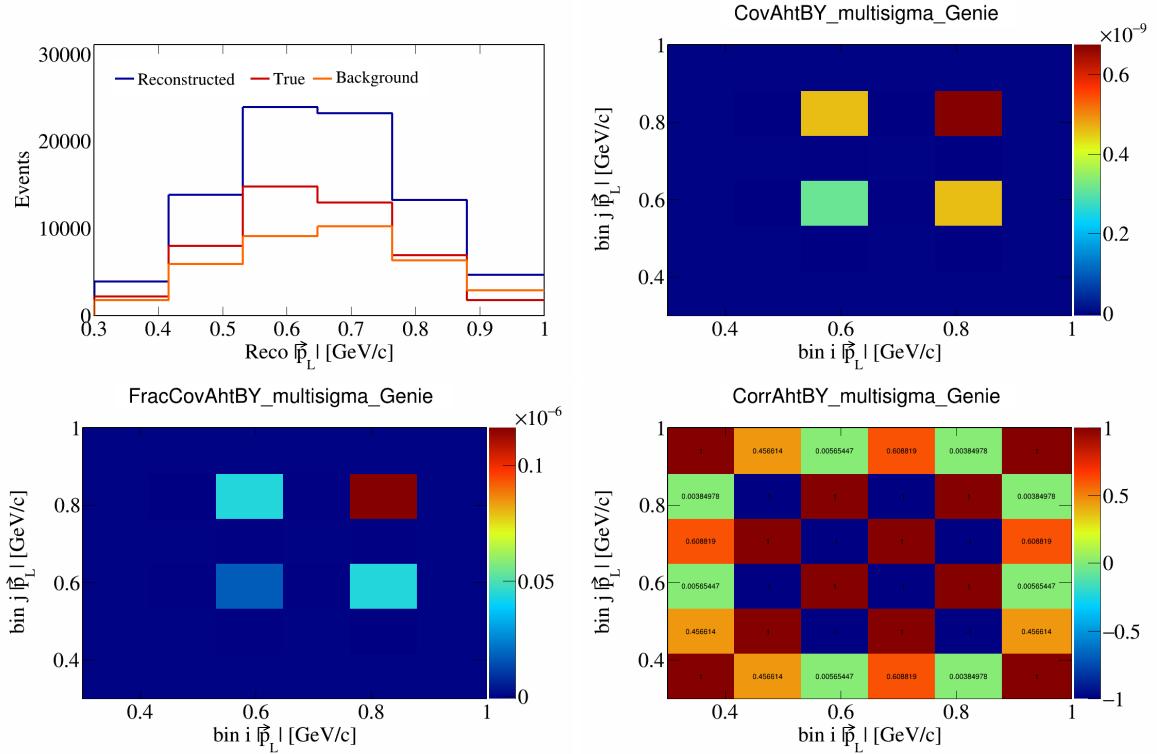


Figure 92: AhtBY variations for $|\vec{p}_L|$.

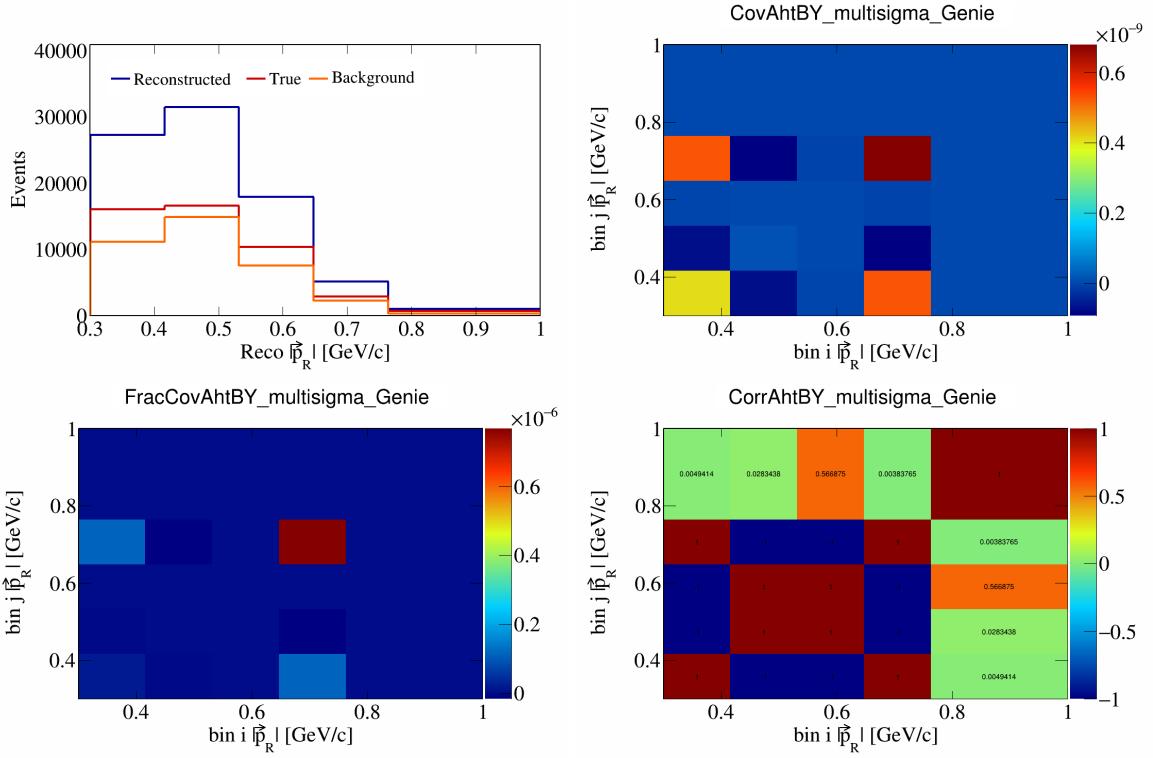


Figure 93: AhtBY variations for $|\vec{p}_R|$.

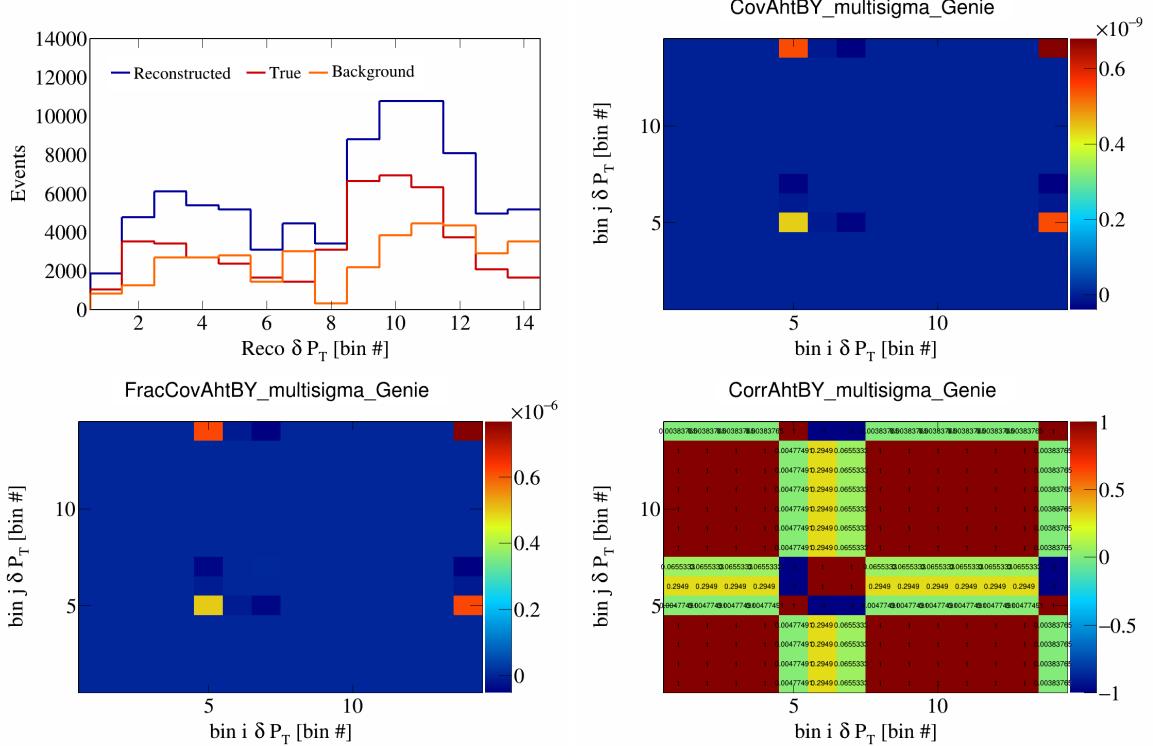


Figure 94: AhtBY variations for δP_T in $\cos(\theta_{\vec{p}_\mu})$.

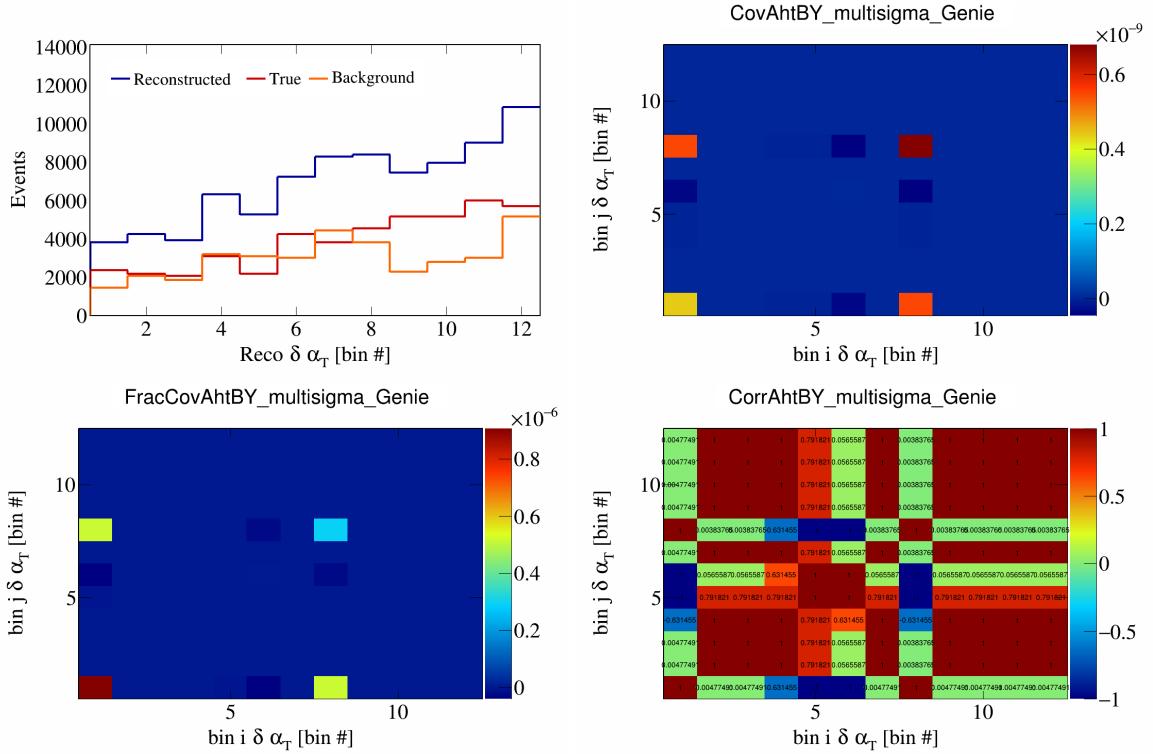


Figure 95: AhtBY variations for $\delta\alpha_T$ in $\cos(\theta_{\vec{p}_\mu})$.

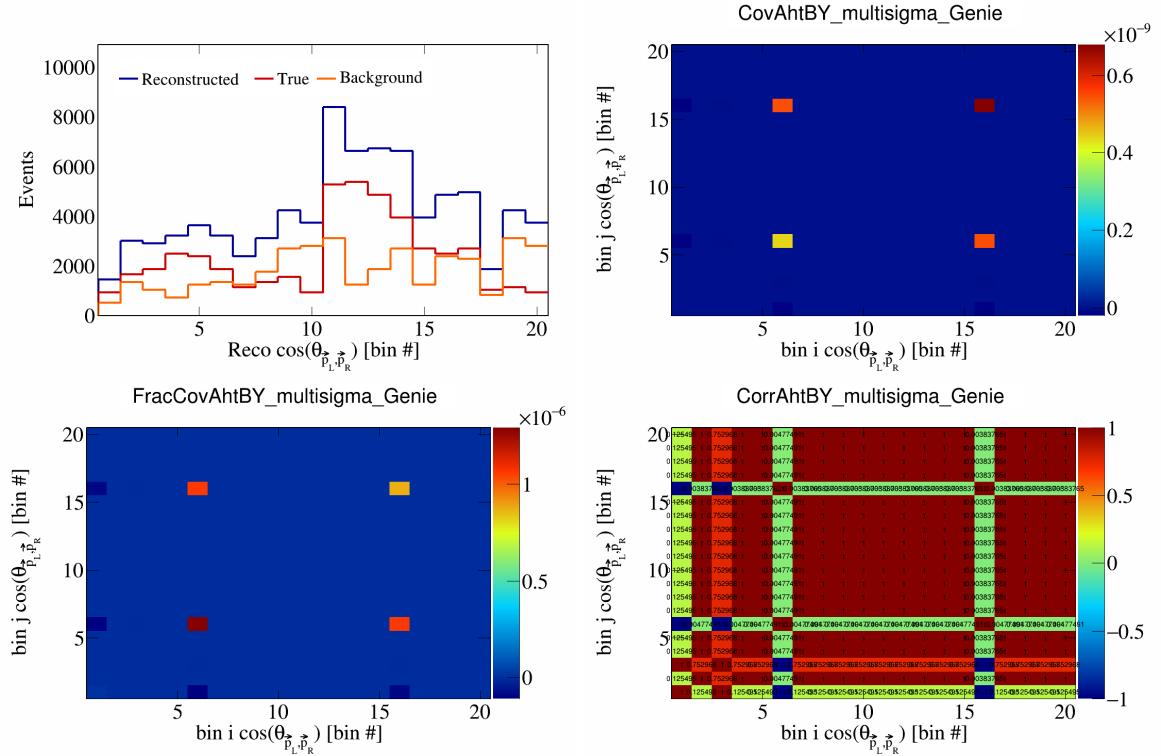


Figure 96: AhtBY variations for $\cos(\theta_{\vec{p}_L, \vec{p}_R})$ in $\cos(\theta_{\vec{p}_\mu})$.

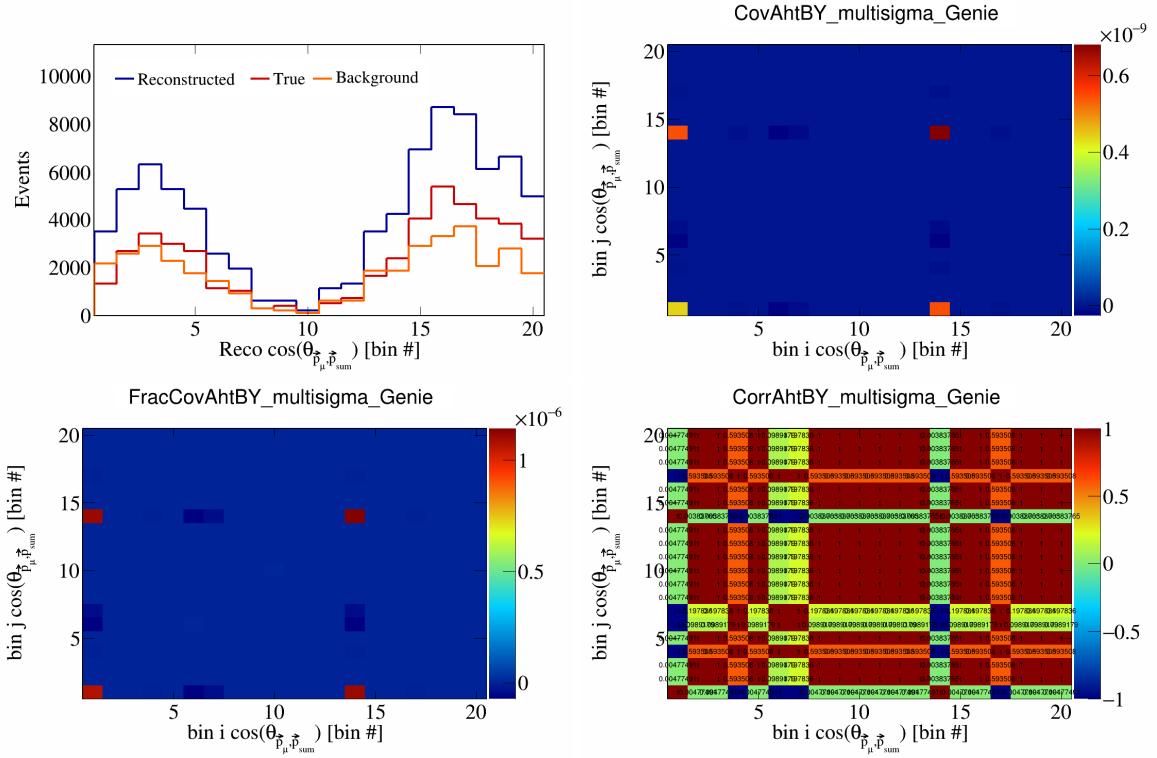


Figure 97: AhtBY variations for $\cos(\theta_{\vec{p}_\mu, \vec{p}_{\text{sum}}})$ in $\cos(\theta_{\vec{p}_\mu})$.

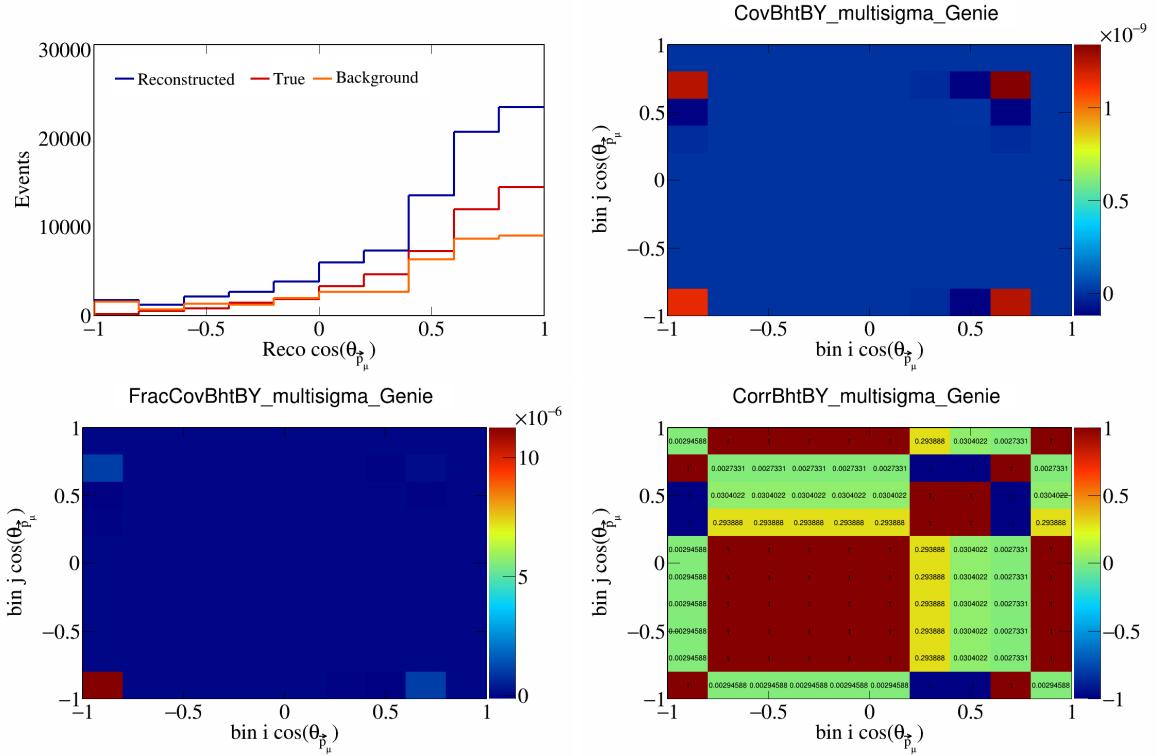


Figure 98: BhtBY variations for $\cos(\theta_{\vec{p}_\mu})$.

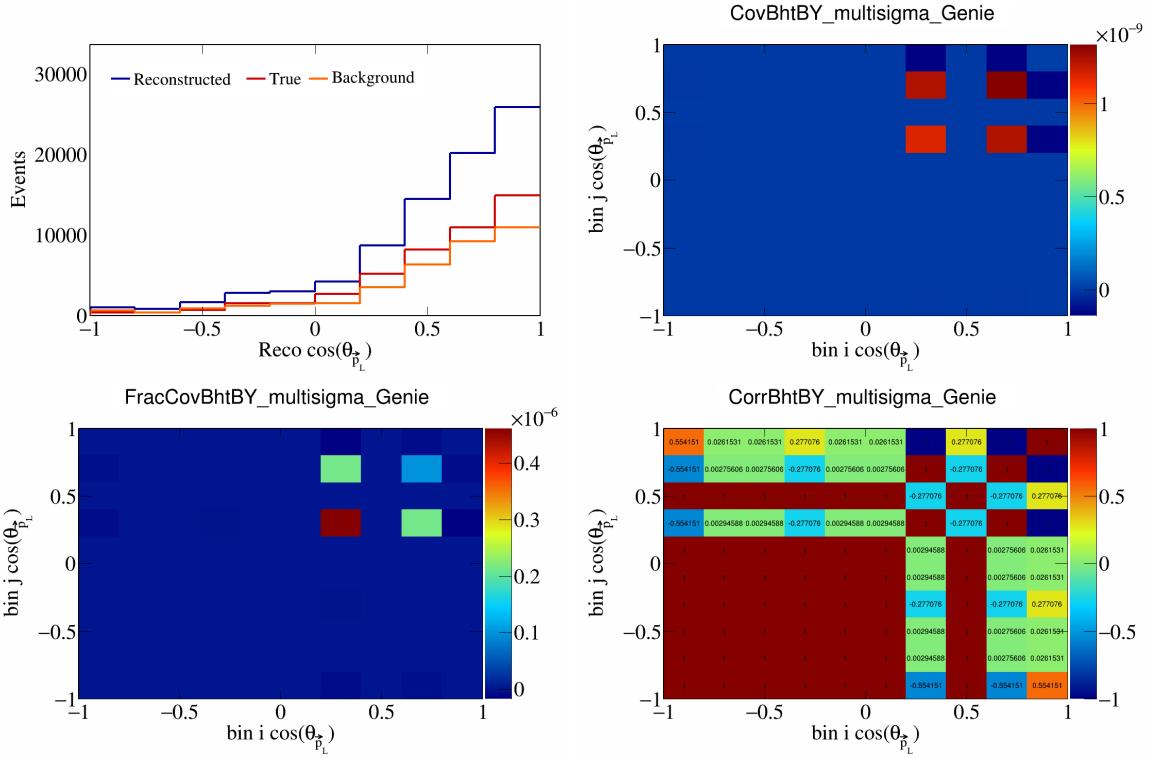


Figure 99: BhtBY variations for $\cos(\theta_{\vec{p}_L})$.

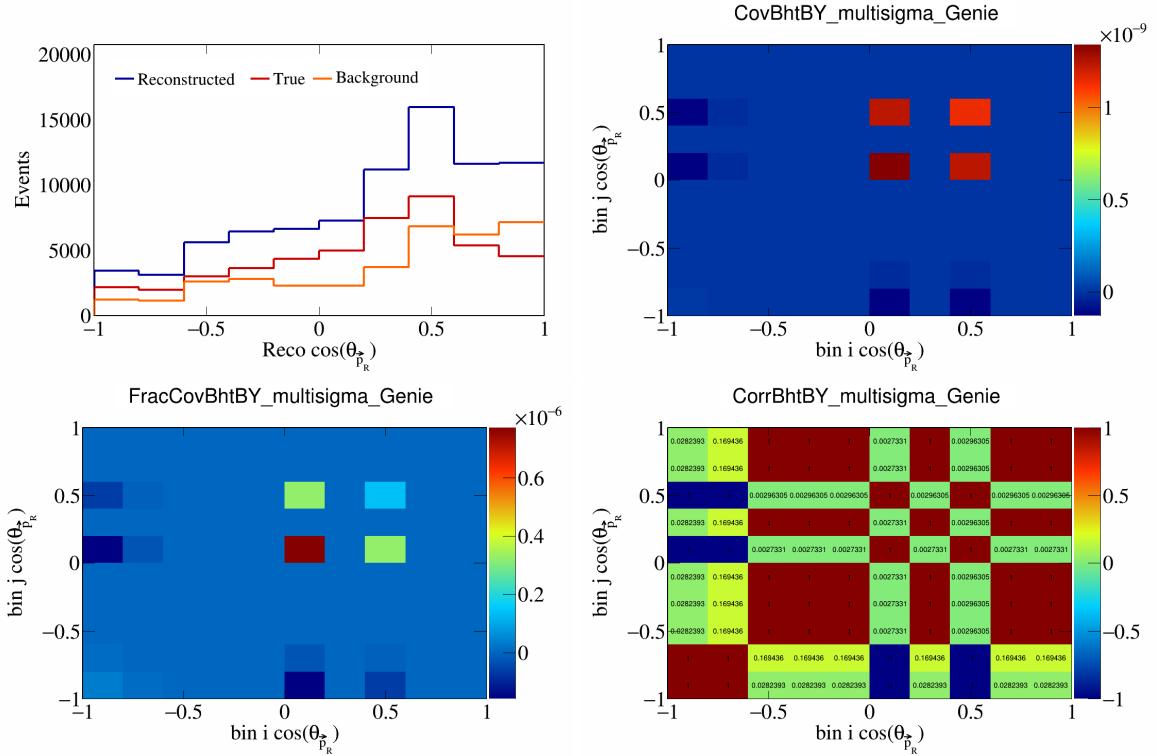


Figure 100: BhtBY variations for $\cos(\theta_{\vec{p}_R})$.

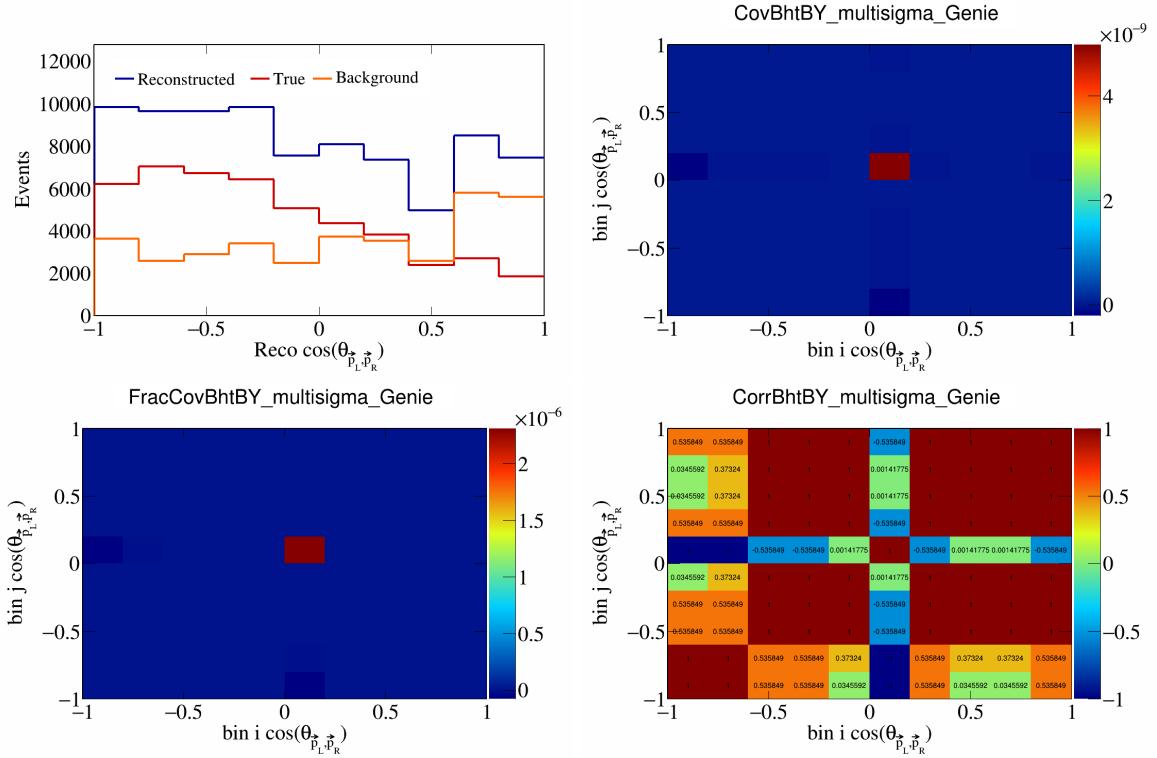


Figure 101: BhtBY variations for $\cos(\theta_{\vec{p}_L, \vec{p}_R})$.

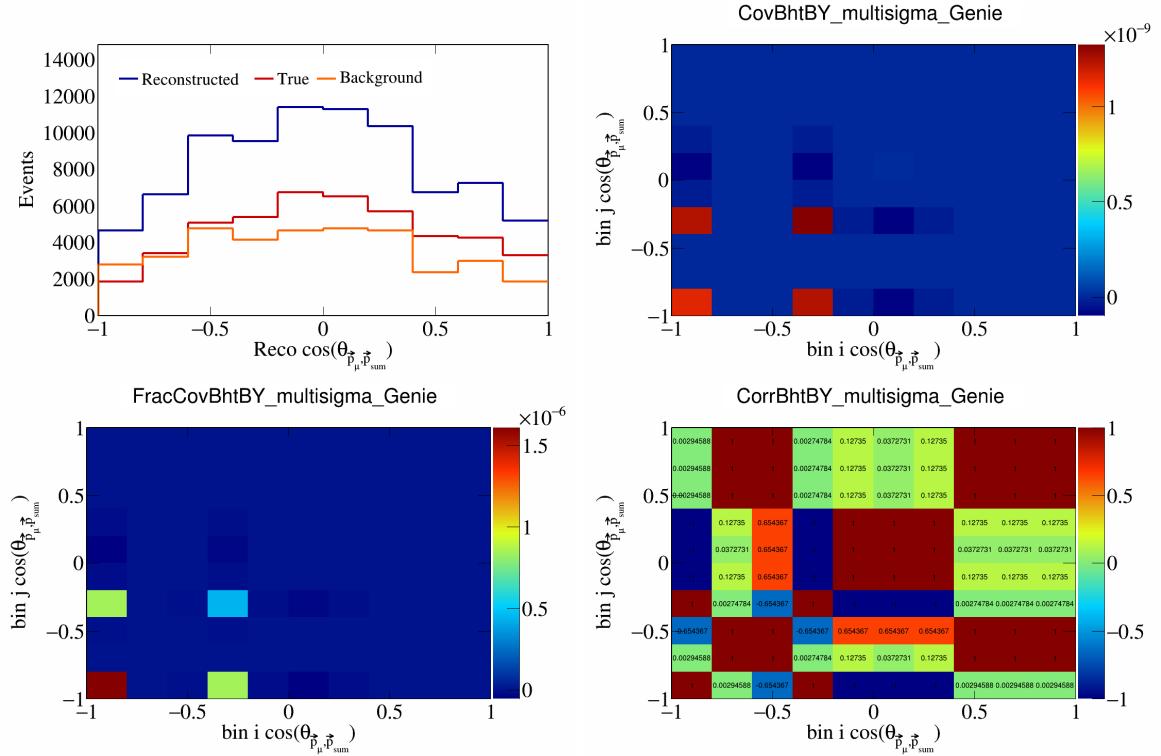


Figure 102: BhtBY variations for $\cos(\theta_{\vec{p}_\mu, \vec{p}_{\text{sum}}})$.

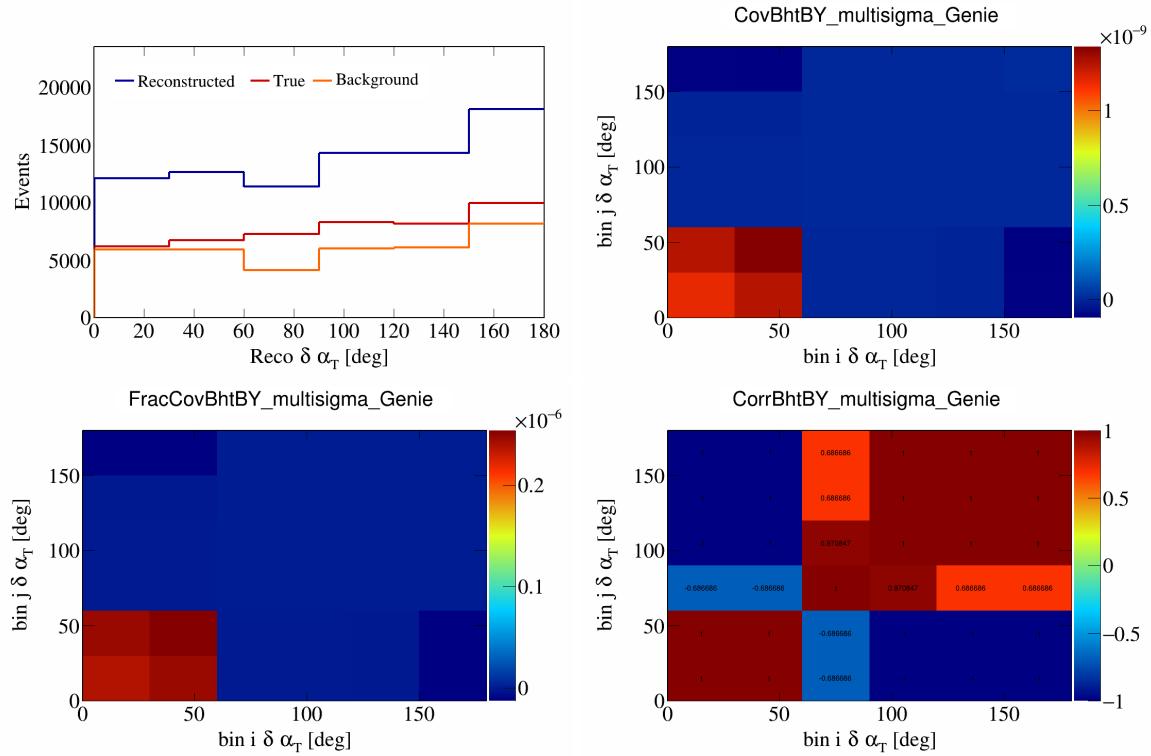


Figure 103: BhtBY variations for $\delta\alpha_T$.

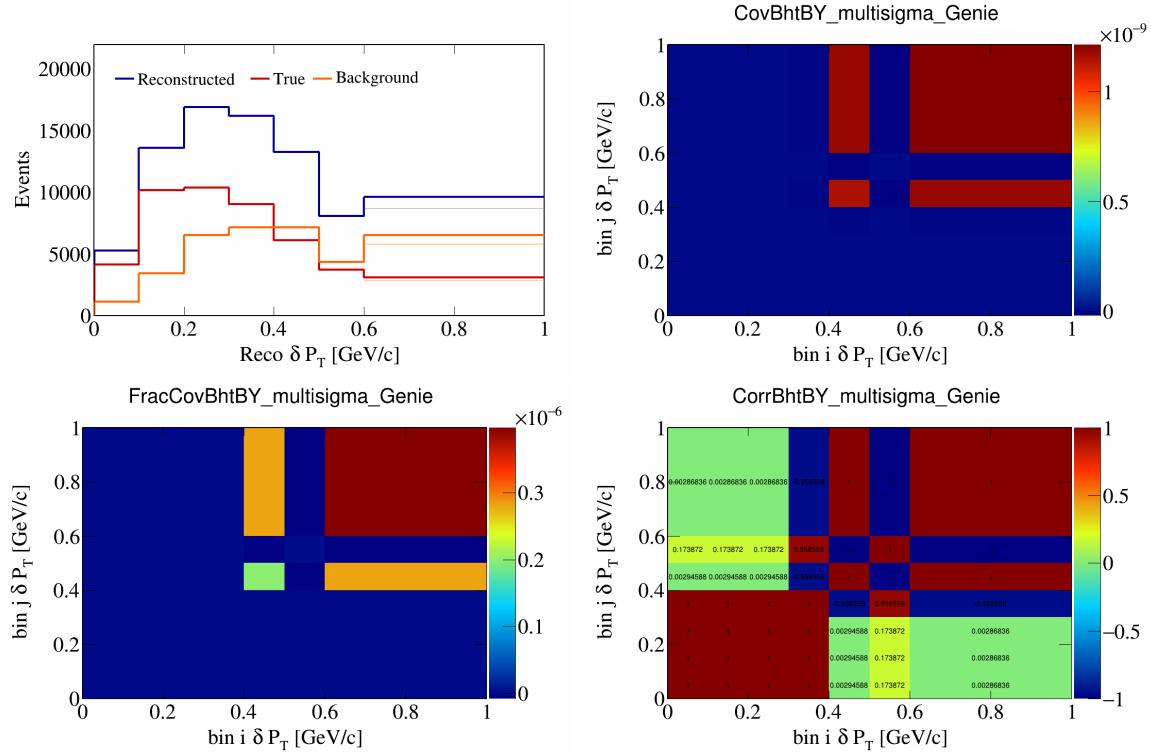


Figure 104: BhtBY variations for δP_T .

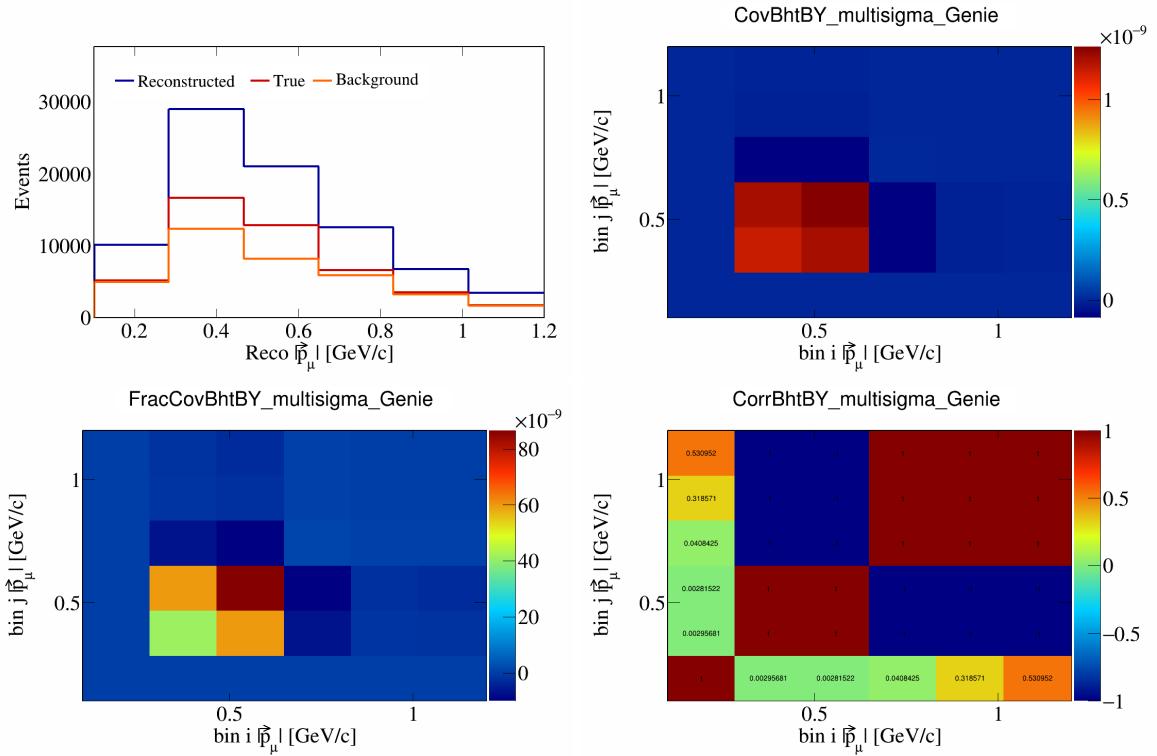


Figure 105: BhtBY variations for $|\vec{p}_\mu|$.

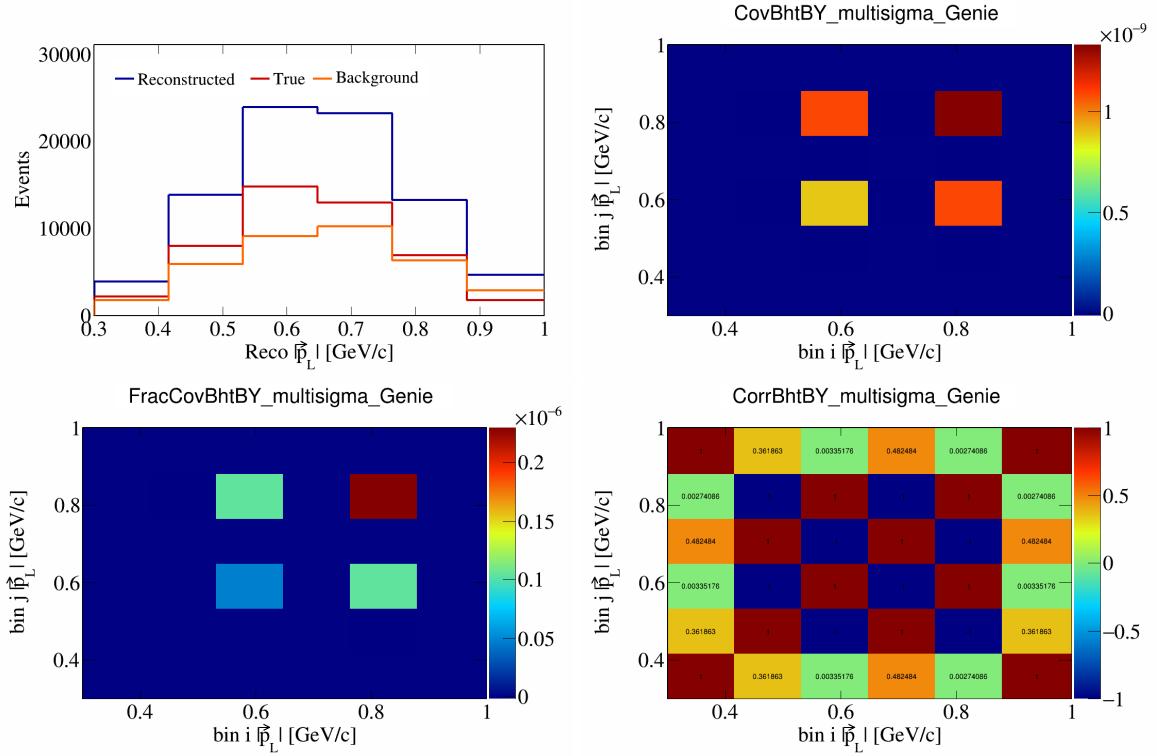


Figure 106: BhtBY variations for $|\vec{p}_L|$.

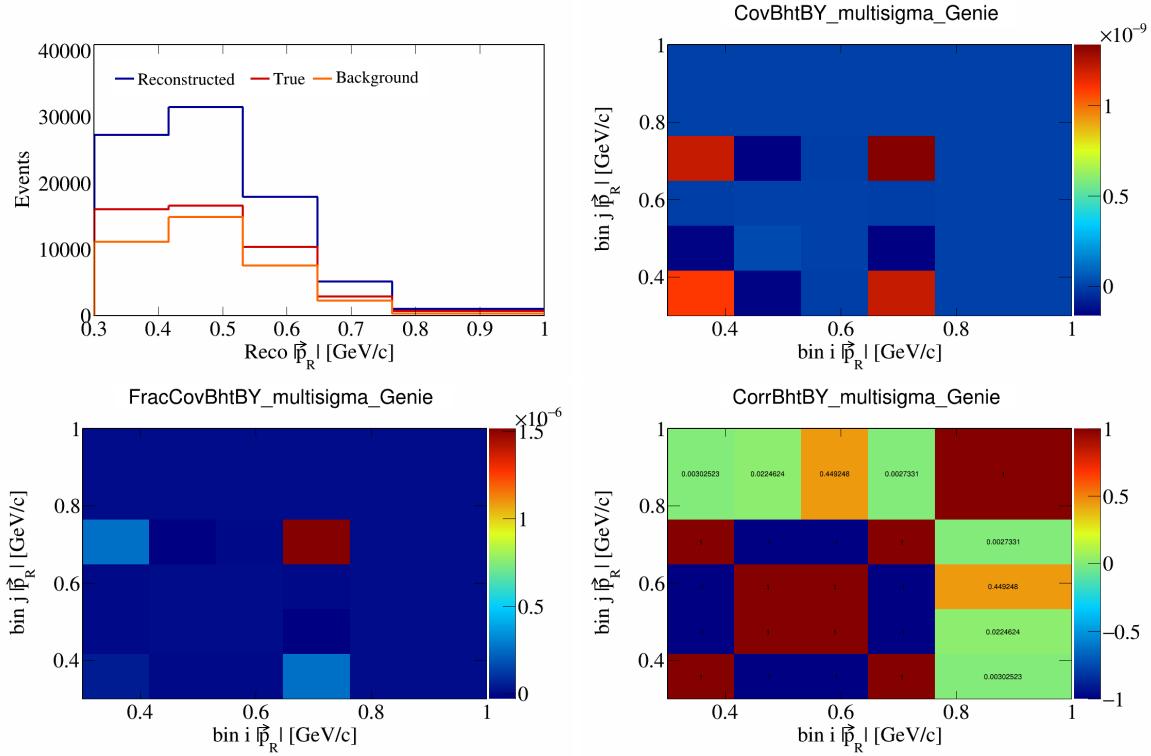


Figure 107: BhtBY variations for $|\vec{p}_R|$.

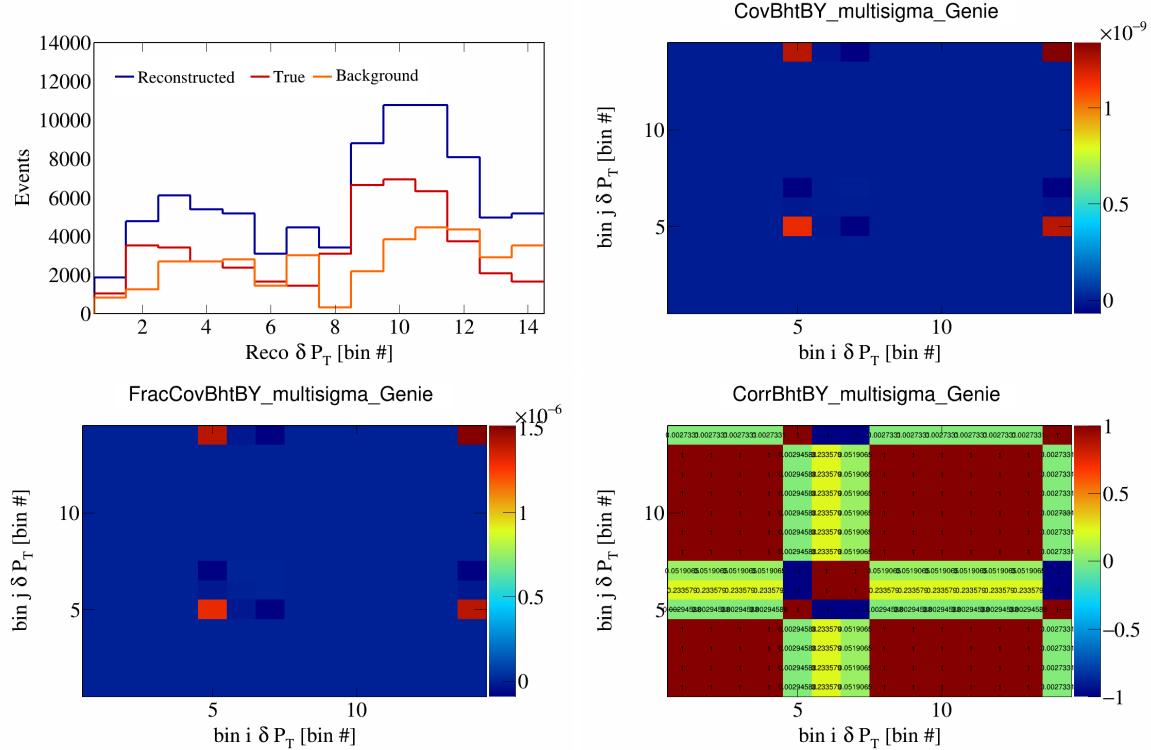


Figure 108: BhtBY variations for δP_T in $\cos(\theta_{\vec{p}_\mu})$.

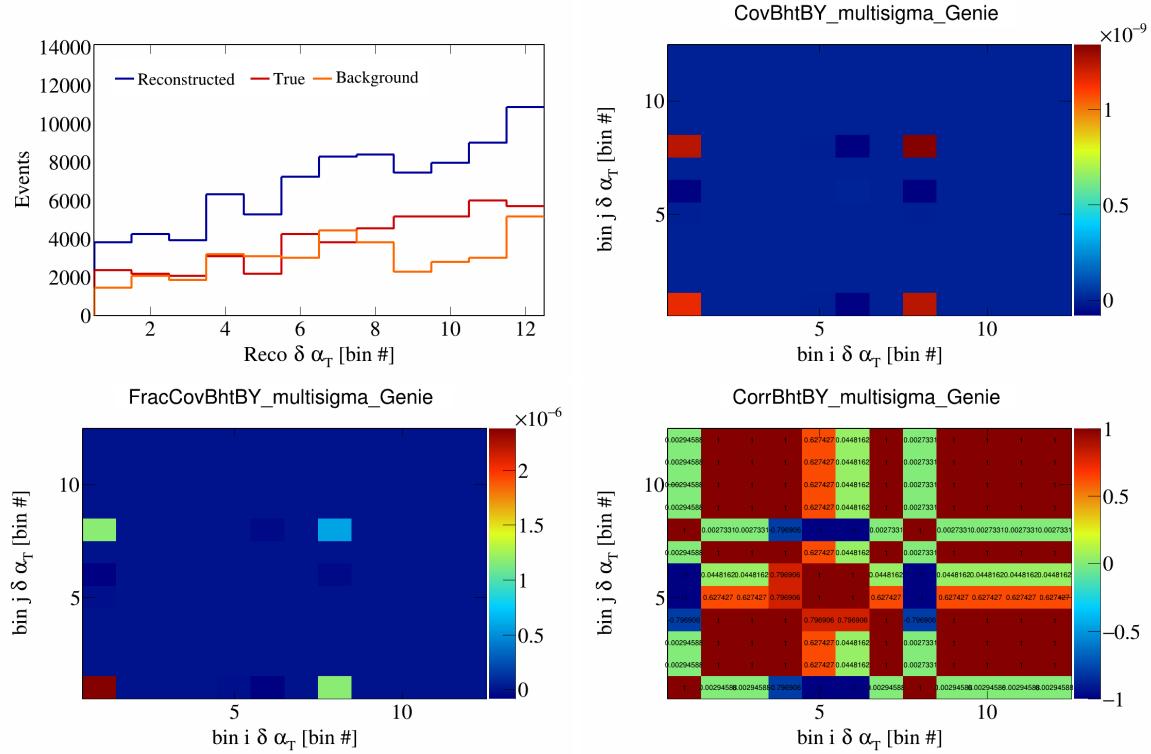


Figure 109: BhtBY variations for $\delta\alpha_T$ in $\cos(\theta_{\vec{p}_\mu})$.

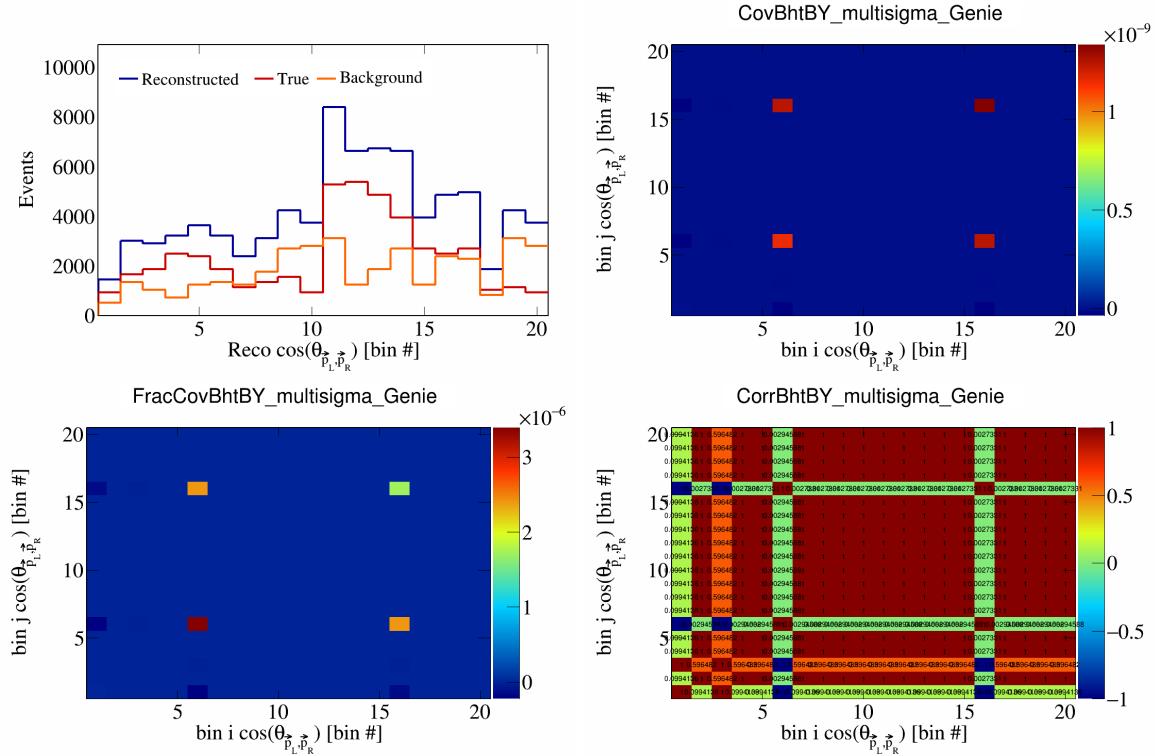


Figure 110: BhtBY variations for $\cos(\theta_{\vec{p}_L, \vec{p}_R})$ in $\cos(\theta_{\vec{p}_\mu})$.

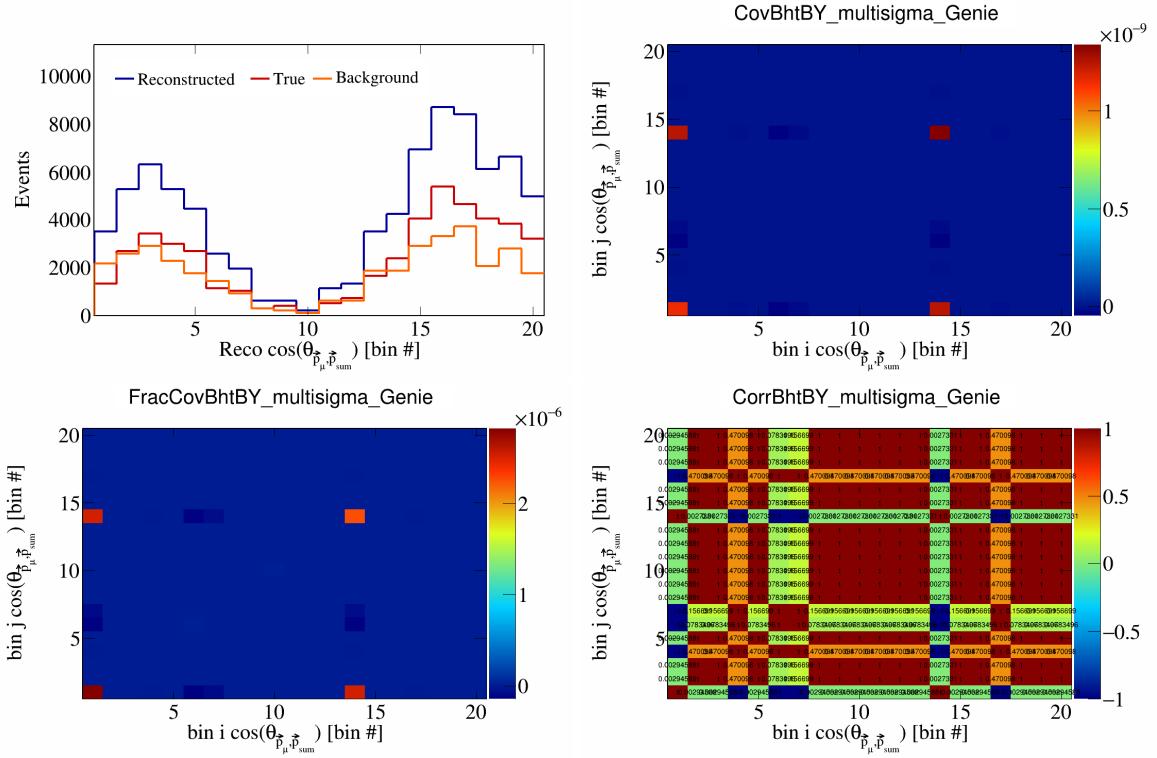


Figure 111: BhtBY variations for $\cos(\theta_{\vec{p}_\mu, \vec{p}_{\text{sum}}})$ in $\cos(\theta_{\vec{p}_\mu})$.

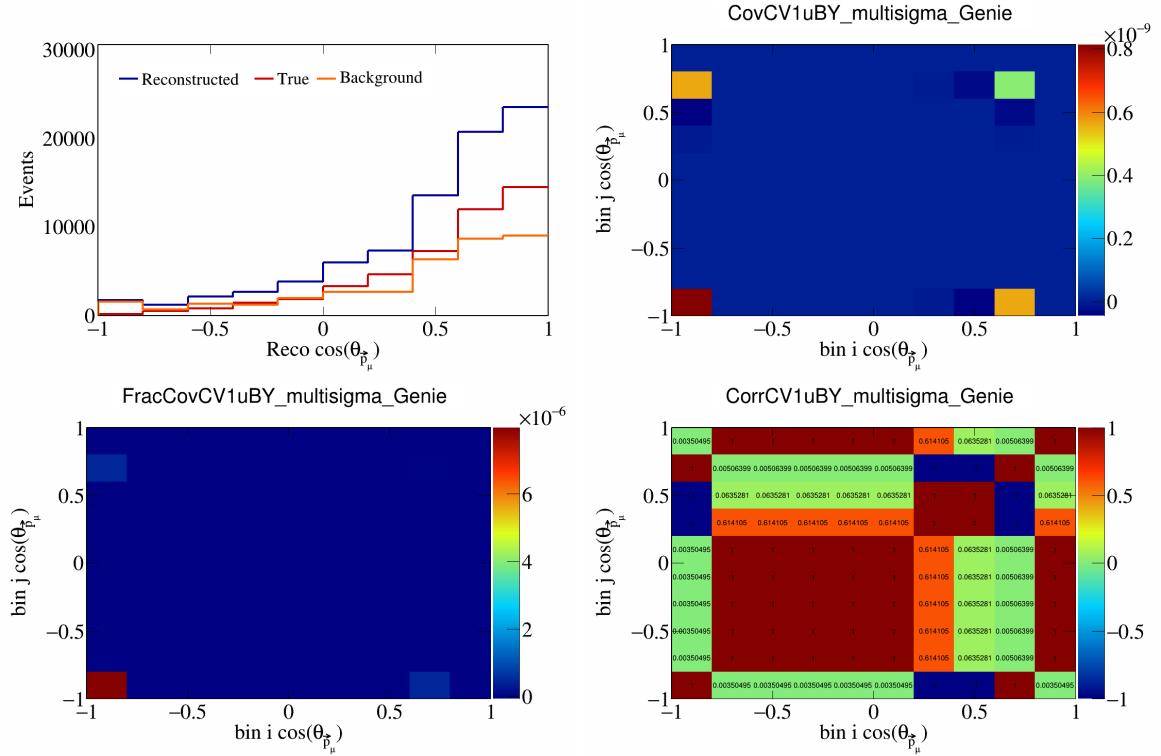


Figure 112: CV1uBY variations for $\cos(\theta_{\vec{p}_\mu})$.

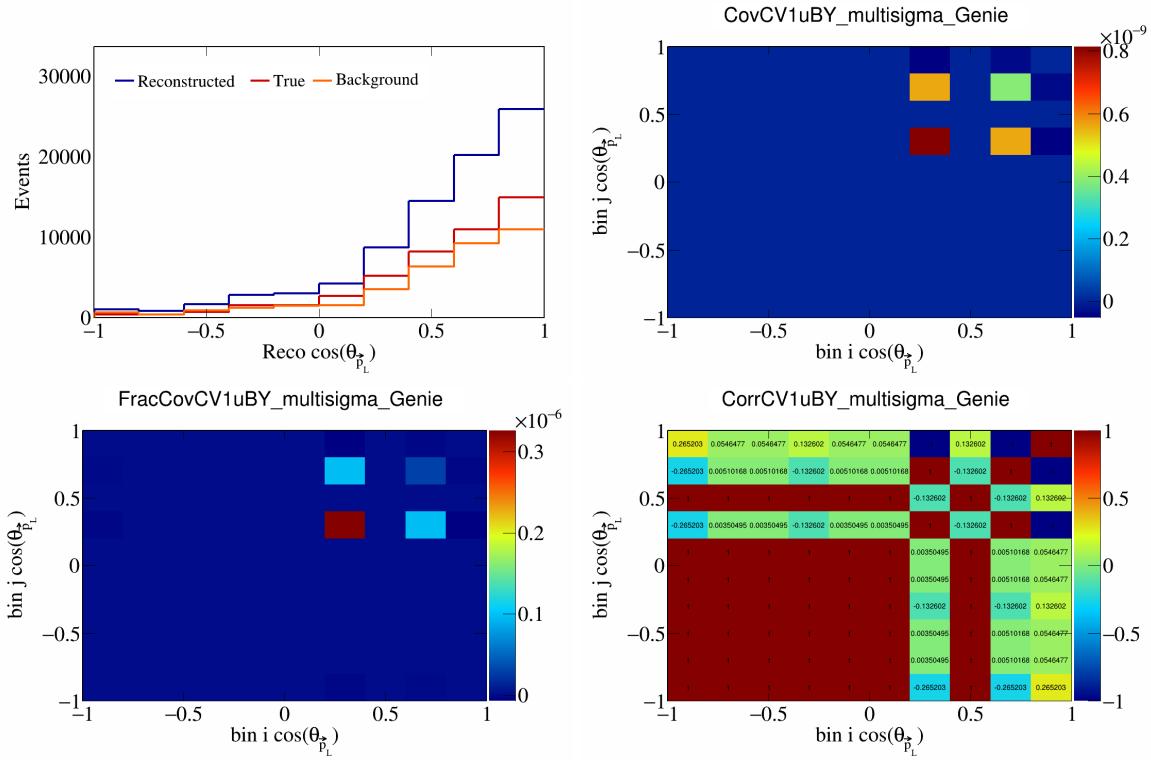


Figure 113: CV1uBY variations for $\cos(\theta_{\vec{p}_L})$.

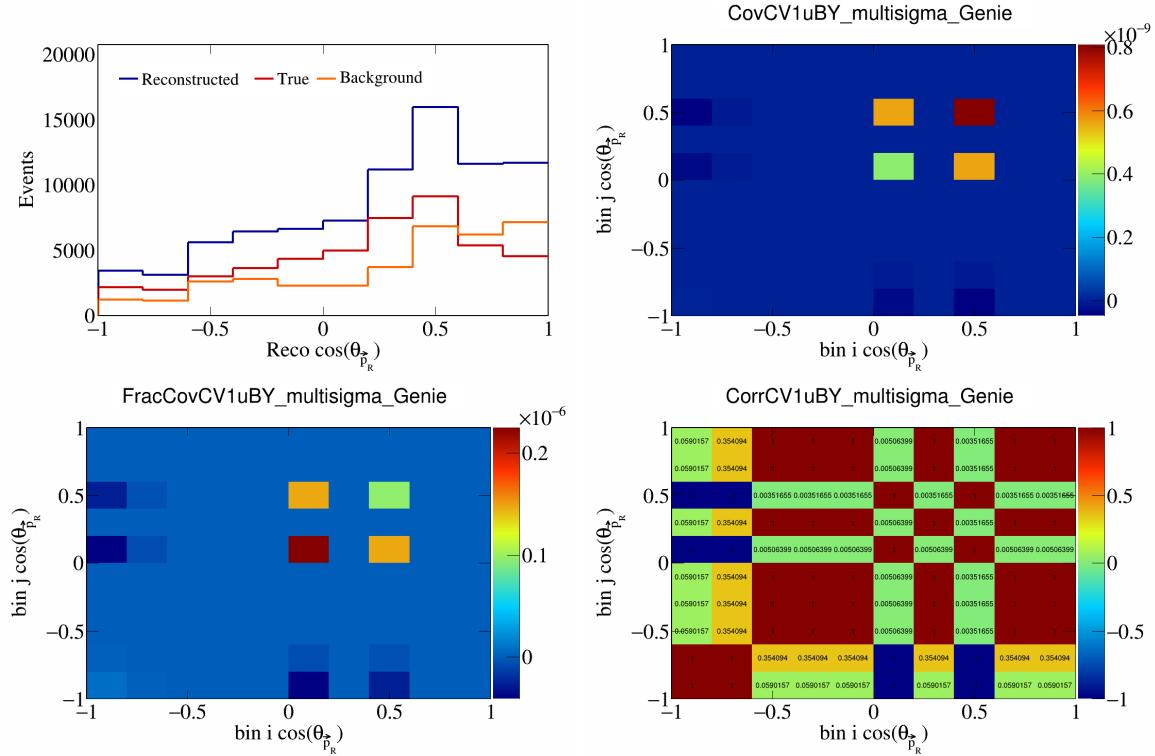


Figure 114: CV1uBY variations for $\cos(\theta_{\vec{p}_R})$.

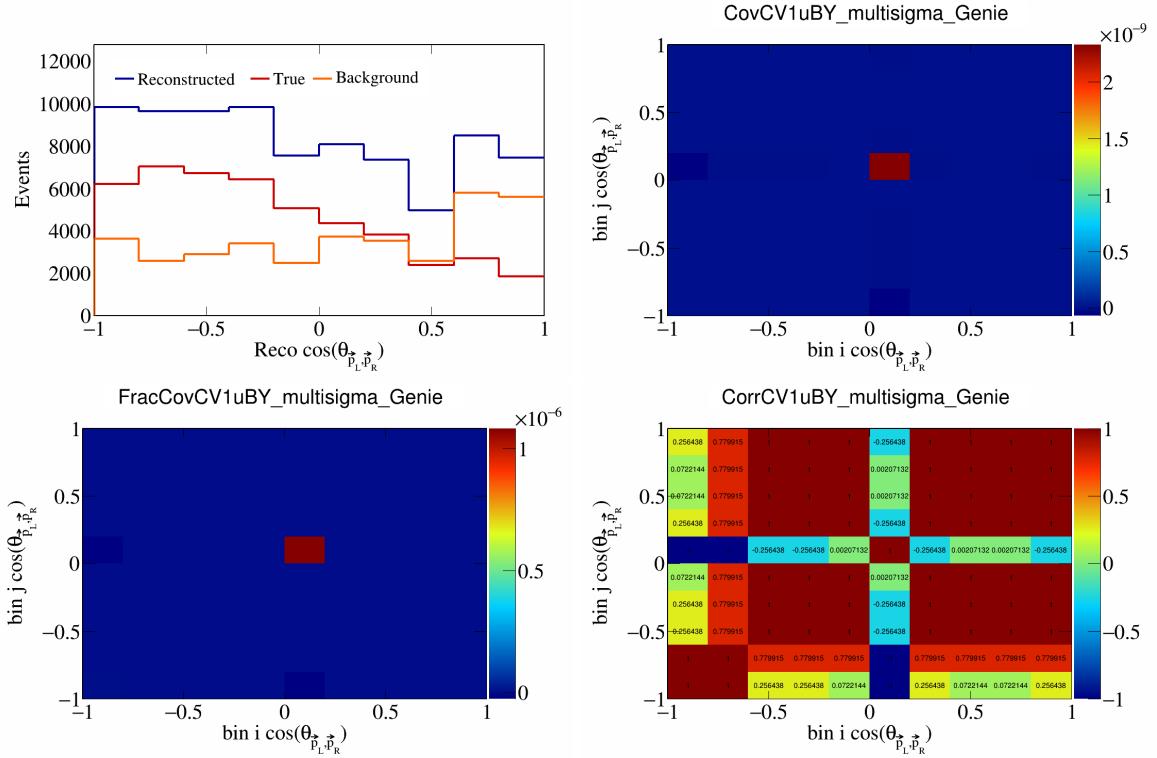


Figure 115: CV1uBY variations for $\cos(\theta_{\vec{p}_L, \vec{p}_R})$.

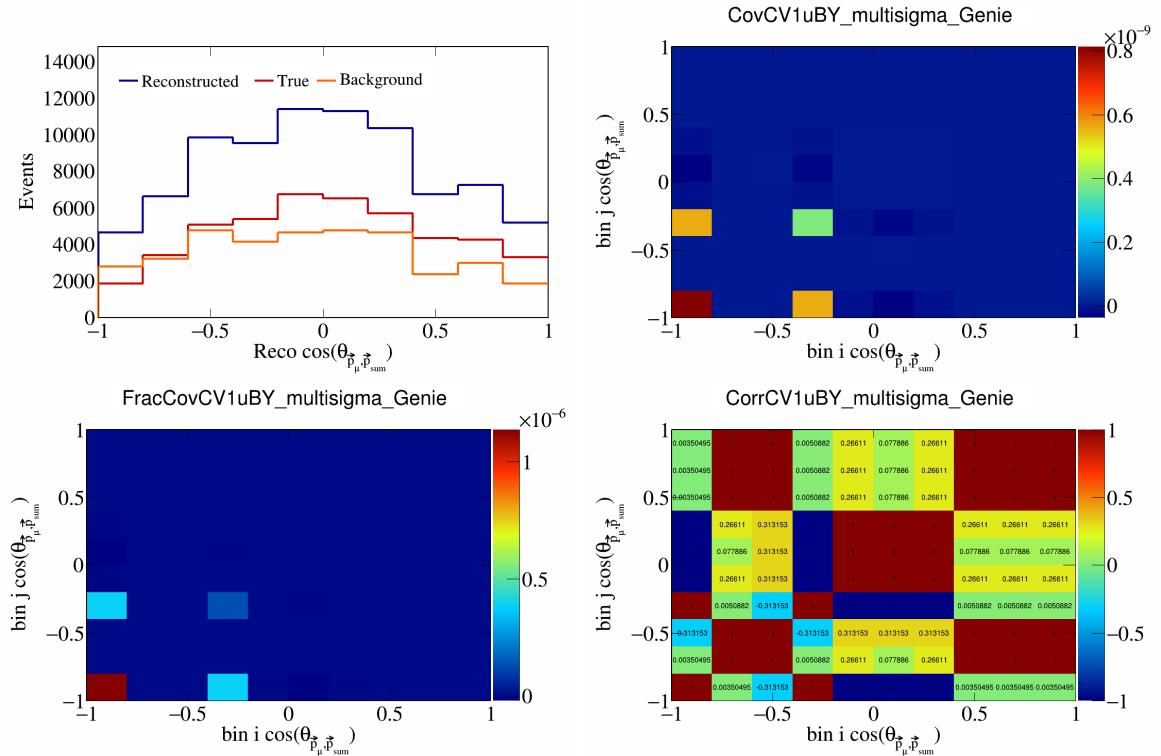


Figure 116: CV1uBY variations for $\cos(\theta_{\vec{p}_\mu, \vec{p}_{\text{sum}}})$.

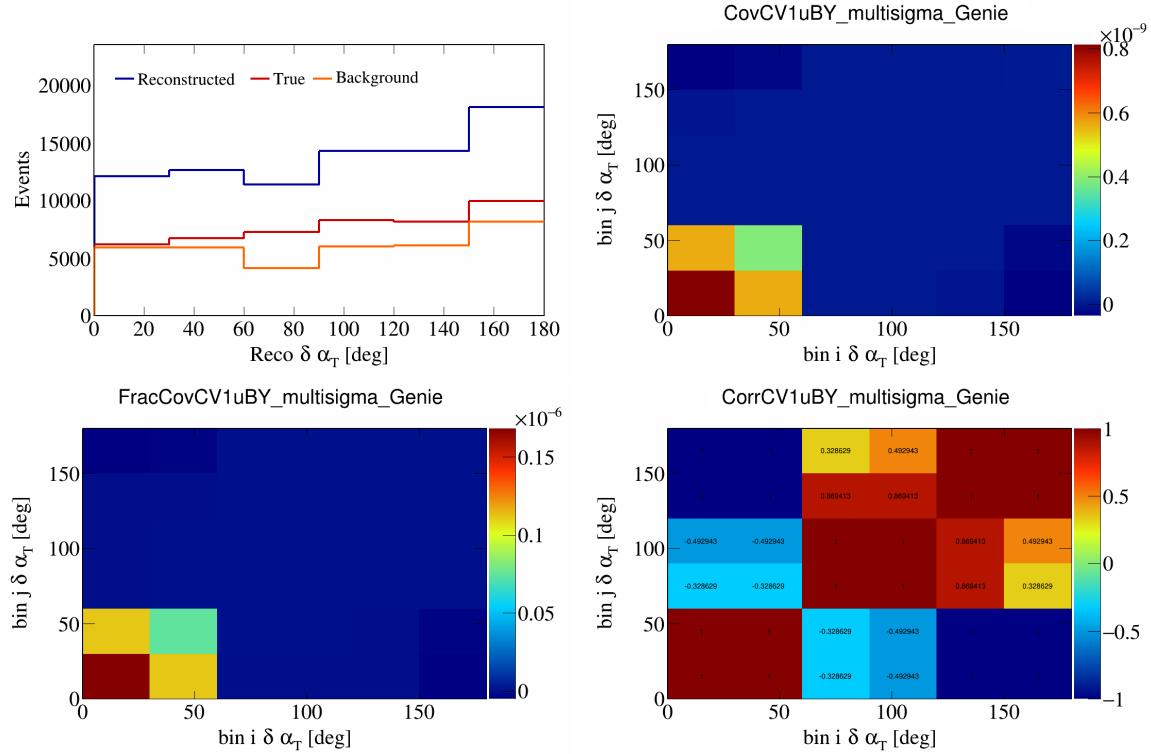


Figure 117: CV1uBY variations for $\delta\alpha_T$.

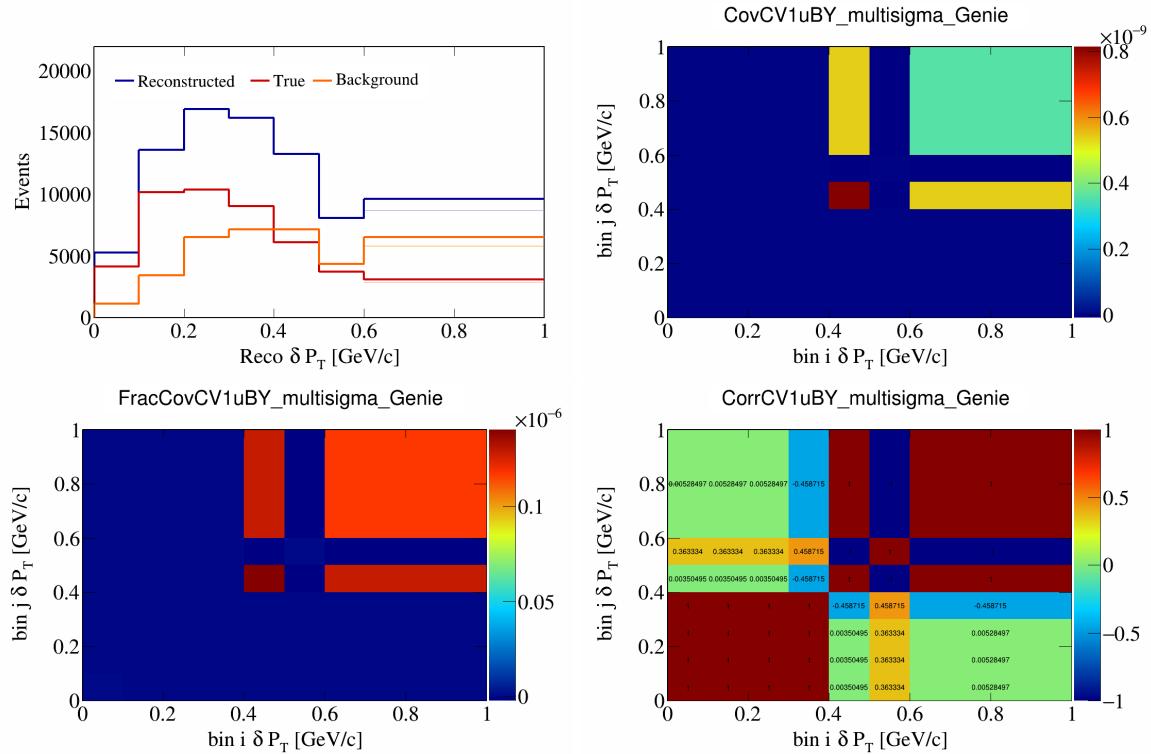


Figure 118: CV1uBY variations for δP_T .

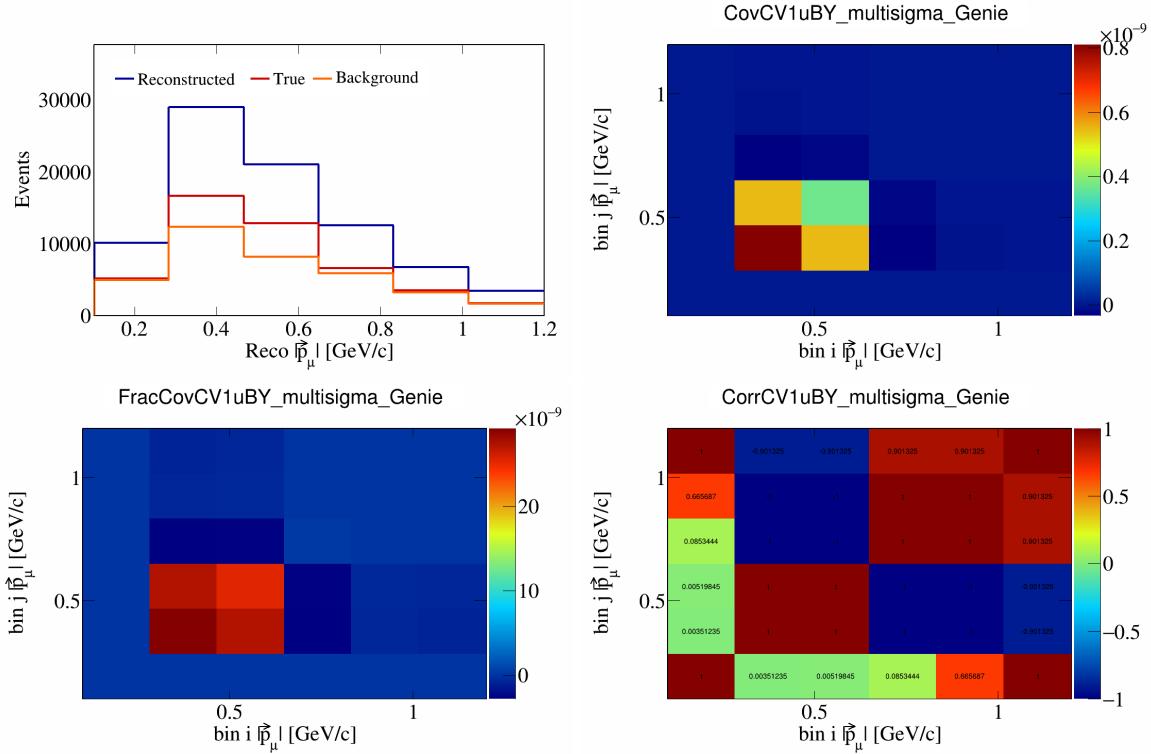


Figure 119: CV1uBY variations for $|\vec{p}_\mu|$.

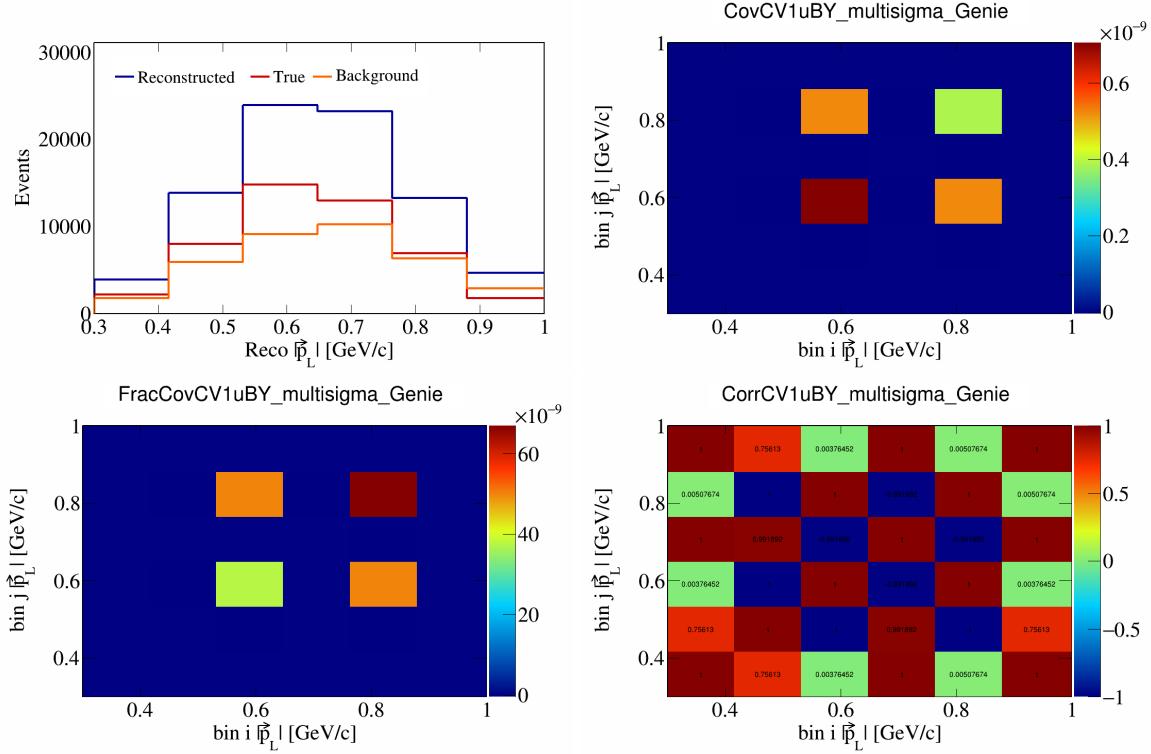


Figure 120: CV1uBY variations for $|\vec{p}_L|$.

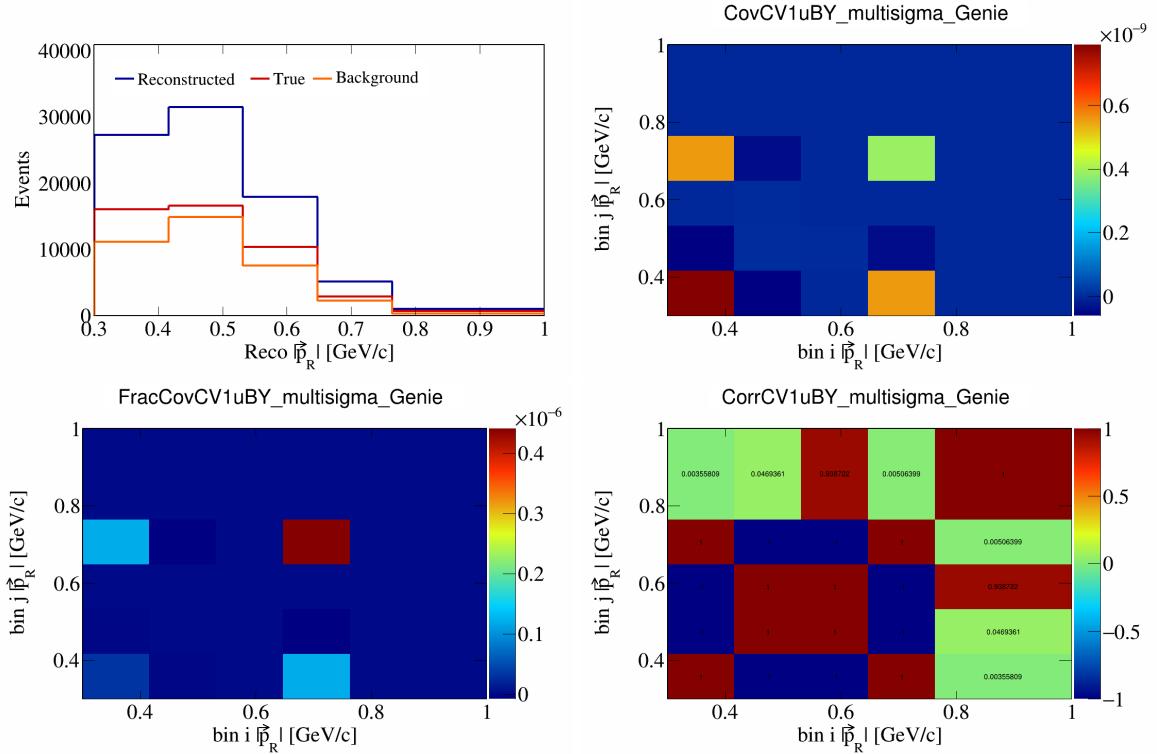


Figure 121: CV1uBY variations for $|\vec{p}_R|$.

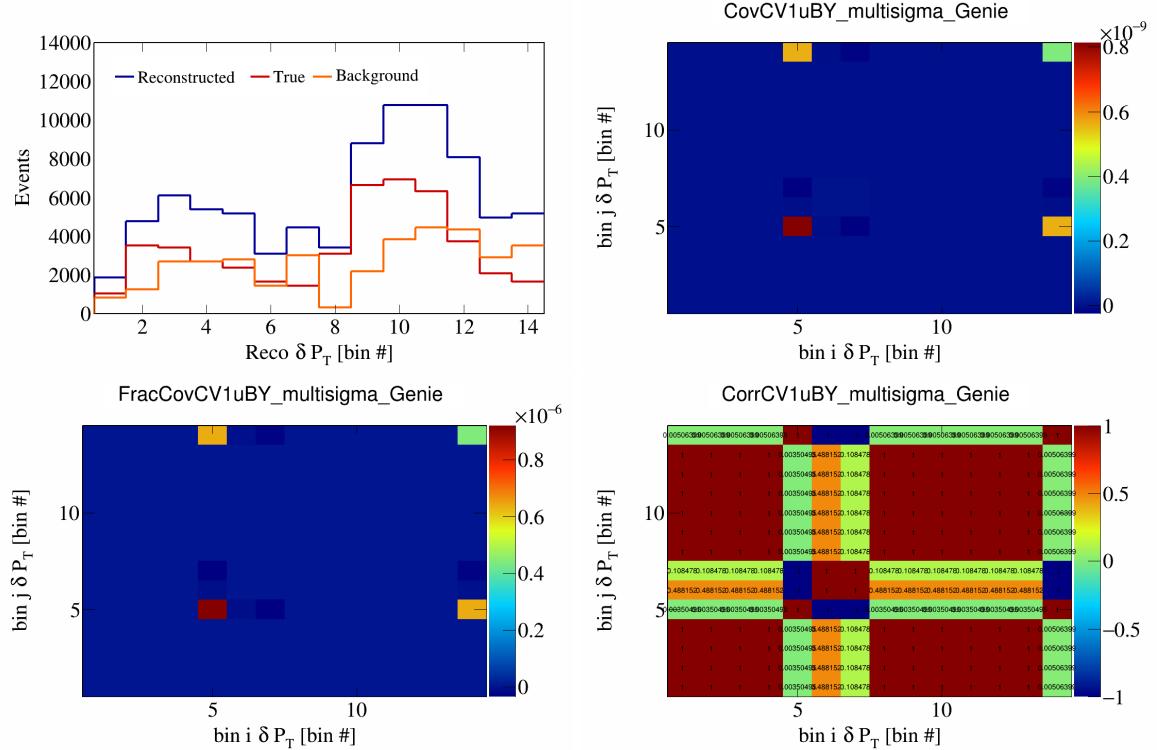


Figure 122: CV1uBY variations for δP_T in $\cos(\theta_{\vec{p}_\mu})$.

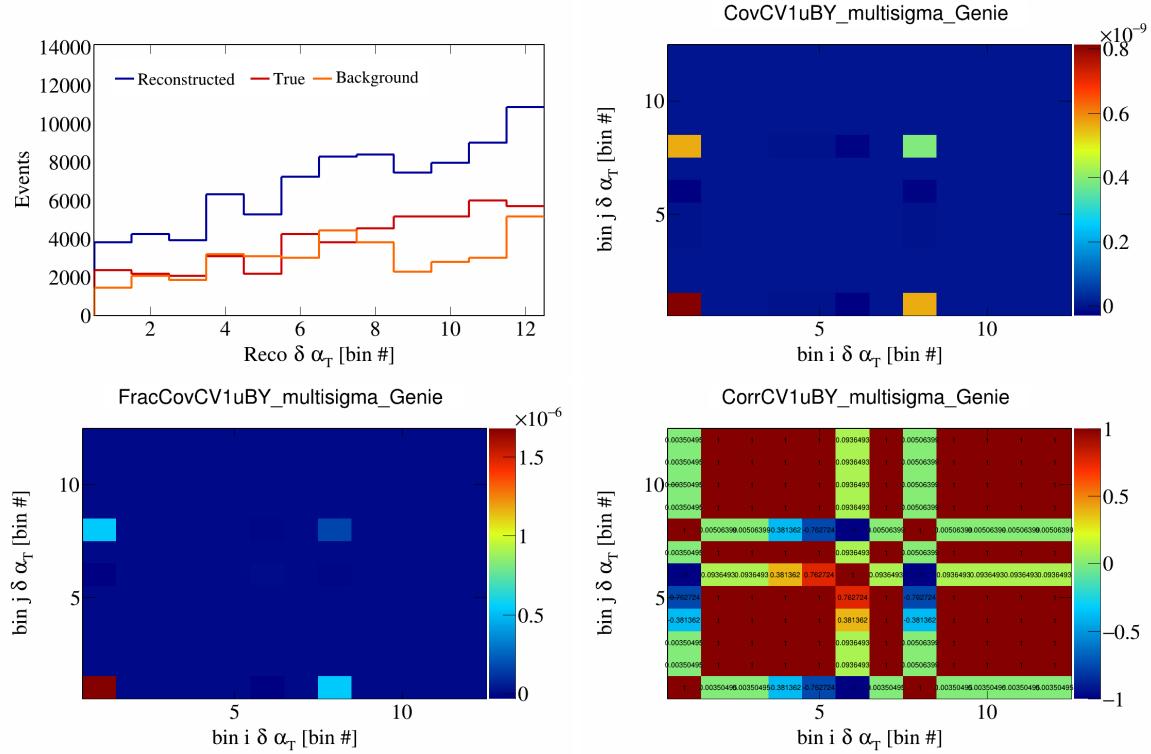


Figure 123: CV1uBY variations for $\delta\alpha_T$ in $\cos(\theta_{\vec{p}_\mu})$.

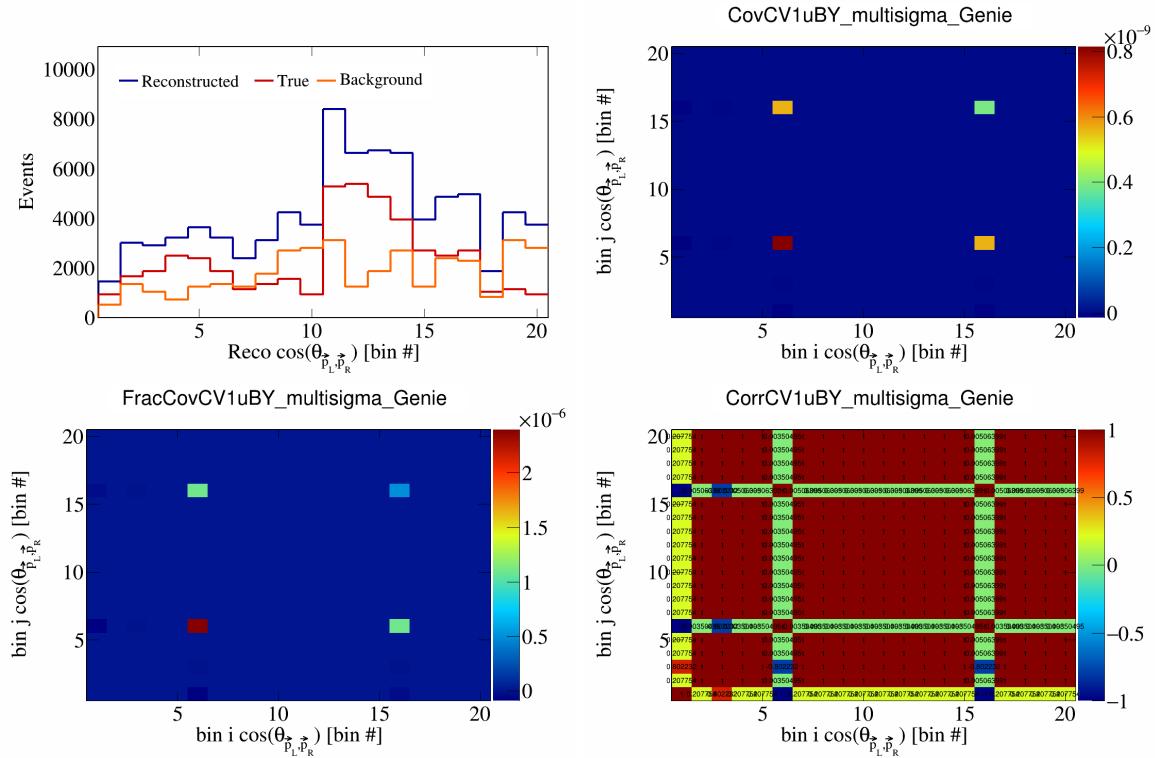


Figure 124: CV1uBY variations for $\cos(\theta_{\vec{p}_L, \vec{p}_R})$ in $\cos(\theta_{\vec{p}_\mu})$.

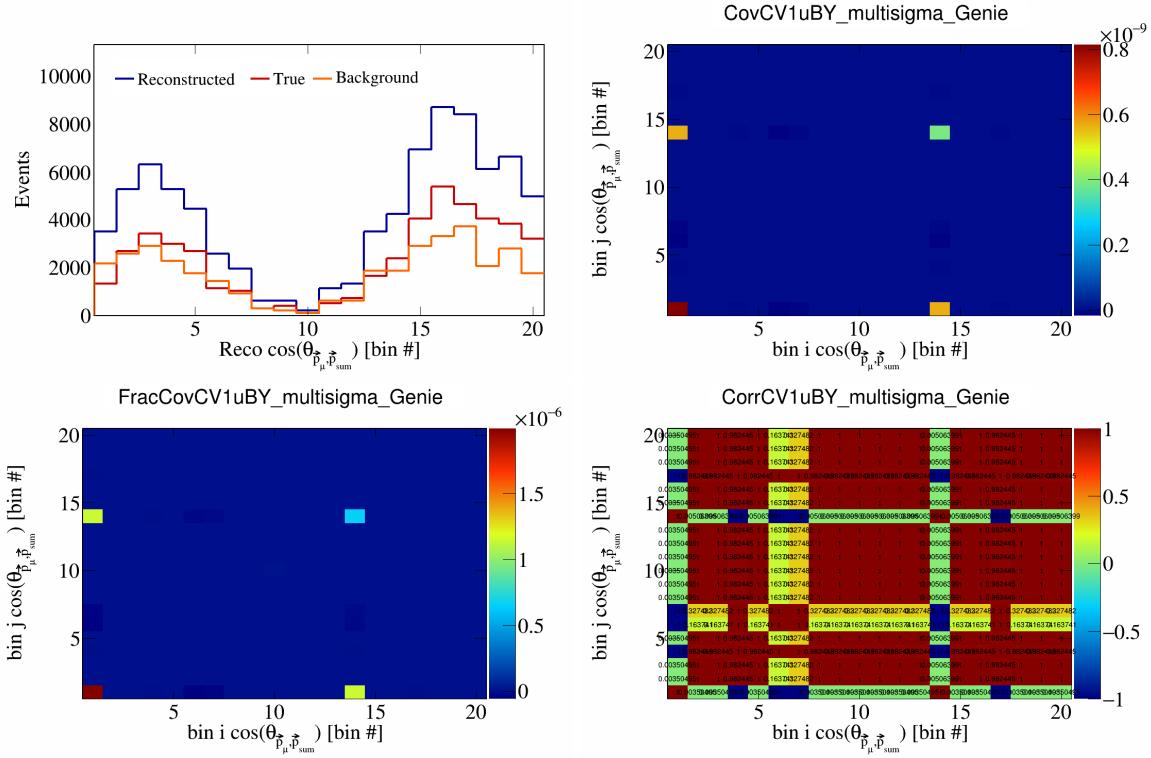


Figure 125: CV1uBY variations for $\cos(\theta_{\vec{p}_\mu, \vec{p}_{\text{sum}}})$ in $\cos(\theta_{\vec{p}_\mu})$.

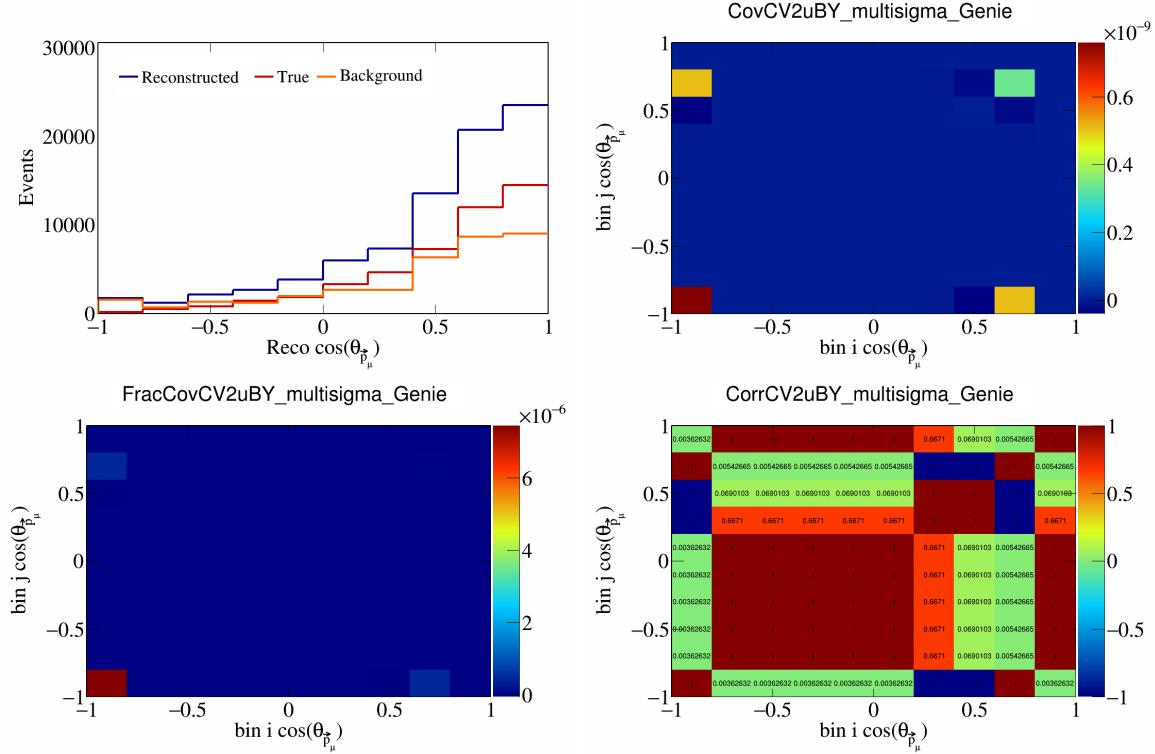


Figure 126: CV2uBY variations for $\cos(\theta_{\vec{p}_\mu})$.

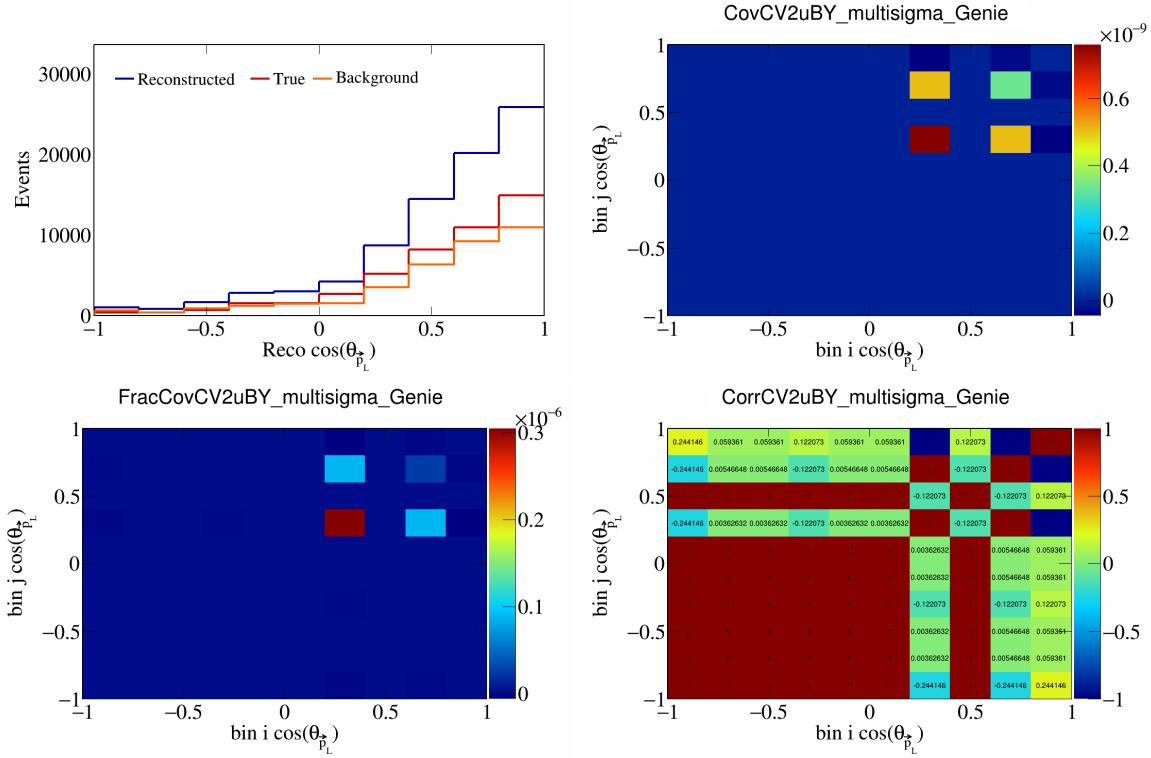


Figure 127: CV2uBY variations for $\cos(\theta_{\vec{p}_L})$.

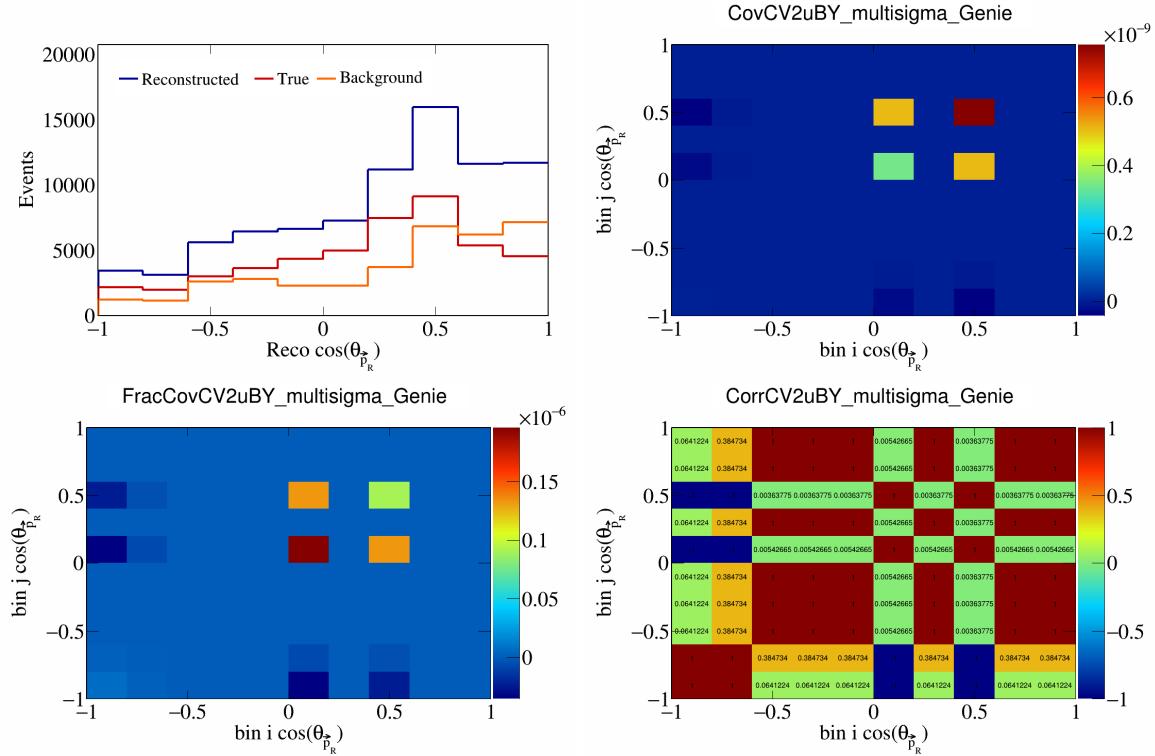


Figure 128: CV2uBY variations for $\cos(\theta_{\vec{p}_R})$.

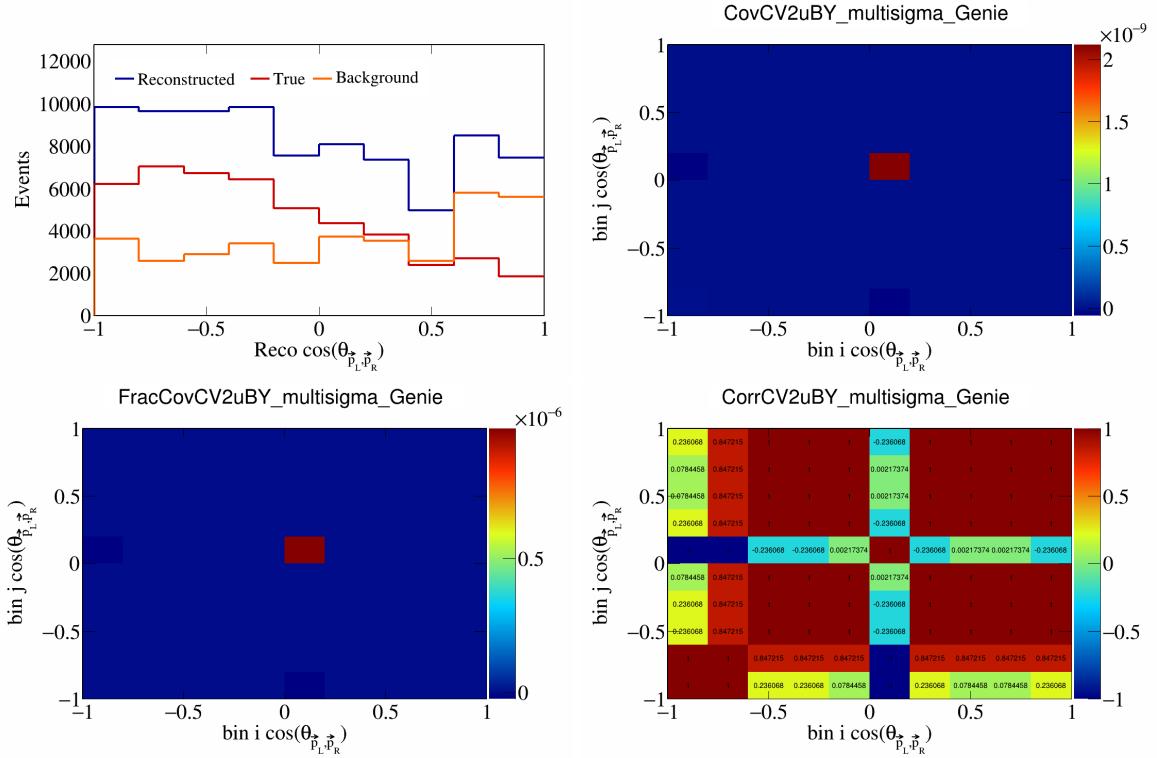


Figure 129: CV2uBY variations for $\cos(\theta_{\vec{p}_L, \vec{p}_R})$.

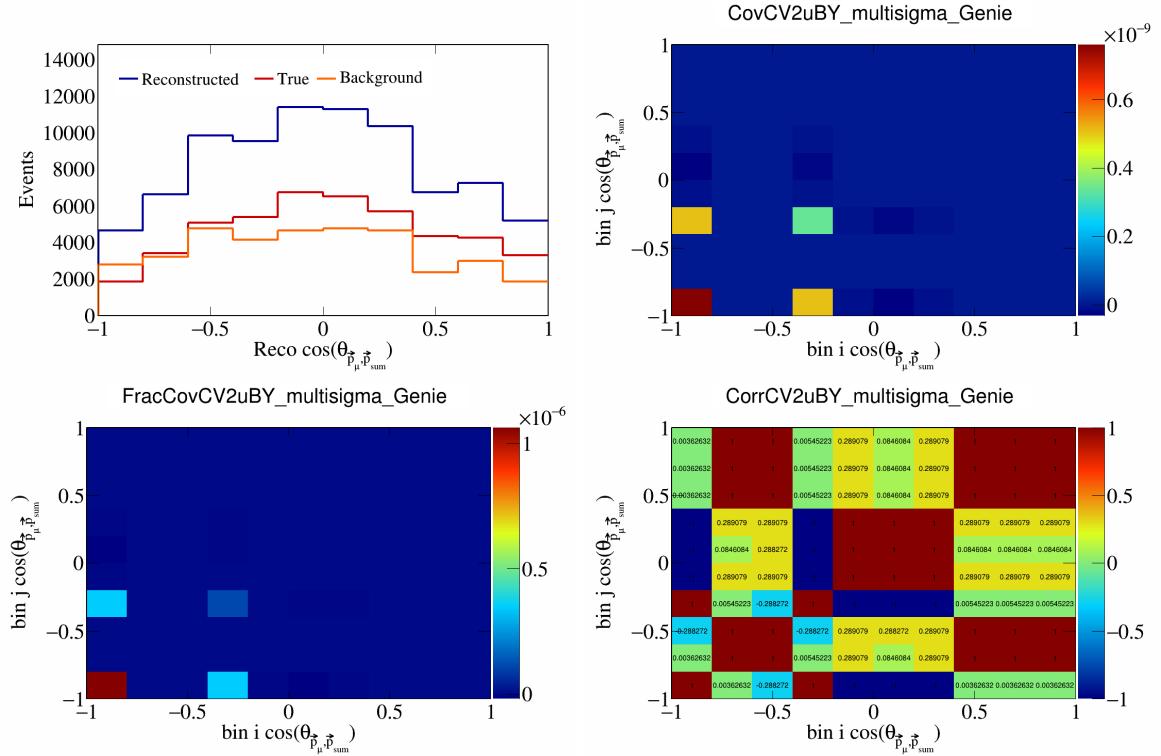


Figure 130: CV2uBY variations for $\cos(\theta_{\vec{p}_\mu, \vec{p}_{\text{sum}}})$.

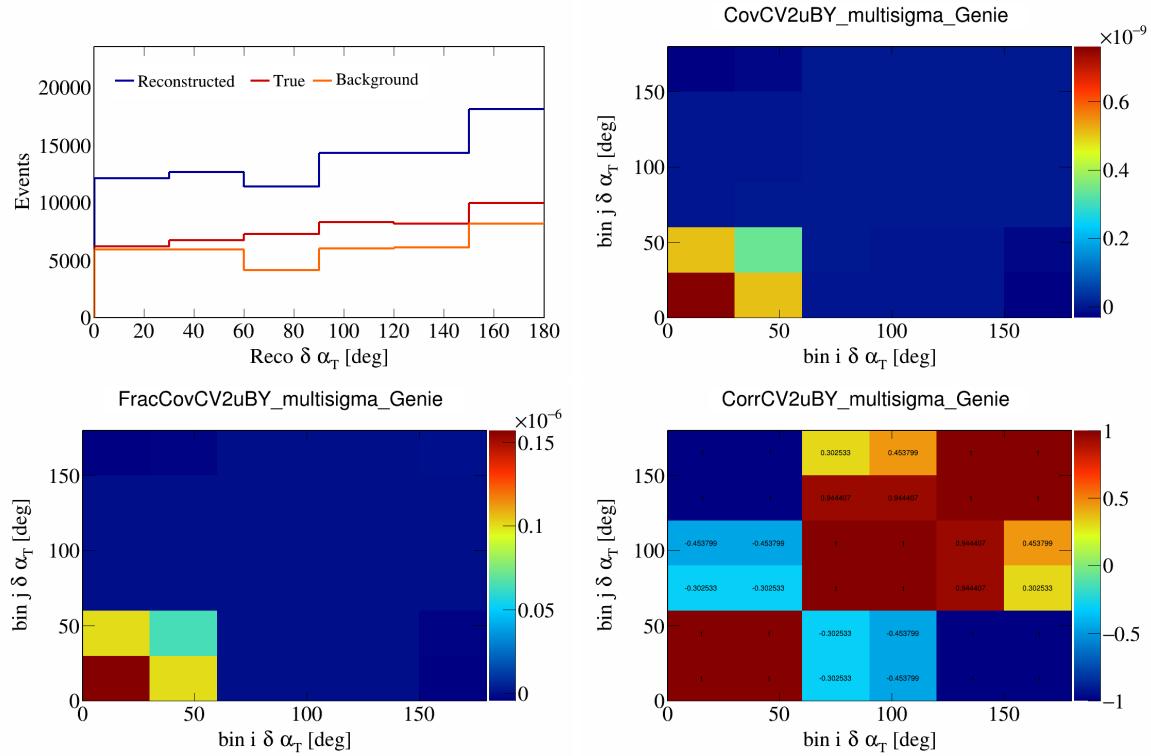


Figure 131: CV2uBY variations for $\delta\alpha_T$.

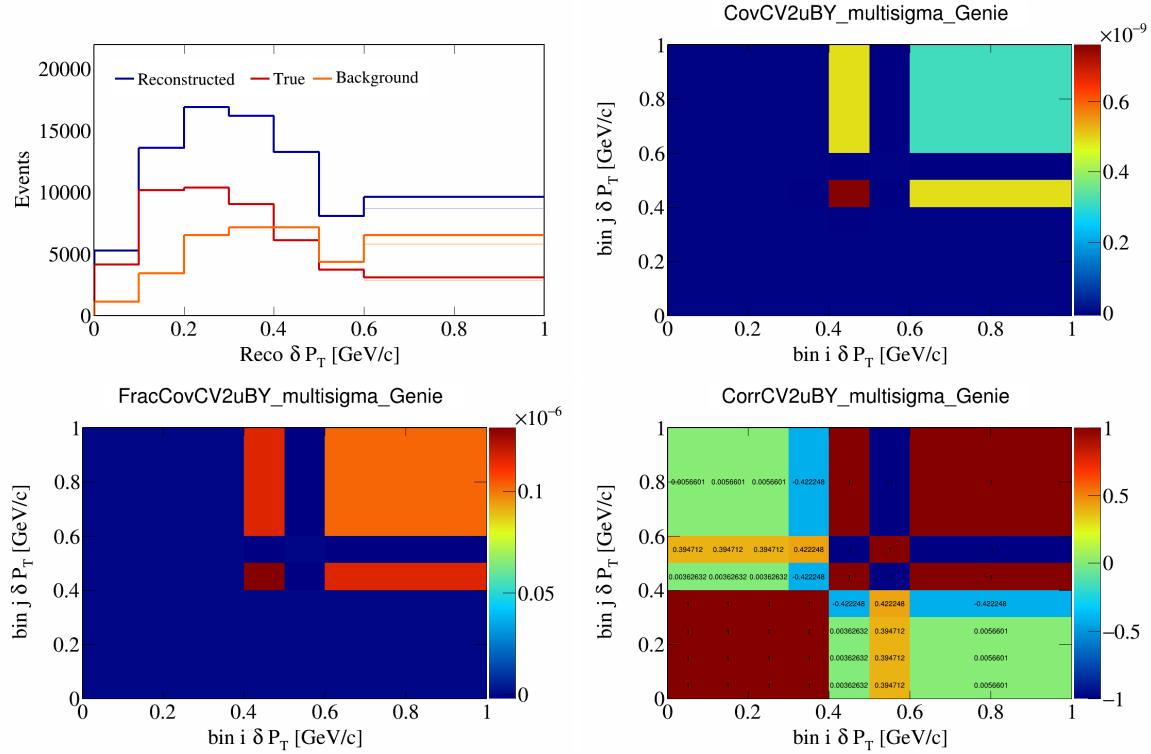


Figure 132: CV2uBY variations for δP_T .

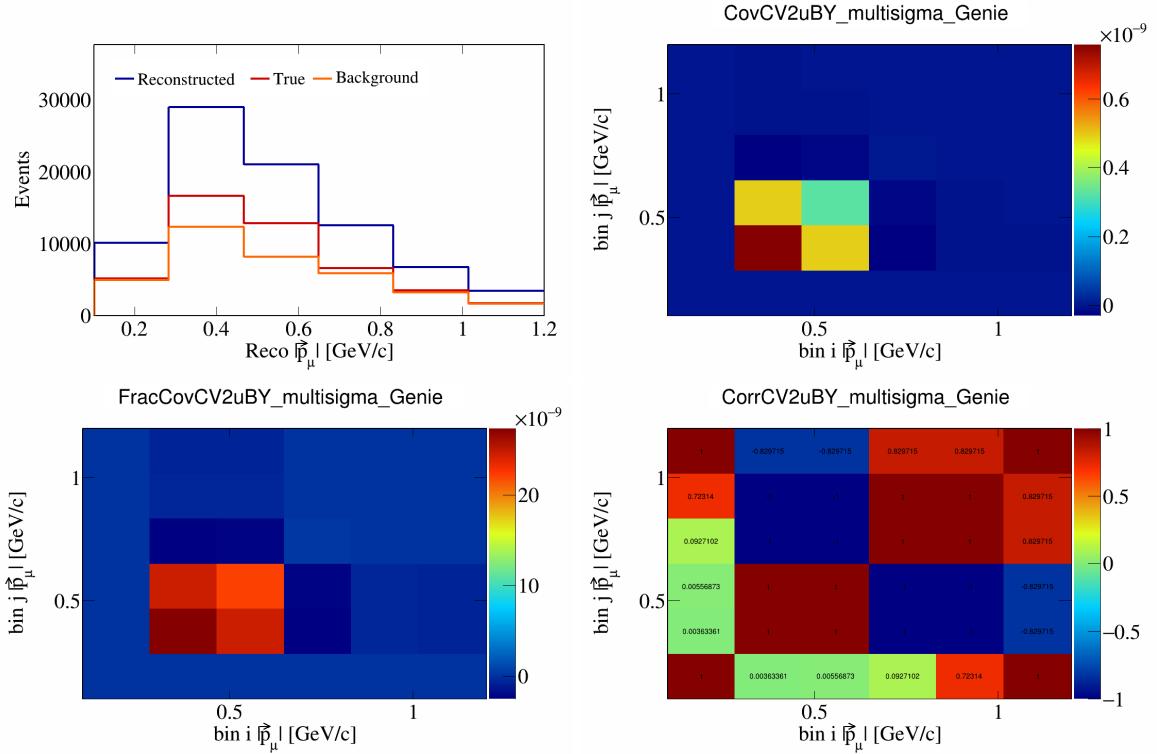


Figure 133: CV2uBY variations for $|\vec{p}_\mu|$.

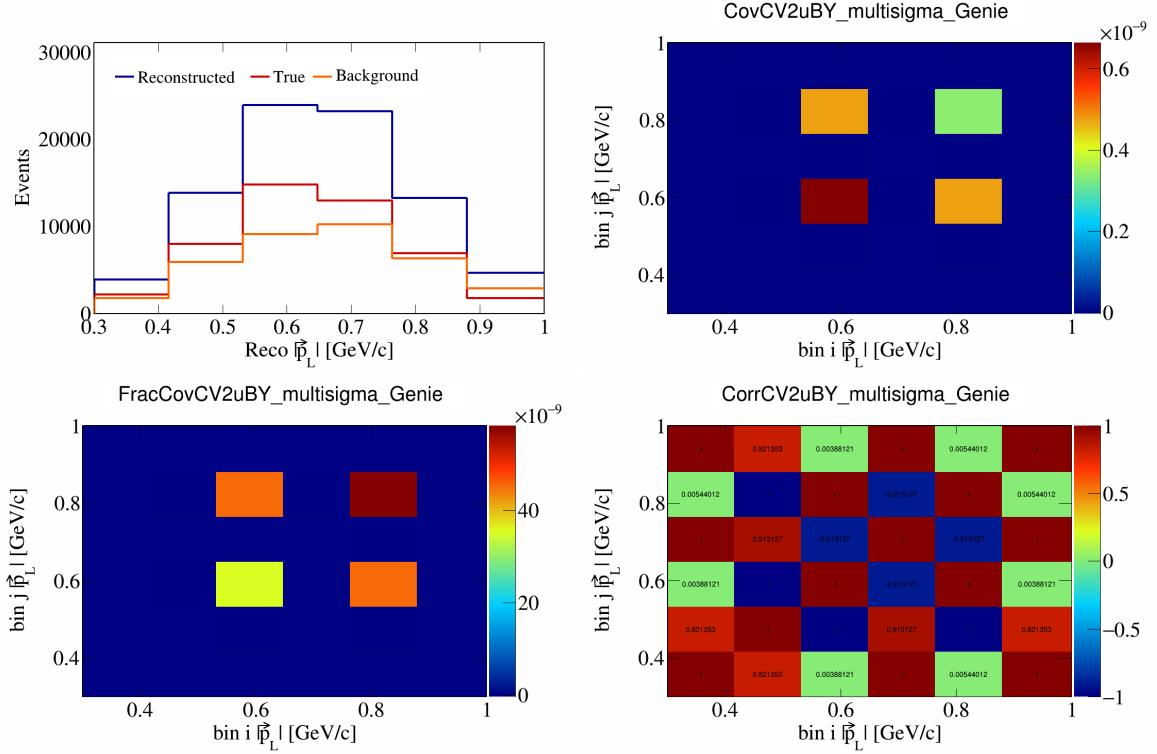


Figure 134: CV2uBY variations for $|\vec{p}_L|$.

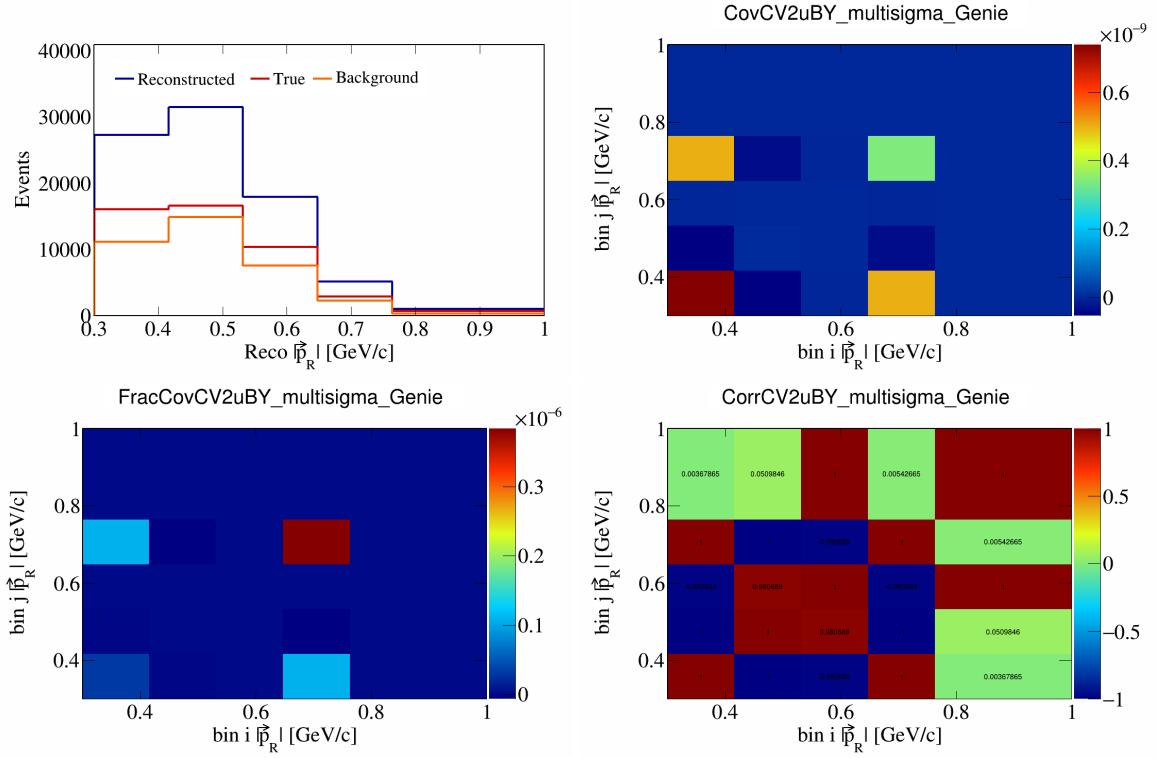


Figure 135: CV2uBY variations for $|\vec{p}_R|$.

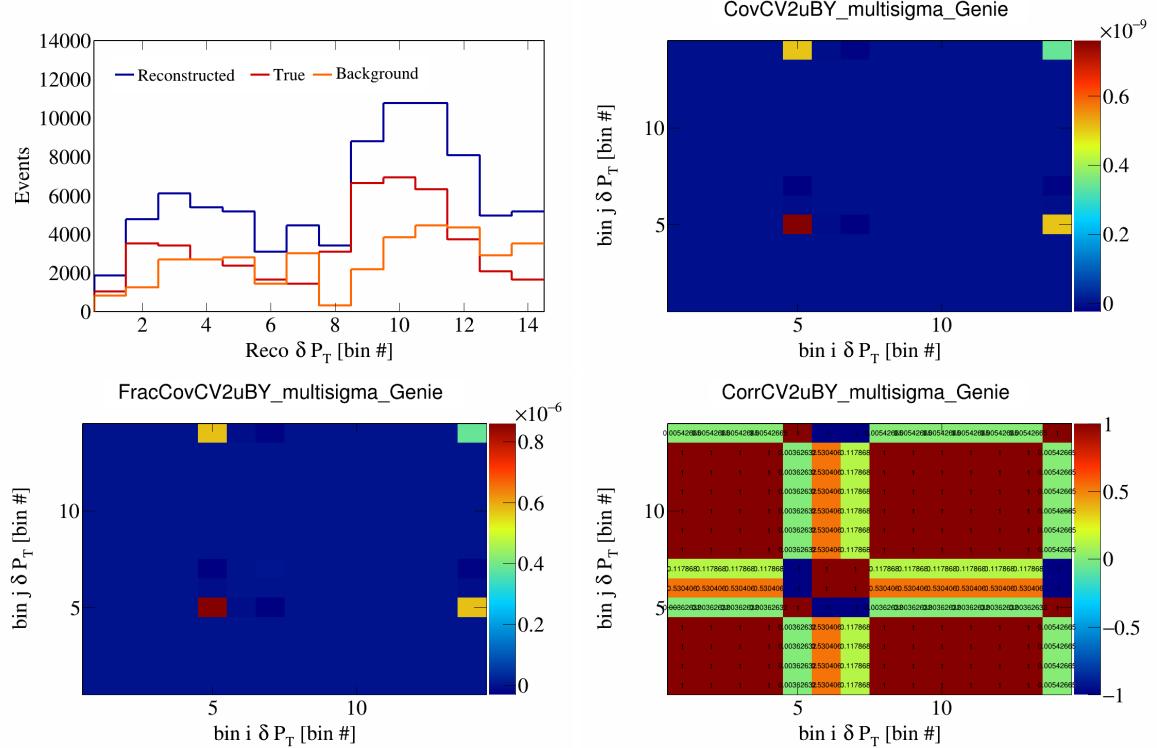


Figure 136: CV2uBY variations for δP_T in $\cos(\theta_{\vec{p}_\mu})$.

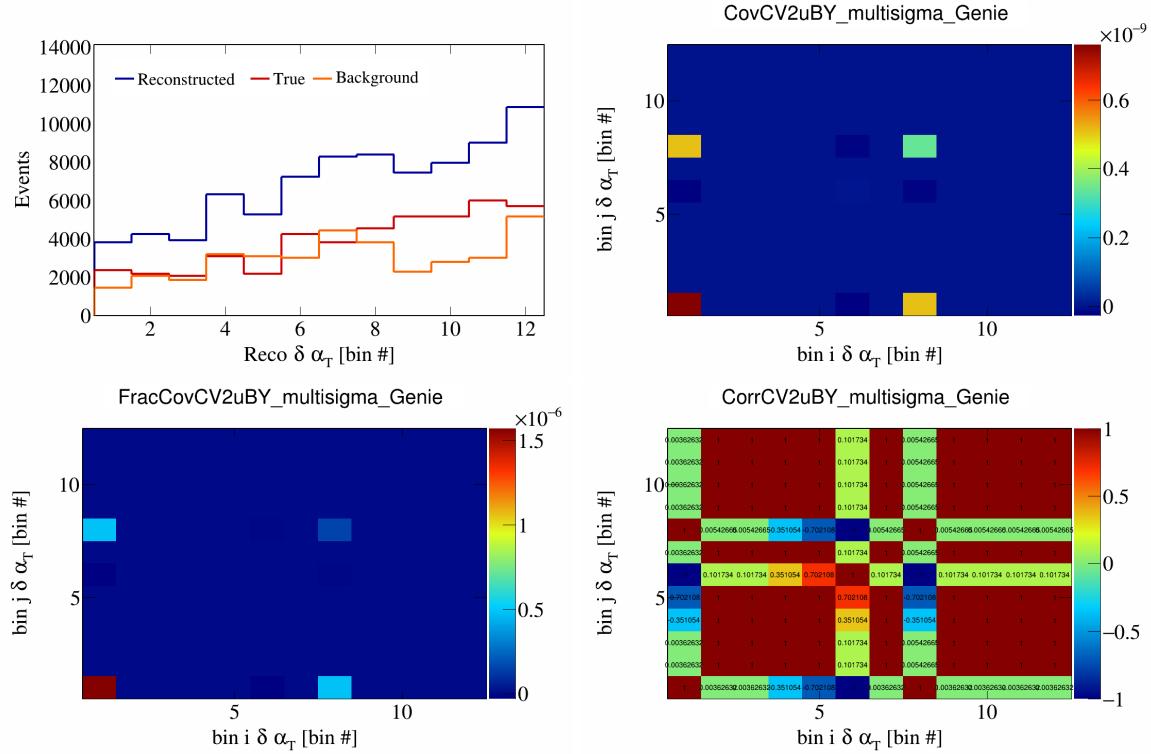


Figure 137: CV2uBY variations for $\delta\alpha_T$ in $\cos(\theta_{\vec{p}_\mu})$.

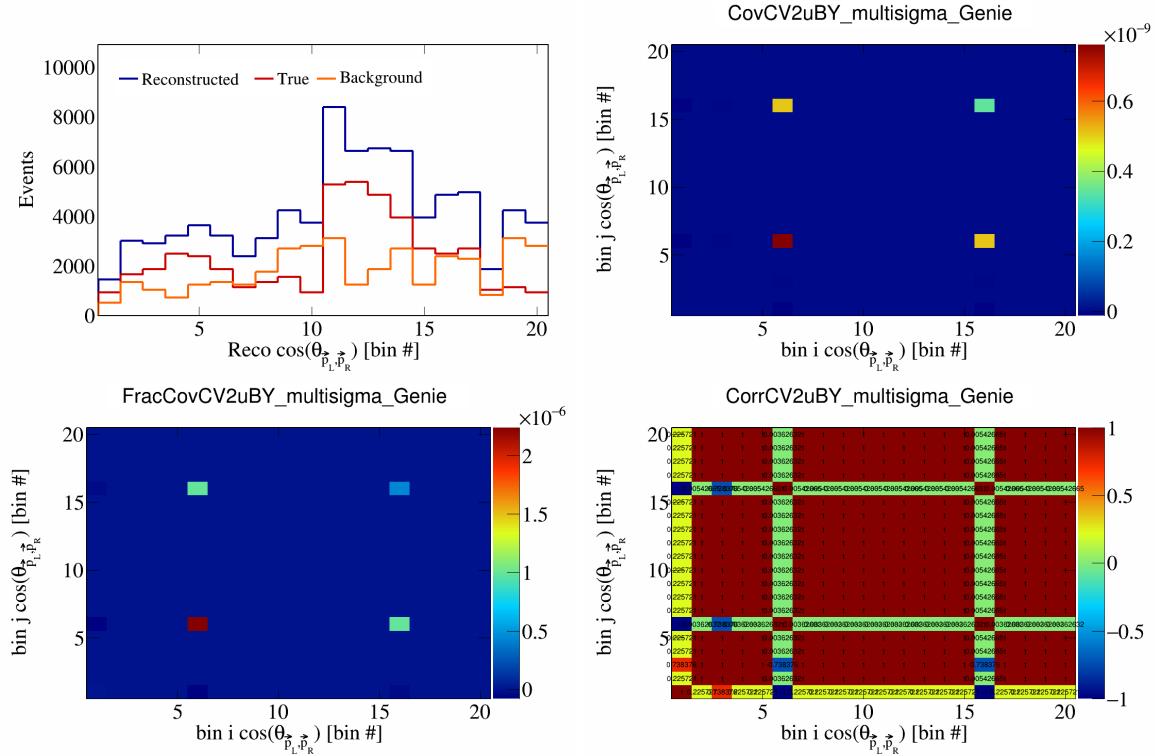


Figure 138: CV2uBY variations for $\cos(\theta_{\vec{p}_L, \vec{p}_R})$ in $\cos(\theta_{\vec{p}_\mu})$.

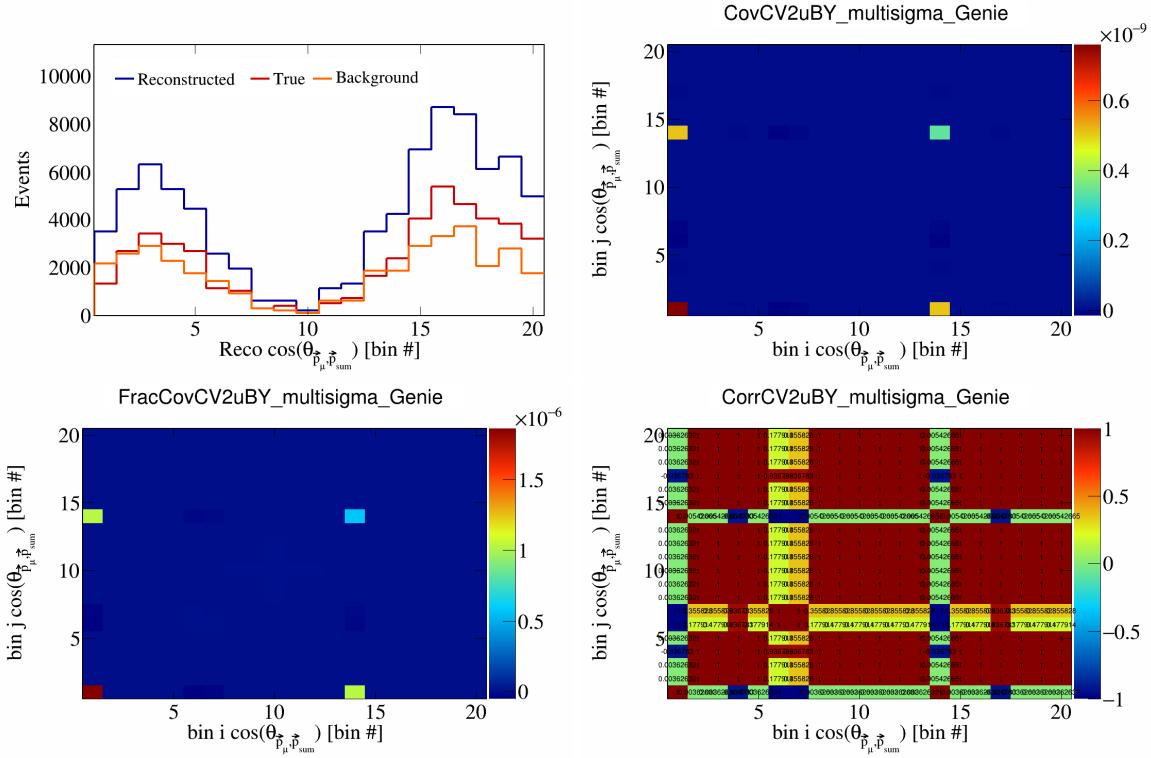


Figure 139: CV2uBY variations for $\cos(\theta_{\vec{p}_\mu, \vec{p}_{\text{sum}}})$ in $\cos(\theta_{\vec{p}_\mu})$.

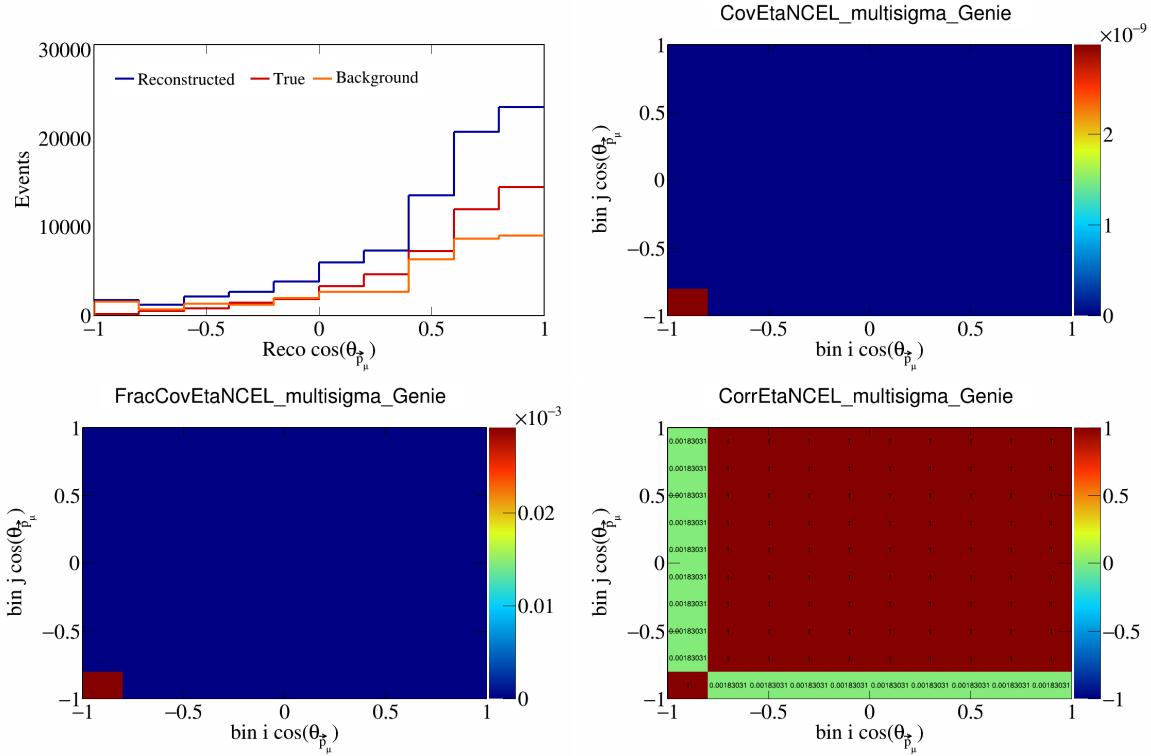


Figure 140: EtaNCEL variations for $\cos(\theta_{\vec{p}_\mu})$.

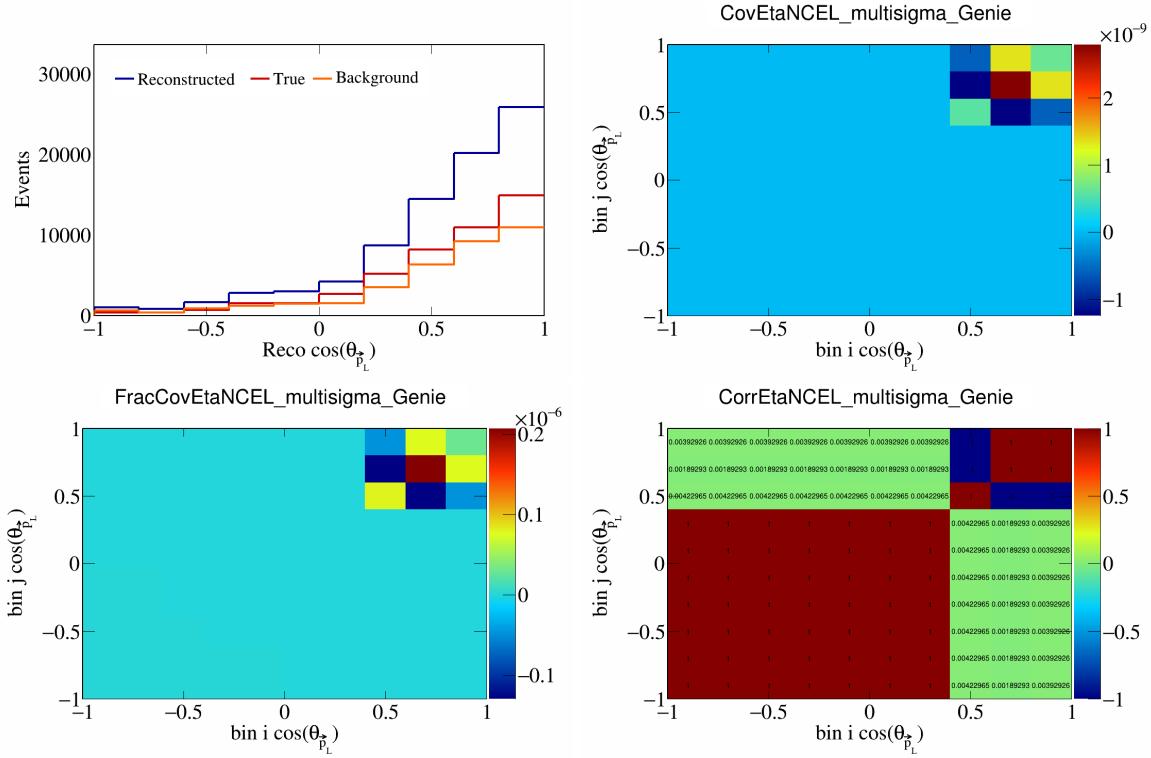


Figure 141: EtaNCEL variations for $\cos(\theta_{\vec{p}_L})$.

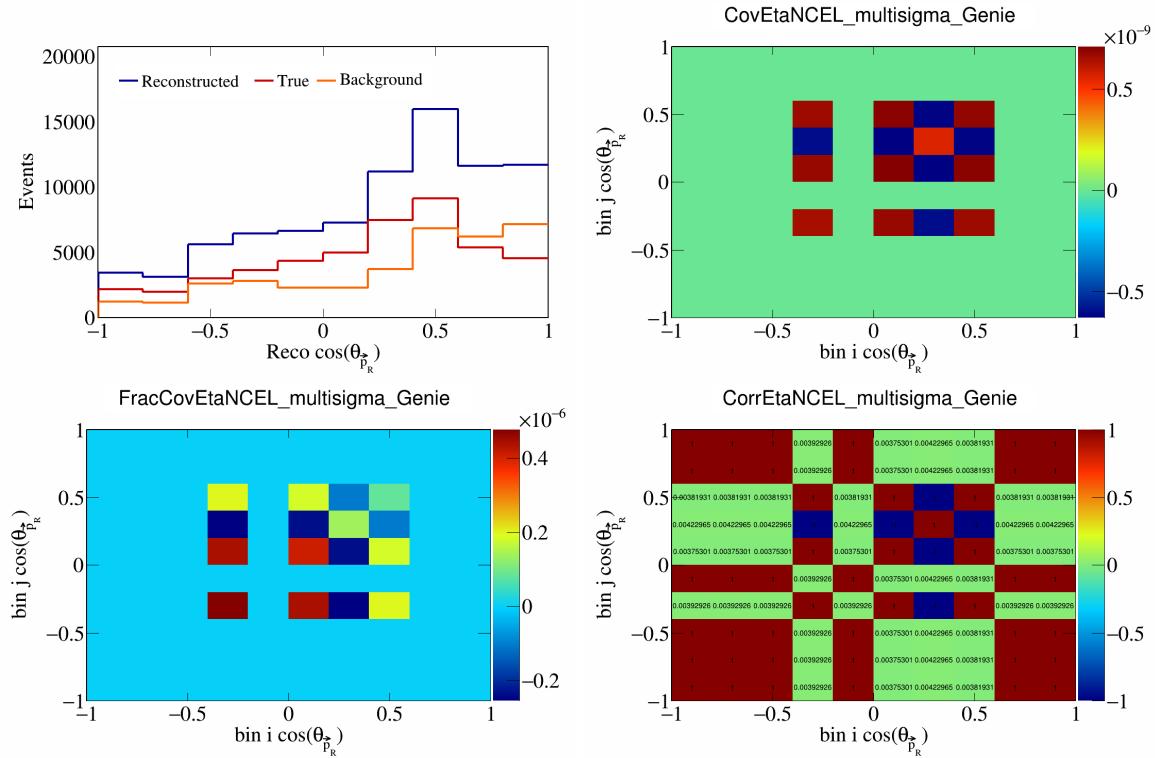


Figure 142: EtaNCEL variations for $\cos(\theta_{\vec{p}_R})$.

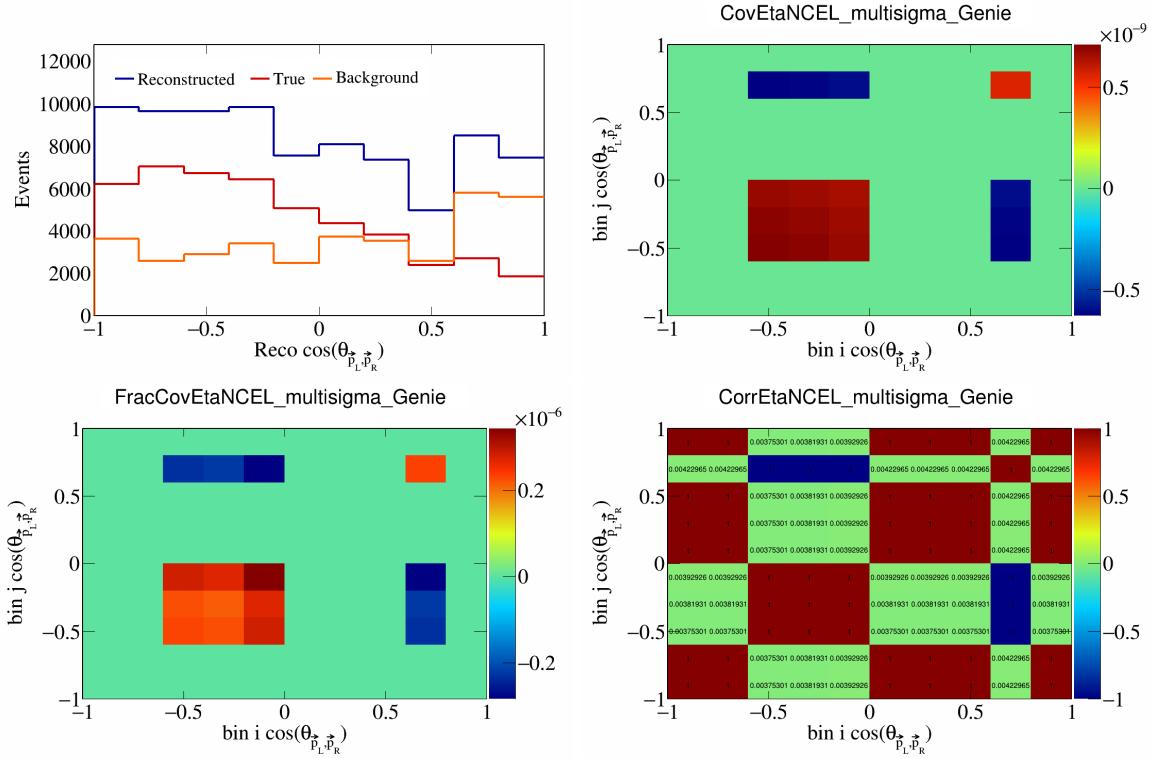


Figure 143: EtaNCEL variations for $\cos(\theta_{\vec{p}_L, \vec{p}_R})$.

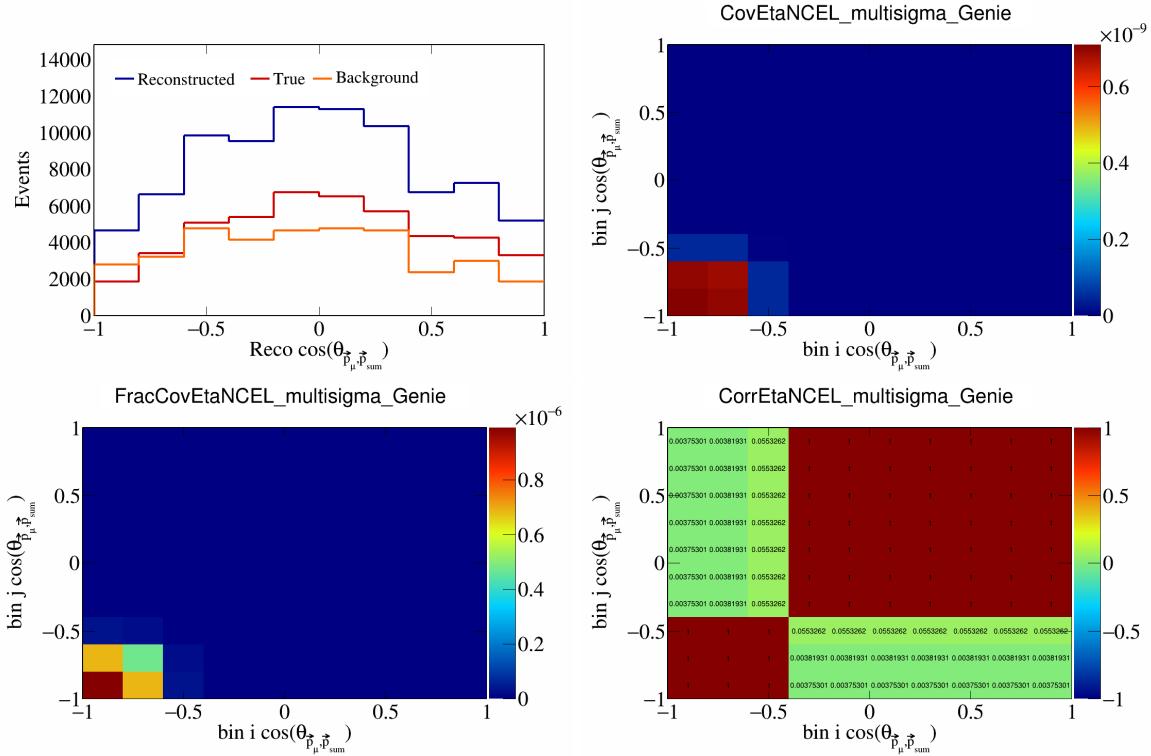


Figure 144: EtaNCEL variations for $\cos(\theta_{\vec{p}_\mu, \vec{p}_{\text{sum}}})$.

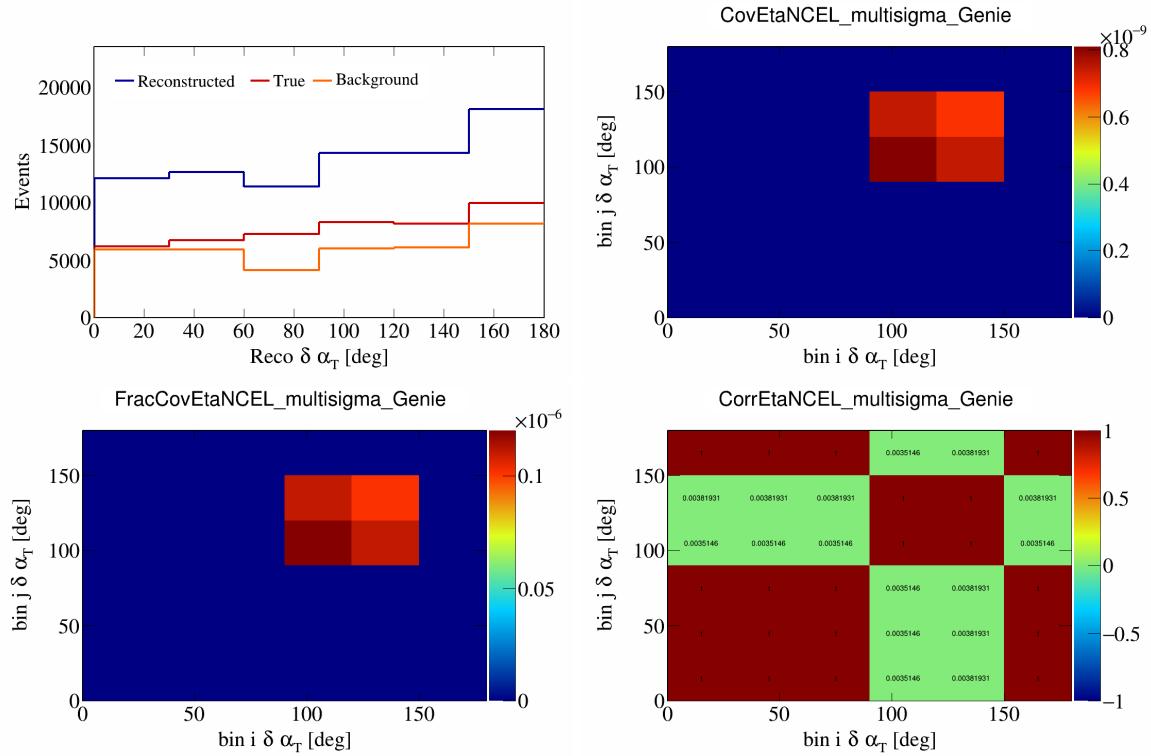


Figure 145: EtaNCEL variations for $\delta\alpha_T$.

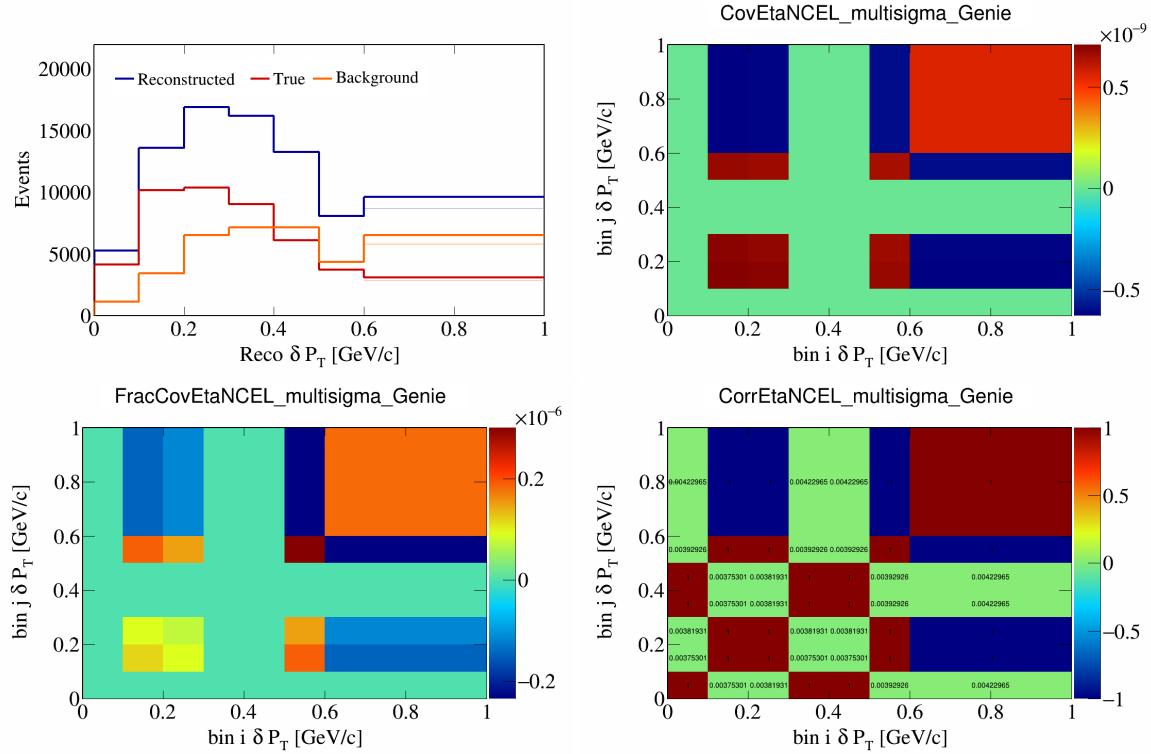


Figure 146: EtaNCEL variations for δP_T .

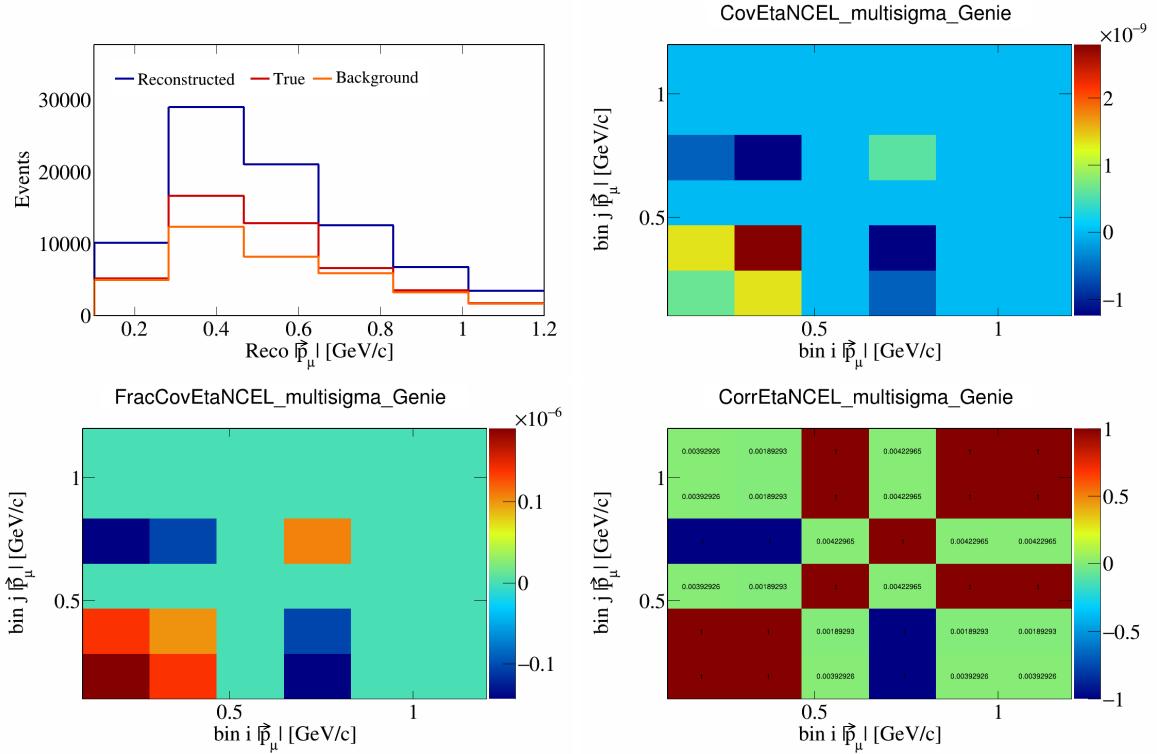


Figure 147: EtaNCEL variations for $|\vec{p}_\mu|$.

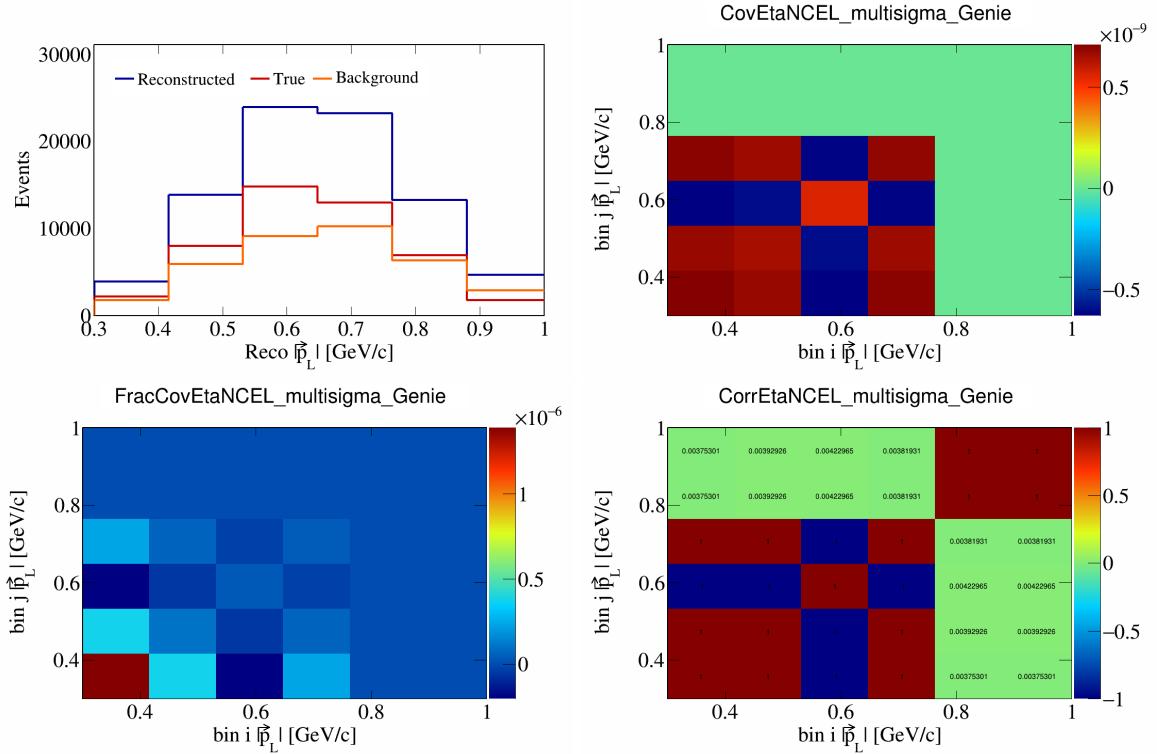


Figure 148: EtaNCEL variations for $|\vec{p}_L|$.

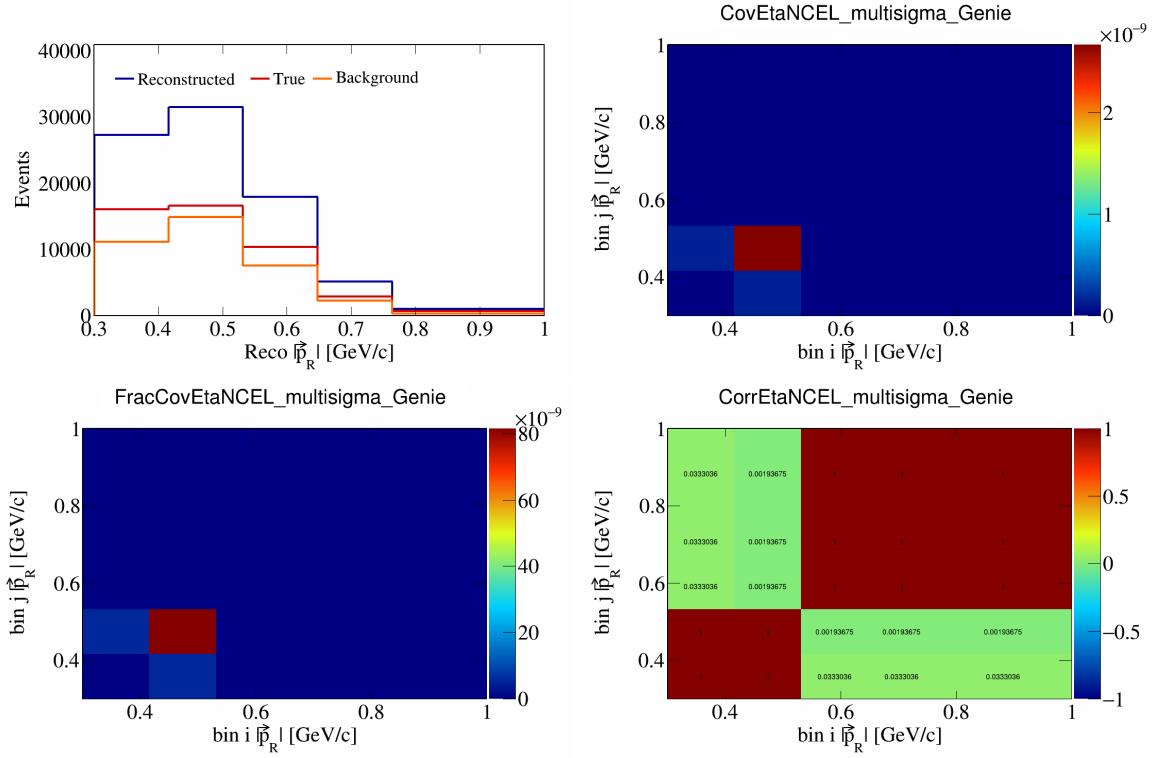


Figure 149: EtaNCEL variations for $|\vec{p}_R|$.

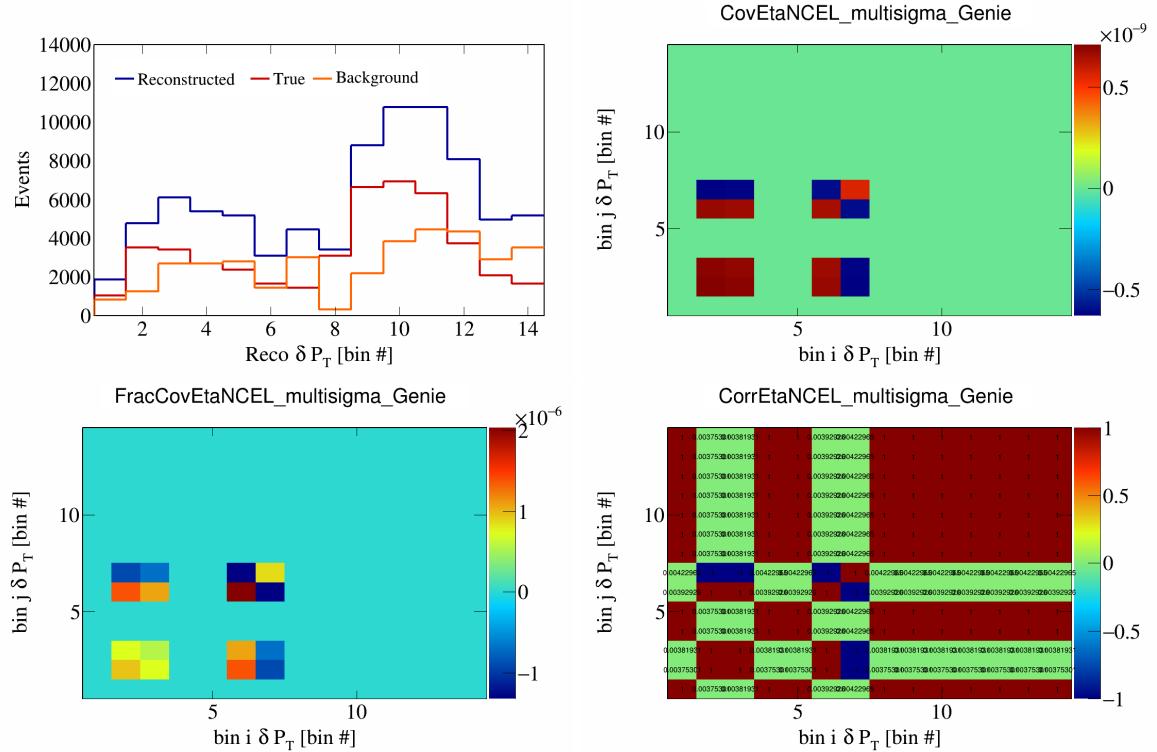


Figure 150: EtaNCEL variations for δP_T in $\cos(\theta_{\vec{p}_\mu})$.

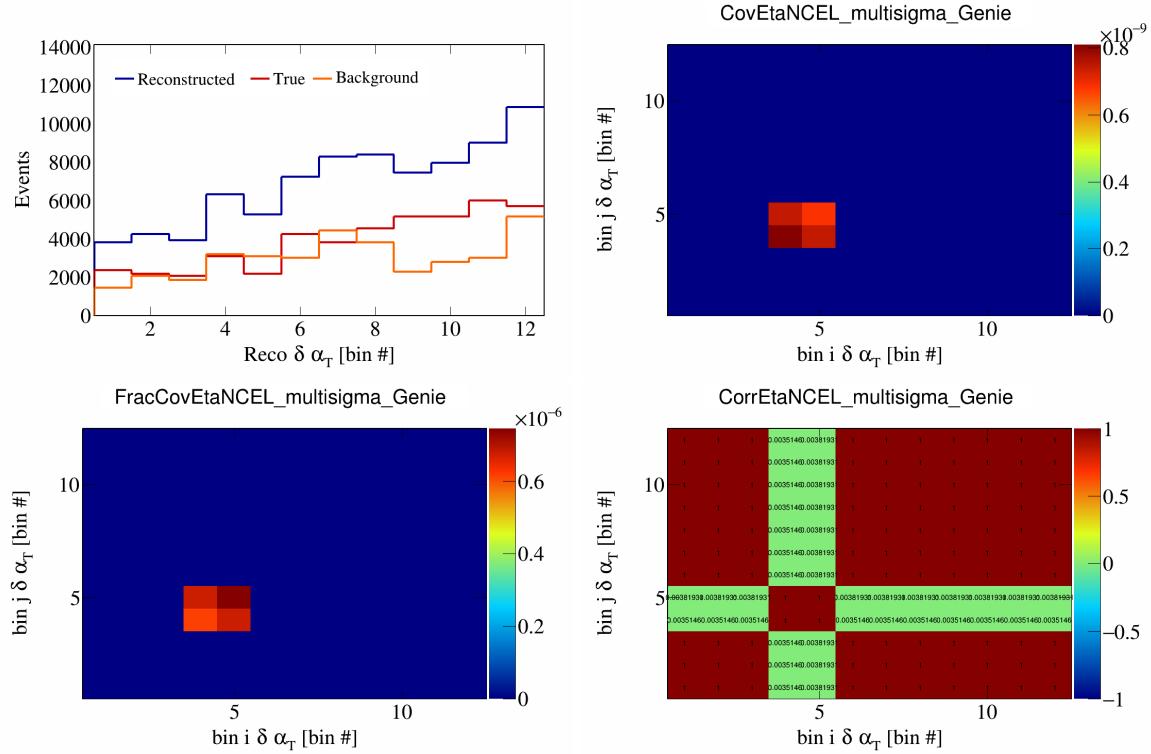


Figure 151: EtaNCEL variations for $\delta \alpha_T$ in $\cos(\theta_{\vec{p}_\mu})$.

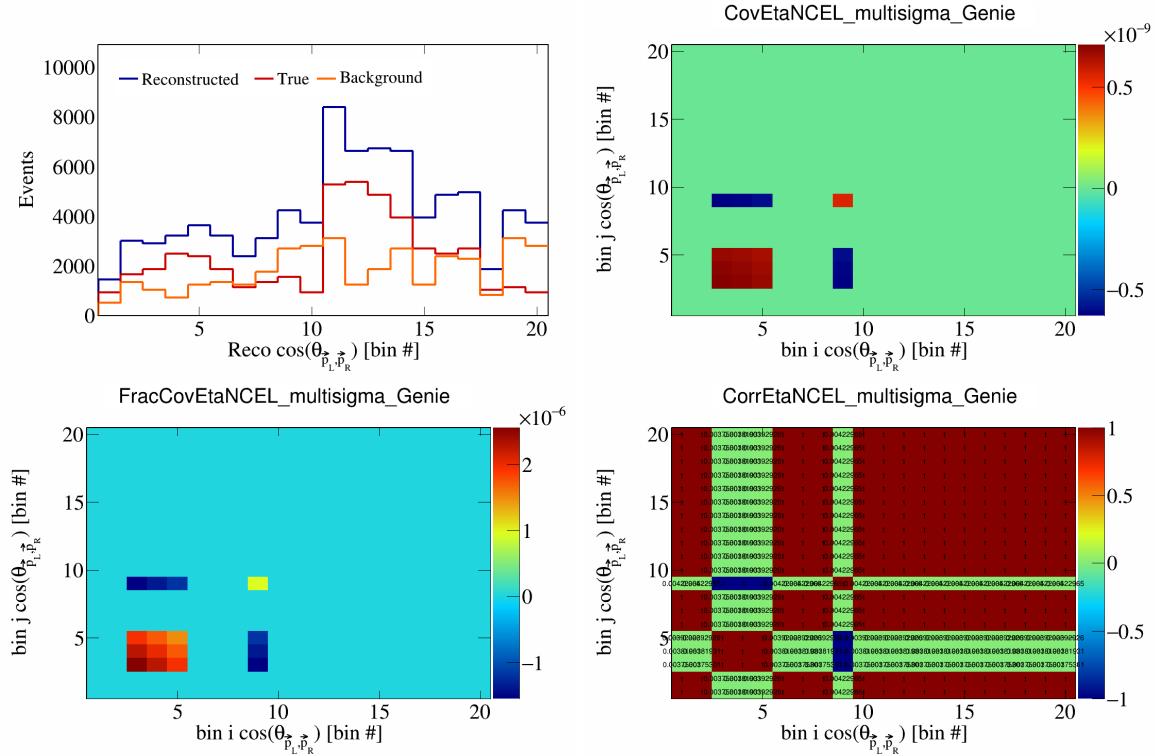


Figure 152: EtaNCEL variations for $\cos(\theta_{\vec{p}_L, \vec{p}_R})$ in $\cos(\theta_{\vec{p}_\mu})$.

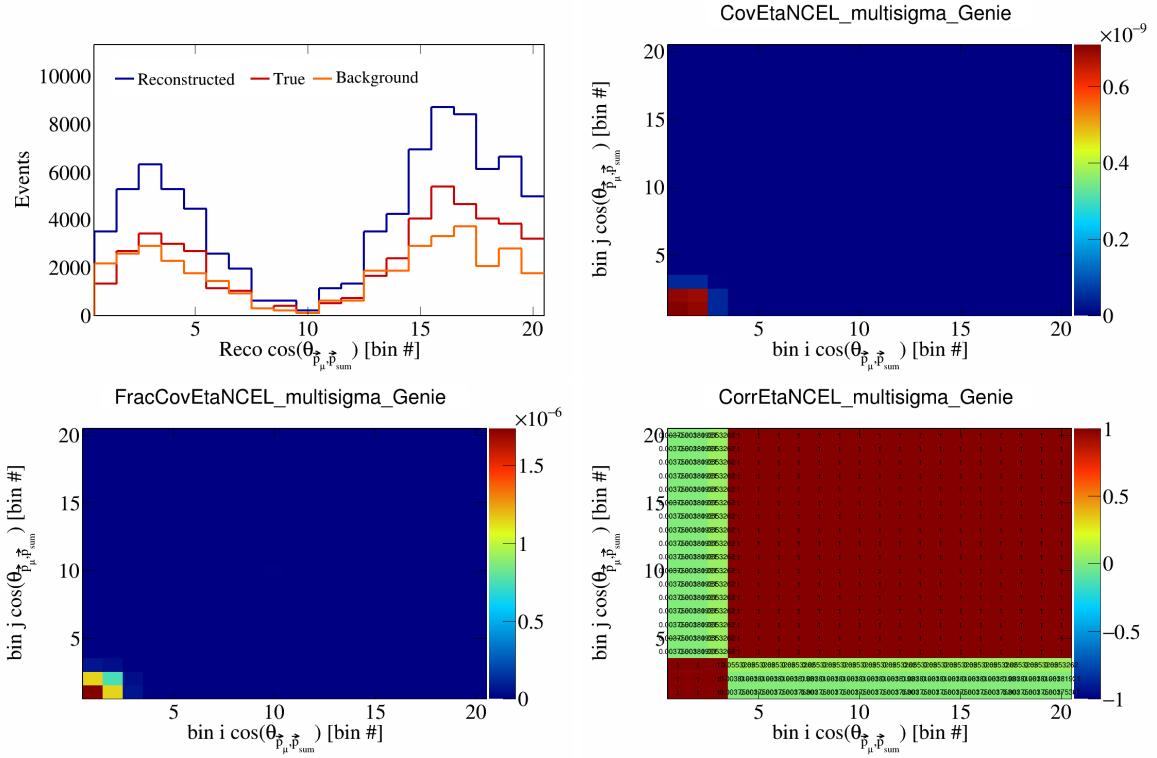


Figure 153: EtaNCEL variations for $\cos(\theta_{\vec{p}_\mu, \vec{p}_{\text{sum}}})$ in $\cos(\theta_{\vec{p}_\mu})$.

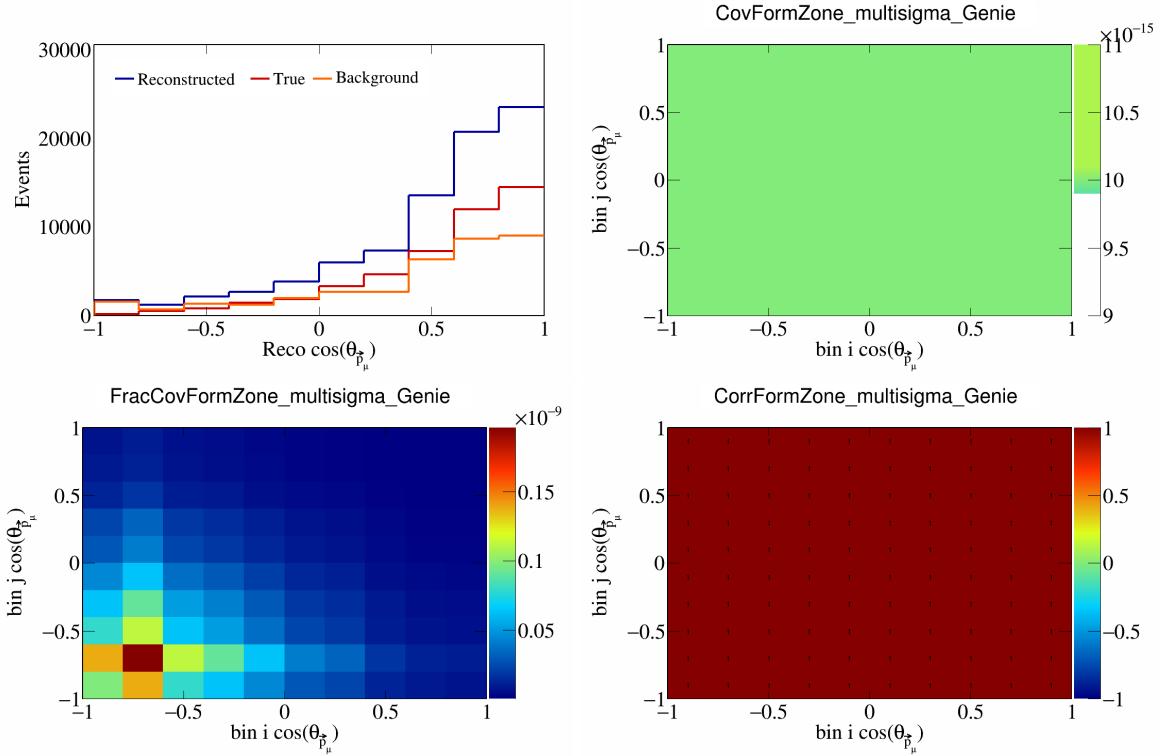


Figure 154: FormZone variations for $\cos(\theta_{\vec{p}_\mu})$.

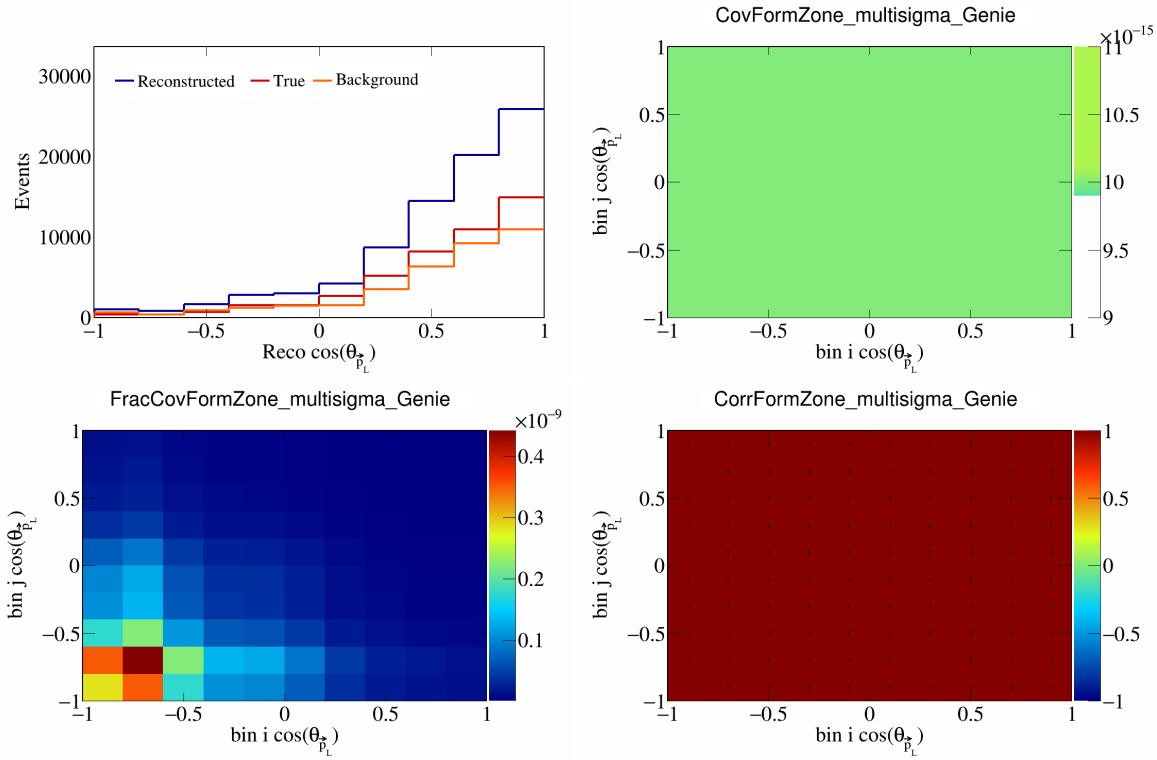


Figure 155: FormZone variations for $\cos(\theta_{\vec{p}_L})$.

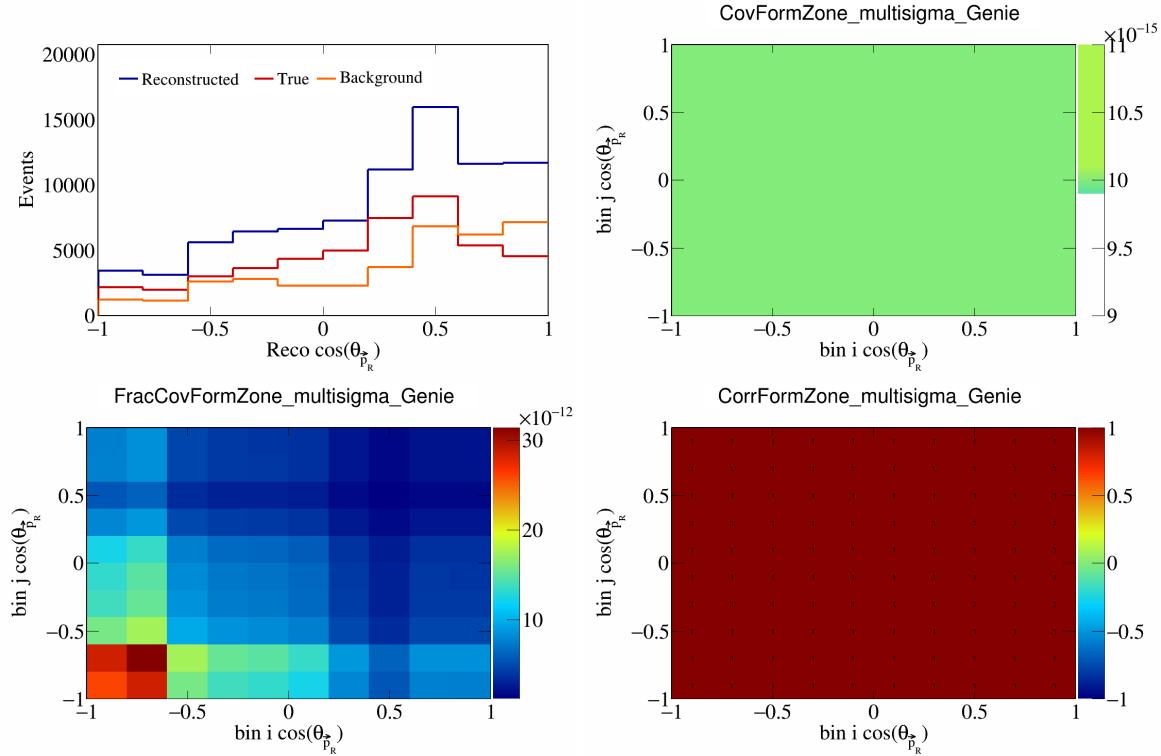


Figure 156: FormZone variations for $\cos(\theta_{\vec{p}_R})$.

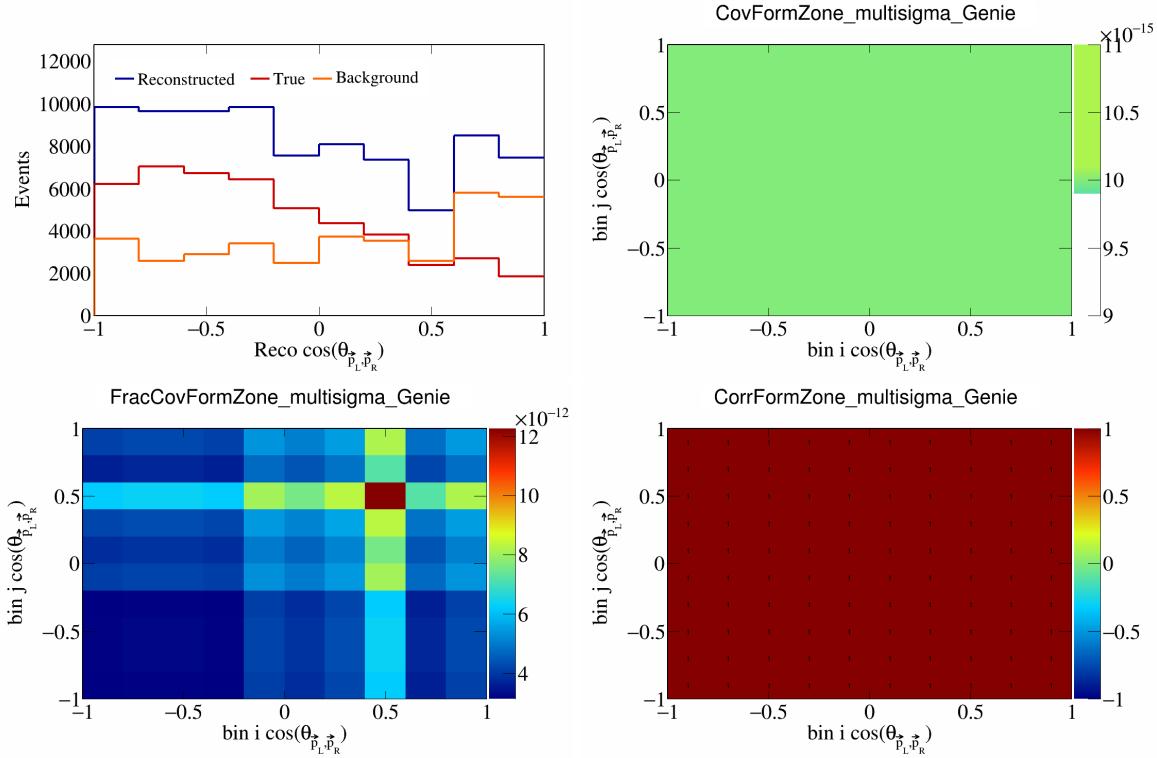


Figure 157: FormZone variations for $\cos(\theta_{\vec{p}_L, \vec{p}_R})$.

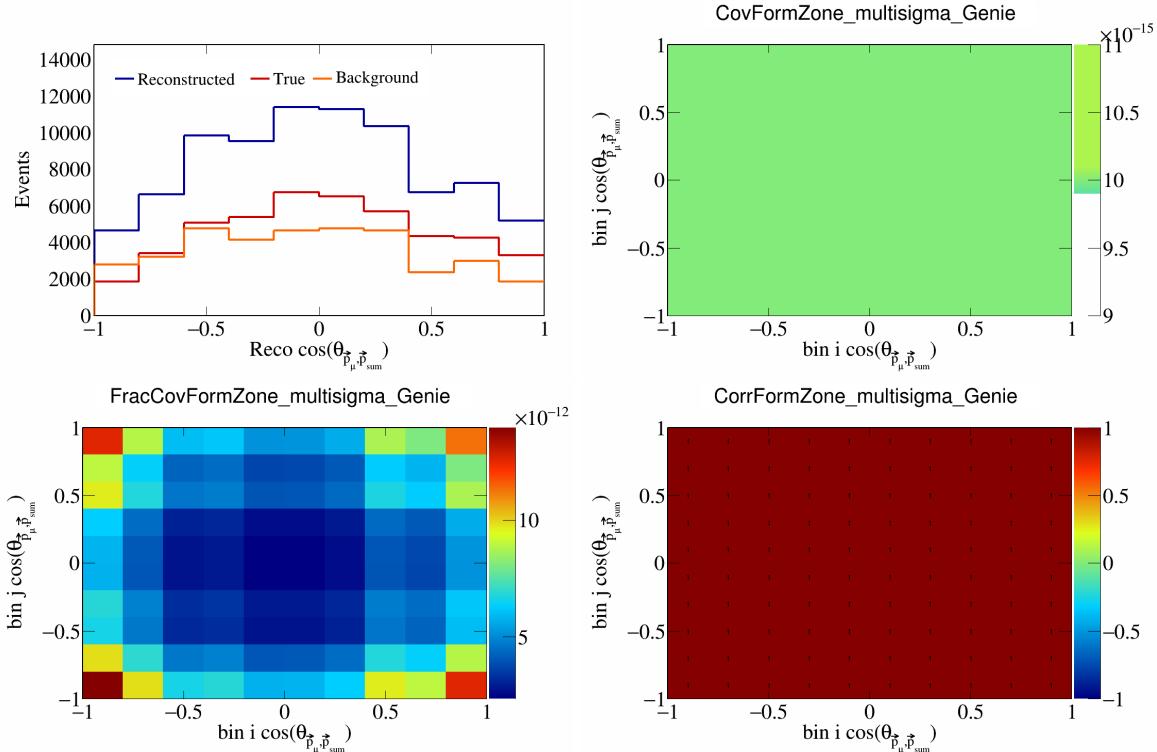


Figure 158: FormZone variations for $\cos(\theta_{\vec{p}_\mu, \vec{p}_{\text{sum}}})$.

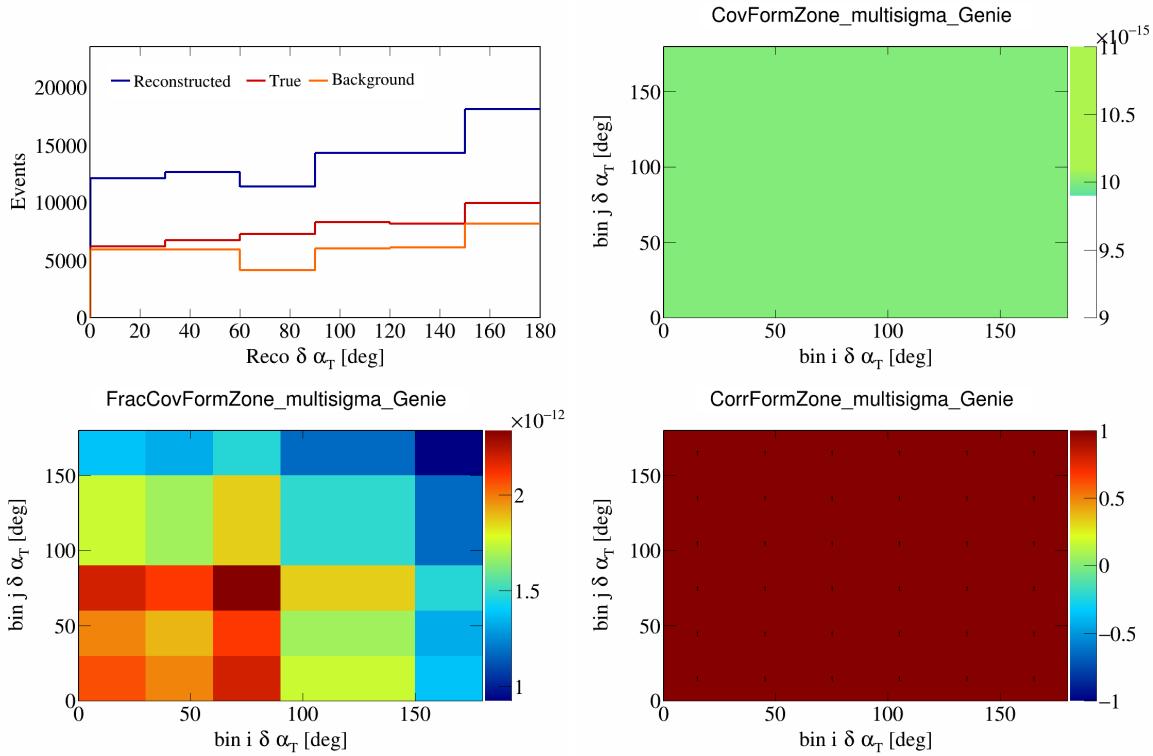


Figure 159: FormZone variations for $\delta \alpha_T$.

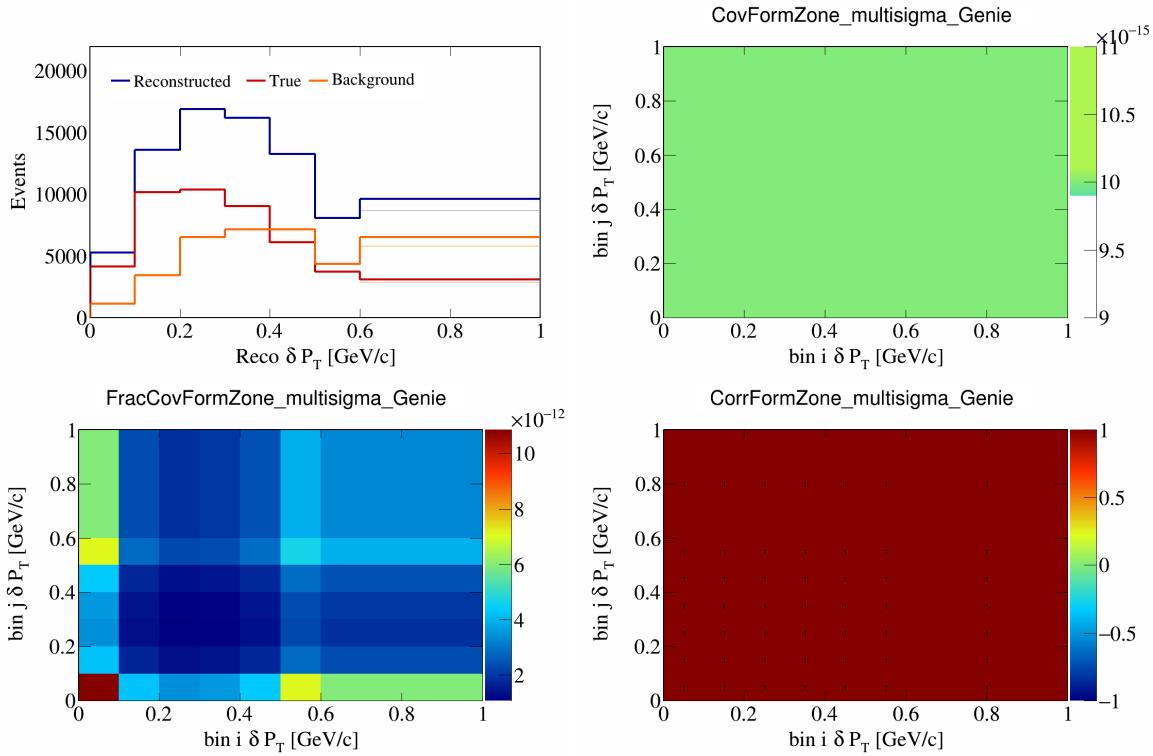


Figure 160: FormZone variations for δP_T .

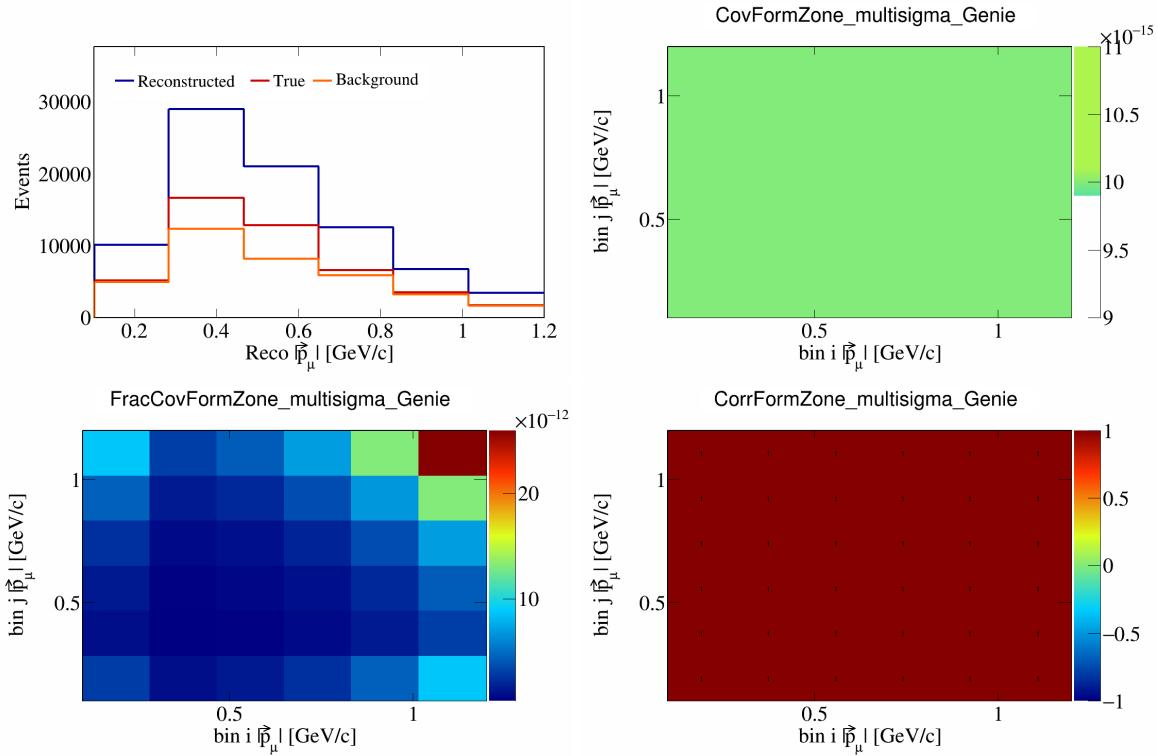


Figure 161: FormZone variations for $|\vec{p}_\mu|$.

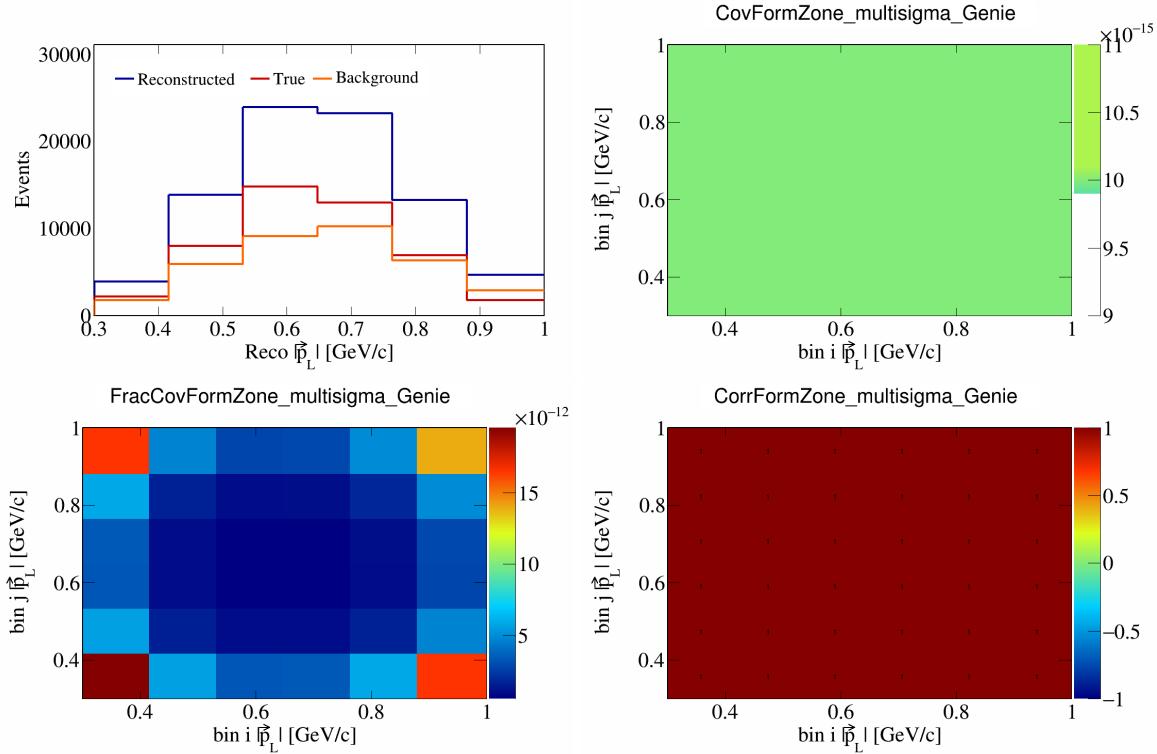


Figure 162: FormZone variations for $|\vec{p}_L|$.

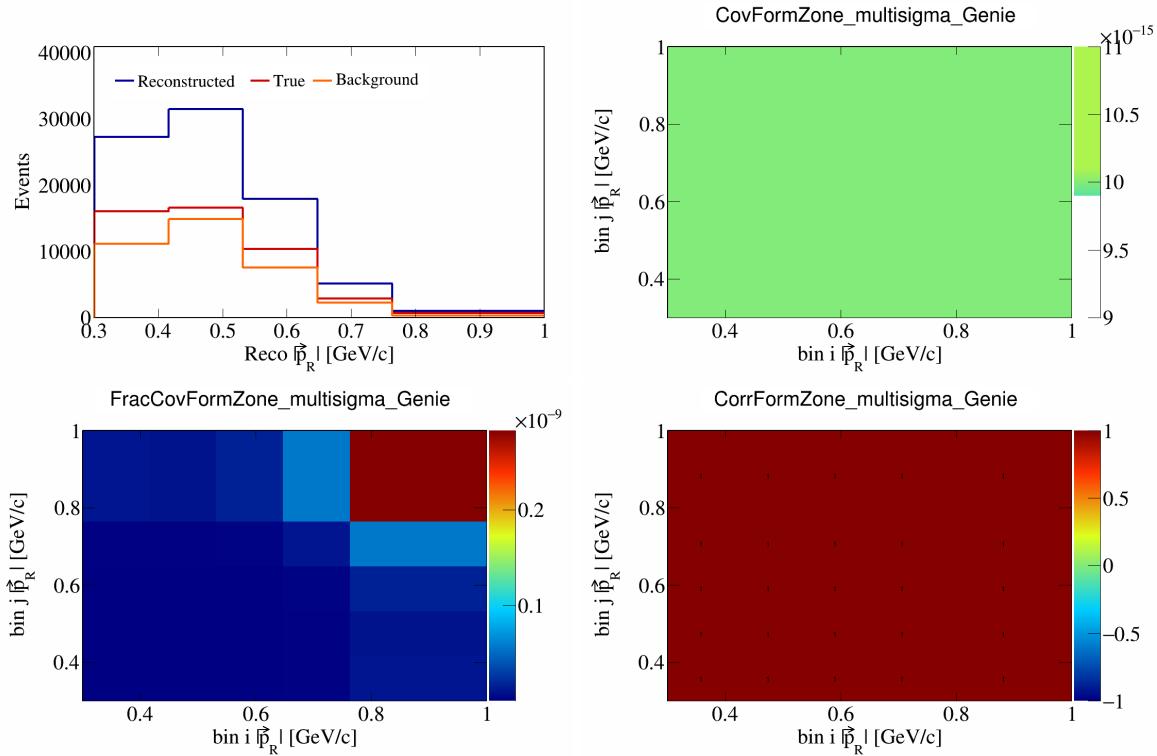


Figure 163: FormZone variations for $|\vec{p}_R|$.

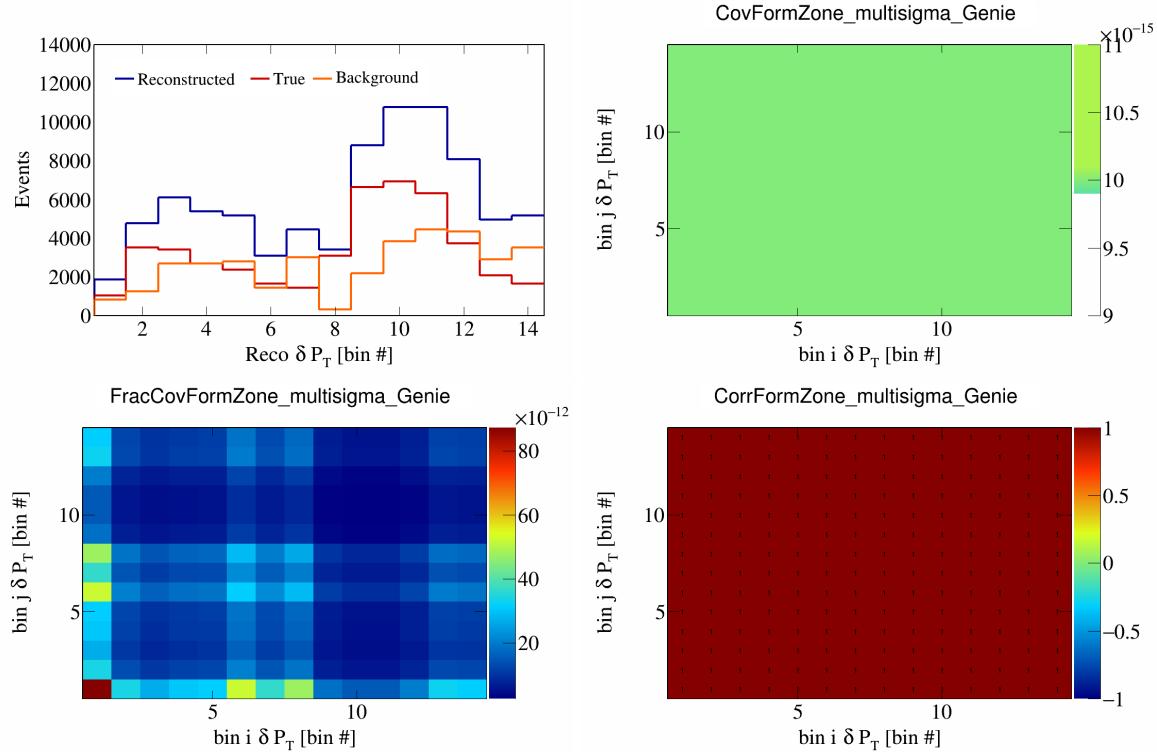


Figure 164: FormZone variations for δP_T in $\cos(\theta_{\vec{p}_\mu})$.

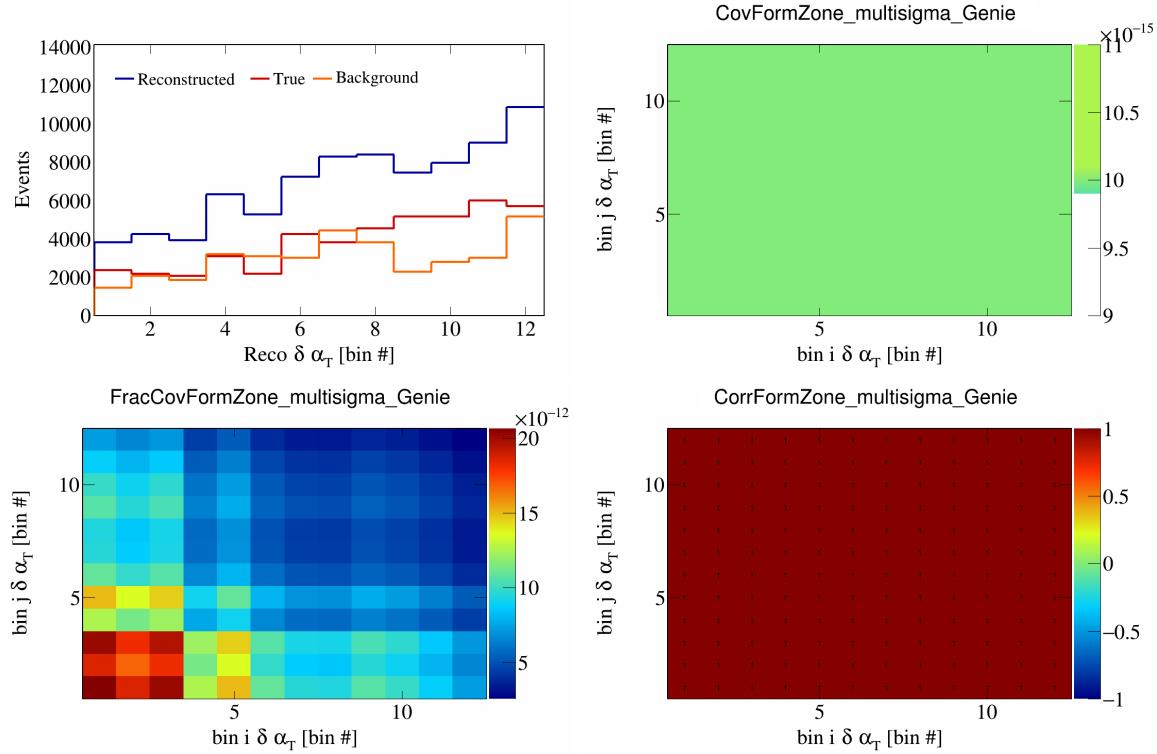


Figure 165: FormZone variations for $\delta\alpha_T$ in $\cos(\theta_{\vec{p}_\mu})$.

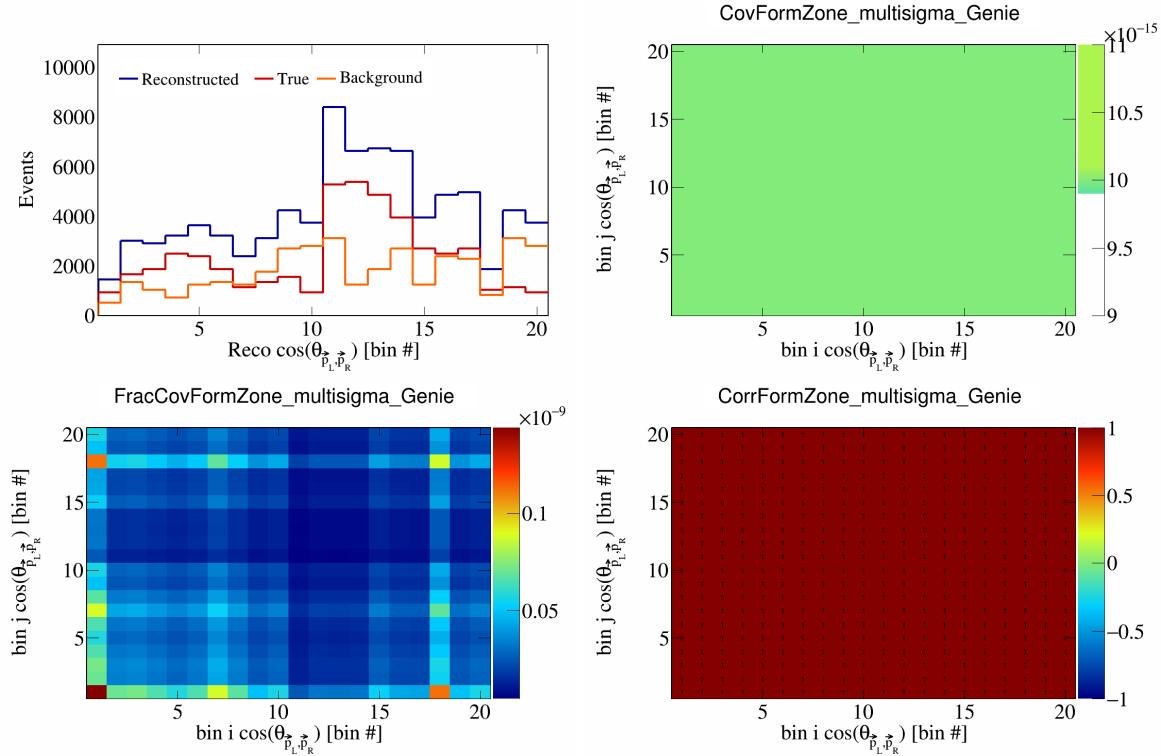


Figure 166: FormZone variations for $\cos(\theta_{\vec{p}_L, \vec{p}_R})$ in $\cos(\theta_{\vec{p}_\mu})$.

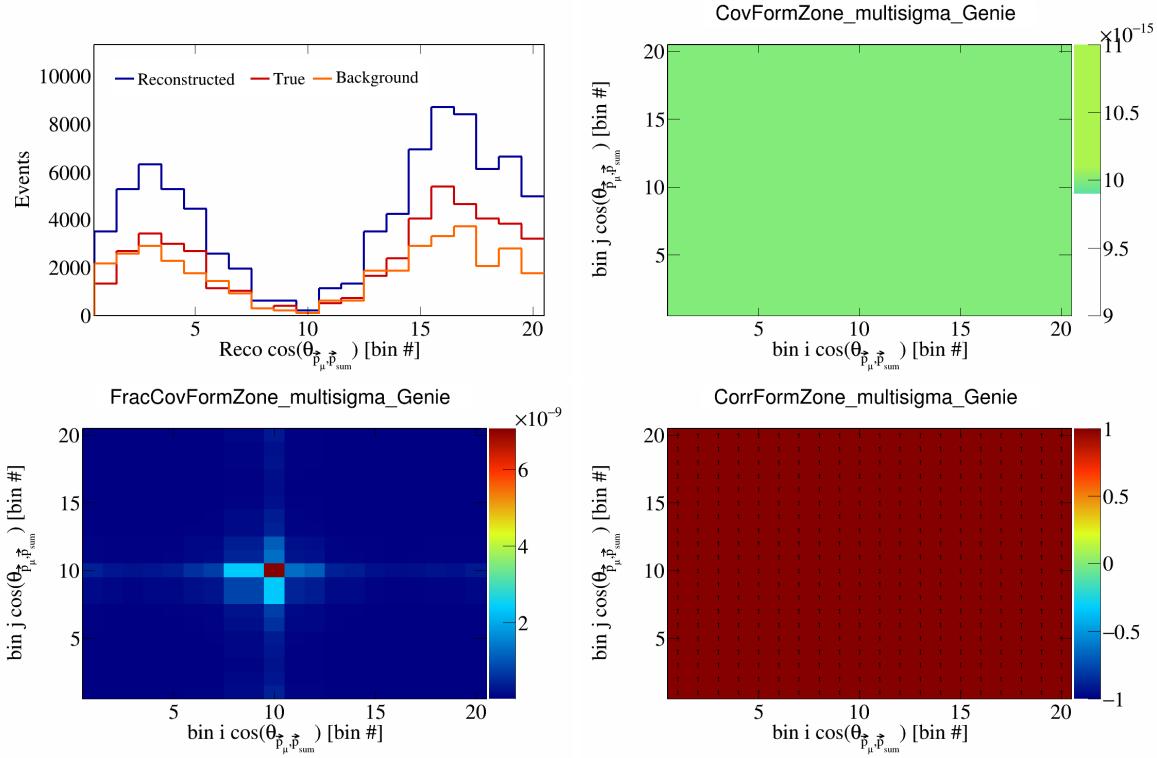


Figure 167: FormZone variations for $\cos(\theta_{\vec{p}_\mu, \vec{p}_{\text{sum}}})$ in $\cos(\theta_{\vec{p}_\mu})$.

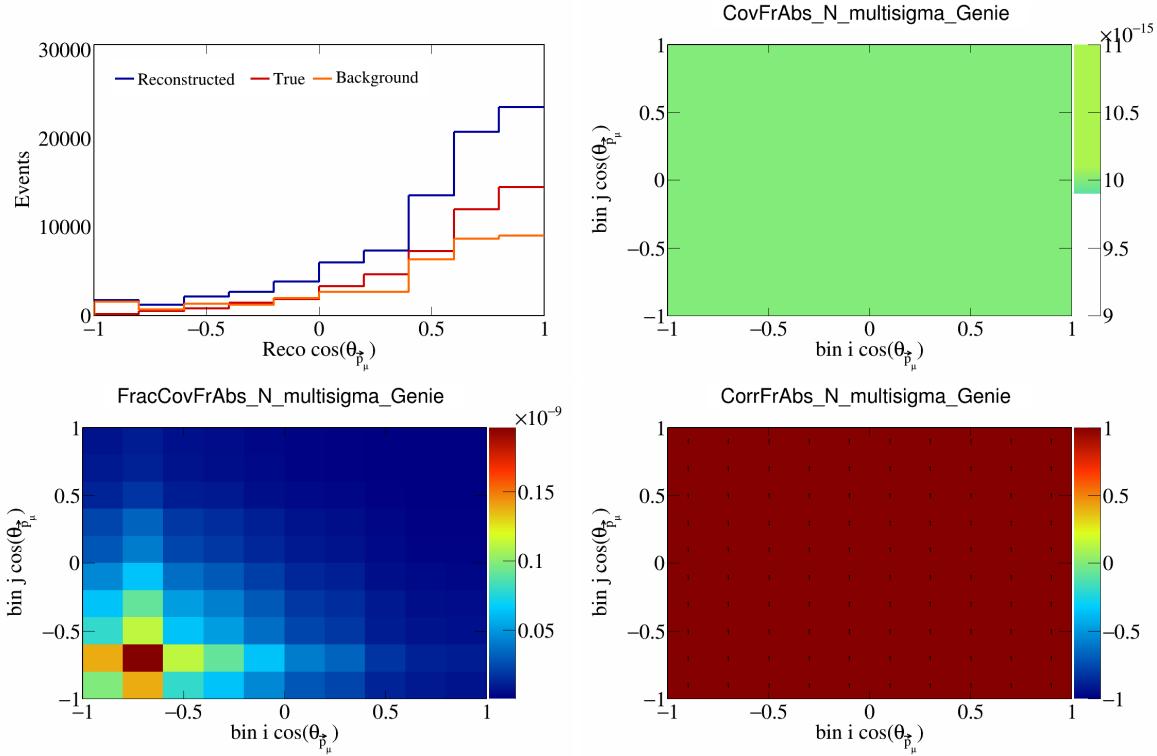


Figure 168: FrAbsN variations for $\cos(\theta_{\vec{p}_\mu})$.

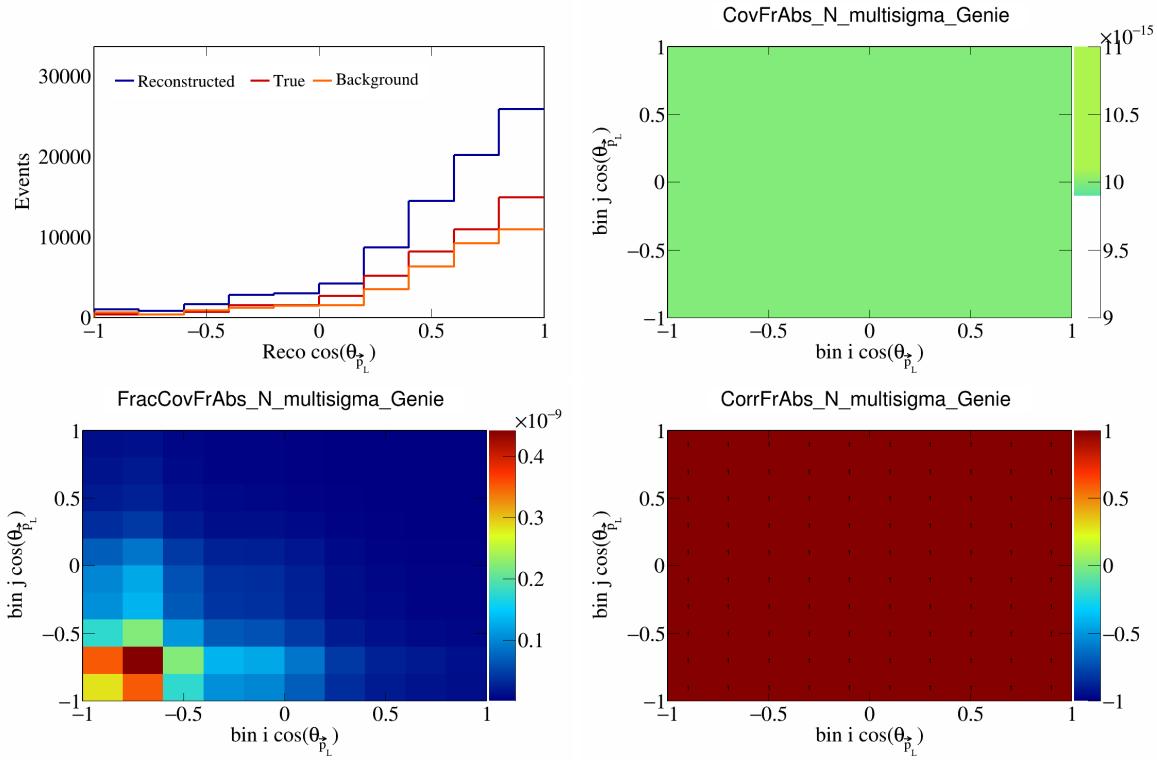


Figure 169: FrAbsN variations for $\cos(\theta_{\vec{p}_L})$.

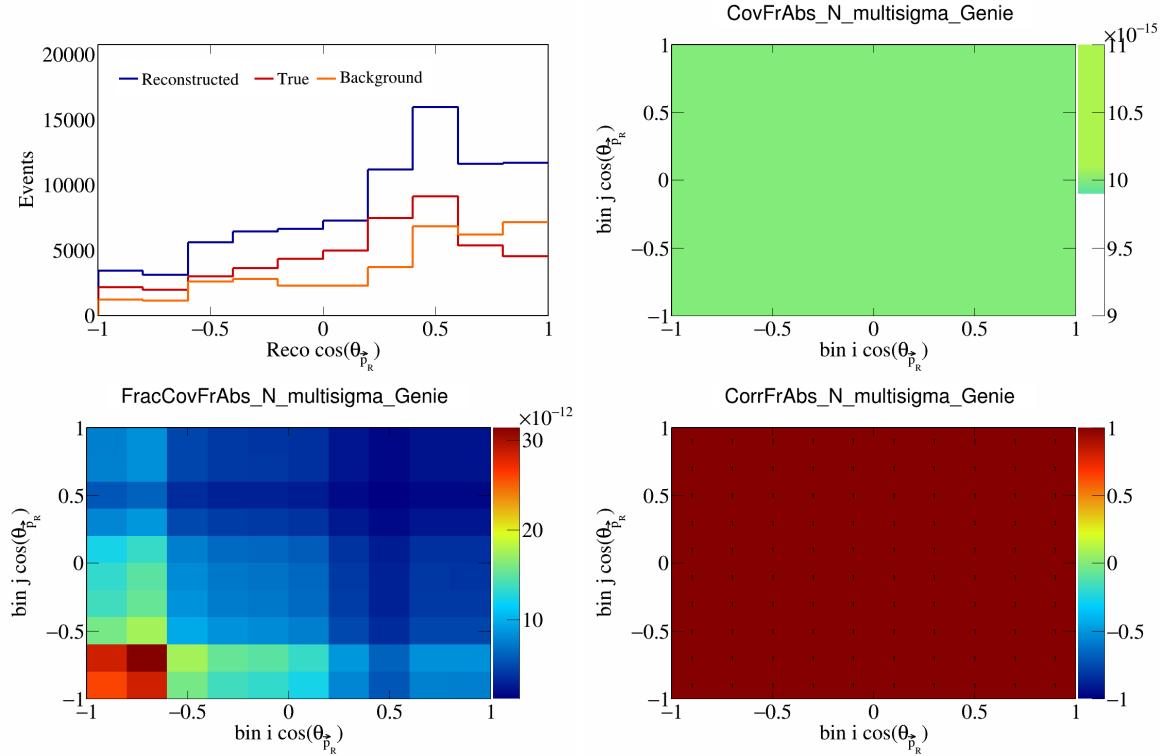


Figure 170: FrAbsN variations for $\cos(\theta_{\vec{p}_R})$.

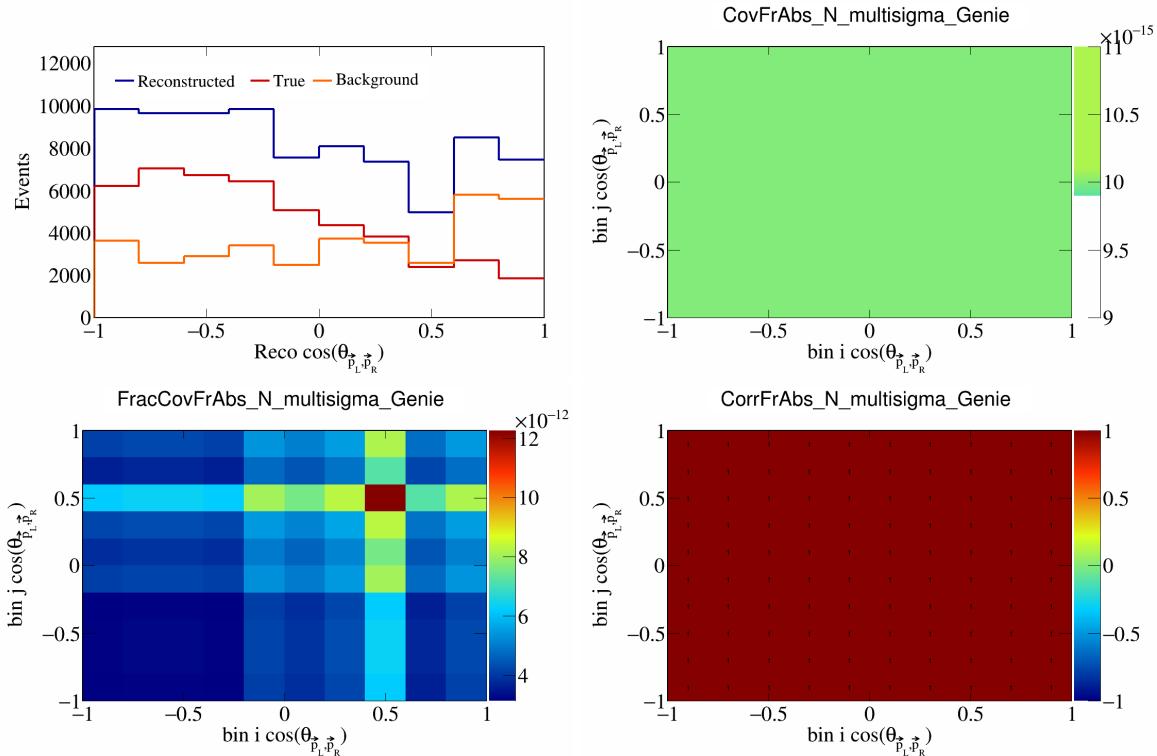


Figure 171: FrAbsN variations for $\cos(\theta_{\vec{p}_L, \vec{p}_R})$.

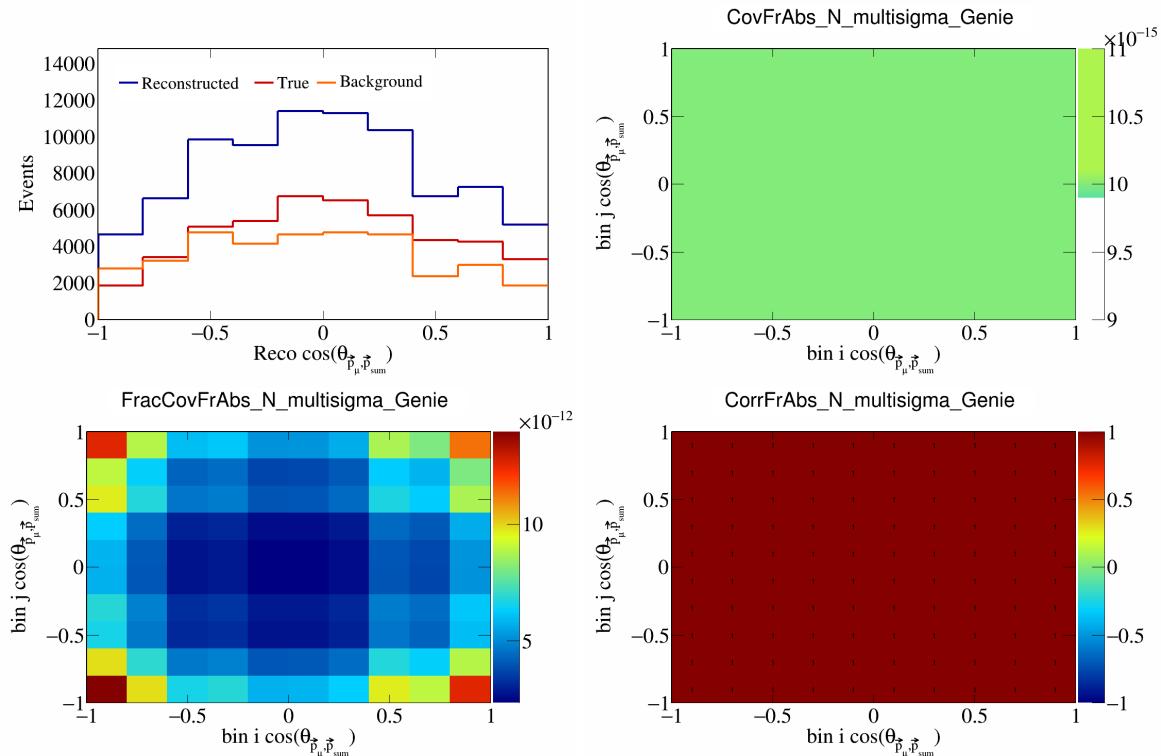


Figure 172: FrAbsN variations for $\cos(\theta_{\vec{p}_\mu, \vec{p}_{\text{sum}}})$.

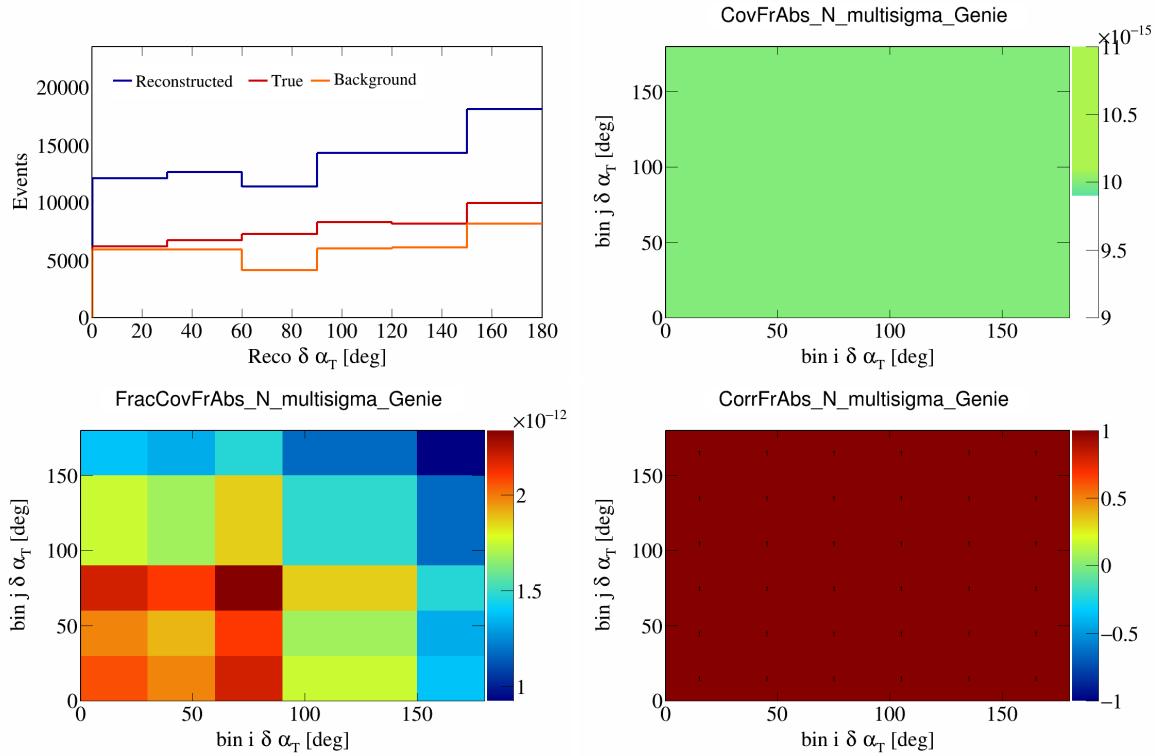


Figure 173: FrAbsN variations for $\delta \alpha_T$.

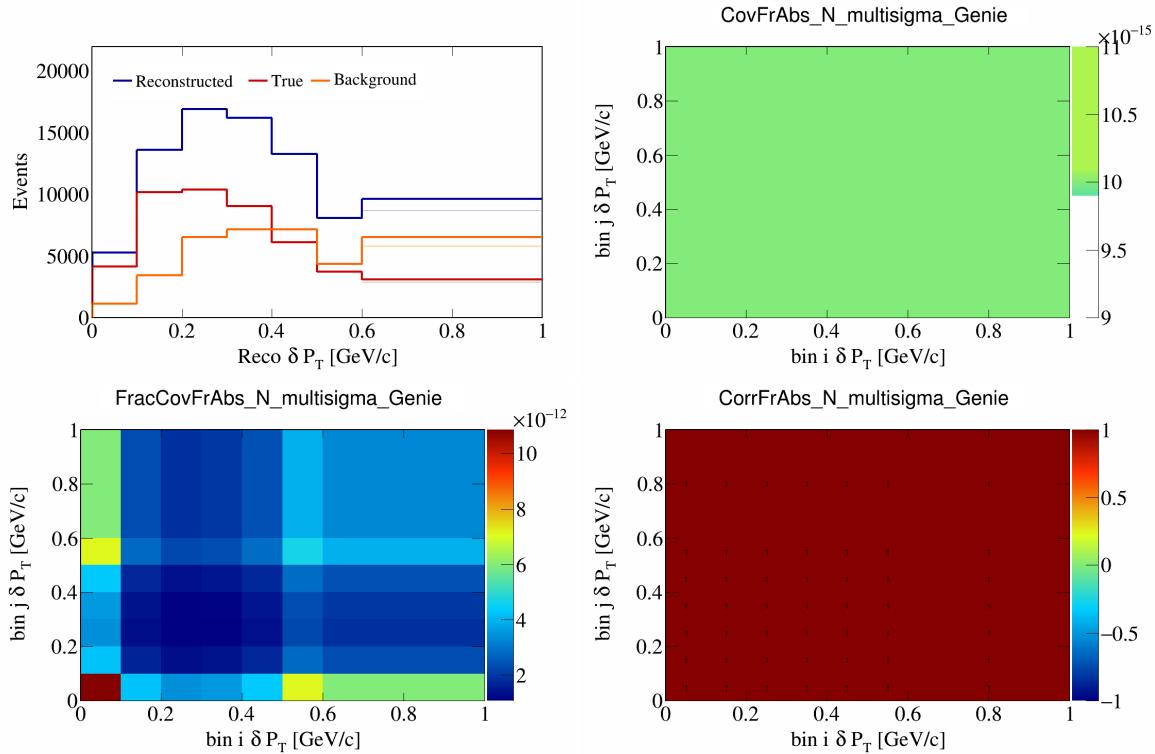


Figure 174: FrAbsN variations for δP_T .

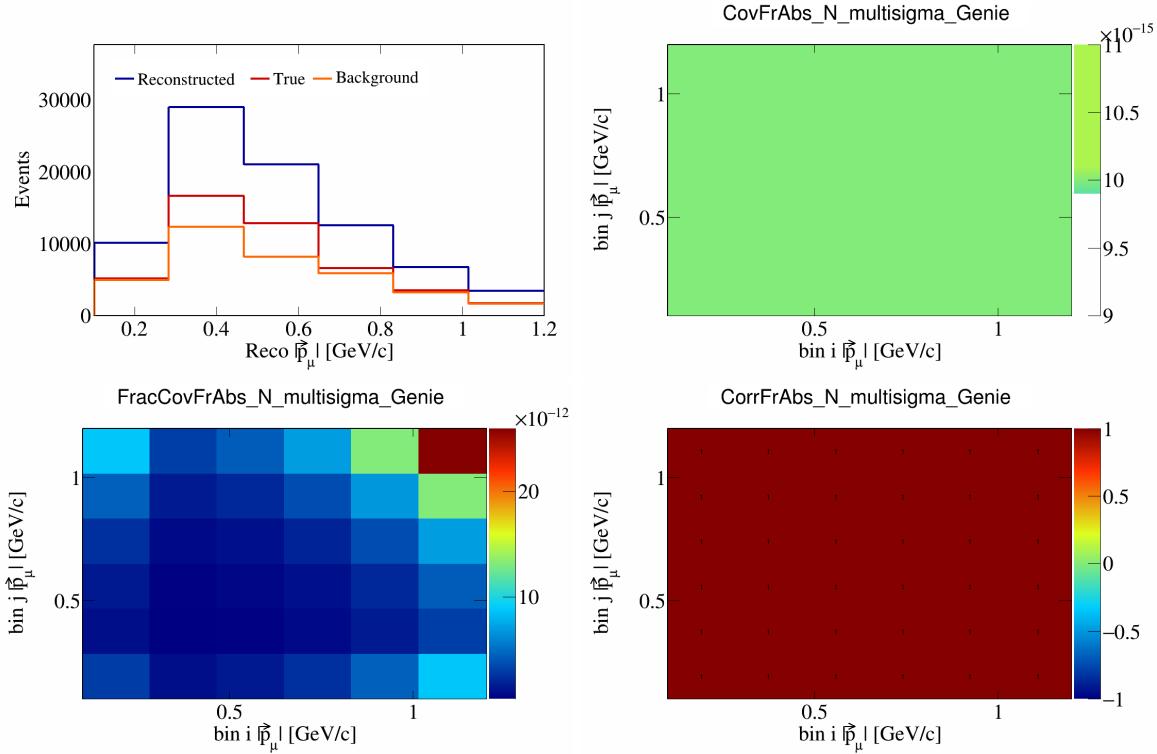


Figure 175: FrAbsN variations for $|\vec{p}_\mu|$.

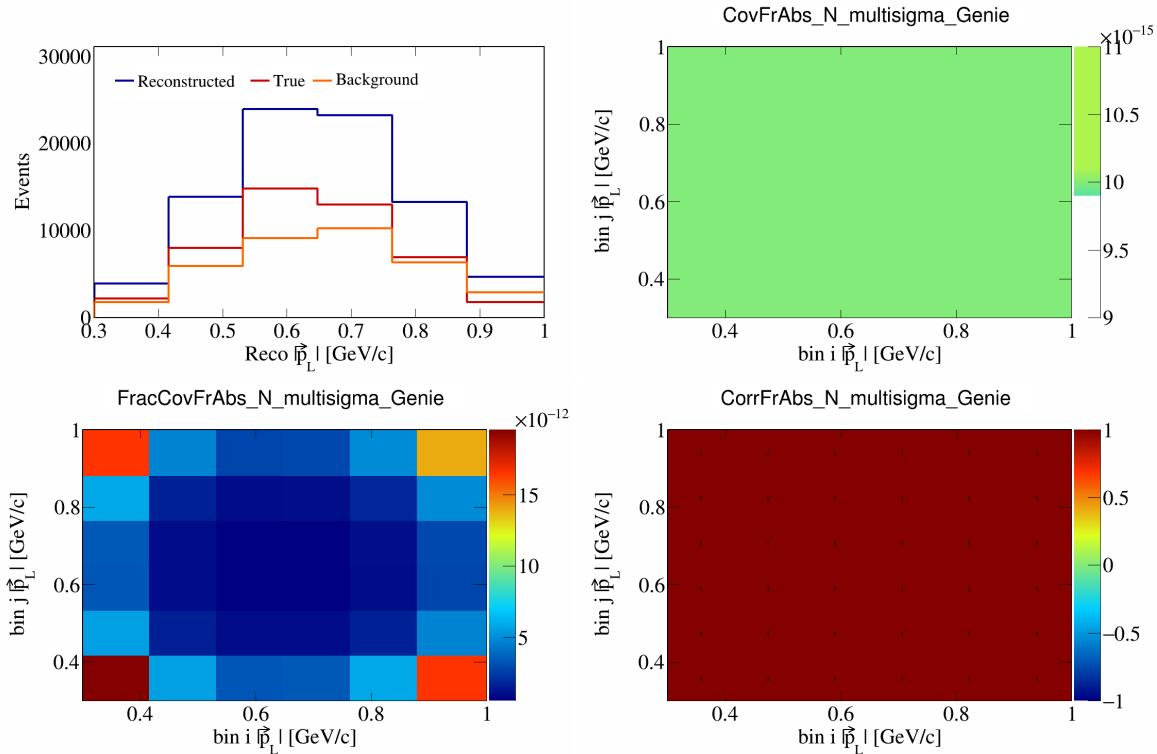


Figure 176: FrAbsN variations for $|\vec{p}_L|$.

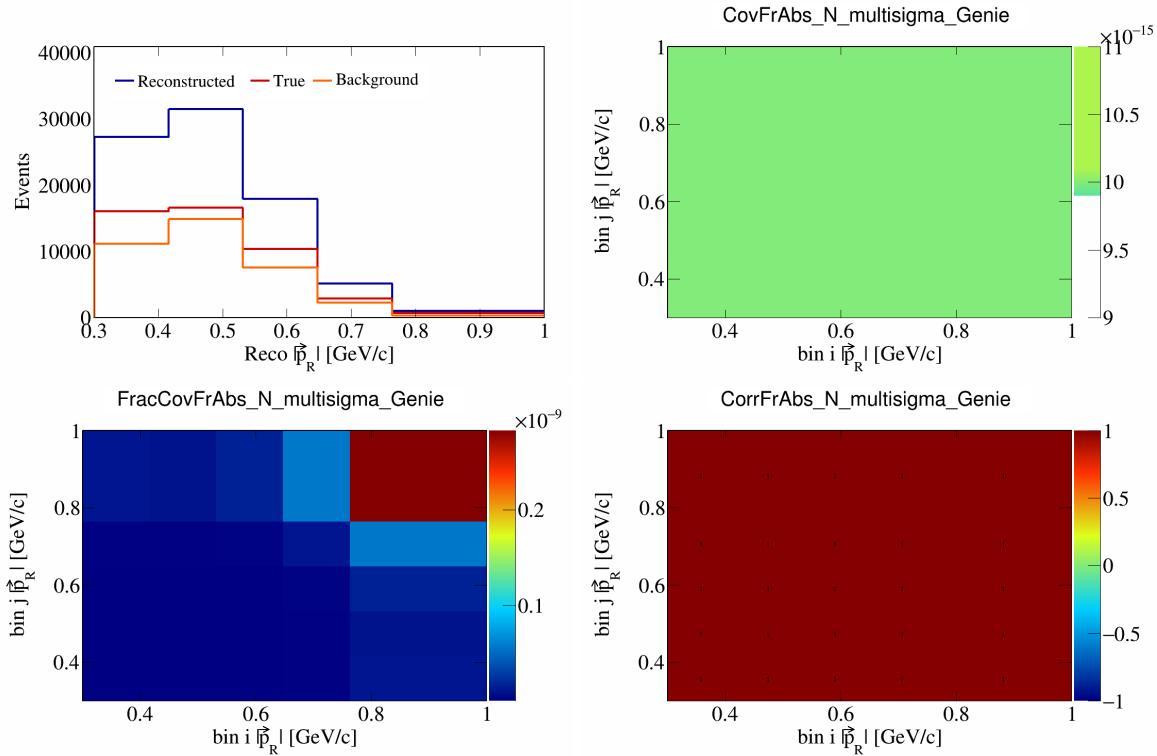


Figure 177: FrAbsN variations for $|\vec{p}_R|$.

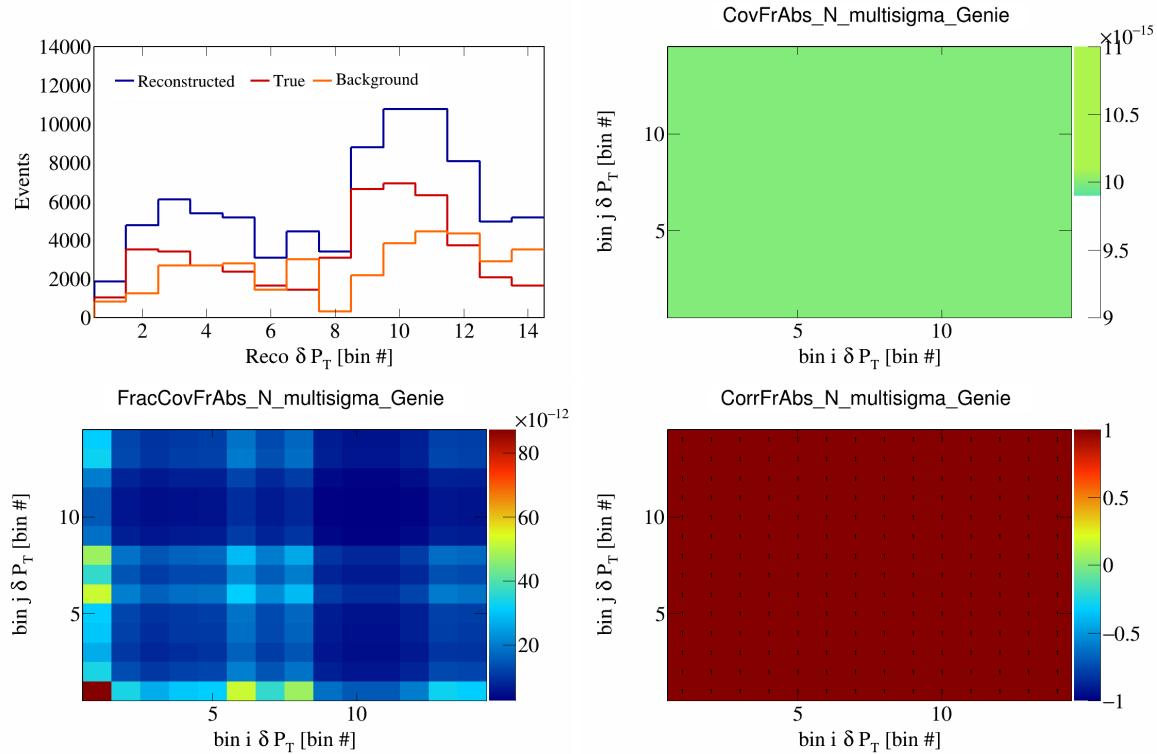


Figure 178: FrAbsN variations for δP_T in $\cos(\theta_{\vec{p}_\mu})$.

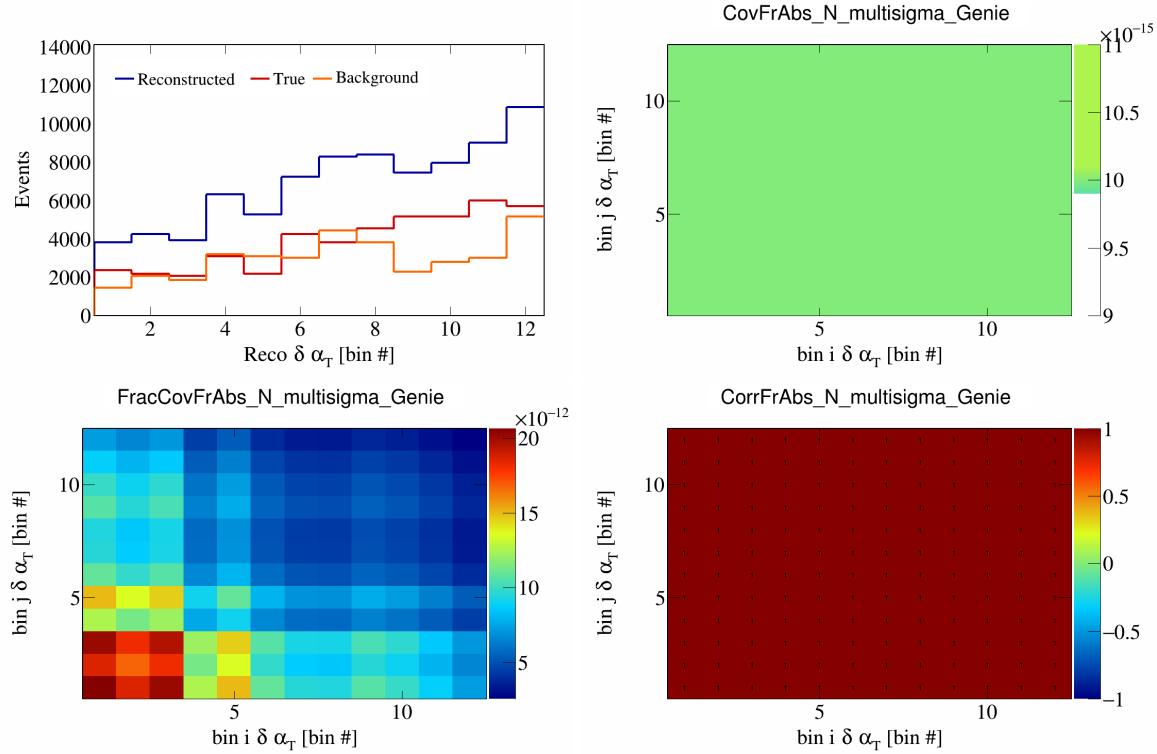


Figure 179: FrAbsN variations for $\delta \alpha_T$ in $\cos(\theta_{\vec{p}_\mu})$.

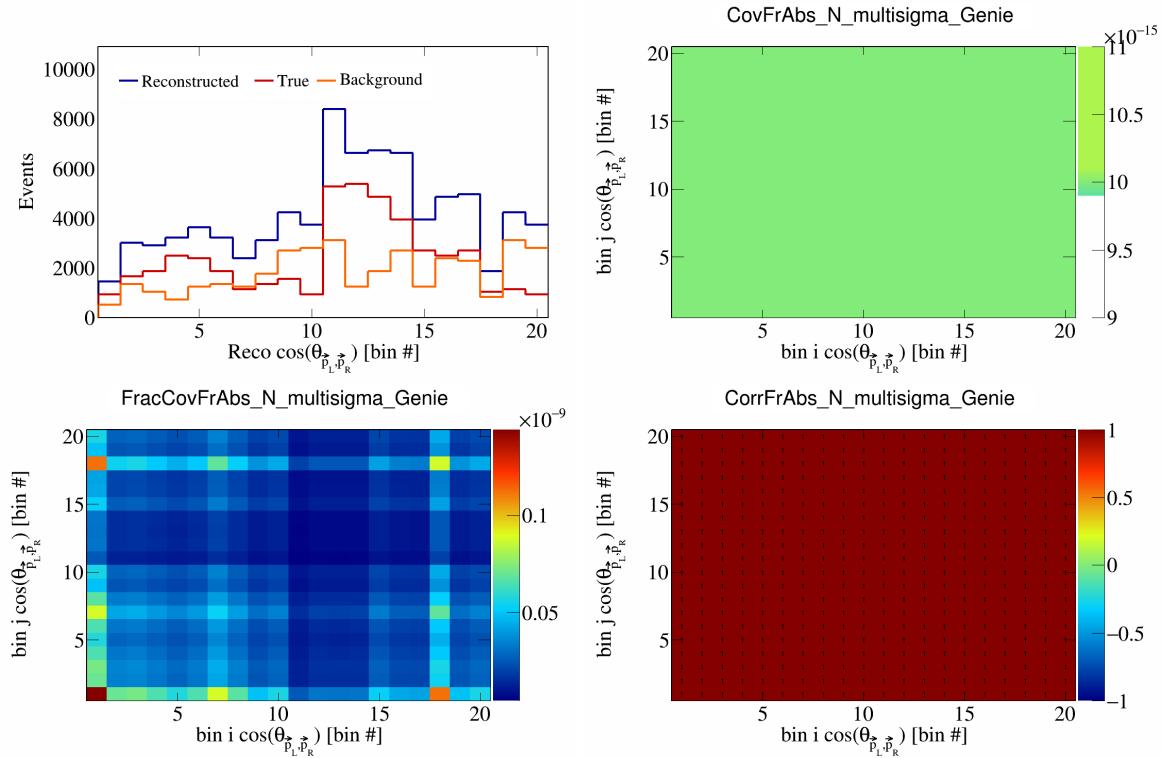


Figure 180: FrAbsN variations for $\cos(\theta_{\vec{p}_L, \vec{p}_R})$ in $\cos(\theta_{\vec{p}_\mu})$.

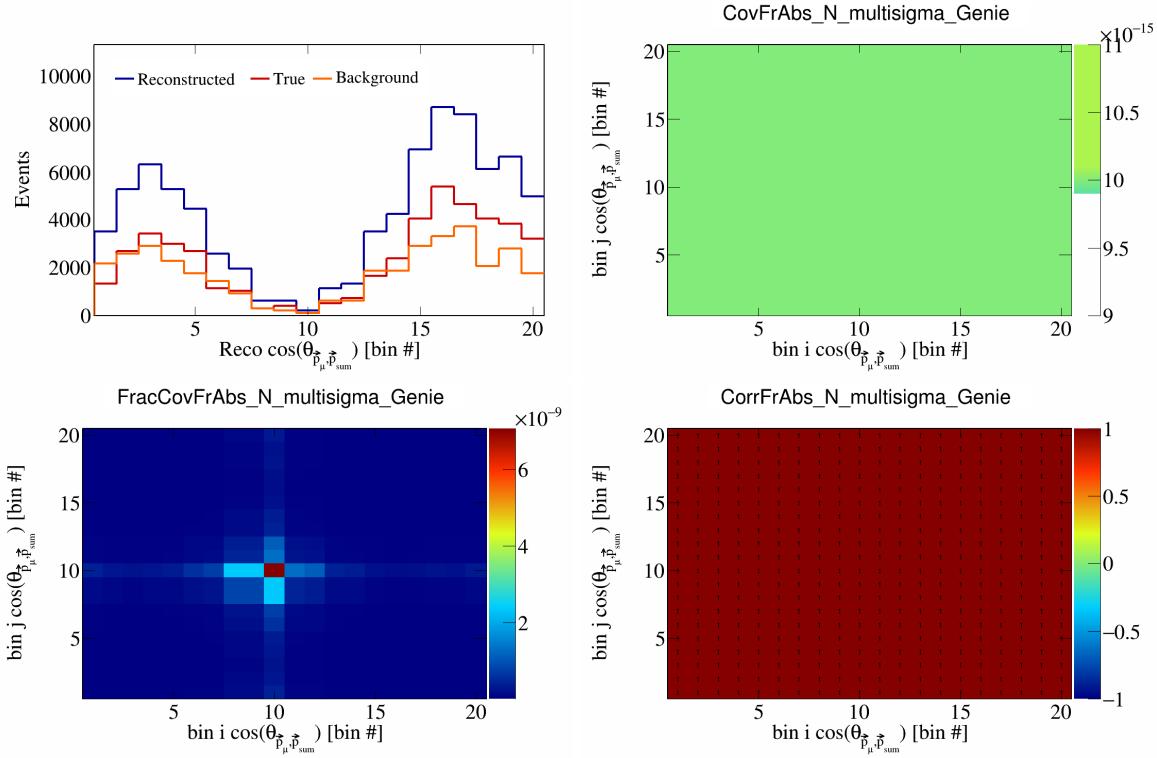


Figure 181: FrAbsN variations for $\cos(\theta_{\vec{p}_\mu, \vec{p}_{\text{sum}}})$ in $\cos(\theta_{\vec{p}_\mu})$.

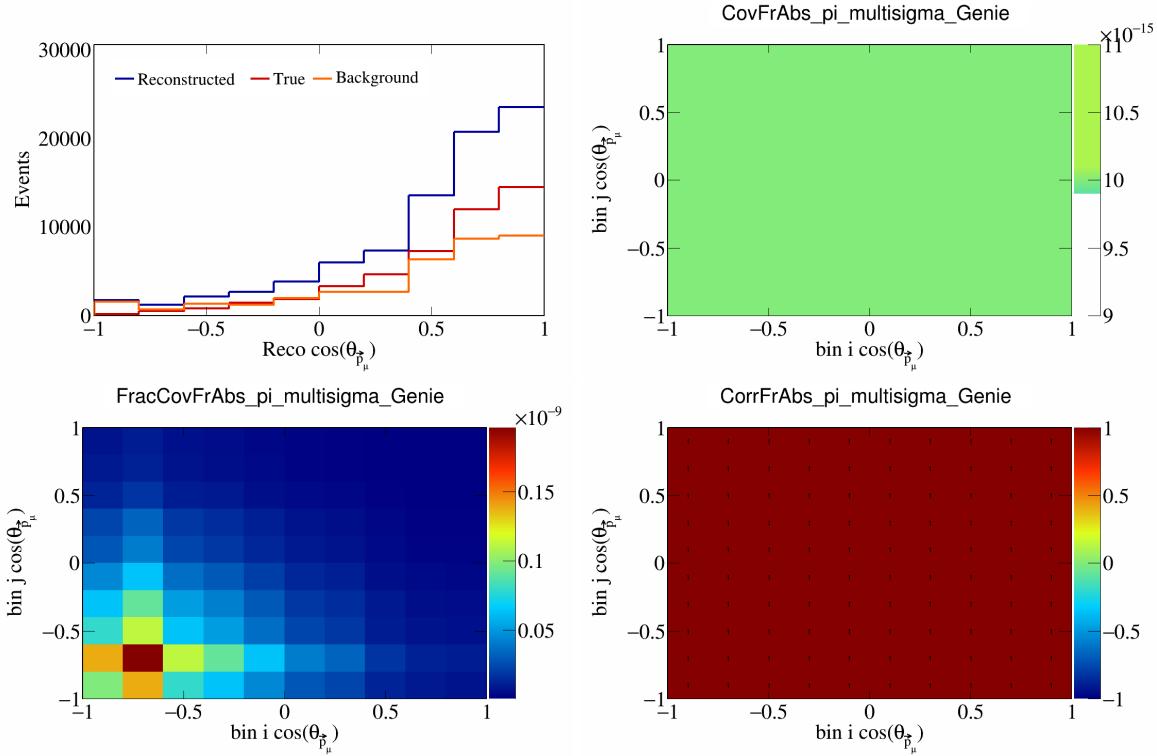


Figure 182: FrAbspi variations for $\cos(\theta_{\vec{p}_\mu})$.

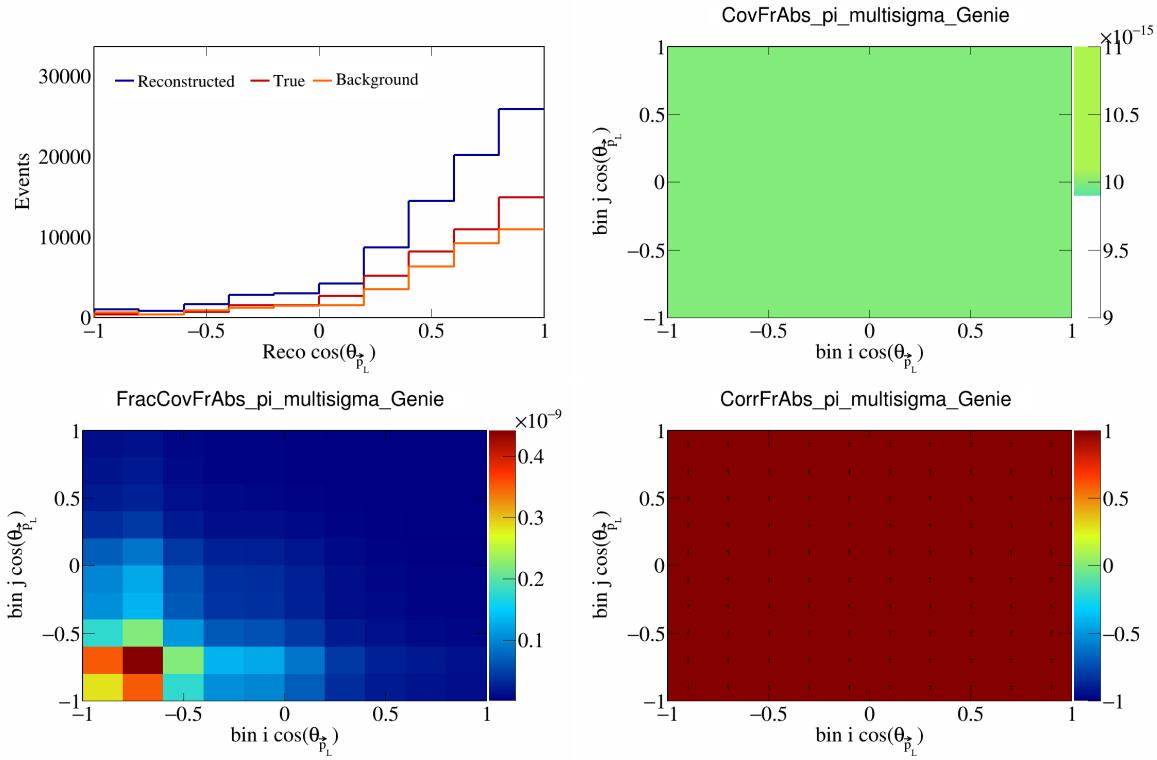


Figure 183: FrAbspi variations for $\cos(\theta_{\vec{p}_L})$.

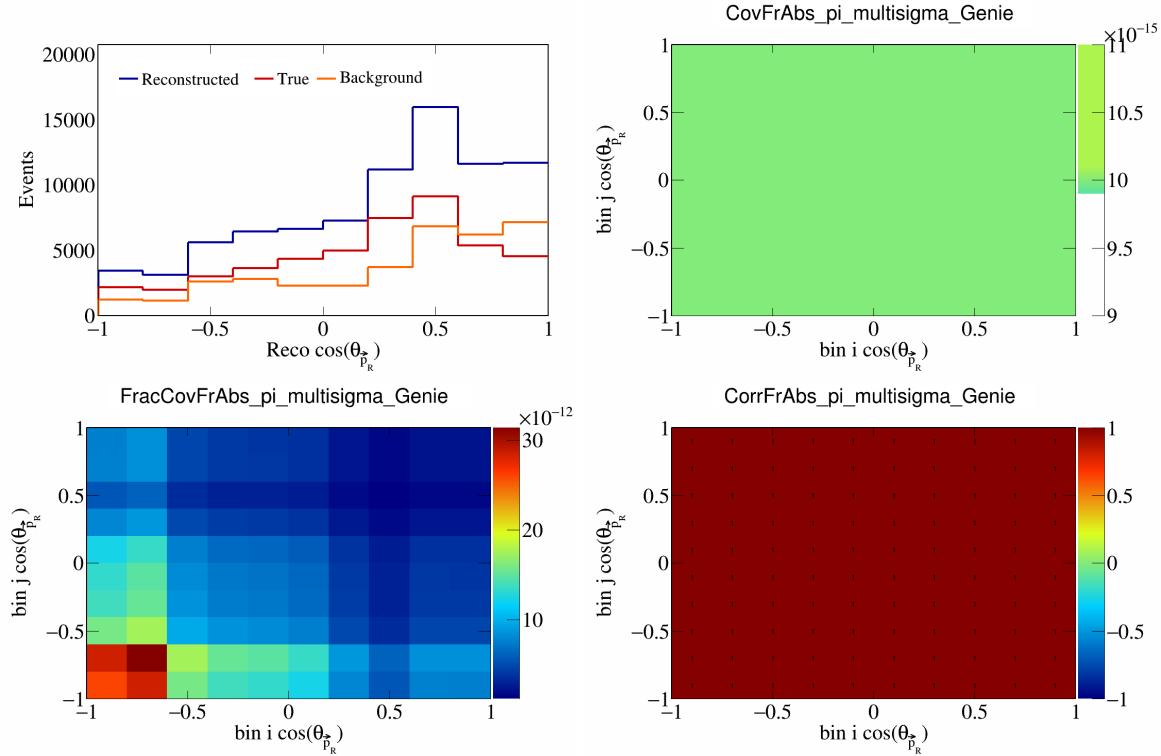


Figure 184: FrAbspi variations for $\cos(\theta_{\vec{p}_R})$.

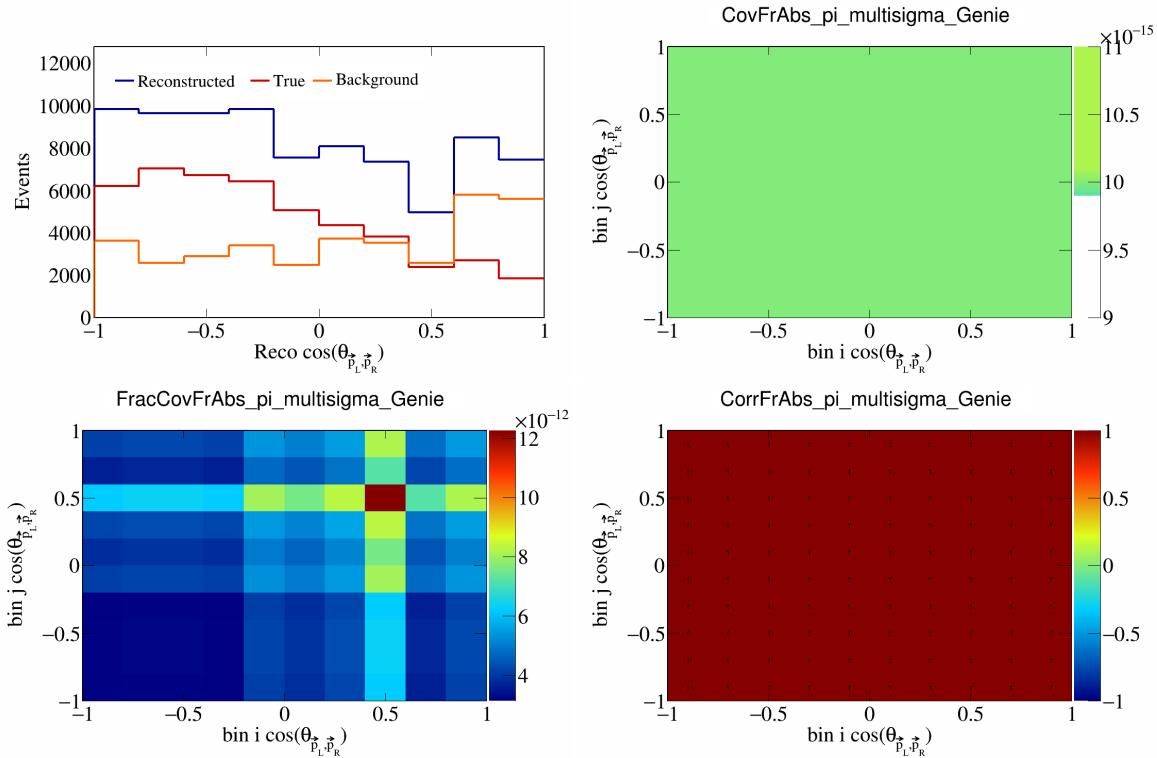


Figure 185: FrAbspi variations for $\cos(\theta_{\vec{p}_L, \vec{p}_R})$.

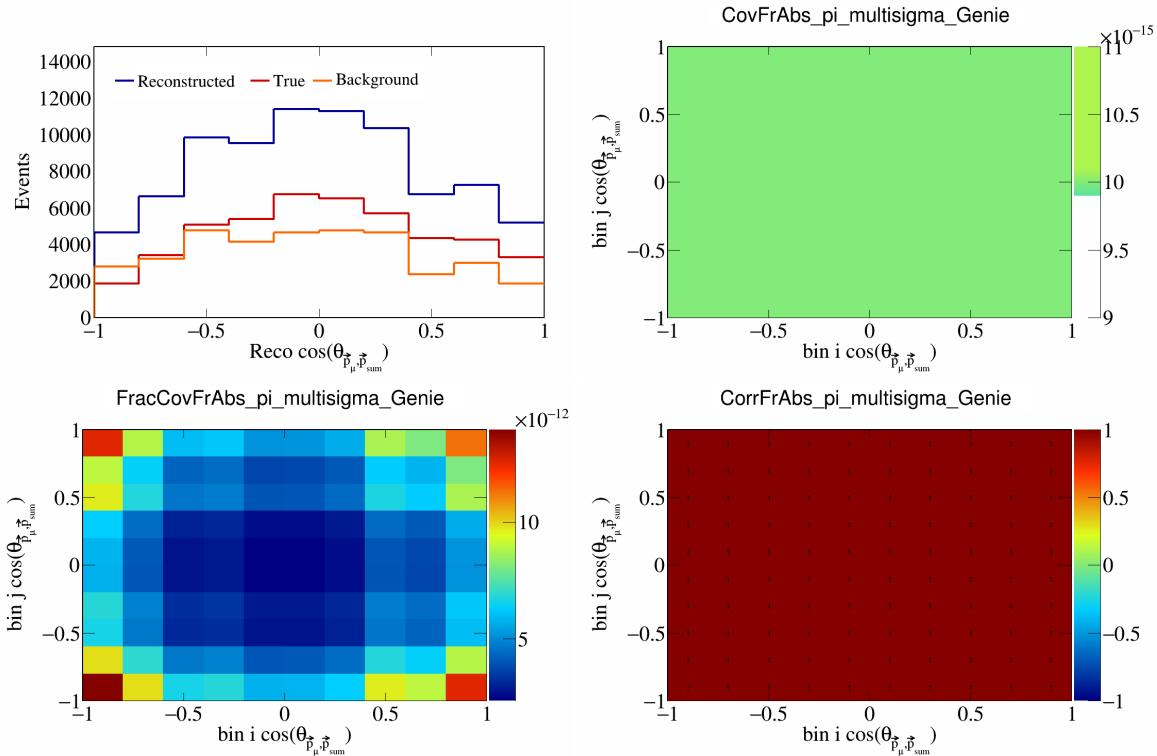


Figure 186: FrAbspi variations for $\cos(\theta_{\vec{p}_\mu, \vec{p}_{\text{sum}}})$.

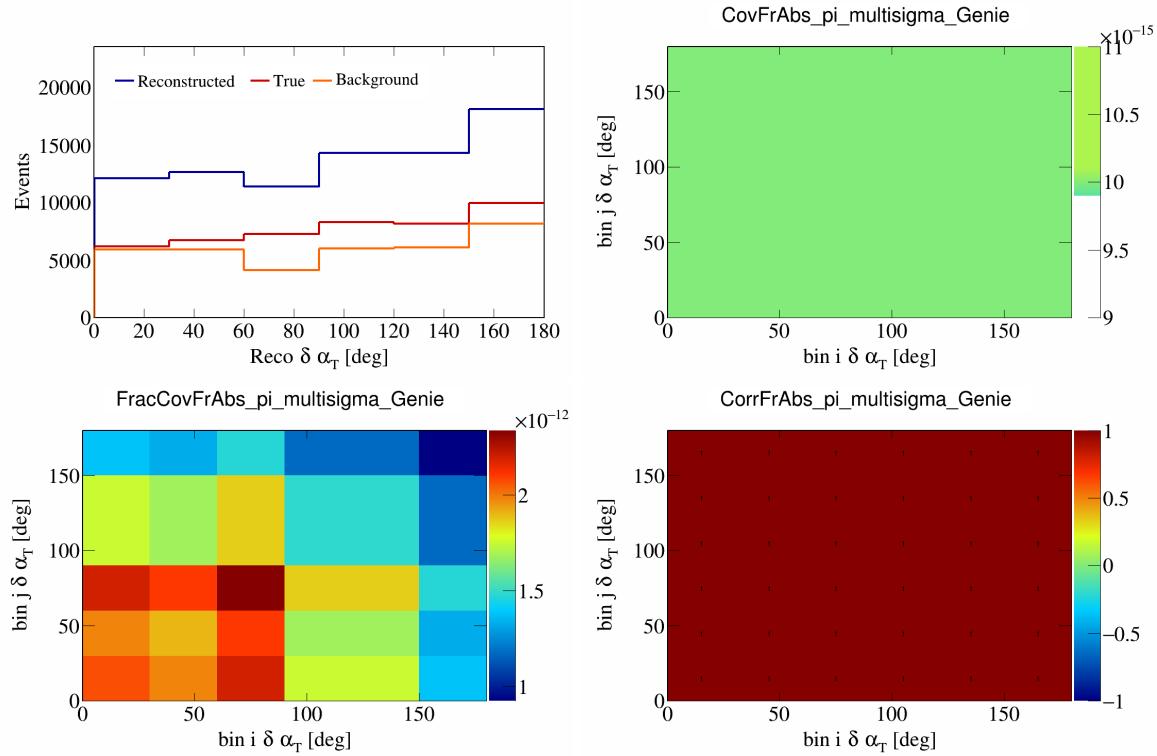


Figure 187: FrAbspi variations for $\delta \alpha_T$.

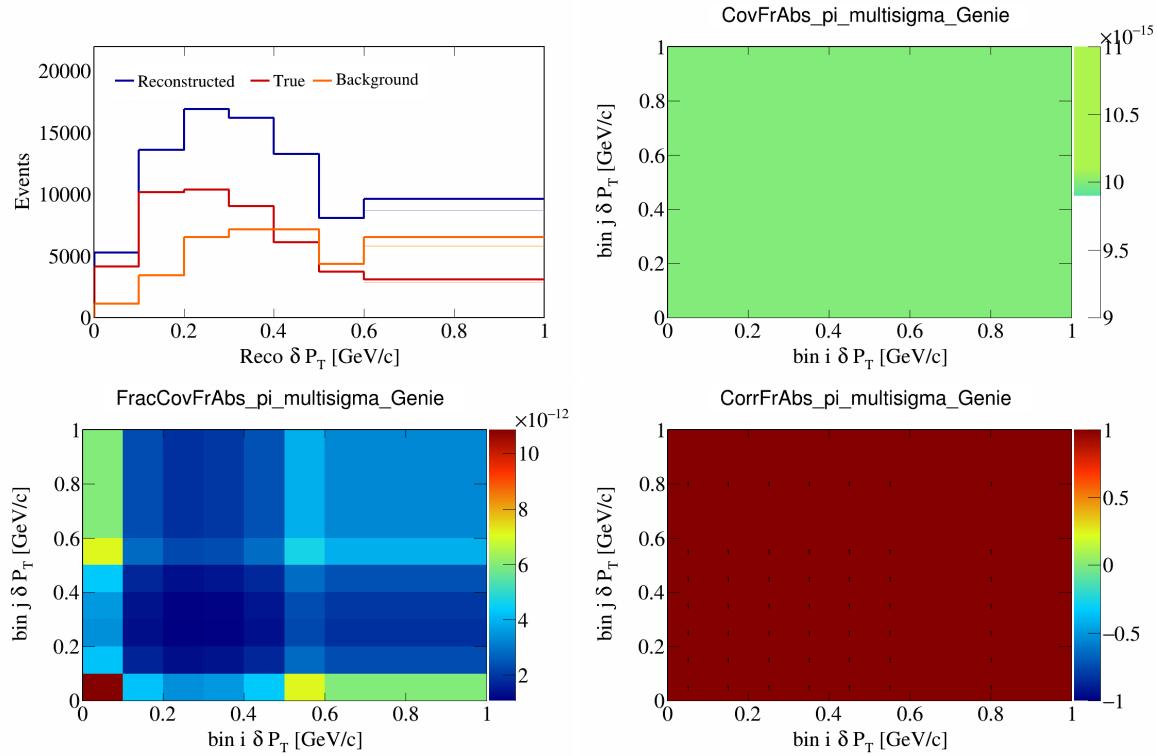


Figure 188: FrAbspi variations for δP_T .

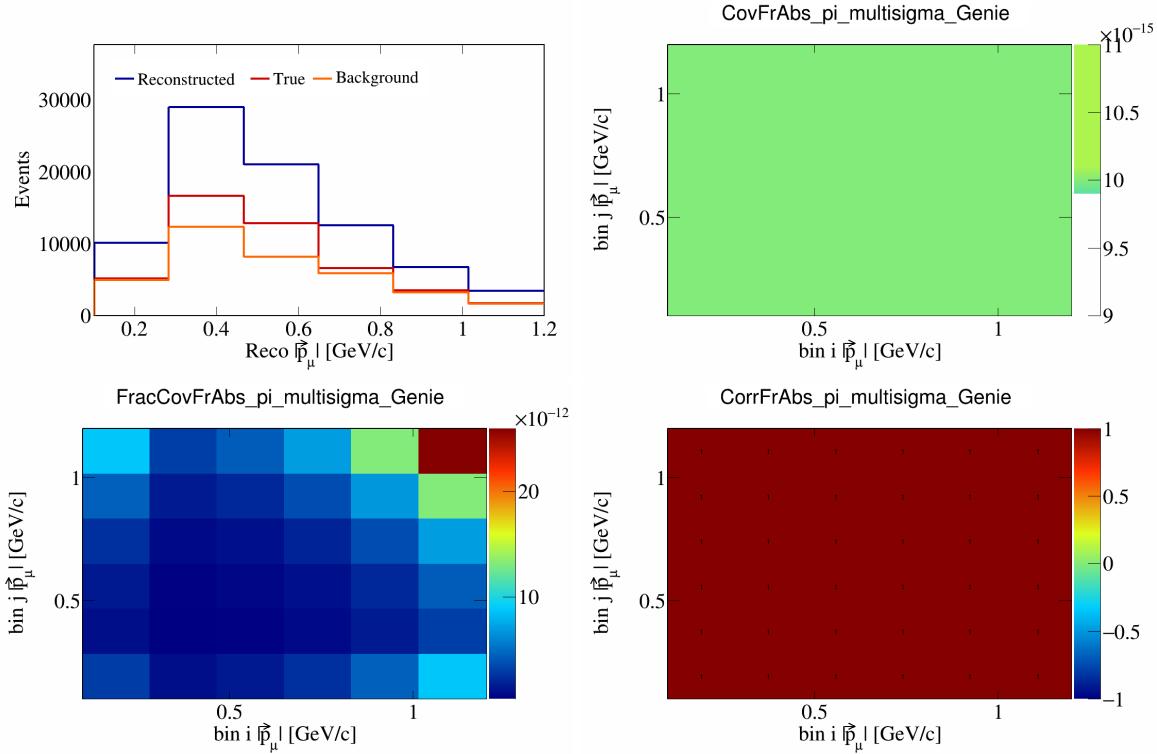


Figure 189: FrAbspi variations for $|\vec{p}_\mu|$.

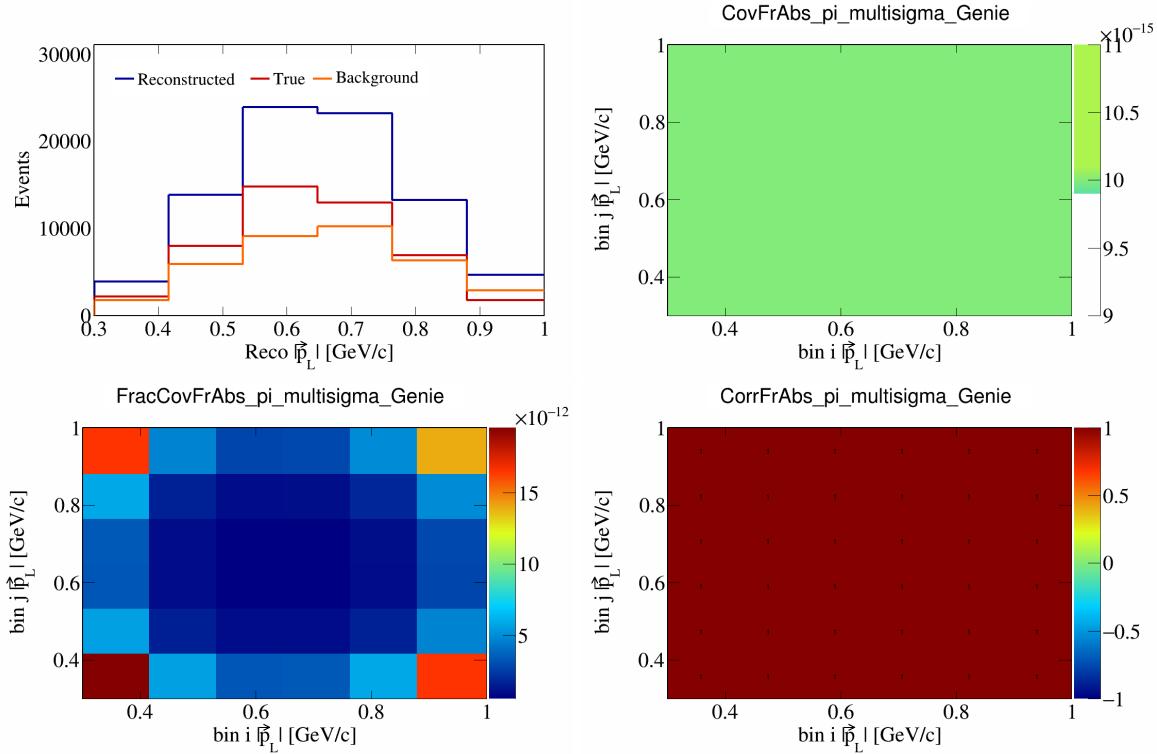


Figure 190: FrAbspi variations for $|\vec{p}_L|$.

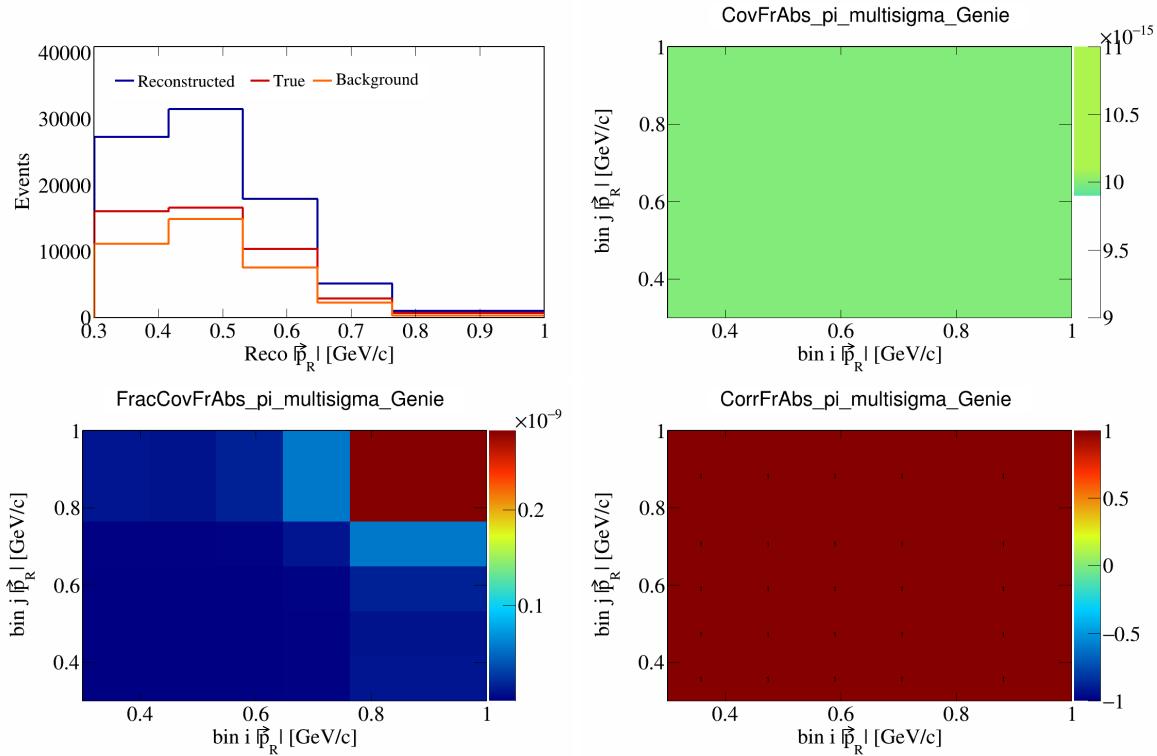


Figure 191: FrAbspi variations for $|\vec{p}_R|$.

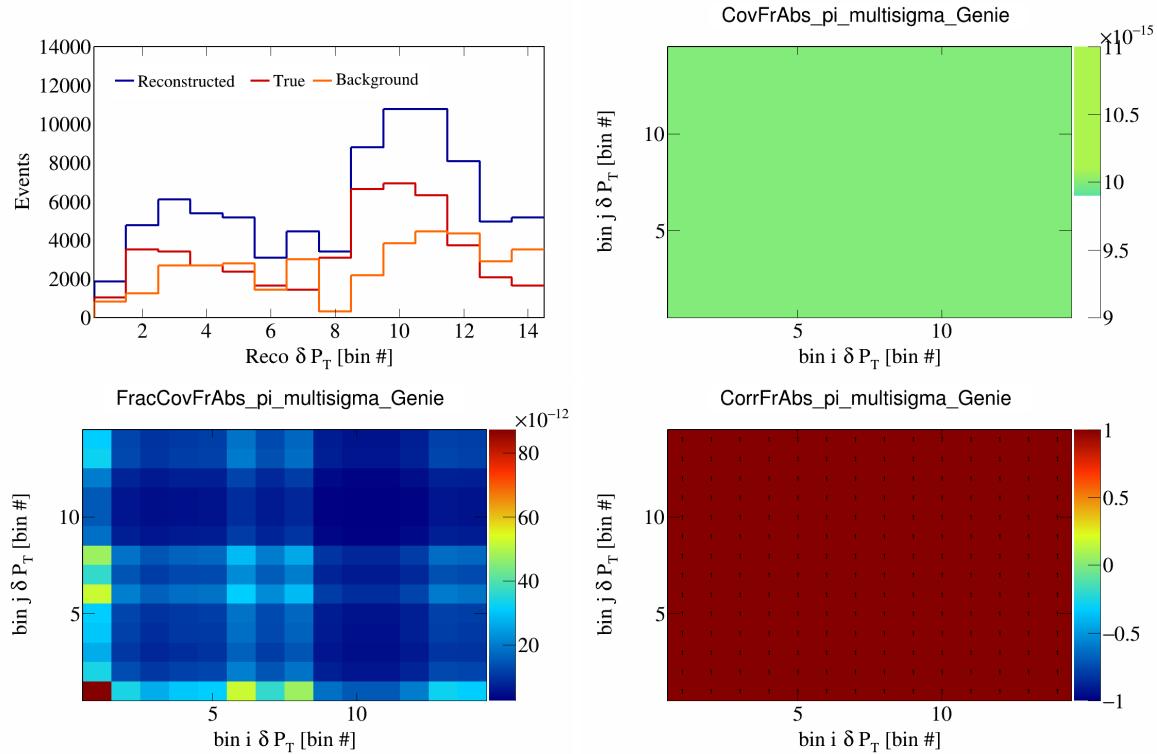


Figure 192: FrAbspi variations for δP_T in $\cos(\theta_{\vec{p}_\mu})$.

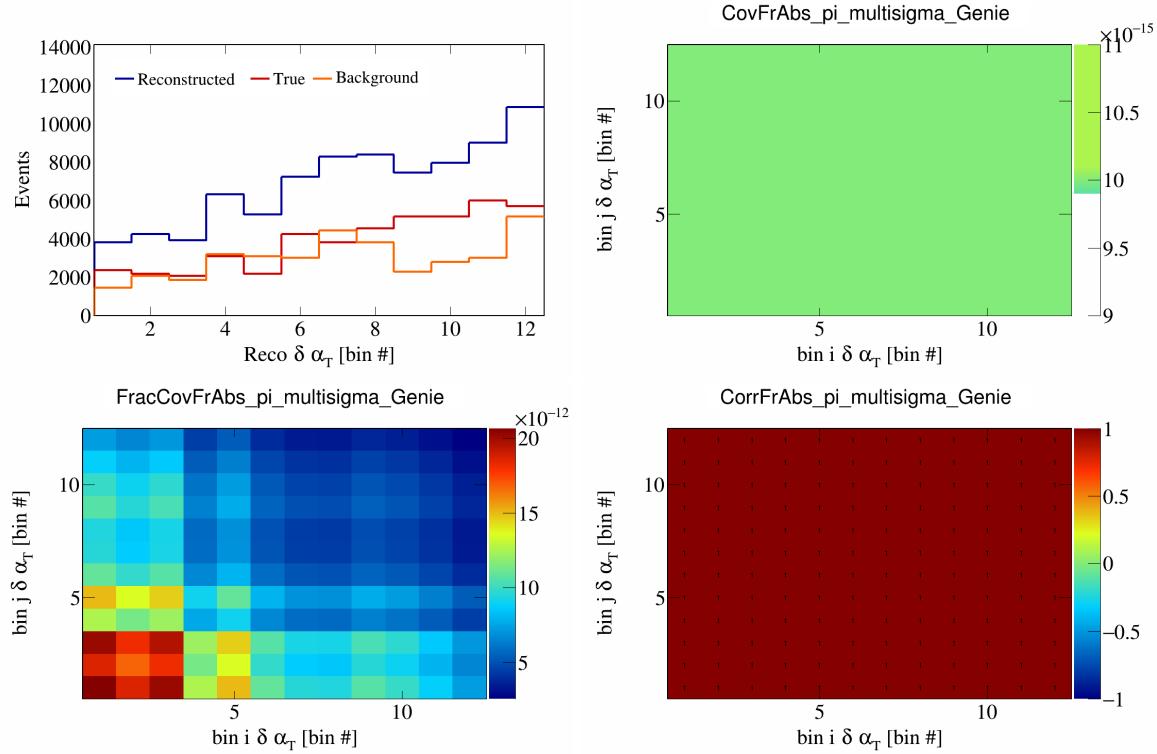


Figure 193: FrAbspi variations for $\delta\alpha_T$ in $\cos(\theta_{\vec{p}_\mu})$.

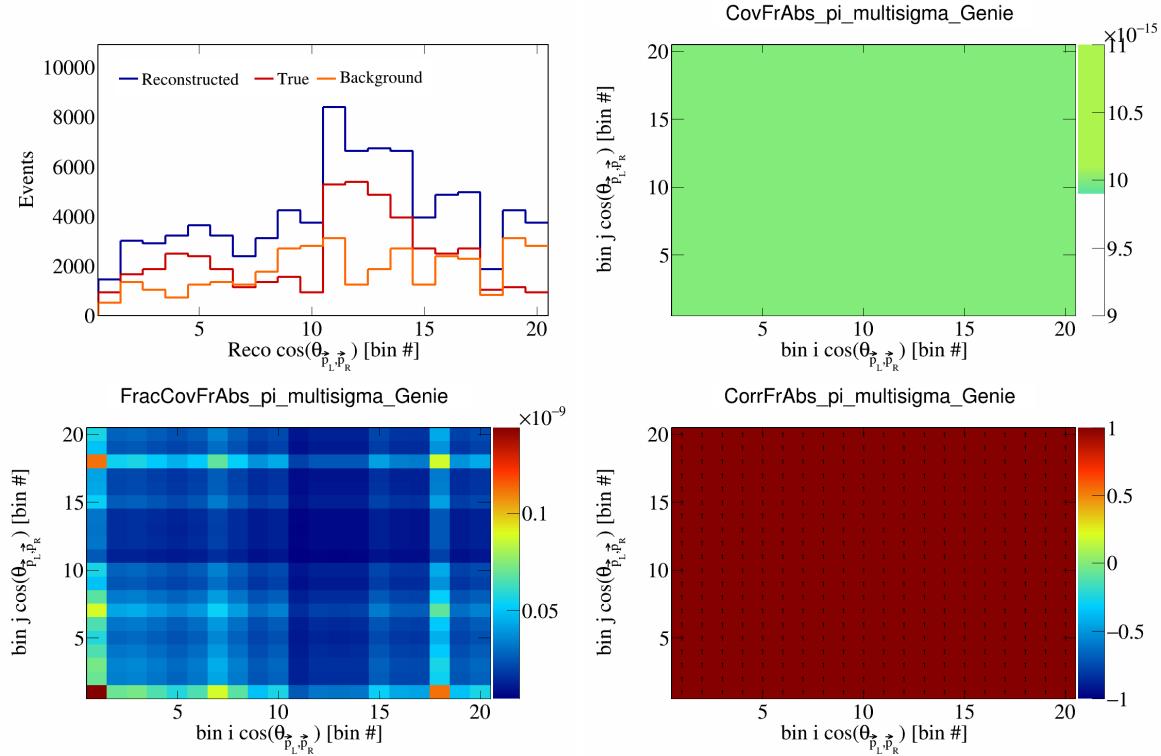


Figure 194: FrAbspi variations for $\cos(\theta_{\vec{p}_L, \vec{p}_R})$ in $\cos(\theta_{\vec{p}_\mu})$.

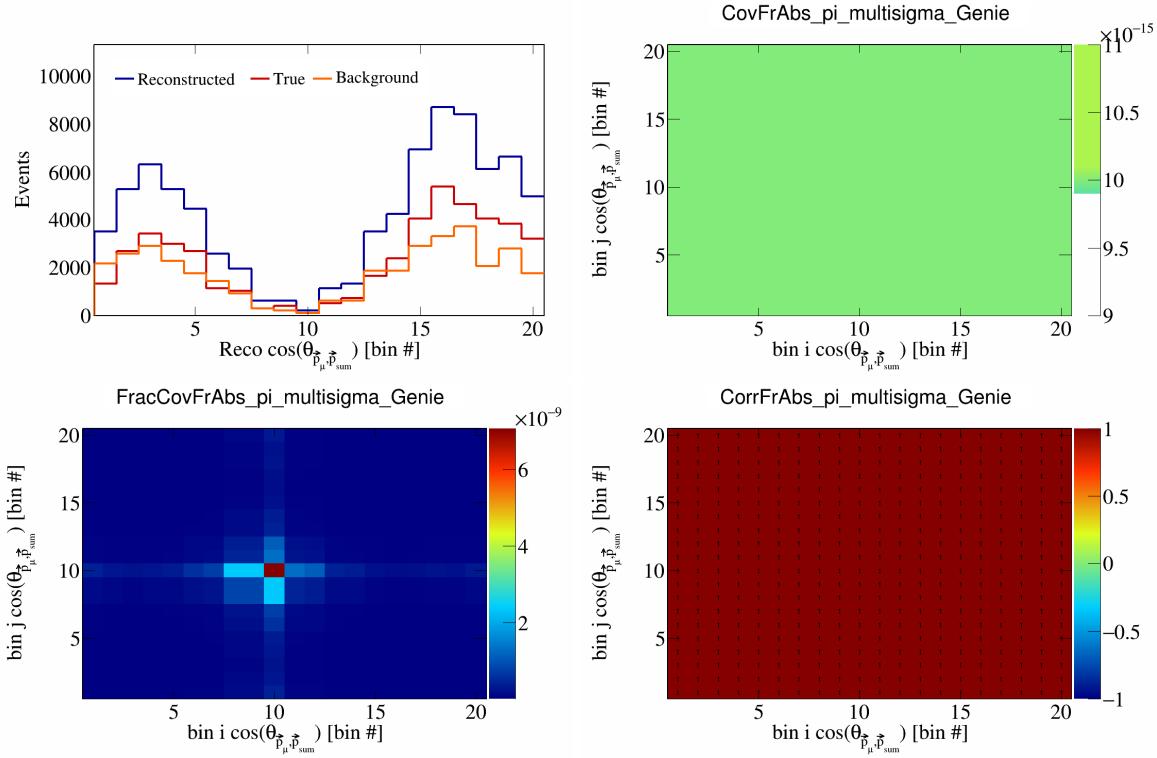


Figure 195: FrAbspi variations for $\cos(\theta_{\vec{p}_\mu, \vec{p}_{\text{sum}}})$ in $\cos(\theta_{\vec{p}_\mu})$.

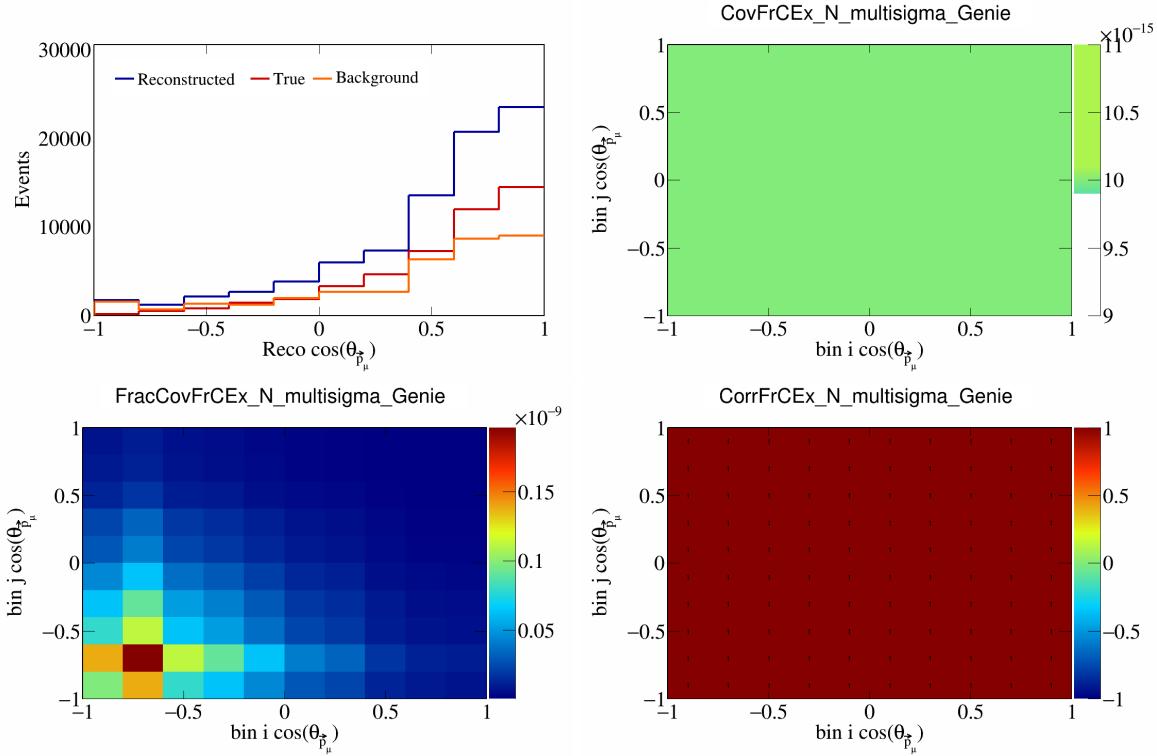


Figure 196: FrCExN variations for $\cos(\theta_{\vec{p}_\mu})$.

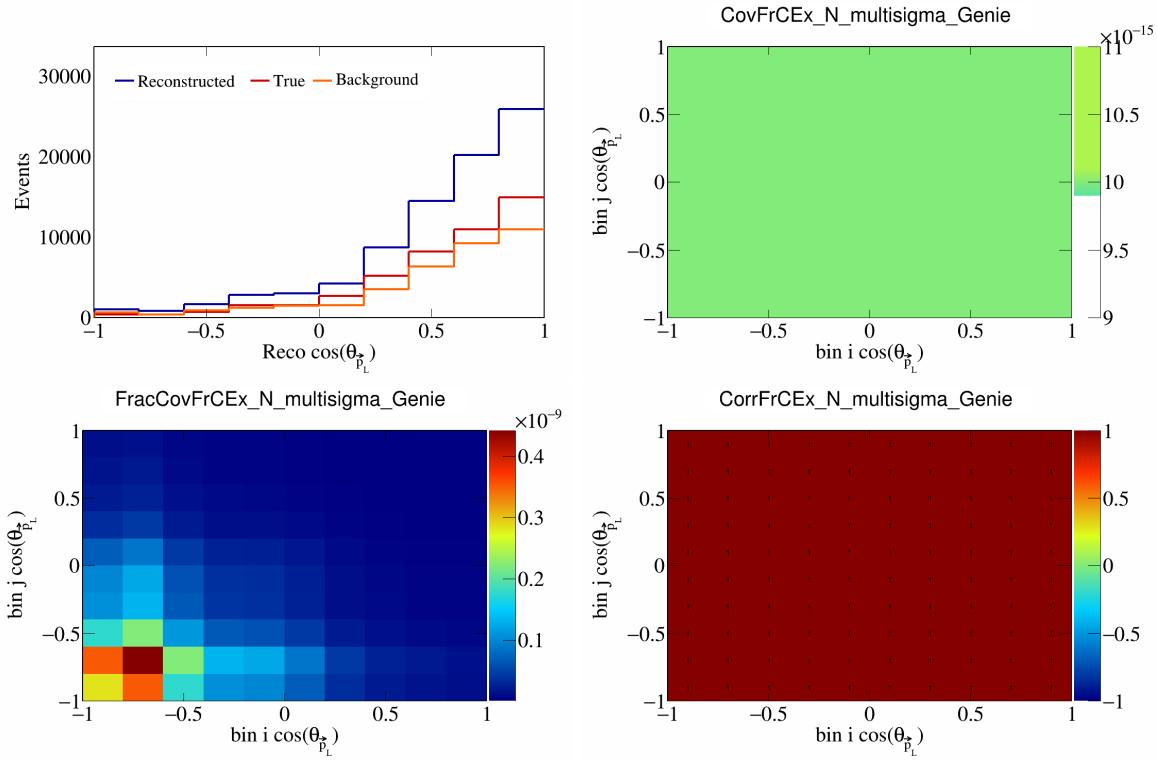


Figure 197: FrCExN variations for $\cos(\theta_{\vec{p}_L})$.

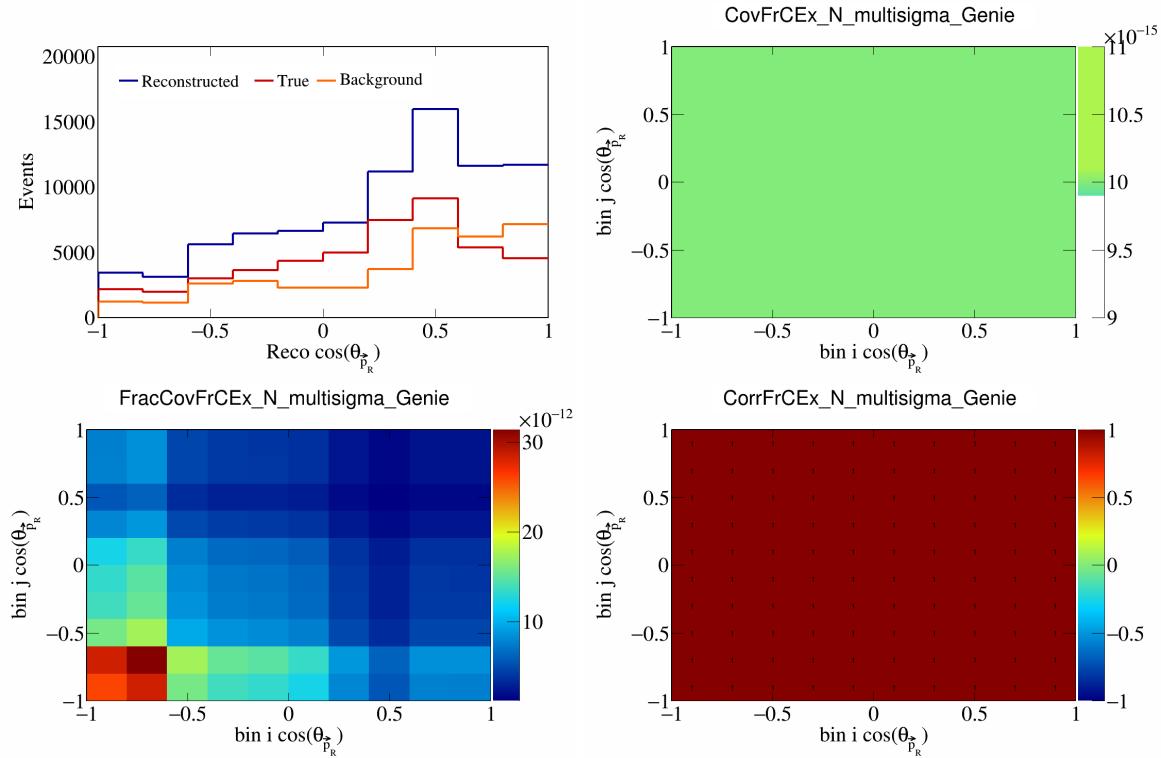


Figure 198: FrCExN variations for $\cos(\theta_{\vec{p}_R})$.

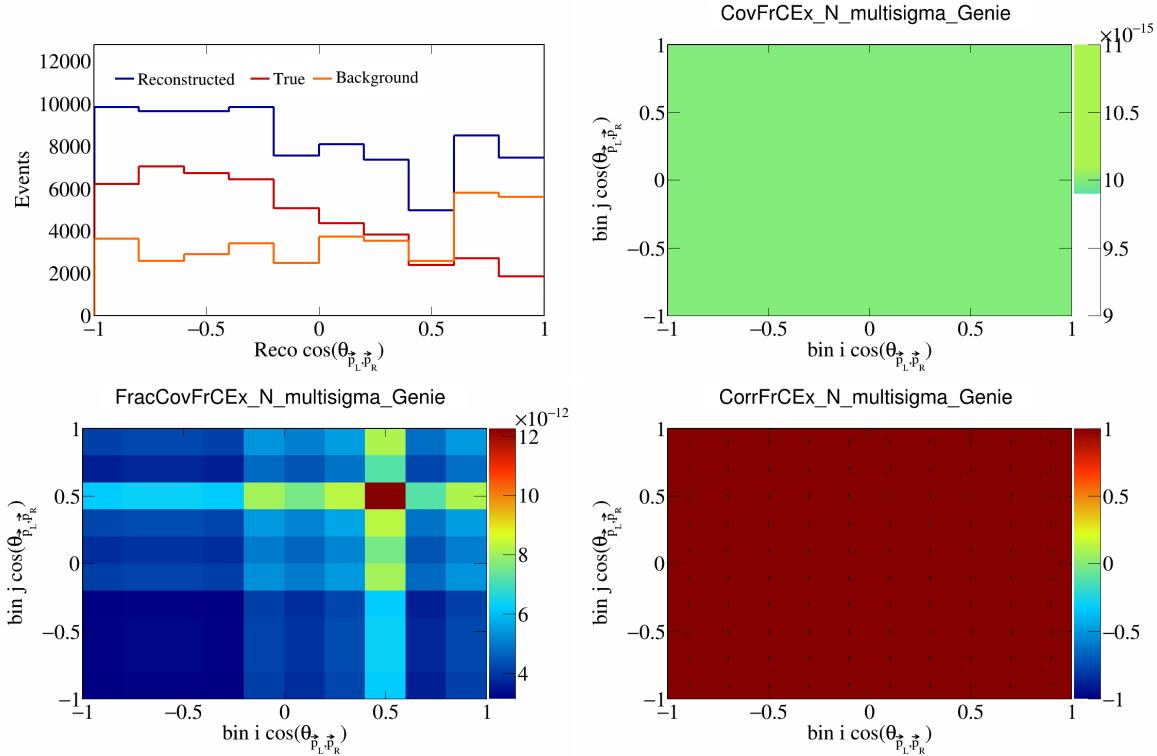


Figure 199: FrCEExN variations for $\cos(\theta_{\vec{p}_L, \vec{p}_R})$.

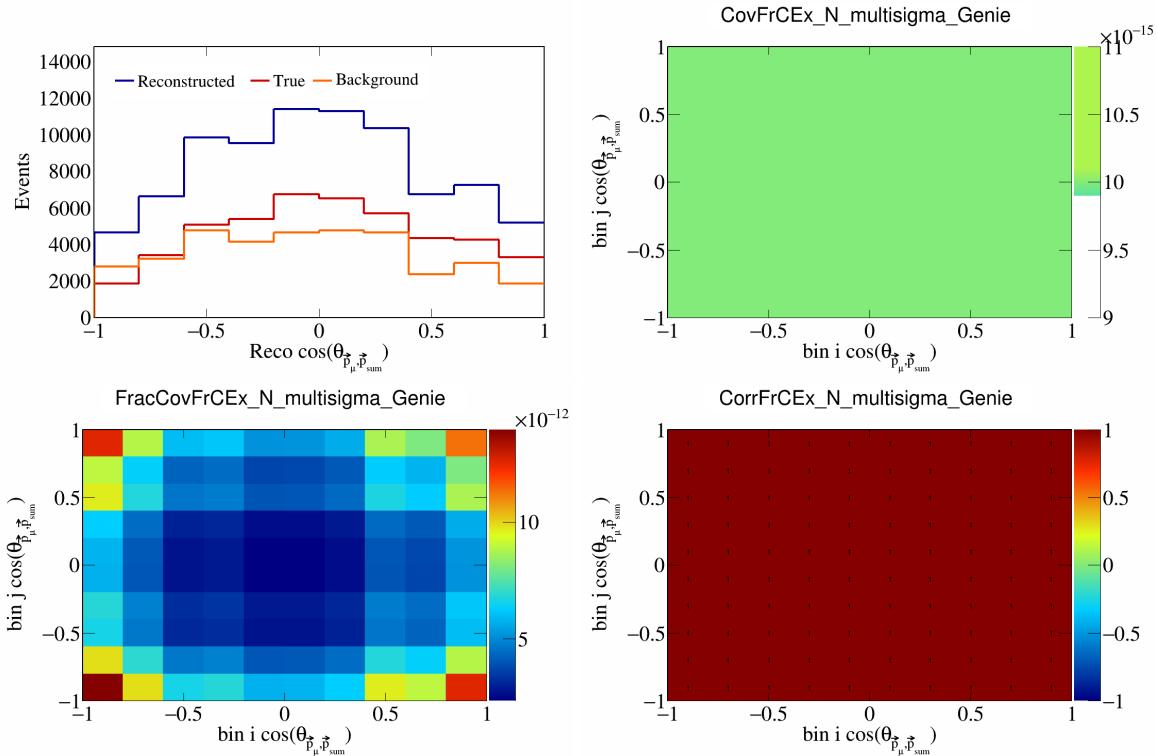


Figure 200: FrCEExN variations for $\cos(\theta_{\vec{p}_\mu, \vec{p}_{\text{sum}}})$.

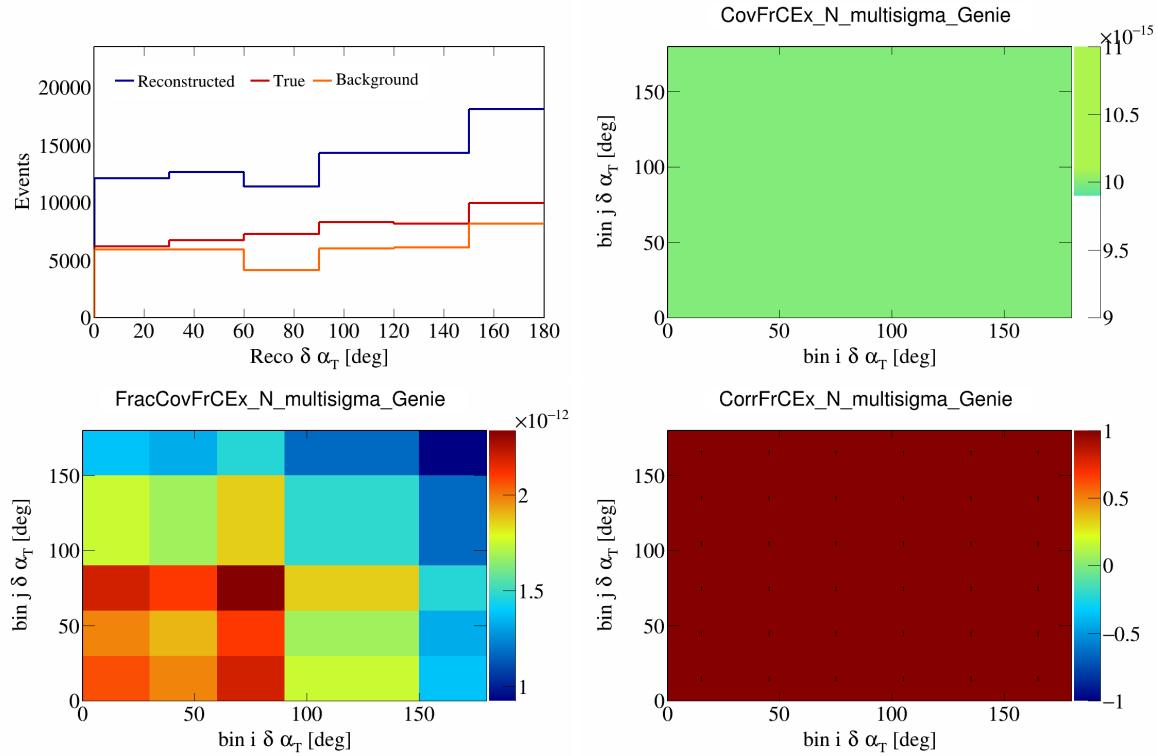


Figure 201: FrCEExN variations for $\delta\alpha_T$.

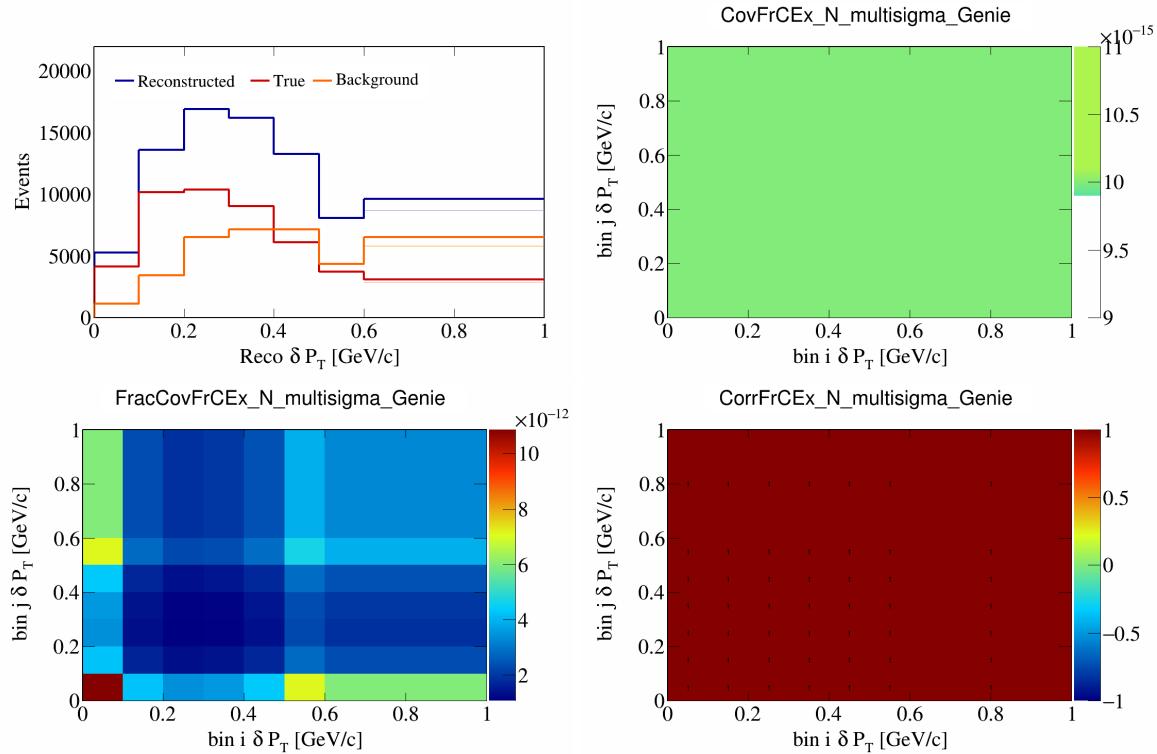


Figure 202: FrCEExN variations for δP_T .

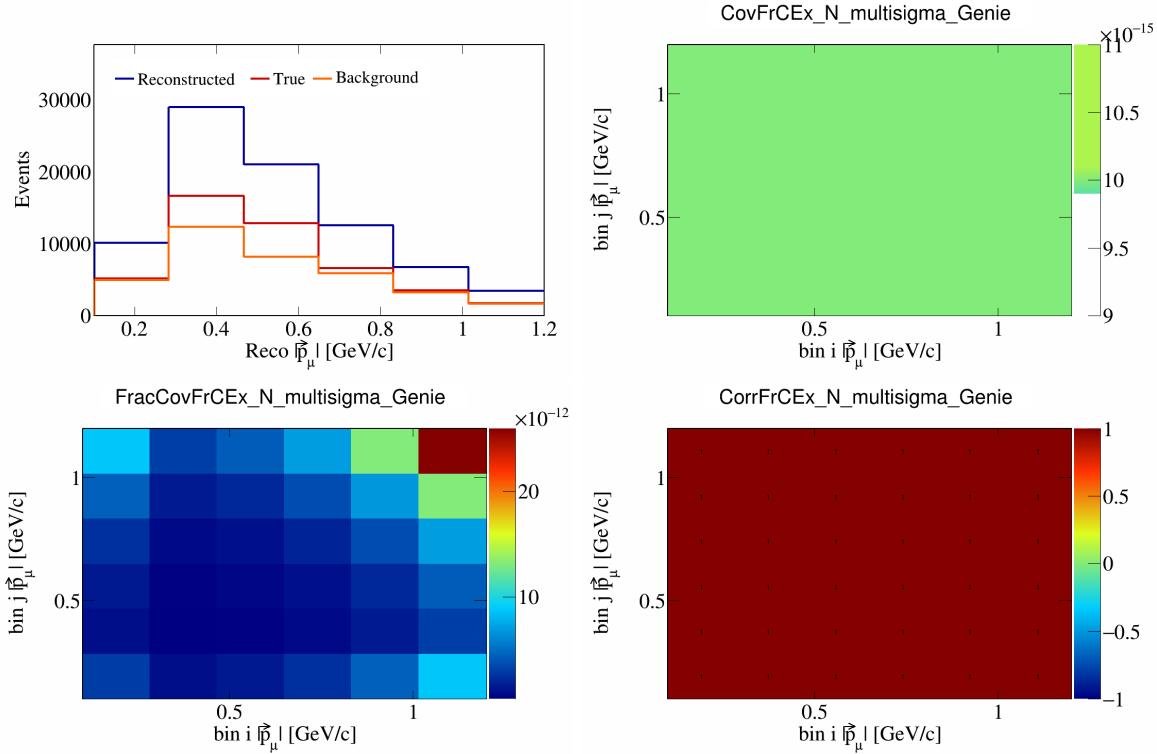


Figure 203: FrCEExN variations for $|\vec{p}_\mu|$.

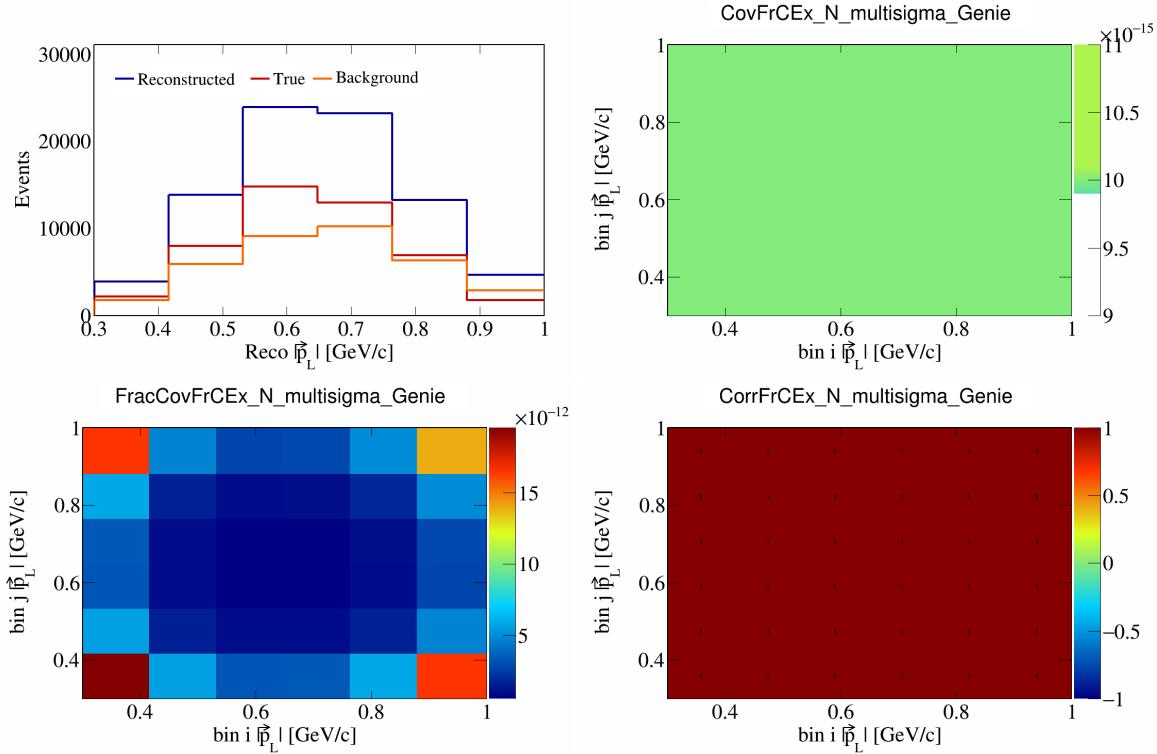


Figure 204: FrCEExN variations for $|\vec{p}_L|$.

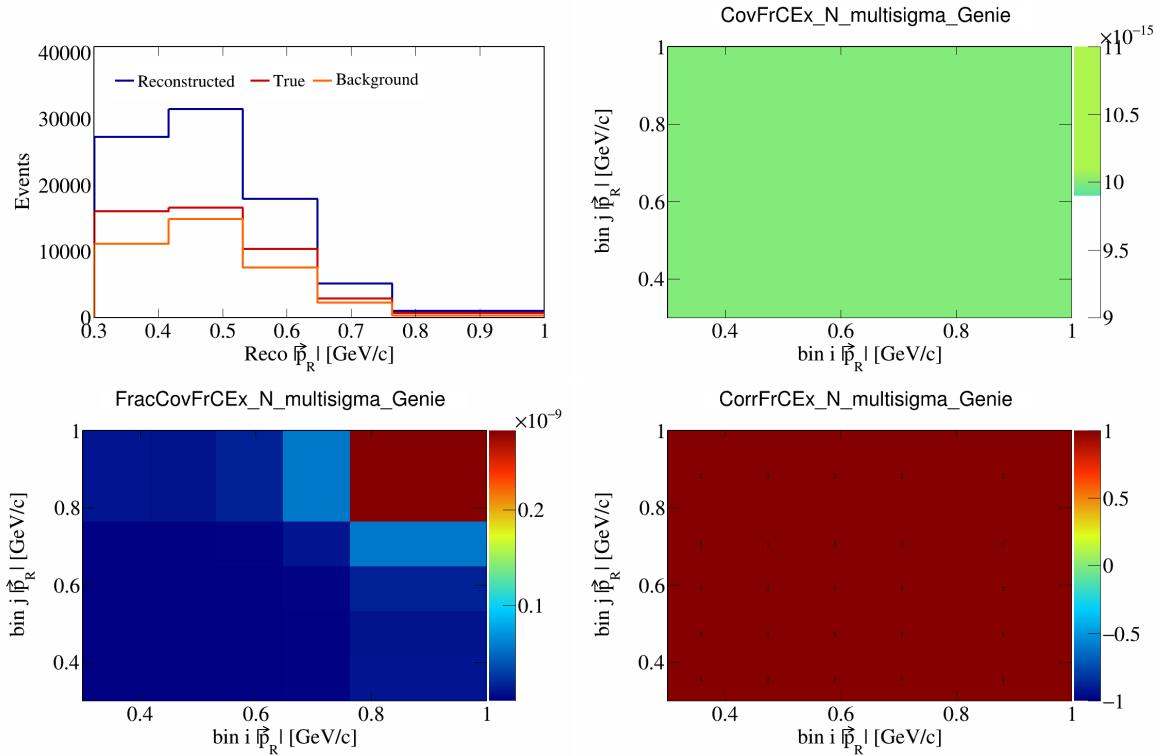


Figure 205: FrCEExN variations for $|\vec{p}_R|$.

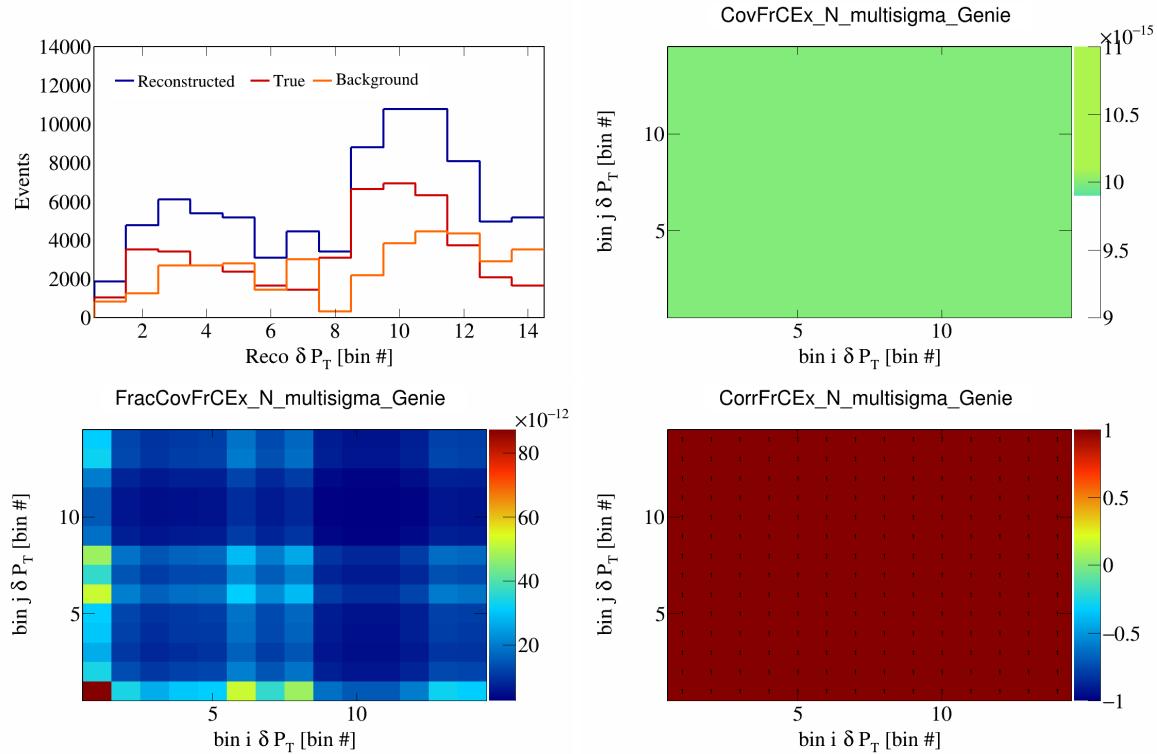


Figure 206: FrCEExN variations for δP_T in $\cos(\theta_{\vec{p}_\mu})$.

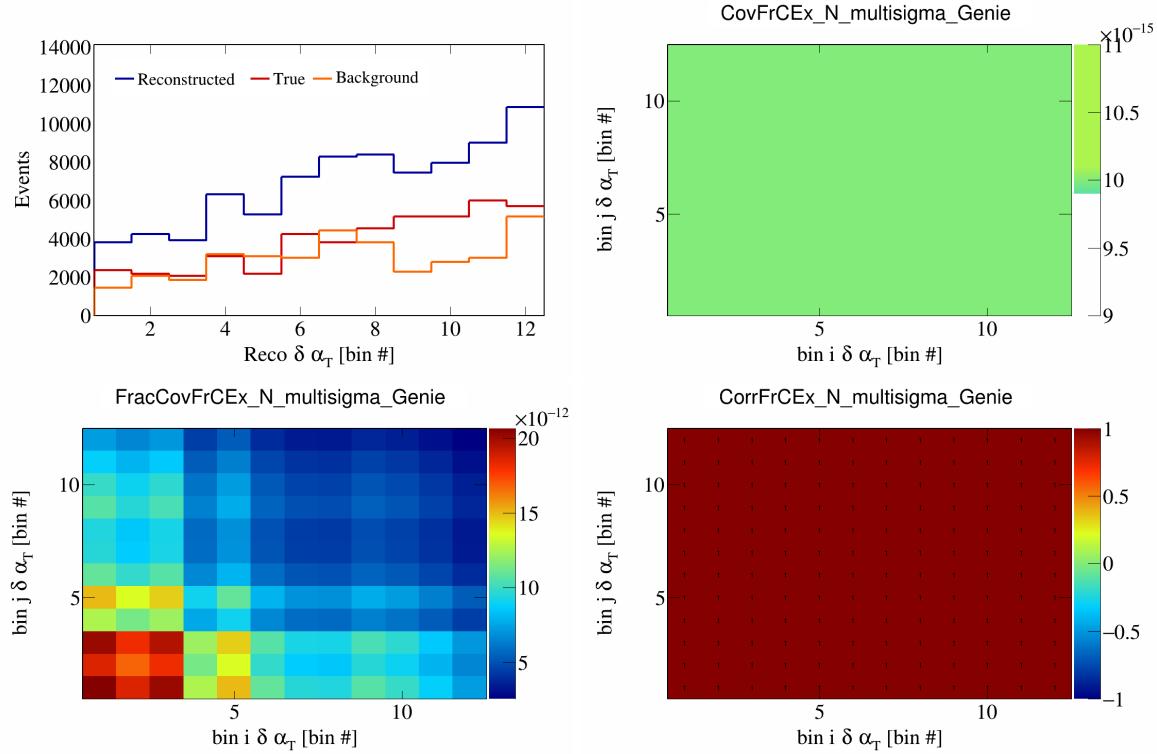


Figure 207: FrCEExN variations for $\delta\alpha_T$ in $\cos(\theta_{\vec{p}_\mu})$.

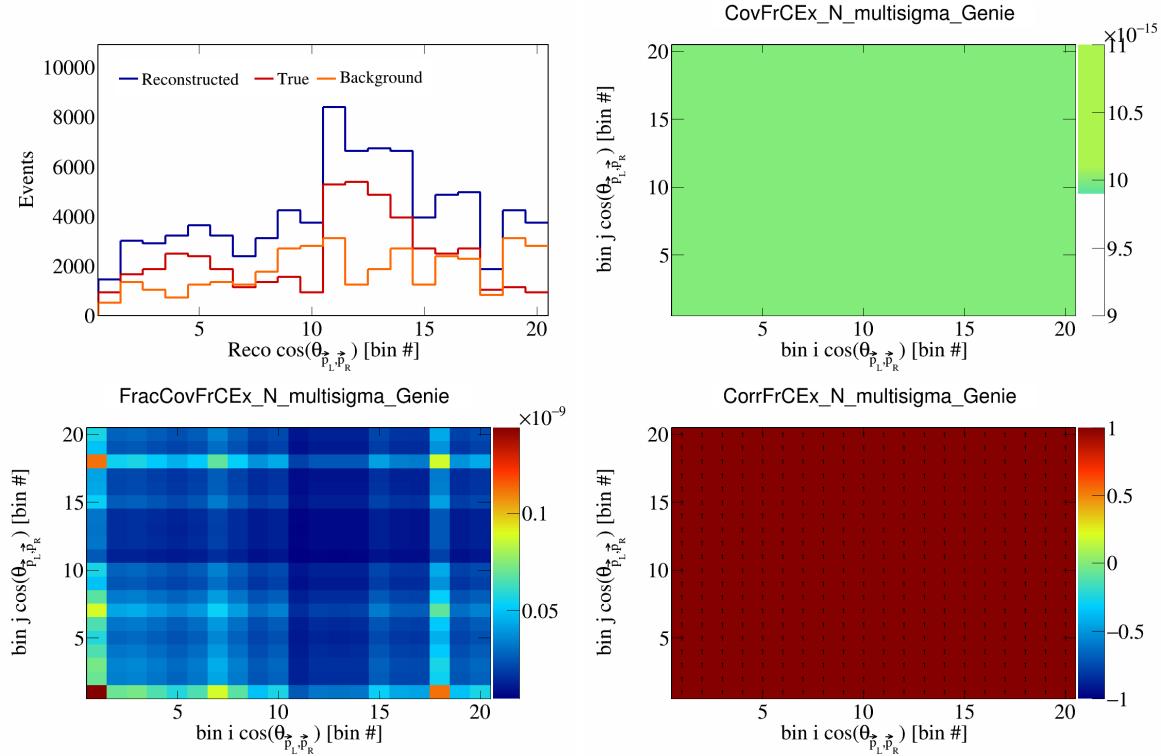


Figure 208: FrCEExN variations for $\cos(\theta_{\vec{p}_L, \vec{p}_R})$ in $\cos(\theta_{\vec{p}_\mu})$.

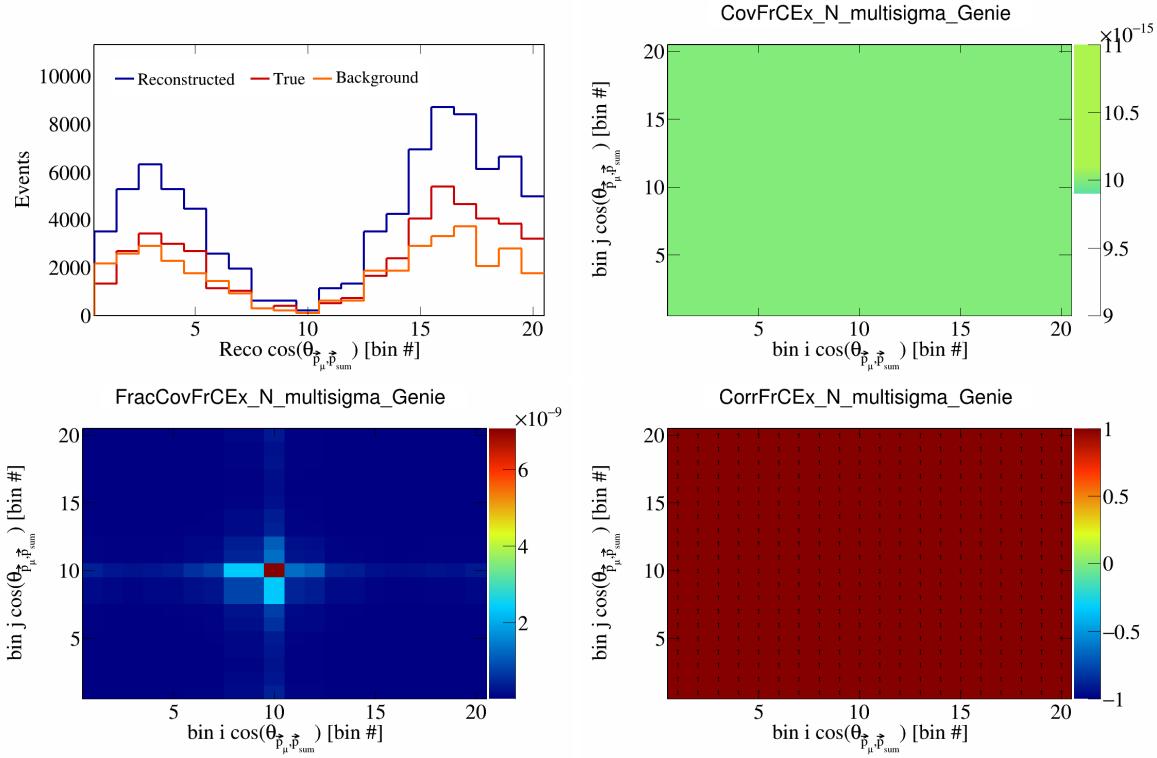


Figure 209: FrCEExN variations for $\cos(\theta_{\vec{p}_\mu, \vec{p}_{\text{sum}}})$ in $\cos(\theta_{\vec{p}_\mu})$.

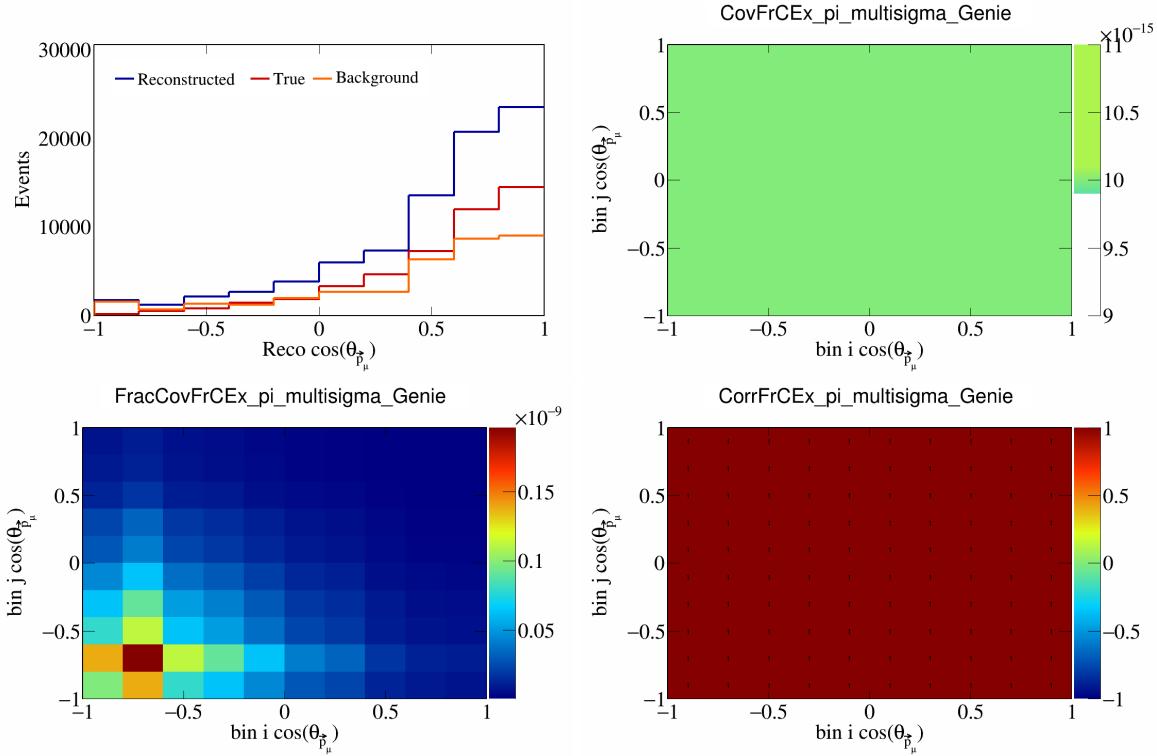


Figure 210: FrCEExpi variations for $\cos(\theta_{\vec{p}_\mu})$.

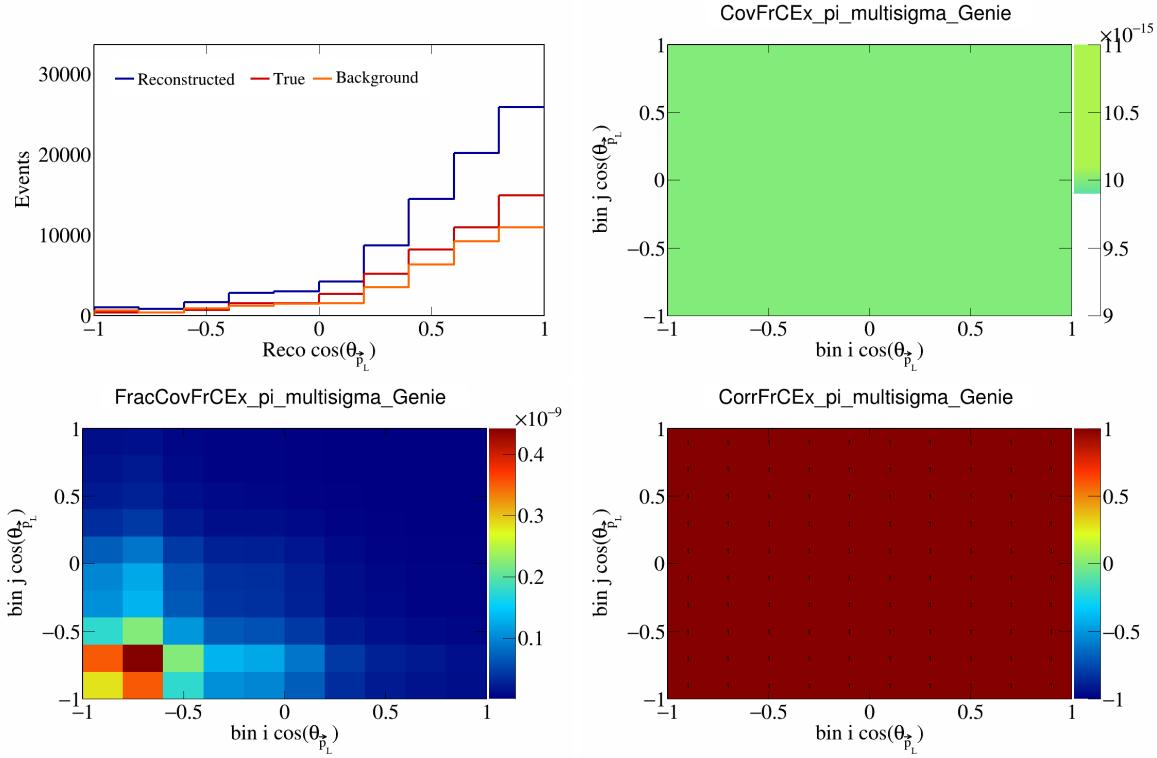


Figure 211: FrCExpi variations for $\cos(\theta_{\vec{p}_L})$.

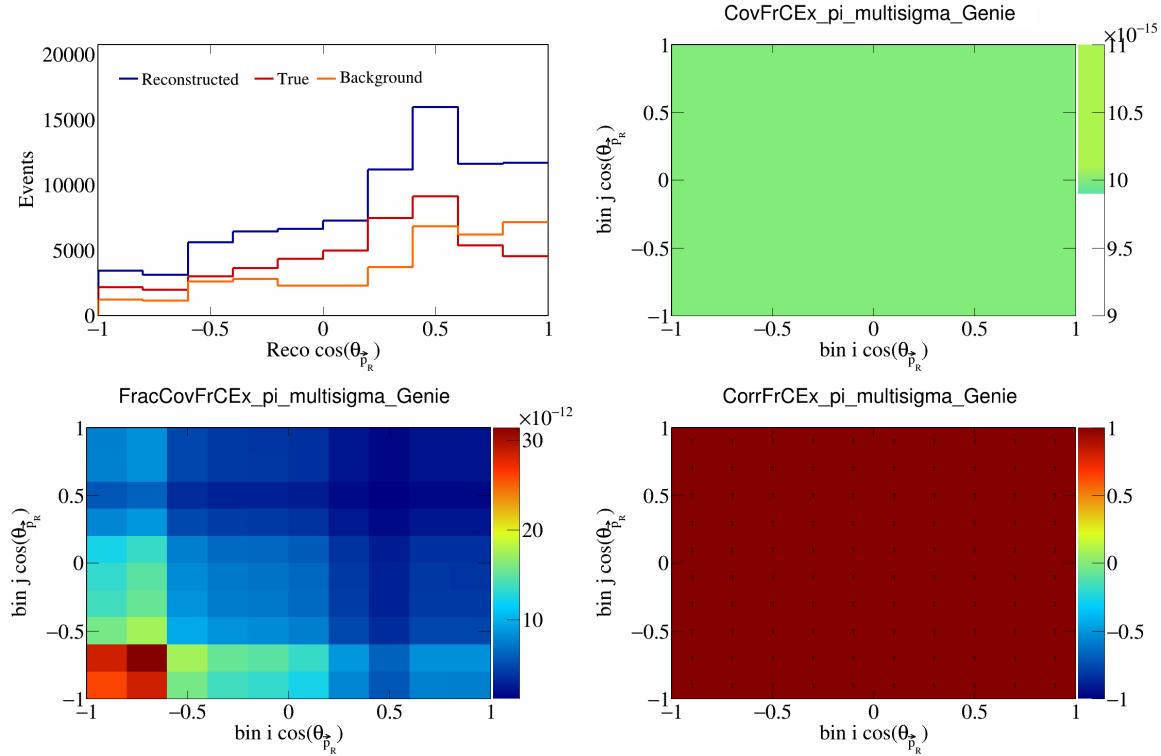


Figure 212: FrCExpi variations for $\cos(\theta_{\vec{p}_R})$.

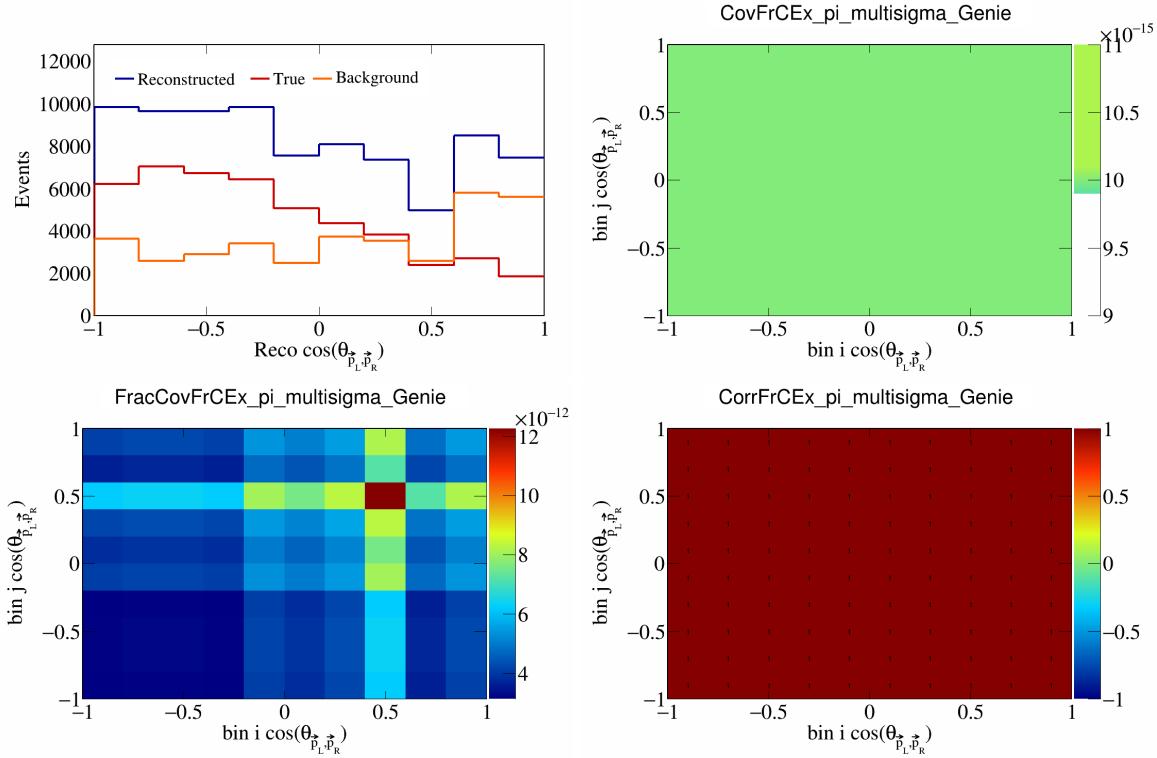


Figure 213: FrCEpi variations for $\cos(\theta_{\vec{p}_L, \vec{p}_R})$.

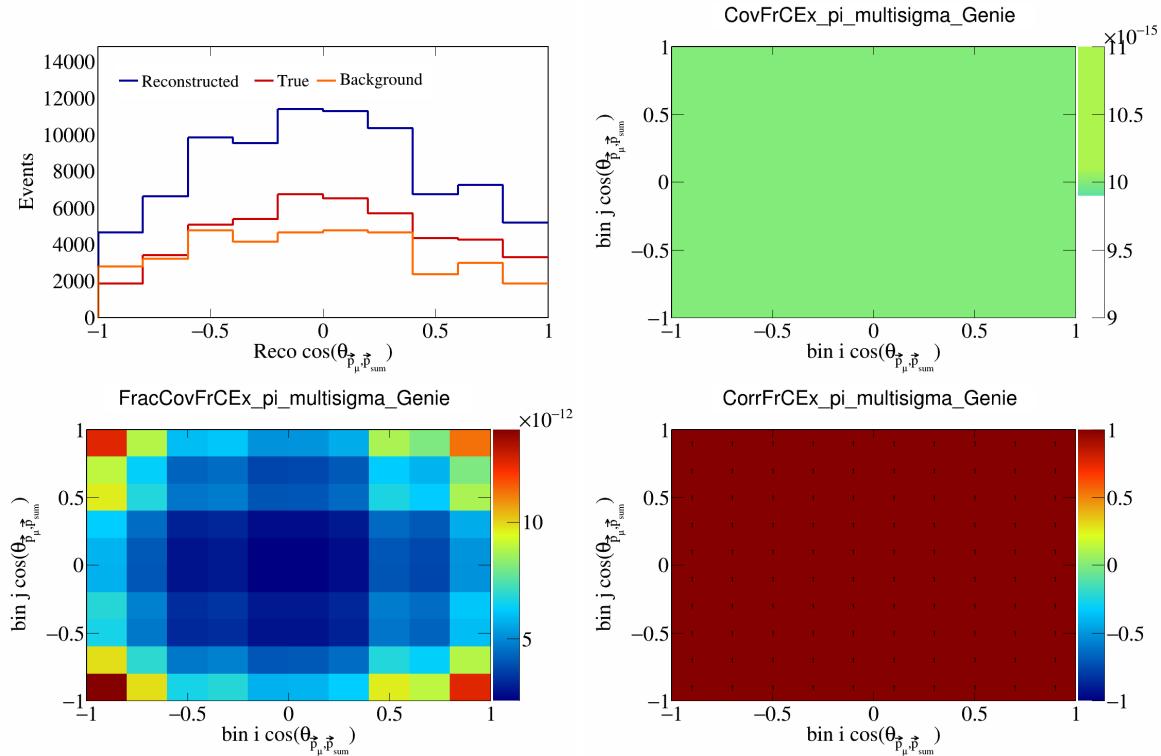


Figure 214: FrCEpi variations for $\cos(\theta_{\vec{p}_\mu, \vec{p}_{\text{sum}}})$.

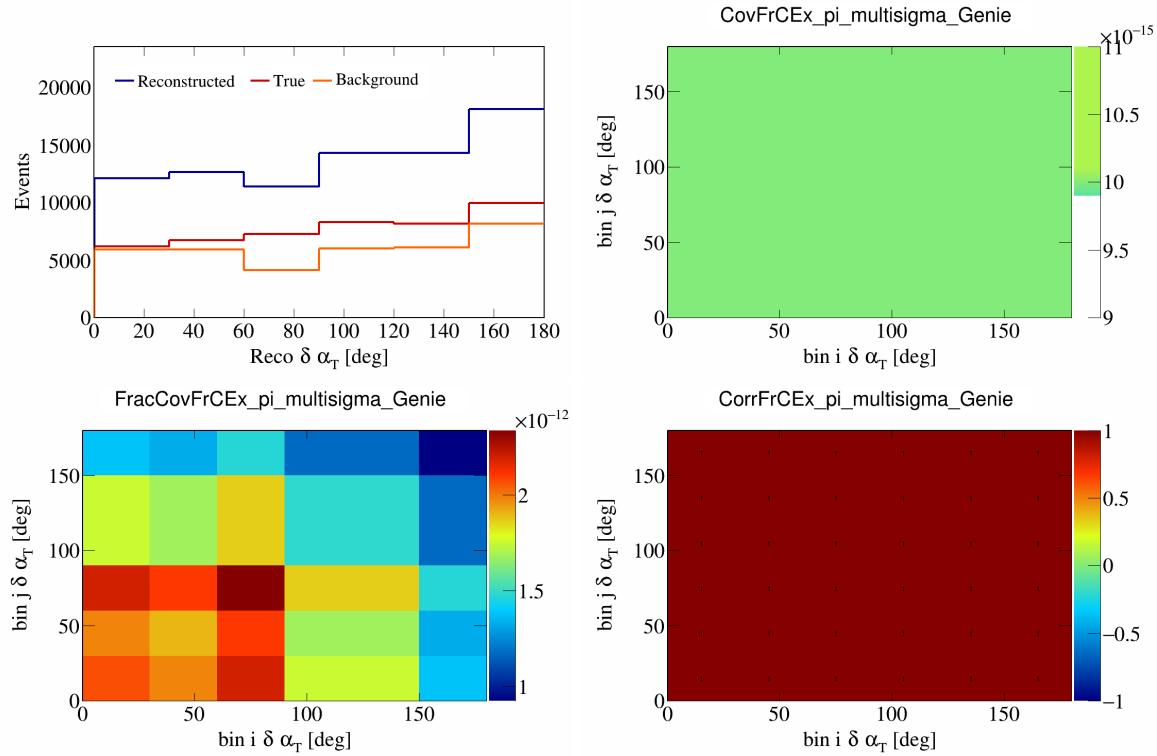


Figure 215: FrCEExpi variations for $\delta\alpha_T$.

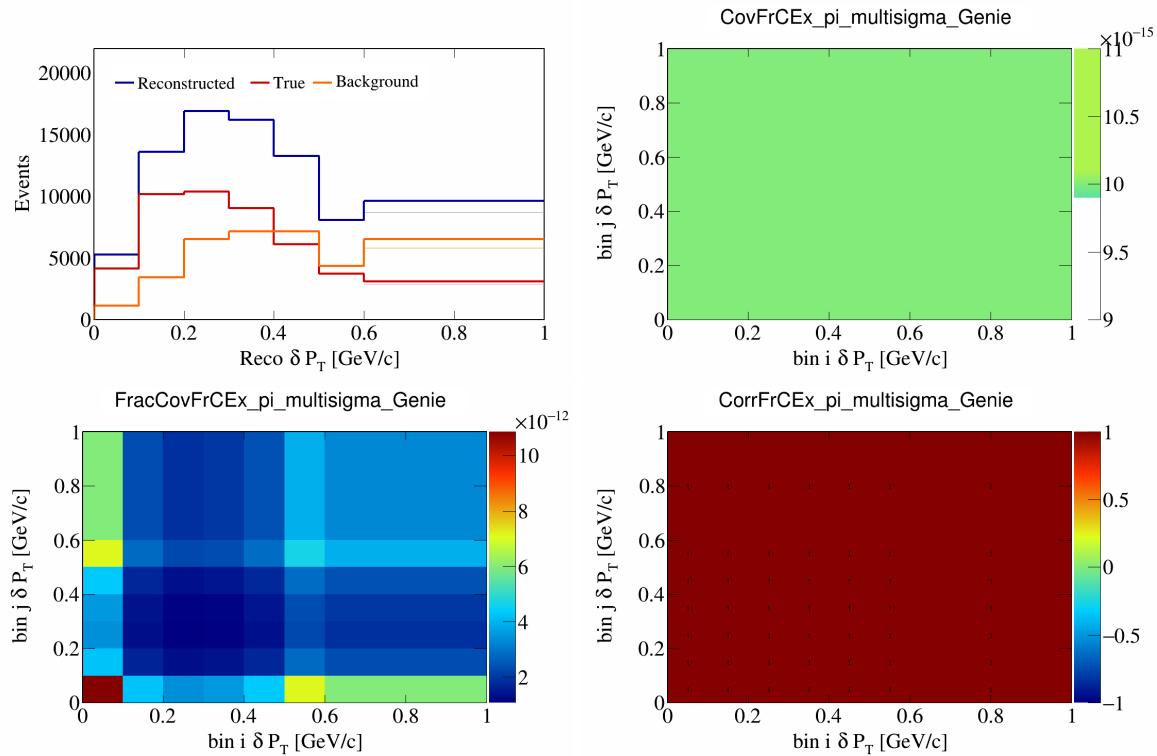


Figure 216: FrCEExpi variations for δP_T .

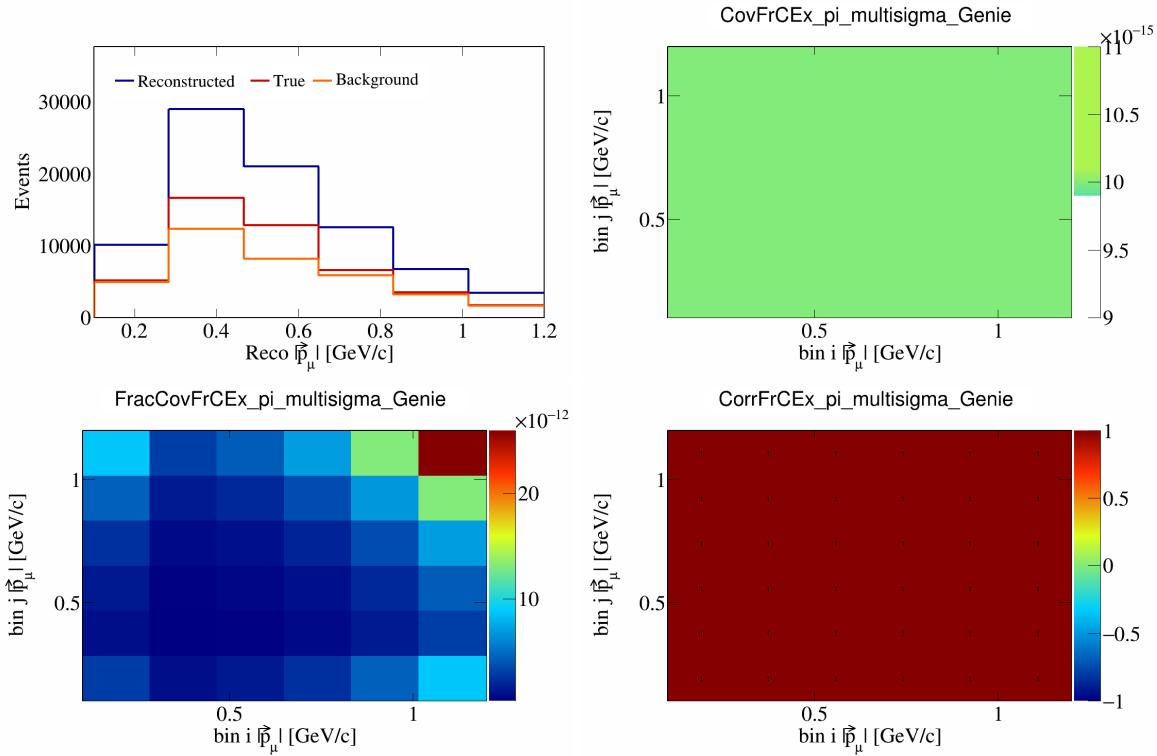


Figure 217: FrCEExpi variations for $|\vec{p}_\mu|$.

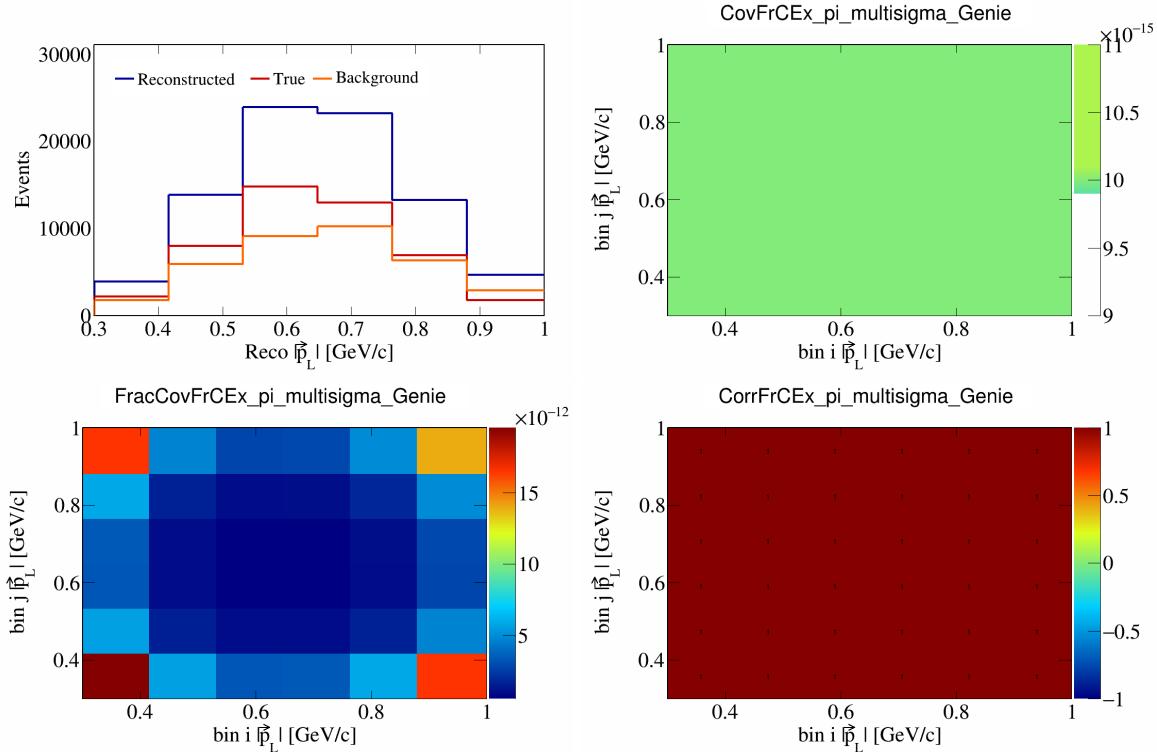


Figure 218: FrCEExpi variations for $|\vec{p}_L|$.

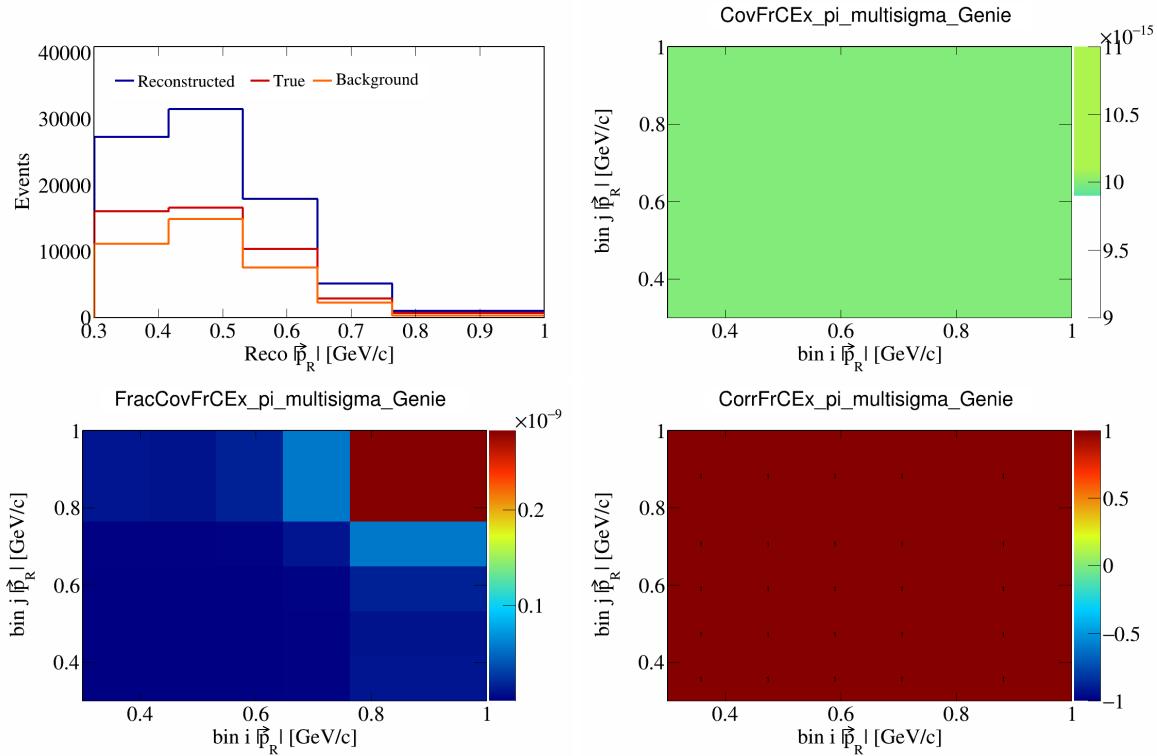


Figure 219: FrCEExpi variations for $|\vec{p}_R|$.

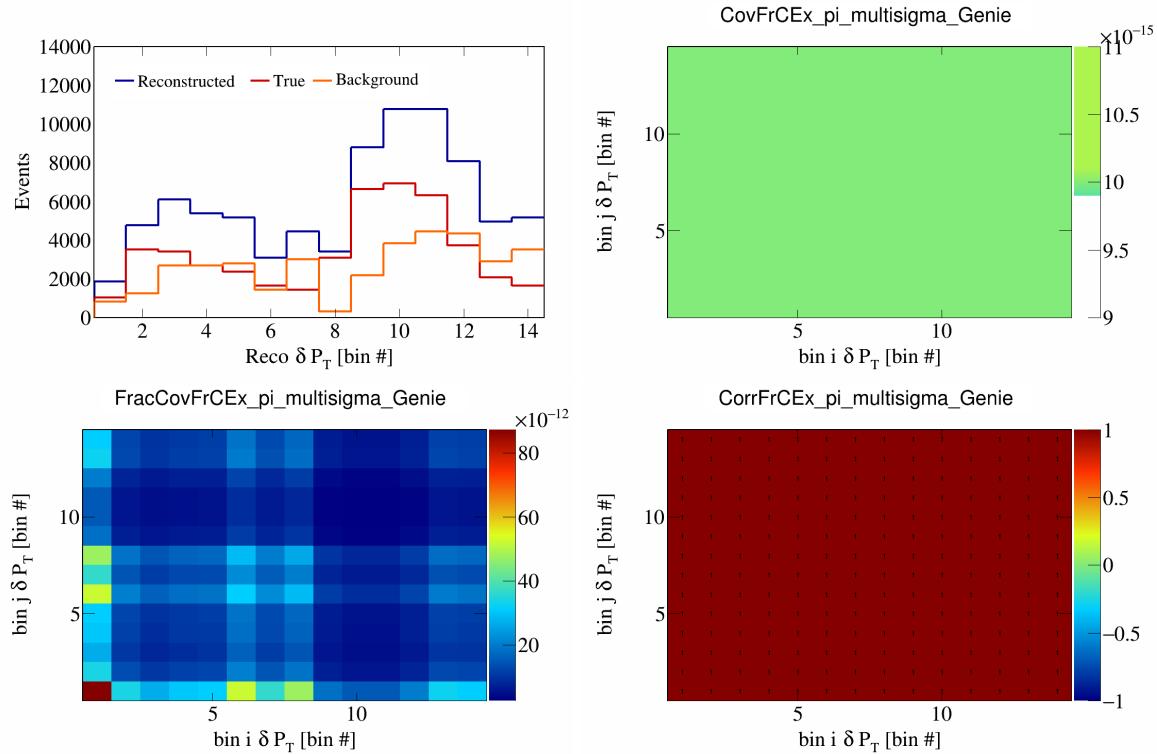


Figure 220: FrCEExpi variations for δP_T in $\cos(\theta_{\vec{p}_\mu})$.

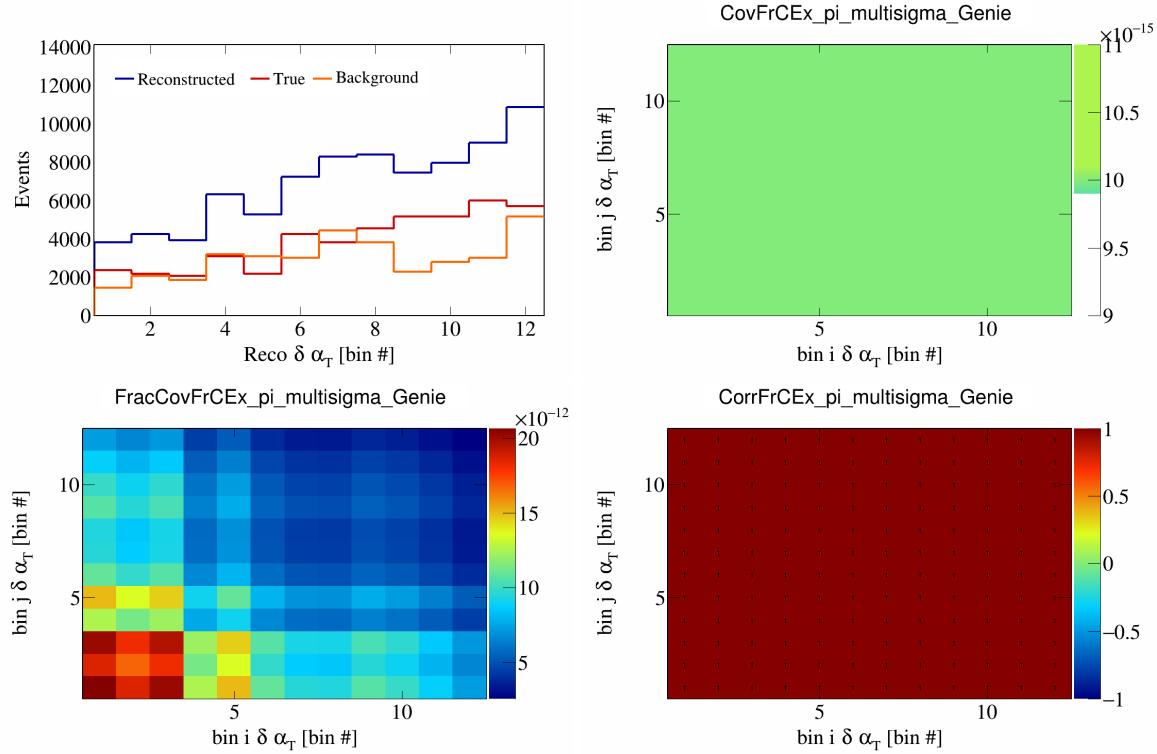


Figure 221: FrCEExpi variations for $\delta\alpha_T$ in $\cos(\theta_{\vec{p}_\mu})$.

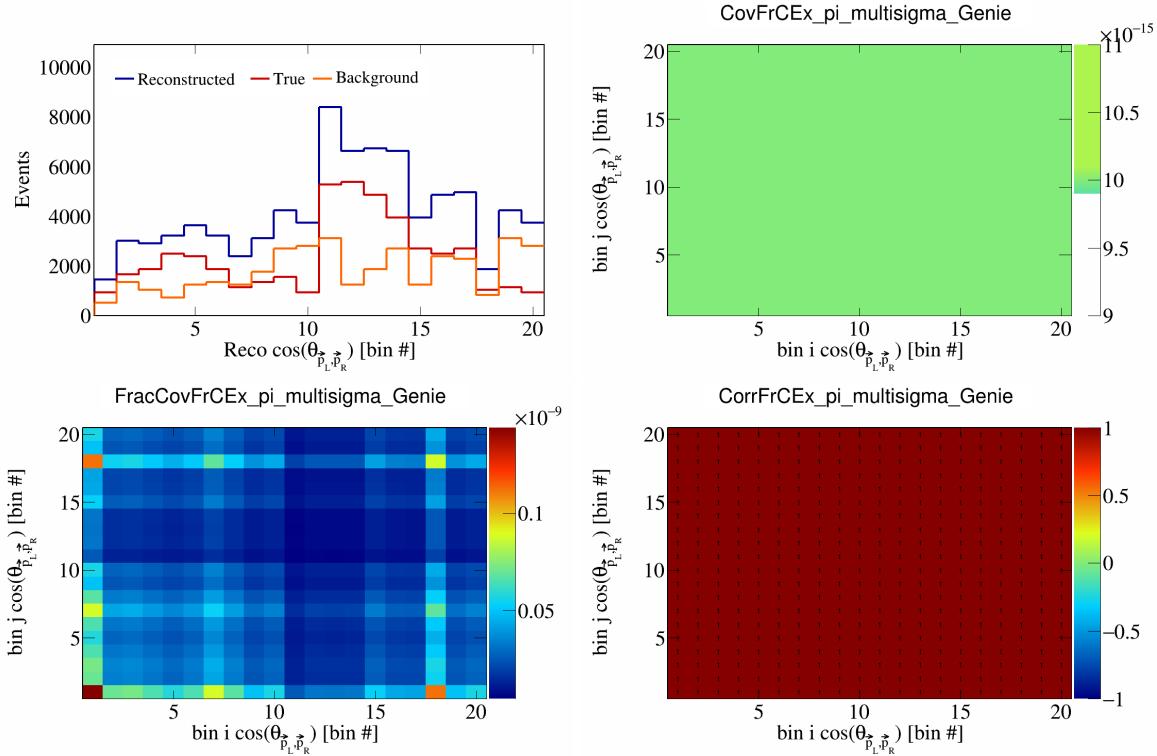


Figure 222: FrCEExpi variations for $\cos(\theta_{\vec{p}_L, \vec{p}_R})$ in $\cos(\theta_{\vec{p}_\mu})$.

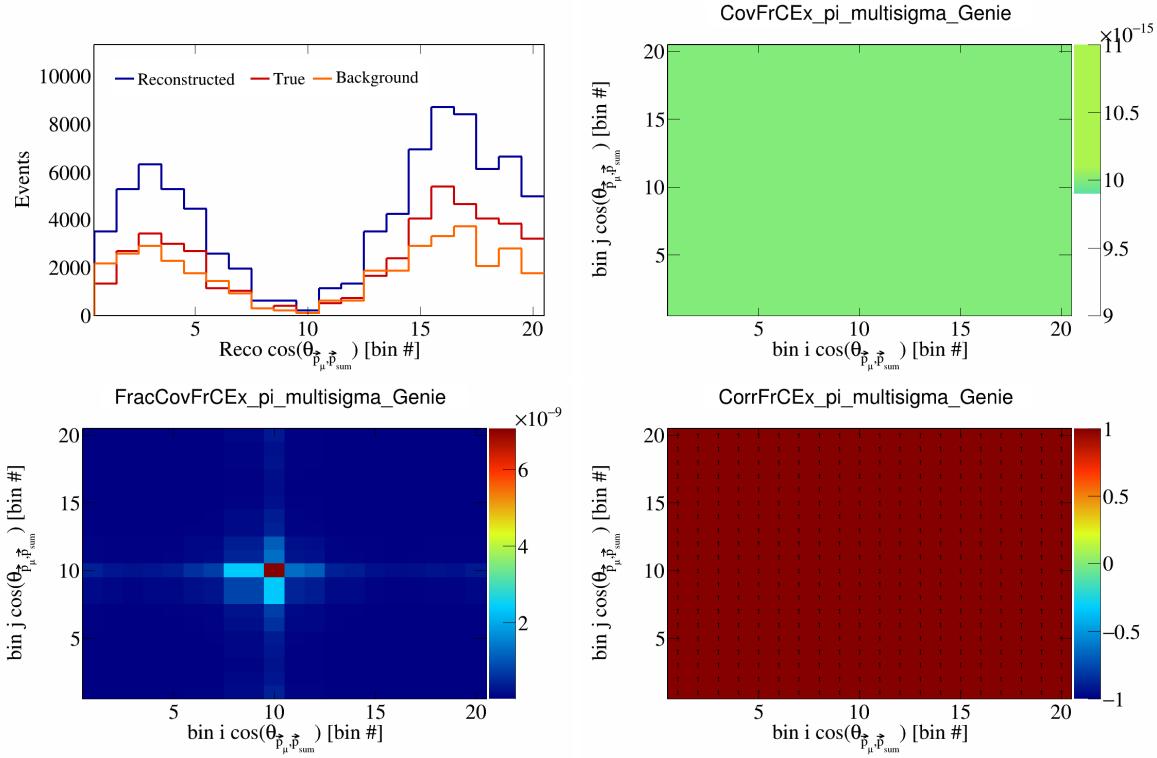


Figure 223: FrCEExpi variations for $\cos(\theta_{\vec{p}_\mu, \vec{p}_{\text{sum}}})$ in $\cos(\theta_{\vec{p}_\mu})$.

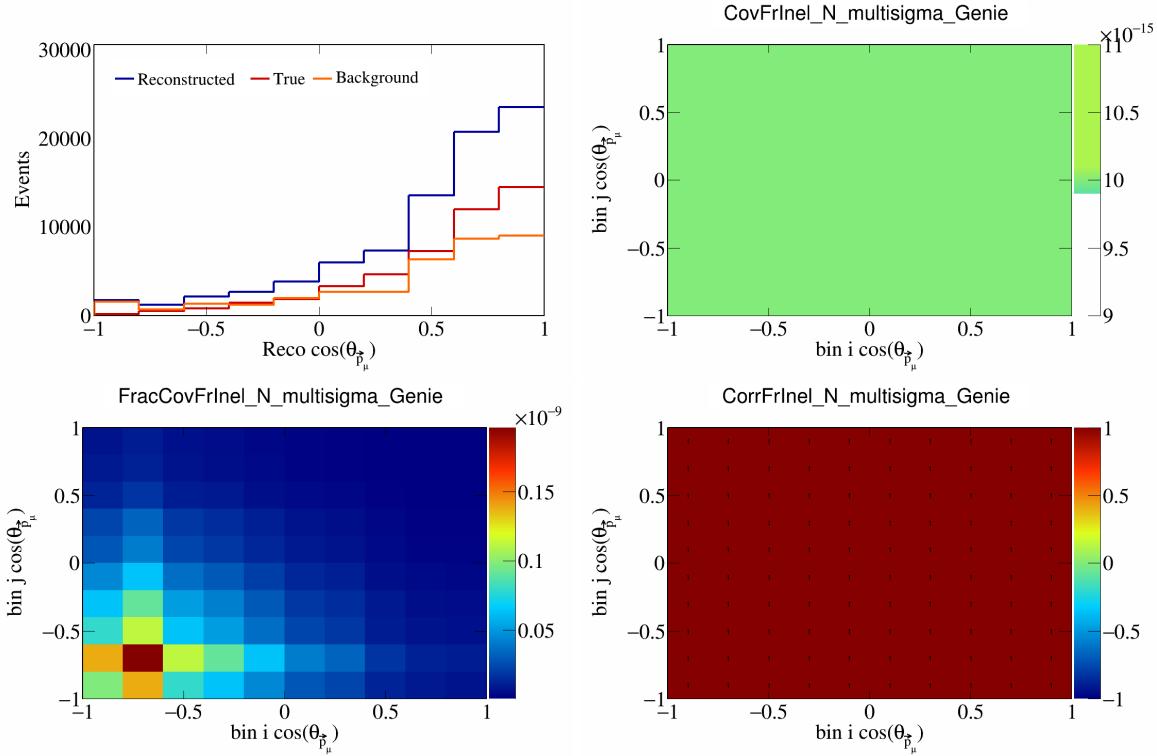


Figure 224: FrInelN variations for $\cos(\theta_{\vec{p}_\mu})$.

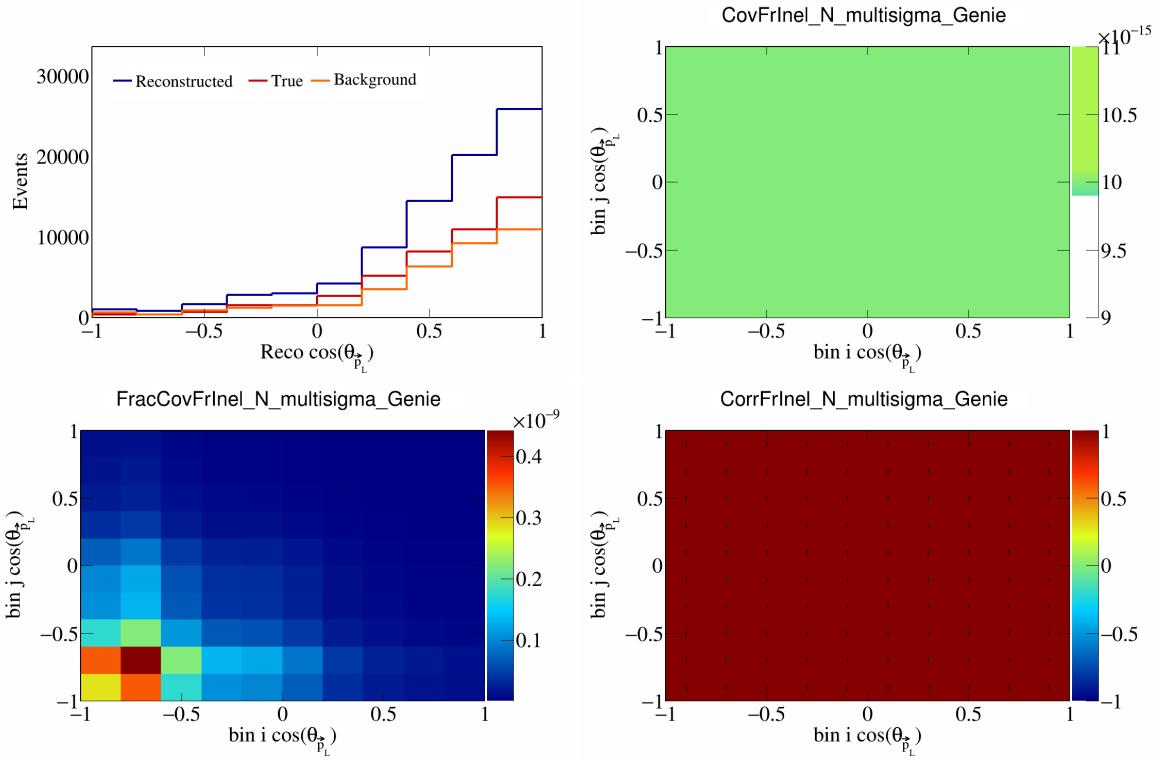


Figure 225: FrInelN variations for $\cos(\theta_{\vec{p}_L})$.

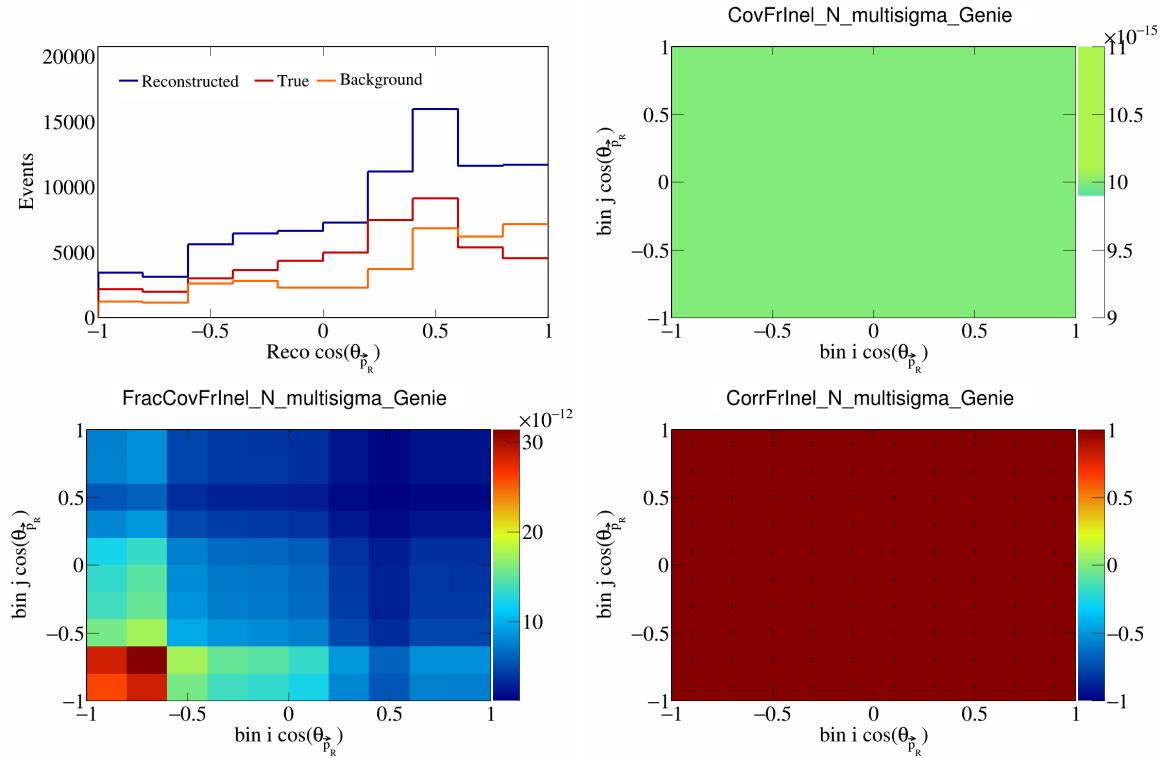


Figure 226: FrInelN variations for $\cos(\theta_{\vec{p}_R})$.

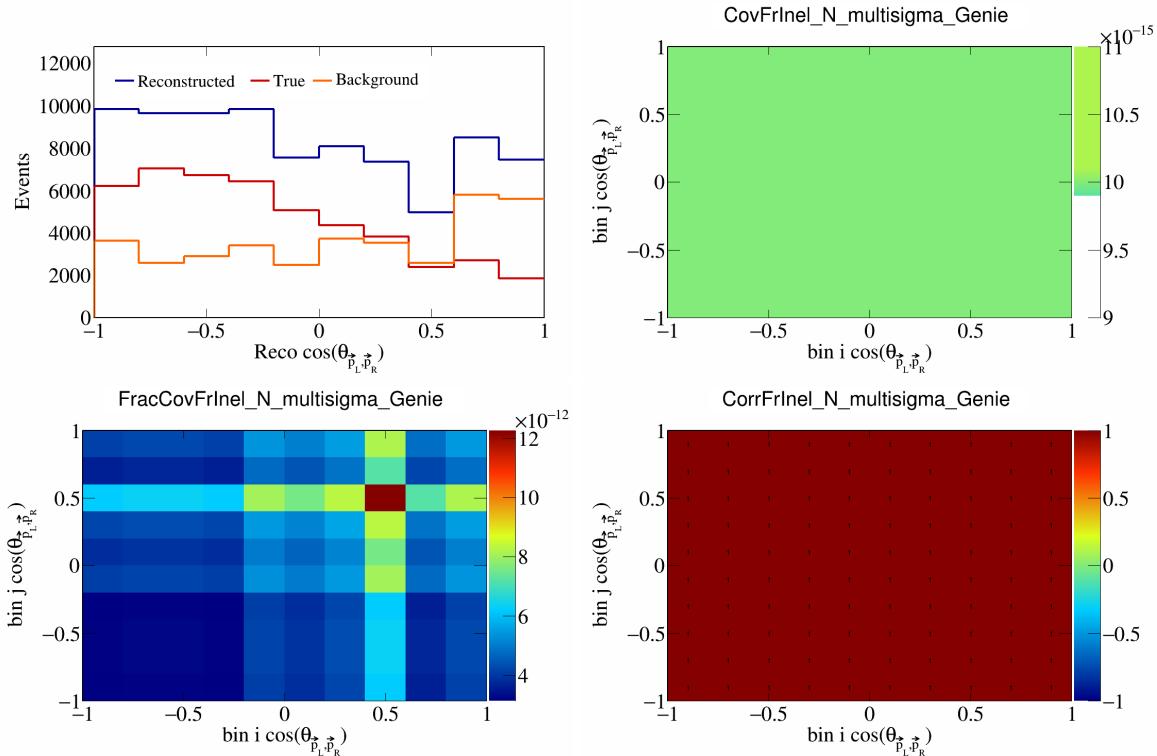


Figure 227: FrInelN variations for $\cos(\theta_{\vec{p}_L, \vec{p}_R})$.

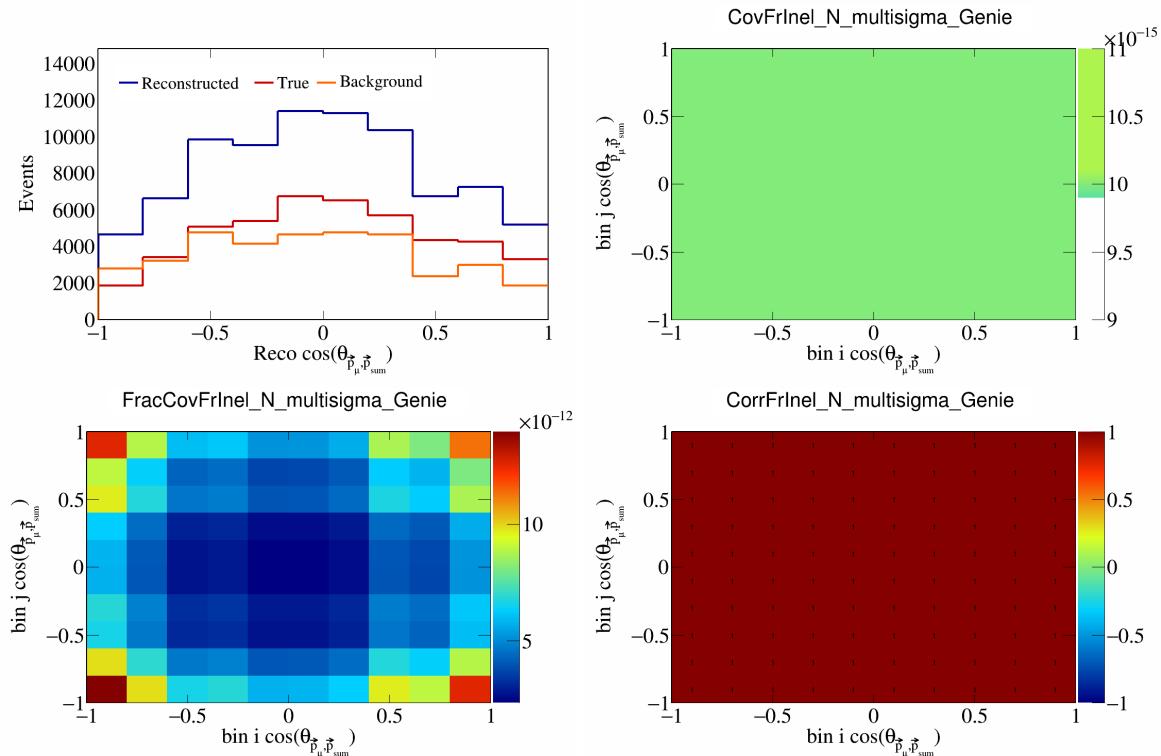


Figure 228: FrInelN variations for $\cos(\theta_{\vec{p}_\mu, \vec{p}_{\text{sum}}})$.

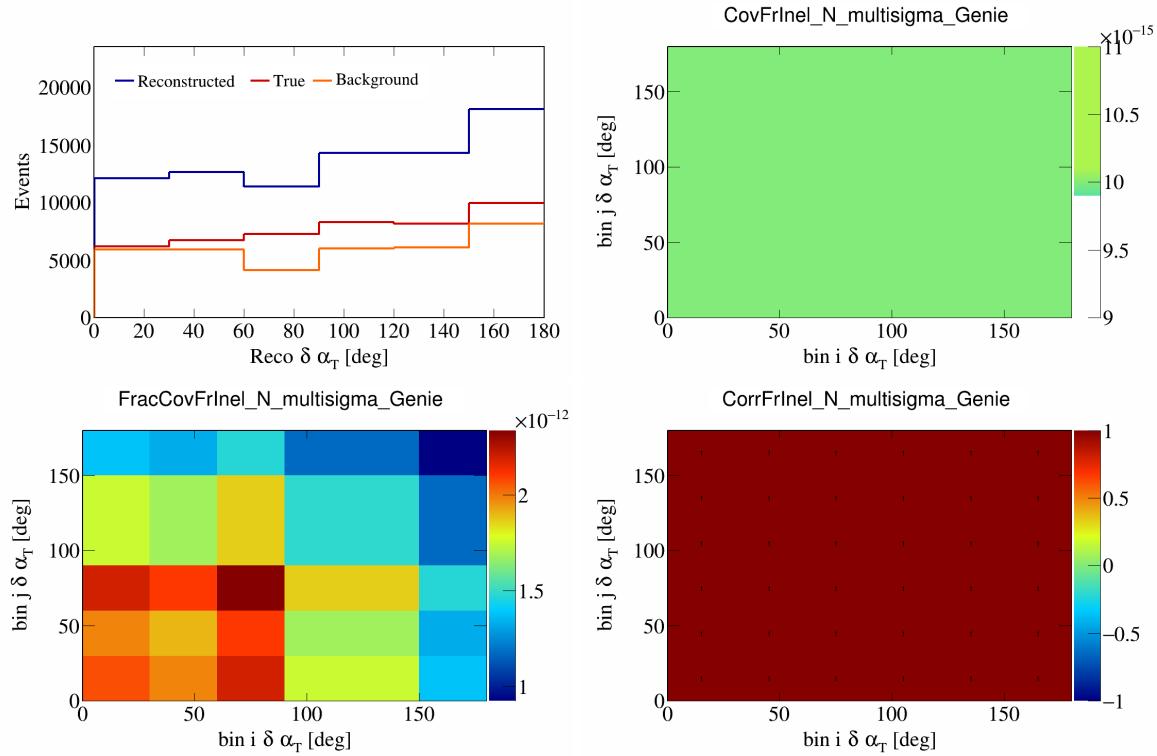


Figure 229: FrInelN variations for $\delta\alpha_T$.

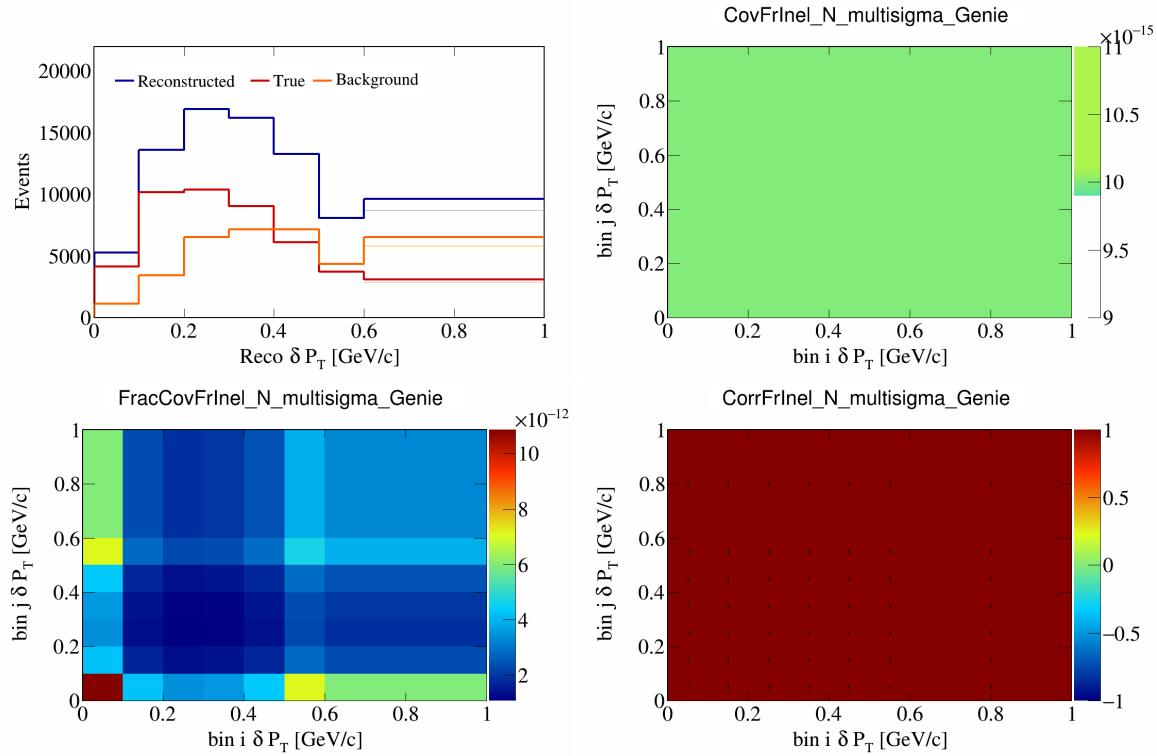


Figure 230: FrInelN variations for δP_T .

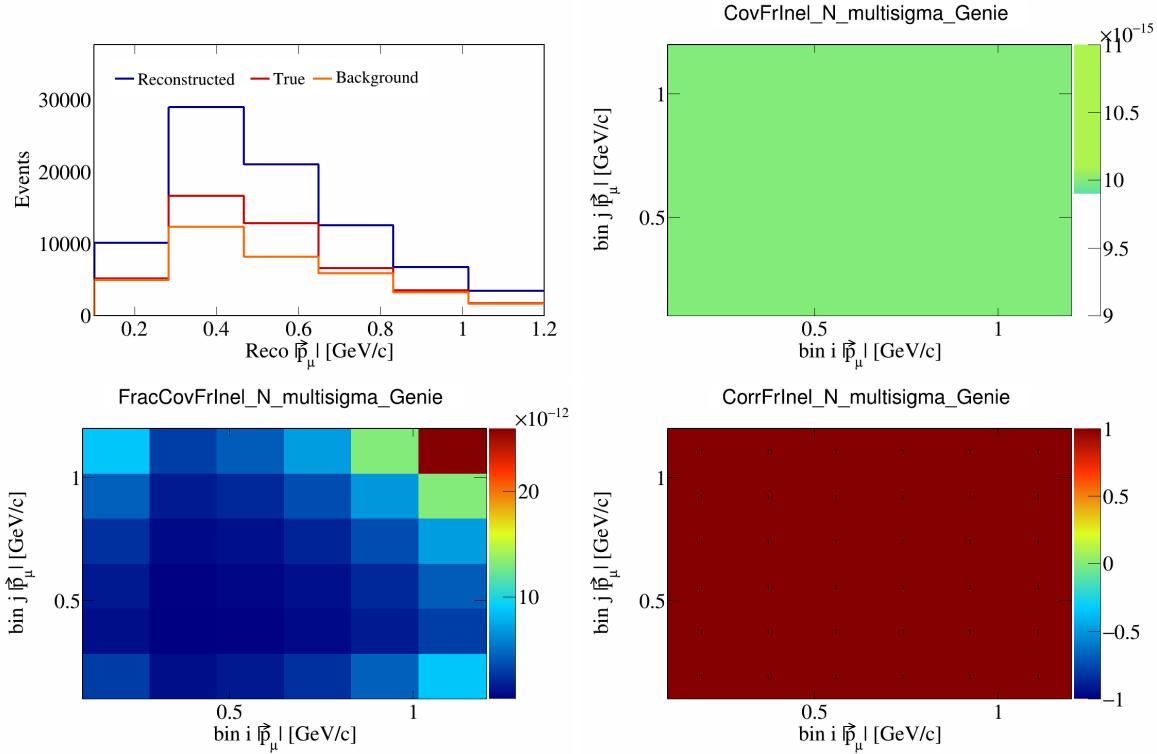


Figure 231: FrInelN variations for $|\vec{p}_\mu|$.

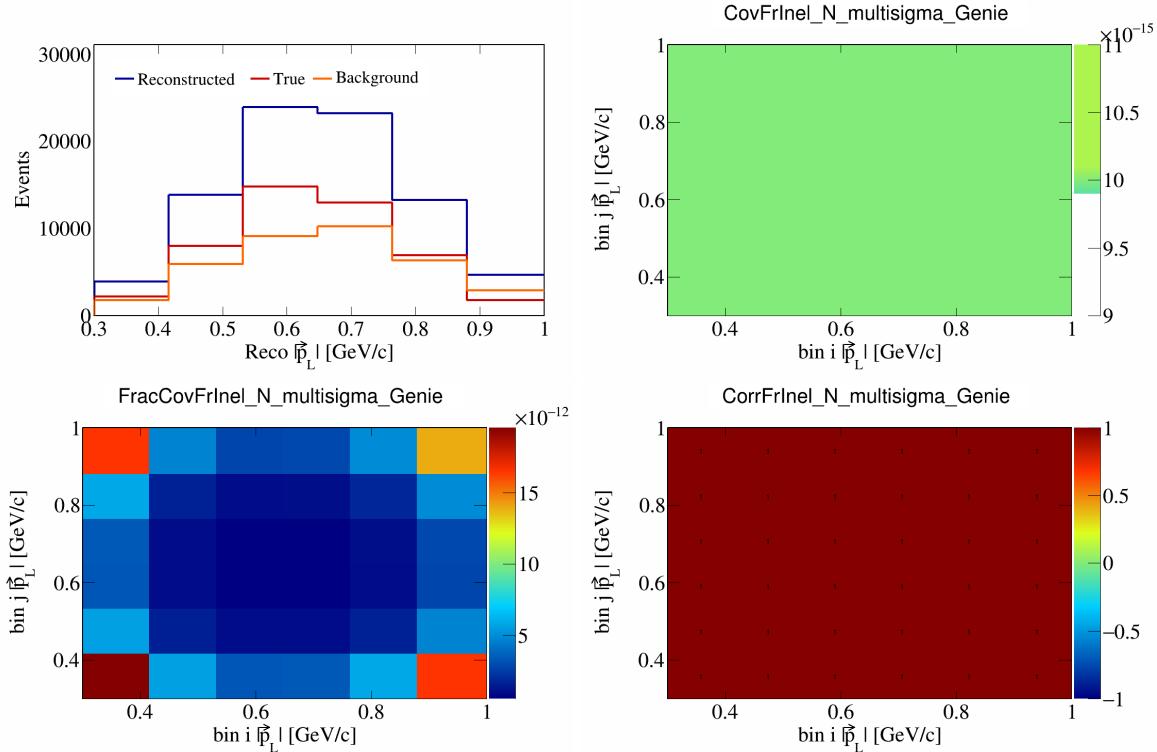


Figure 232: FrInelN variations for $|\vec{p}_L|$.

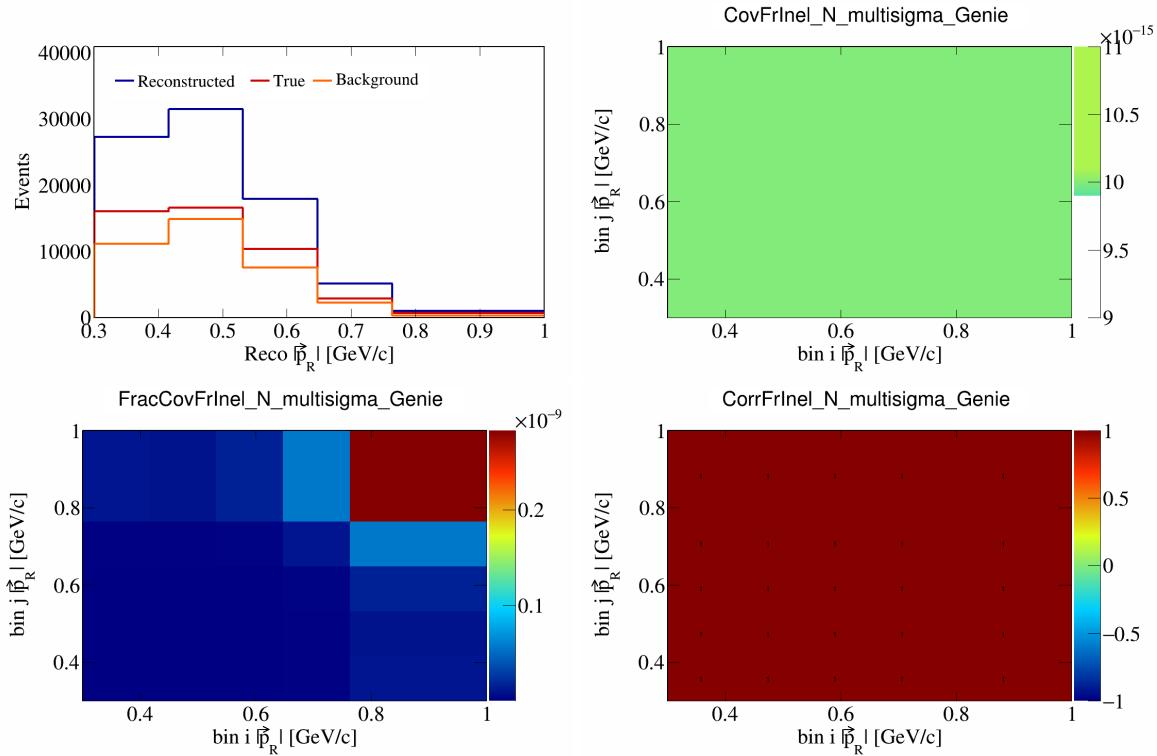


Figure 233: FrInelN variations for $|\vec{p}_R|$.

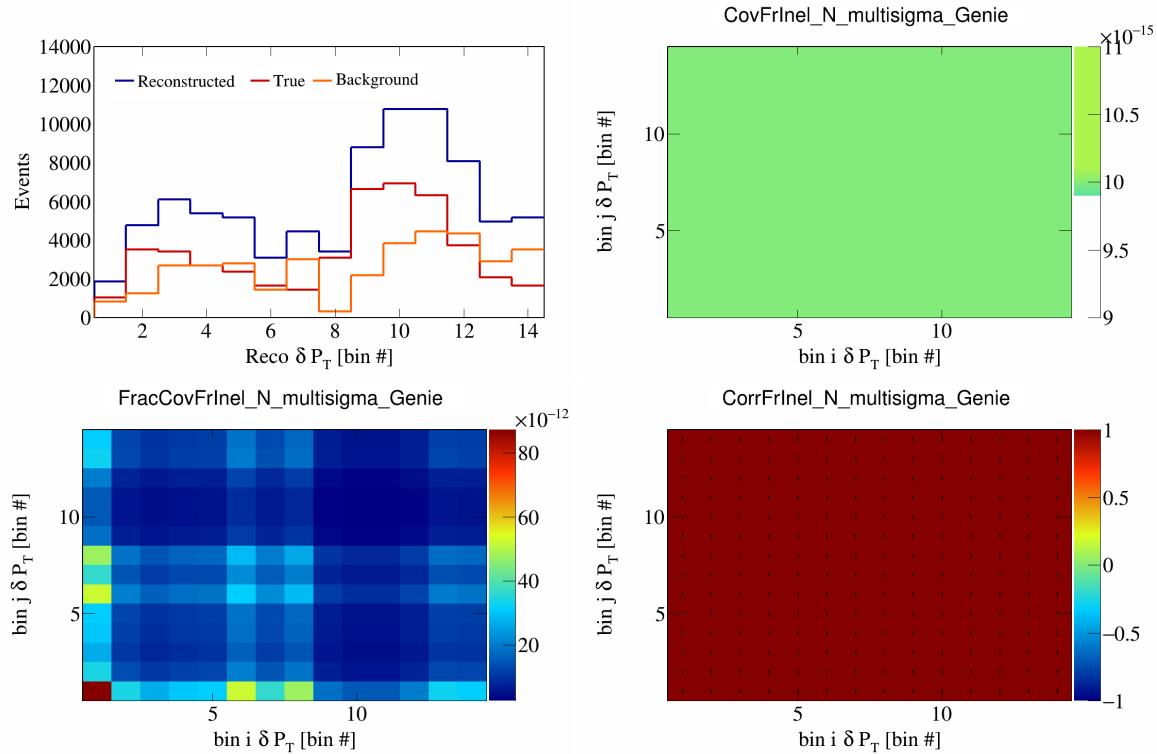


Figure 234: FrInelN variations for δP_T in $\cos(\theta_{\vec{p}_\mu})$.

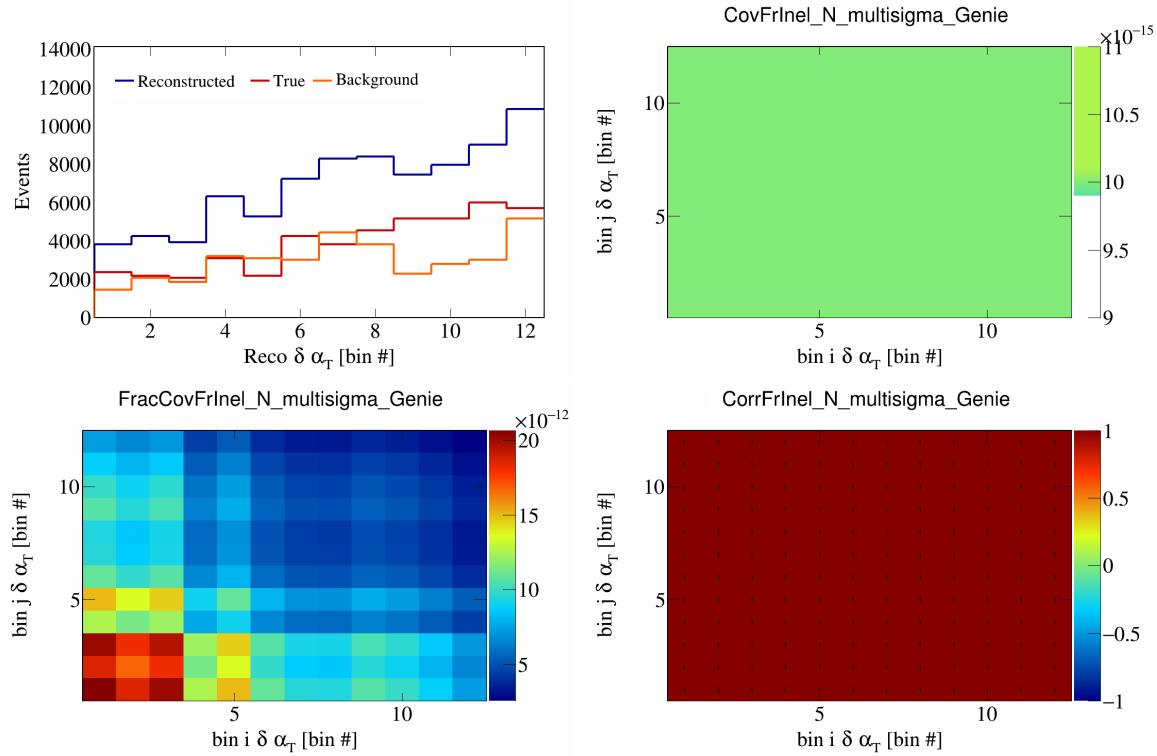


Figure 235: FrInelN variations for $\delta \alpha_T$ in $\cos(\theta_{\vec{p}_\mu})$.

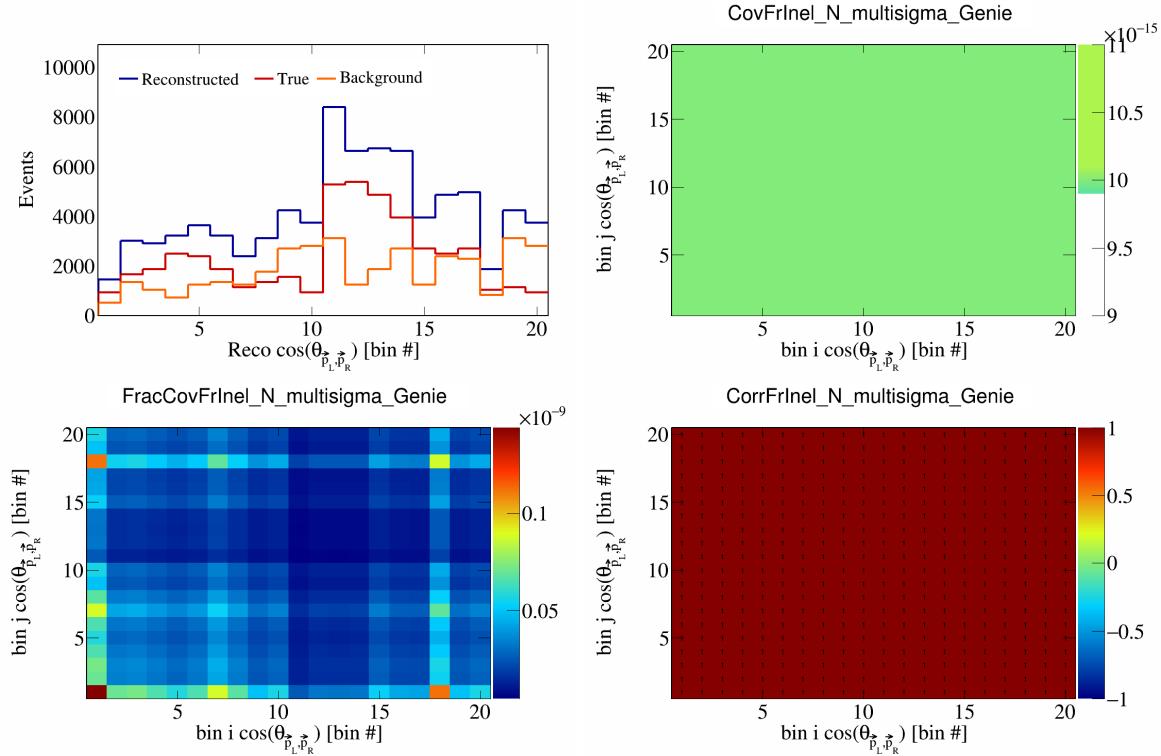


Figure 236: FrInelN variations for $\cos(\theta_{\vec{p}_L, \vec{p}_R})$ in $\cos(\theta_{\vec{p}_\mu})$.

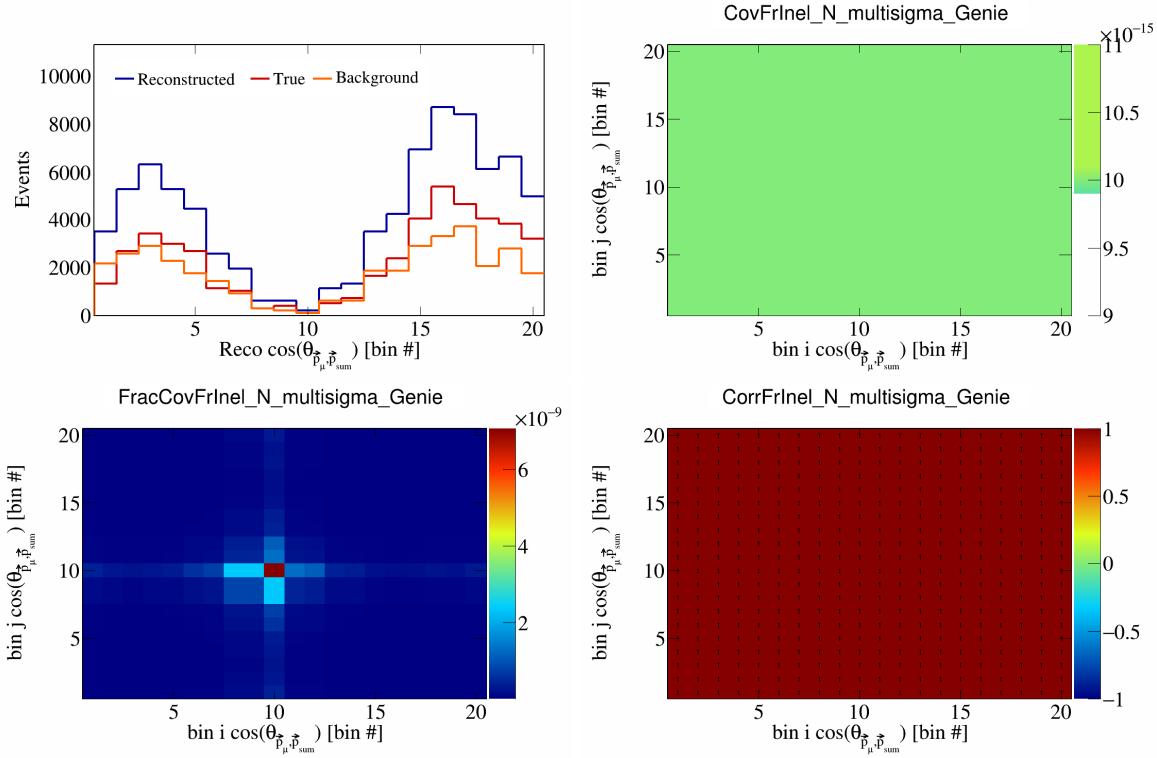


Figure 237: FrInelN variations for $\cos(\theta_{\vec{p}_\mu, \vec{p}_{\text{sum}}})$ in $\cos(\theta_{\vec{p}_\mu})$.

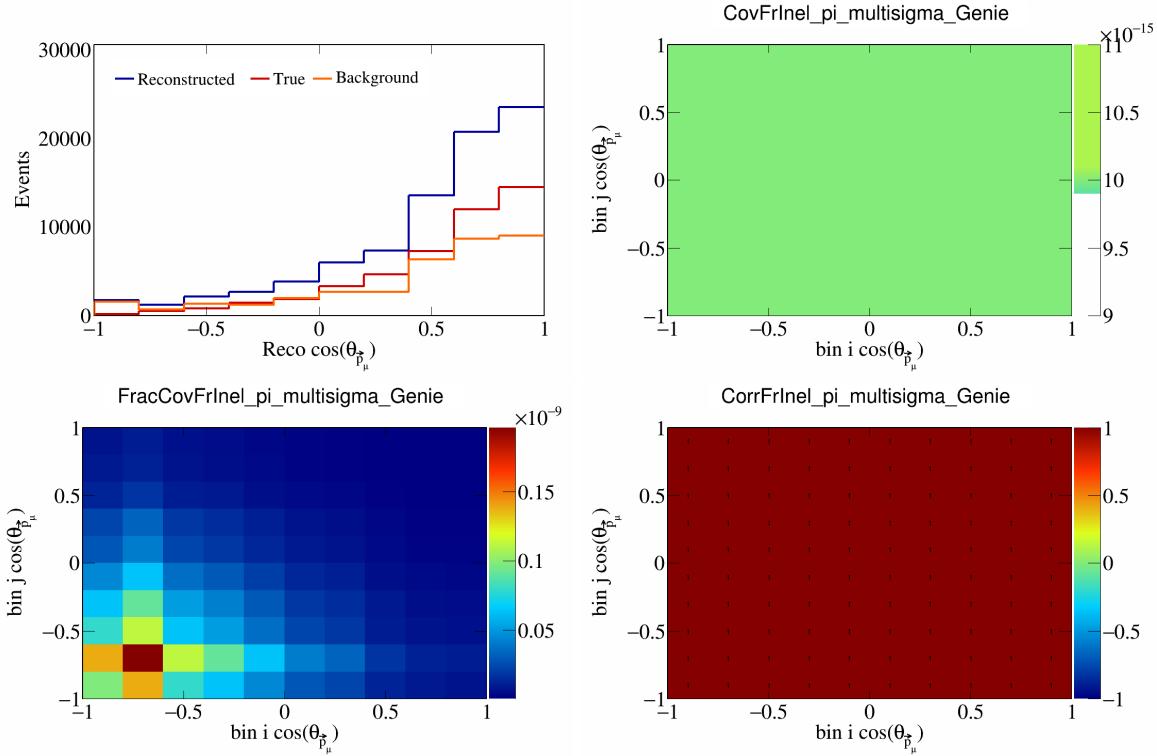


Figure 238: FrInelpi variations for $\cos(\theta_{\vec{p}_\mu})$.

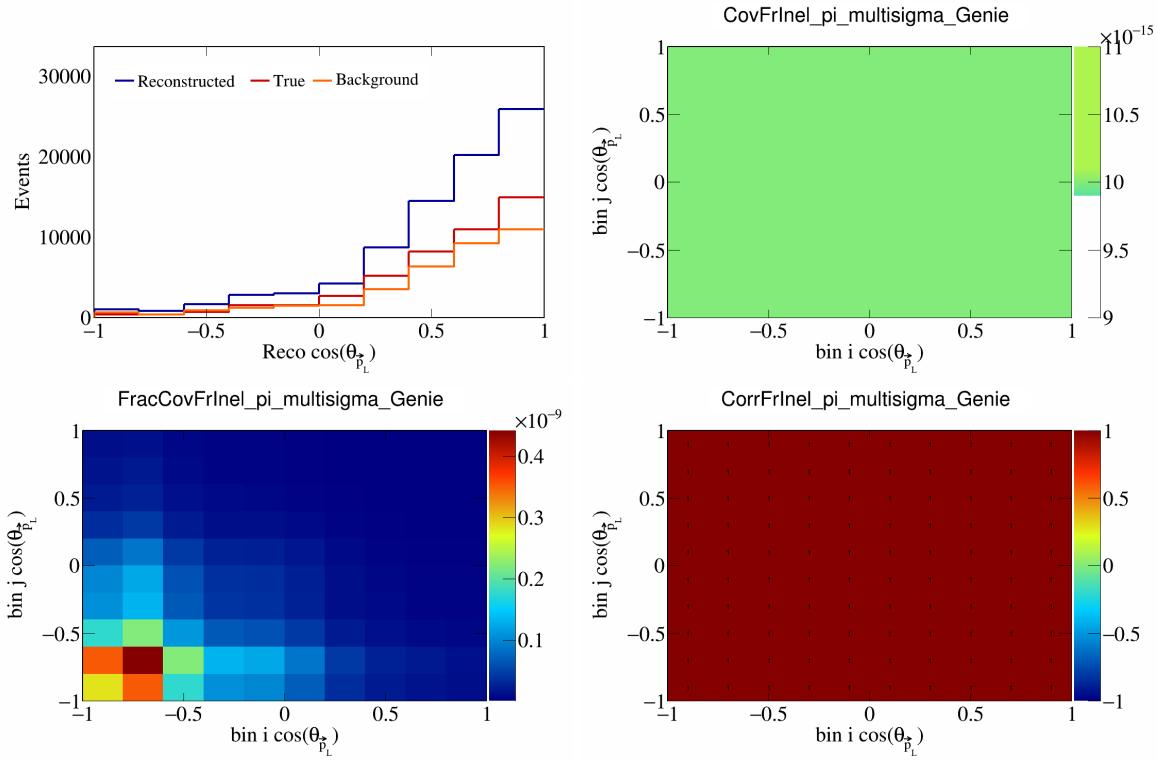


Figure 239: FrInelpi variations for $\cos(\theta_{\vec{p}_L})$.

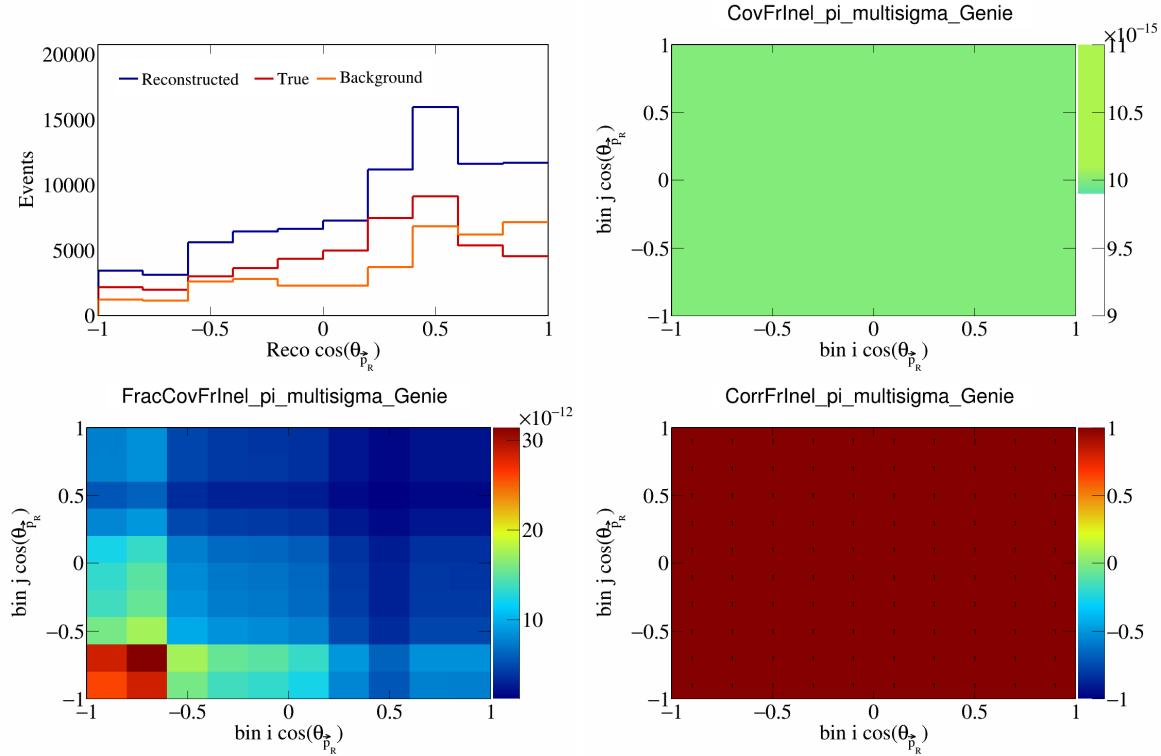


Figure 240: FrInelpi variations for $\cos(\theta_{\vec{p}_R})$.

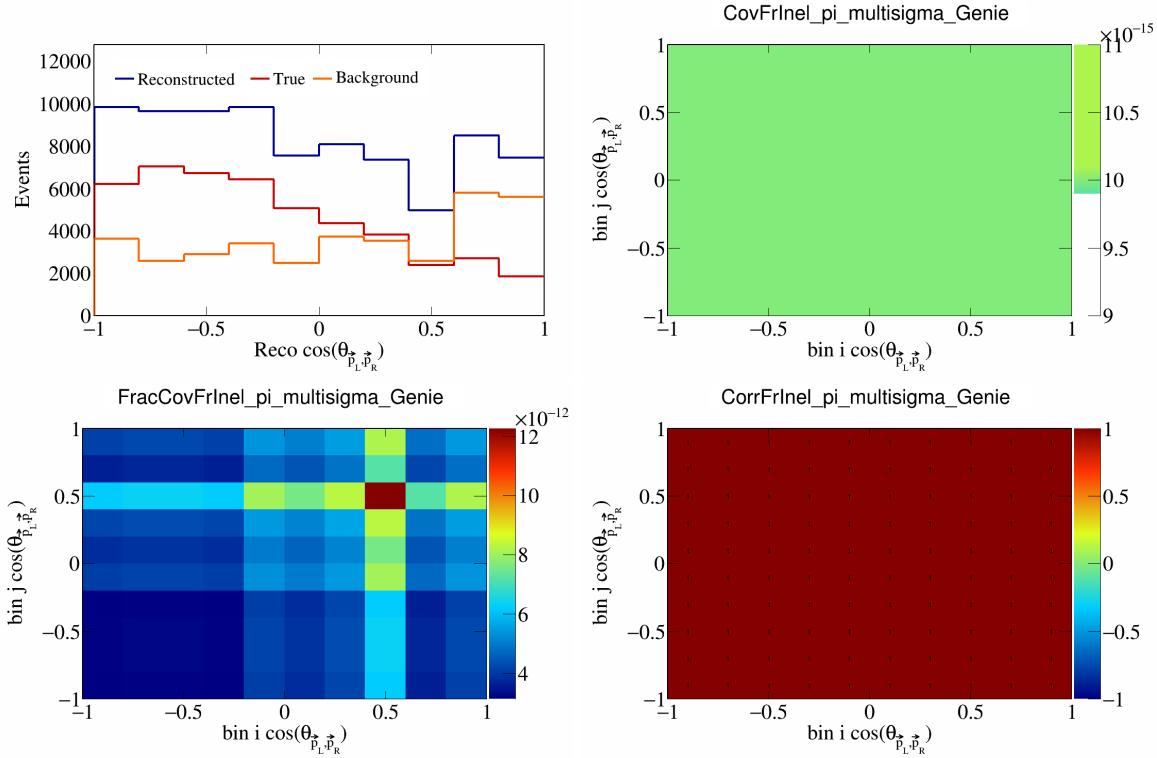


Figure 241: FrInelpi variations for $\cos(\theta_{\vec{p}_L, \vec{p}_R})$.

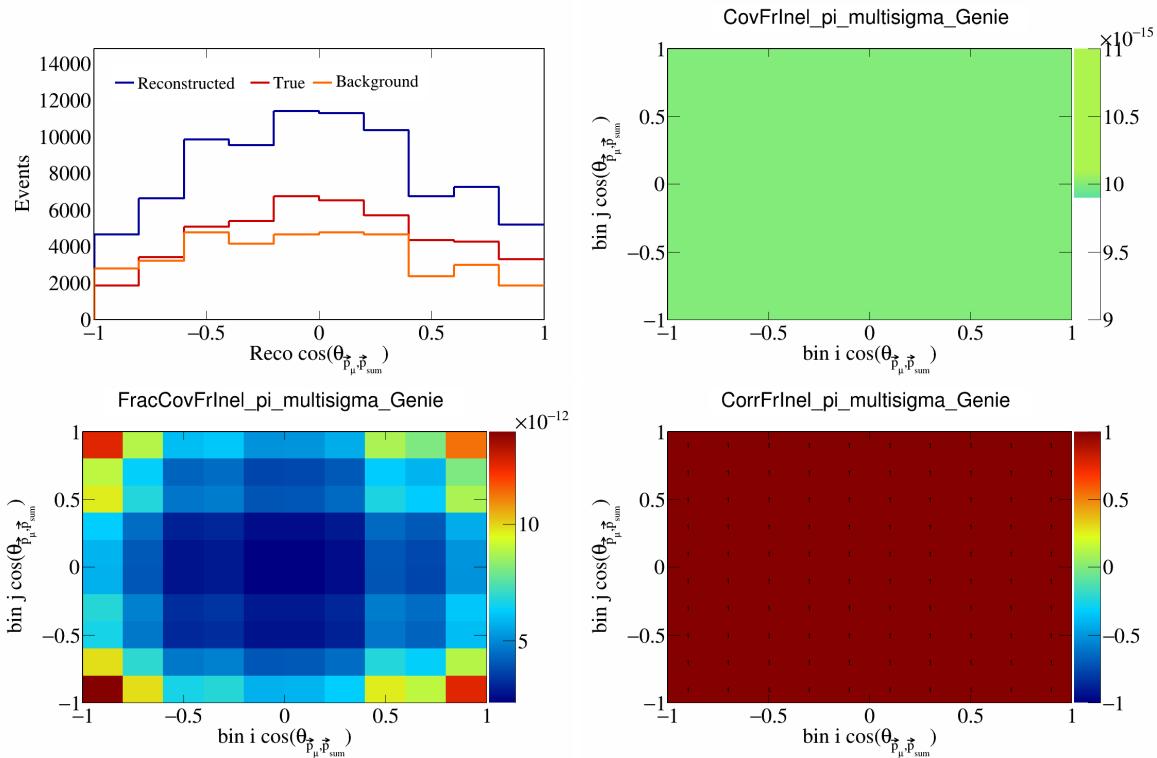


Figure 242: FrInelpi variations for $\cos(\theta_{\vec{p}_\mu, \vec{p}_{\text{sum}}})$.

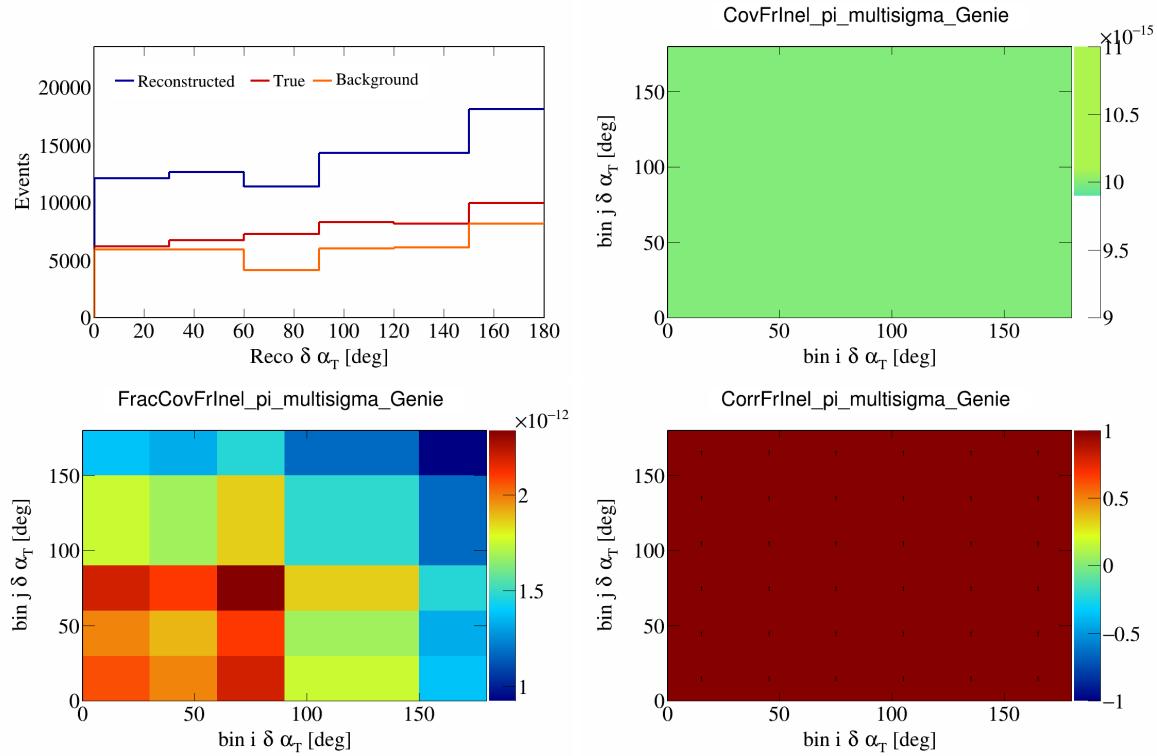


Figure 243: FrInelpi variations for $\delta \alpha_T$.

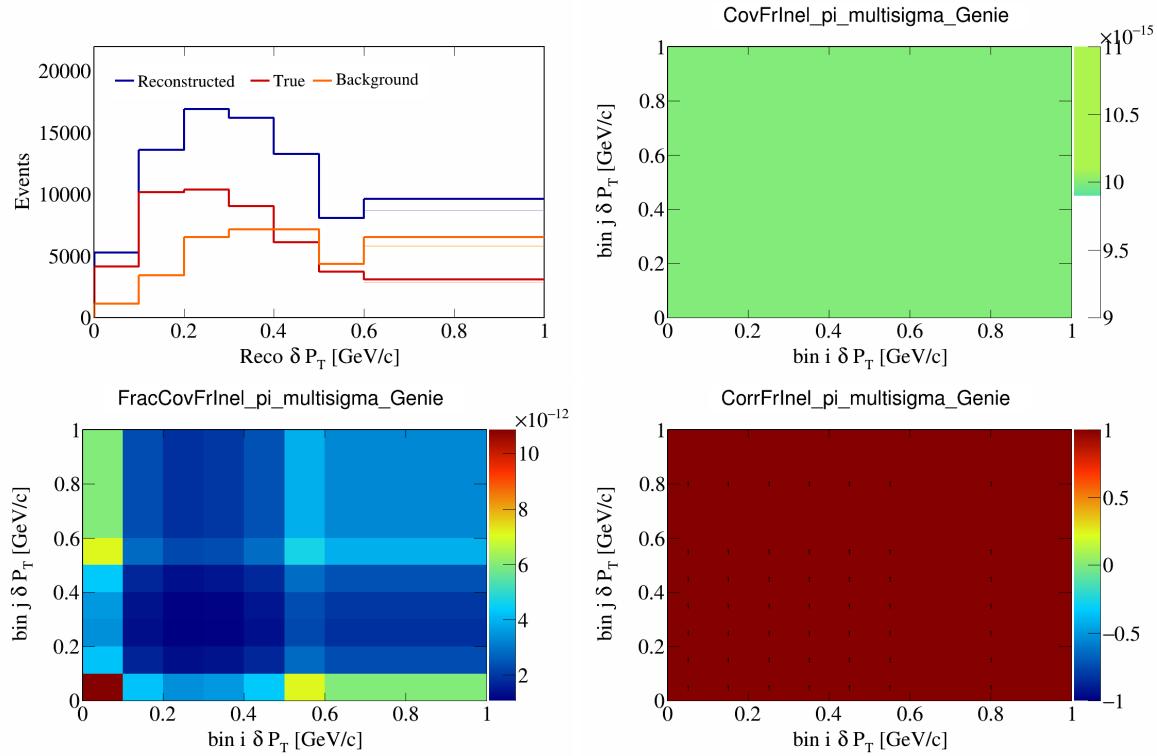


Figure 244: FrInelpi variations for δP_T .

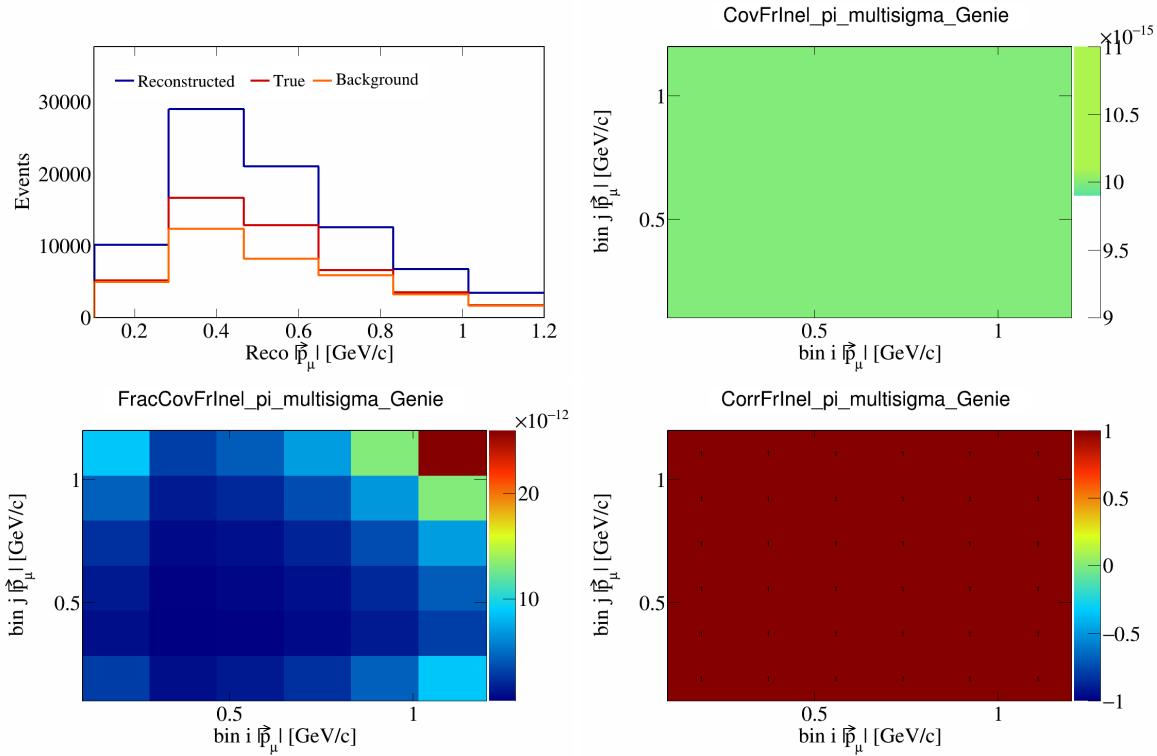


Figure 245: FrInelpi variations for $|\vec{p}_\mu|$.

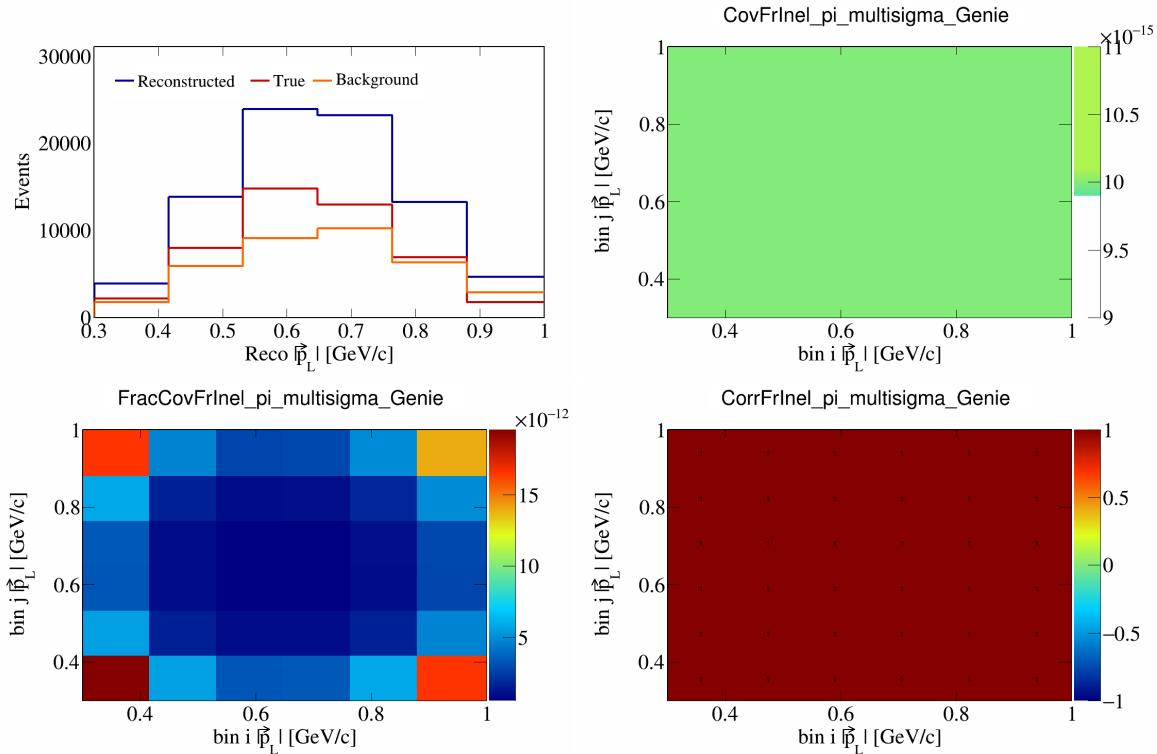


Figure 246: FrInelpi variations for $|\vec{p}_L|$.

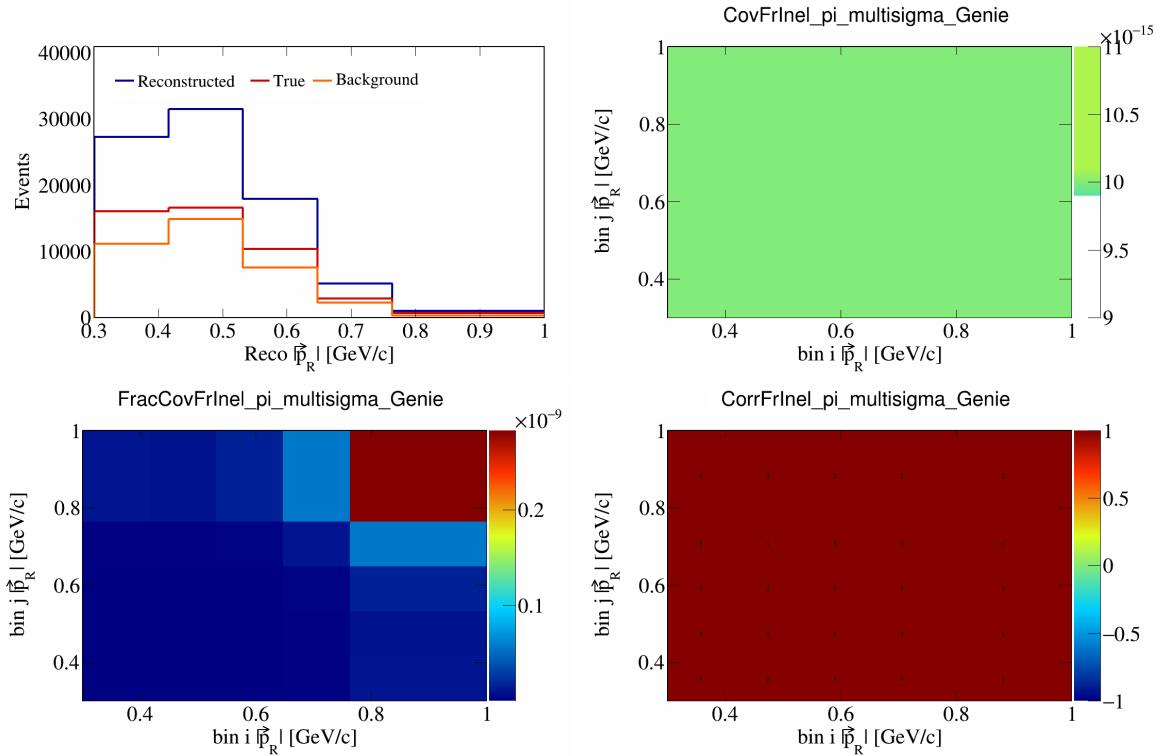


Figure 247: FrInelpi variations for $|\vec{p}_R|$.

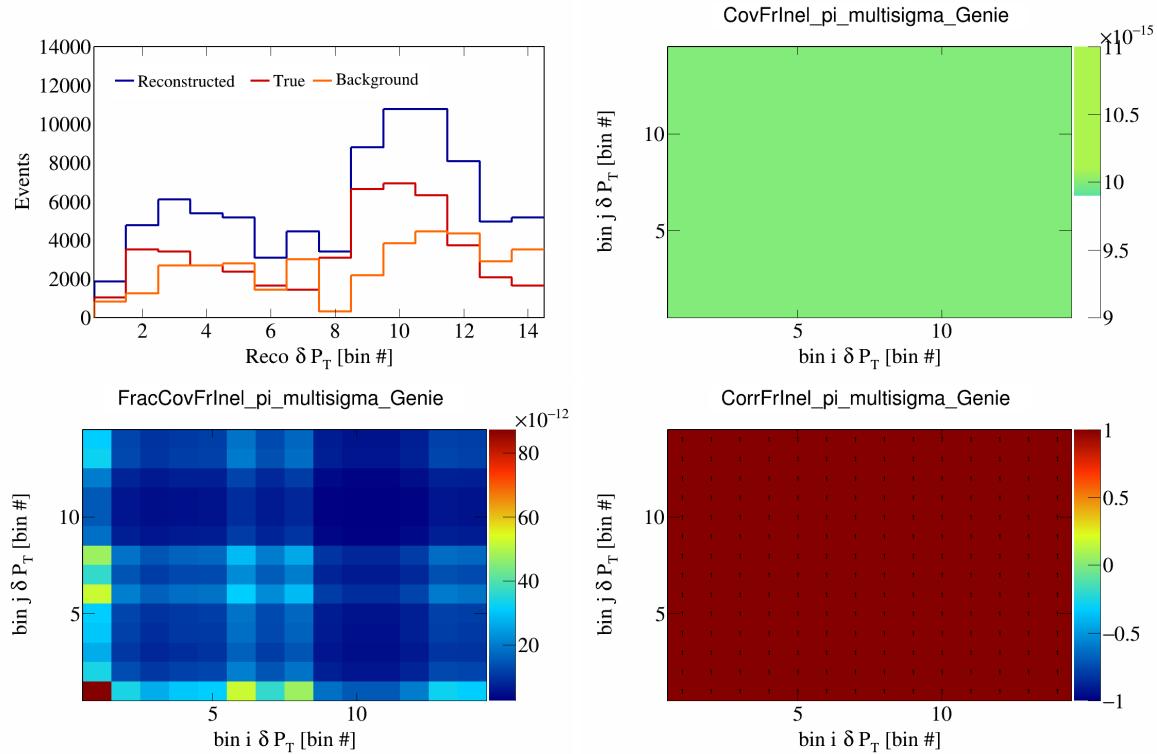


Figure 248: FrInelpi variations for δP_T in $\cos(\theta_{\vec{p}_\mu})$.

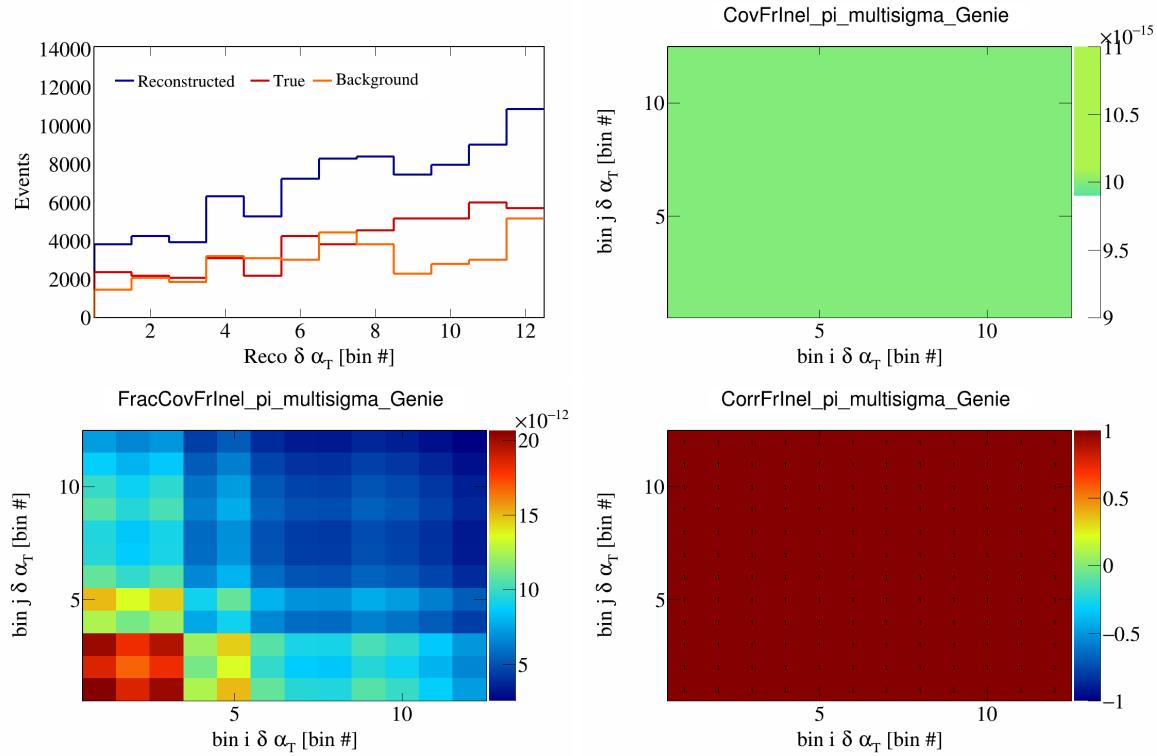


Figure 249: FrInelpi variations for $\delta\alpha_T$ in $\cos(\theta_{\vec{p}_\mu})$.

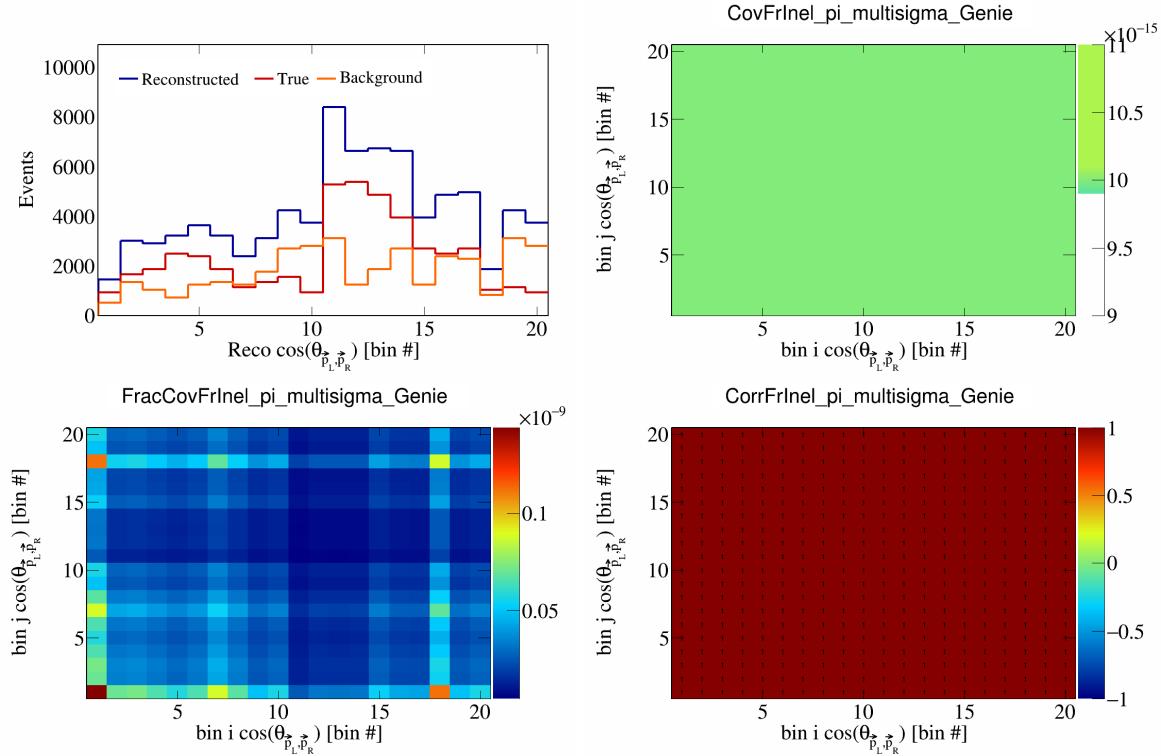


Figure 250: FrInelpi variations for $\cos(\theta_{\vec{p}_L, \vec{p}_R})$ in $\cos(\theta_{\vec{p}_\mu})$.

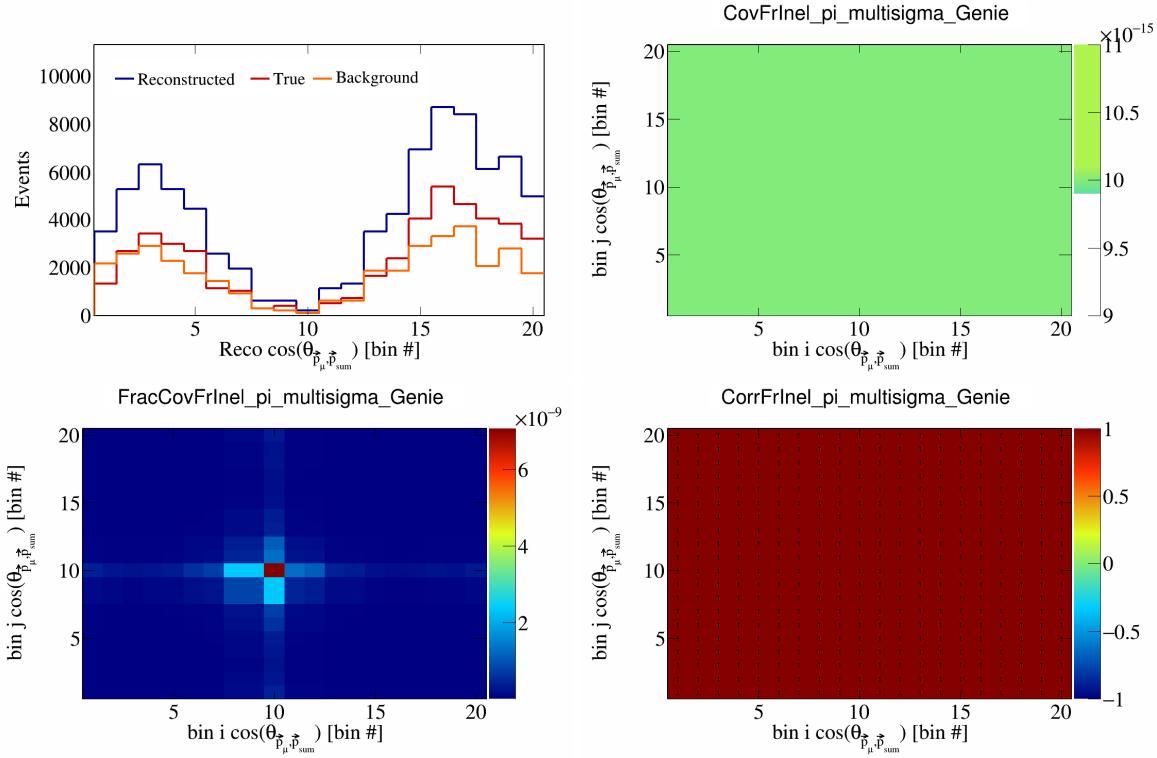


Figure 251: FrInelpi variations for $\cos(\theta_{\vec{p}_\mu, \vec{p}_{\text{sum}}})$ in $\cos(\theta_{\vec{p}_\mu})$.

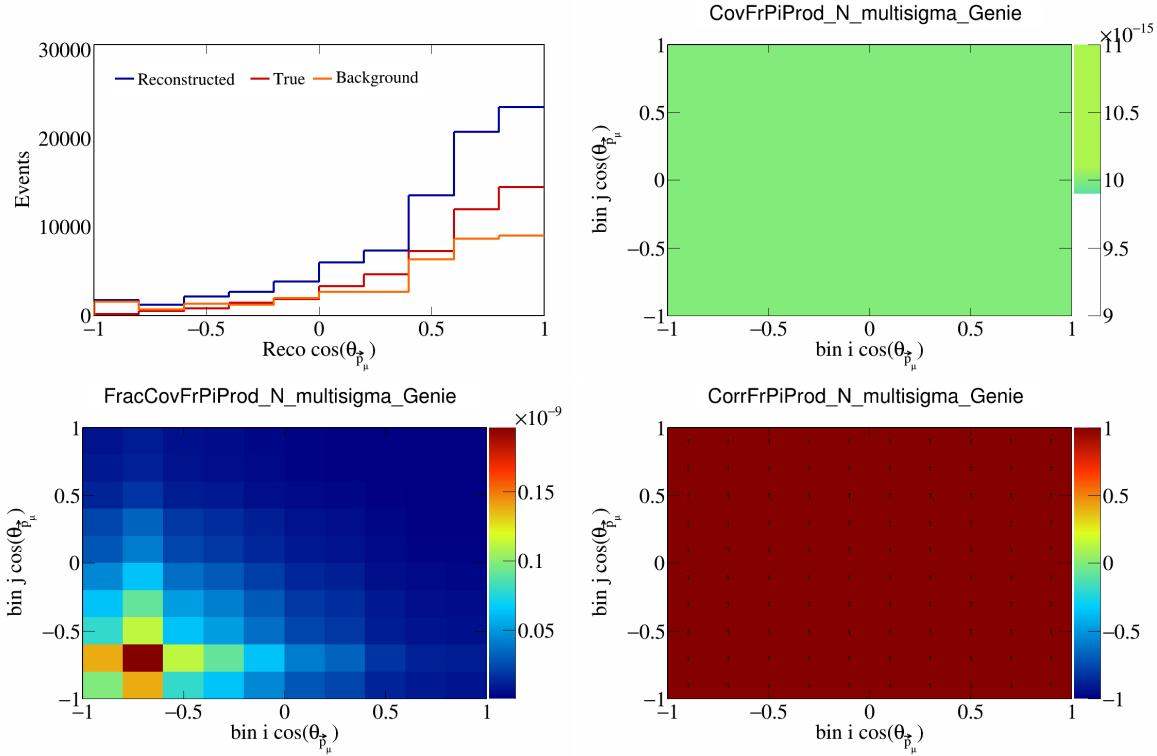


Figure 252: FrPiProdN variations for $\cos(\theta_{\vec{p}_\mu})$.

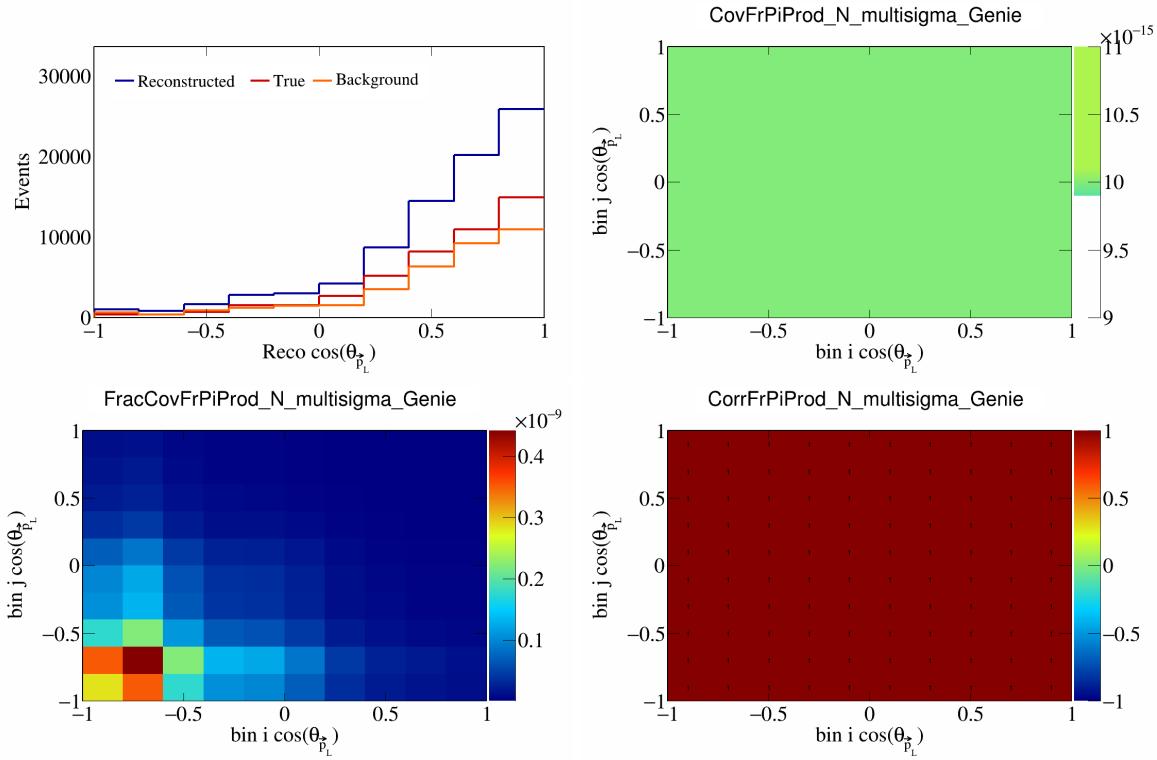


Figure 253: FrPiProdN variations for $\cos(\theta_{\vec{p}_L})$.

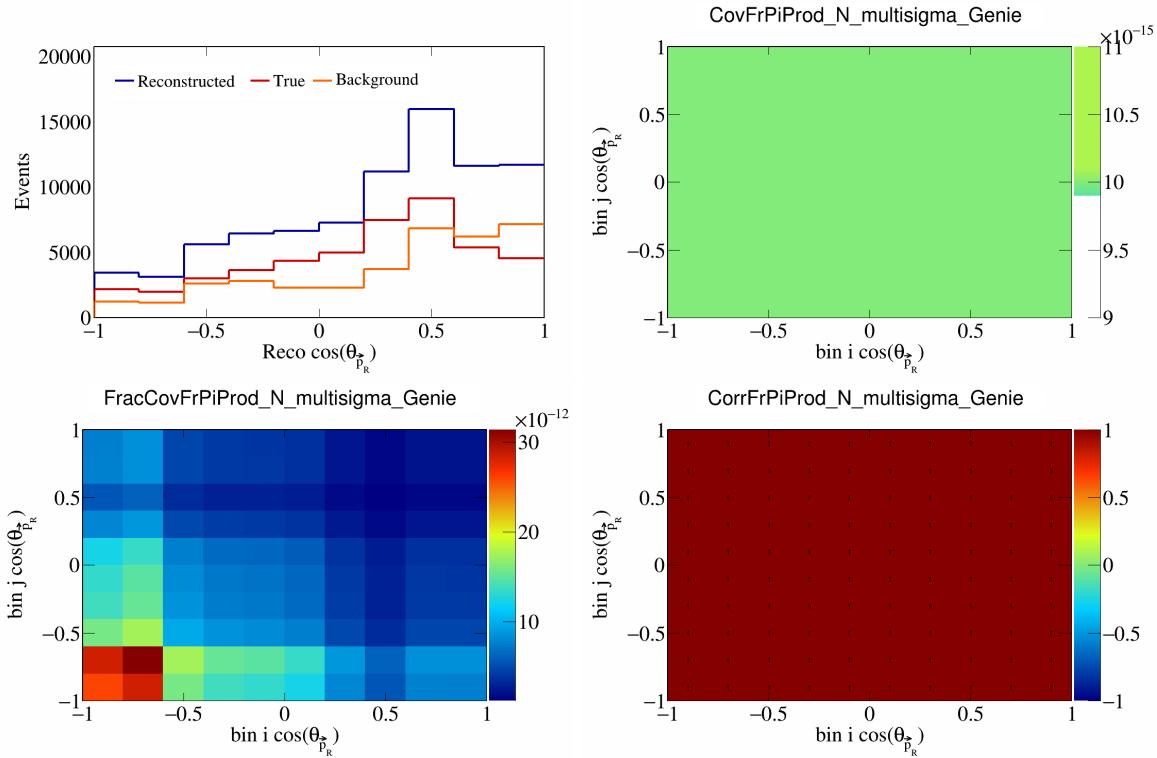


Figure 254: FrPiProdN variations for $\cos(\theta_{\vec{p}_R})$.

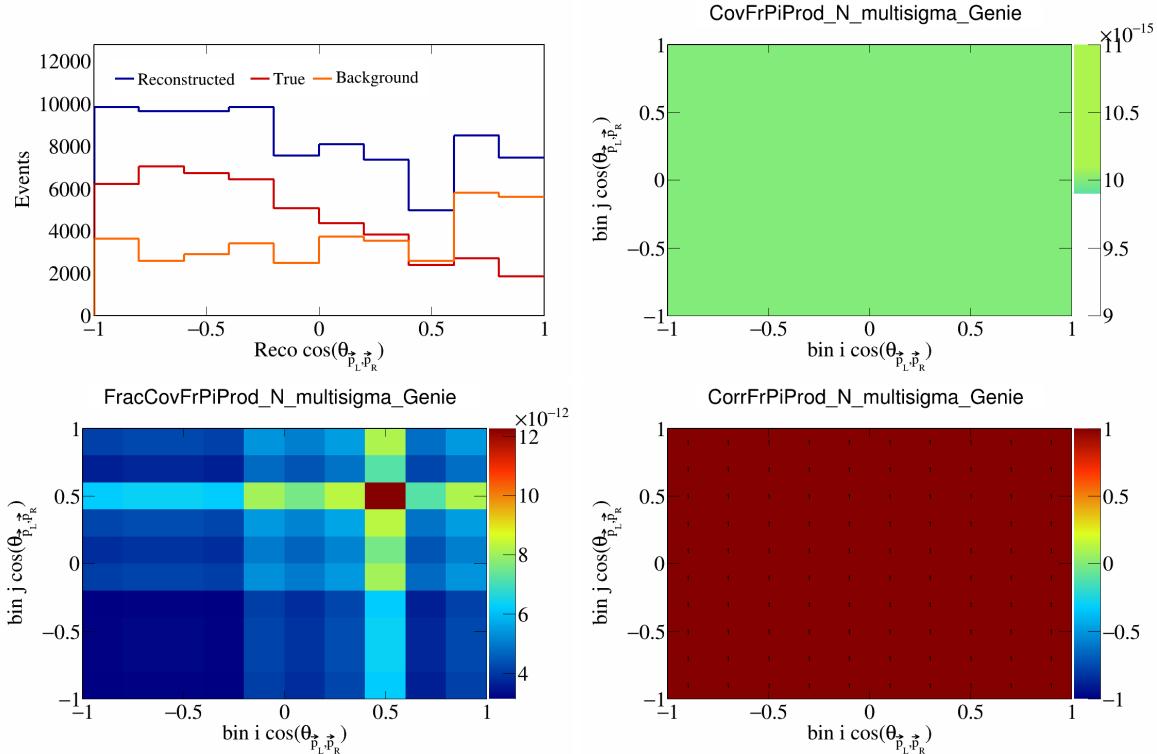


Figure 255: FrPiProdN variations for $\cos(\theta_{\vec{p}_L, \vec{p}_R})$.

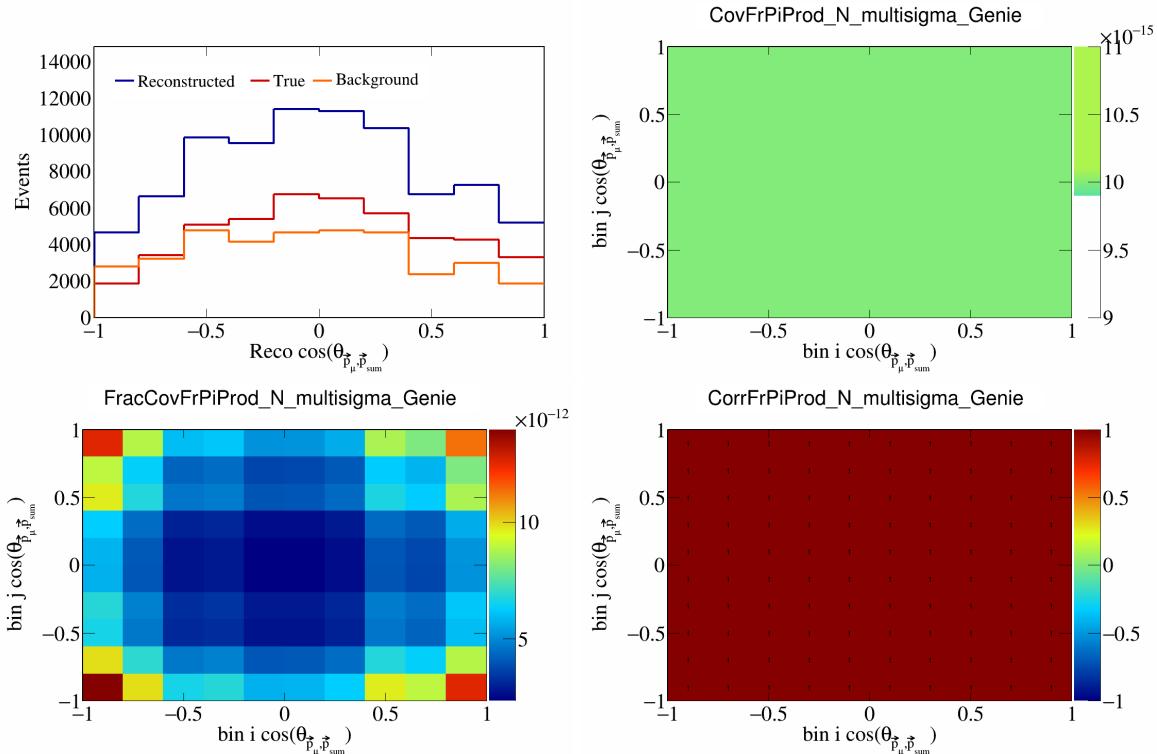


Figure 256: FrPiProdN variations for $\cos(\theta_{\vec{p}_\mu, \vec{p}_{\text{sum}}})$.

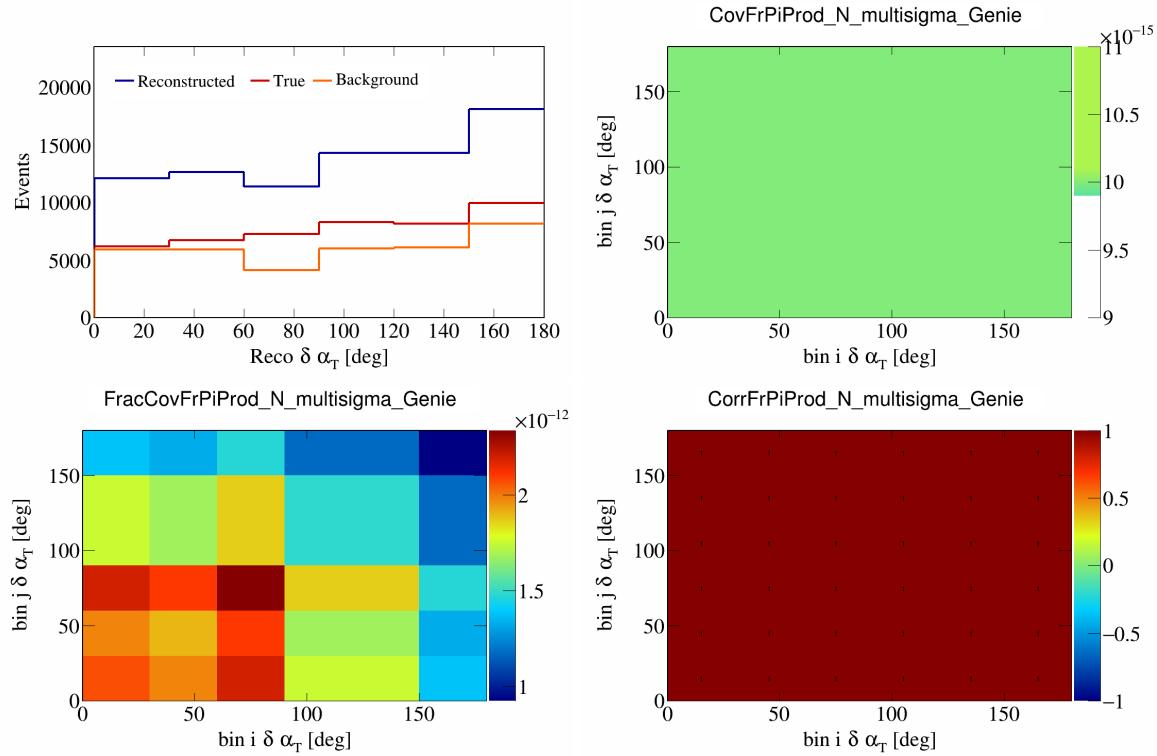


Figure 257: FrPiProdN variations for $\delta\alpha_T$.

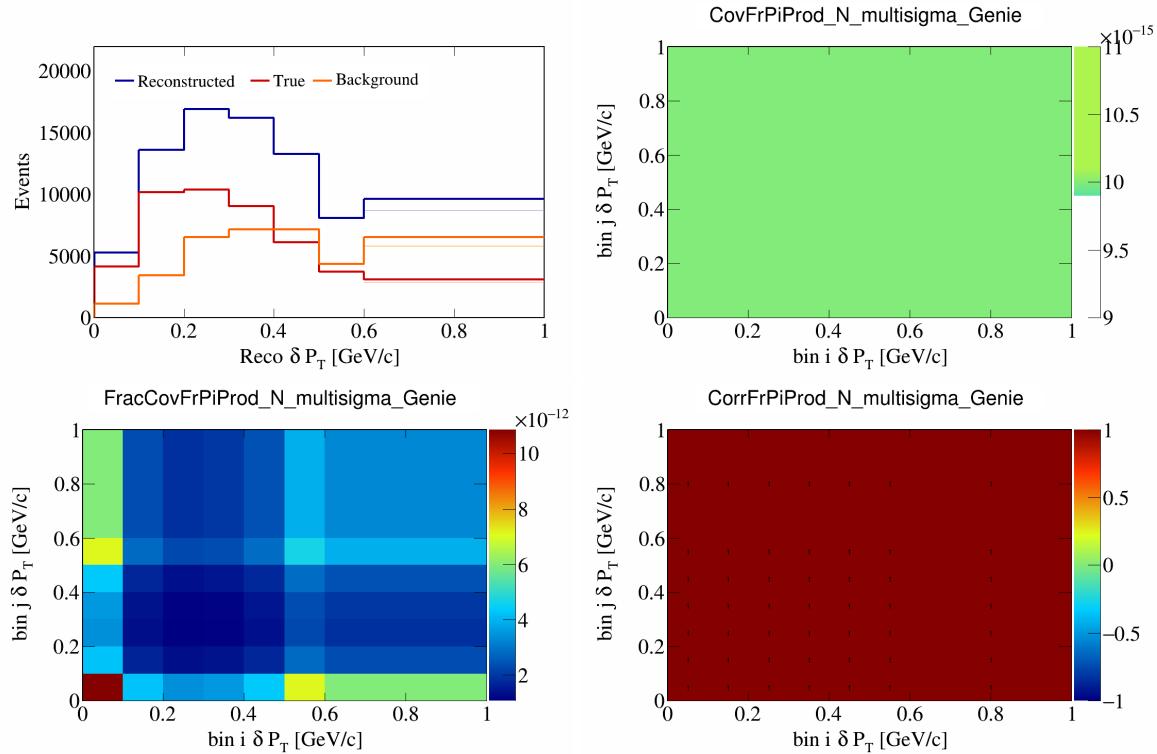


Figure 258: FrPiProdN variations for δP_T .

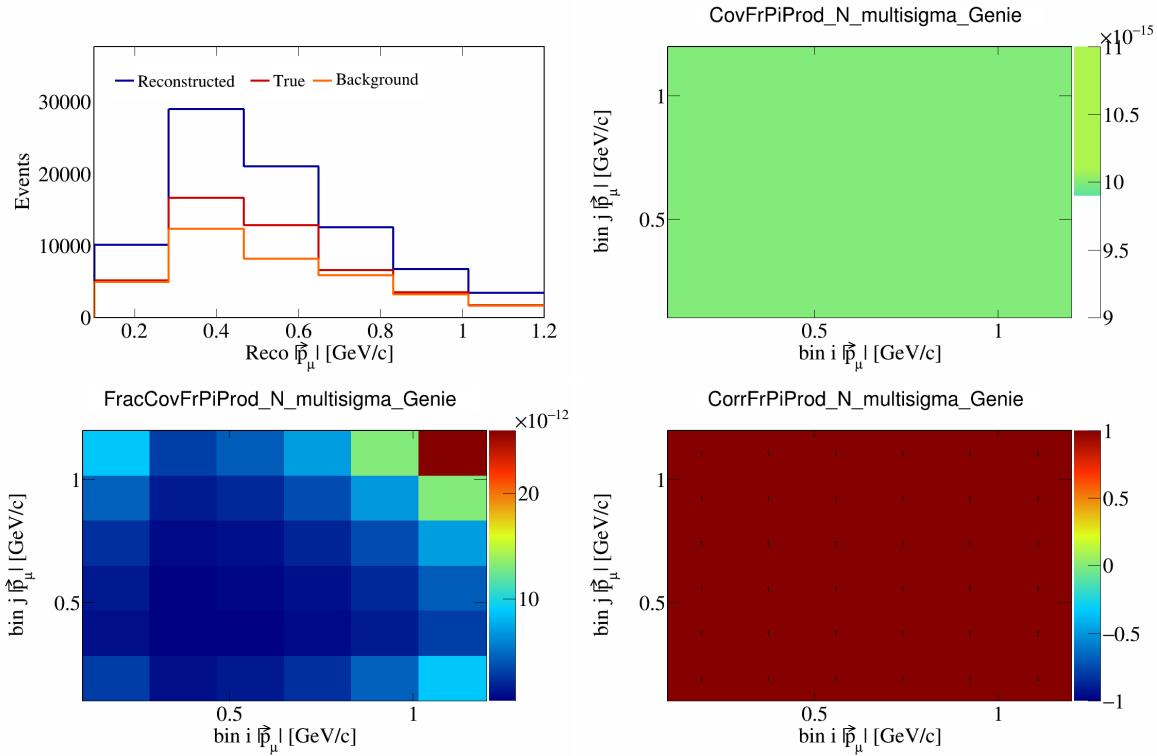


Figure 259: FrPiProdN variations for $|\vec{p}_\mu|$.

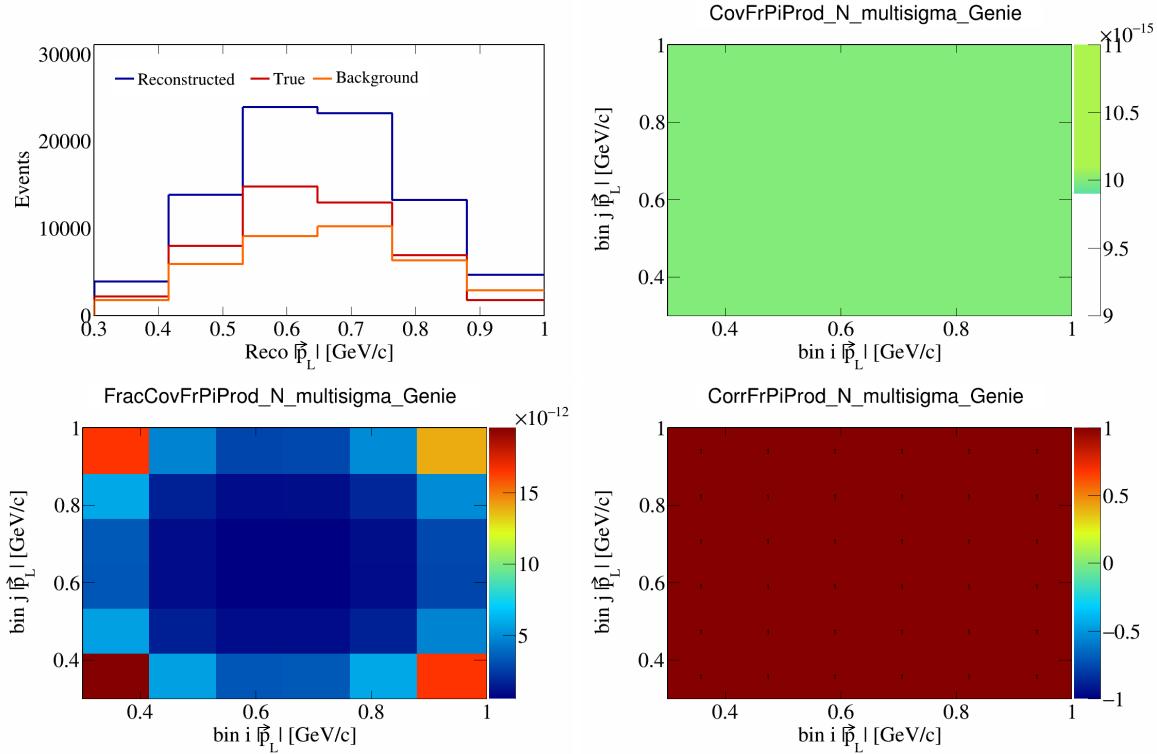


Figure 260: FrPiProdN variations for $|\vec{p}_L|$.

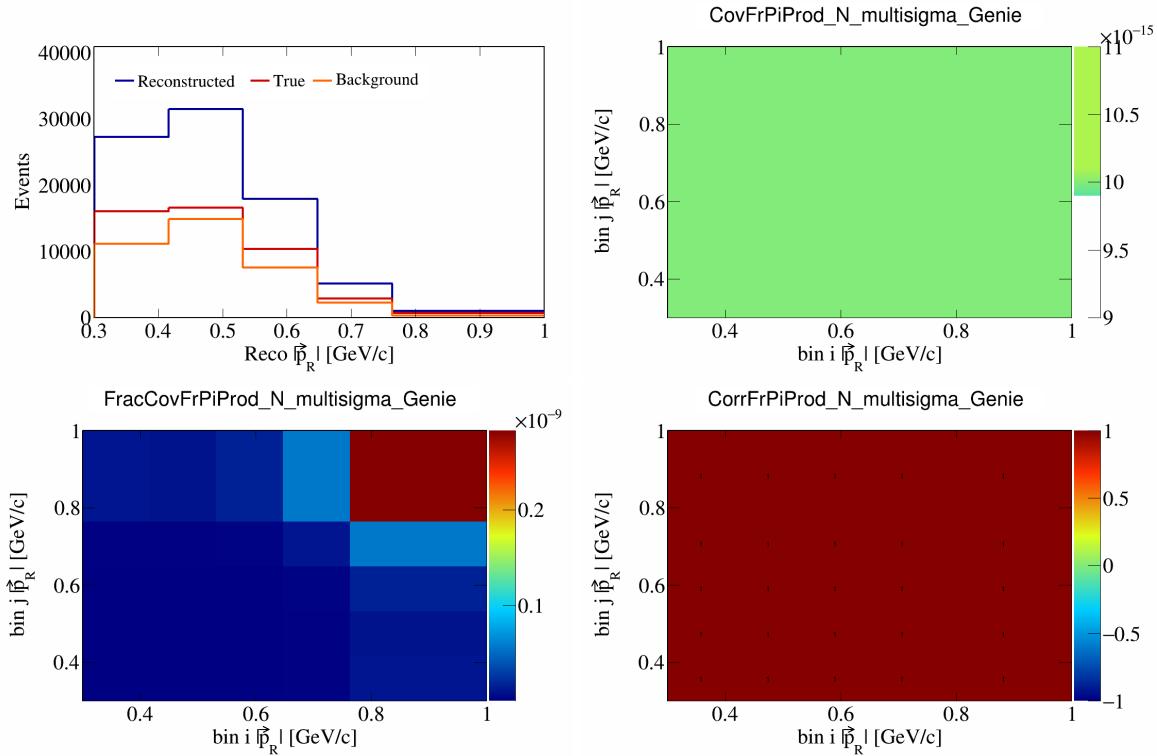


Figure 261: FrPiProdN variations for $|\vec{p}_R|$.

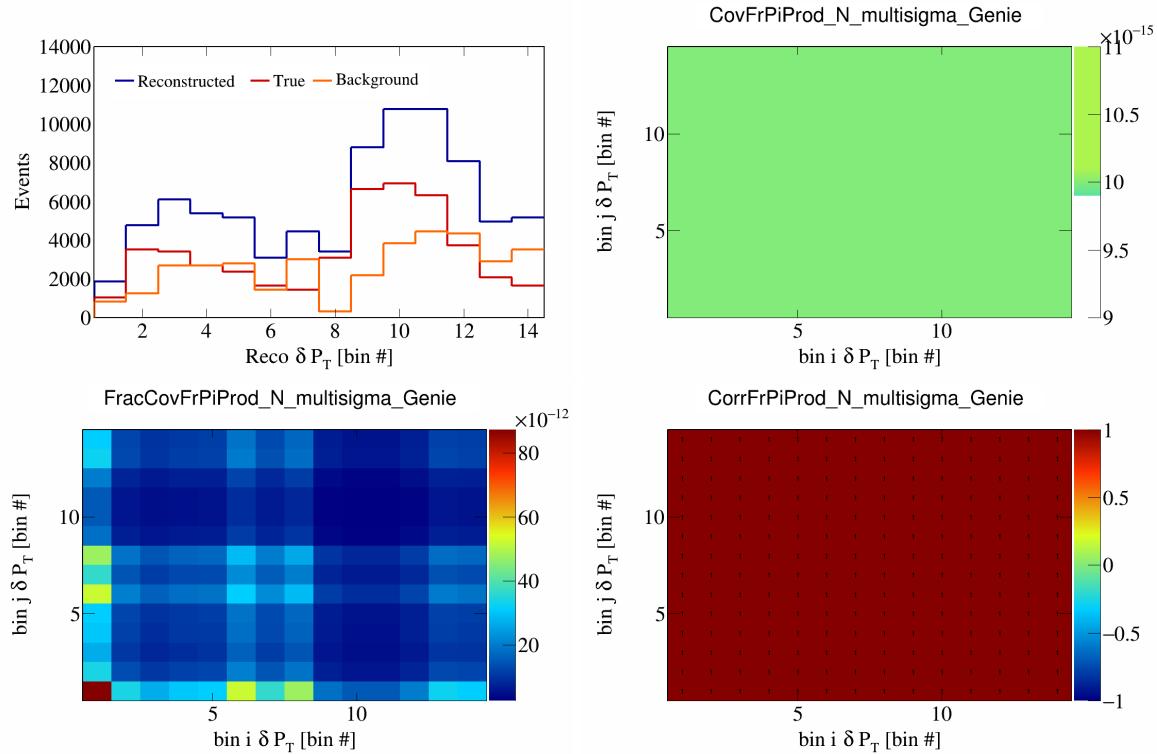


Figure 262: FrPiProdN variations for δP_T in $\cos(\theta_{\vec{p}_\mu})$.

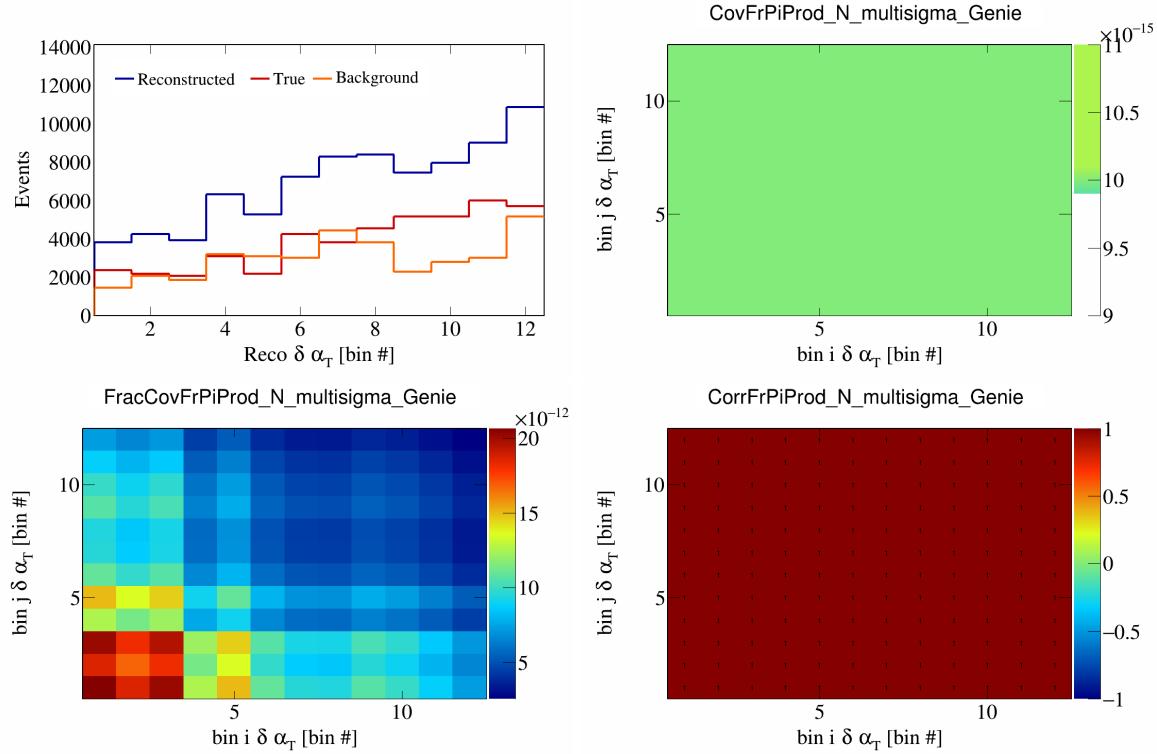


Figure 263: FrPiProdN variations for $\delta\alpha_T$ in $\cos(\theta_{\vec{p}_\mu})$.

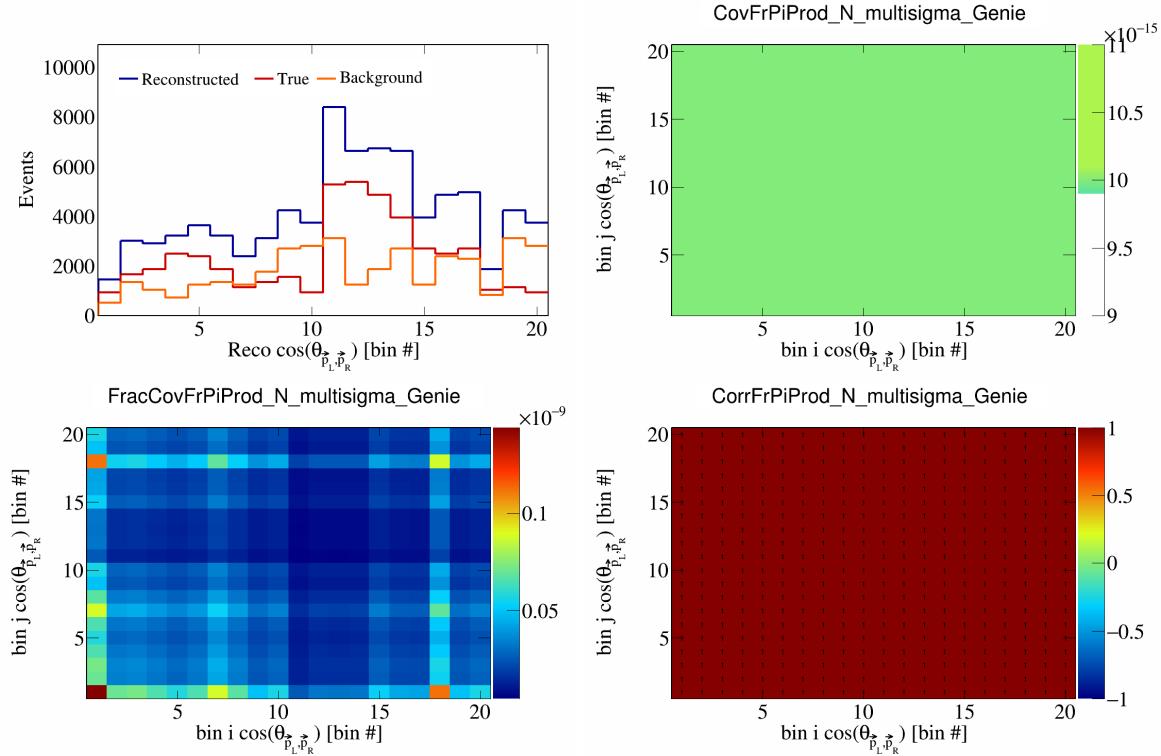


Figure 264: FrPiProdN variations for $\cos(\theta_{\vec{p}_L, \vec{p}_R})$ in $\cos(\theta_{\vec{p}_\mu})$.

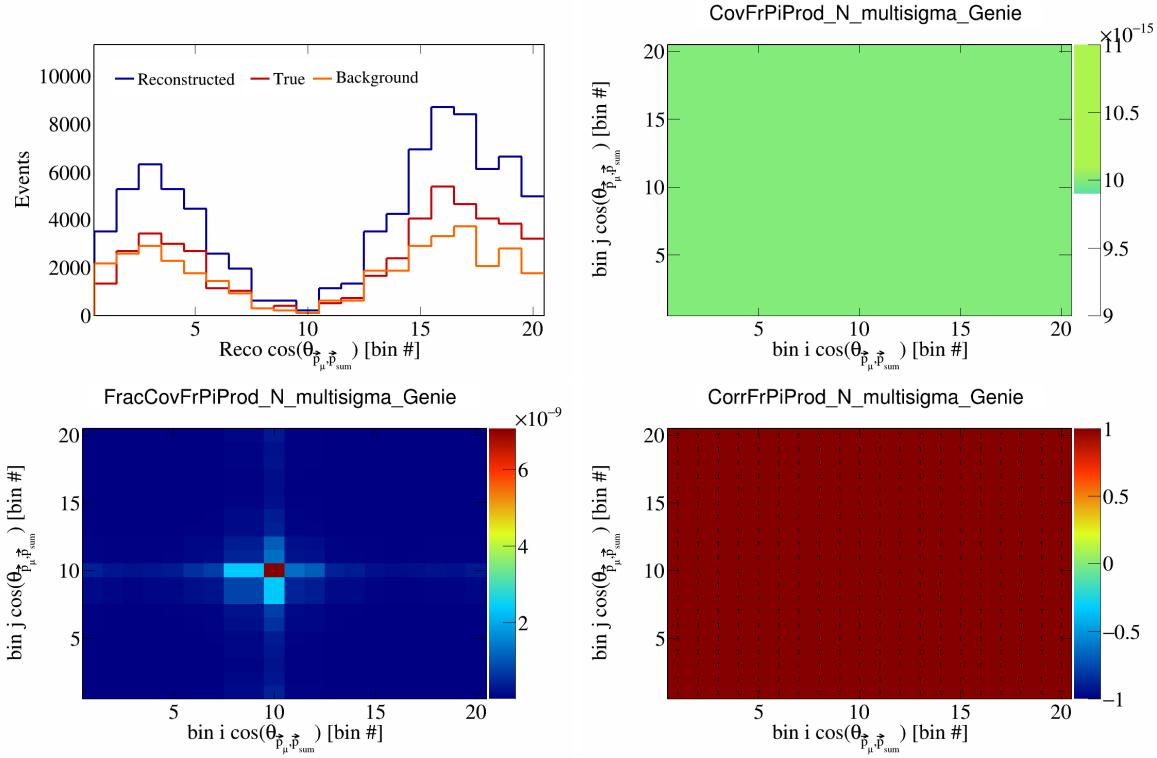


Figure 265: FrPiProdN variations for $\cos(\theta_{\vec{p}_\mu, \vec{p}_{\text{sum}}})$ in $\cos(\theta_{\vec{p}_\mu})$.

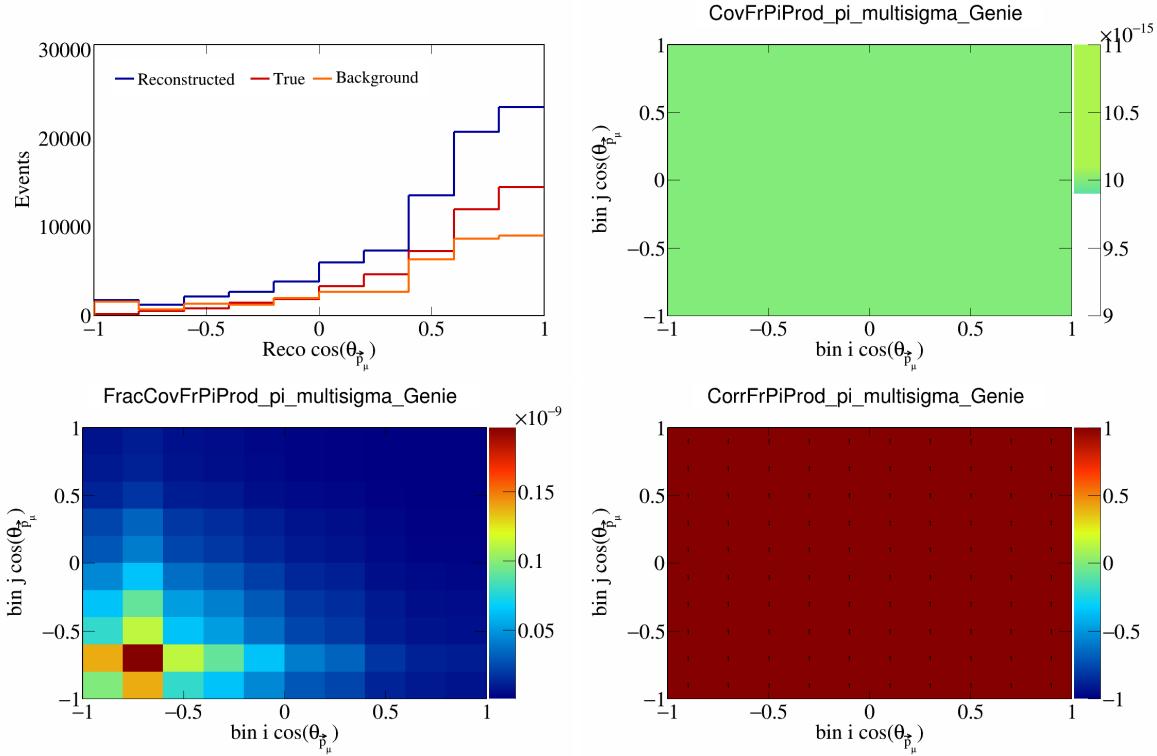


Figure 266: FrPiProdpi variations for $\cos(\theta_{\vec{p}_\mu, \vec{p}_\pi})$ in $\cos(\theta_{\vec{p}_\mu})$.

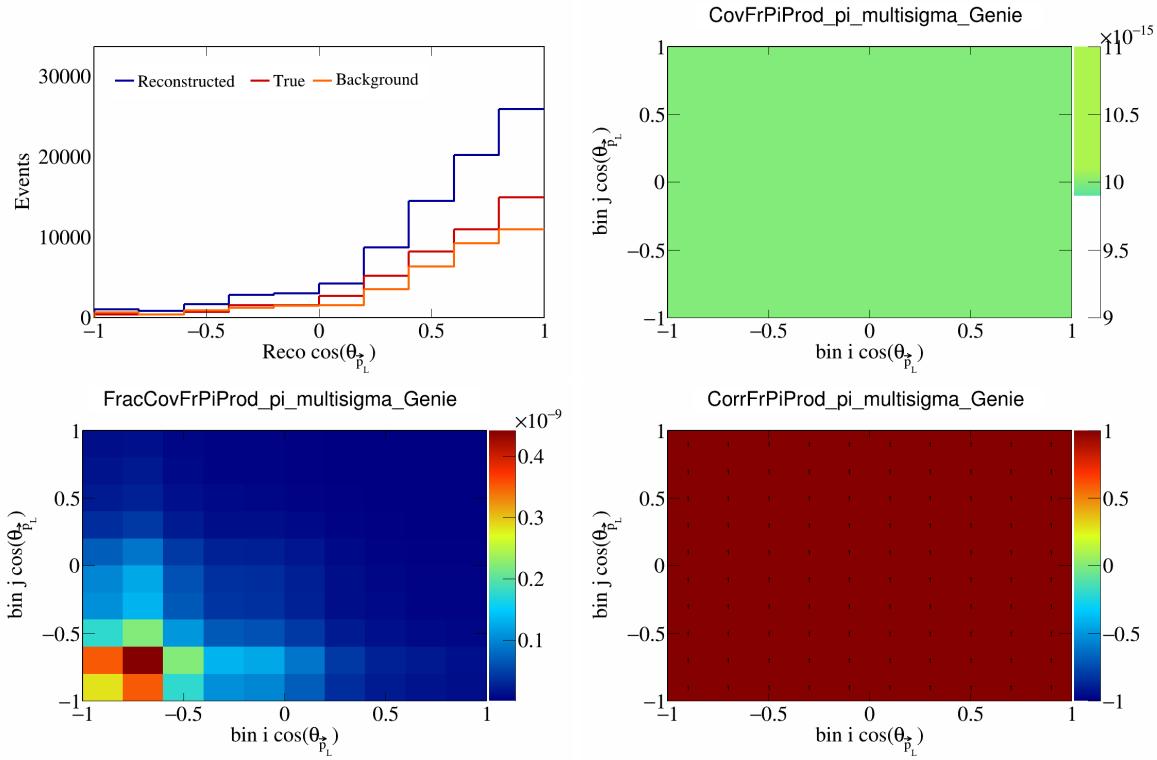


Figure 267: FrPiProdpi variations for $\cos(\theta_{\vec{p}_L})$.

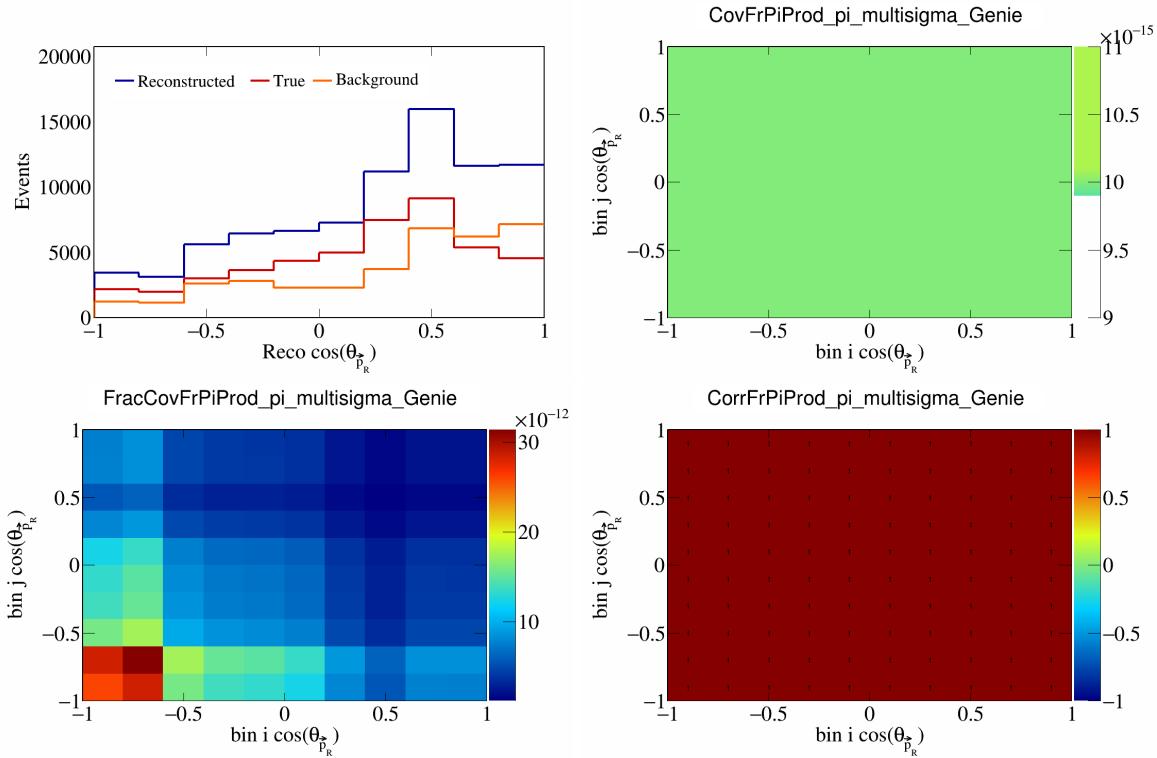


Figure 268: FrPiProdpi variations for $\cos(\theta_{\vec{p}_R})$.

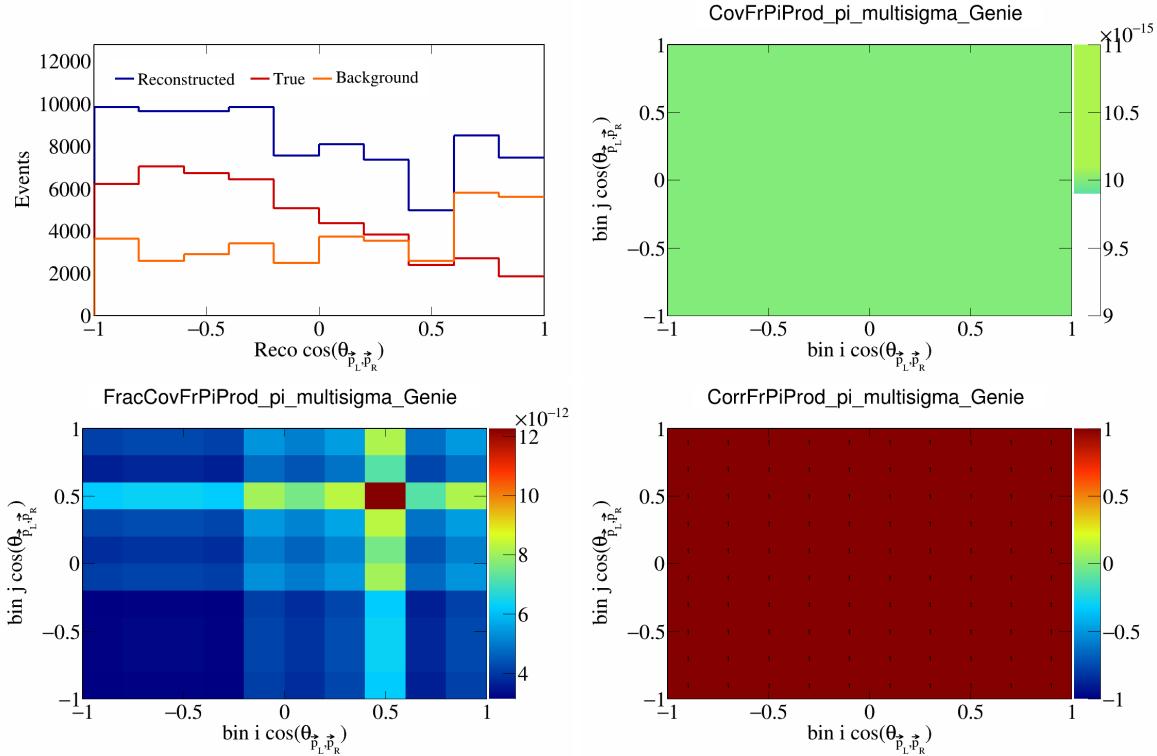


Figure 269: FrPiProdpi variations for $\cos(\theta_{\vec{p}_L, \vec{p}_R})$.

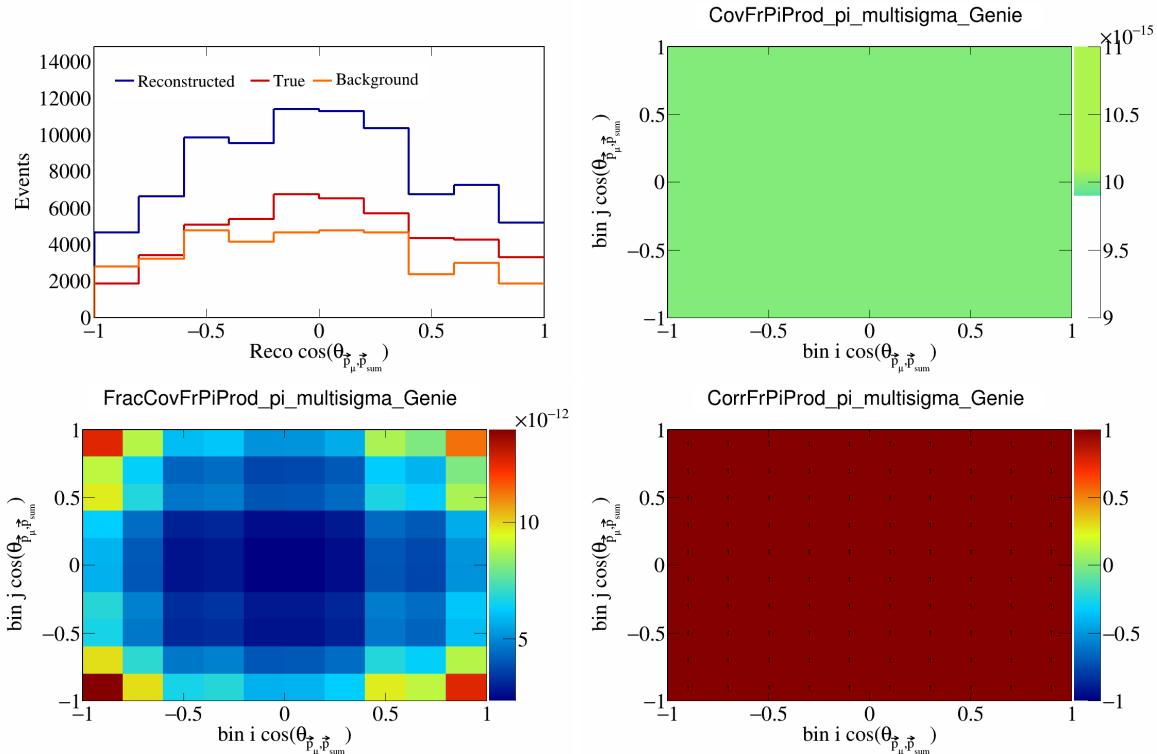


Figure 270: FrPiProdpi variations for $\cos(\theta_{\vec{p}_\mu, \vec{p}_{\text{sum}}})$.

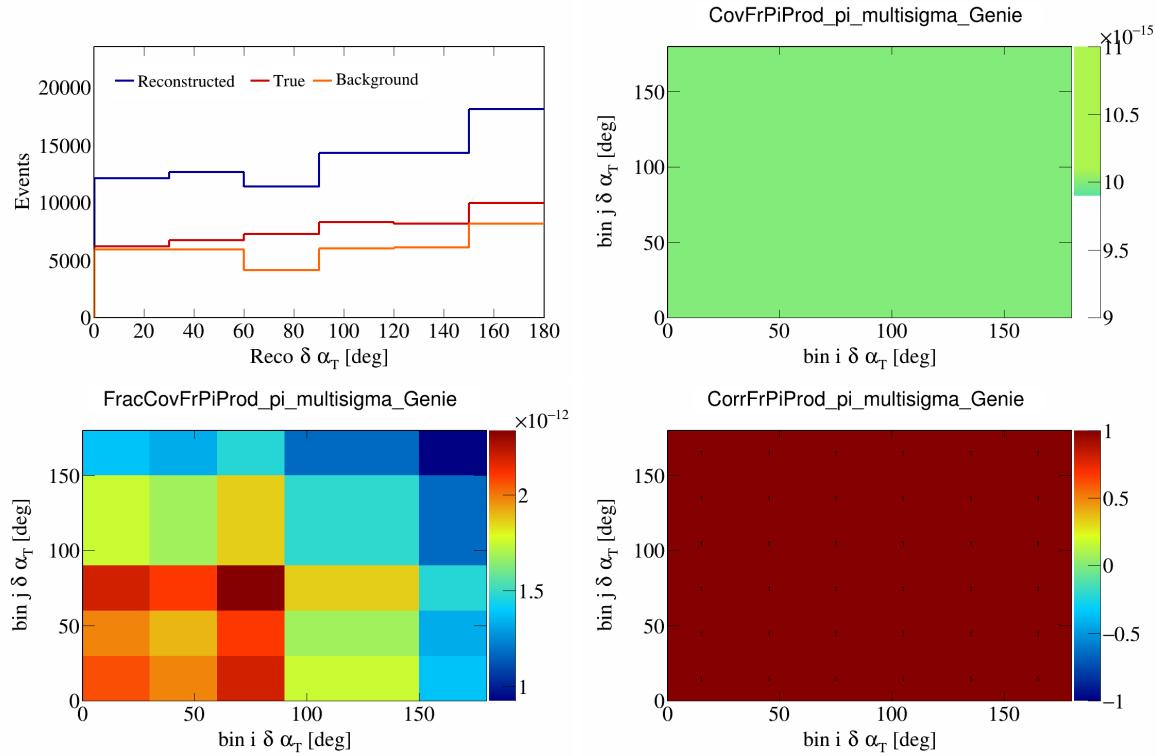


Figure 271: FrPiProdpi variations for $\delta\alpha_T$.

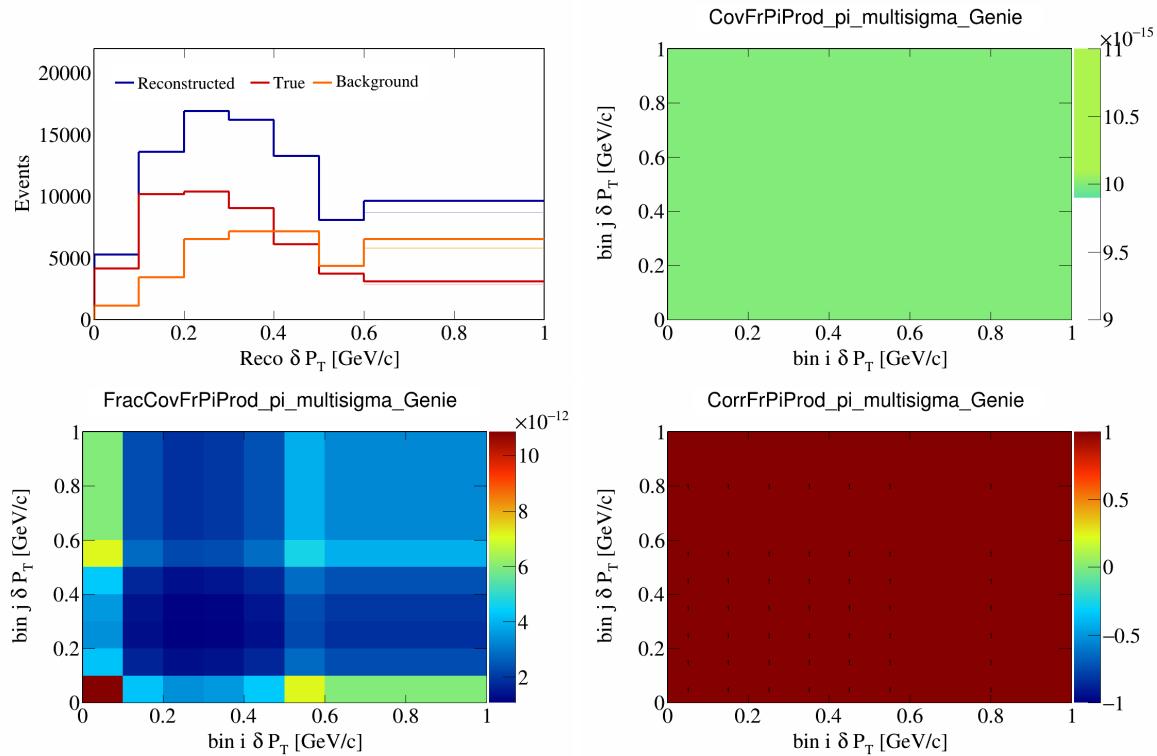


Figure 272: FrPiProdpi variations for δP_T .

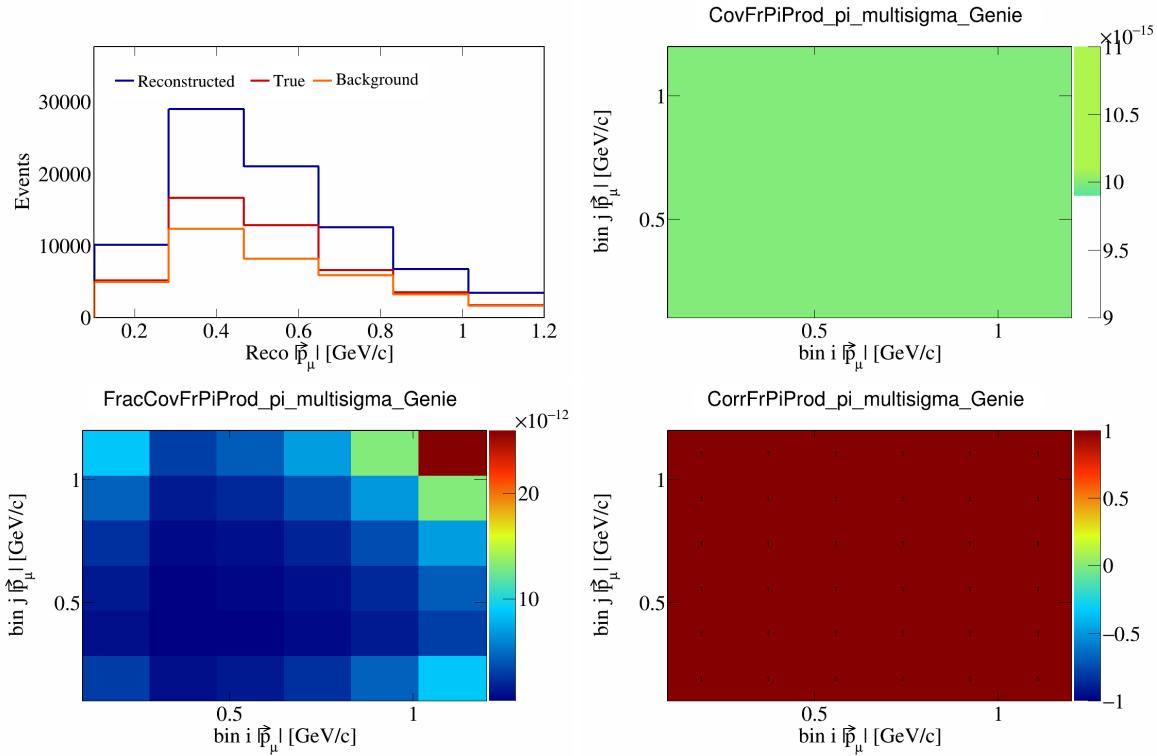


Figure 273: FrPiProdpi variations for $|{\vec p}_\mu|$.

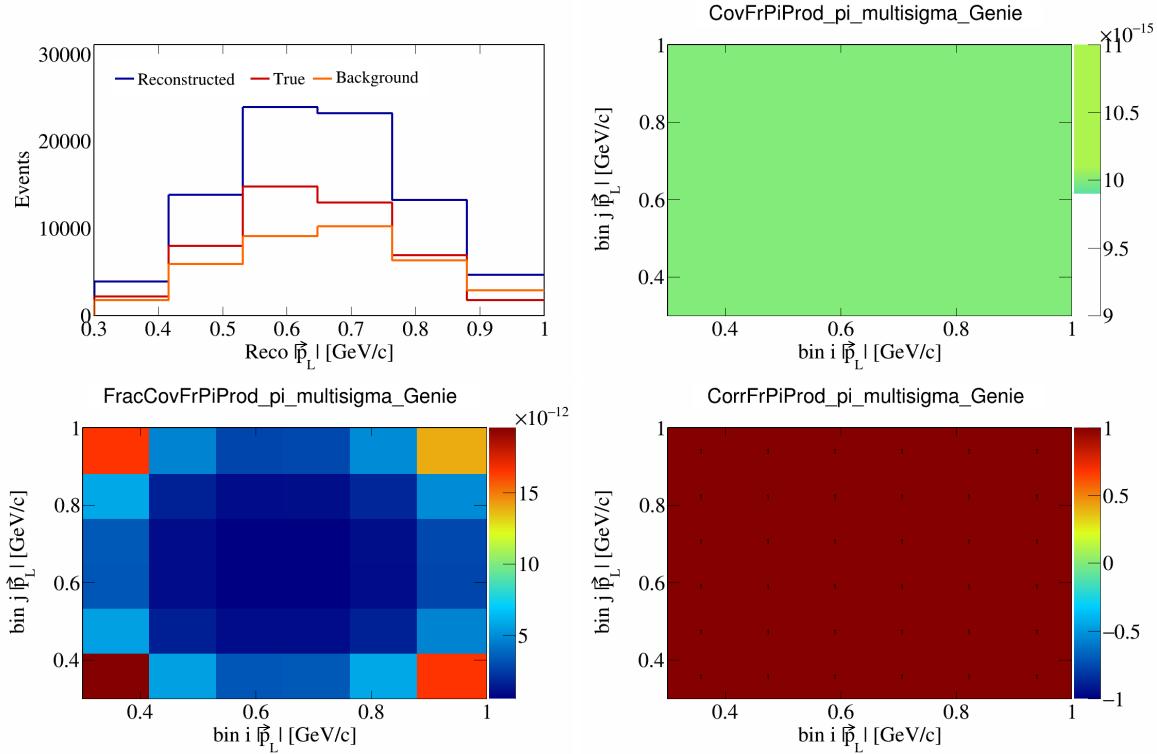


Figure 274: FrPiProdpi variations for $|{\vec p}_L|$.

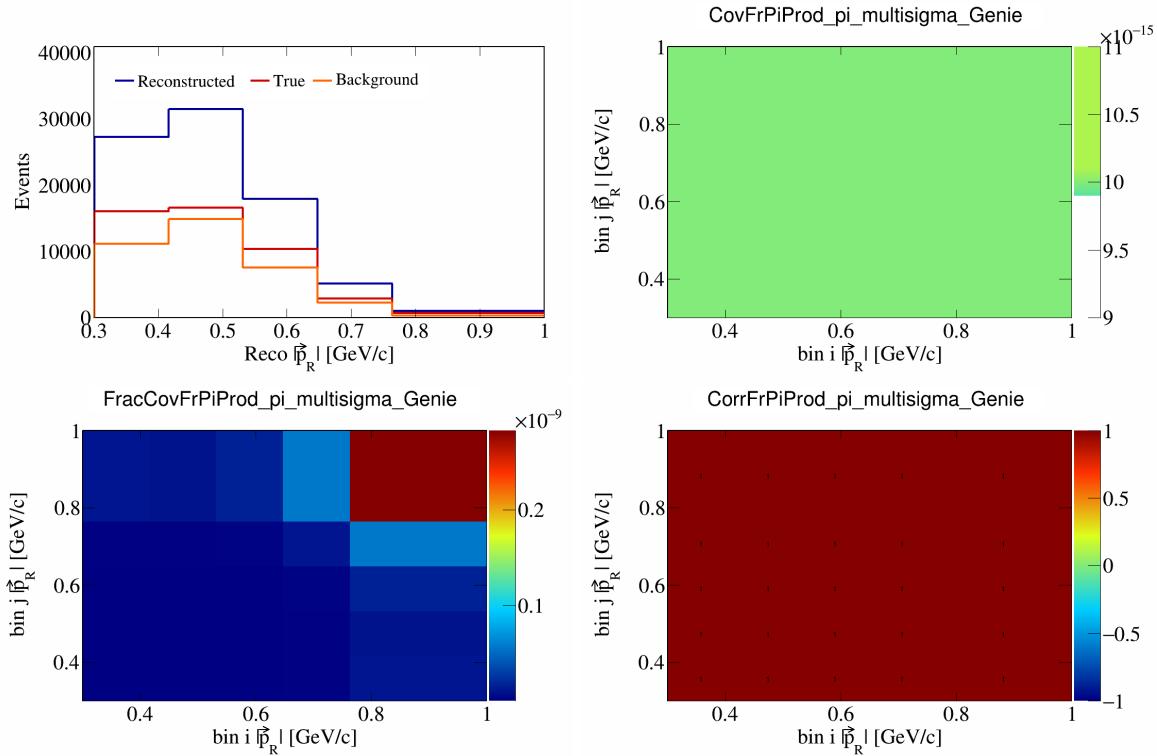


Figure 275: FrPiProdpi variations for $|\vec{p}_R|$.

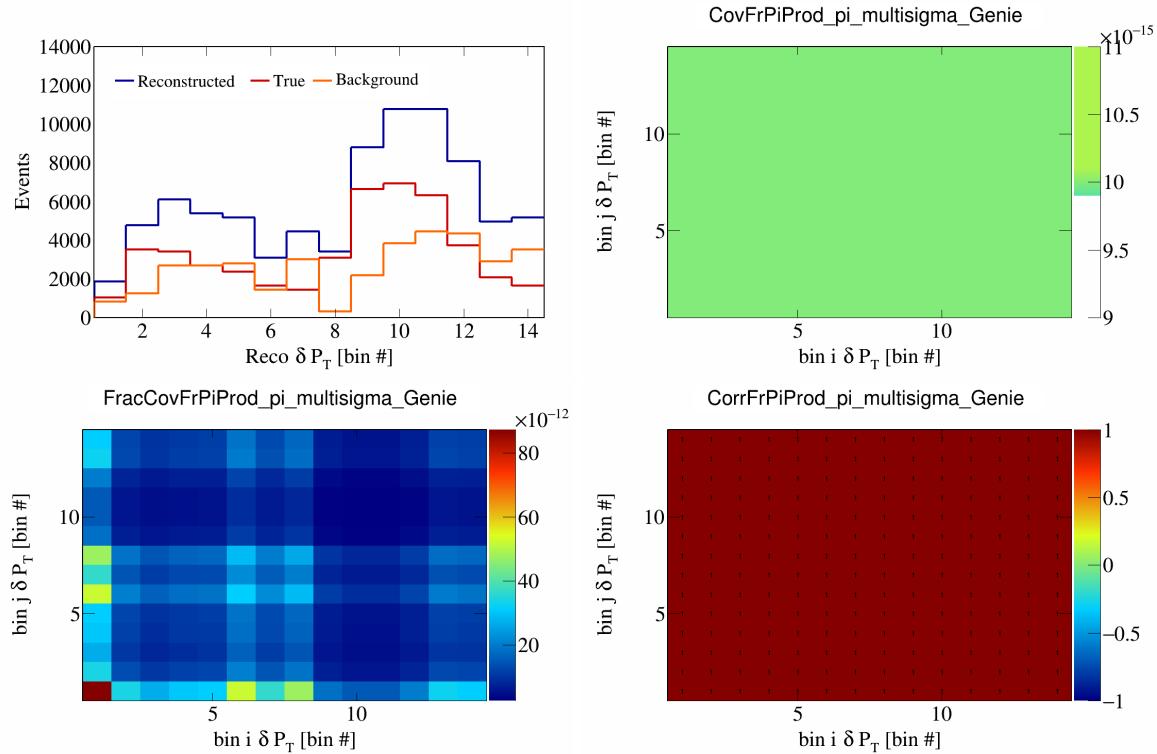


Figure 276: FrPiProdpi variations for δP_T in $\cos(\theta_{\vec{p}_\mu})$.

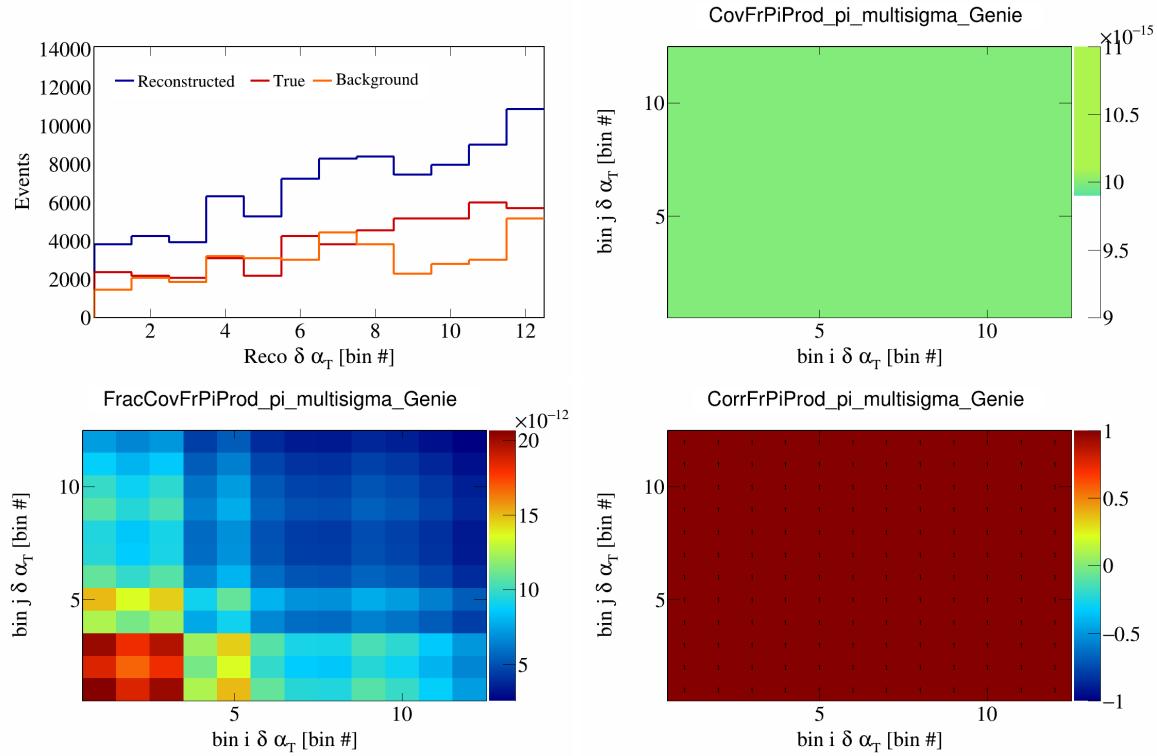


Figure 277: FrPiProdpi variations for $\delta\alpha_T$ in $\cos(\theta_{\vec{p}_\mu})$.

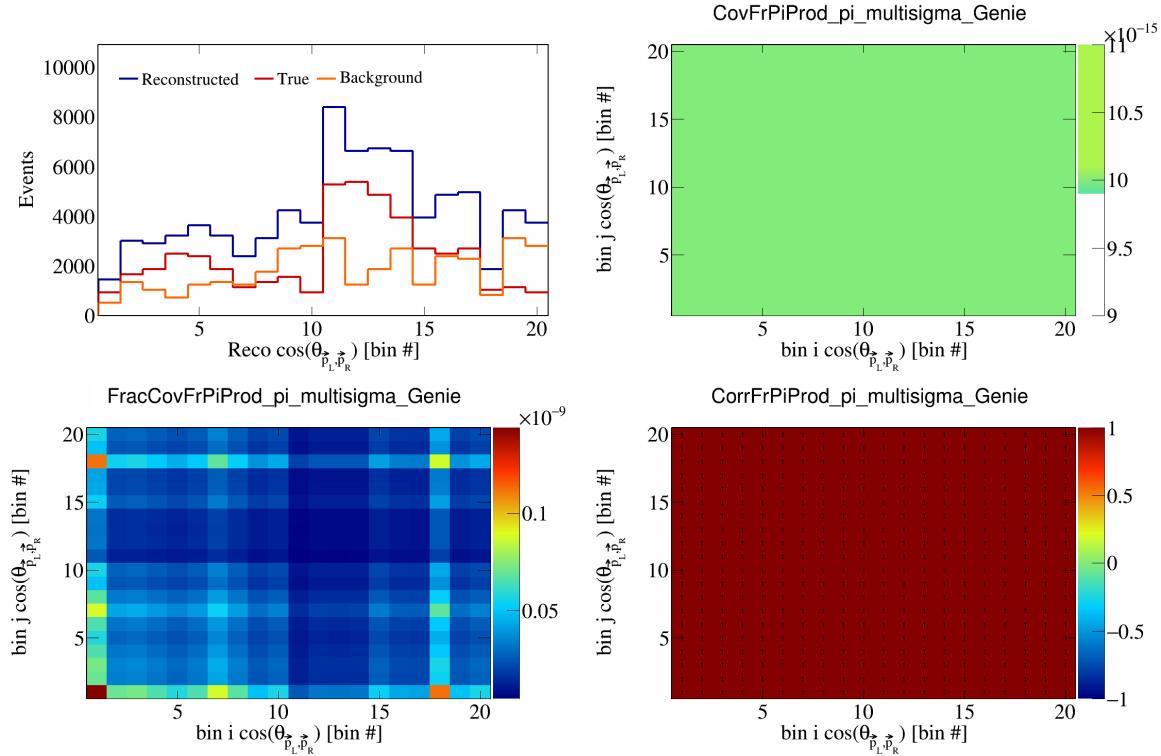


Figure 278: FrPiProdpi variations for $\cos(\theta_{\vec{p}_L, \vec{p}_R})$ in $\cos(\theta_{\vec{p}_\mu})$.

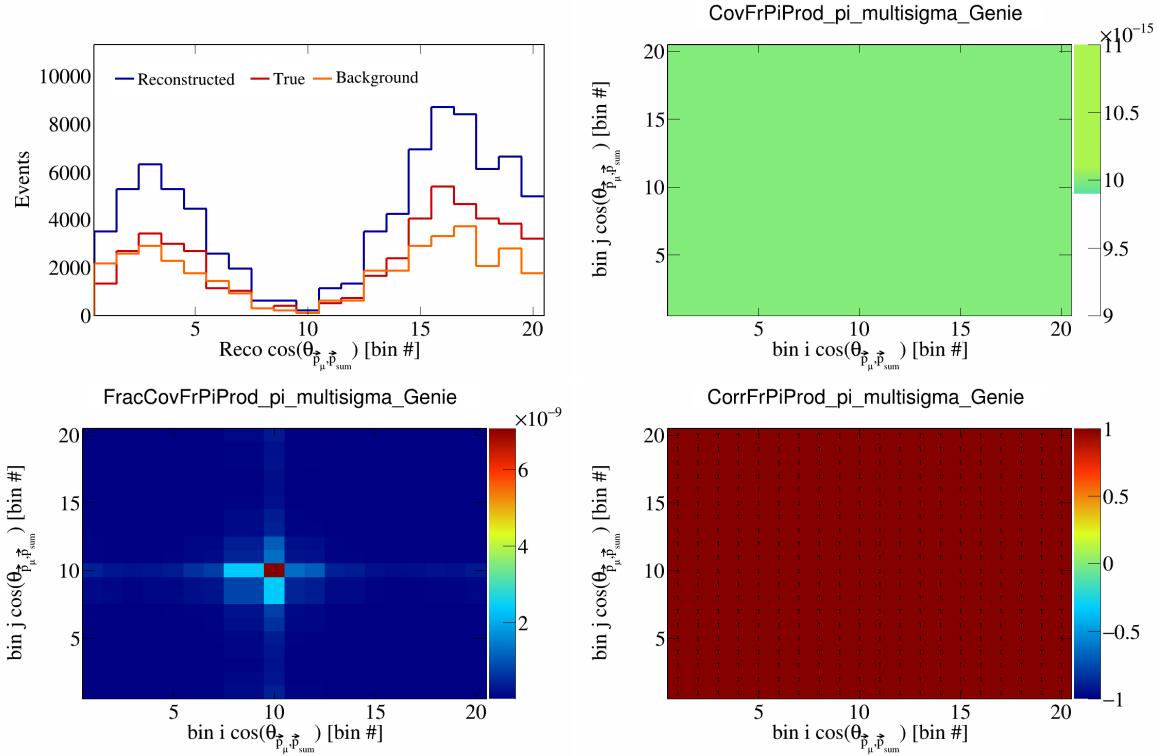


Figure 279: FrPiProdpi variations for $\cos(\theta_{\vec{p}_\mu})$ in $\cos(\theta_{\vec{p}_\mu})$.

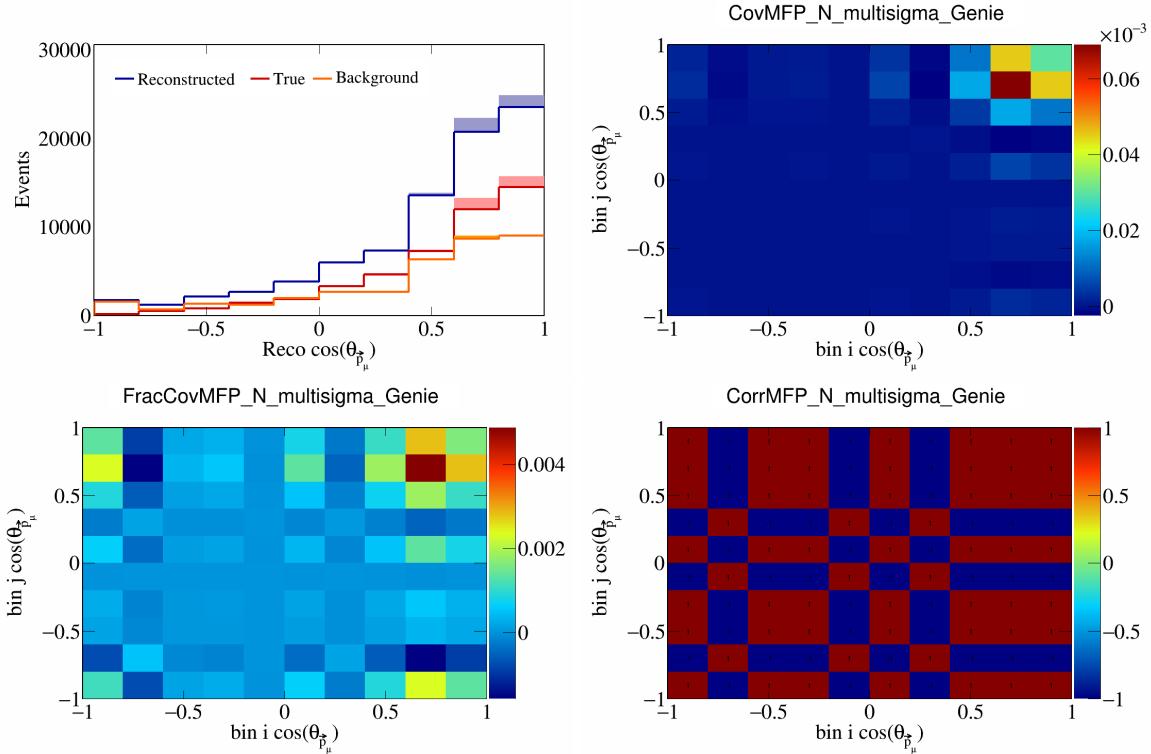


Figure 280: MFPN variations for $\cos(\theta_{\vec{p}_\mu})$.

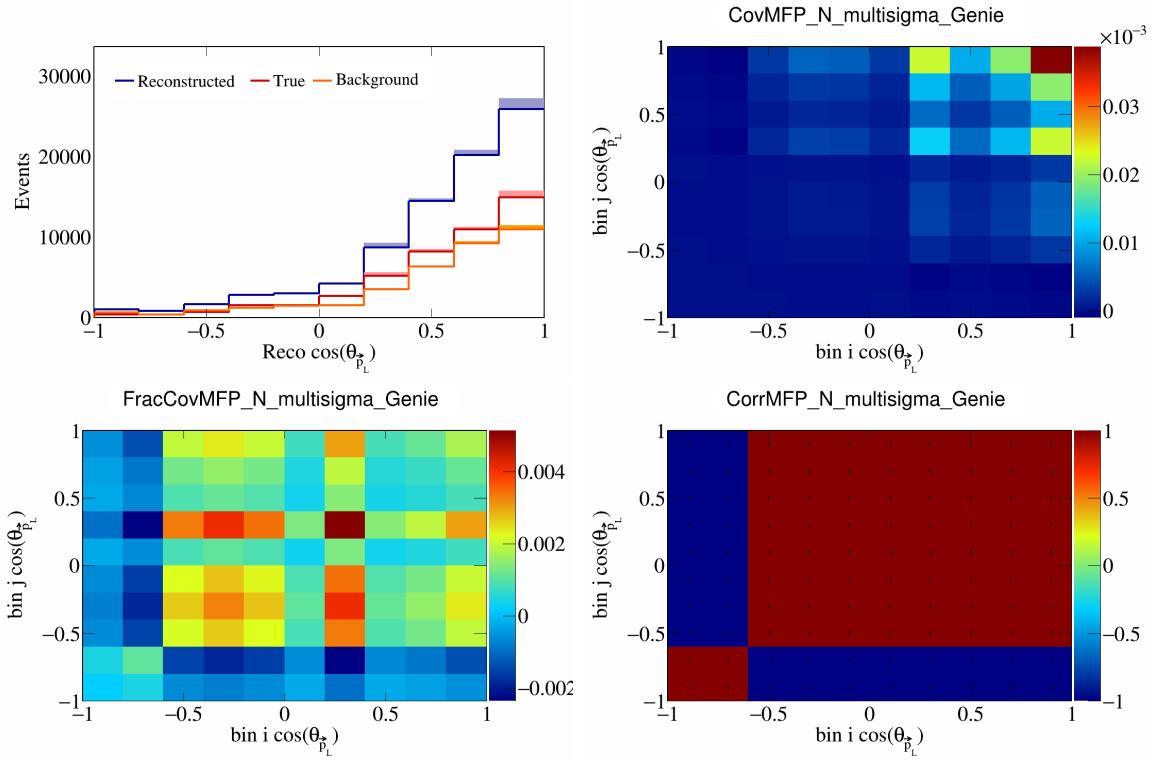


Figure 281: MFPN variations for $\cos(\theta_{\vec{p}_L})$.

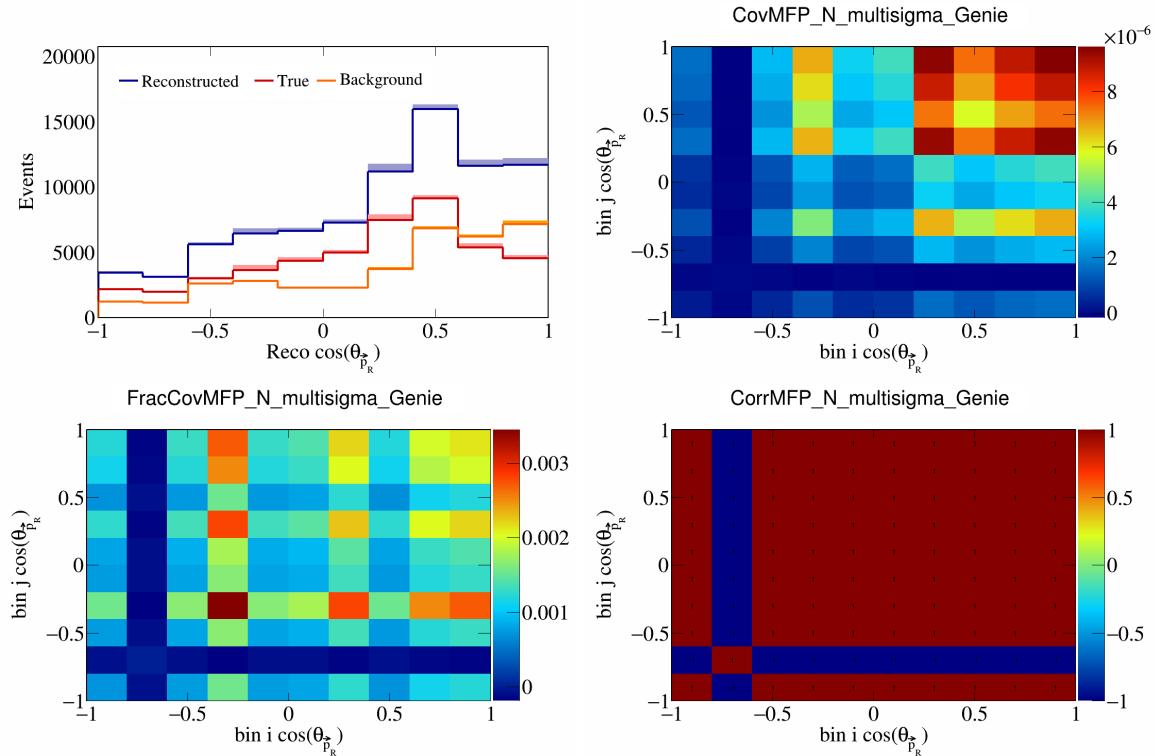


Figure 282: MFPN variations for $\cos(\theta_{\vec{p}_R})$.

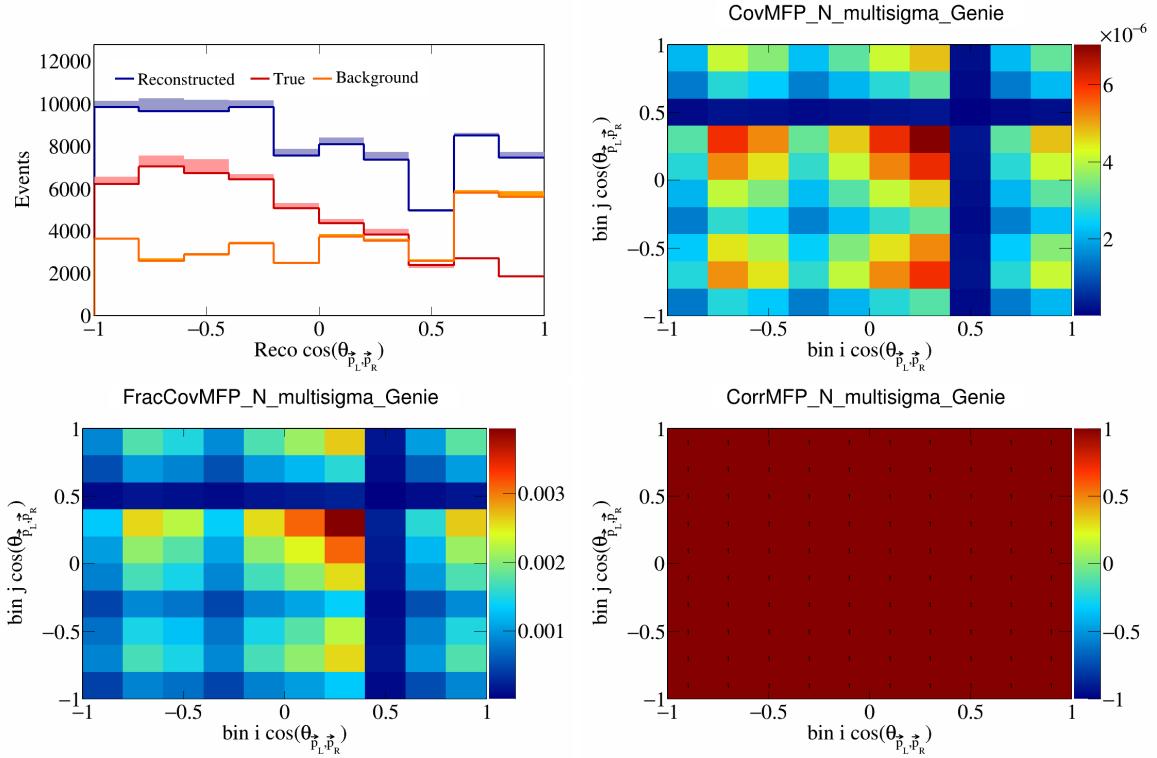


Figure 283: MFPN variations for $\cos(\theta_{\vec{p}_L, \vec{p}_R})$.

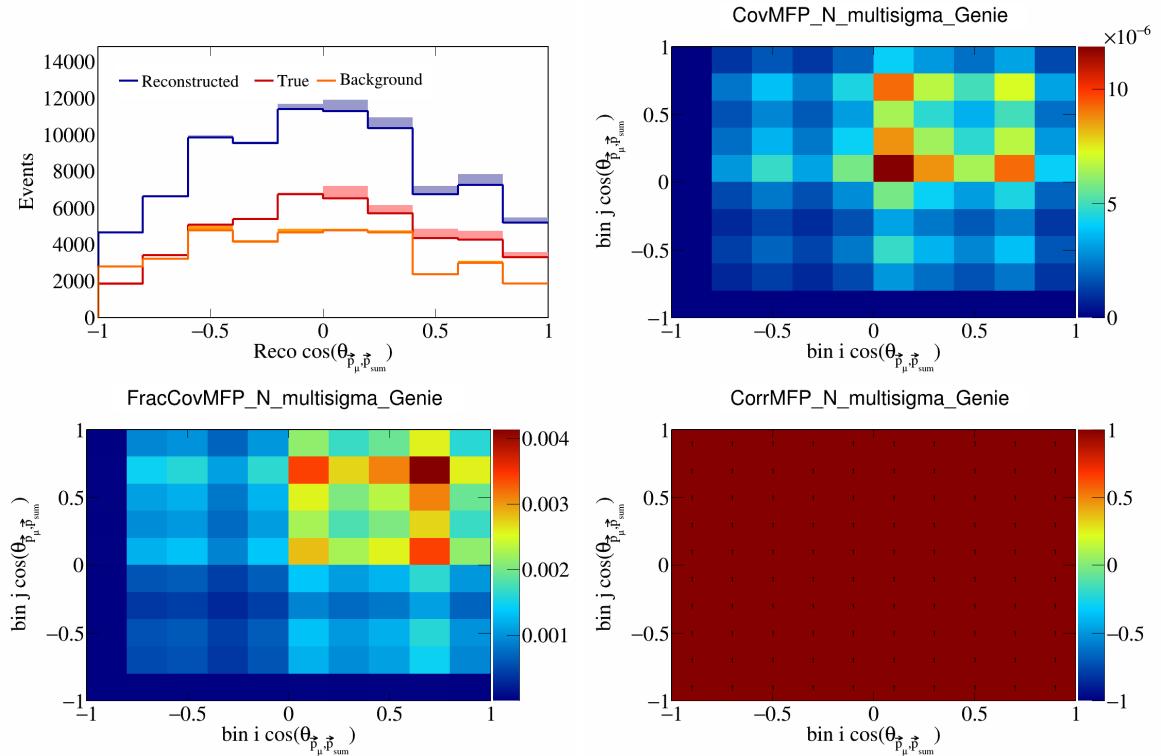


Figure 284: MFPN variations for $\cos(\theta_{\vec{p}_\mu, \vec{p}_{\text{sum}}})$.

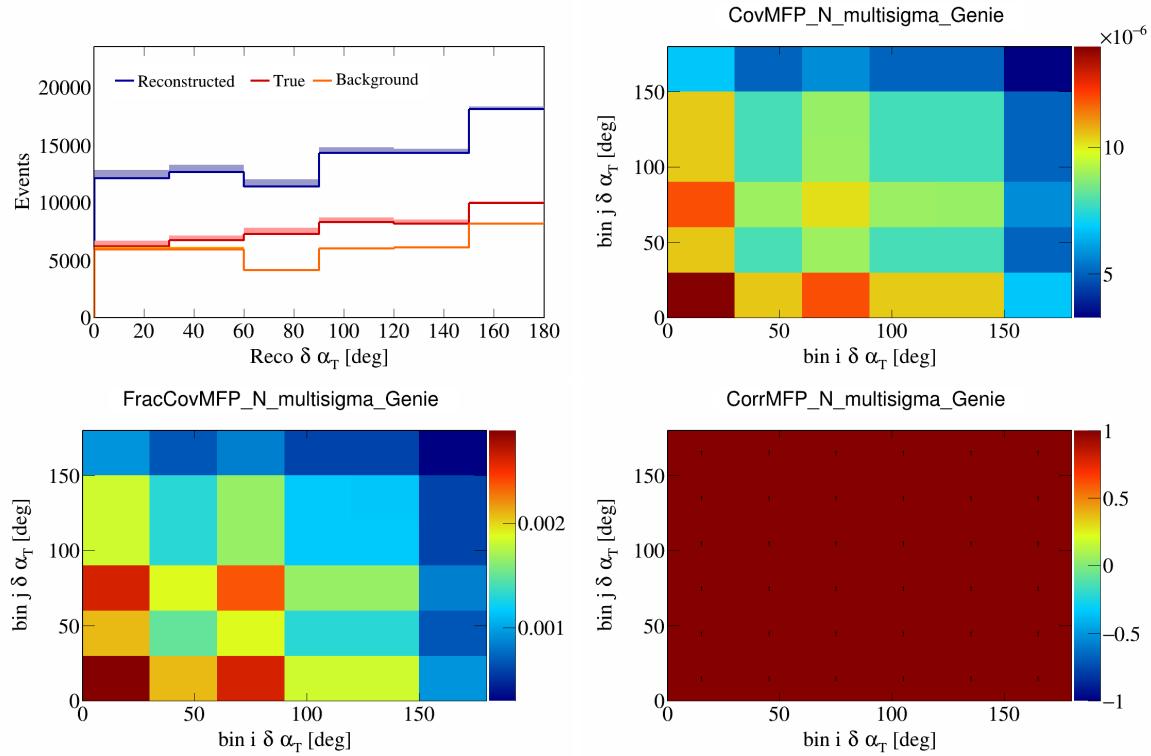


Figure 285: MFPN variations for $\delta\alpha_T$.

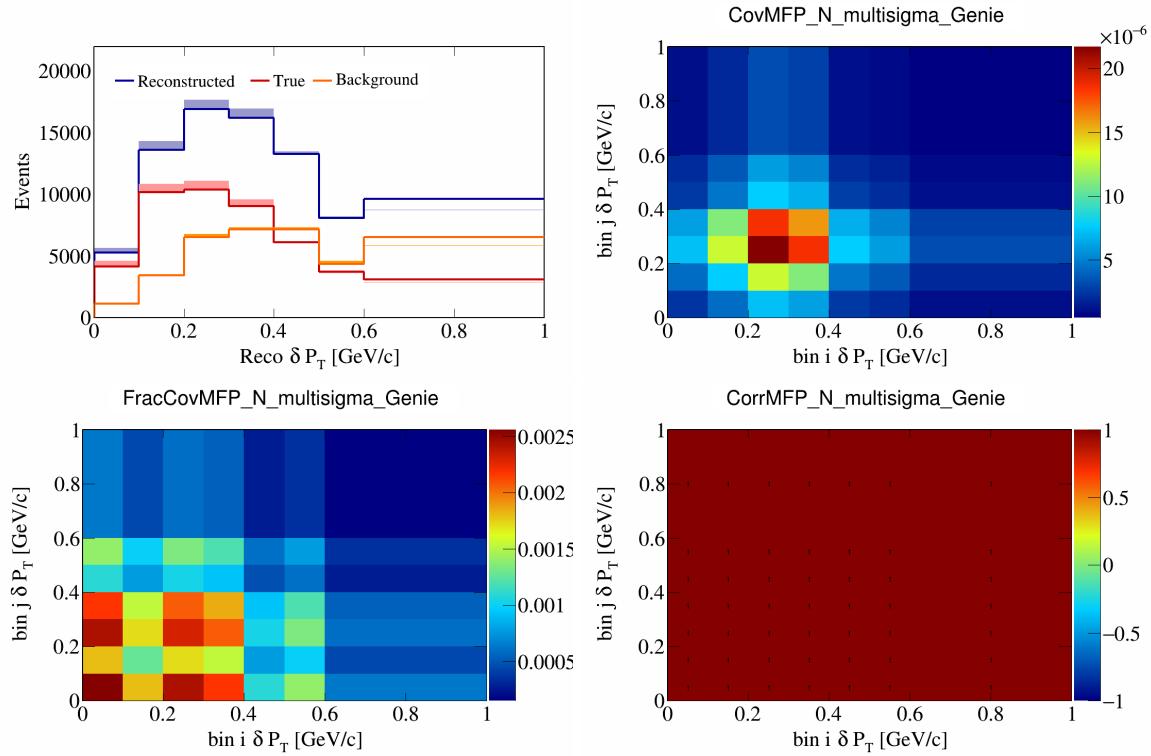


Figure 286: MFPN variations for δP_T .

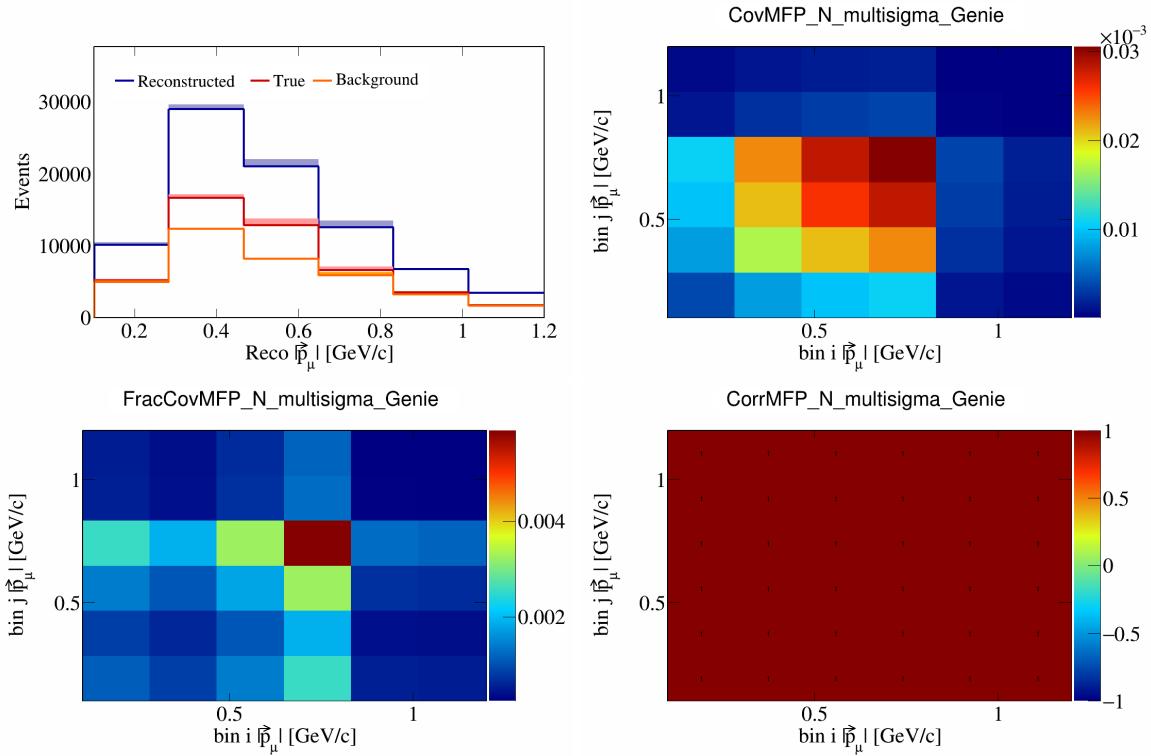


Figure 287: MFPN variations for $|\vec{p}_\mu|$.

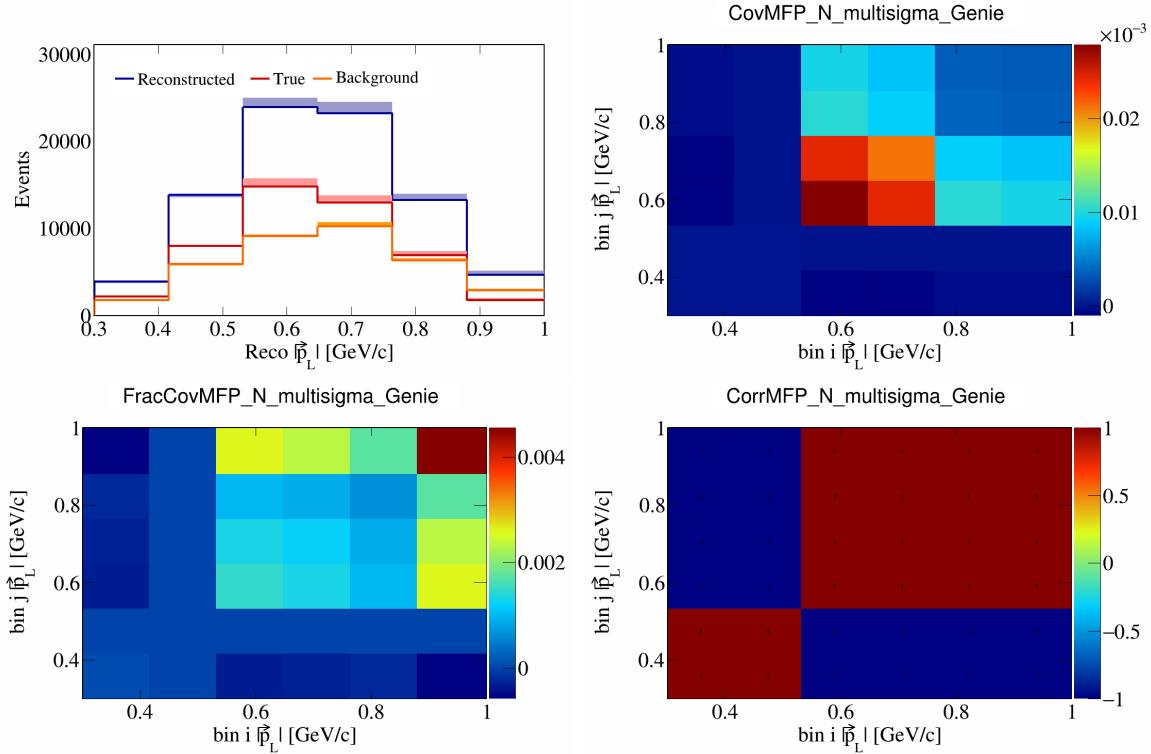


Figure 288: MFPN variations for $|\vec{p}_L|$.

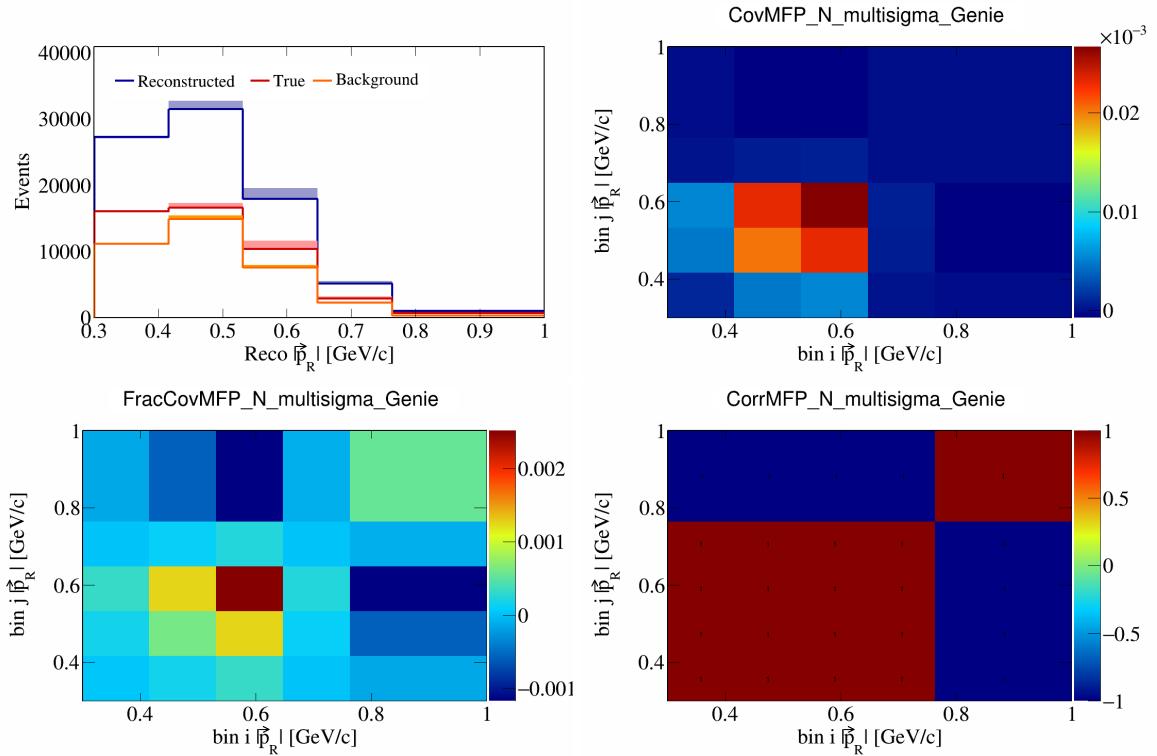


Figure 289: MFPN variations for $|\vec{p}_R|$.

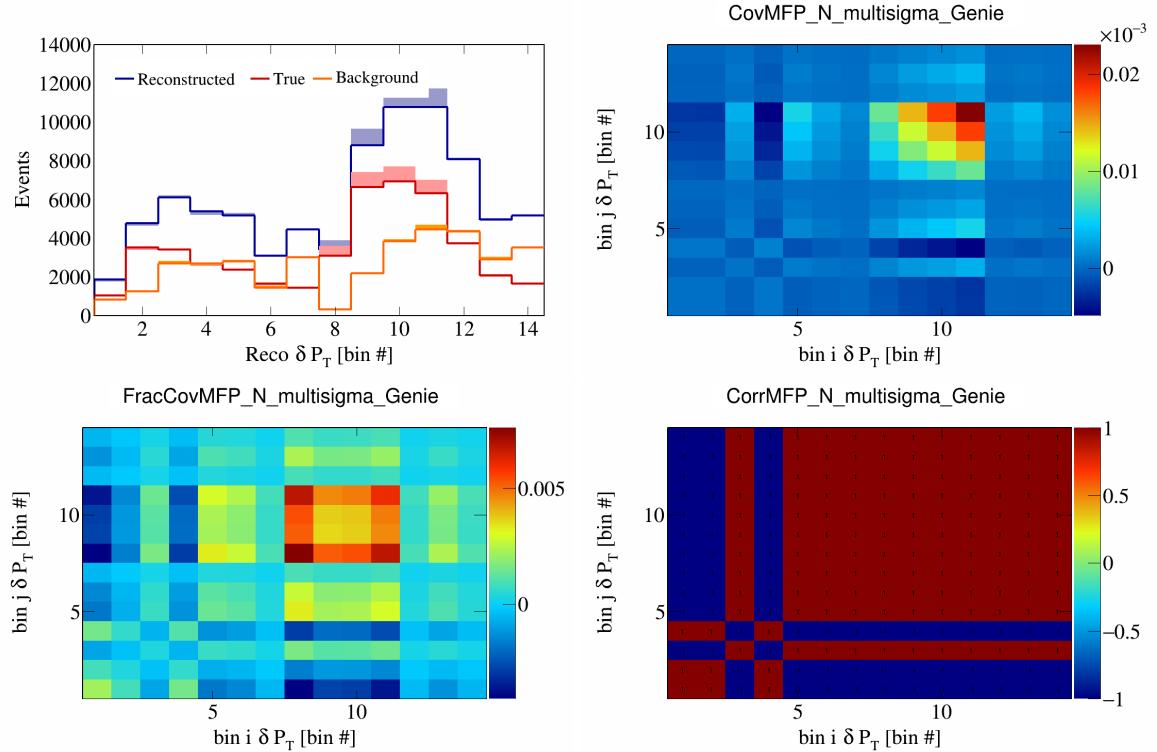


Figure 290: MFPN variations for δP_T in $\cos(\theta_{\vec{p}_\mu})$.

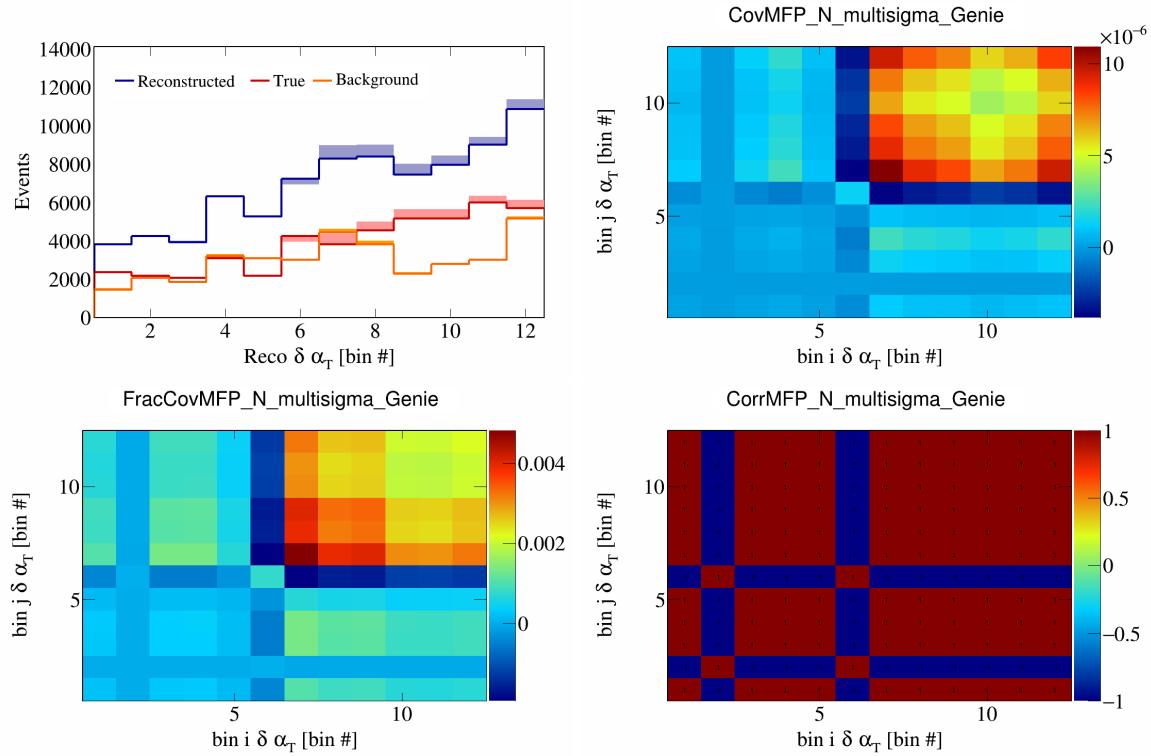


Figure 291: MFPN variations for $\delta \alpha_T$ in $\cos(\theta_{\vec{p}_\mu})$.

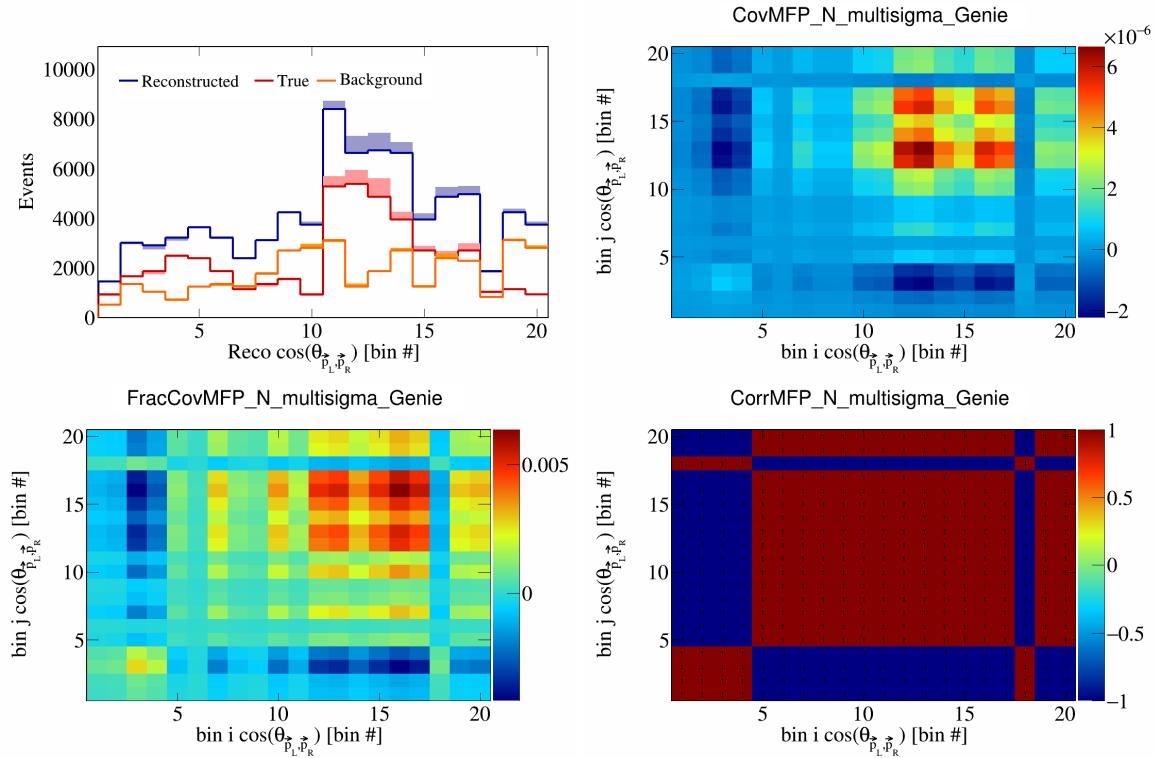


Figure 292: MFPN variations for $\cos(\theta_{\vec{p}_L, \vec{p}_R})$ in $\cos(\theta_{\vec{p}_\mu})$.

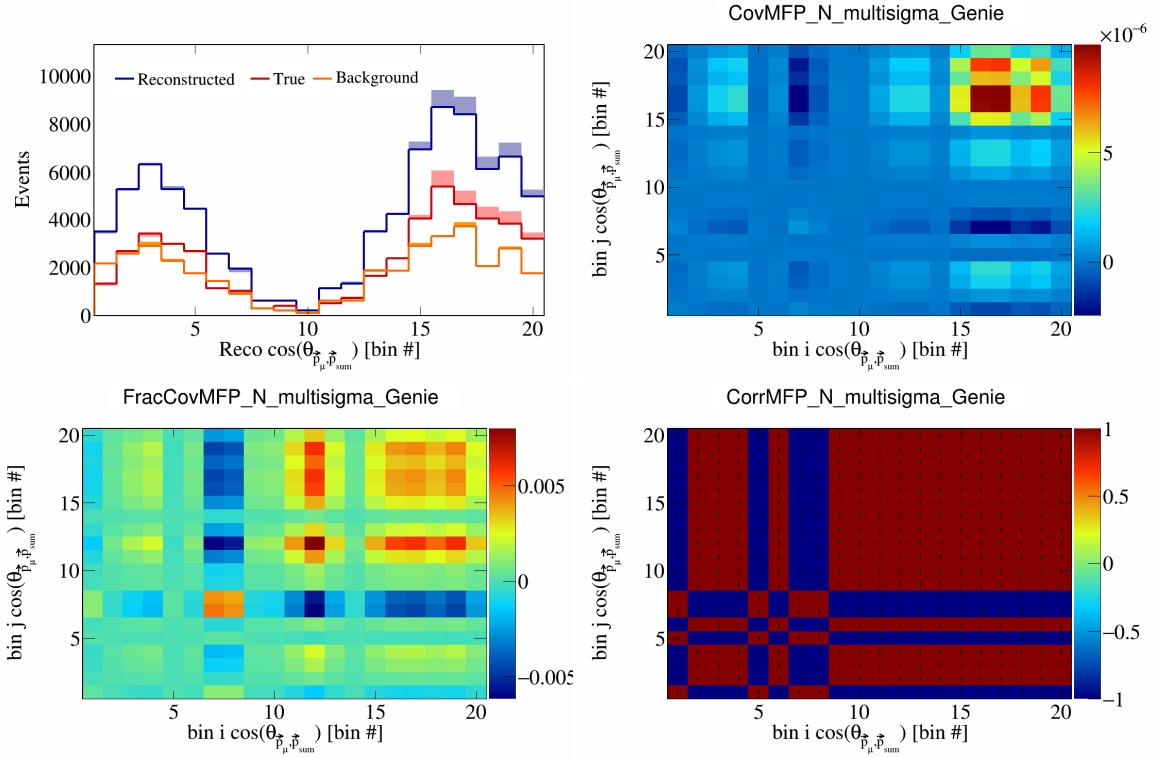


Figure 293: MFPN variations for $\cos(\theta_{\vec{p}_\mu, \vec{p}_{\text{sum}}})$ in $\cos(\theta_{\vec{p}_\mu})$.

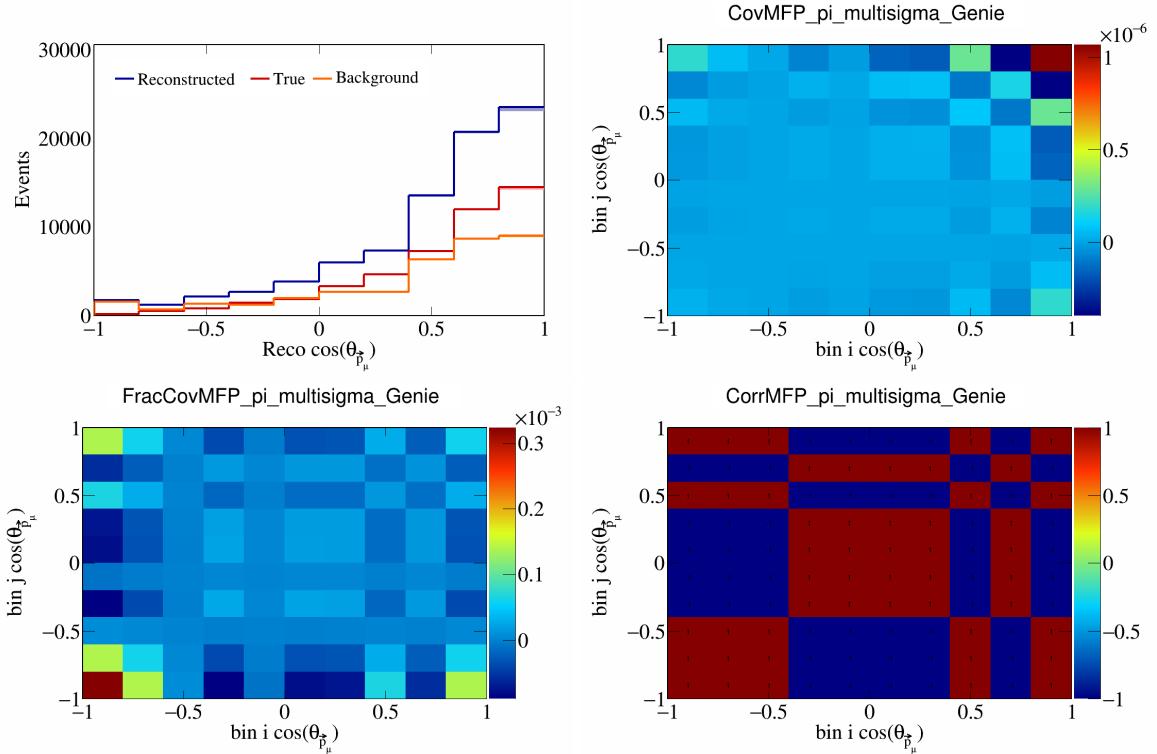


Figure 294: MFPpi variations for $\cos(\theta_{\vec{p}_\mu})$.

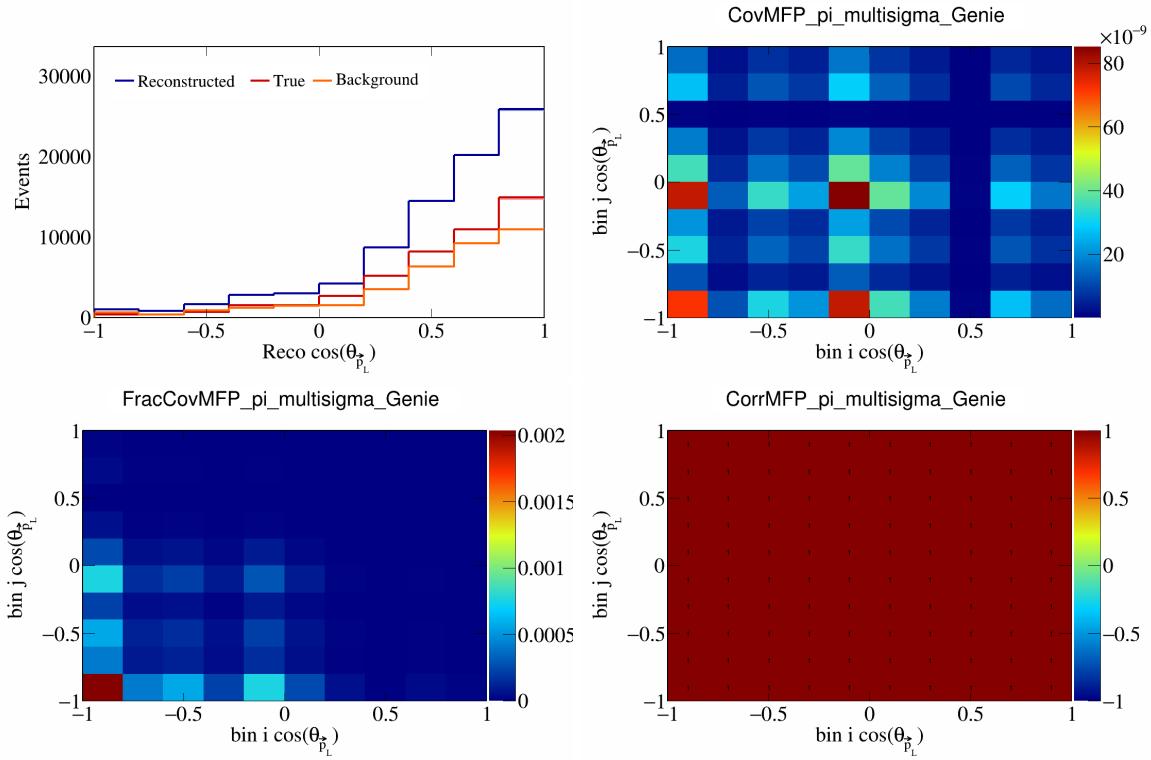


Figure 295: MFPpi variations for $\cos(\theta_{\vec{p}_L})$.

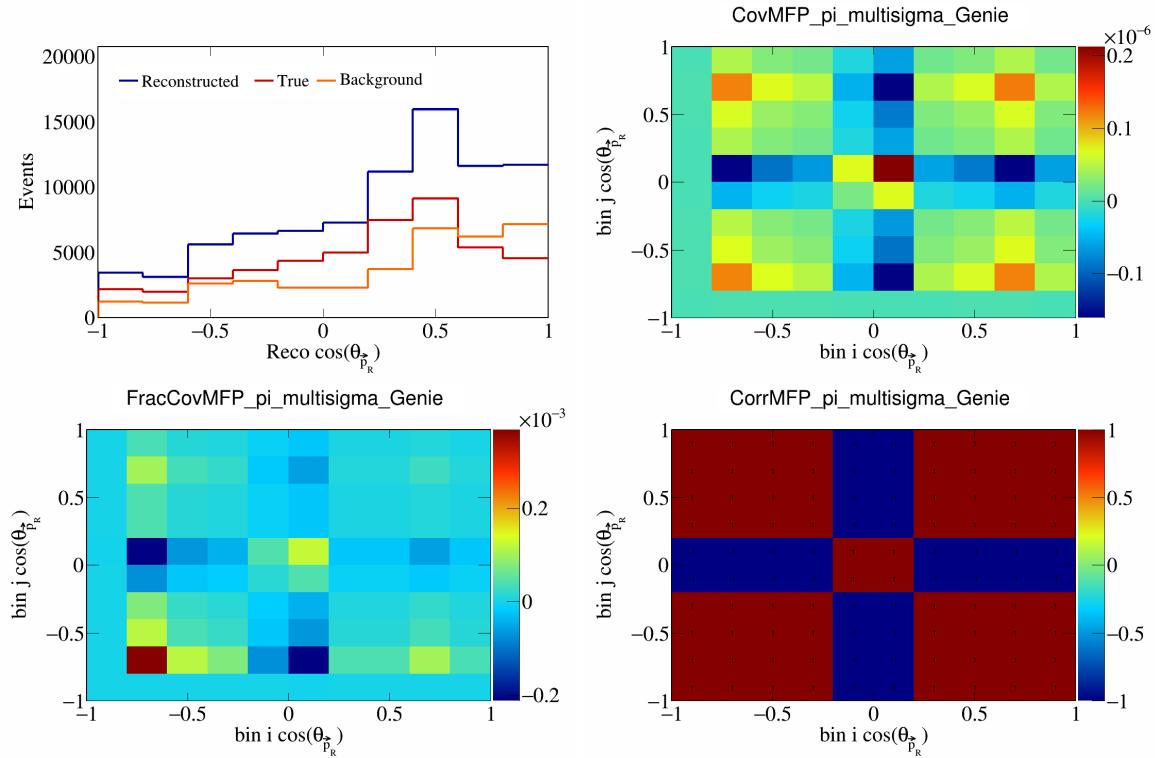


Figure 296: MFPpi variations for $\cos(\theta_{\vec{p}_R})$.

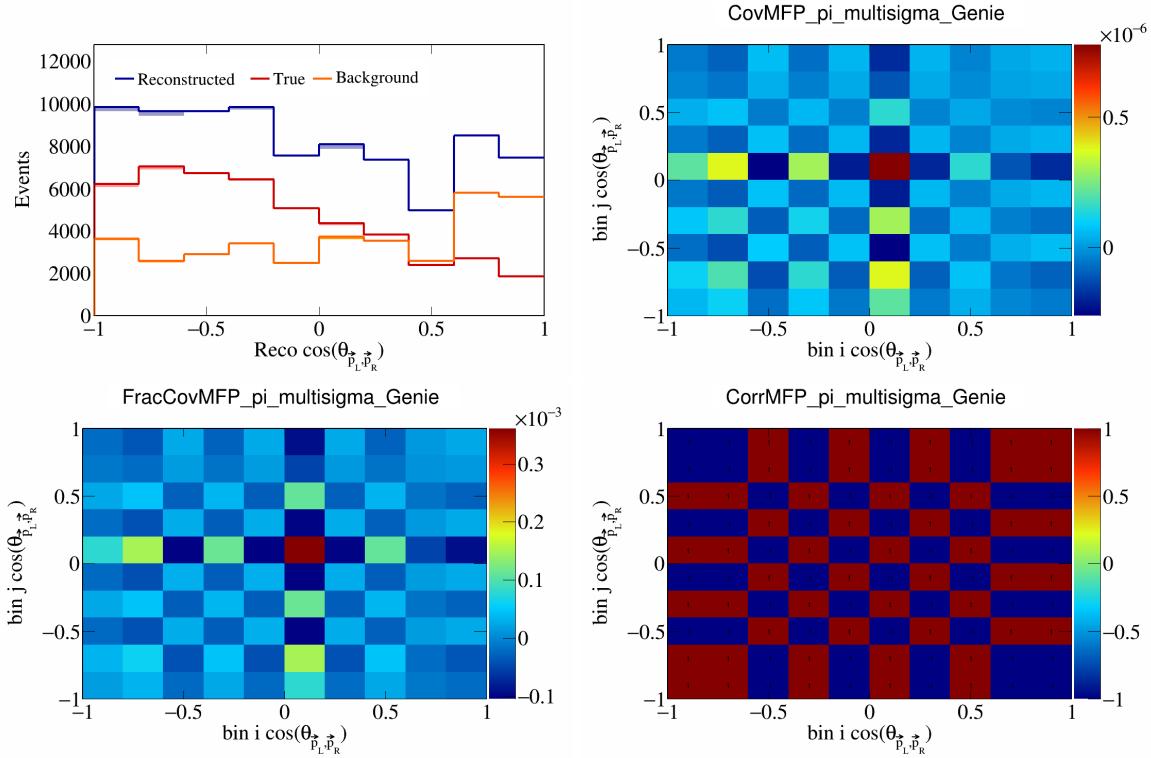


Figure 297: MFPpi variations for $\cos(\theta_{\vec{p}_L, \vec{p}_R})$.

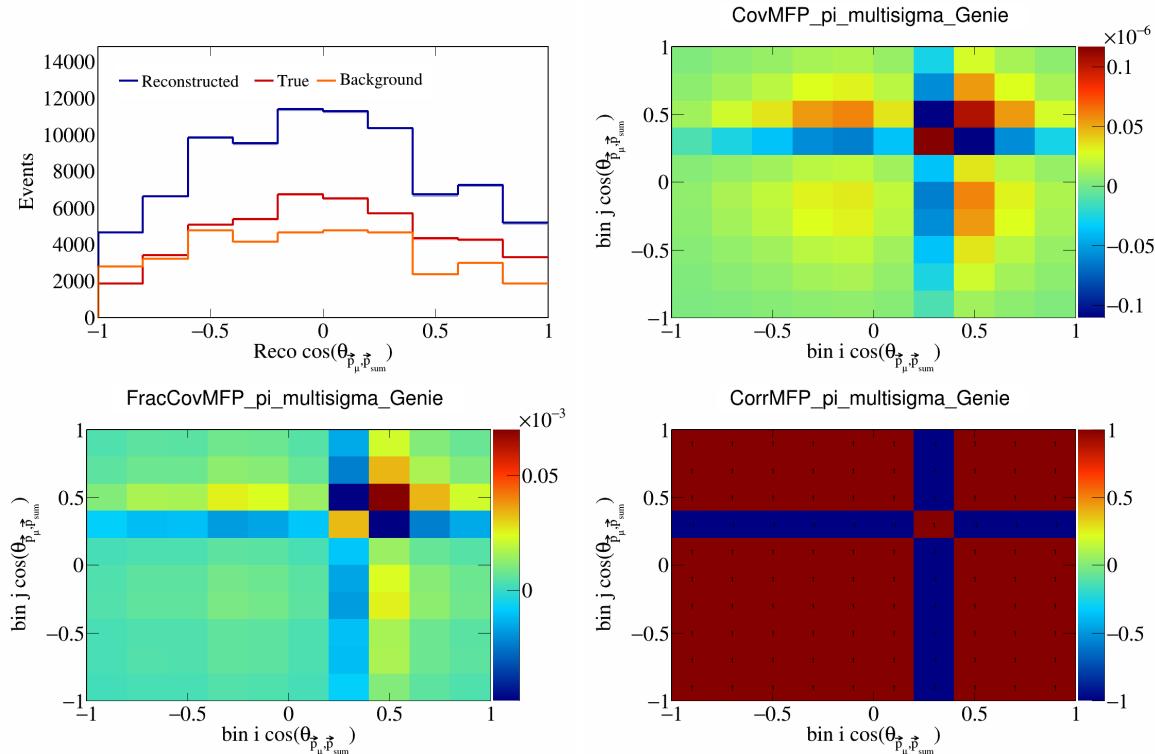


Figure 298: MFPpi variations for $\cos(\theta_{\vec{p}_\mu, \vec{p}_{\text{sum}}})$.

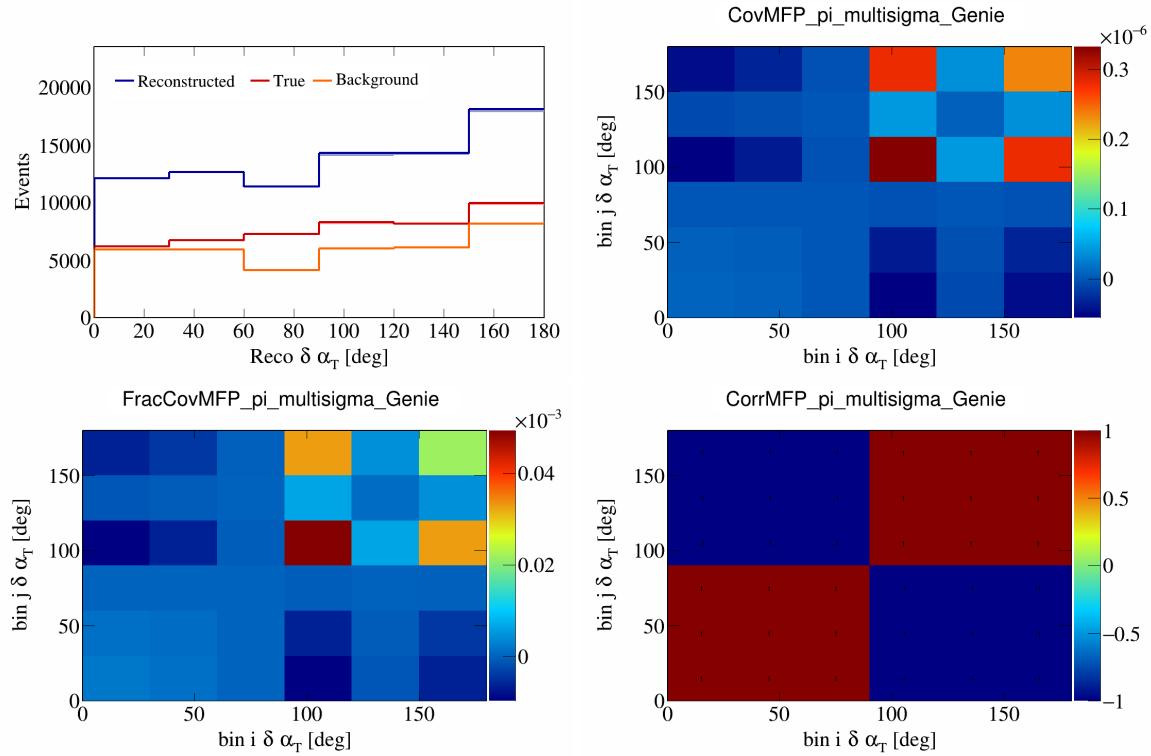


Figure 299: MFPPi variations for $\delta\alpha_T$.

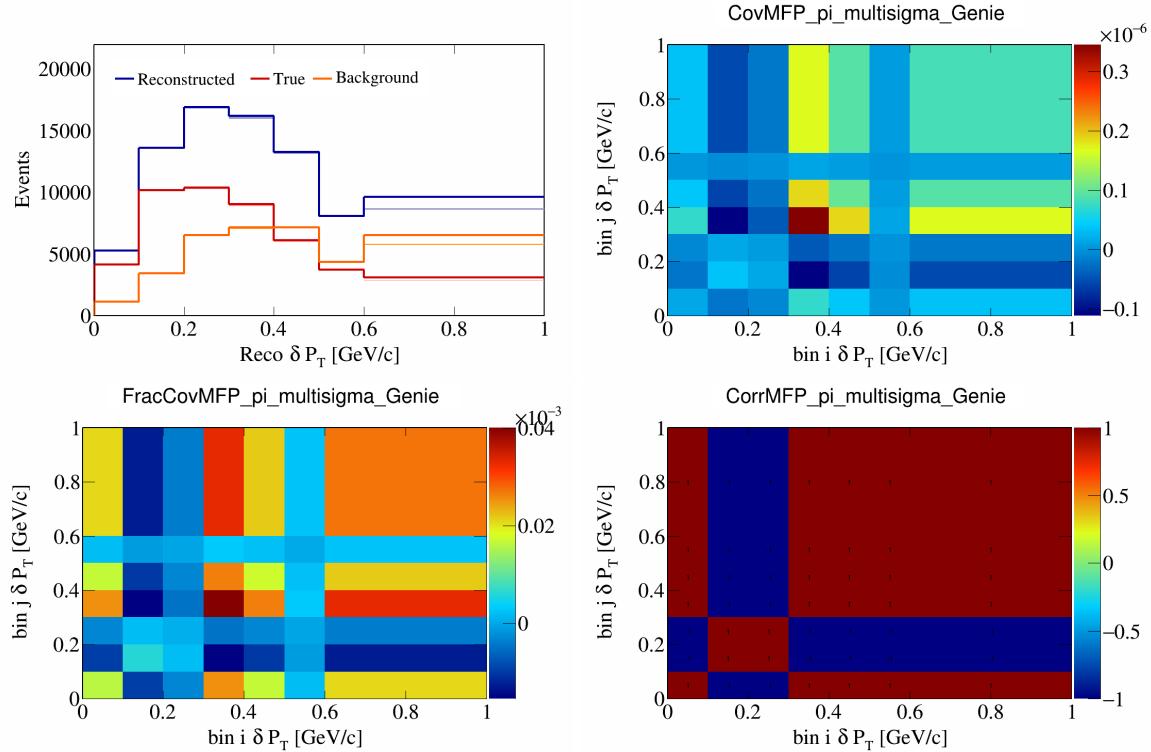


Figure 300: MFPPi variations for δP_T .

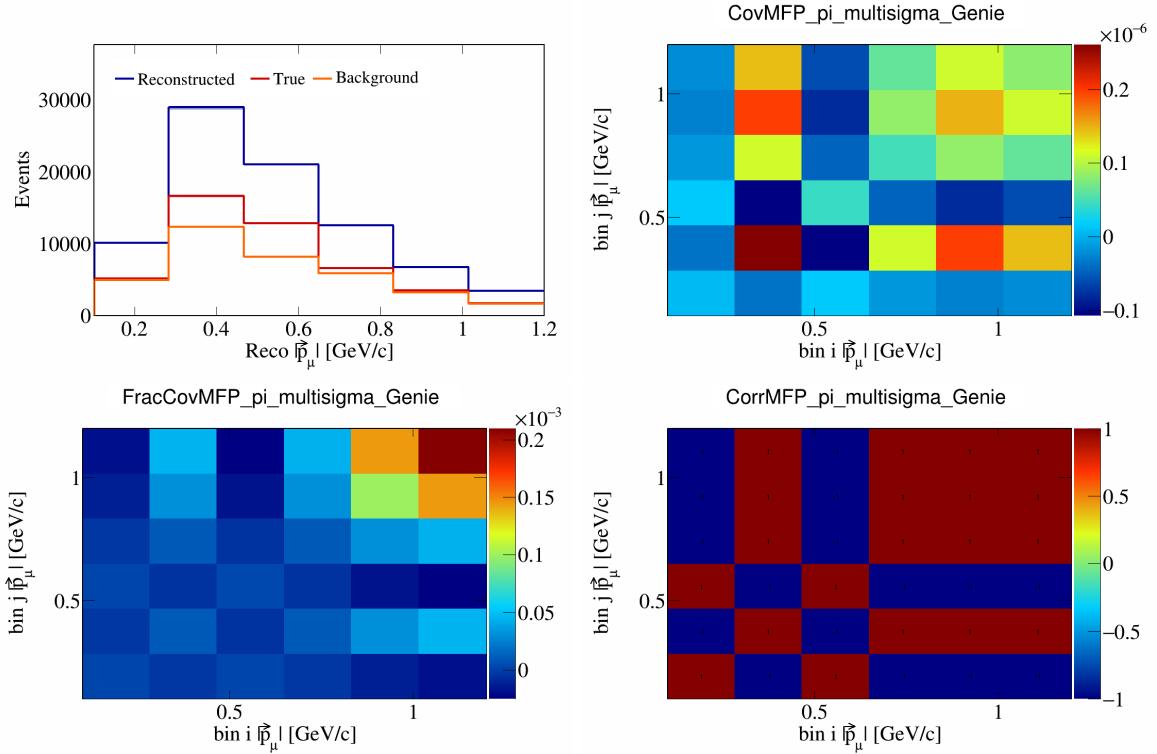


Figure 301: MFPpi variations for $|\vec{p}_\mu|$.

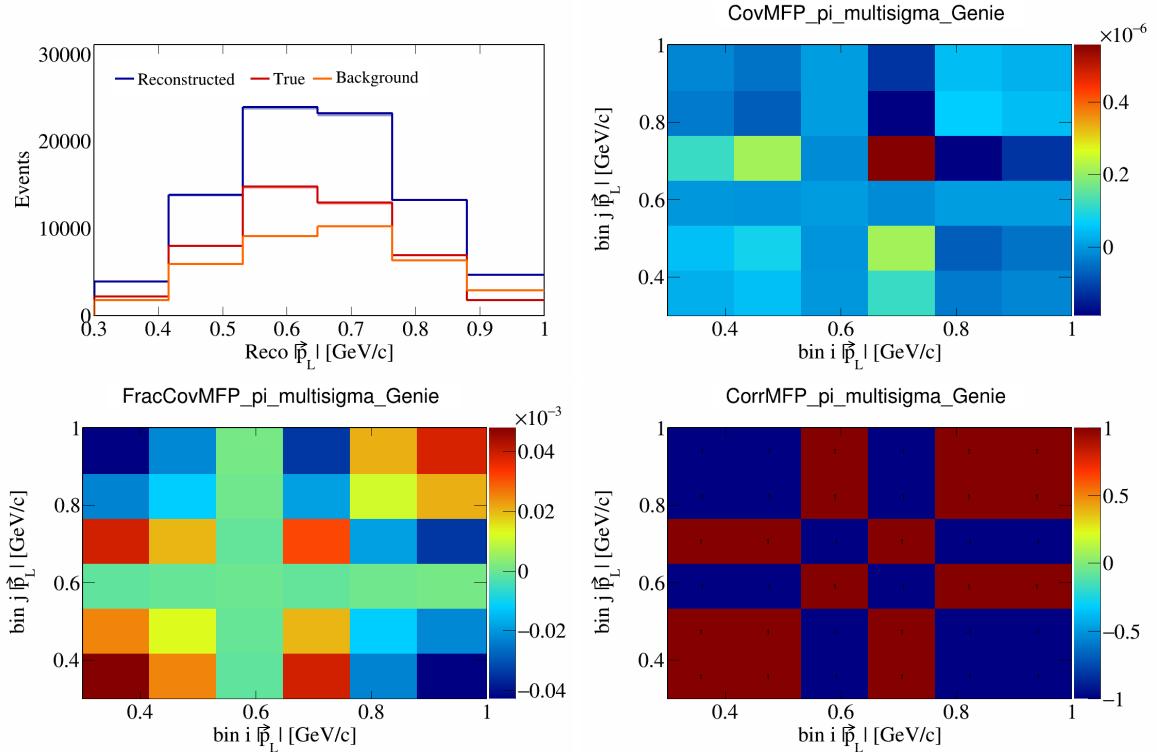


Figure 302: MFPpi variations for $|\vec{p}_L|$.

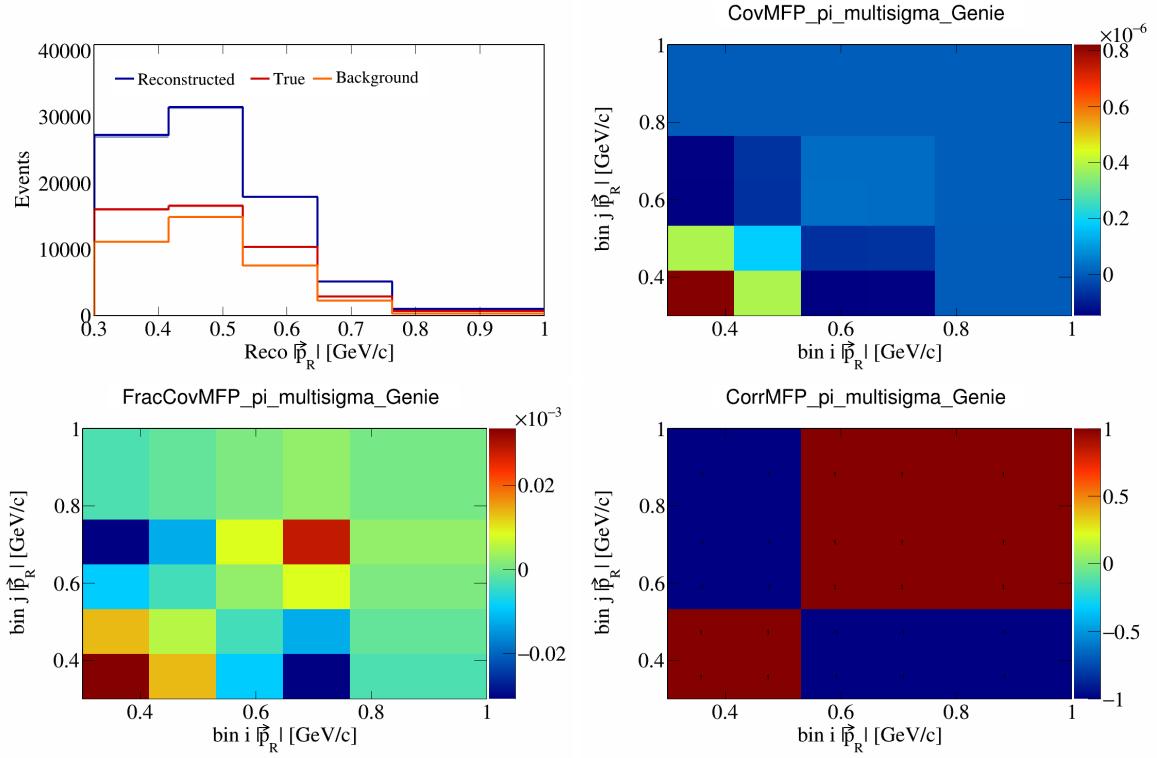


Figure 303: MFPPi variations for $|\vec{p}_R|$.

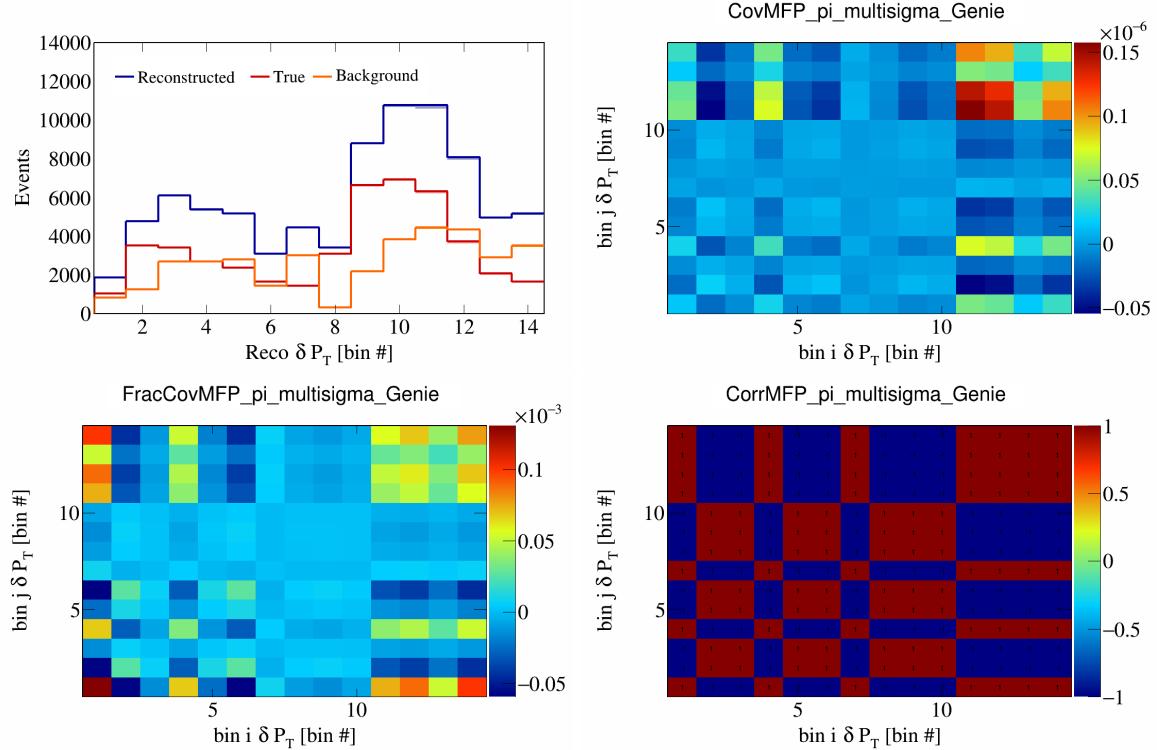


Figure 304: MFPPi variations for δP_T in $\cos(\theta_{\vec{p}_\mu})$.

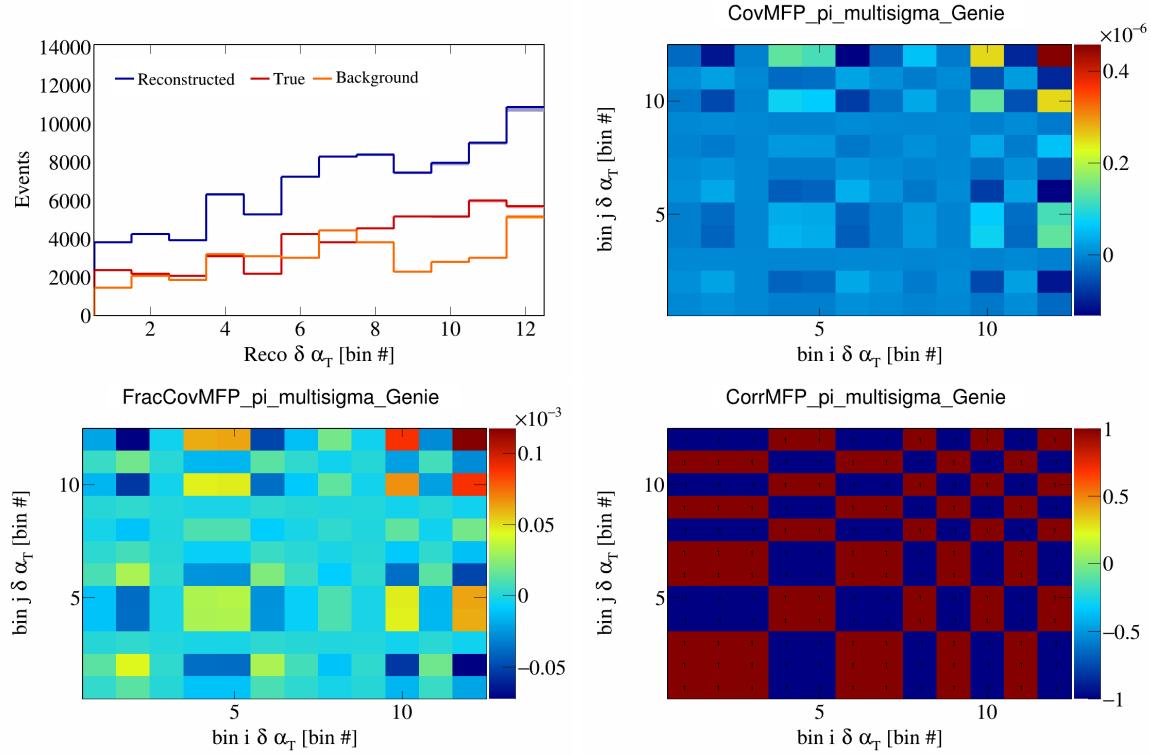


Figure 305: MFPpi variations for $\delta \alpha_T$ in $\cos(\theta_{\vec{p}_\mu})$.

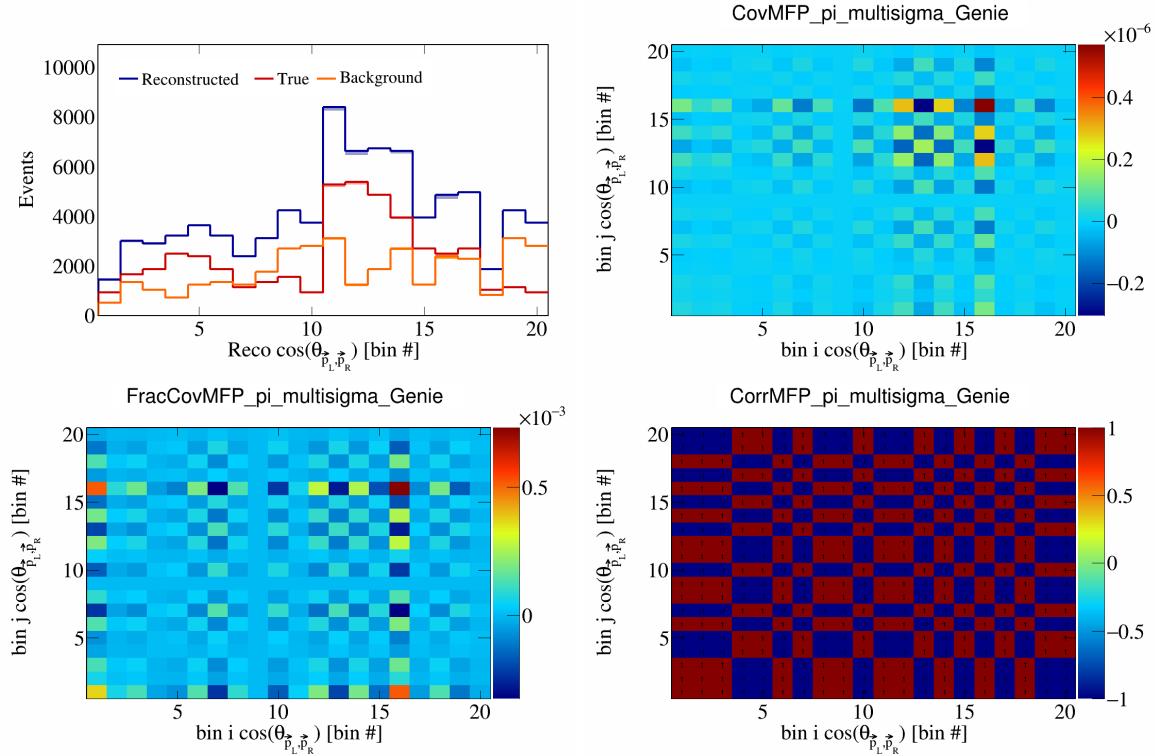


Figure 306: MFPpi variations for $\cos(\theta_{\vec{p}_L, \vec{p}_R})$ in $\cos(\theta_{\vec{p}_\mu})$.

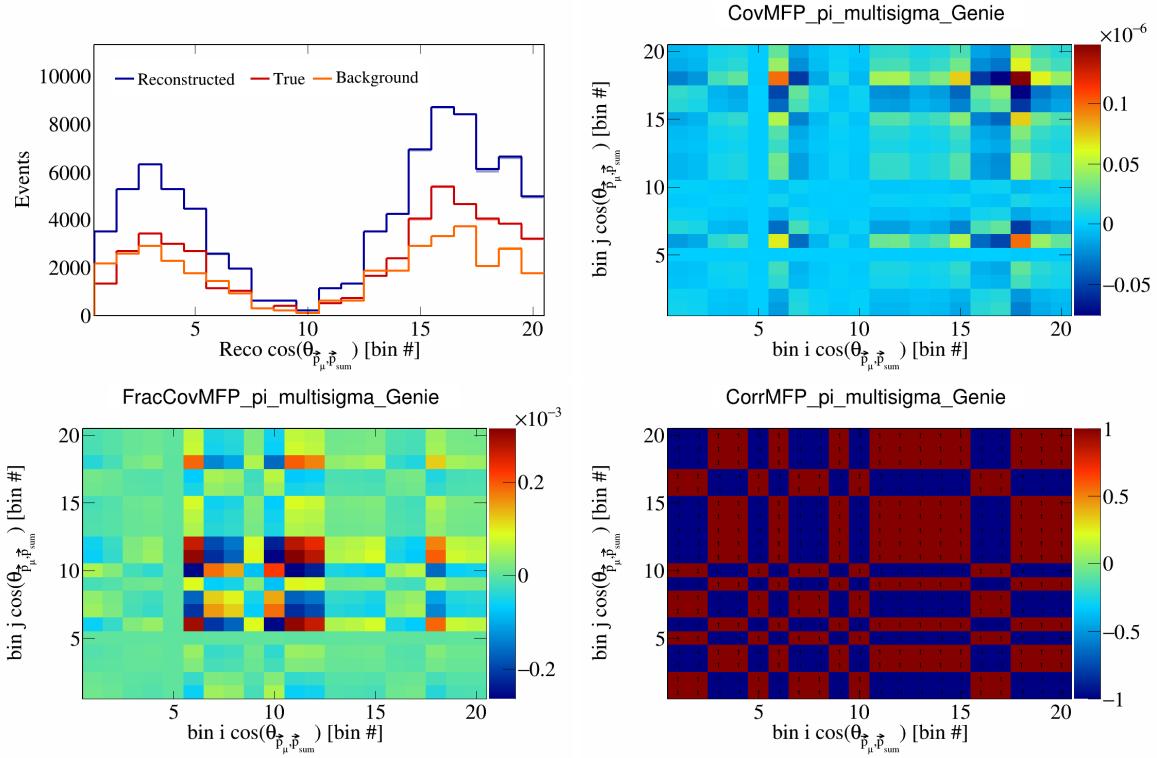


Figure 307: MFPpi variations for $\cos(\theta_{\vec{p}_\mu, \vec{p}_{\text{sum}}})$ in $\cos(\theta_{\vec{p}_\mu})$.

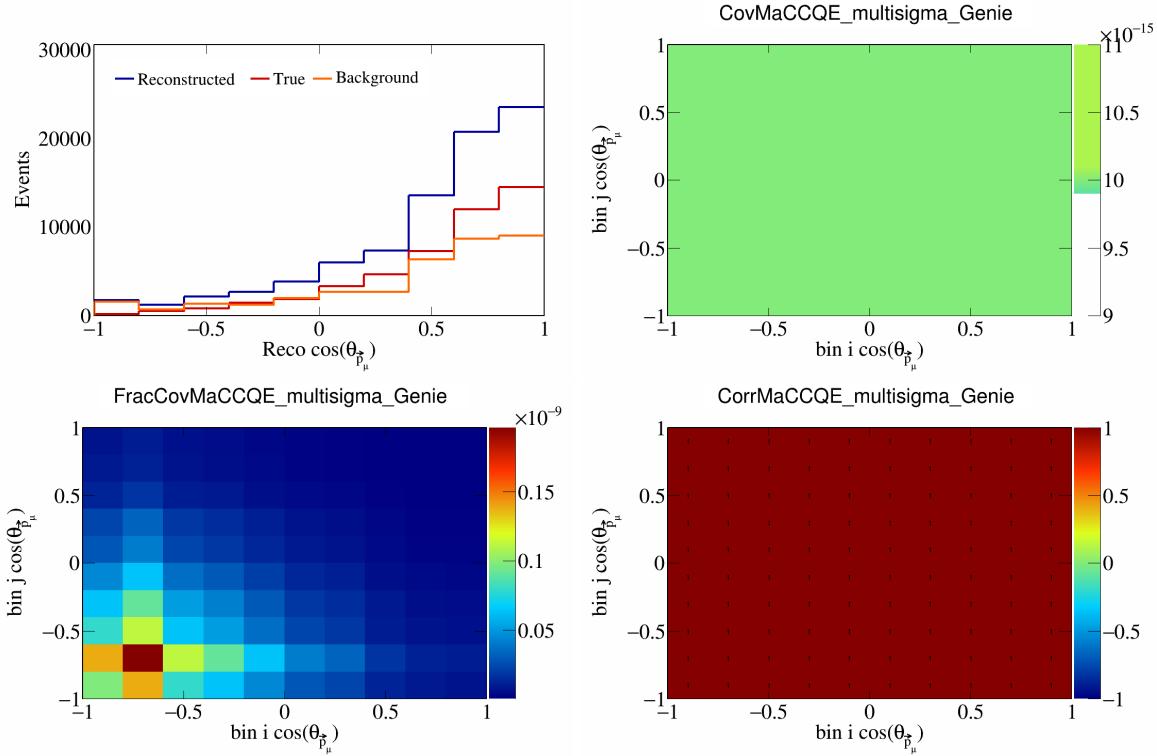


Figure 308: MaCCQE variations for $\cos(\theta_{\vec{p}_\mu})$.

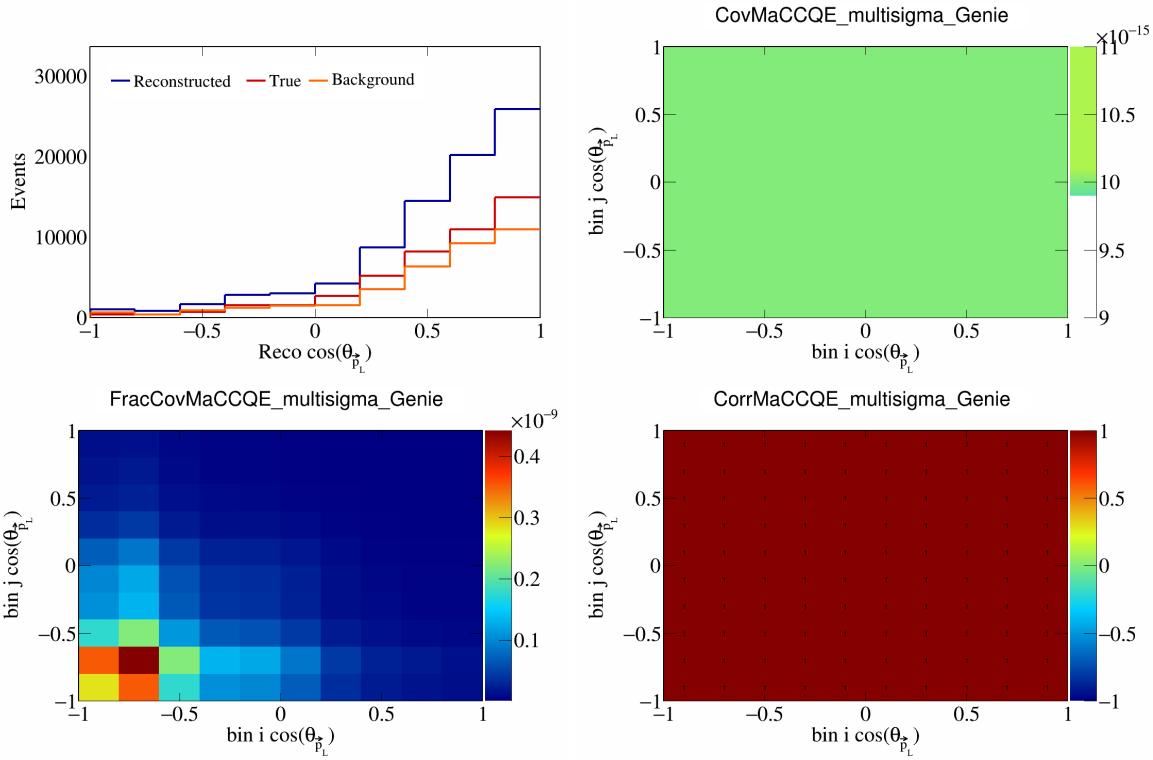


Figure 309: MaCCQE variations for $\cos(\theta_{\vec{p}_L})$.

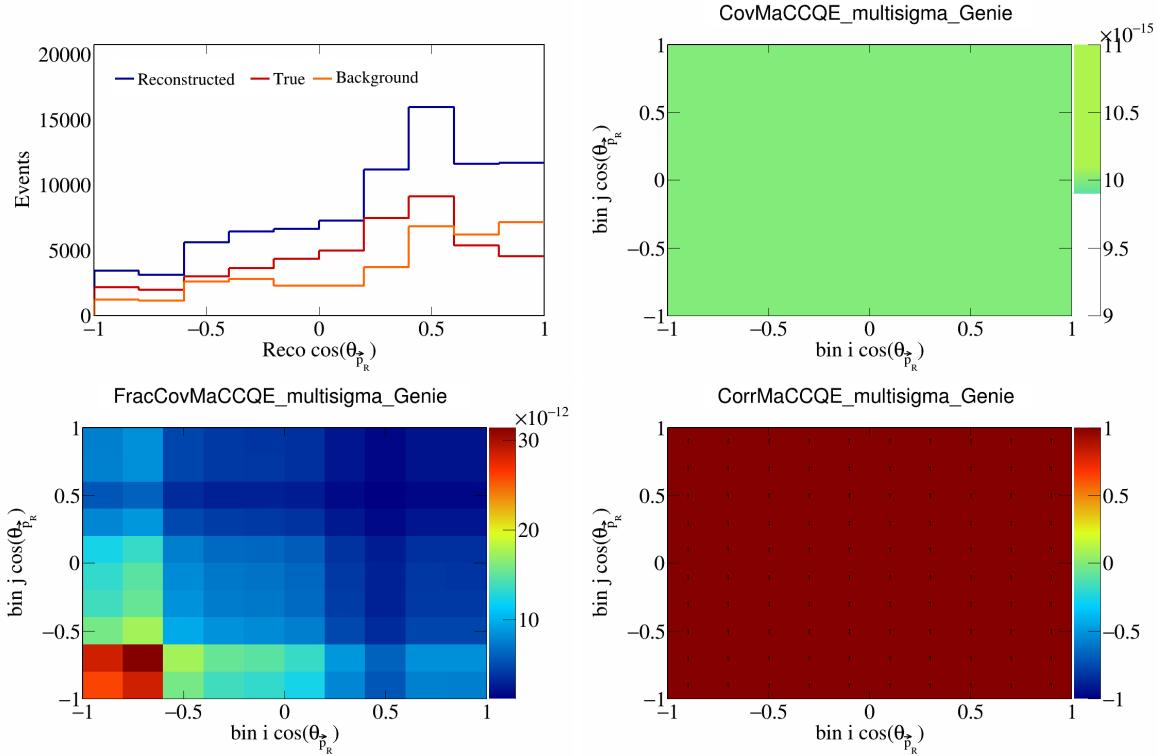


Figure 310: MaCCQE variations for $\cos(\theta_{\vec{p}_R})$.

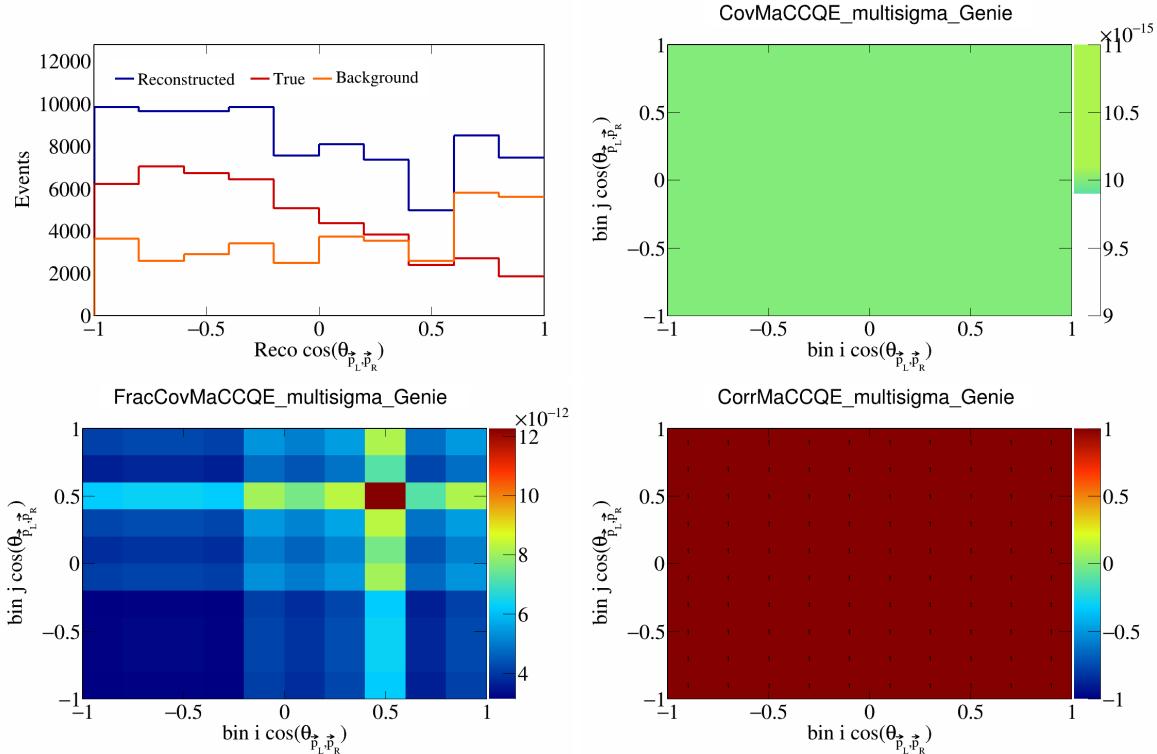


Figure 311: MaCCQE variations for $\cos(\theta_{\vec{p}_L, \vec{p}_R})$.

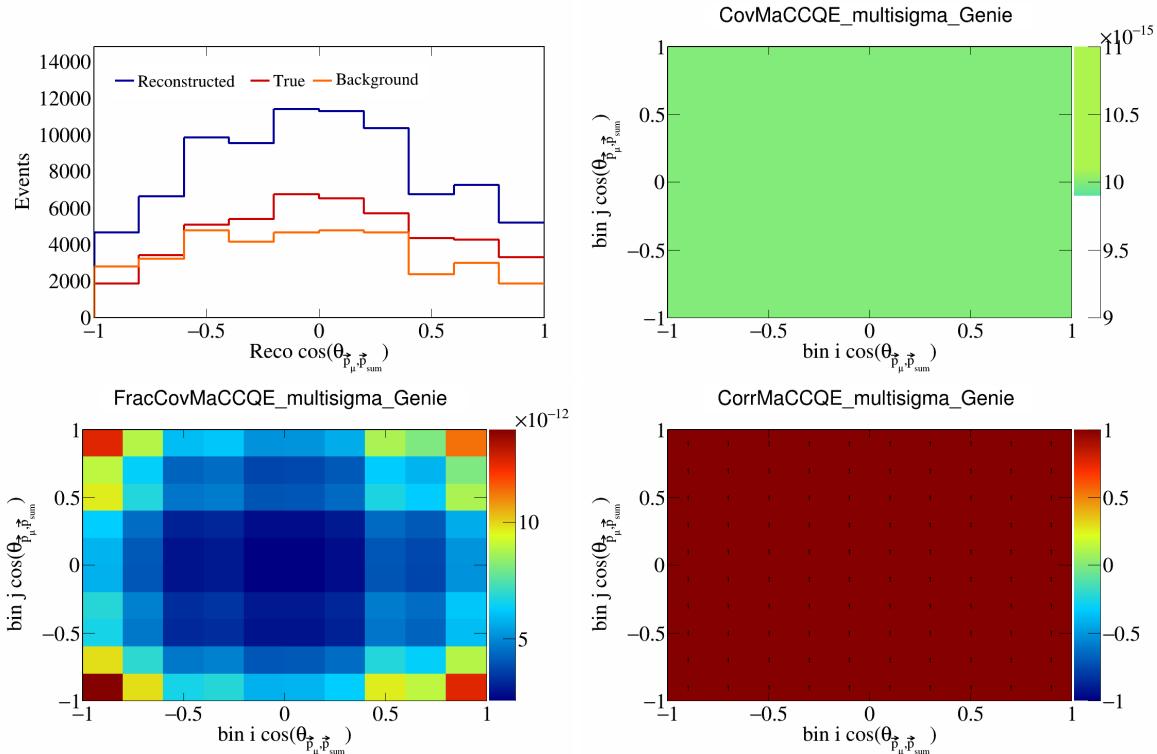


Figure 312: MaCCQE variations for $\cos(\theta_{\vec{p}_\mu, \vec{p}_{\text{sum}}})$.

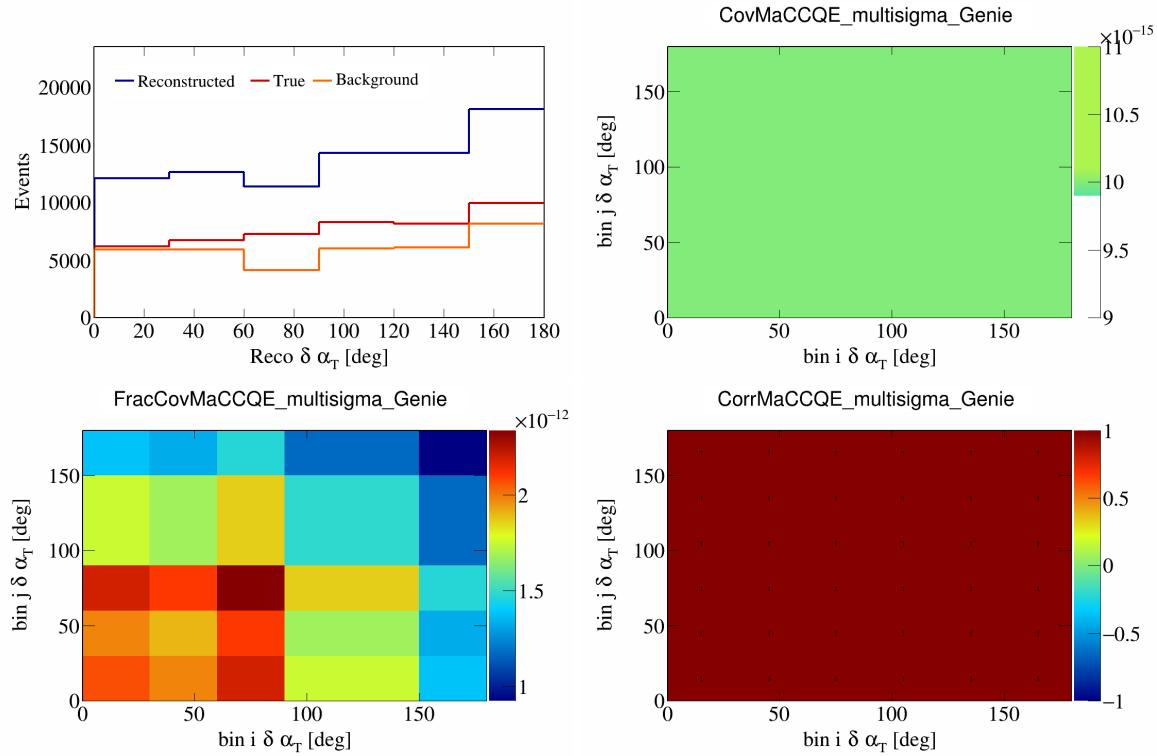


Figure 313: MaCCQE variations for $\delta\alpha_T$.

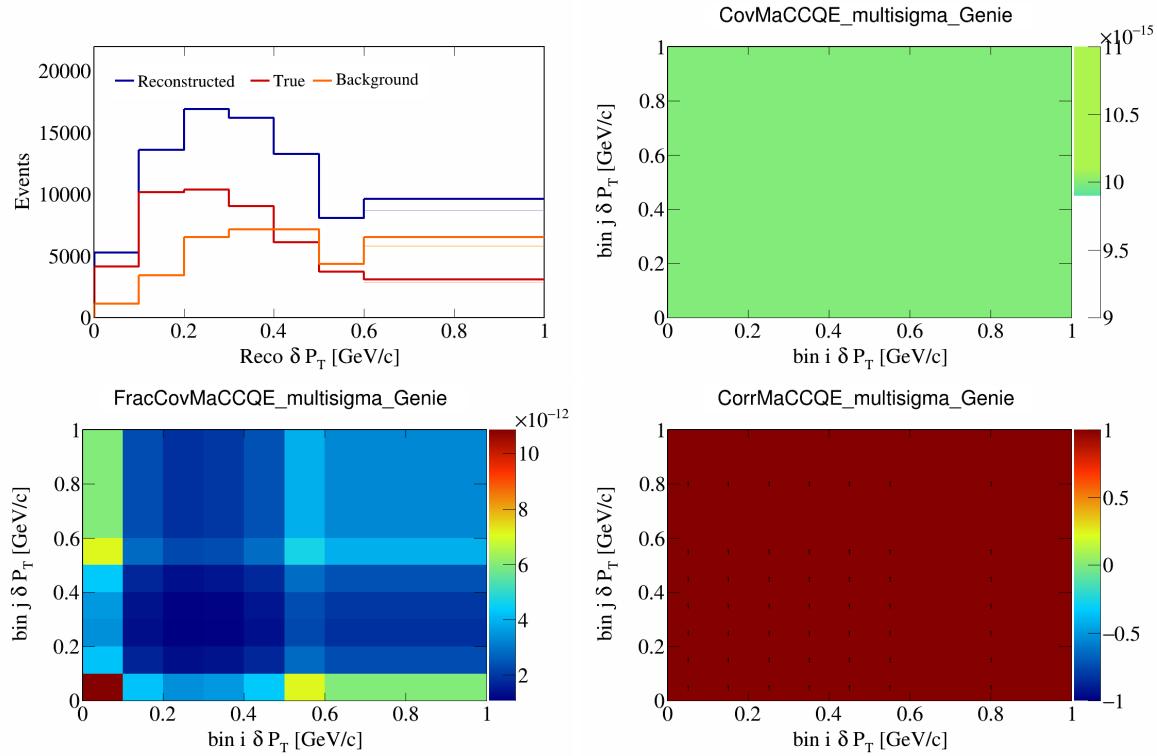


Figure 314: MaCCQE variations for δP_T .

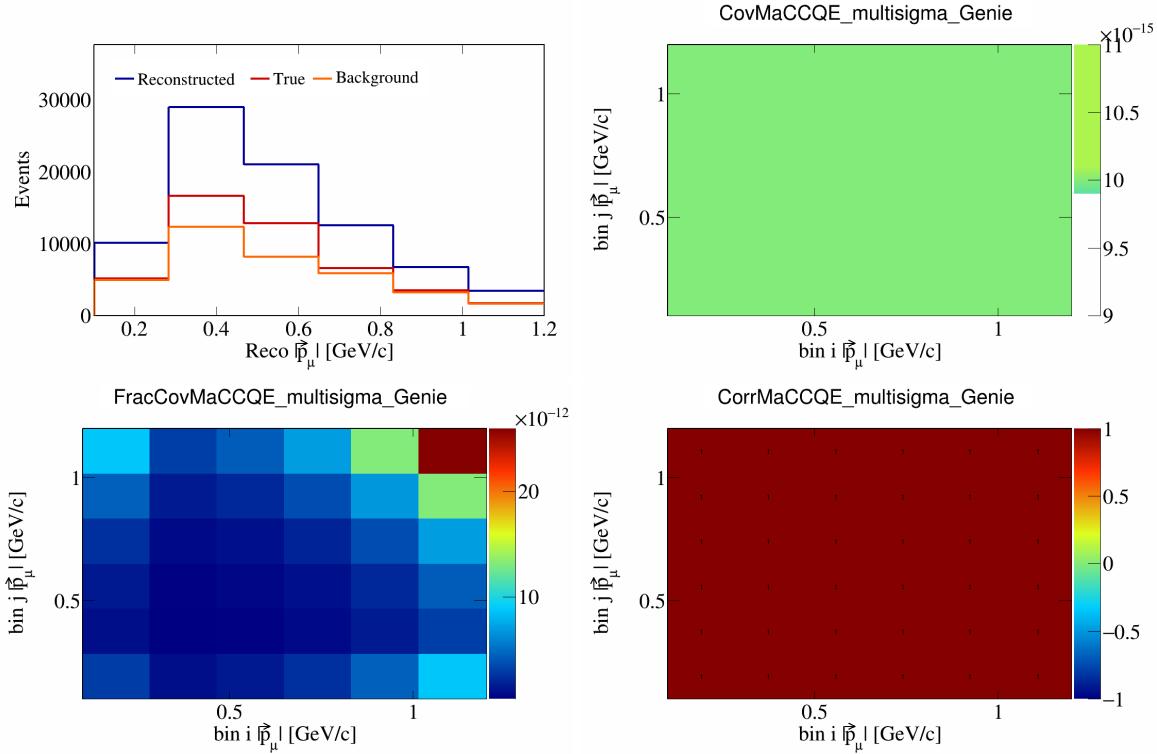


Figure 315: MaCCQE variations for $|\vec{p}_\mu|$.

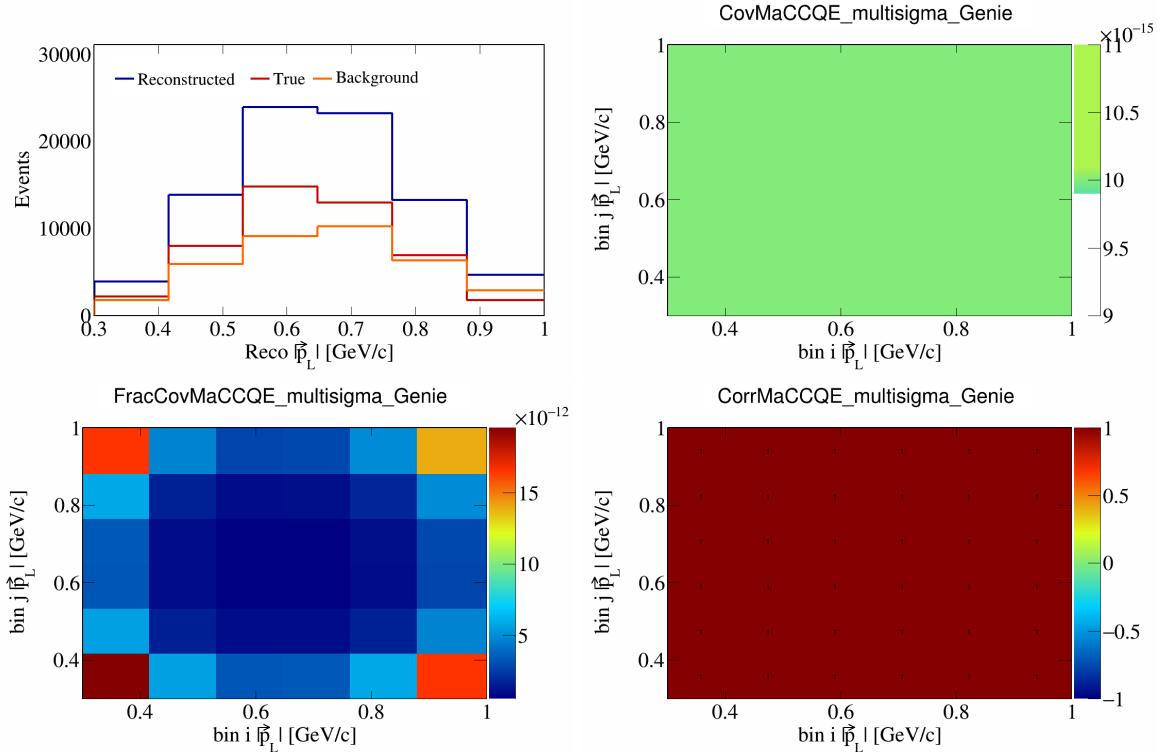


Figure 316: MaCCQE variations for $|\vec{p}_L|$.

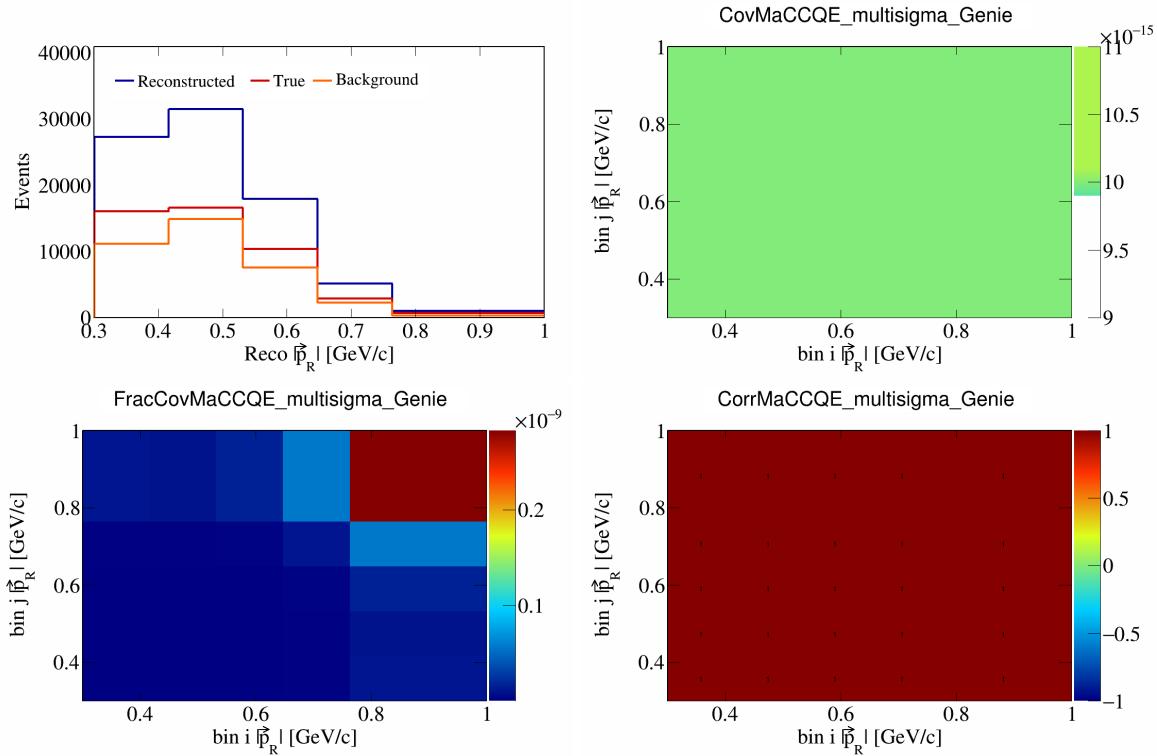


Figure 317: MaCCQE variations for $|\vec{p}_R|$.

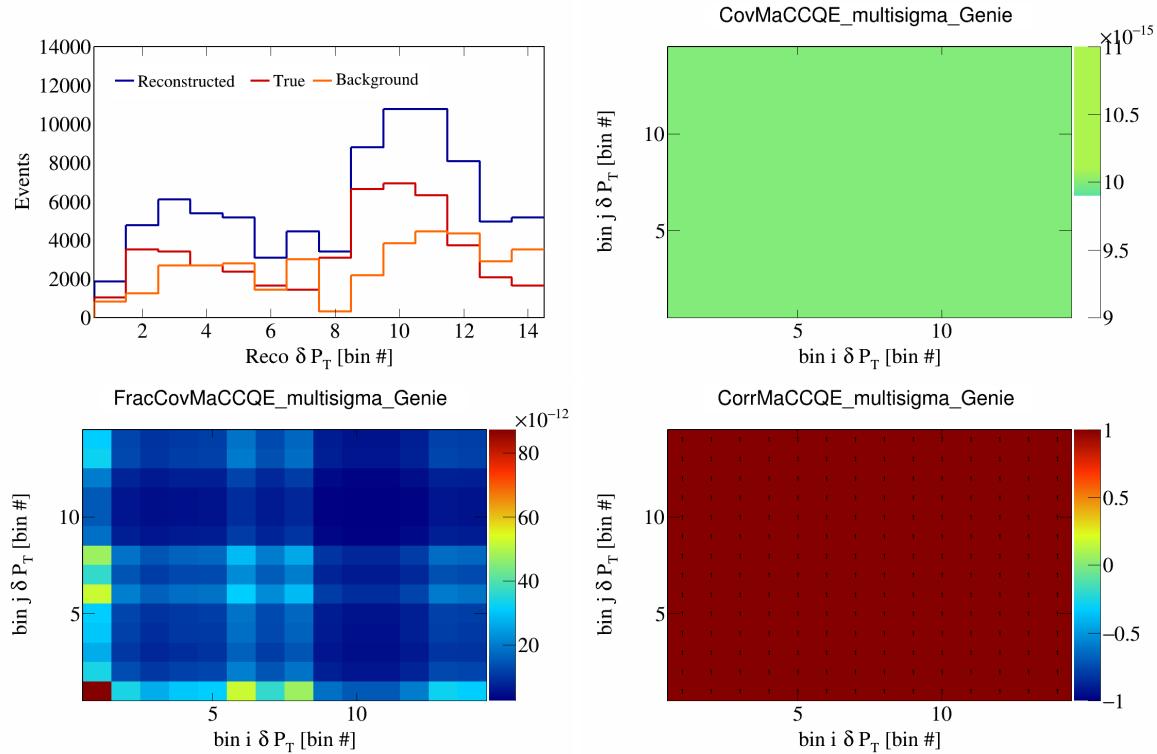


Figure 318: MaCCQE variations for δP_T in $\cos(\theta_{\vec{p}_\mu})$.

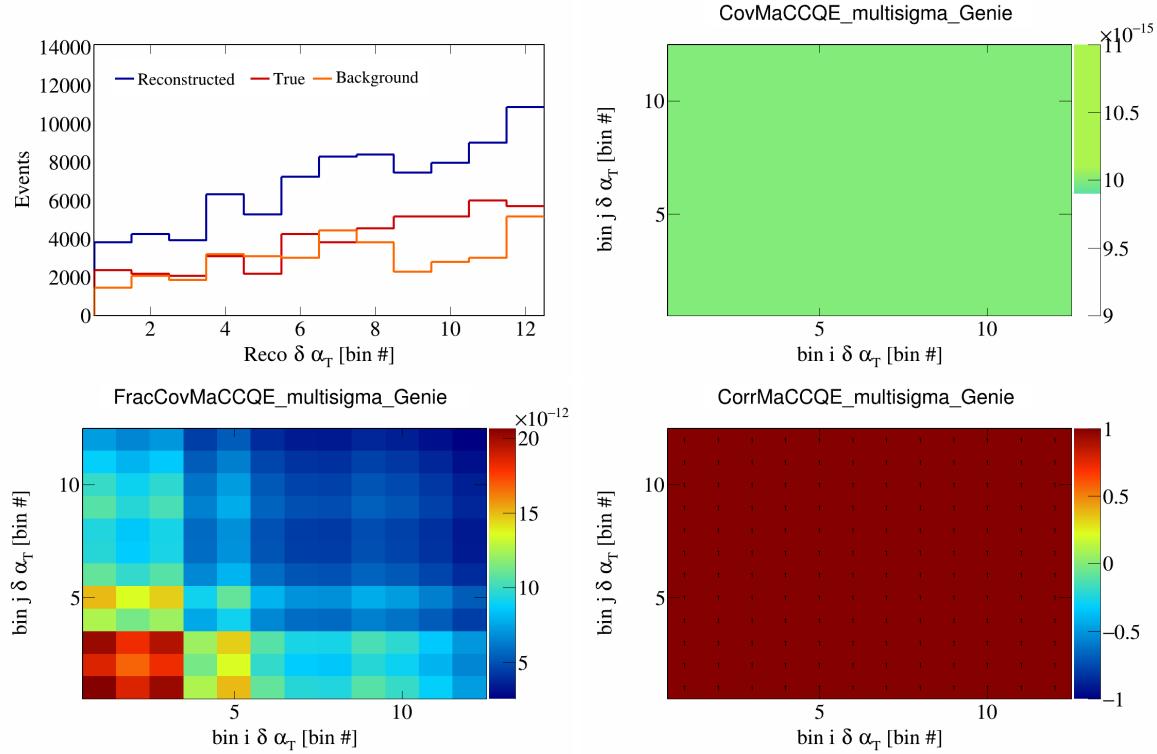


Figure 319: MaCCQE variations for $\delta\alpha_T$ in $\cos(\theta_{\vec{p}_\mu})$.

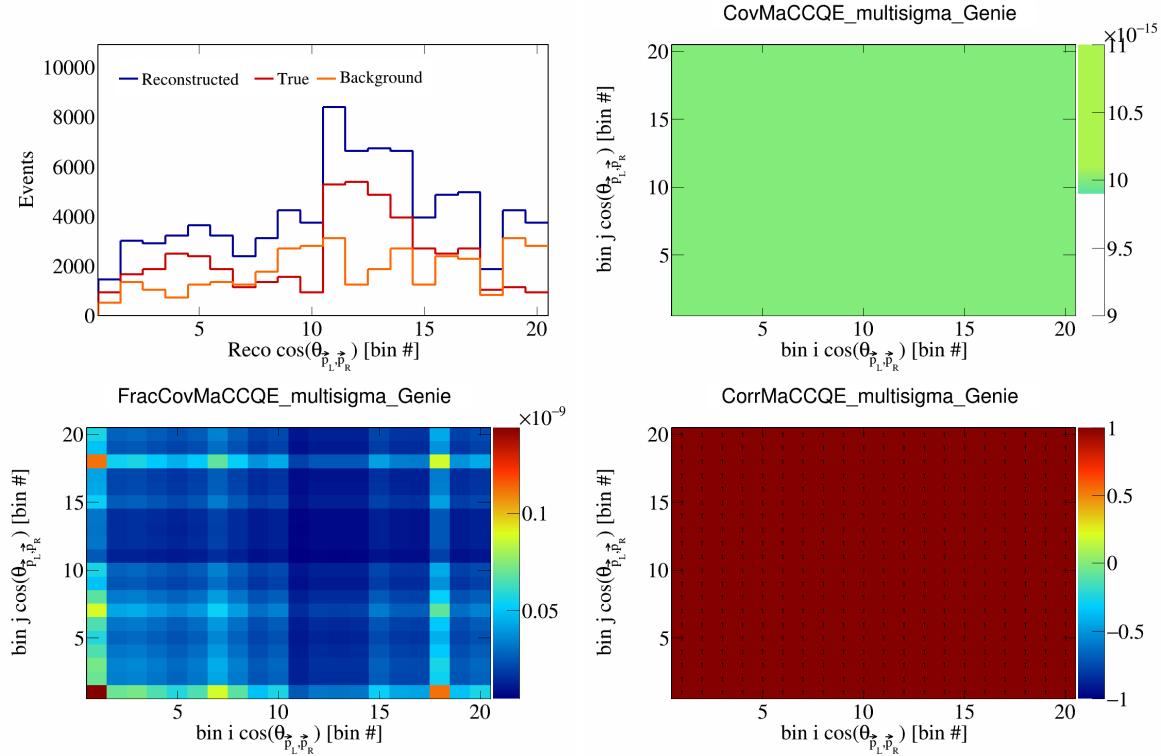


Figure 320: MaCCQE variations for $\cos(\theta_{\vec{p}_L, \vec{p}_R})$ in $\cos(\theta_{\vec{p}_\mu})$.

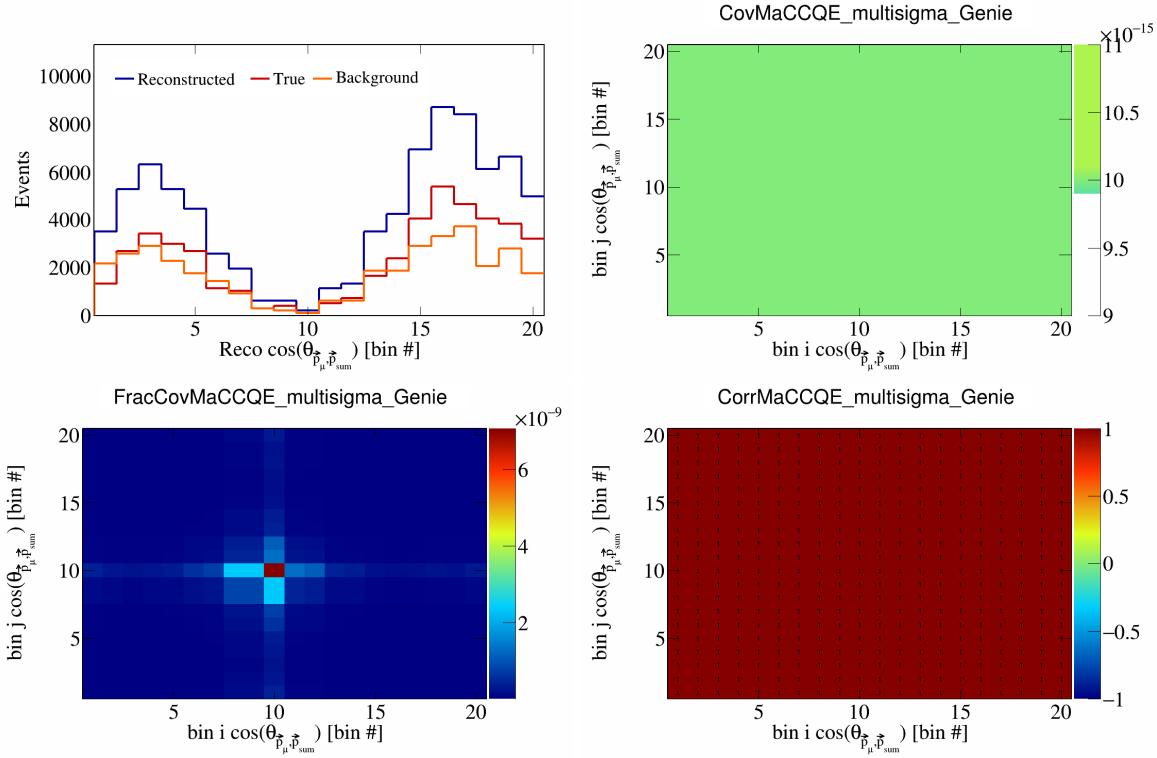


Figure 321: MaCCQE variations for $\cos(\theta_{\vec{p}_\mu, \vec{p}_{\text{sum}}})$ in $\cos(\theta_{\vec{p}_\mu})$.

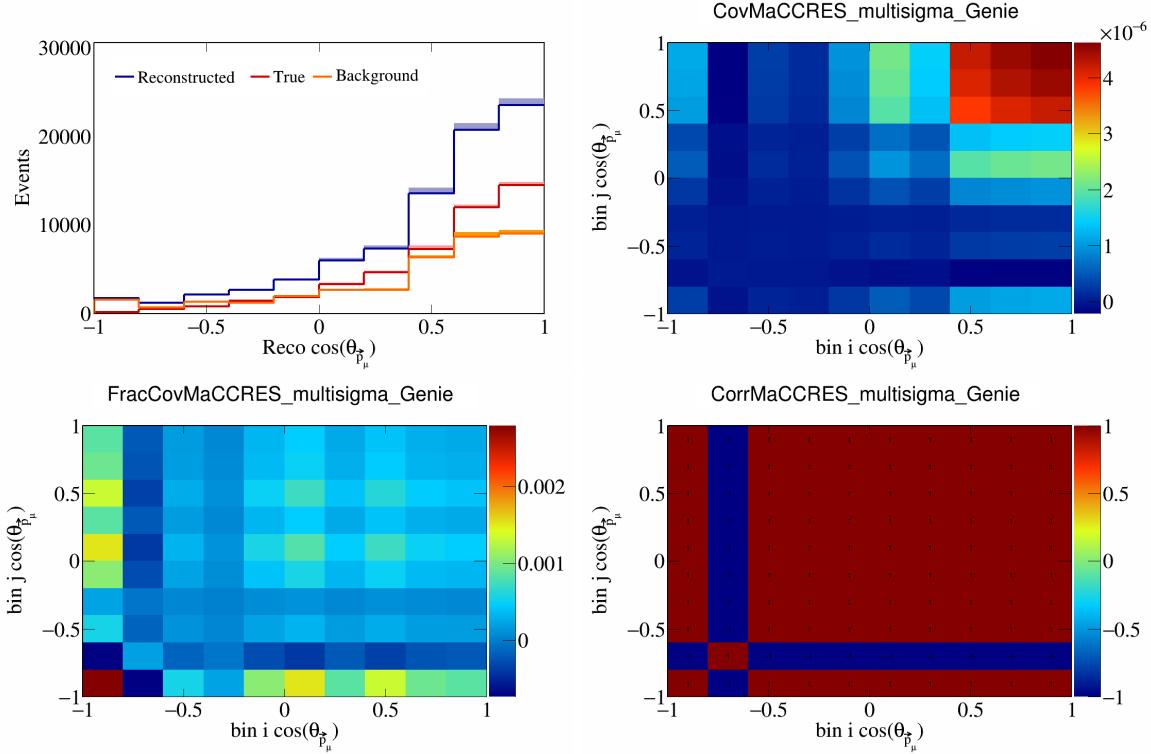


Figure 322: MaCCRES variations for $\cos(\theta_{\vec{p}_\mu})$.

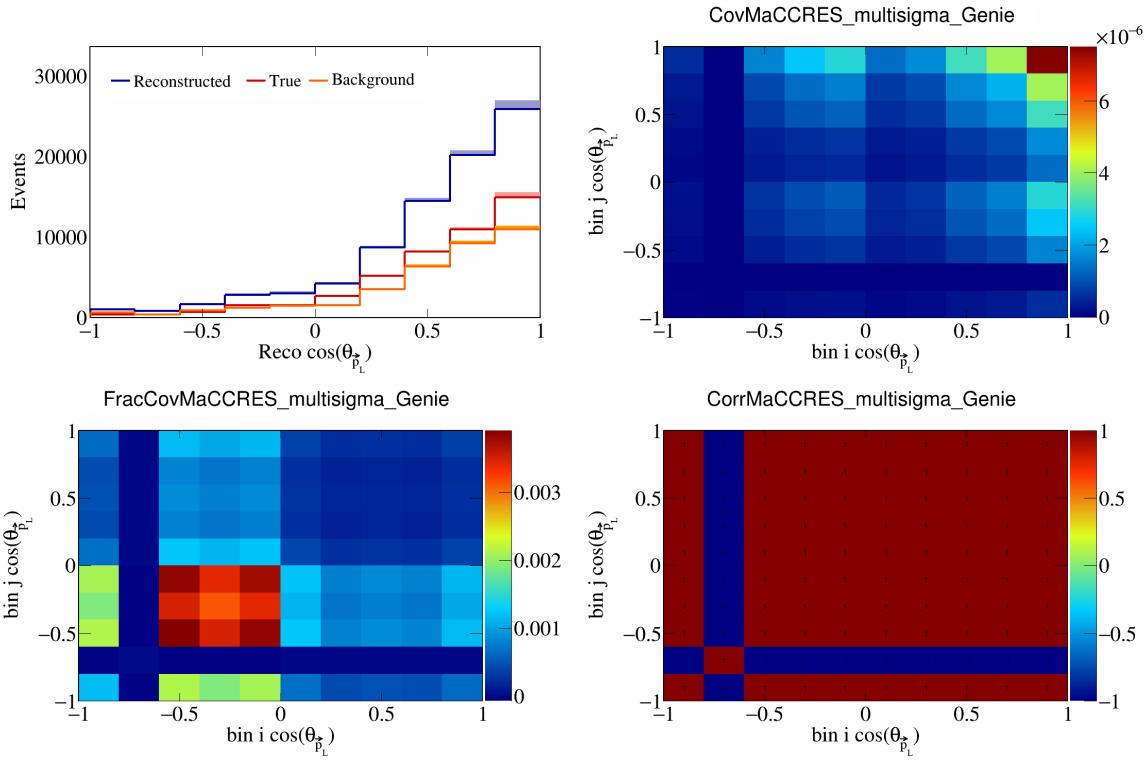


Figure 323: MaCCRES variations for $\cos(\theta_{\vec{p}_L})$.

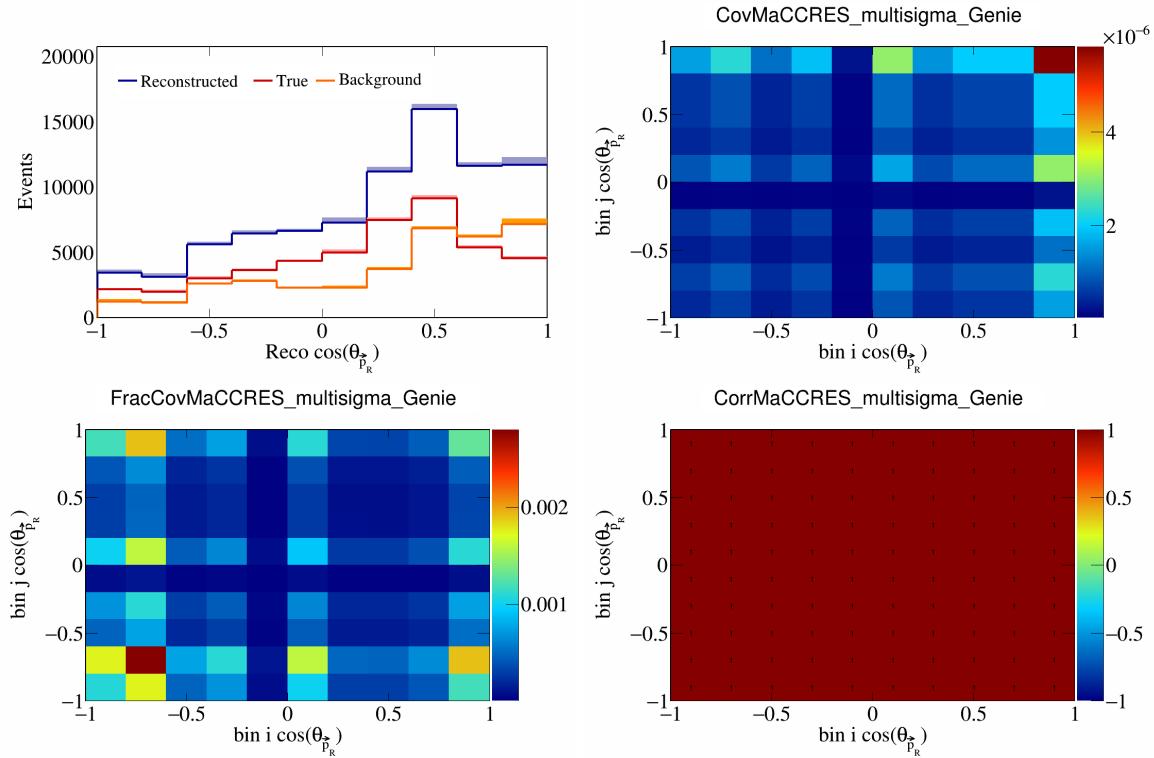


Figure 324: MaCCRES variations for $\cos(\theta_{\vec{p}_R})$.

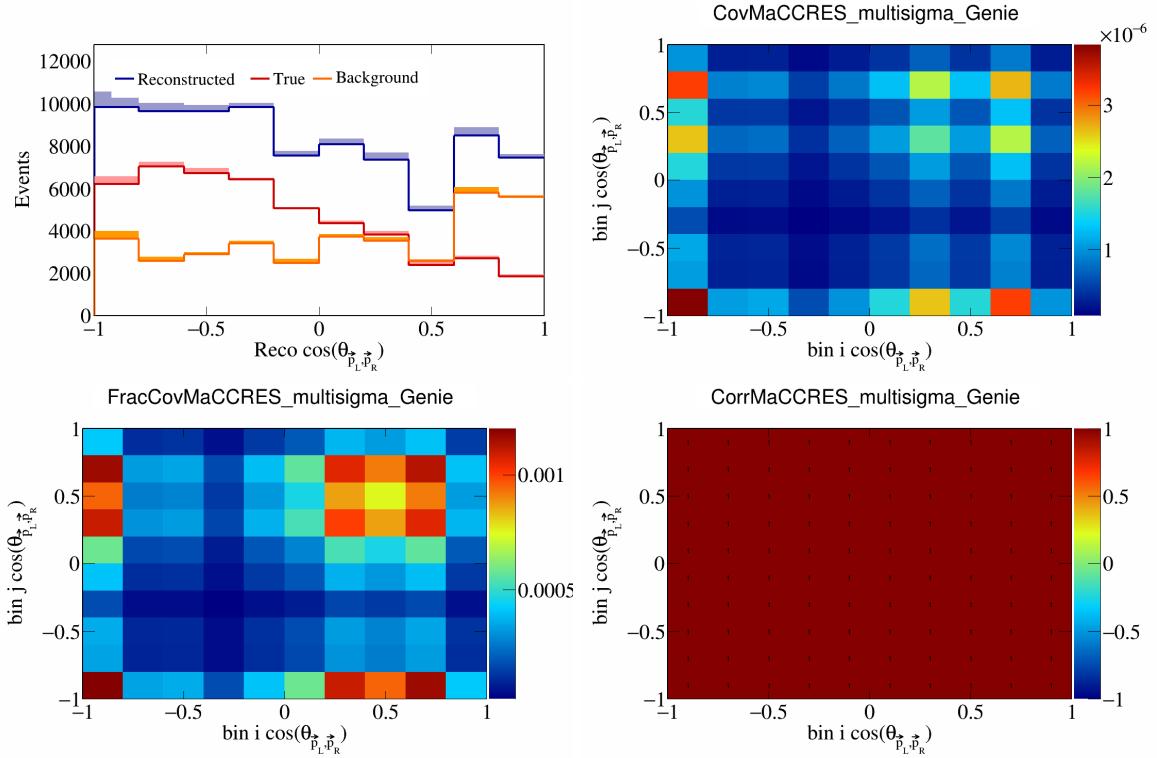


Figure 325: MaCCRES variations for $\cos(\theta_{\vec{p}_L, \vec{p}_R})$.

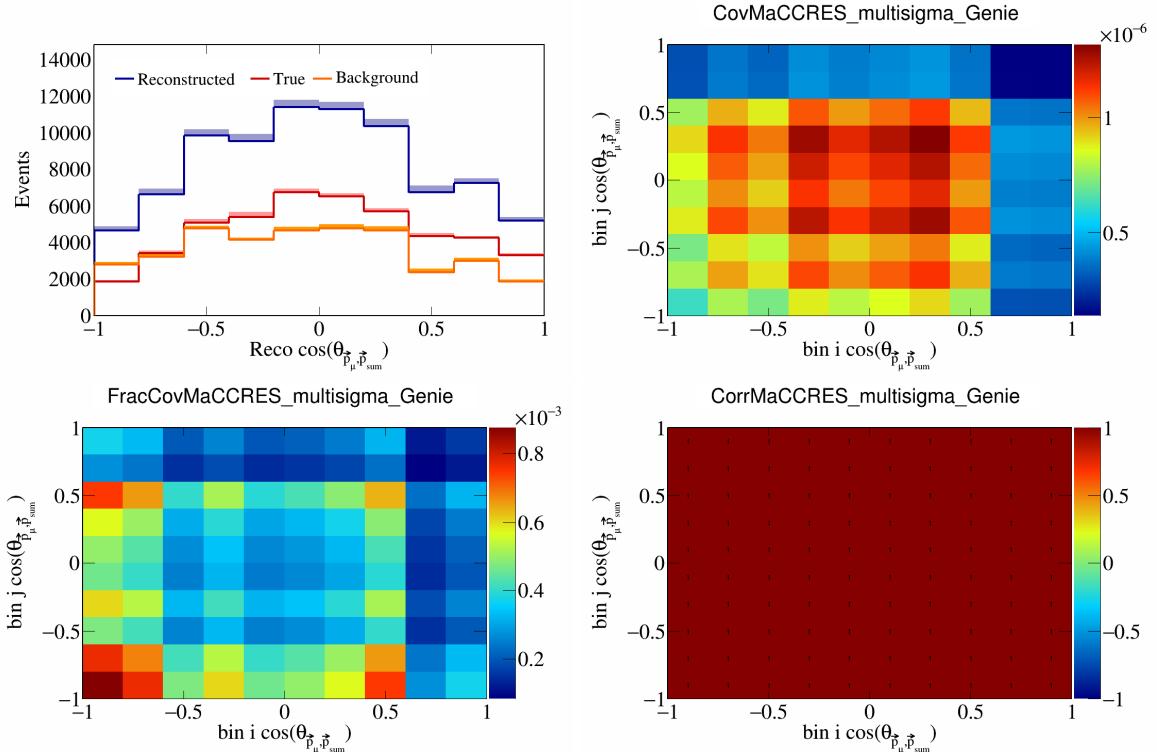


Figure 326: MaCCRES variations for $\cos(\theta_{\vec{p}_\mu, \vec{p}_{\text{sum}}})$.

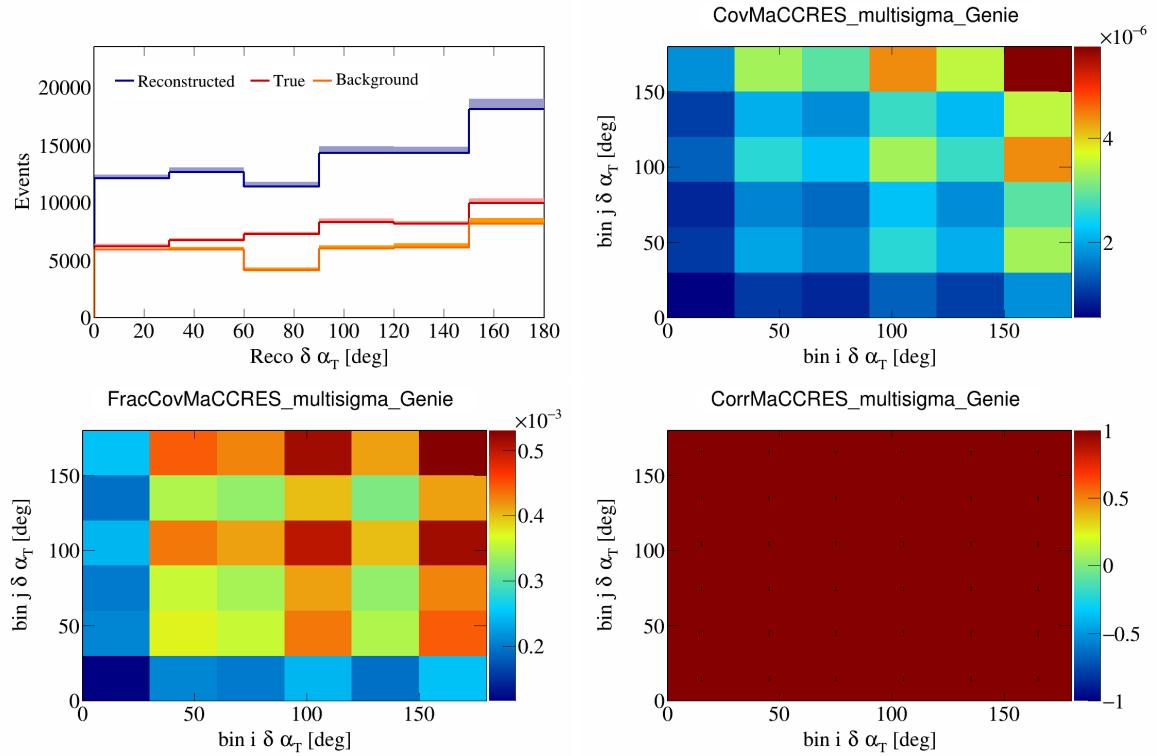


Figure 327: MaCCRES variations for $\delta\alpha_T$.

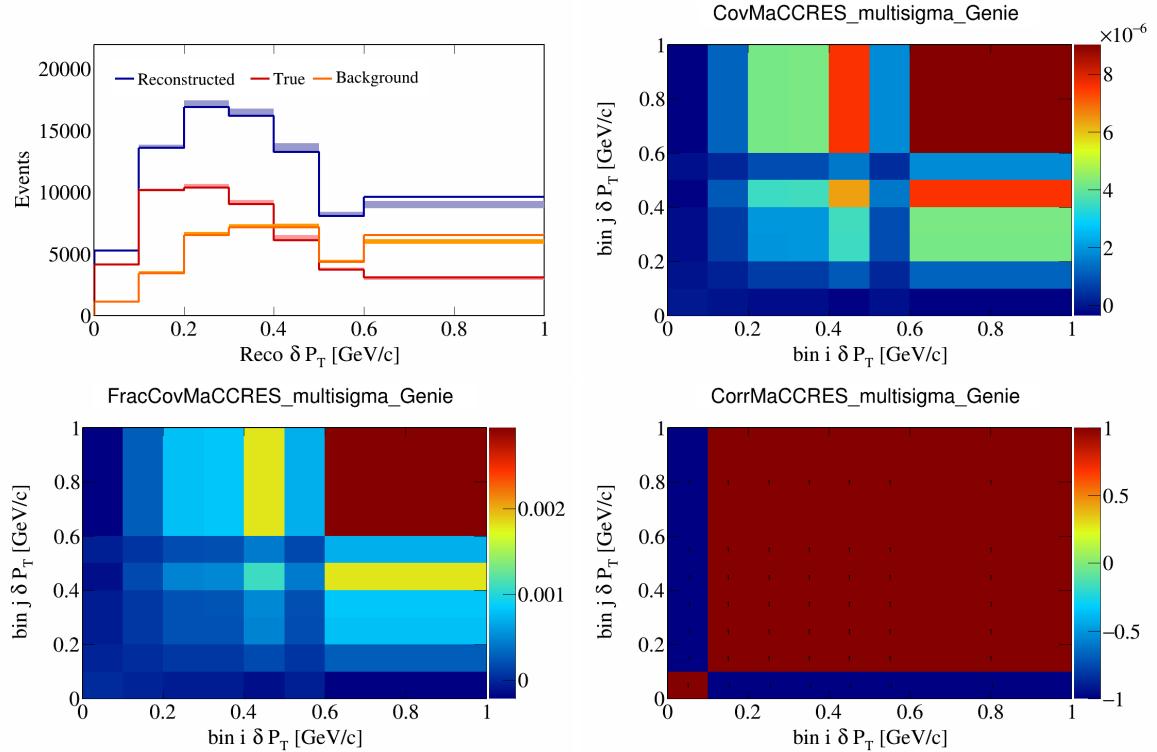


Figure 328: MaCCRES variations for δP_T .

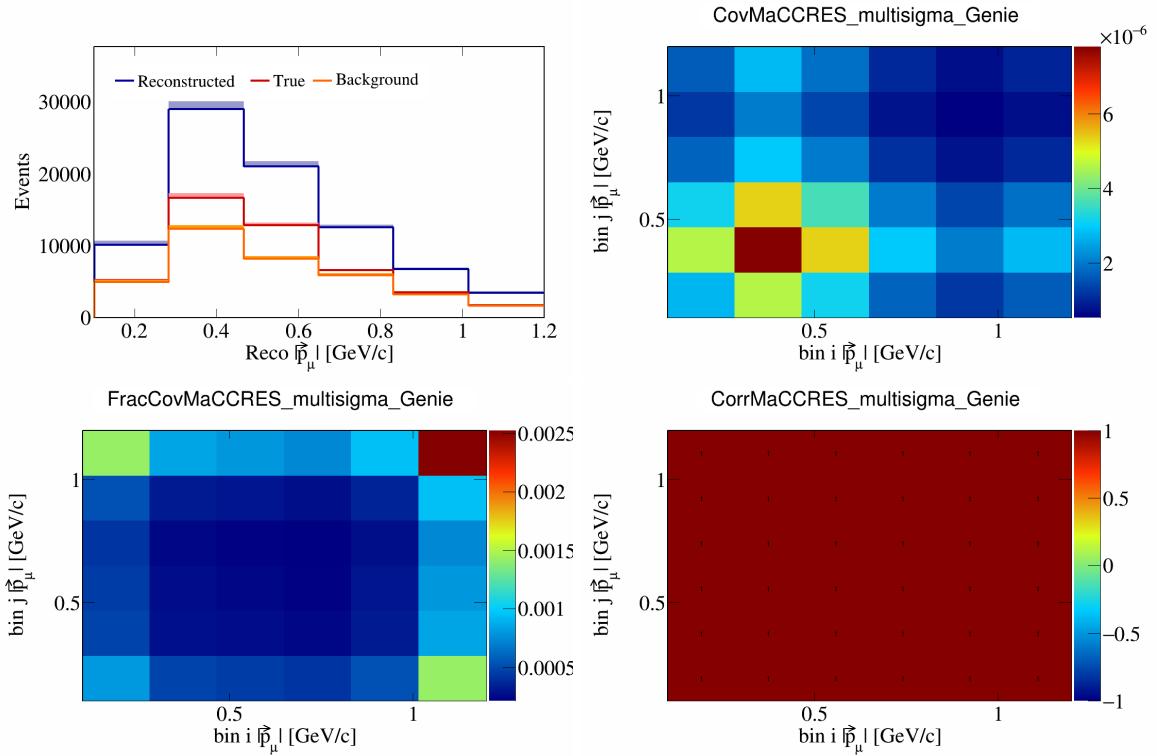


Figure 329: MaCCRES variations for $|\vec{p}_\mu|$.

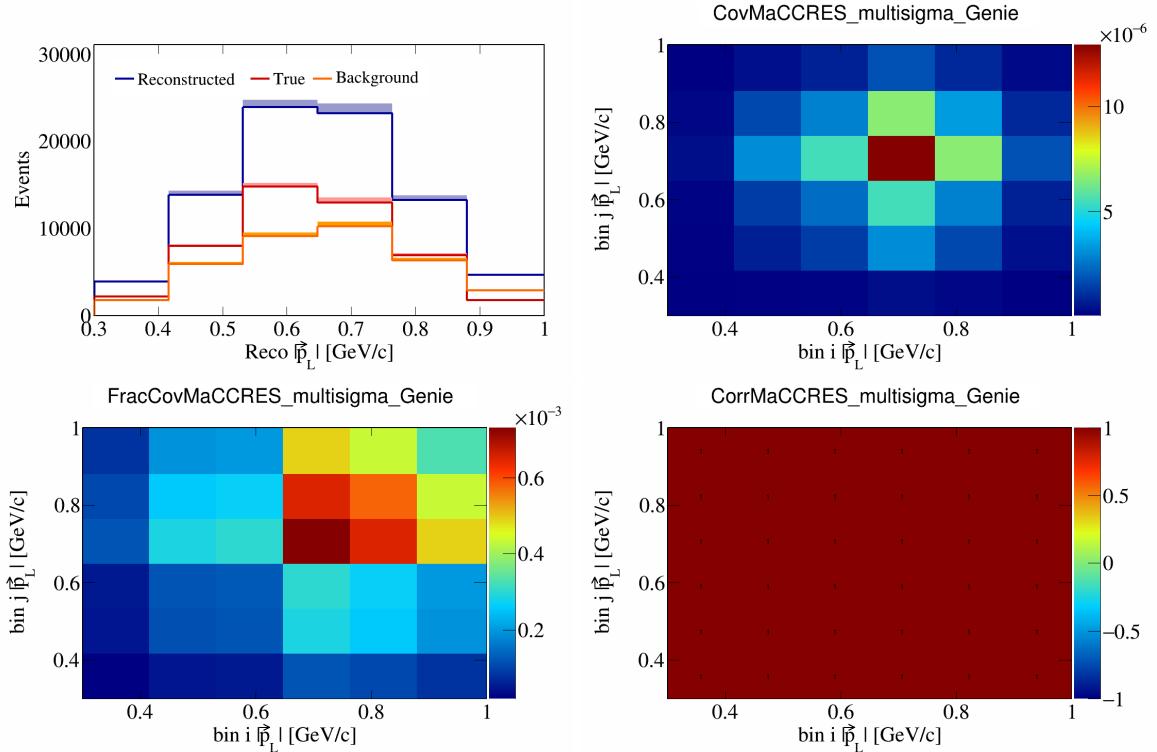


Figure 330: MaCCRES variations for $|\vec{p}_L|$.

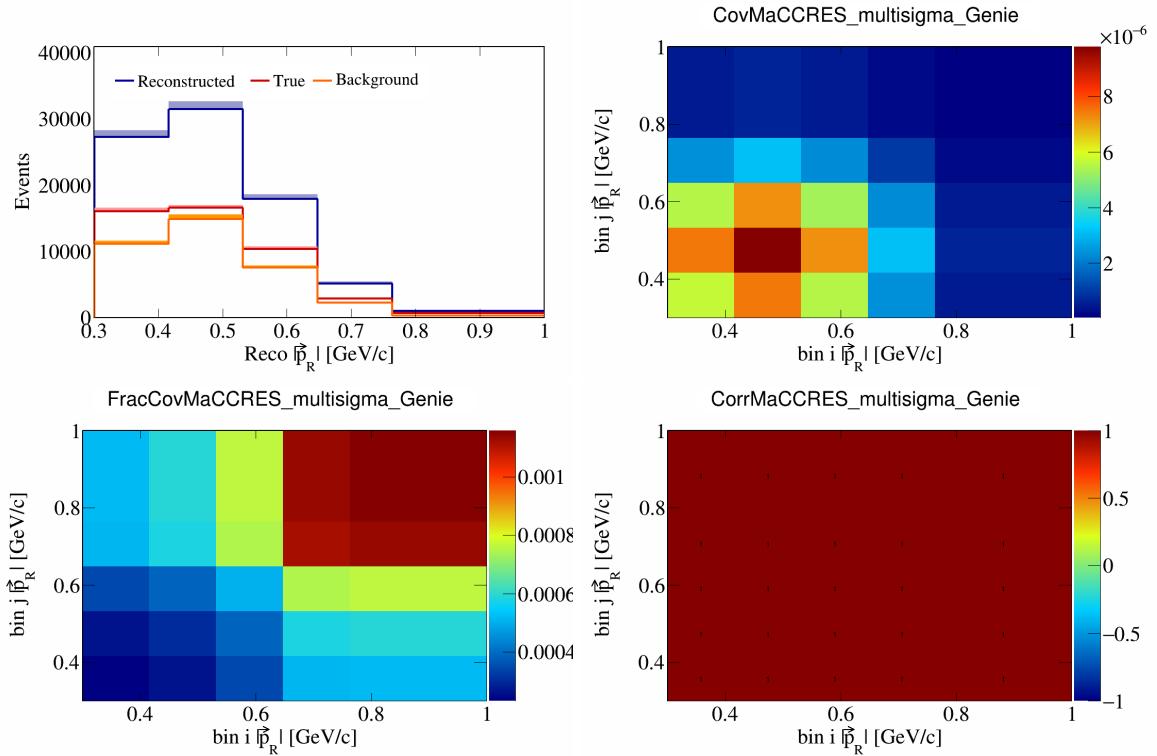


Figure 331: MaCCRES variations for $|\vec{p}_R|$.

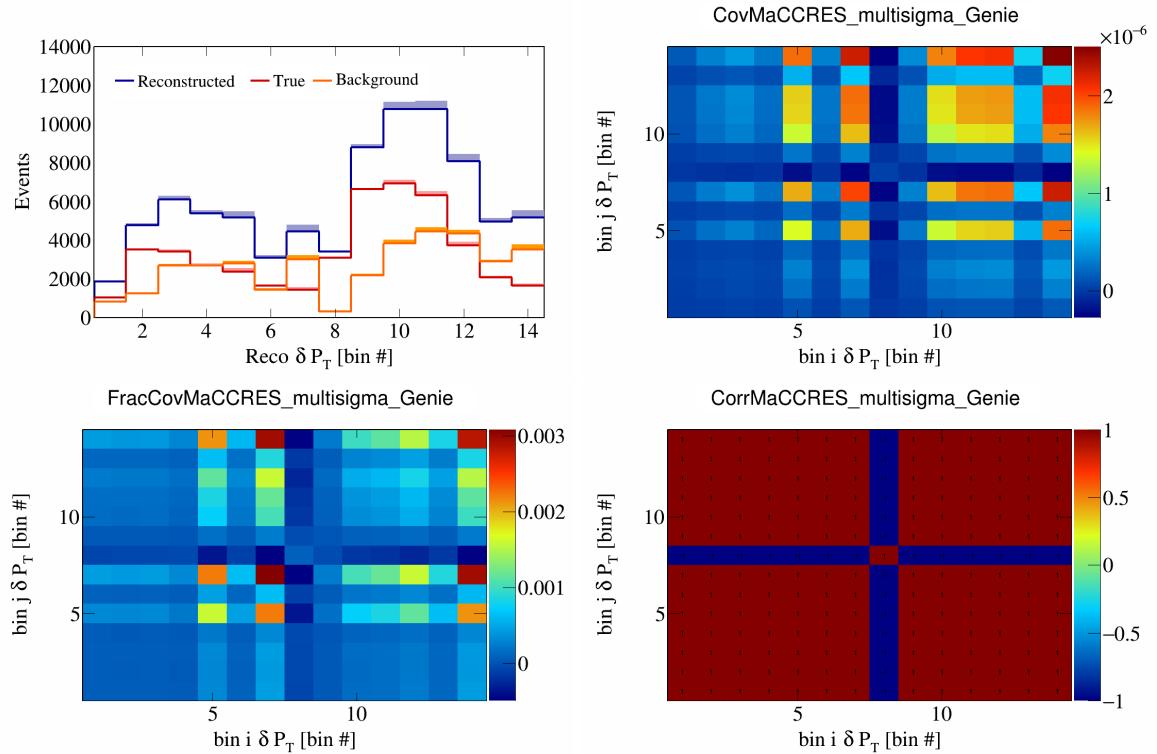


Figure 332: MaCCRES variations for δP_T in $\cos(\theta_{\vec{p}_\mu})$.

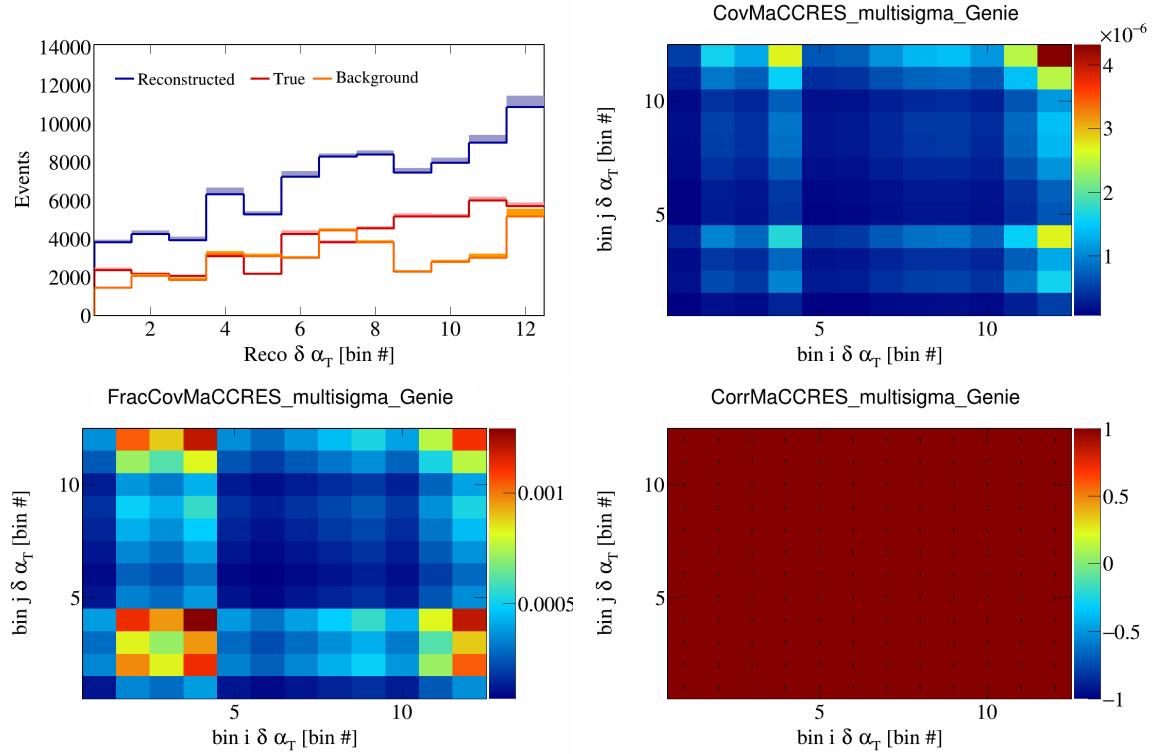


Figure 333: MaCCRES variations for $\delta \alpha_T$ in $\cos(\theta_{\vec{p}_\mu})$.

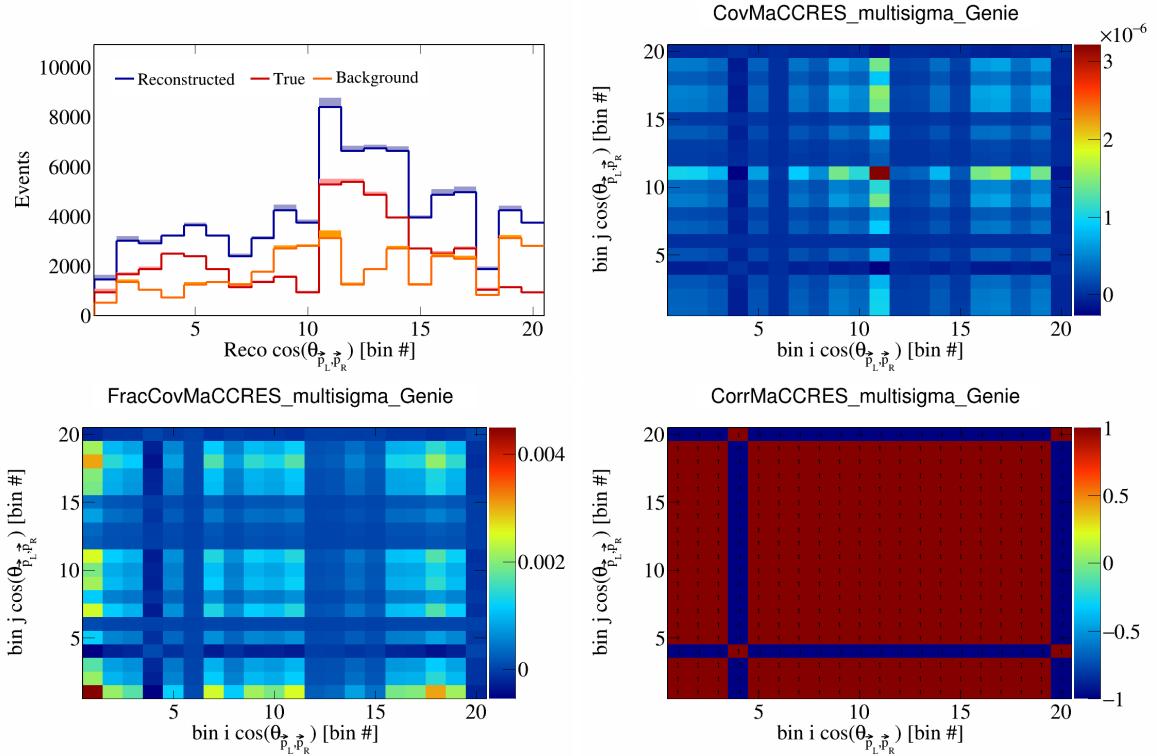


Figure 334: MaCCRES variations for $\cos(\theta_{\vec{p}_L, \vec{p}_R})$ in $\cos(\theta_{\vec{p}_\mu})$.

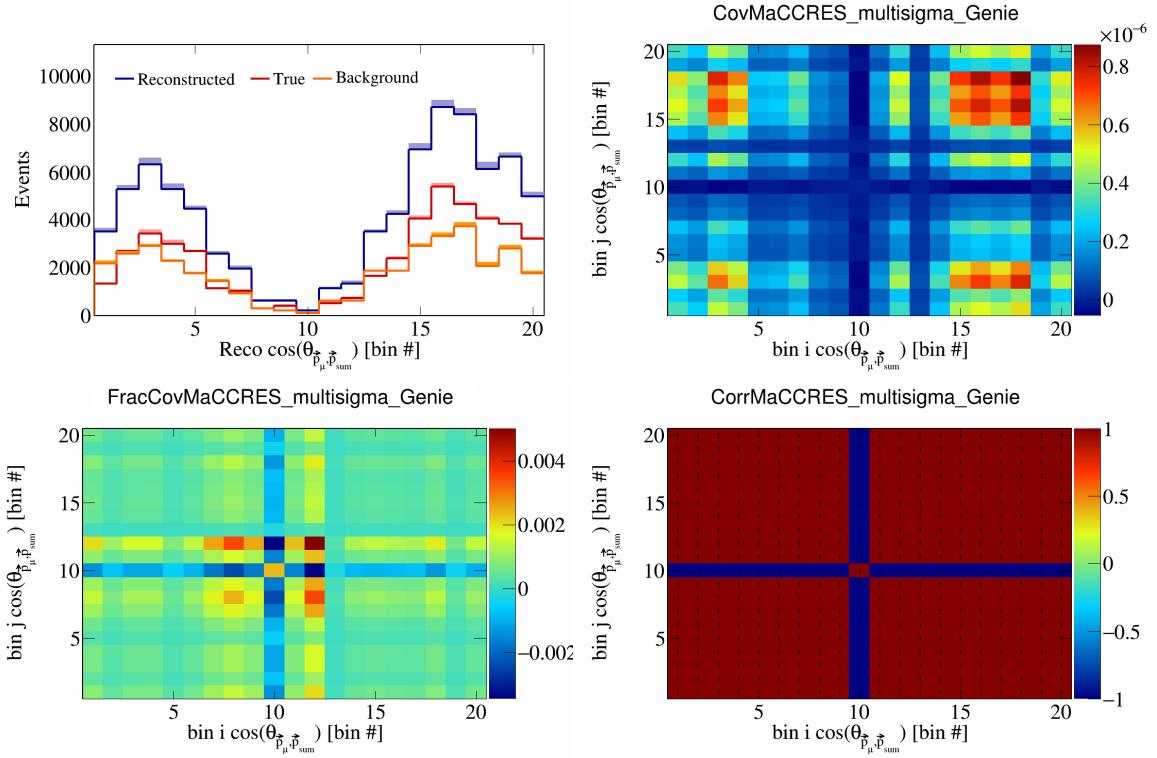


Figure 335: MaCCRES variations for $\cos(\theta_{\vec{p}_\mu, \vec{p}_{\text{sum}}})$ in $\cos(\theta_{\vec{p}_\mu})$.

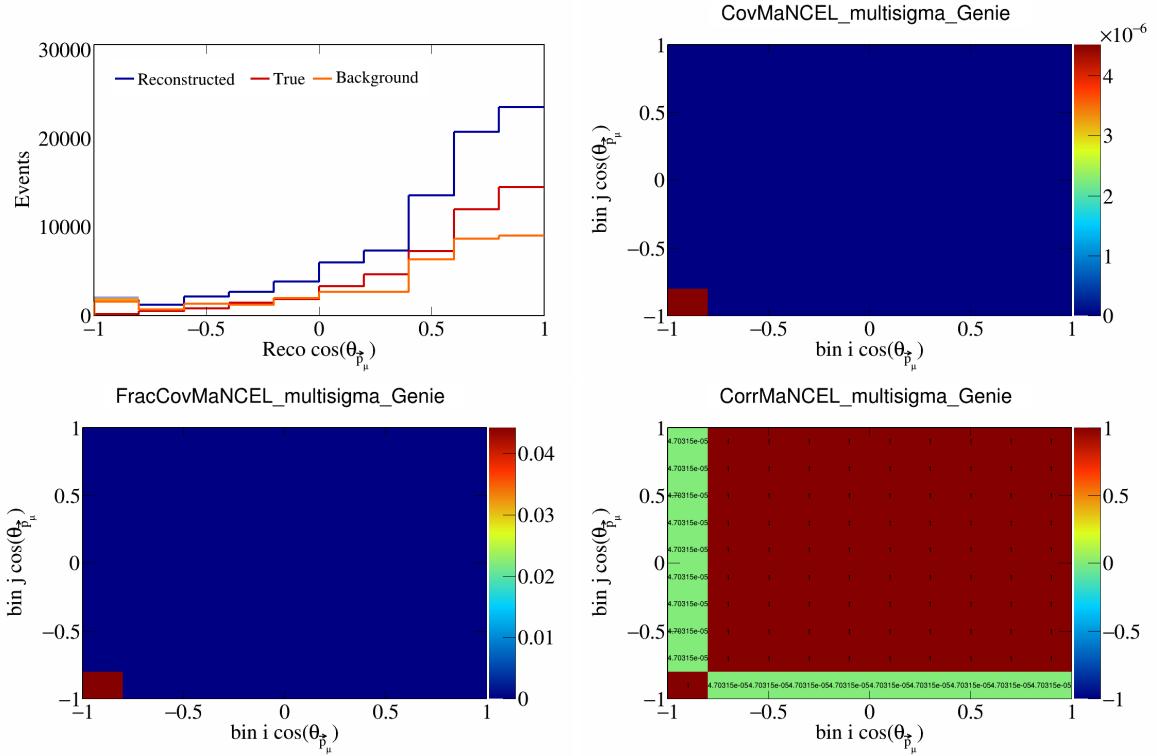


Figure 336: MaNCEL variations for $\cos(\theta_{\vec{p}_\mu})$.

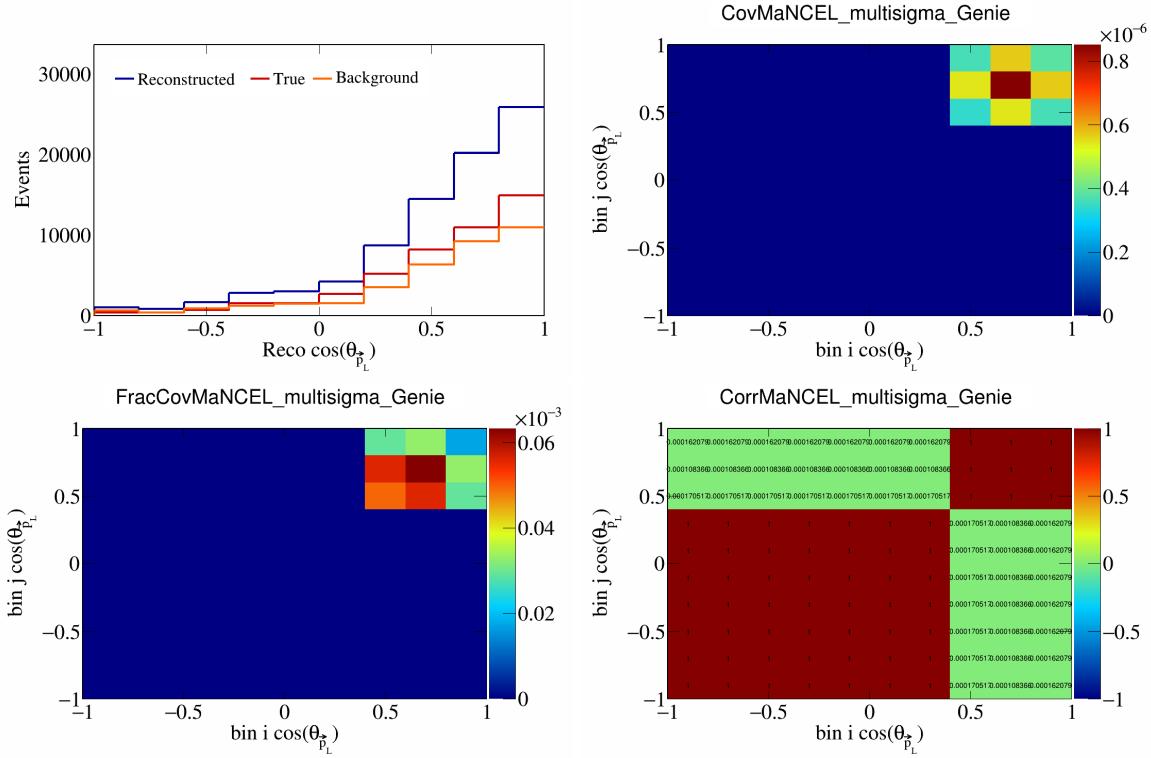


Figure 337: MaNCEL variations for $\cos(\theta_{\vec{p}_L})$.

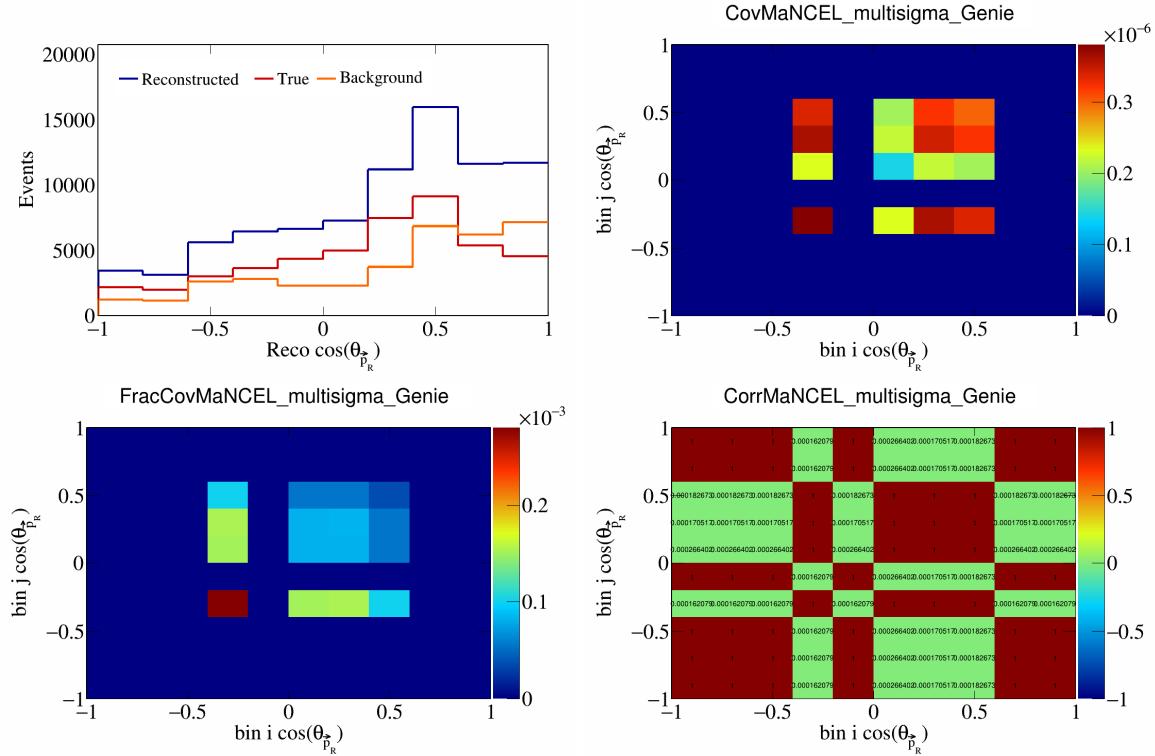


Figure 338: MaNCEL variations for $\cos(\theta_{\vec{p}_R})$.

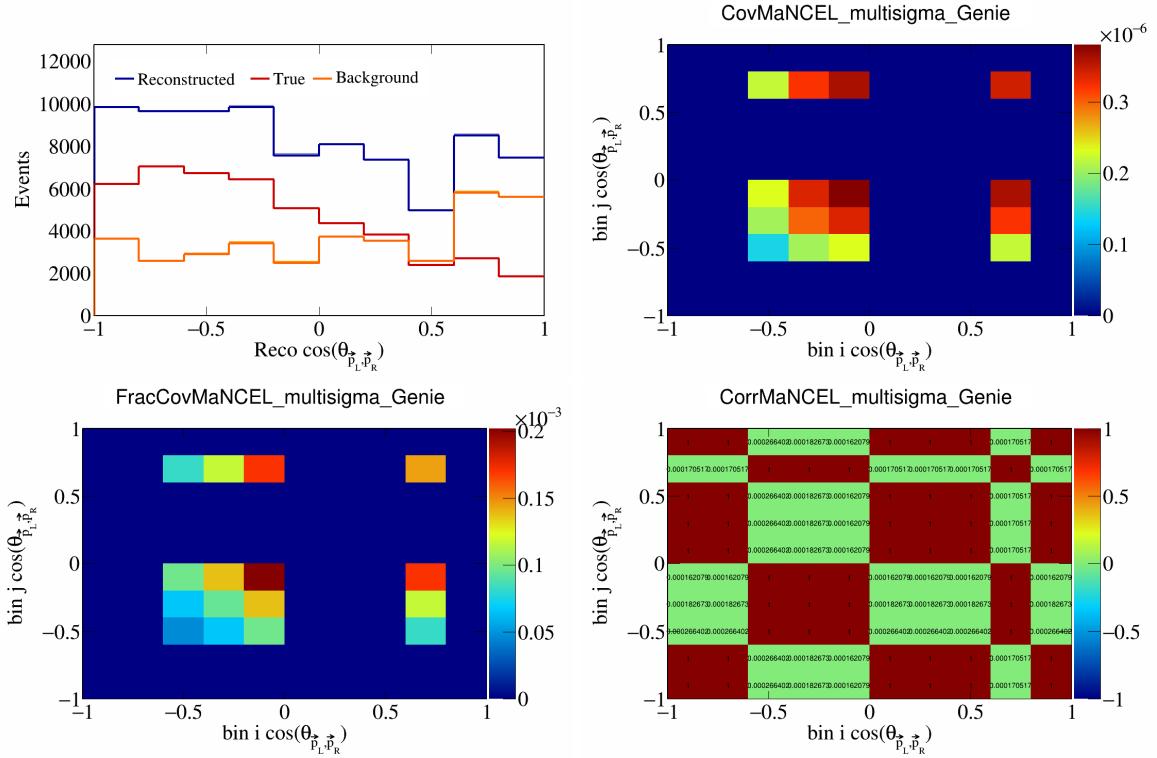


Figure 339: MaNCEL variations for $\cos(\theta_{\vec{p}_L, \vec{p}_R})$.

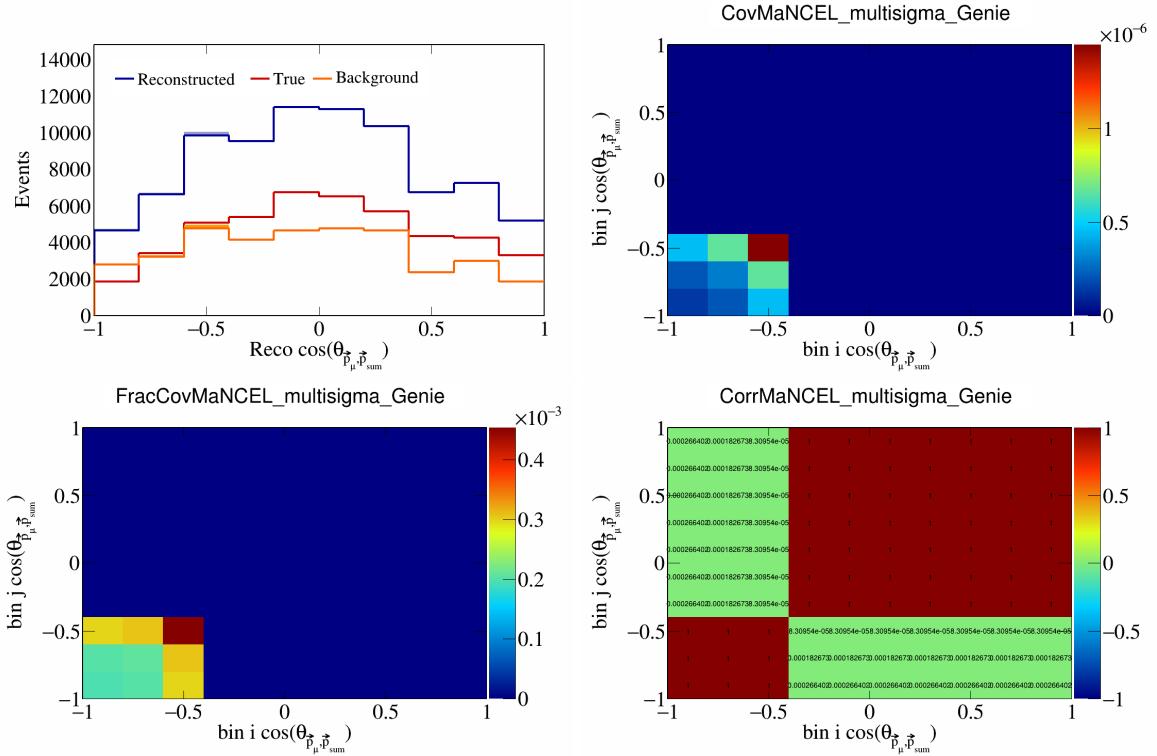


Figure 340: MaNCEL variations for $\cos(\theta_{\vec{p}_\mu, \vec{p}_{\text{sum}}})$.

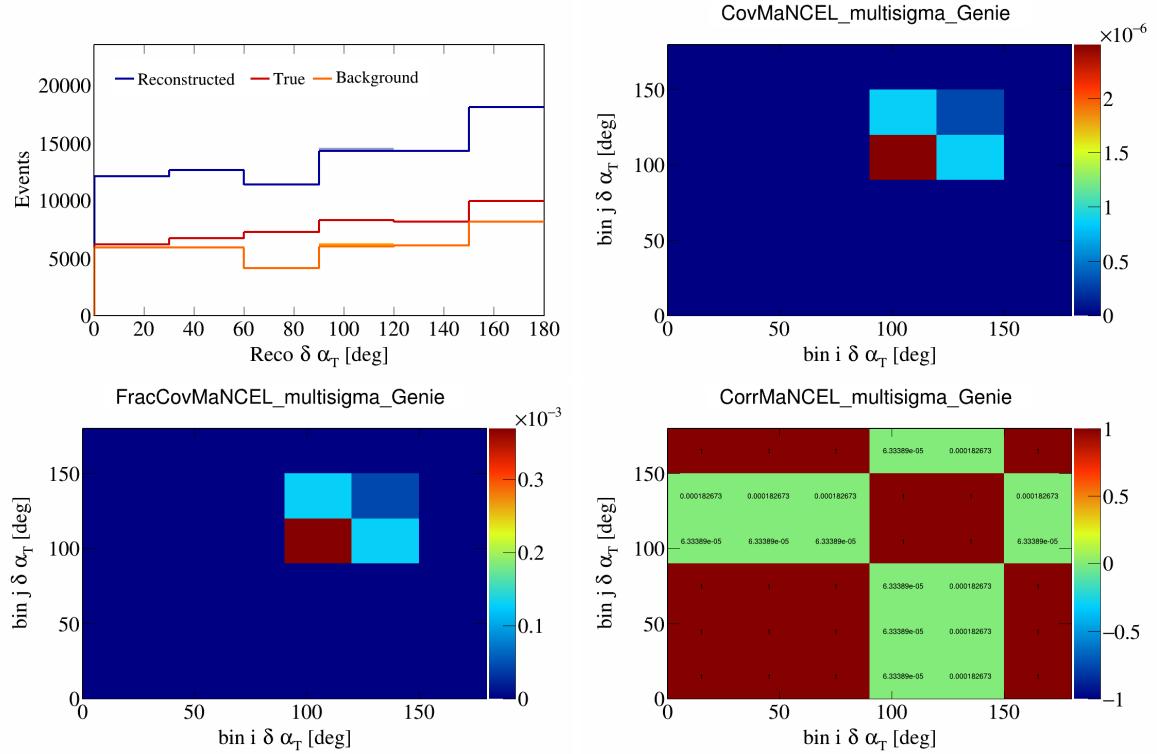


Figure 341: MaNCEL variations for $\delta\alpha_T$.

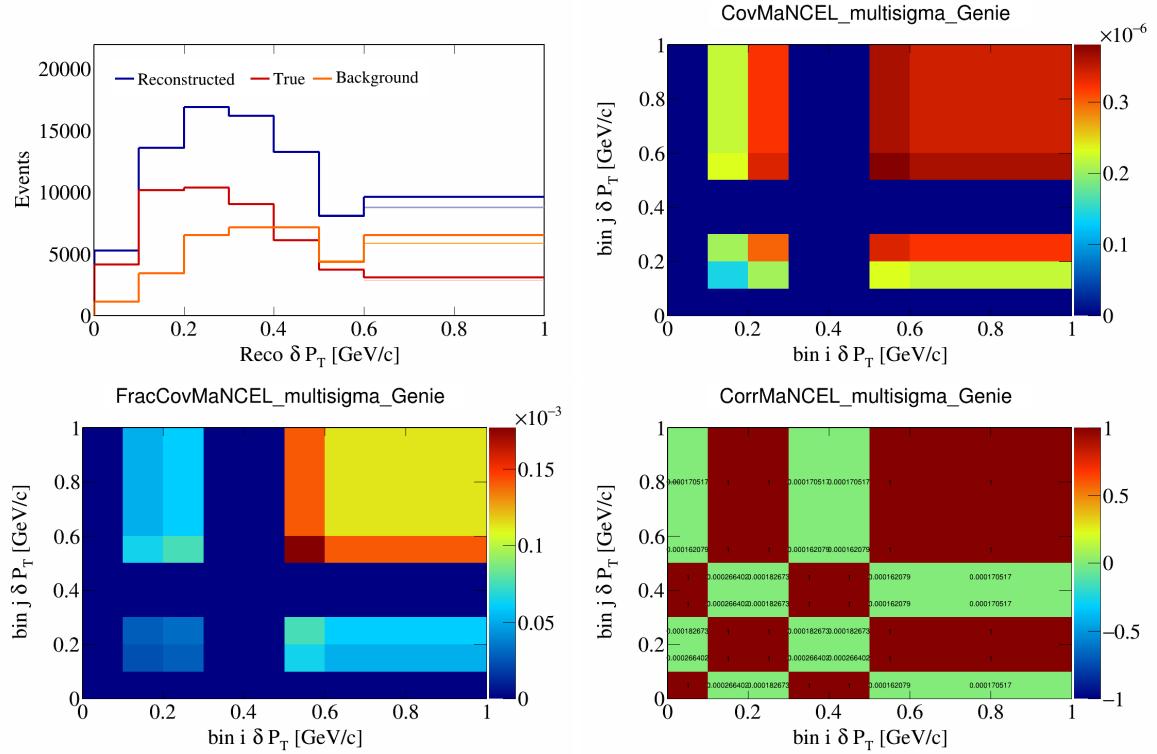


Figure 342: MaNCEL variations for δP_T .

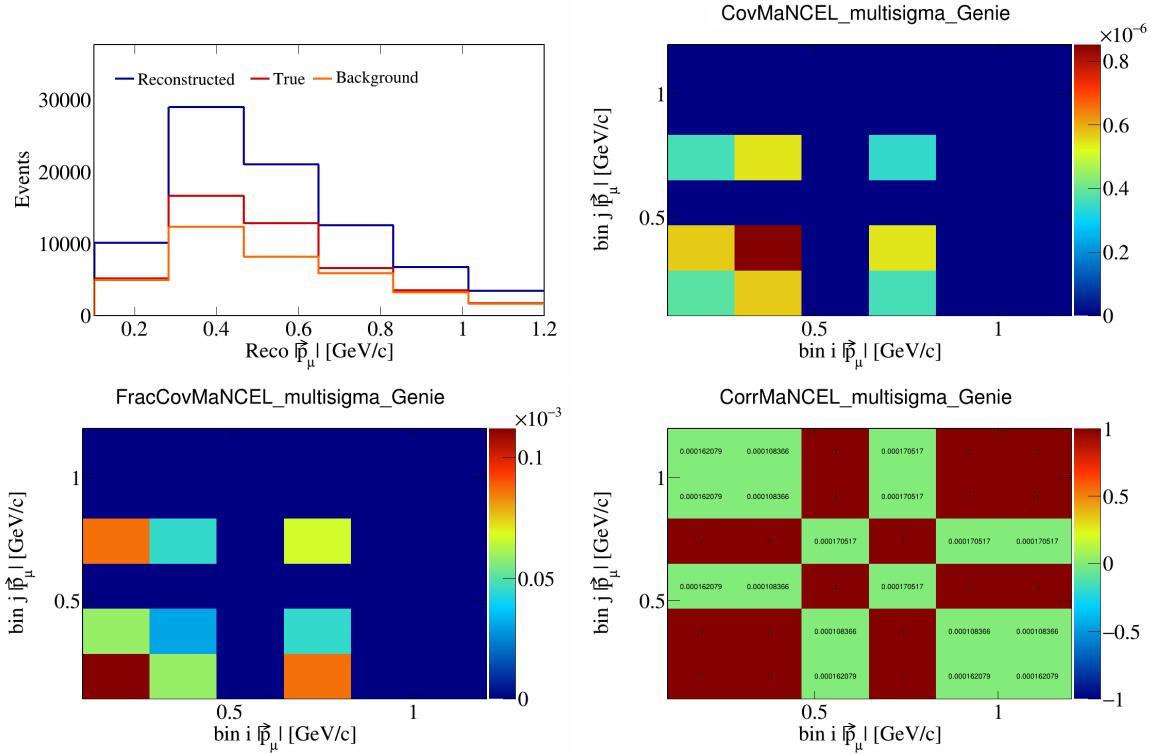


Figure 343: MaNCEL variations for $|\vec{p}_\mu|$.

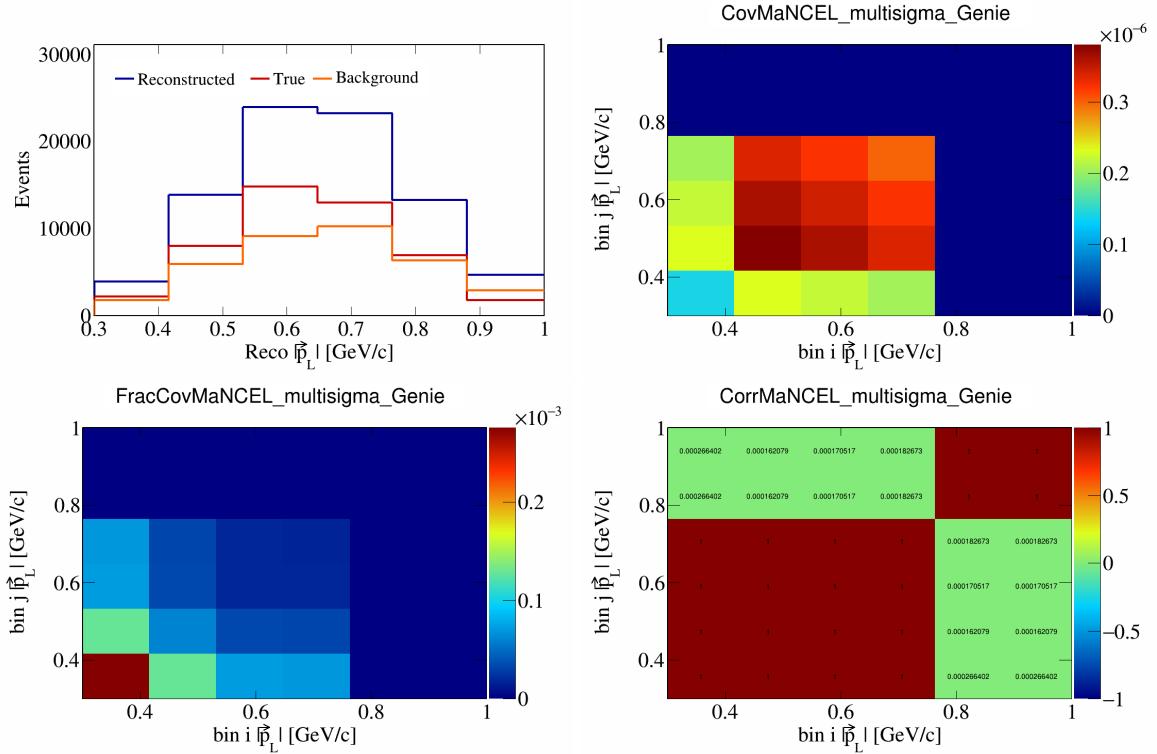


Figure 344: MaNCEL variations for $|\vec{p}_L|$.

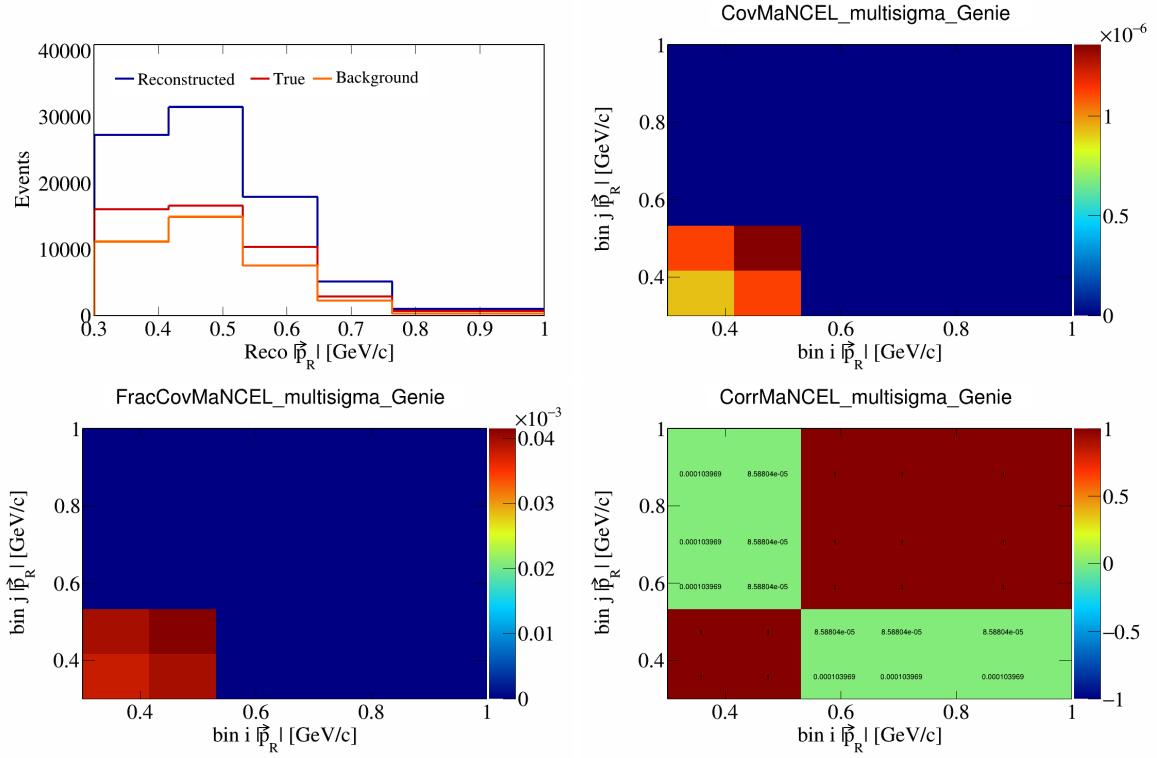


Figure 345: MaNCEL variations for $|\vec{p}_R|$.

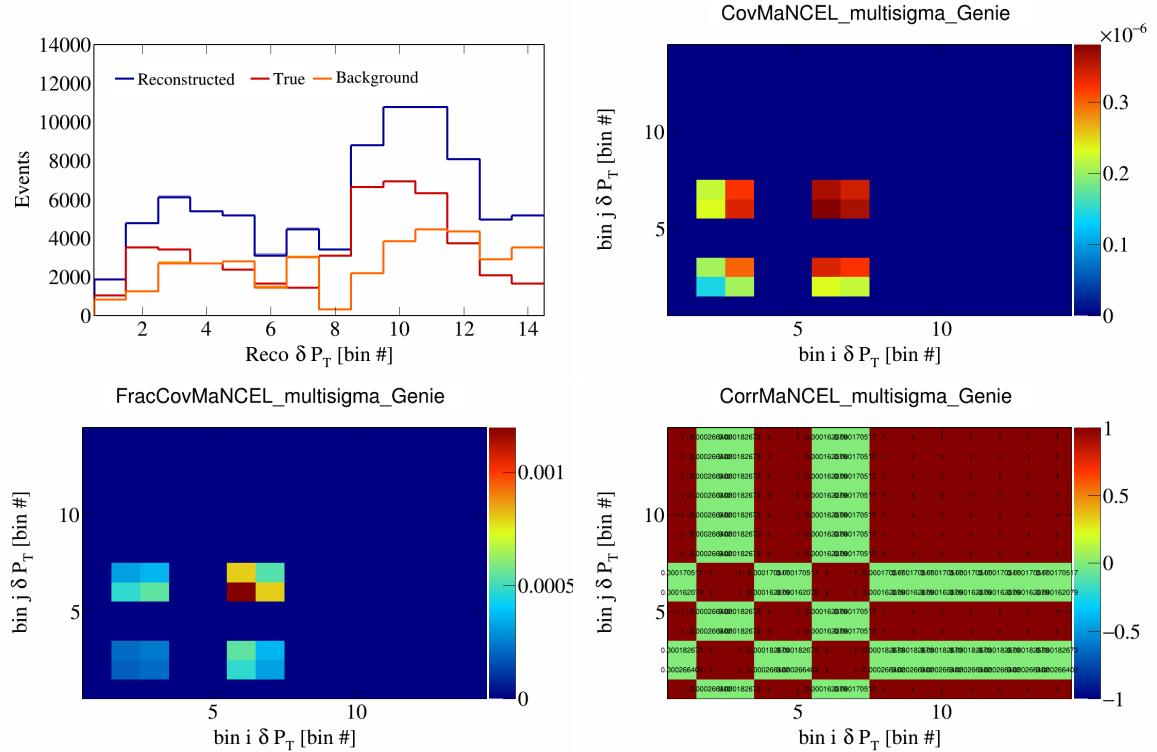


Figure 346: MaNCEL variations for δP_T in $\cos(\theta_{\vec{p}_\mu})$.

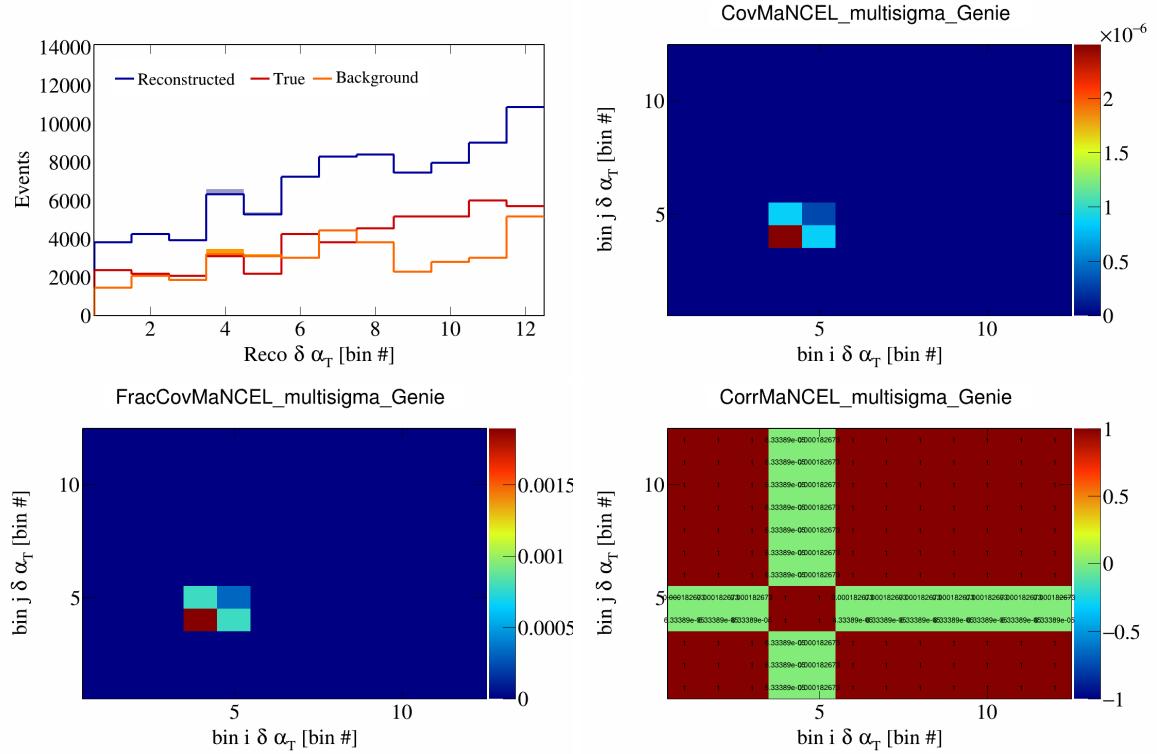


Figure 347: MaNCEL variations for $\delta\alpha_T$ in $\cos(\theta_{\vec{p}_\mu})$.

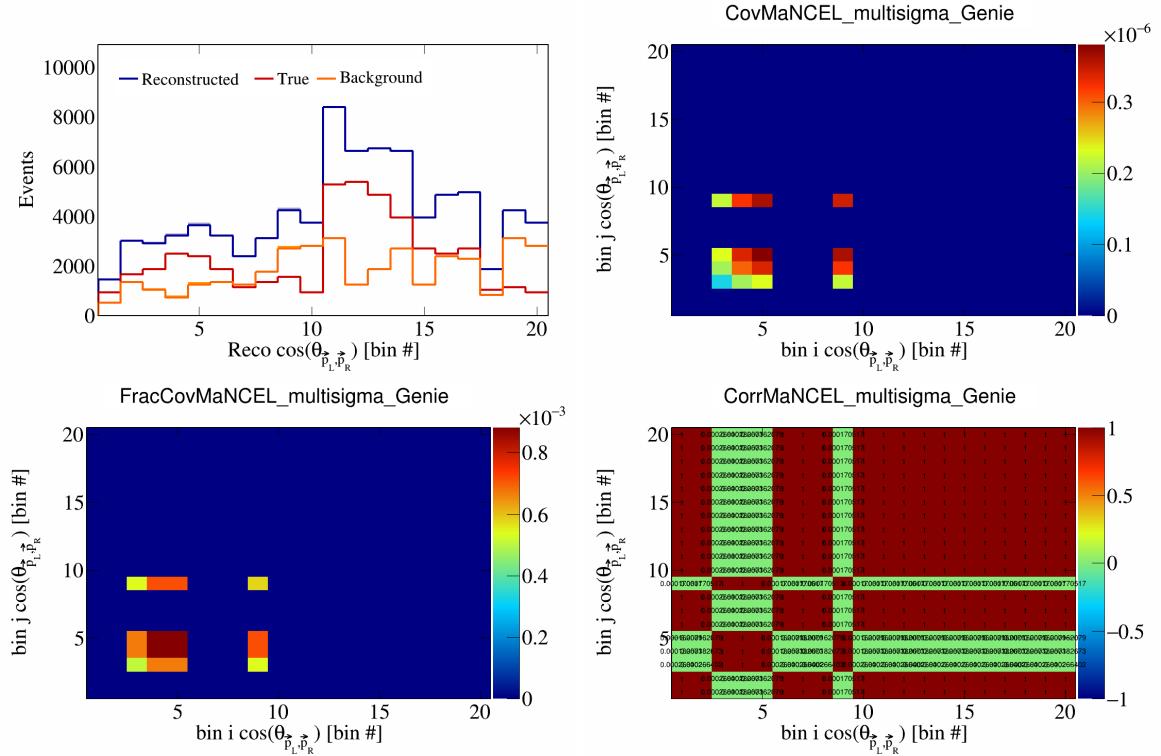


Figure 348: MaNCEL variations for $\cos(\theta_{\vec{p}_L, \vec{p}_R})$ in $\cos(\theta_{\vec{p}_\mu})$.

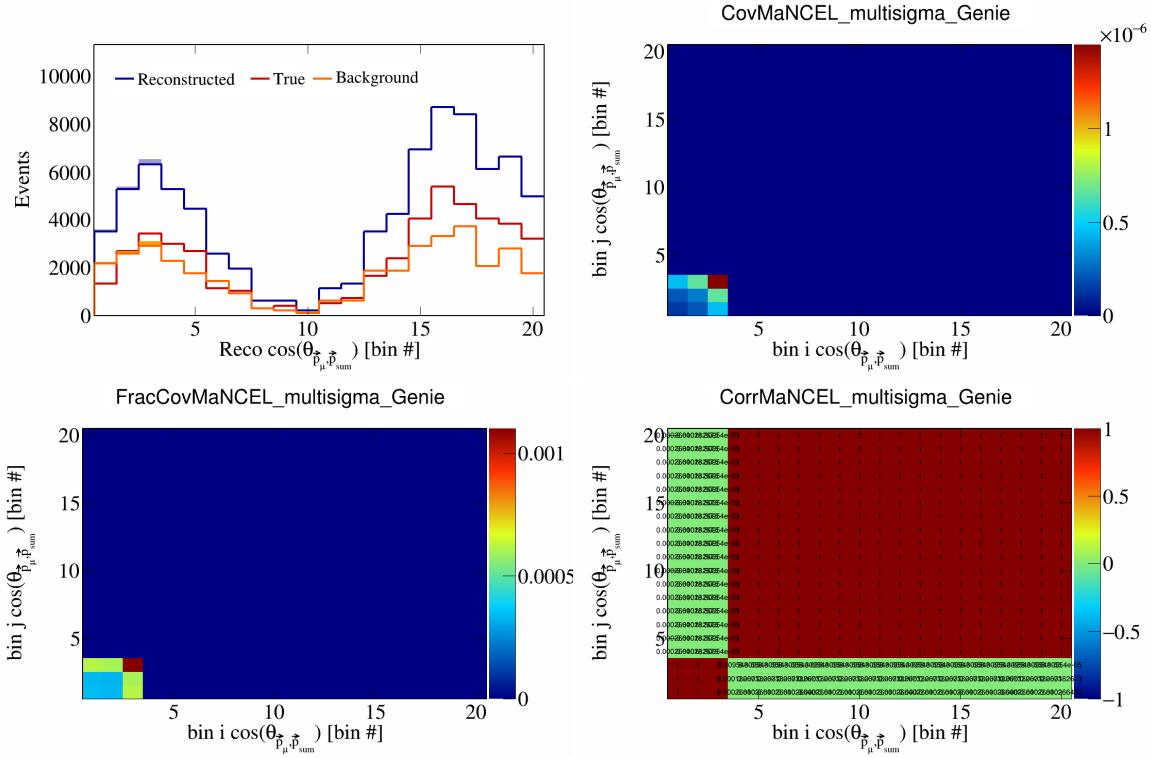


Figure 349: MaNCEL variations for $\cos(\theta_{\vec{p}_\mu, \vec{p}_{\text{sum}}})$ in $\cos(\theta_{\vec{p}_\mu})$.

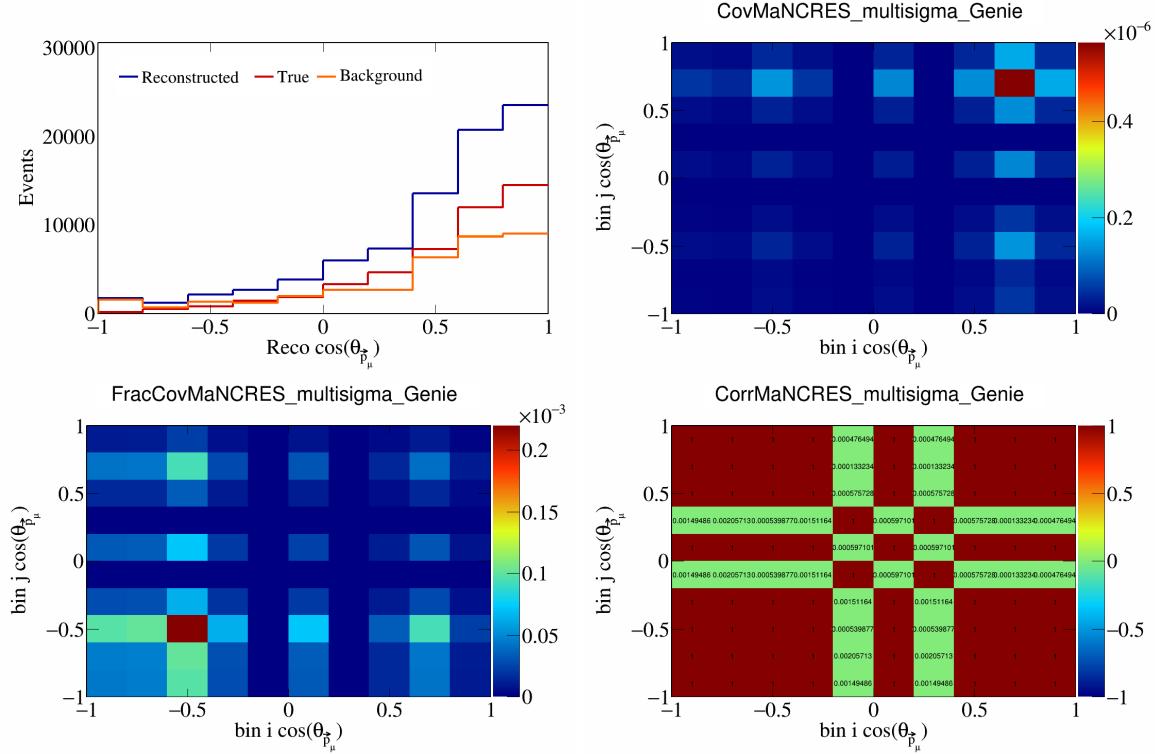


Figure 350: MaNCRES variations for $\cos(\theta_{\vec{p}_\mu, \vec{p}_{\text{sum}}})$.

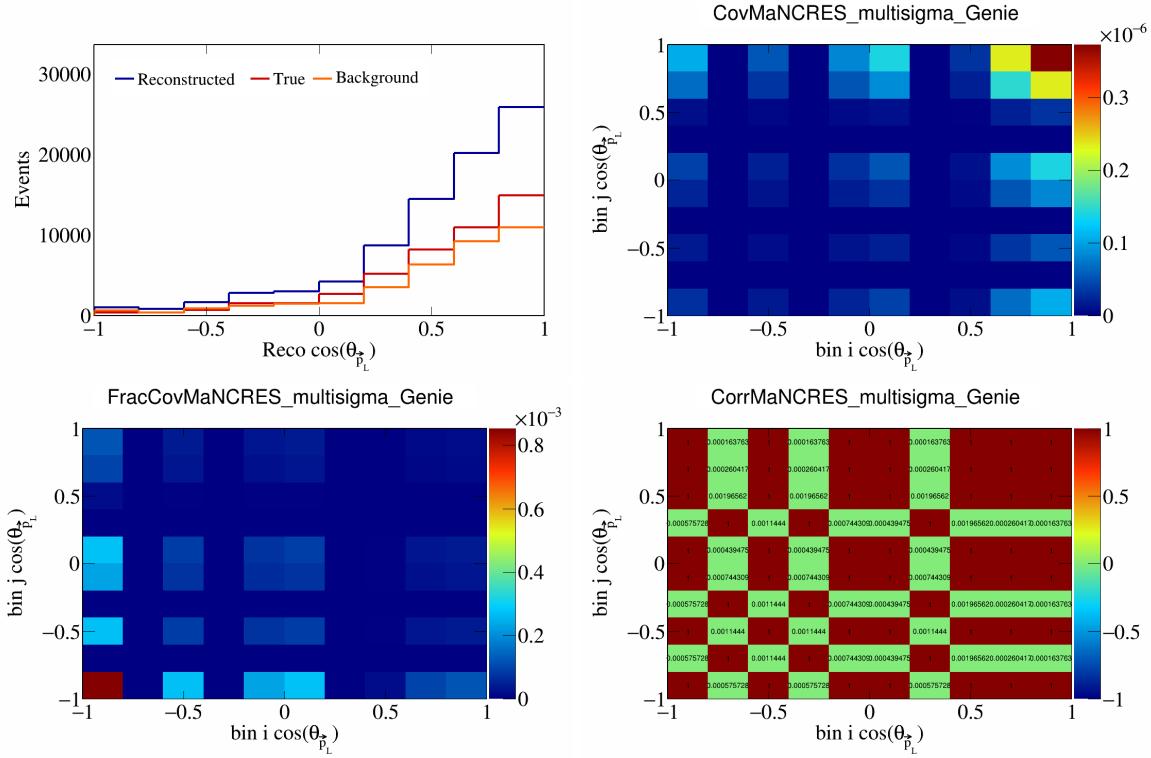


Figure 351: MaNCRES variations for $\cos(\theta_{\vec{p}_L})$.

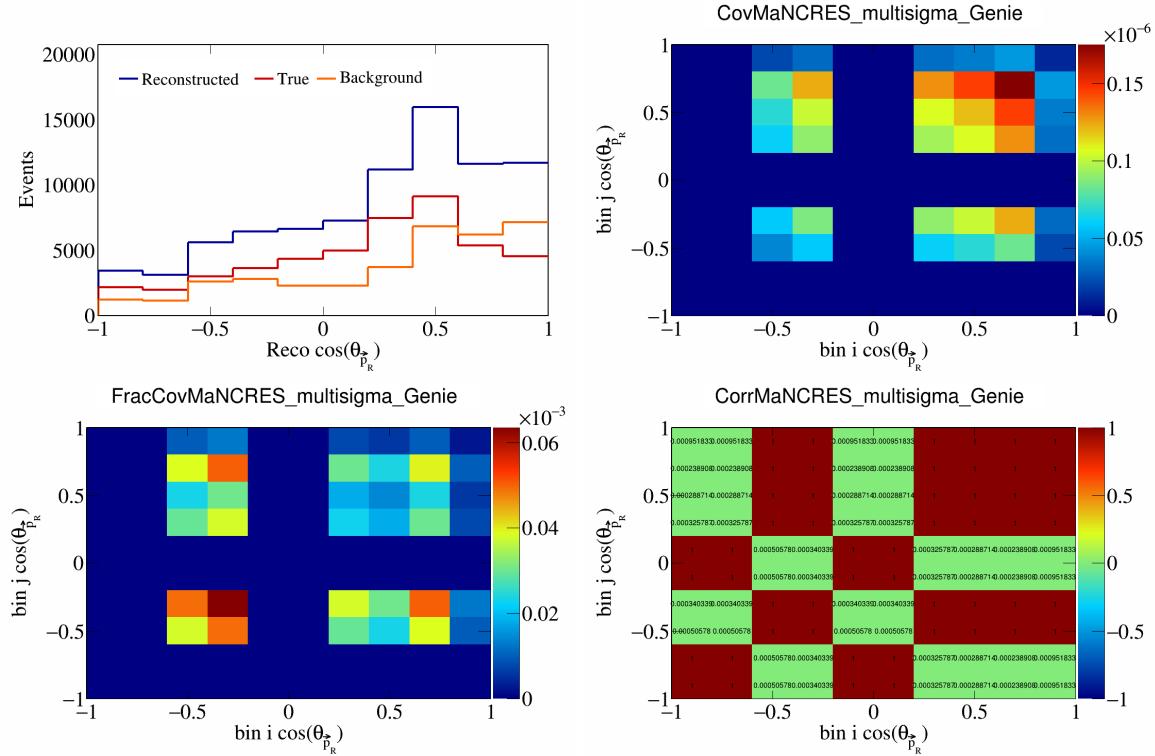


Figure 352: MaNCRES variations for $\cos(\theta_{\vec{p}_R})$.

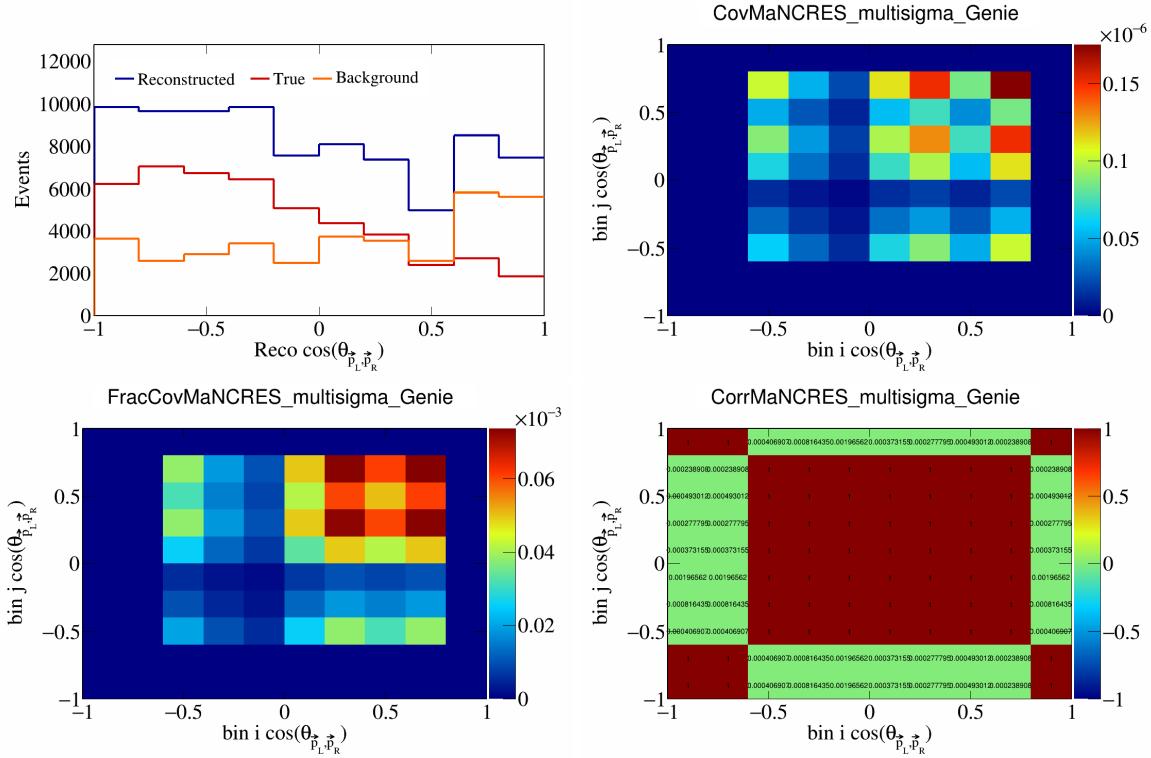


Figure 353: MaNCRES variations for $\cos(\theta_{\vec{p}_L, \vec{p}_R})$.

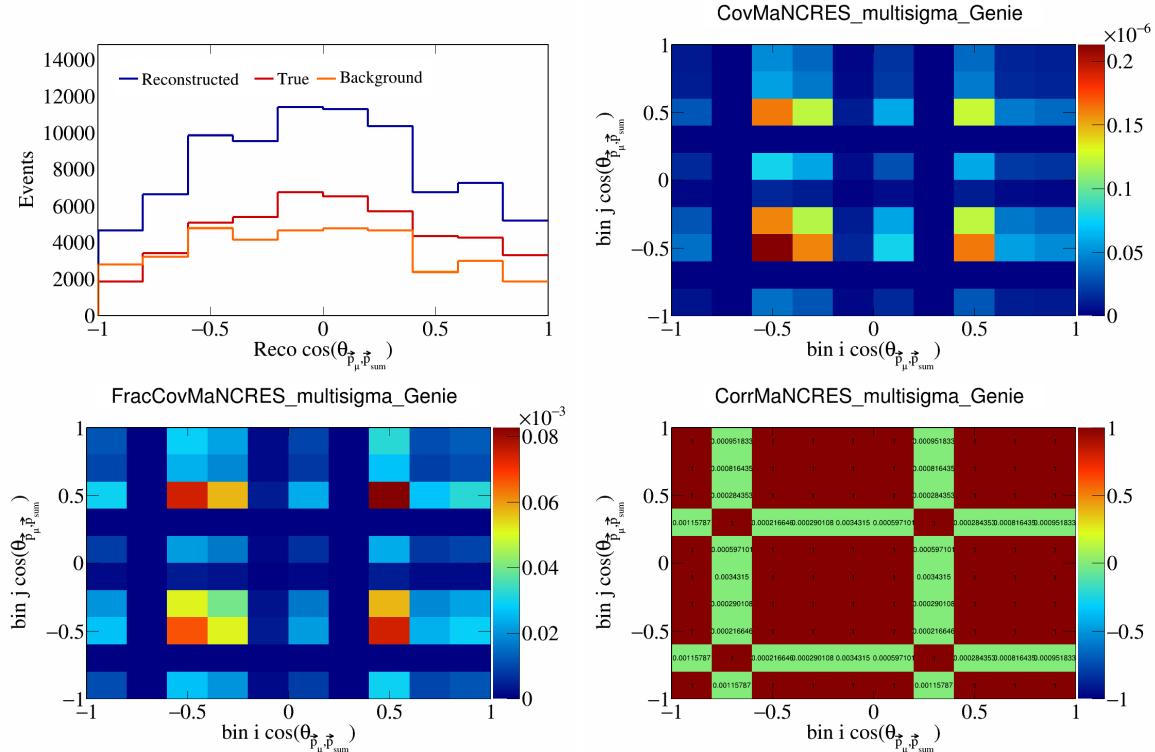


Figure 354: MaNCRES variations for $\cos(\theta_{\vec{p}_\mu, \vec{p}_{\text{sum}}})$.

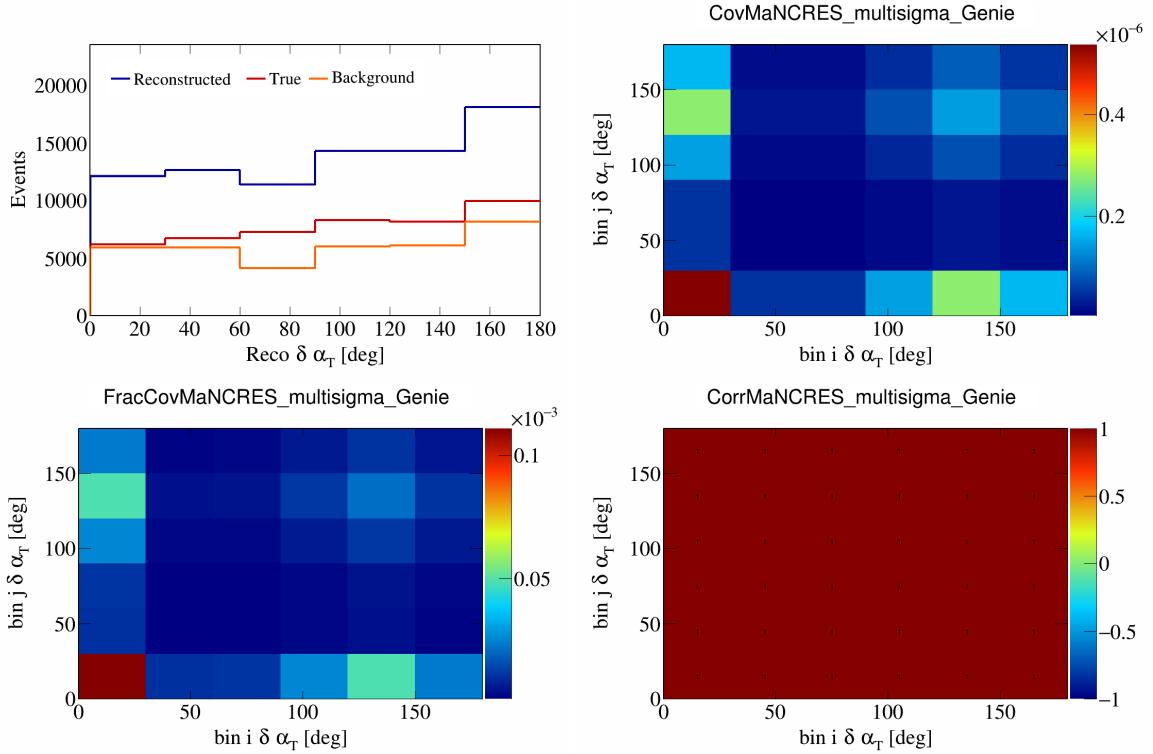


Figure 355: MaNCRES variations for $\delta\alpha_T$.

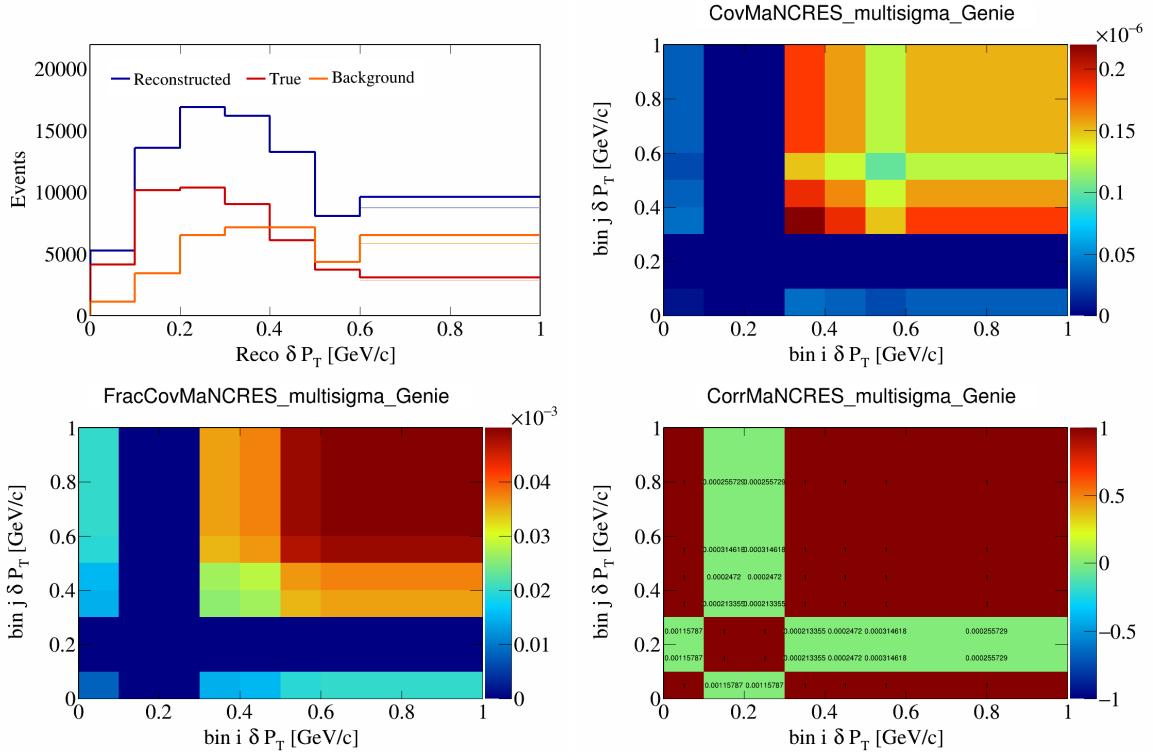


Figure 356: MaNCRES variations for δP_T .

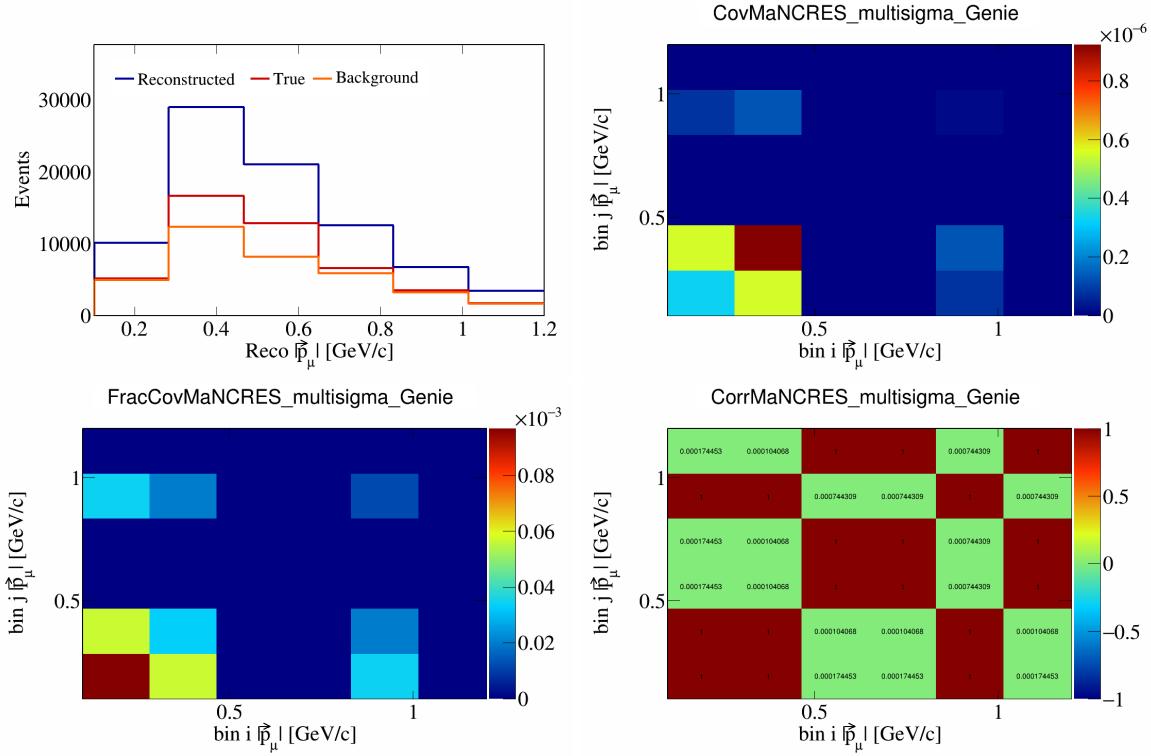


Figure 357: MaNCRES variations for $|\vec{p}_\mu|$.

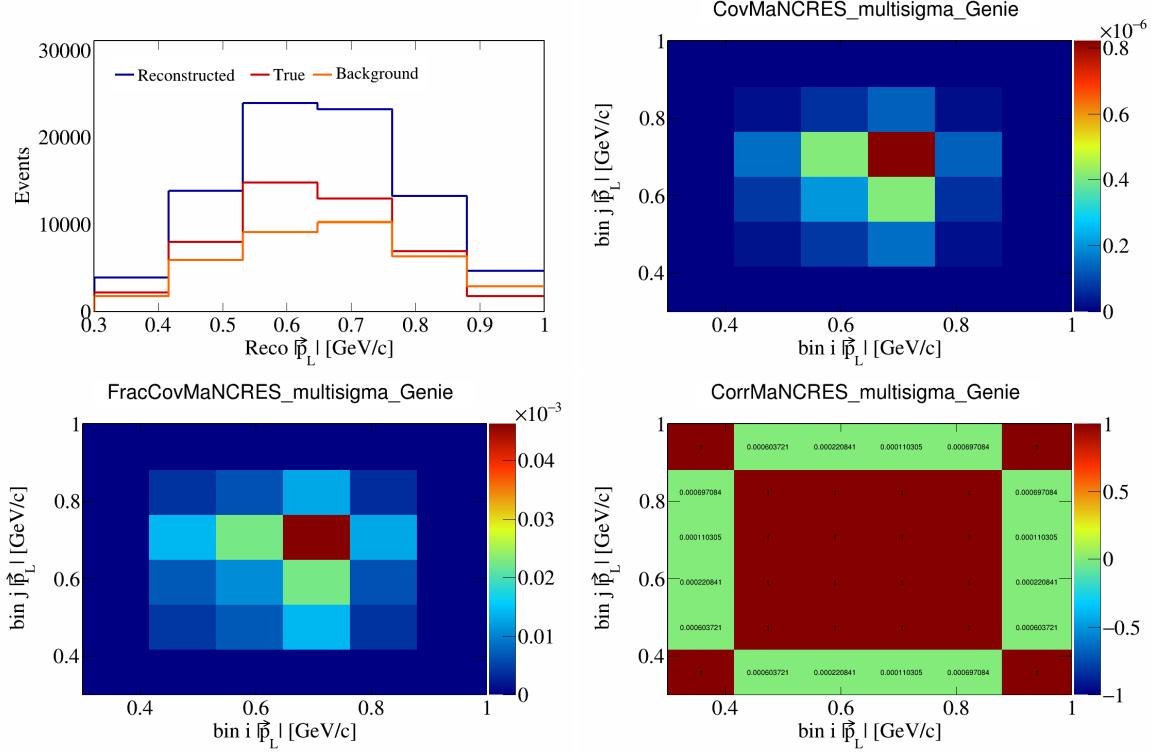


Figure 358: MaNCRES variations for $|\vec{p}_L|$.

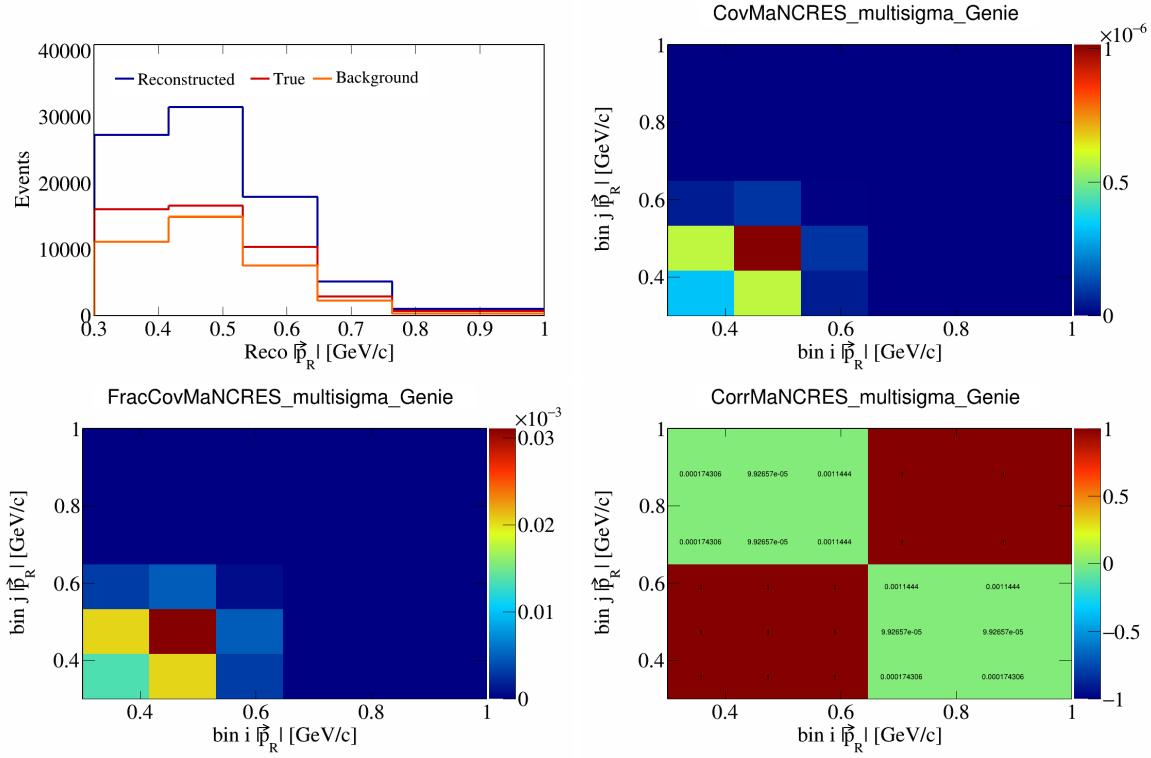


Figure 359: MaNCRES variations for $|\vec{p}_R|$.

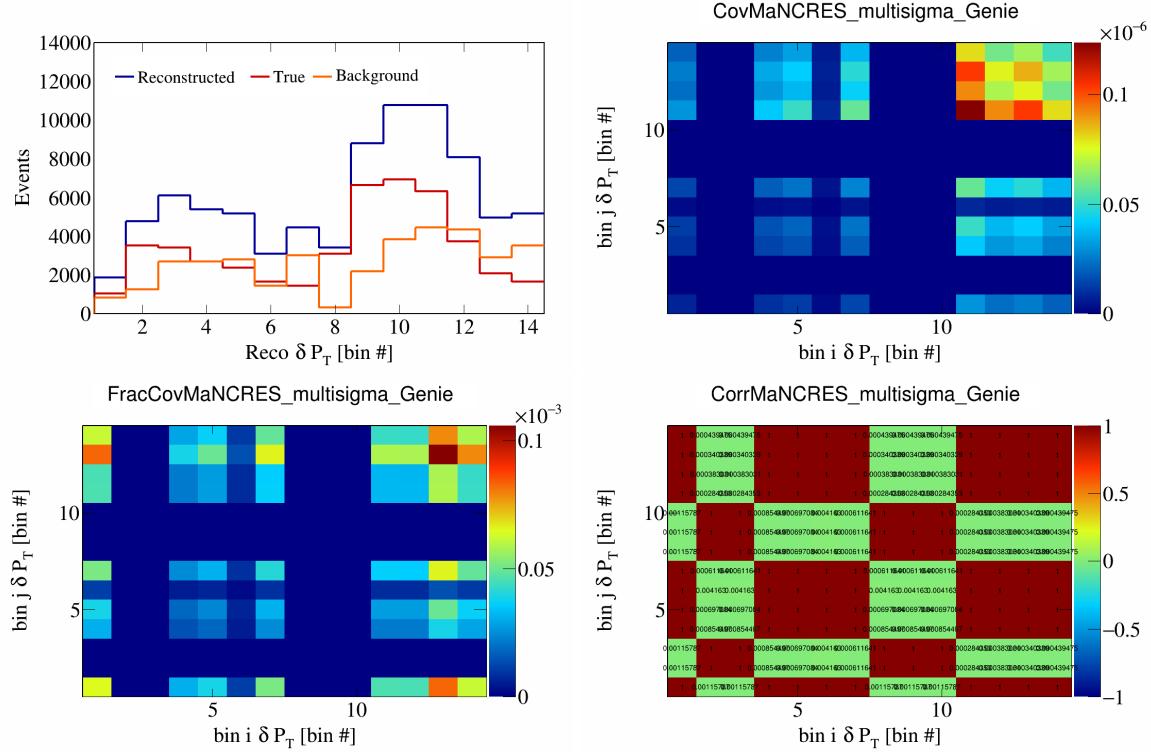


Figure 360: MaNCRES variations for δP_T in $\cos(\theta_{\vec{p}_\mu})$.

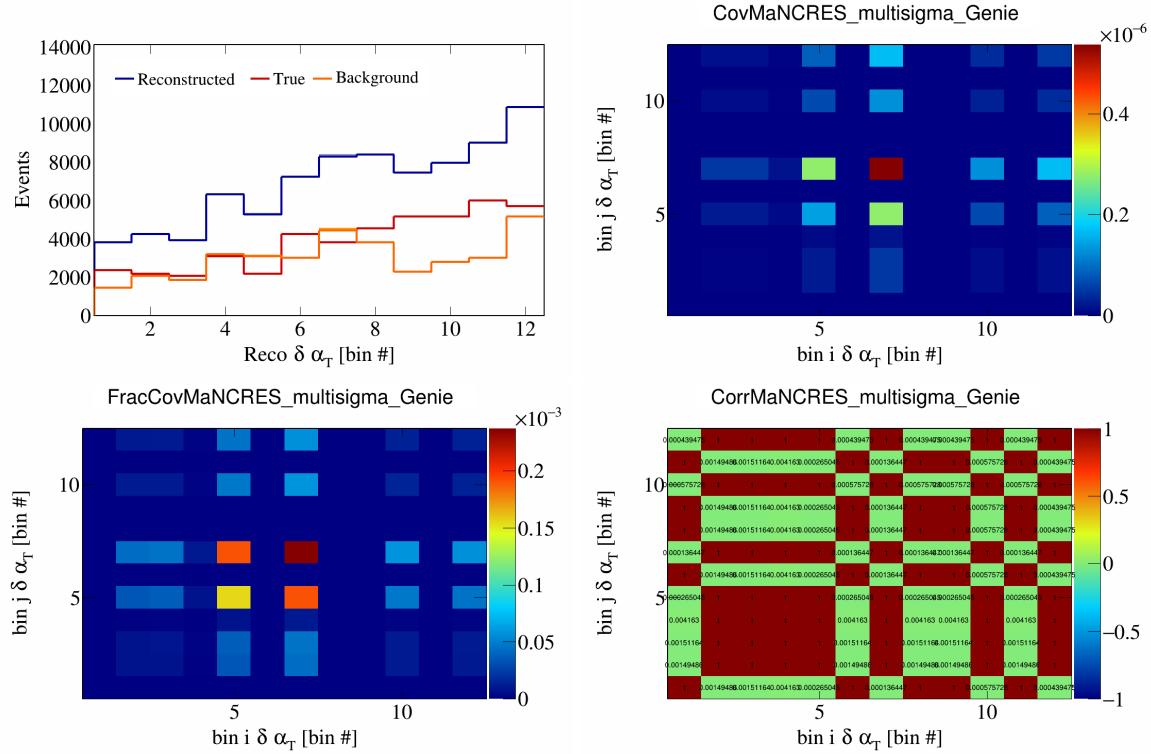


Figure 361: MaNCRES variations for $\delta\alpha_T$ in $\cos(\theta_{\vec{p}_\mu})$.

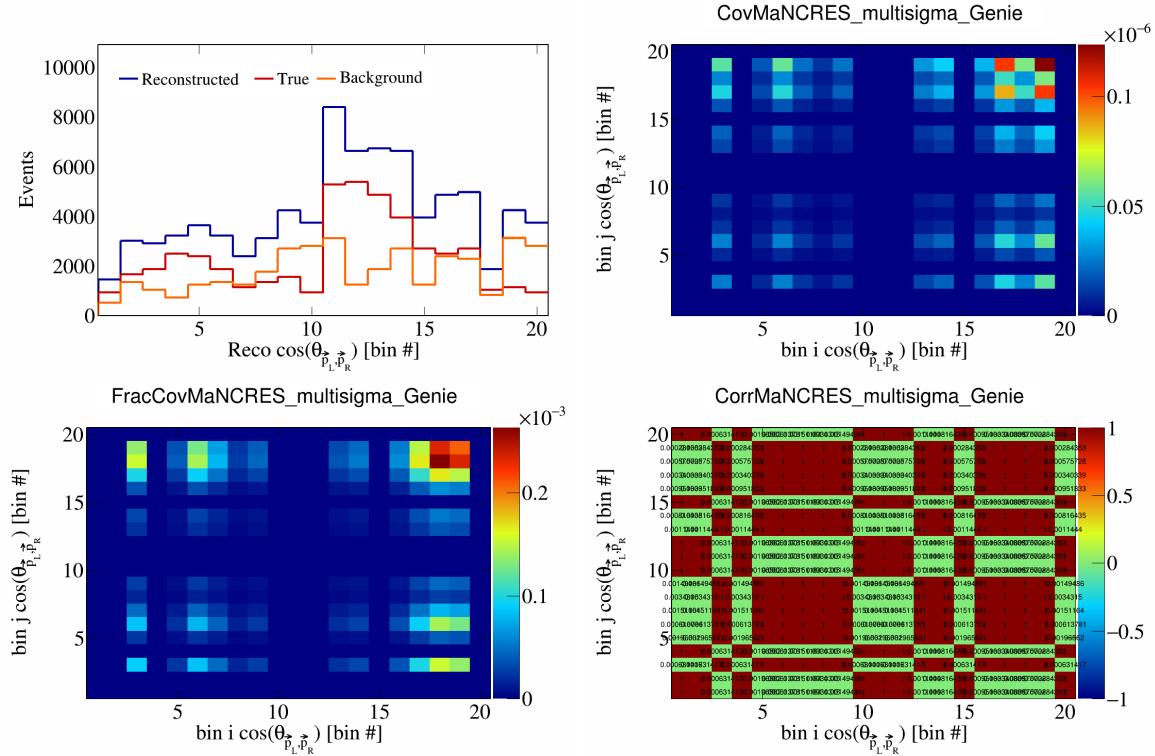


Figure 362: MaNCRES variations for $\cos(\theta_{\vec{p}_L, \vec{p}_R})$ in $\cos(\theta_{\vec{p}_\mu})$.

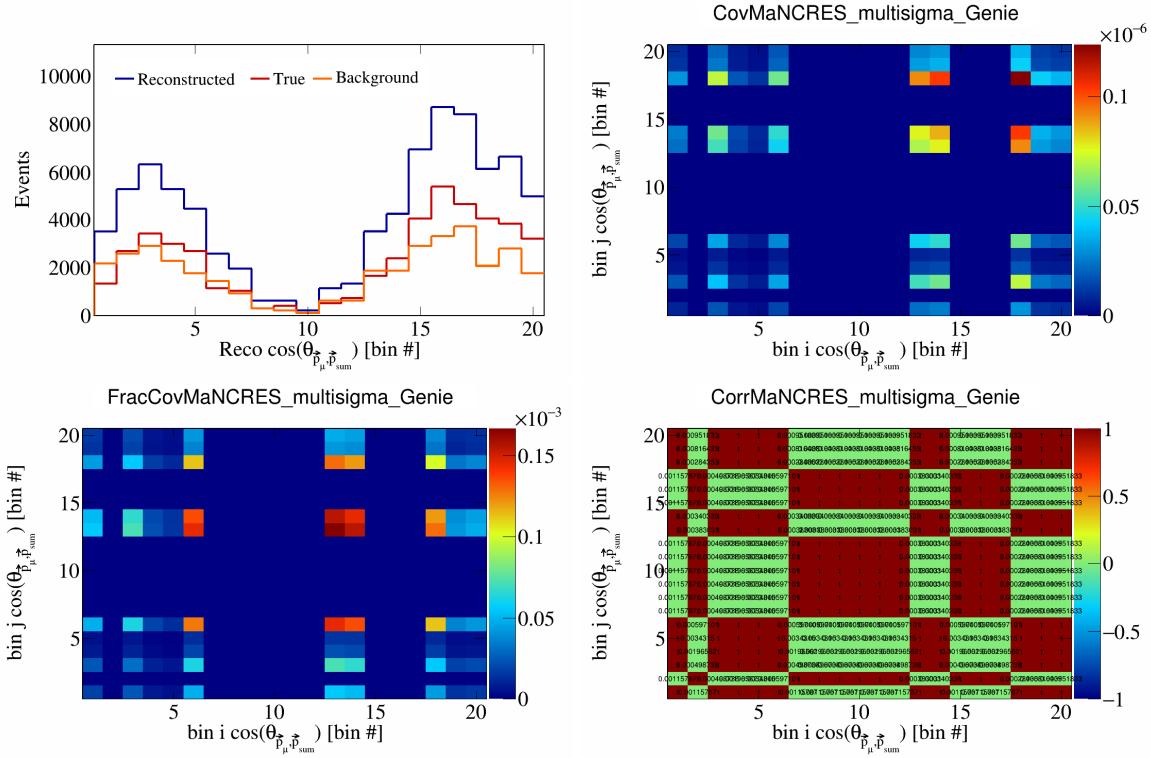


Figure 363: MaNCRES variations for $\cos(\theta_{\vec{p}_\mu, \vec{p}_{\text{sum}}})$ in $\cos(\theta_{\vec{p}_\mu})$.

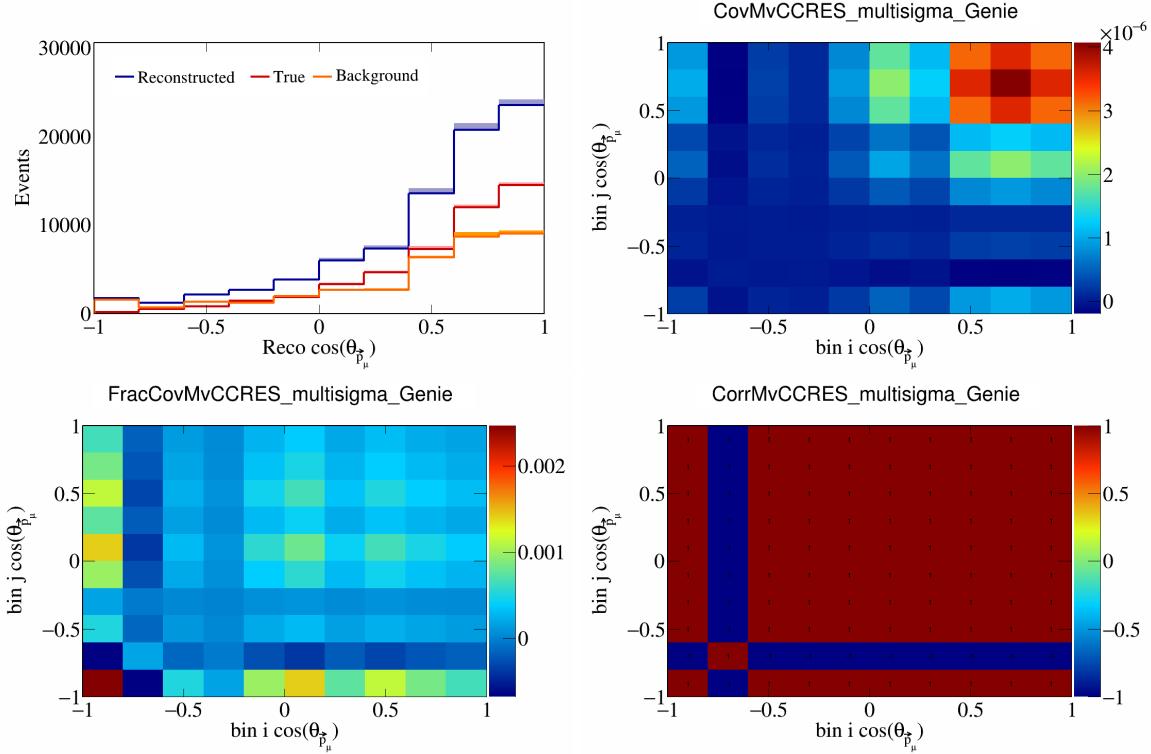


Figure 364: MvCCRES variations for $\cos(\theta_{\vec{p}_\mu})$.

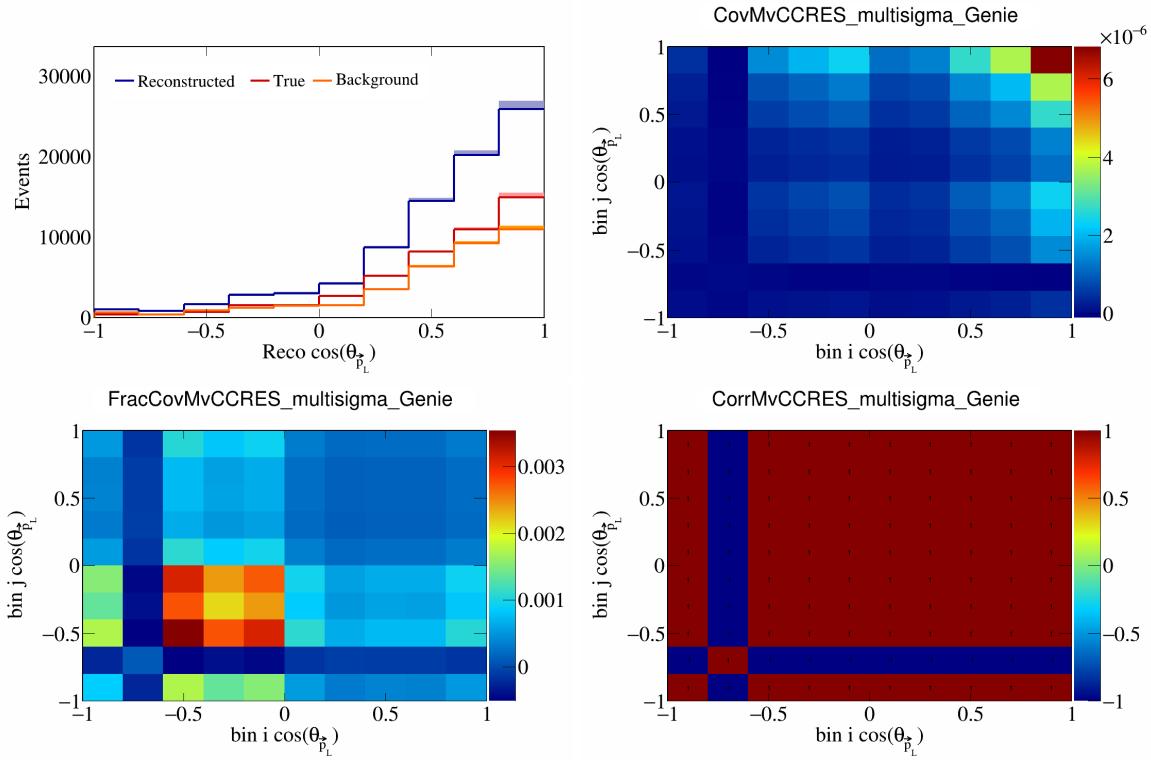


Figure 365: MvCCRES variations for $\cos(\theta_{\vec{p}_L})$.

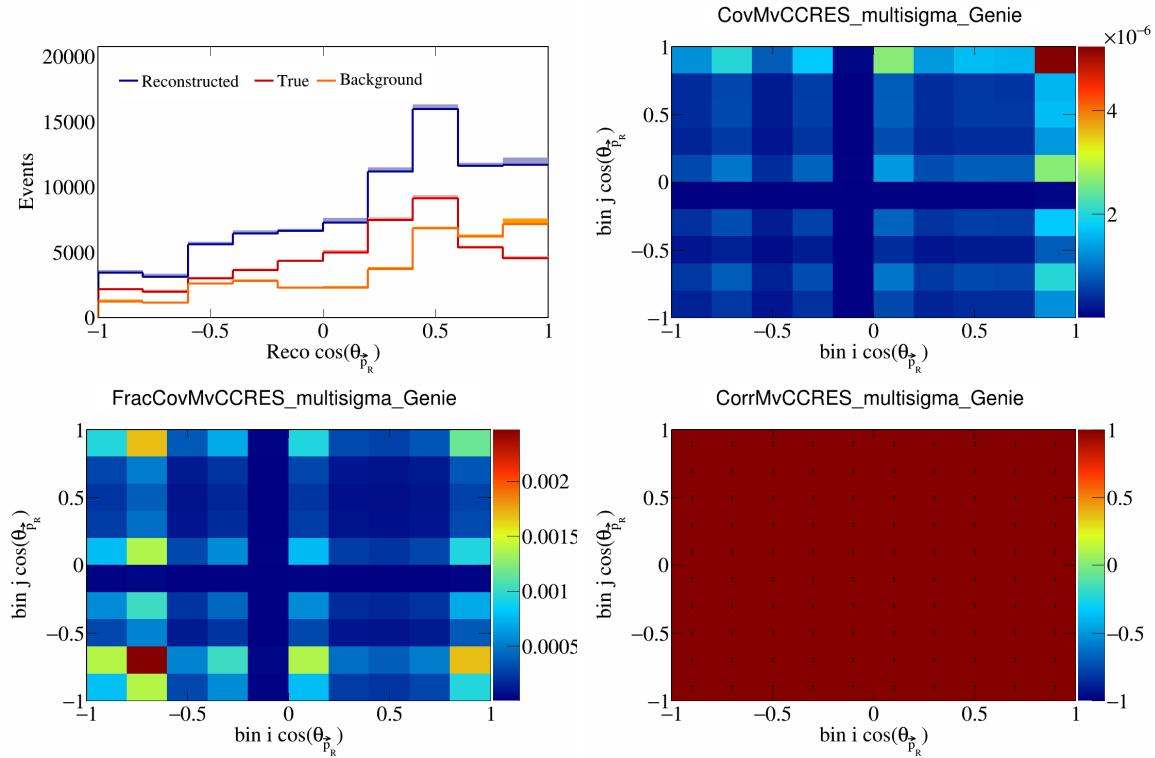


Figure 366: MvCCRES variations for $\cos(\theta_{\vec{p}_R})$.

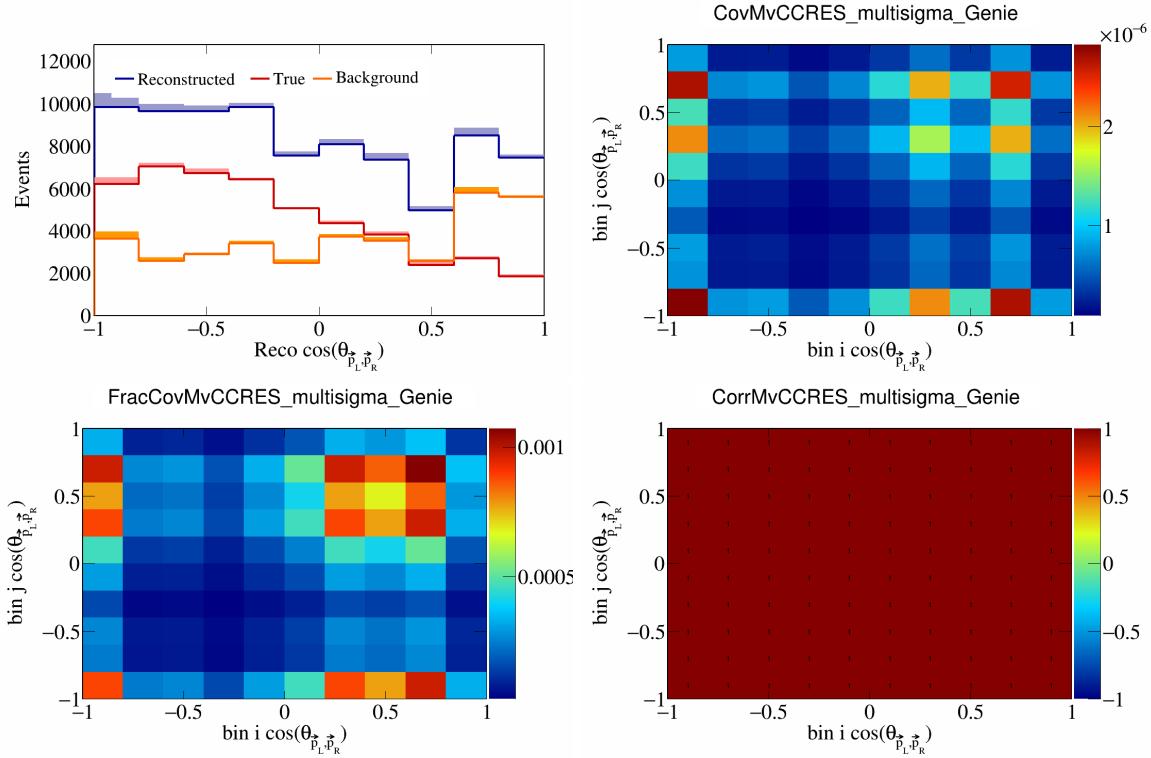


Figure 367: MvCCRES variations for $\cos(\theta_{\vec{p}_L, \vec{p}_R})$.

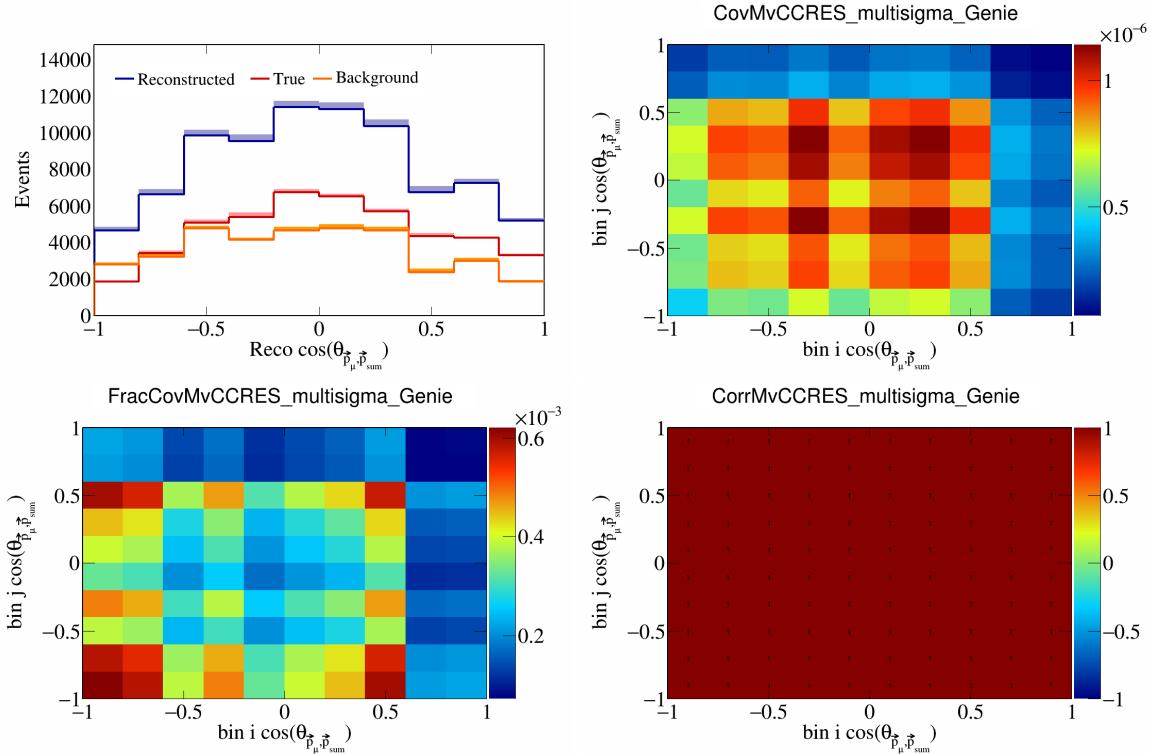


Figure 368: MvCCRES variations for $\cos(\theta_{\vec{p}_\mu, \vec{p}_{\text{sum}}})$.

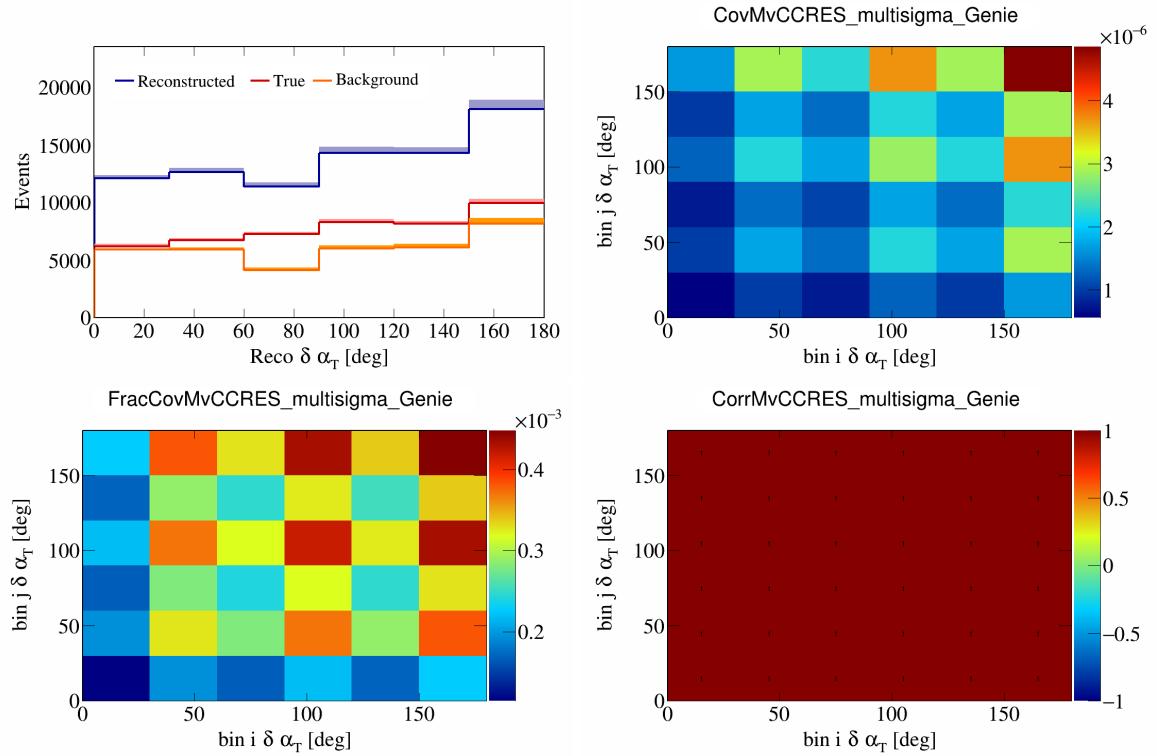


Figure 369: MvCCRES variations for $\delta\alpha_T$.

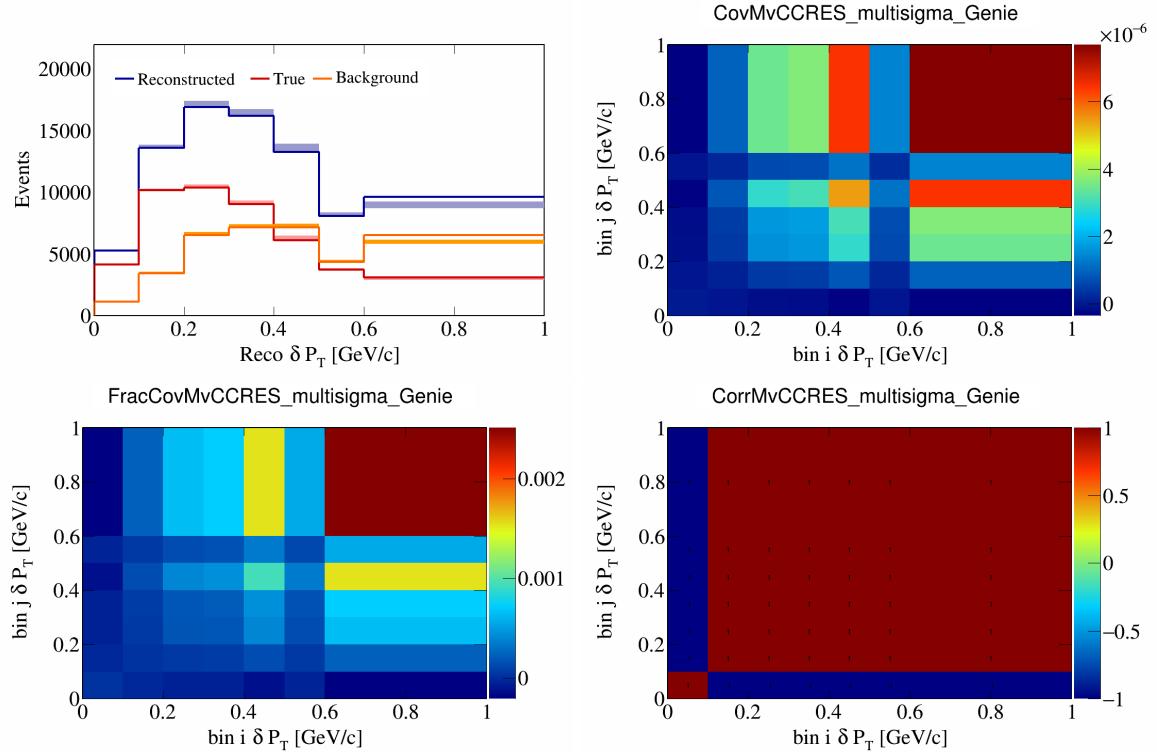


Figure 370: MvCCRES variations for δP_T .

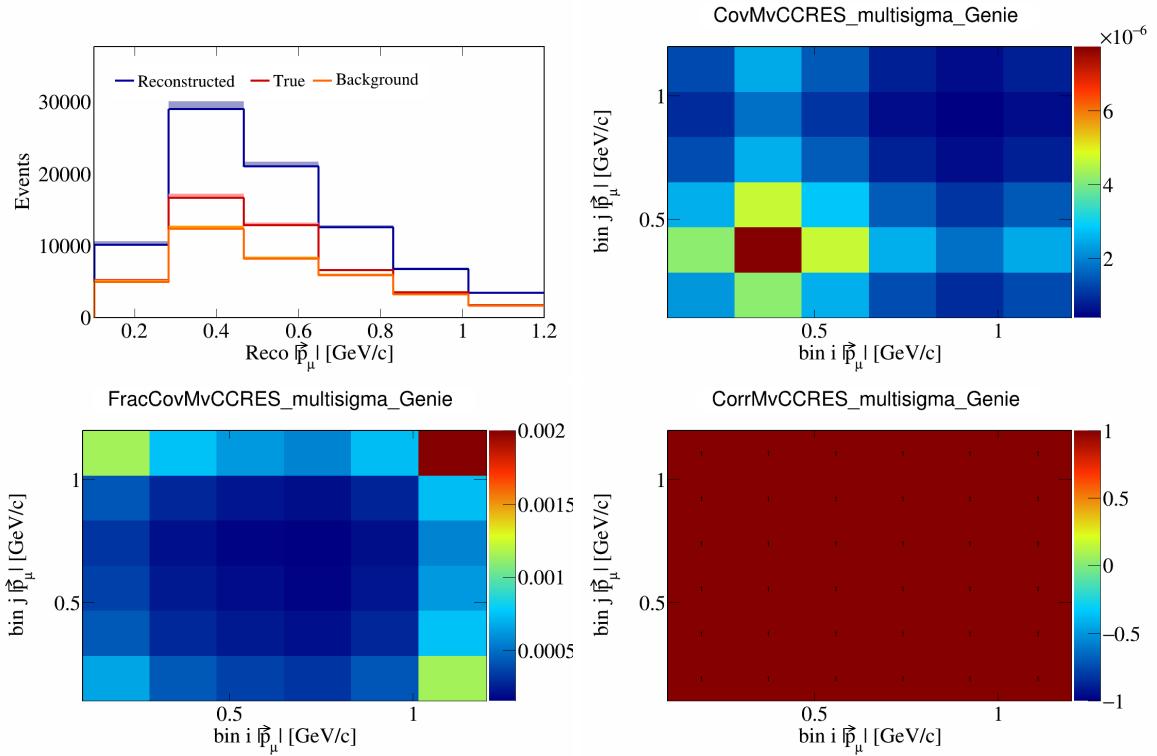


Figure 371: MvCCRES variations for $|\vec{p}_\mu|$.

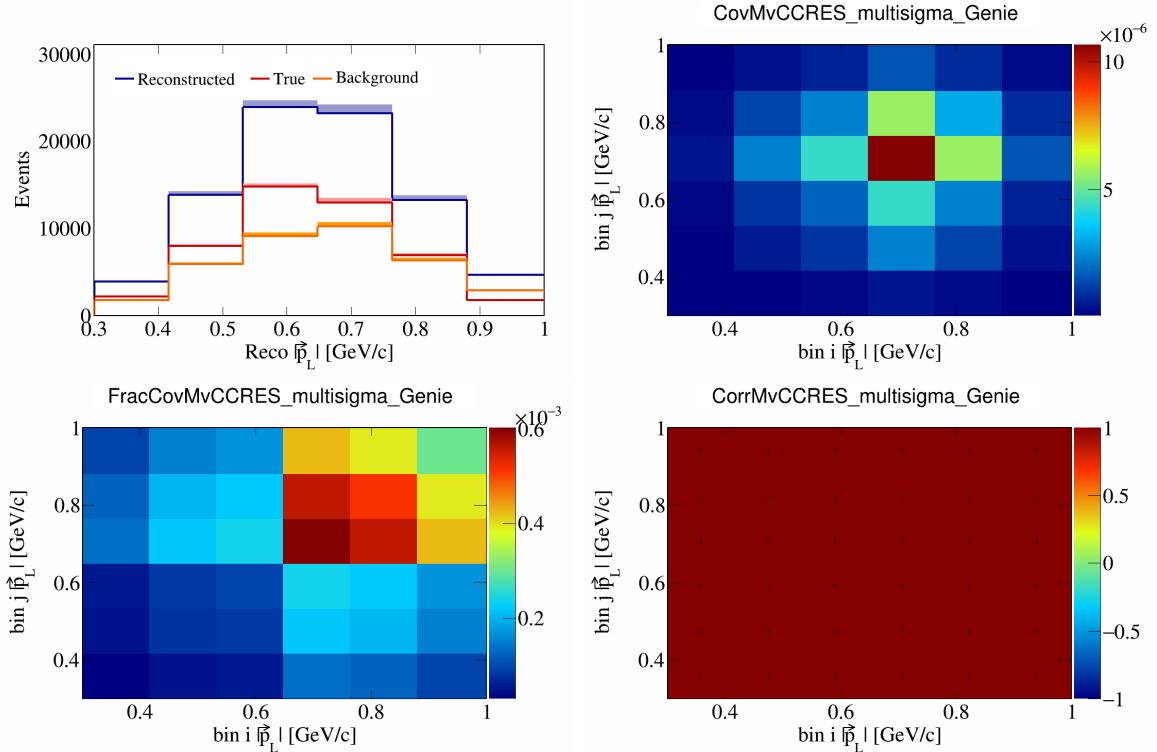


Figure 372: MvCCRES variations for $|\vec{p}_L|$.

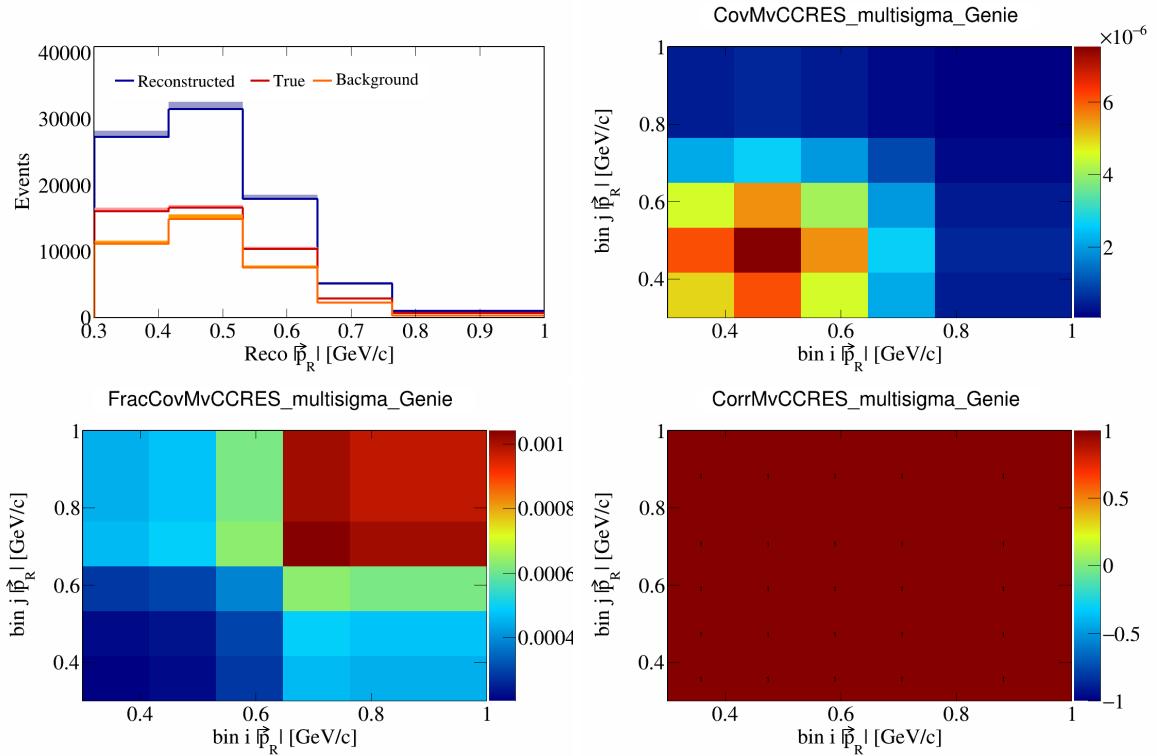


Figure 373: MvCCRES variations for $|\vec{p}_R|$.

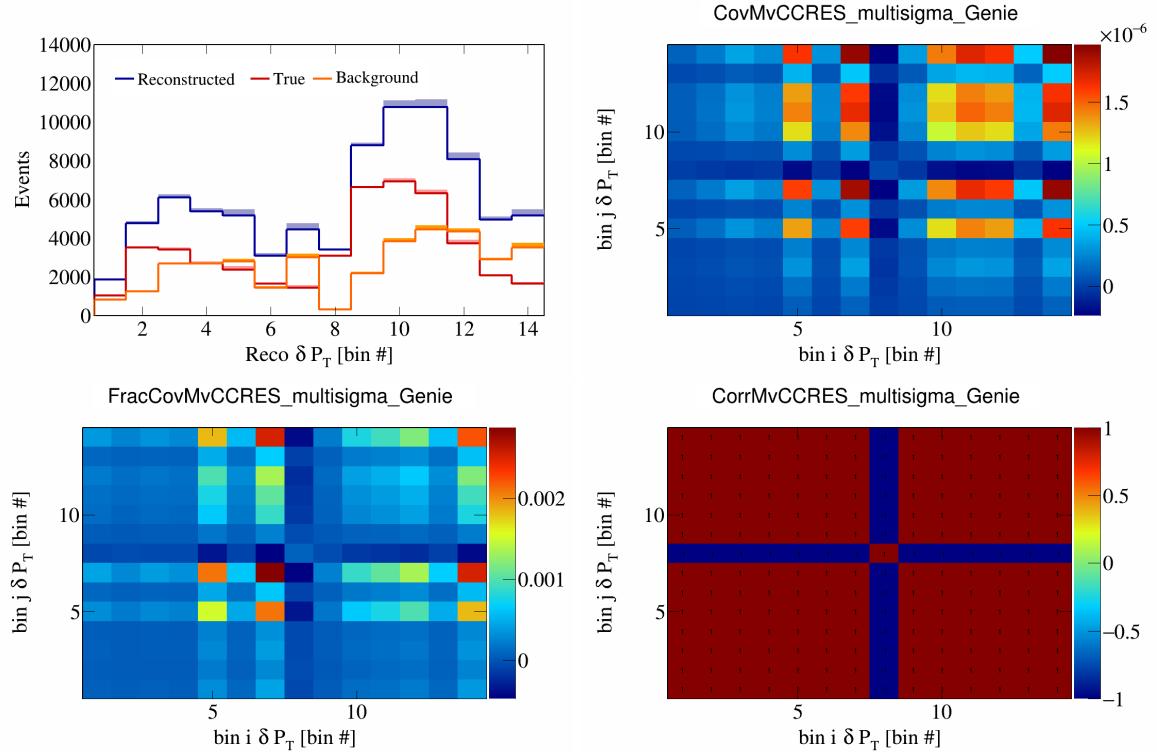


Figure 374: MvCCRES variations for δP_T in $\cos(\theta_{\vec{p}_\mu})$.

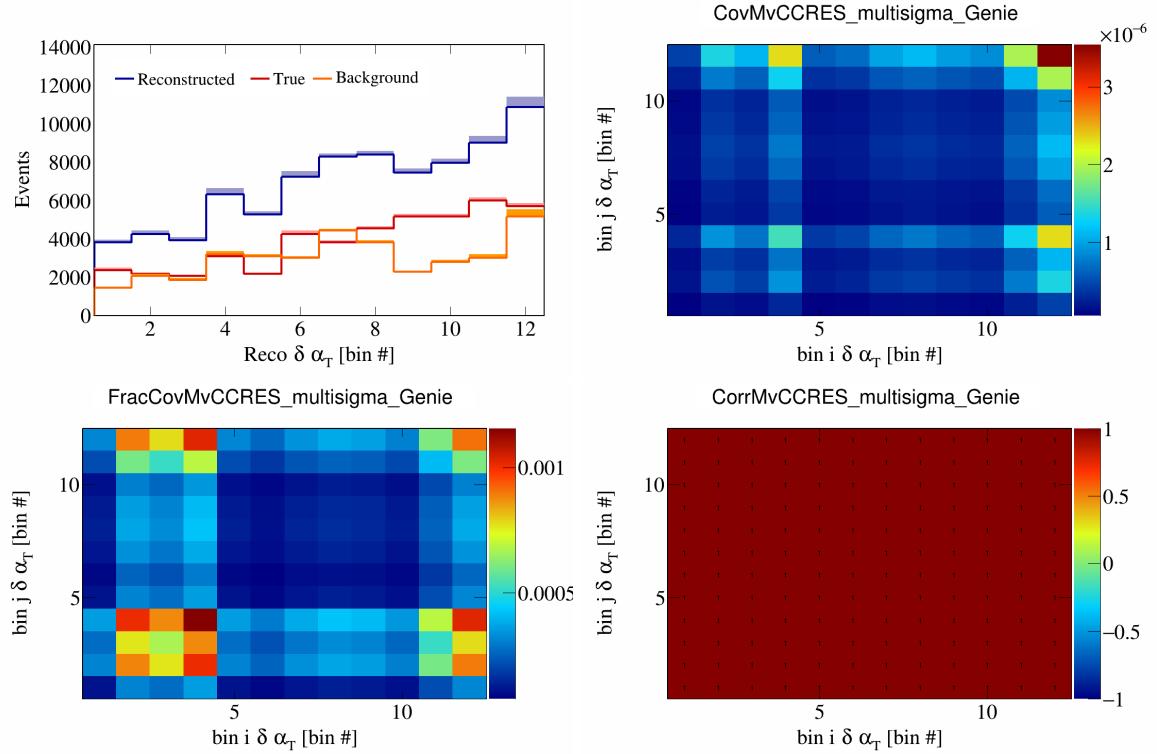


Figure 375: MvCCRES variations for $\delta\alpha_T$ in $\cos(\theta_{\vec{p}_\mu})$.

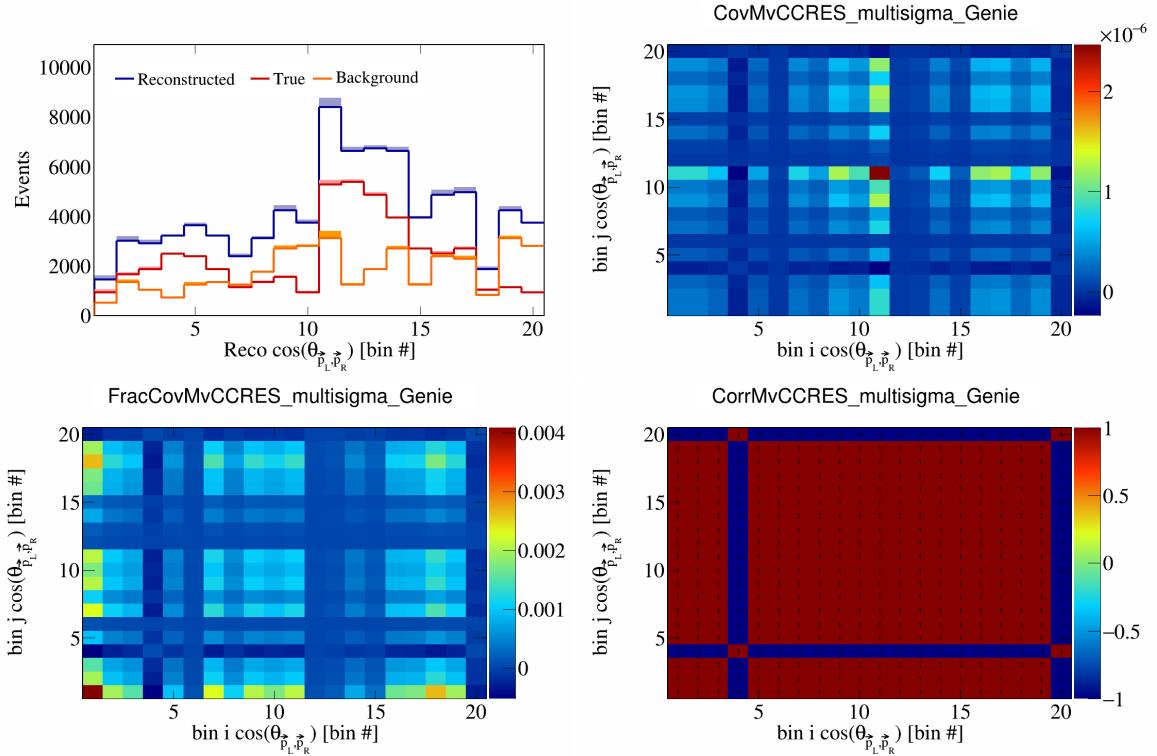


Figure 376: MvCCRES variations for $\cos(\theta_{\vec{p}_L, \vec{p}_R})$ in $\cos(\theta_{\vec{p}_\mu})$.

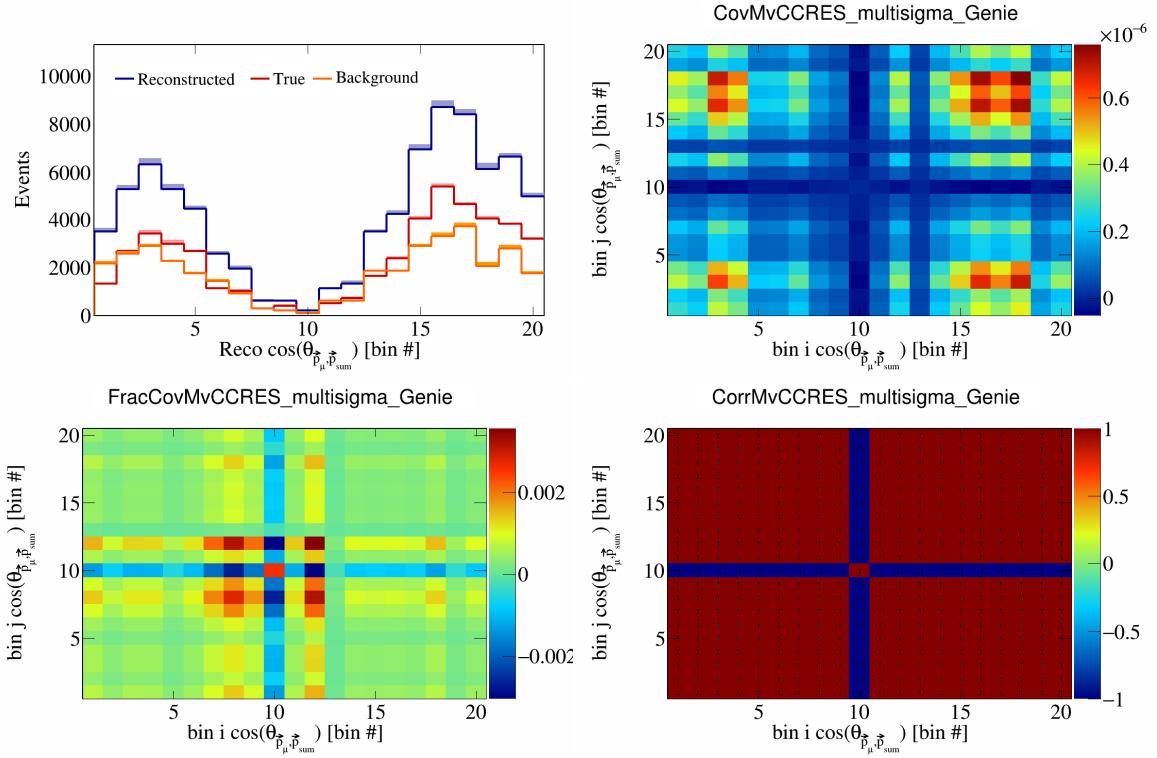


Figure 377: MvCCRES variations for $\cos(\theta_{\vec{p}_\mu, \vec{p}_{\text{sum}}})$ in $\cos(\theta_{\vec{p}_\mu})$.

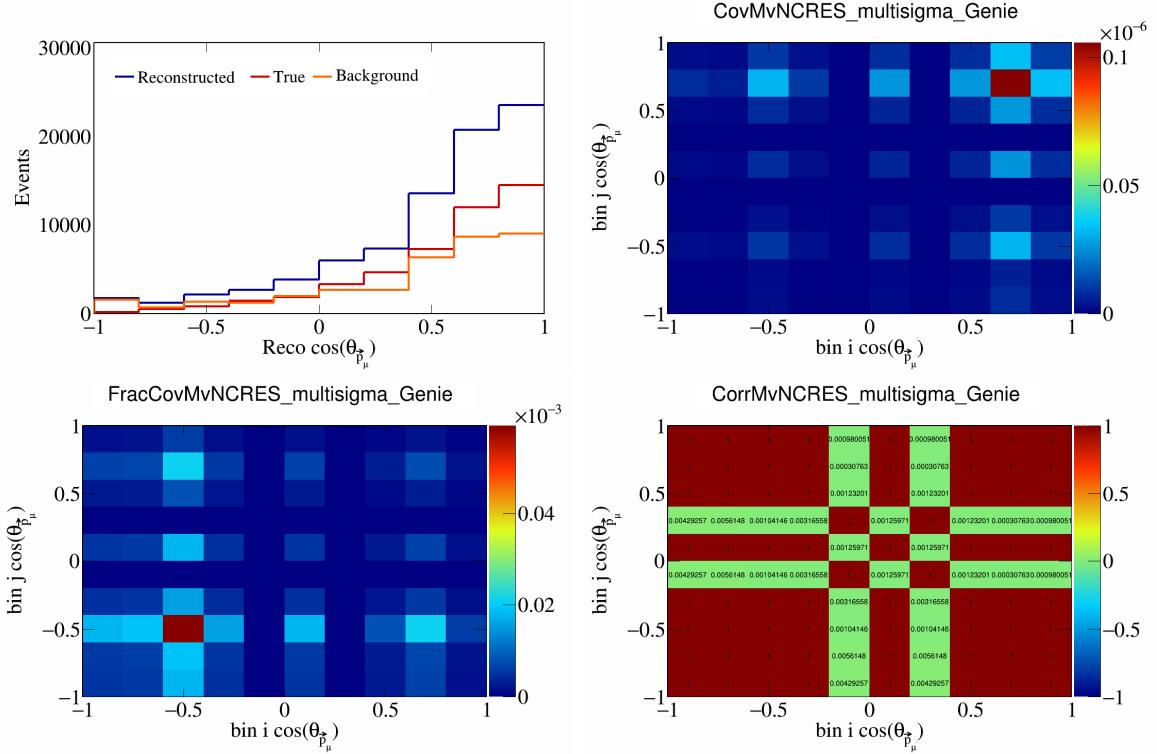


Figure 378: MvNCRES variations for $\cos(\theta_{\vec{p}_\mu})$.

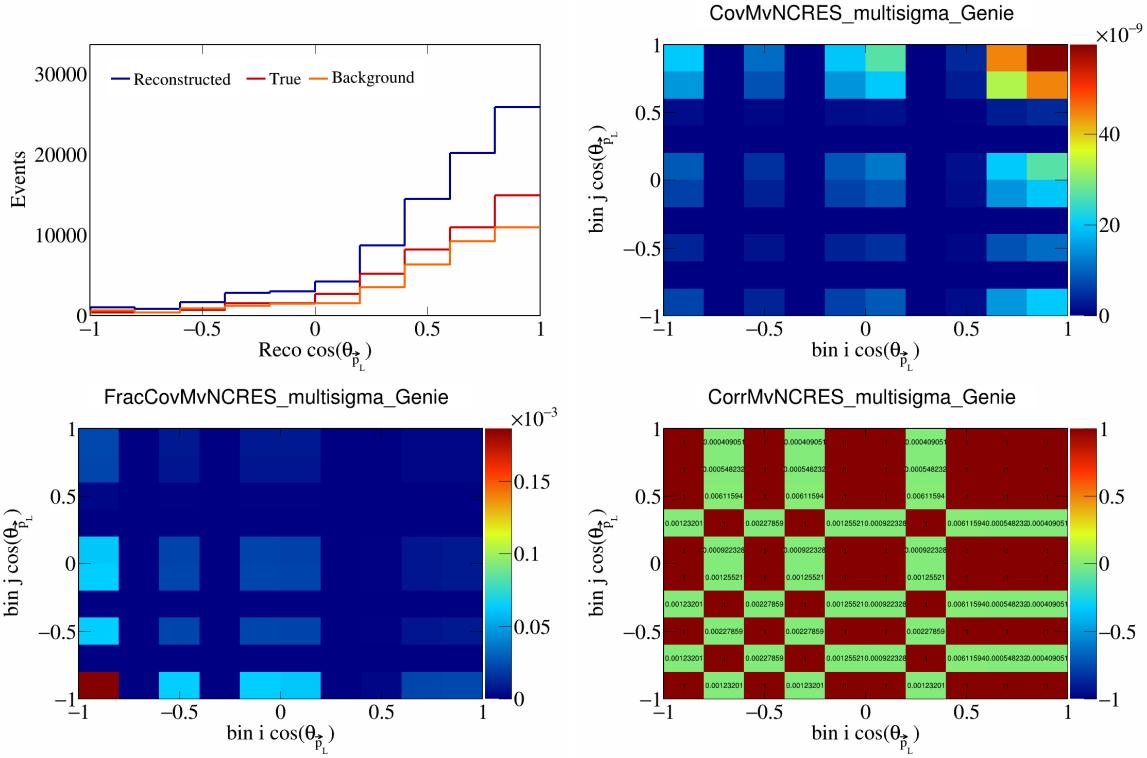


Figure 379: MvNCRES variations for $\cos(\theta_{\vec{p}_L})$.

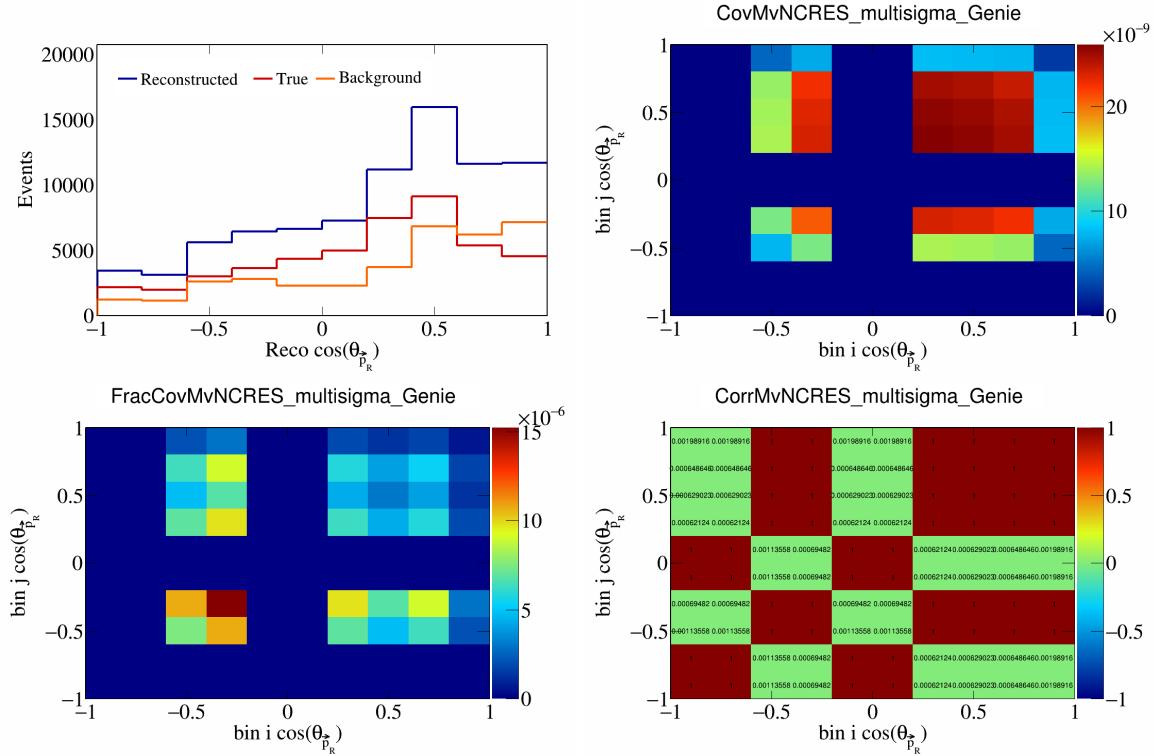


Figure 380: MvNCRES variations for $\cos(\theta_{\vec{p}_R})$.

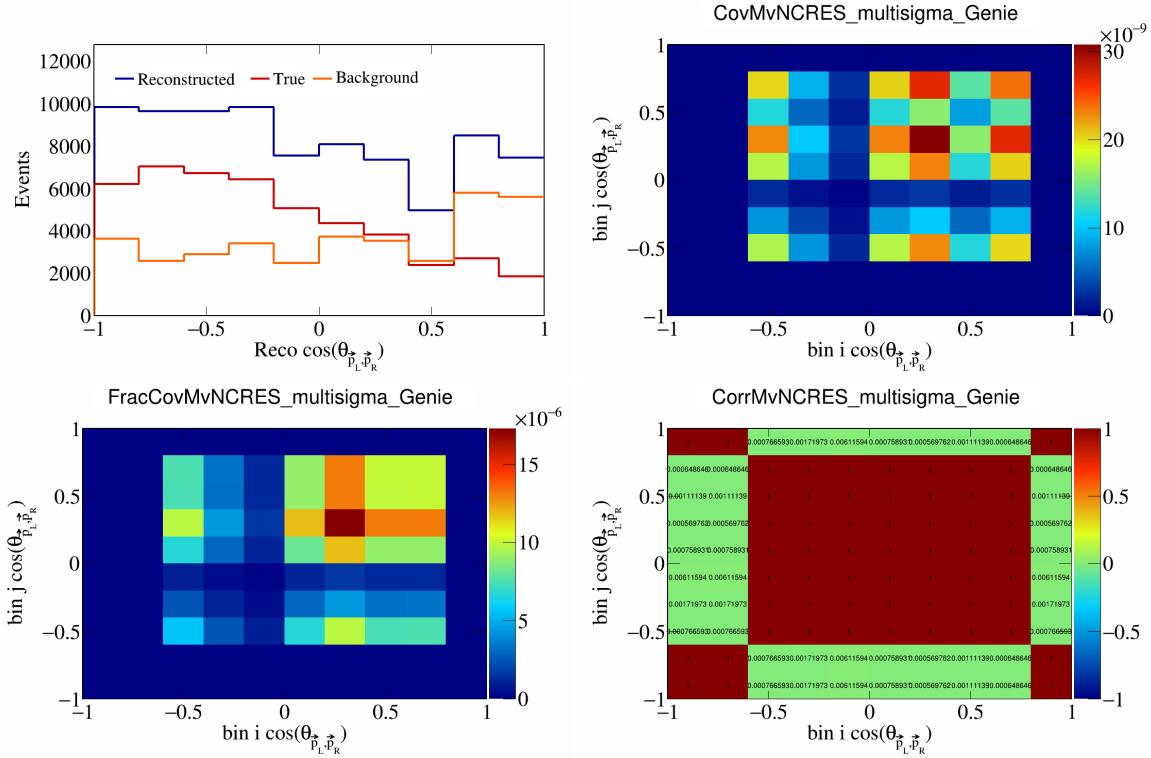


Figure 381: MvNCRES variations for $\cos(\theta_{\vec{p}_L, \vec{p}_R})$.

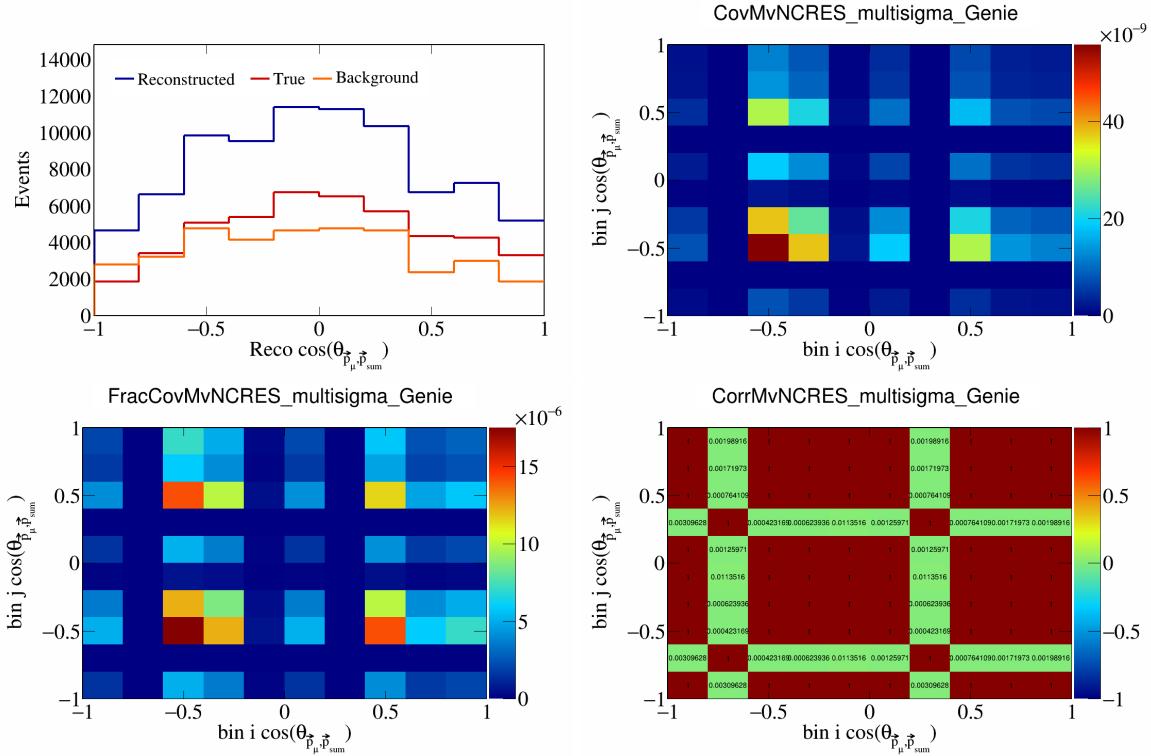


Figure 382: MvNCRES variations for $\cos(\theta_{\vec{p}_\mu, \vec{p}_{\text{sum}}})$.

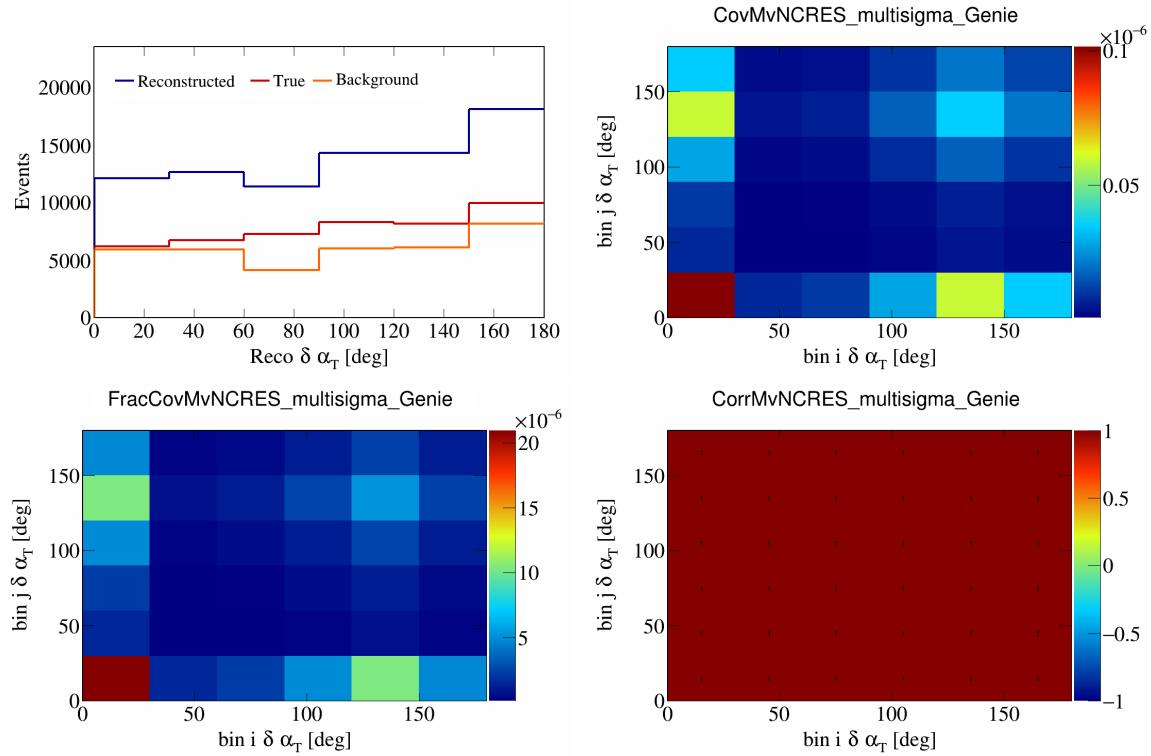


Figure 383: MvNCRES variations for $\delta\alpha_T$.

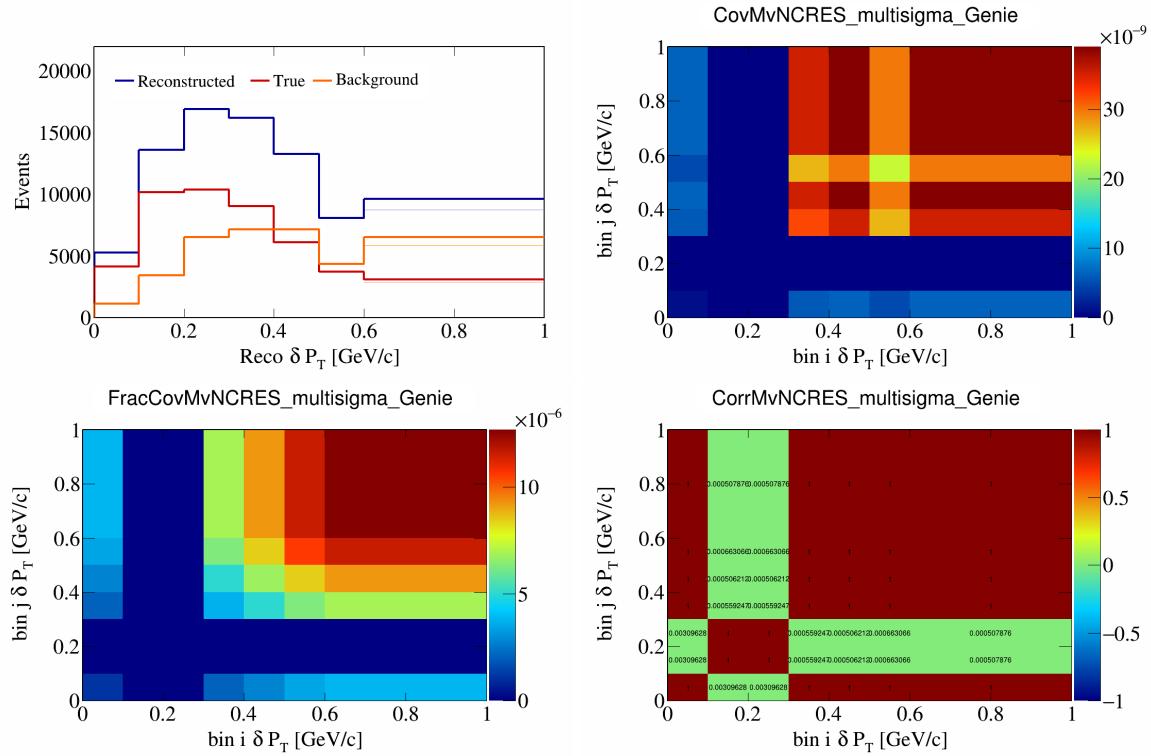


Figure 384: MvNCRES variations for δP_T .

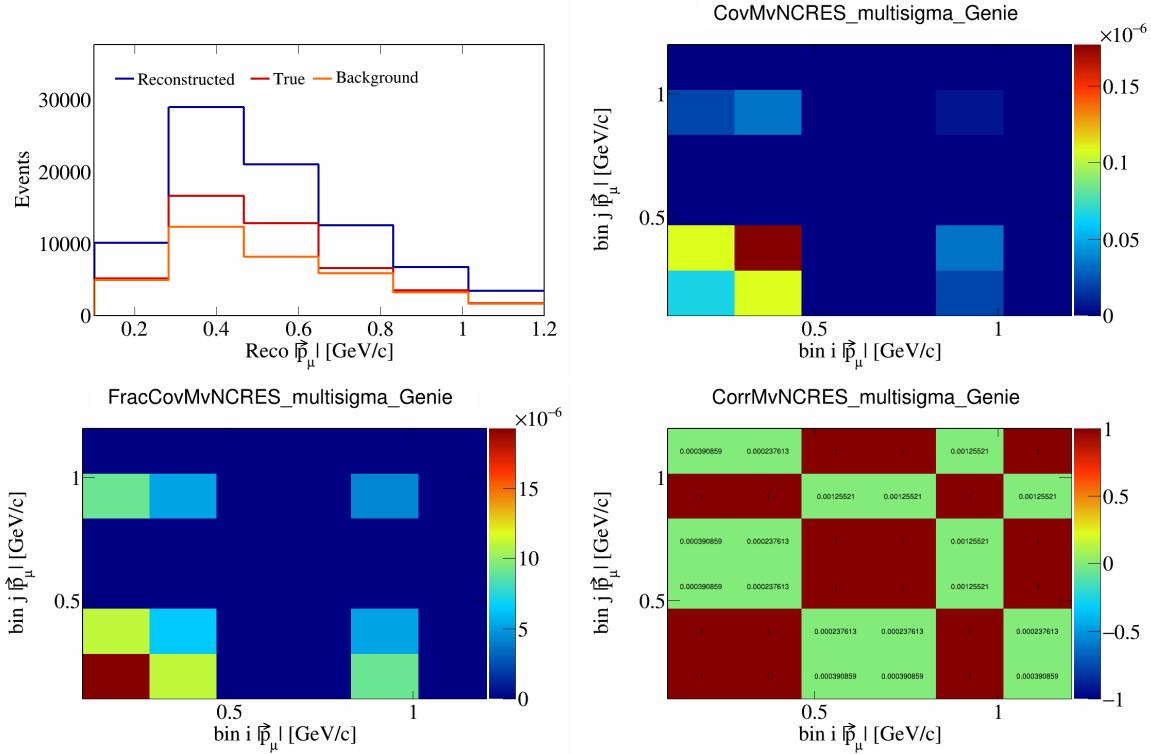


Figure 385: MvNCRES variations for $|\vec{p}_\mu|$.

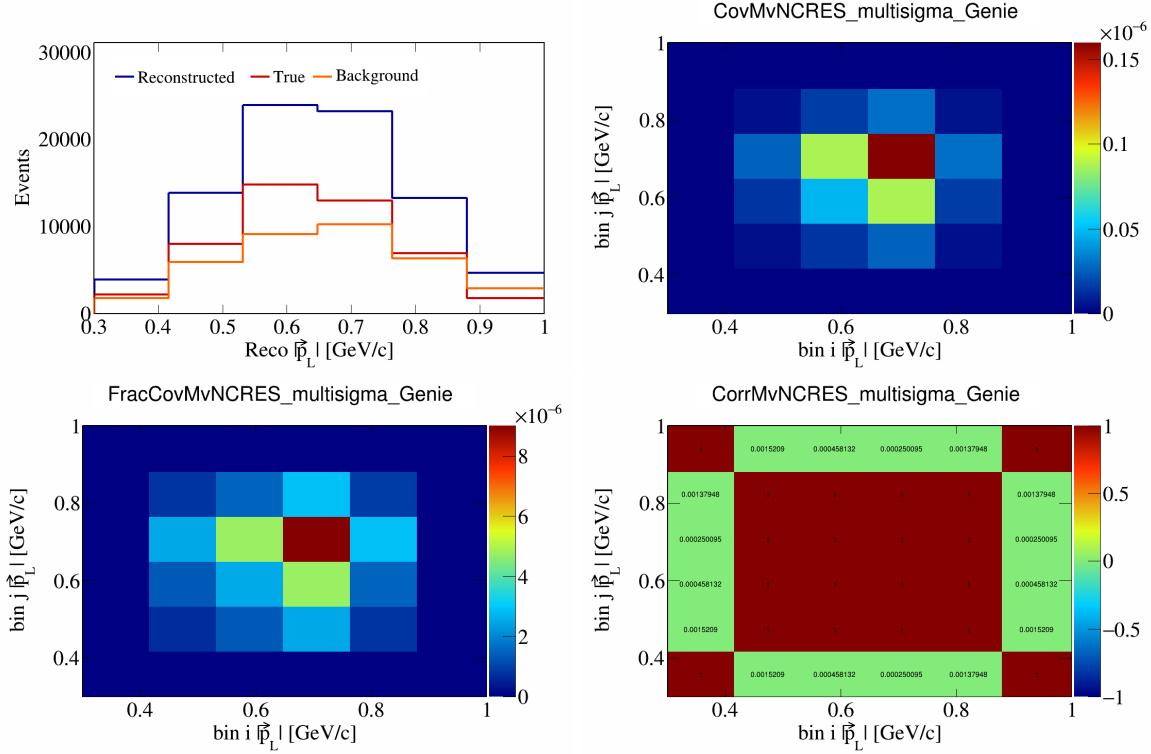


Figure 386: MvNCRES variations for $|\vec{p}_L|$.

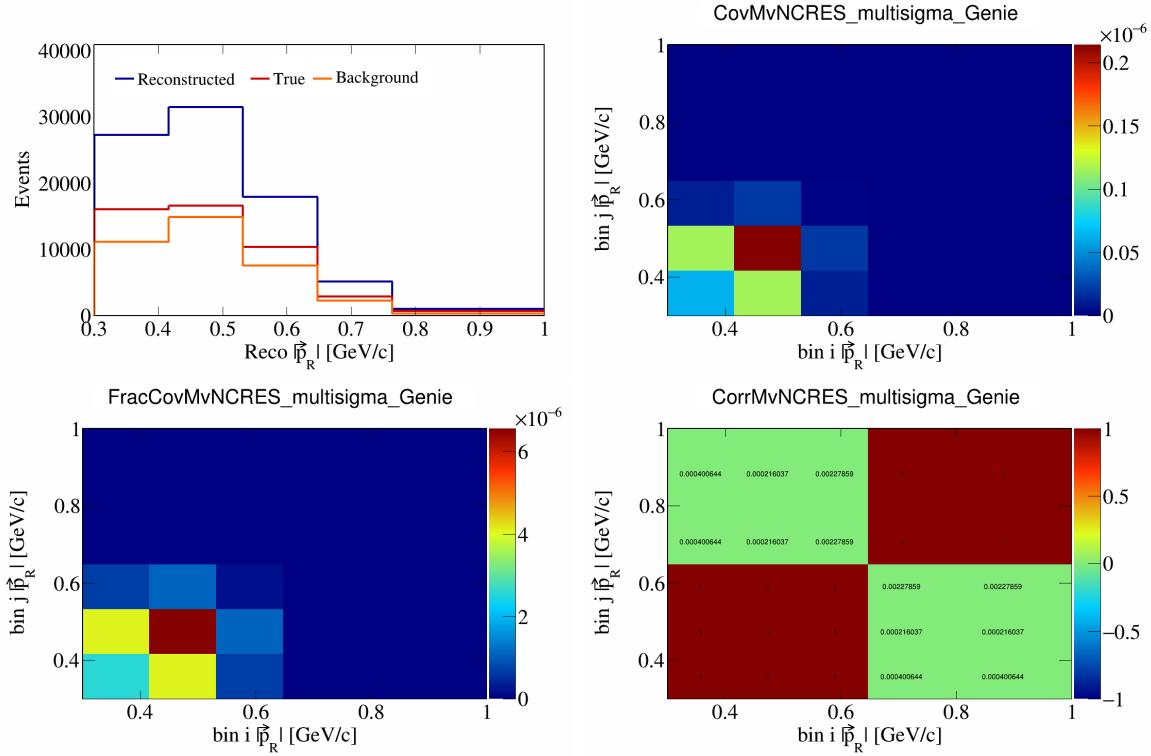


Figure 387: MvNCRES variations for $|\vec{p}_R|$.

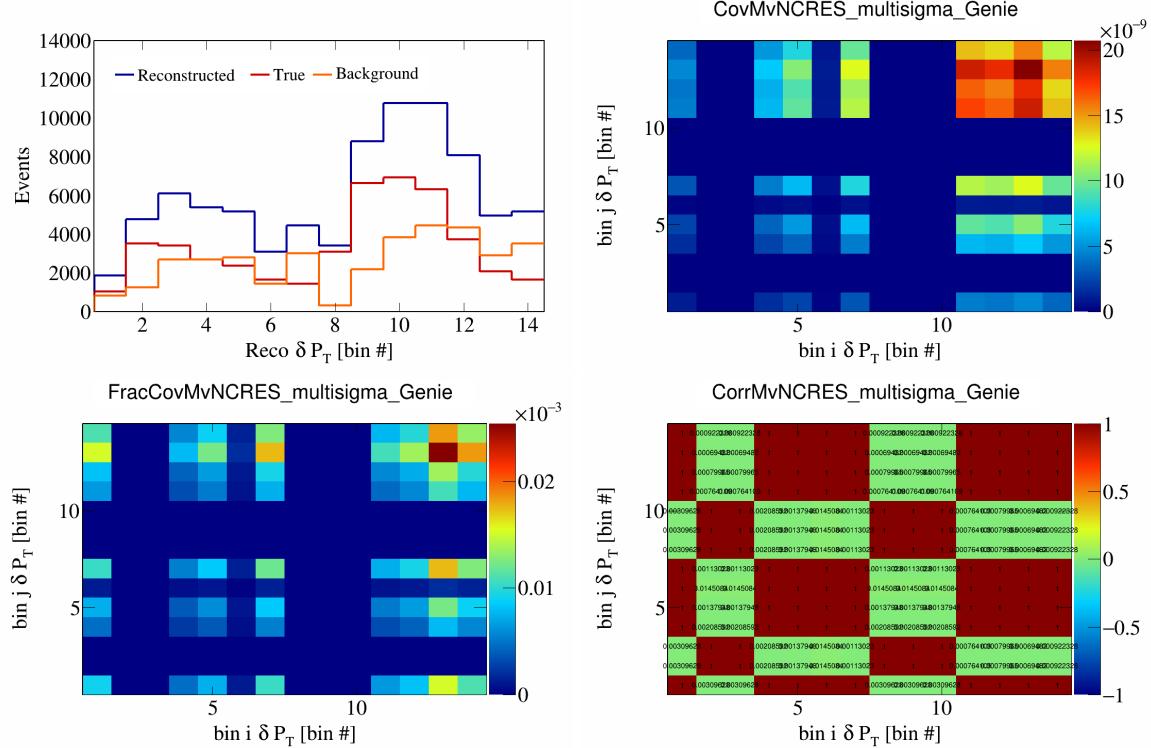


Figure 388: MvNCRES variations for δP_T in $\cos(\theta_{\vec{p}_\mu})$.

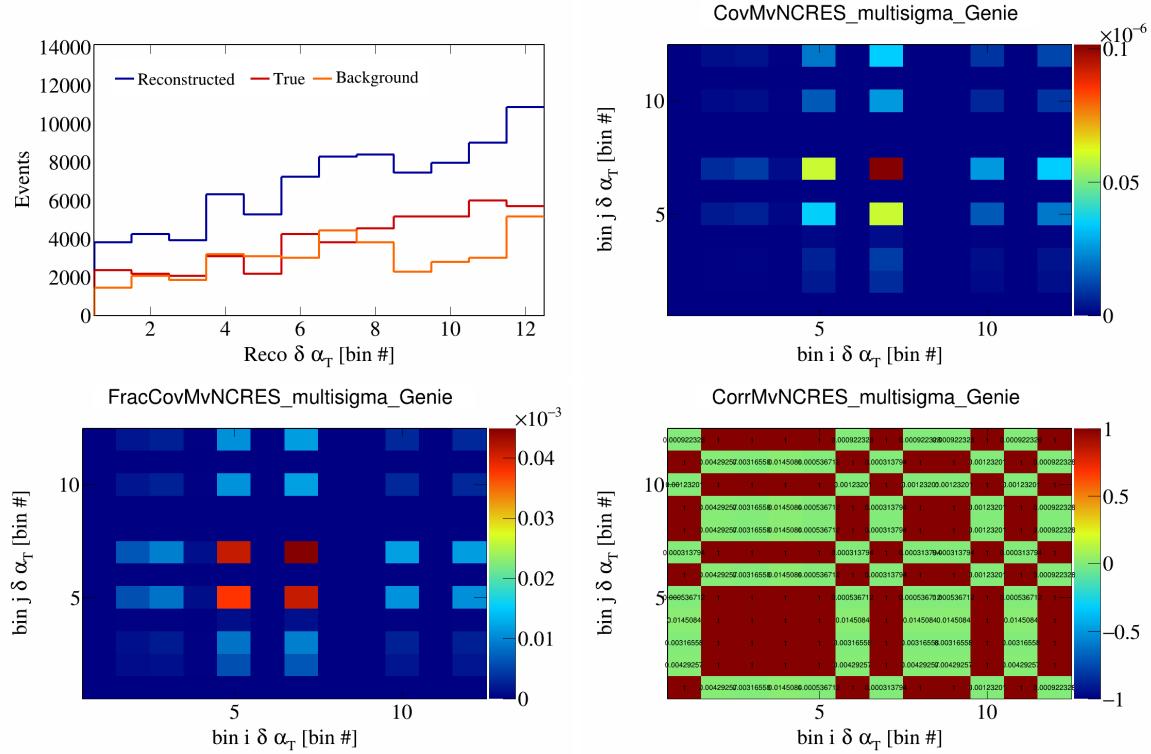


Figure 389: MvNCRES variations for $\delta\alpha_T$ in $\cos(\theta_{\vec{p}_\mu})$.

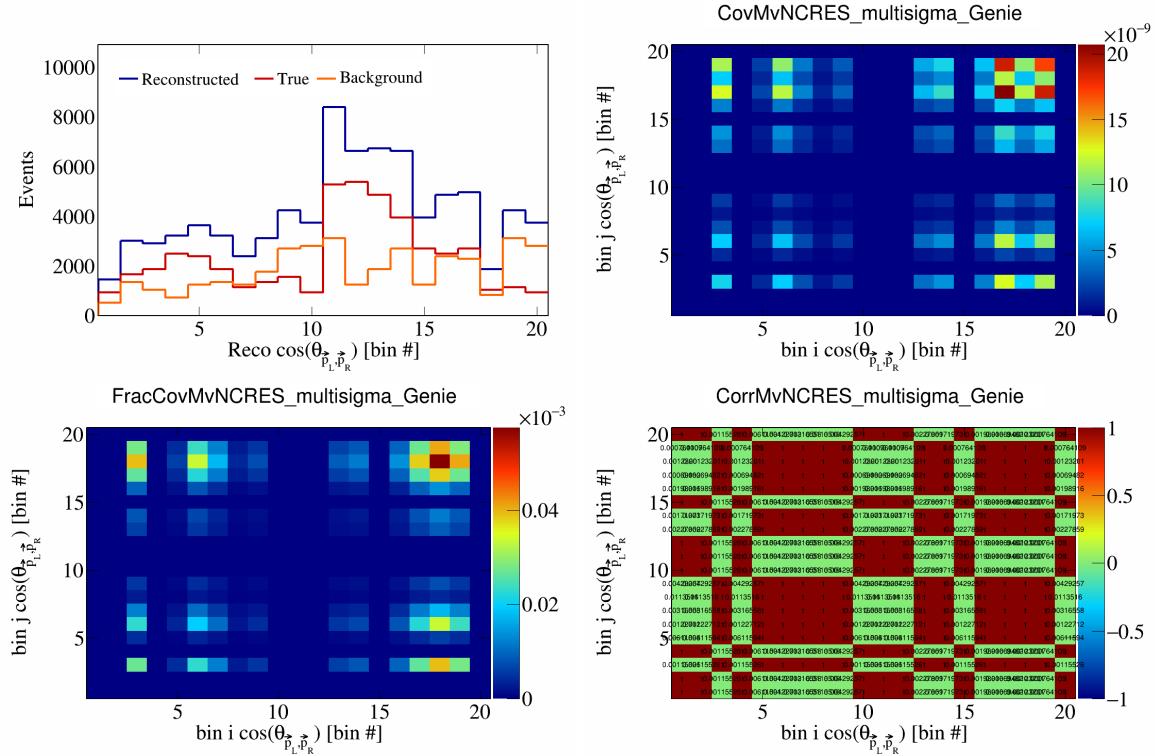


Figure 390: MvNCRES variations for $\cos(\theta_{\vec{p}_L, \vec{p}_R})$ in $\cos(\theta_{\vec{p}_\mu})$.

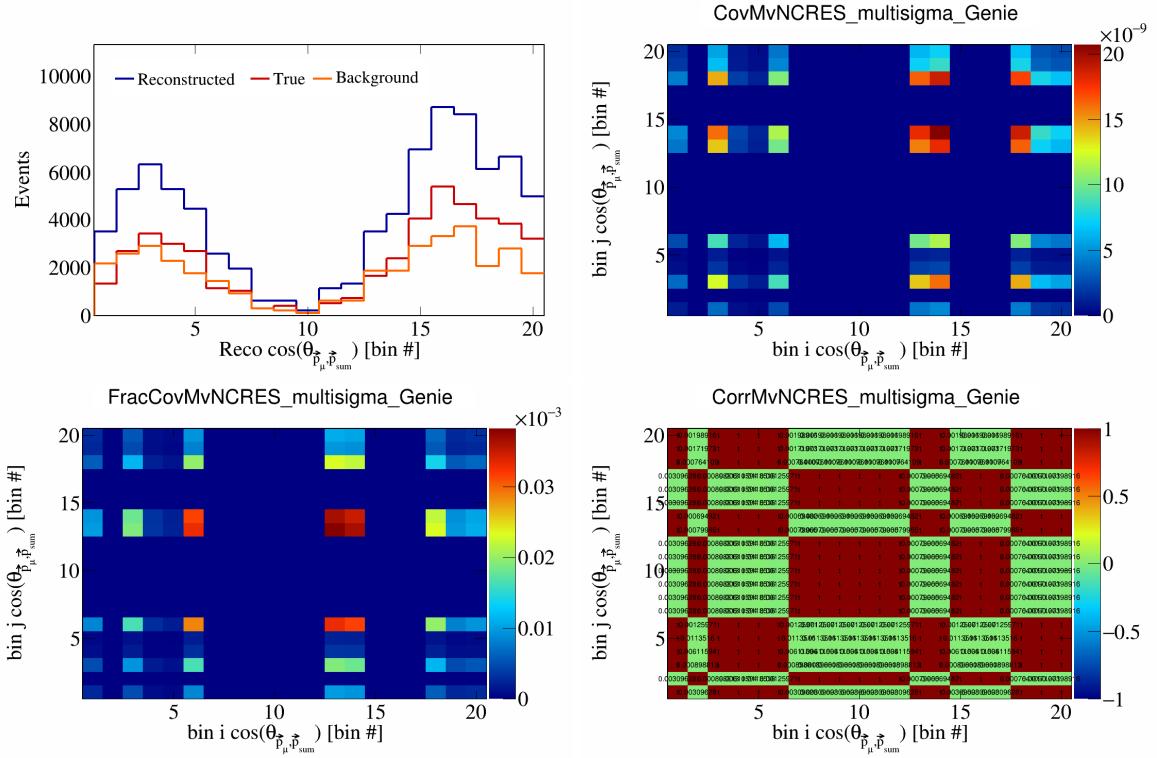


Figure 391: MvNCRES variations for $\cos(\theta_{\vec{p}_\mu, \vec{p}_{\text{sum}}})$ in $\cos(\theta_{\vec{p}_\mu})$.

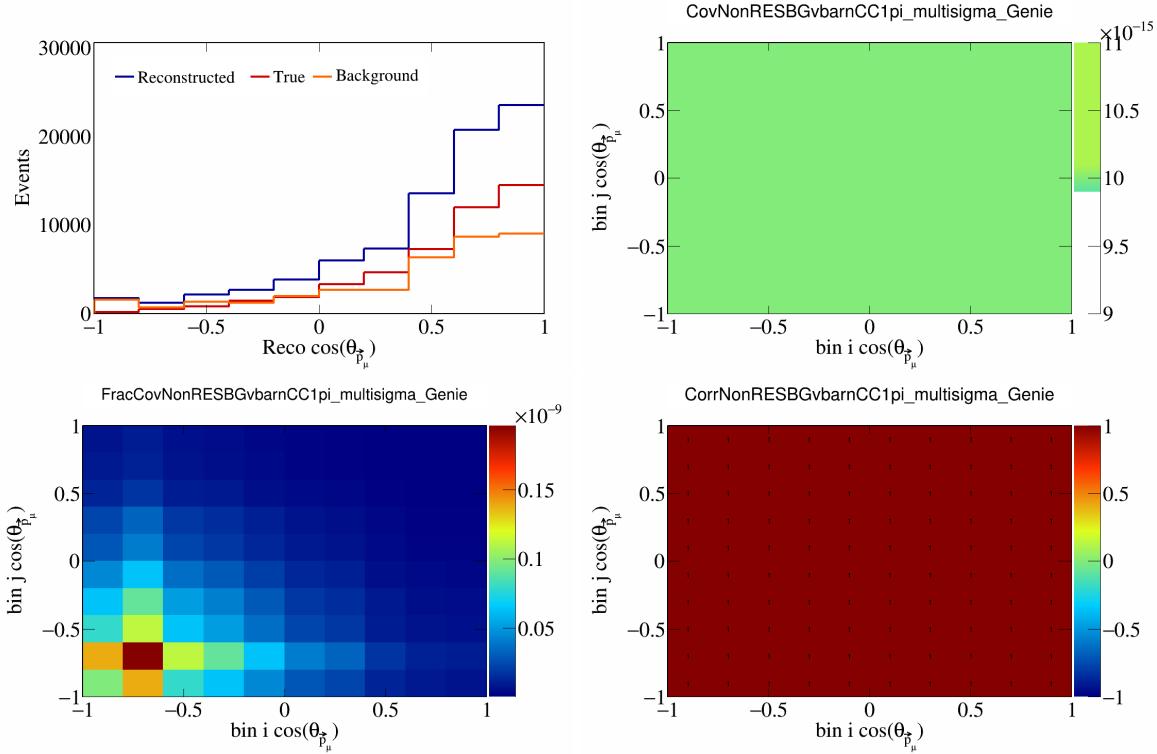


Figure 392: NonRESBGvbarCC1pi variations for $\cos(\theta_{\vec{p}_\mu})$.

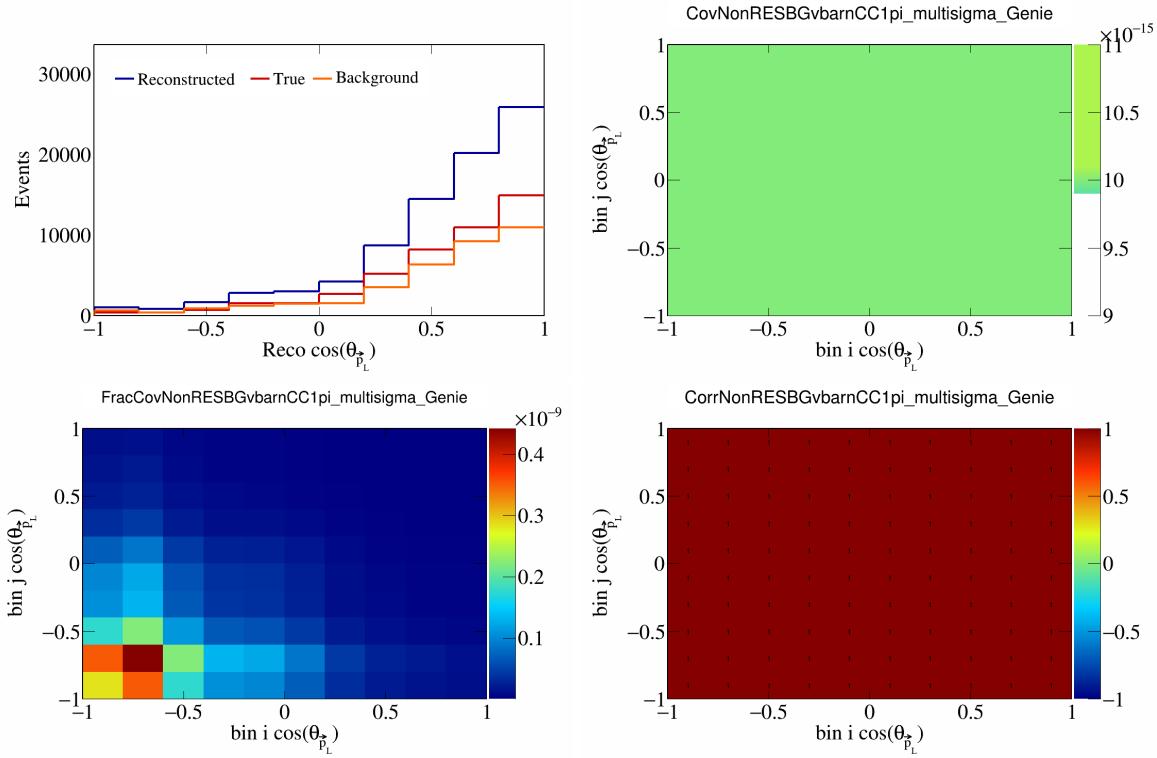


Figure 393: NonRESBGvbarCC1pi variations for $\cos(\theta_{\vec{p}_L})$.

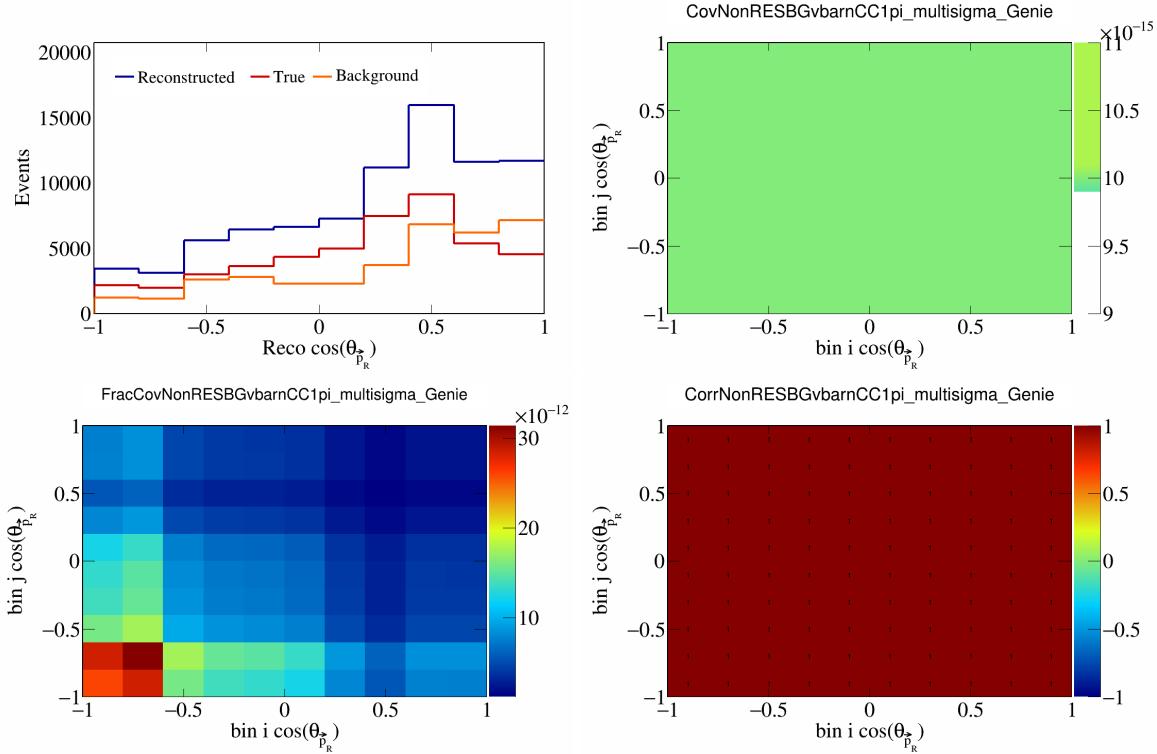


Figure 394: NonRESBGvbarCC1pi variations for $\cos(\theta_{\vec{p}_R})$.

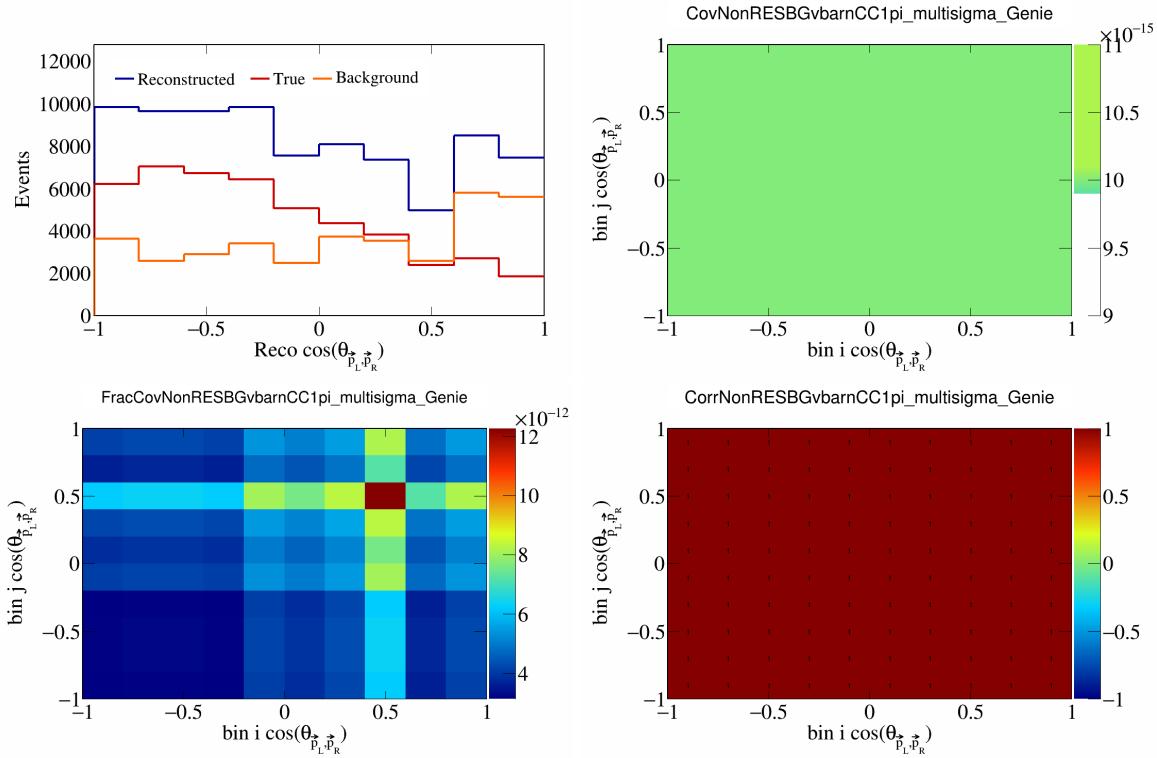


Figure 395: NonRESBGvbarCC1pi variations for $\cos(\theta_{\vec{p}_L, \vec{p}_R})$.

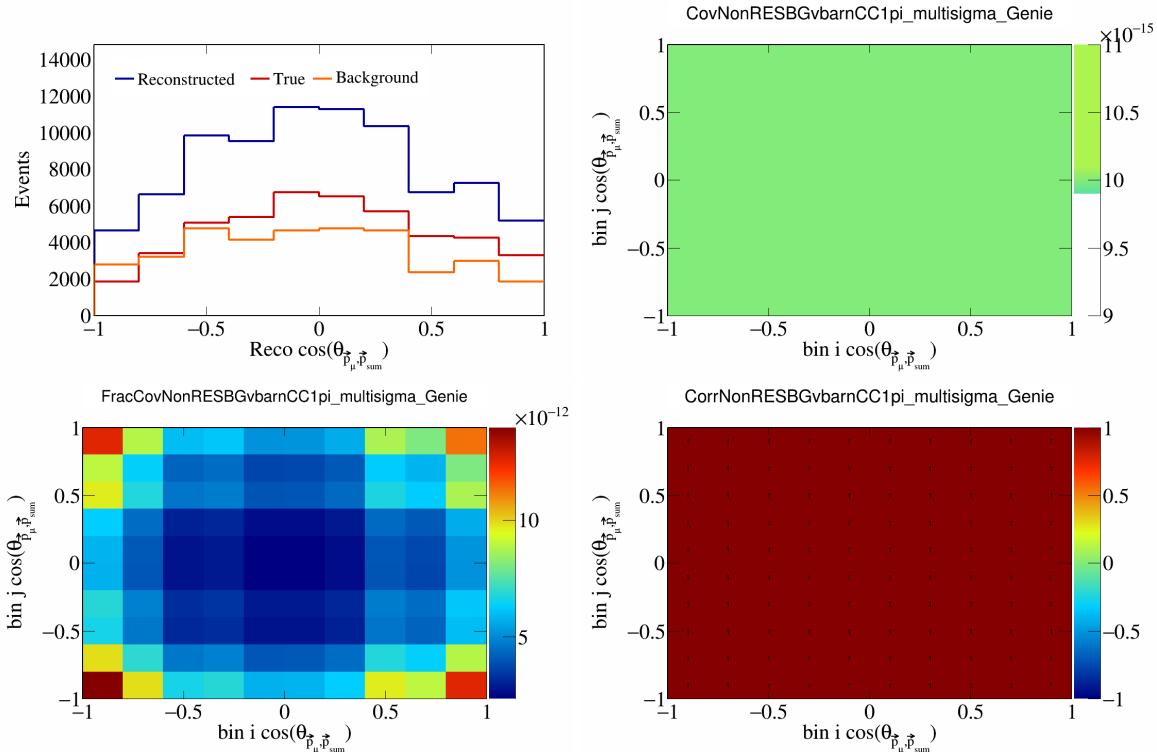


Figure 396: NonRESBGvbarCC1pi variations for $\cos(\theta_{\vec{p}_\mu, \vec{p}_{\text{sum}}})$.

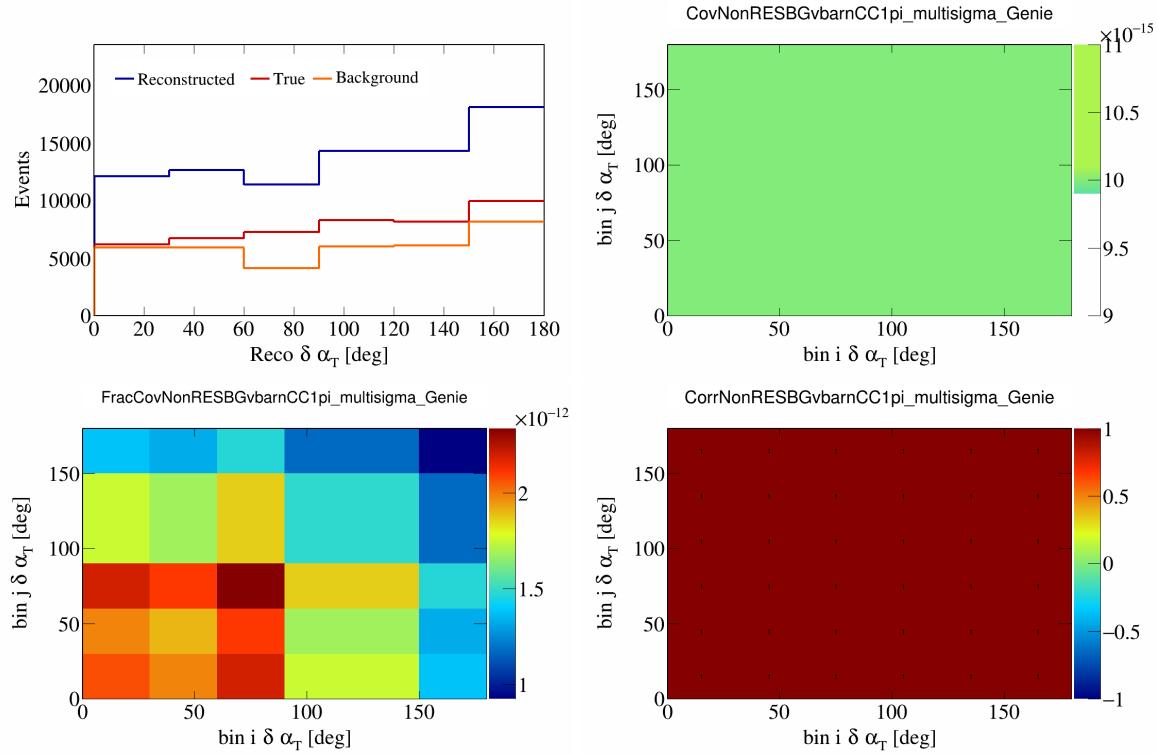


Figure 397: NonRESBGvbarCC1pi variations for $\delta\alpha_T$.

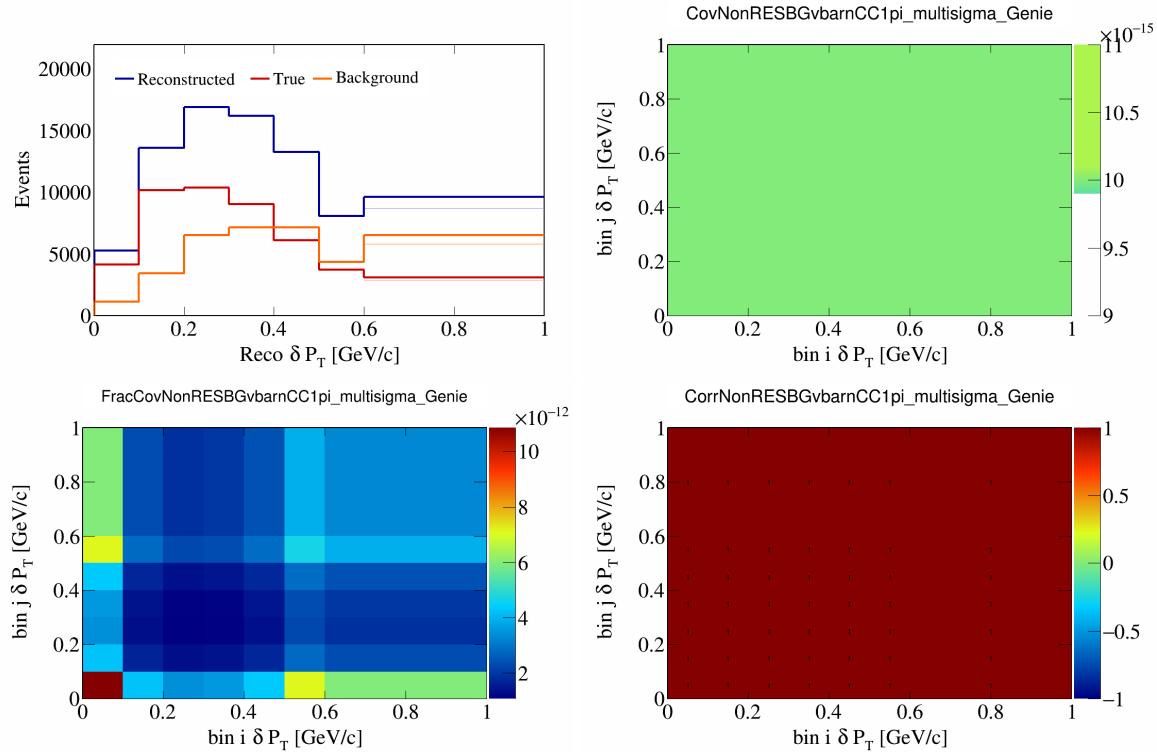


Figure 398: NonRESBGvbarCC1pi variations for δP_T .

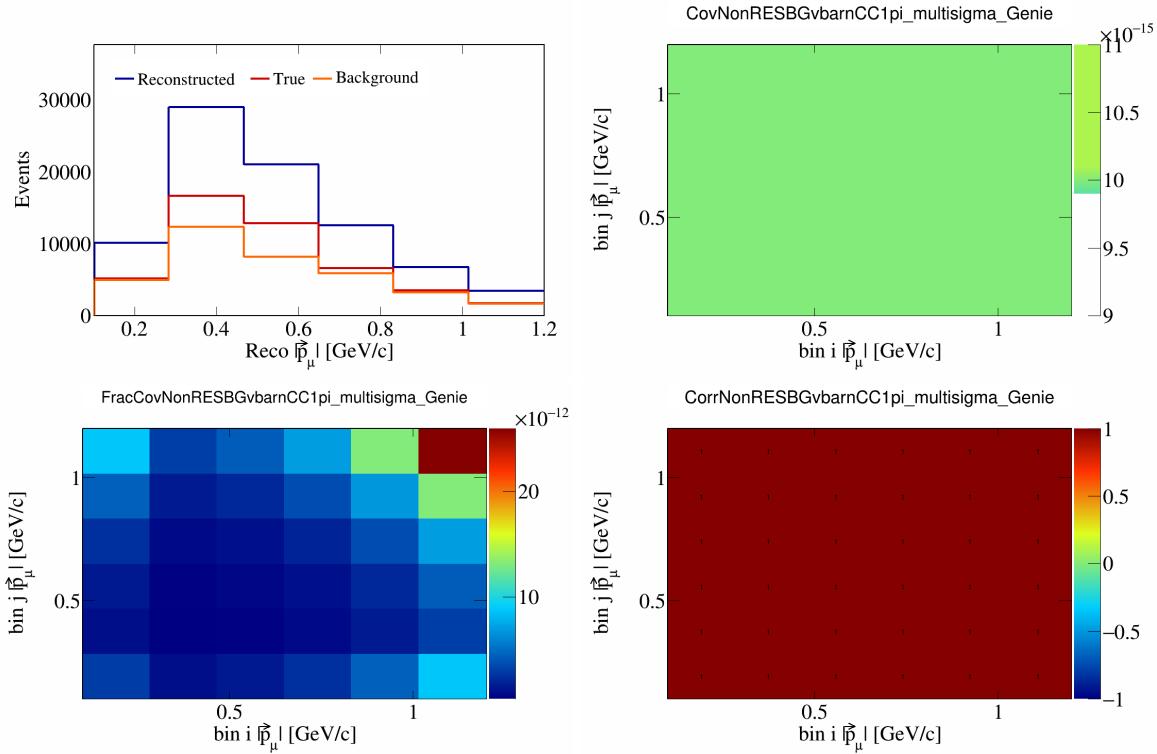


Figure 399: NonRESBGvbarCC1pi variations for $|\vec{p}_\mu|$.

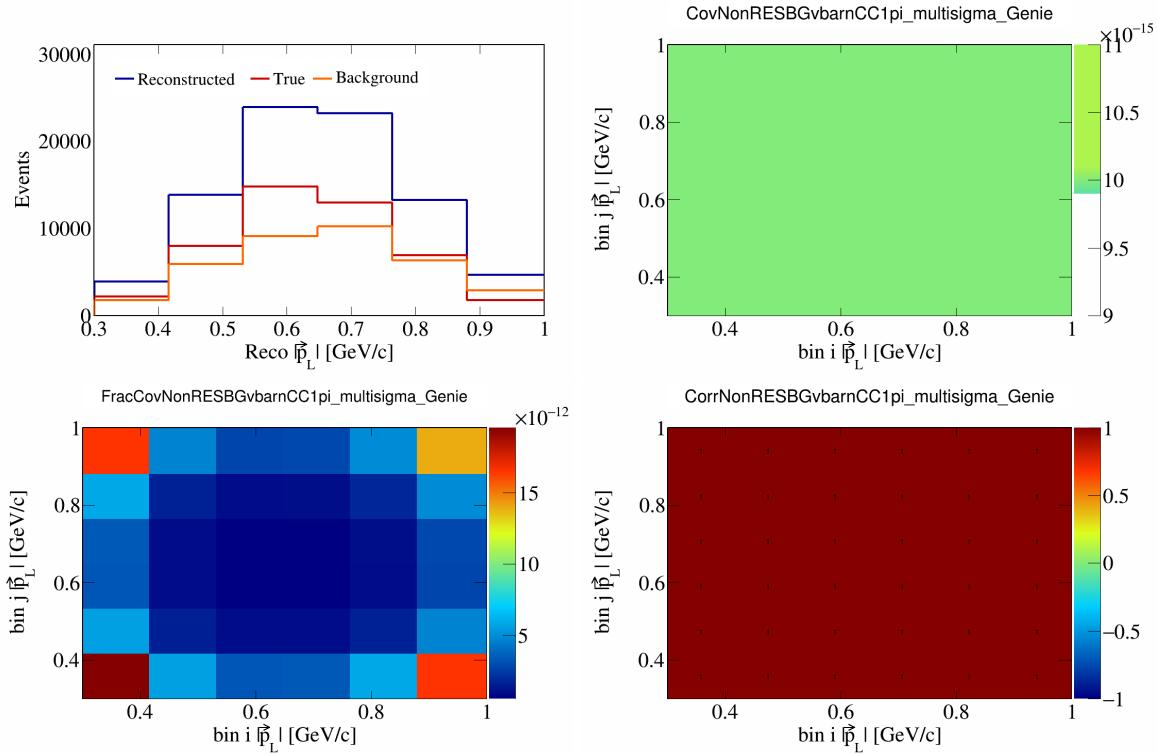


Figure 400: NonRESBGvbarCC1pi variations for $|\vec{p}_L|$.

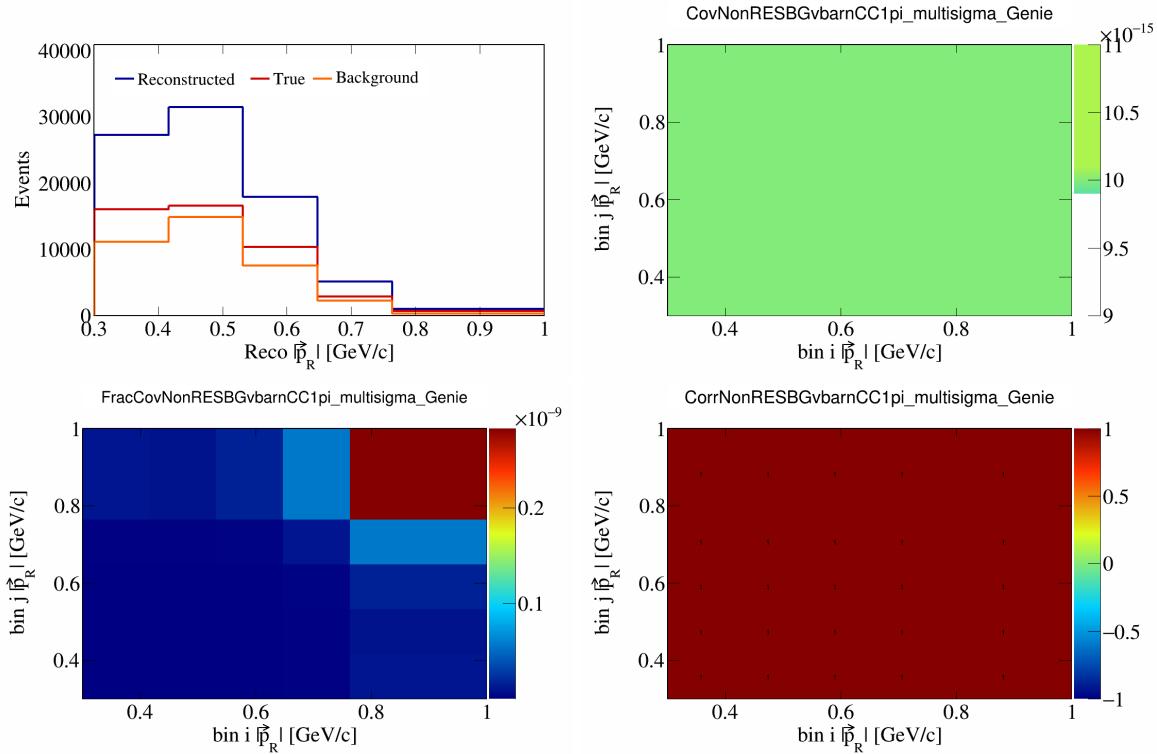


Figure 401: NonRESBGvbarCC1pi variations for $|\vec{p}_R|$.

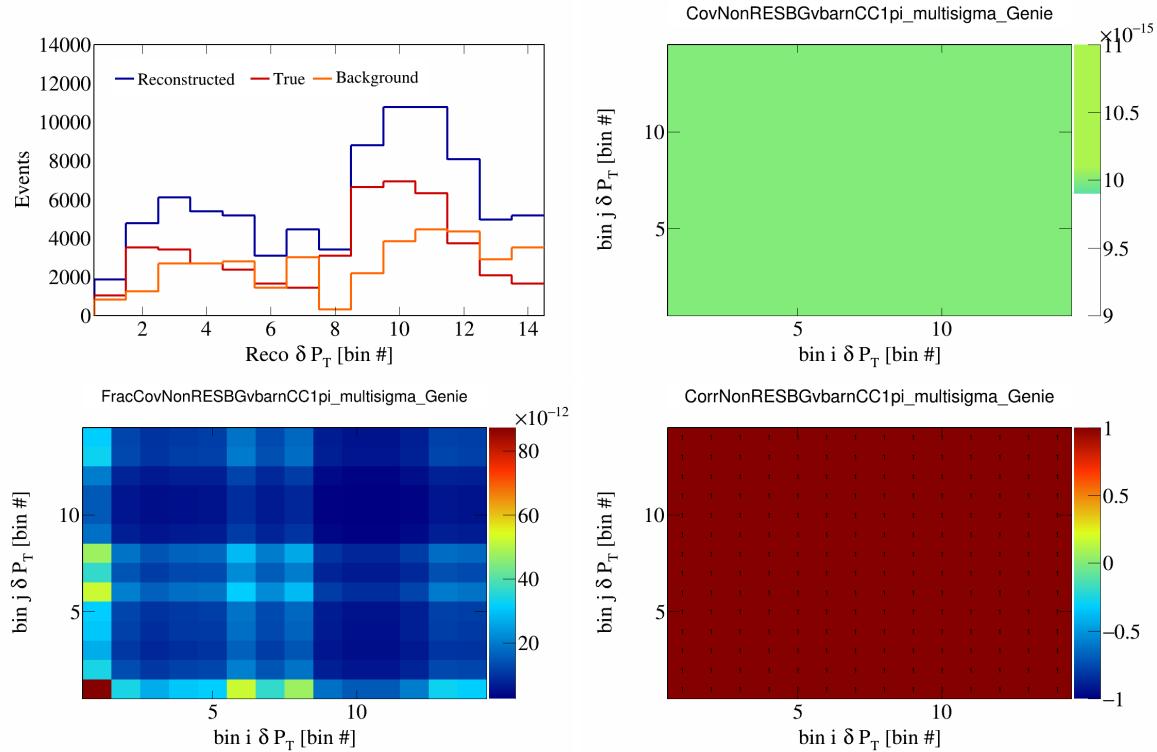


Figure 402: NonRESBGvbarCC1pi variations for δP_T in $\cos(\theta_{\vec{p}_\mu})$.

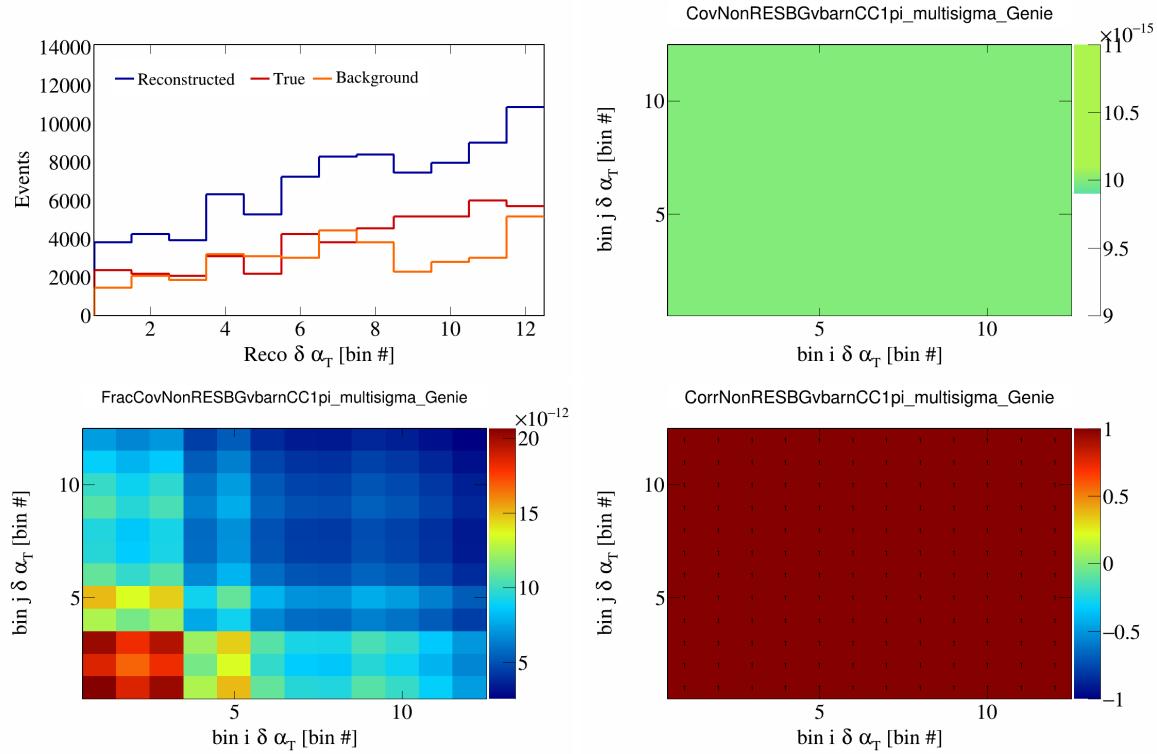


Figure 403: NonRESBGvbarCC1pi variations for $\delta \alpha_T$ in $\cos(\theta_{\vec{p}_\mu})$.

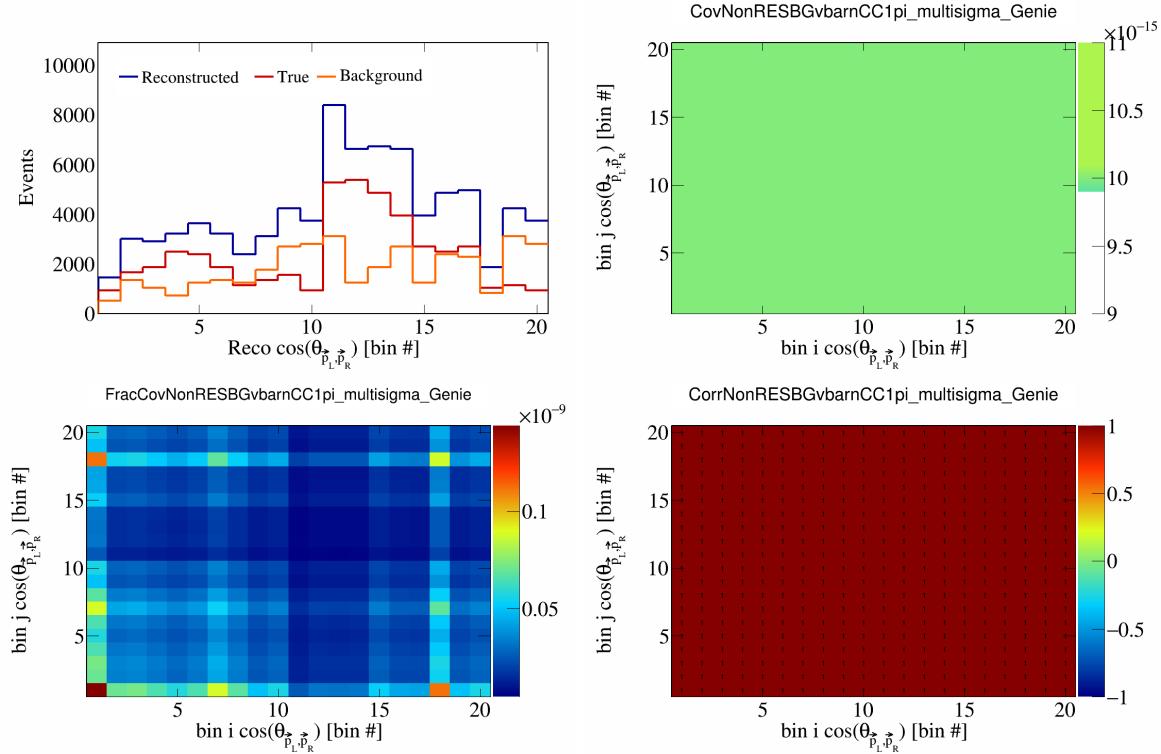


Figure 404: NonRESBGvbarCC1pi variations for $\cos(\theta_{\vec{p}_L, \vec{p}_R})$ in $\cos(\theta_{\vec{p}_\mu})$.

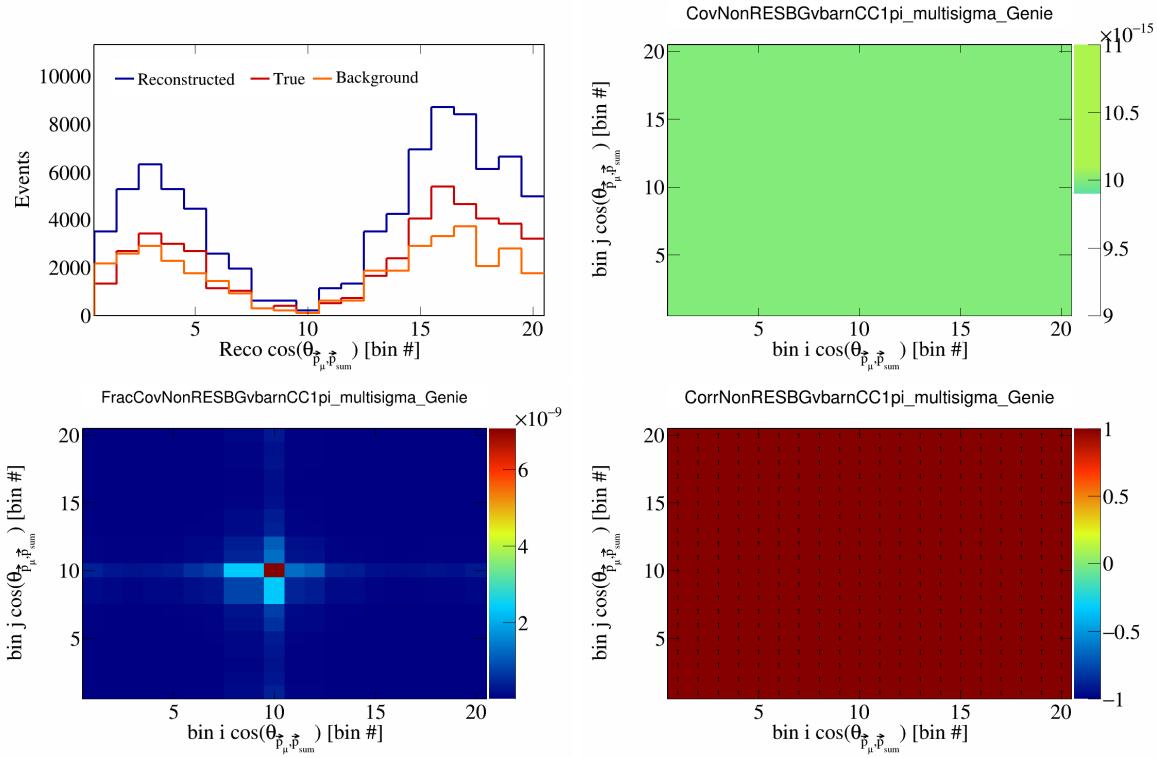


Figure 405: NonRESBGvbarCC1pi variations for $\cos(\theta_{\vec{p}_\mu})$ in $\cos(\theta_{\vec{p}_\mu})$.

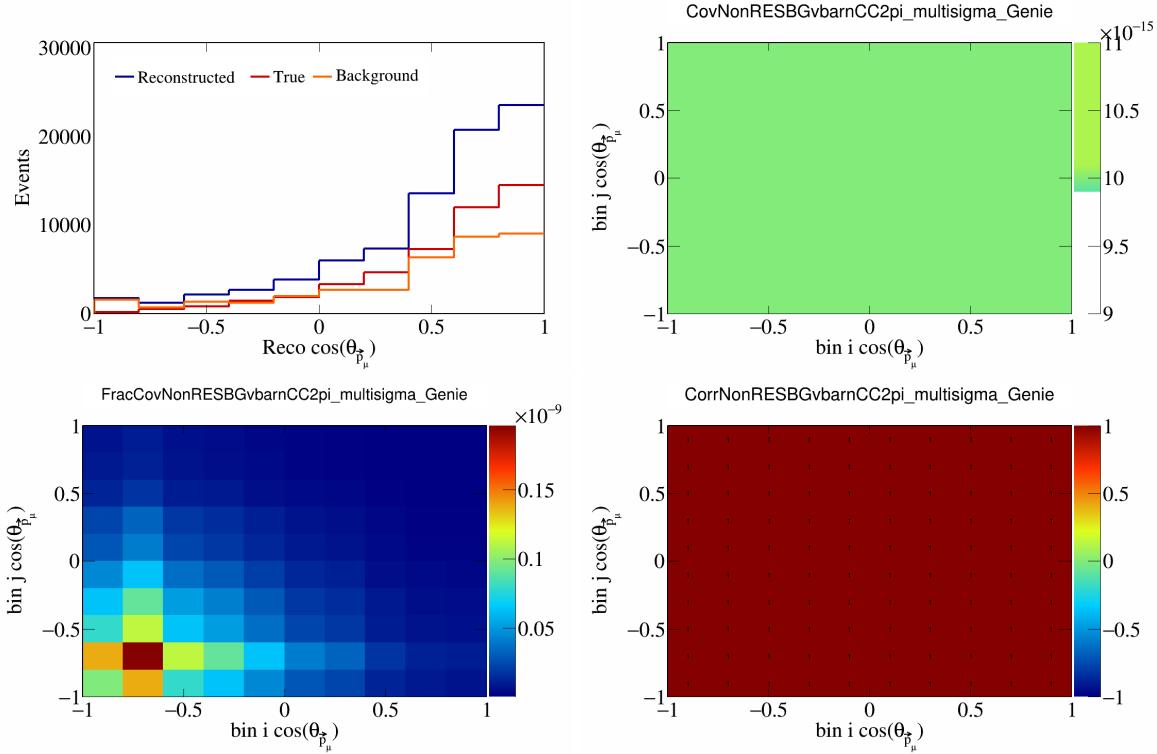


Figure 406: NonRESBGvbarCC2pi variations for $\cos(\theta_{\vec{p}_\mu})$.

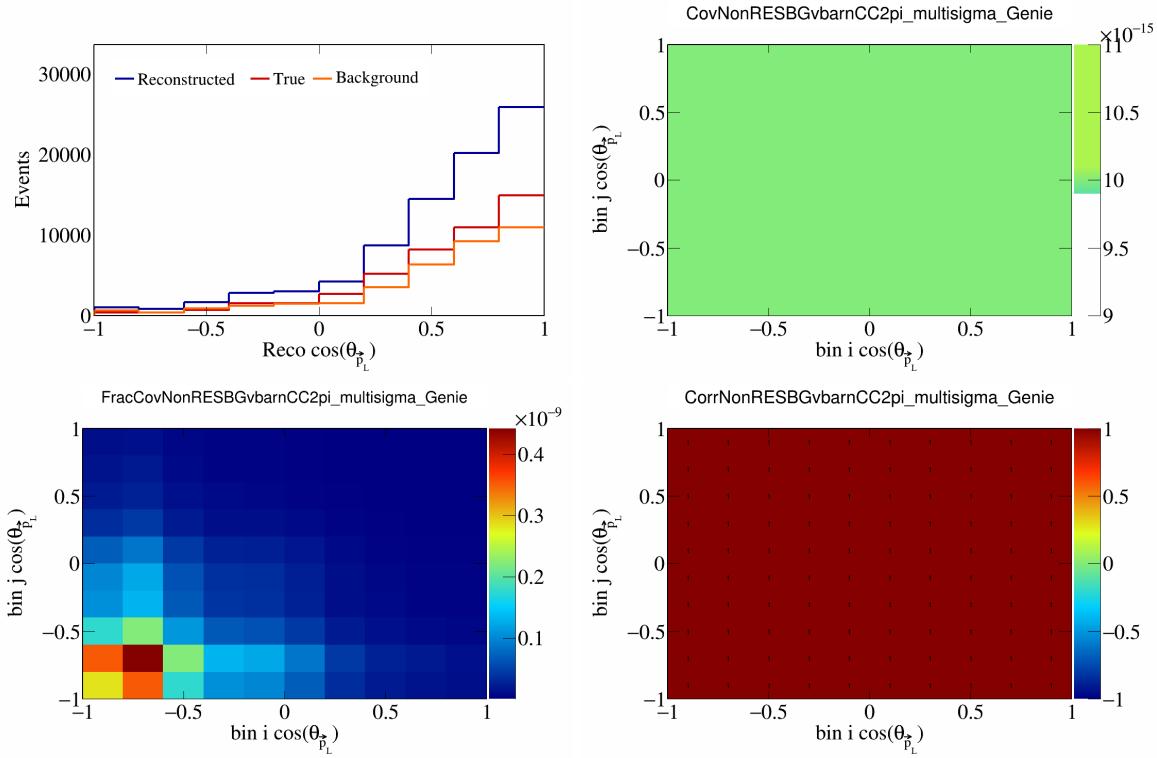


Figure 407: NonRESBGvbarCC2pi variations for $\cos(\theta_{\vec{F}_L})$.

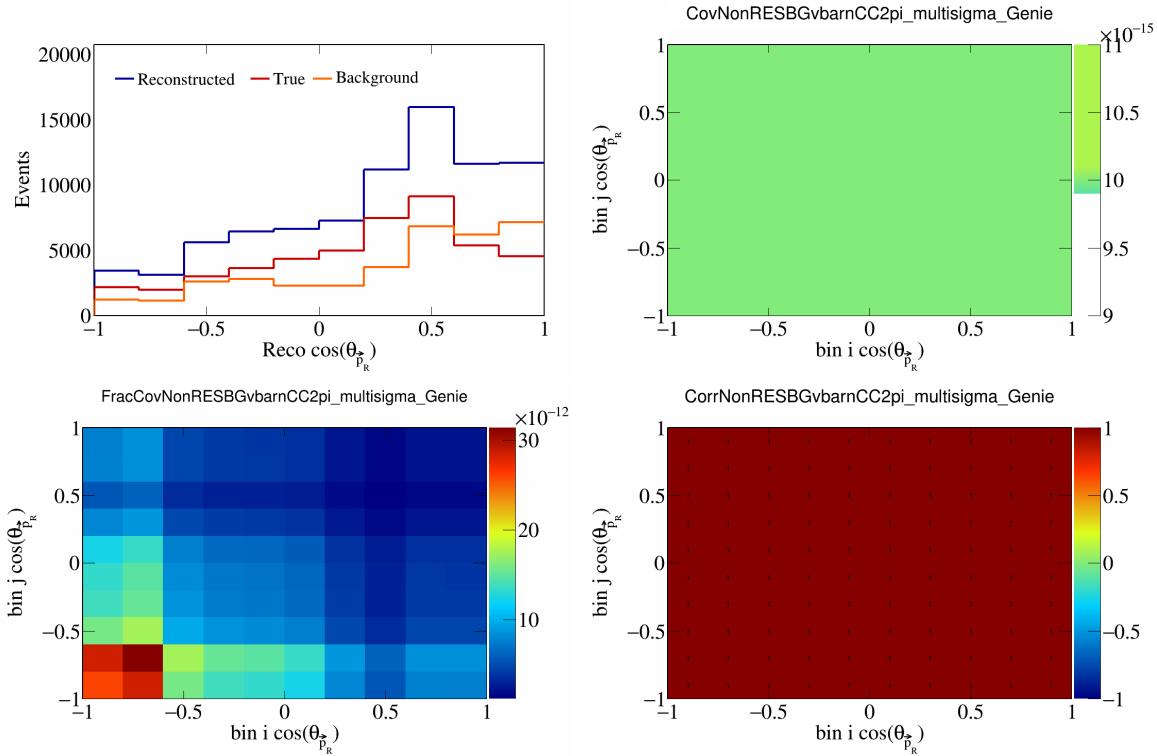


Figure 408: NonRESBGvbarCC2pi variations for $\cos(\theta_{\vec{F}_R})$.

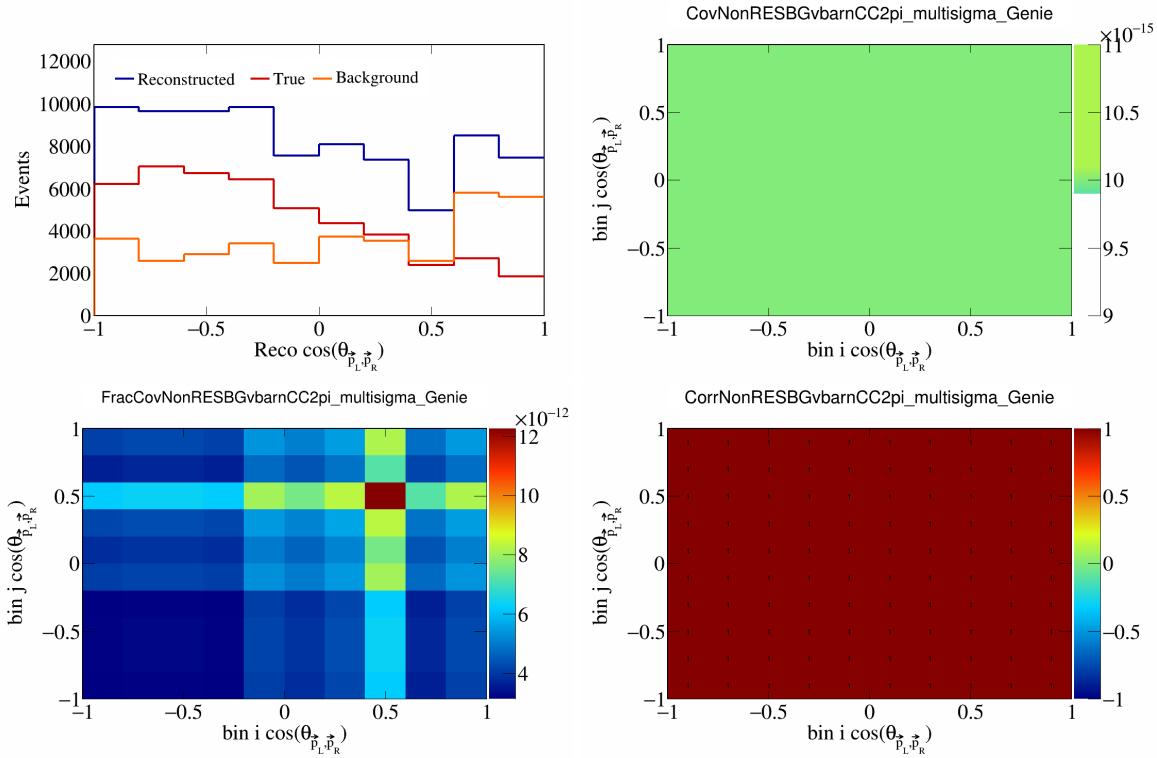


Figure 409: NonRESBGvbarCC2pi variations for $\cos(\theta_{\vec{p}_L, \vec{p}_R})$.

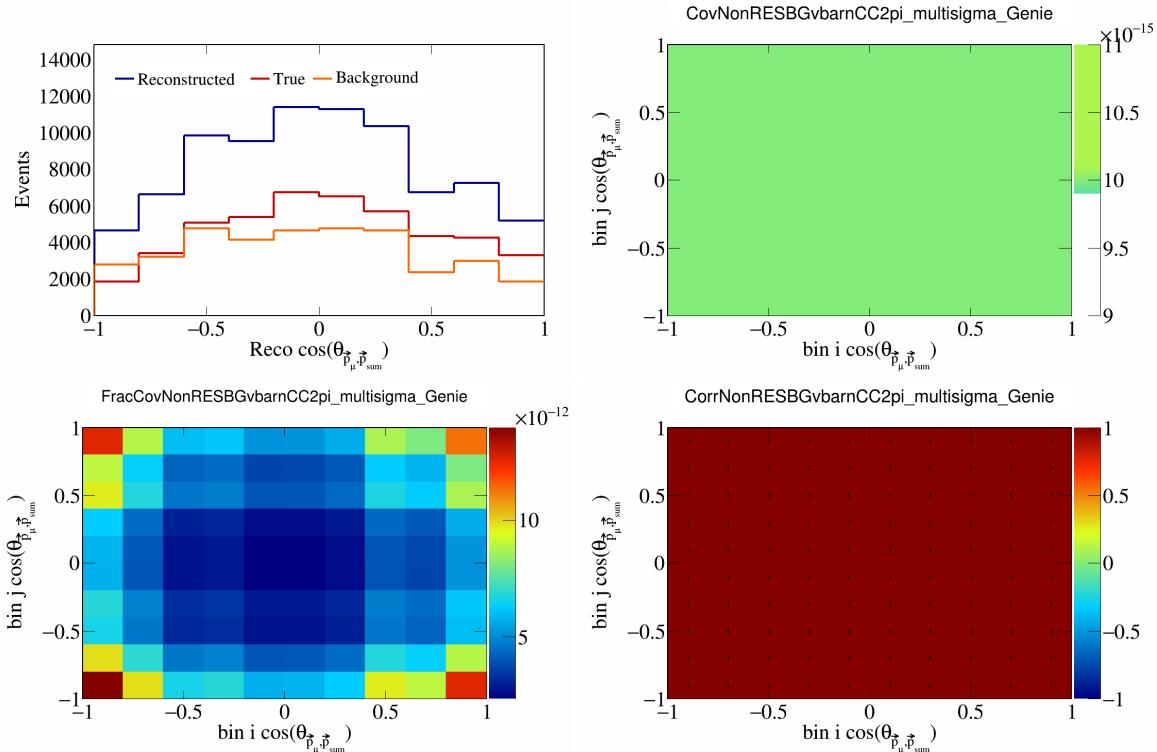


Figure 410: NonRESBGvbarCC2pi variations for $\cos(\theta_{\vec{p}_\mu, \vec{p}_{\text{sum}}})$.

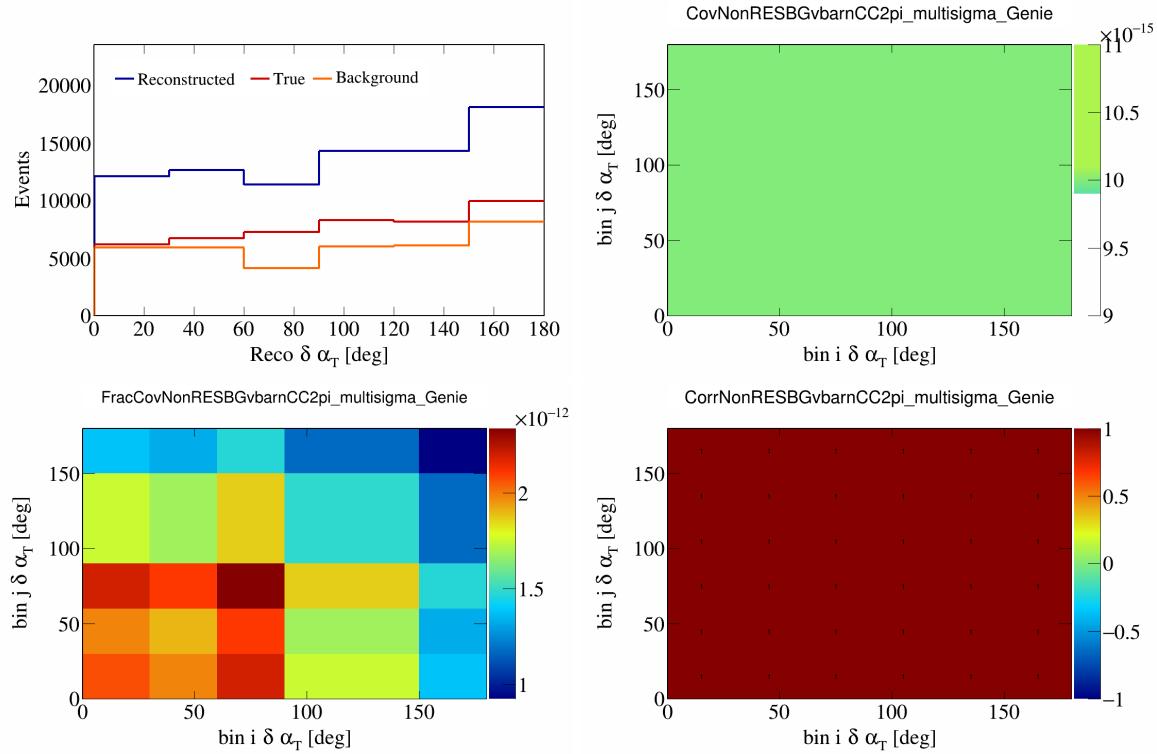


Figure 411: NonRESBGvbarCC2pi variations for $\delta\alpha_T$.

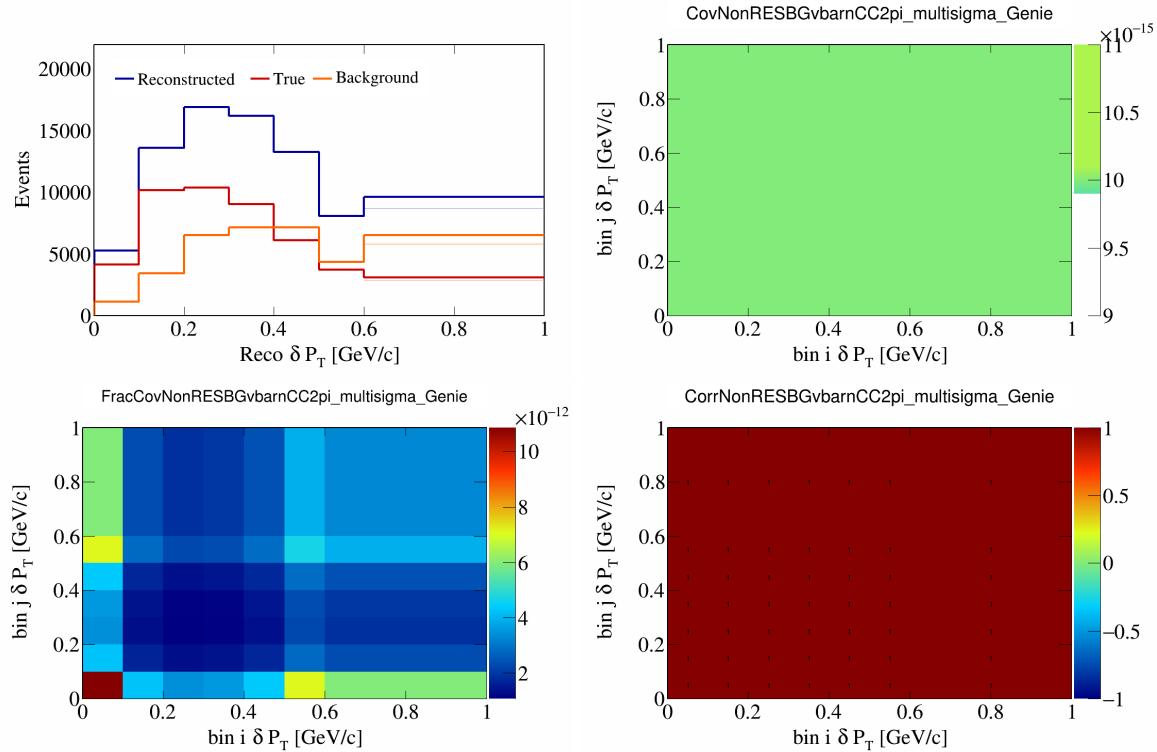


Figure 412: NonRESBGvbarCC2pi variations for δP_T .

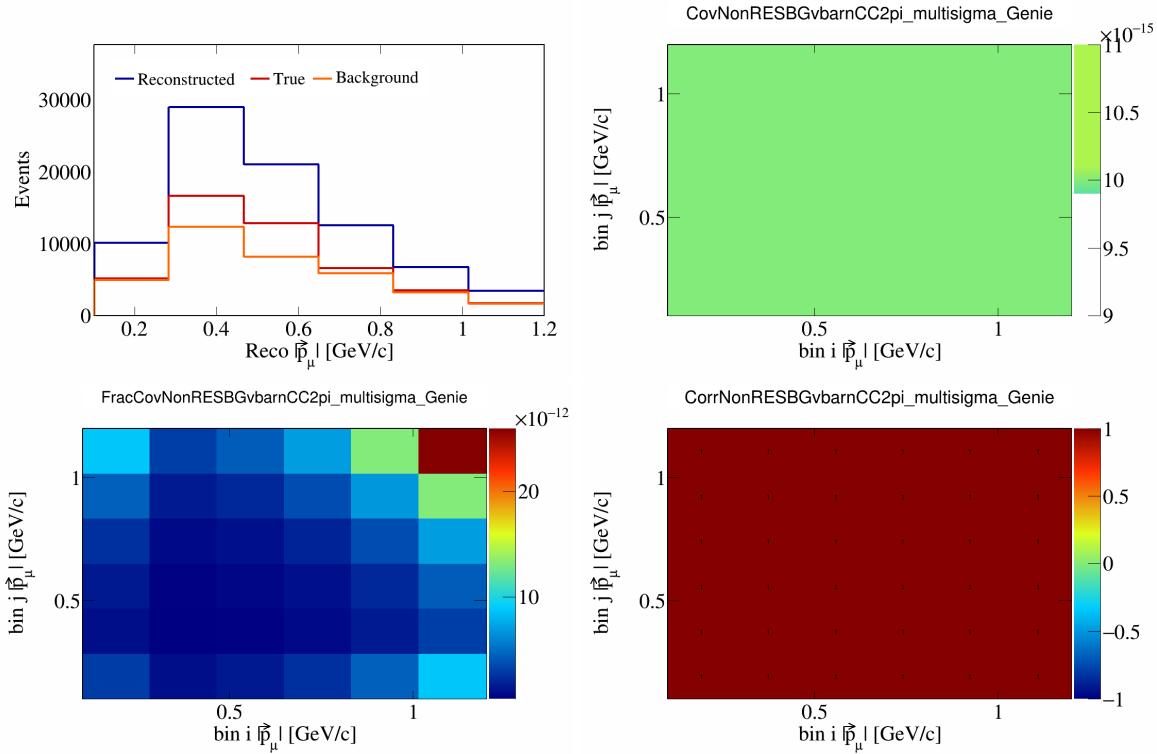


Figure 413: NonRESBGvbarCC2pi variations for $|\vec{p}_\mu|$.

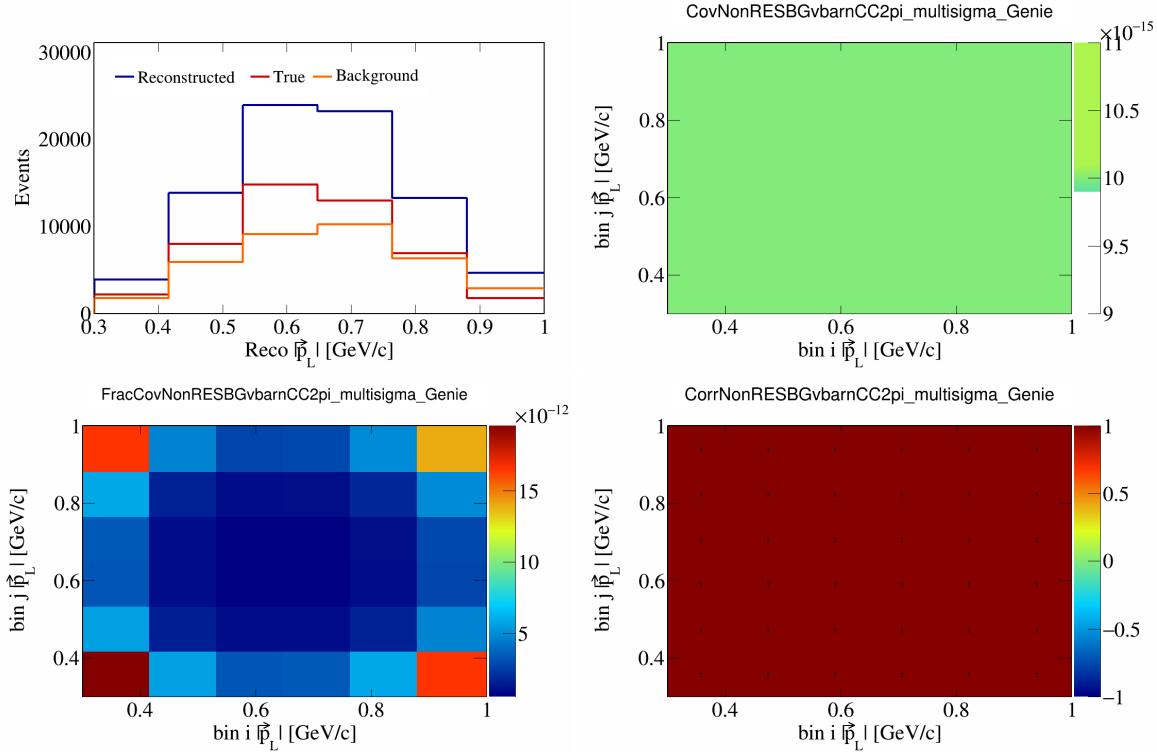


Figure 414: NonRESBGvbarCC2pi variations for $|\vec{p}_L|$.

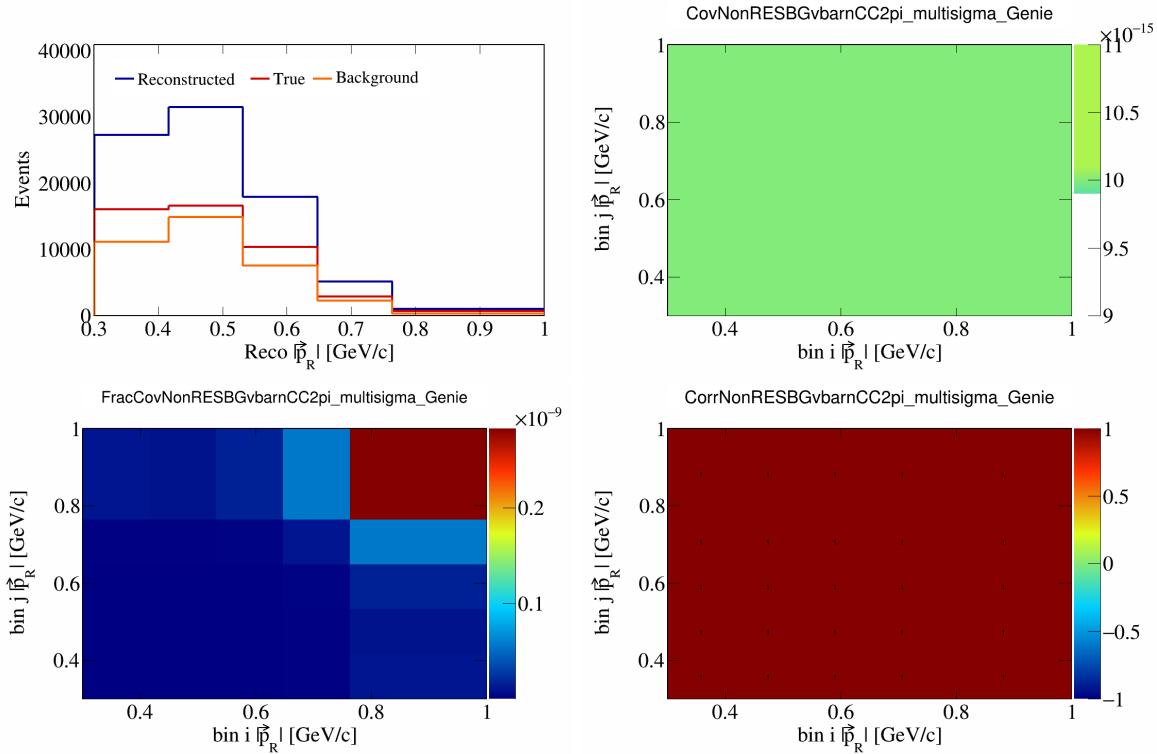


Figure 415: NonRESBGvbarCC2pi variations for $|\vec{p}_R|$.

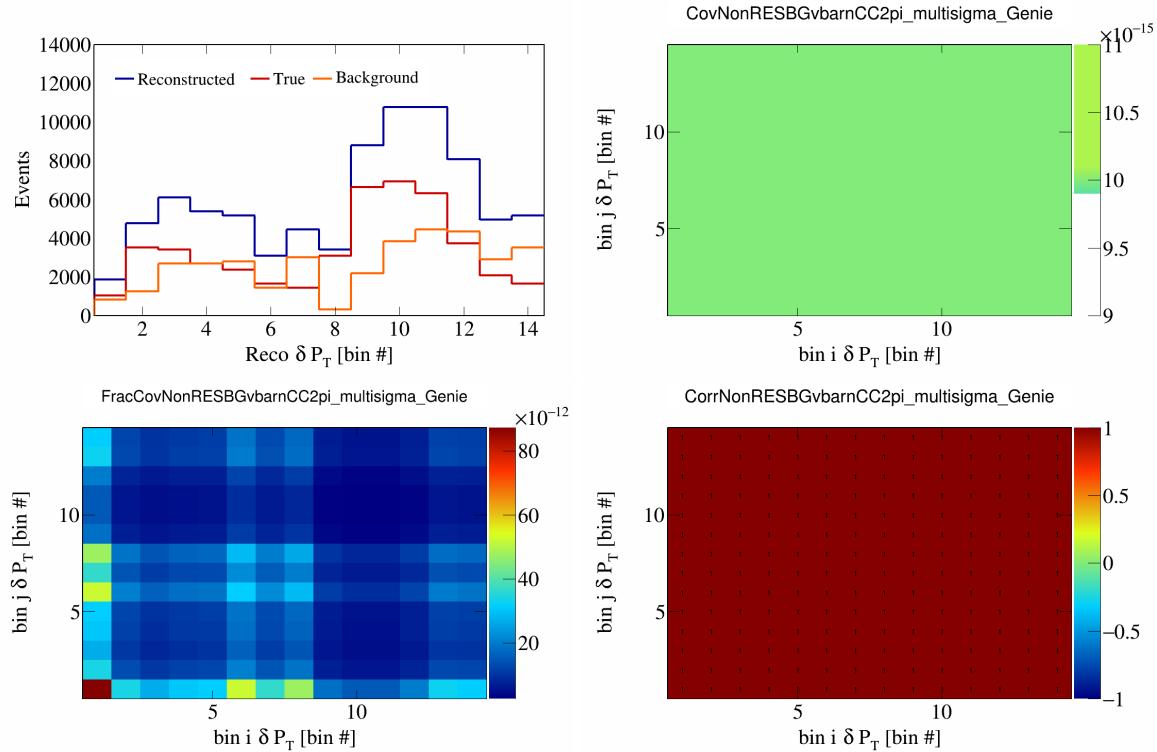


Figure 416: NonRESBGvbarCC2pi variations for δP_T in $\cos(\theta_{\vec{p}_\mu})$.

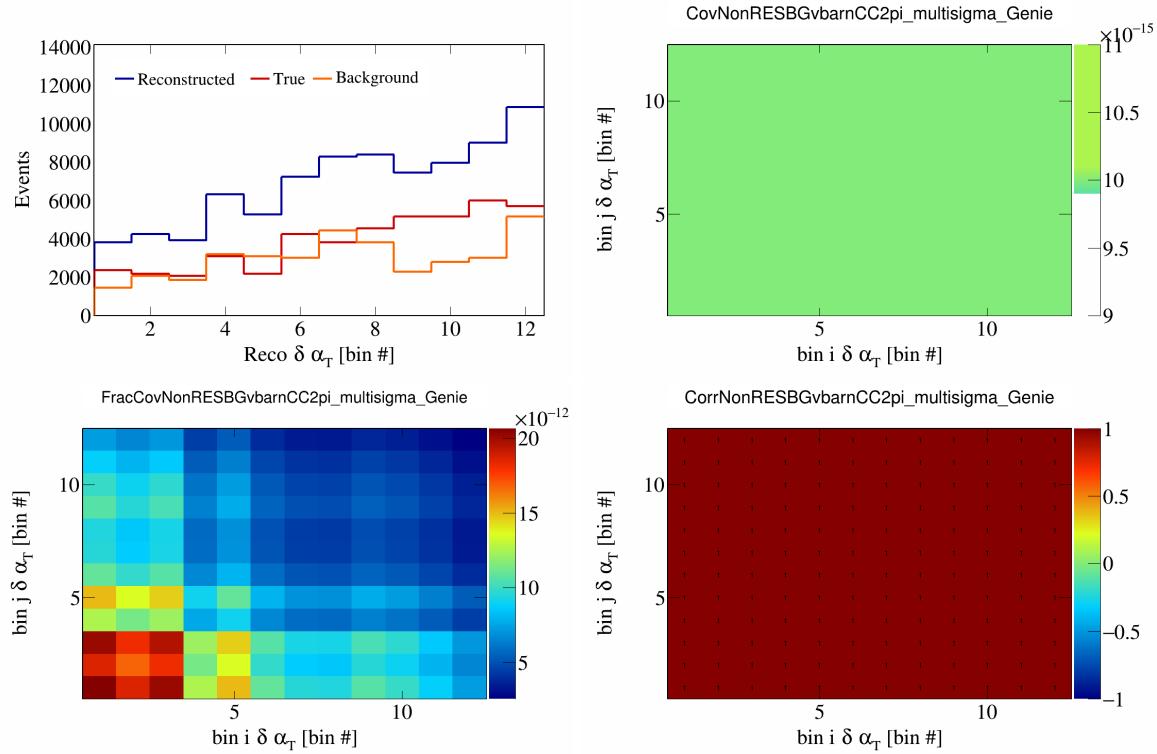


Figure 417: NonRESBGvbarCC2pi variations for $\delta \alpha_T$ in $\cos(\theta_{\vec{p}_\mu})$.

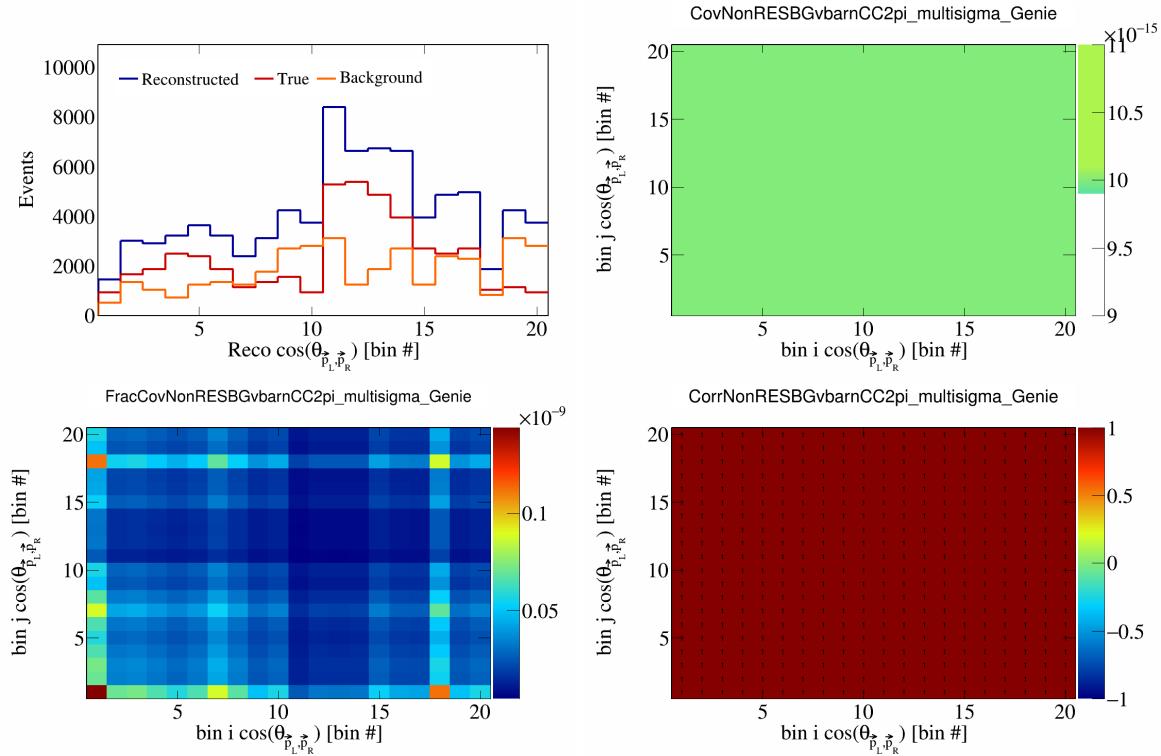


Figure 418: NonRESBGvbarCC2pi variations for $\cos(\theta_{\vec{p}_L, \vec{p}_R})$ in $\cos(\theta_{\vec{p}_\mu})$.

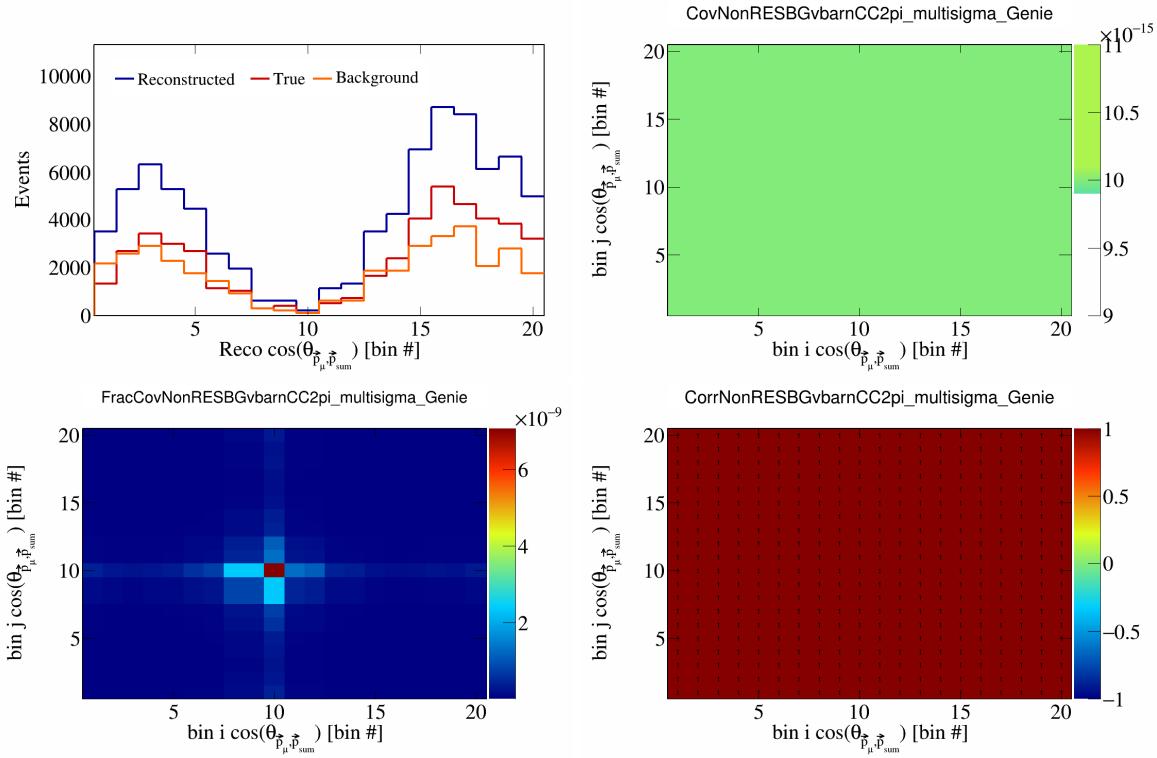


Figure 419: NonRESBGvbarCC2pi variations for $\cos(\theta_{\vec{p}_\mu, \vec{p}_{\text{sum}}})$ in $\cos(\theta_{\vec{p}_\mu})$.

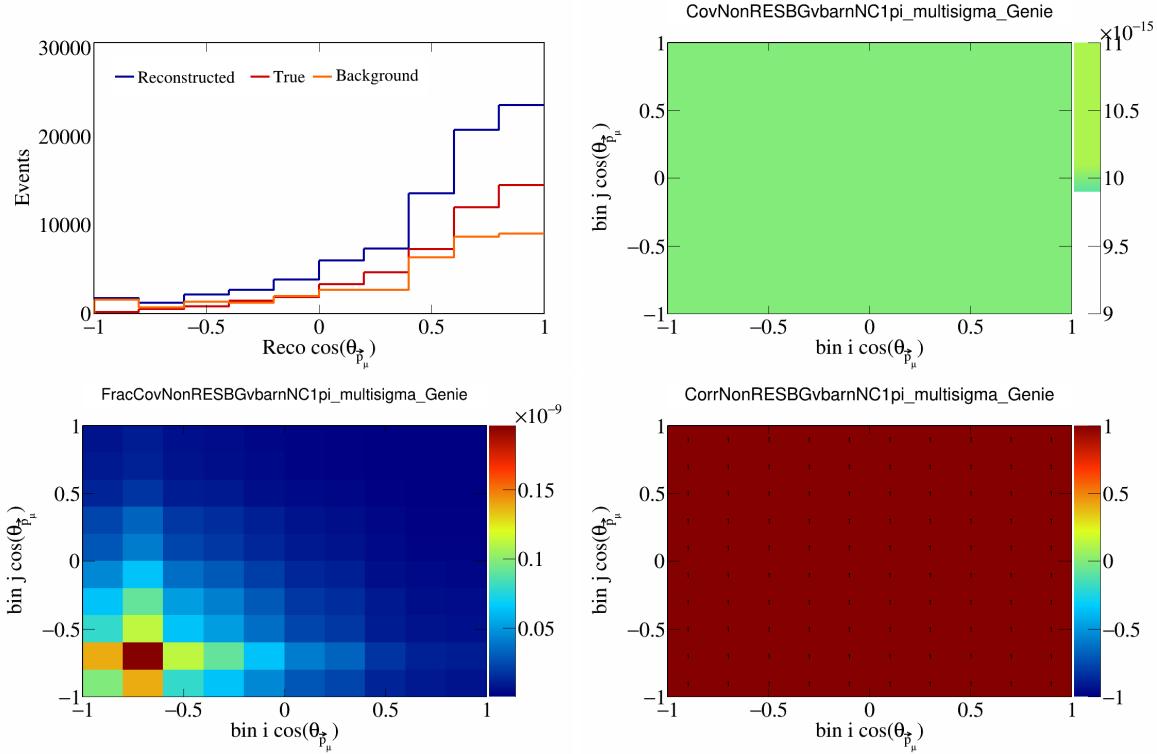


Figure 420: NonRESBGvbarNC1pi variations for $\cos(\theta_{\vec{p}_\mu})$.

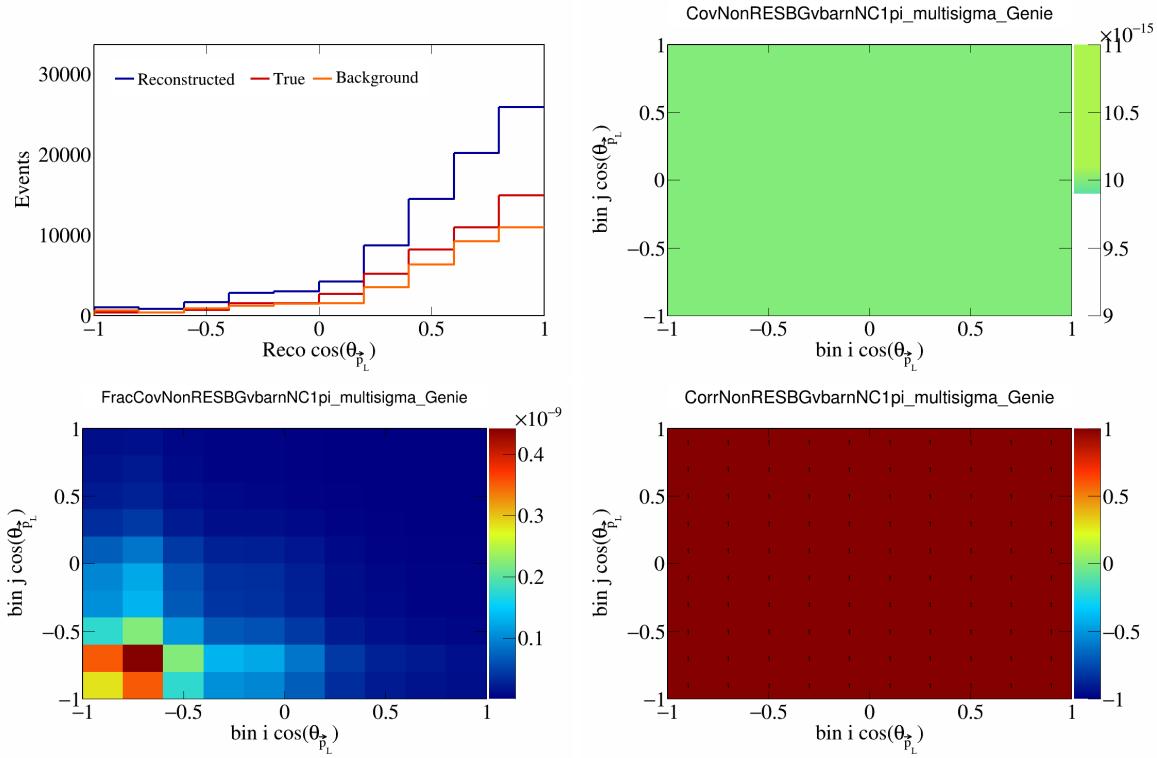


Figure 421: NonRESBGvbarNC1pi variations for $\cos(\theta_{\vec{p}_L})$.

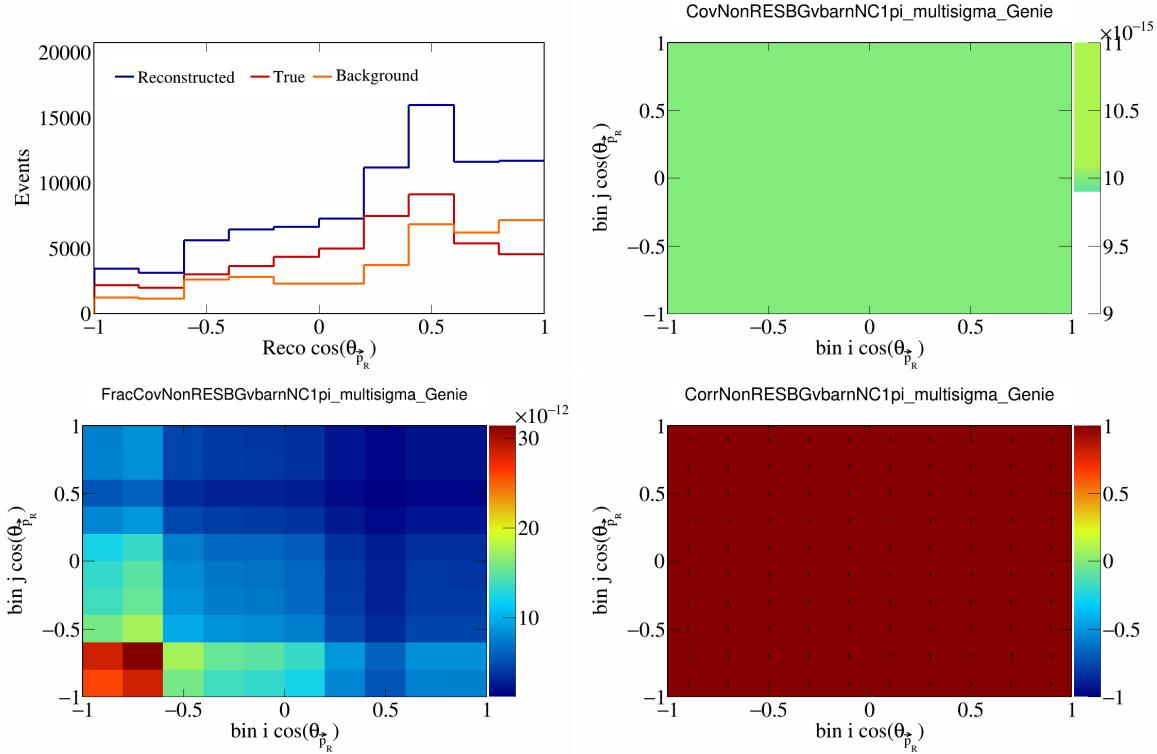


Figure 422: NonRESBGvbarNC1pi variations for $\cos(\theta_{\vec{p}_R})$.

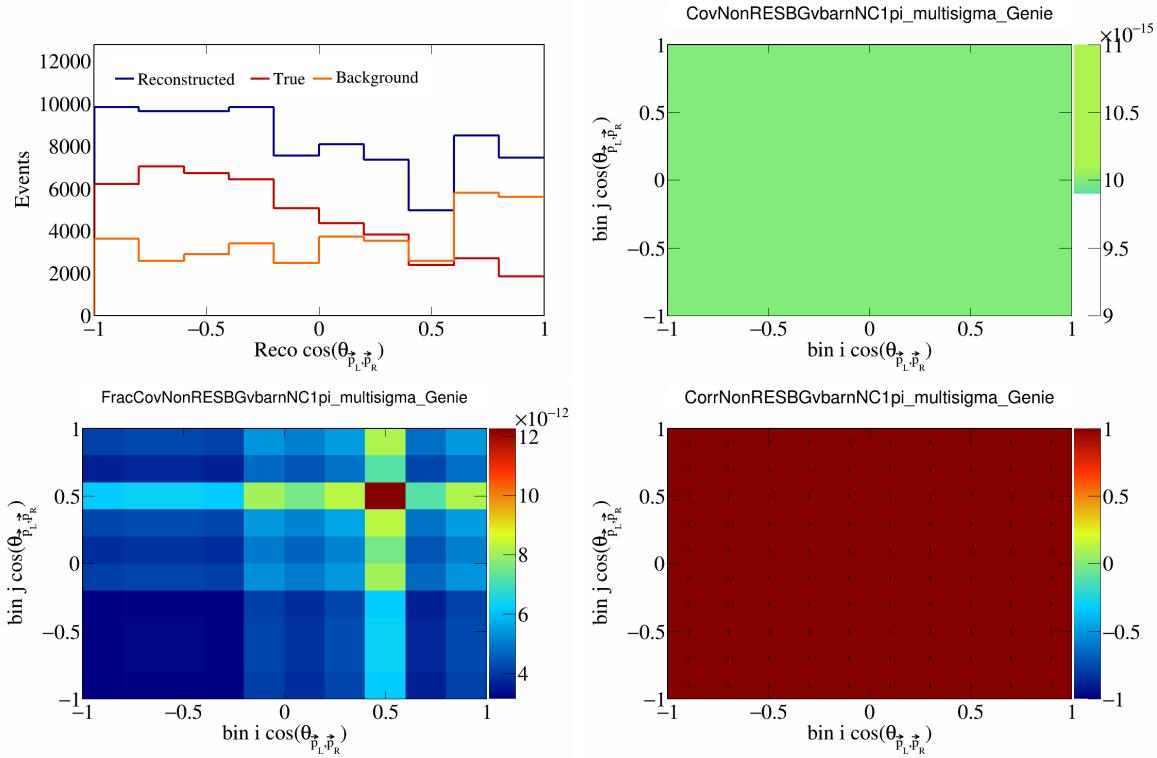


Figure 423: NonRESBGvbarNC1pi variations for $\cos(\theta_{\vec{p}_L, \vec{p}_R})$.

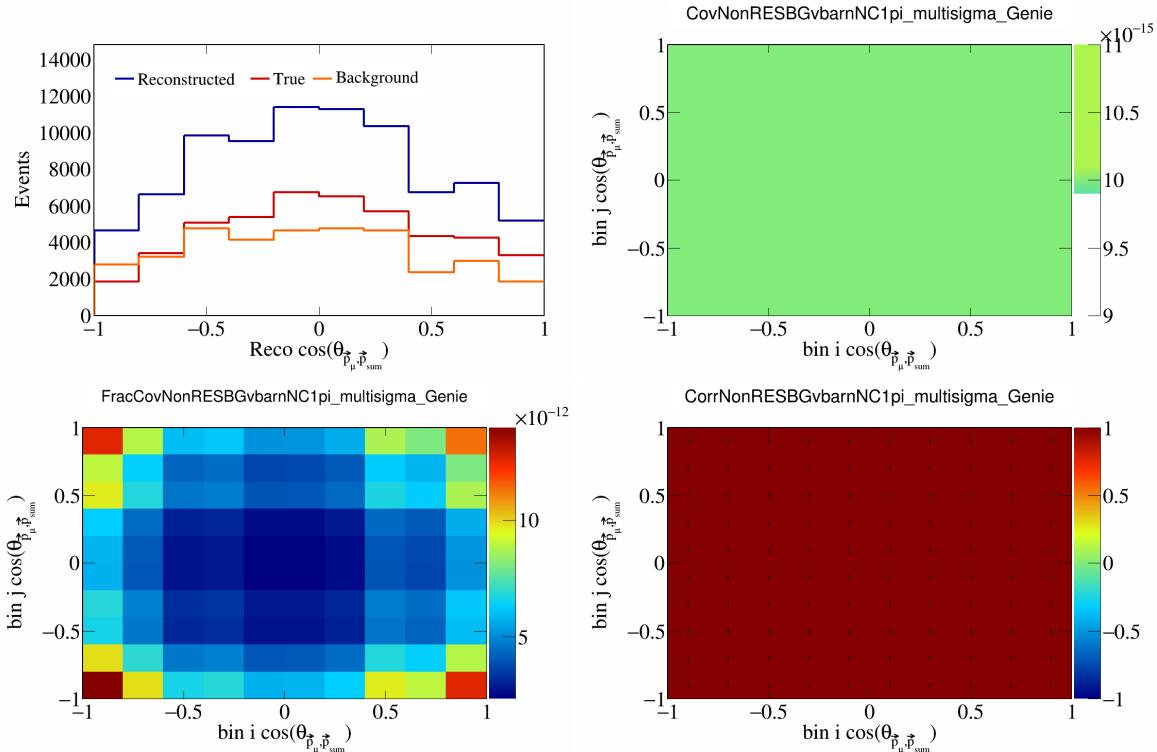


Figure 424: NonRESBGvbarNC1pi variations for $\cos(\theta_{\vec{p}_\mu, \vec{p}_{\text{sum}}})$.

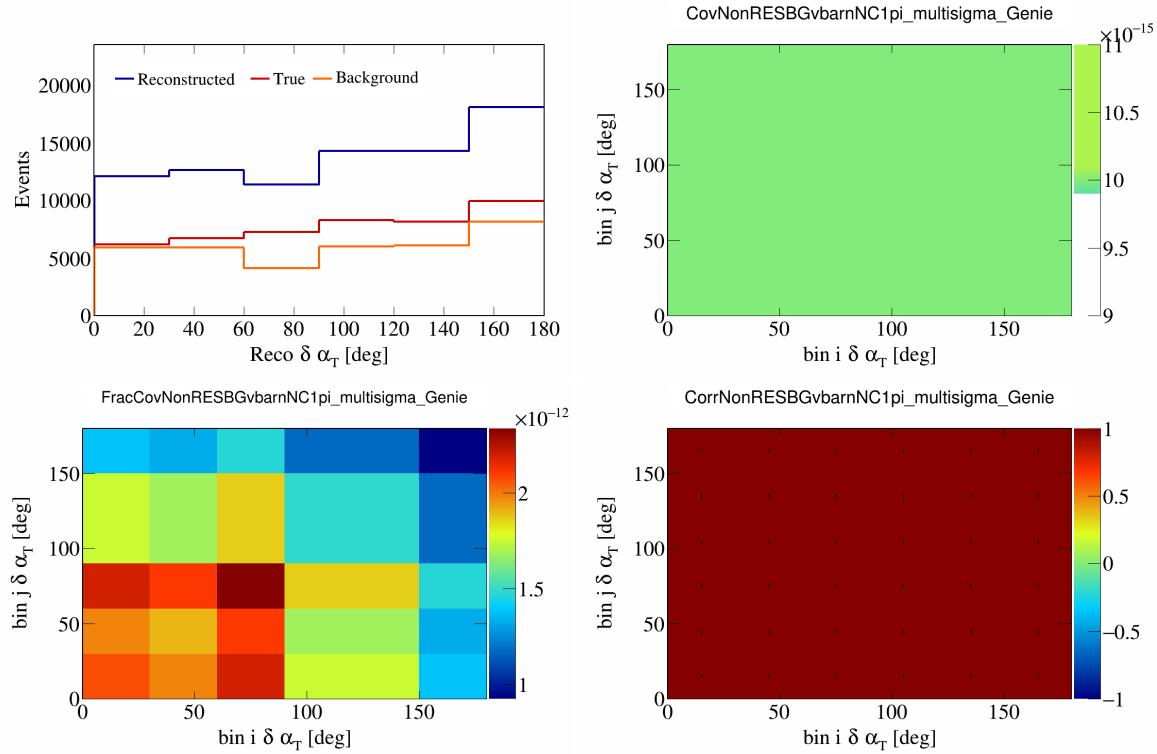


Figure 425: NonRESBGvbarNC1pi variations for $\delta\alpha_T$.

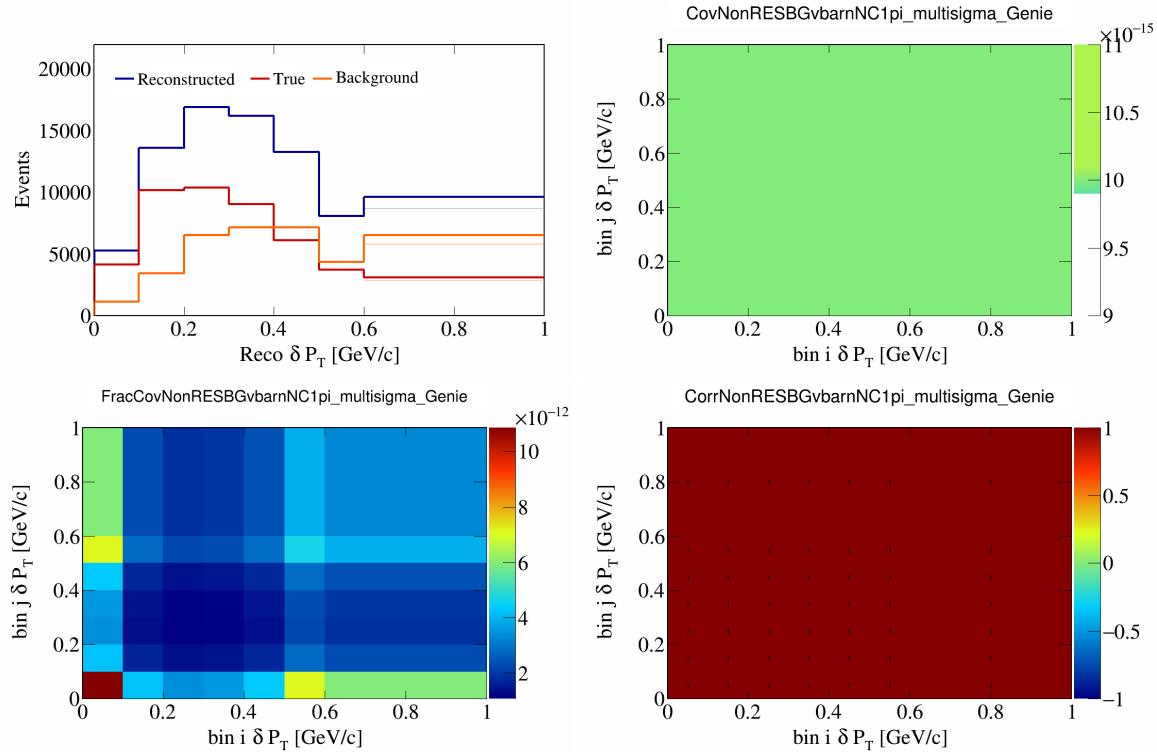


Figure 426: NonRESBGvbarNC1pi variations for δP_T .

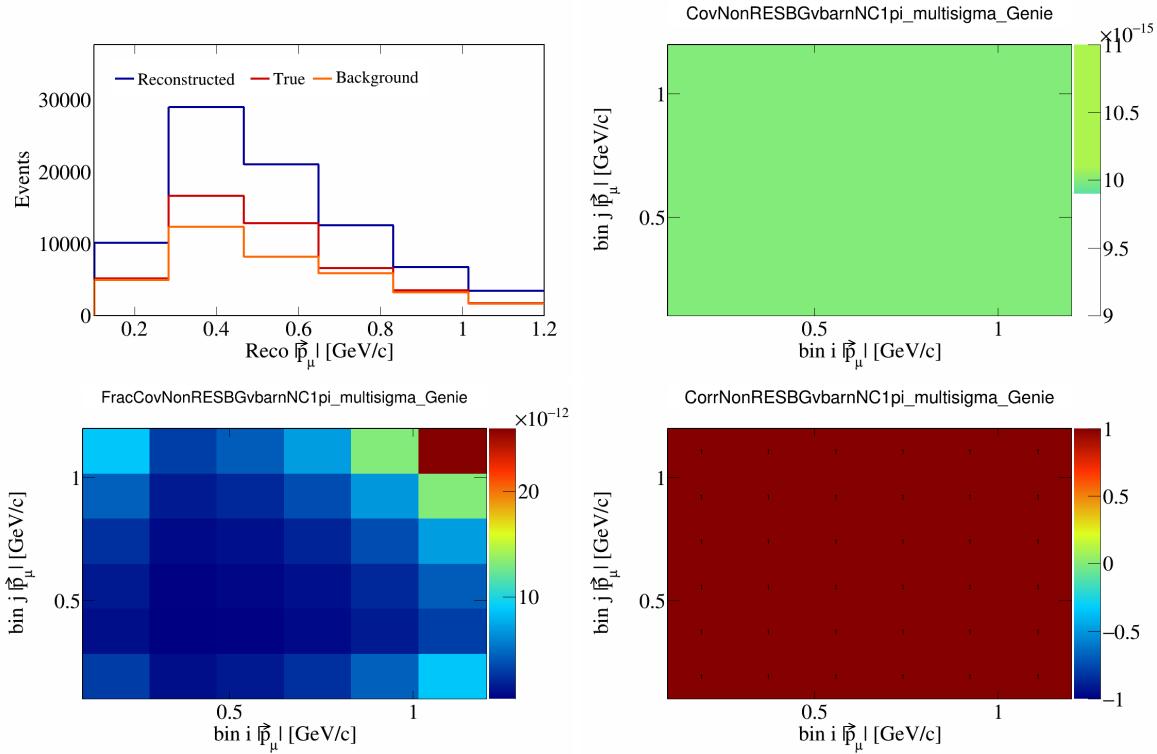


Figure 427: NonRESBGvbarNC1pi variations for $|\vec{p}_\mu|$.

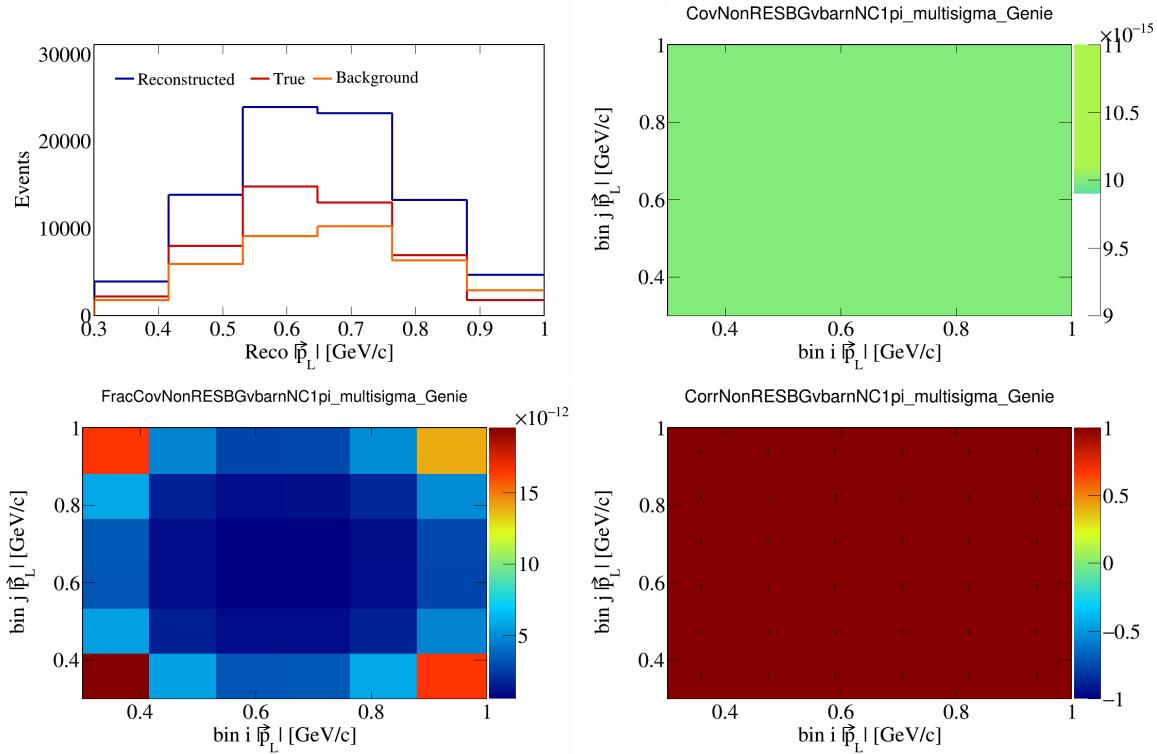


Figure 428: NonRESBGvbarNC1pi variations for $|\vec{p}_L|$.

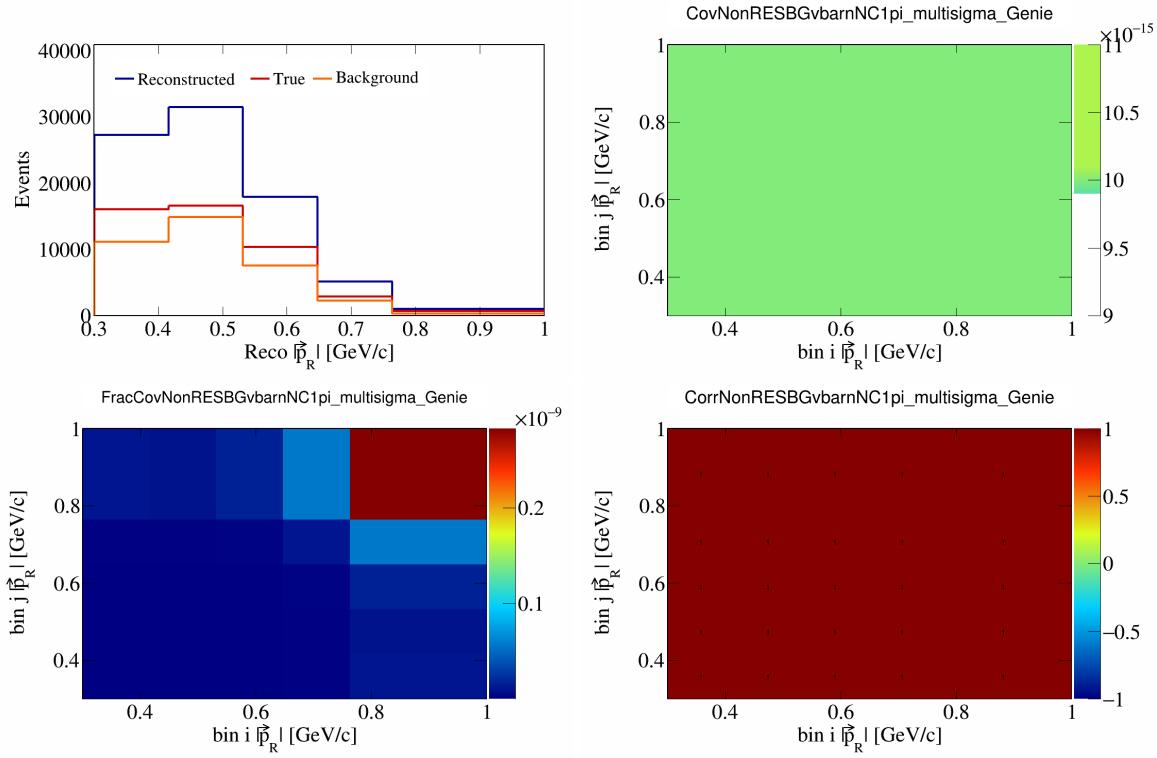


Figure 429: NonRESBGvbarNC1pi variations for $|\vec{p}_R|$.

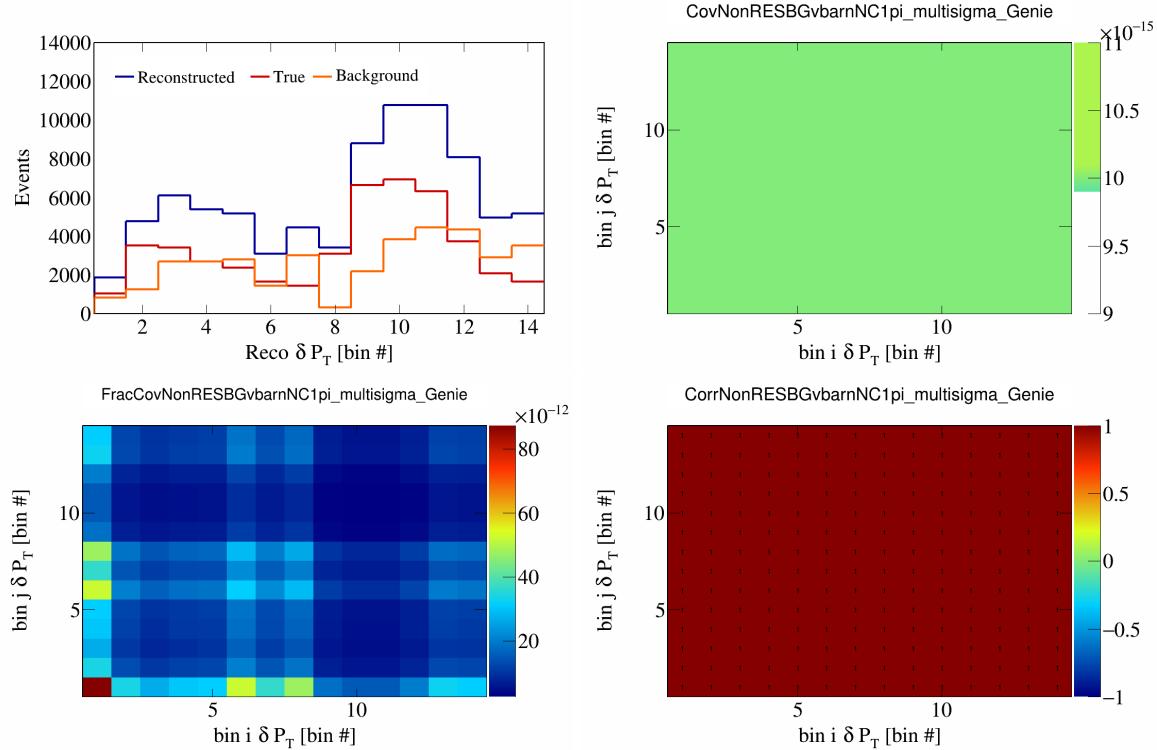


Figure 430: NonRESBGvbarNC1pi variations for δP_T in $\cos(\theta_{\vec{p}_\mu})$.

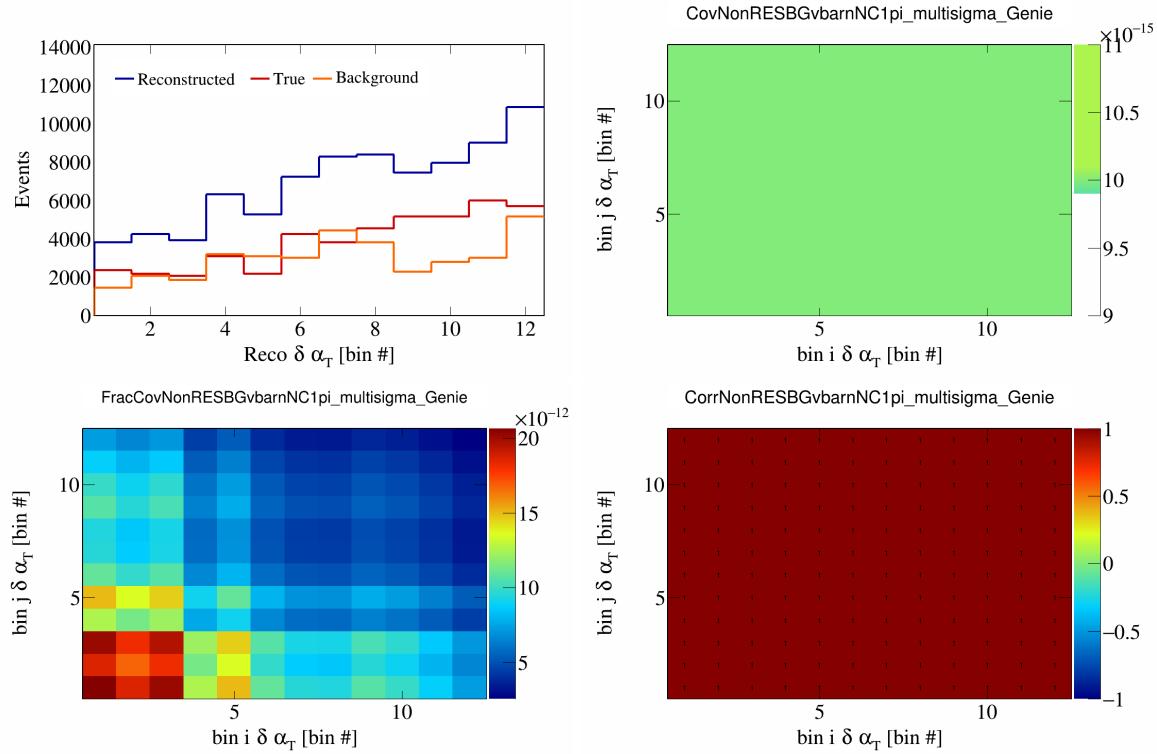


Figure 431: NonRESBGvbarNC1pi variations for $\delta\alpha_T$ in $\cos(\theta_{\vec{p}_\mu})$.

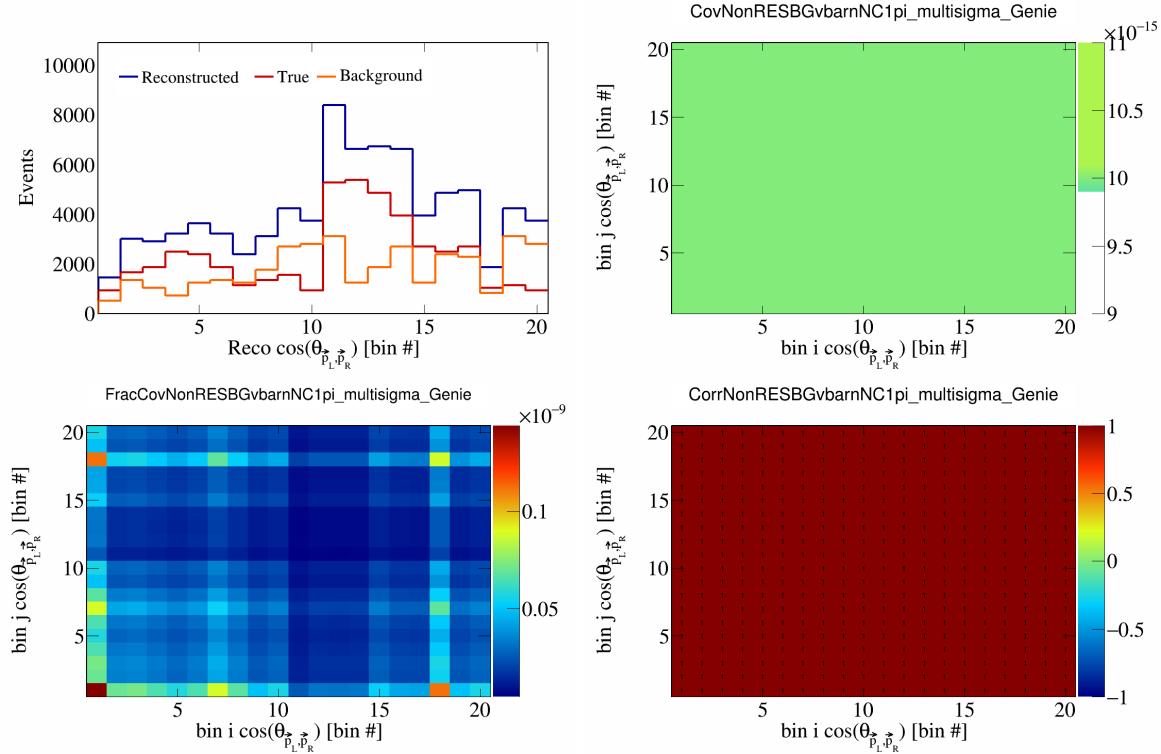


Figure 432: NonRESBGvbarNC1pi variations for $\cos(\theta_{\vec{p}_L, \vec{p}_R})$ in $\cos(\theta_{\vec{p}_\mu})$.

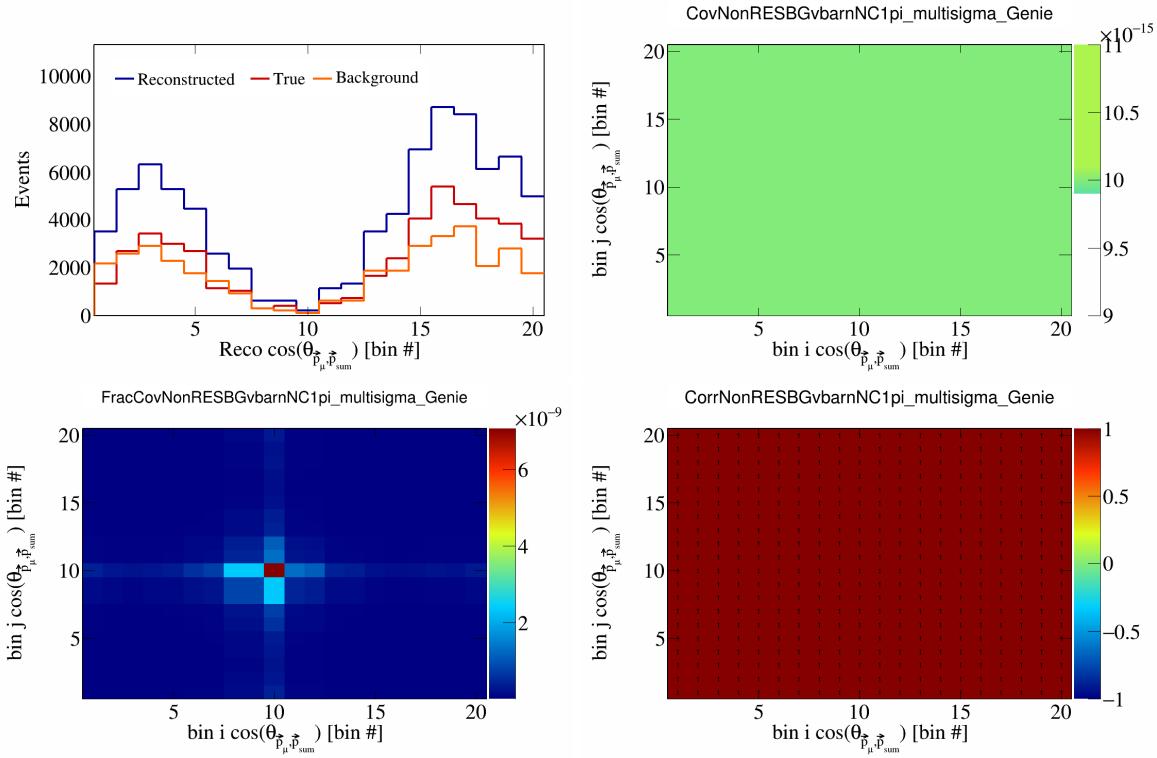


Figure 433: NonRESBGvbarNC1pi variations for $\cos(\theta_{\vec{p}_\mu})$ in $\cos(\theta_{\vec{p}_\mu})$.

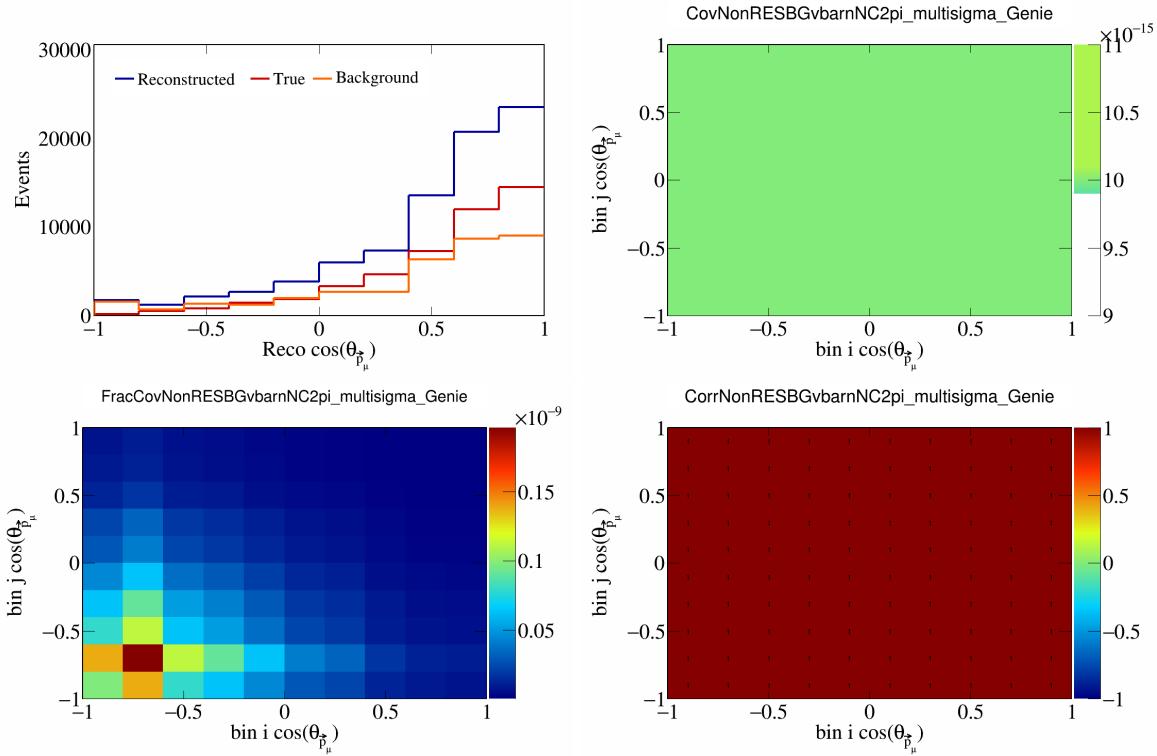


Figure 434: NonRESBGvbarNC2pi variations for $\cos(\theta_{\vec{p}_\mu})$.

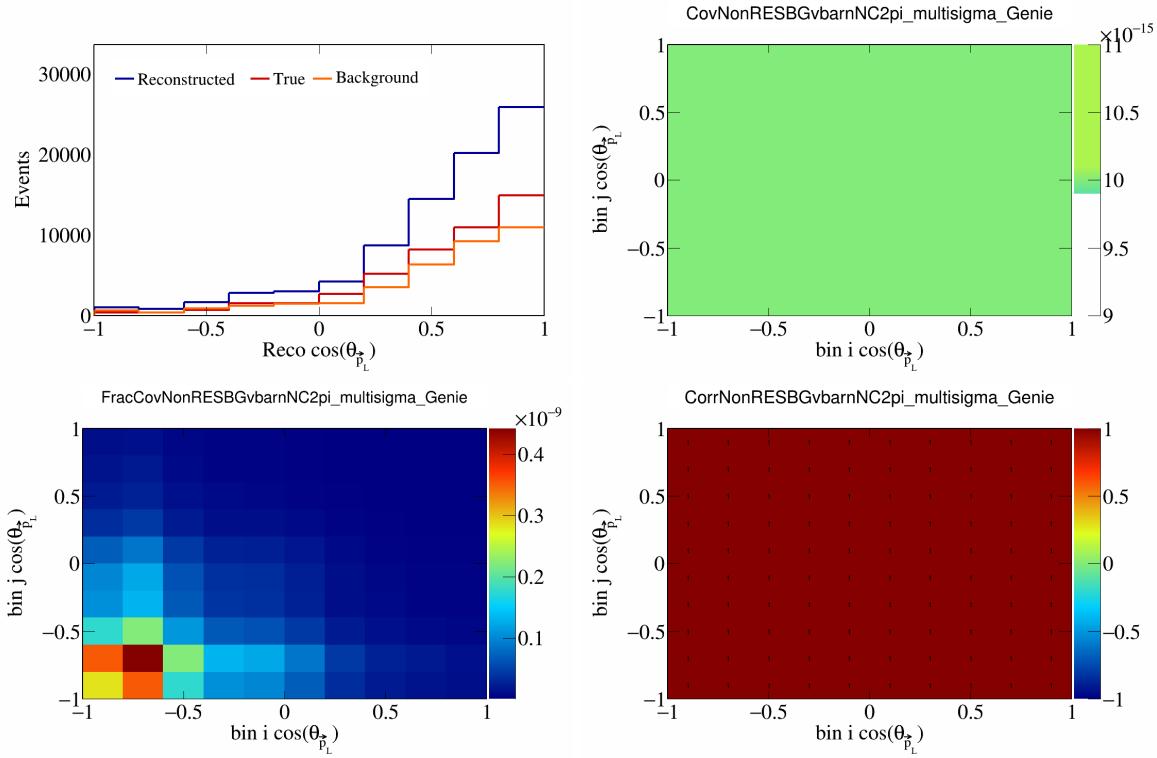


Figure 435: NonRESBGvbarNC2pi variations for $\cos(\theta_{\vec{p}_L})$.

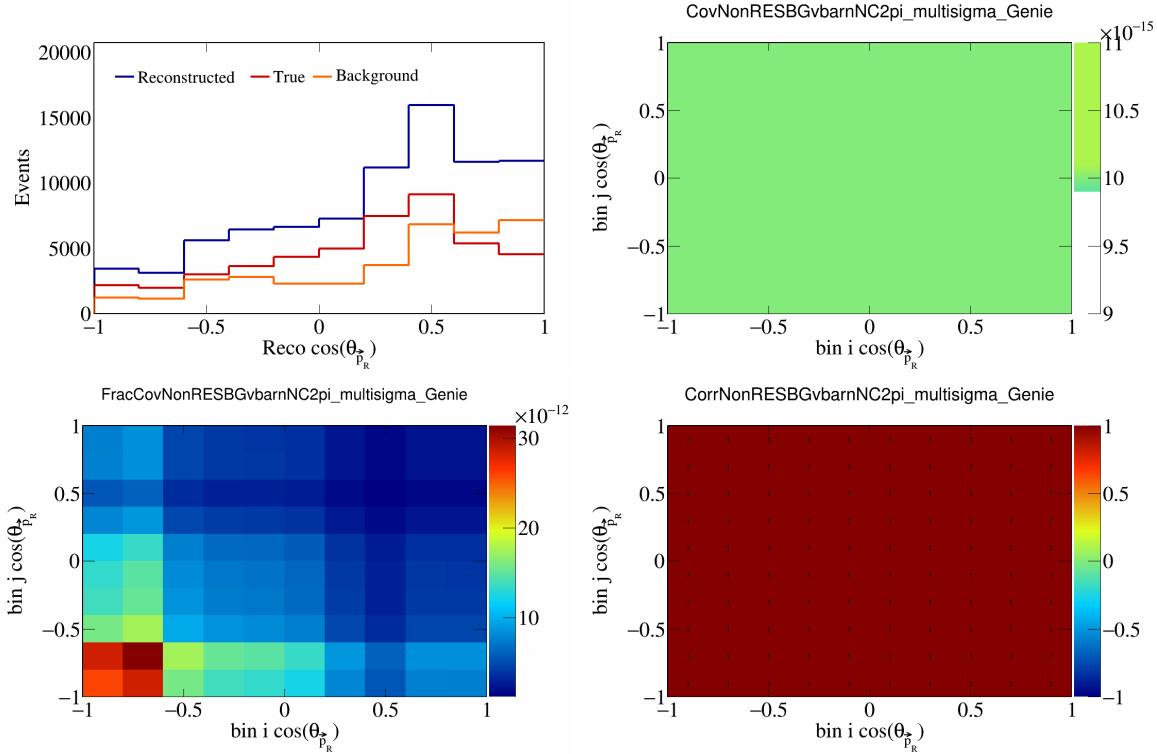


Figure 436: NonRESBGvbarNC2pi variations for $\cos(\theta_{\vec{p}_R})$.

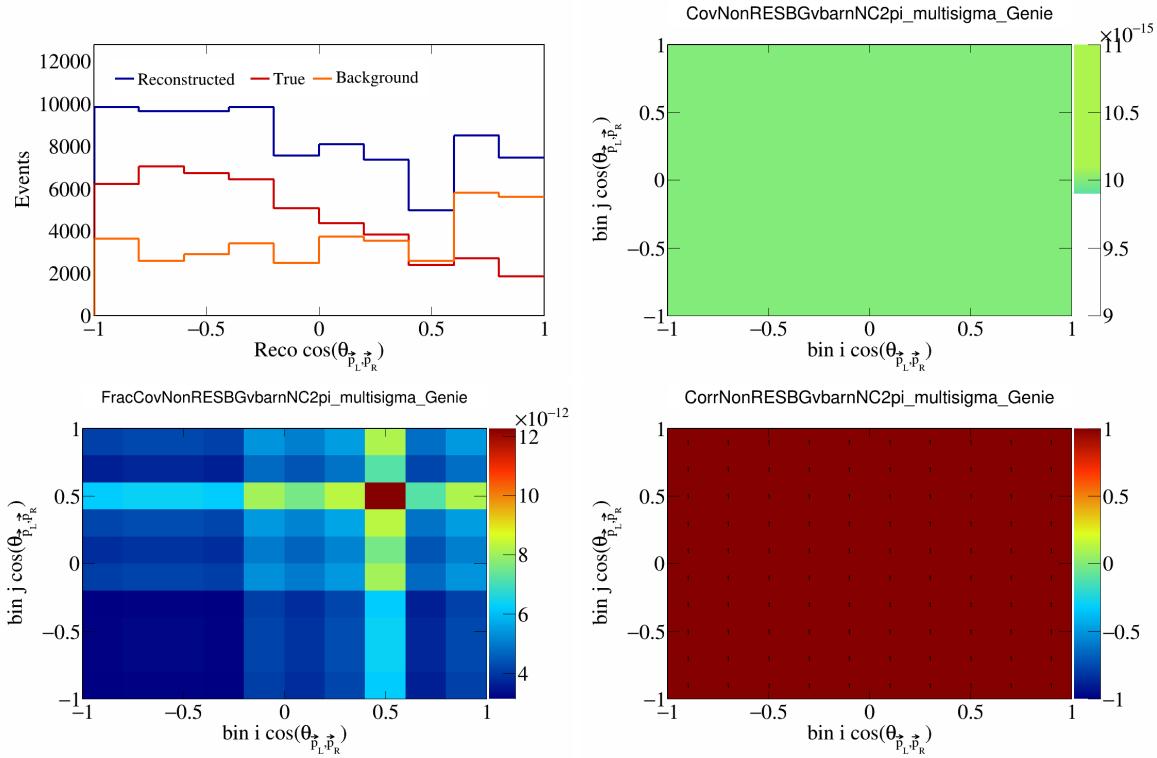


Figure 437: NonRESBGvbarNC2pi variations for $\cos(\theta_{\vec{p}_L, \vec{p}_R})$.

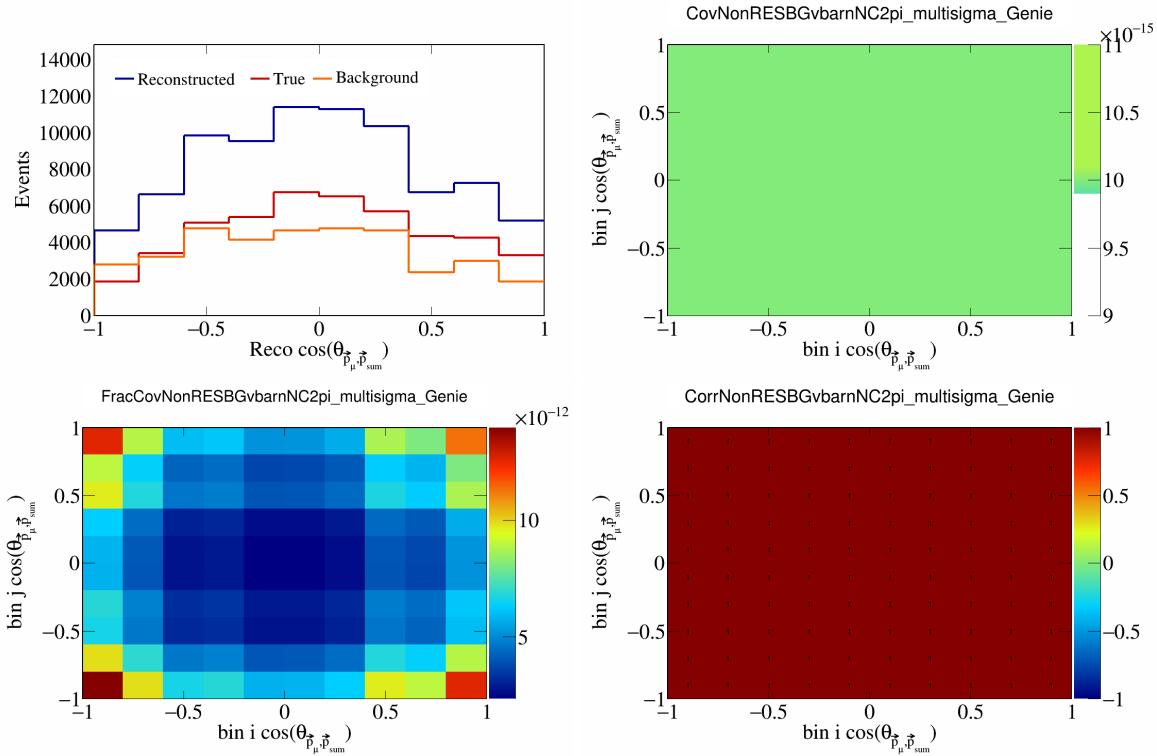


Figure 438: NonRESBGvbarNC2pi variations for $\cos(\theta_{\vec{p}_\mu, \vec{p}_{\text{sum}}})$.

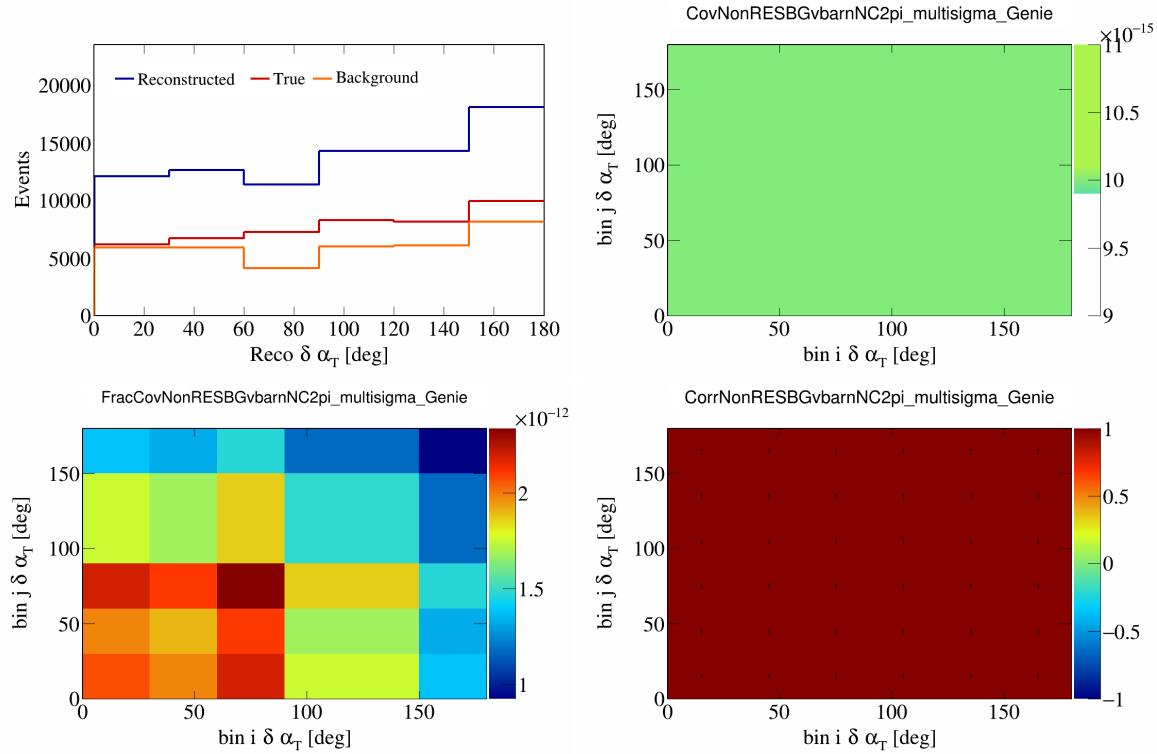


Figure 439: NonRESBGvbarNC2pi variations for $\delta\alpha_T$.

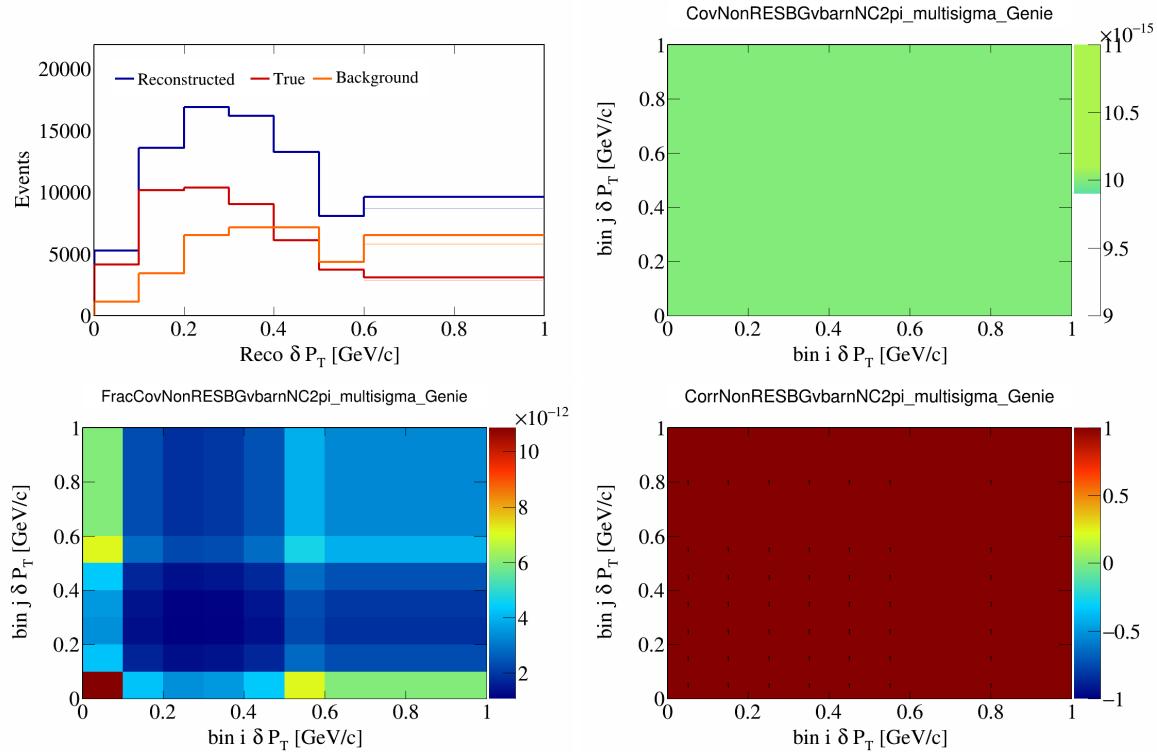


Figure 440: NonRESBGvbarNC2pi variations for δP_T .

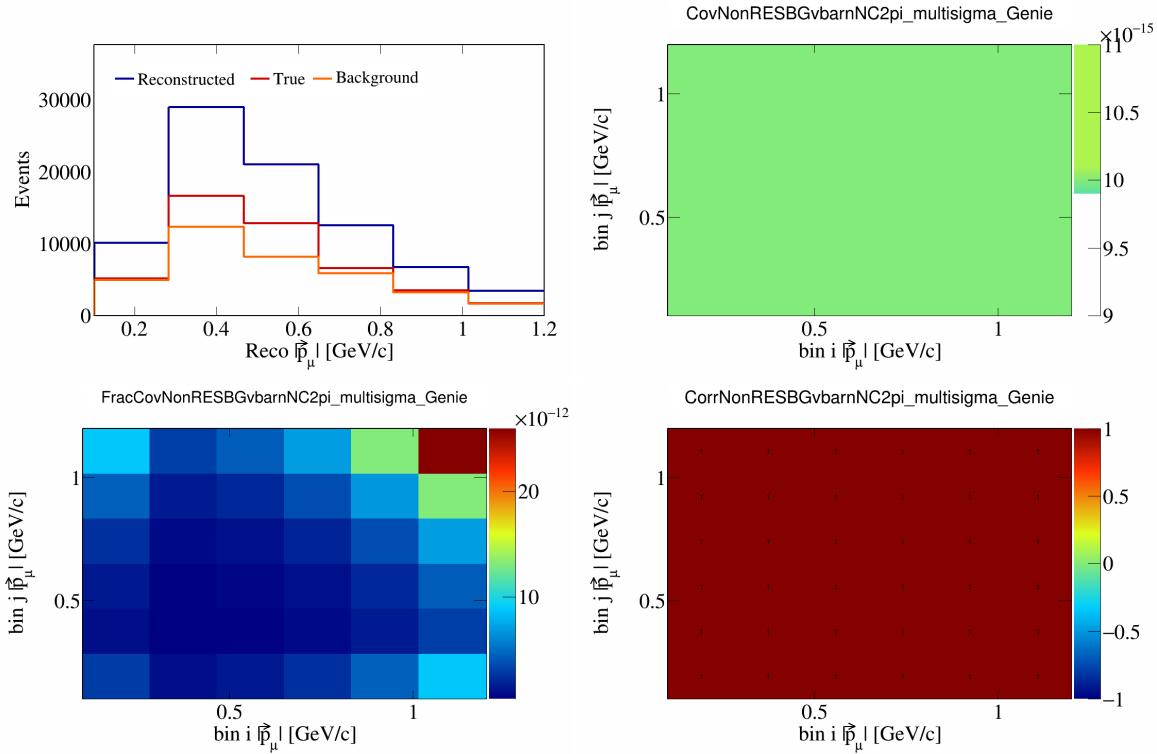


Figure 441: NonRESBGvbarNC2pi variations for $|\vec{p}_\mu|$.

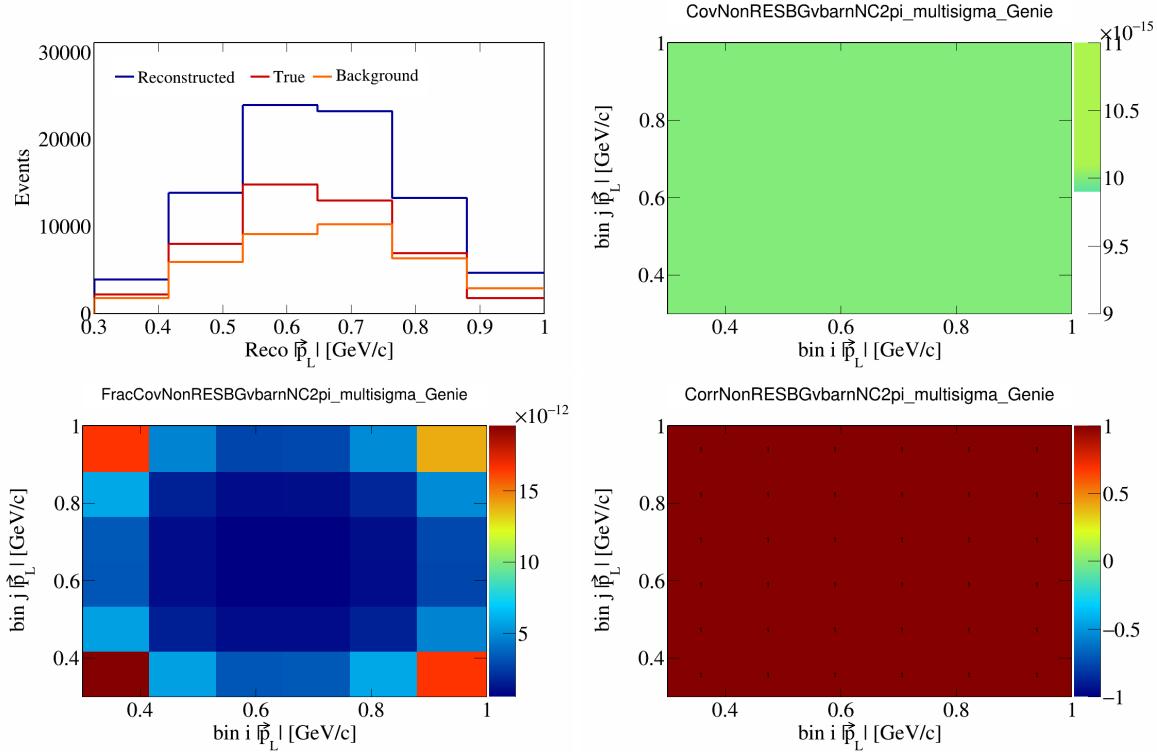


Figure 442: NonRESBGvbarNC2pi variations for $|\vec{p}_L|$.

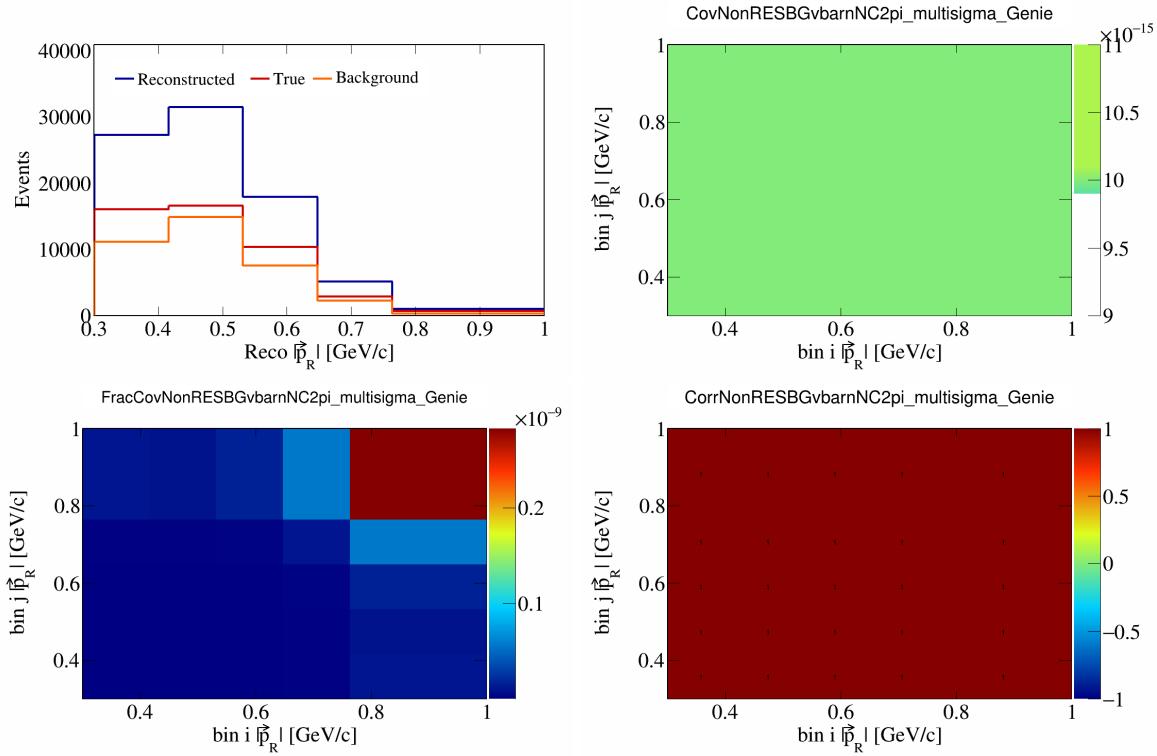


Figure 443: NonRESBGvbarNC2pi variations for $|\vec{p}_R|$.

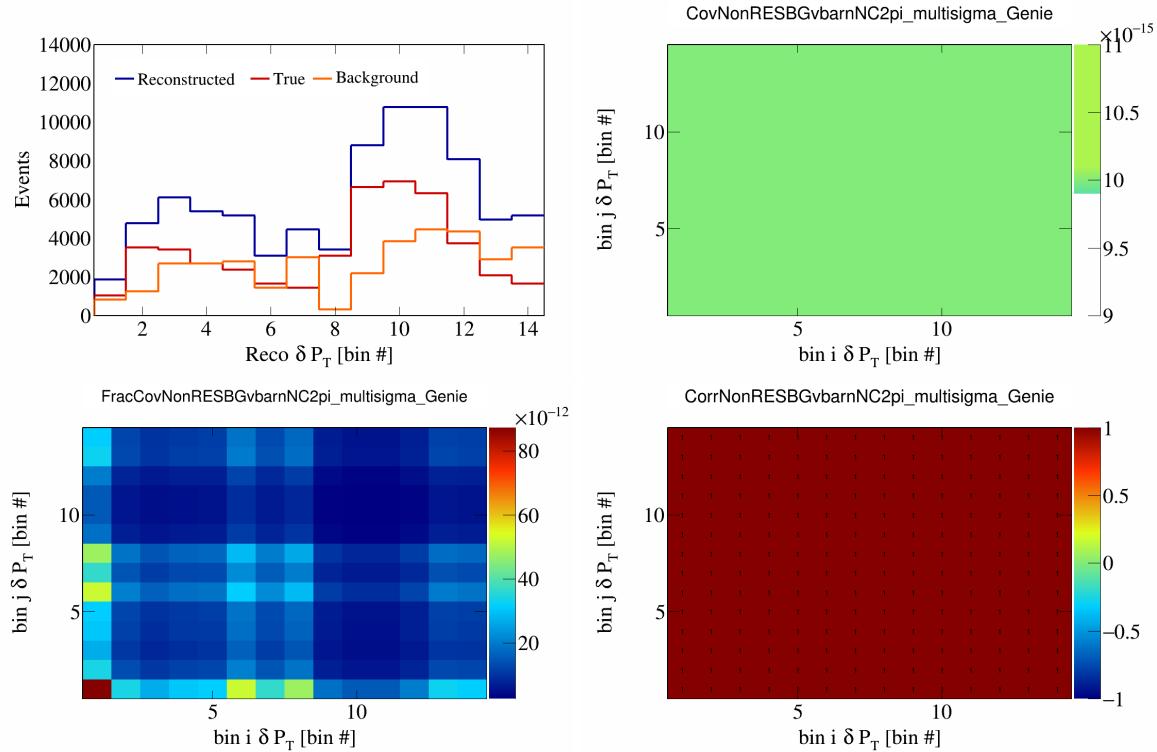


Figure 444: NonRESBGvbarNC2pi variations for δP_T in $\cos(\theta_{\vec{p}_\mu})$.

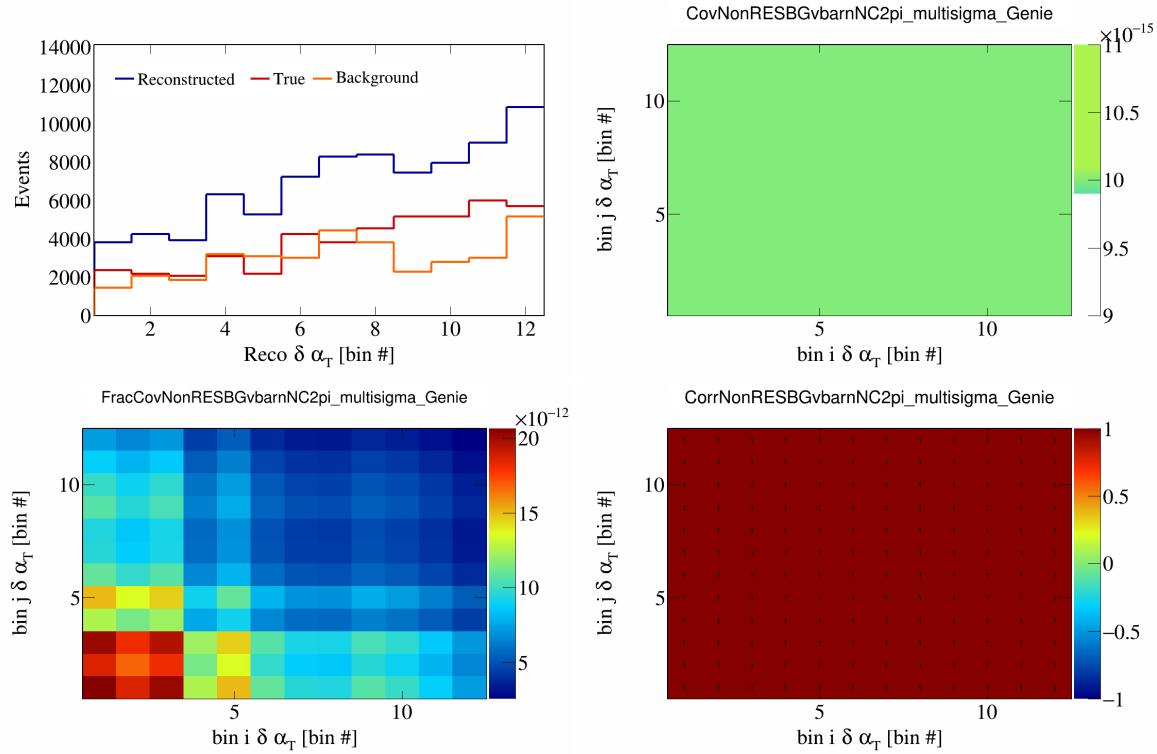


Figure 445: NonRESBGvbarNC2pi variations for $\delta \alpha_T$ in $\cos(\theta_{\vec{p}_\mu})$.

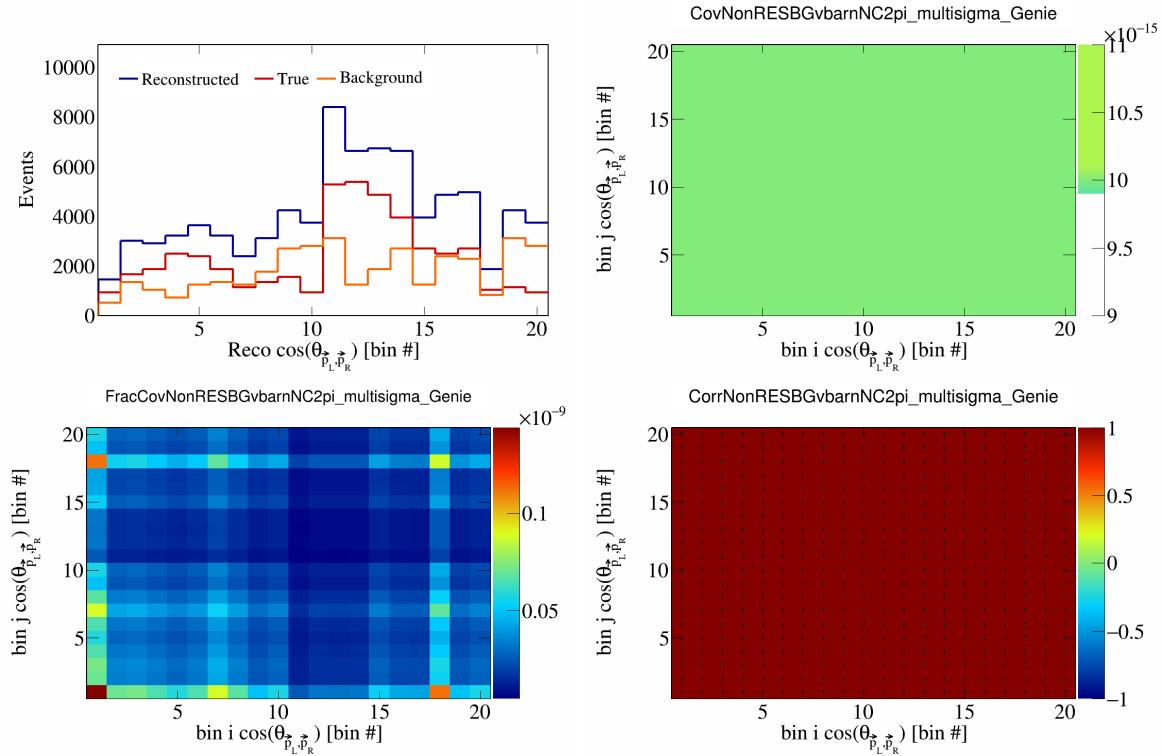


Figure 446: NonRESBGvbarNC2pi variations for $\cos(\theta_{\vec{p}_L, \vec{p}_R})$ in $\cos(\theta_{\vec{p}_\mu})$.

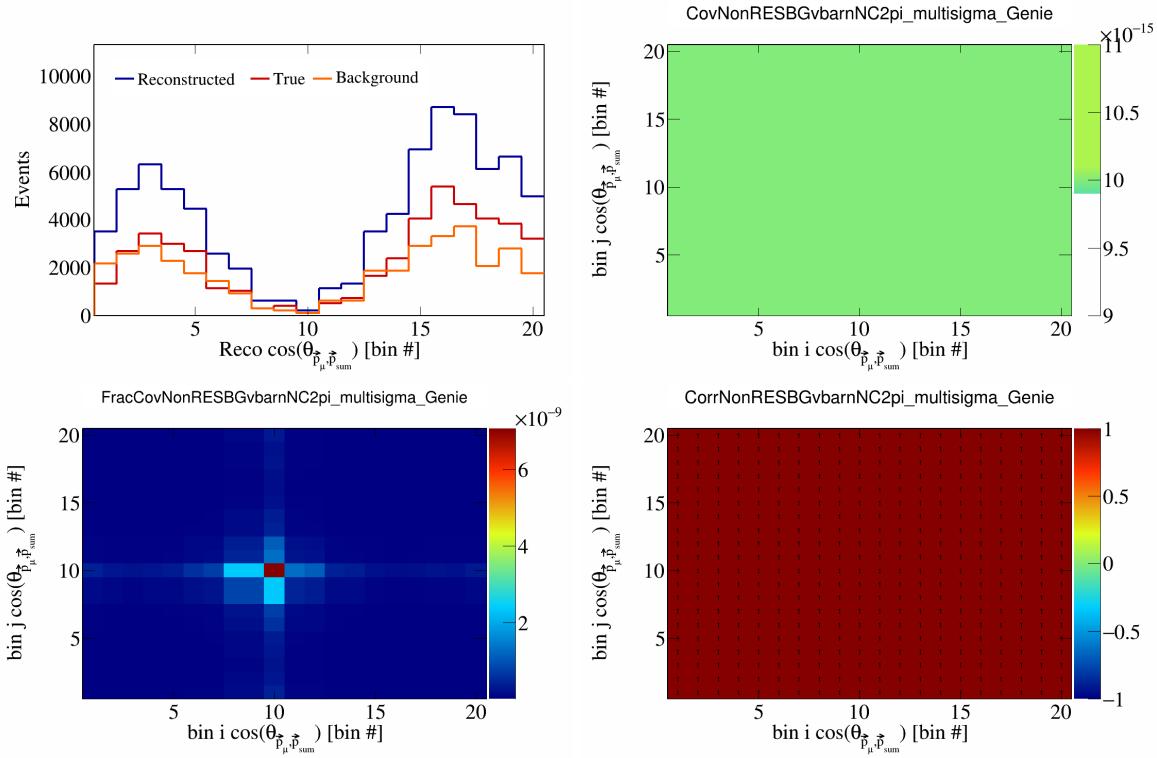


Figure 447: NonRESBGvbarNC2pi variations for $\cos(\theta_{\vec{p}_\mu, \vec{p}_{\text{sum}}})$ in $\cos(\theta_{\vec{p}_\mu})$.

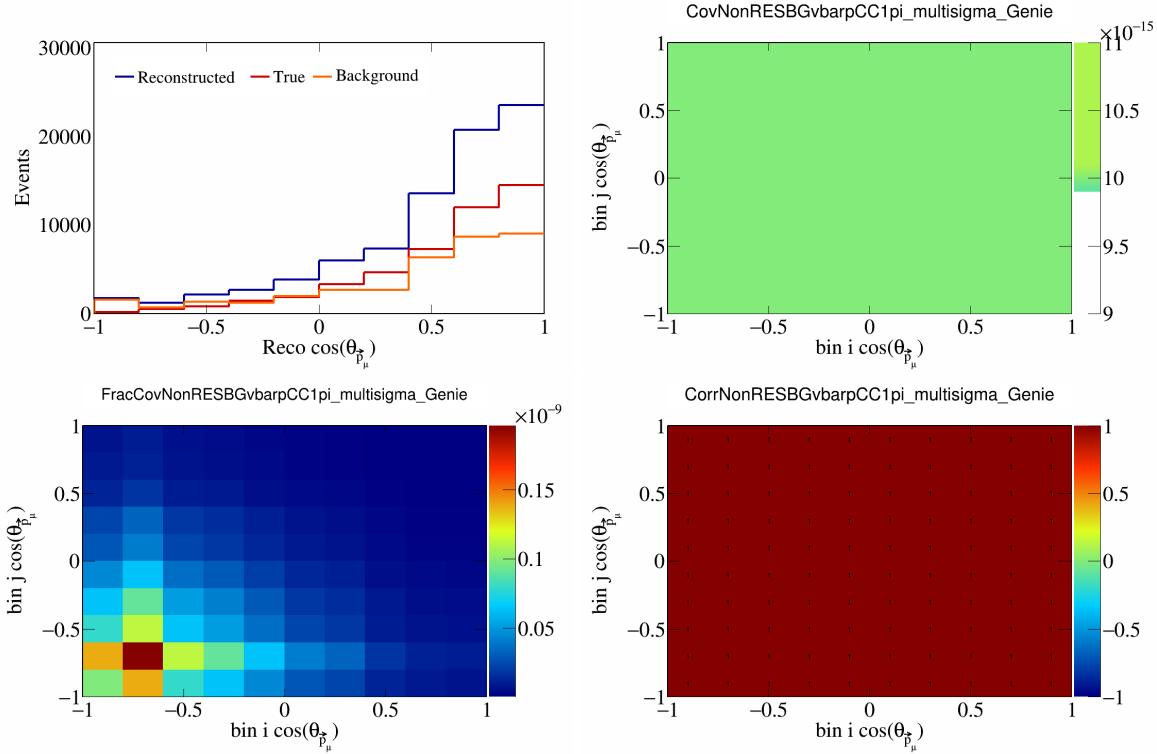


Figure 448: NonRESBGvbarCC1pi variations for $\cos(\theta_{\vec{p}_\mu})$.

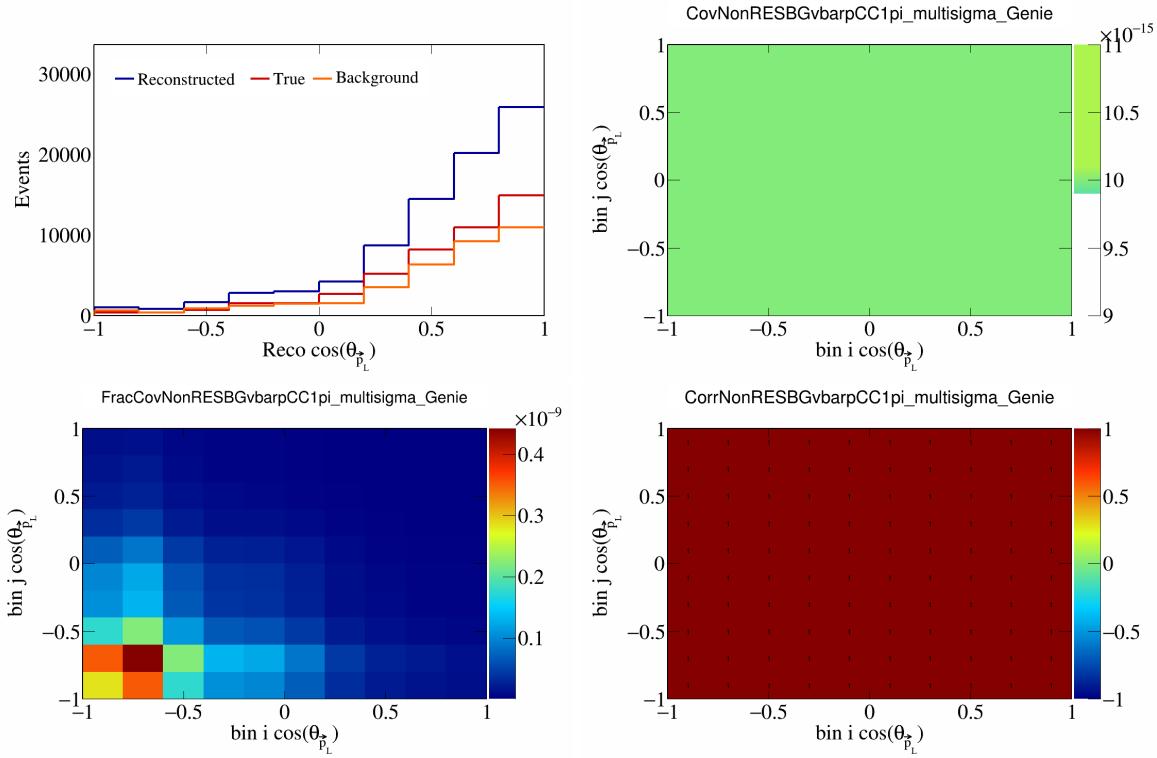


Figure 449: NonRESBGvbarpCC1pi variations for $\cos(\theta_{\vec{p}_L})$.

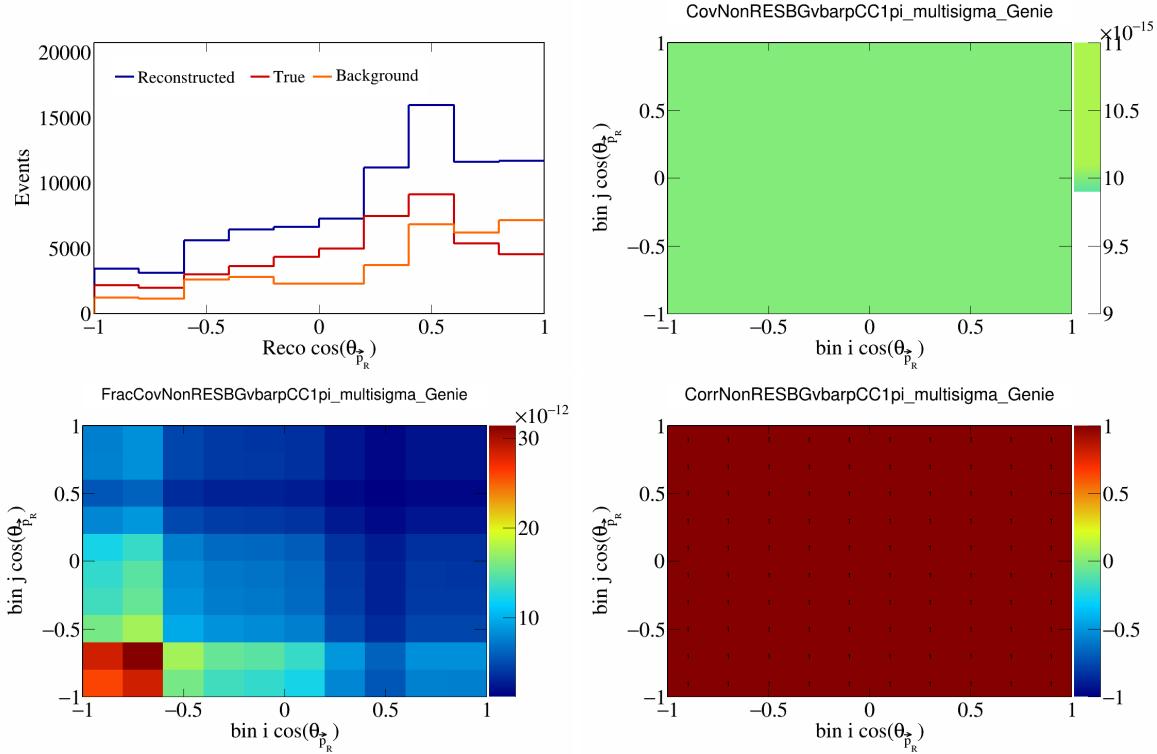


Figure 450: NonRESBGvbarpCC1pi variations for $\cos(\theta_{\vec{p}_R})$.

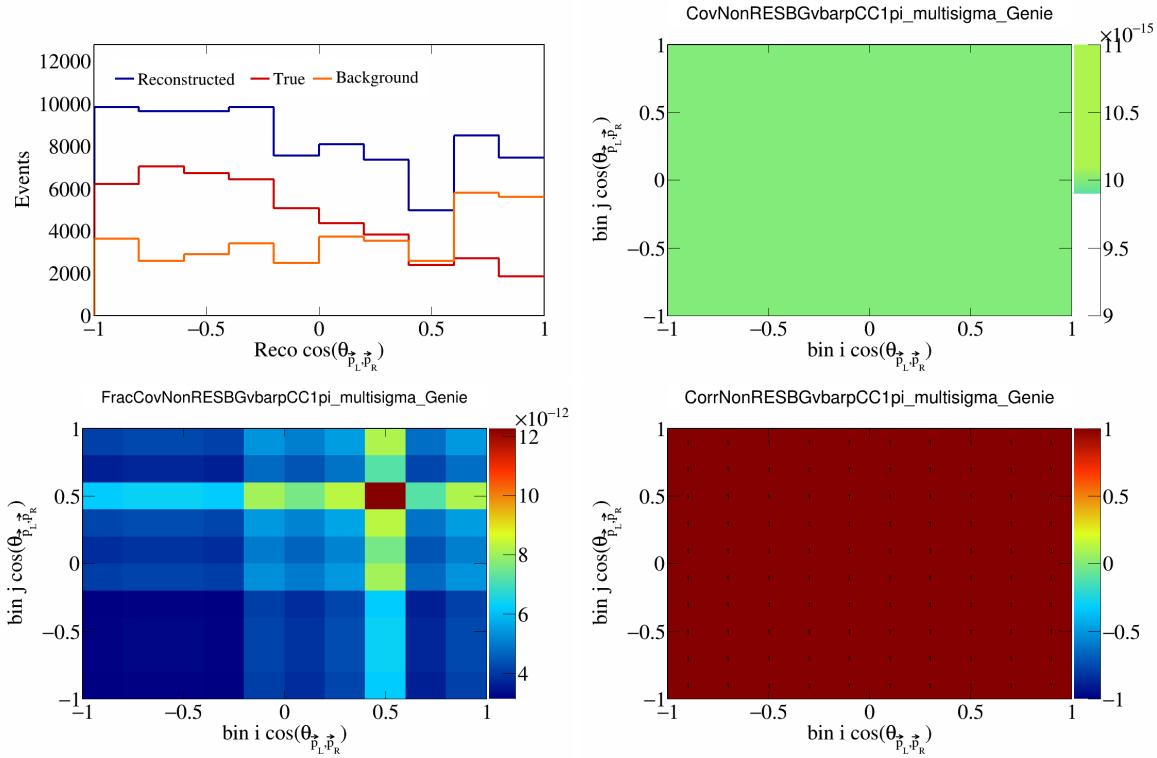


Figure 451: NonRESBGvbarpCC1pi variations for $\cos(\theta_{\vec{p}_L, \vec{p}_R})$.

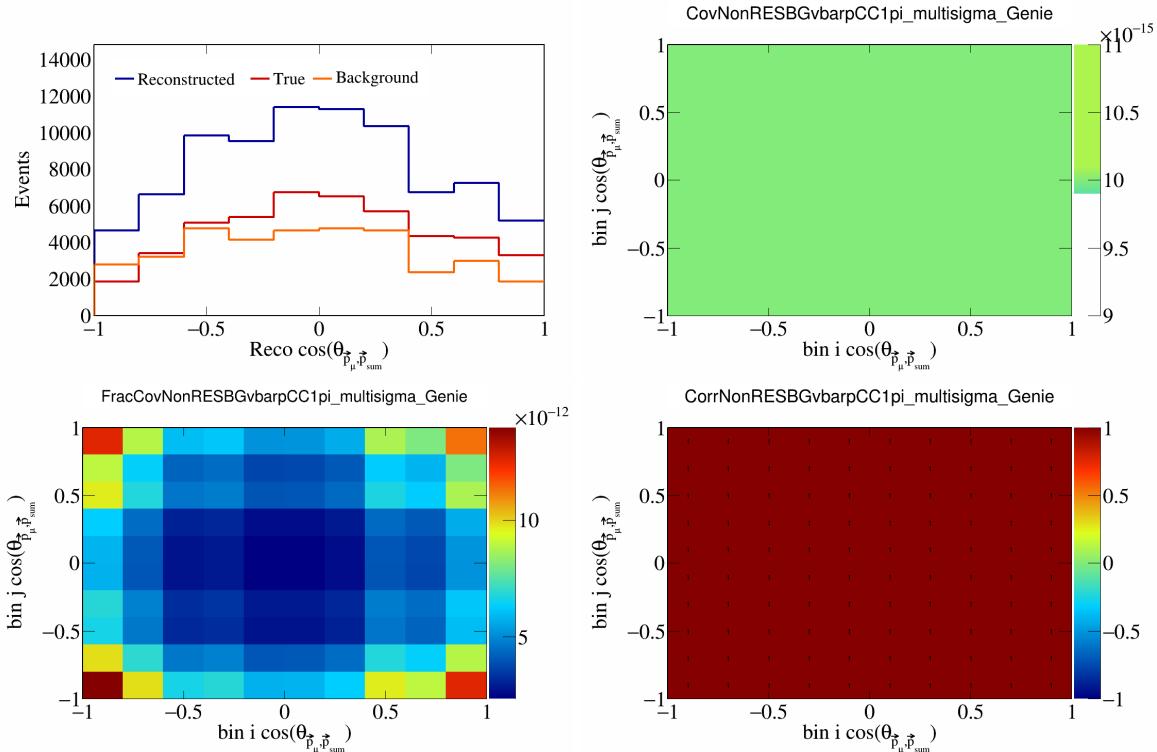


Figure 452: NonRESBGvbarpCC1pi variations for $\cos(\theta_{\vec{p}_\mu, \vec{p}_{\text{sum}}})$.

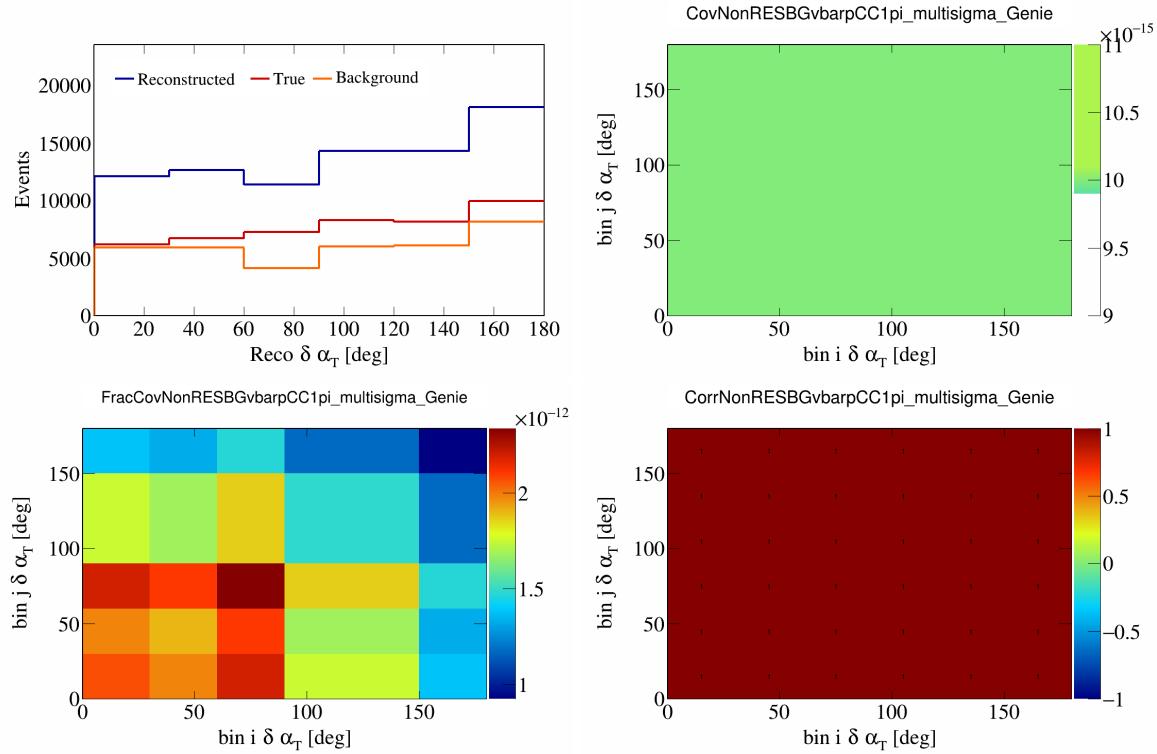


Figure 453: NonRESBGvbarpCC1pi variations for $\delta\alpha_T$.

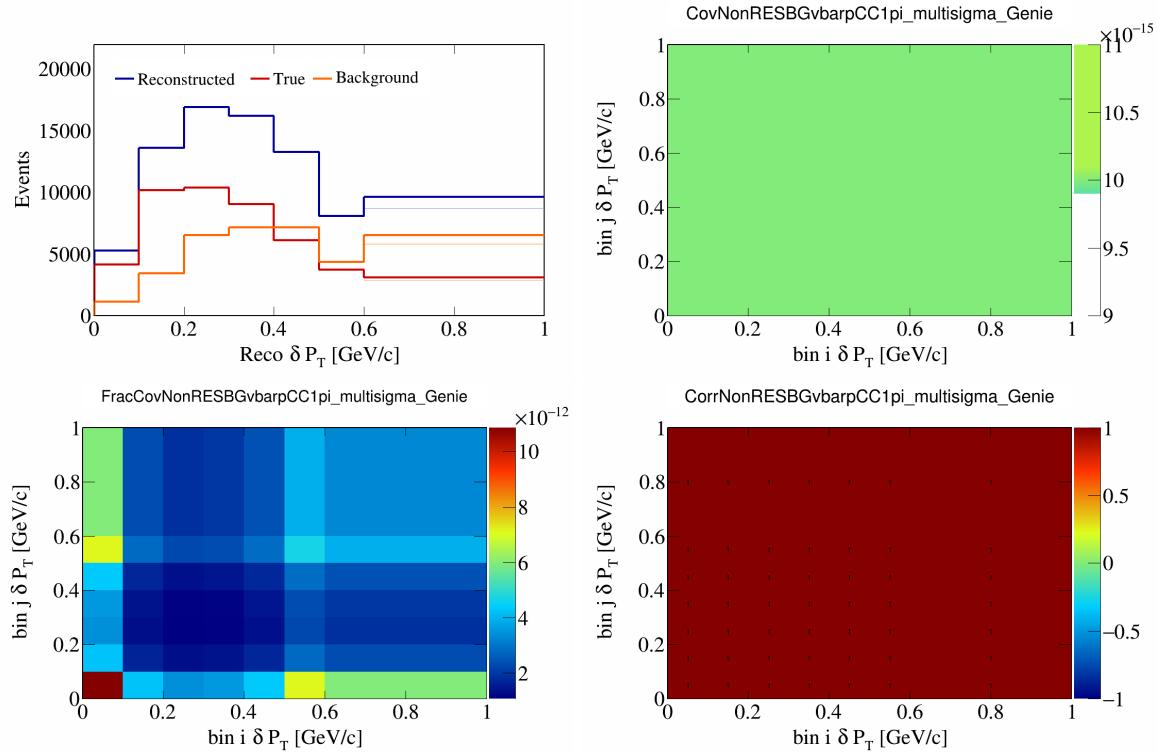


Figure 454: NonRESBGvbarpCC1pi variations for δP_T .

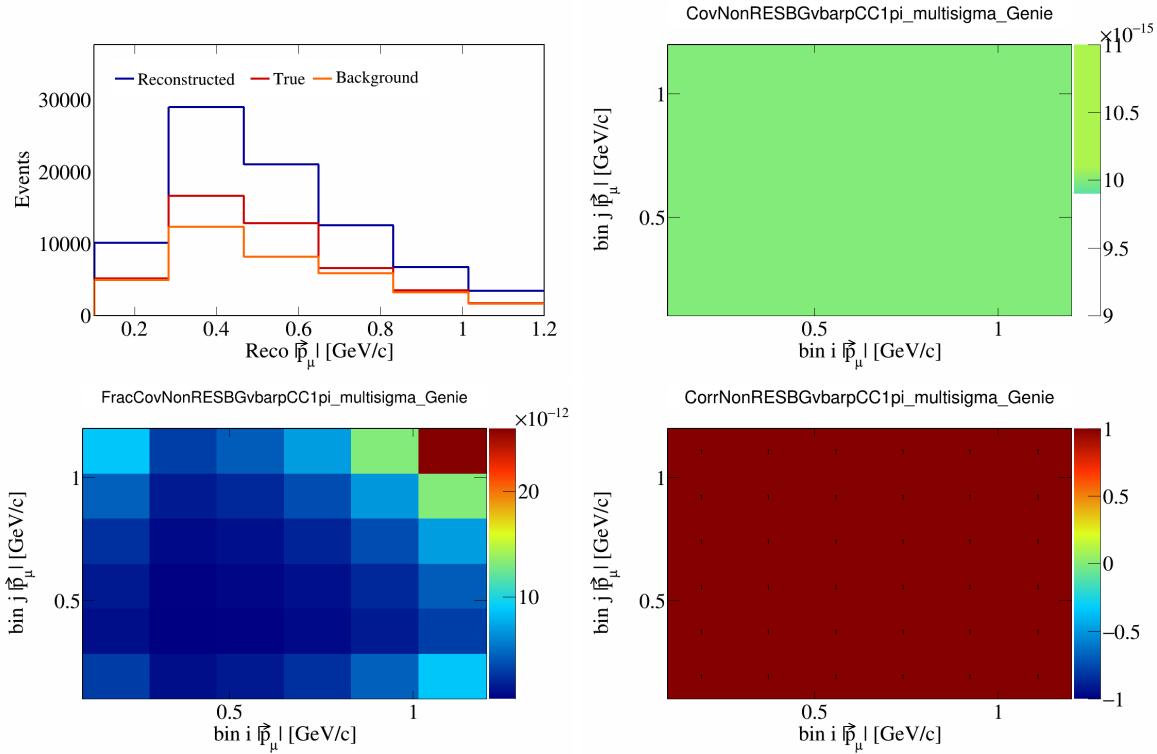


Figure 455: NonRESBGvbarpCC1pi variations for $|\vec{p}_\mu|$.

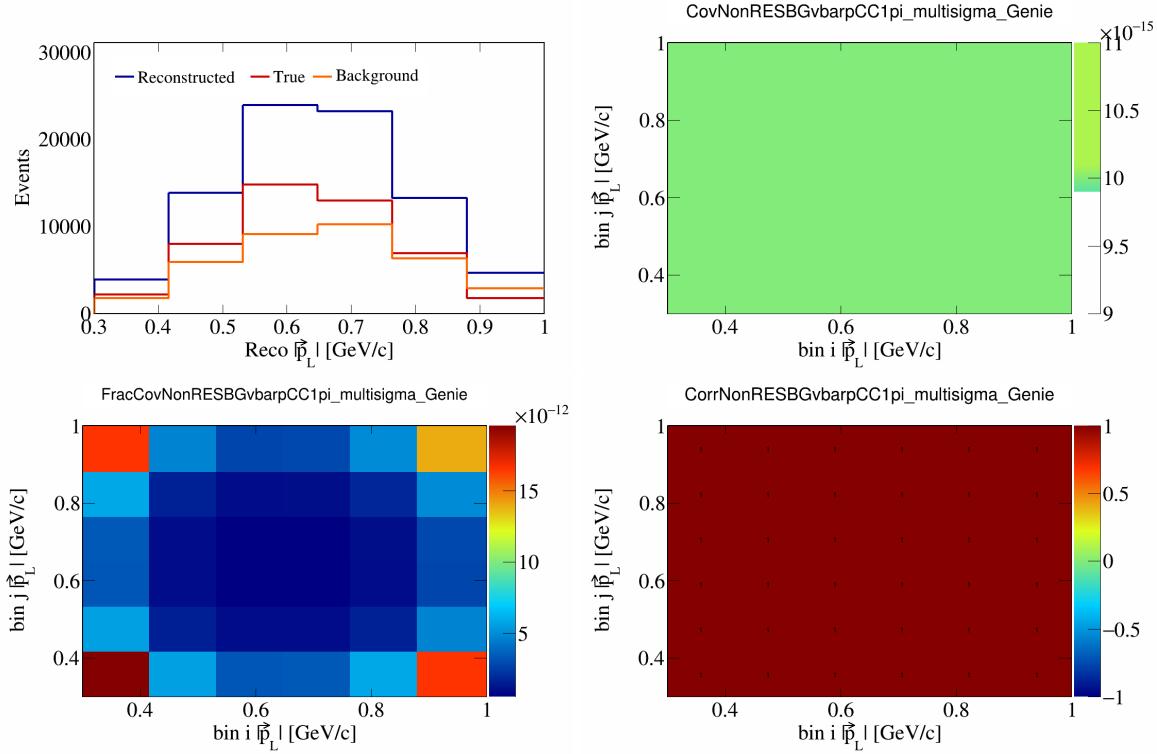


Figure 456: NonRESBGvbarpCC1pi variations for $|\vec{p}_L|$.

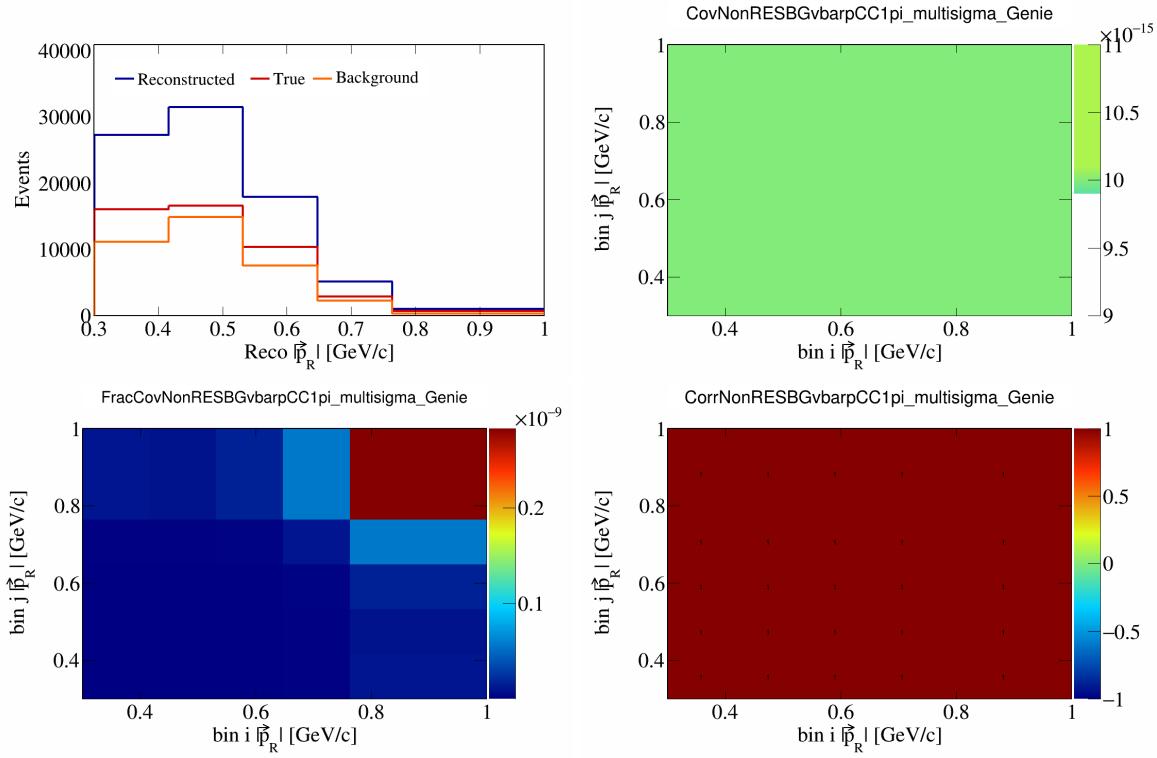


Figure 457: NonRESBGvbarpCC1pi variations for $|\vec{p}_R|$.

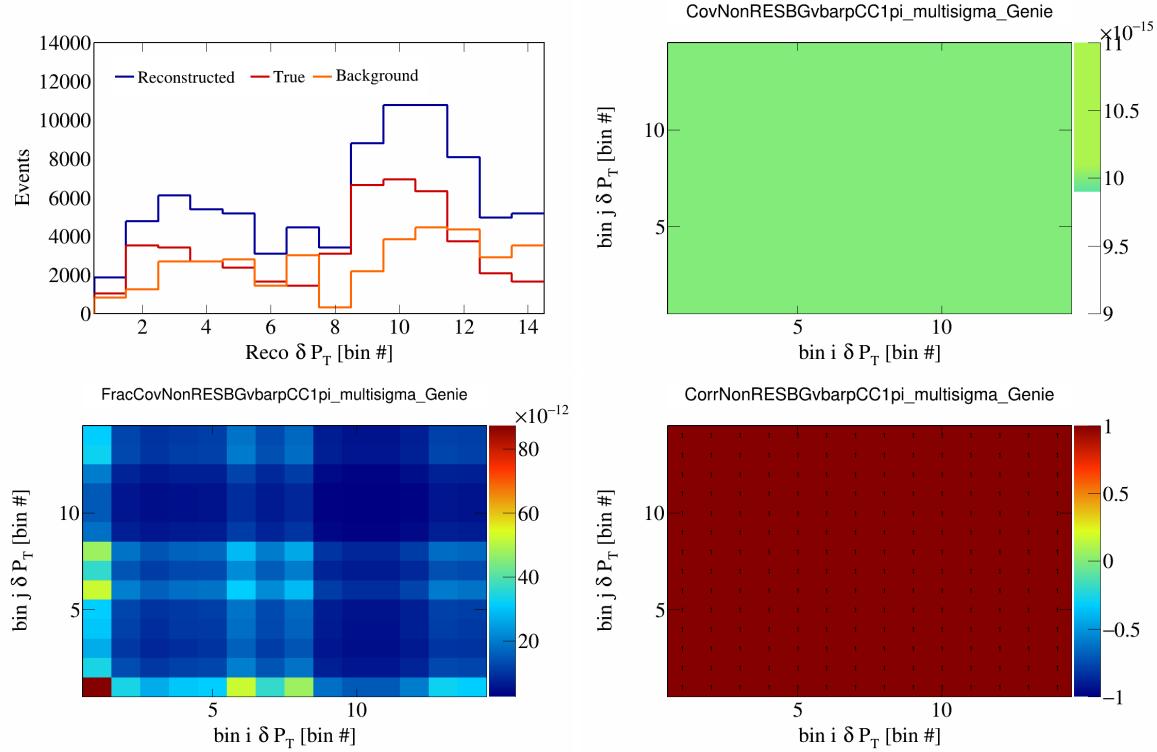


Figure 458: NonRESBGvbarpCC1pi variations for δP_T in $\cos(\theta_{\vec{p}_\mu})$.

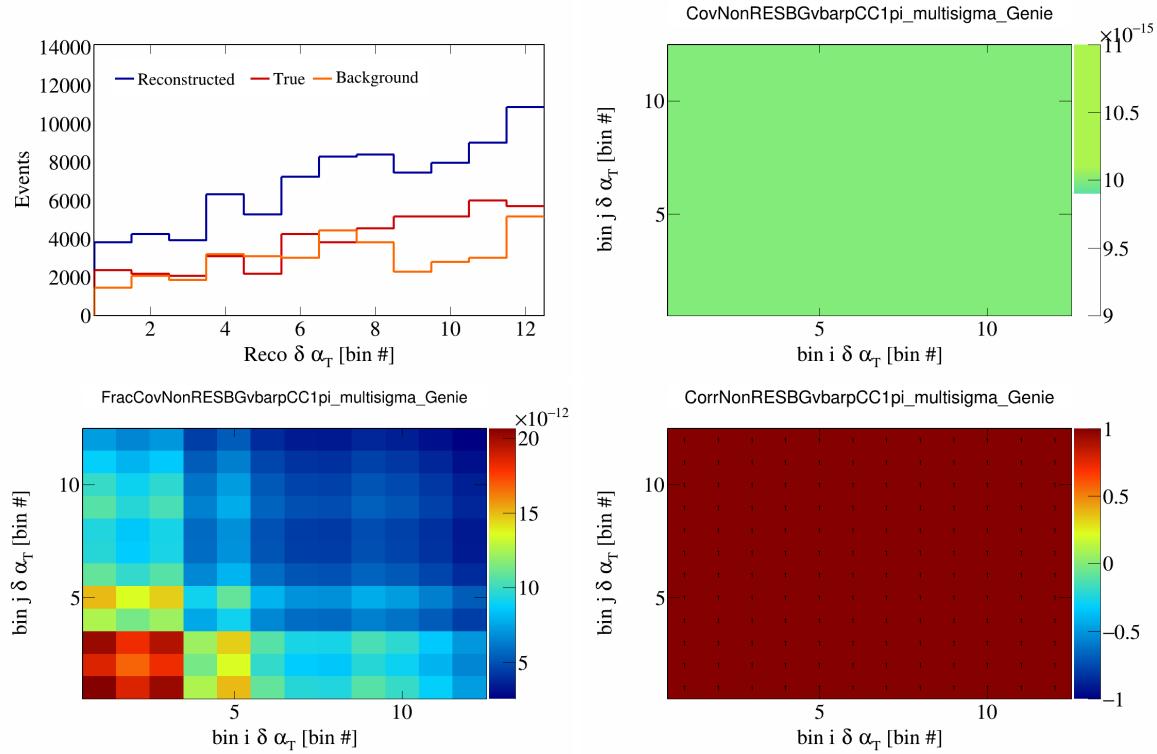


Figure 459: NonRESBGvbarpCC1pi variations for $\delta \alpha_T$ in $\cos(\theta_{\vec{p}_\mu})$.

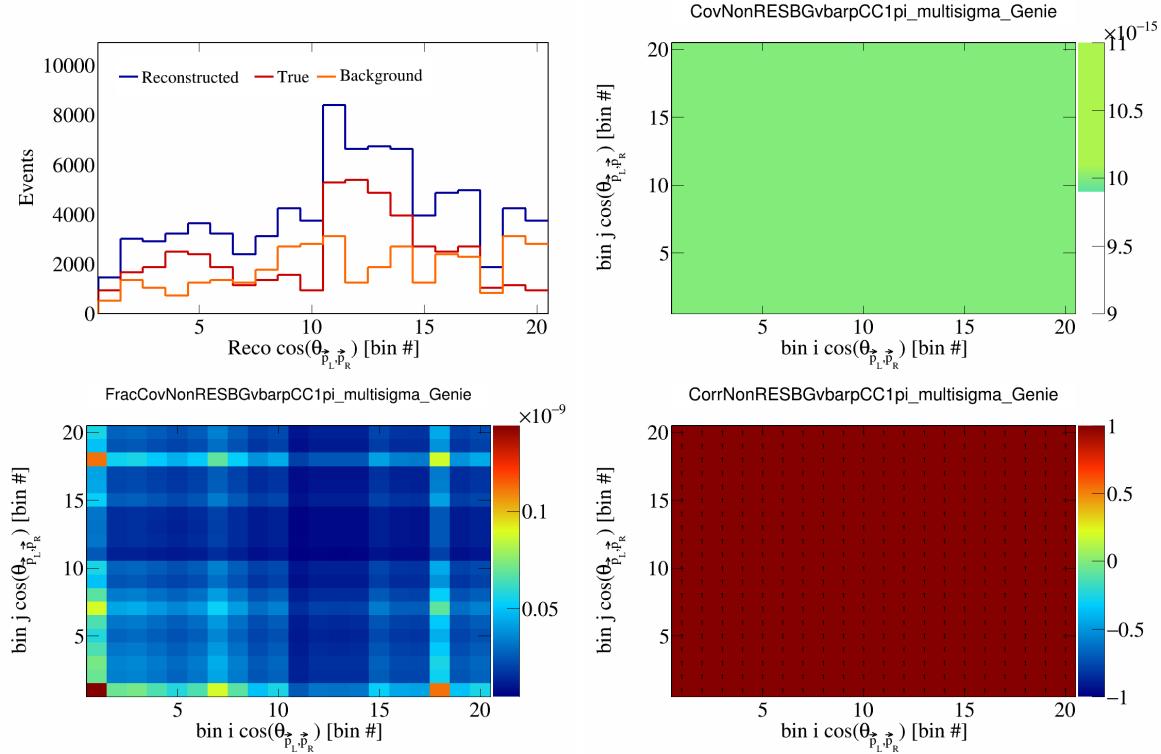


Figure 460: NonRESBGvbarpCC1pi variations for $\cos(\theta_{\vec{p}_L, \vec{p}_R})$ in $\cos(\theta_{\vec{p}_\mu})$.

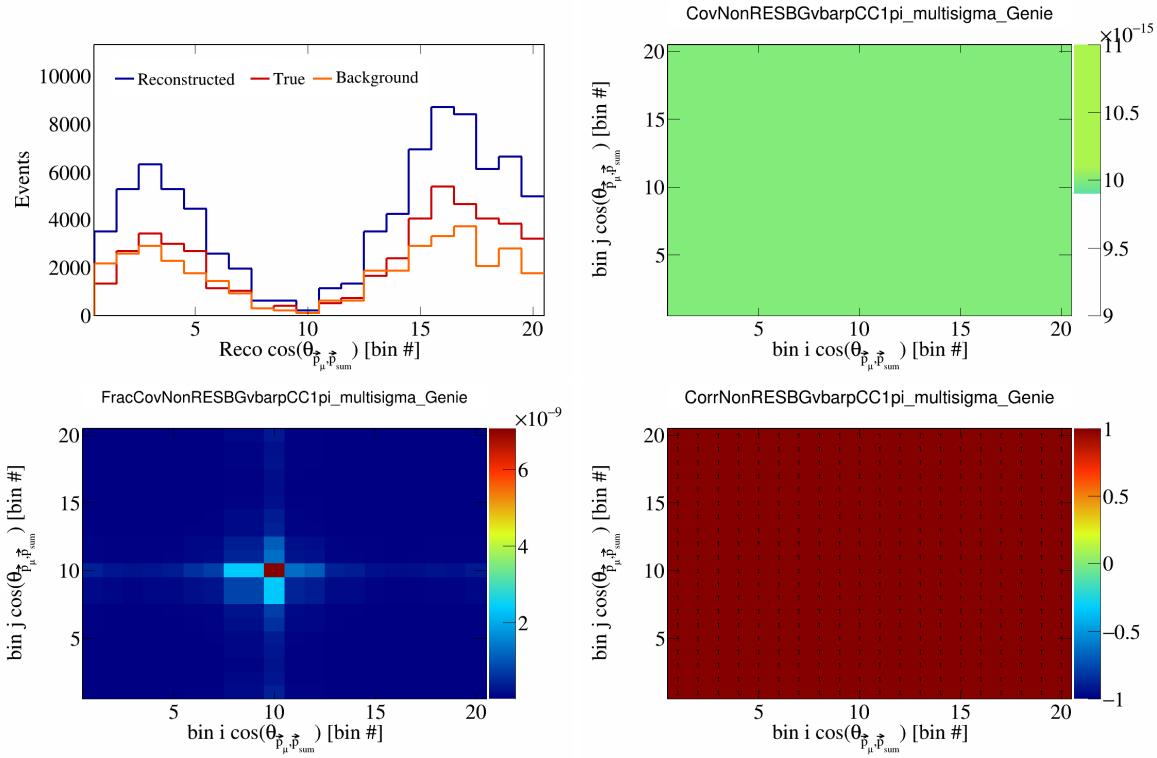


Figure 461: NonRESBGvbarpCC1pi variations for $\cos(\theta_{\vec{p}_\mu})$ in $\cos(\theta_{\vec{p}_\mu})$.

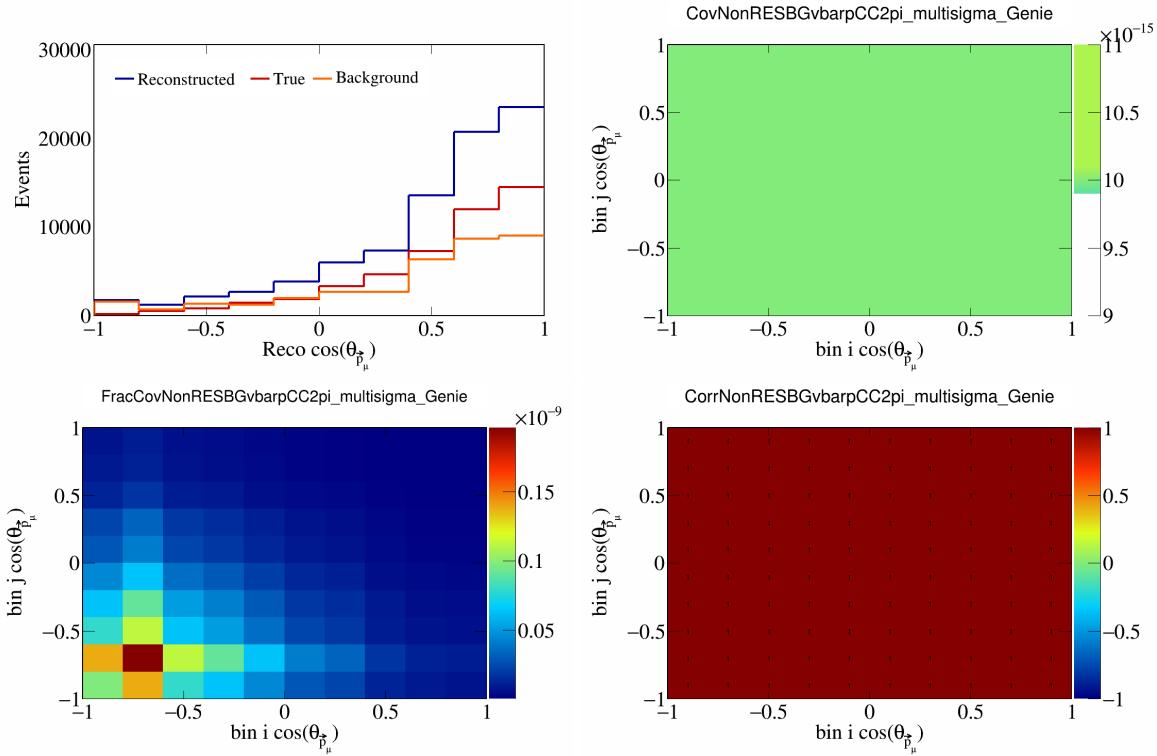


Figure 462: NonRESBGvbarpCC2pi variations for $\cos(\theta_{\vec{p}_\mu})$.

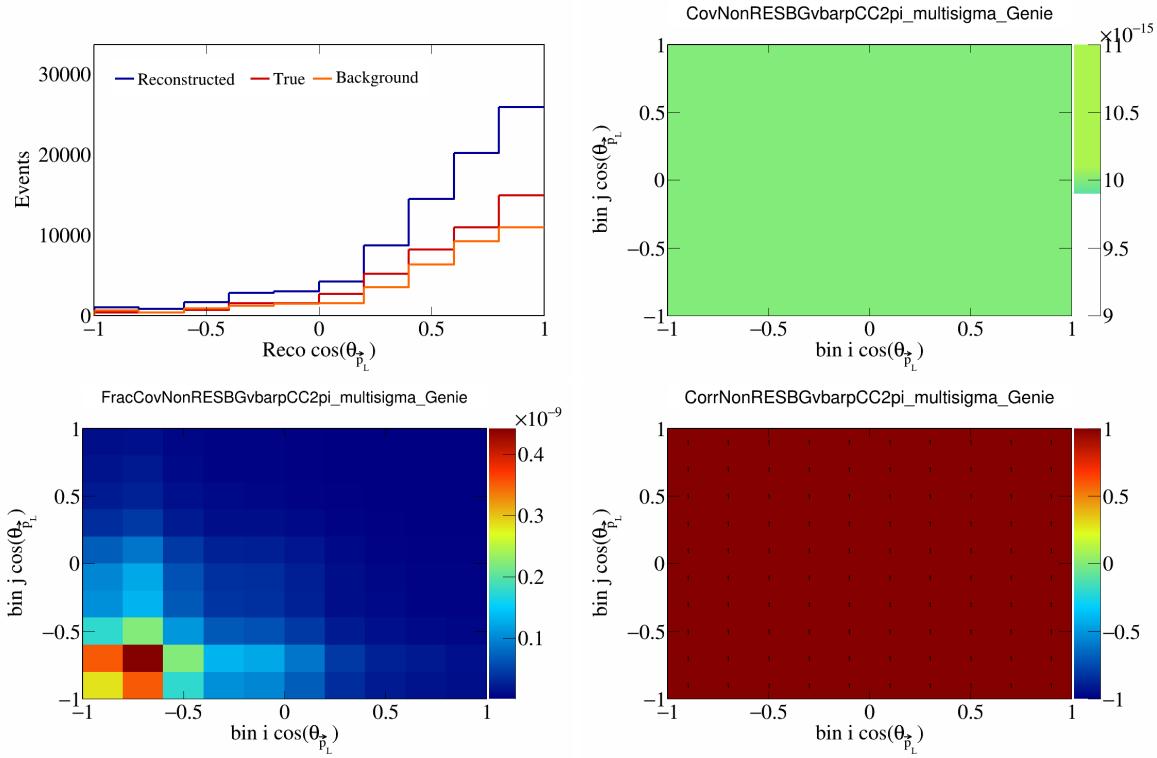


Figure 463: NonRESBGvbarpCC2pi variations for $\cos(\theta_{\vec{F}_L})$.

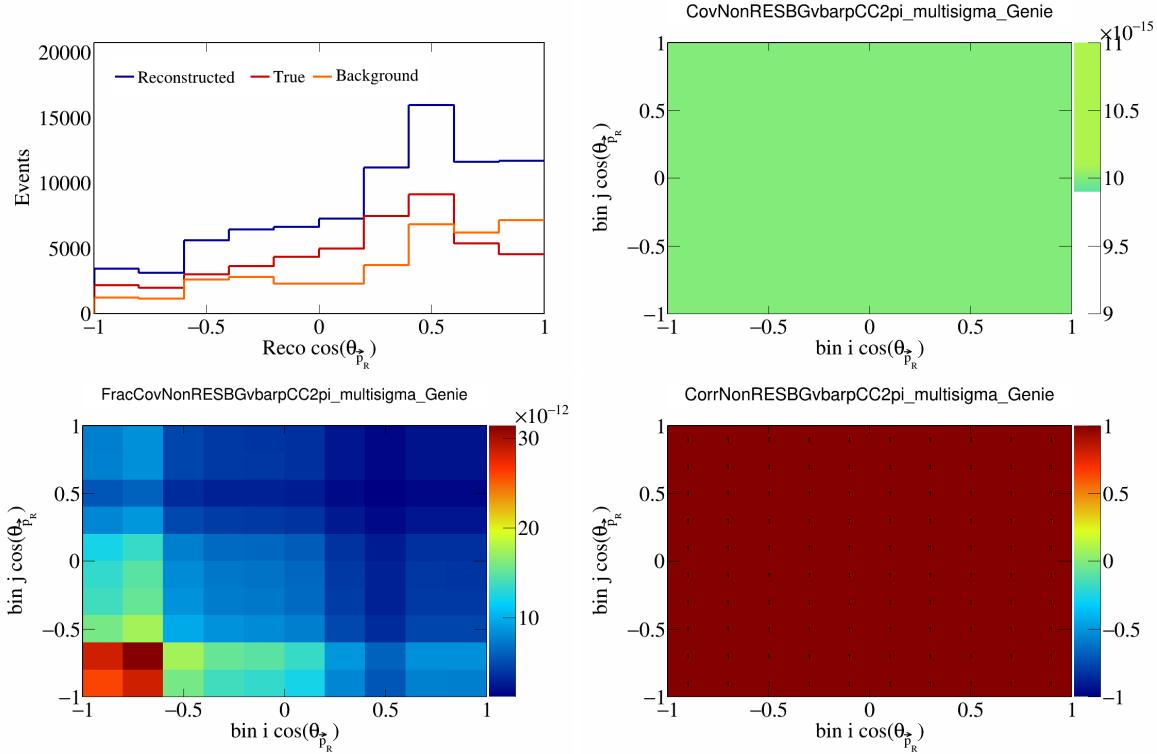


Figure 464: NonRESBGvbarpCC2pi variations for $\cos(\theta_{\vec{F}_R})$.

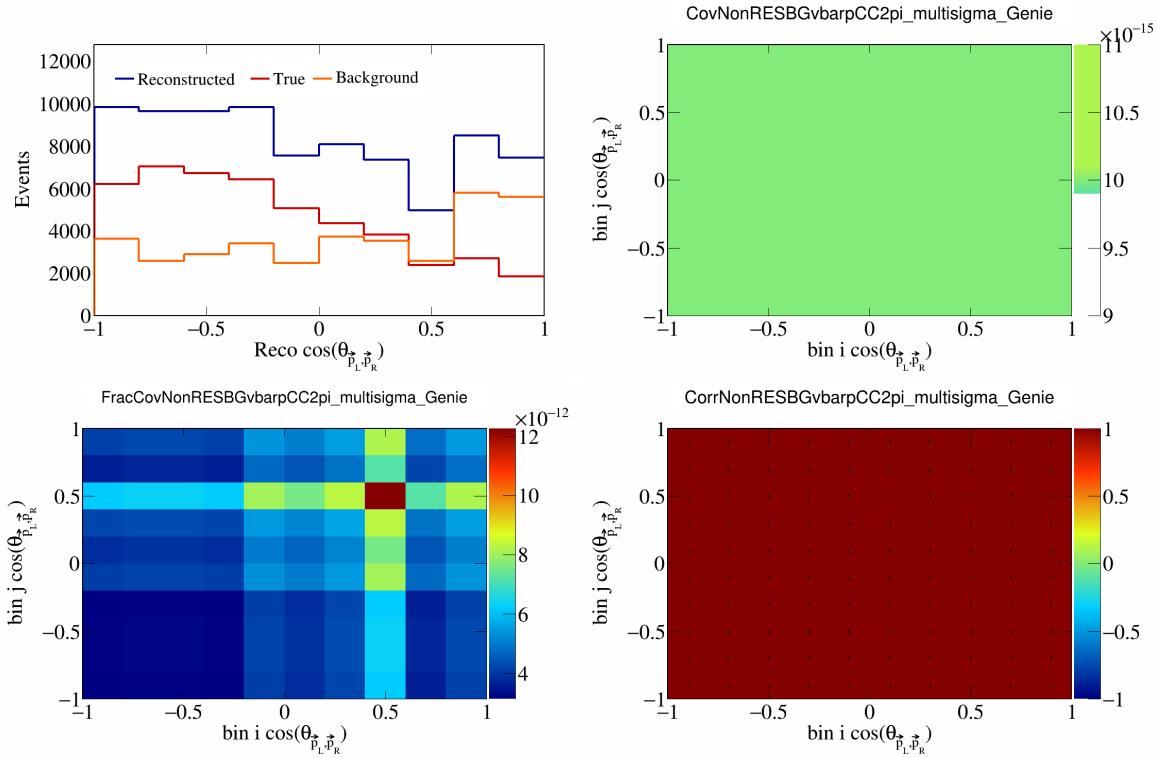


Figure 465: NonRESBGvbarpCC2pi variations for $\cos(\theta_{\vec{p}_L, \vec{p}_R})$.

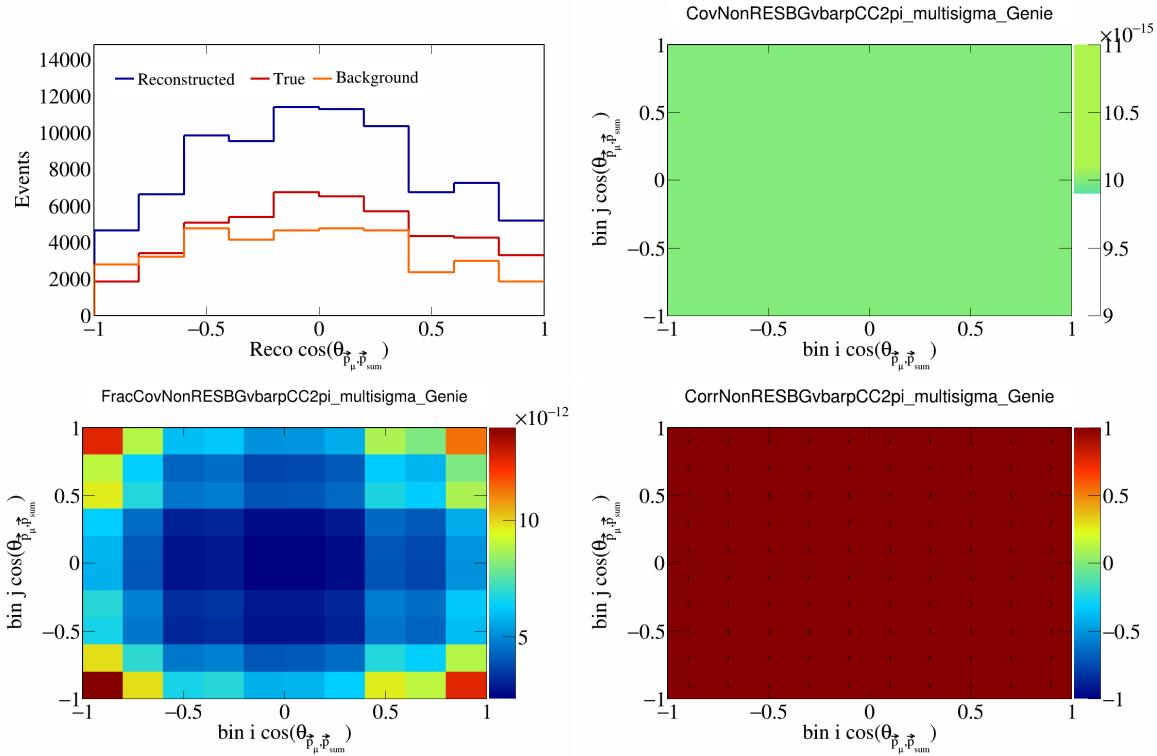


Figure 466: NonRESBGvbarpCC2pi variations for $\cos(\theta_{\vec{p}_\mu, \vec{p}_{\text{sum}}})$.

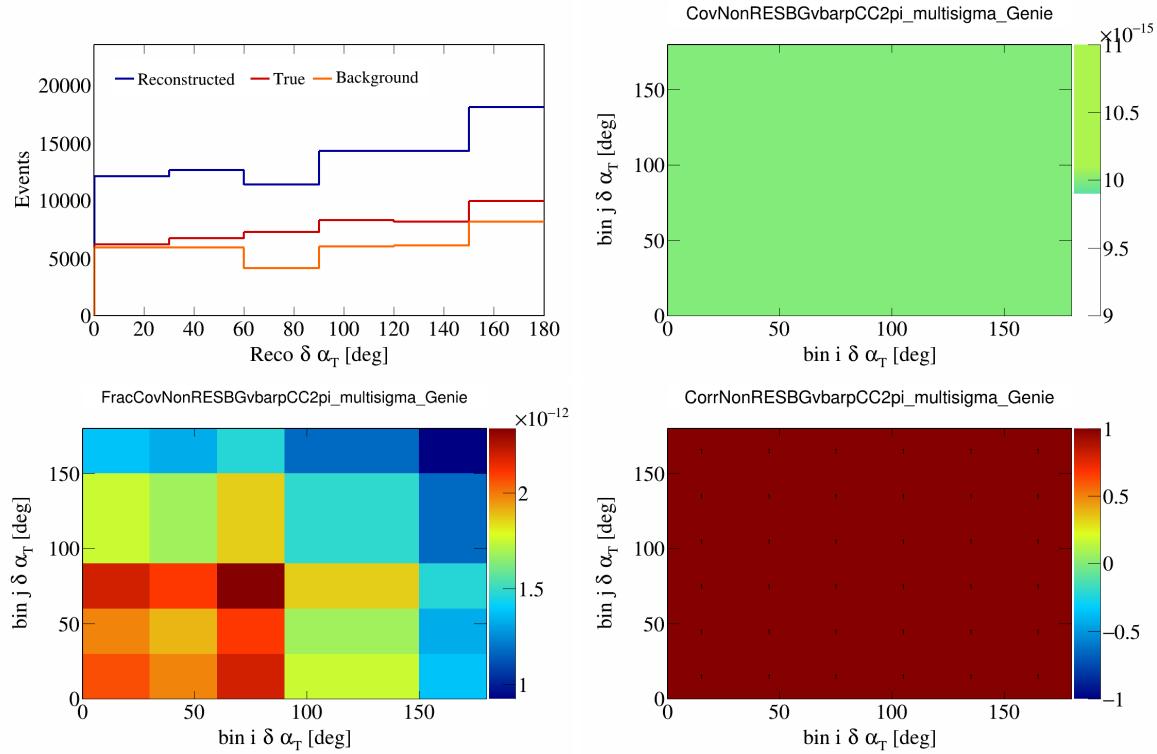


Figure 467: NonRESBGvbarpCC2pi variations for $\delta\alpha_T$.

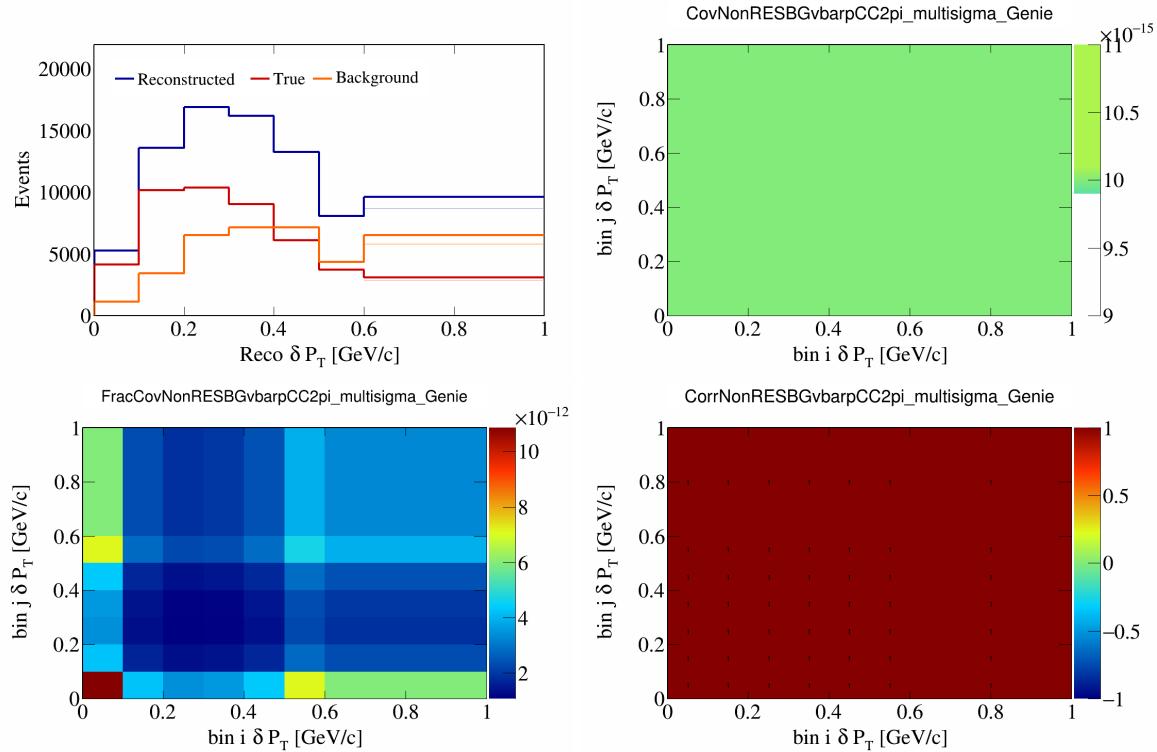


Figure 468: NonRESBGvbarpCC2pi variations for δP_T .

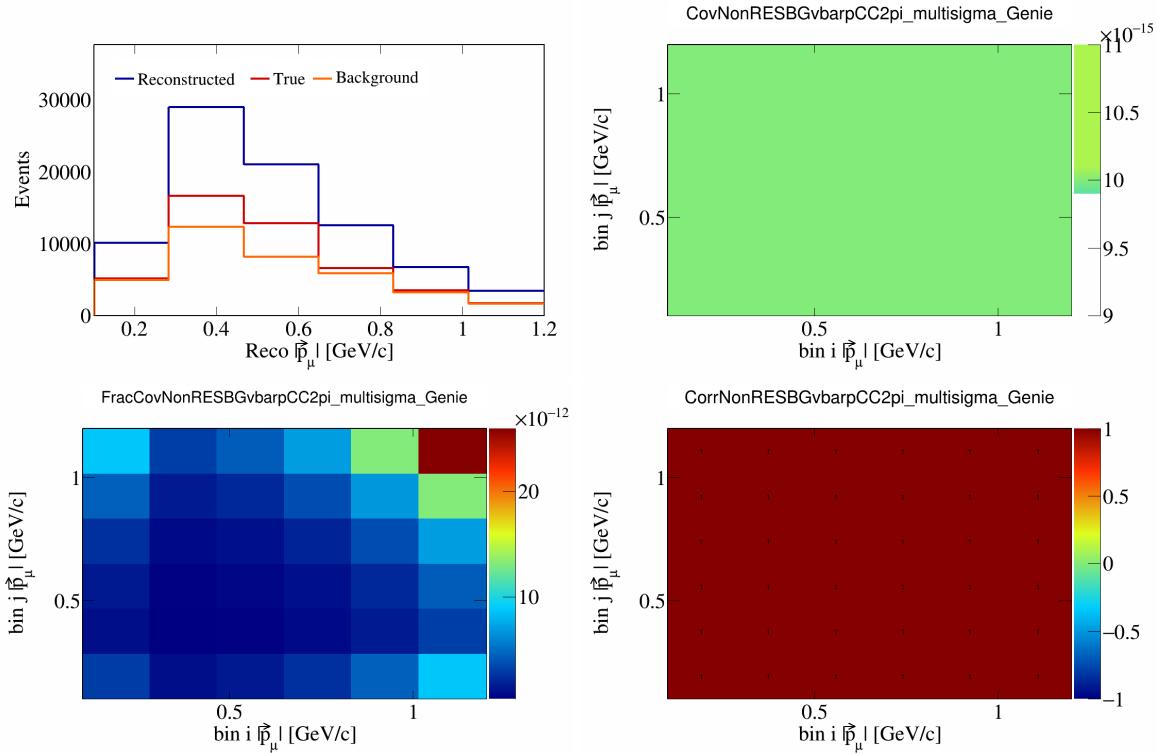


Figure 469: NonRESBGvbarpCC2pi variations for $|\vec{p}_\mu|$.

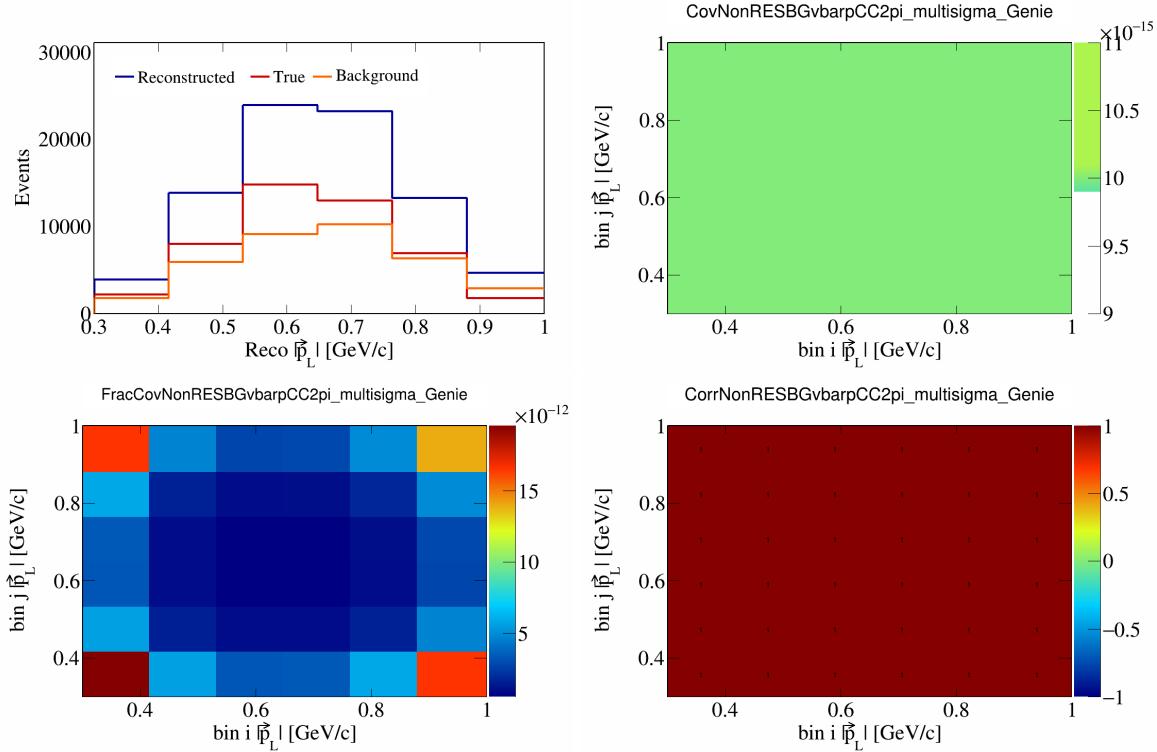


Figure 470: NonRESBGvbarpCC2pi variations for $|\vec{p}_L|$.

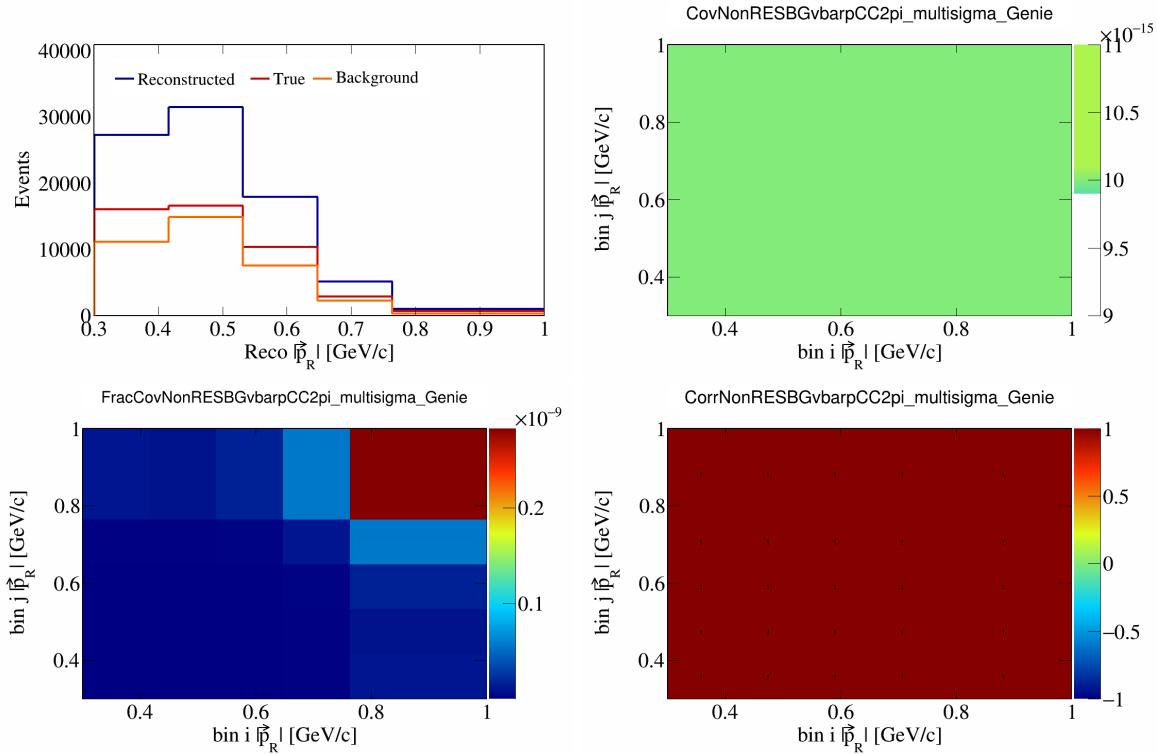


Figure 471: NonRESBGvbarpCC2pi variations for $|\vec{p}_R|$.

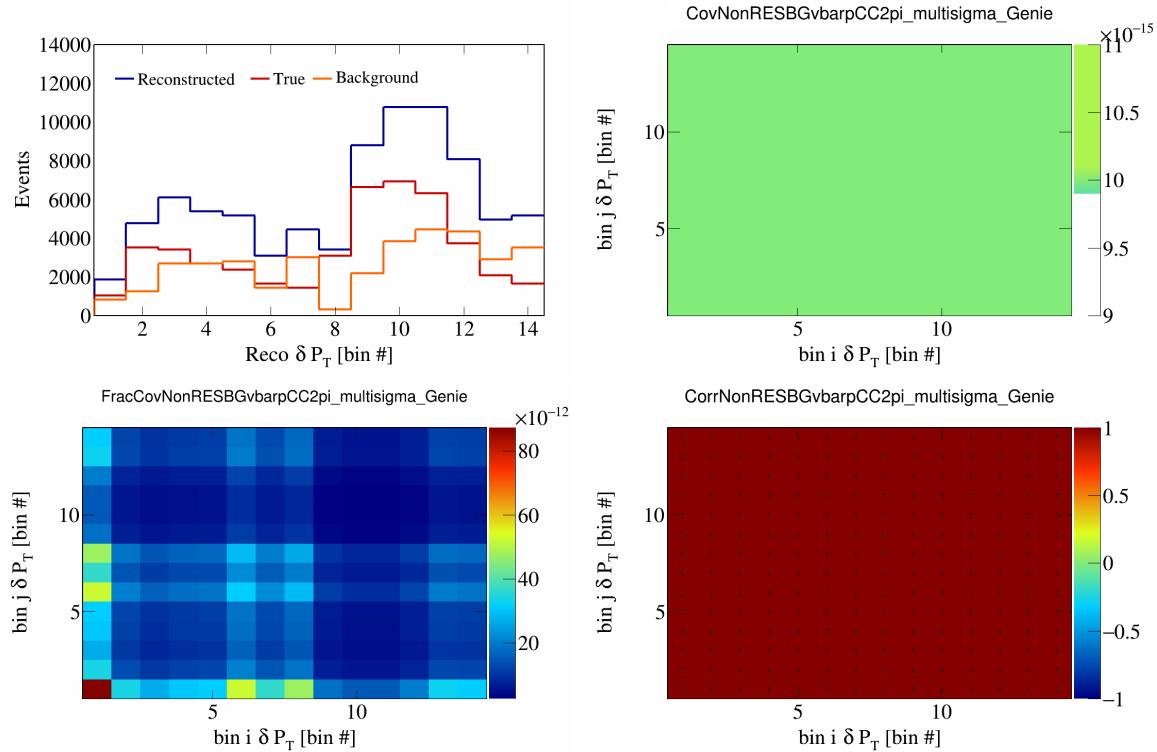


Figure 472: NonRESBGvbarpCC2pi variations for δP_T in $\cos(\theta_{\vec{p}_\mu})$.

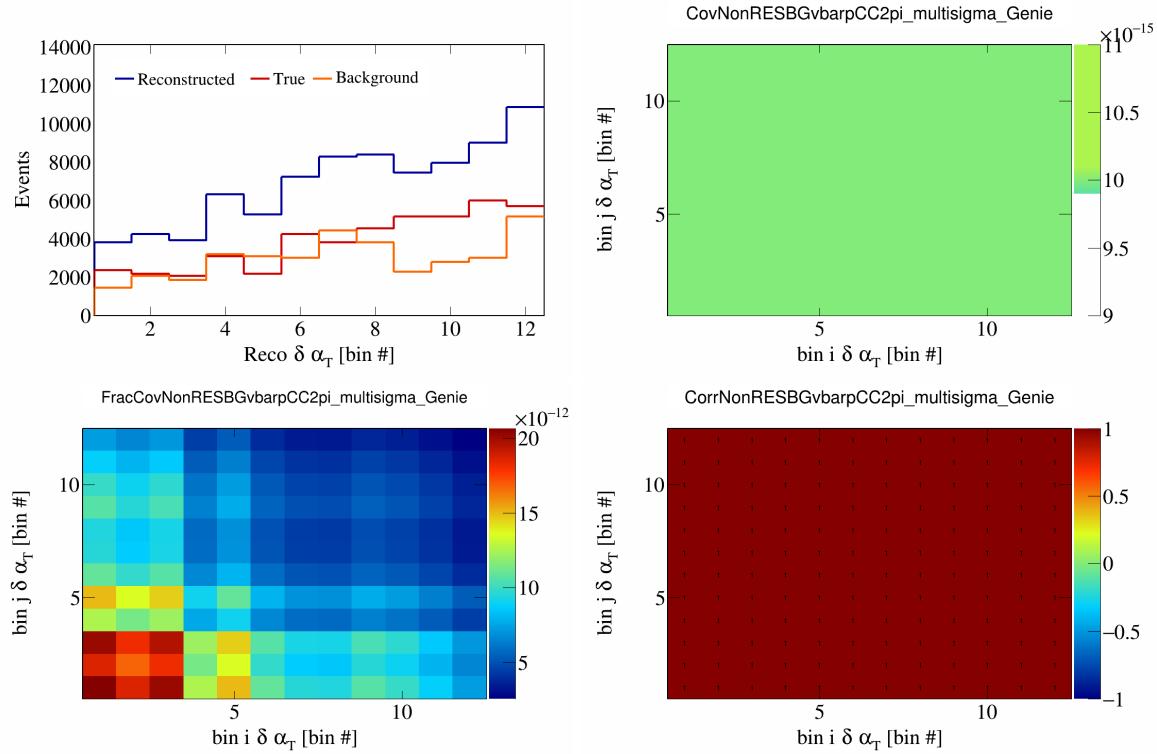


Figure 473: NonRESBGvbarpCC2pi variations for $\delta \alpha_T$ in $\cos(\theta_{\vec{p}_\mu})$.

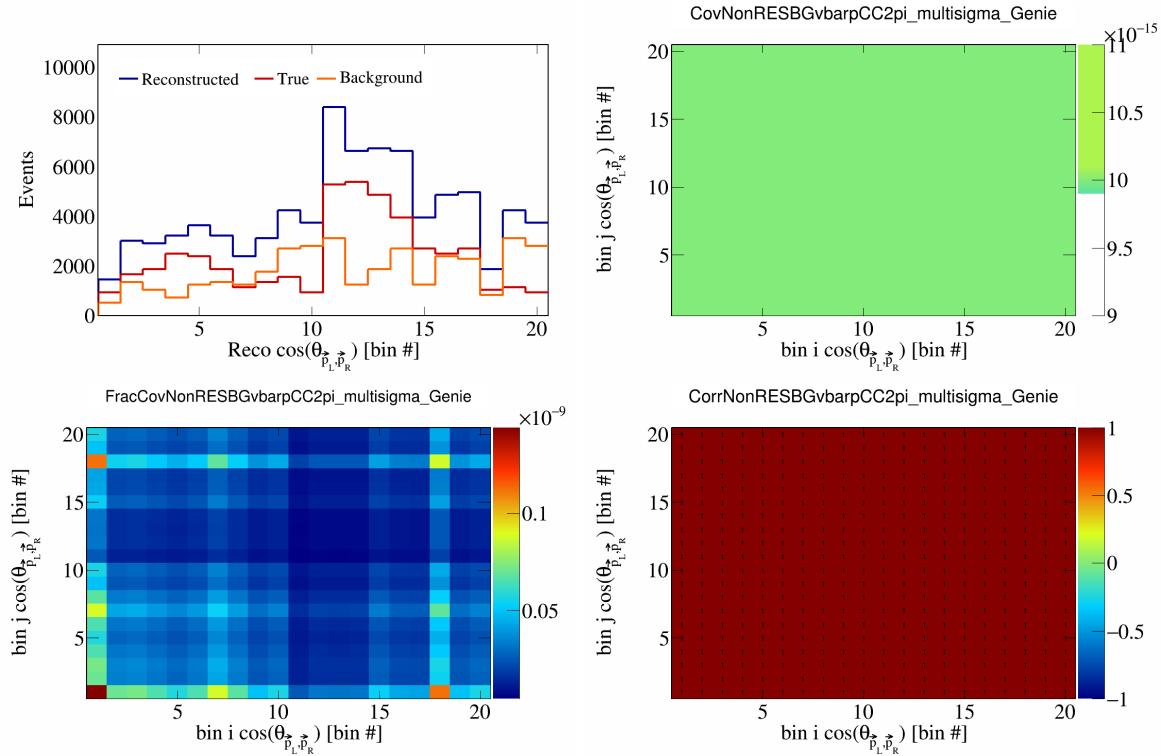


Figure 474: NonRESBGvbarpCC2pi variations for $\cos(\theta_{\vec{p}_L, \vec{p}_R})$ in $\cos(\theta_{\vec{p}_\mu})$.

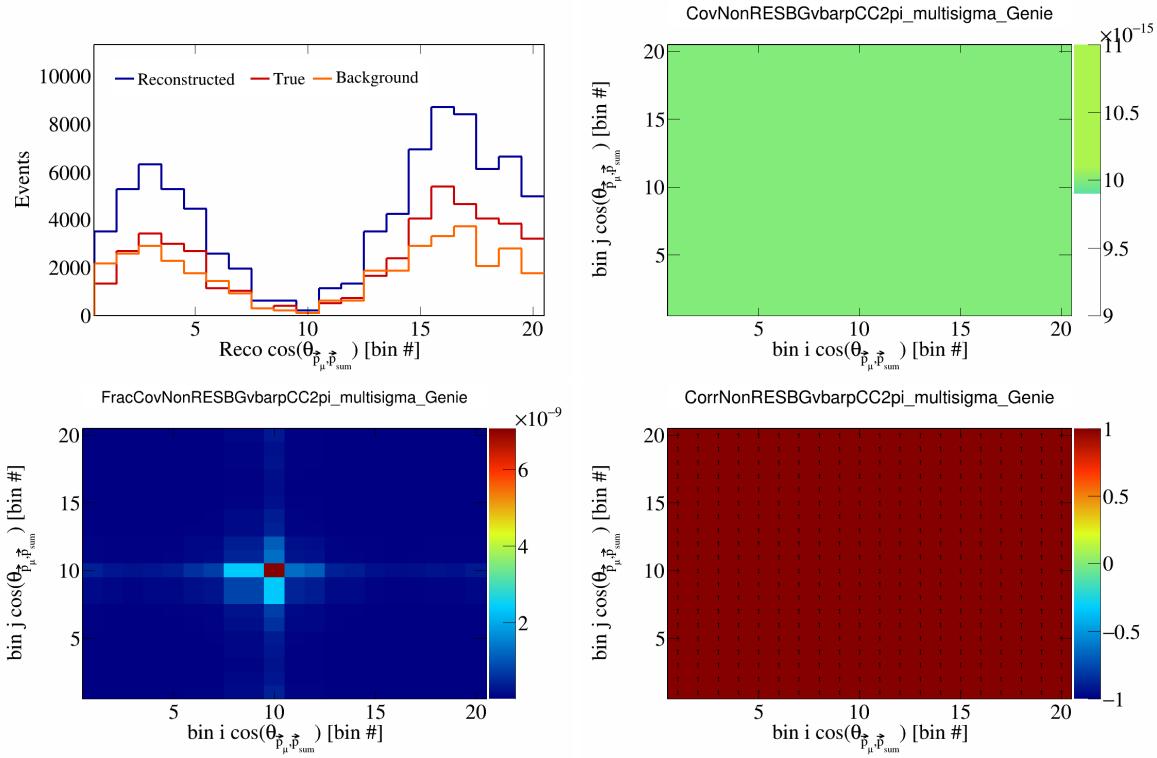


Figure 475: NonRESBGvbarpCC2pi variations for $\cos(\theta_{\vec{p}_\mu, \vec{p}_{\text{sum}}})$ in $\cos(\theta_{\vec{p}_\mu})$.

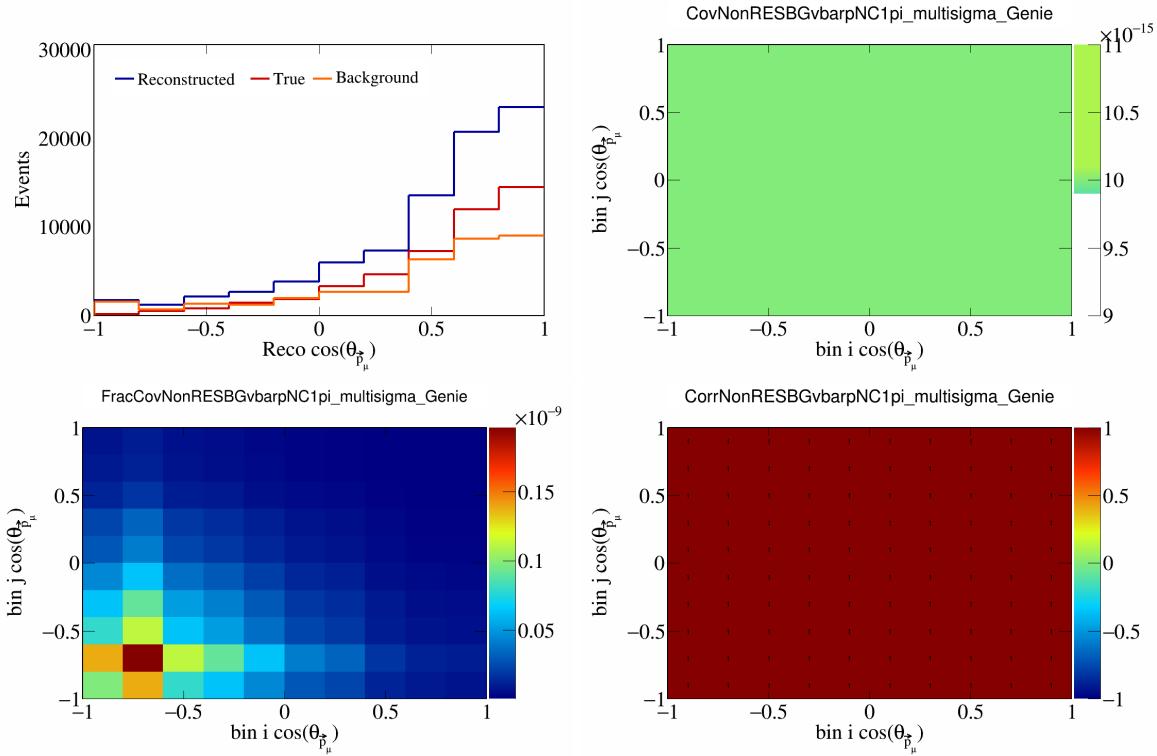


Figure 476: NonRESBGvbarpNC1pi variations for $\cos(\theta_{\vec{p}_\mu})$.

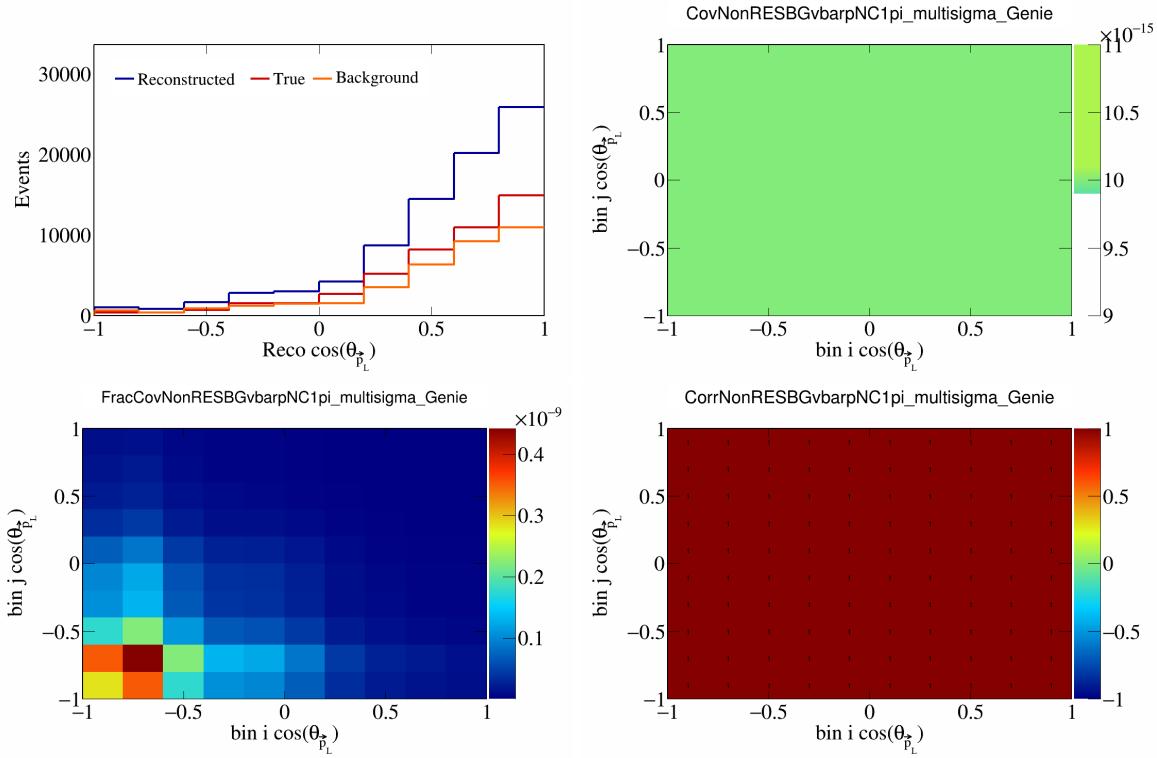


Figure 477: NonRESBGvbarpNC1pi variations for $\cos(\theta_{\vec{p}_L})$.

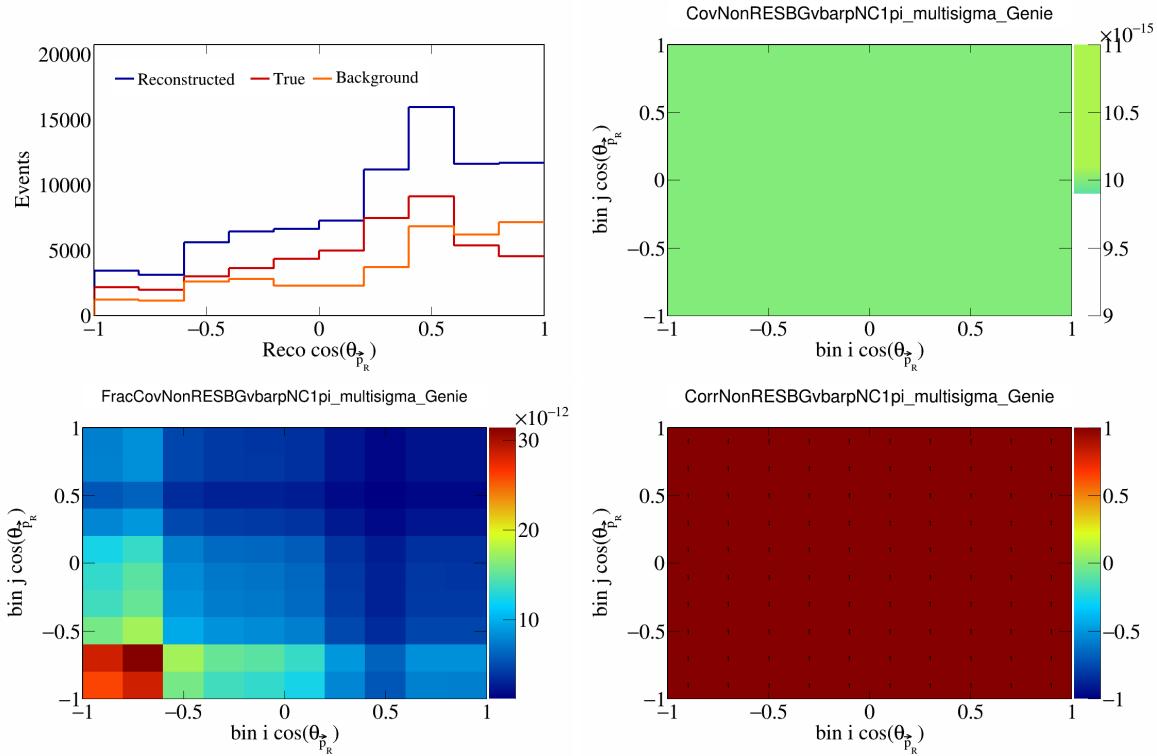


Figure 478: NonRESBGvbarpNC1pi variations for $\cos(\theta_{\vec{p}_R})$.

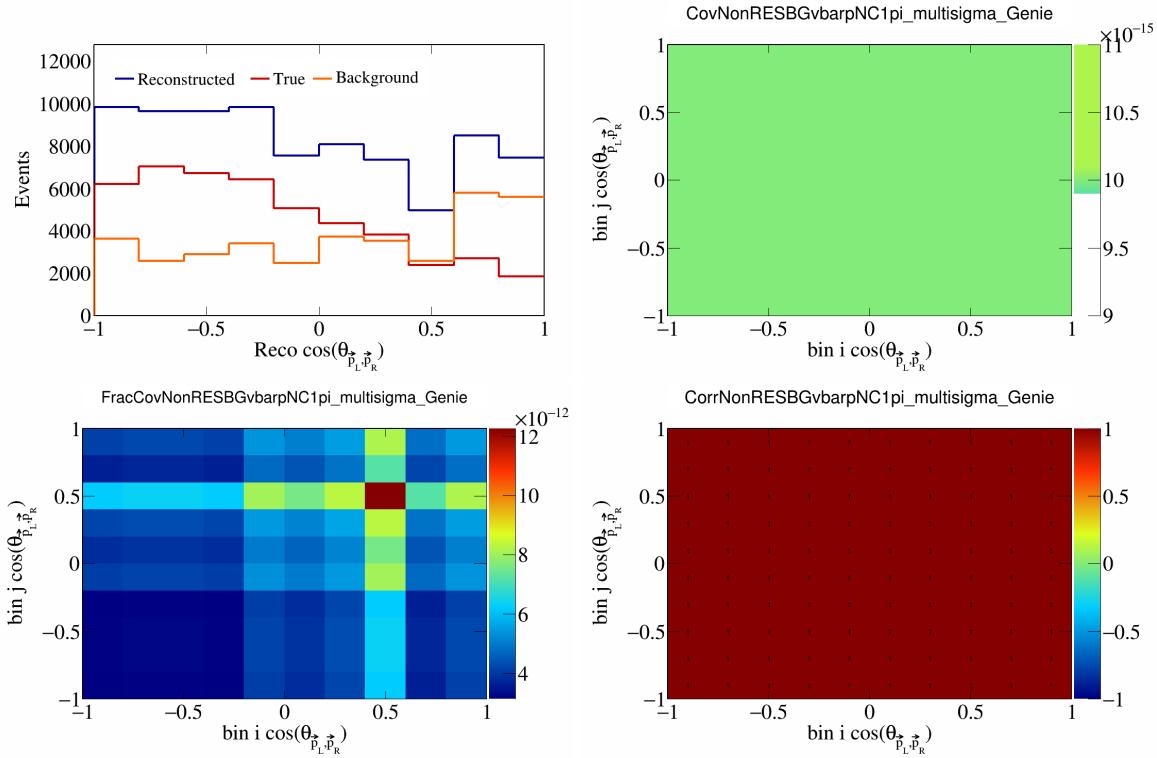


Figure 479: NonRESBGvbarpNC1pi variations for $\cos(\theta_{\vec{p}_L, \vec{p}_R})$.

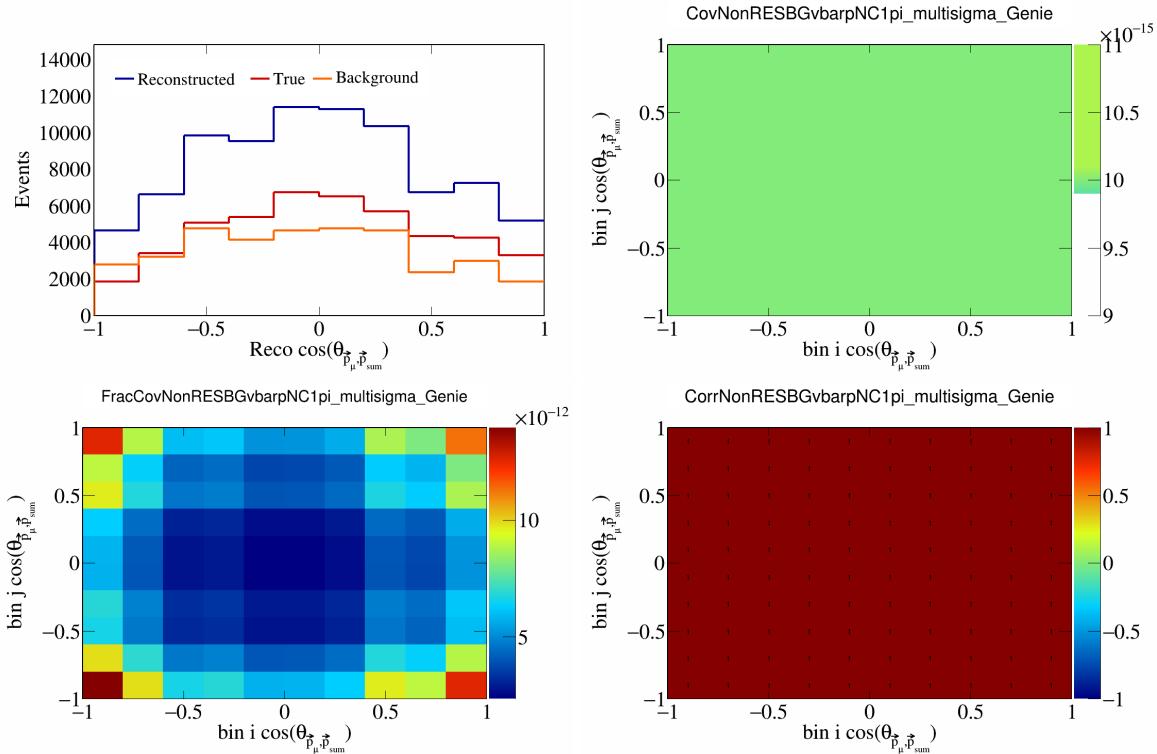


Figure 480: NonRESBGvbarpNC1pi variations for $\cos(\theta_{\vec{p}_\mu, \vec{p}_{\text{sum}}})$.

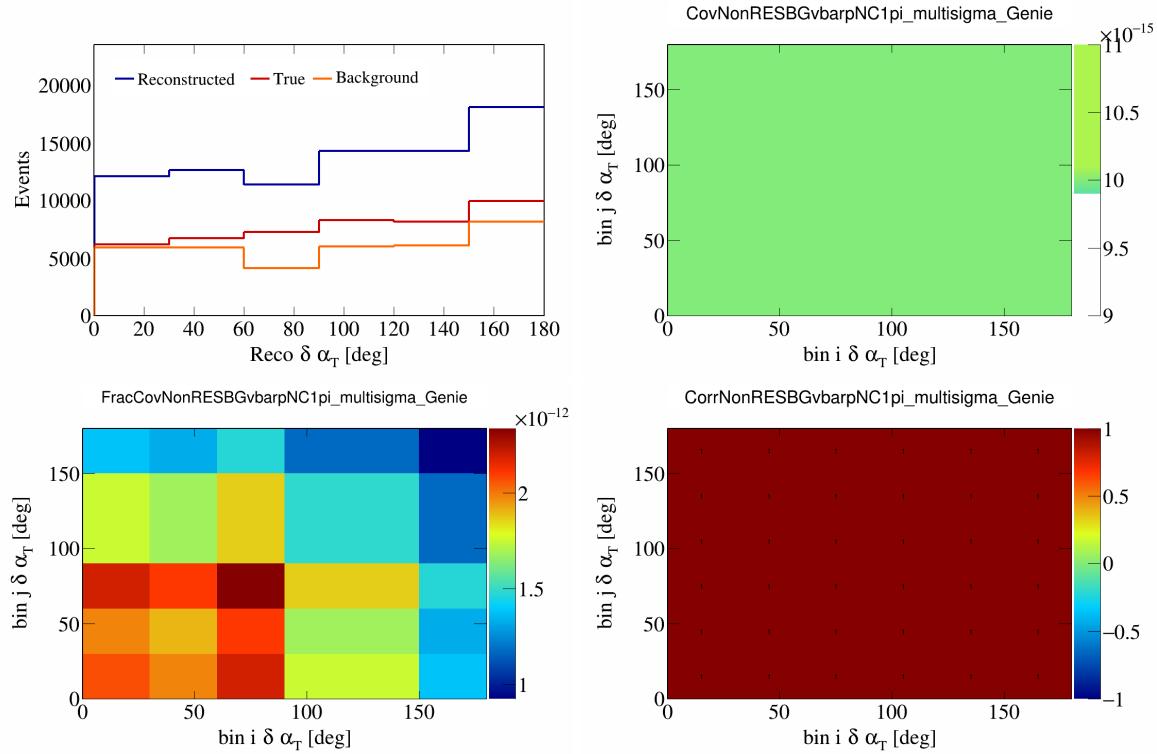


Figure 481: NonRESBGvbarpNC1pi variations for $\delta\alpha_T$.

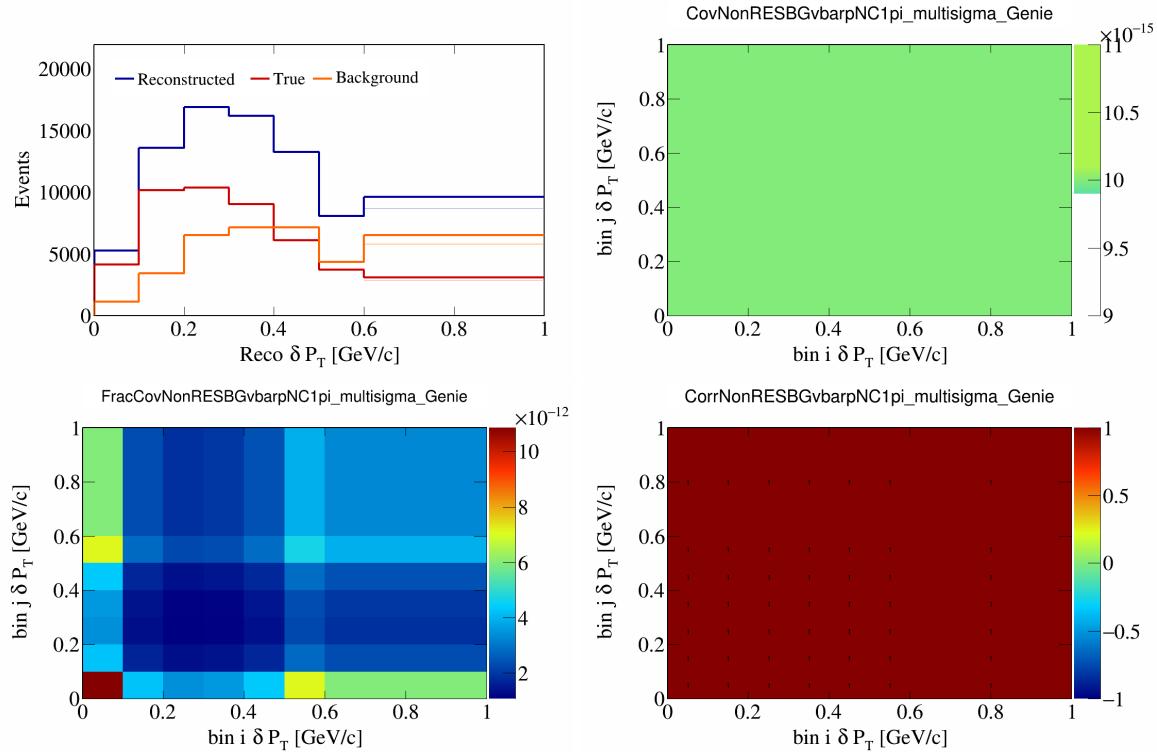


Figure 482: NonRESBGvbarpNC1pi variations for δP_T .

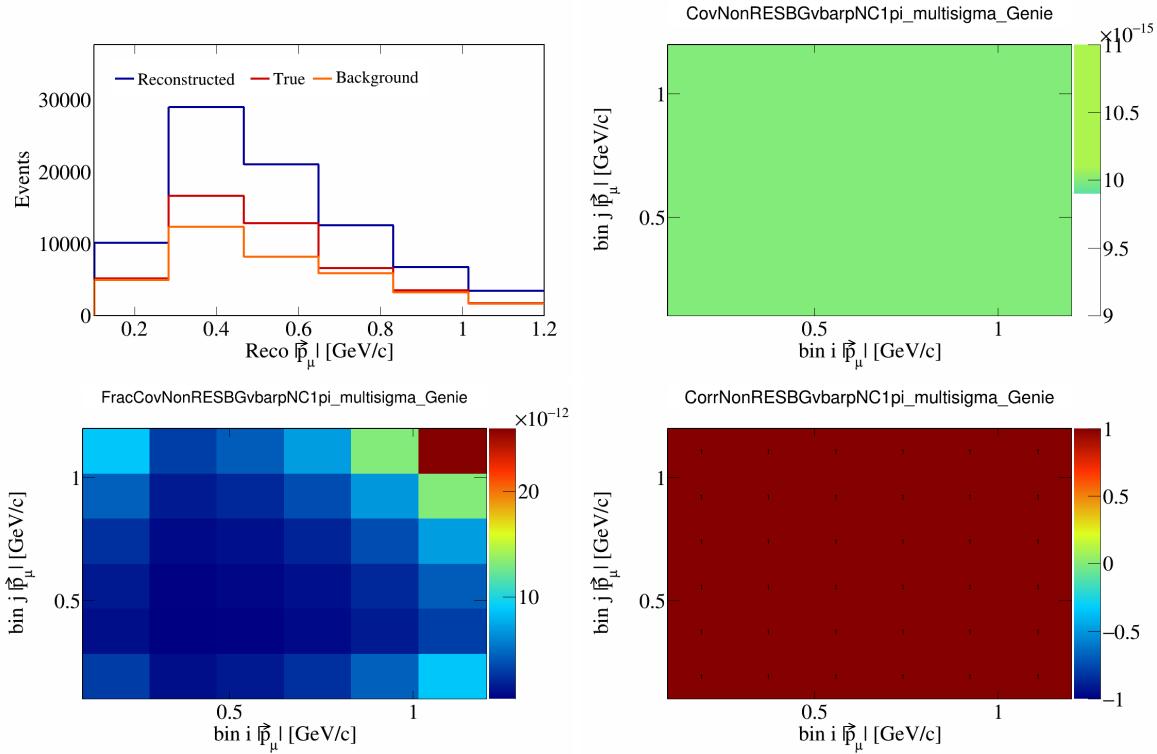


Figure 483: NonRESBGvbarpNC1pi variations for $|\vec{p}_\mu|$.

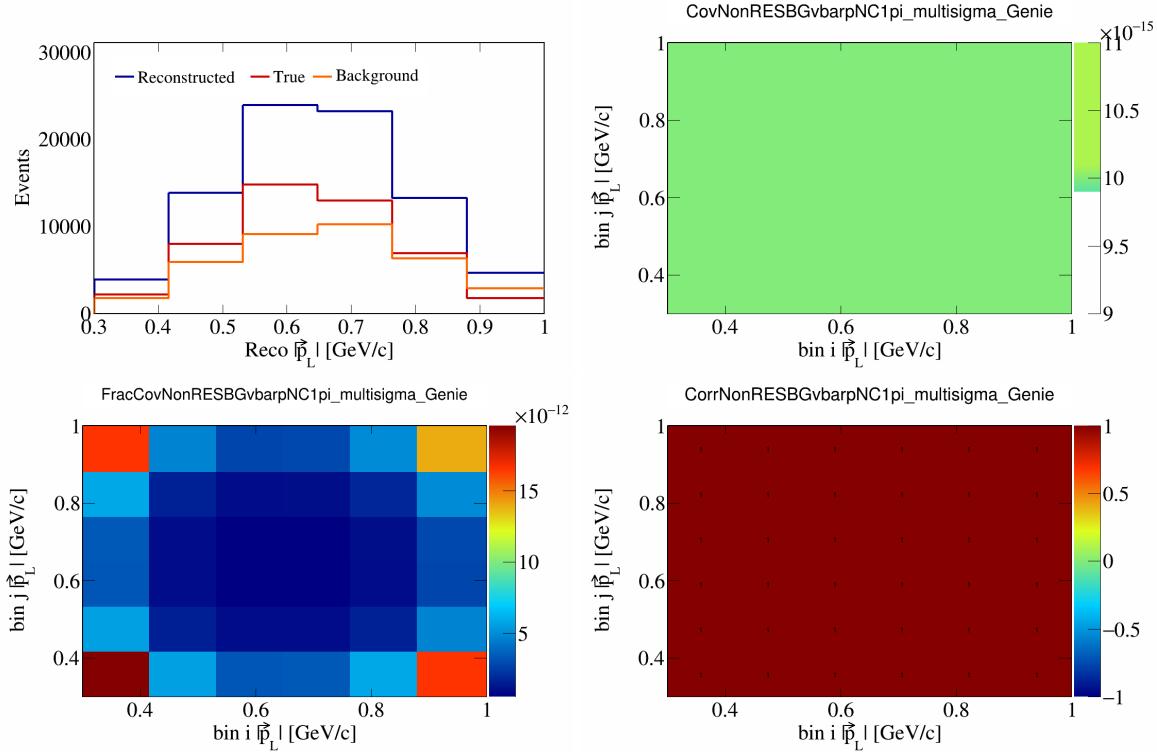


Figure 484: NonRESBGvbarpNC1pi variations for $|\vec{p}_L|$.

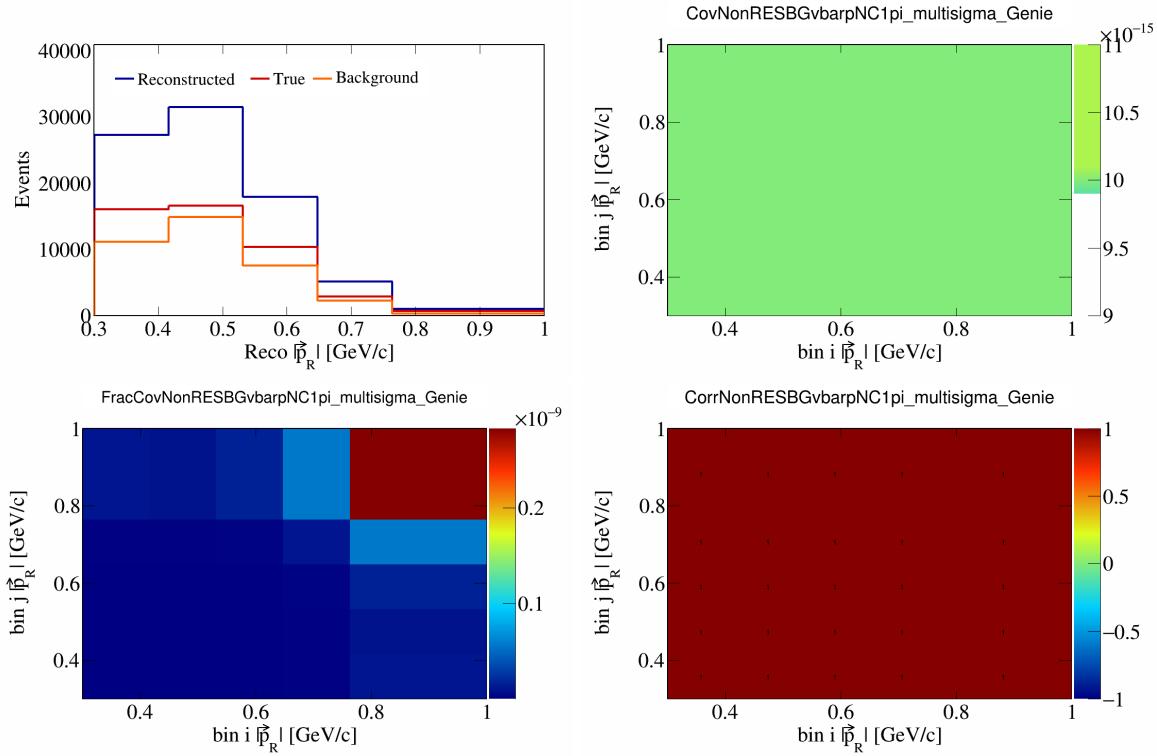


Figure 485: NonRESBGvbarpNC1pi variations for $|\vec{p}_R|$.

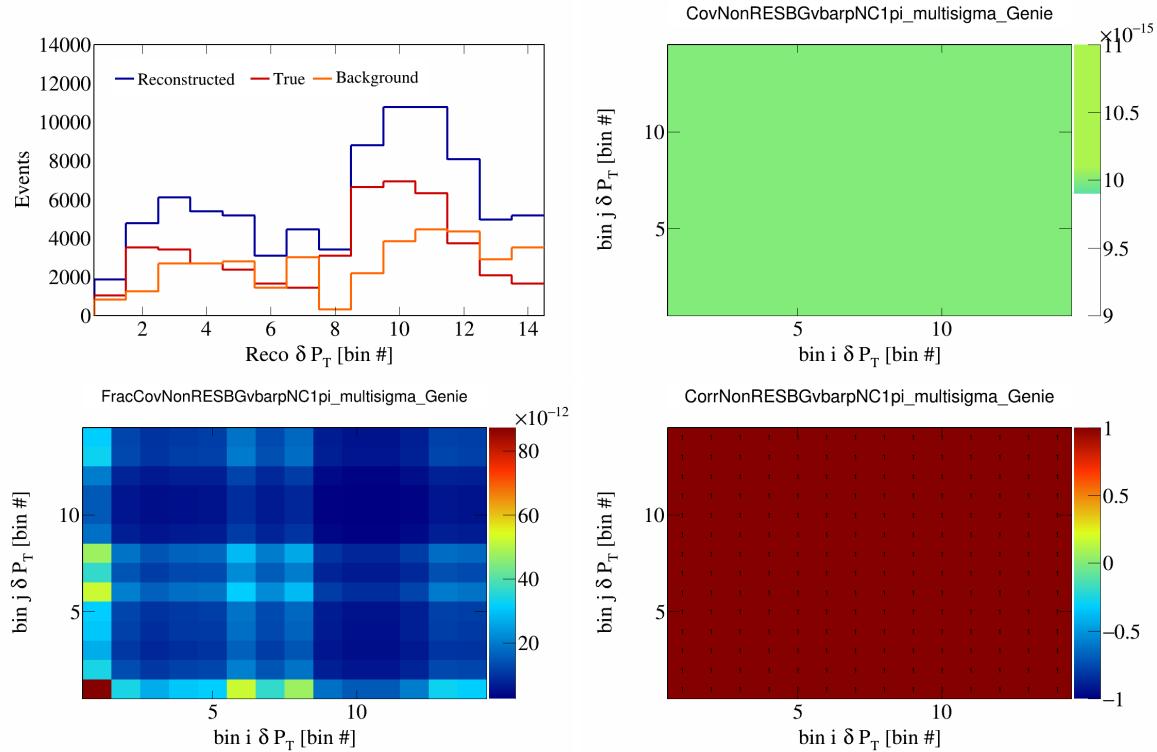


Figure 486: NonRESBGvbarpNC1pi variations for δP_T in $\cos(\theta_{\vec{p}_\mu})$.

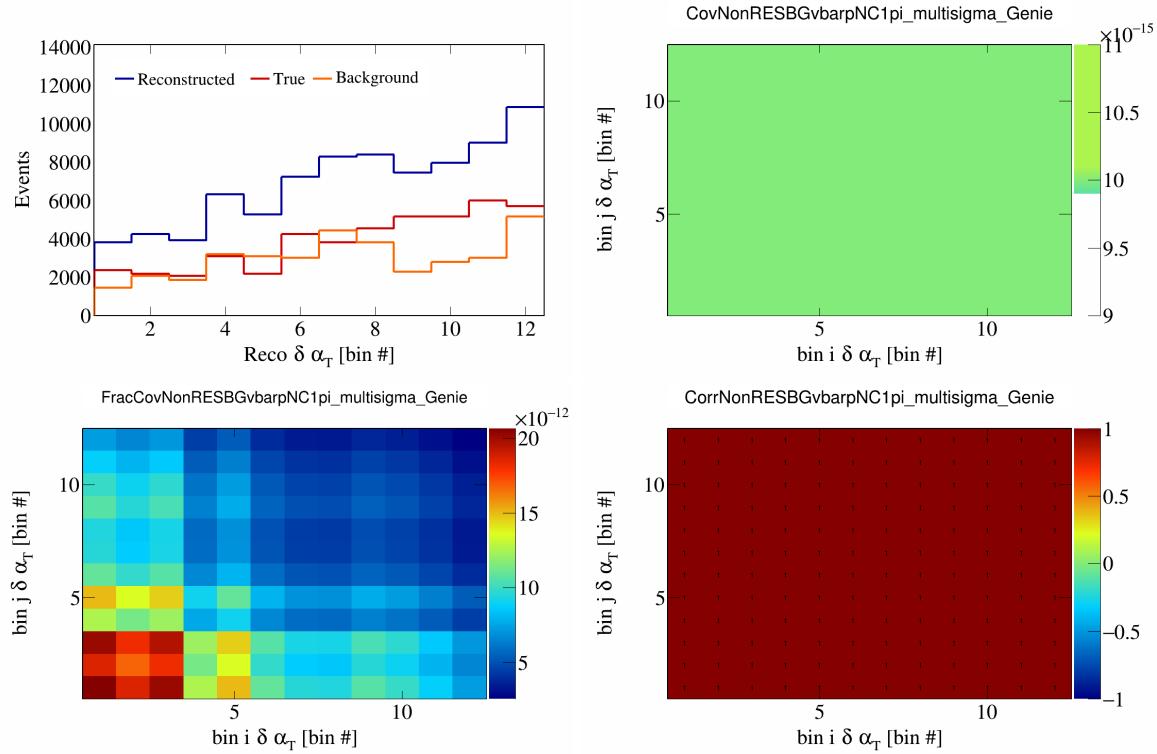


Figure 487: NonRESBGvbarpNC1pi variations for $\delta\alpha_T$ in $\cos(\theta_{\vec{p}_\mu})$.

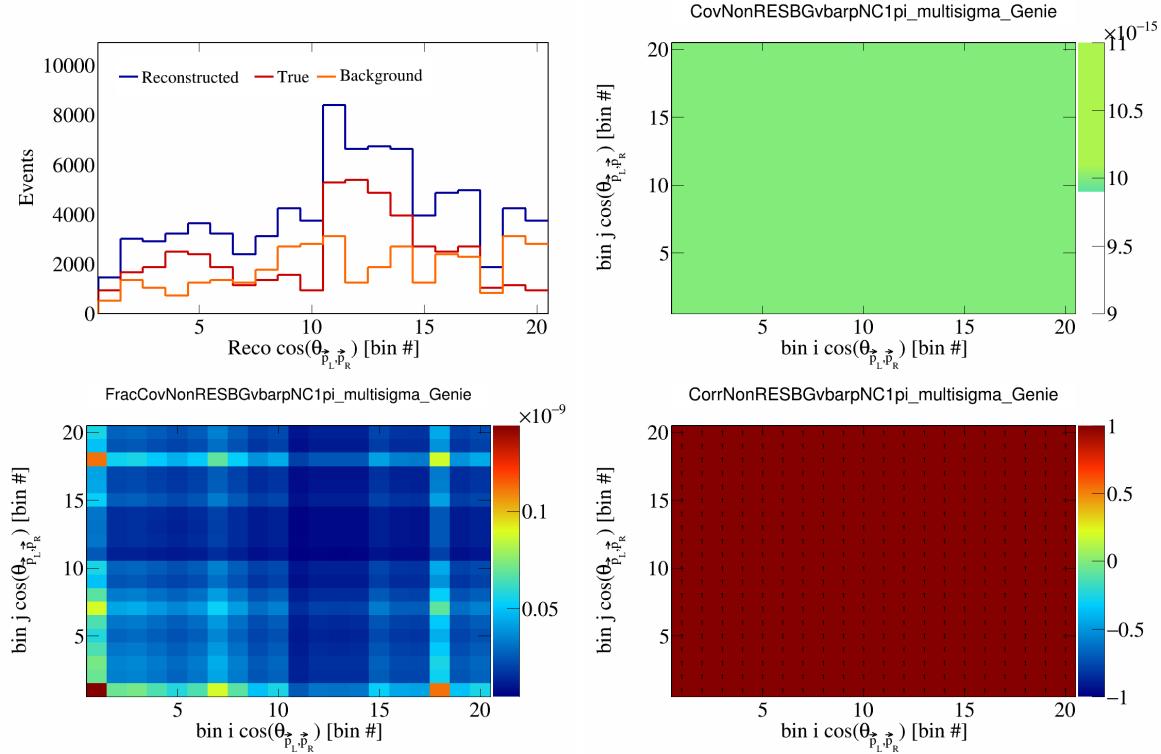


Figure 488: NonRESBGvbarpNC1pi variations for $\cos(\theta_{\vec{p}_L, \vec{p}_R})$ in $\cos(\theta_{\vec{p}_\mu})$.

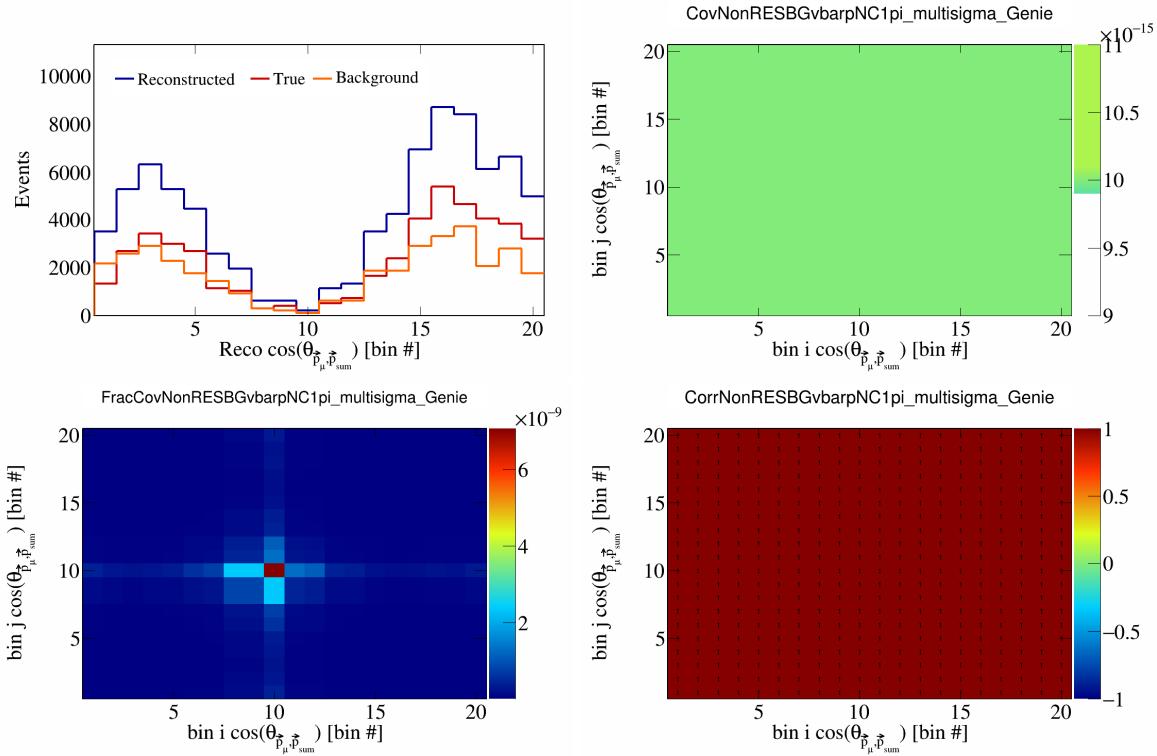


Figure 489: NonRESBGvbarpNC1pi variations for $\cos(\theta_{\vec{p}_\mu})$ in $\cos(\theta_{\vec{p}_\mu})$.

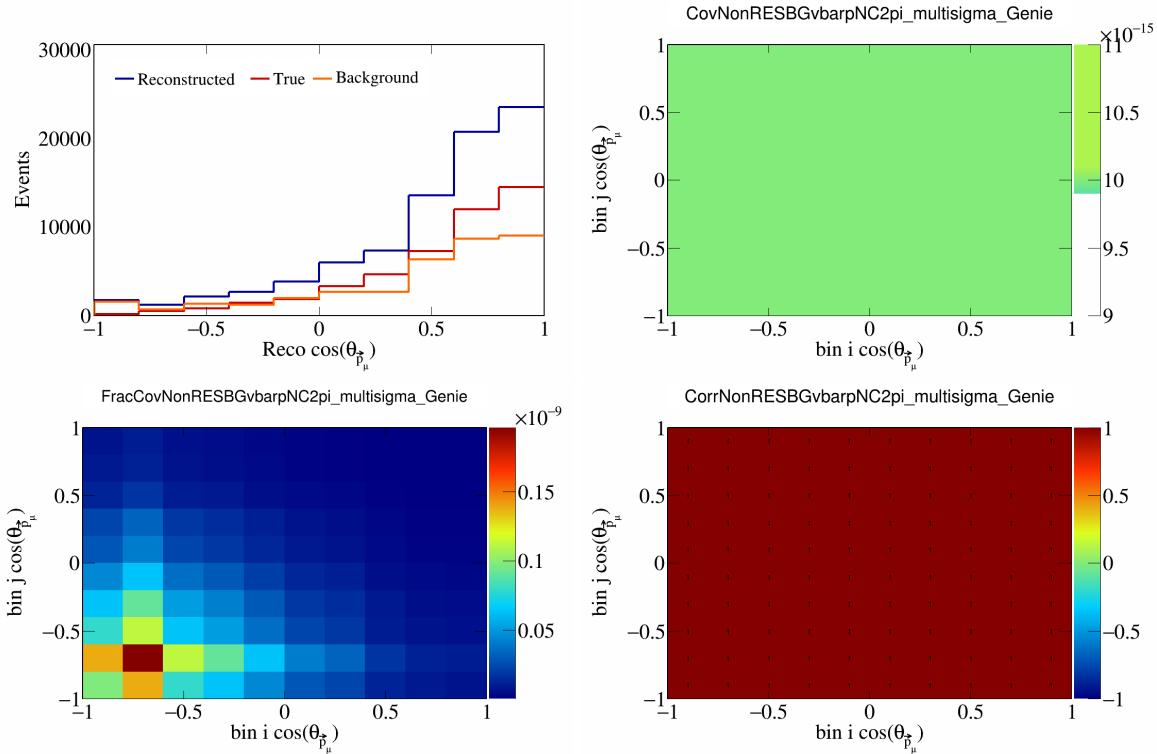


Figure 490: NonRESBGvbarpNC2pi variations for $\cos(\theta_{\vec{p}_\mu})$.

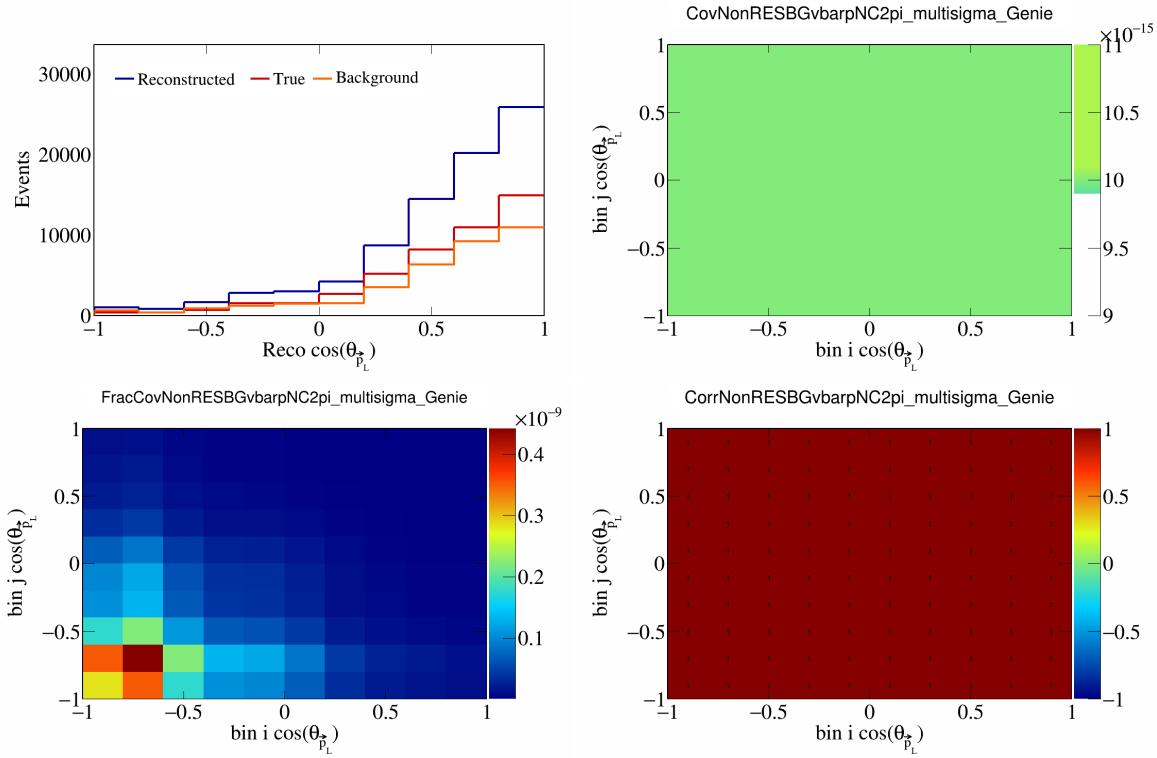


Figure 491: NonRESBGvbarpNC2pi variations for $\cos(\theta_{\vec{p}_L})$.

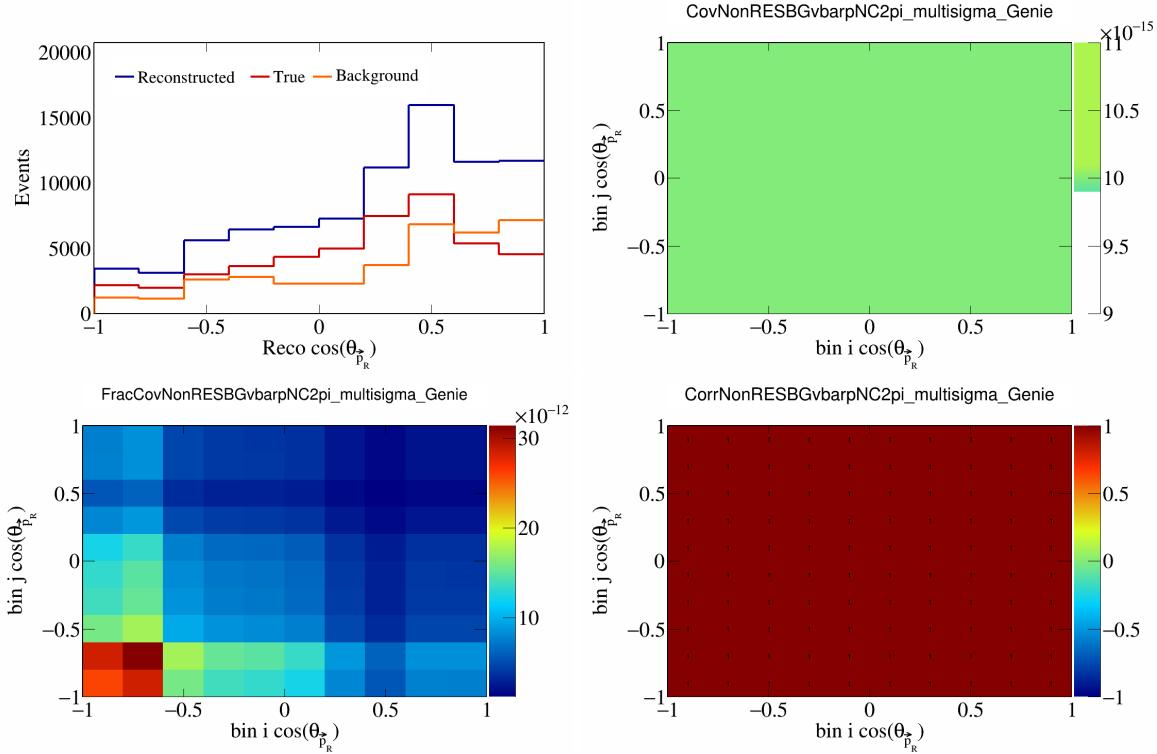


Figure 492: NonRESBGvbarpNC2pi variations for $\cos(\theta_{\vec{p}_R})$.

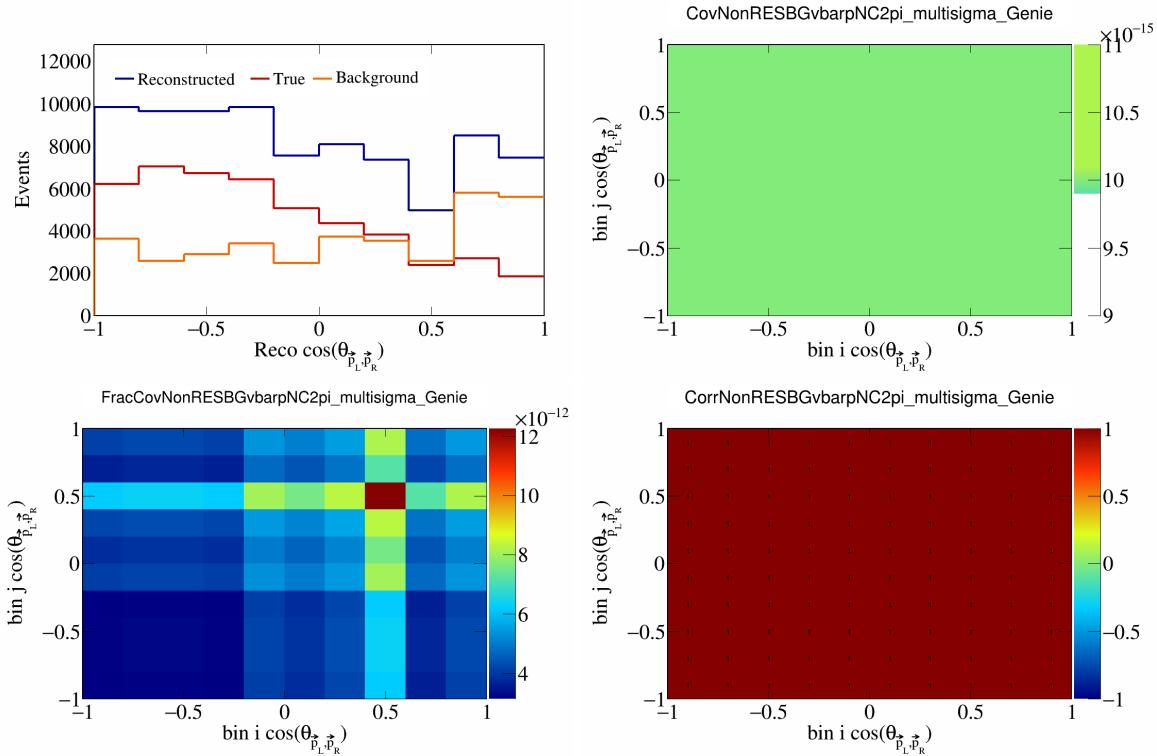


Figure 493: NonRESBGvbarpNC2pi variations for $\cos(\theta_{\vec{p}_L, \vec{p}_R})$.

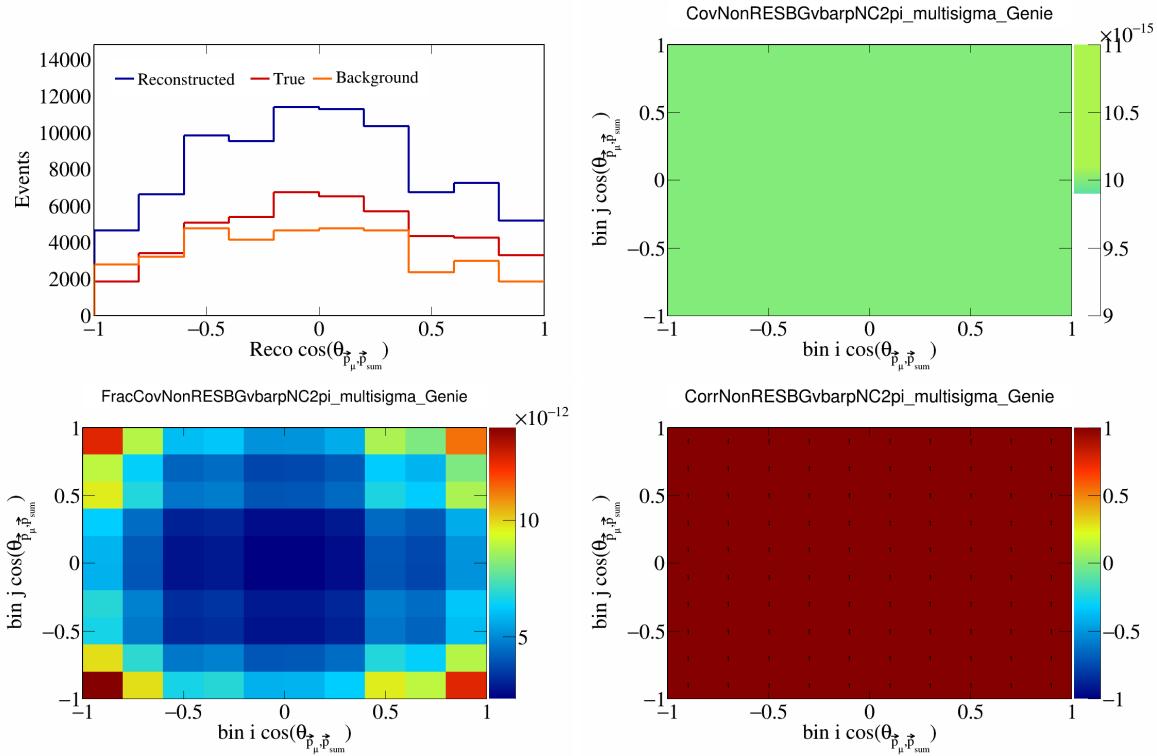


Figure 494: NonRESBGvbarpNC2pi variations for $\cos(\theta_{\vec{p}_\mu, \vec{p}_{\text{sum}}})$.

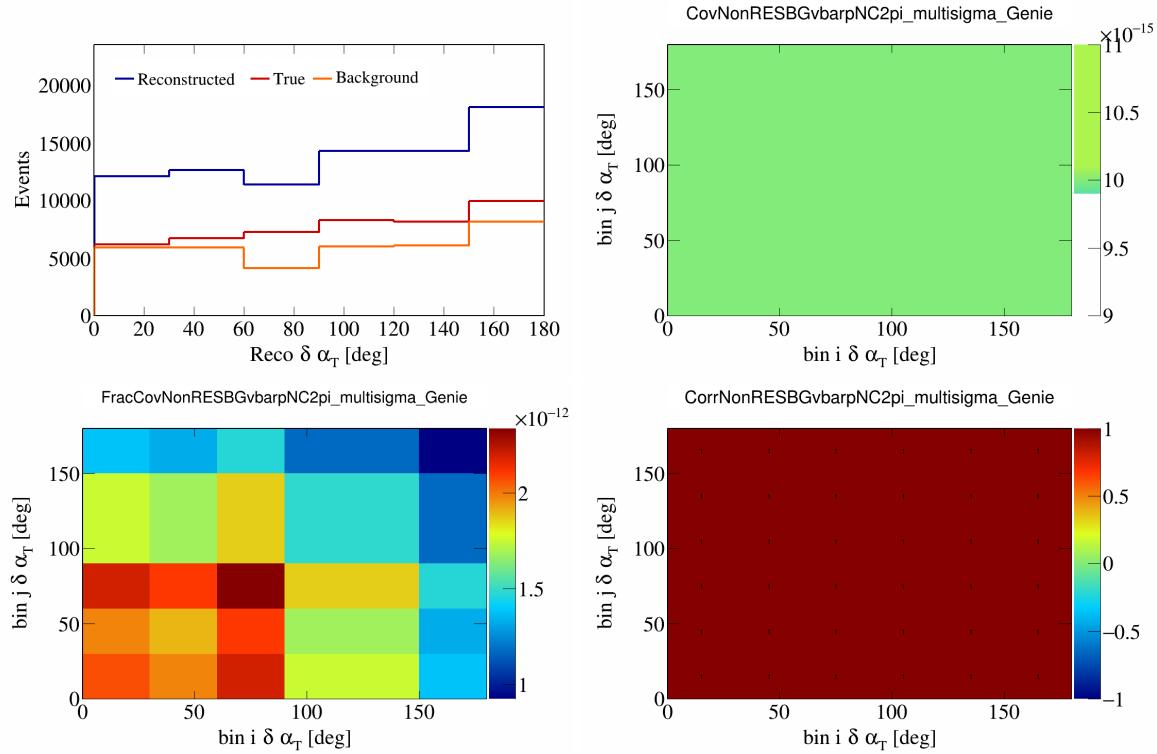


Figure 495: NonRESBGvbarpNC2pi variations for $\delta\alpha_T$.

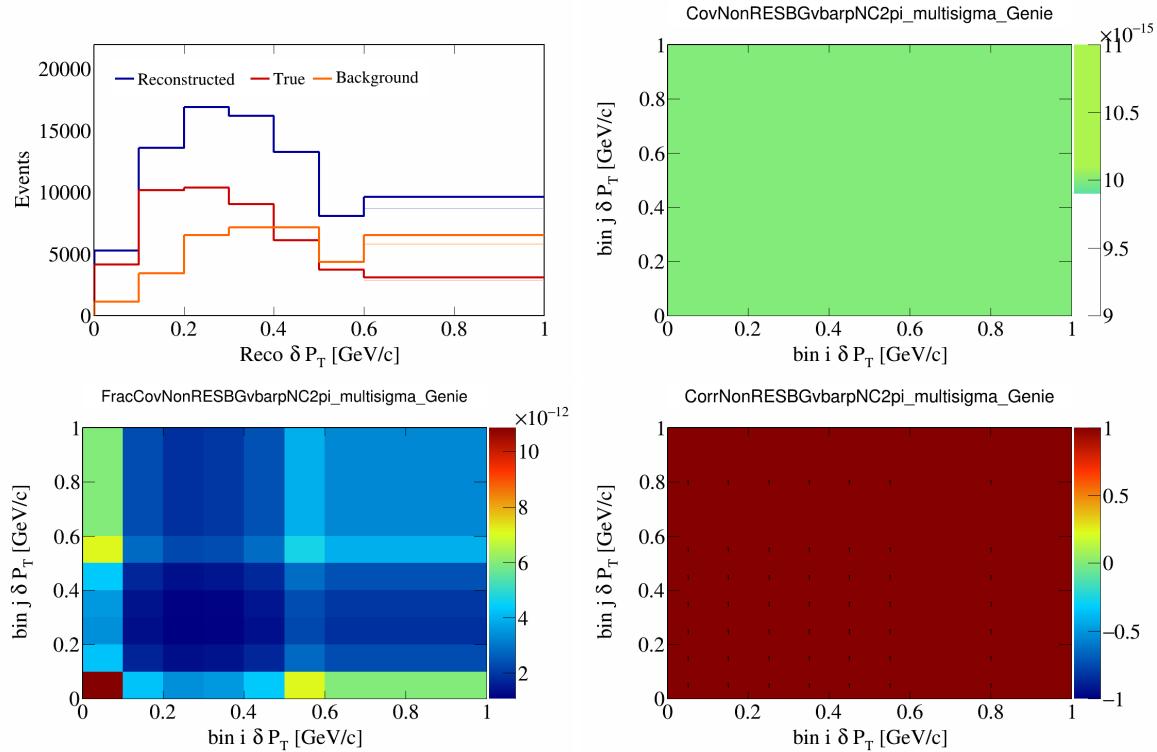


Figure 496: NonRESBGvbarpNC2pi variations for δP_T .

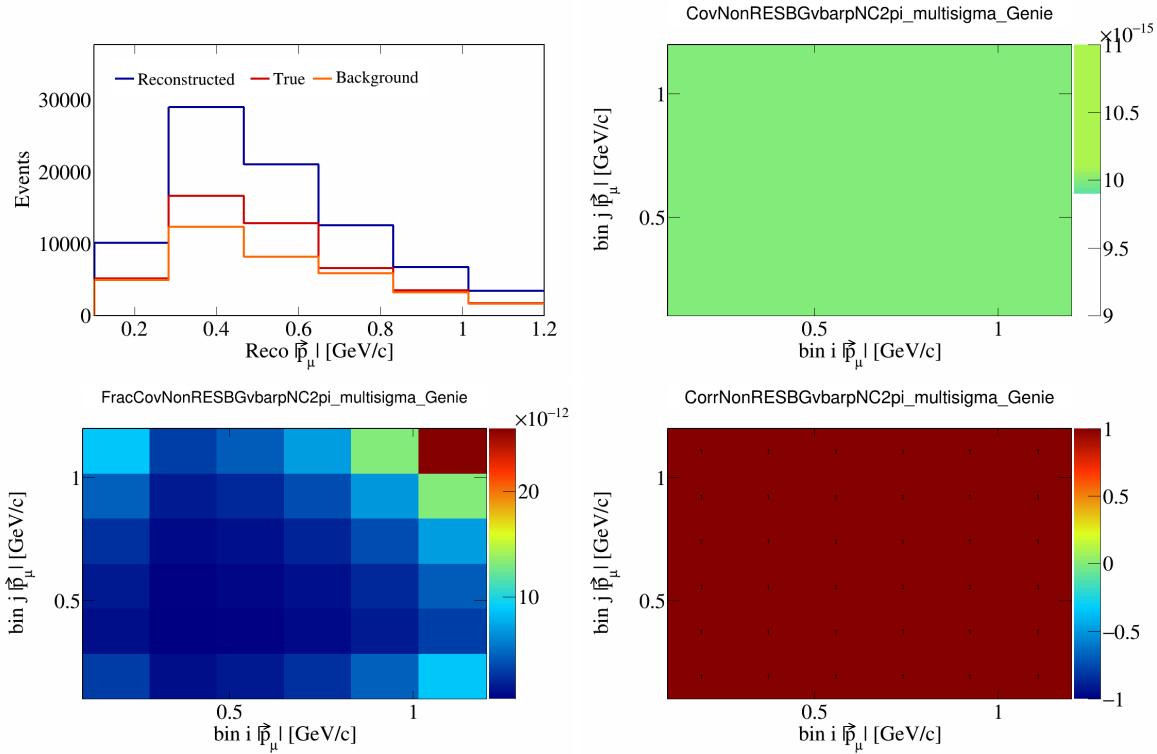


Figure 497: NonRESBGvbarpNC2pi variations for $|\vec{p}_\mu|$.

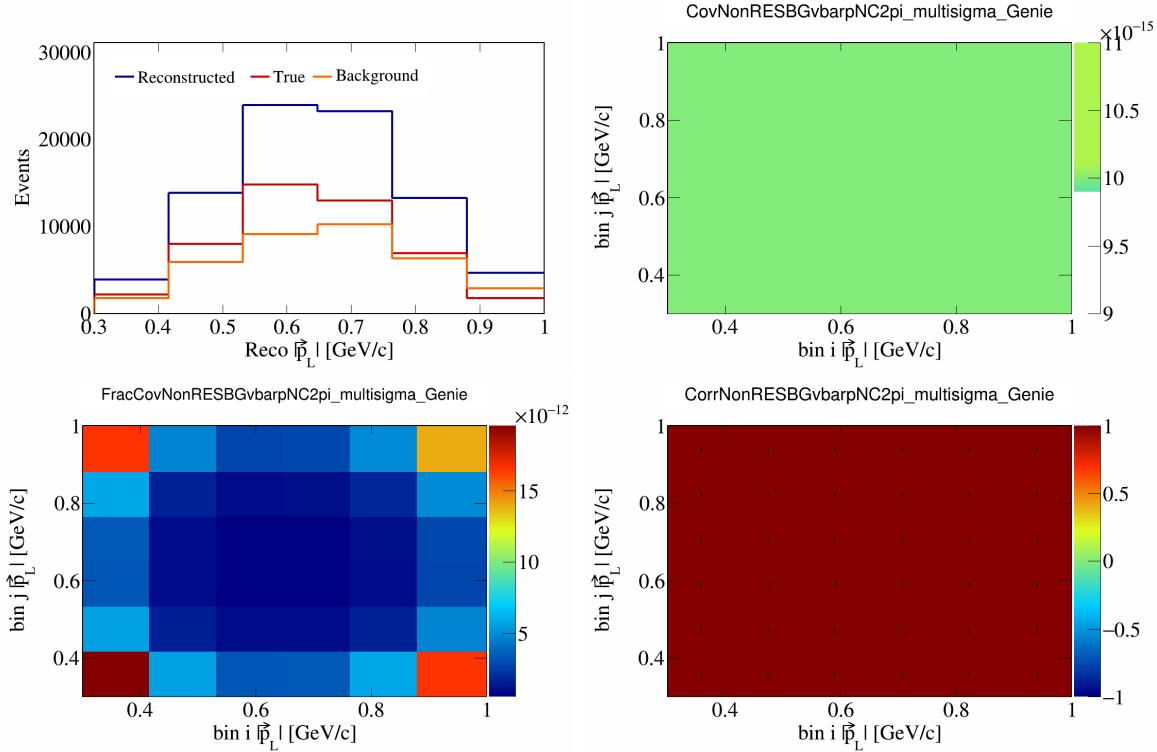


Figure 498: NonRESBGvbarpNC2pi variations for $|\vec{p}_L|$.

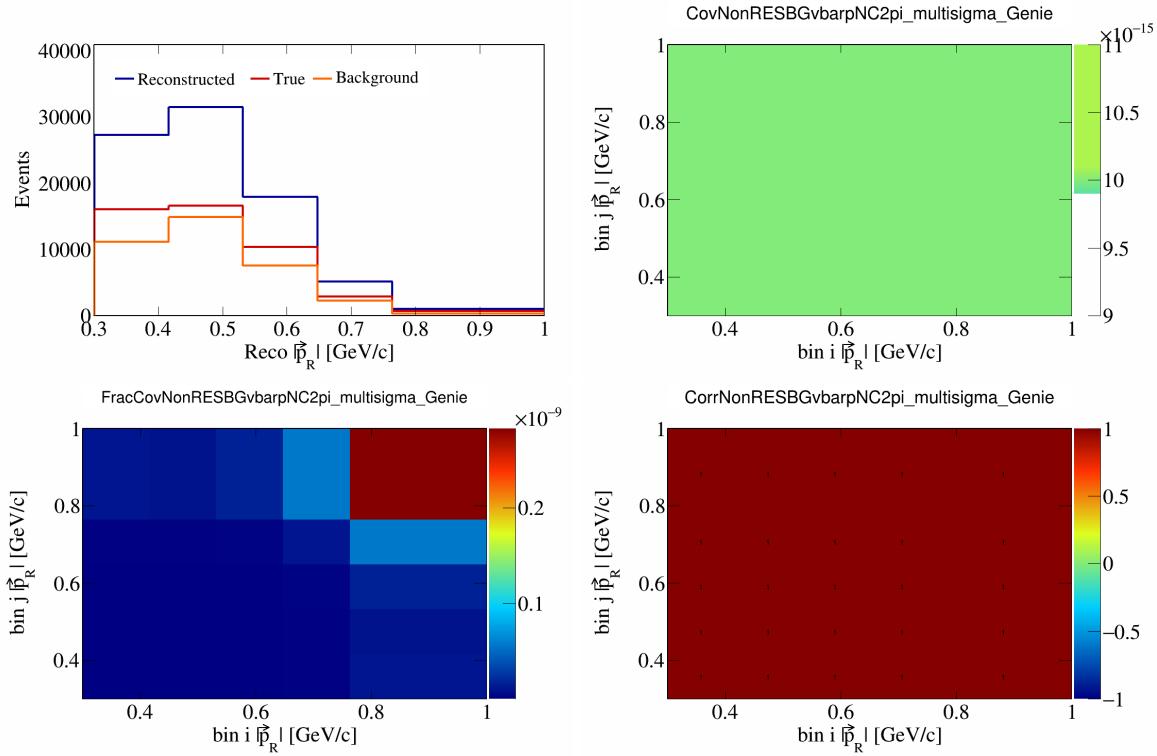


Figure 499: NonRESBGvbarpNC2pi variations for $|\vec{p}_R|$.

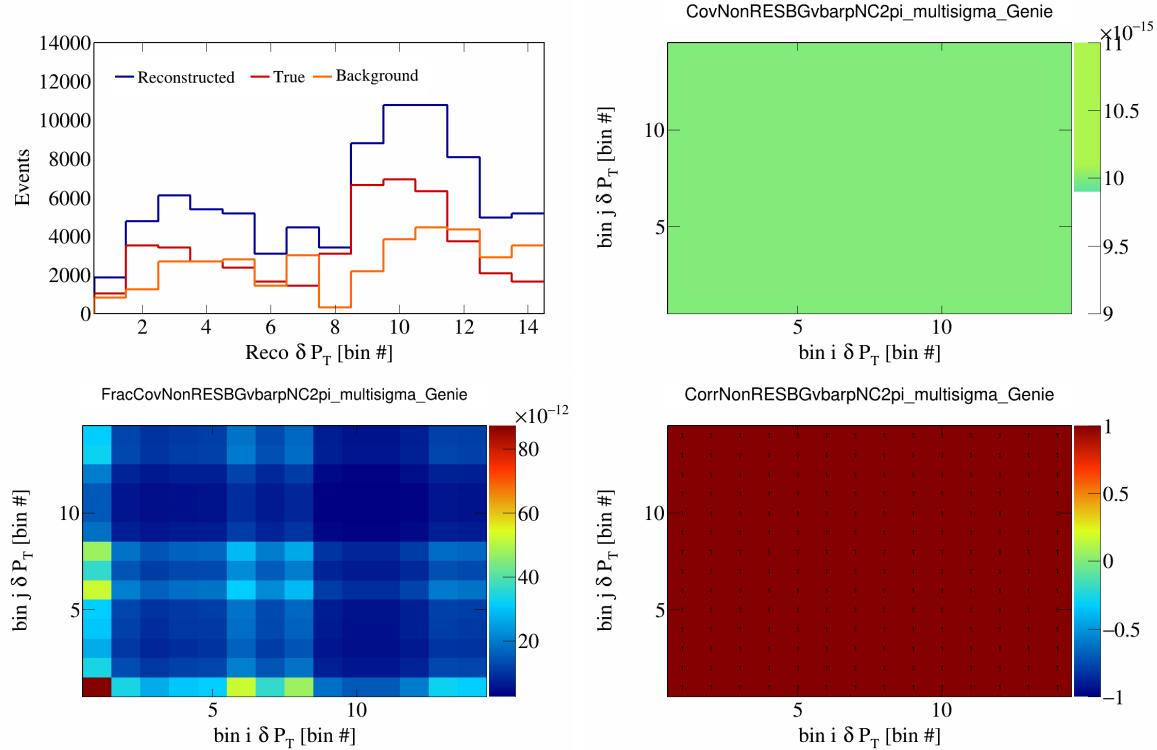


Figure 500: NonRESBGvbarpNC2pi variations for δP_T in $\cos(\theta_{\vec{p}_\mu})$.

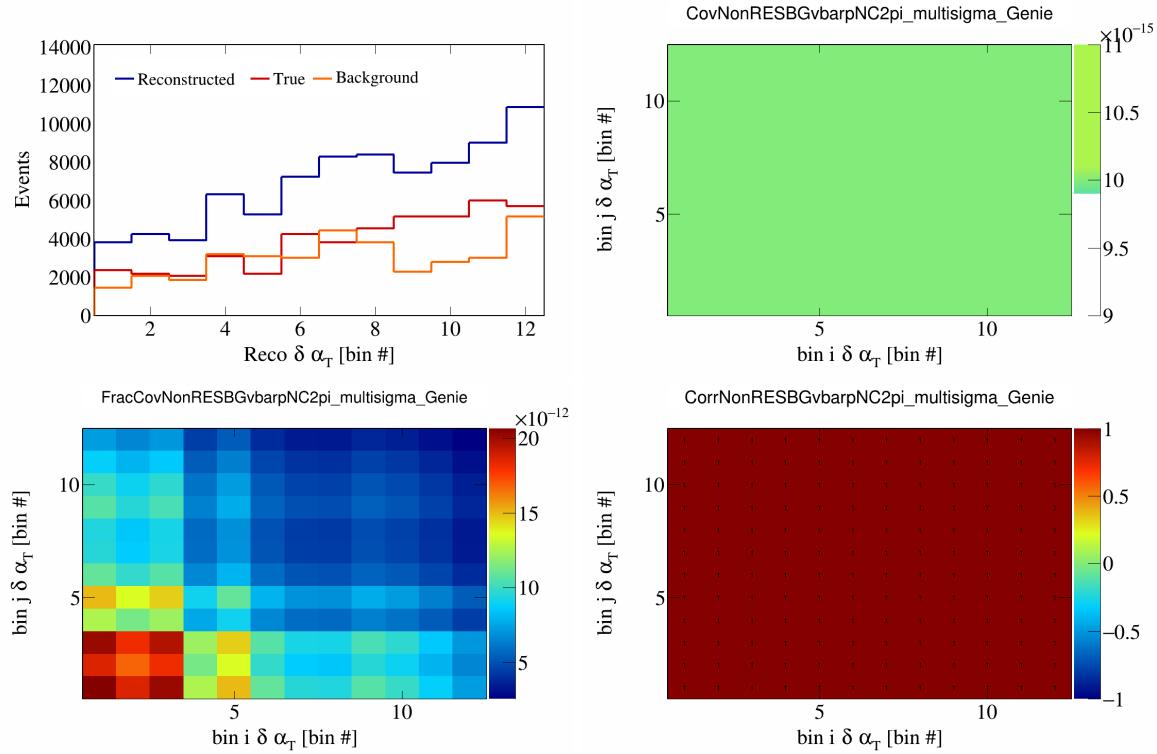


Figure 501: NonRESBGvbarpNC2pi variations for $\delta\alpha_T$ in $\cos(\theta_{\vec{p}_\mu})$.

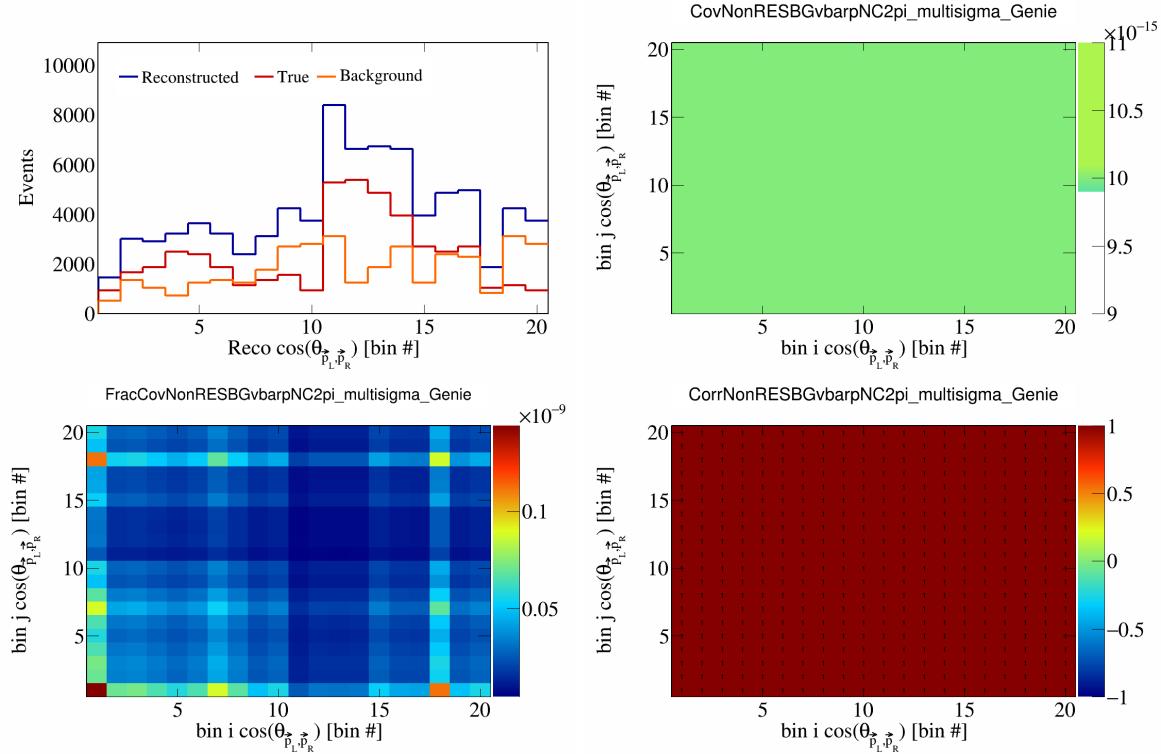


Figure 502: NonRESBGvbarpNC2pi variations for $\cos(\theta_{\vec{p}_L, \vec{p}_R})$ in $\cos(\theta_{\vec{p}_\mu})$.

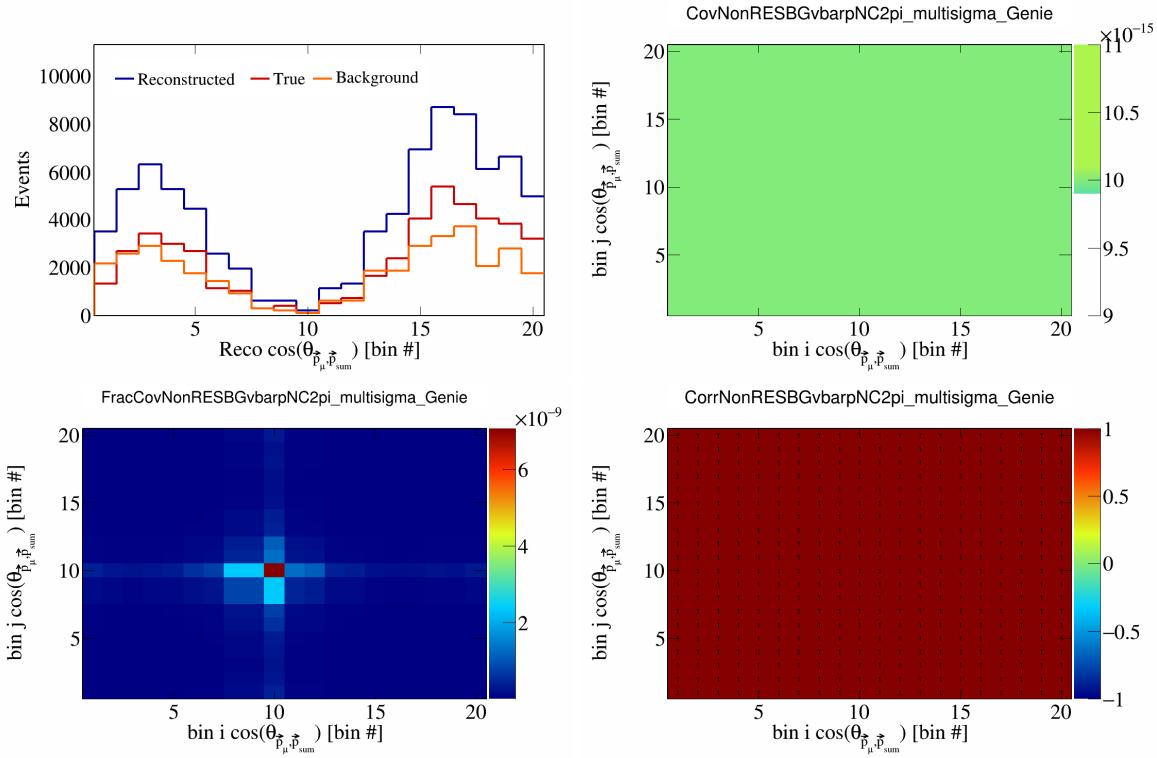


Figure 503: NonRESBGvbarpNC2pi variations for $\cos(\theta_{\vec{p}_\mu})$ in $\cos(\theta_{\vec{p}_\mu})$.

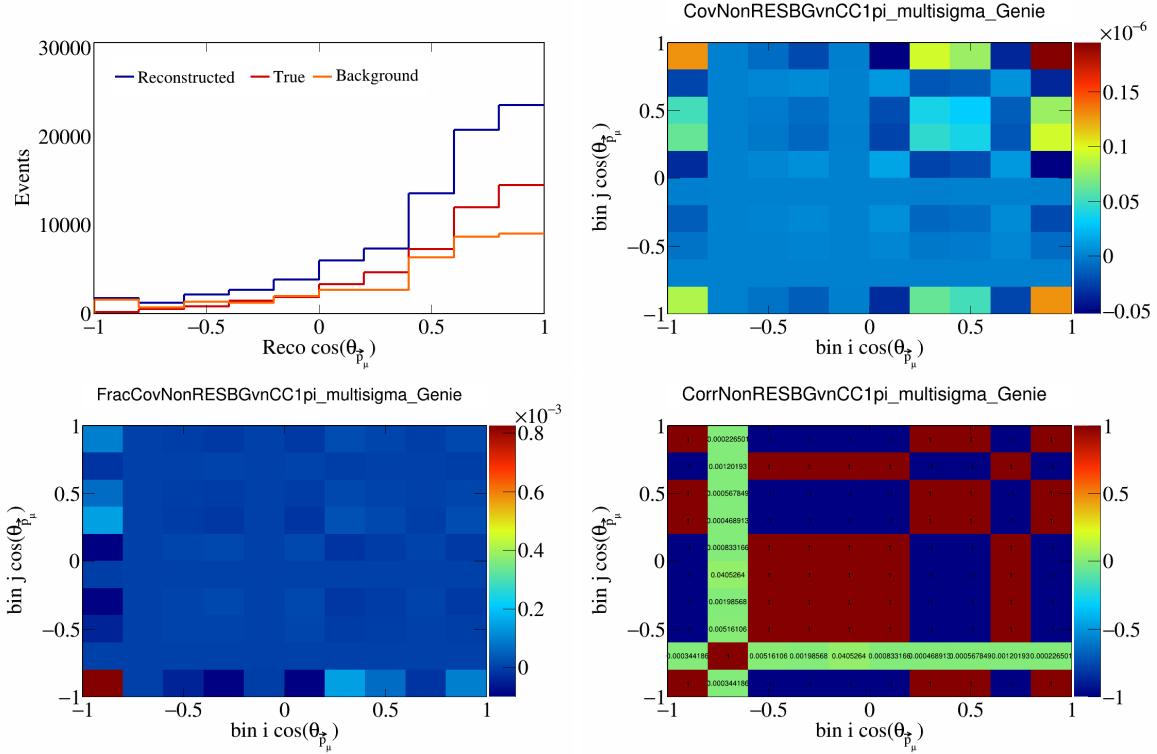


Figure 504: NonRESBGvnCC1pi variations for $\cos(\theta_{\vec{p}_\mu})$.

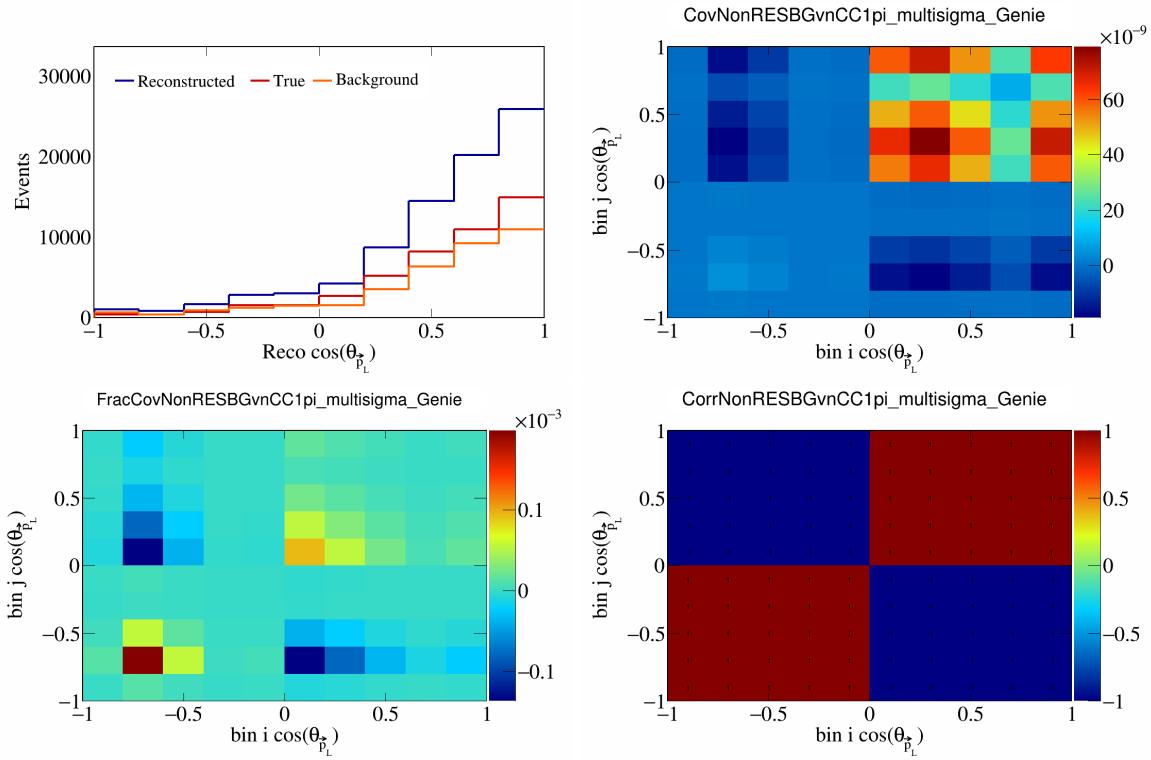


Figure 505: NonRESBGvnCC1pi variations for $\cos(\theta_{\vec{p}_L})$.

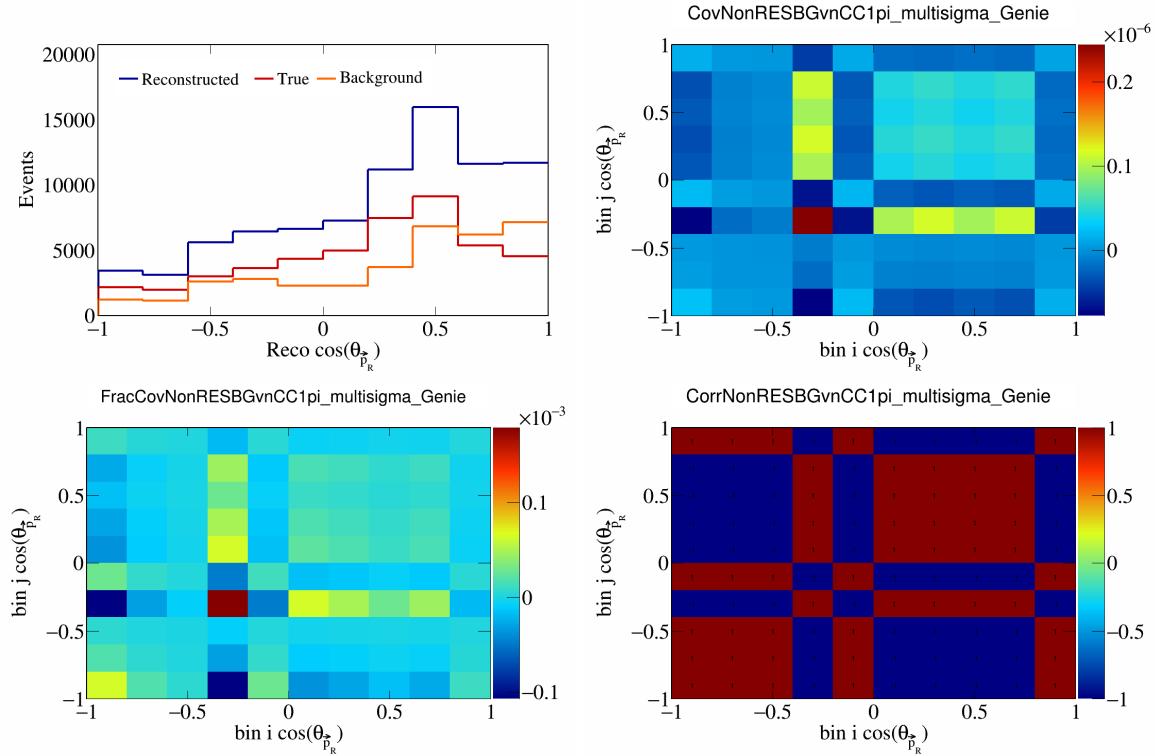


Figure 506: NonRESBGvnCC1pi variations for $\cos(\theta_{\vec{p}_R})$.

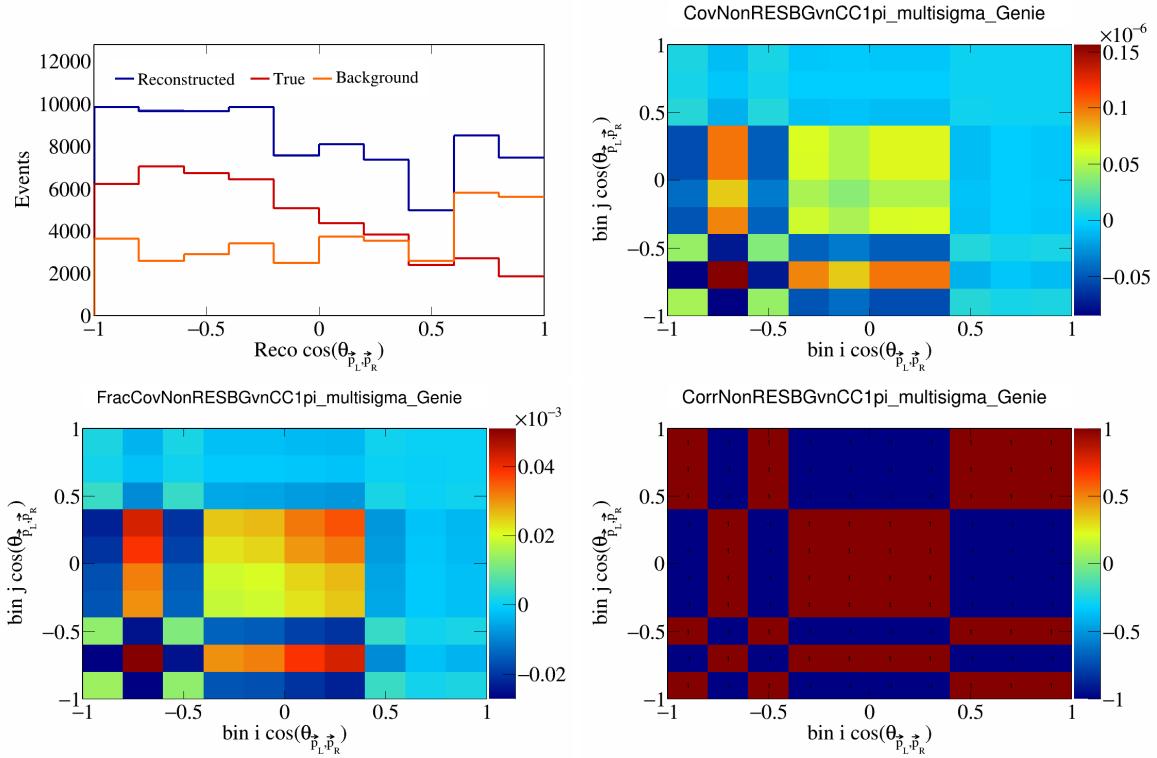


Figure 507: NonRESBGvnCC1pi variations for $\cos(\theta_{\vec{p}_L, \vec{p}_R})$.

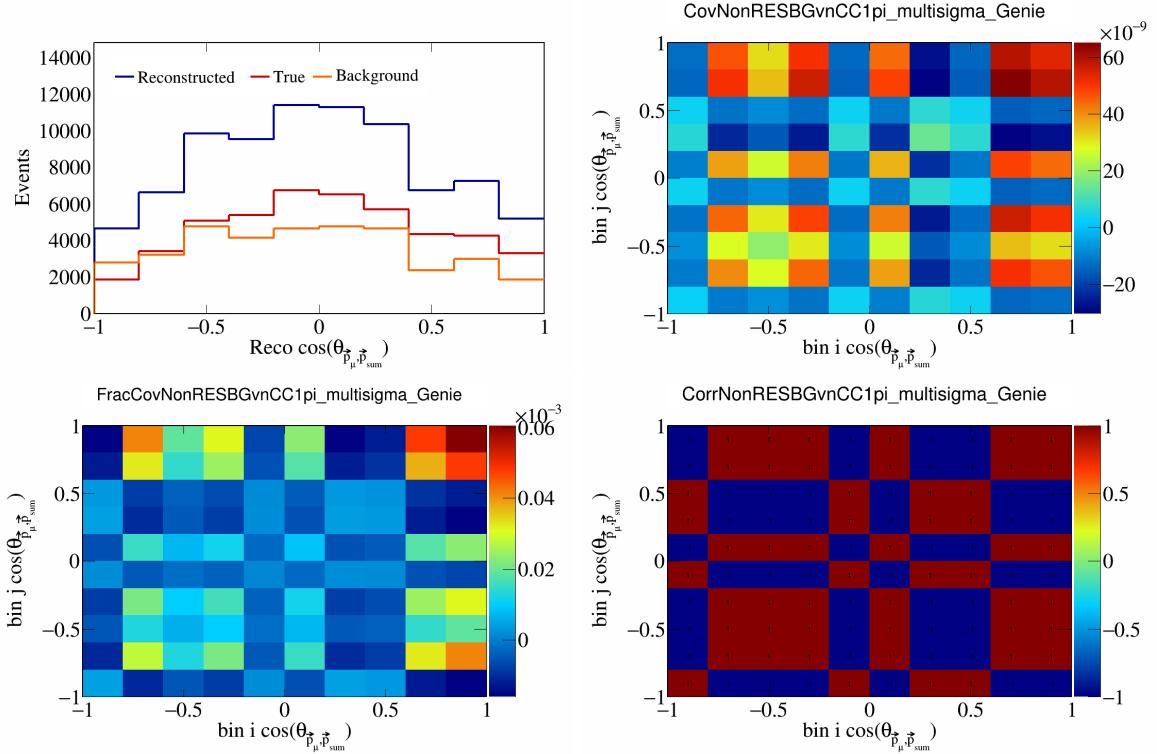


Figure 508: NonRESBGvnCC1pi variations for $\cos(\theta_{\vec{p}_\mu, \vec{p}_{\text{sum}}})$.

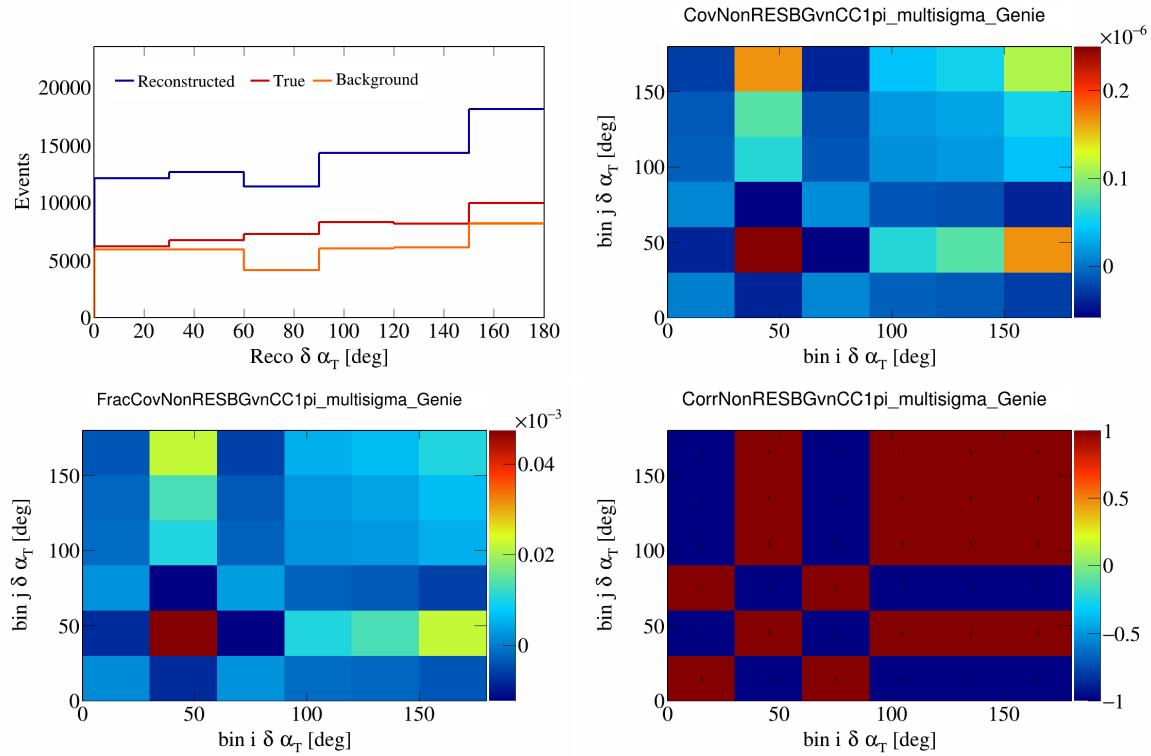


Figure 509: NonRESBGvnCC1pi variations for $\delta\alpha_T$.

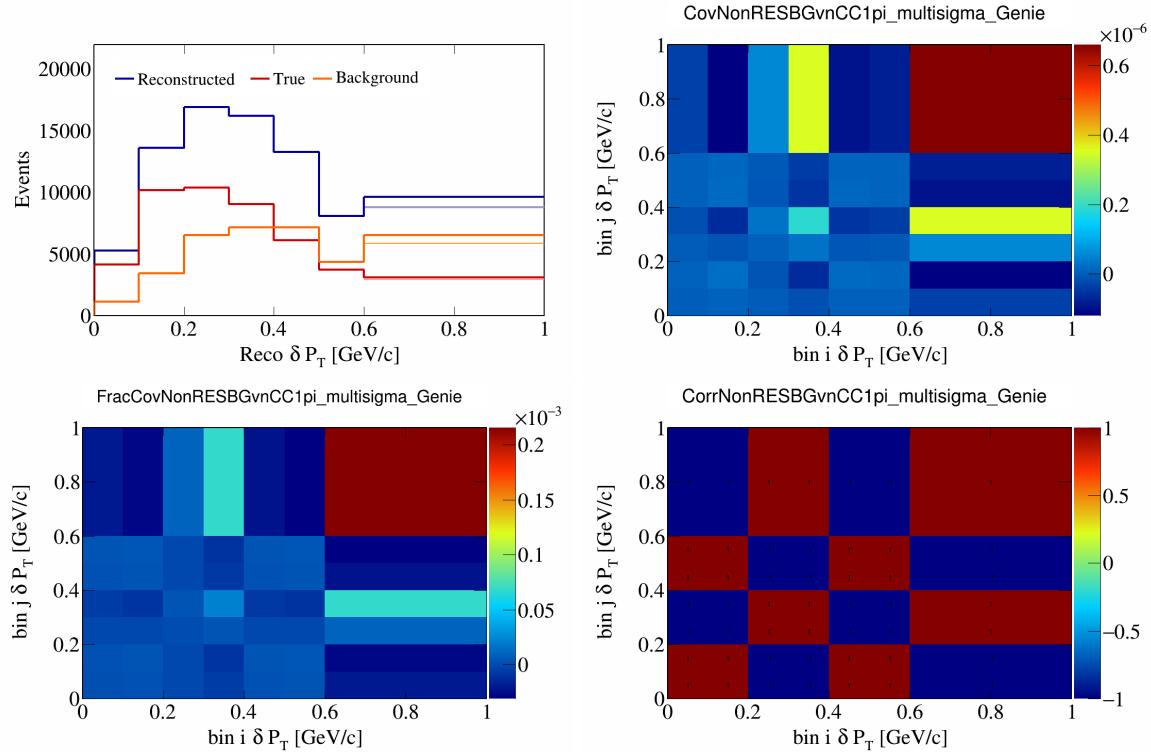


Figure 510: NonRESBGvnCC1pi variations for δP_T .

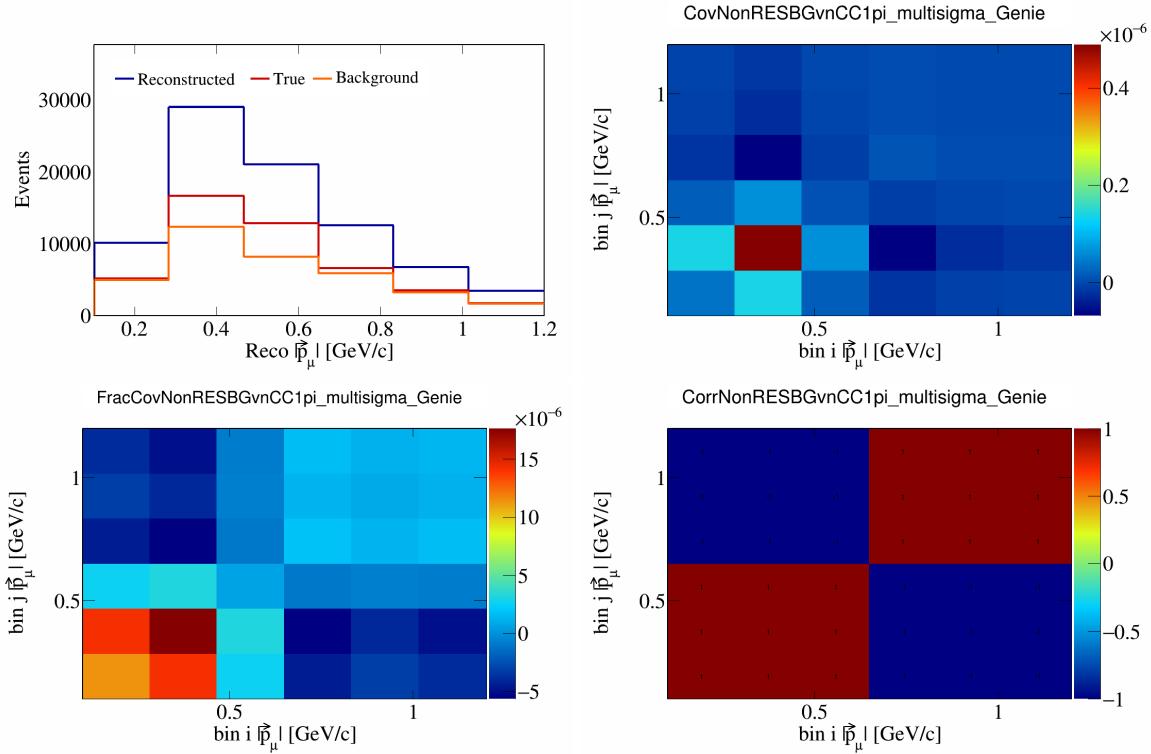


Figure 511: NonRESBGvnCC1pi variations for $|p_\mu|$.

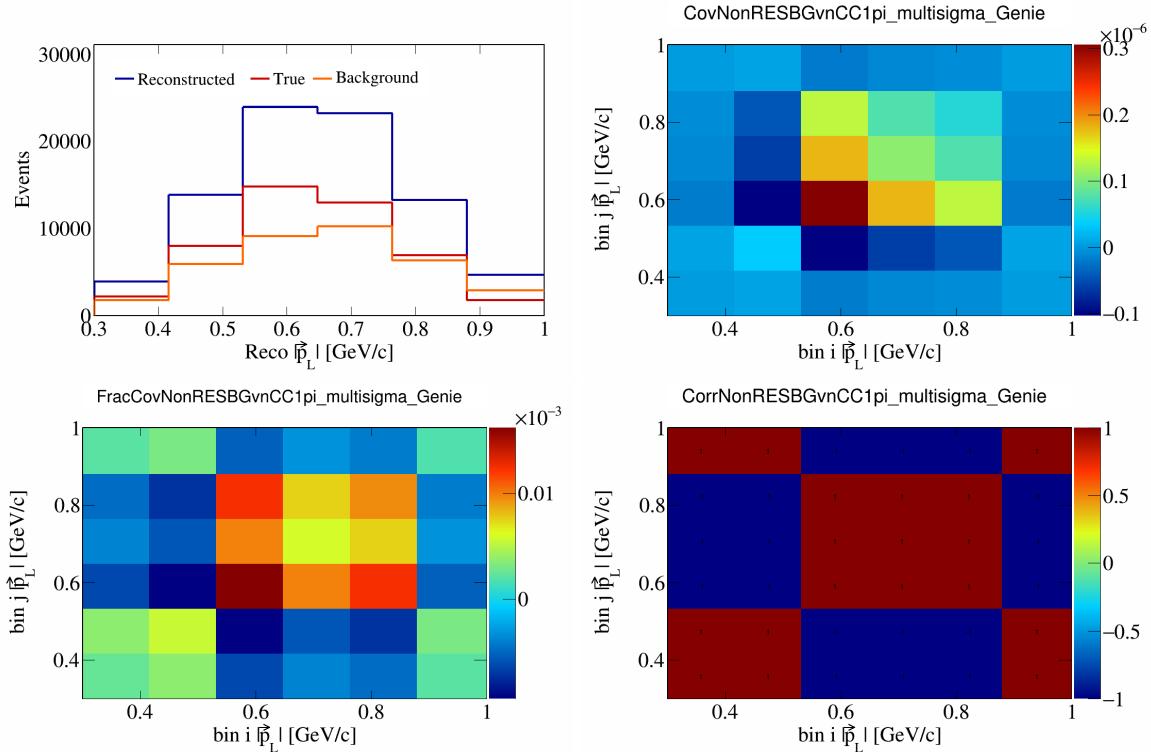


Figure 512: NonRESBGvnCC1pi variations for $|p_L|$.

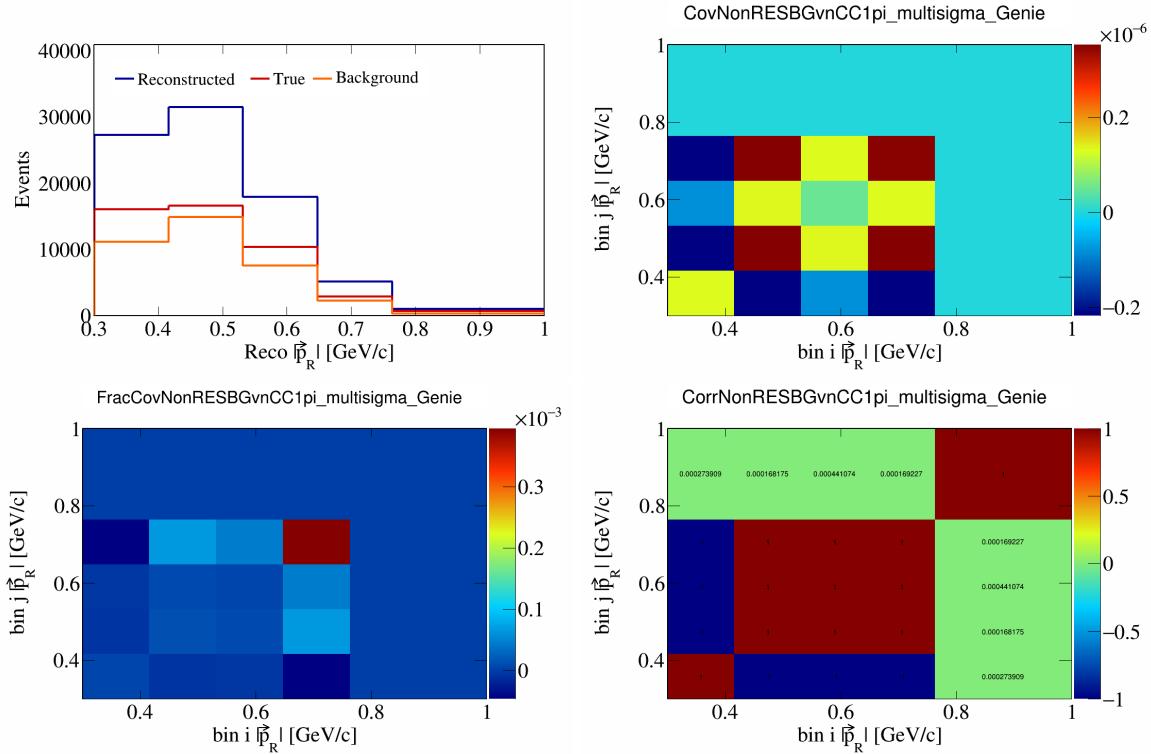


Figure 513: NonRESBGvnCC1pi variations for $|\vec{p}_R|$.

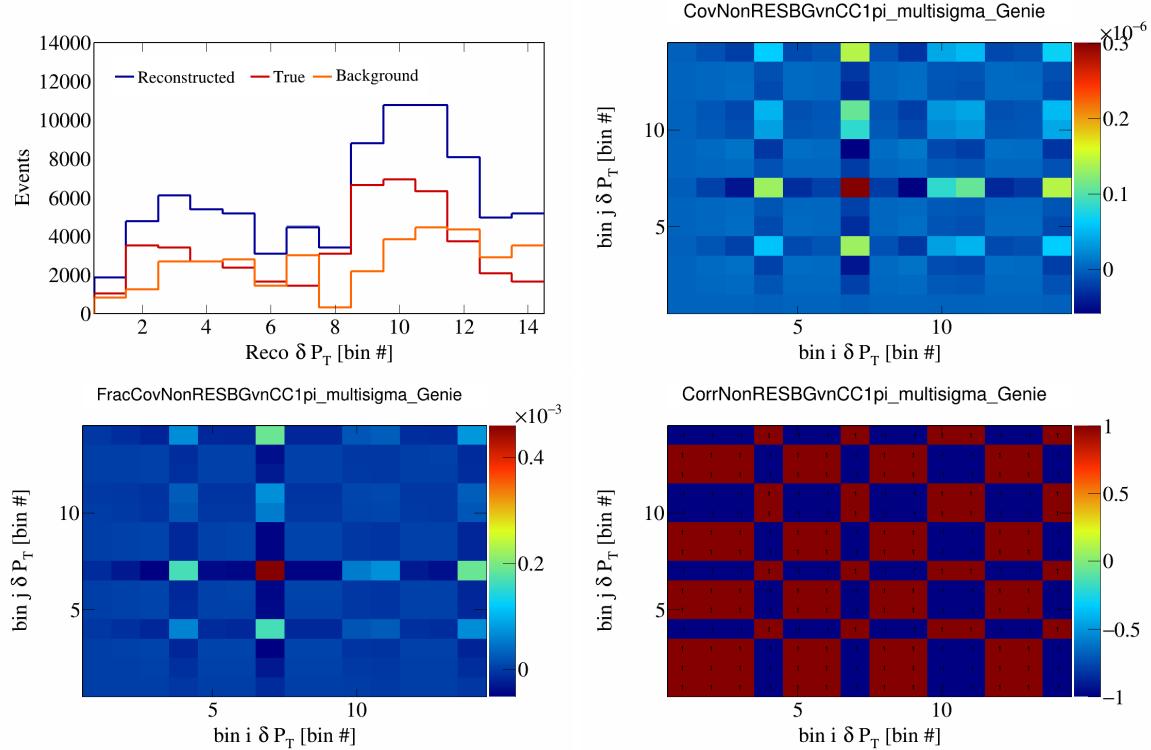


Figure 514: NonRESBGvnCC1pi variations for δP_T in $\cos(\theta_{\vec{p}_\mu})$.

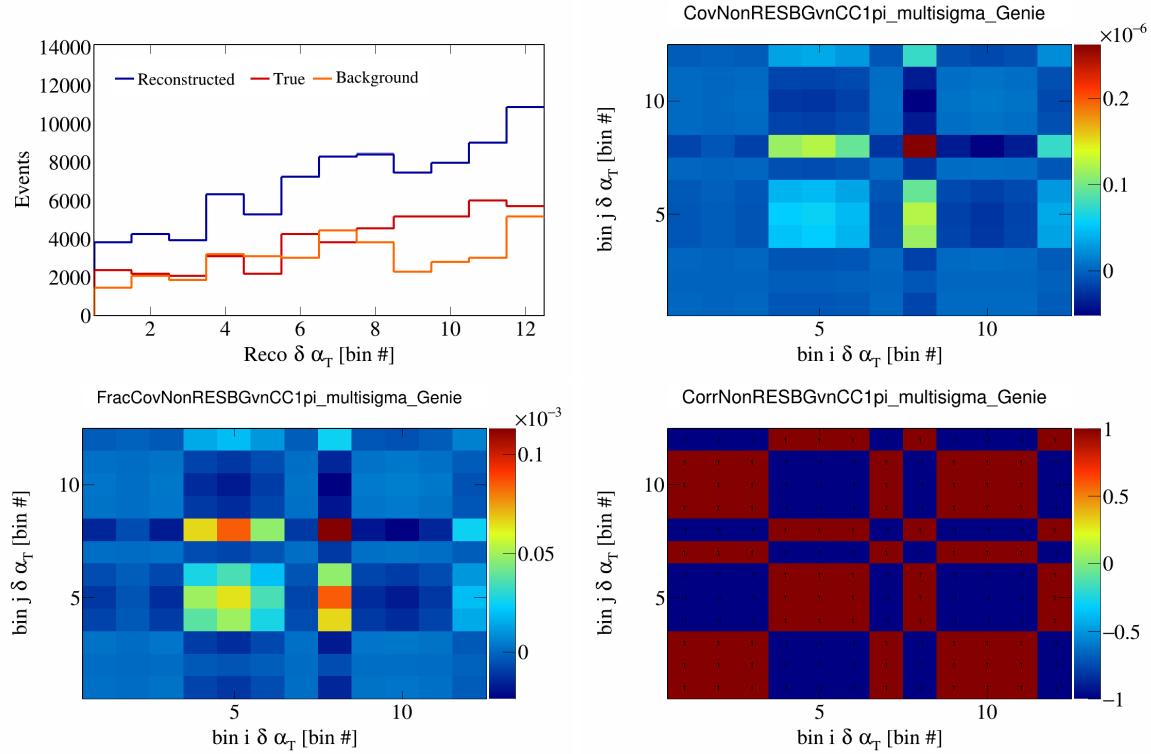


Figure 515: NonRESBGvnCC1pi variations for $\delta \alpha_T$ in $\cos(\theta_{\vec{p}_\mu})$.

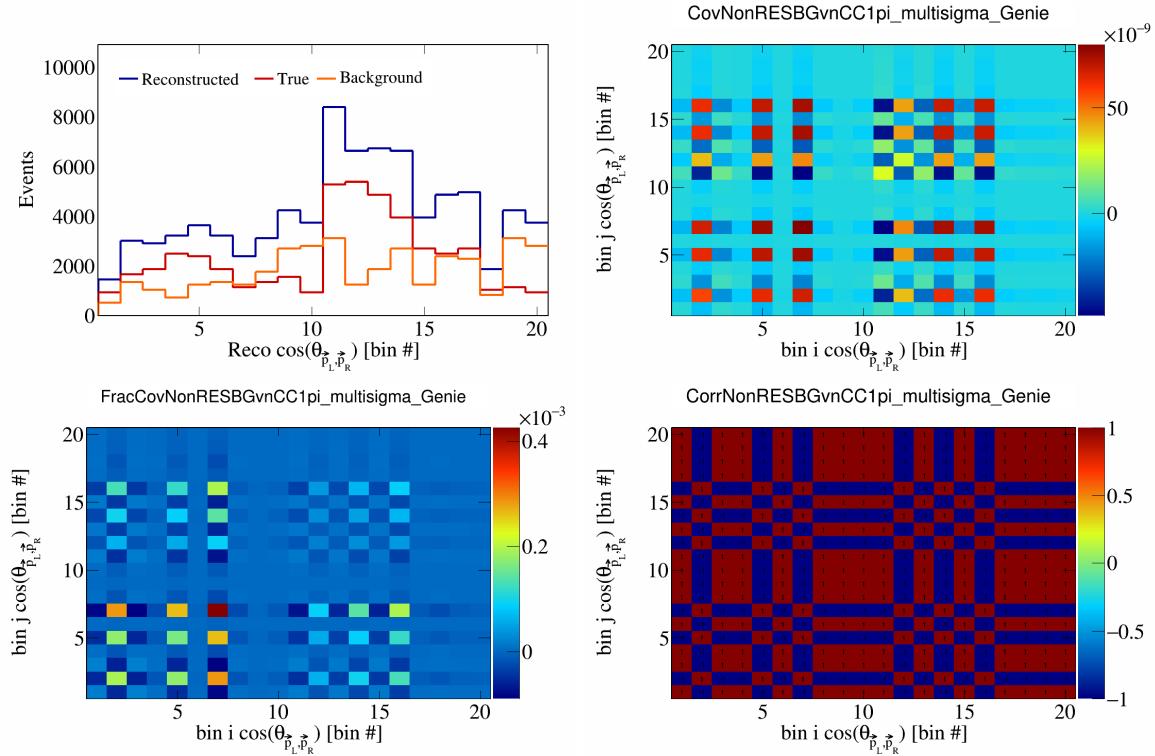


Figure 516: NonRESBGvnCC1pi variations for $\cos(\theta_{\vec{p}_L, \vec{p}_R})$ in $\cos(\theta_{\vec{p}_\mu})$.

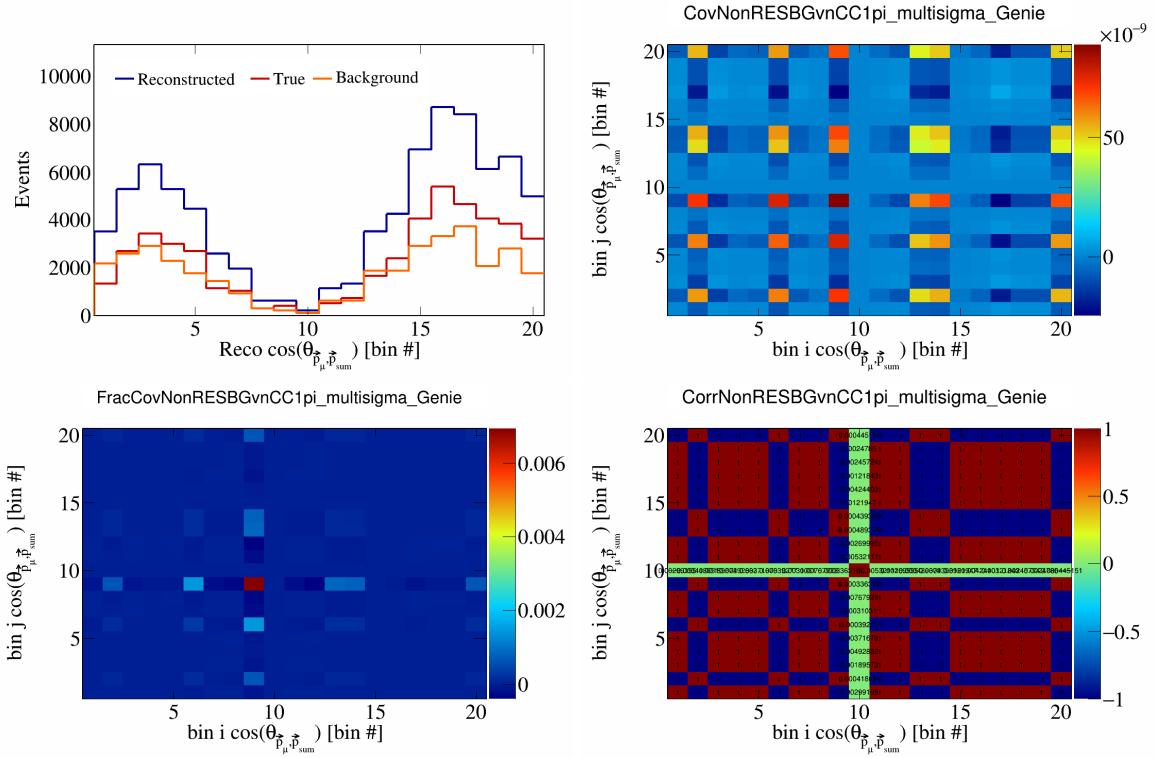


Figure 517: NonRESBGvnCC1pi variations for $\cos(\theta_{\vec{p}_\mu})$ in $\cos(\theta_{\vec{p}_\mu})$.

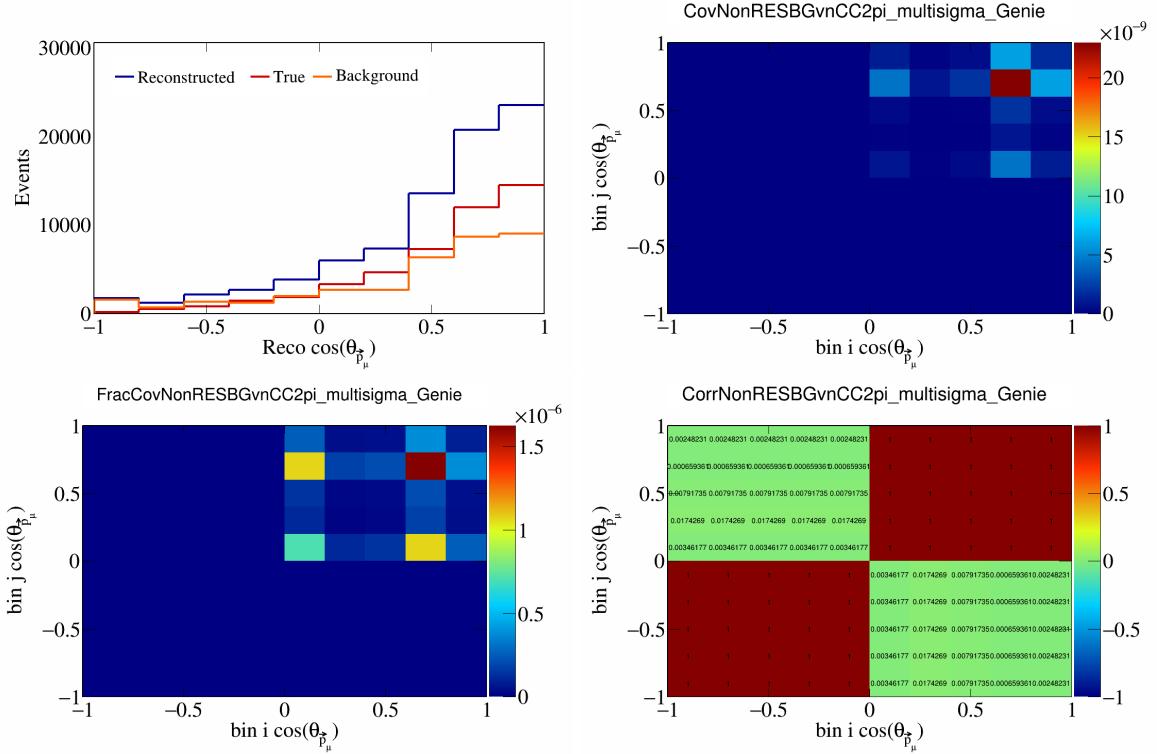


Figure 518: NonRESBGvnCC2pi variations for $\cos(\theta_{\vec{p}_\mu})$.

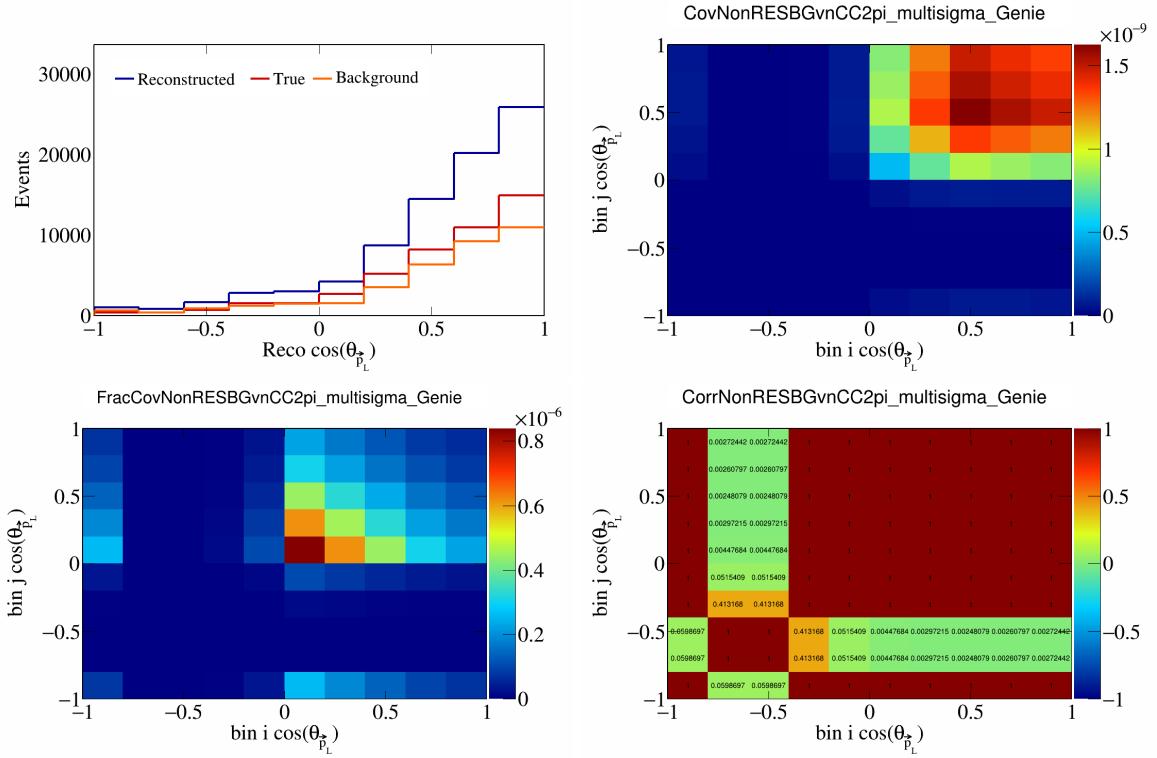


Figure 519: NonRESBGvnCC2pi variations for $\cos(\theta_{\vec{p}_L})$.

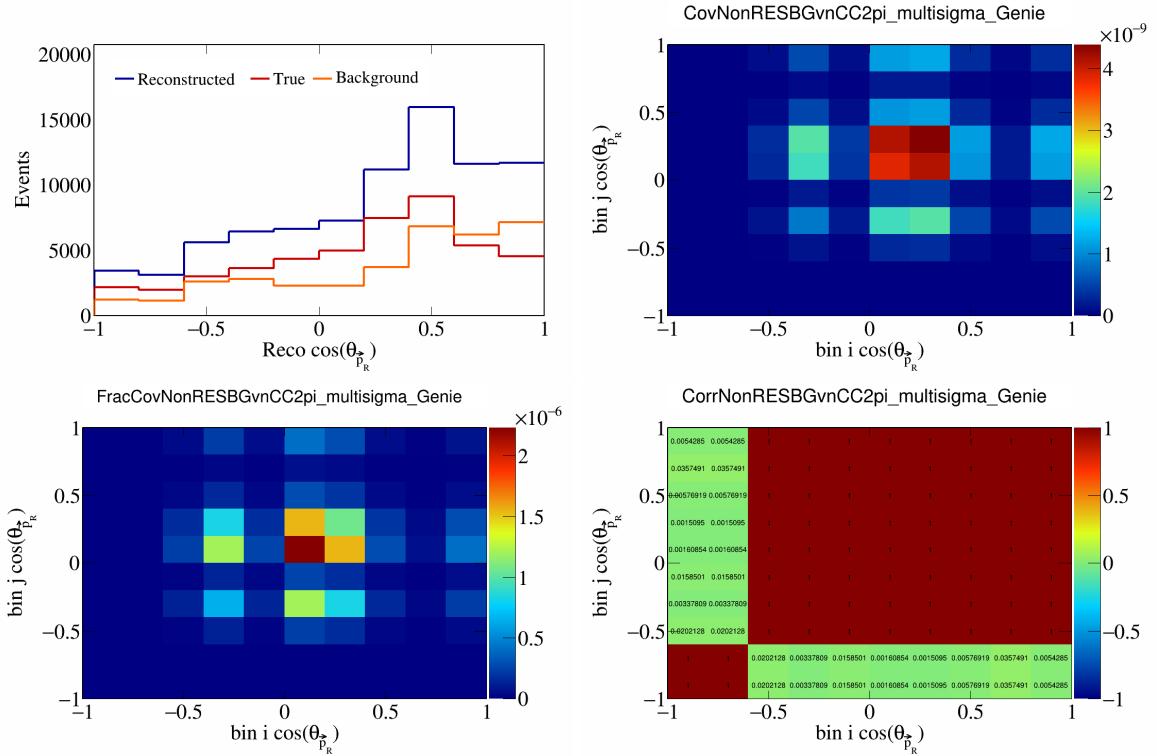


Figure 520: NonRESBGvnCC2pi variations for $\cos(\theta_{\vec{p}_R})$.

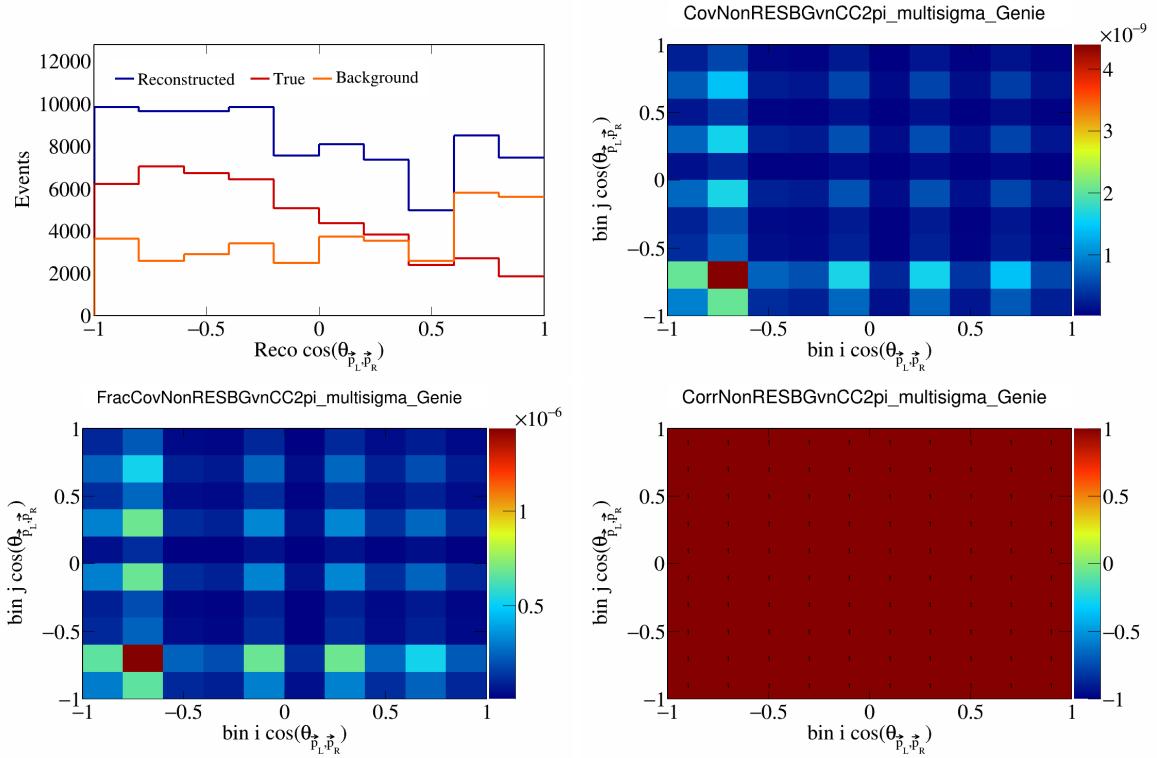


Figure 521: NonRESBGvnCC2pi variations for $\cos(\theta_{\vec{p}_L, \vec{p}_R})$.

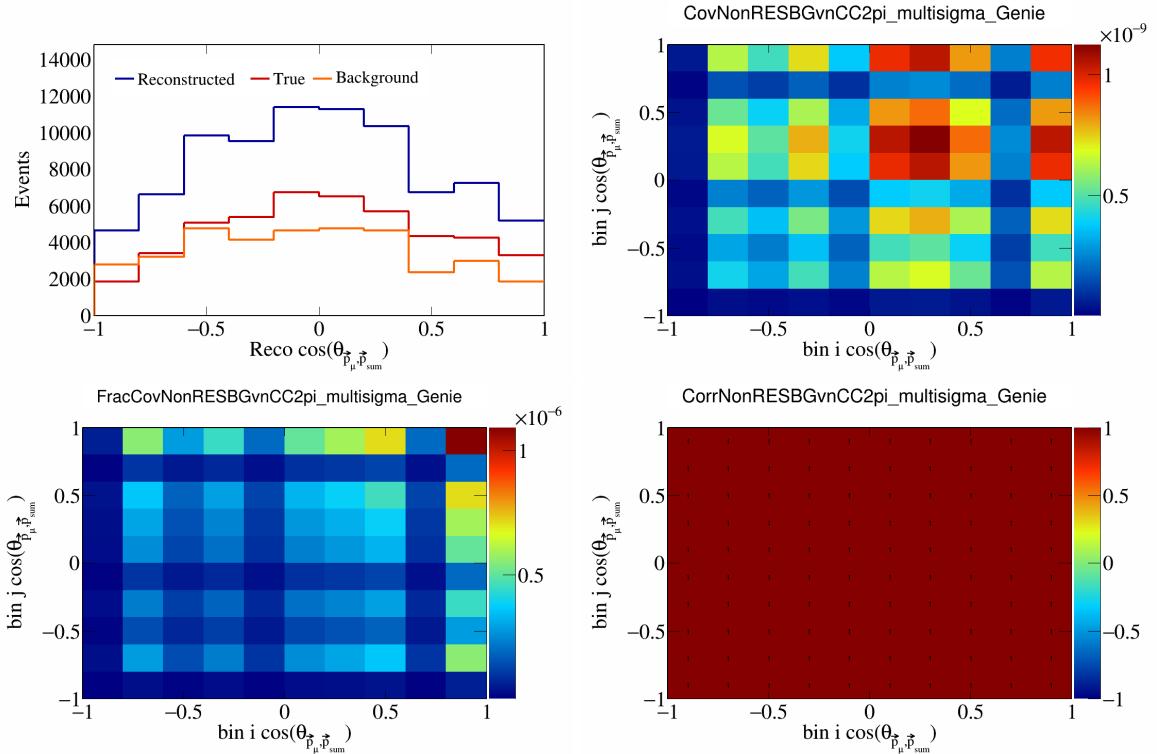


Figure 522: NonRESBGvnCC2pi variations for $\cos(\theta_{\vec{p}_\mu, \vec{p}_{\text{sum}}})$.

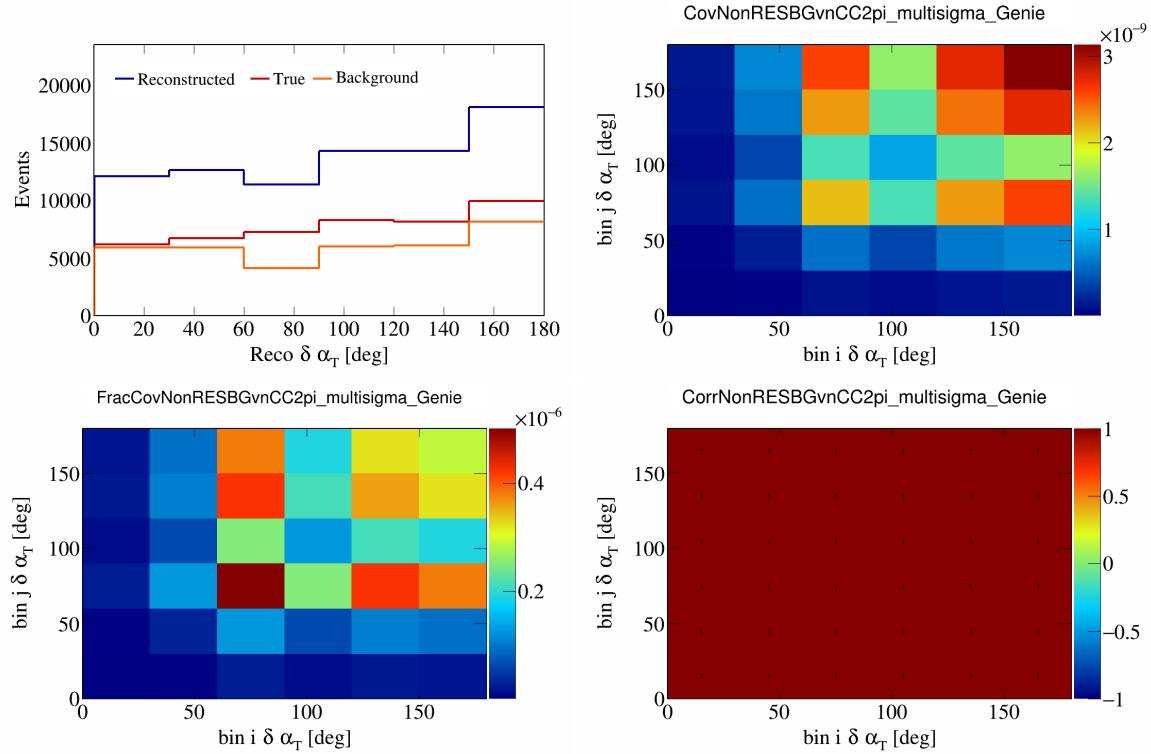


Figure 523: NonRESBGvnCC2pi variations for $\delta\alpha_T$.

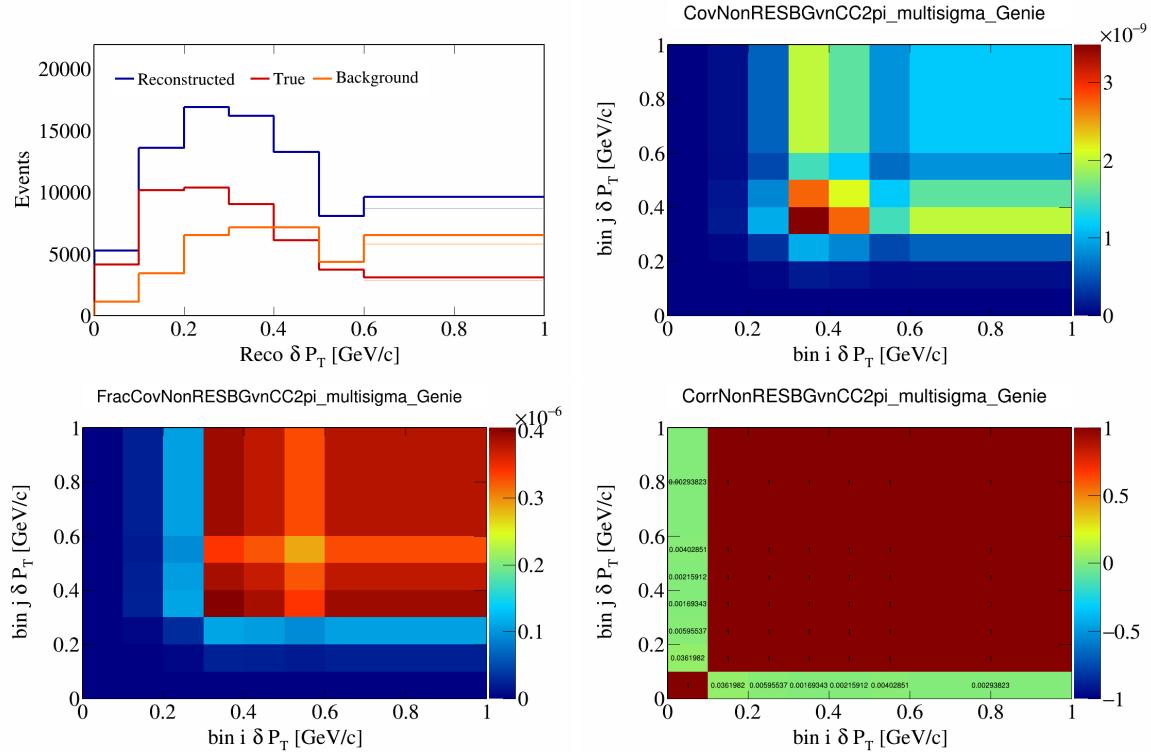


Figure 524: NonRESBGvnCC2pi variations for δP_T .

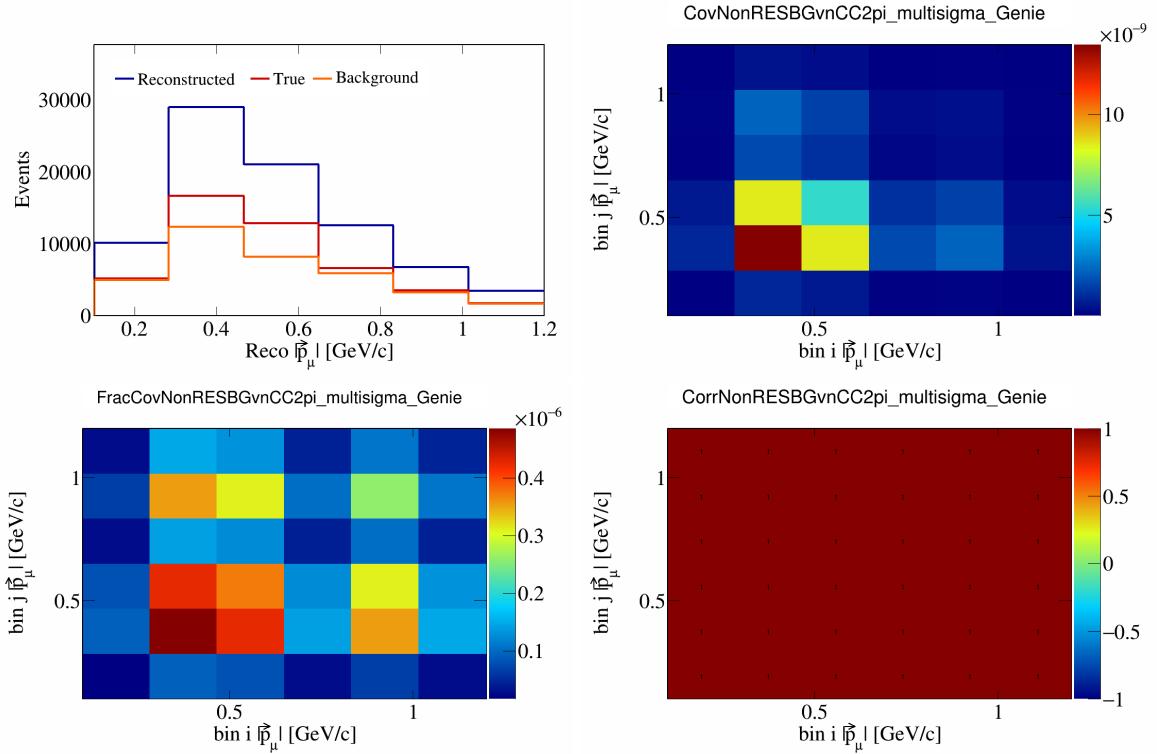


Figure 525: NonRESBGvnCC2pi variations for $|\vec{p}_\mu|$.

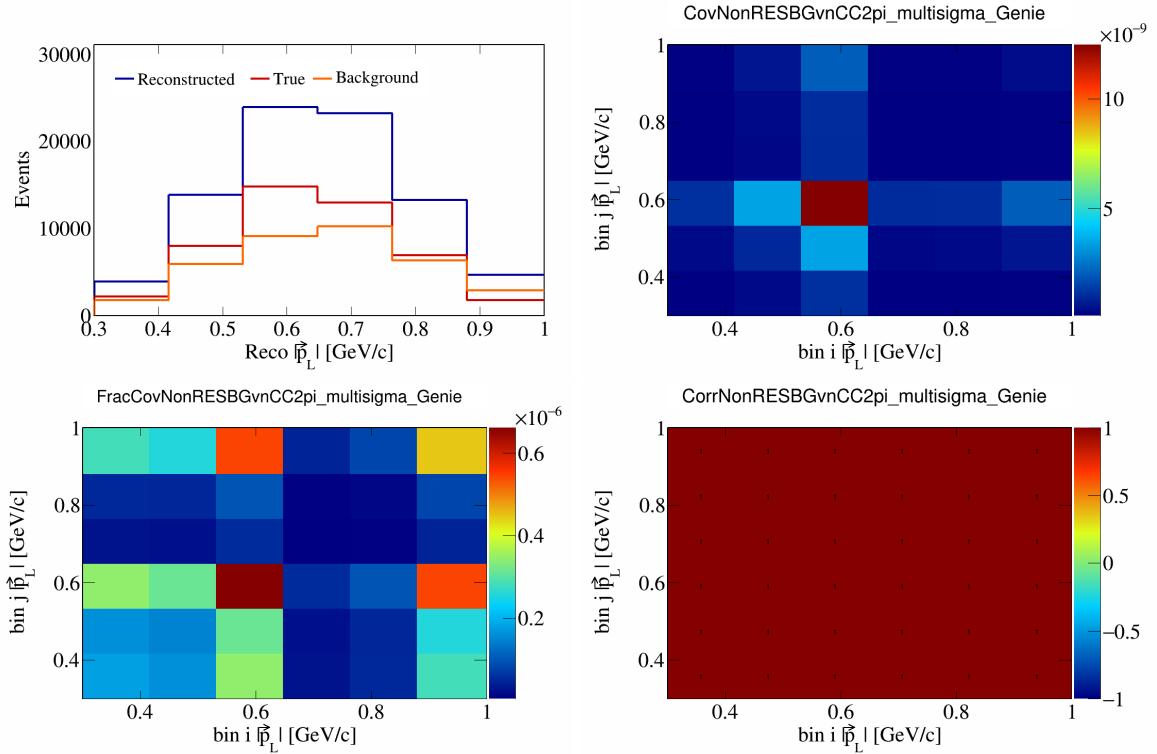


Figure 526: NonRESBGvnCC2pi variations for $|\vec{p}_L|$.

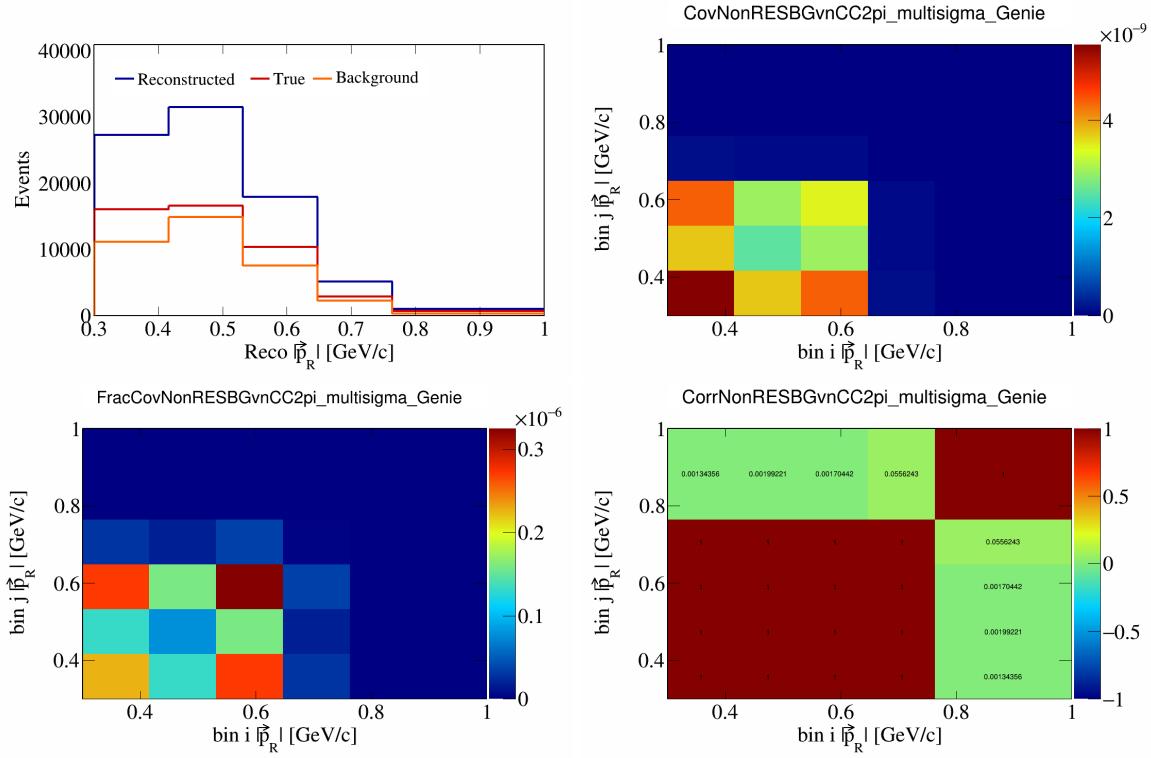


Figure 527: NonRESBGvnCC2pi variations for $|\vec{p}_R|$.

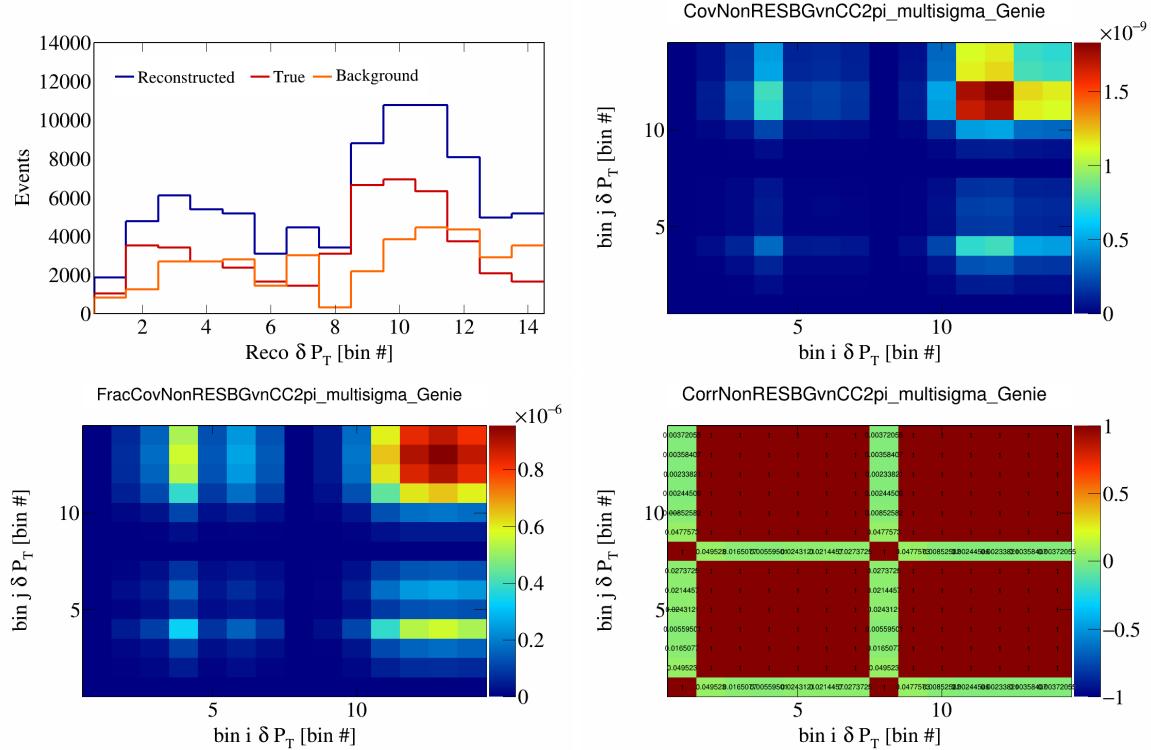


Figure 528: NonRESBGvnCC2pi variations for δP_T in $\cos(\theta_{\vec{p}_\mu})$.

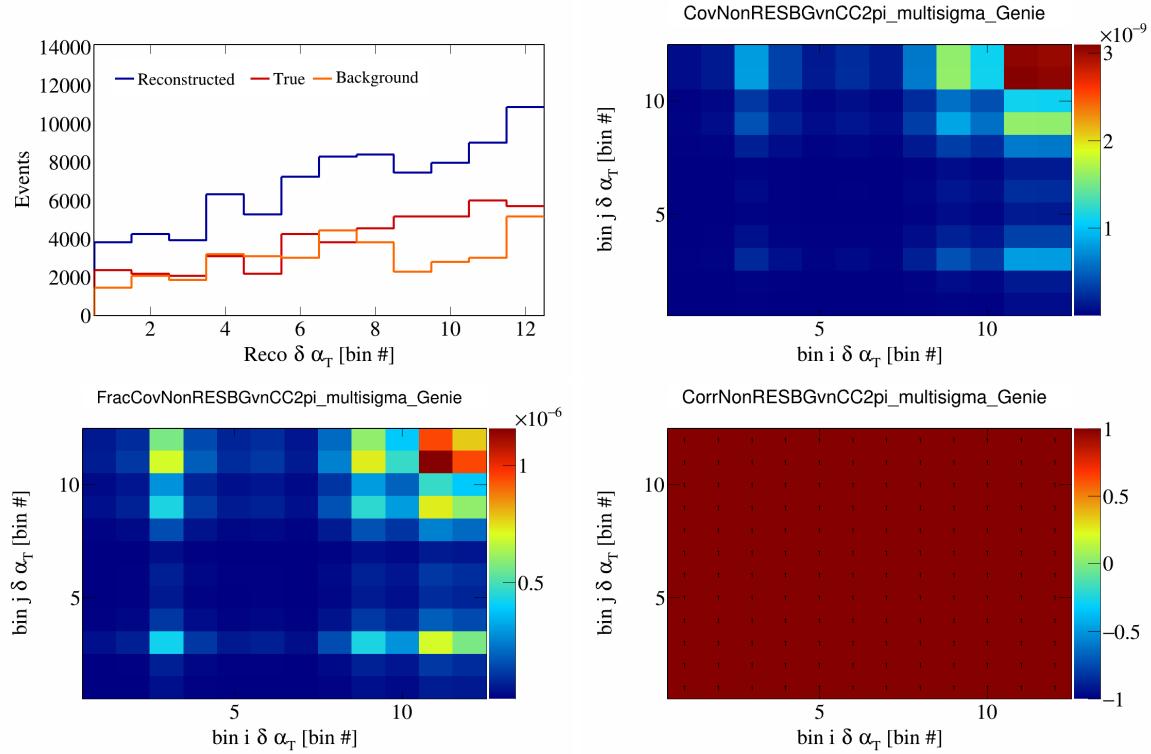


Figure 529: NonRESBGvnCC2pi variations for $\delta\alpha_T$ in $\cos(\theta_{\vec{p}_\mu})$.

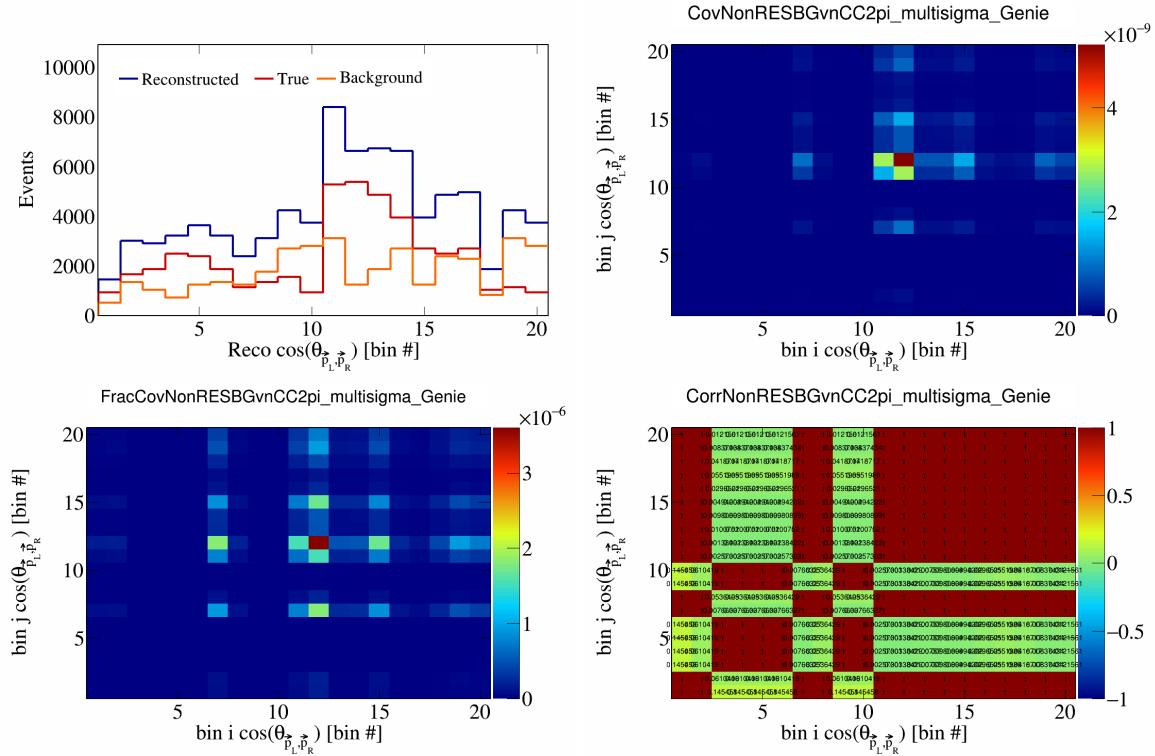


Figure 530: NonRESBGvnCC2pi variations for $\cos(\theta_{\vec{p}_L, \vec{p}_R})$ in $\cos(\theta_{\vec{p}_\mu})$.

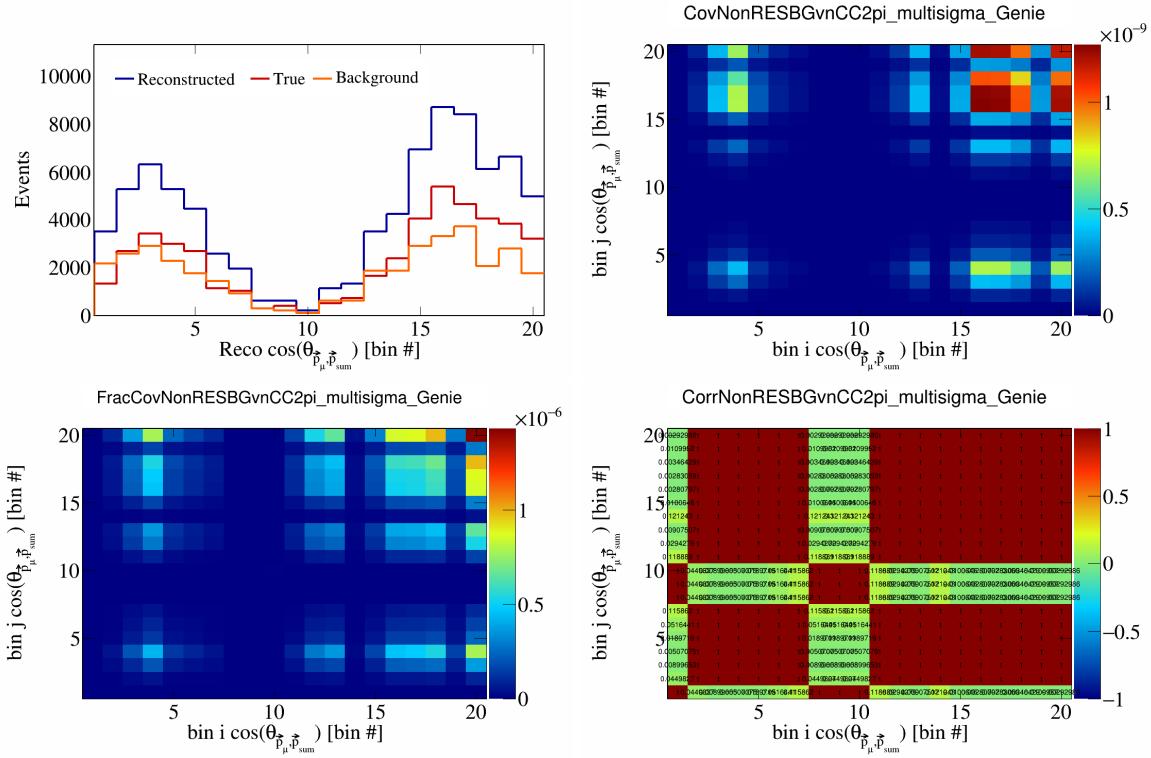


Figure 531: NonRESBGvnCC2pi variations for $\cos(\theta_{\vec{p}_\mu})$ in $\cos(\theta_{\vec{p}_\mu})$.

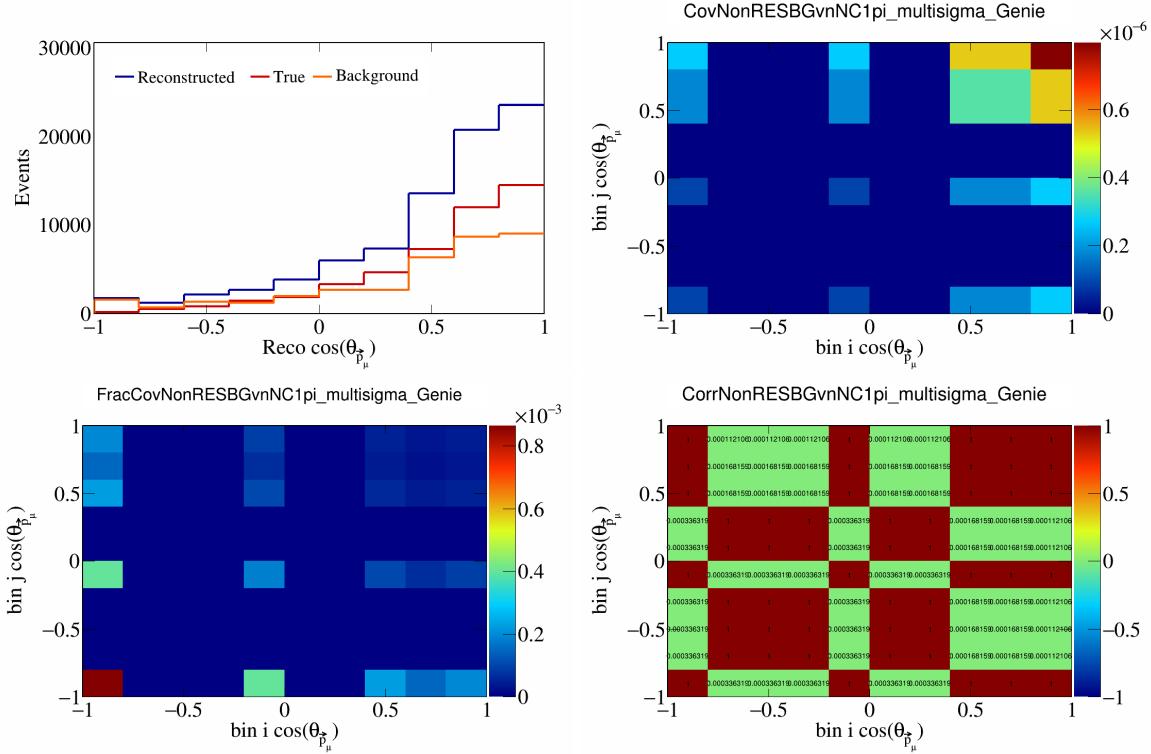


Figure 532: NonRESBGvnNC1pi variations for $\cos(\theta_{\vec{p}_\mu})$.

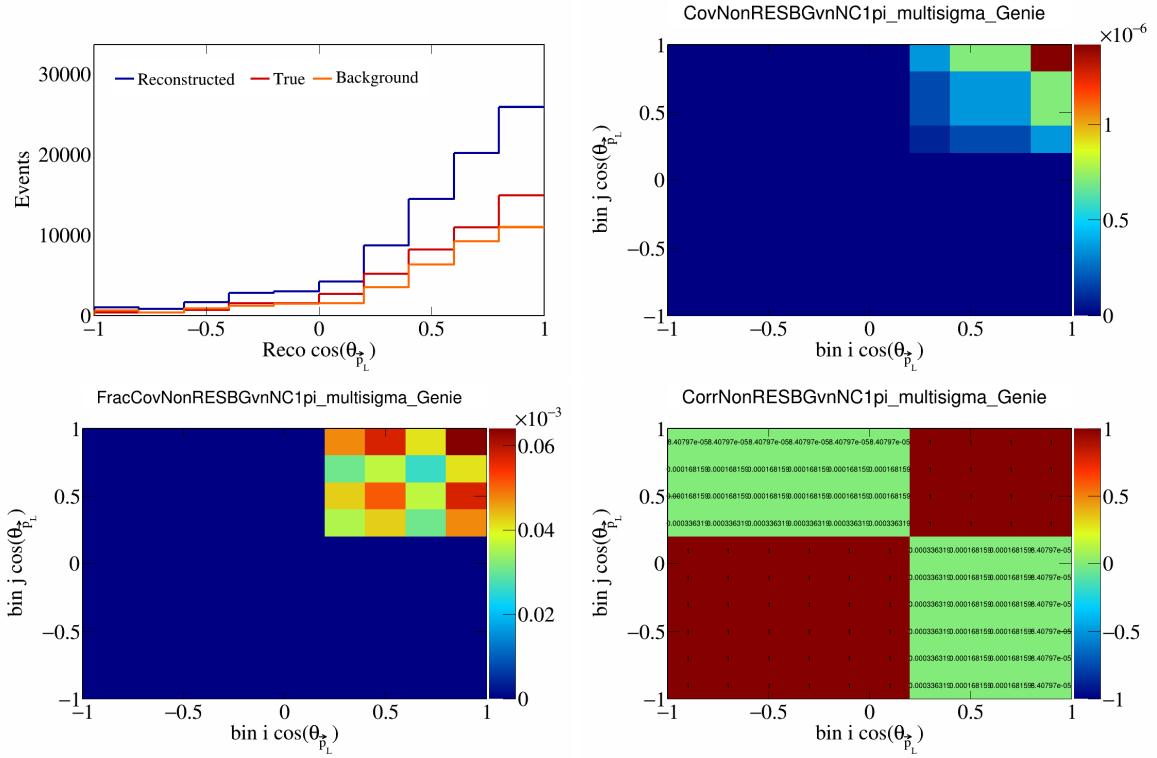


Figure 533: NonRESBGvnNC1pi variations for $\cos(\theta_{\vec{p}_L})$.

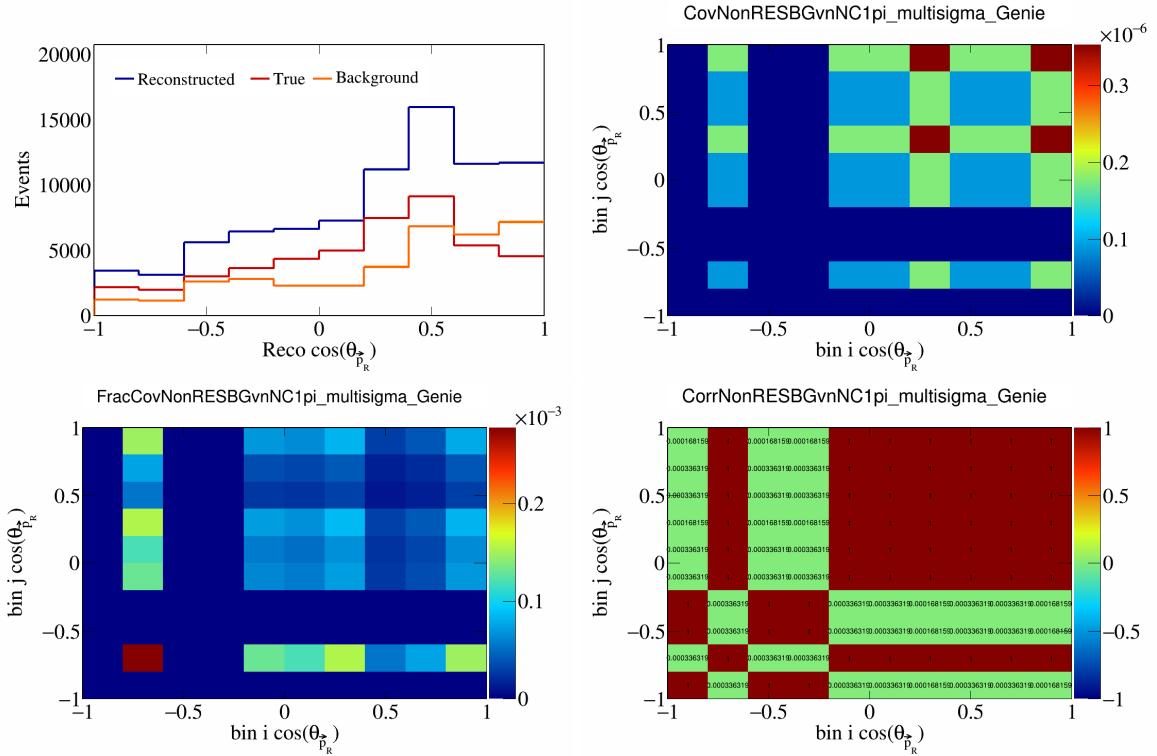


Figure 534: NonRESBGvnNC1pi variations for $\cos(\theta_{\vec{p}_R})$.

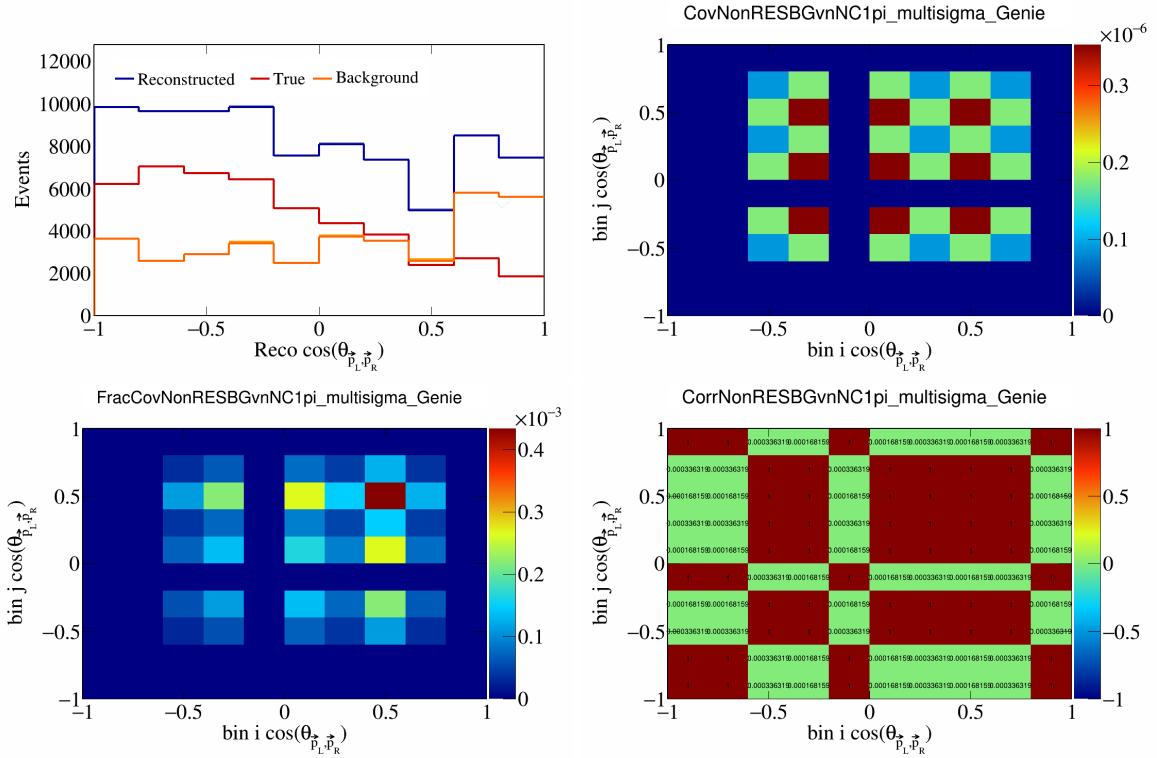


Figure 535: NonRESBGvnNC1pi variations for $\cos(\theta_{\vec{p}_L, \vec{p}_R})$.

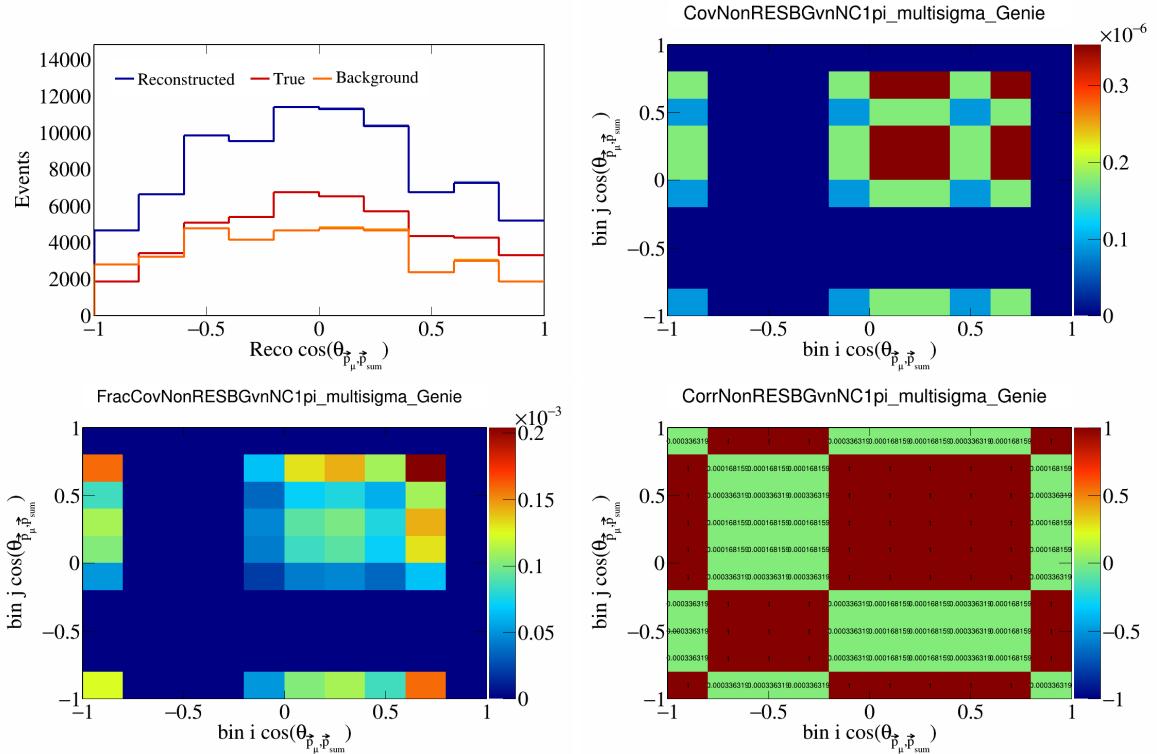


Figure 536: NonRESBGvnNC1pi variations for $\cos(\theta_{\vec{p}_\mu, \vec{p}_{\text{sum}}})$.

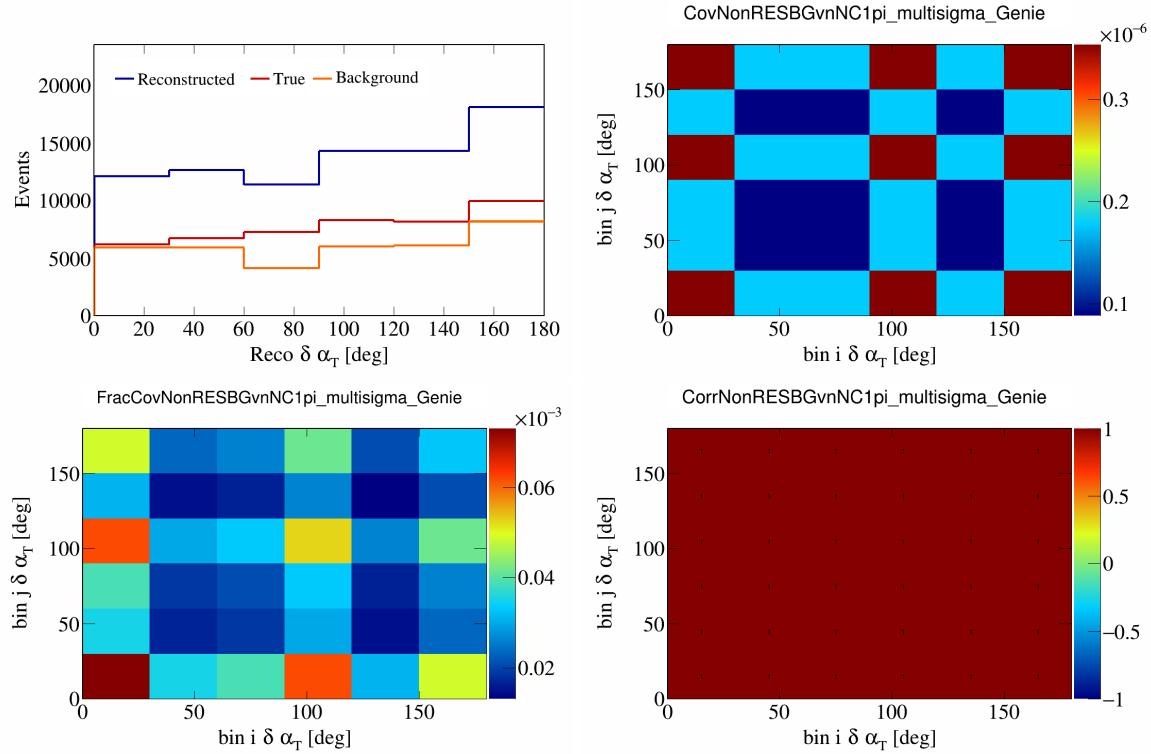


Figure 537: NonRESBGvnNC1pi variations for $\delta \alpha_T$.

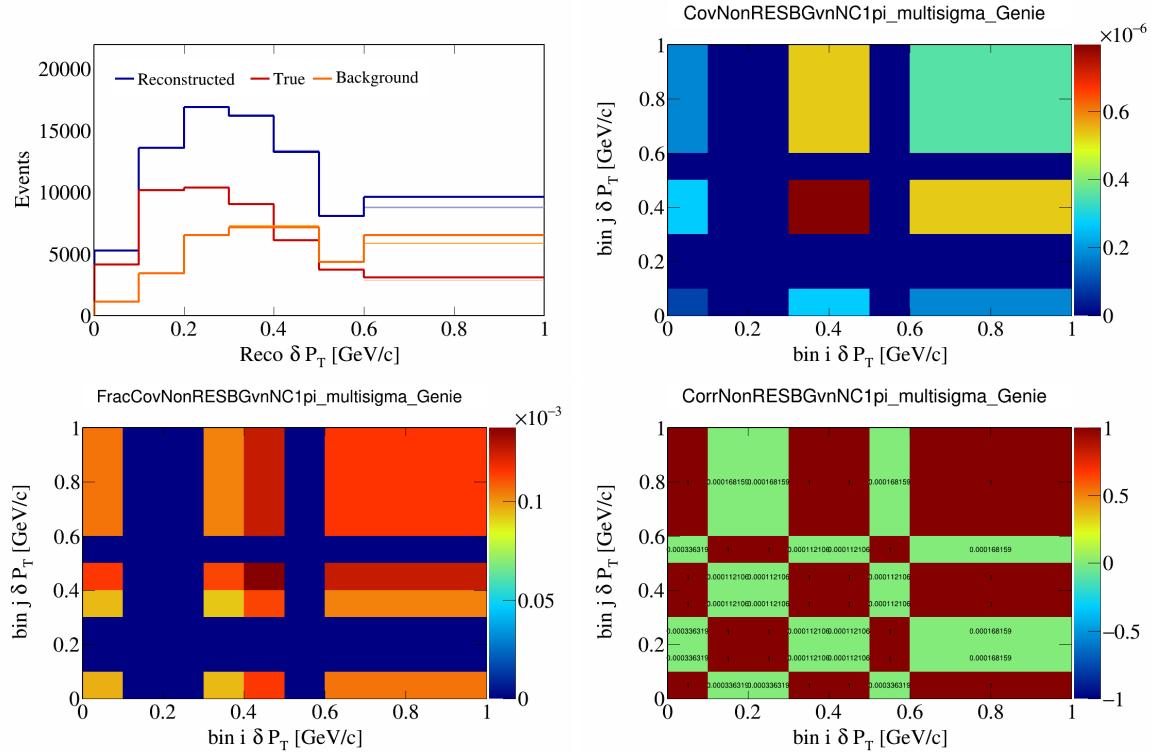


Figure 538: NonRESBGvnNC1pi variations for δP_T .

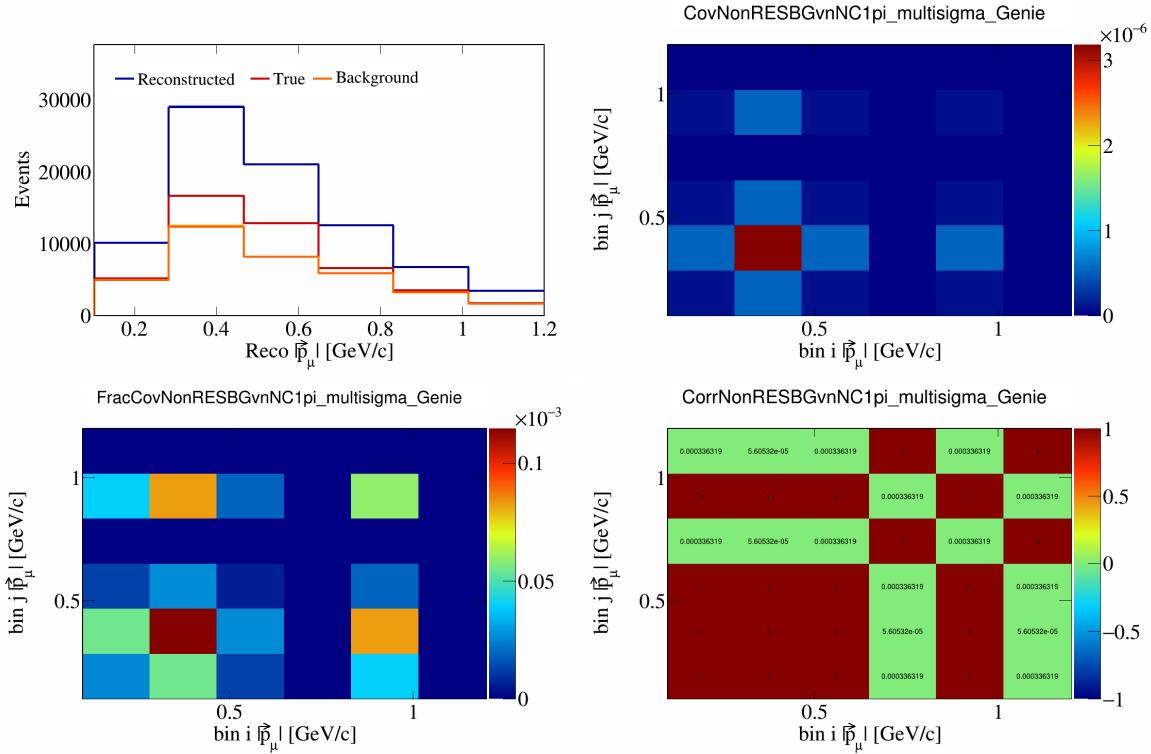
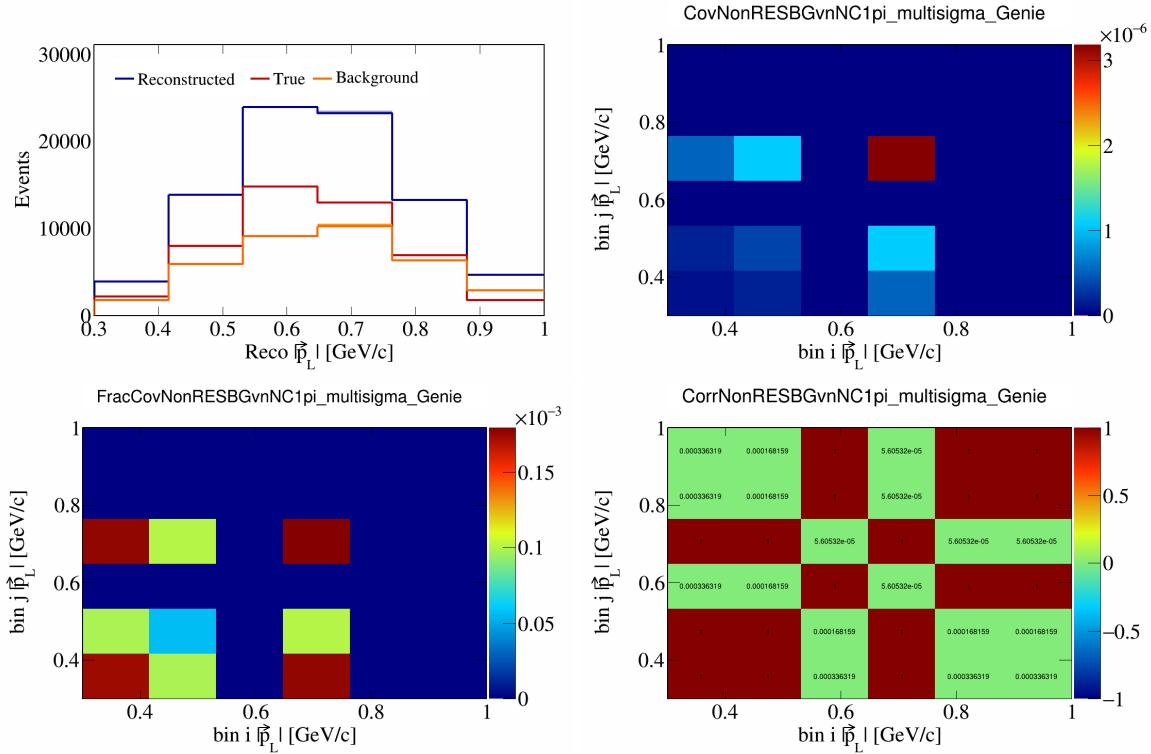


Figure 539: NonRESBGvnNC1pi variations for $|\vec{p}_\mu|$.



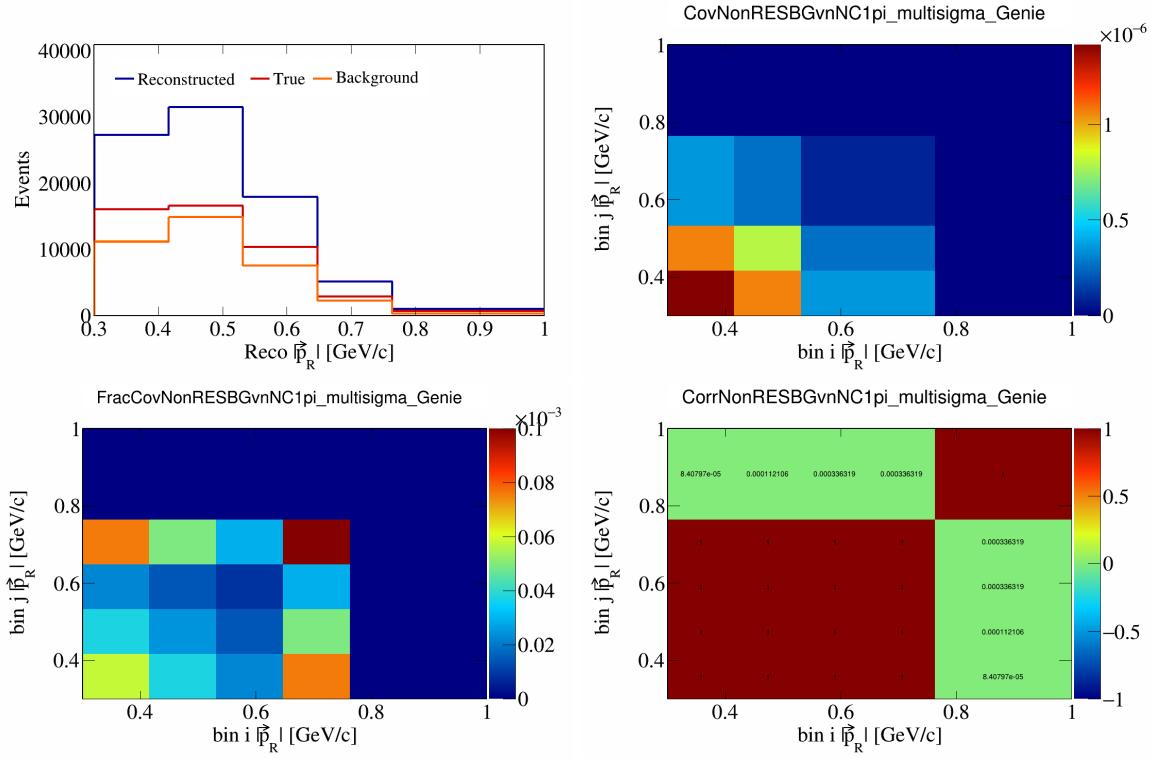


Figure 541: NonRESBGvnNC1pi variations for $|\vec{p}_R|$.

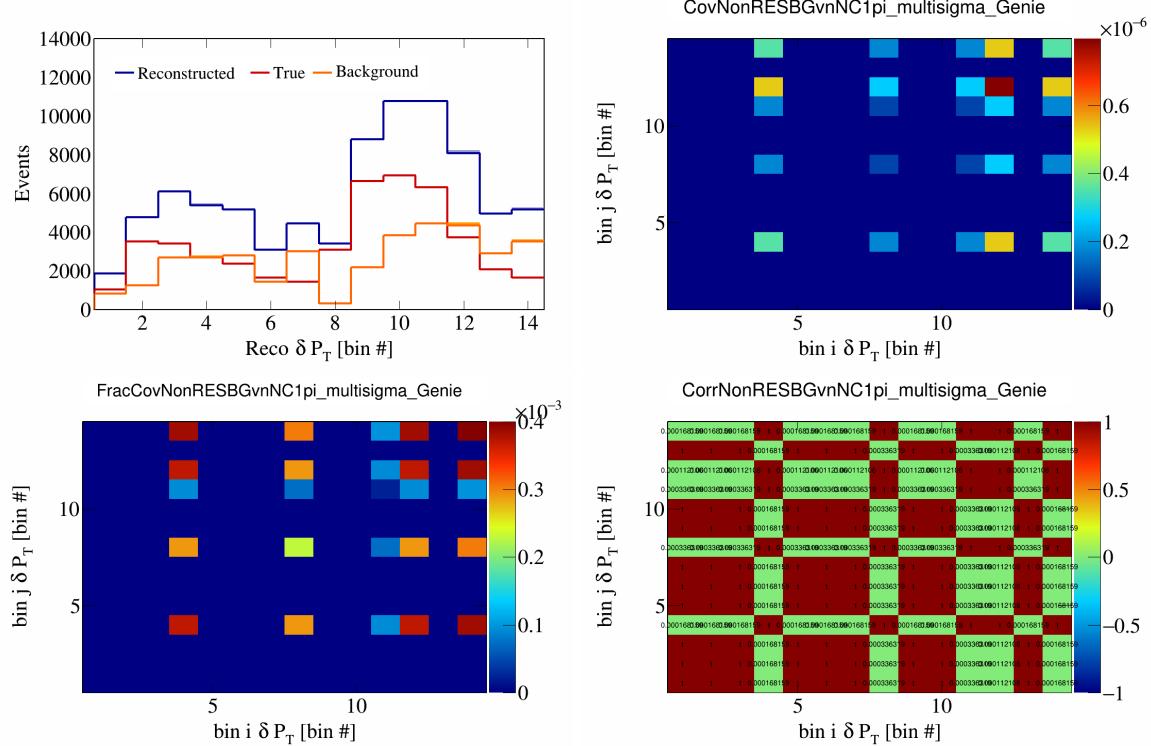


Figure 542: NonRESBGvnNC1pi variations for δP_T in $\cos(\theta_{\vec{p}_\mu})$.

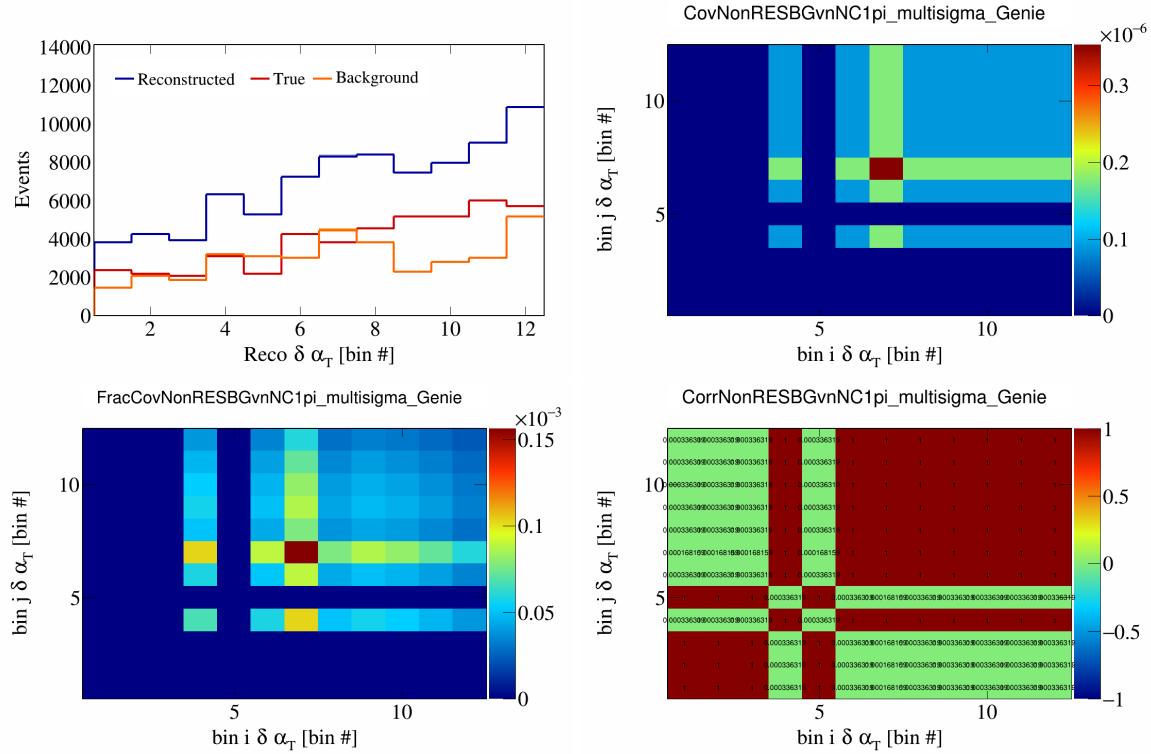


Figure 543: NonRESBGvnNC1pi variations for $\delta\alpha_T$ in $\cos(\theta_{\vec{p}_\mu})$.

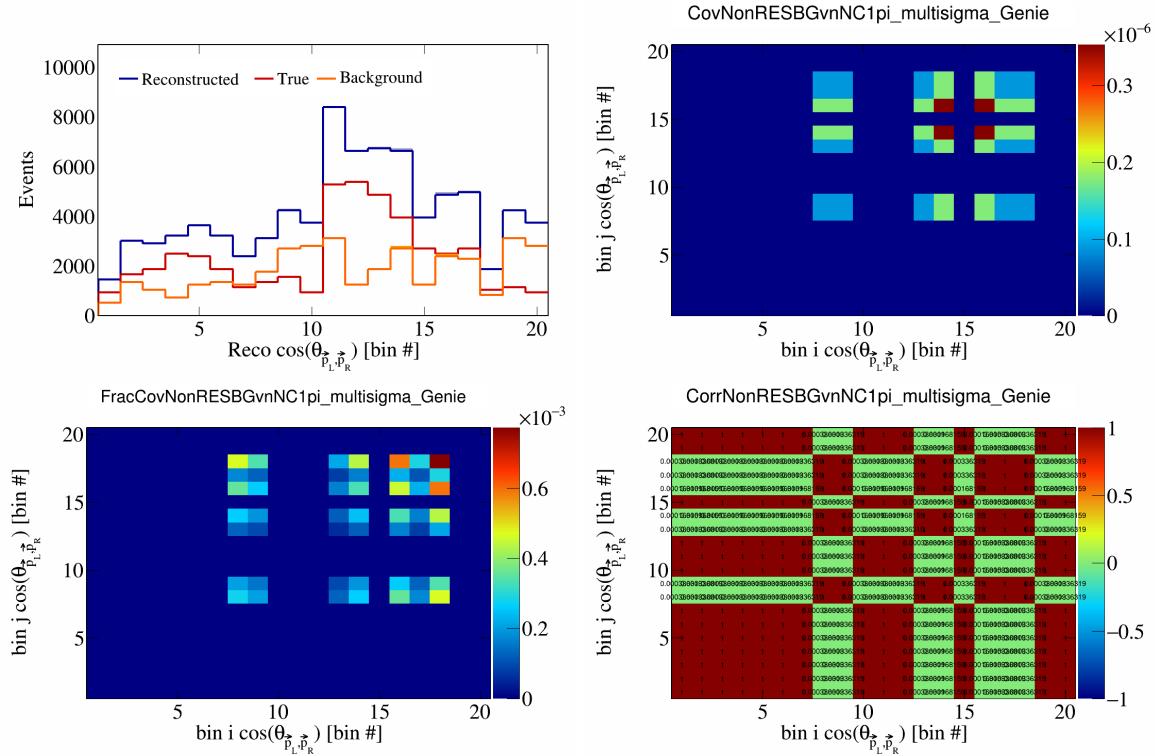


Figure 544: NonRESBGvnNC1pi variations for $\cos(\theta_{\vec{p}_L, \vec{p}_R})$ in $\cos(\theta_{\vec{p}_\mu})$.

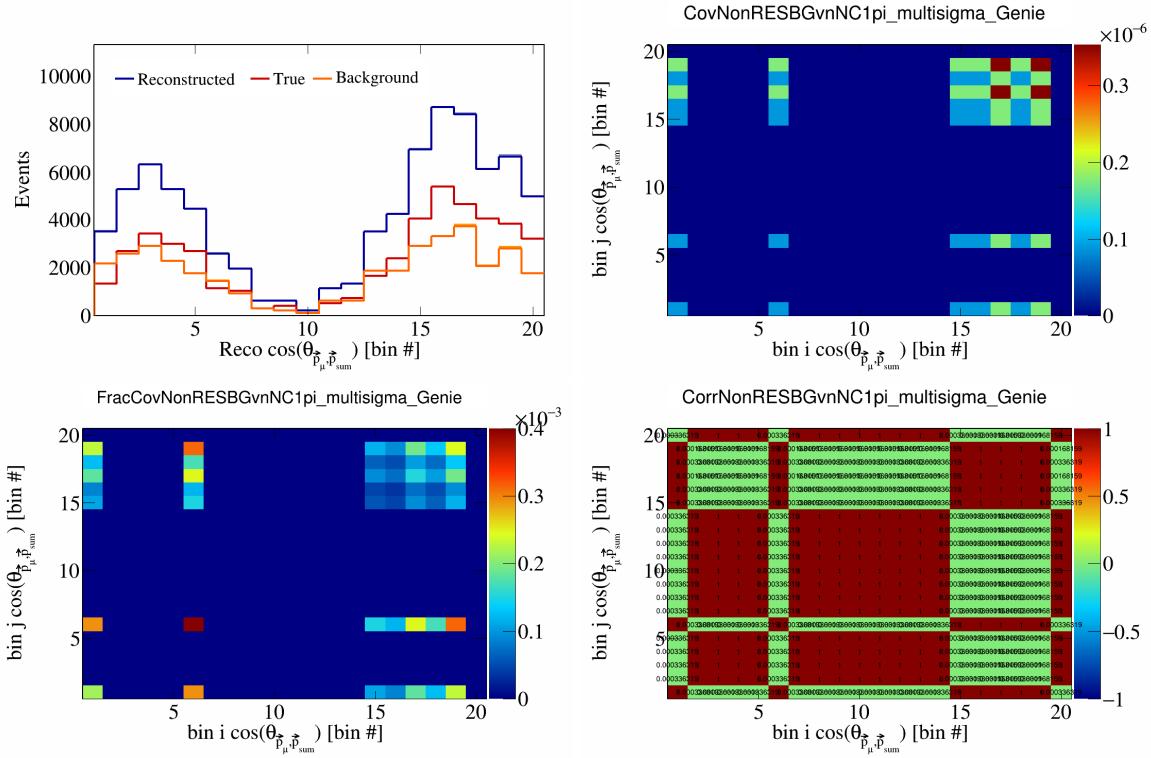


Figure 545: NonRESBGvnNC1pi variations for $\cos(\theta_{\vec{p}_\mu, \vec{p}_{\text{sum}}})$ in $\cos(\theta_{\vec{p}_\mu})$.

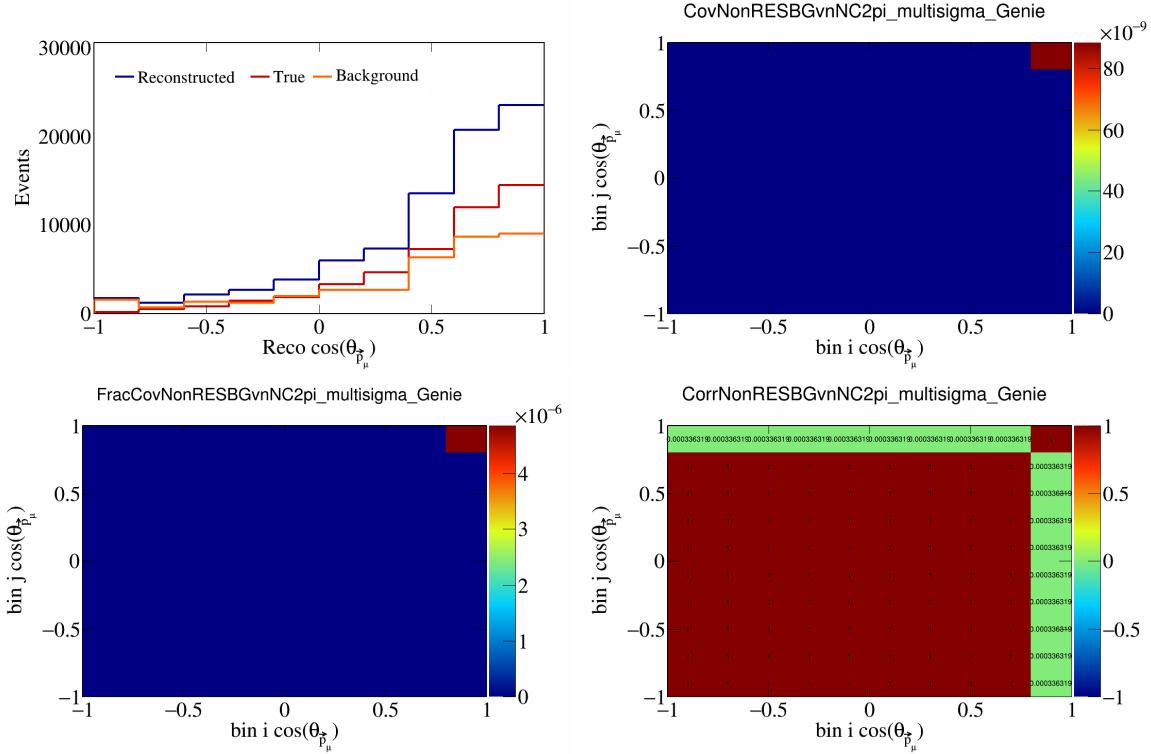


Figure 546: NonRESBGvnNC2pi variations for $\cos(\theta_{\vec{p}_\mu})$.

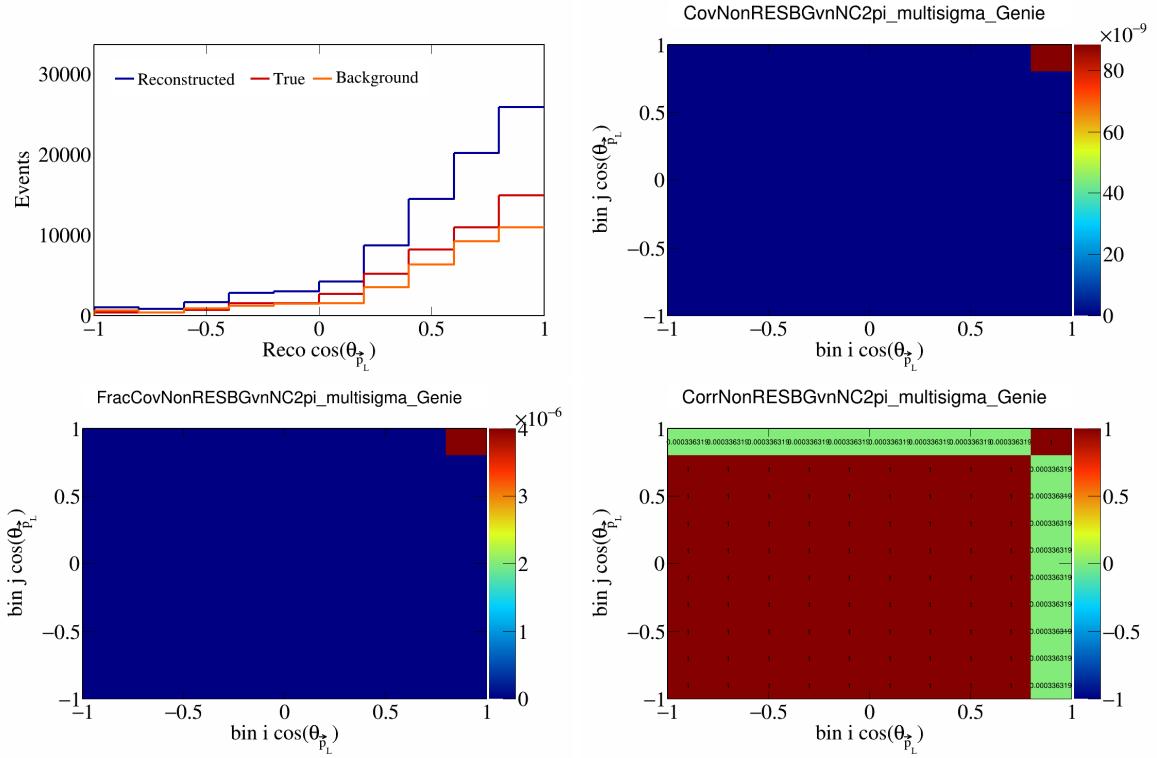


Figure 547: NonRESBGvnNC2pi variations for $\cos(\theta_{\vec{p}_L})$.

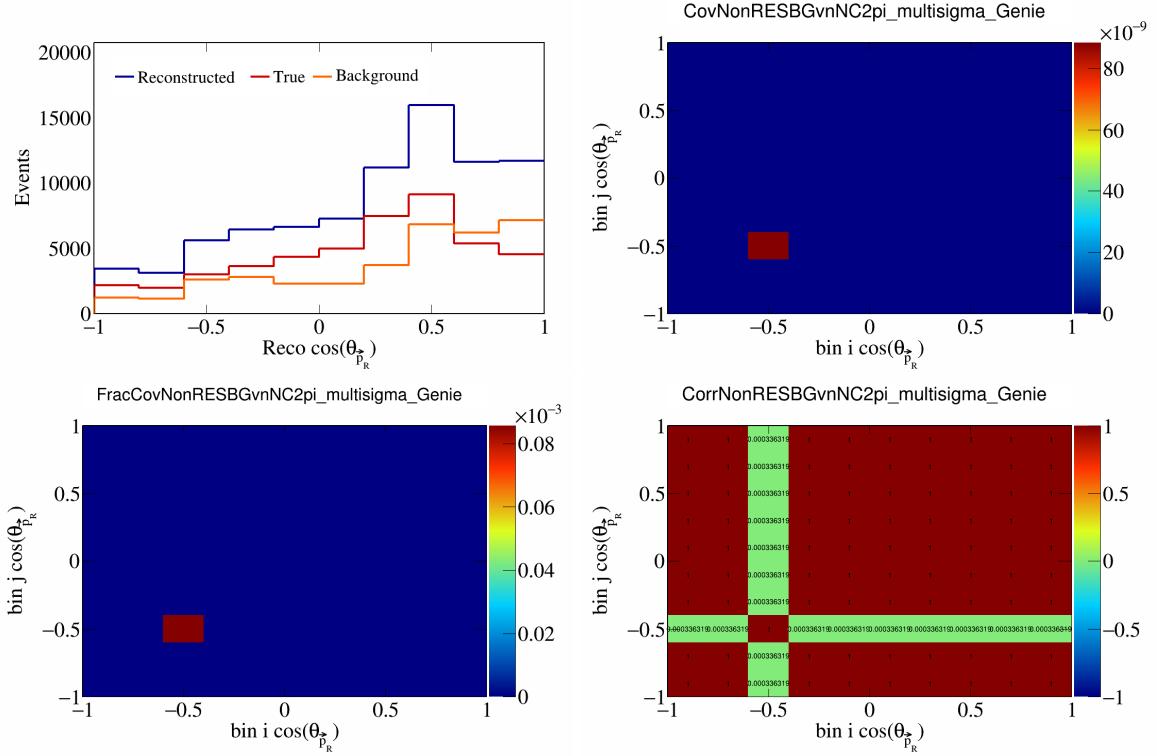


Figure 548: NonRESBGvnNC2pi variations for $\cos(\theta_{\vec{p}_R})$.

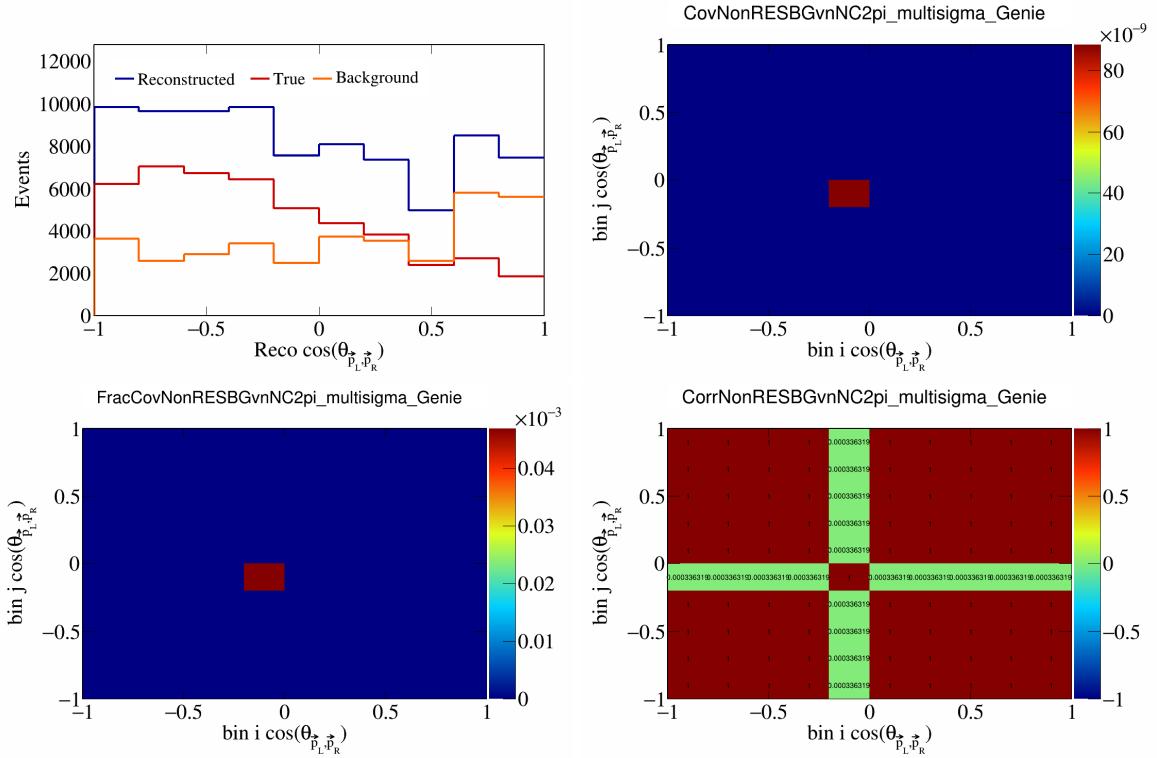


Figure 549: NonRESBGvnNC2pi variations for $\cos(\theta_{\vec{p}_L, \vec{p}_R})$.

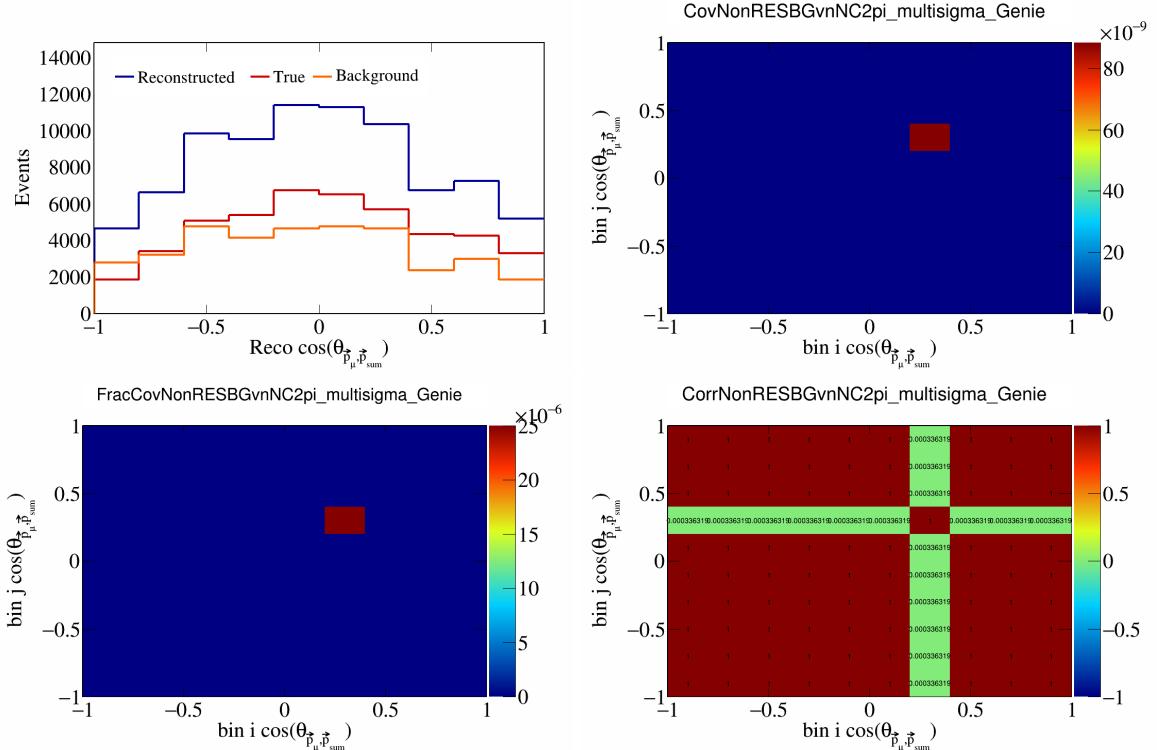


Figure 550: NonRESBGvnNC2pi variations for $\cos(\theta_{\vec{p}_\mu, \vec{p}_{\text{sum}}})$.

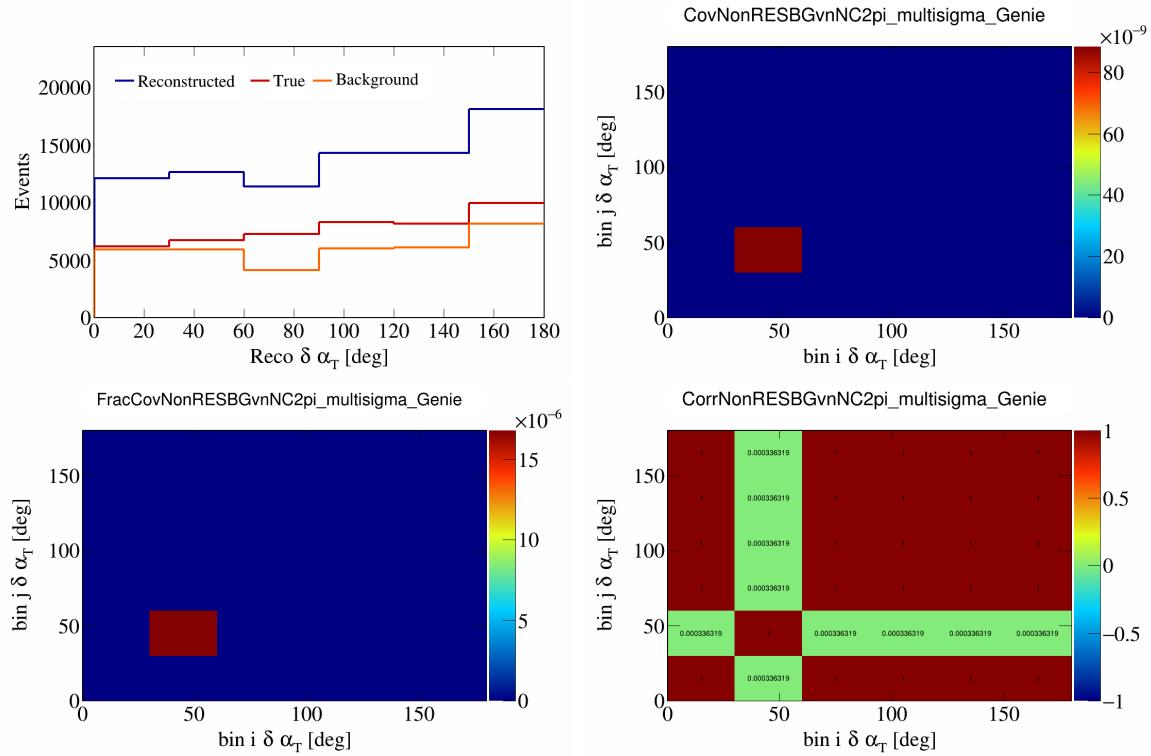


Figure 551: NonRESBGvnNC2pi variations for $\delta \alpha_T$.

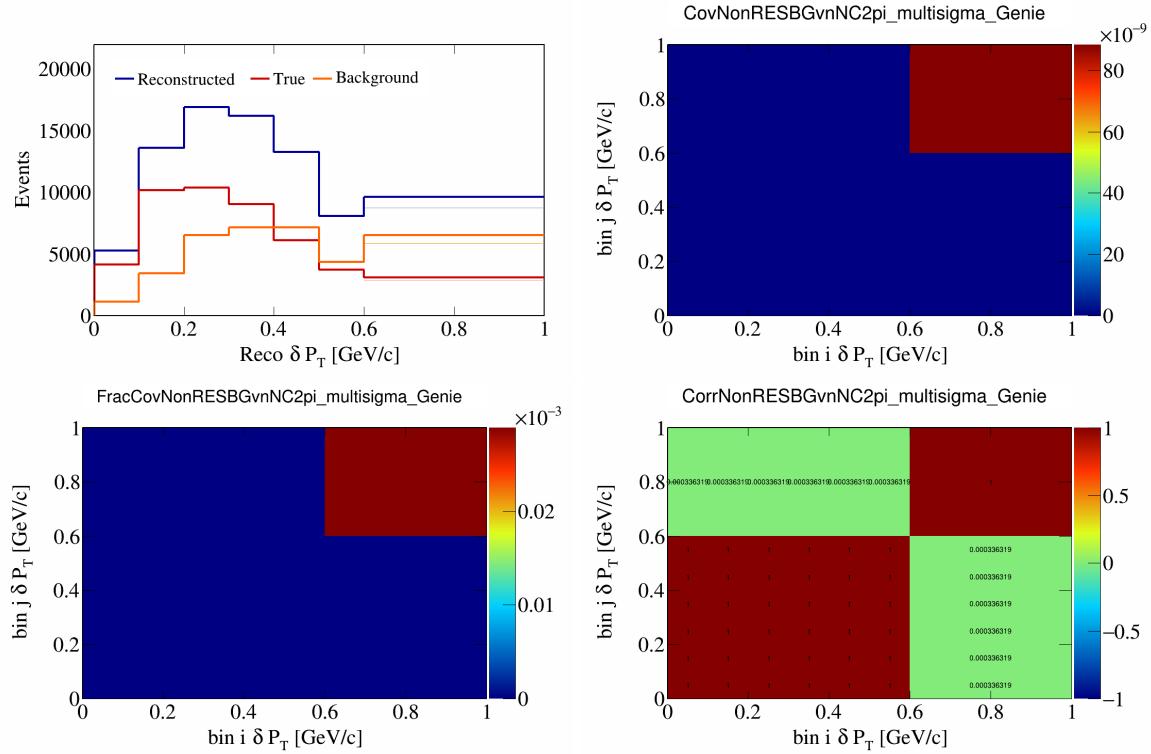


Figure 552: NonRESBGvnNC2pi variations for δP_T .

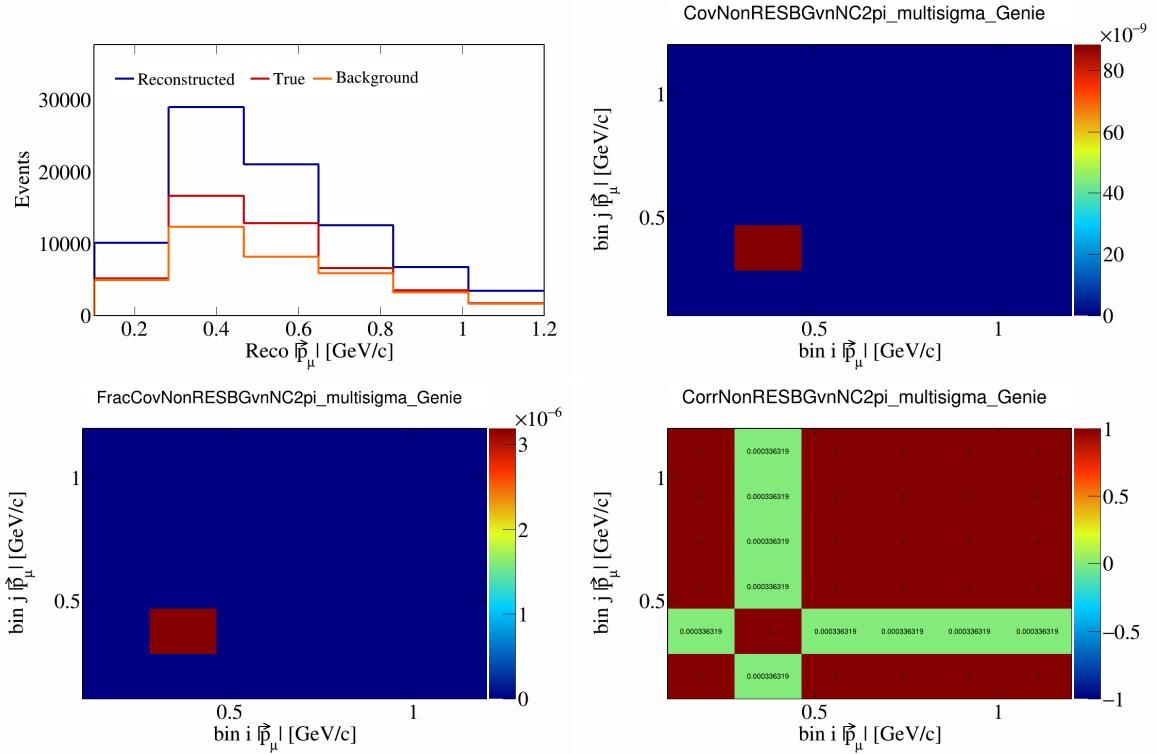


Figure 553: NonRESBGvnNC2pi variations for $|\vec{p}_\mu|$.

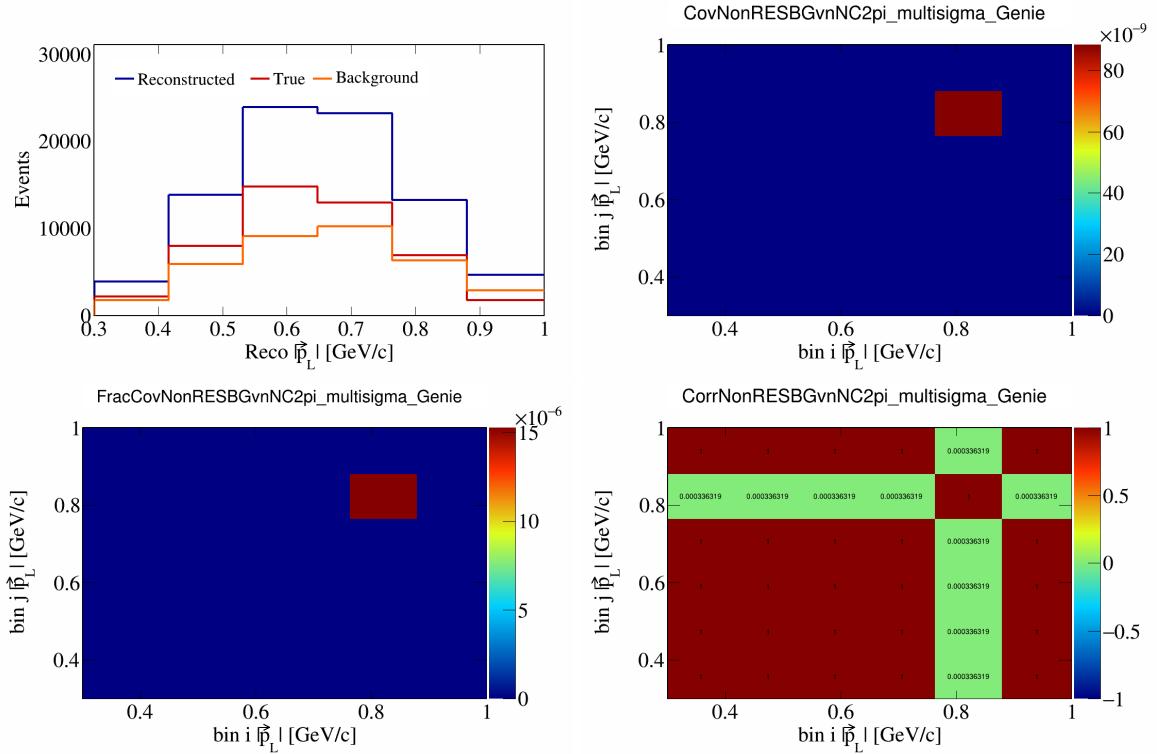


Figure 554: NonRESBGvnNC2pi variations for $|\vec{p}_L|$.

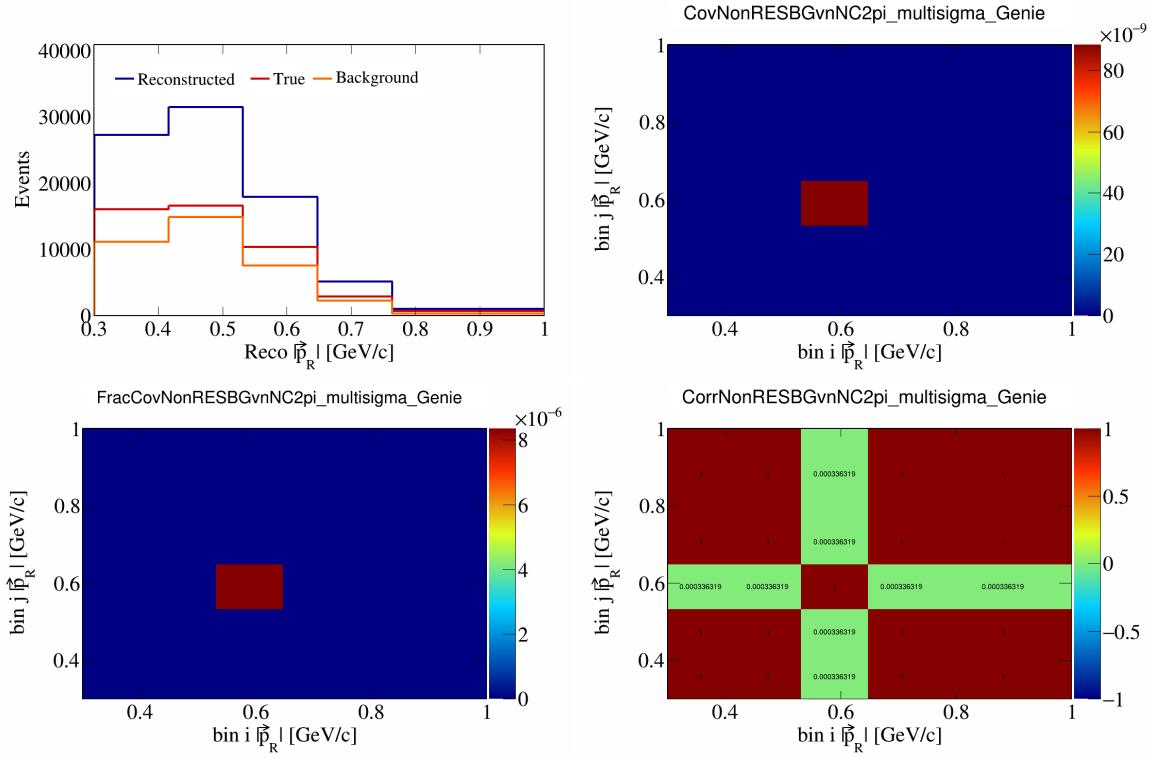


Figure 555: NonRESBGvnNC2pi variations for $|\vec{p}_R|$.

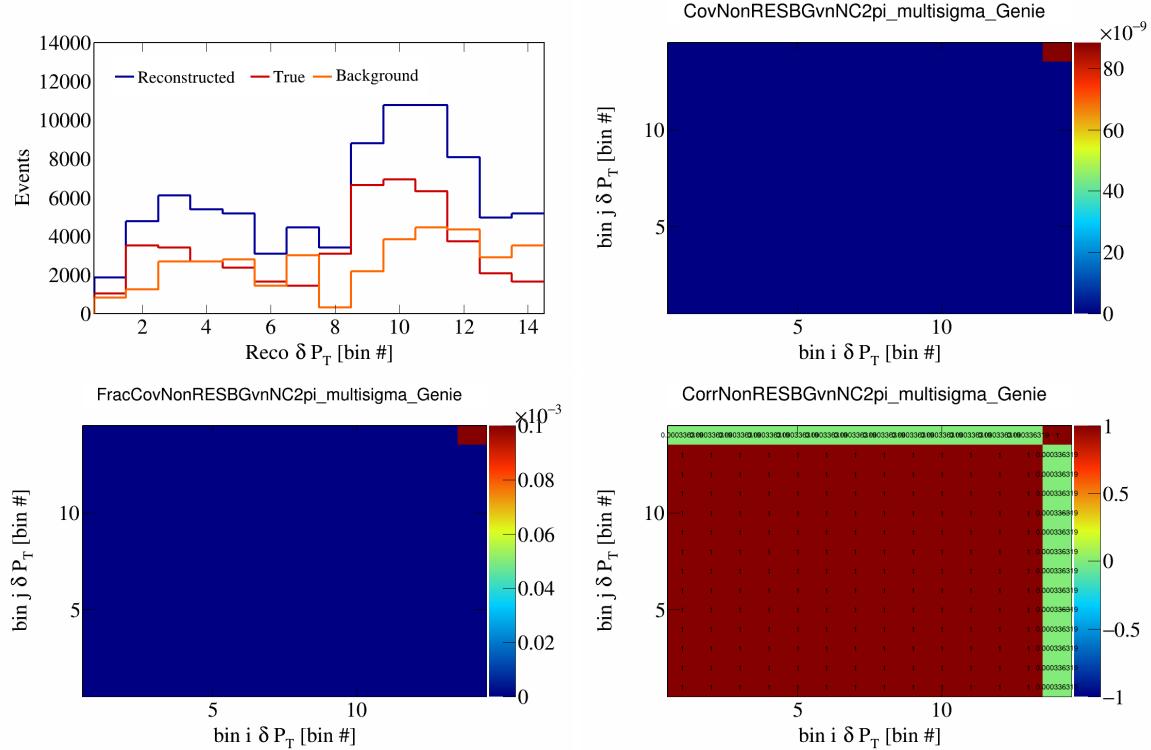


Figure 556: NonRESBGvnNC2pi variations for δP_T in $\cos(\theta_{\vec{p}_\mu})$.

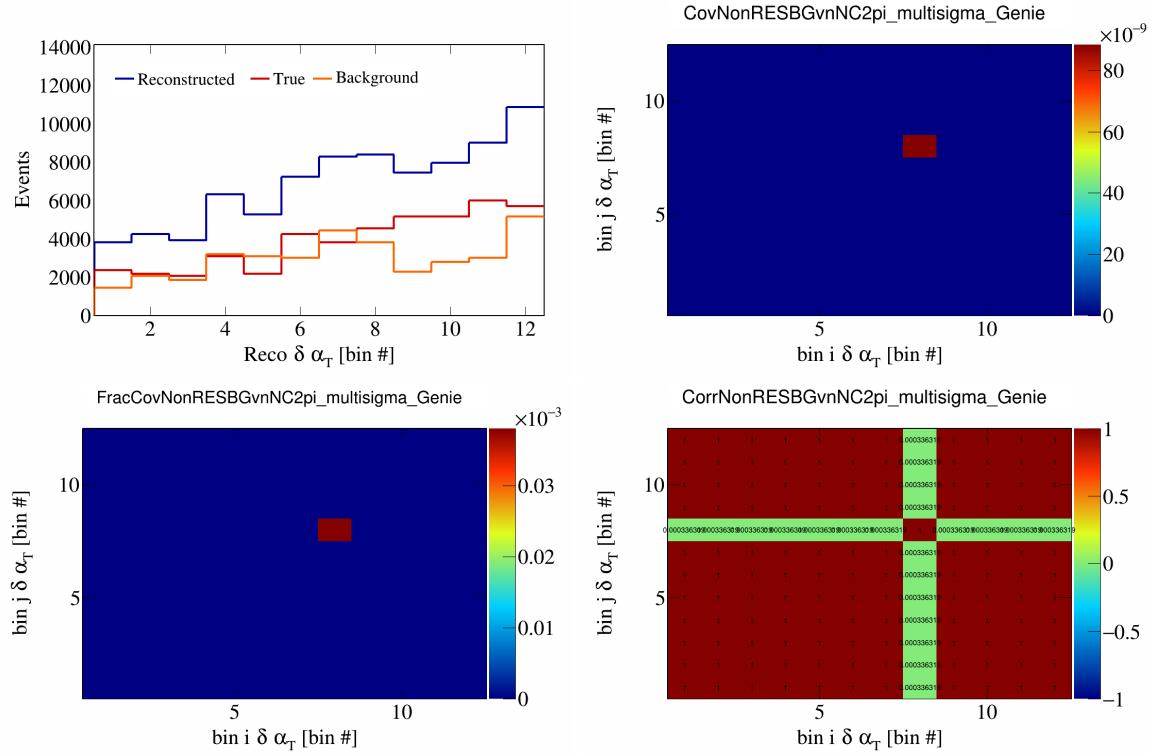


Figure 557: NonRESBGvnNC2pi variations for $\delta\alpha_T$ in $\cos(\theta_{\vec{p}_\mu})$.

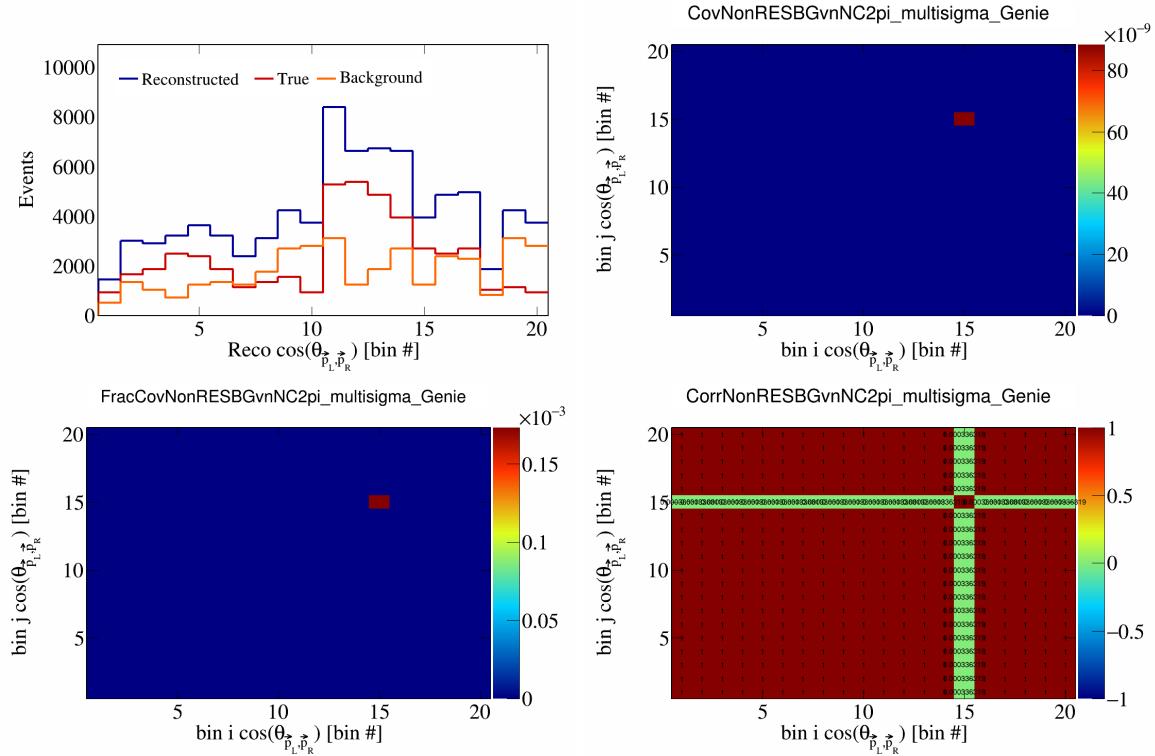


Figure 558: NonRESBGvnNC2pi variations for $\cos(\theta_{\vec{p}_L, \vec{p}_R})$ in $\cos(\theta_{\vec{p}_\mu})$.

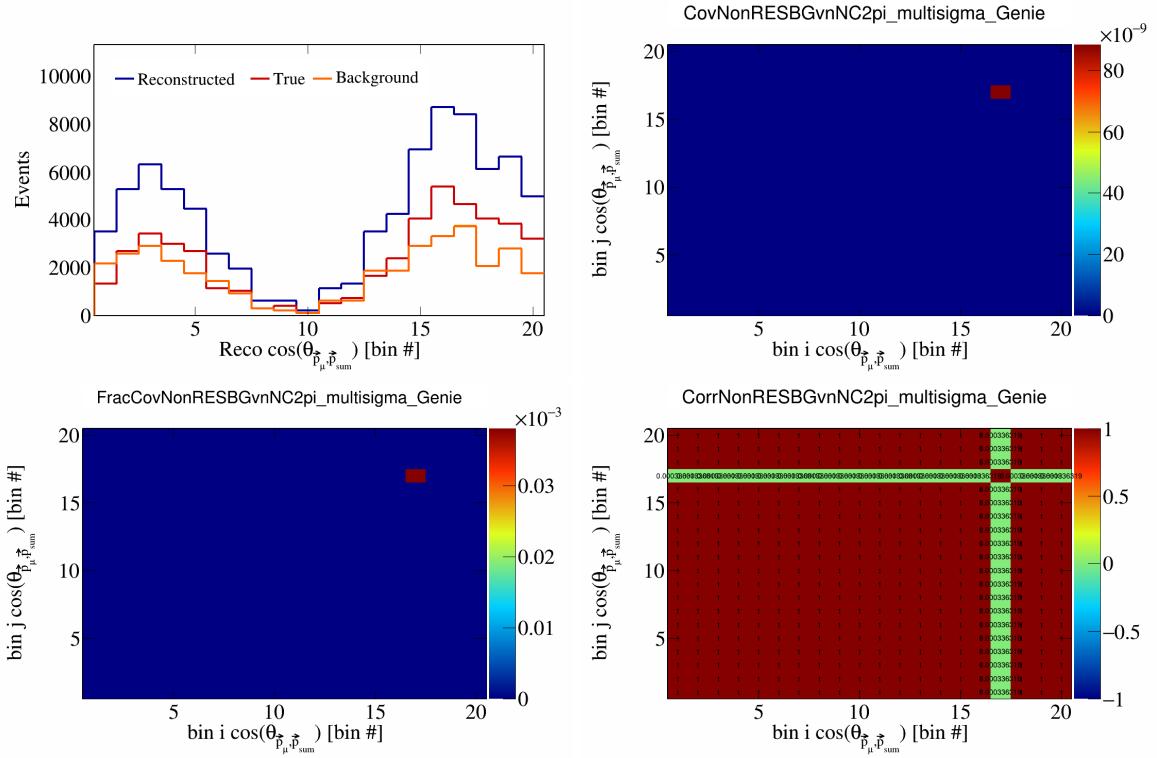


Figure 559: NonRESBGvnNC2pi variations for $\cos(\theta_{\vec{p}_\mu})$ in $\cos(\theta_{\vec{p}_\mu})$.

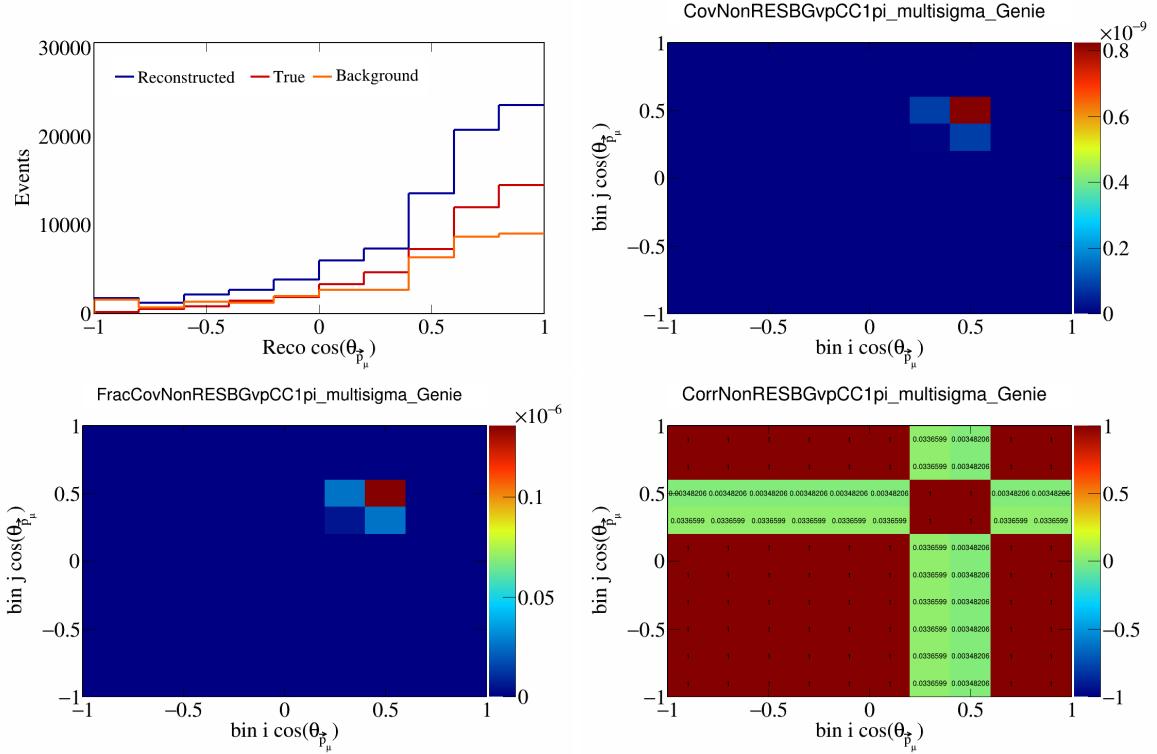


Figure 560: NonRESBGvpCC1pi variations for $\cos(\theta_{\vec{p}_\mu})$.

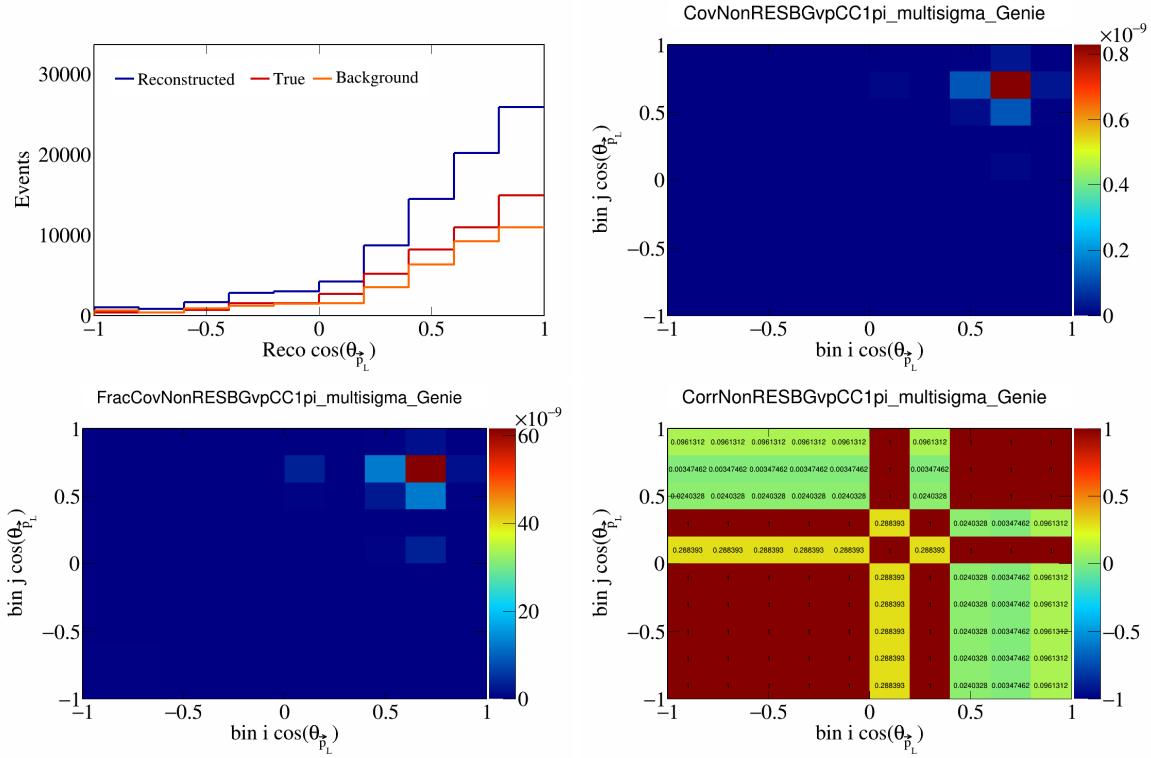


Figure 561: NonRESBGvpCC1pi variations for $\cos(\theta_{\vec{p}_L})$.

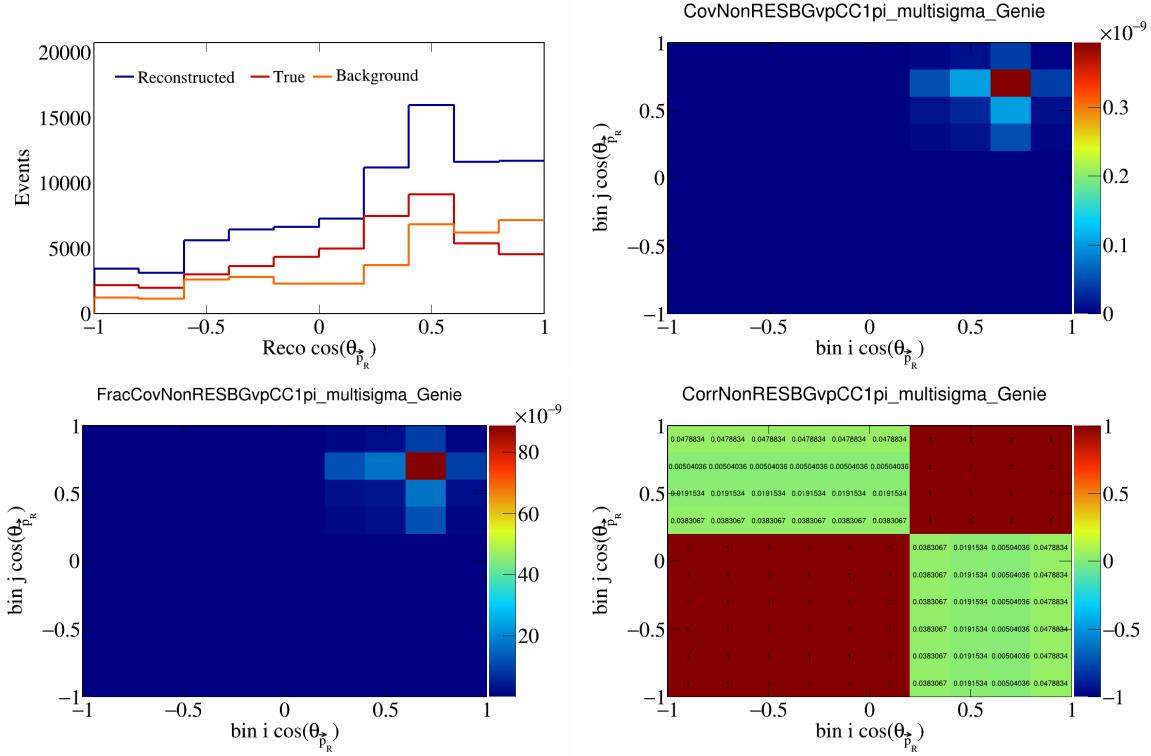


Figure 562: NonRESBGvpCC1pi variations for $\cos(\theta_{\vec{p}_R})$.

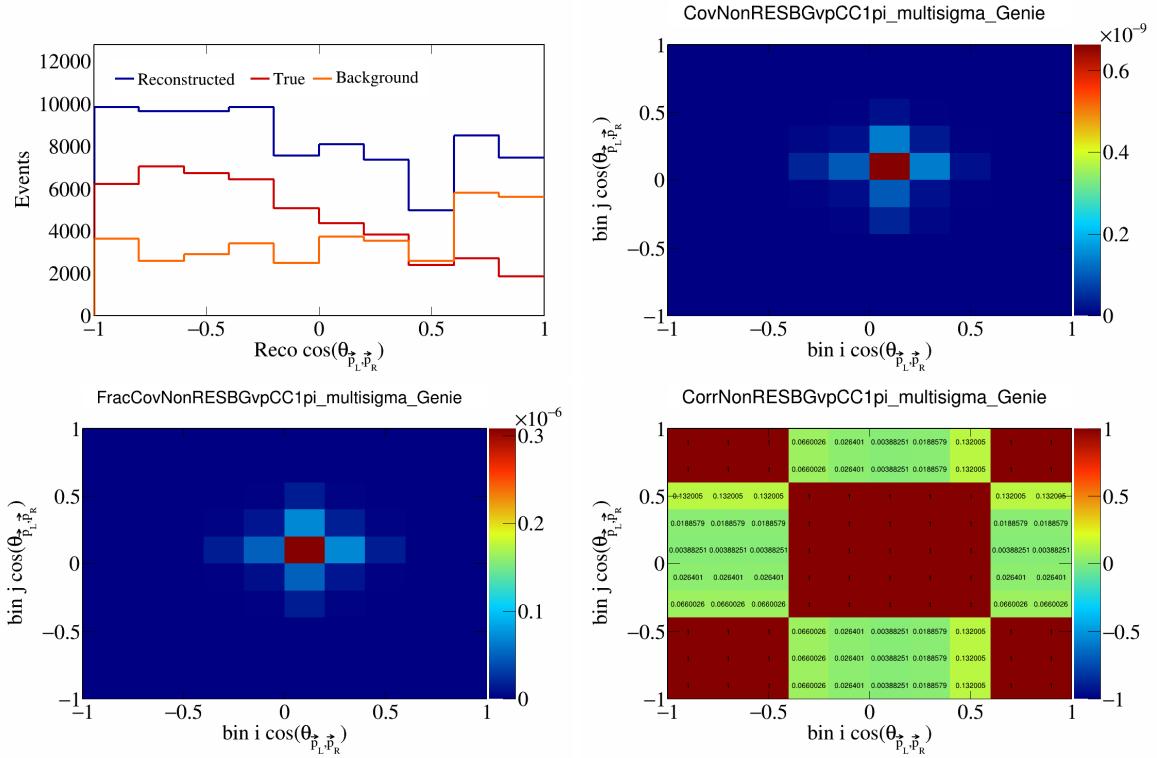


Figure 563: NonRESBGvpCC1pi variations for $\cos(\theta_{\vec{p}_L, \vec{p}_R})$.

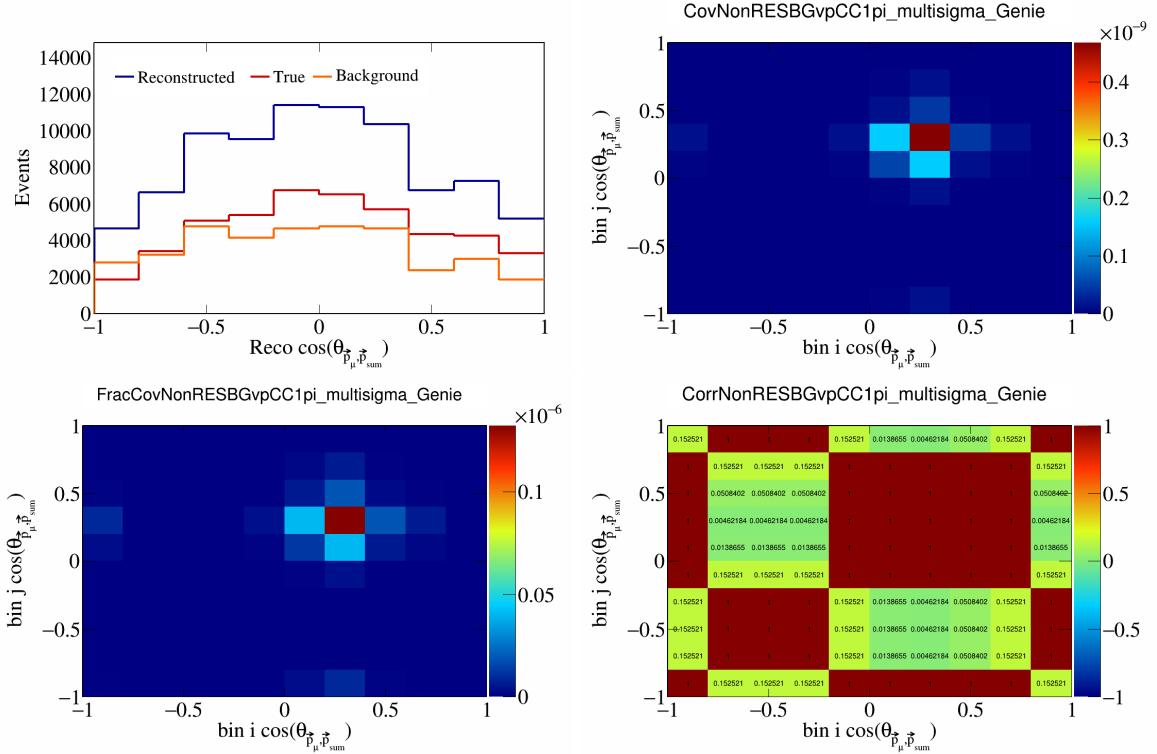


Figure 564: NonRESBGvpCC1pi variations for $\cos(\theta_{\vec{p}_\mu, \vec{p}_{\text{sum}}})$.

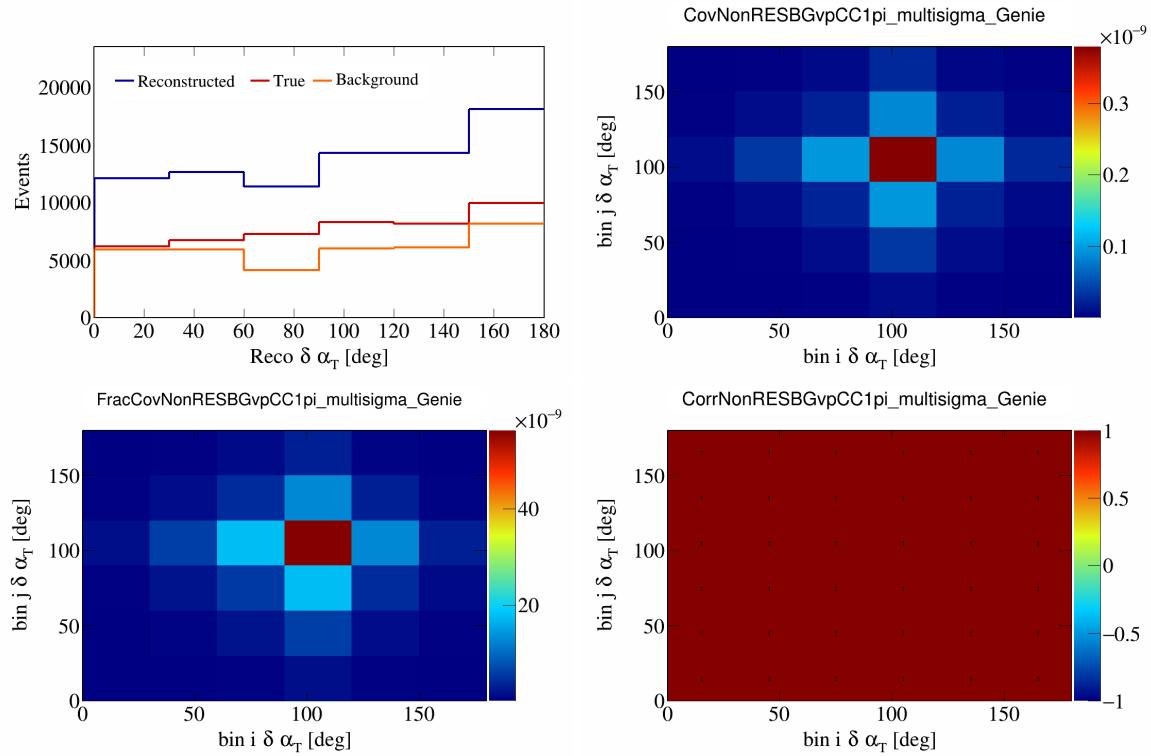


Figure 565: NonRESBGvpCC1pi variations for $\delta\alpha_T$.

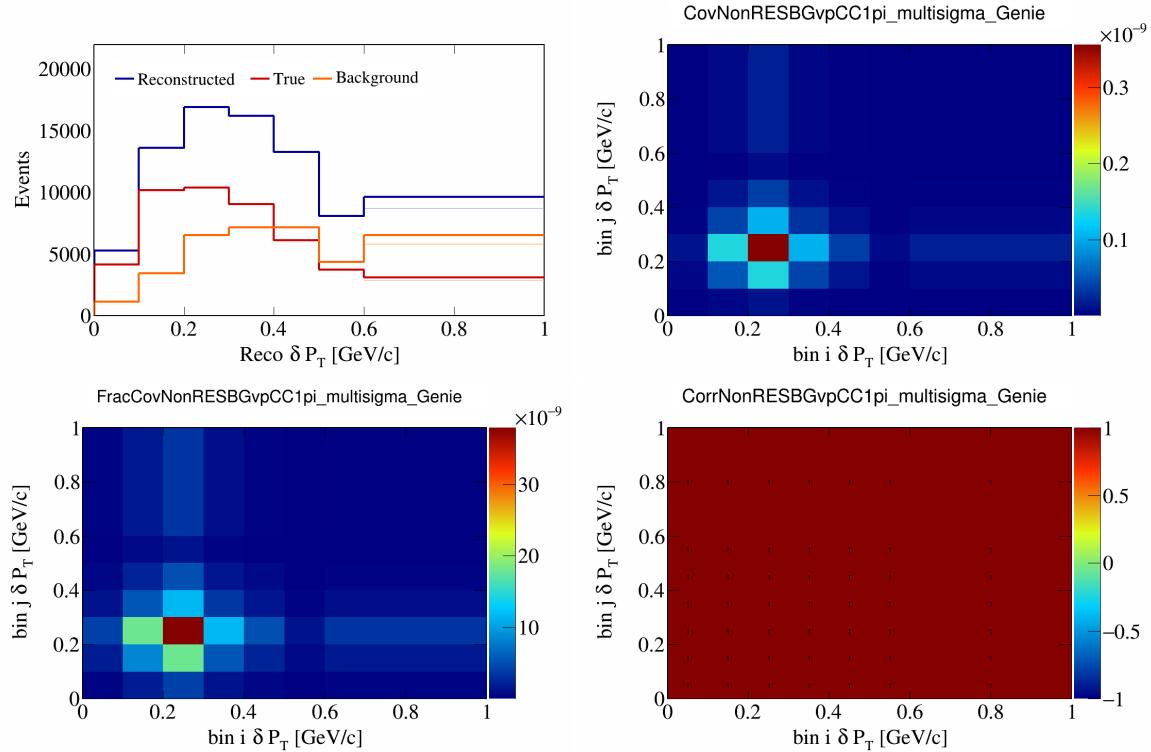


Figure 566: NonRESBGvpCC1pi variations for δP_T .

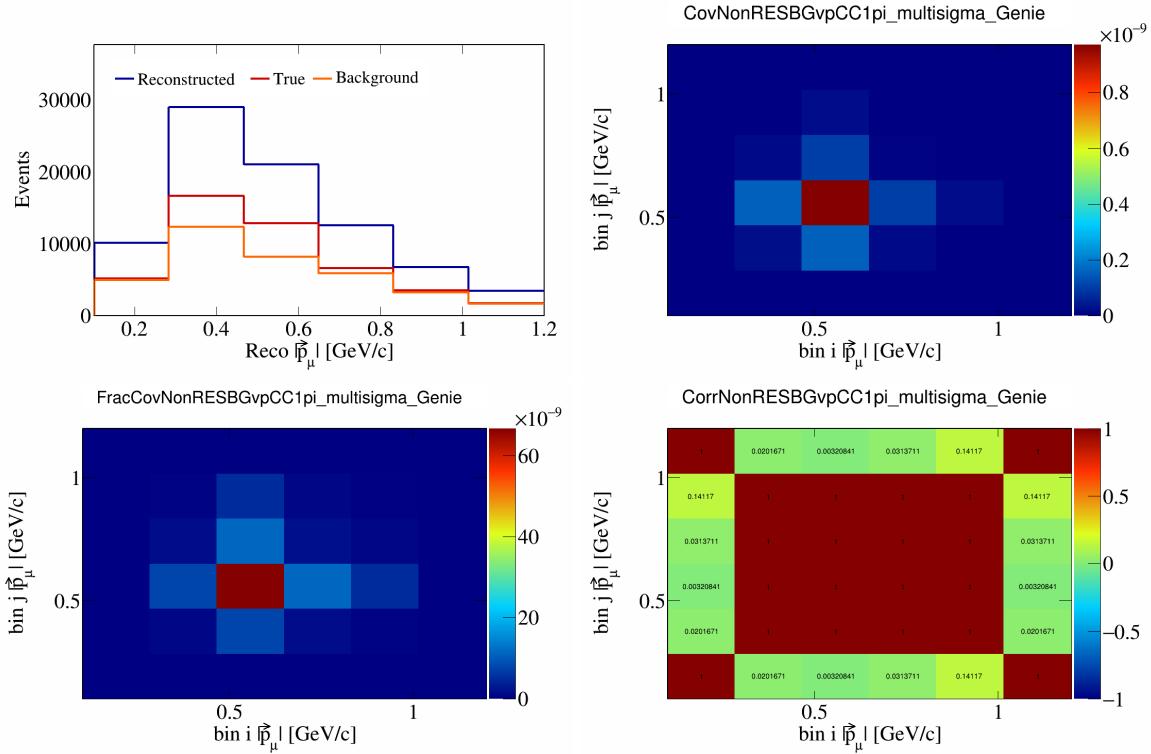


Figure 567: NonRESBGvpCC1pi variations for $|\vec{p}_\mu|$.

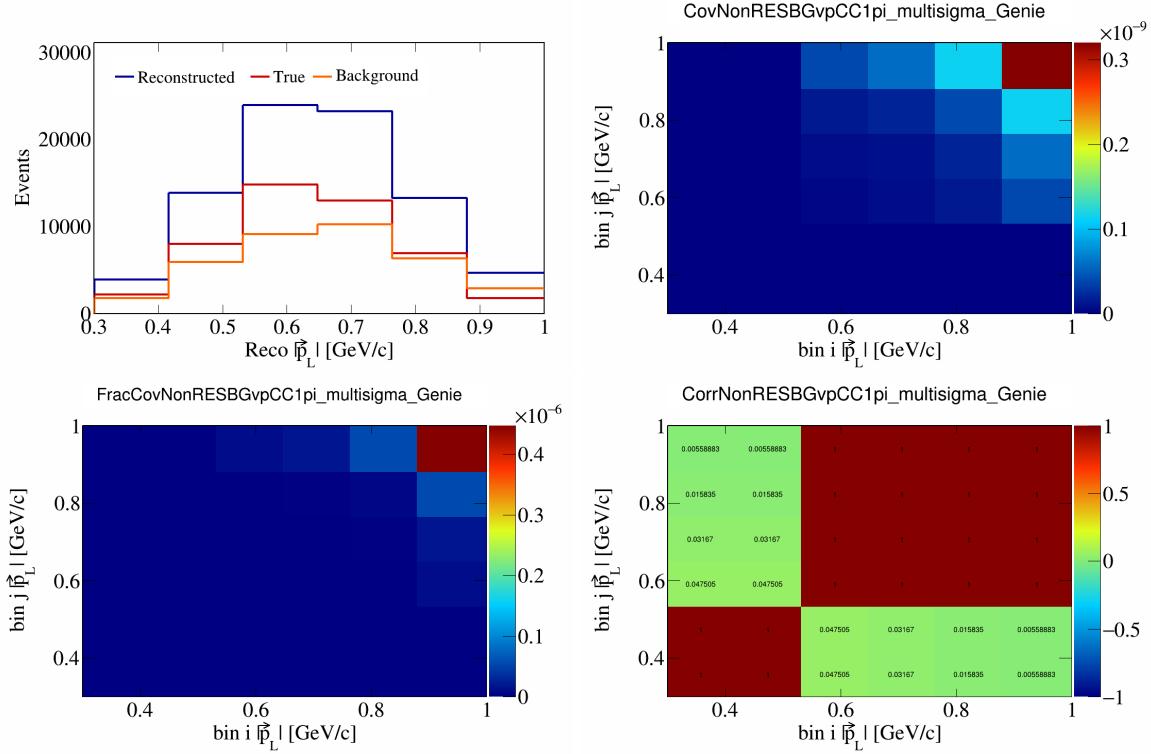


Figure 568: NonRESBGvpCC1pi variations for $|\vec{p}_L|$.

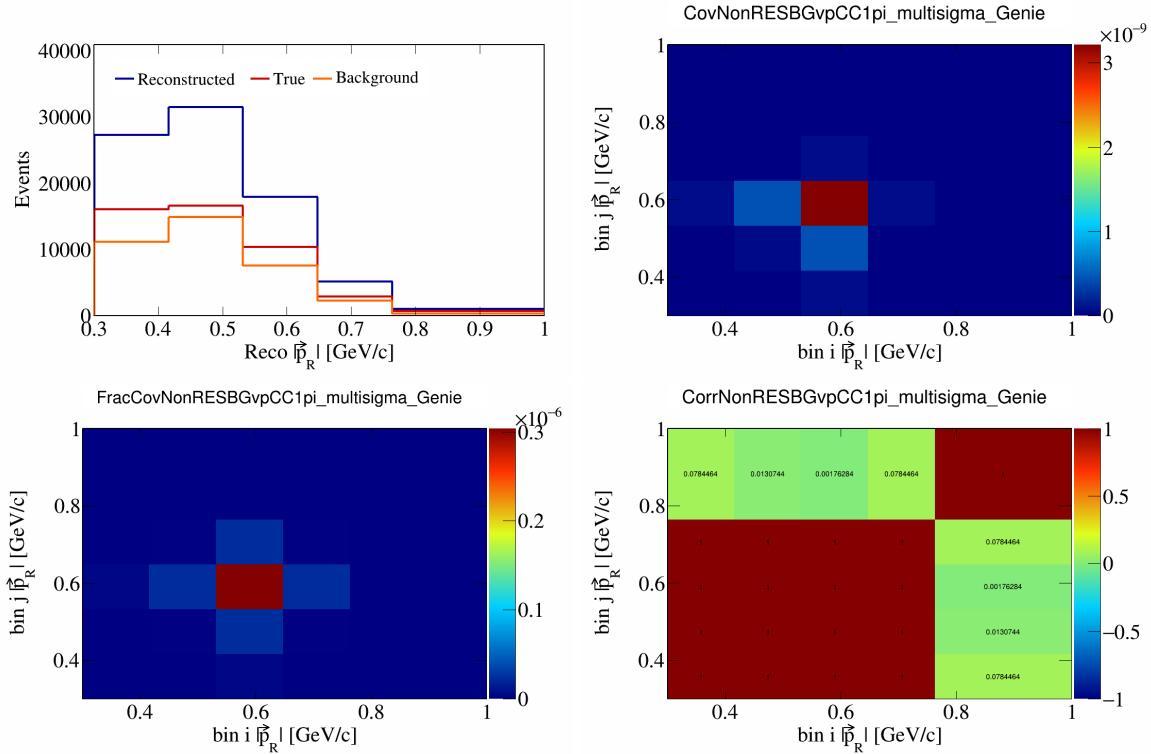


Figure 569: NonRESBGvpCC1pi variations for $|\vec{p}_R|$.

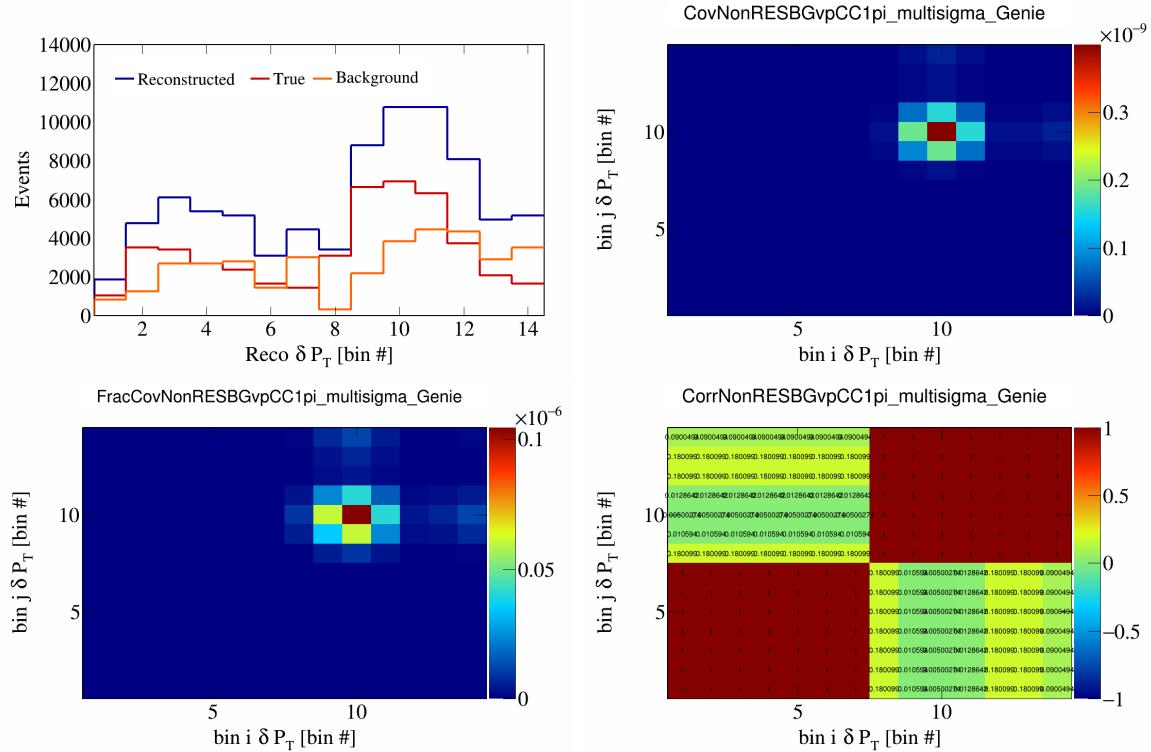


Figure 570: NonRESBGvpCC1pi variations for δP_T in $\cos(\theta_{\vec{p}_\mu})$.

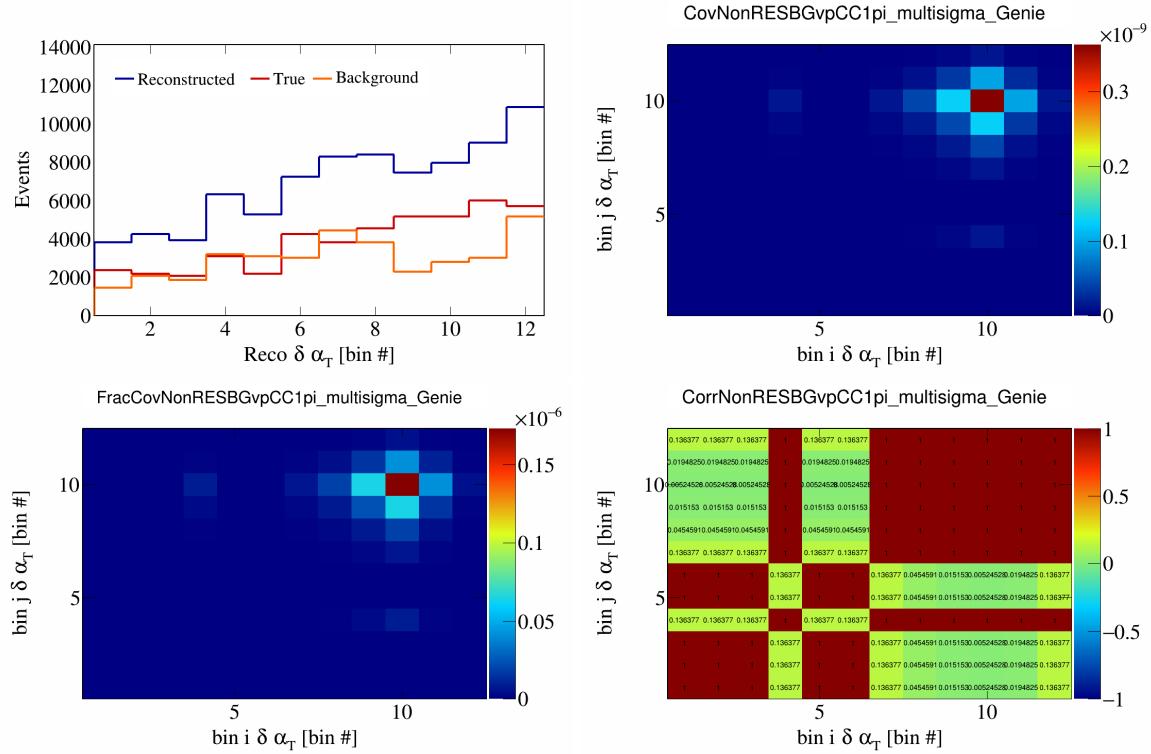


Figure 571: NonRESBGvpCC1pi variations for $\delta\alpha_T$ in $\cos(\theta_{\vec{p}_\mu})$.

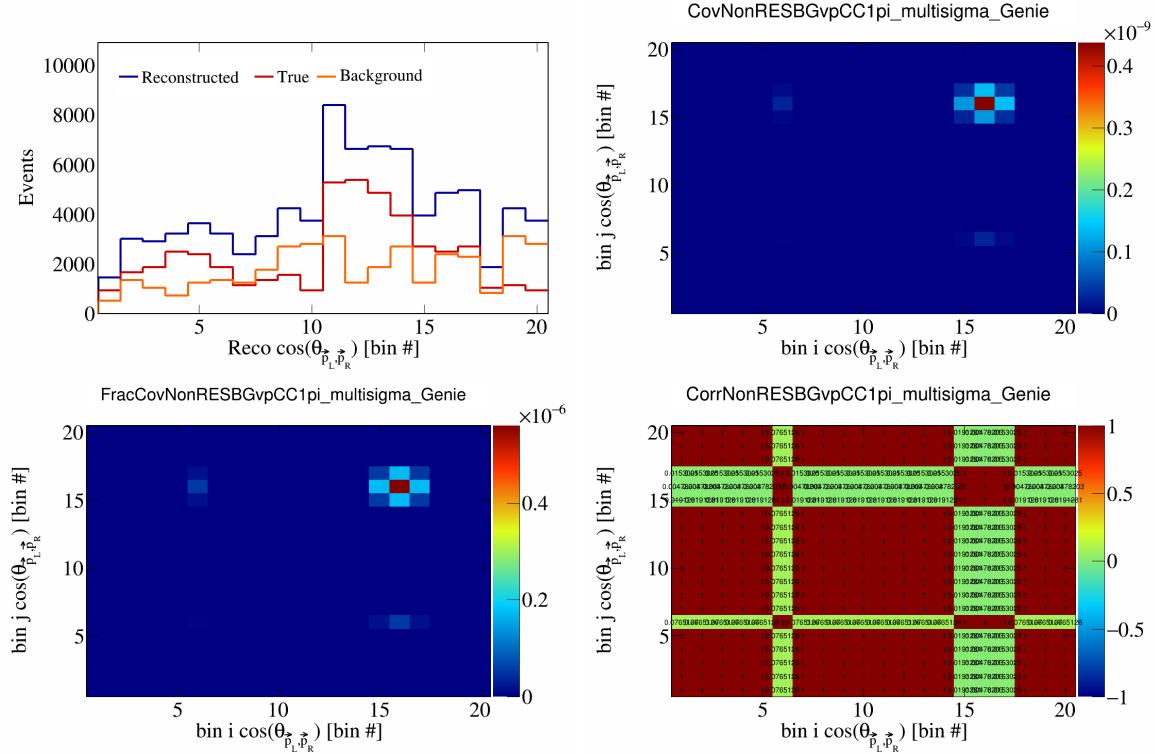


Figure 572: NonRESBGvpCC1pi variations for $\cos(\theta_{\vec{p}_L, \vec{p}_R})$ in $\cos(\theta_{\vec{p}_\mu})$.

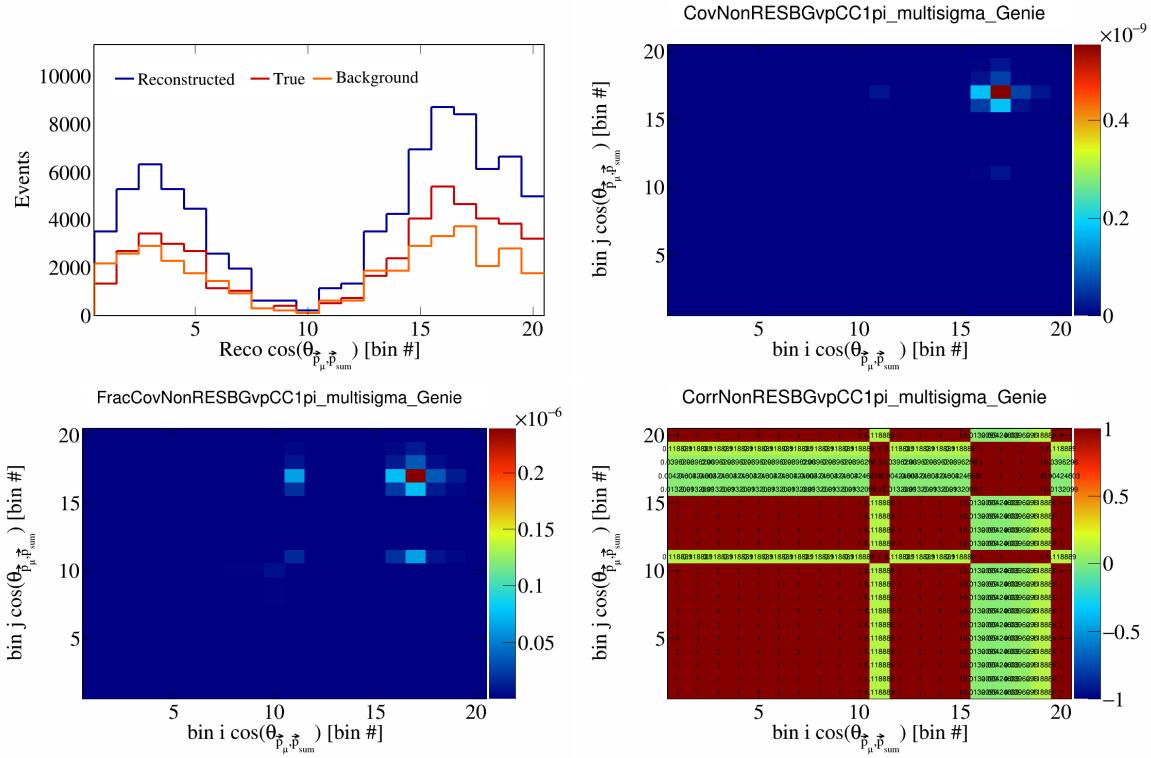


Figure 573: NonRESBGvpCC1pi variations for $\cos(\theta_{\vec{p}_\mu})$ in $\cos(\theta_{\vec{p}_\mu})$.

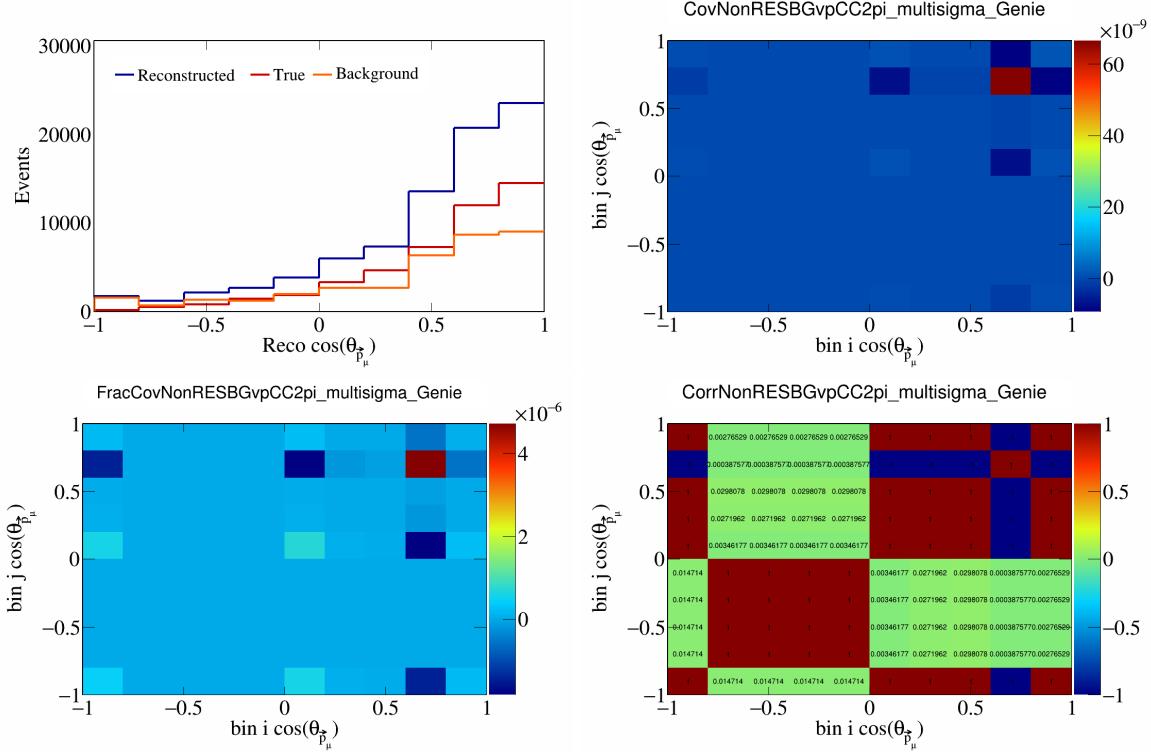


Figure 574: NonRESBGvpCC2pi variations for $\cos(\theta_{\vec{p}_\mu})$.

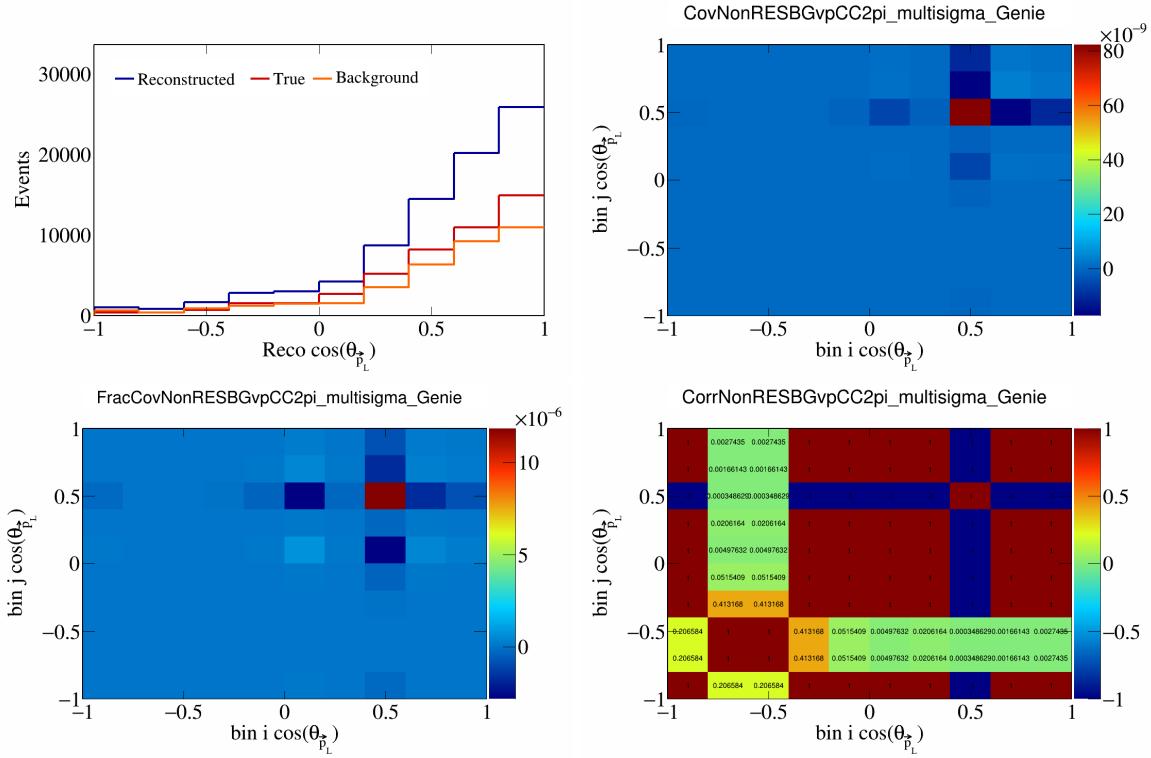


Figure 575: NonRESBGvpCC2pi variations for $\cos(\theta_{\vec{p}_L})$.

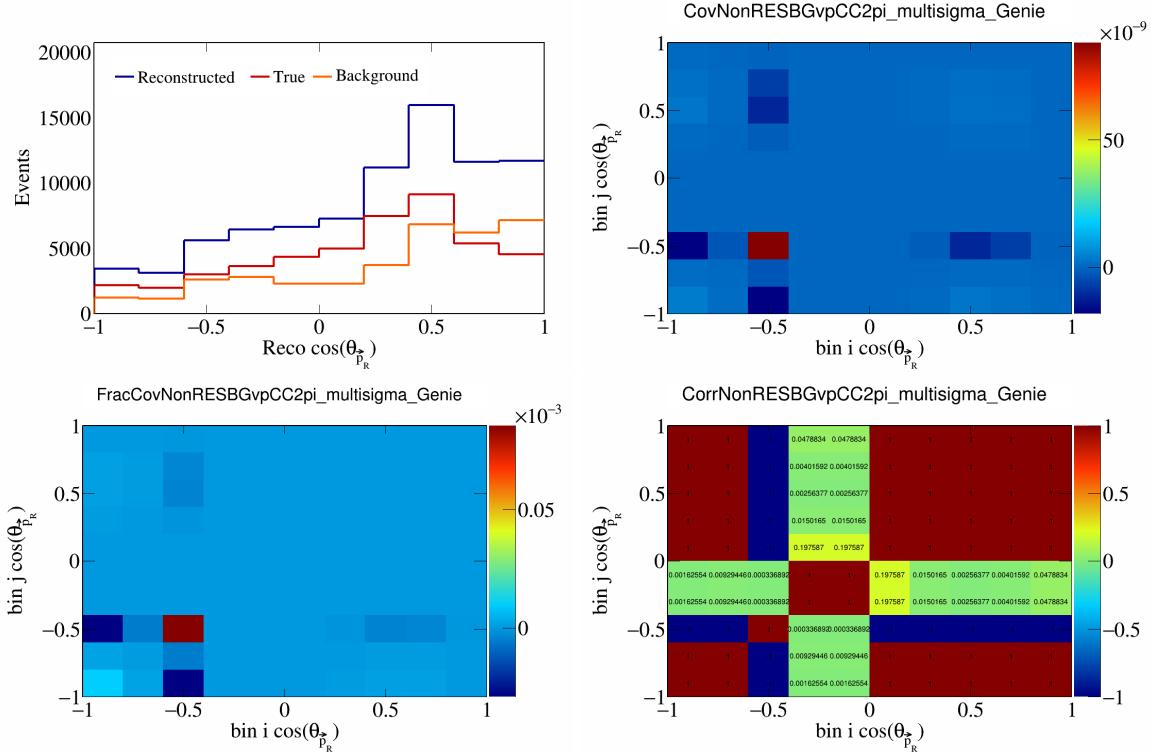


Figure 576: NonRESBGvpCC2pi variations for $\cos(\theta_{\vec{p}_R})$.

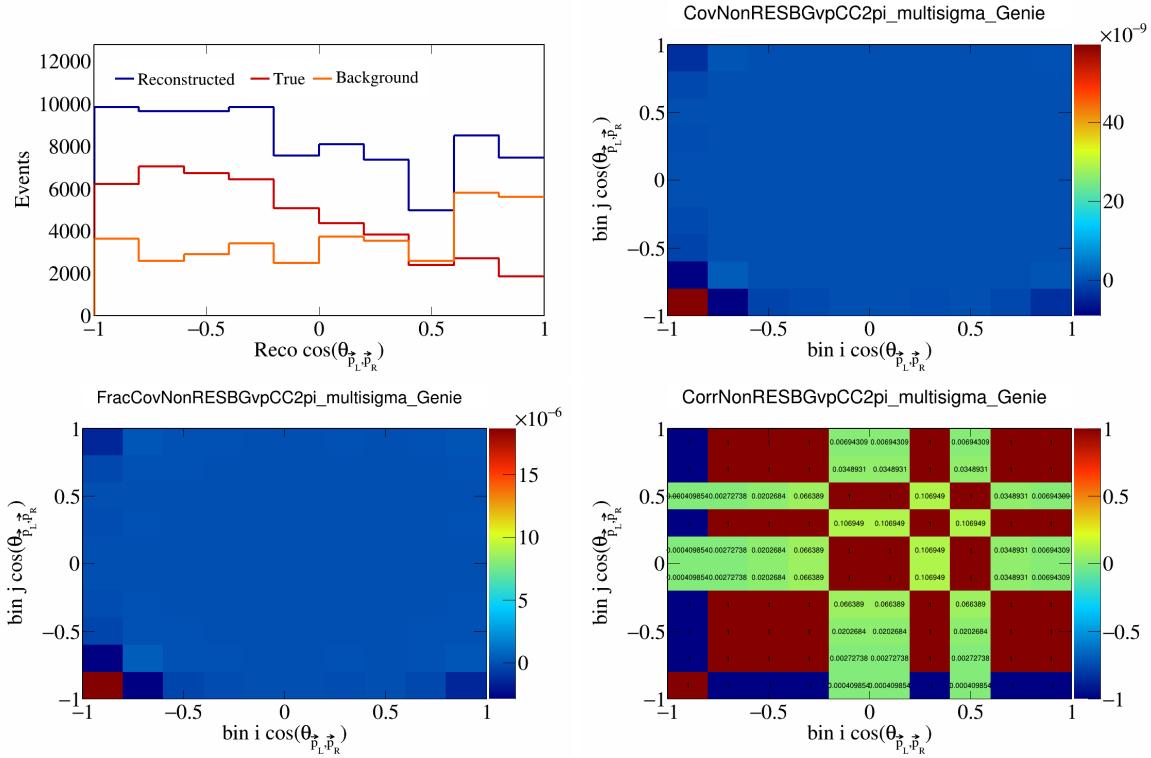


Figure 577: NonRESBGvpCC2pi variations for $\cos(\theta_{\vec{p}_L, \vec{p}_R})$.

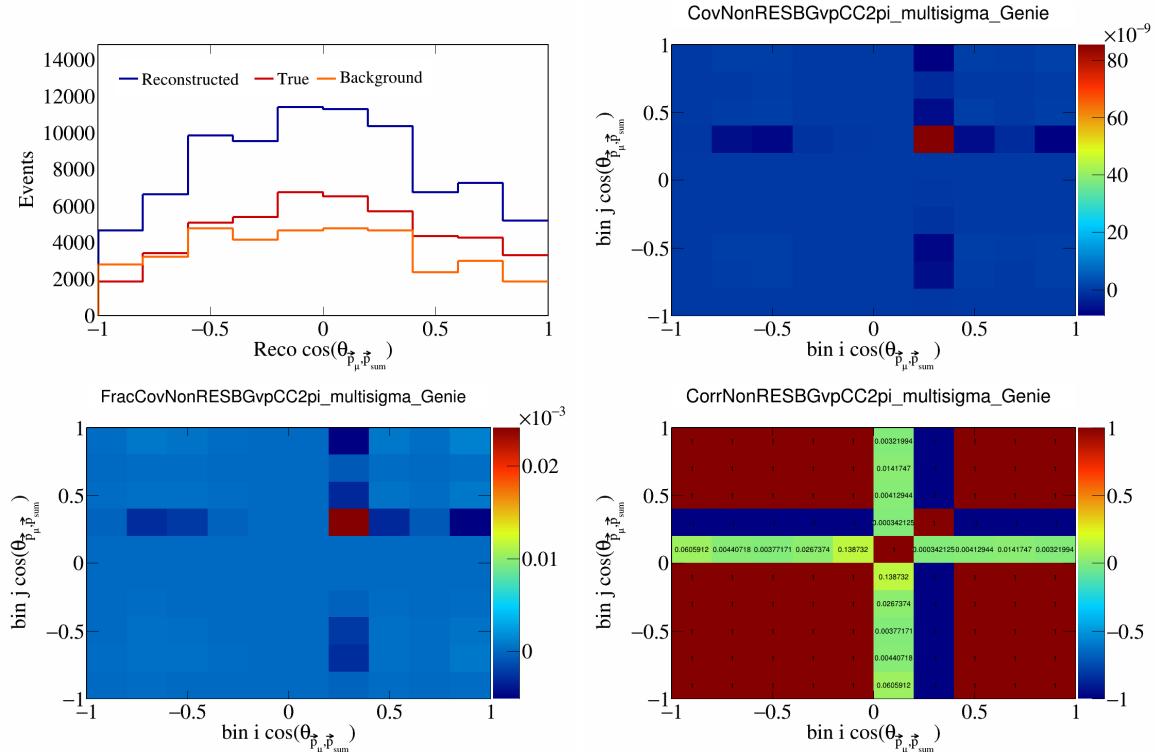


Figure 578: NonRESBGvpCC2pi variations for $\cos(\theta_{\vec{p}_\mu, \vec{p}_{\text{sum}}})$.

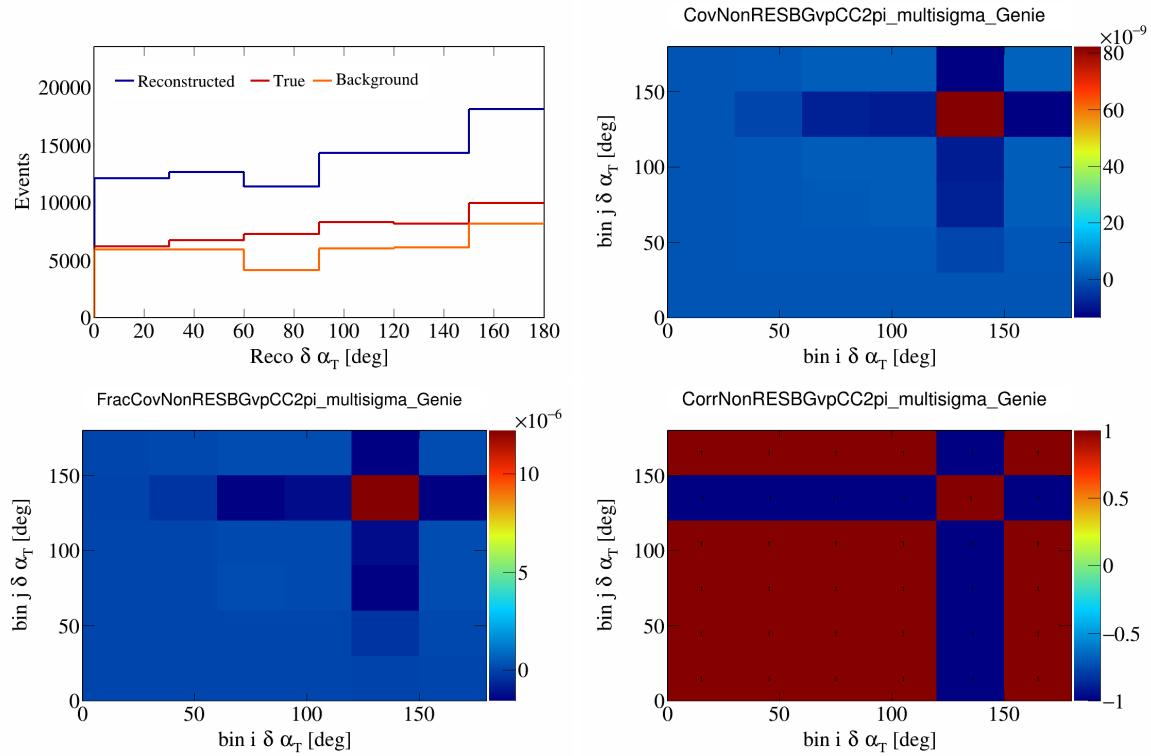


Figure 579: NonRESBGvpCC2pi variations for $\delta \alpha_T$.

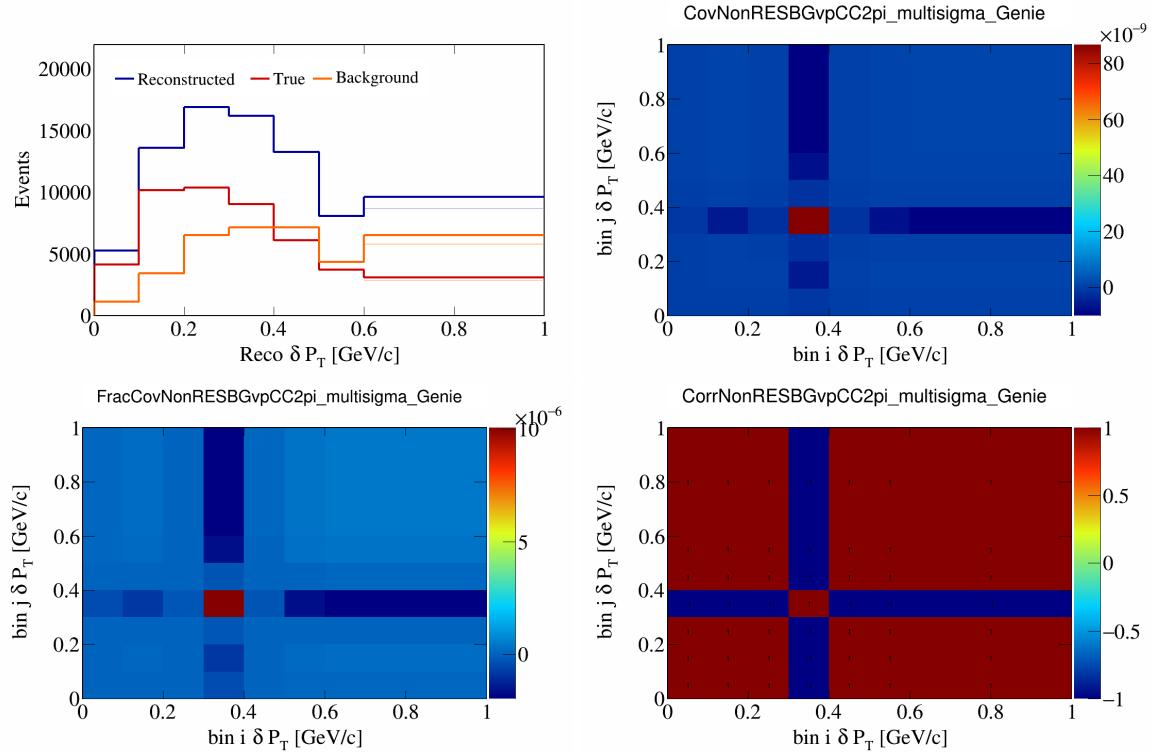


Figure 580: NonRESBGvpCC2pi variations for δP_T .

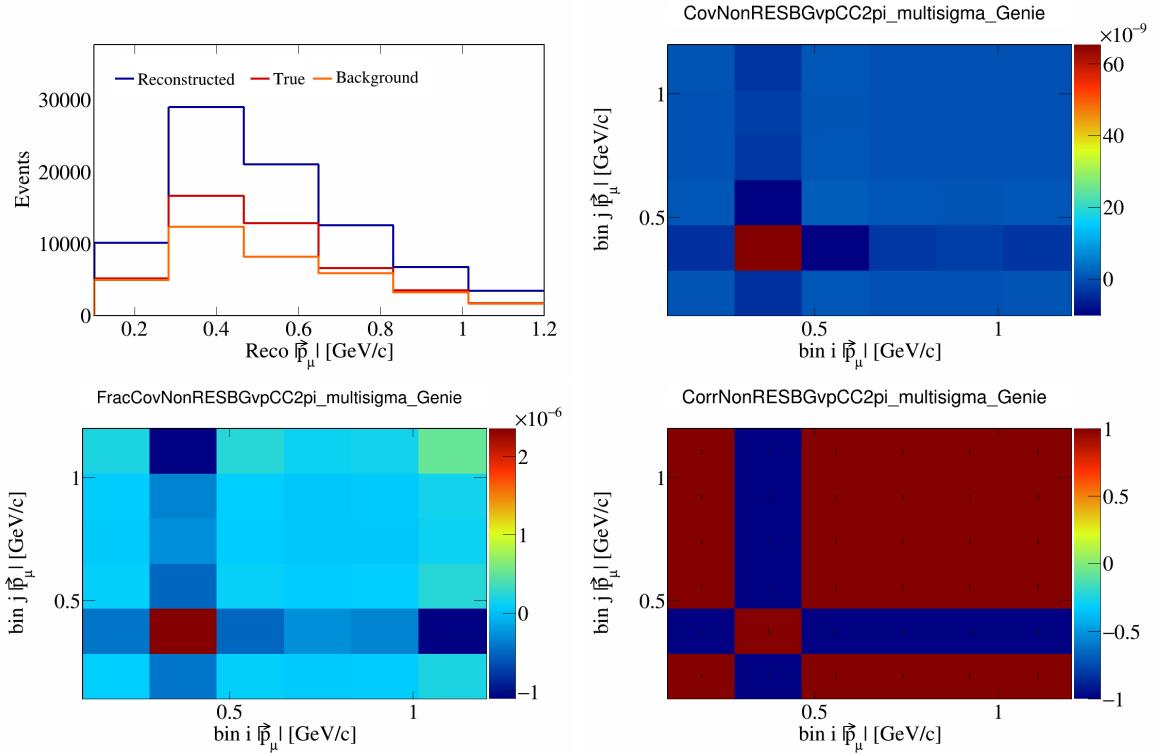


Figure 581: NonRESBGvpCC2pi variations for $|\vec{p}_\mu|$.

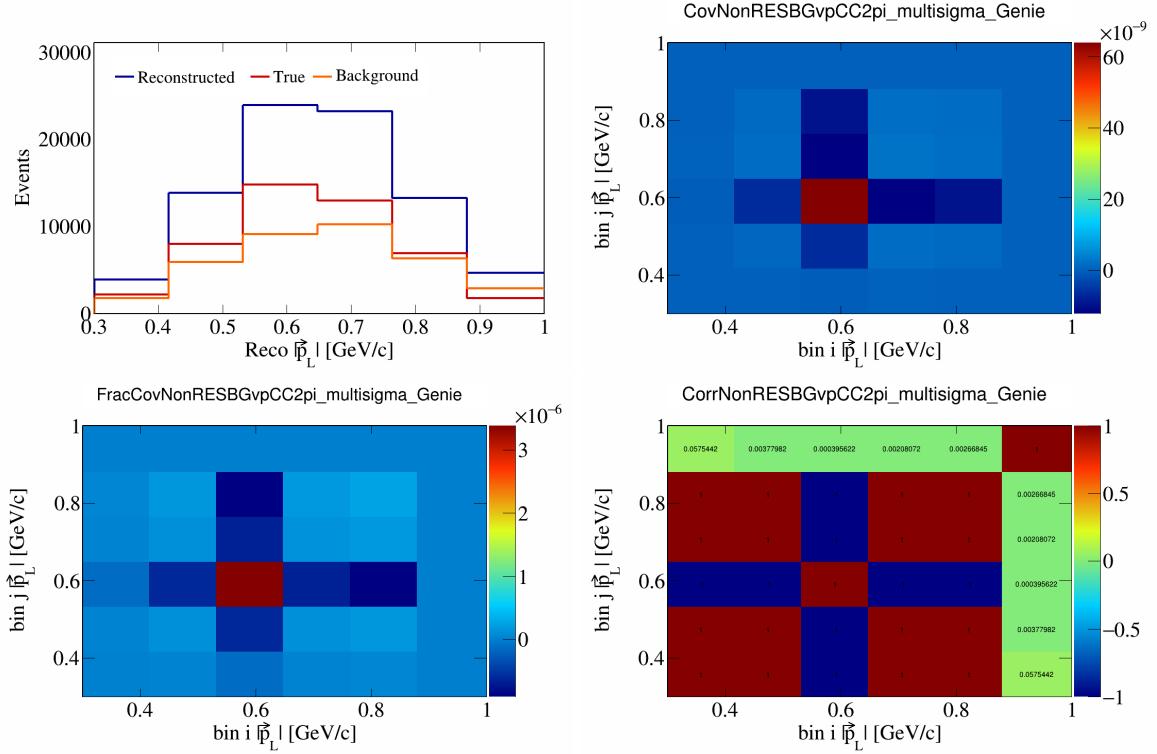


Figure 582: NonRESBGvpCC2pi variations for $|\vec{p}_L|$.

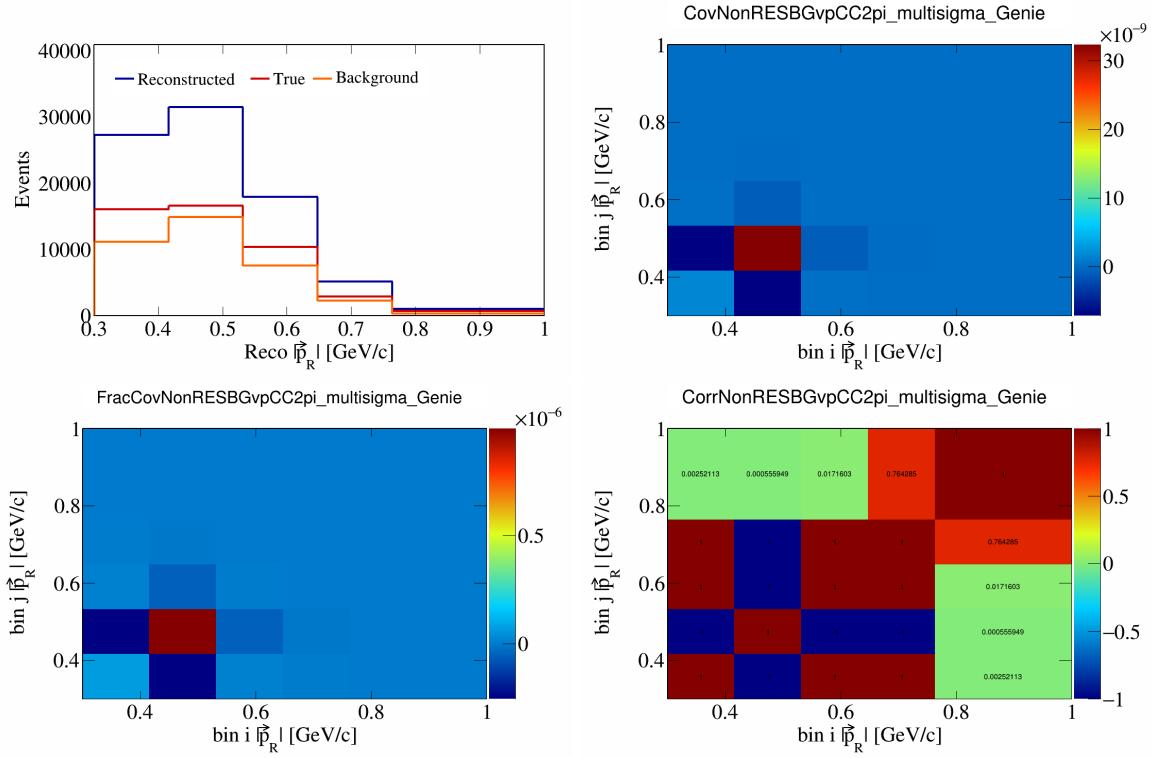


Figure 583: NonRESBGvpCC2pi variations for $|\vec{p}_R|$.

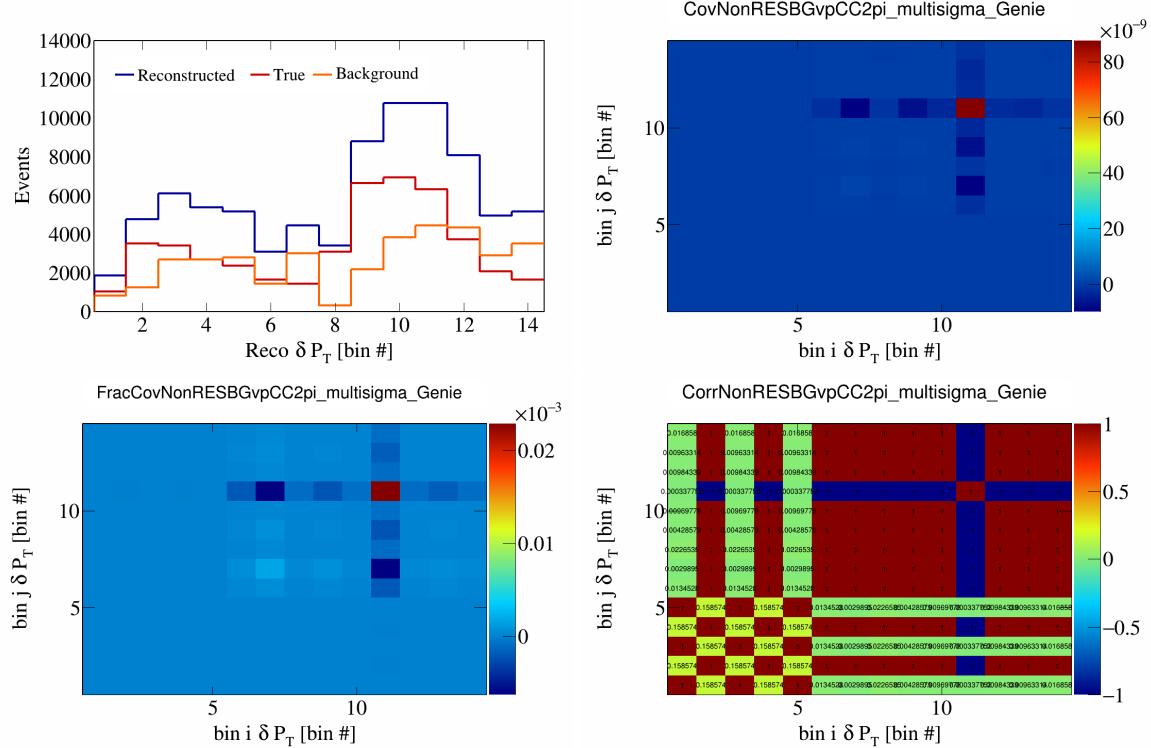


Figure 584: NonRESBGvpCC2pi variations for δP_T in $\cos(\theta_{\vec{p}_\mu})$.

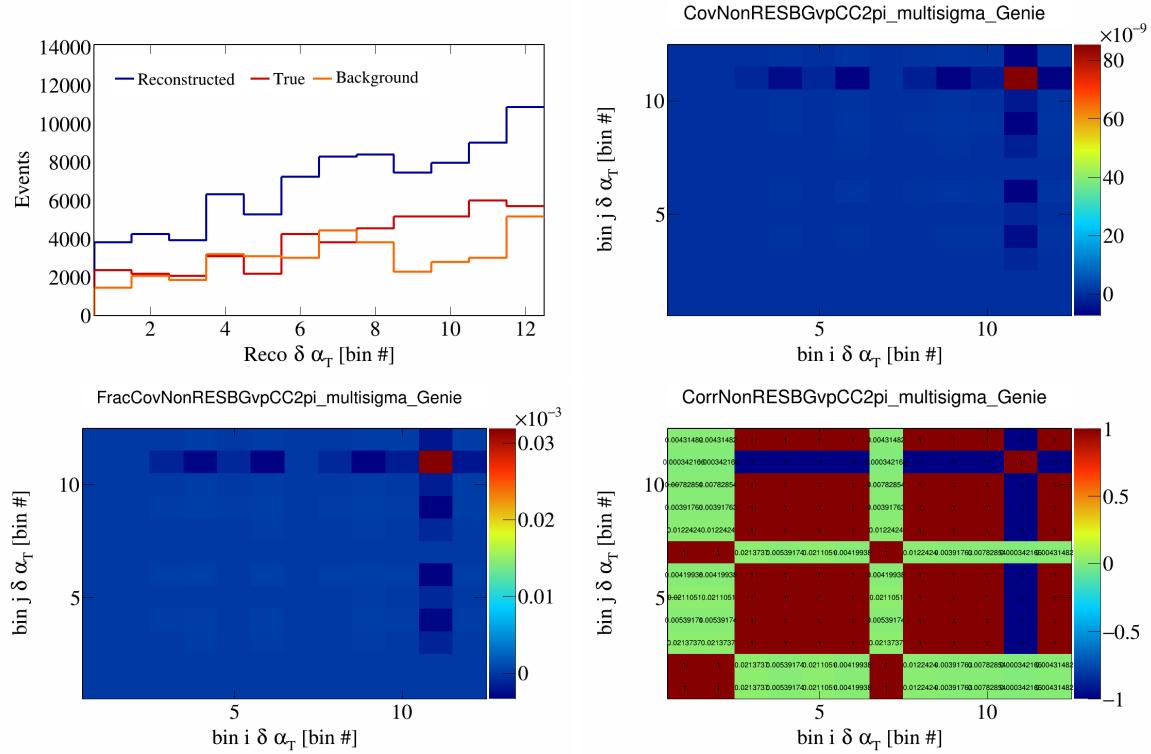


Figure 585: NonRESBGvpCC2pi variations for $\delta\alpha_T$ in $\cos(\theta_{\vec{p}_\mu})$.

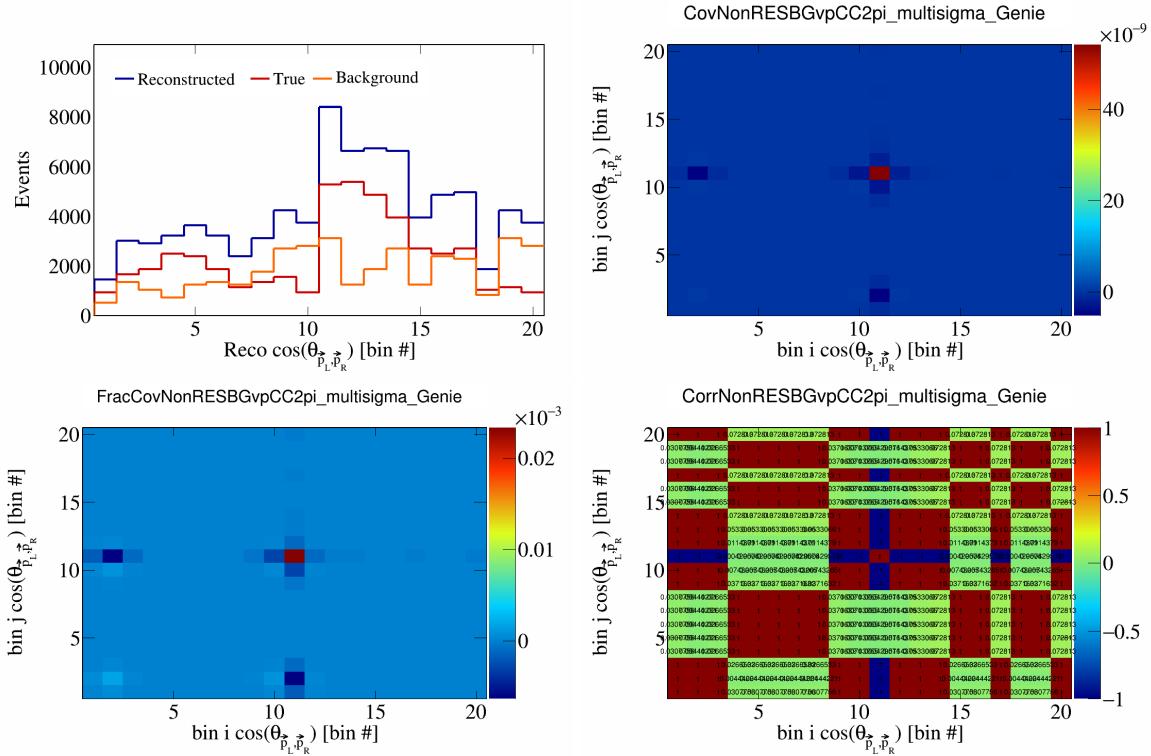


Figure 586: NonRESBGvpCC2pi variations for $\cos(\theta_{\vec{p}_L, \vec{p}_R})$ in $\cos(\theta_{\vec{p}_\mu})$.

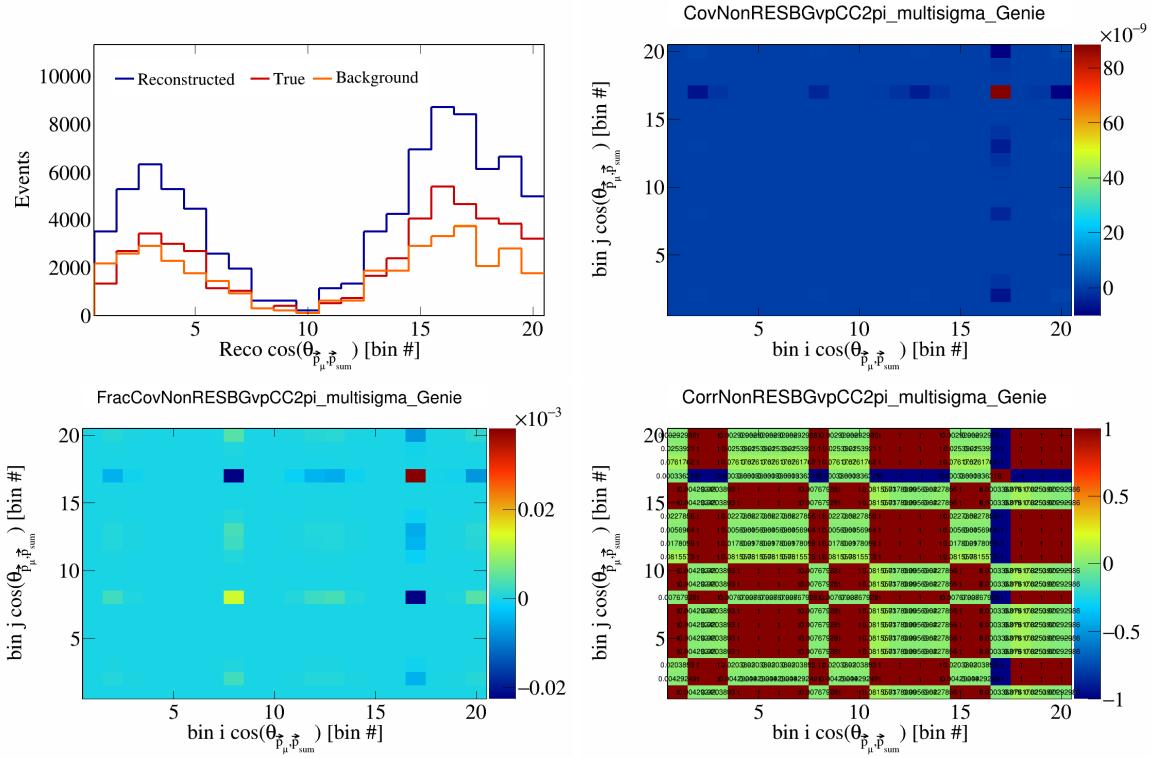


Figure 587: NonRESBGvpCC2pi variations for $\cos(\theta_{\vec{p}_\mu, \vec{p}_{\text{sum}}})$ in $\cos(\theta_{\vec{p}_\mu})$.

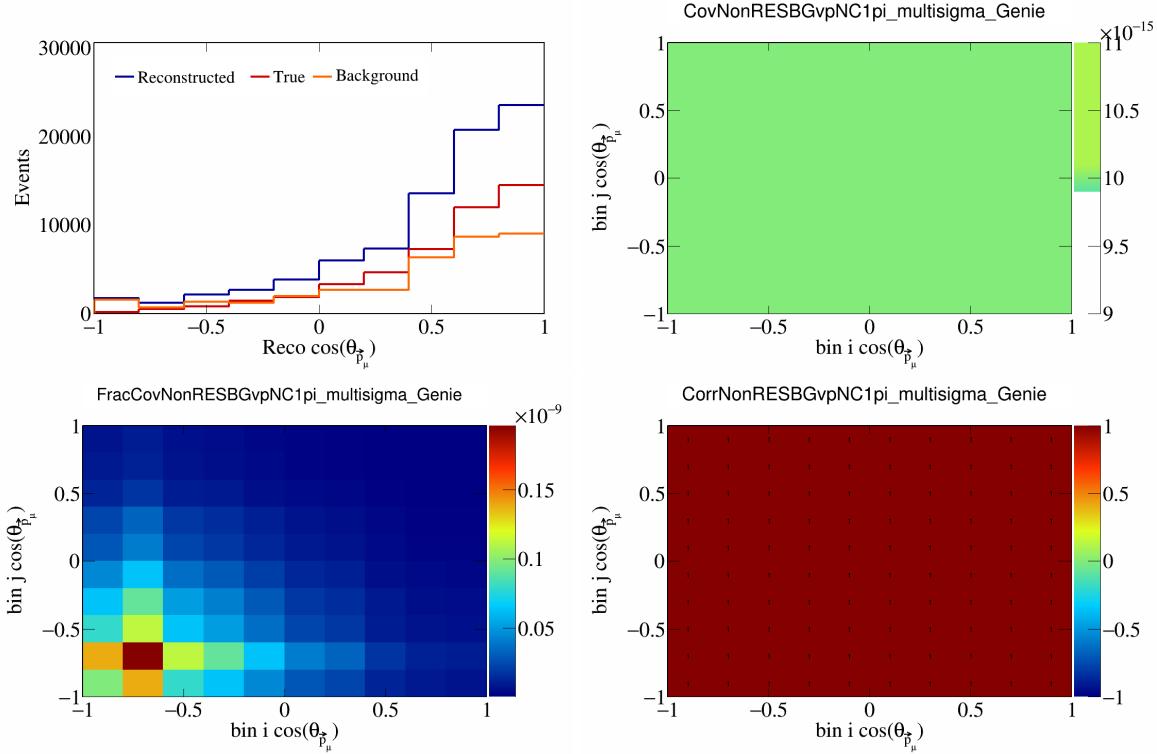


Figure 588: NonRESBGvpNC1pi variations for $\cos(\theta_{\vec{p}_\mu})$.

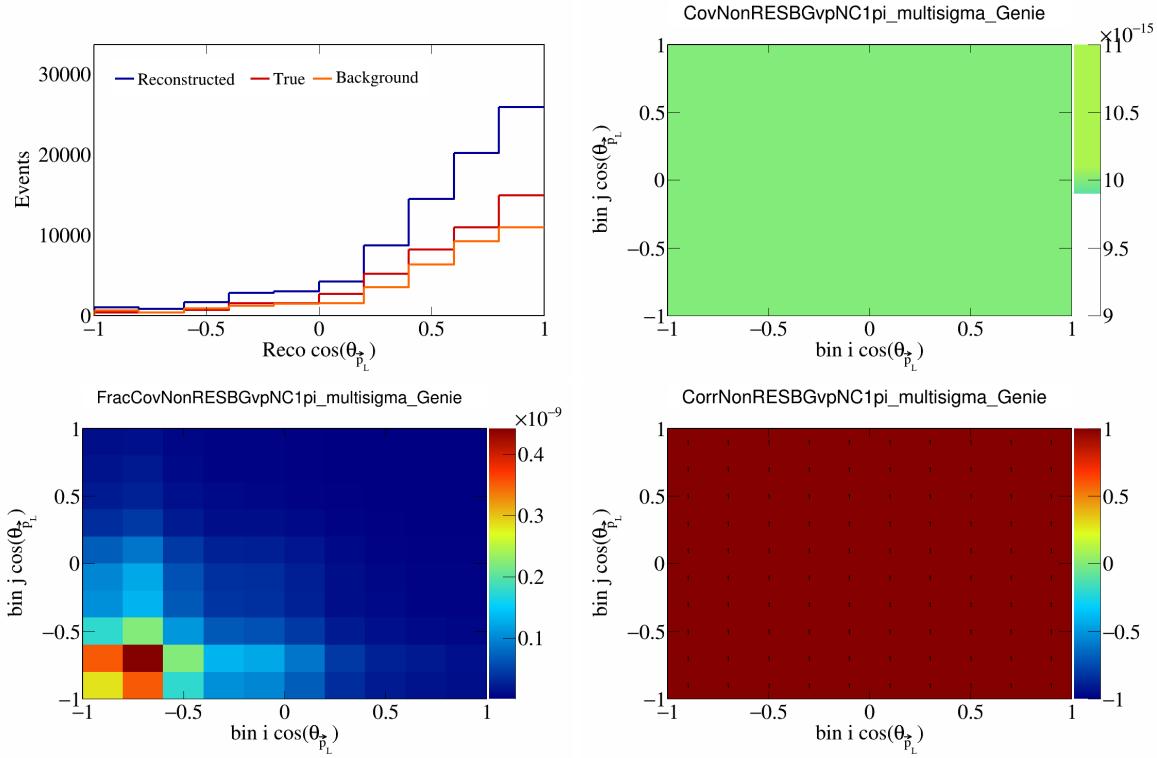


Figure 589: NonRESBGvpNC1pi variations for $\cos(\theta_{\vec{p}_L})$.

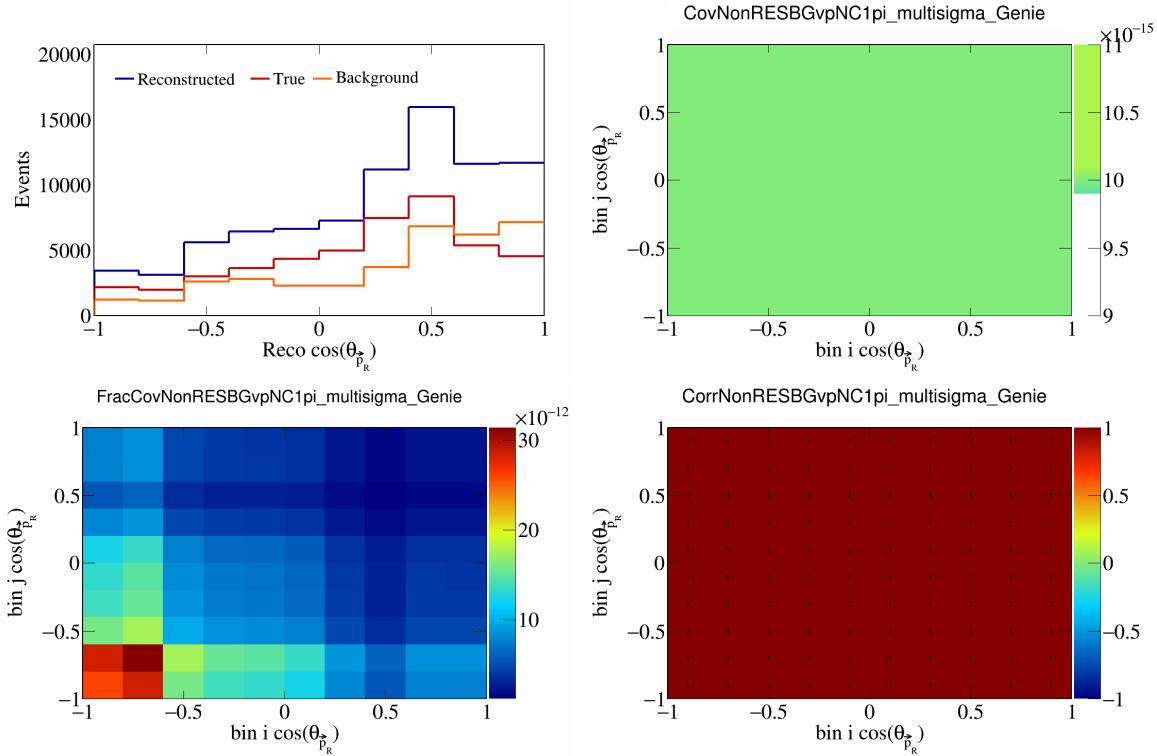


Figure 590: NonRESBGvpNC1pi variations for $\cos(\theta_{\vec{p}_R})$.

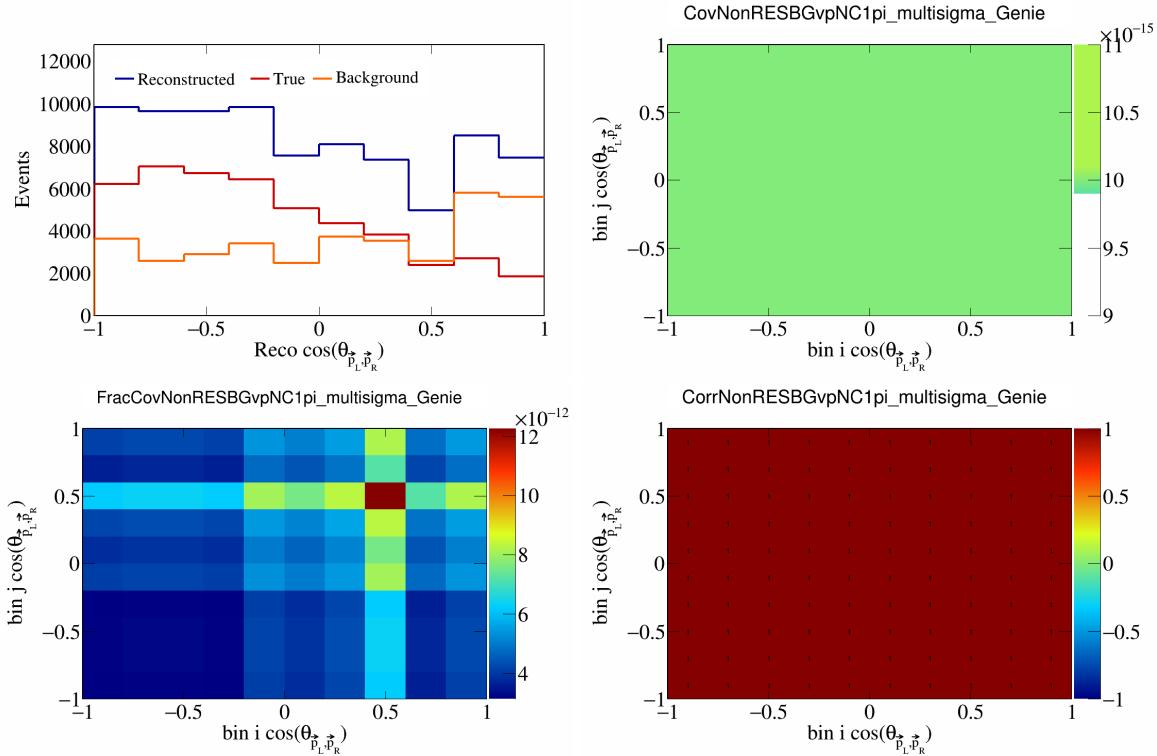


Figure 591: NonRESBGvpNC1pi variations for $\cos(\theta_{\vec{p}_L, \vec{p}_R})$.

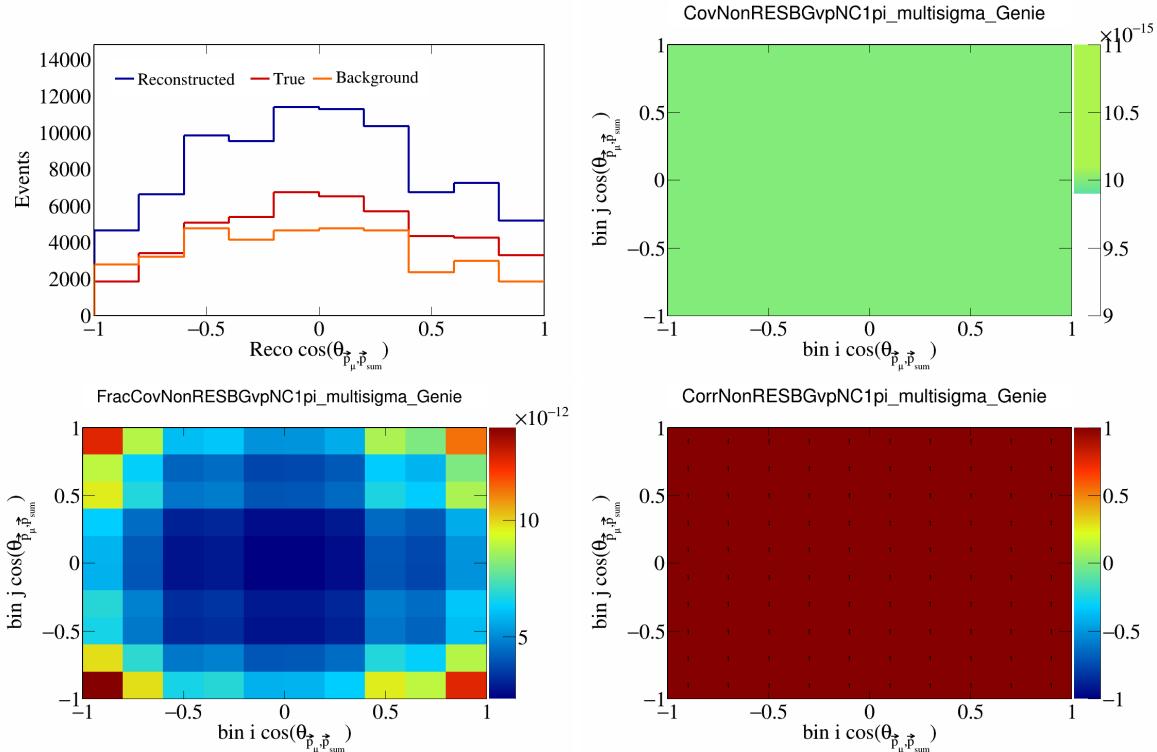


Figure 592: NonRESBGvpNC1pi variations for $\cos(\theta_{\vec{p}_\mu, \vec{p}_{\text{sum}}})$.

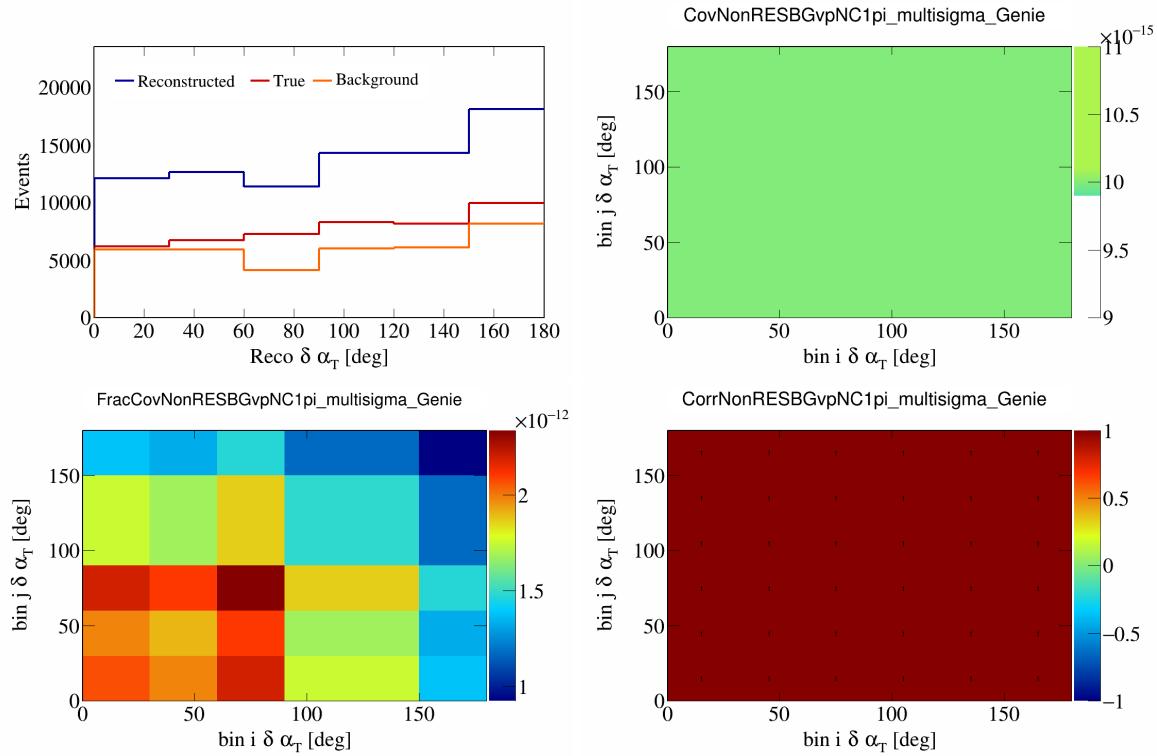


Figure 593: NonRESBGvpNC1pi variations for $\delta\alpha_T$.

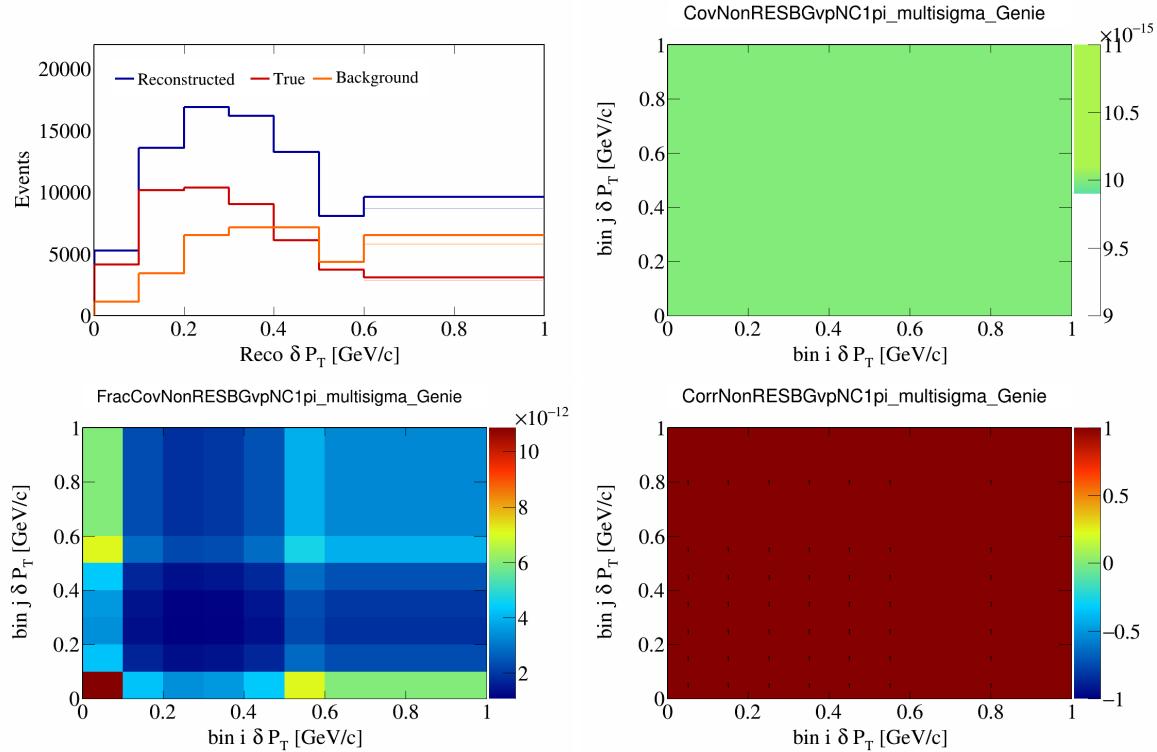


Figure 594: NonRESBGvpNC1pi variations for δP_T .

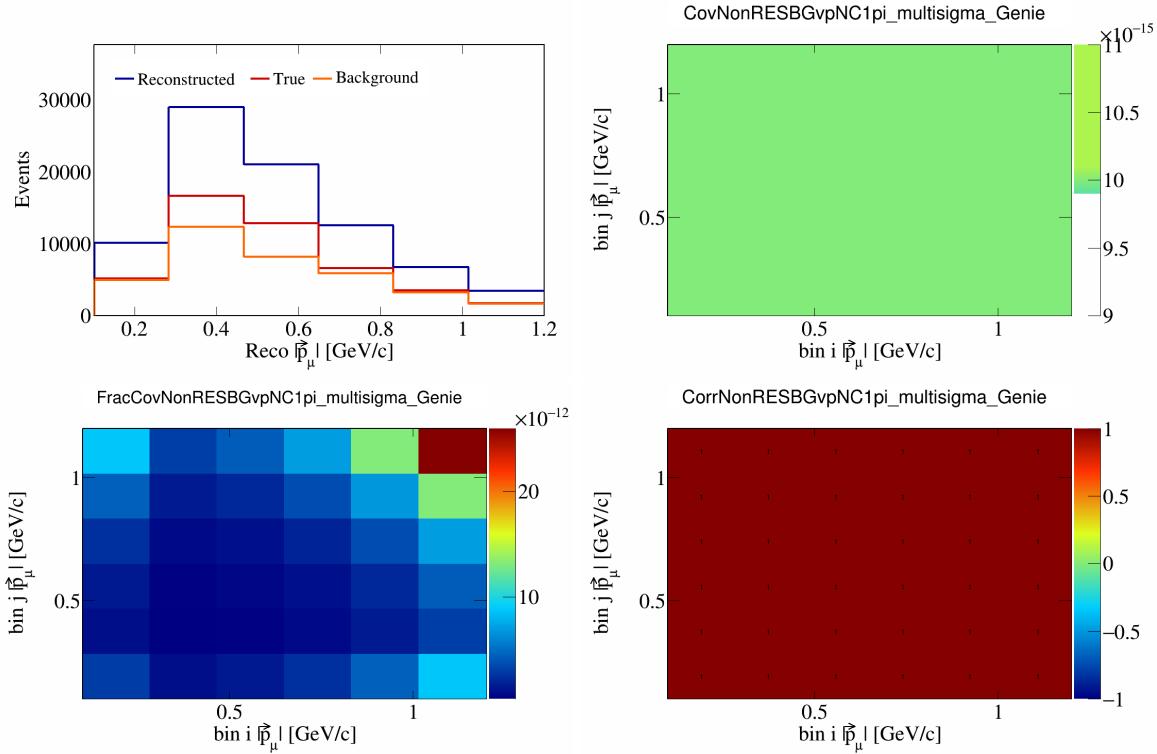


Figure 595: NonRESBGvpNC1pi variations for $|\vec{p}_\mu|$.

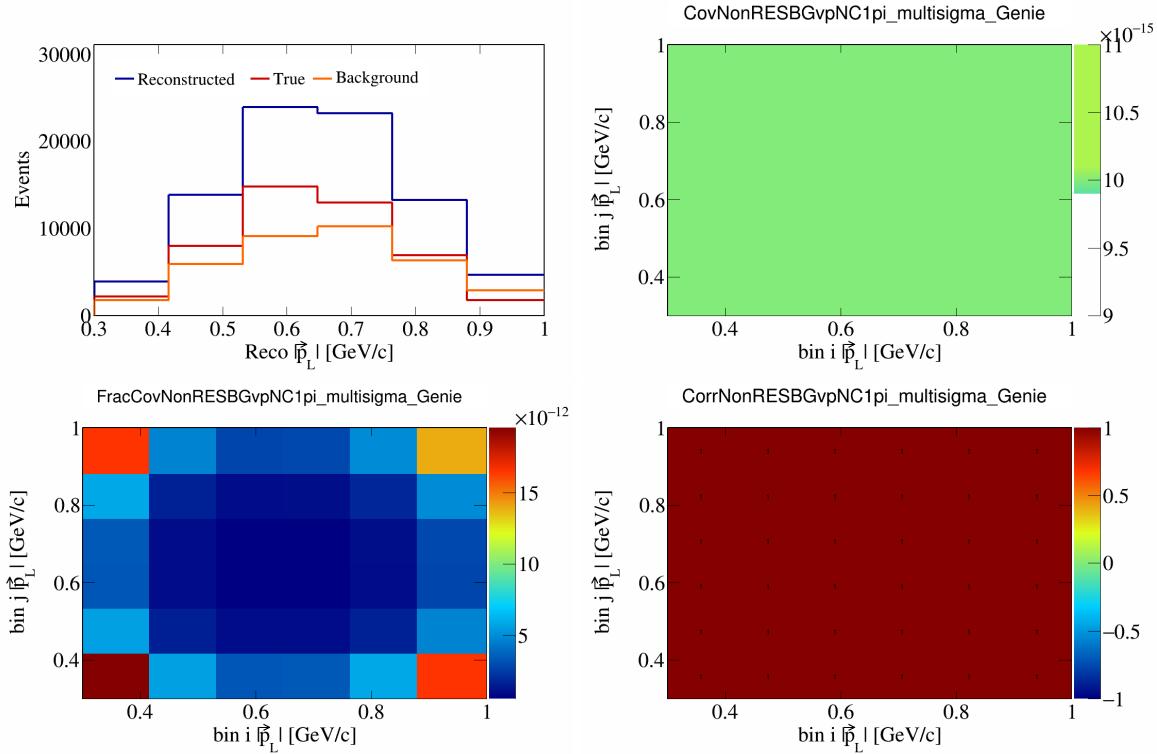


Figure 596: NonRESBGvpNC1pi variations for $|\vec{p}_L|$.

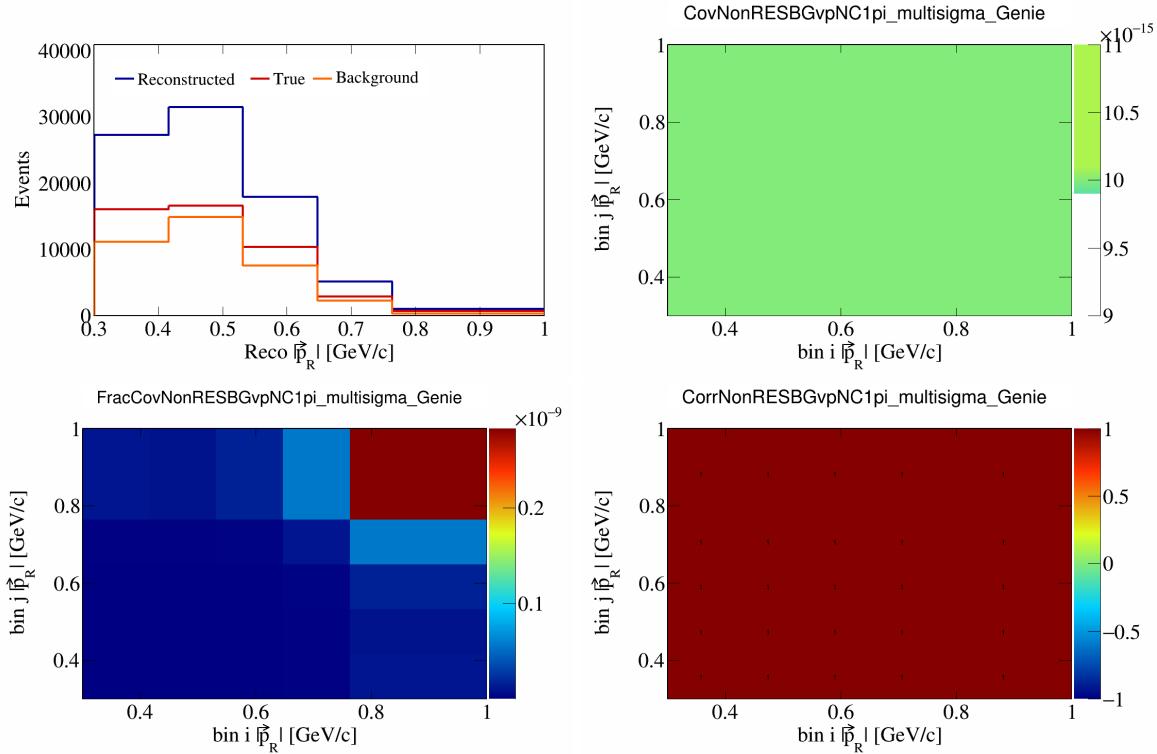


Figure 597: NonRESBGvpNC1pi variations for $|\vec{p}_R|$.

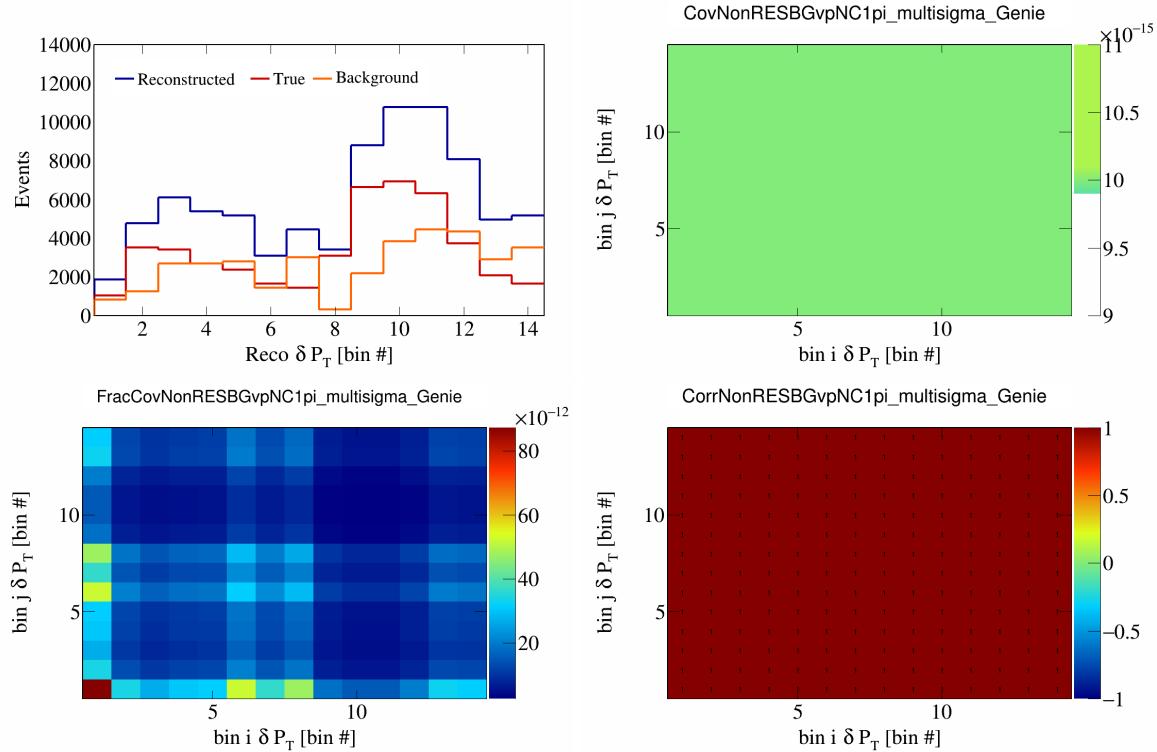


Figure 598: NonRESBGvpNC1pi variations for δP_T in $\cos(\theta_{\vec{p}_\mu})$.

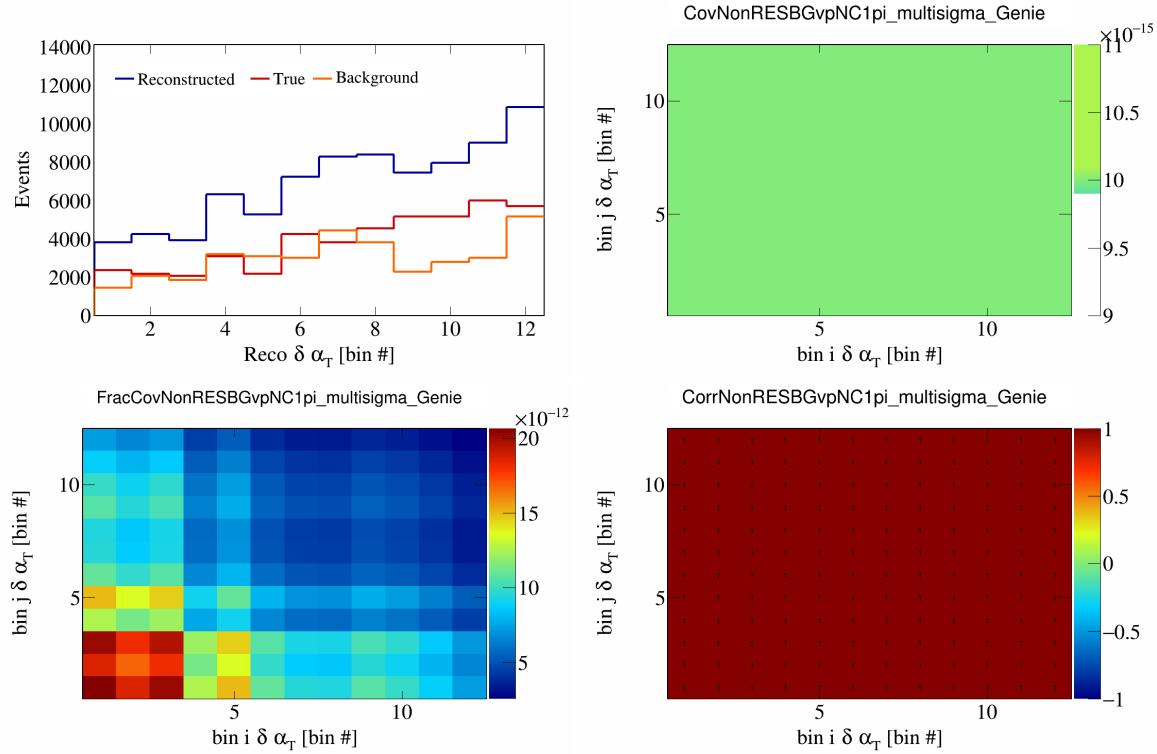


Figure 599: NonRESBGvpNC1pi variations for $\delta\alpha_T$ in $\cos(\theta_{\vec{p}_\mu})$.

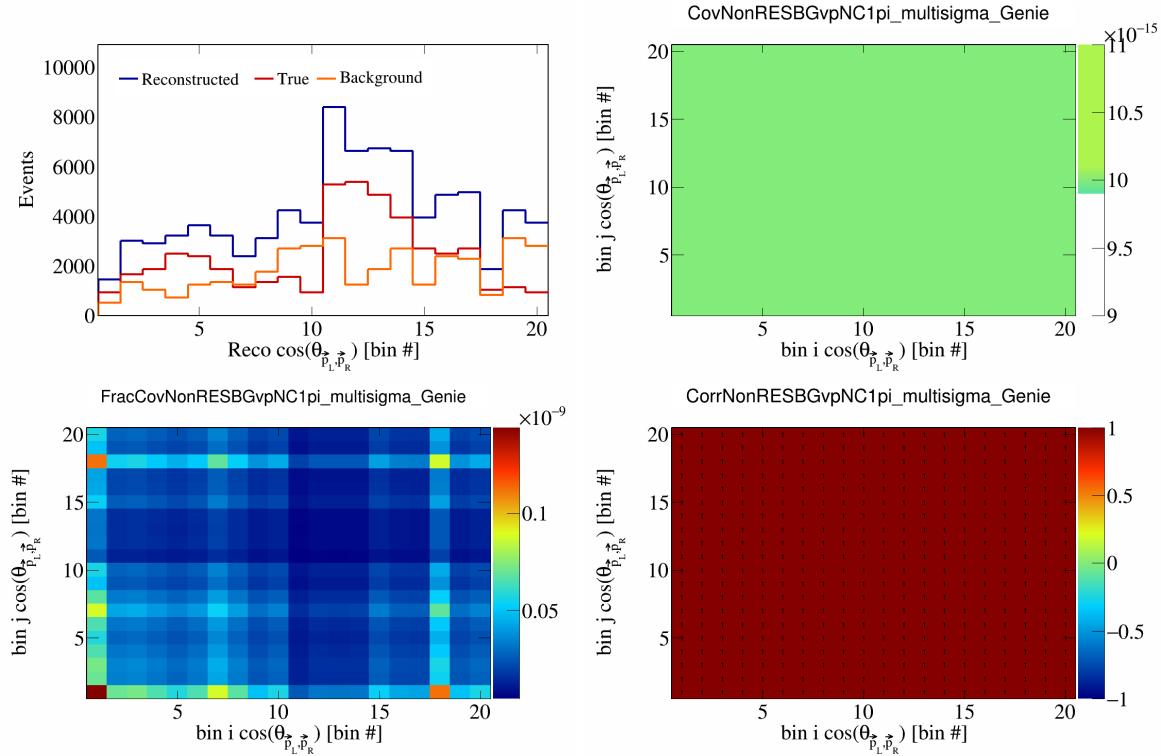


Figure 600: NonRESBGvpNC1pi variations for $\cos(\theta_{\vec{p}_L, \vec{p}_R})$ in $\cos(\theta_{\vec{p}_\mu})$.

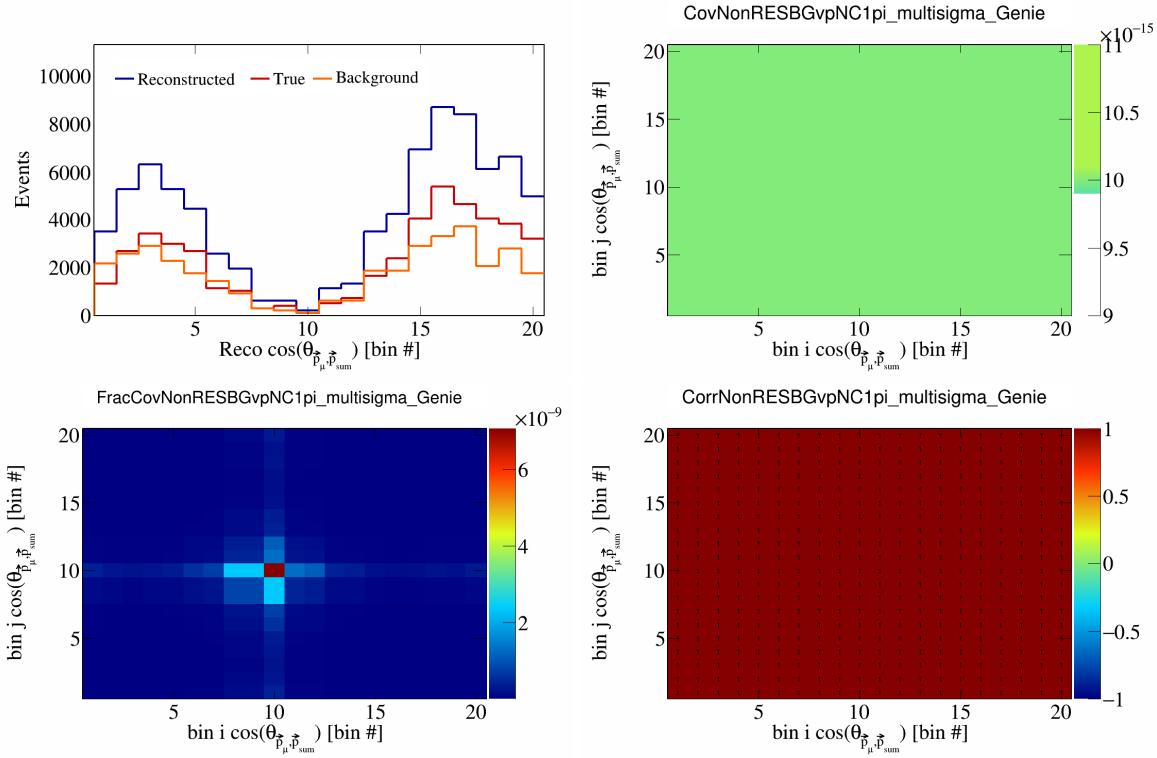


Figure 601: NonRESBGvpNC1pi variations for $\cos(\theta_{\vec{p}_\mu})$ in $\cos(\theta_{\vec{p}_\mu})$.

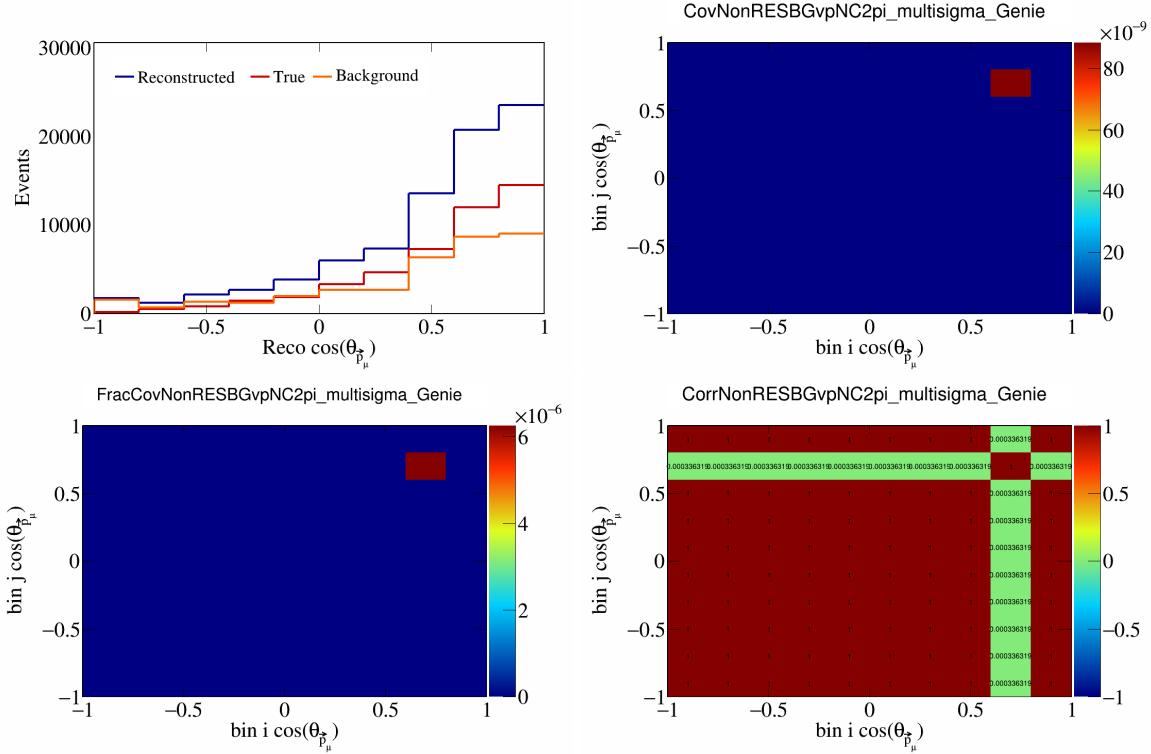


Figure 602: NonRESBGvpNC2pi variations for $\cos(\theta_{\vec{p}_\mu})$.

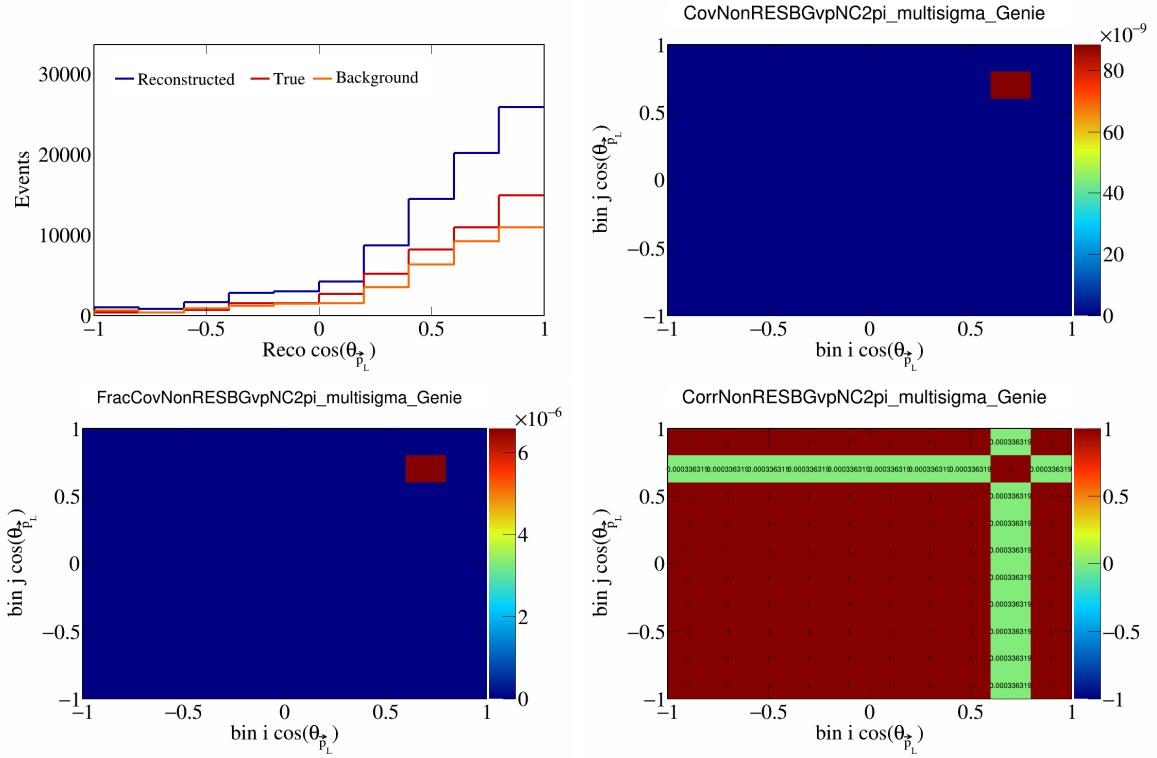


Figure 603: NonRESBGvpNC2pi variations for $\cos(\theta_{\vec{p}_L})$.

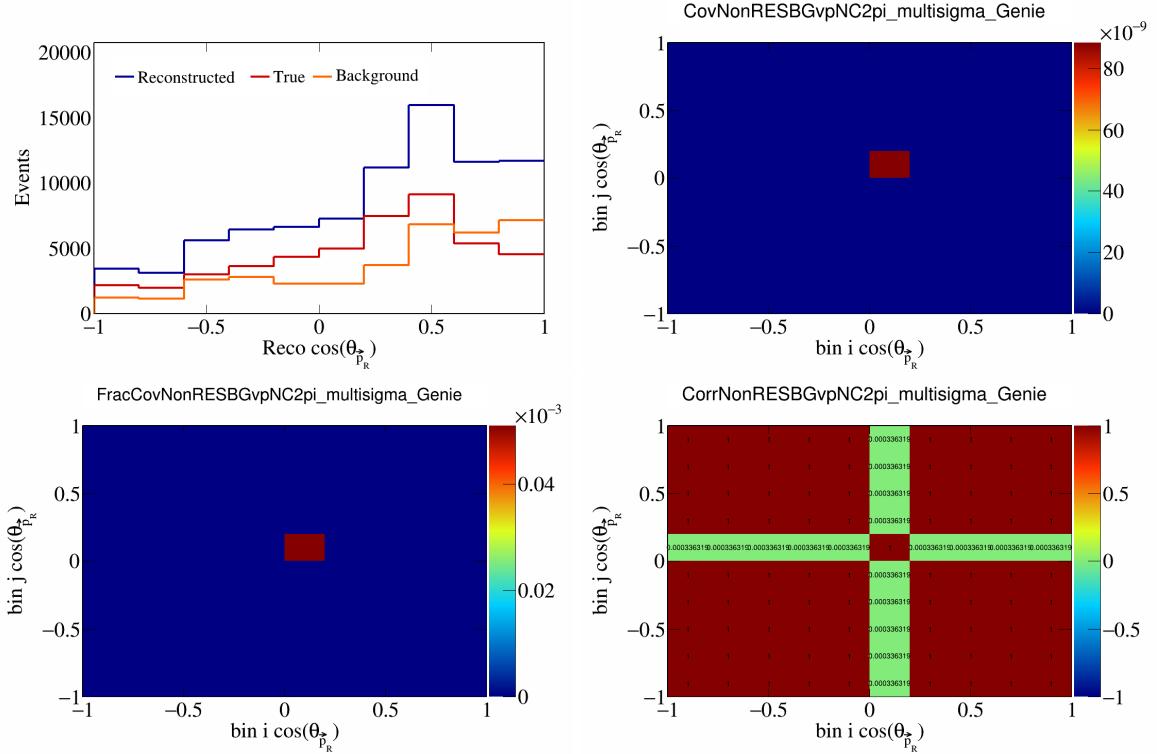


Figure 604: NonRESBGvpNC2pi variations for $\cos(\theta_{\vec{p}_R})$.

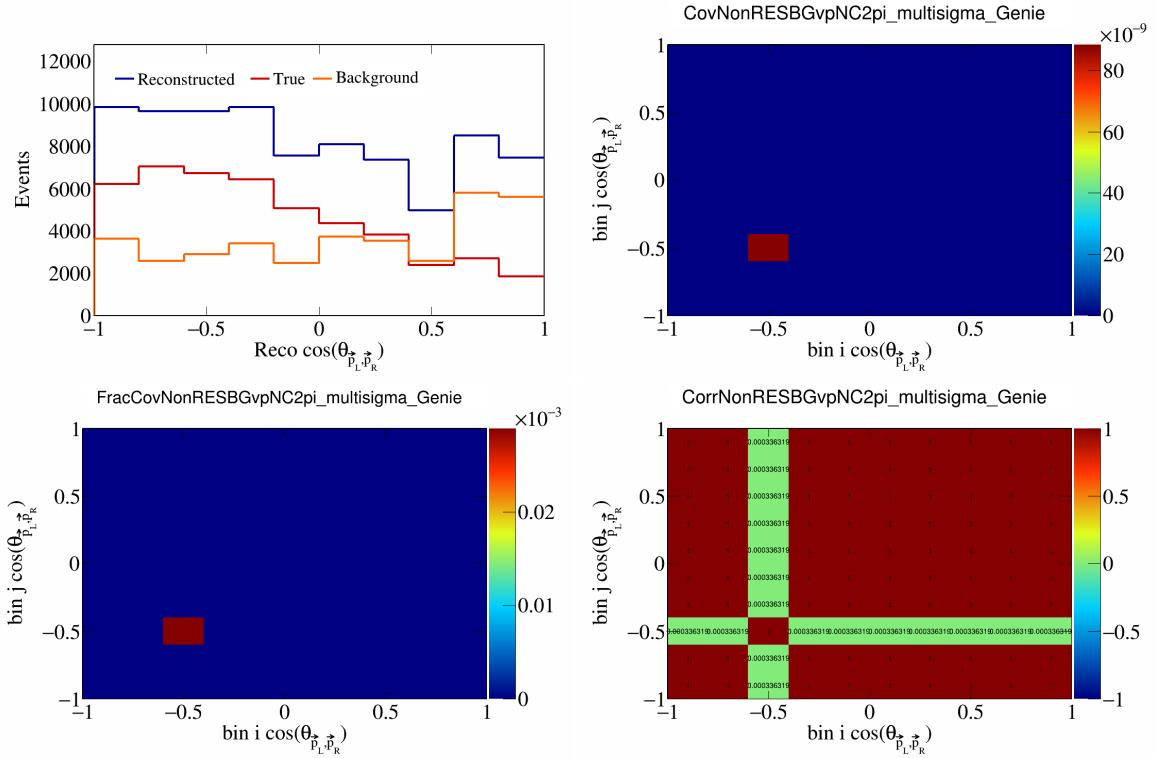


Figure 605: NonRESBGvpNC2pi variations for $\cos(\theta_{\vec{p}_L, \vec{p}_R})$.

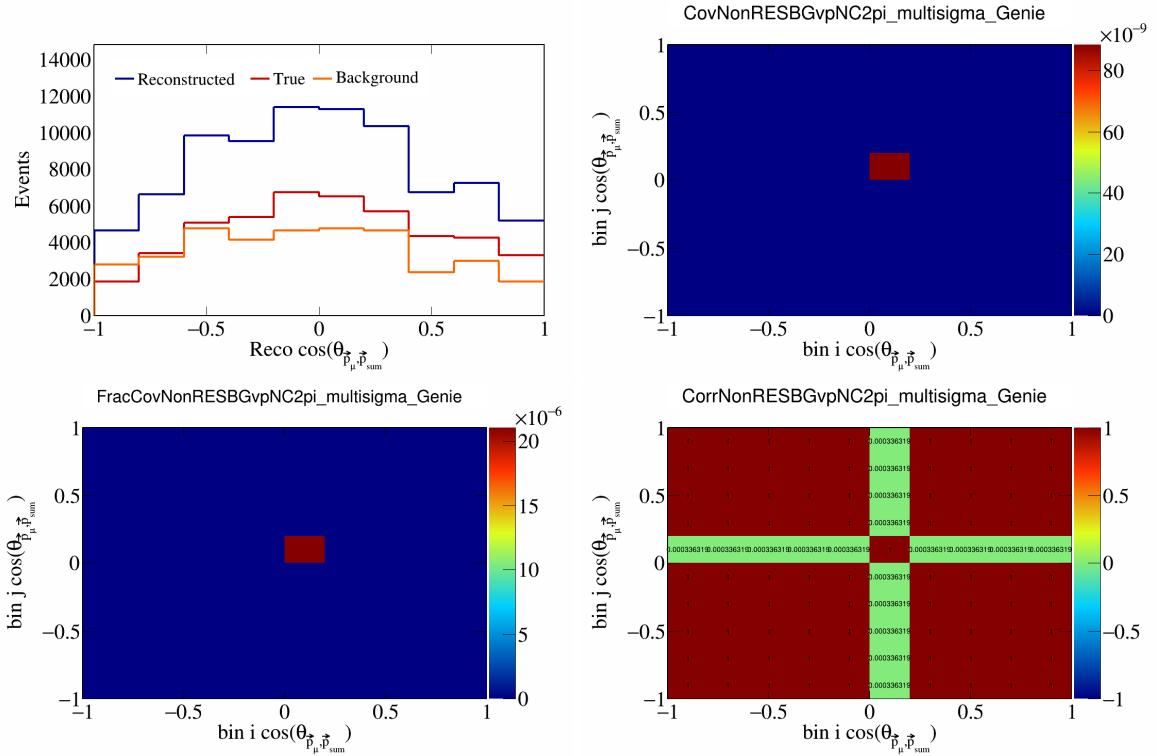


Figure 606: NonRESBGvpNC2pi variations for $\cos(\theta_{\vec{p}_\mu, \vec{p}_{\text{sum}}})$.

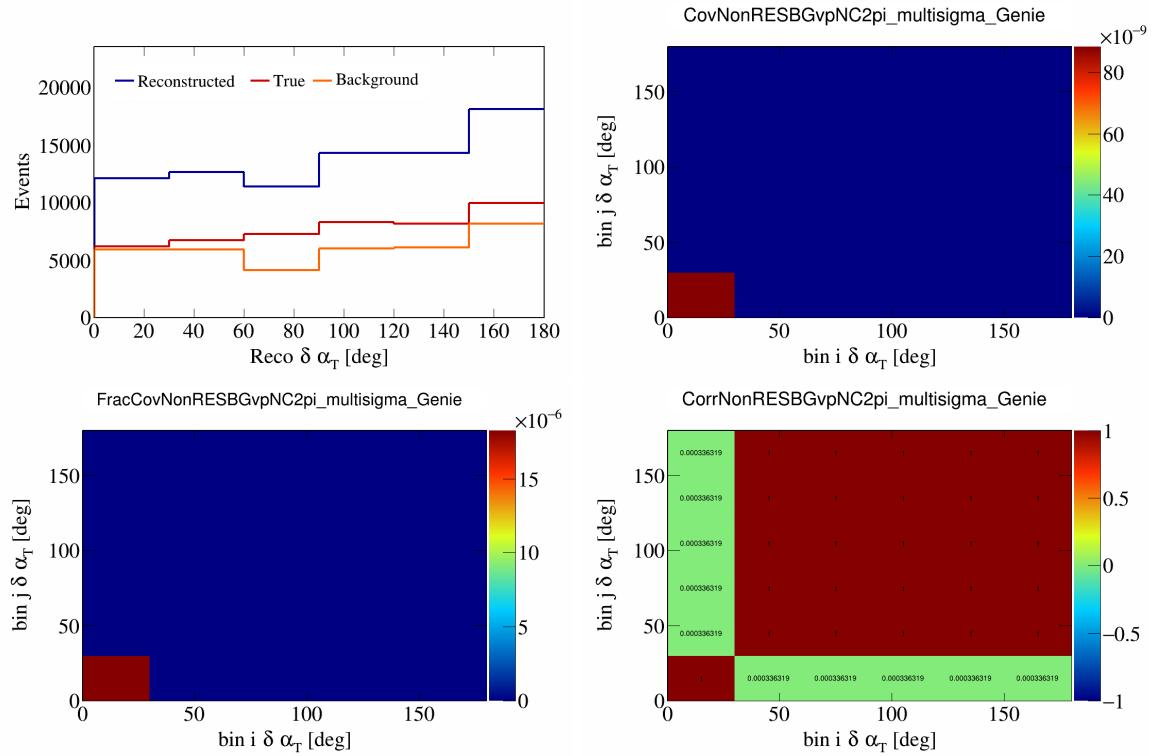


Figure 607: NonRESBGvpNC2pi variations for $\delta\alpha_T$.

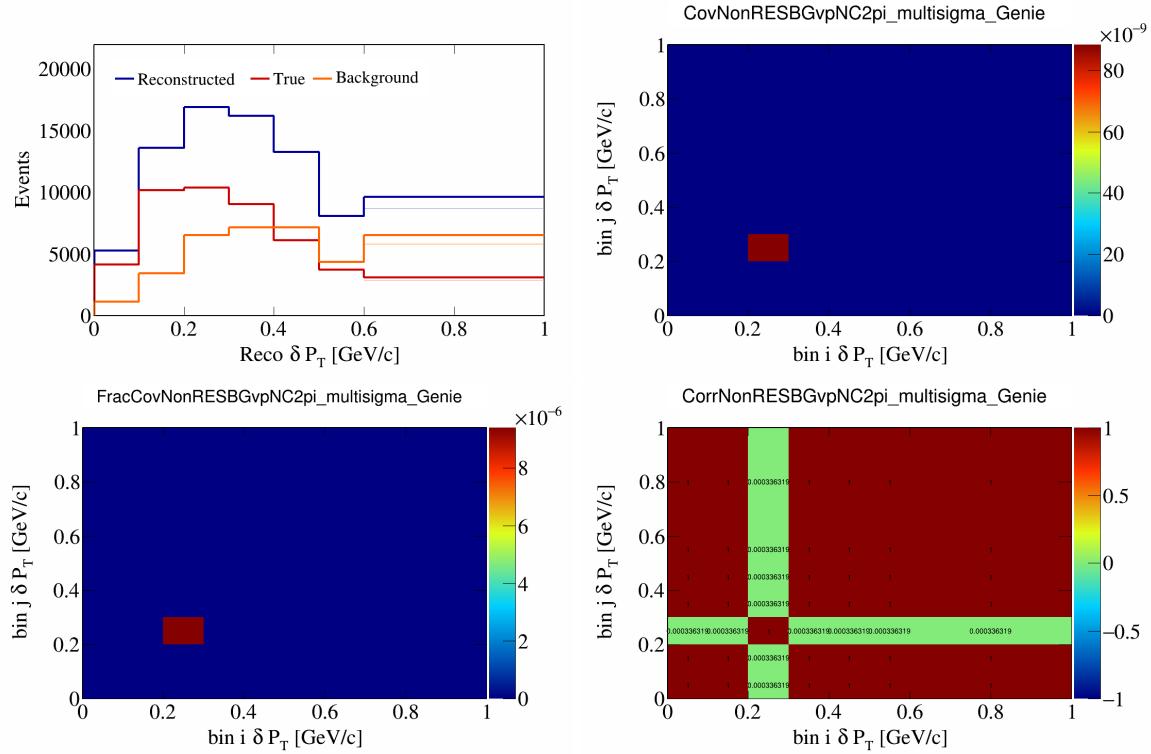


Figure 608: NonRESBGvpNC2pi variations for δP_T .

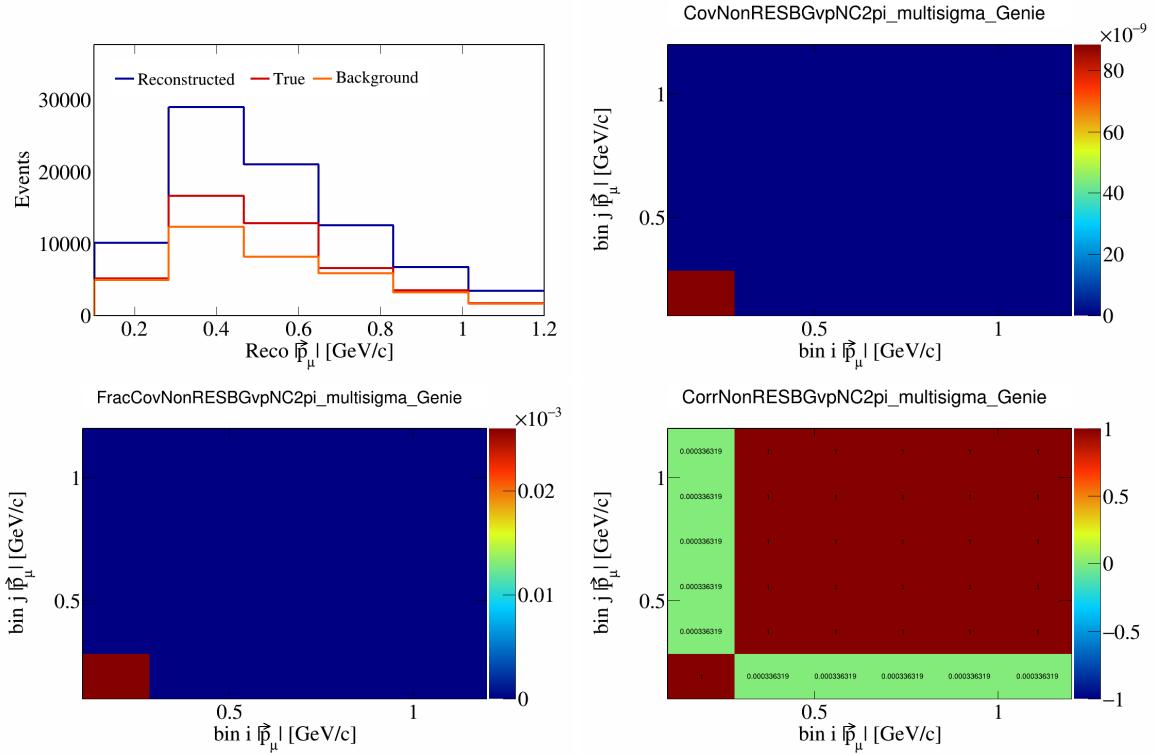


Figure 609: NonRESBGvpNC2pi variations for $|\vec{p}_\mu|$.

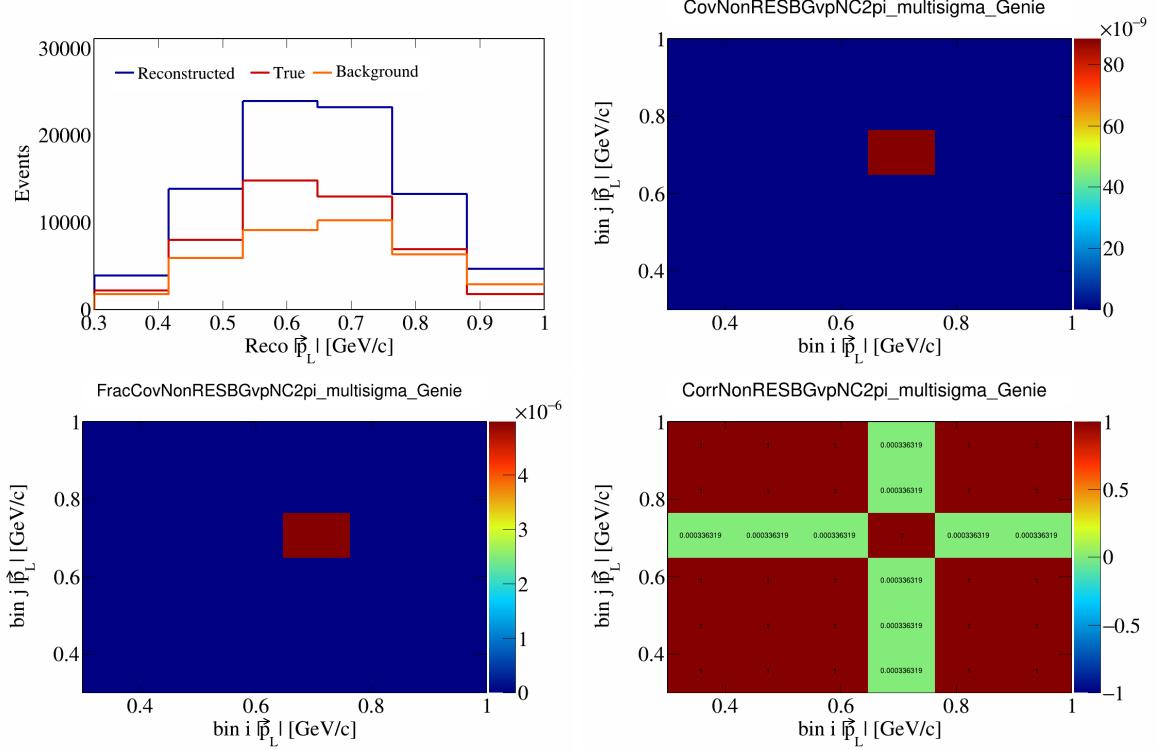


Figure 610: NonRESBGvpNC2pi variations for $|\vec{p}_L|$.

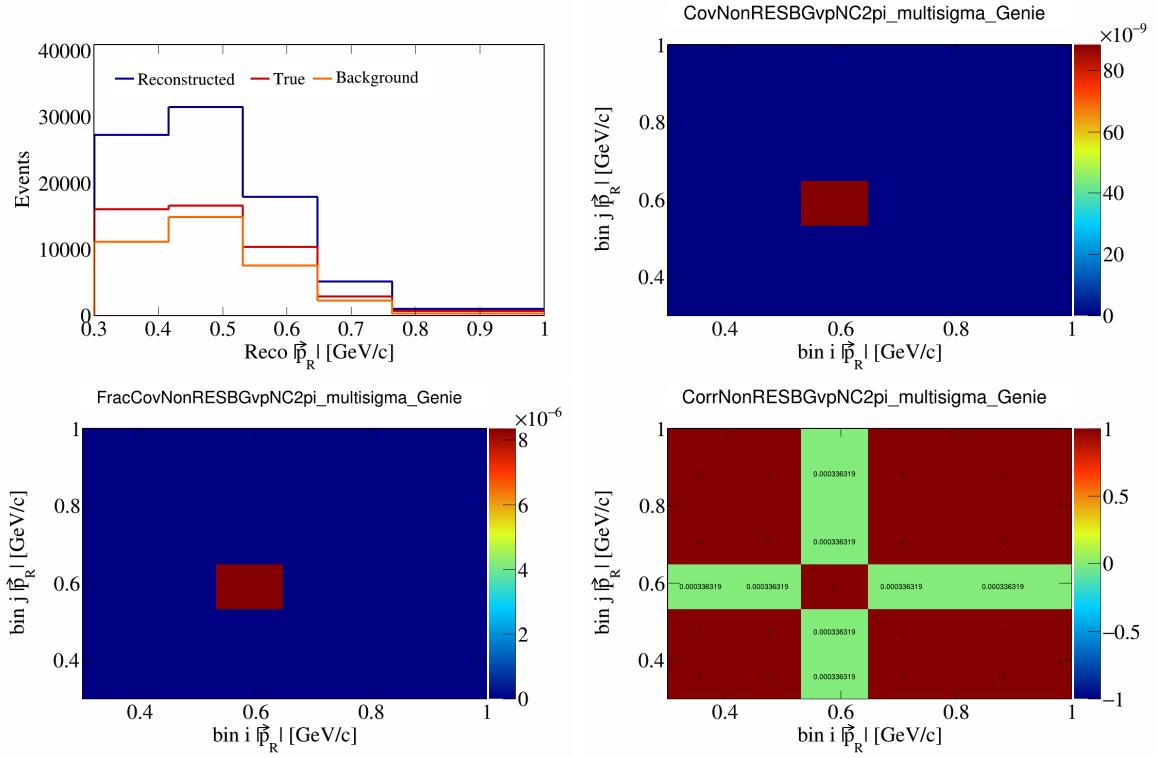


Figure 611: NonRESBGvpNC2pi variations for $|\vec{p}_R|$.

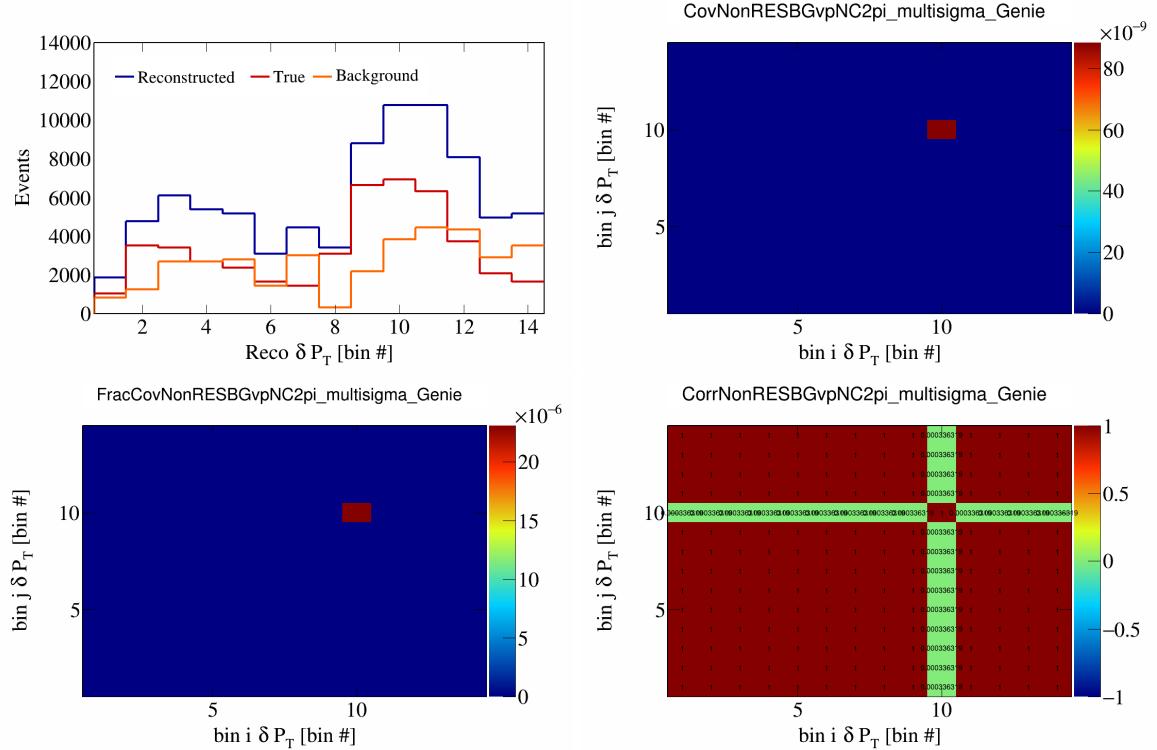


Figure 612: NonRESBGvpNC2pi variations for δP_T in $\cos(\theta_{\vec{p}_\mu})$.

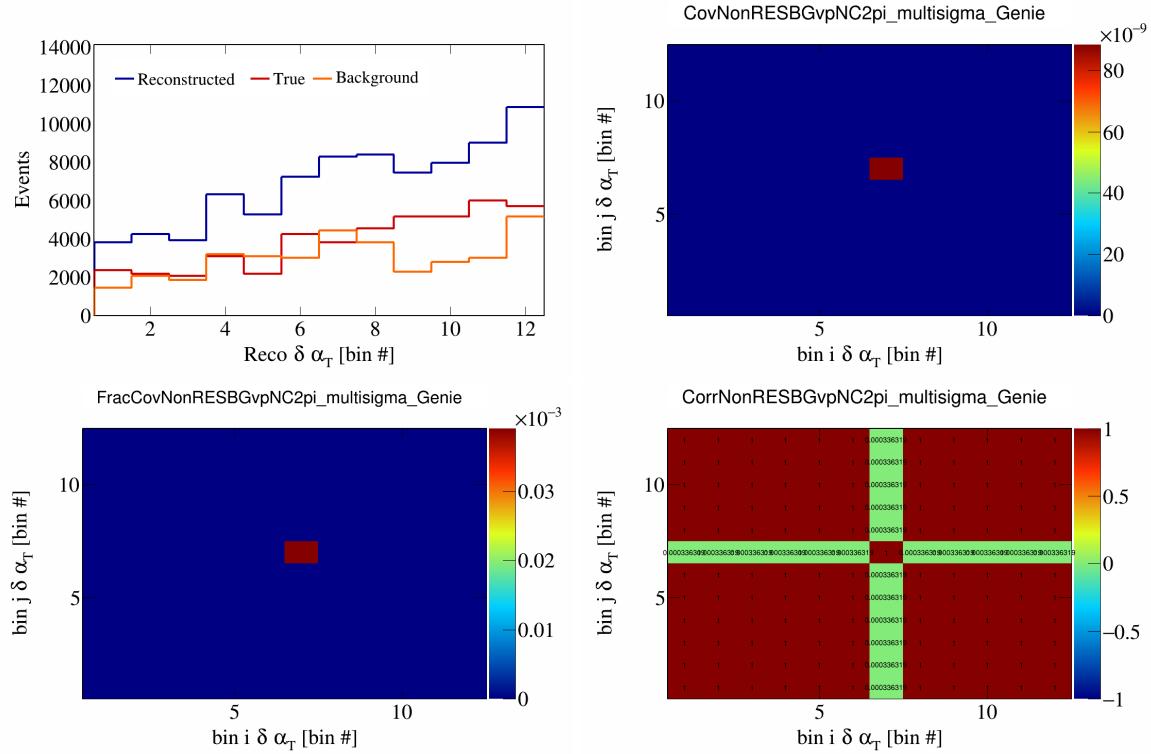


Figure 613: NonRESBGvpNC2pi variations for $\delta\alpha_T$ in $\cos(\theta_{\vec{p}_\mu})$.

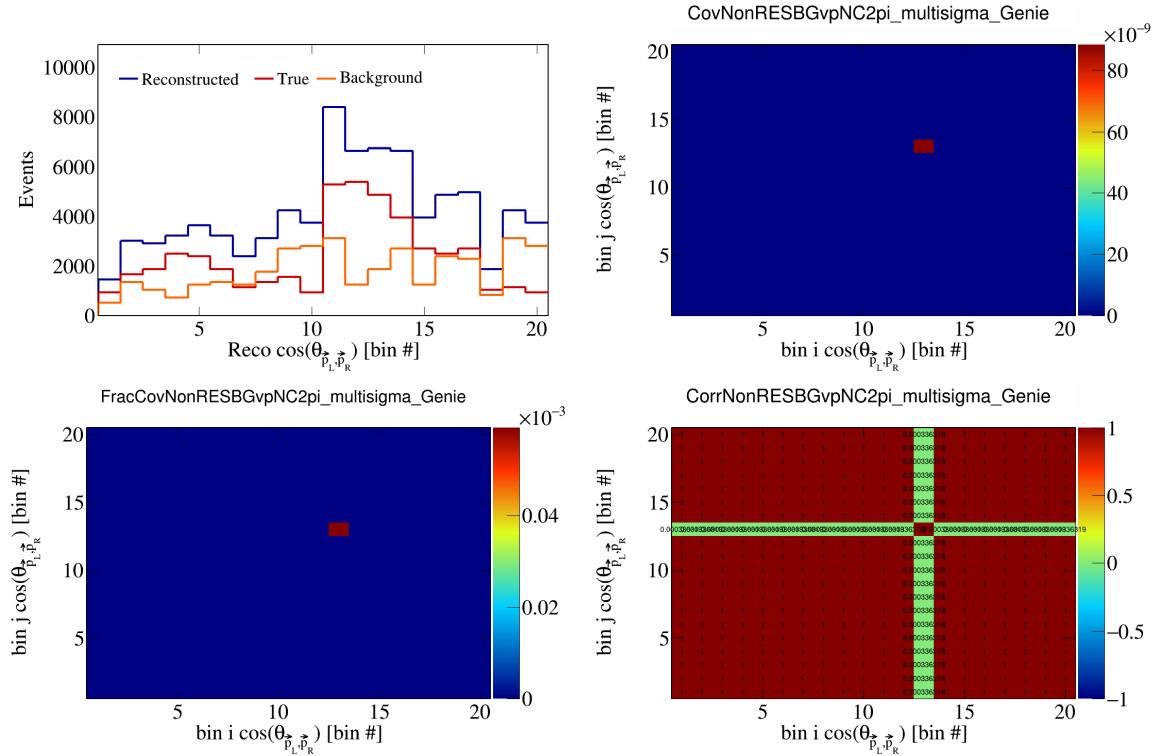


Figure 614: NonRESBGvpNC2pi variations for $\cos(\theta_{\vec{p}_L, \vec{p}_R})$ in $\cos(\theta_{\vec{p}_\mu})$.

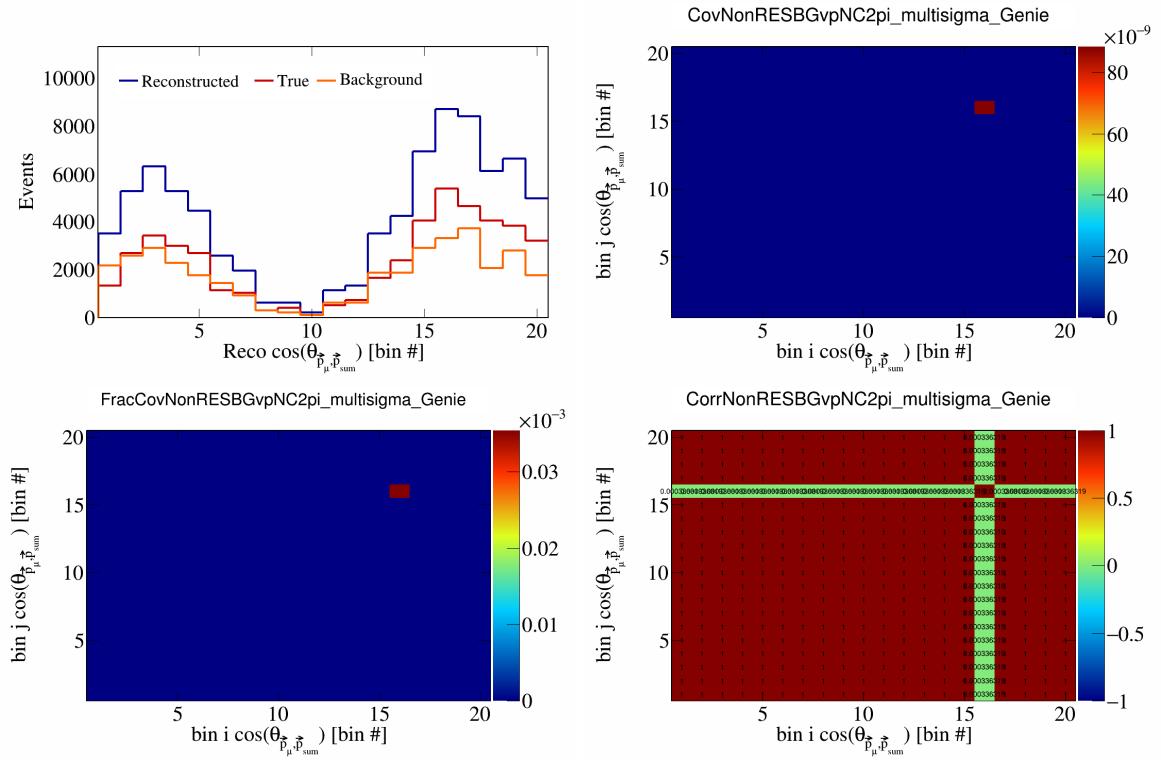


Figure 615: NonRESBGvpNC2pi variations for $\cos(\theta_{\vec{p}_\mu, \vec{p}_{\text{sum}}})$ in $\cos(\theta_{\vec{p}_\mu})$.

310 7.2 Flux systematics

311 In this appendix, the variations, covariance matrices, fractional covariance matrices, and correlation matrices
 312 are plotted for all of the flux systematics and variables.

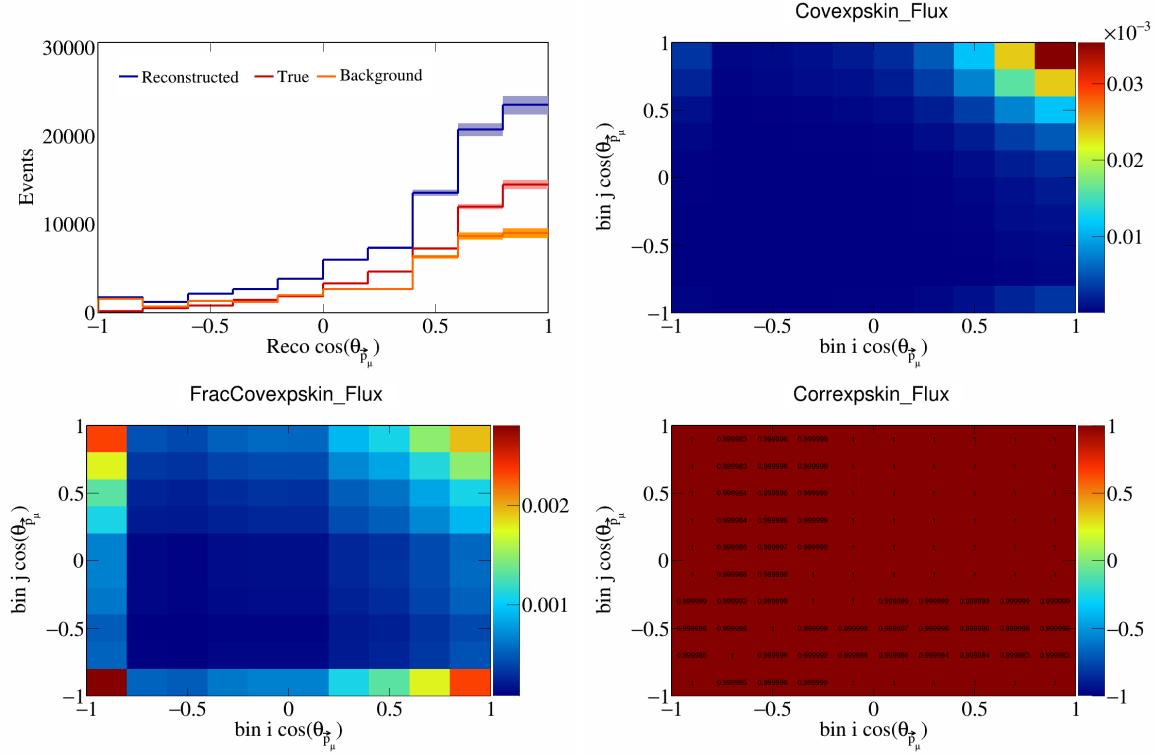


Figure 616: Epskin variations for $\cos(\theta_{\vec{p}_\mu})$.

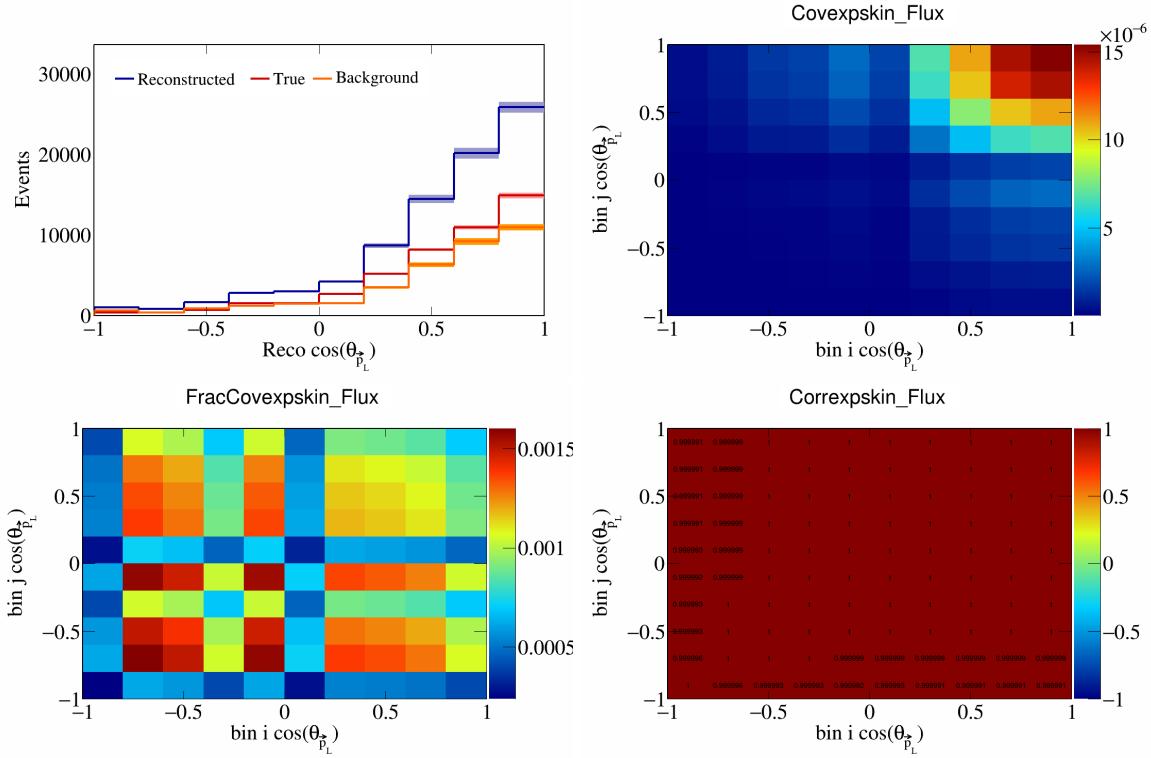


Figure 617: ExpSkin variations for $\cos(\theta_{\vec{p}_L})$.

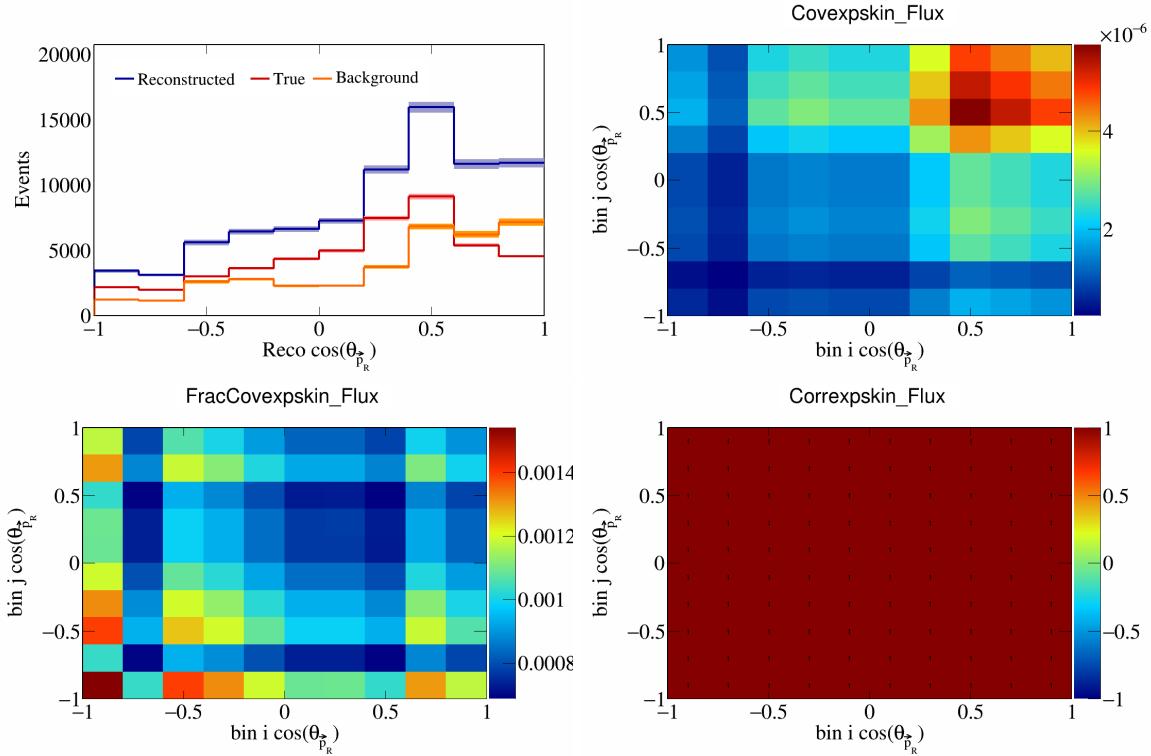


Figure 618: ExpSkin variations for $\cos(\theta_{\vec{p}_R})$.

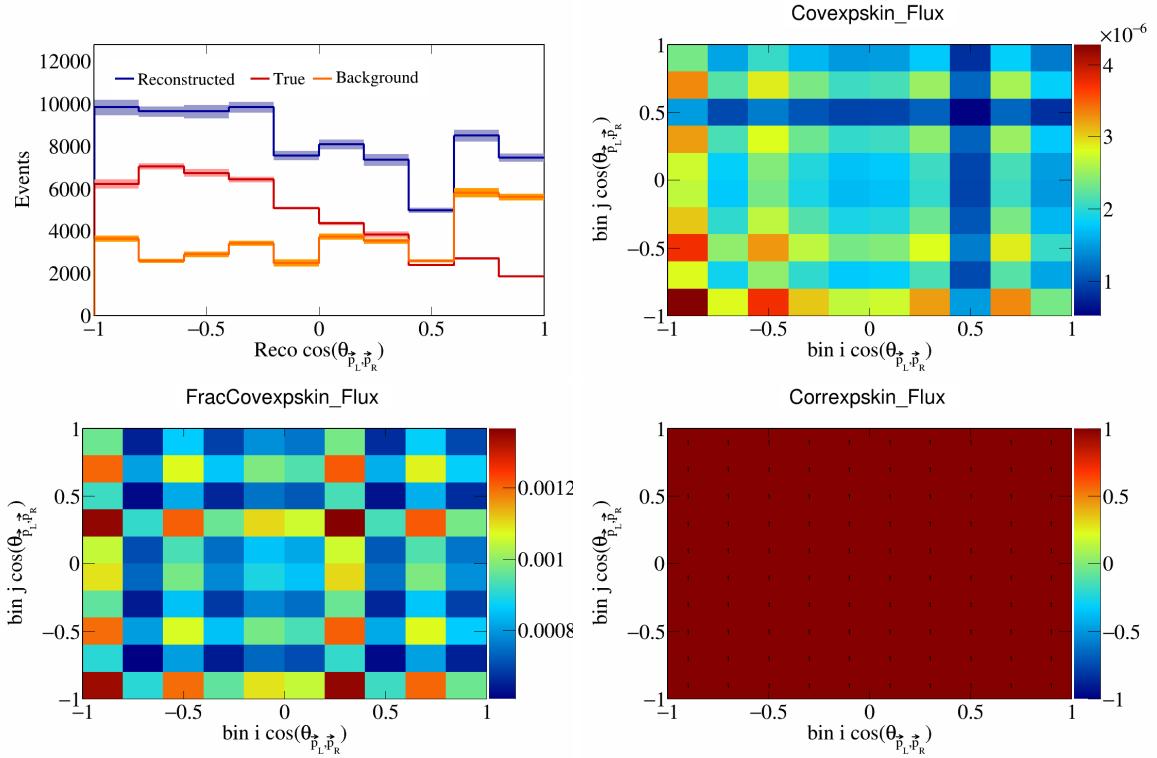


Figure 619: Exp skin variations for $\cos(\theta_{\vec{p}_L, \vec{p}_R})$.

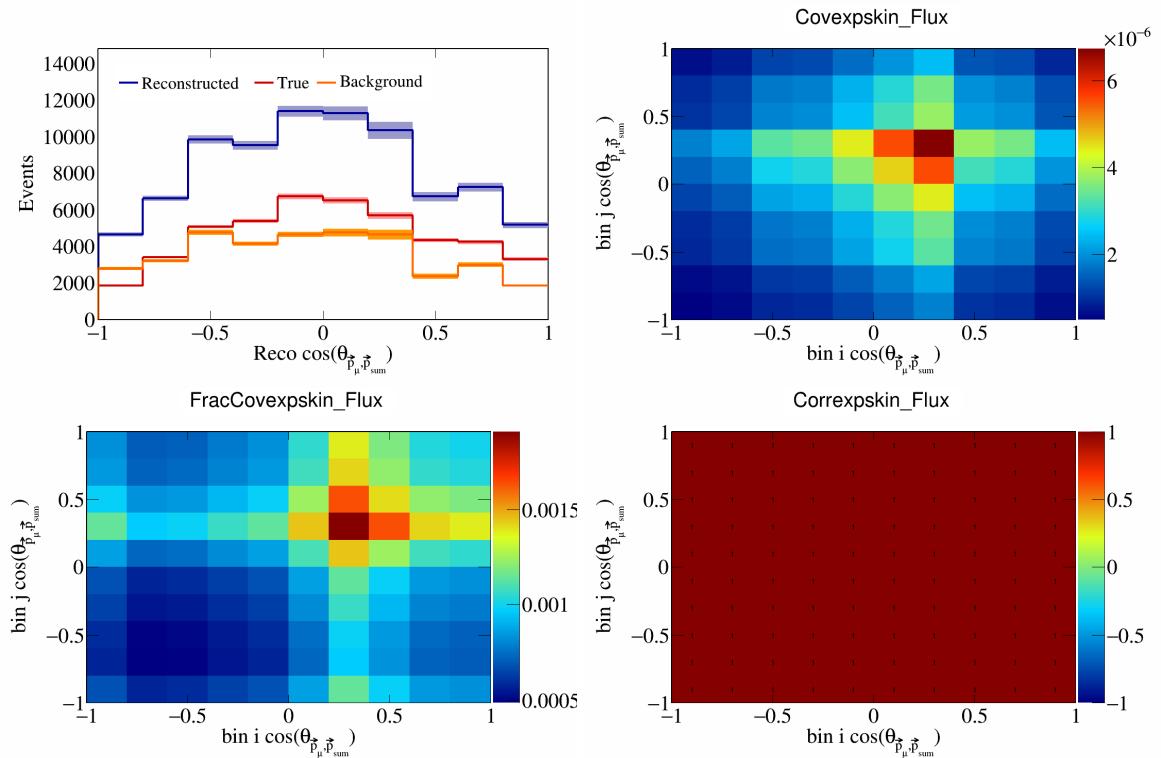


Figure 620: Exp skin variations for $\cos(\theta_{\vec{p}_\mu, \vec{p}_{\text{sum}}})$.

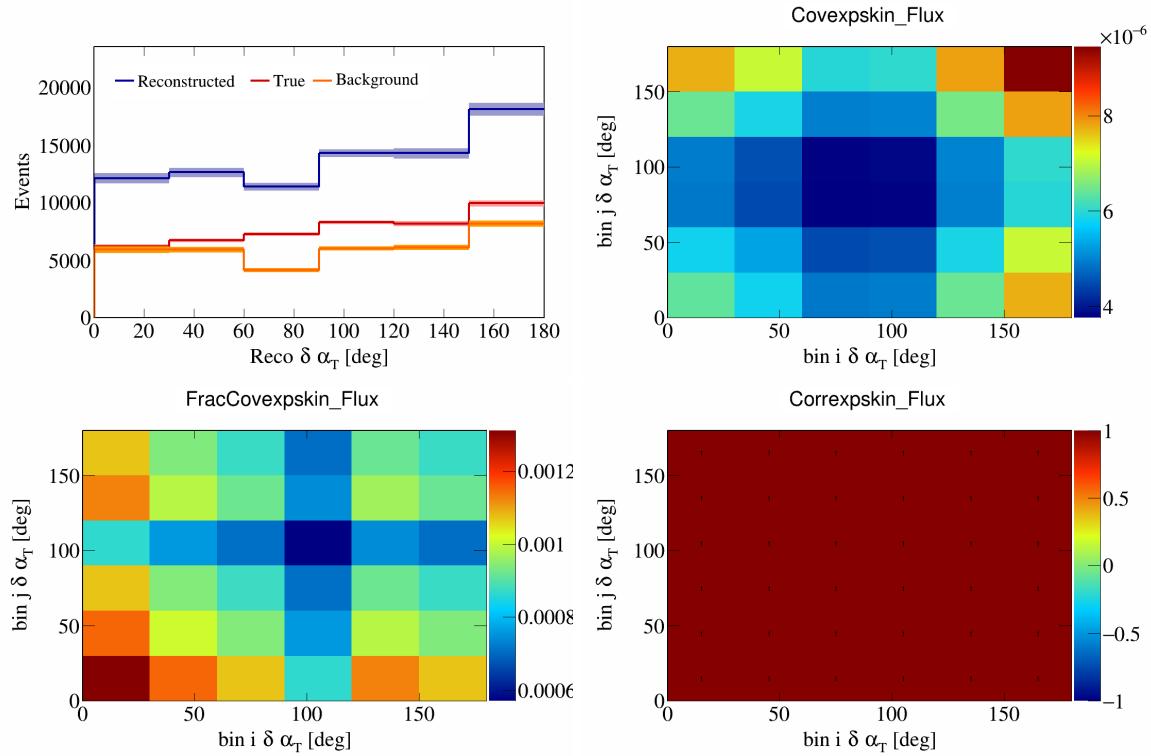


Figure 621: Expskin variations for $\delta \alpha_T$.

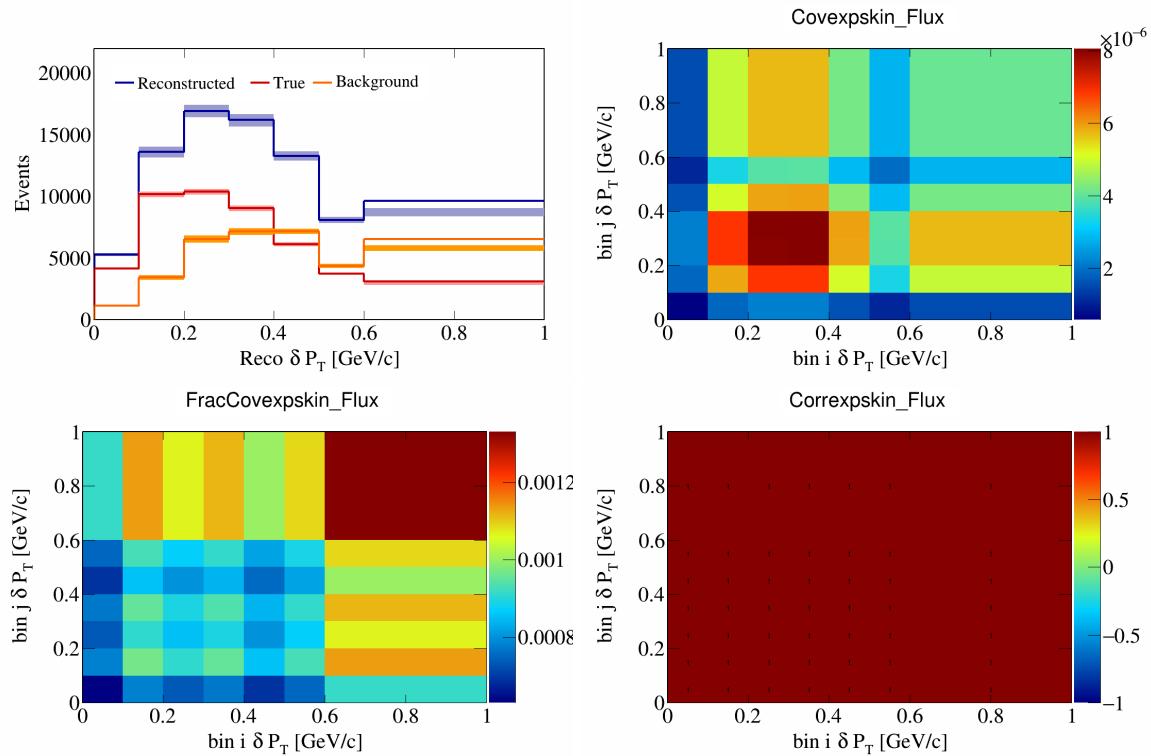


Figure 622: Expskin variations for δP_T .

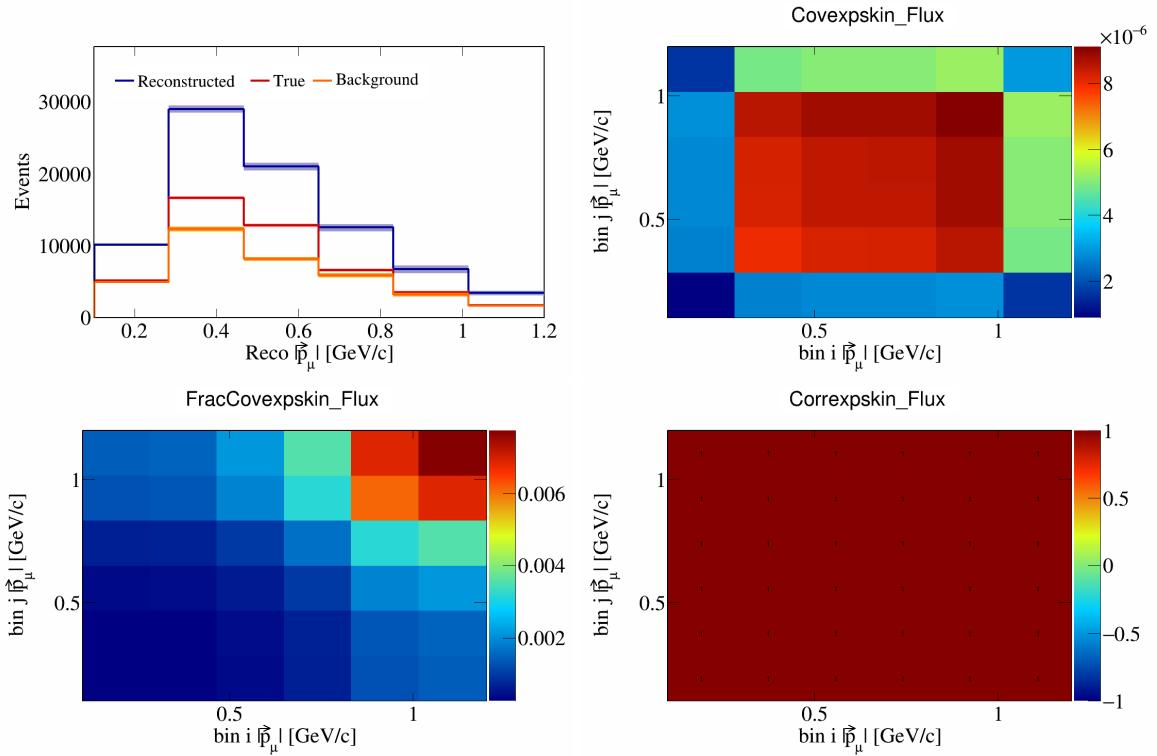


Figure 623: Epskin variations for $|\vec{p}_\mu|$.

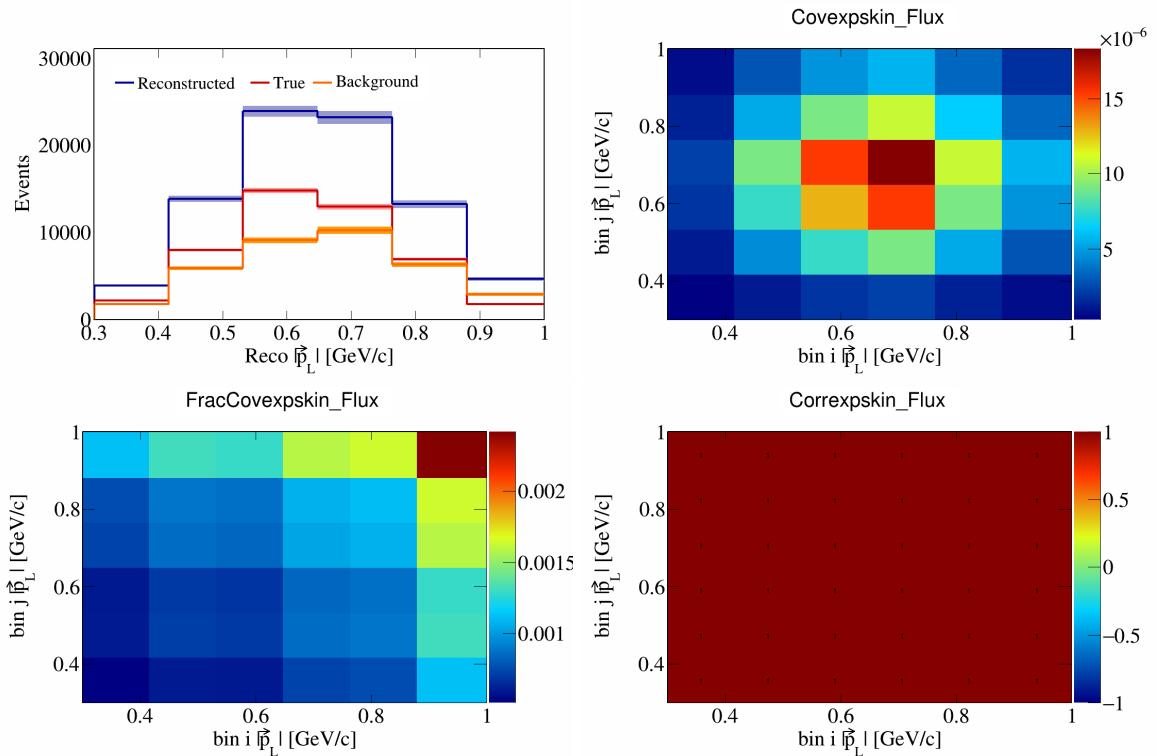


Figure 624: Epskin variations for $|\vec{p}_L|$.

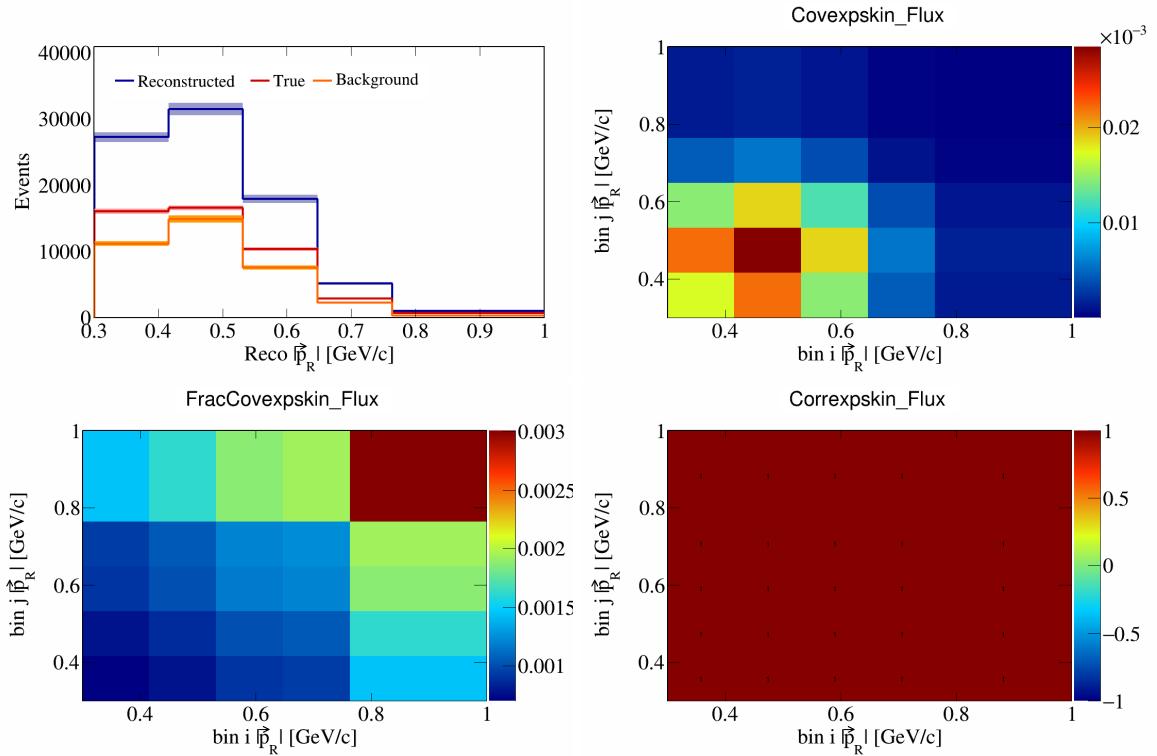


Figure 625: Expskin variations for $|\vec{p}_R|$.

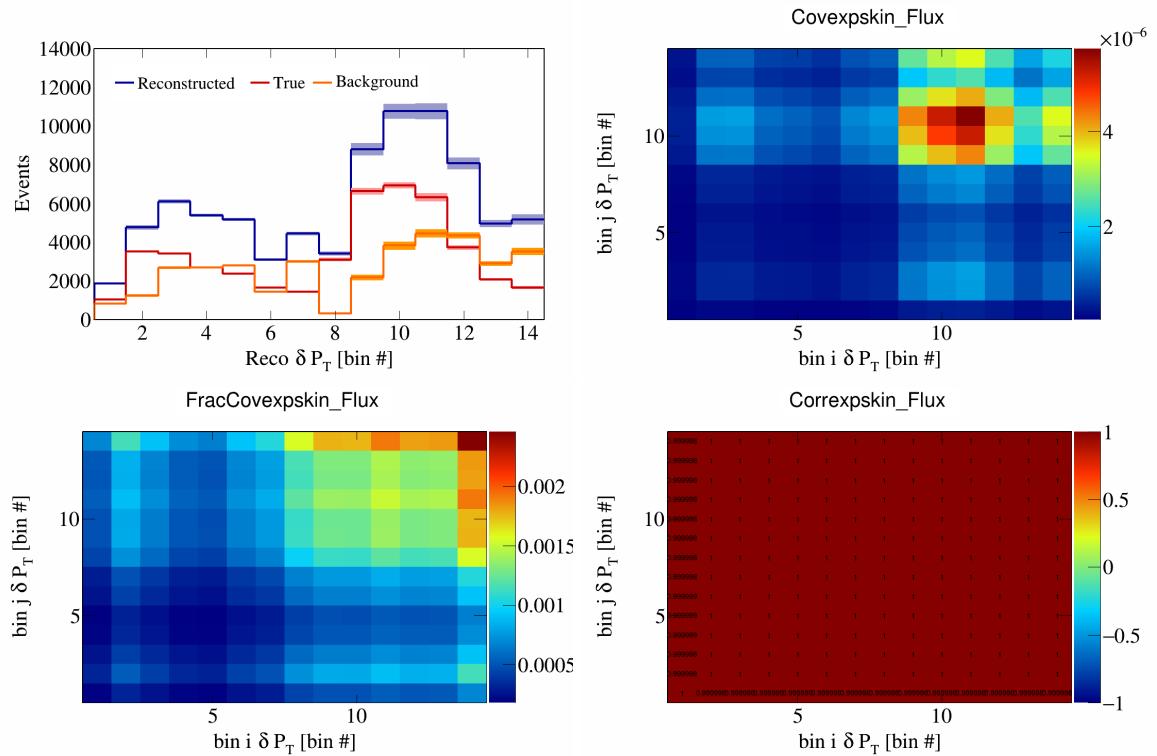


Figure 626: Expskin variations for δP_T in $\cos(\theta_{\vec{p}_\mu})$.

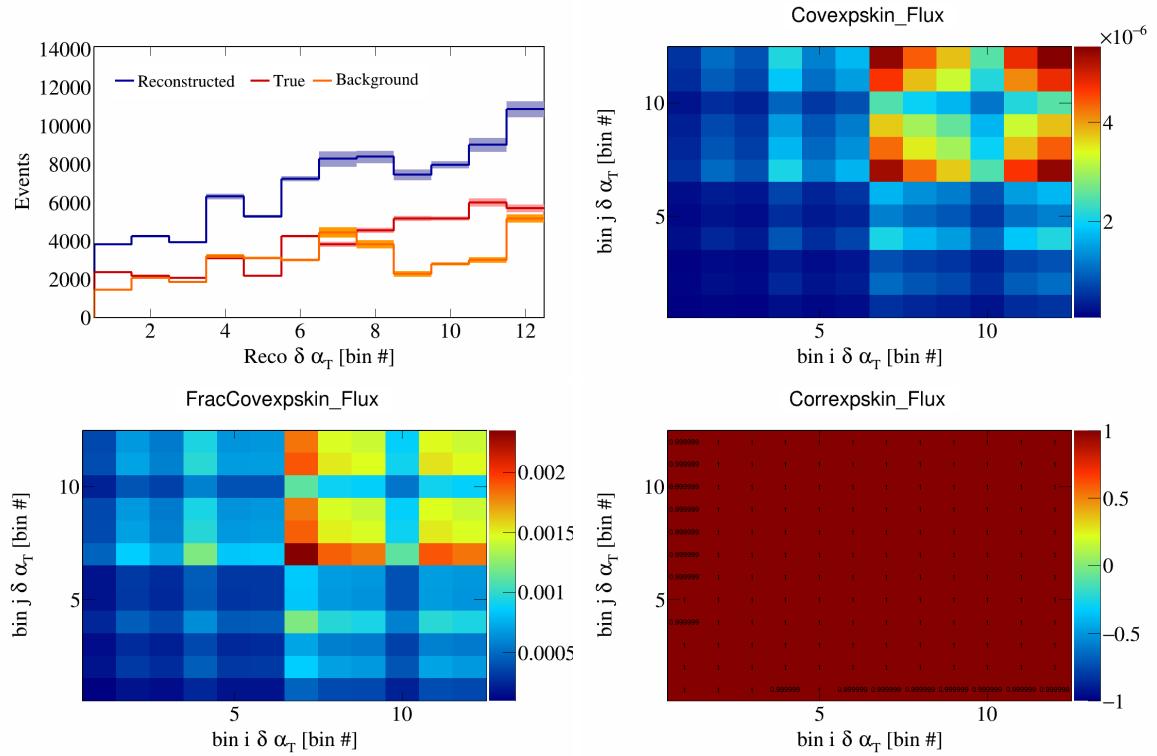


Figure 627: Expskin variations for $\delta\alpha_T$ in $\cos(\theta_{\vec{p}_\mu})$.

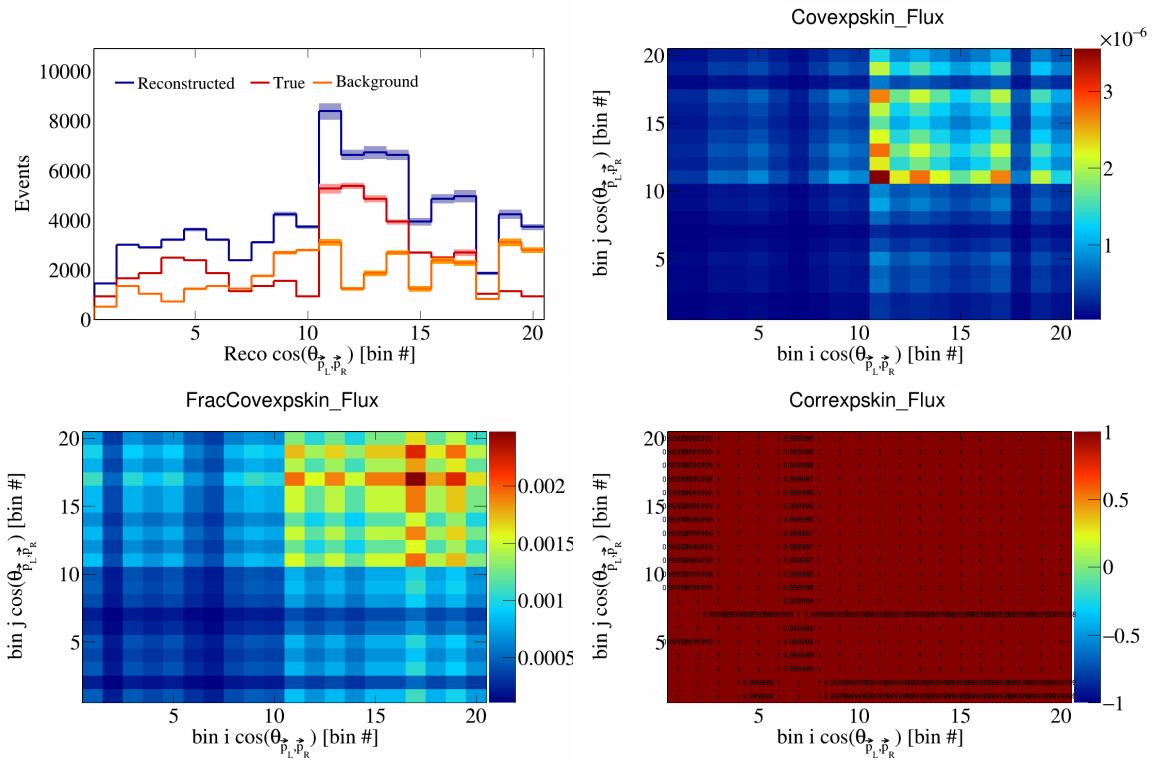


Figure 628: Expskin variations for $\cos(\theta_{\vec{p}_L, \vec{p}_R})$ in $\cos(\theta_{\vec{p}_\mu})$.

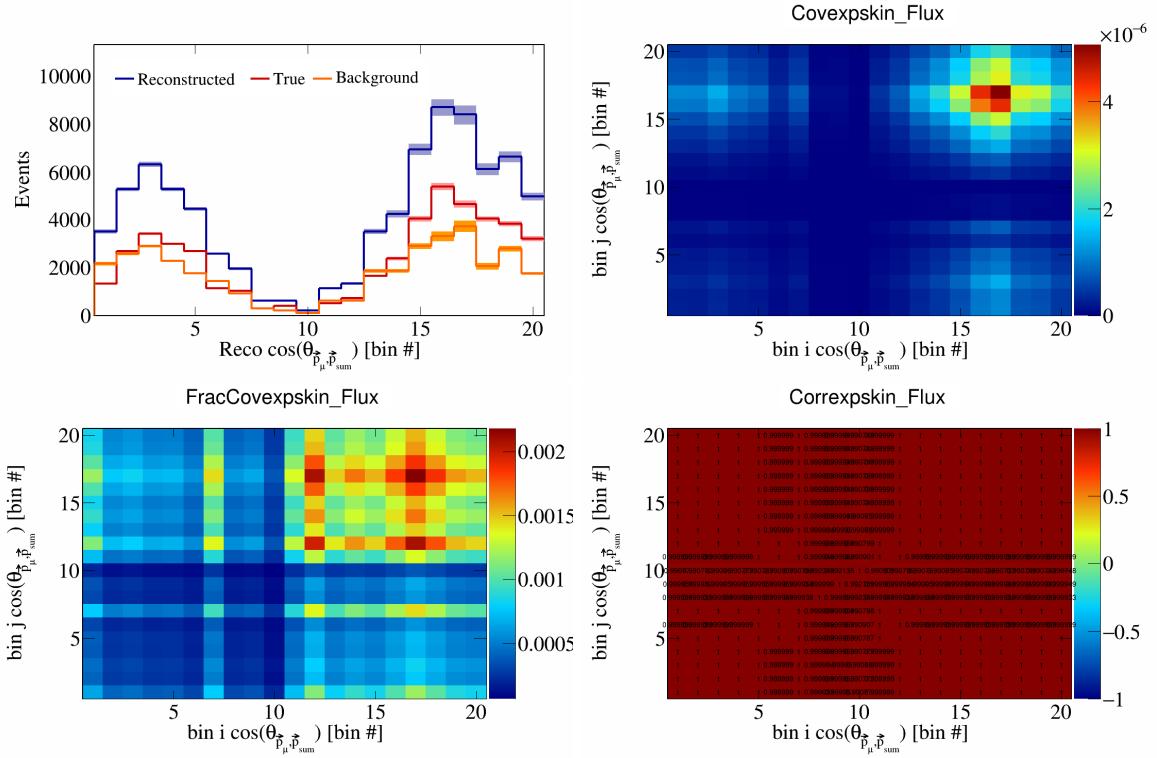


Figure 629: Expskin variations for $\cos(\theta_{\vec{p}_\mu, \vec{p}_{\text{sum}}})$ in $\cos(\theta_{\vec{p}_\mu})$.

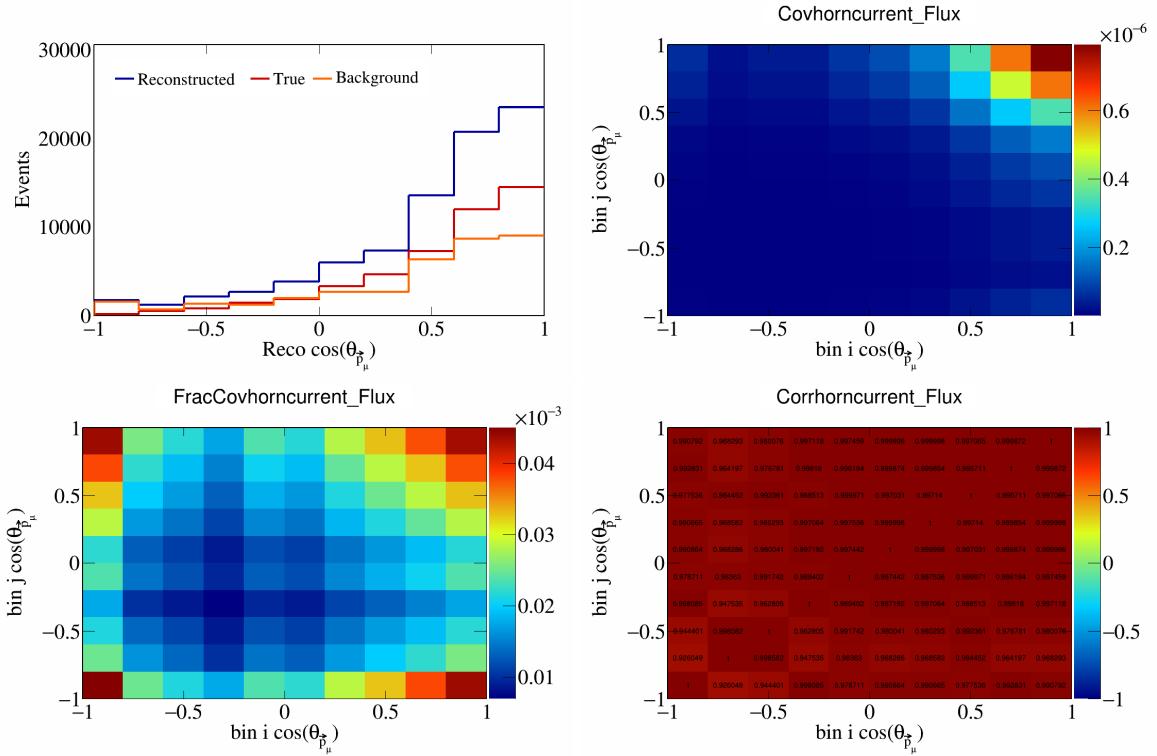


Figure 630: HornCurrent variations for $\cos(\theta_{\vec{p}_\mu})$.

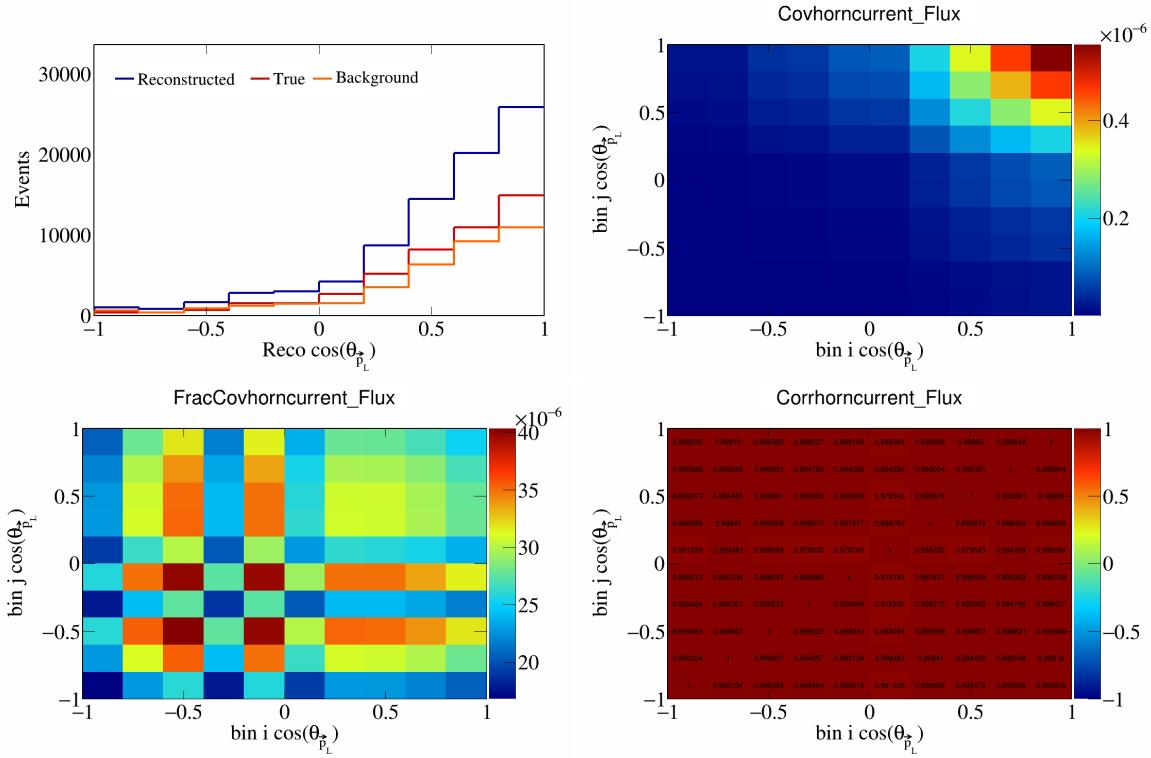


Figure 631: HornCurrent variations for $\cos(\theta_{\vec{p}_L})$.

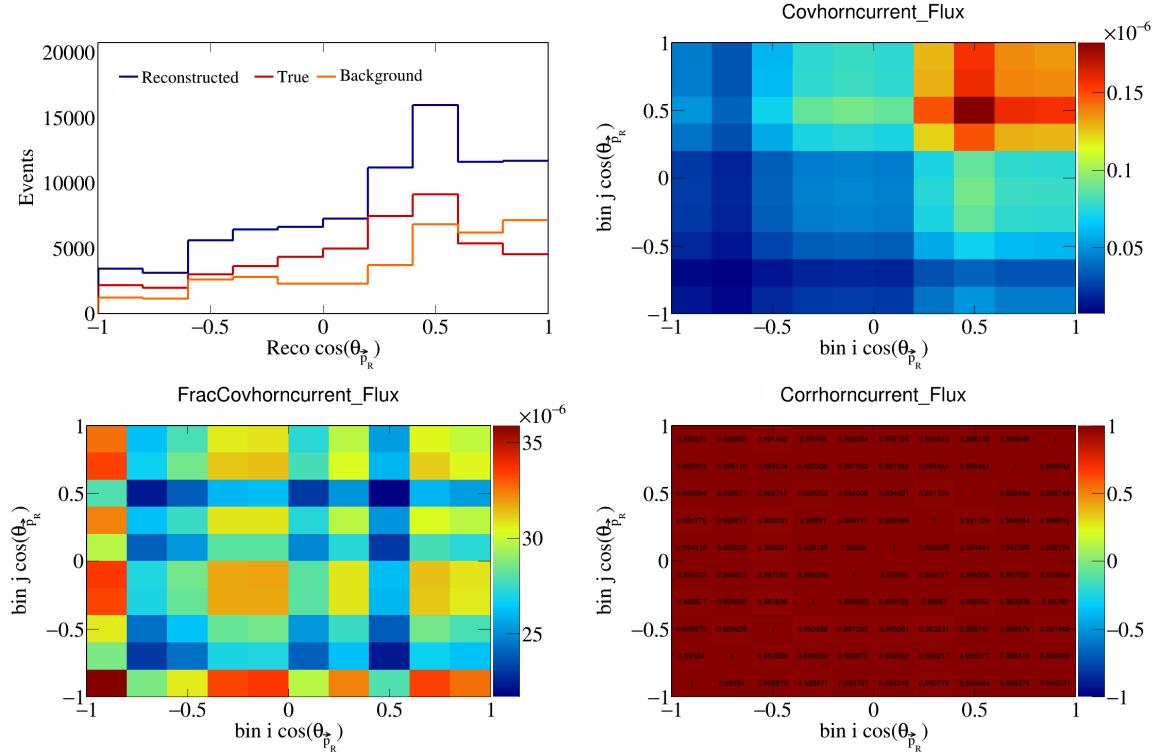


Figure 632: HornCurrent variations for $\cos(\theta_{\vec{p}_R})$.

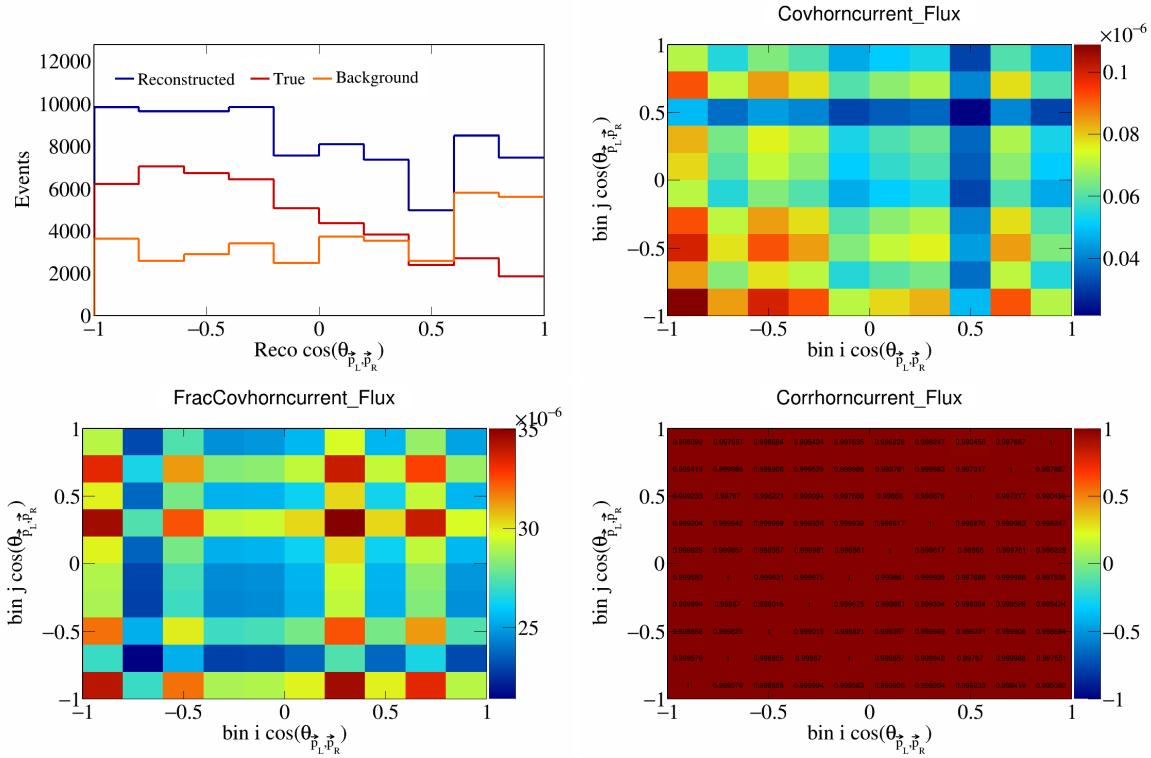


Figure 633: HornCurrent variations for $\cos(\theta_{\vec{p}_L, \vec{p}_R})$.

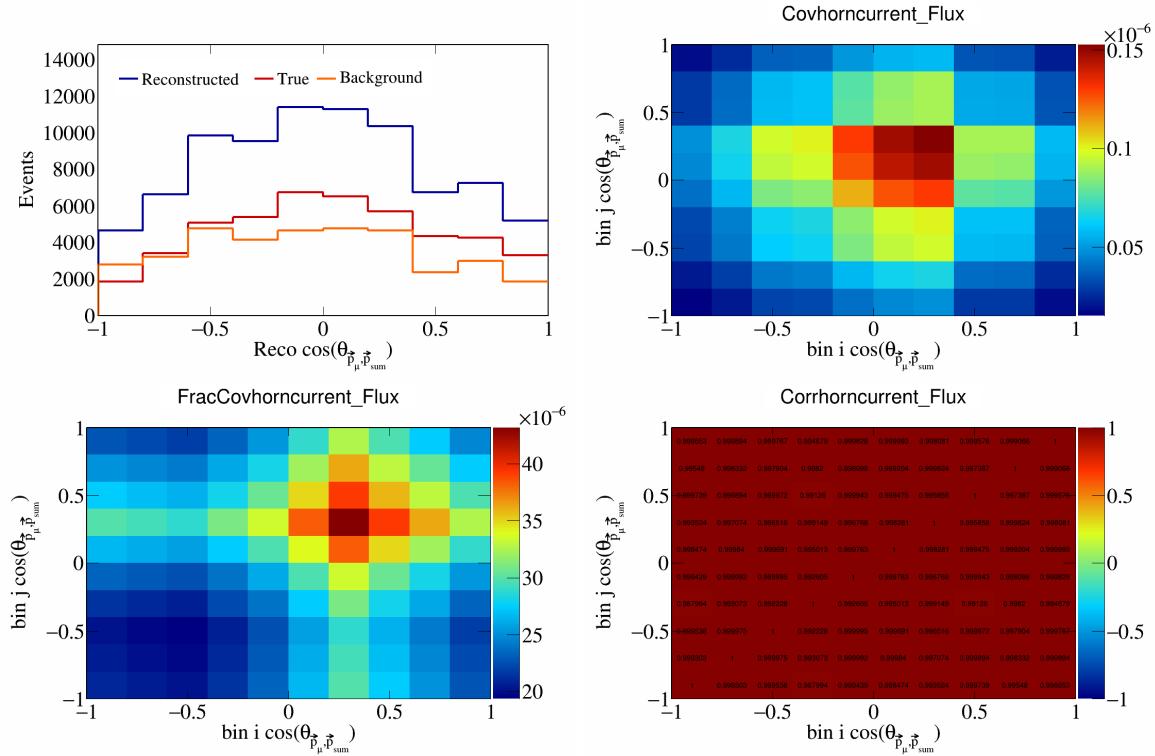


Figure 634: HornCurrent variations for $\cos(\theta_{\vec{p}_\mu, \vec{p}_{\text{sum}}})$.

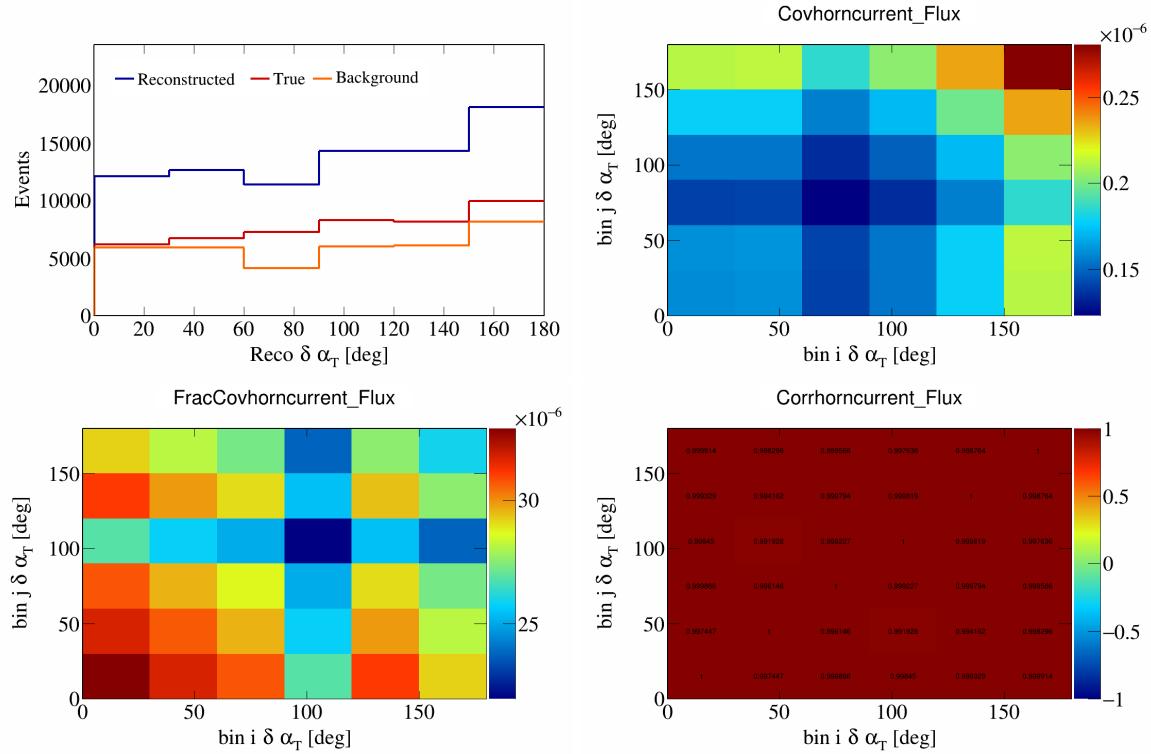


Figure 635: HornCurrent variations for $\delta\alpha_T$.

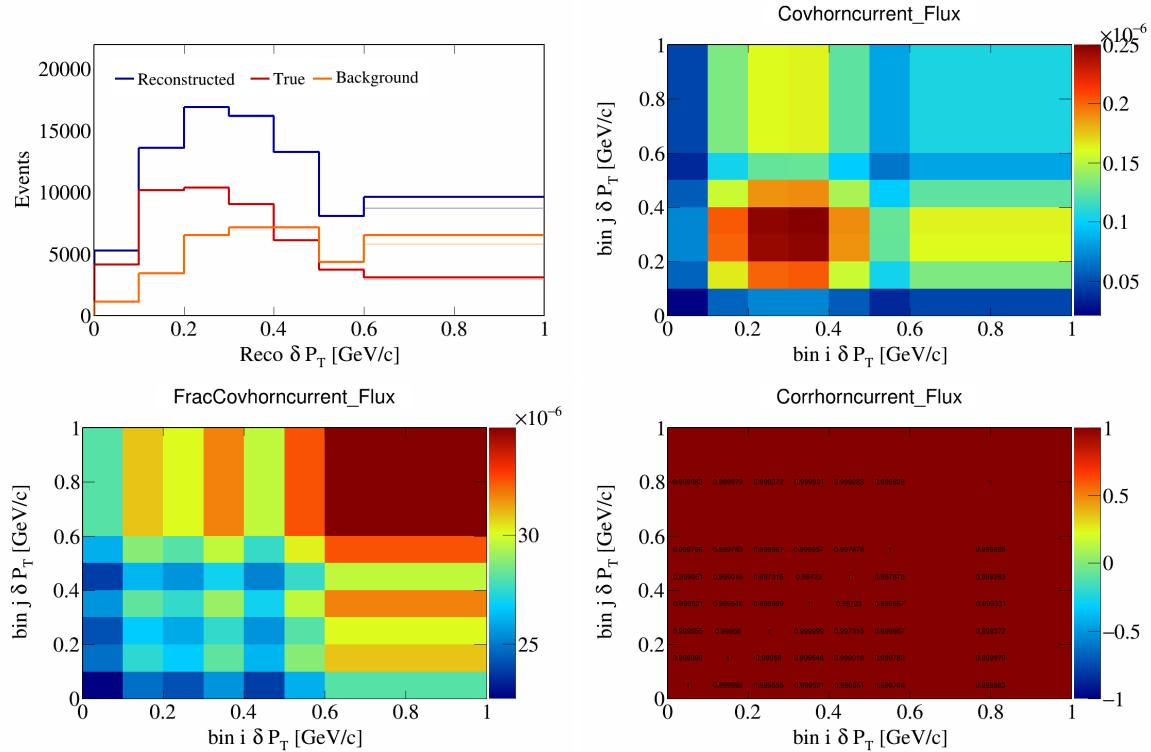


Figure 636: HornCurrent variations for δP_T .

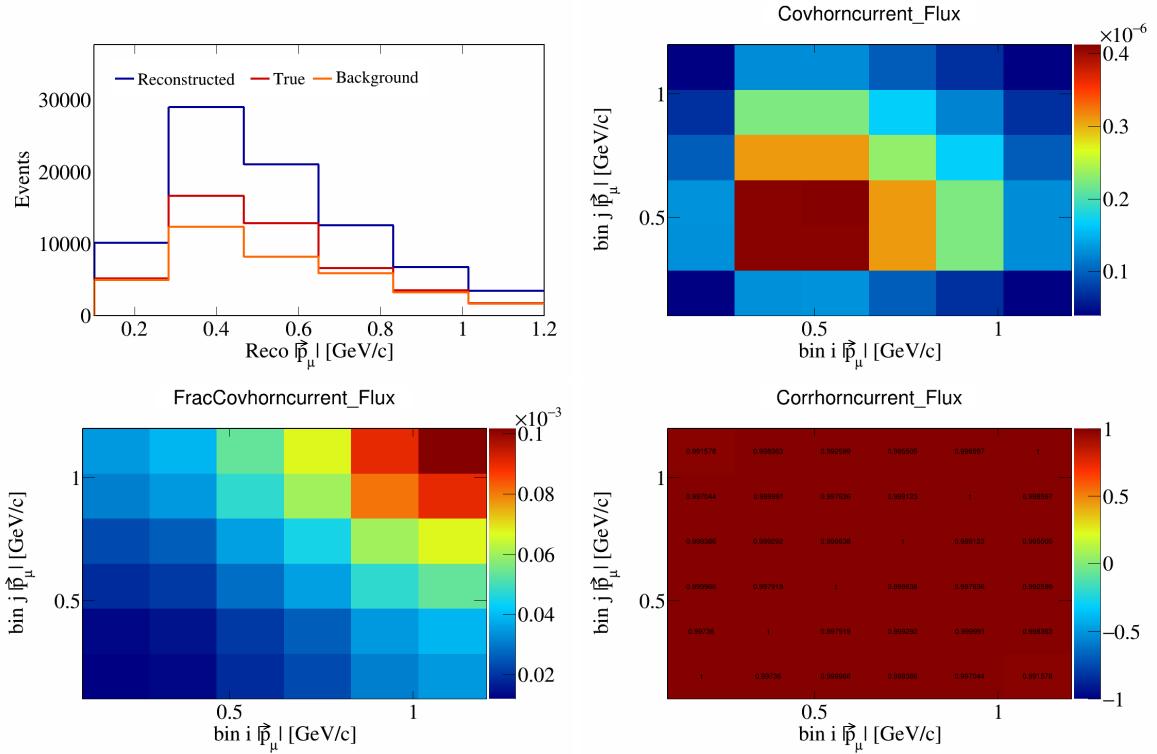


Figure 637: HornCurrent variations for $|\vec{p}_\mu|$.

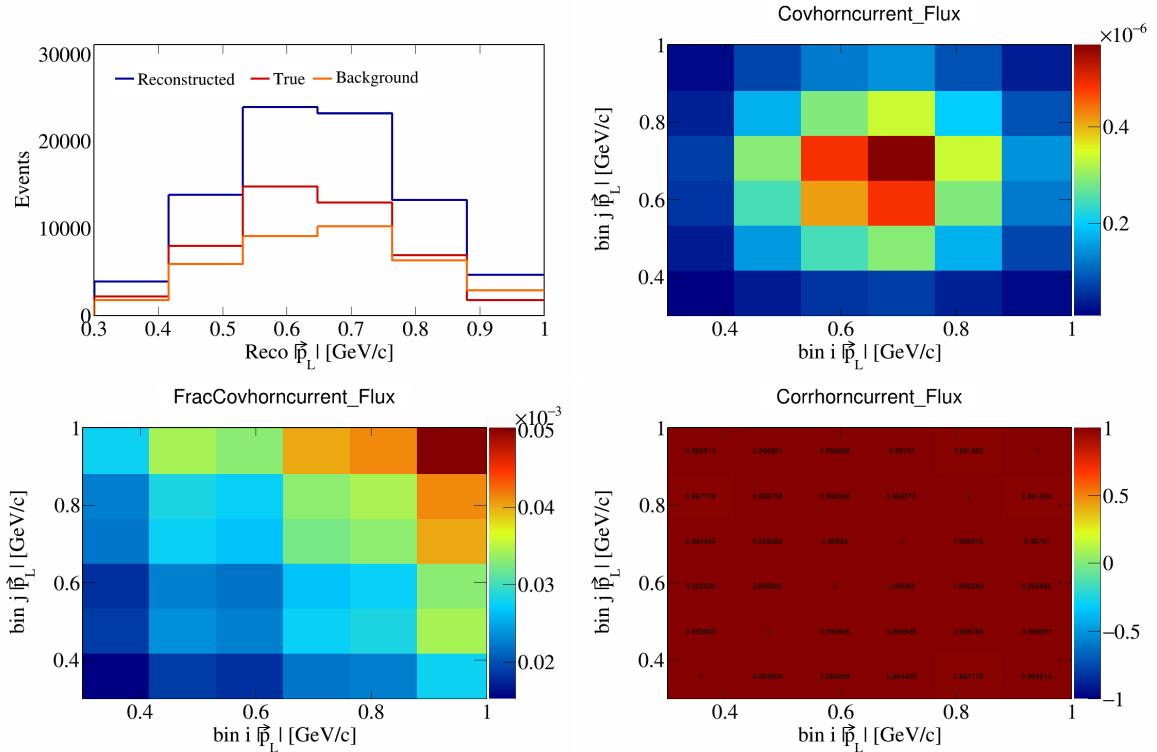


Figure 638: HornCurrent variations for $|\vec{p}_L|$.

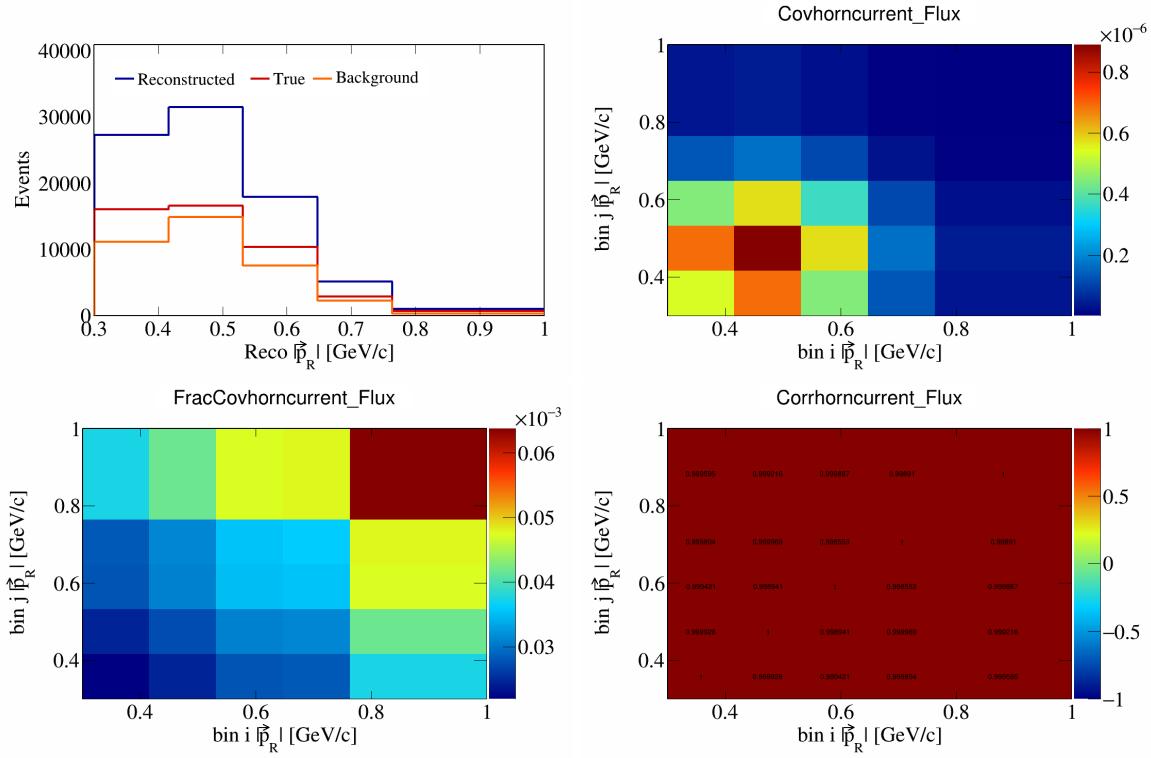


Figure 639: HornCurrent variations for $|\vec{p}_R|$.

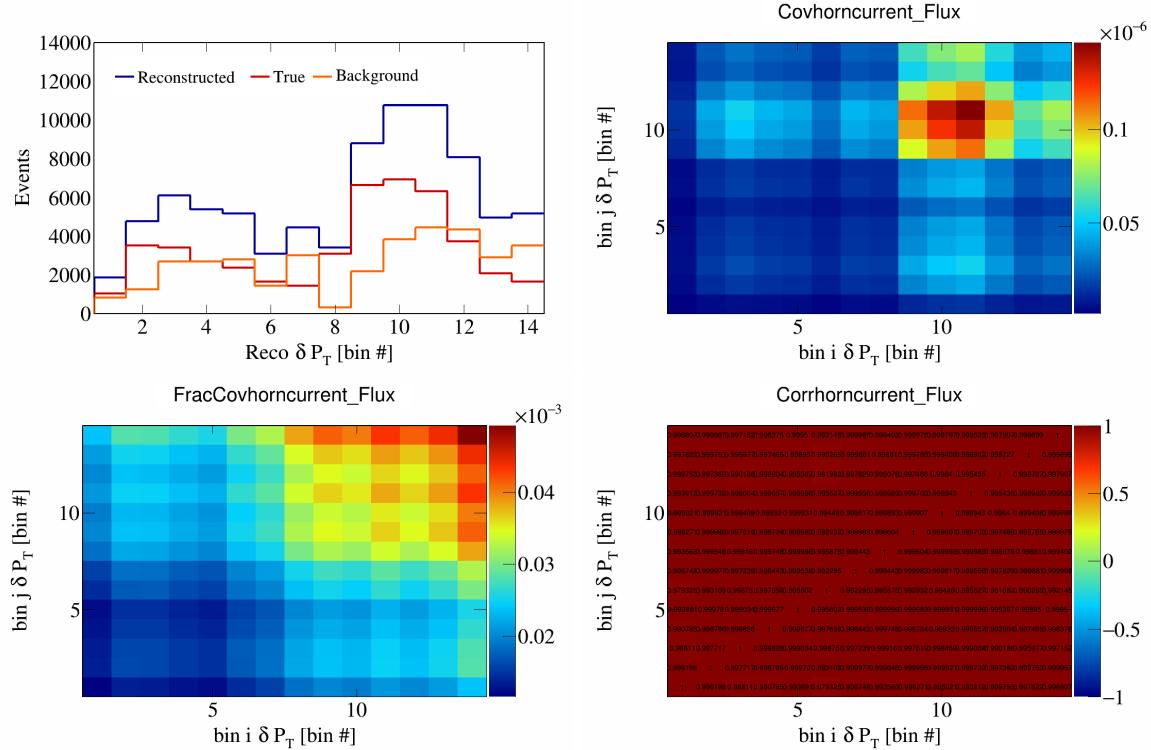


Figure 640: HornCurrent variations for δP_T in $\cos(\theta_{\vec{p}_\mu})$.

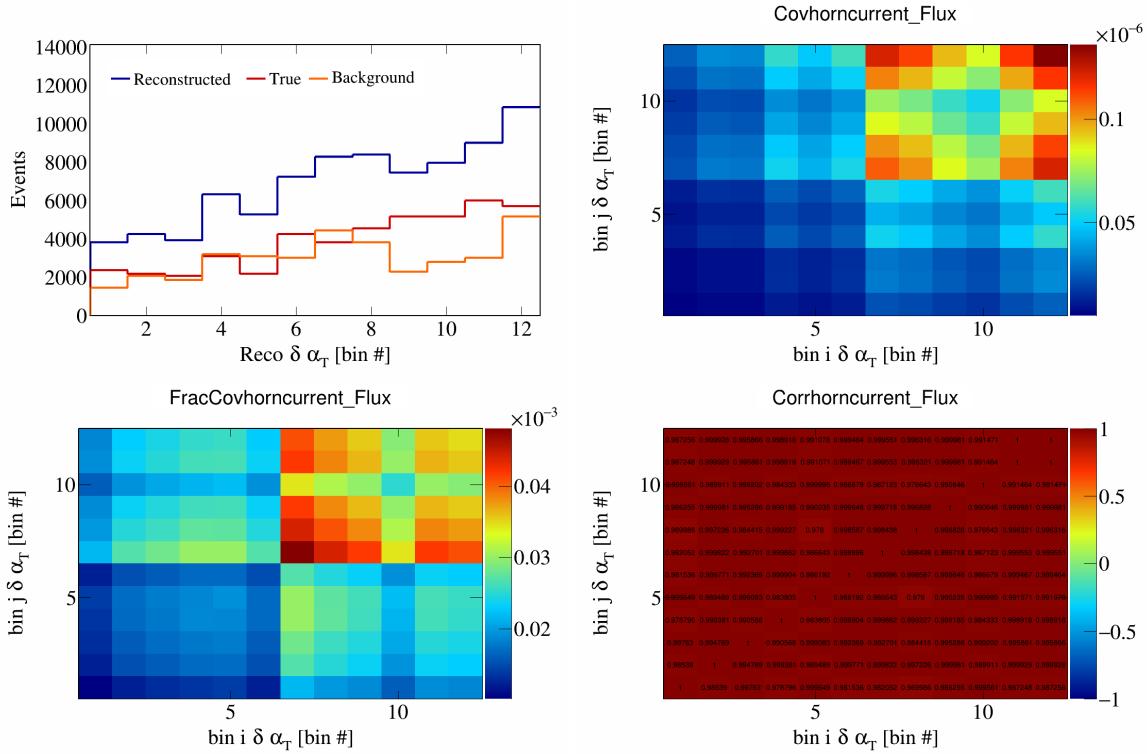


Figure 641: HornCurrent variations for $\delta \alpha_T$ in $\cos(\theta_{\vec{p}_\mu})$.

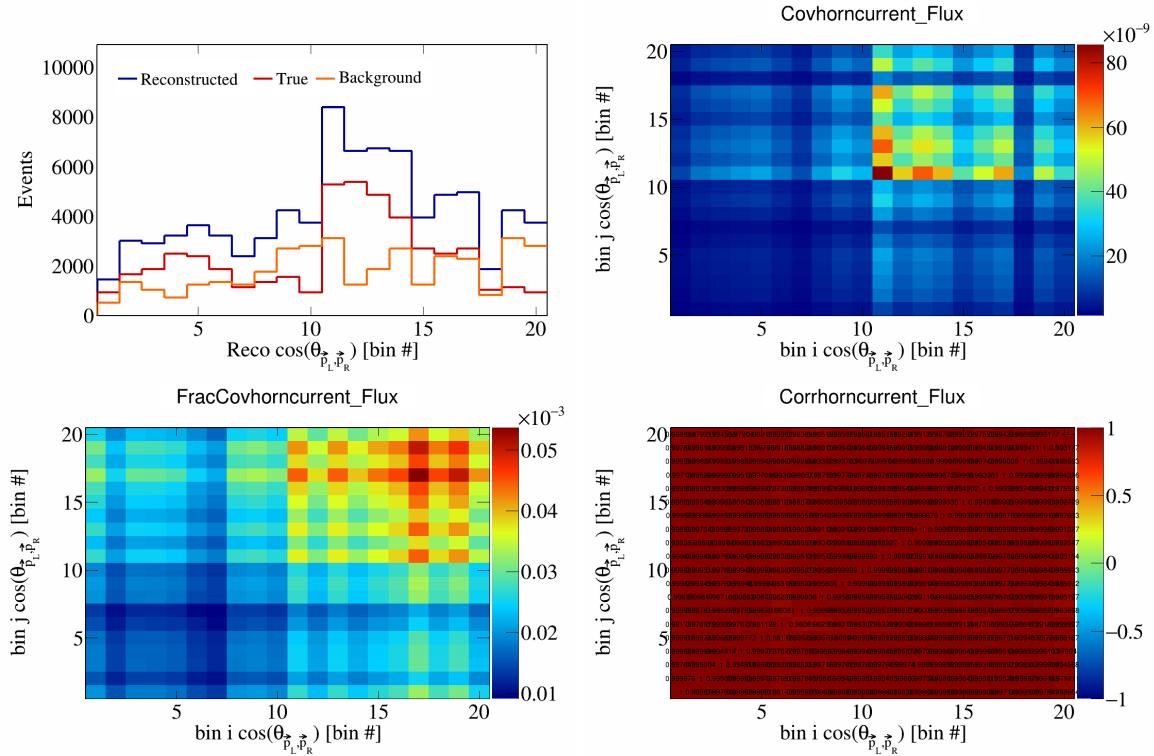


Figure 642: HornCurrent variations for $\cos(\theta_{\vec{p}_L, \vec{p}_R})$ in $\cos(\theta_{\vec{p}_\mu})$.

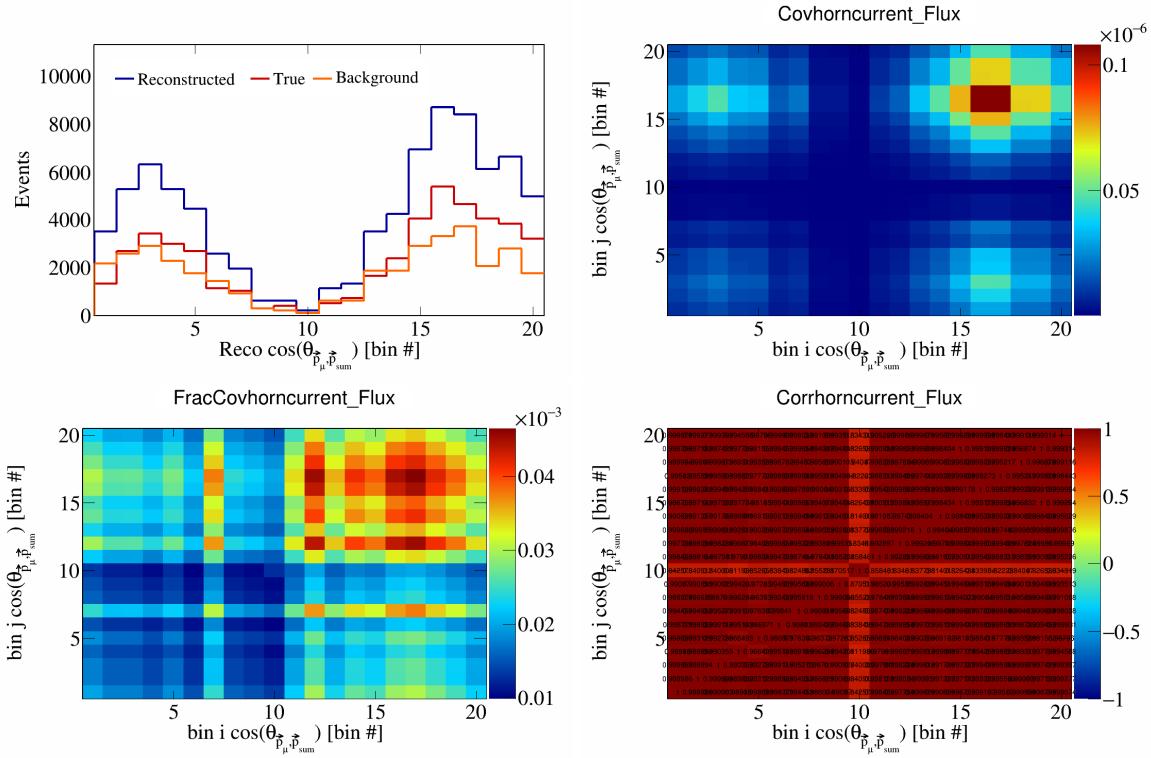


Figure 643: HornCurrent variations for $\cos(\theta_{\vec{p}_\mu} \cdot \vec{p}_{\text{sum}})$ in $\cos(\theta_{\vec{p}_\mu})$.

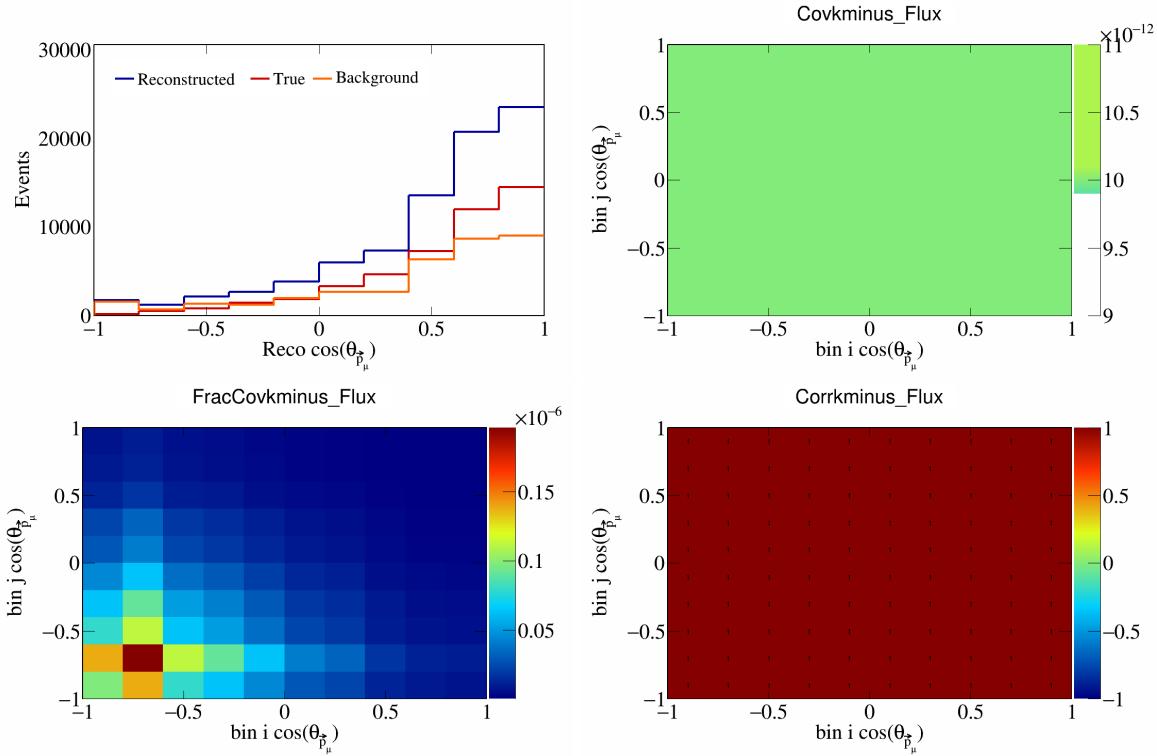


Figure 644: KMinus variations for $\cos(\theta_{\vec{p}_\mu})$.

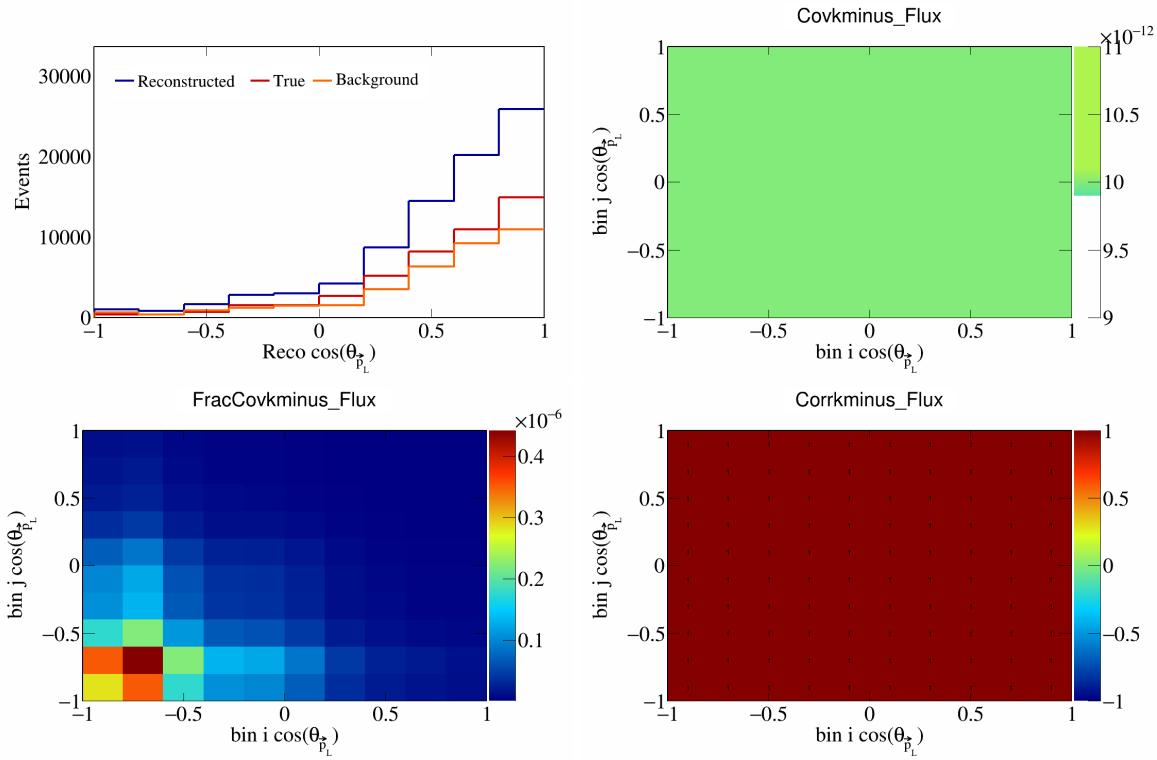


Figure 645: KMinus variations for $\cos(\theta_{\vec{p}_L})$.

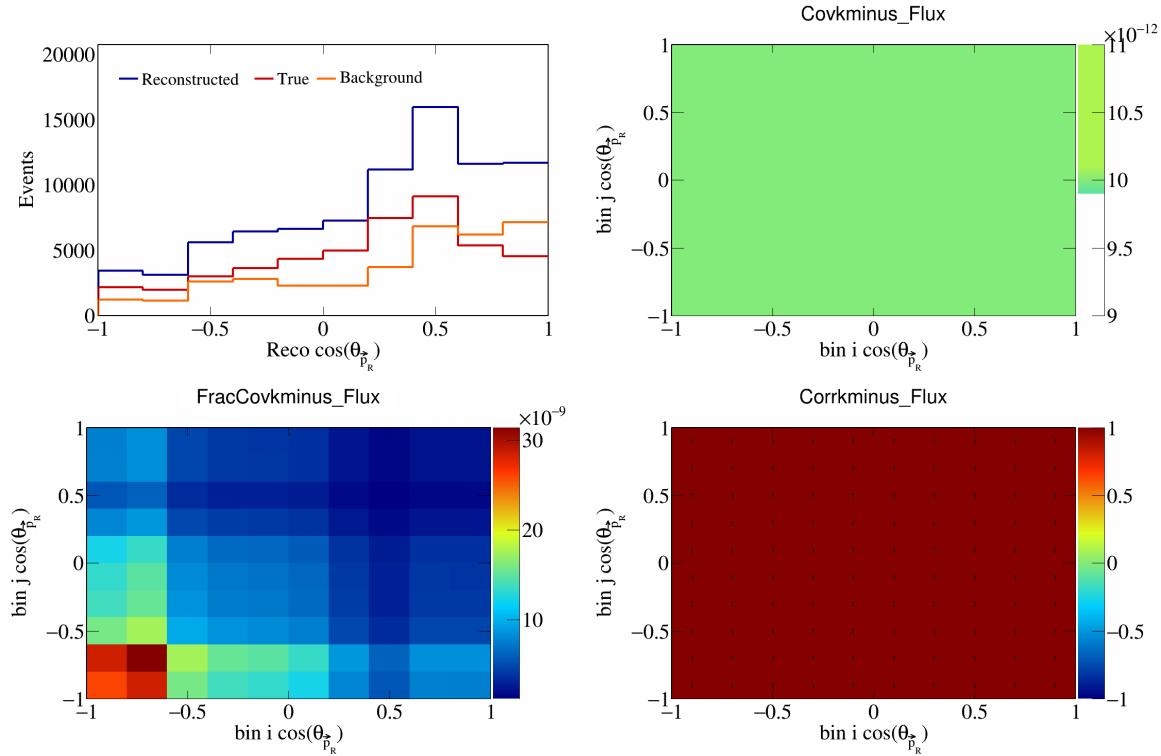


Figure 646: KMinus variations for $\cos(\theta_{\vec{p}_R})$.

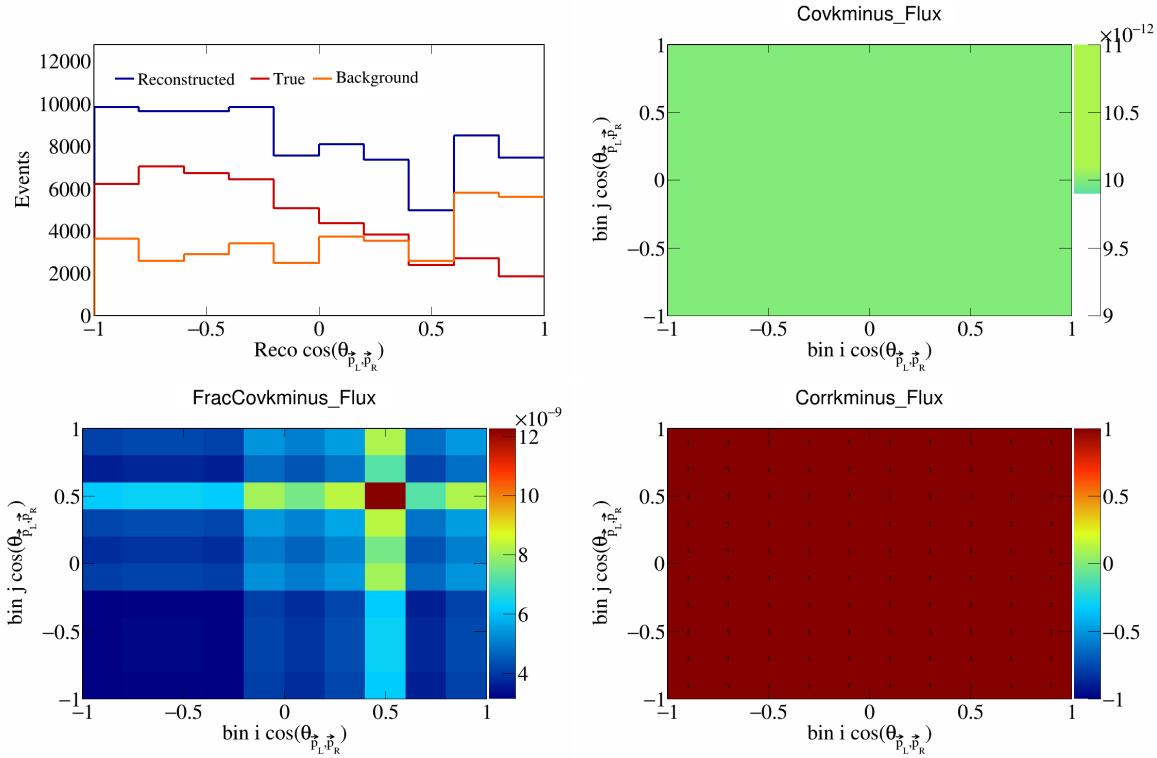


Figure 647: KMinus variations for $\cos(\theta_{\vec{p}_L, \vec{p}_R})$.

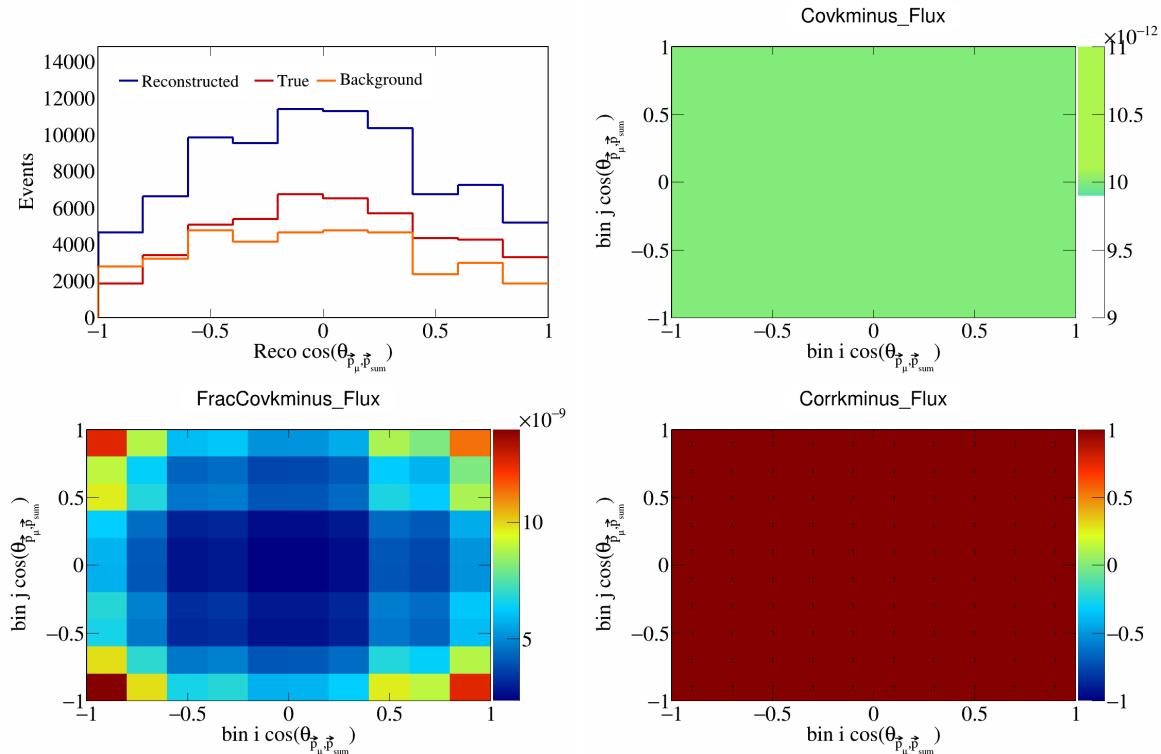


Figure 648: KMinus variations for $\cos(\theta_{\vec{p}_\mu, \vec{p}_{\text{sum}}})$.

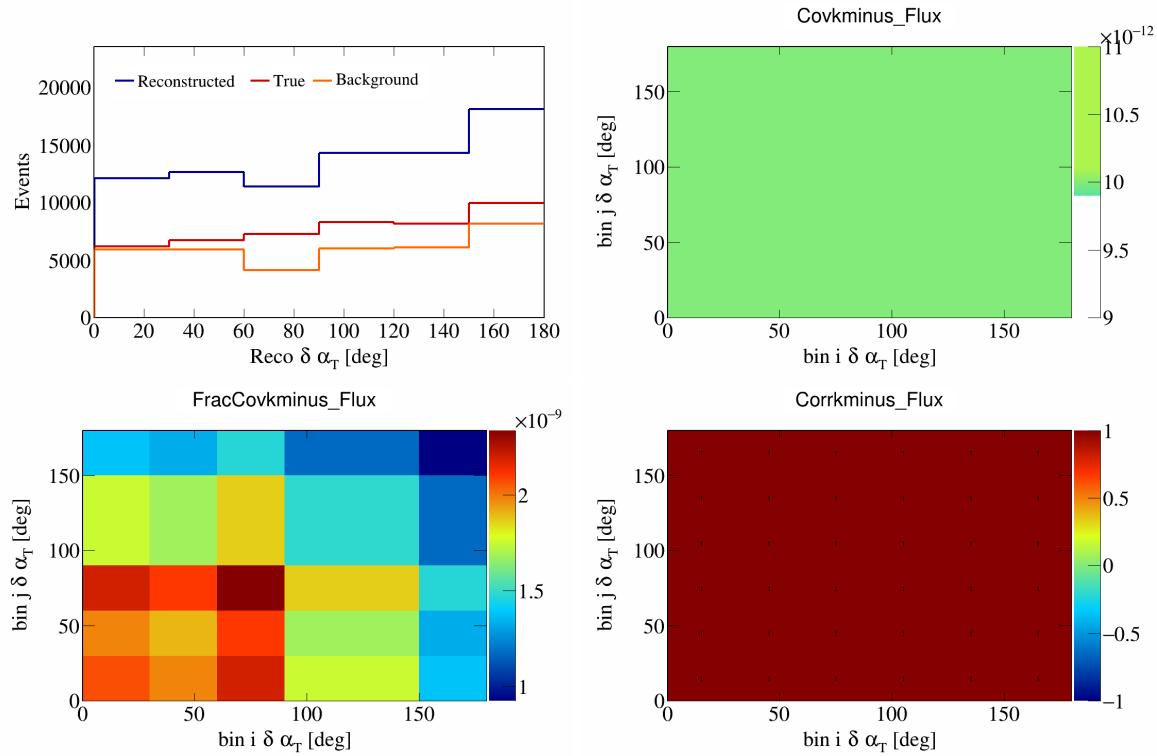


Figure 649: KMinus variations for $\delta\alpha_T$.

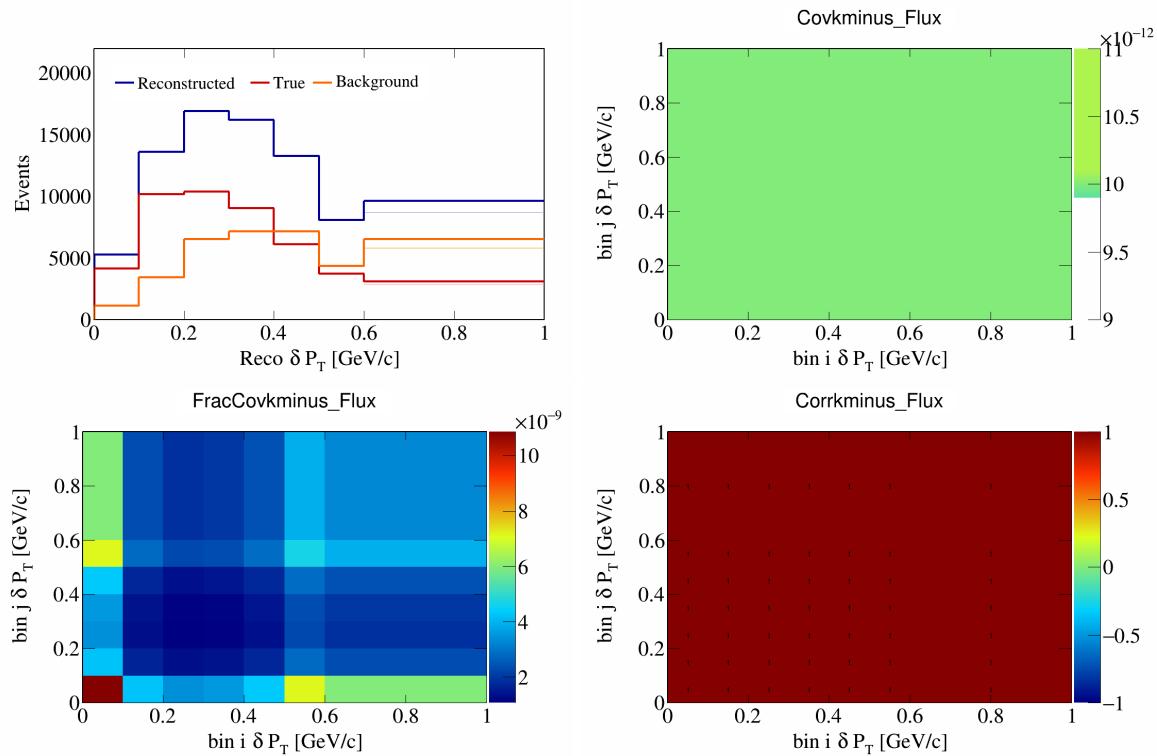


Figure 650: KMinus variations for δP_T .

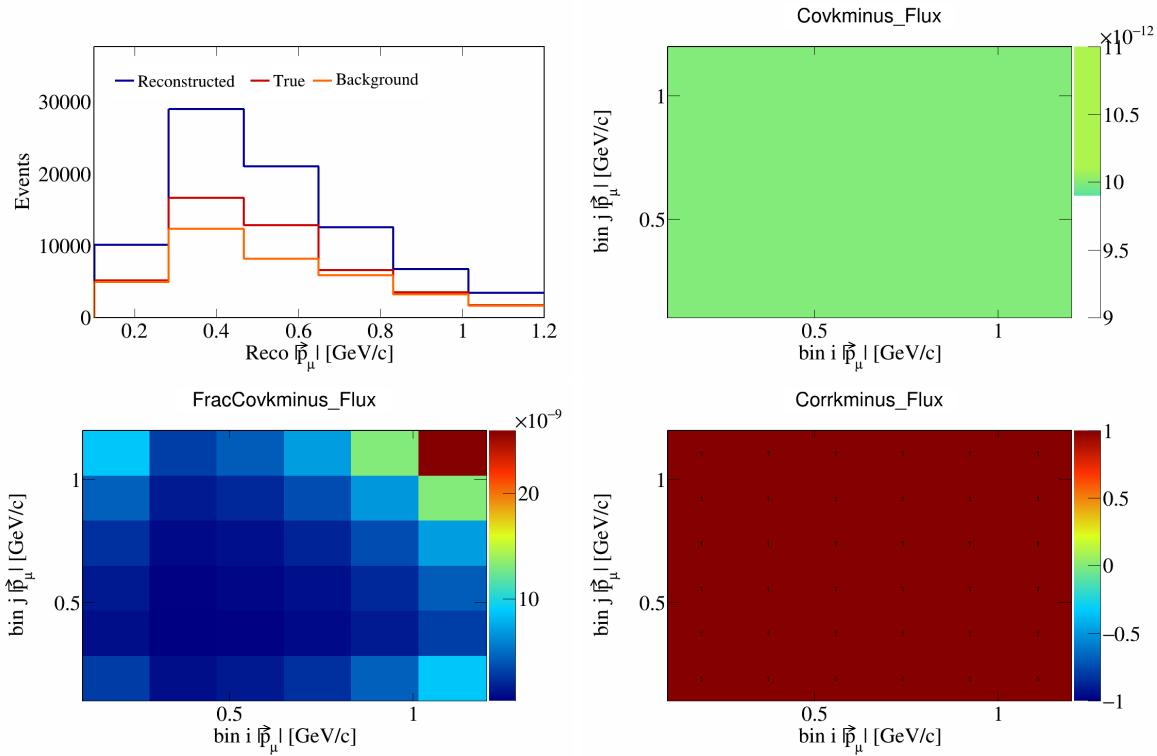


Figure 651: KMinus variations for $|\vec{p}_\mu|$.

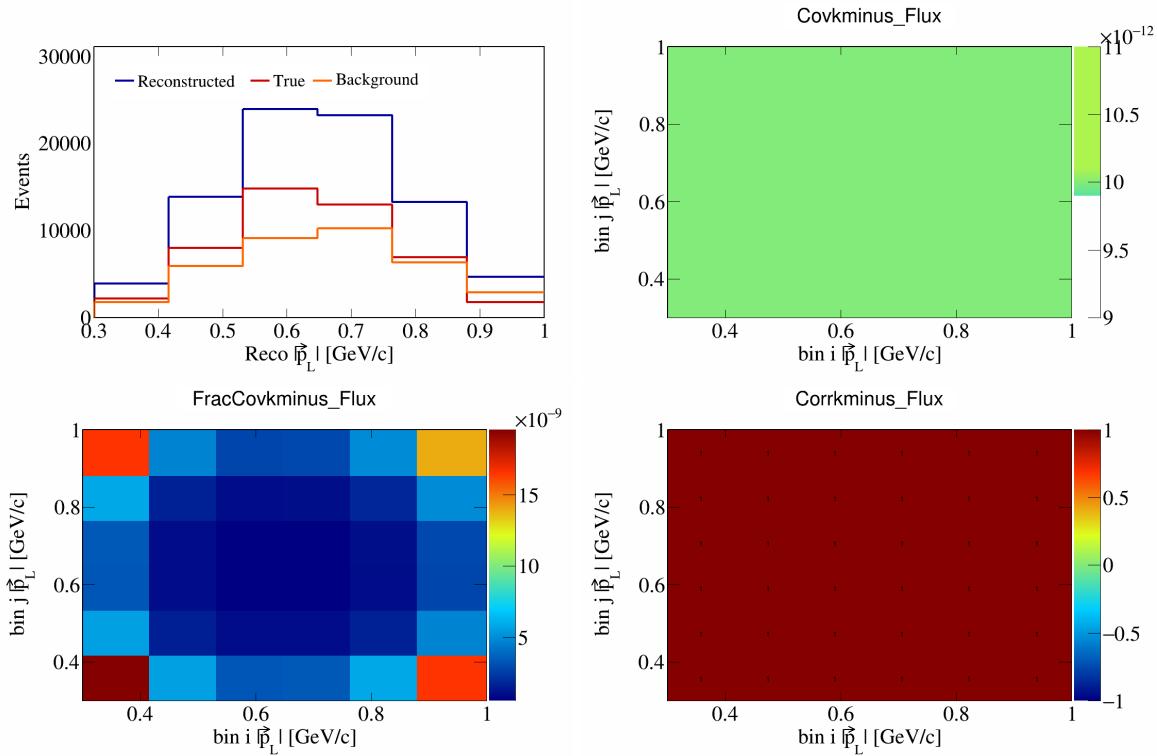


Figure 652: KMinus variations for $|\vec{p}_L|$.

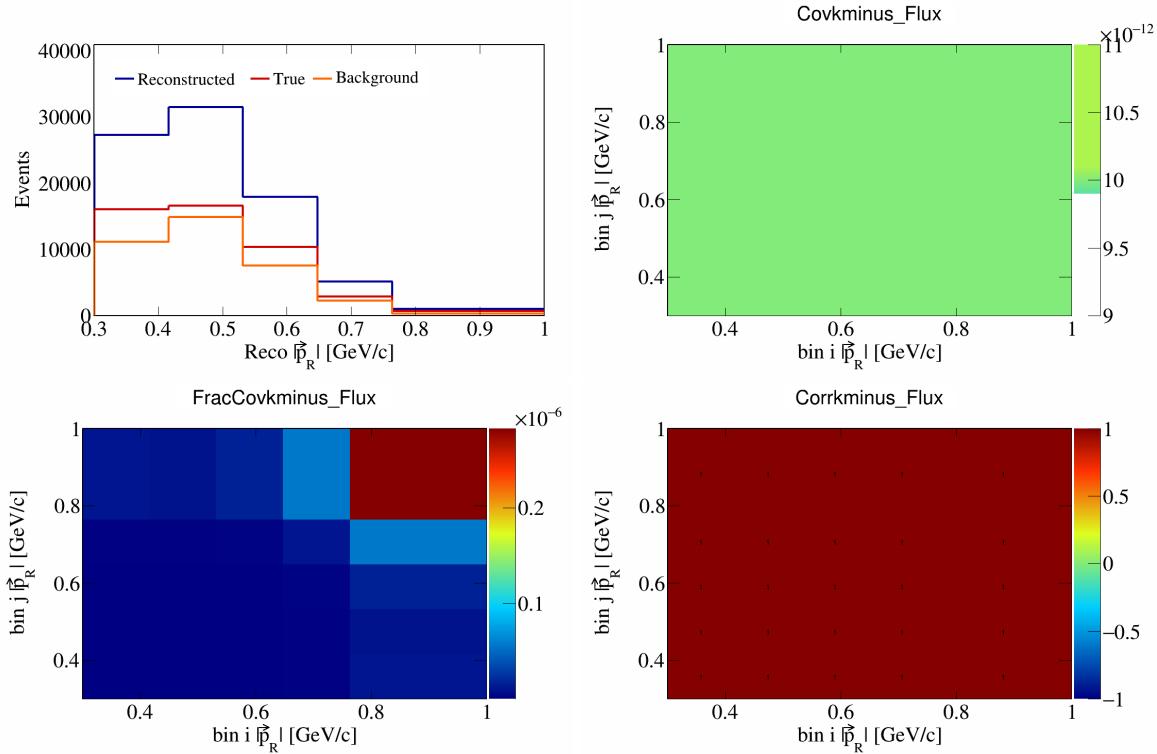


Figure 653: KMinus variations for $|\vec{p}_R|$.

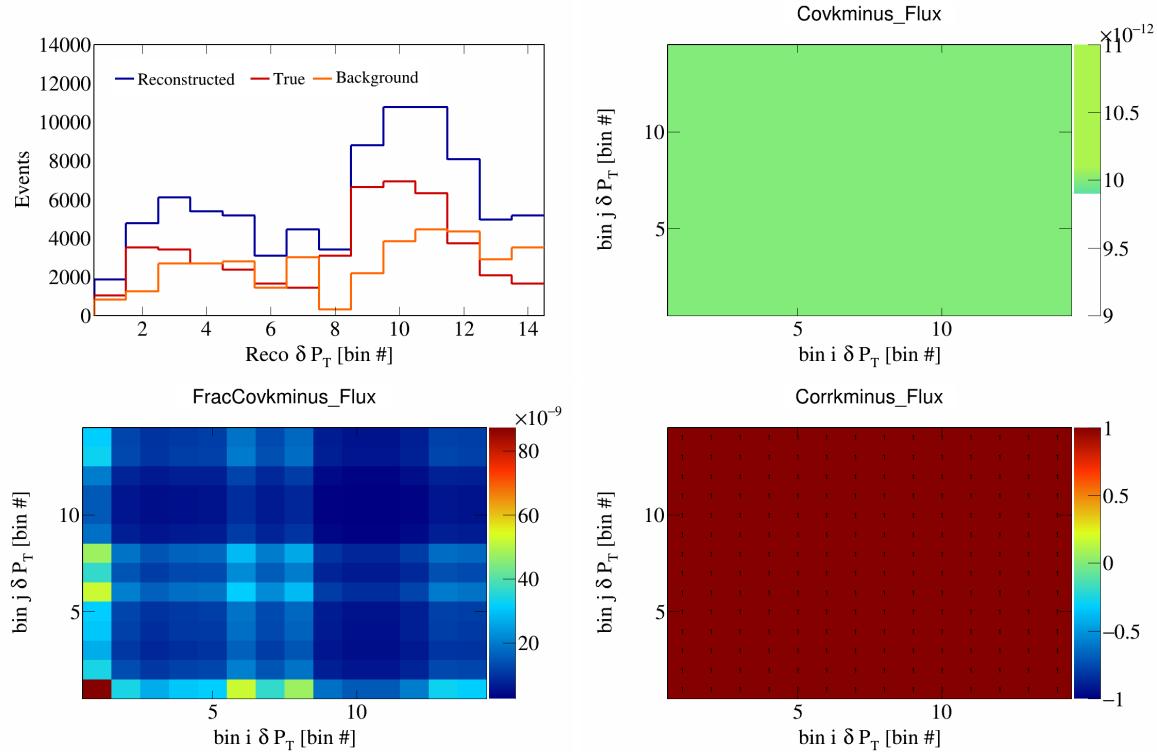


Figure 654: KMinus variations for δP_T in $\cos(\theta_{\vec{p}_\mu})$.

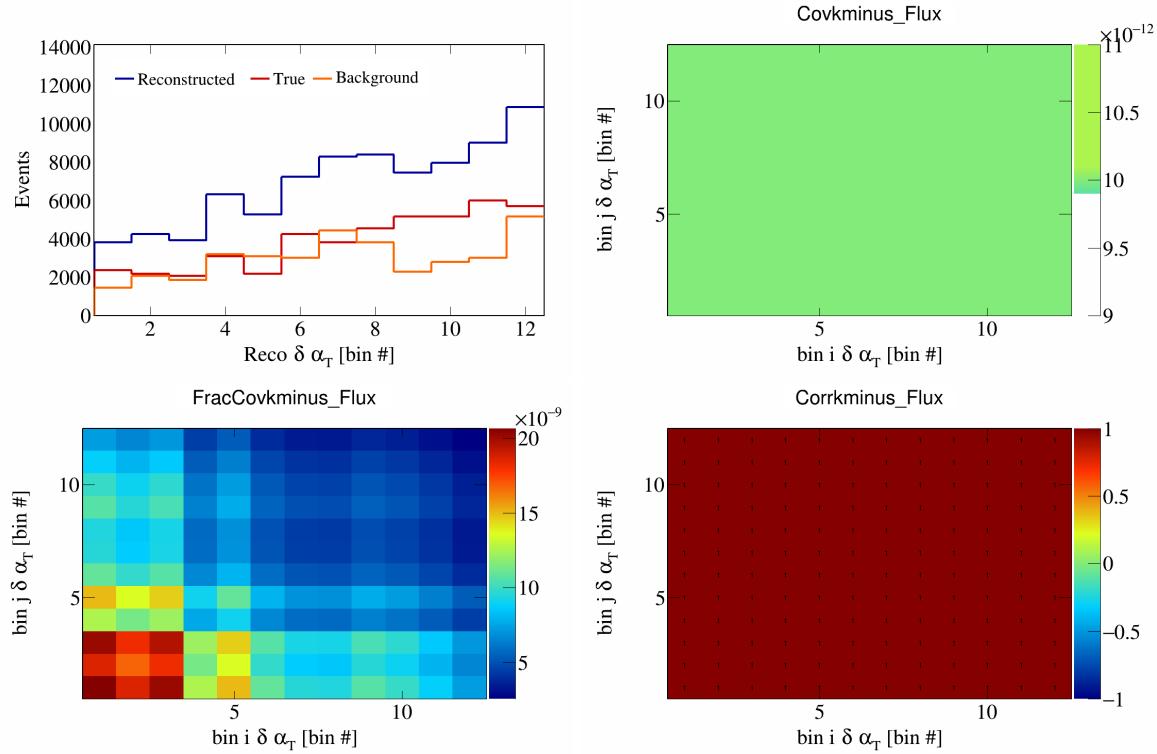


Figure 655: KMinus variations for $\delta\alpha_T$ in $\cos(\theta_{\vec{p}_\mu})$.

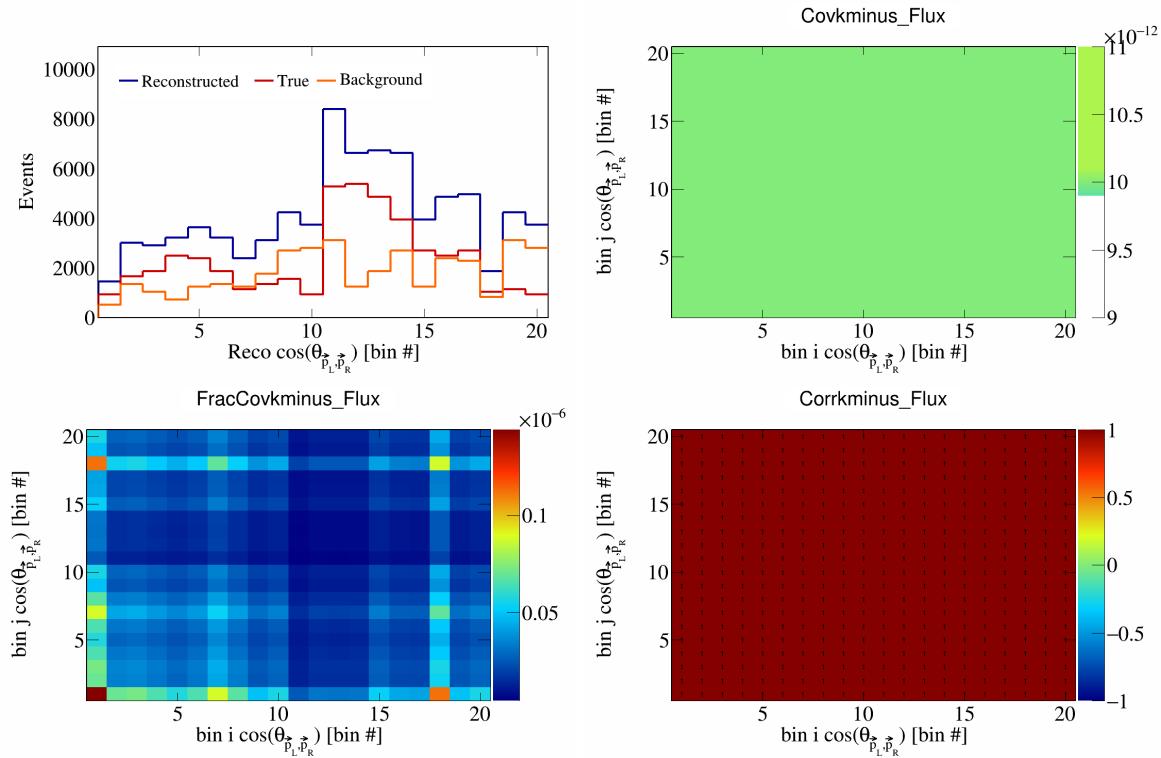


Figure 656: KMinus variations for $\cos(\theta_{\vec{p}_L, \vec{p}_R})$ in $\cos(\theta_{\vec{p}_\mu})$.

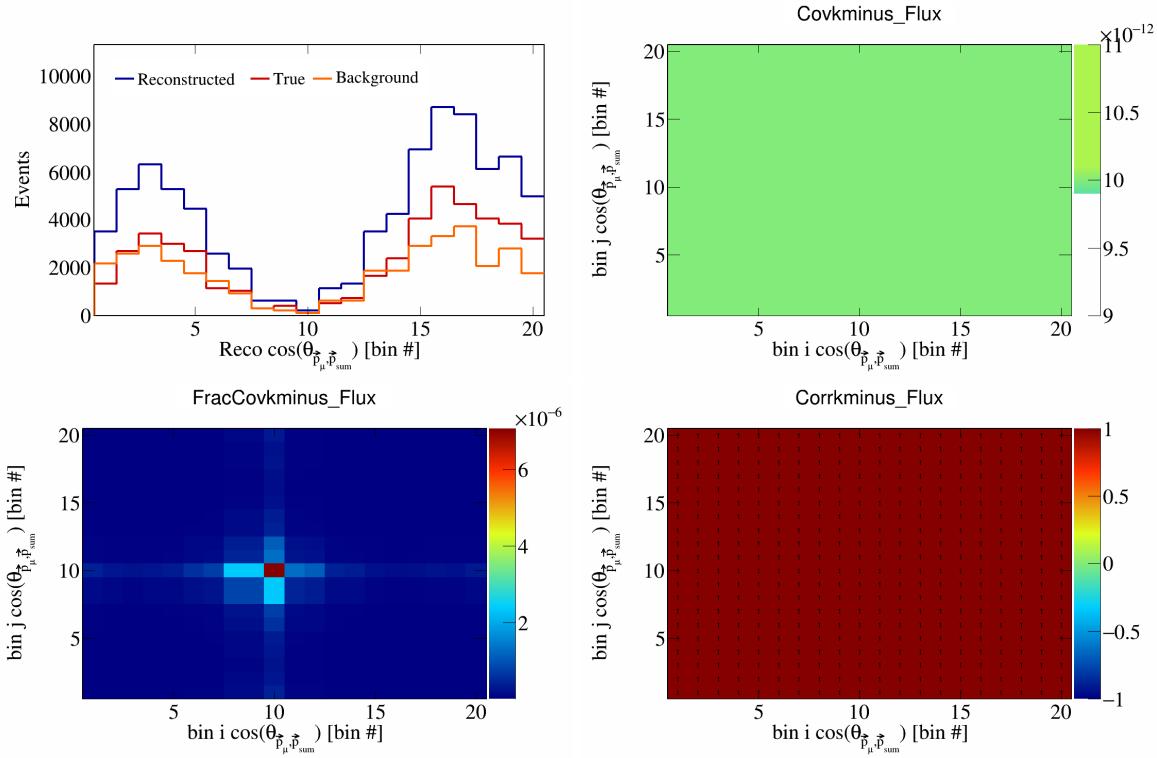


Figure 657: KMinus variations for $\cos(\theta_{\vec{p}_\mu}^*, \vec{p}_{\text{sum}}^*)$ in $\cos(\theta_{\vec{p}_\mu}^*)$.

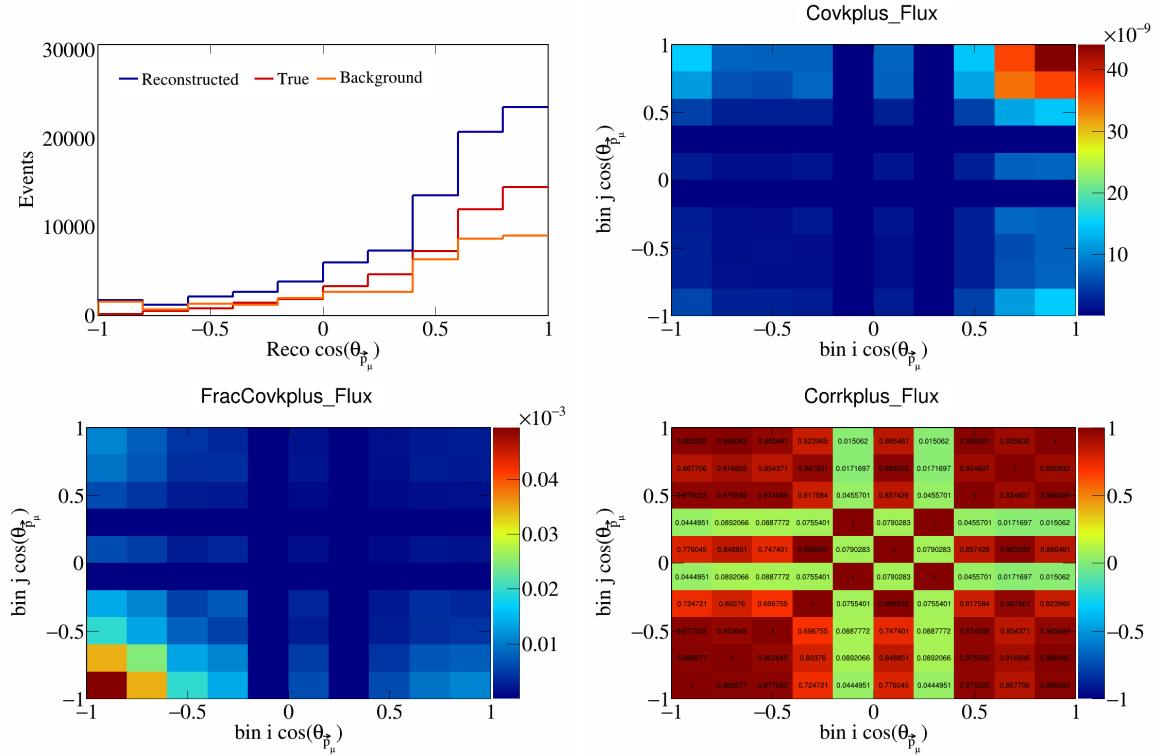


Figure 658: KPlus variations for $\cos(\theta_{\vec{p}_\mu}^*, \vec{p}_{\text{sum}}^*)$ in $\cos(\theta_{\vec{p}_\mu}^*)$.

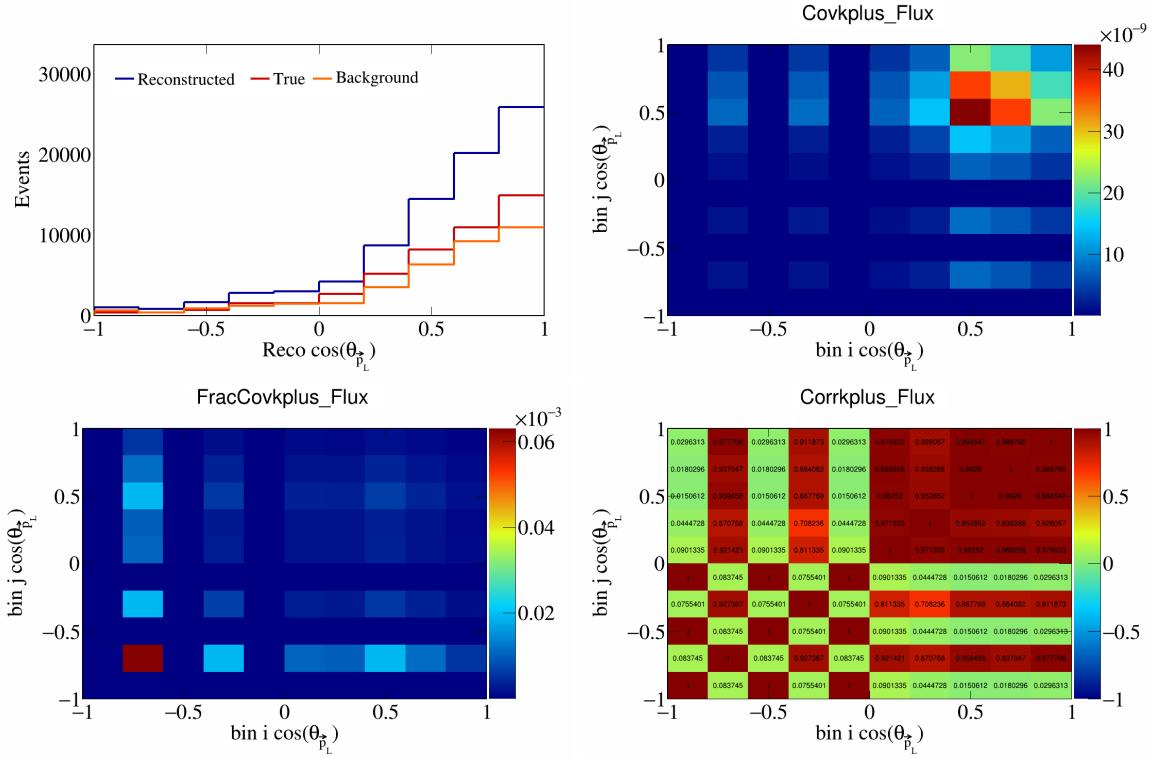


Figure 659: KPlus variations for $\cos(\theta_{\vec{p}_L})$.

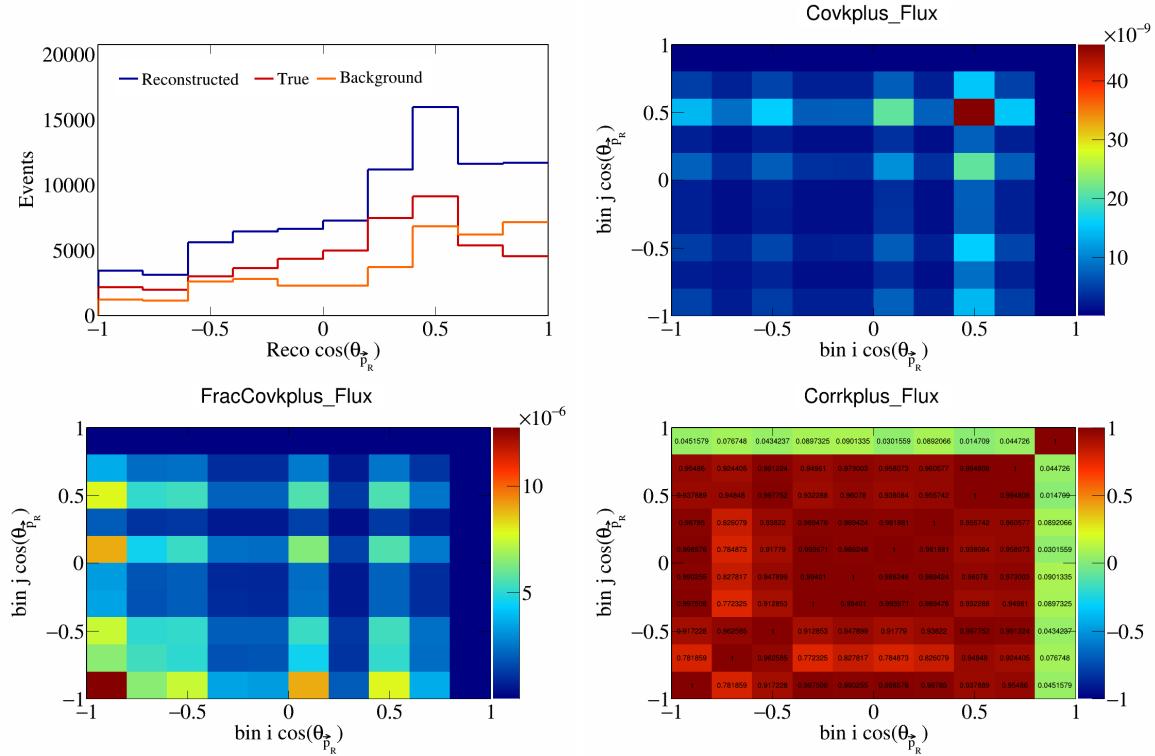


Figure 660: KPlus variations for $\cos(\theta_{\vec{p}_R})$.

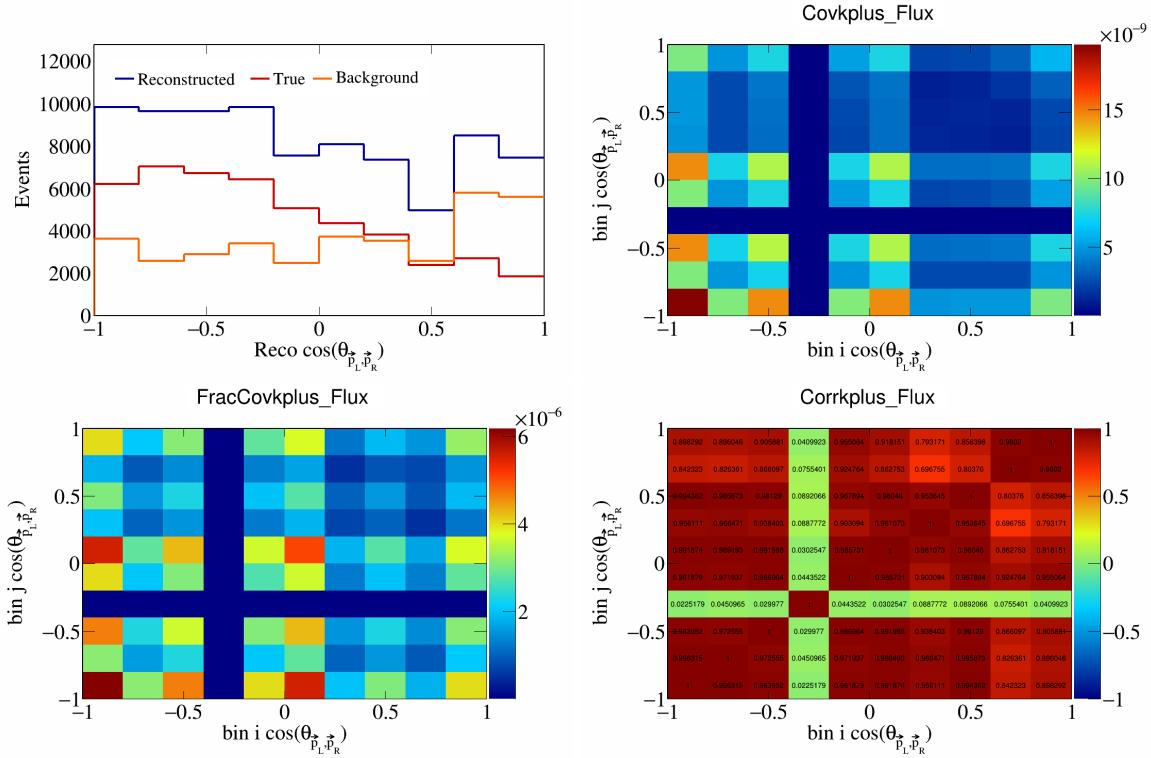


Figure 661: KPlus variations for $\cos(\theta_{\vec{p}_L, \vec{p}_R})$.

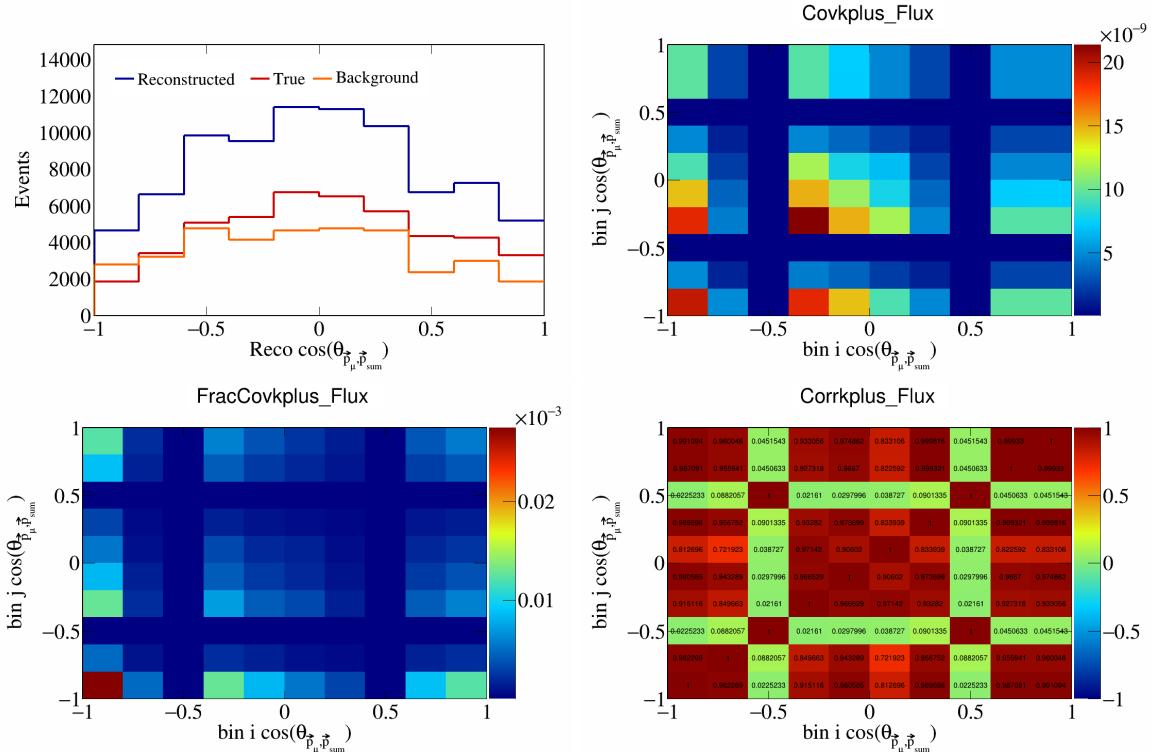


Figure 662: KPlus variations for $\cos(\theta_{\vec{p}_\mu, \vec{p}_{\text{sum}}})$.

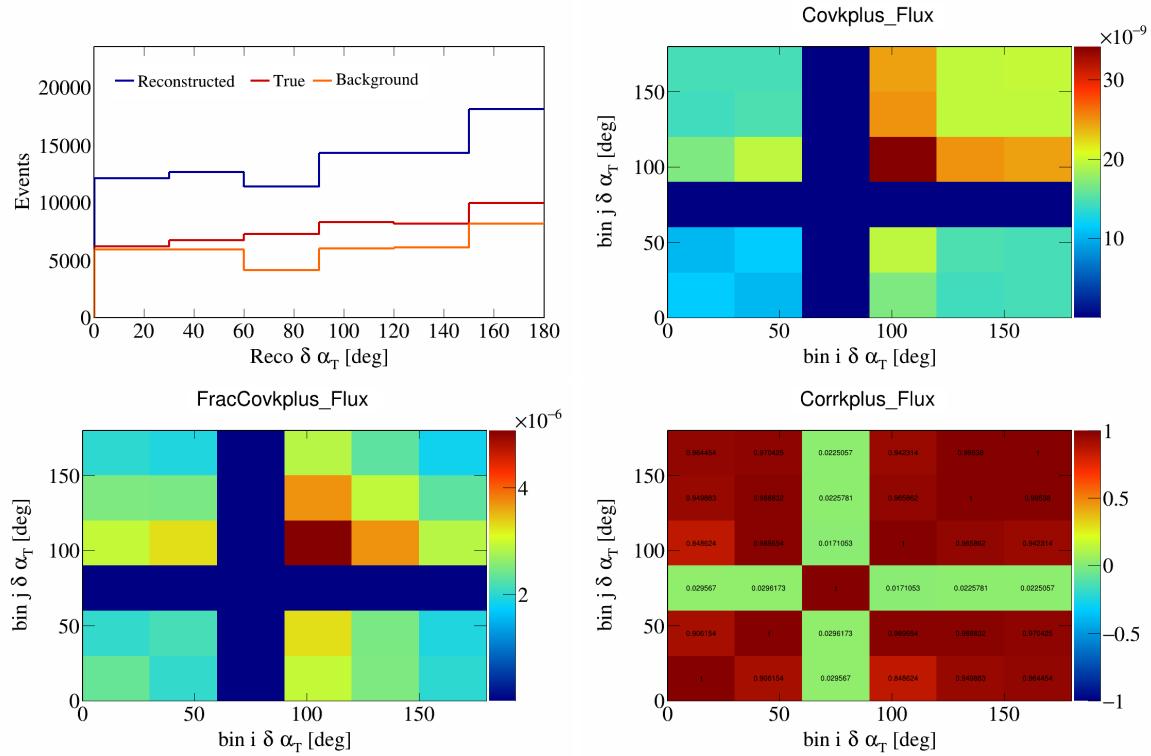


Figure 663: KPlus variations for $\delta\alpha_T$.

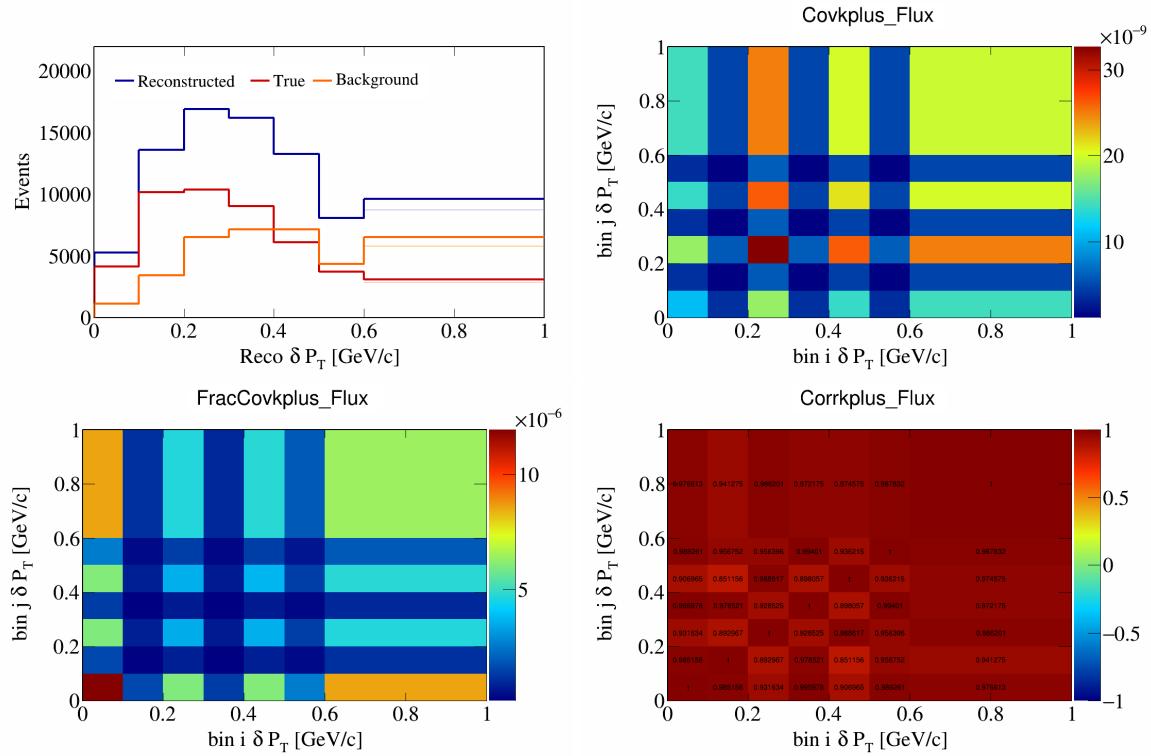


Figure 664: KPlus variations for δP_T .

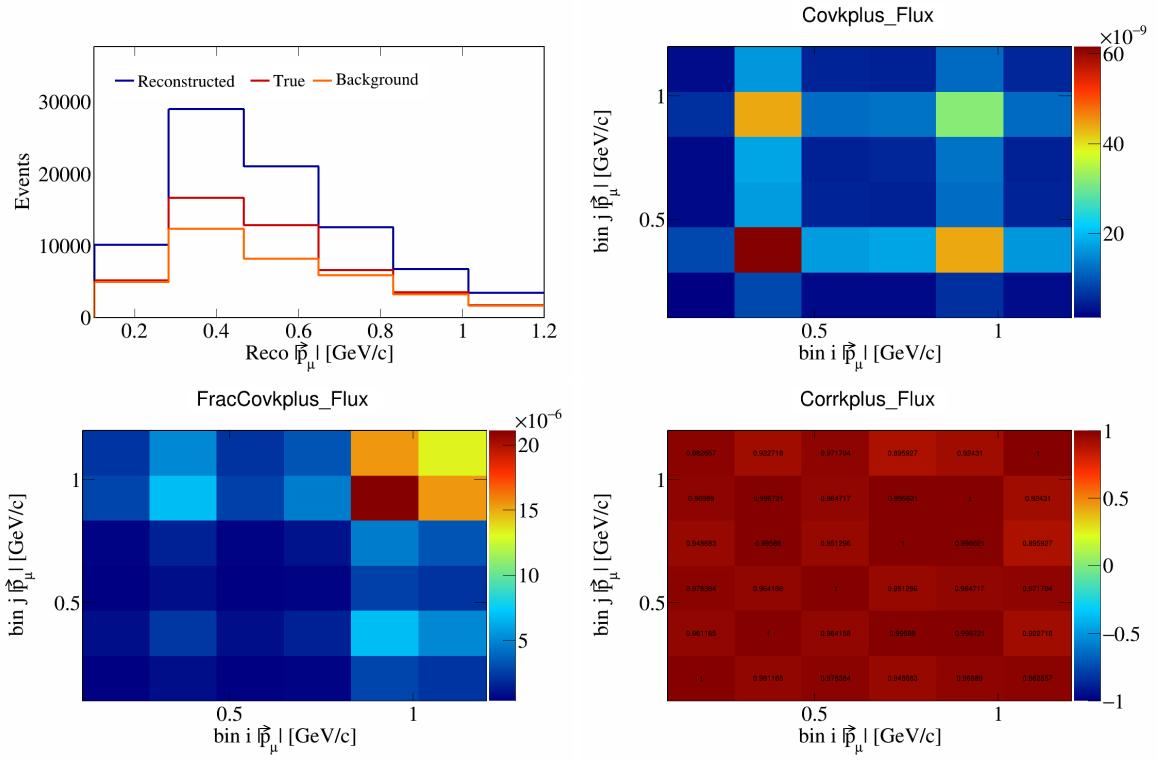


Figure 665: KPlus variations for $|\vec{p}_\mu|$.

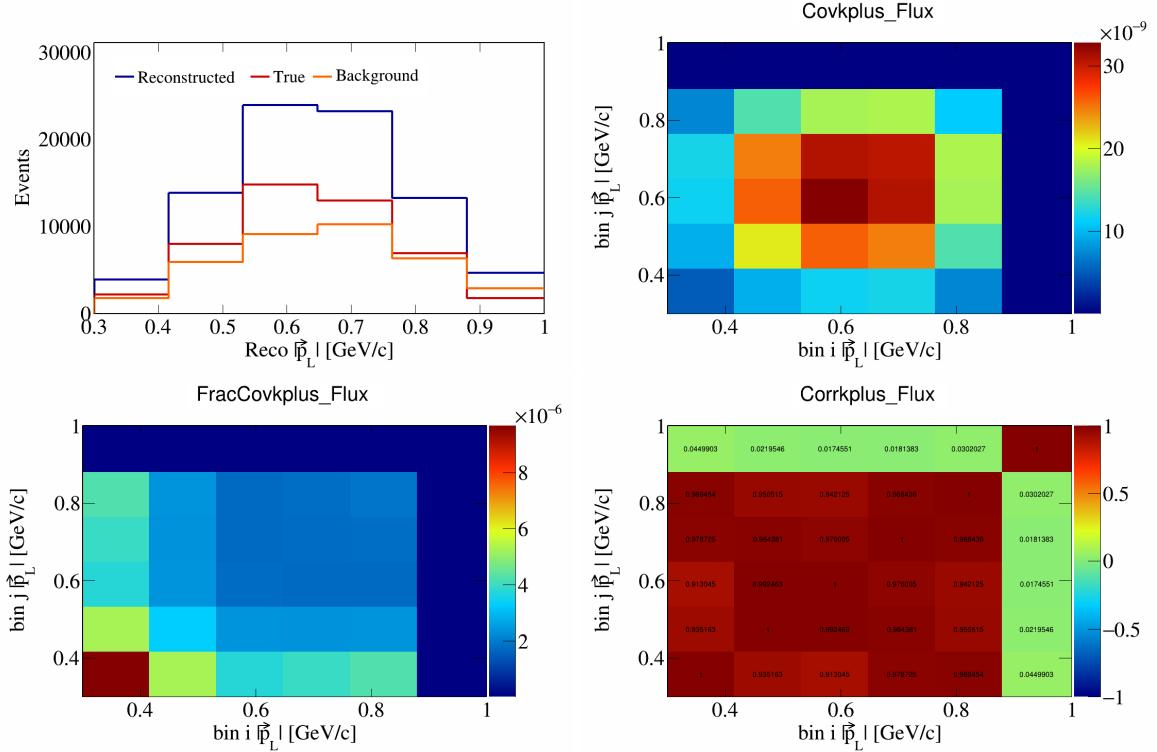


Figure 666: KPlus variations for $|\vec{p}_L|$.

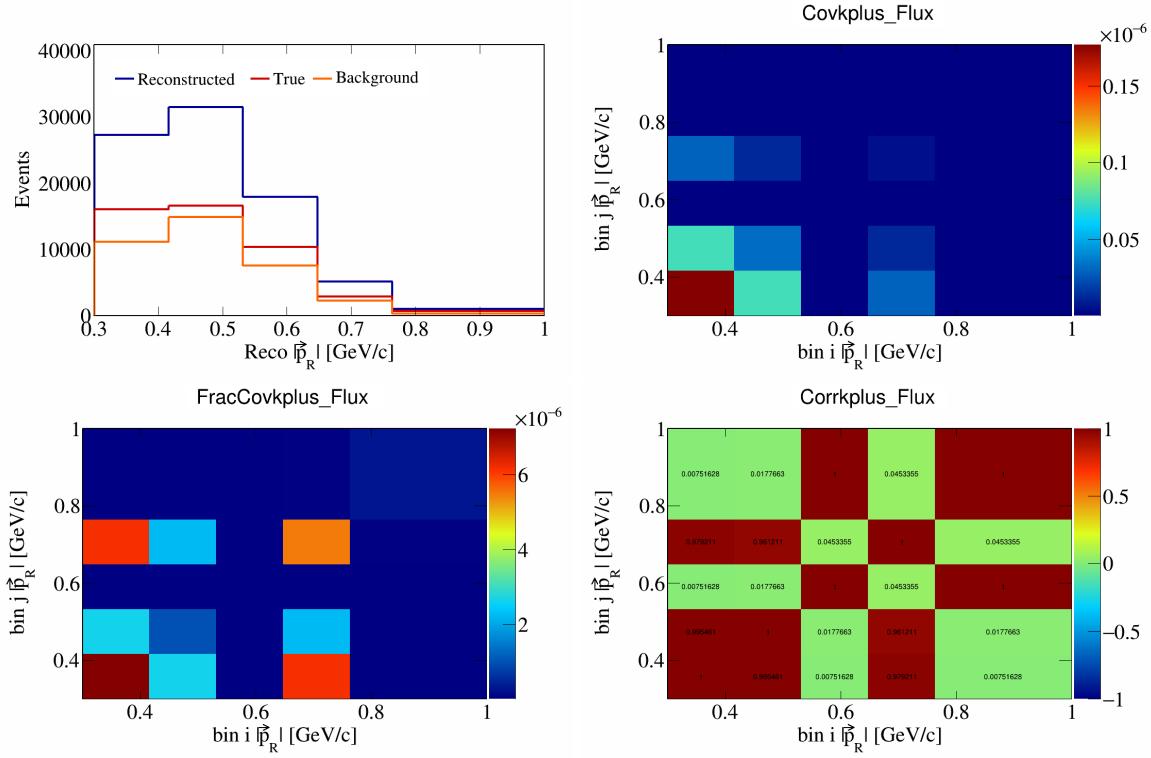


Figure 667: KPlus variations for $|\vec{p}_R|$.

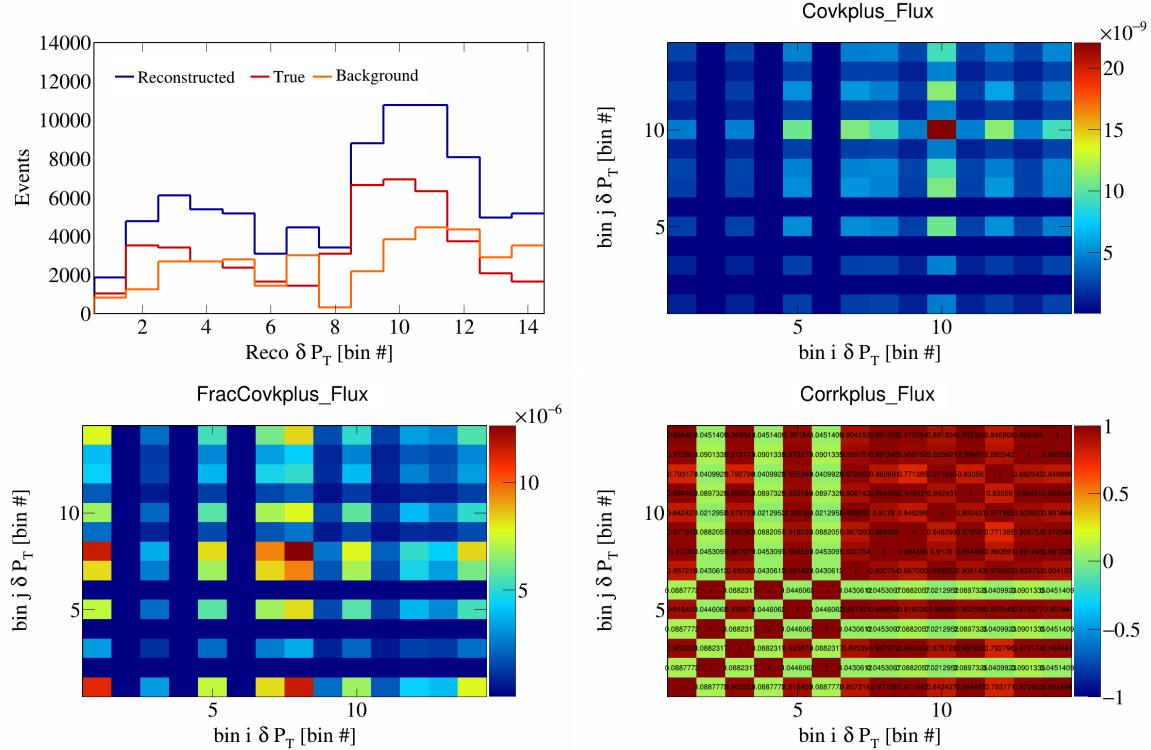


Figure 668: KPlus variations for δP_T in $\cos(\theta_{\vec{p}_\mu})$.

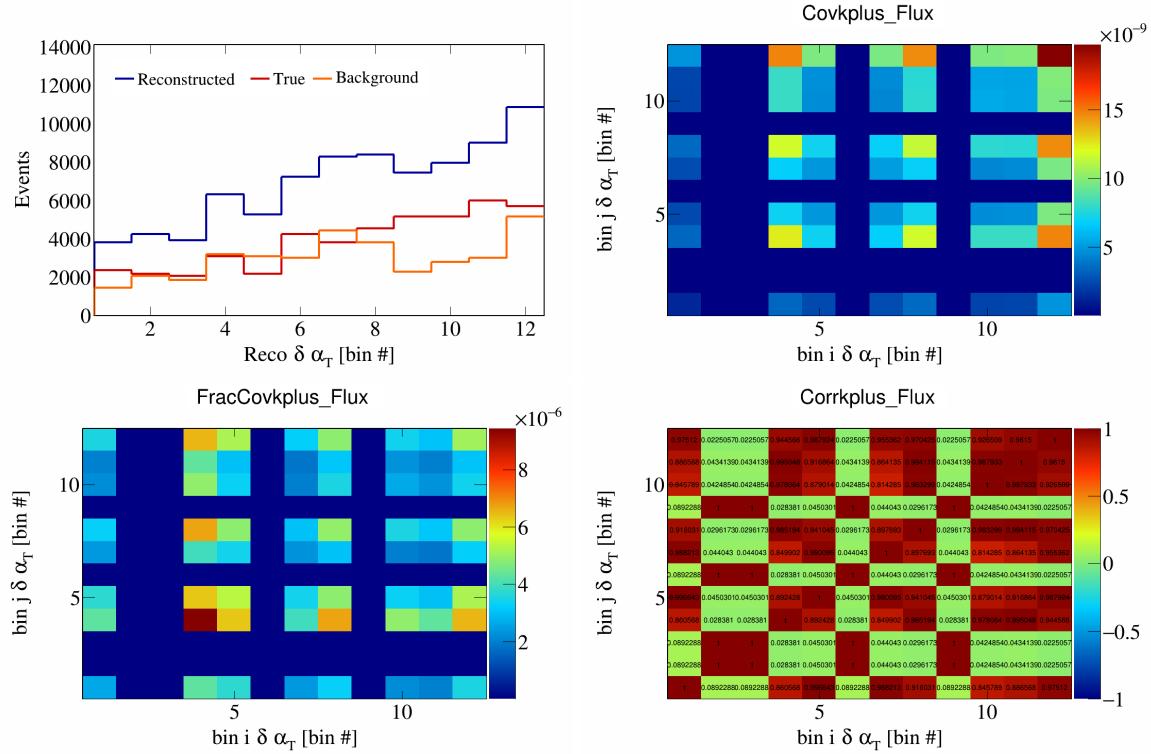


Figure 669: KPlus variations for $\delta\alpha_T$ in $\cos(\theta_{\vec{p}_\mu})$.

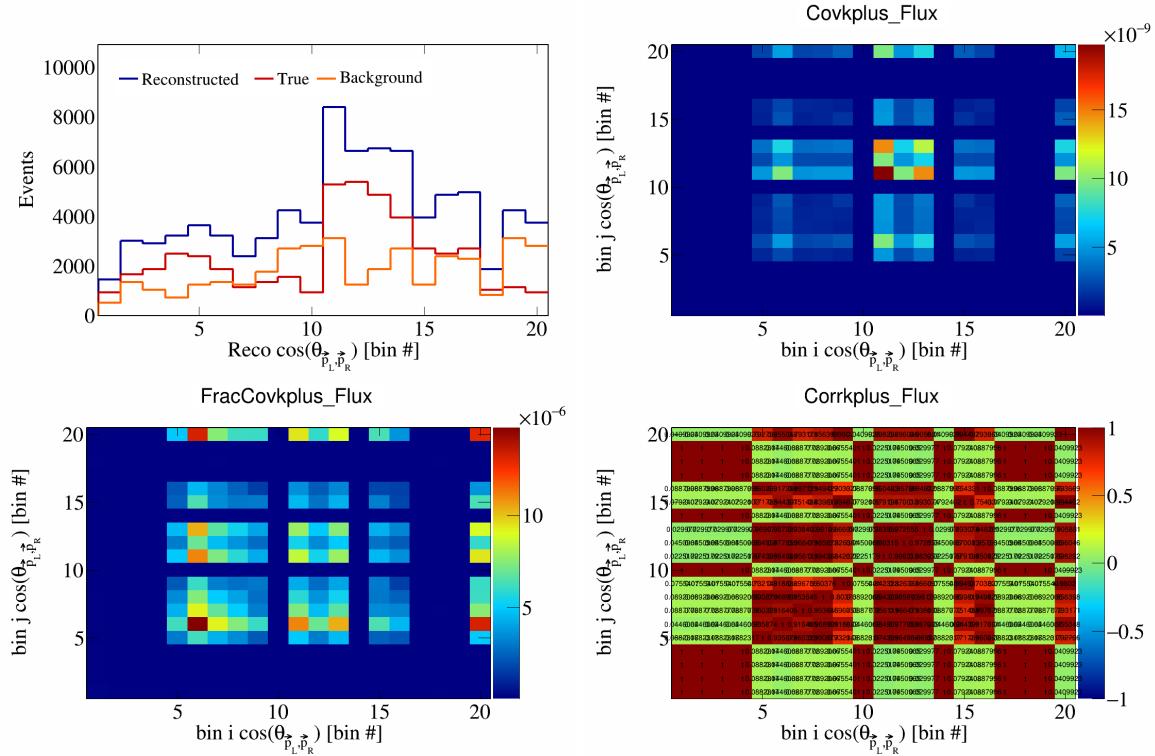


Figure 670: KPlus variations for $\cos(\theta_{\vec{p}_L, \vec{p}_R})$ in $\cos(\theta_{\vec{p}_\mu})$.

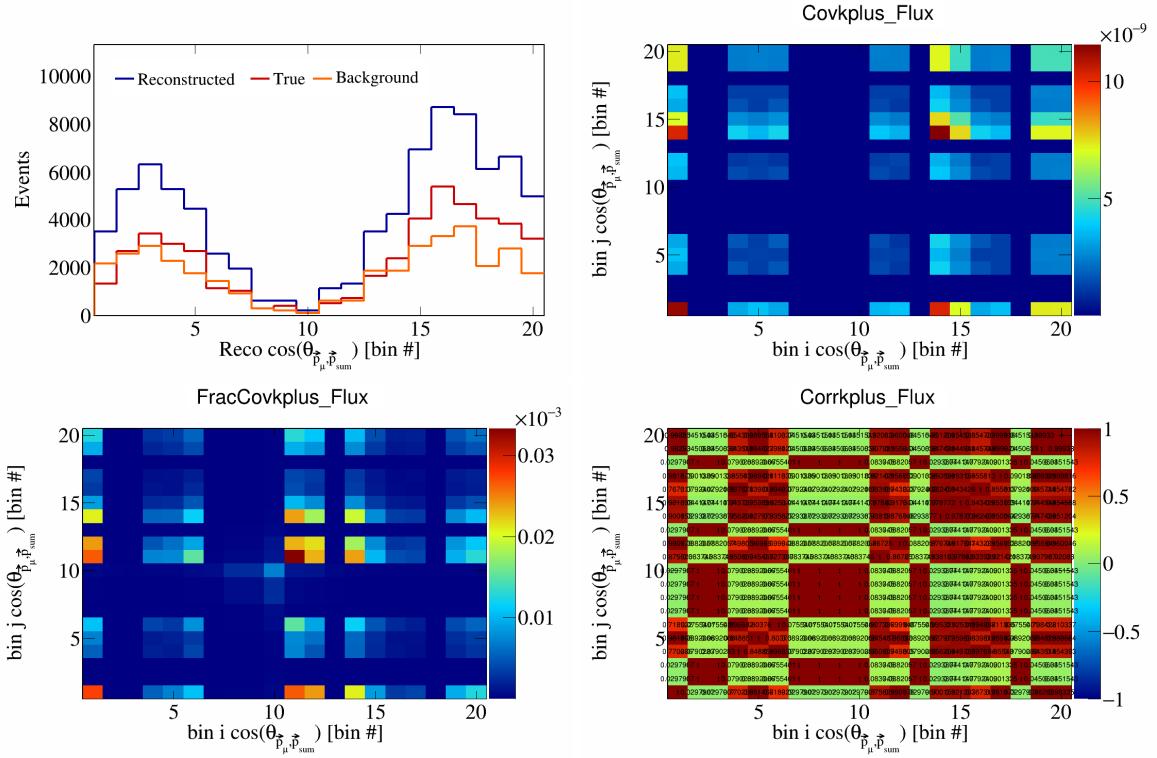


Figure 671: KPlus variations for $\cos(\theta_{\vec{p}_\mu, \vec{p}_{\text{sum}}})$ in $\cos(\theta_{\vec{p}_\mu})$.

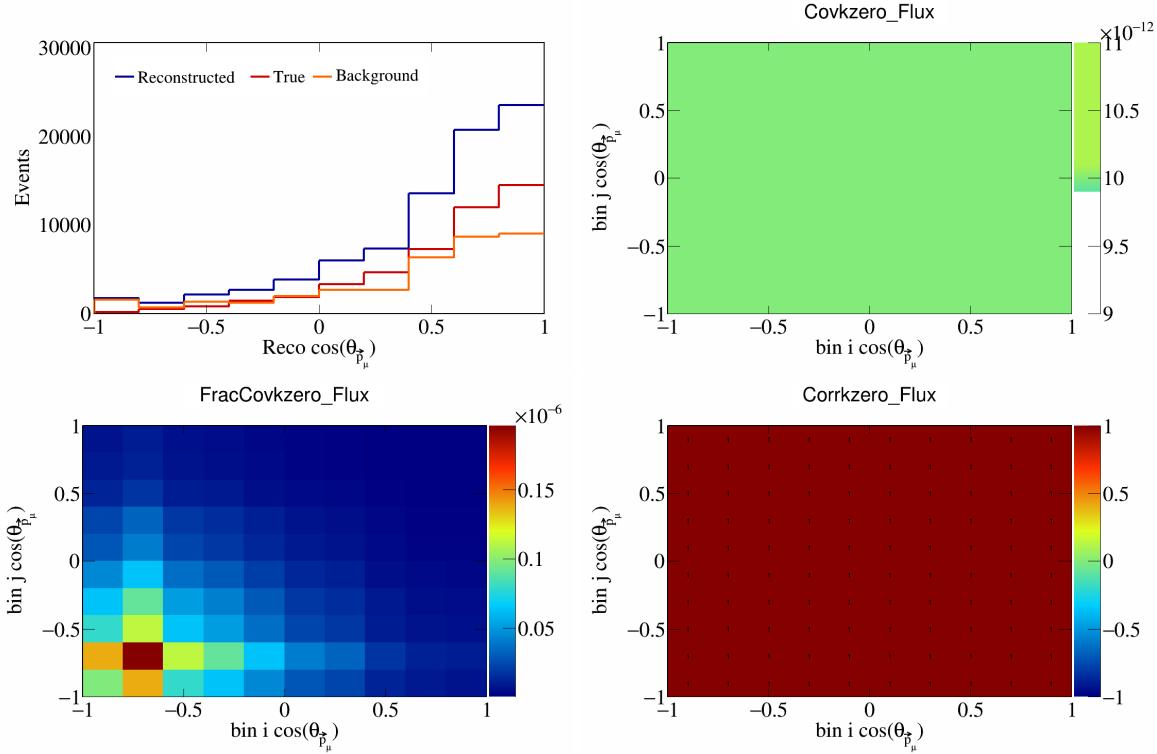


Figure 672: KZero variations for $\cos(\theta_{\vec{p}_\mu, \vec{p}_{\text{sum}}})$ in $\cos(\theta_{\vec{p}_\mu})$.

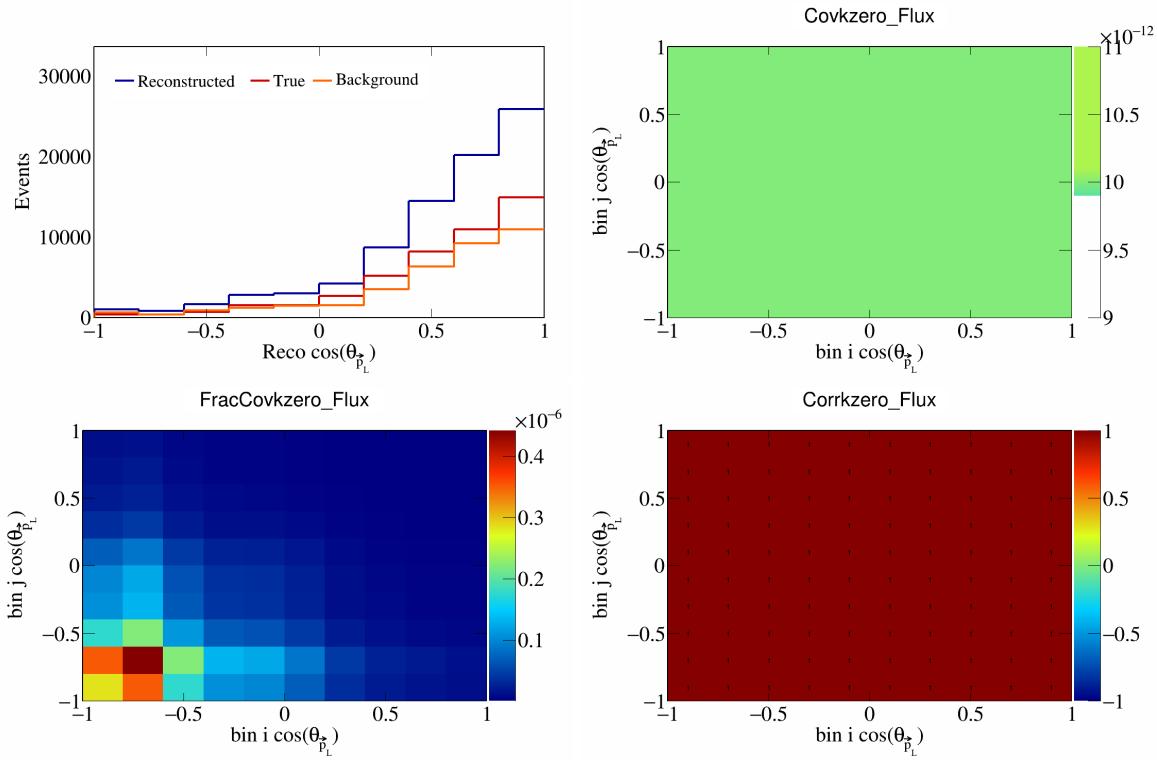


Figure 673: KZero variations for $\cos(\theta_{\vec{p}_L})$.

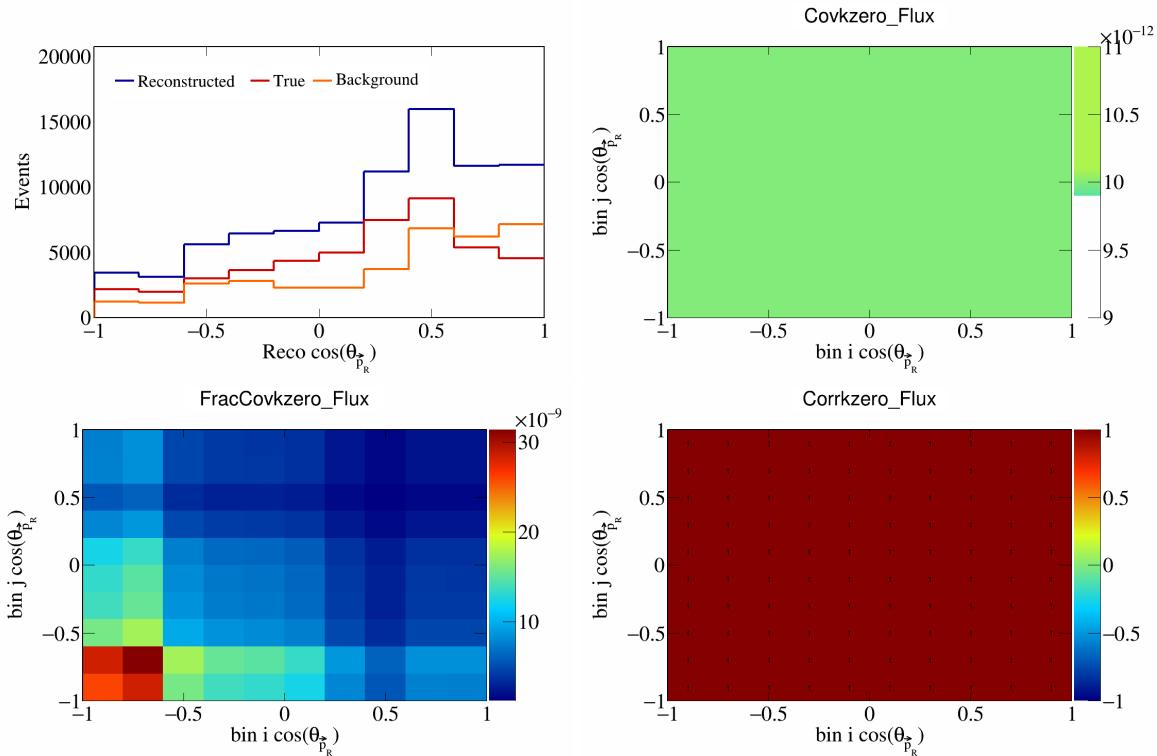


Figure 674: KZero variations for $\cos(\theta_{\vec{p}_R})$.

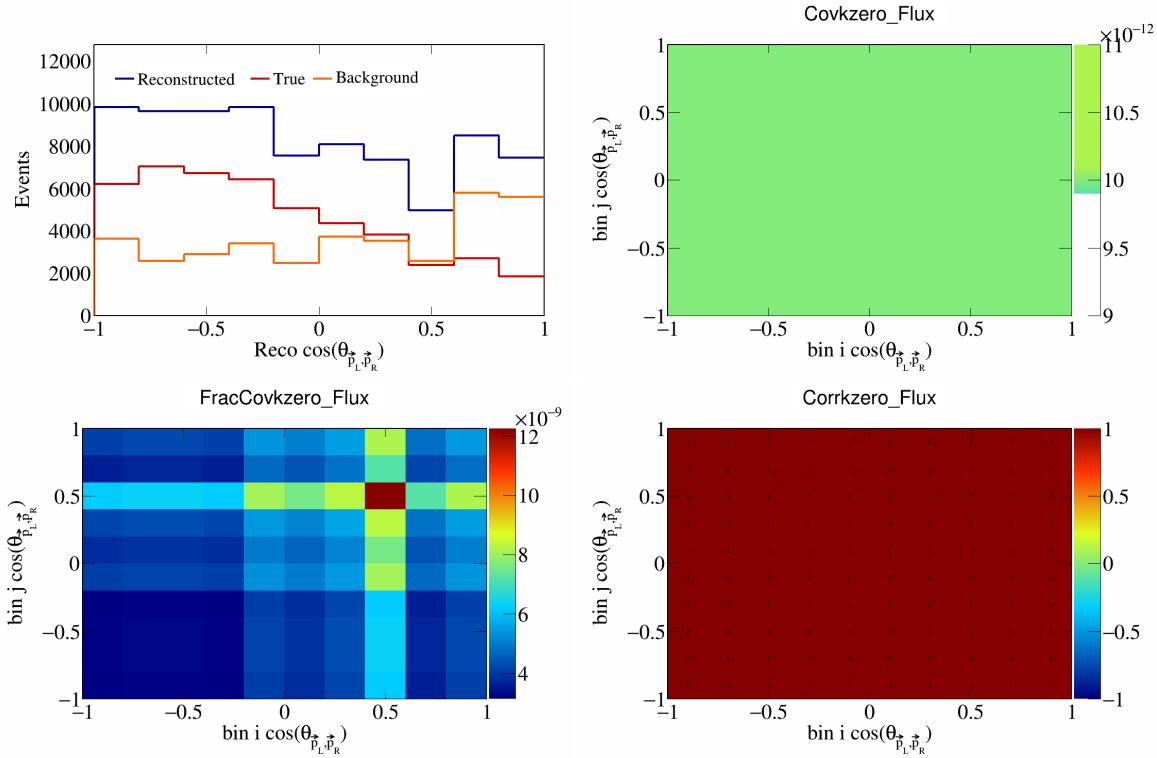


Figure 675: KZero variations for $\cos(\theta_{\vec{p}_L, \vec{p}_R})$.

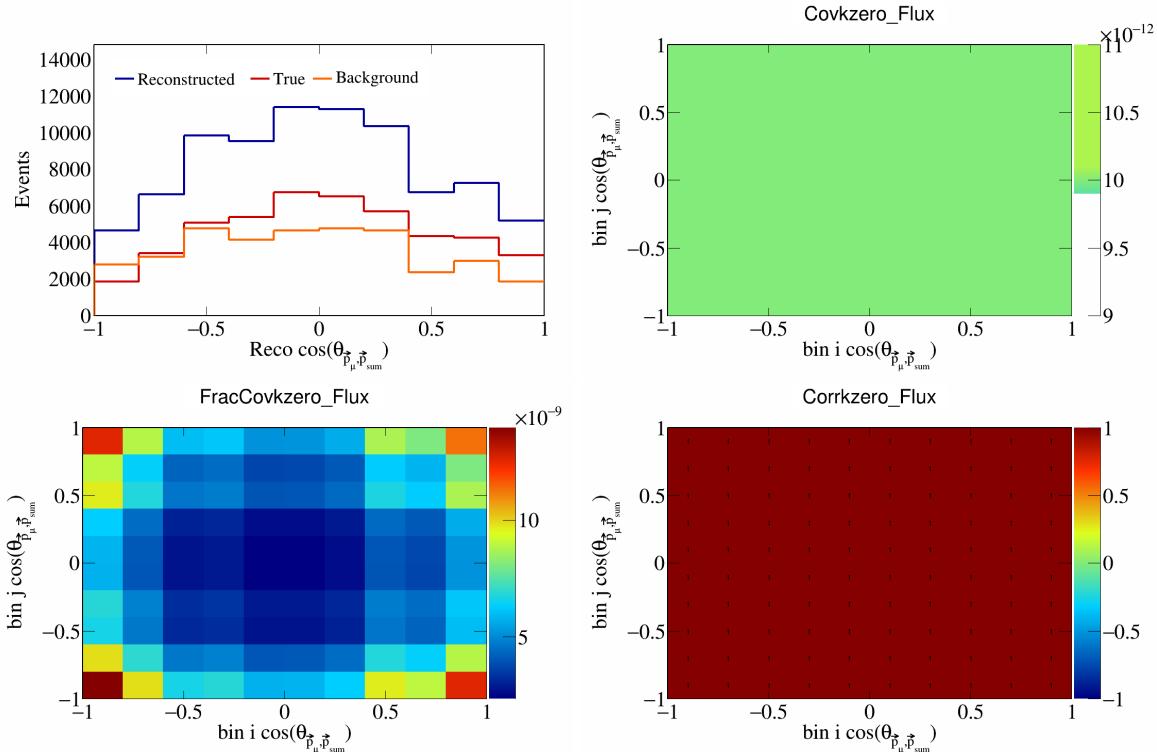


Figure 676: KZero variations for $\cos(\theta_{\vec{p}_\mu, \vec{p}_{\text{sum}}})$.

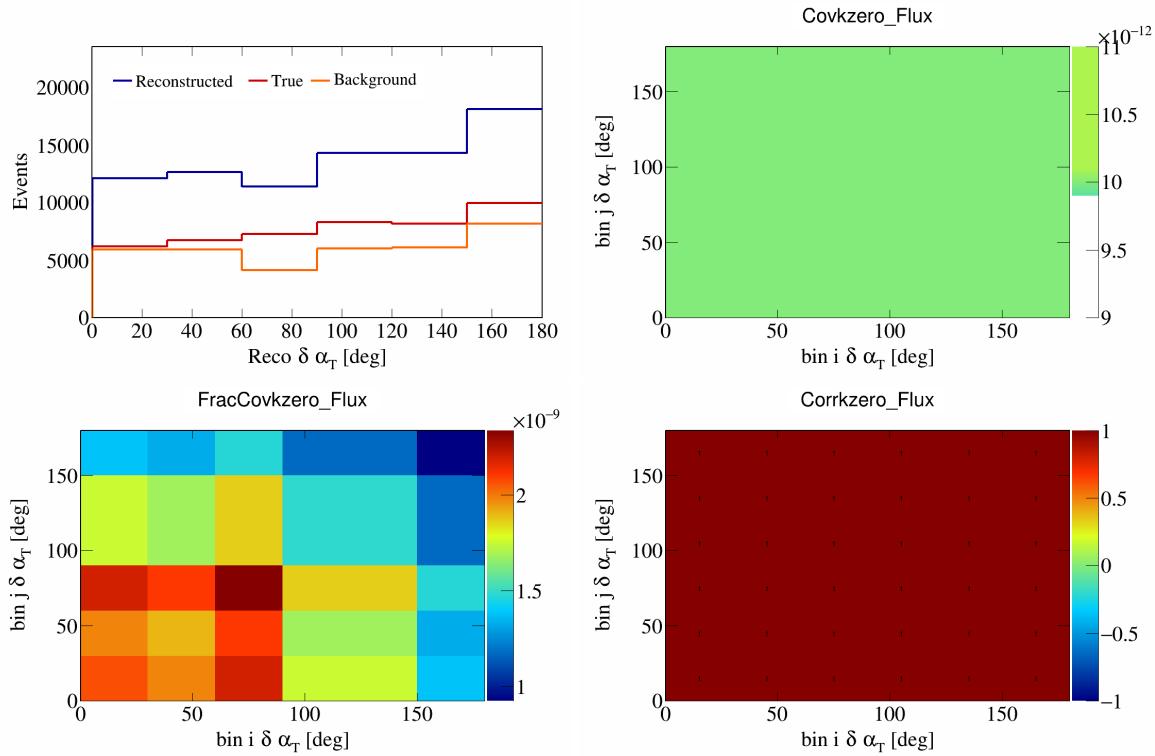


Figure 677: KZero variations for $\delta\alpha_T$.

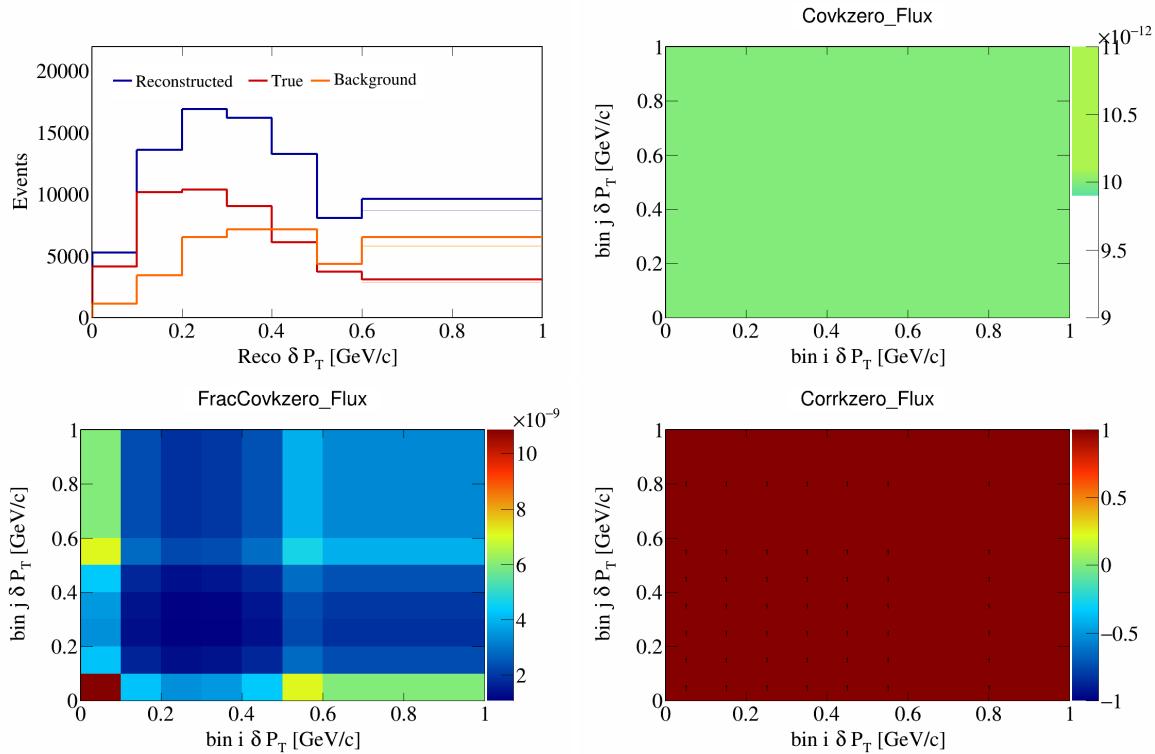


Figure 678: KZero variations for δP_T .

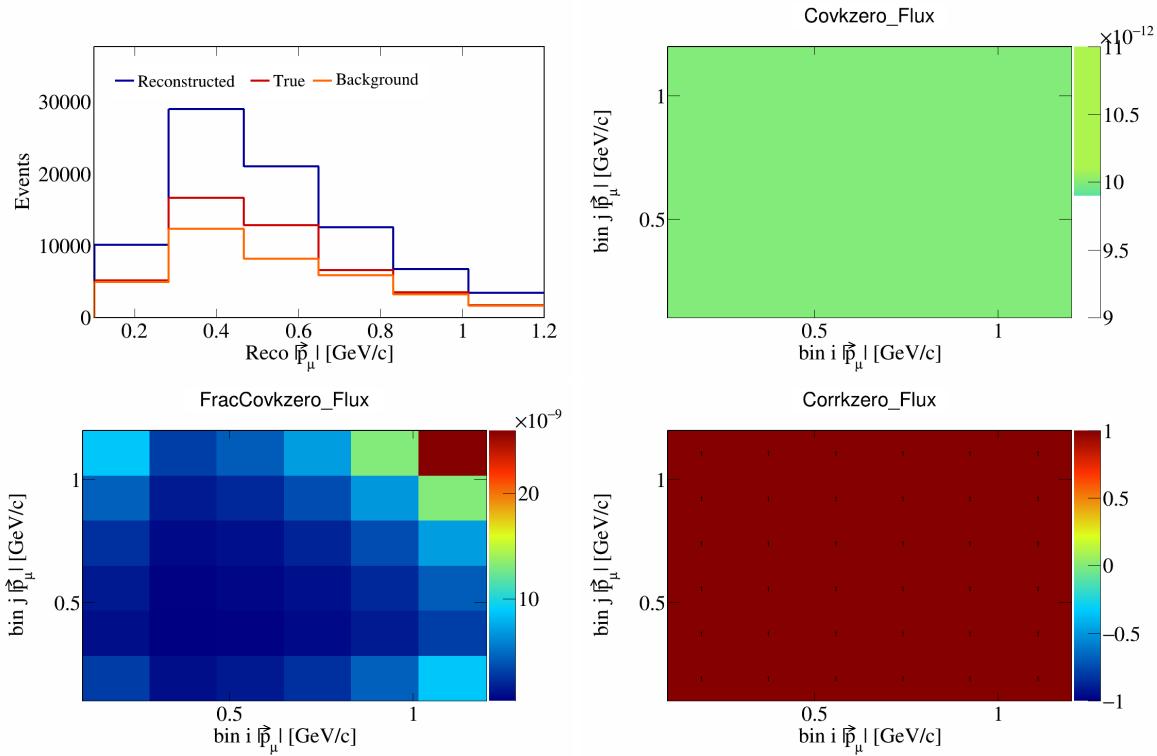


Figure 679: KZero variations for $|\vec{p}_\mu|$.

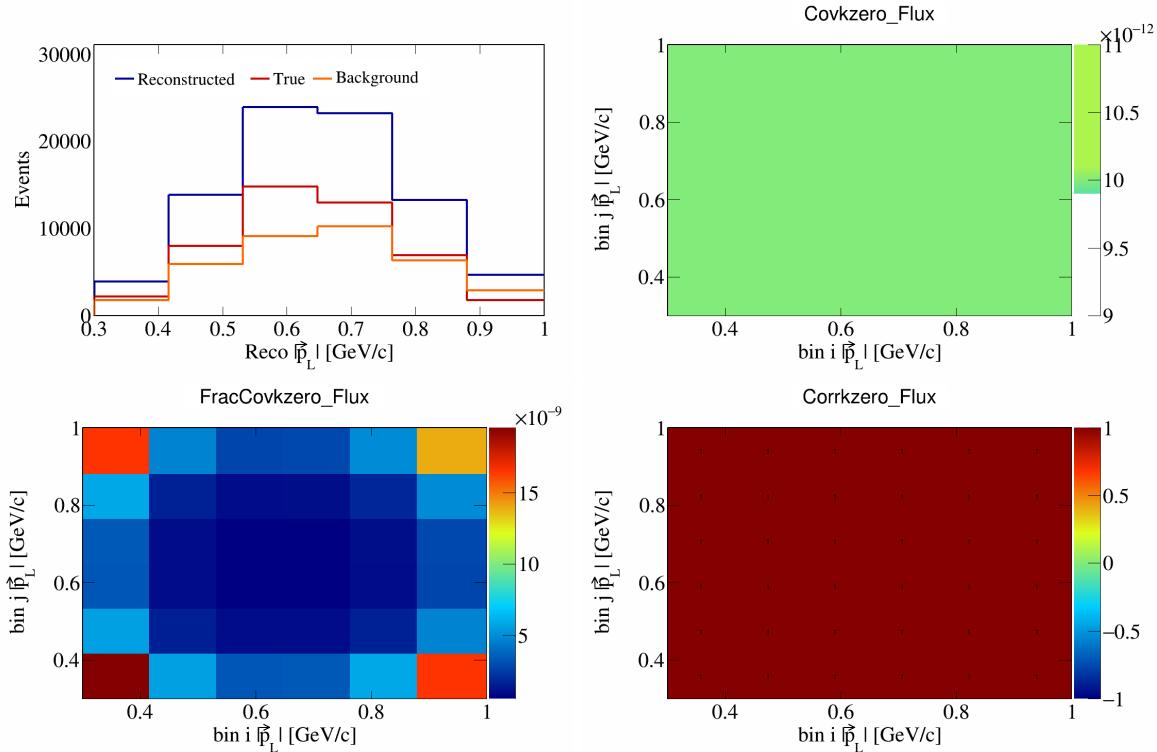


Figure 680: KZero variations for $|\vec{p}_L|$.

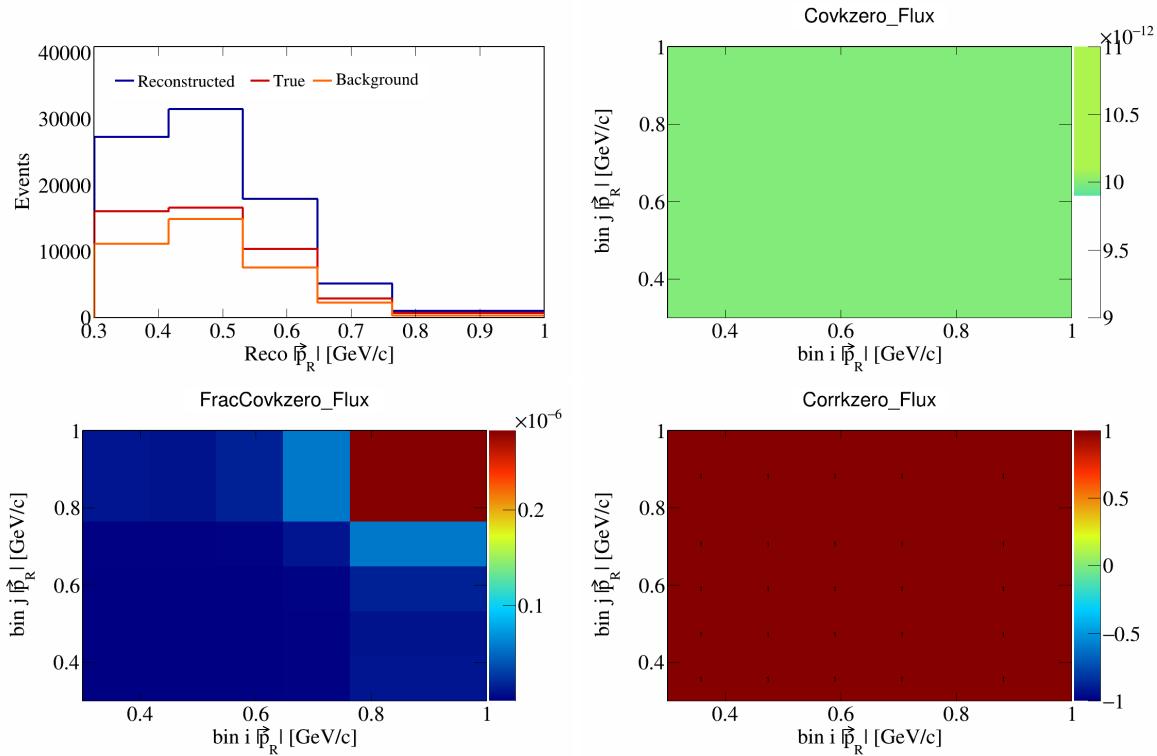


Figure 681: KZero variations for $|\vec{p}_R|$.

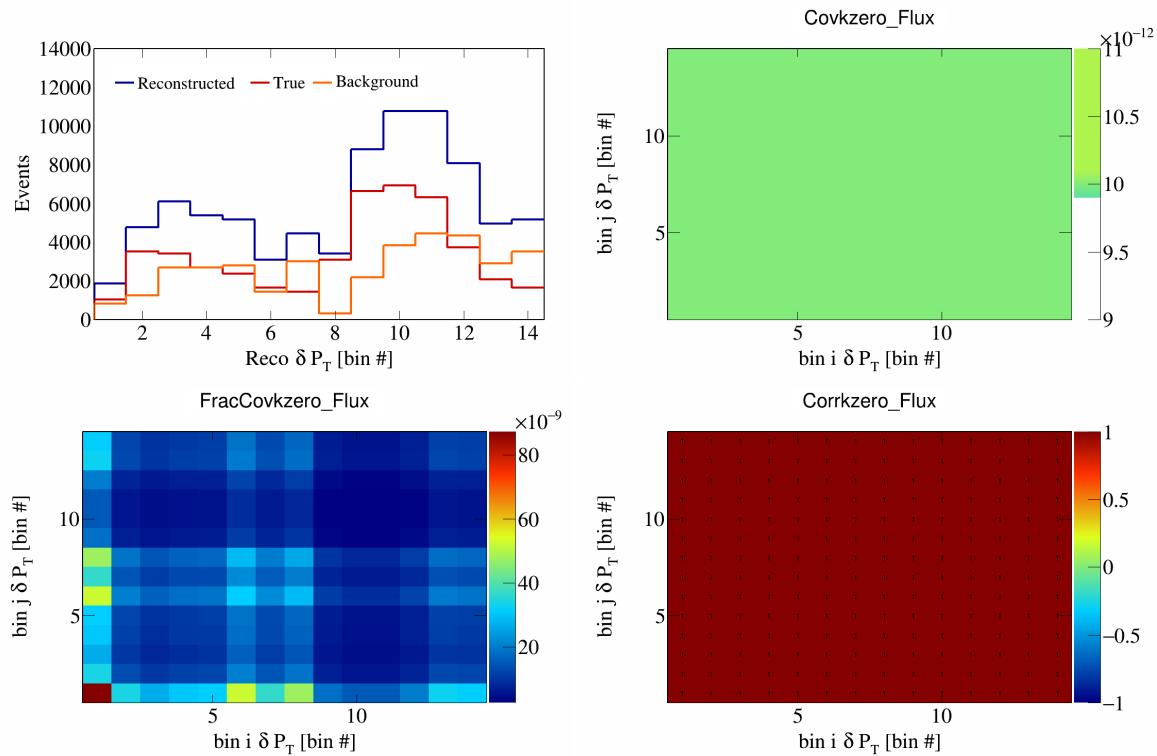


Figure 682: KZero variations for δP_T in $\cos(\theta_{\vec{p}_\mu})$.

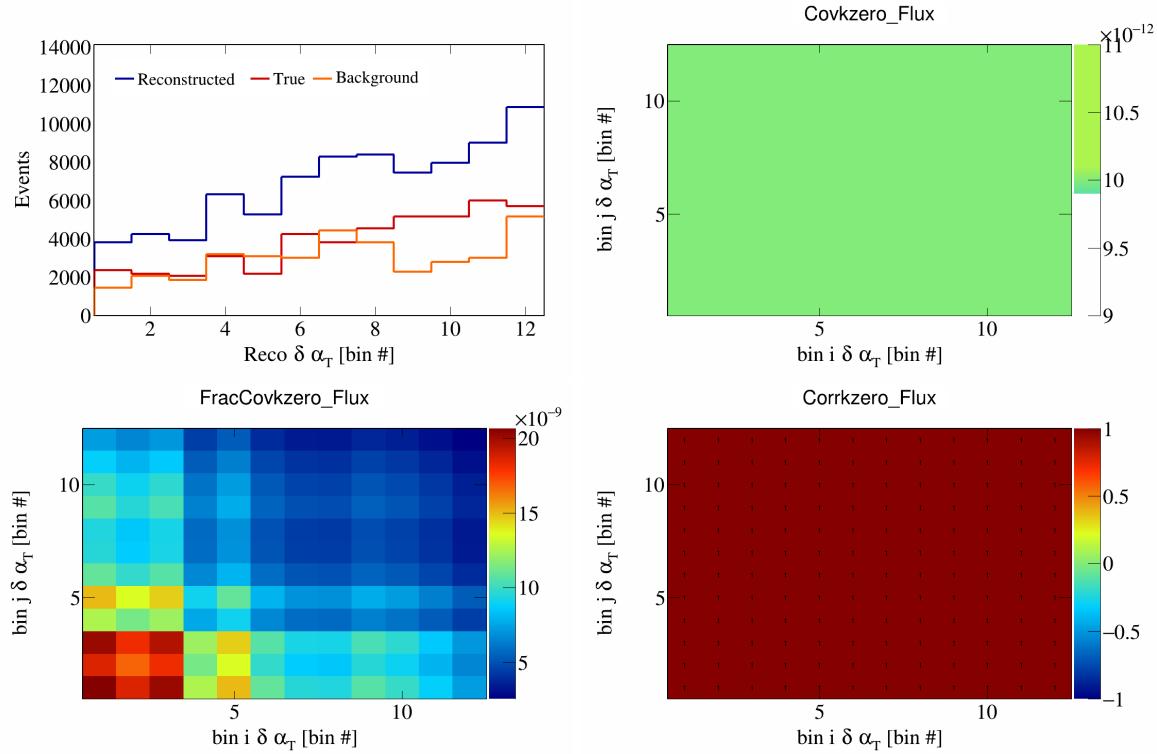


Figure 683: KZero variations for $\delta\alpha_T$ in $\cos(\theta_{\vec{p}_\mu})$.

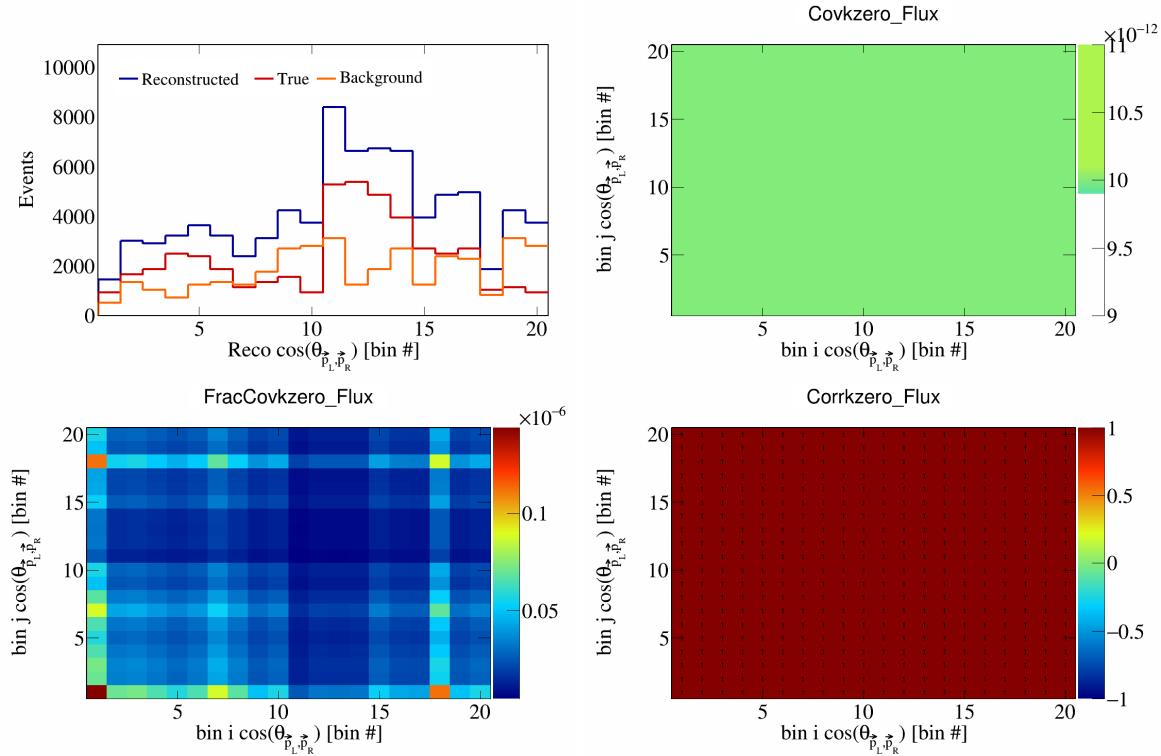


Figure 684: KZero variations for $\cos(\theta_{\vec{p}_L, \vec{p}_R})$ in $\cos(\theta_{\vec{p}_\mu})$.

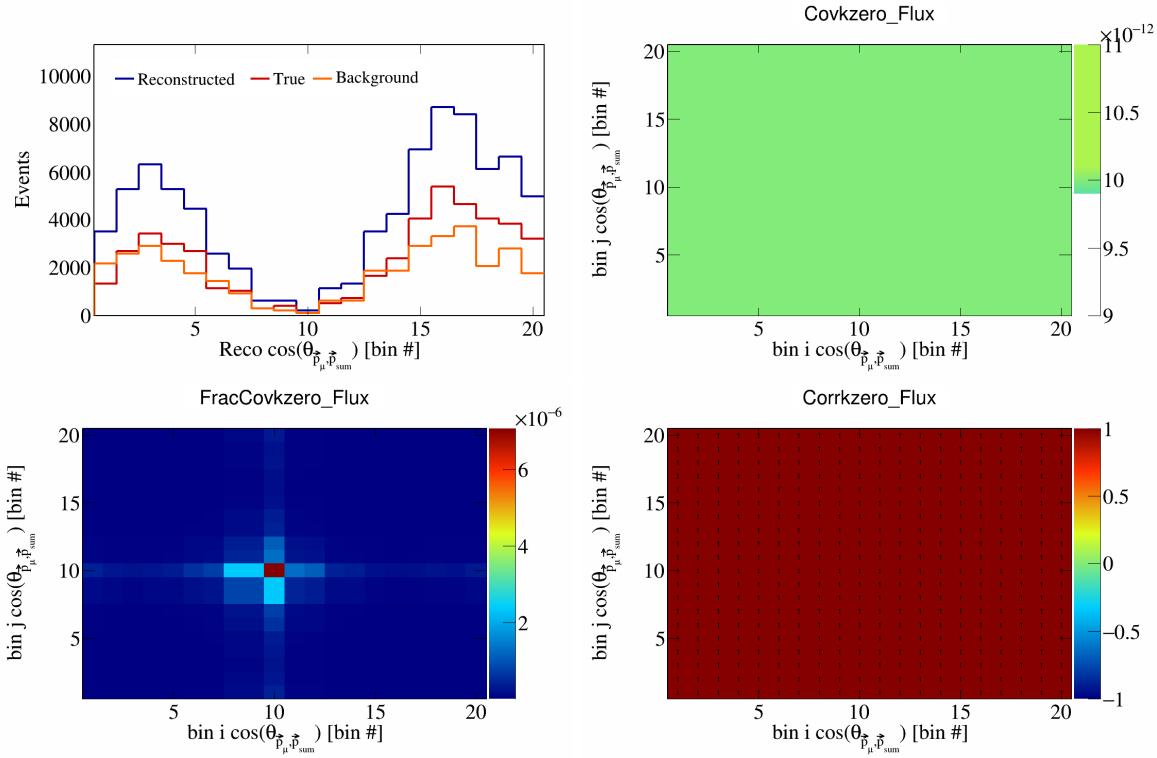


Figure 685: KZero variations for $\cos(\theta_{\vec{p}_\mu, \vec{p}_{\text{sum}}})$ in $\cos(\theta_{\vec{p}_\mu})$.

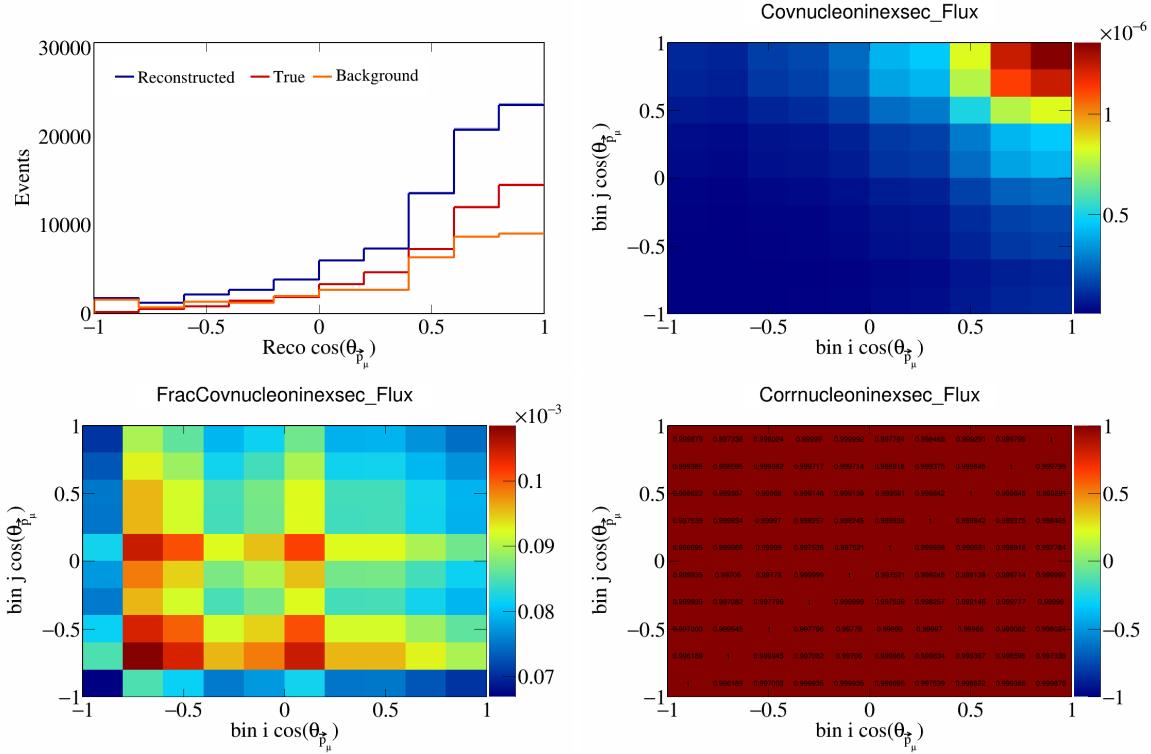


Figure 686: NucleonIneXSec variations for $\cos(\theta_{\vec{p}_\mu})$.

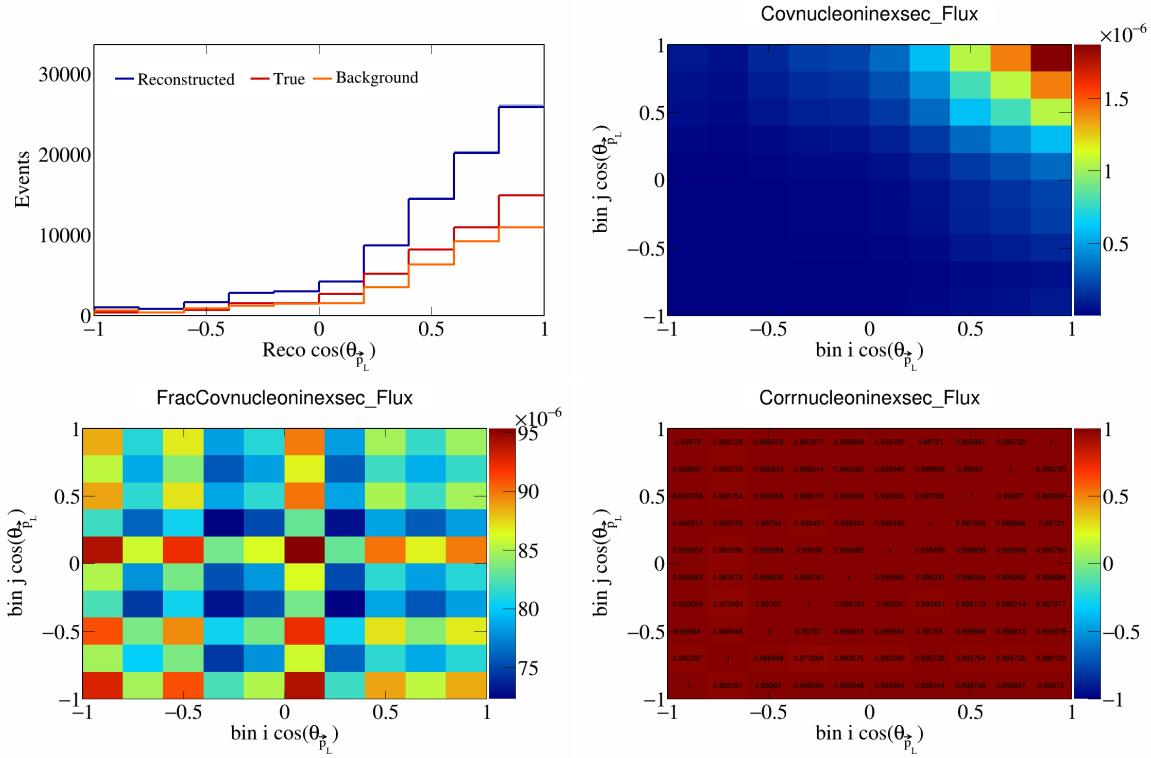


Figure 687: NucleonIneXSec variations for $\cos(\theta_{\vec{p}_L})$.

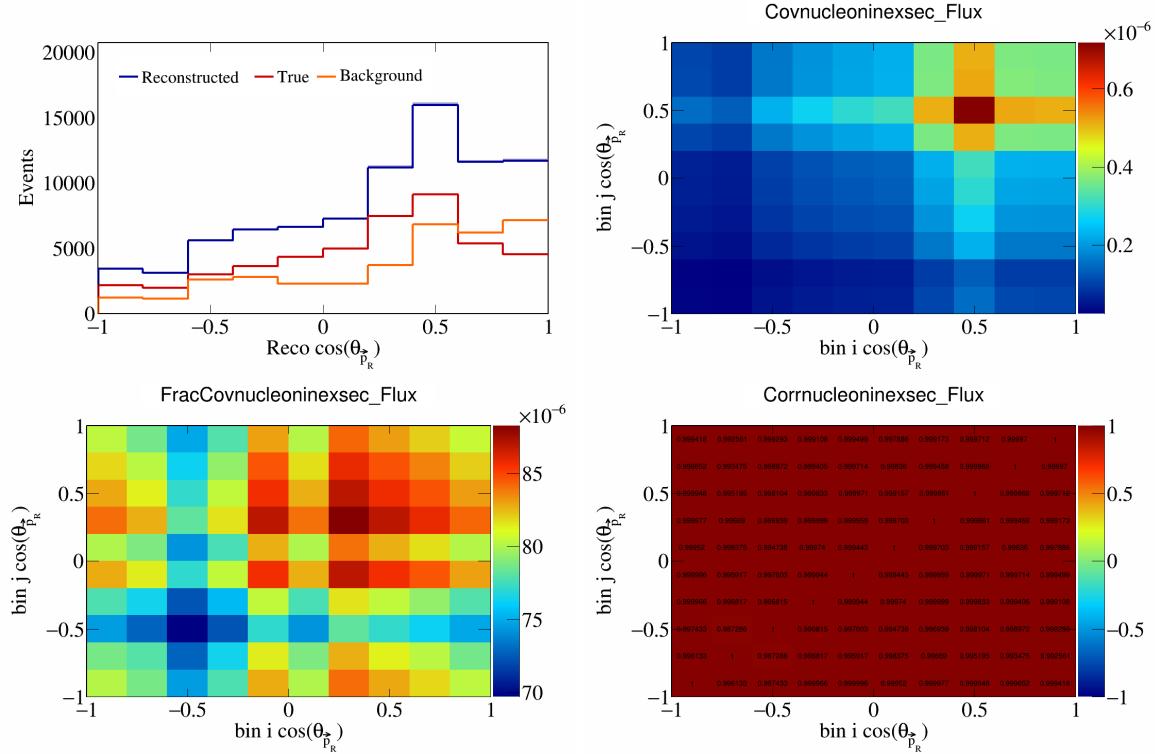


Figure 688: NucleonIneXSec variations for $\cos(\theta_{\vec{p}_R})$.

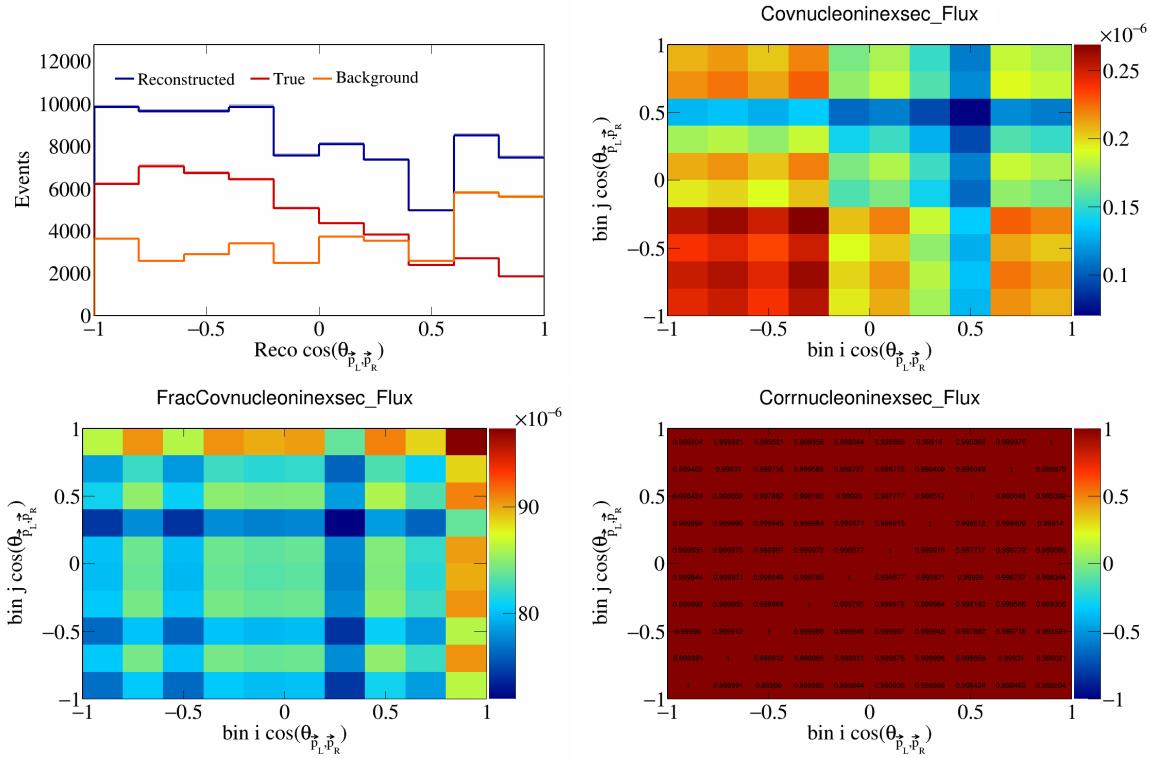


Figure 689: NucleonIneXSec variations for $\cos(\theta_{\vec{p}_L, \vec{p}_R})$.

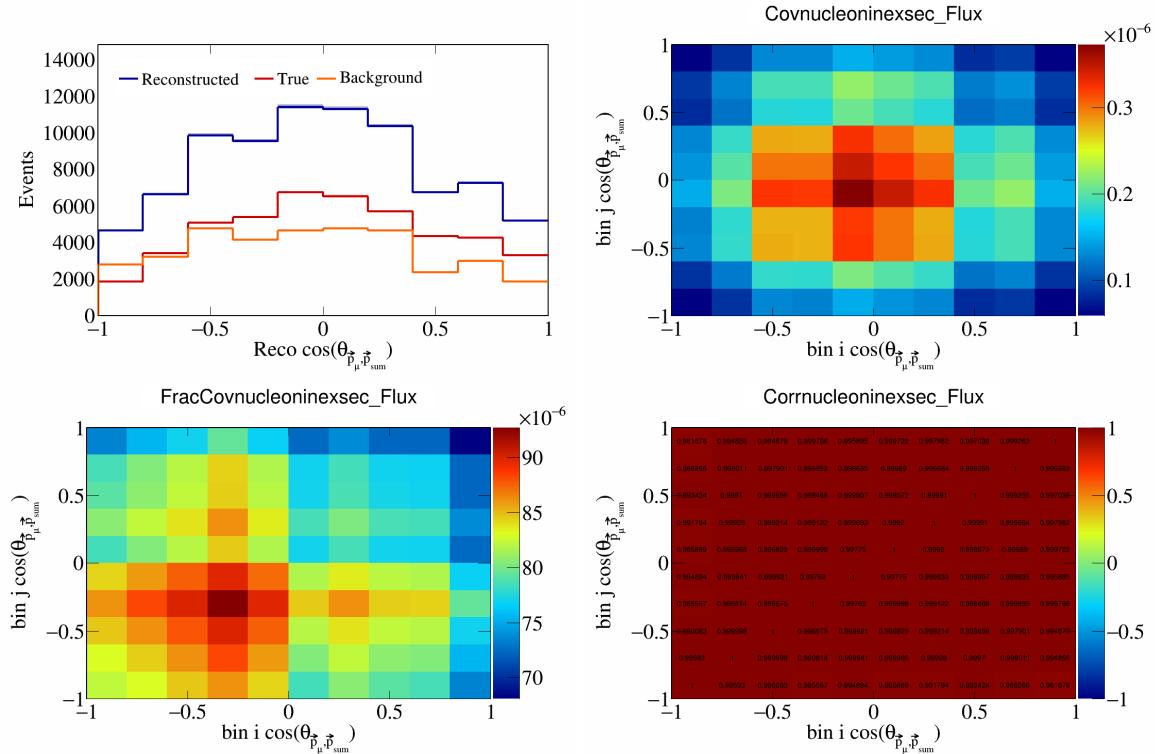


Figure 690: NucleonIneXSec variations for $\cos(\theta_{\vec{p}_\mu, \vec{p}_{\text{sum}}})$.

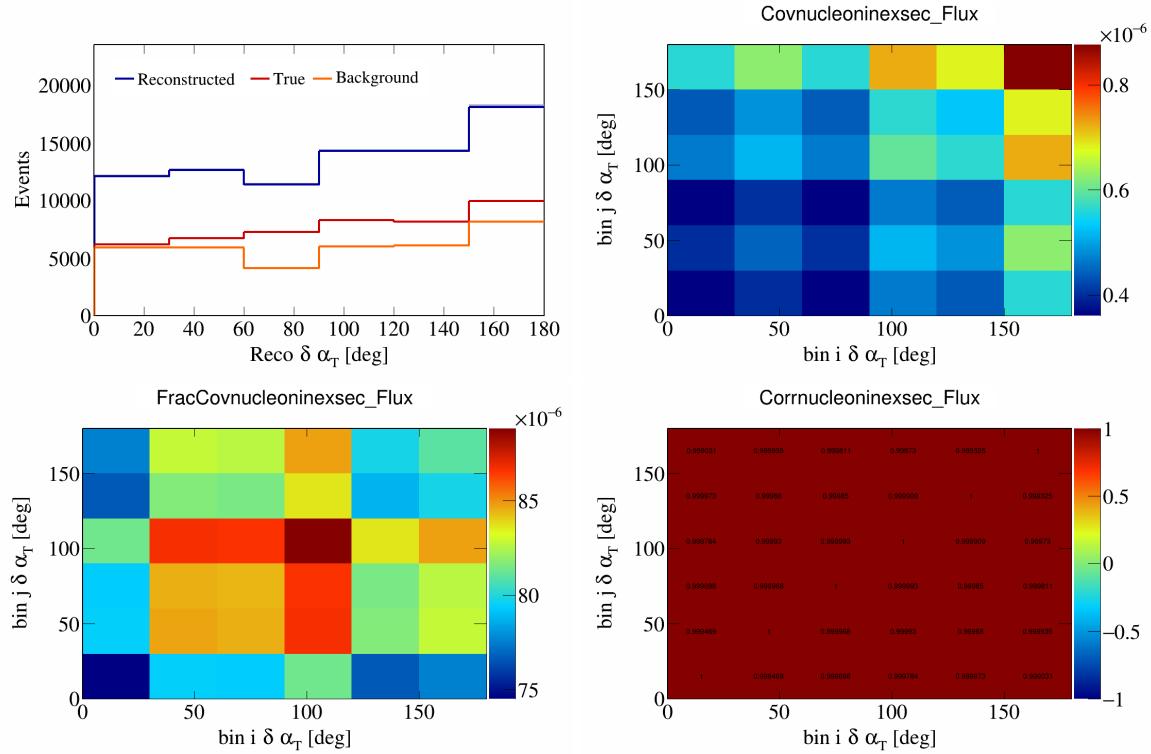


Figure 691: NucleonIneXSec variations for $\delta\alpha_T$.

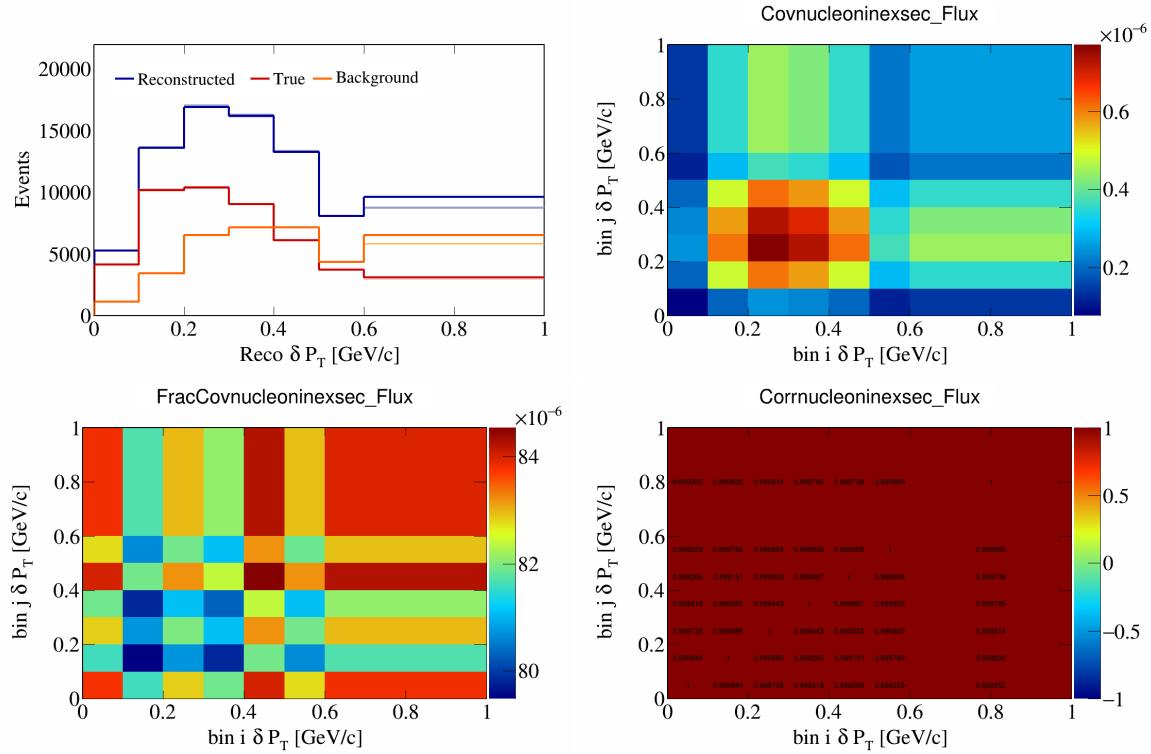


Figure 692: NucleonIneXSec variations for δP_T .

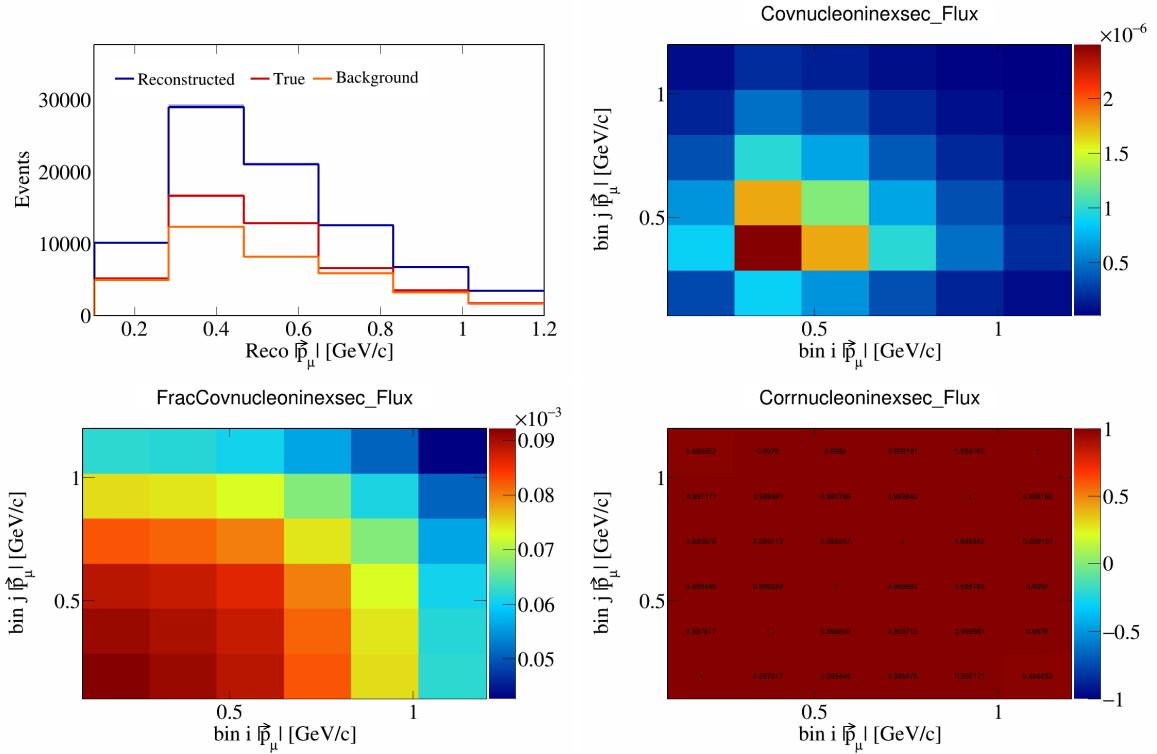


Figure 693: NucleonIneXSec variations for $|\vec{p}_\mu|$.

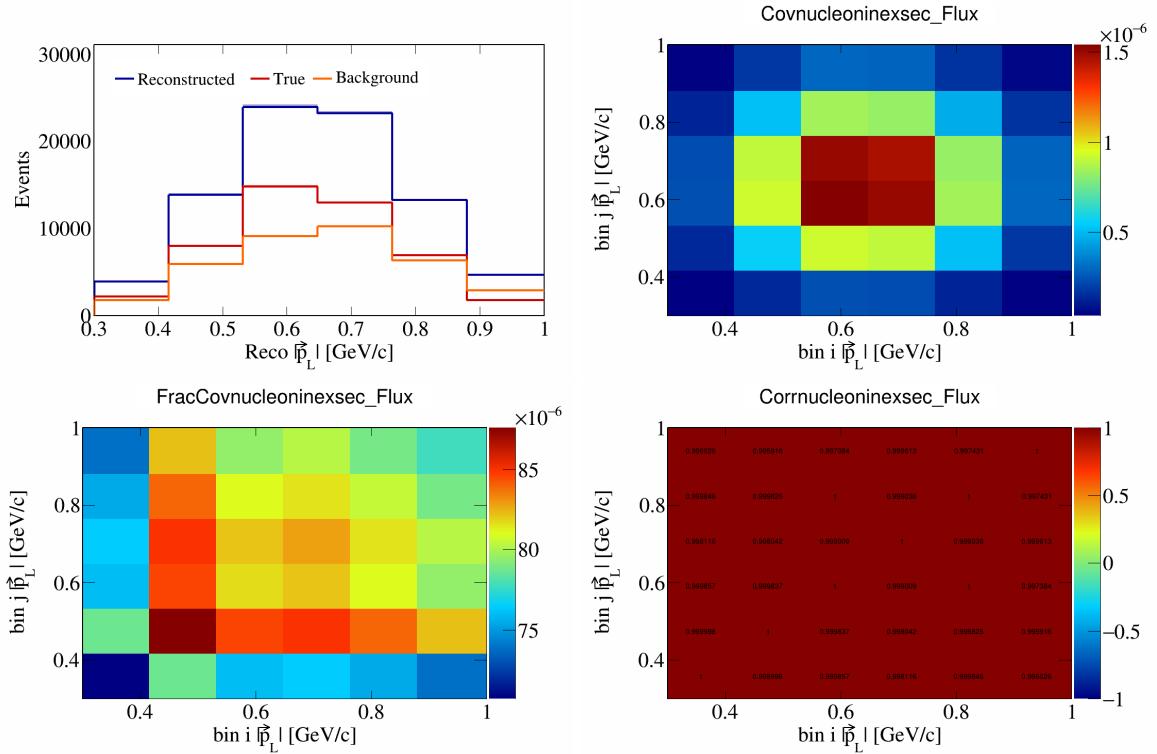


Figure 694: NucleonIneXSec variations for $|\vec{p}_L|$.

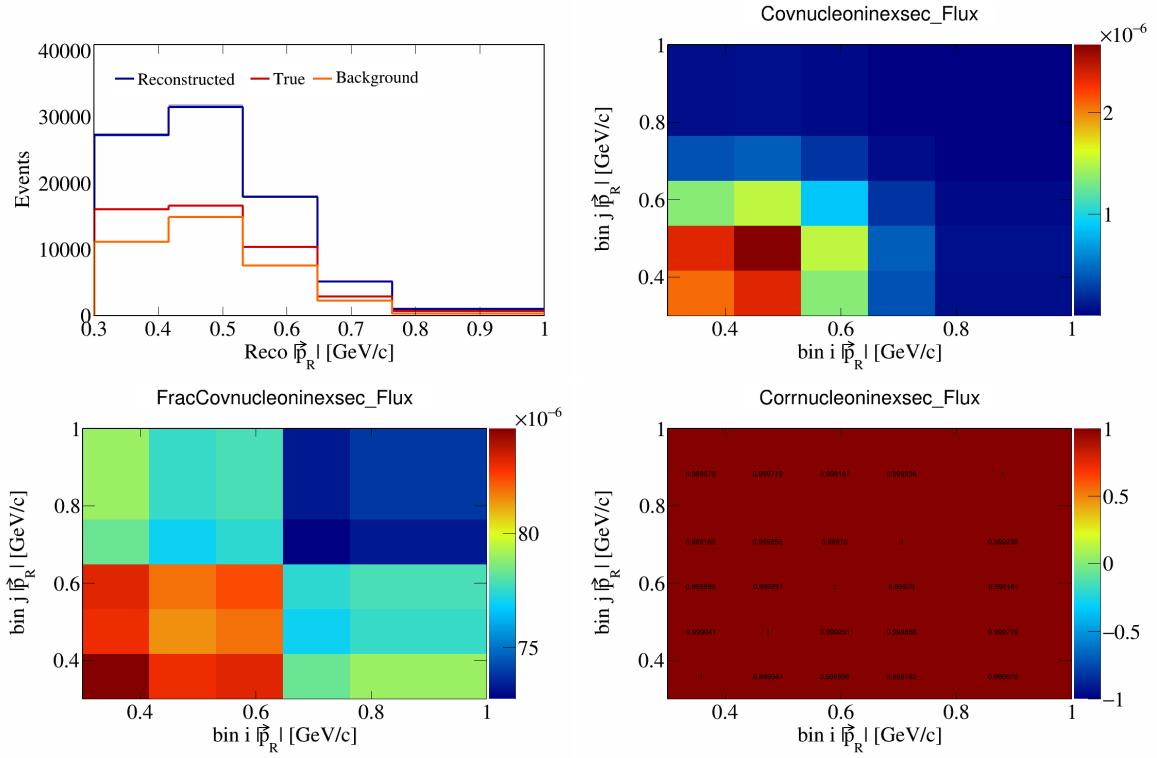


Figure 695: NucleonIneXSec variations for $|\vec{p}_R|$.

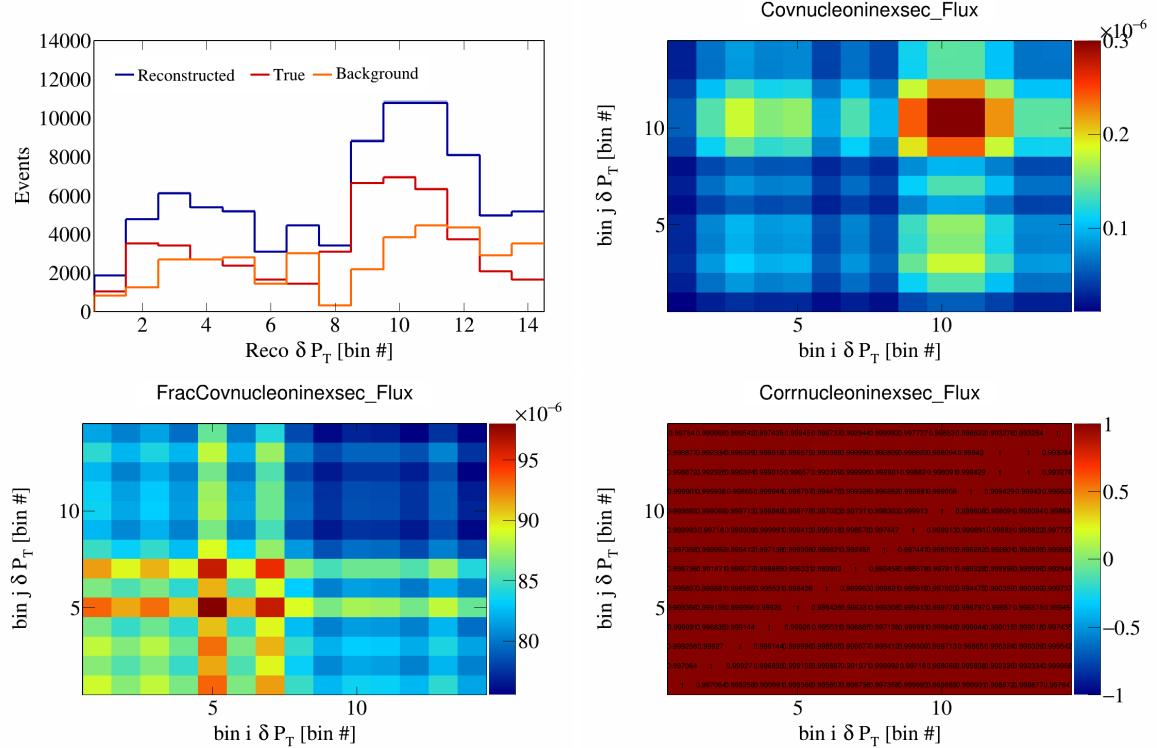


Figure 696: NucleonIneXSec variations for δP_T in $\cos(\theta_{\vec{p}_\mu})$.

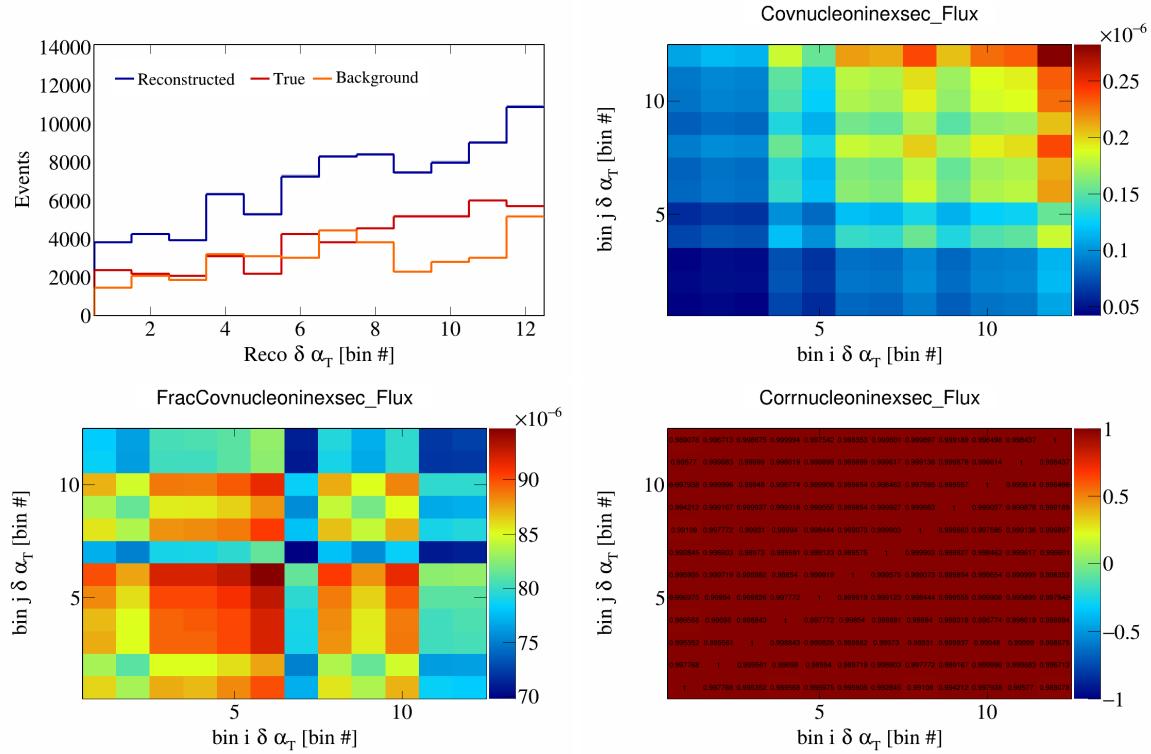


Figure 697: NucleonIneXSec variations for $\delta\alpha_T$ in $\cos(\theta_{\vec{p}_\mu})$.

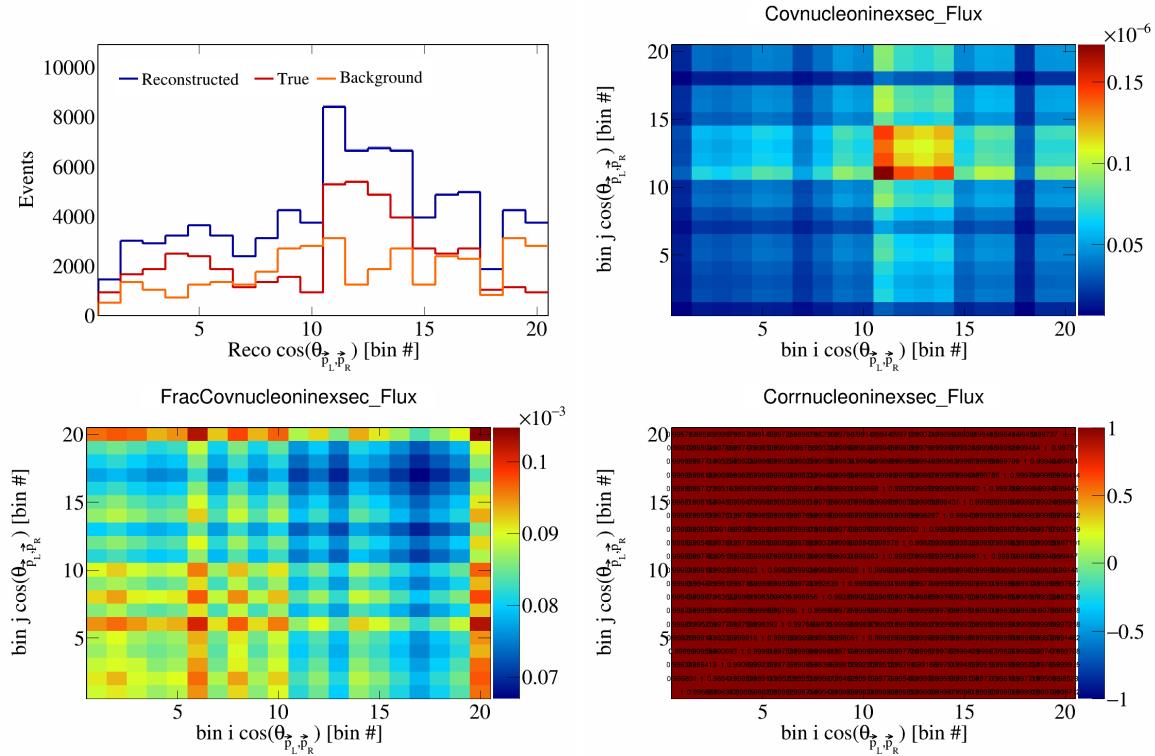


Figure 698: NucleonIneXSec variations for $\cos(\theta_{\vec{p}_L, \vec{p}_R})$ in $\cos(\theta_{\vec{p}_\mu})$.

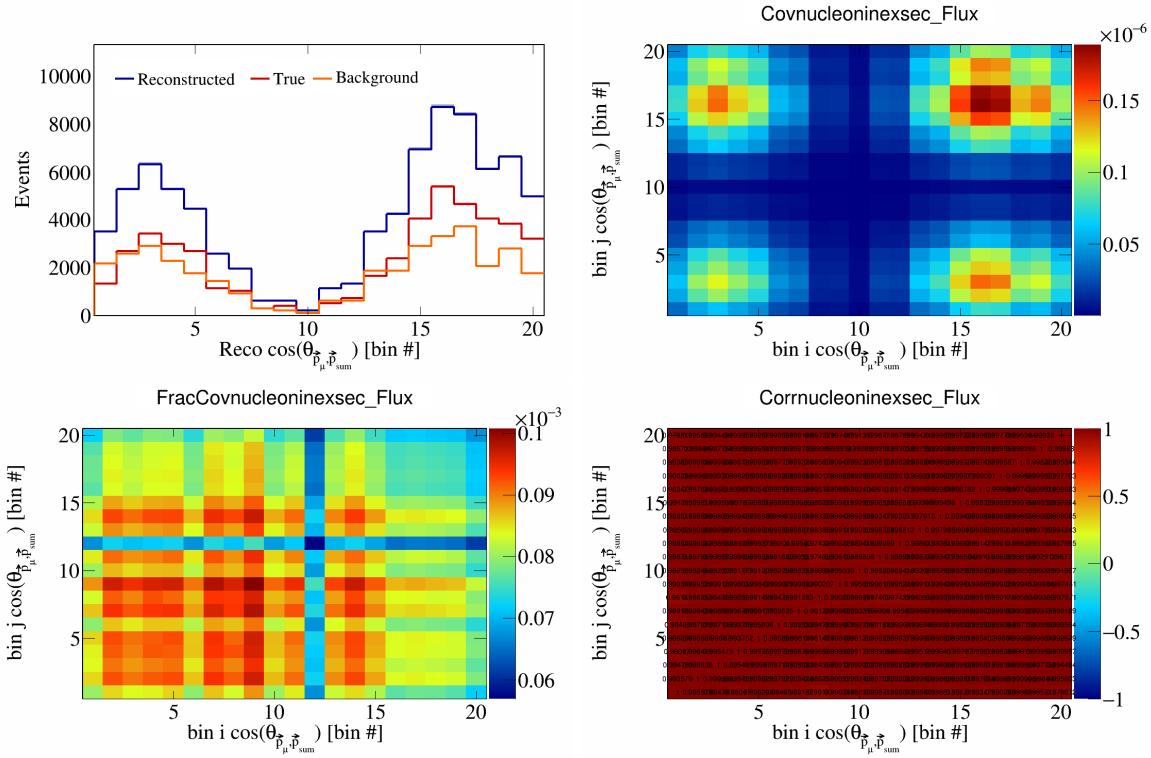


Figure 699: NucleonIneXSec variations for $\cos(\theta_{\vec{p}_\mu})$ in $\cos(\theta_{\vec{p}_\mu})$.

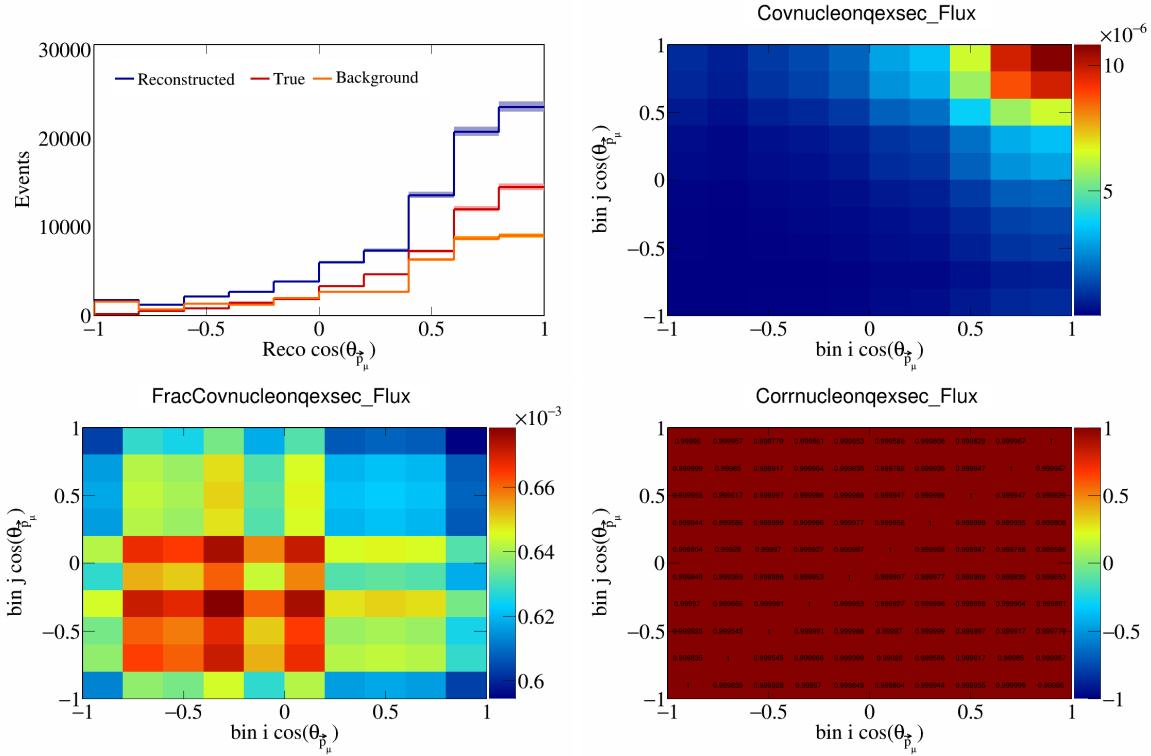


Figure 700: NucleonQeXSec variations for $\cos(\theta_{\vec{p}_\mu})$.

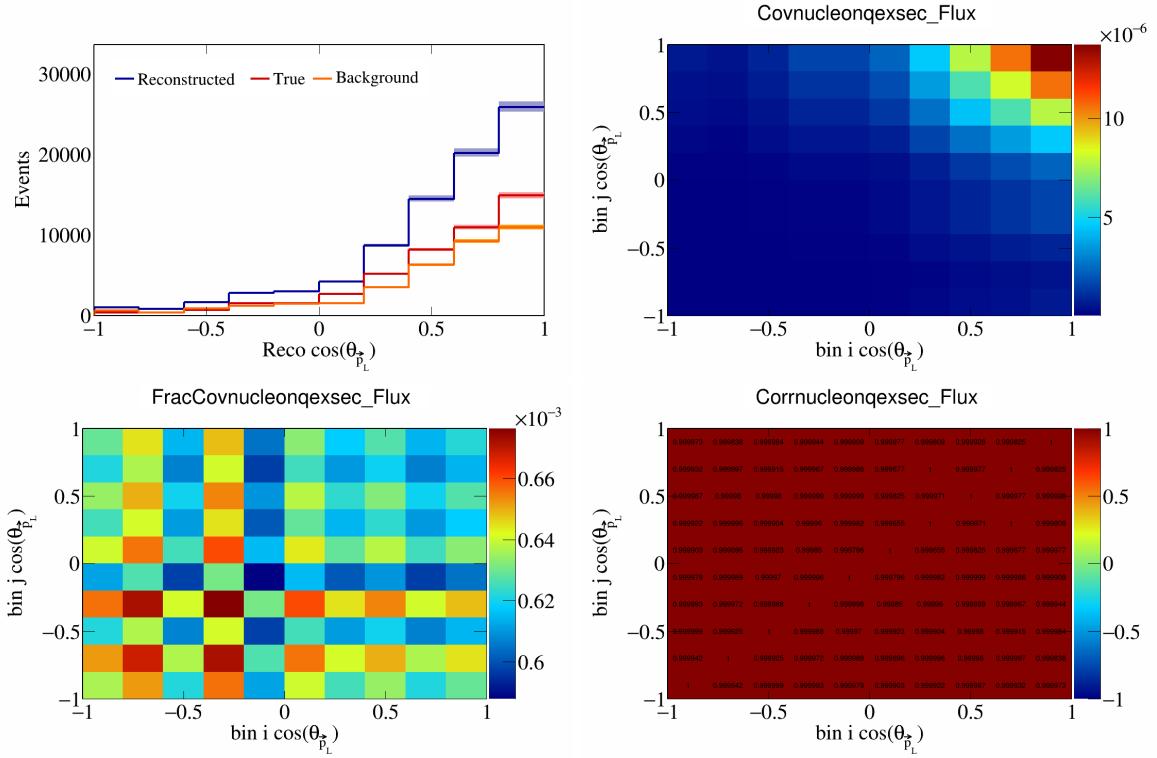


Figure 701: NucleonQeXSec variations for $\cos(\theta_{\vec{p}_L})$.

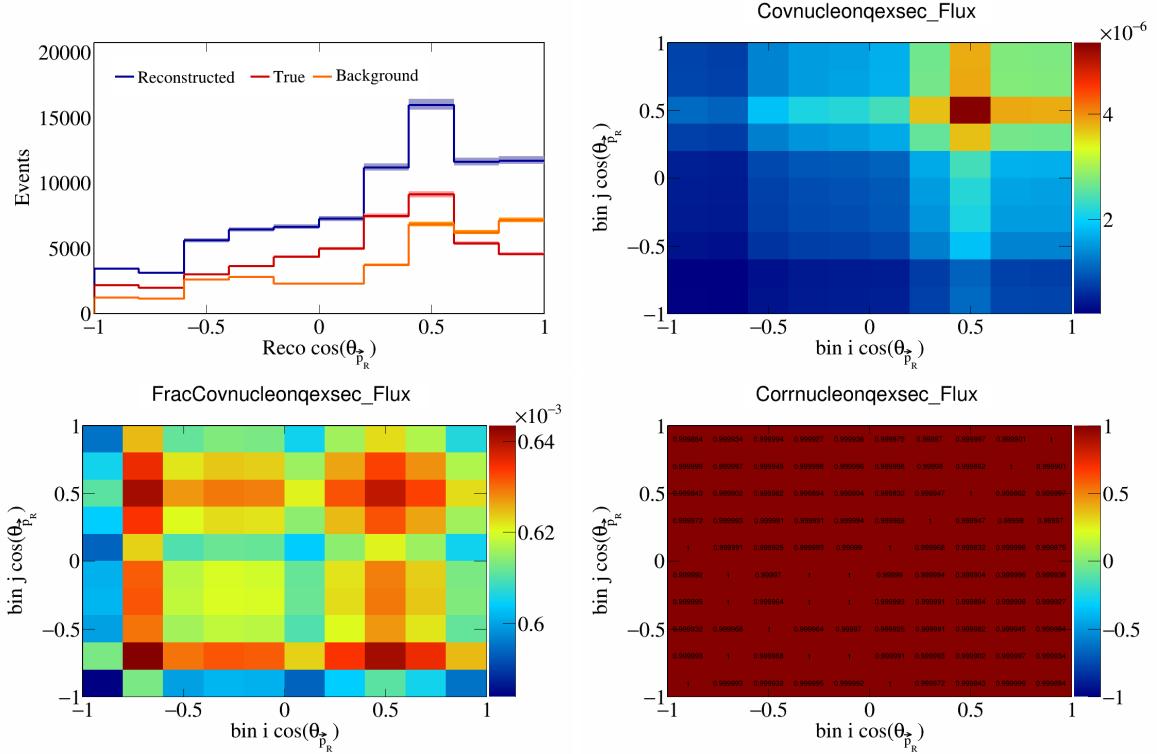


Figure 702: NucleonQeXSec variations for $\cos(\theta_{\vec{p}_R})$.

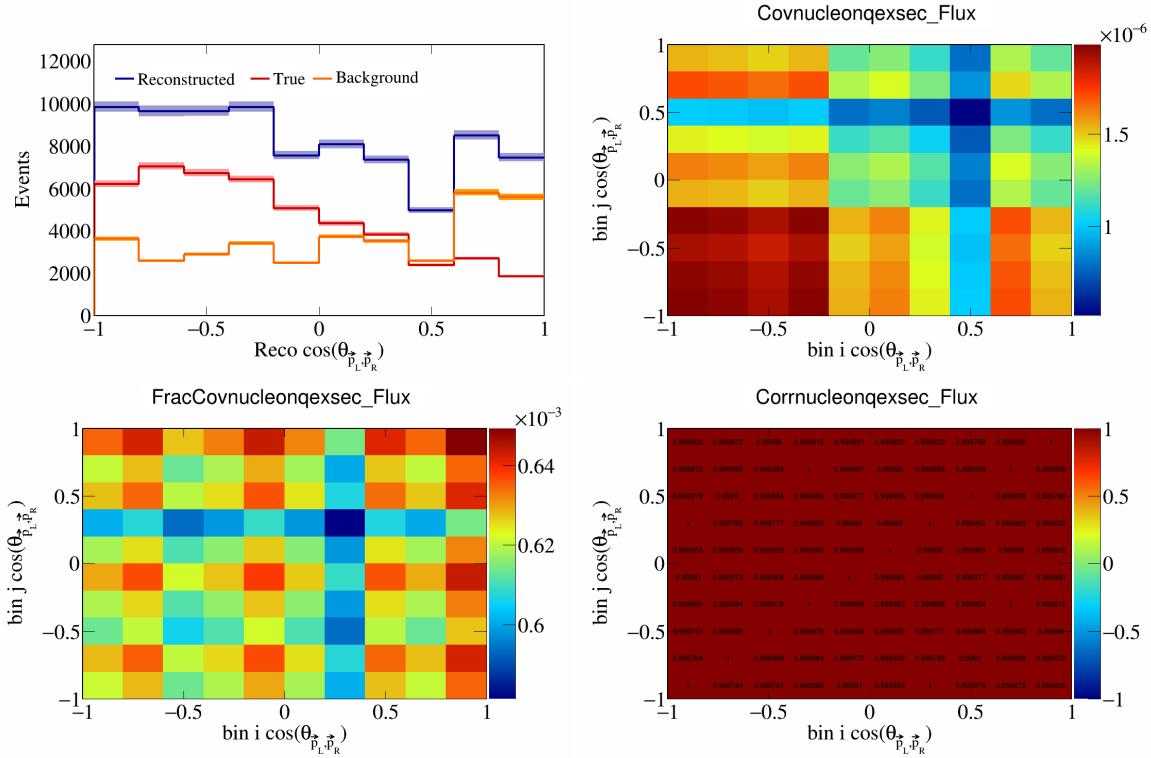


Figure 703: NucleonQeXSec variations for $\cos(\theta_{\vec{p}_L, \vec{p}_R})$.

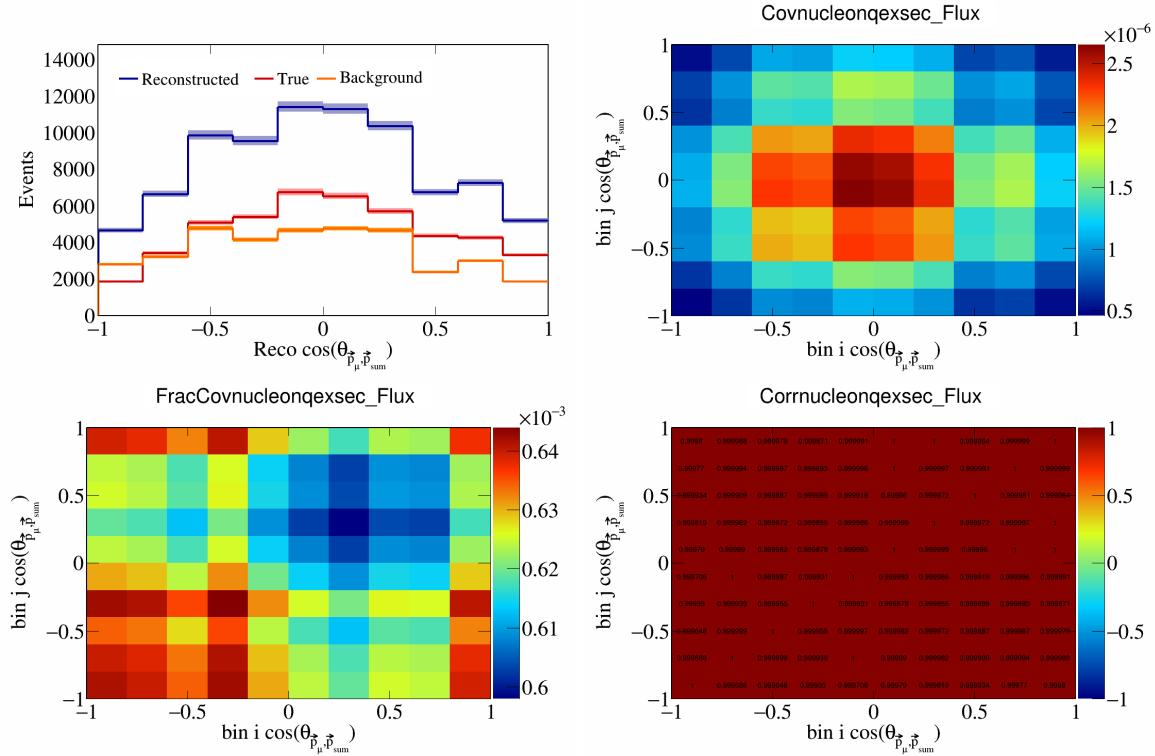


Figure 704: NucleonQeXSec variations for $\cos(\theta_{\vec{p}_\mu, \vec{p}_{\text{sum}}})$.

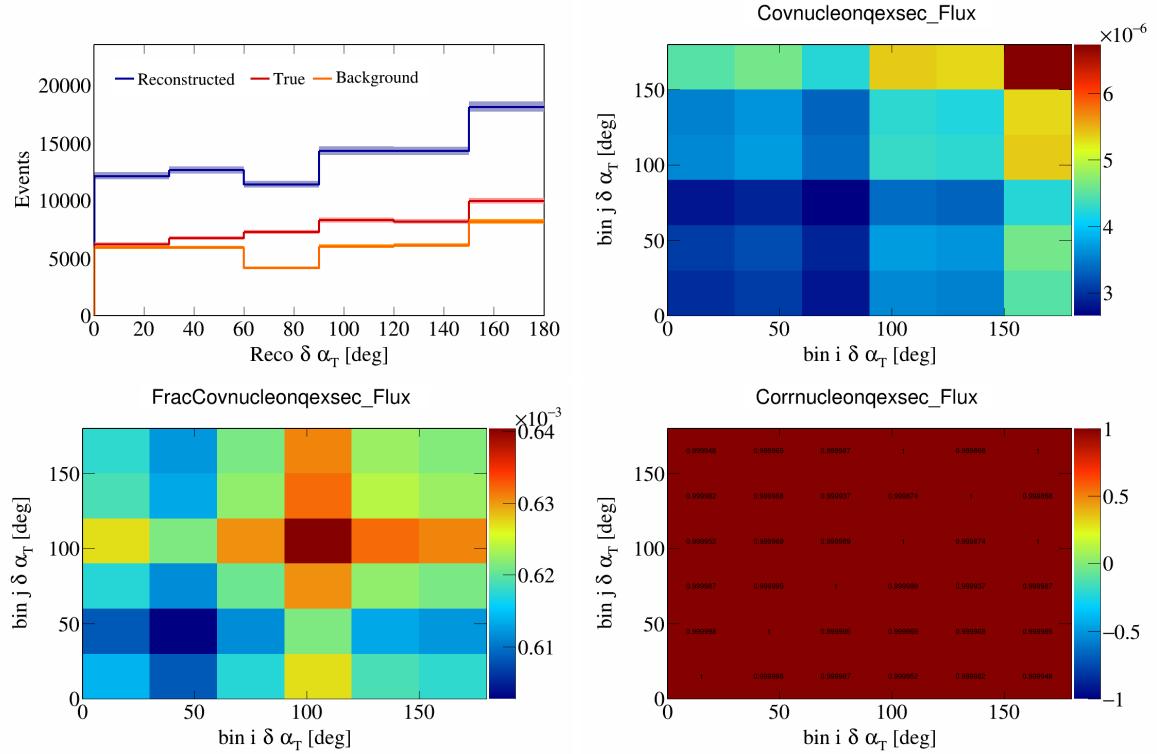


Figure 705: NucleonQeXSec variations for $\delta\alpha_T$.

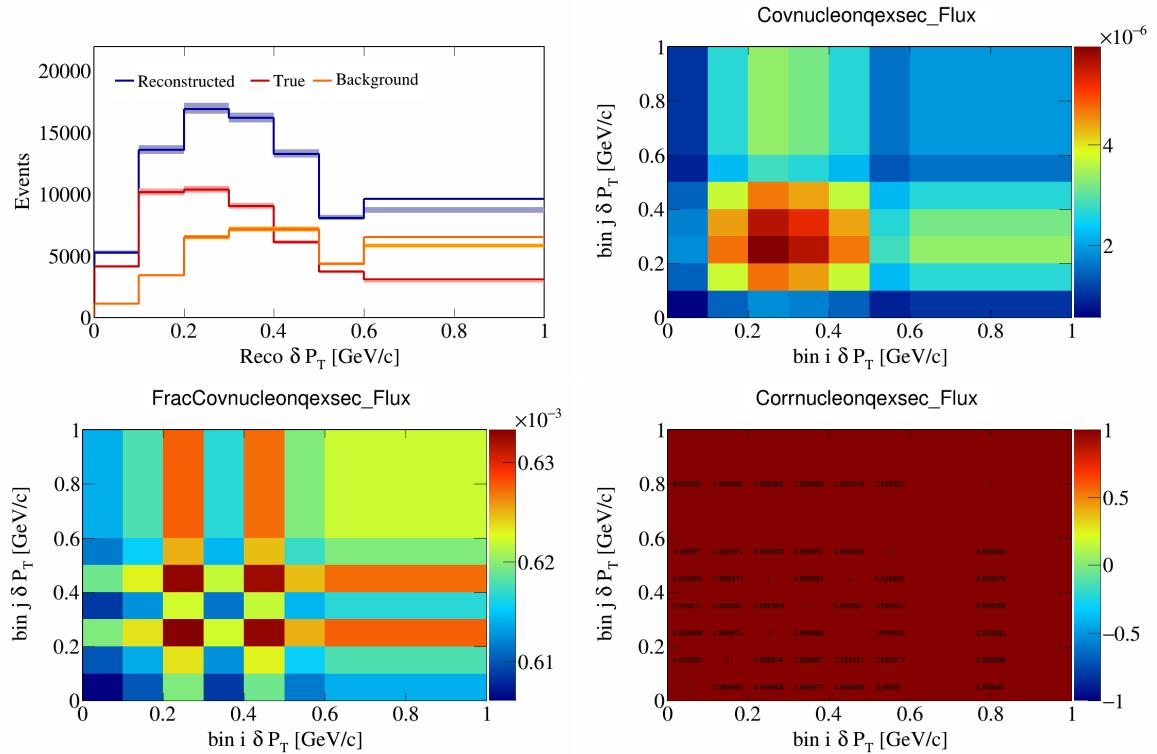


Figure 706: NucleonQeXSec variations for δP_T .

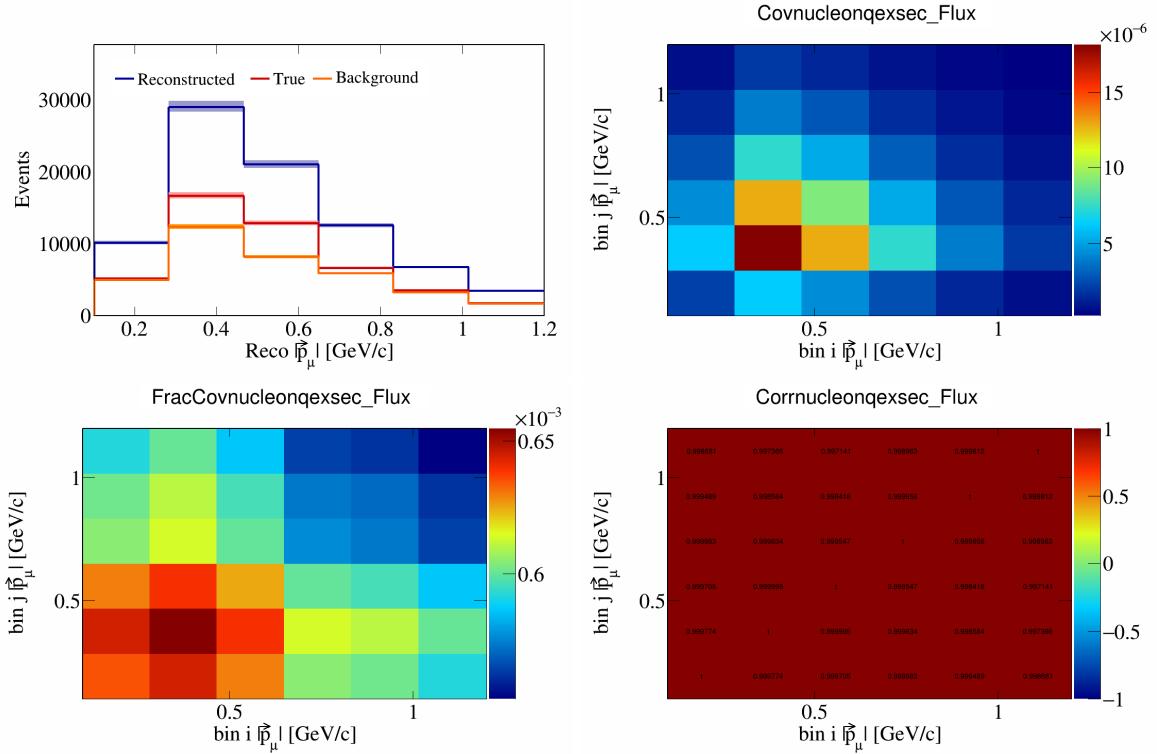


Figure 707: NucleonQeXSec variations for $|\vec{p}_\mu|$.

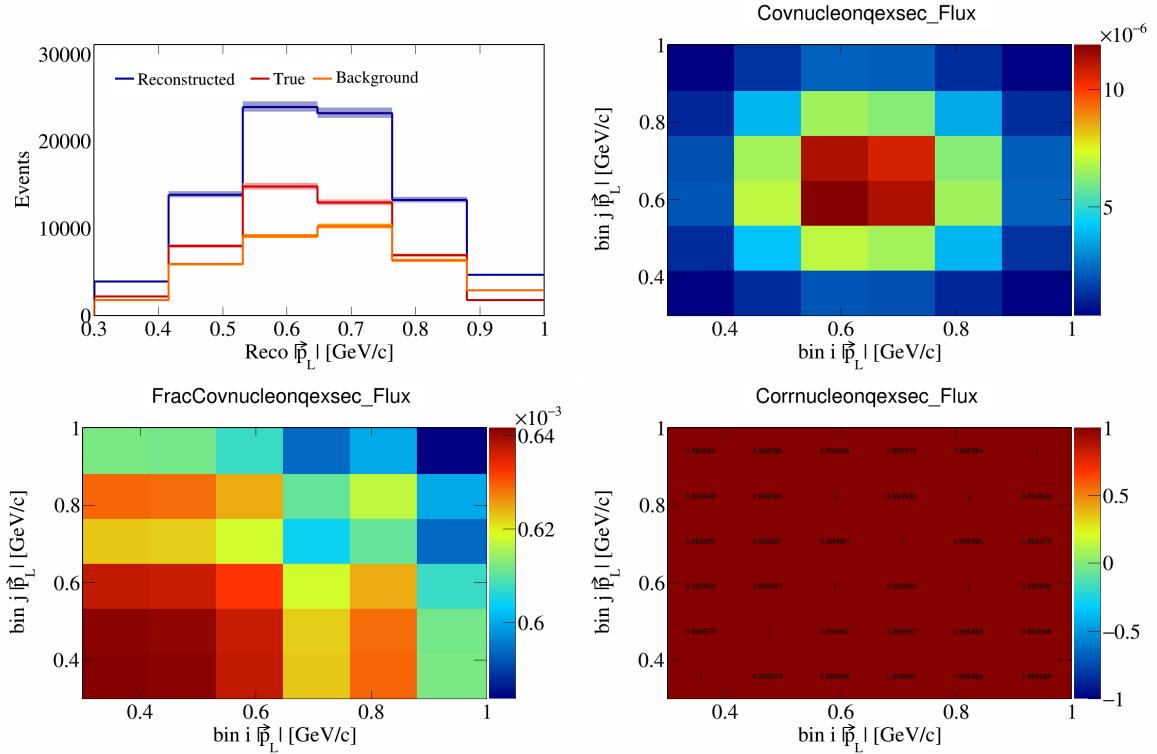


Figure 708: NucleonQeXSec variations for $|\vec{p}_L|$.

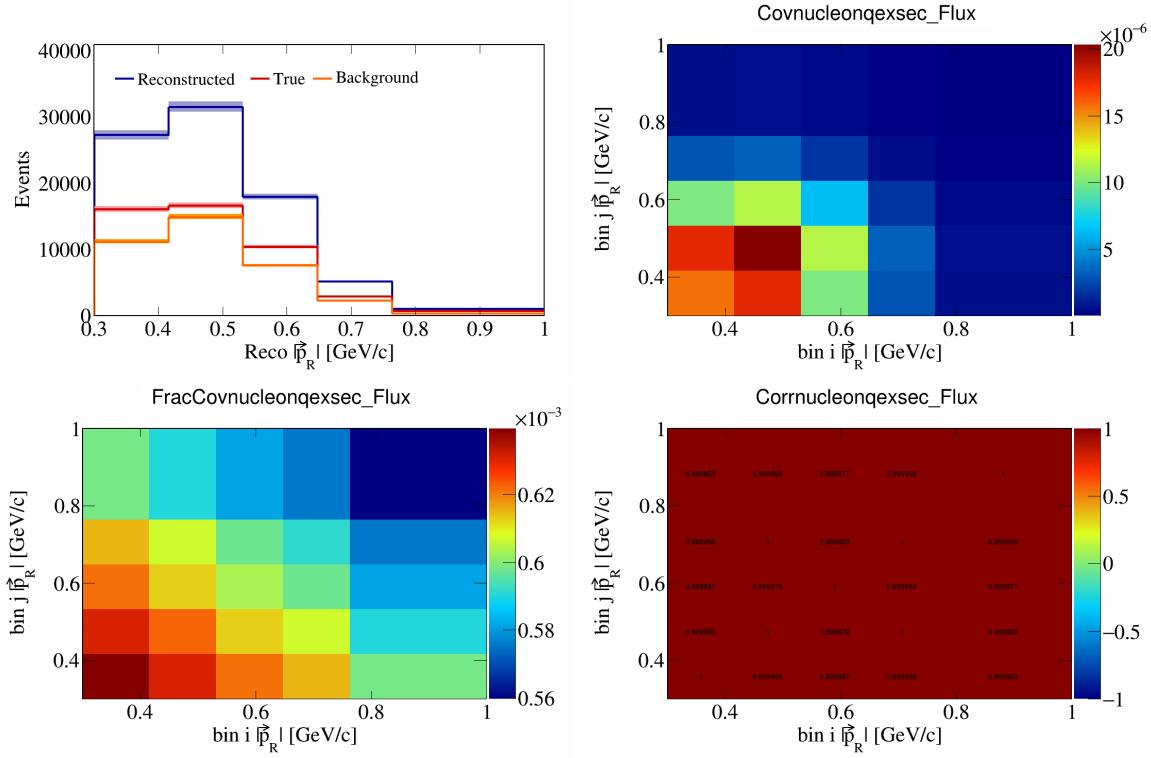


Figure 709: NucleonQeXSec variations for $|\vec{p}_R|$.

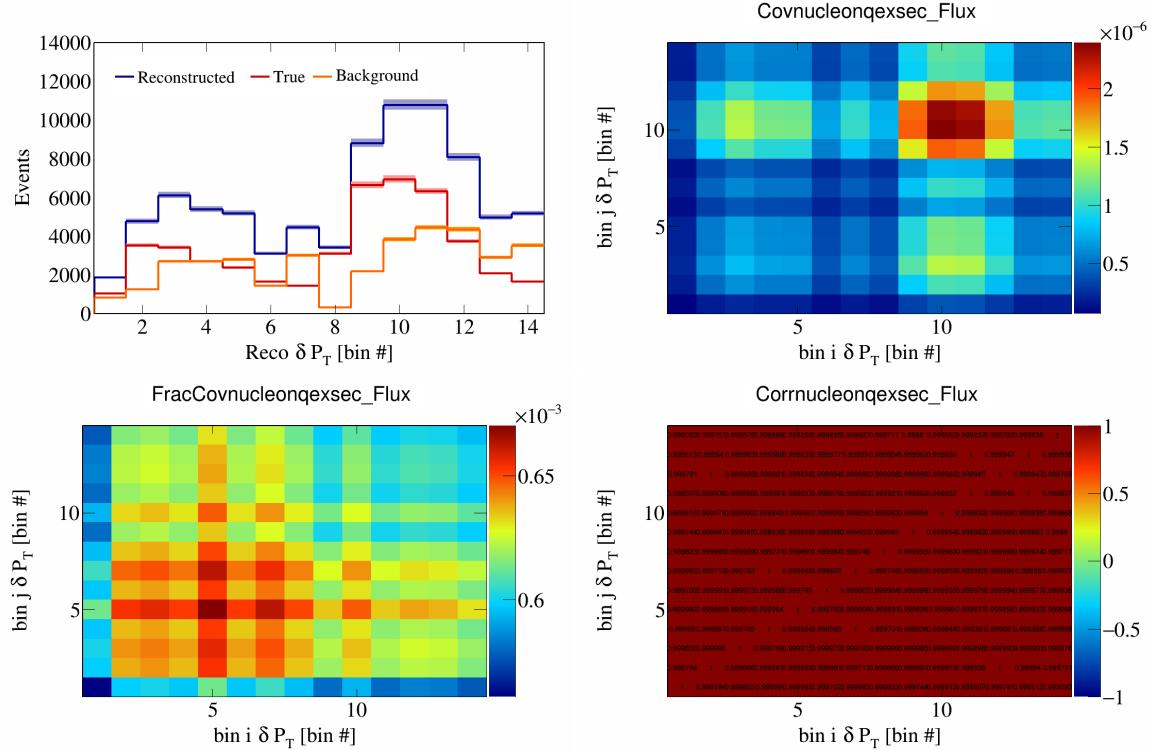


Figure 710: NucleonQeXSec variations for δP_T in $\cos(\theta_{\vec{p}_T})$.

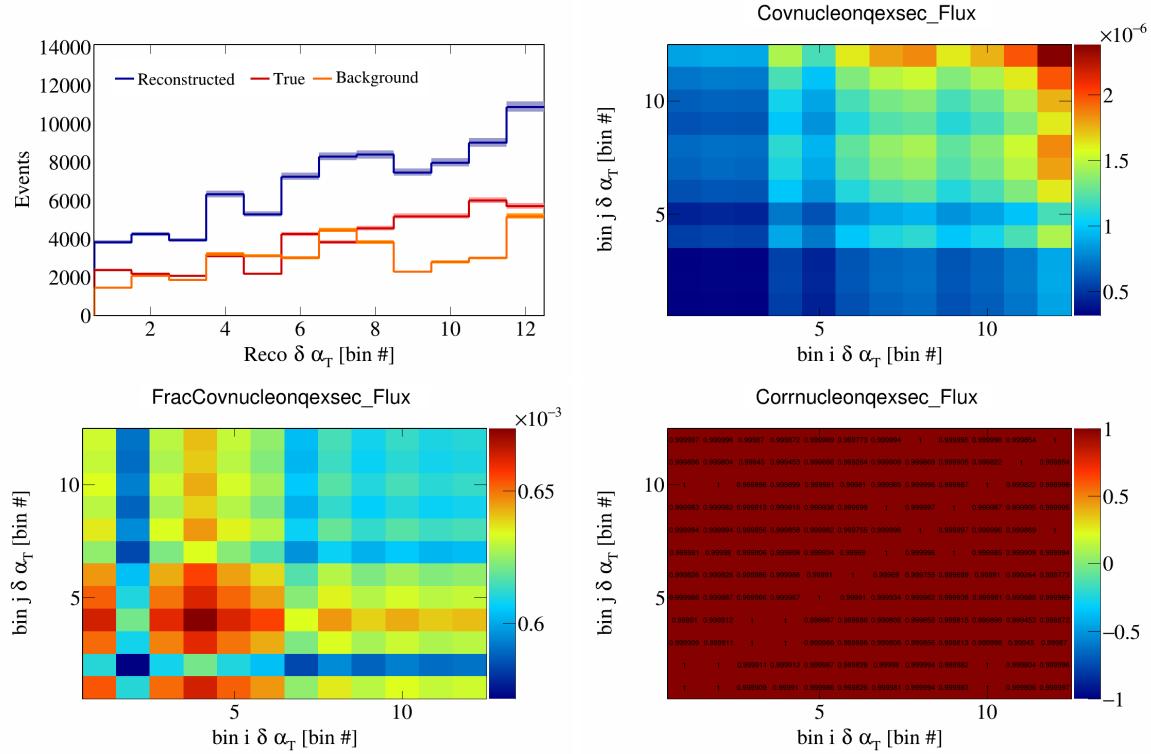


Figure 711: NucleonQeXSec variations for $\delta\alpha_T$ in $\cos(\theta_{\vec{p}_\mu})$.

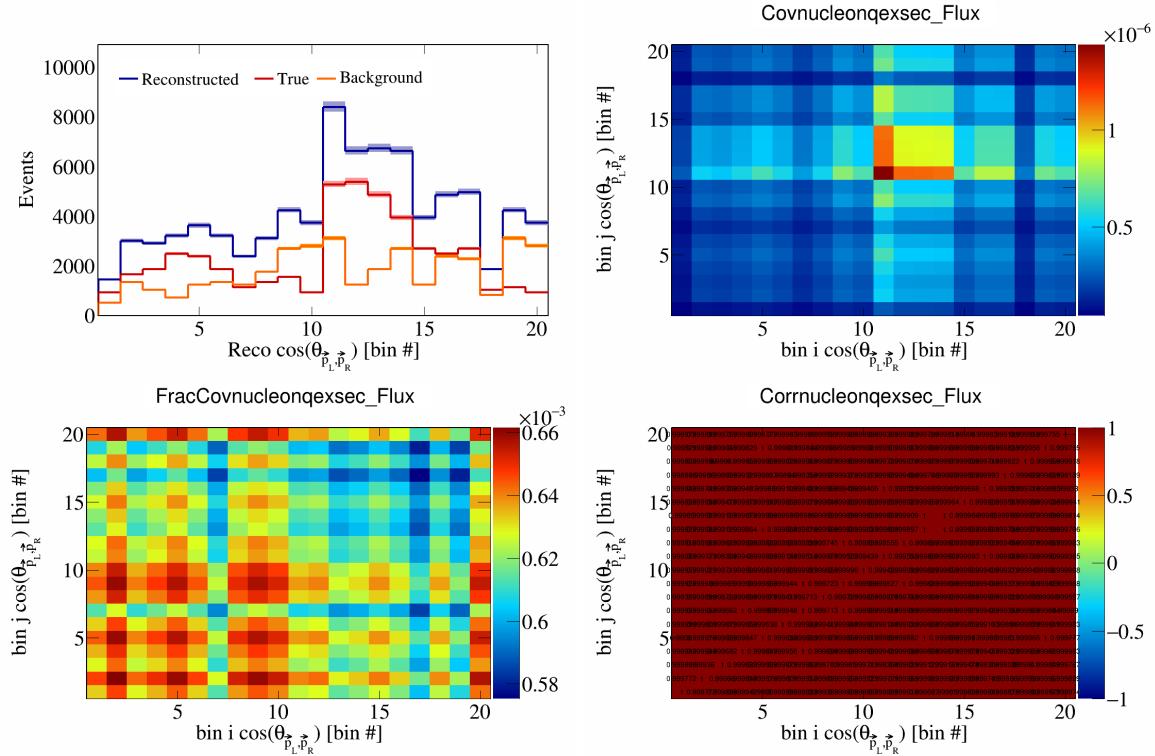


Figure 712: NucleonQeXSec variations for $\cos(\theta_{\vec{p}_L, \vec{p}_R})$ in $\cos(\theta_{\vec{p}_\mu})$.

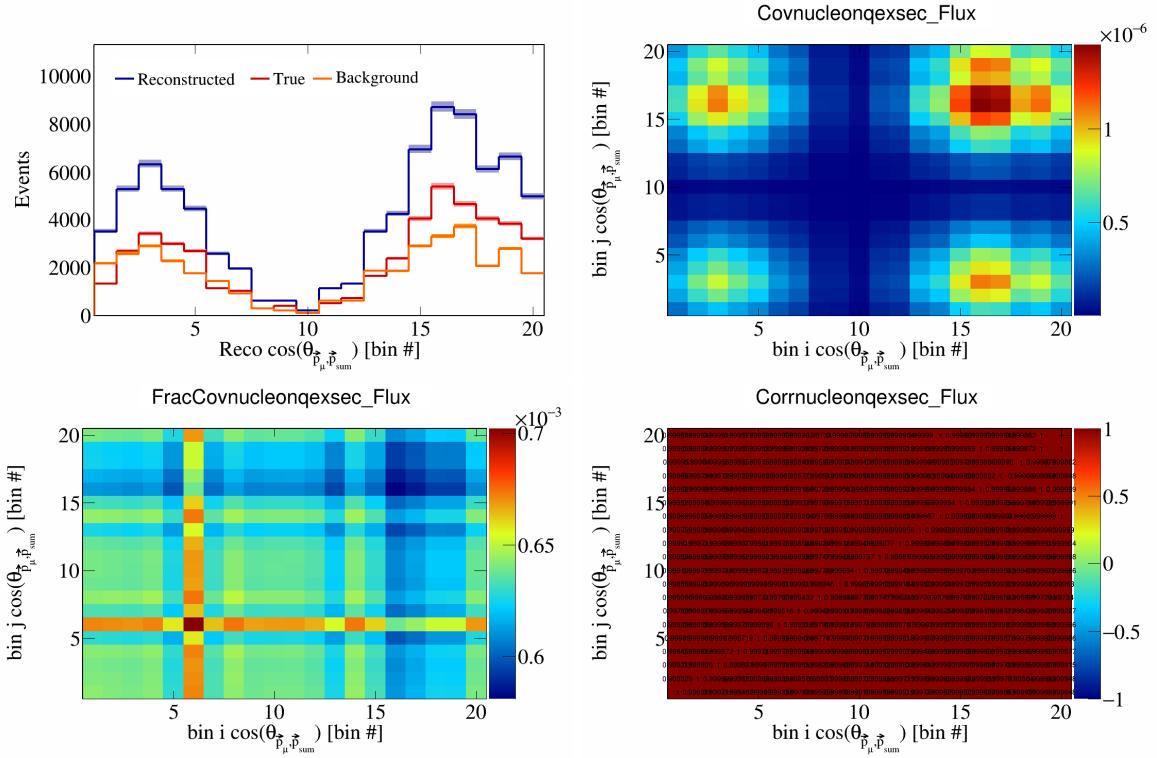


Figure 713: NucleonQeXSec variations for $\cos(\theta_{\vec{p}_\mu, \vec{p}_{\text{sum}}})$ in $\cos(\theta_{\vec{p}_\mu})$.

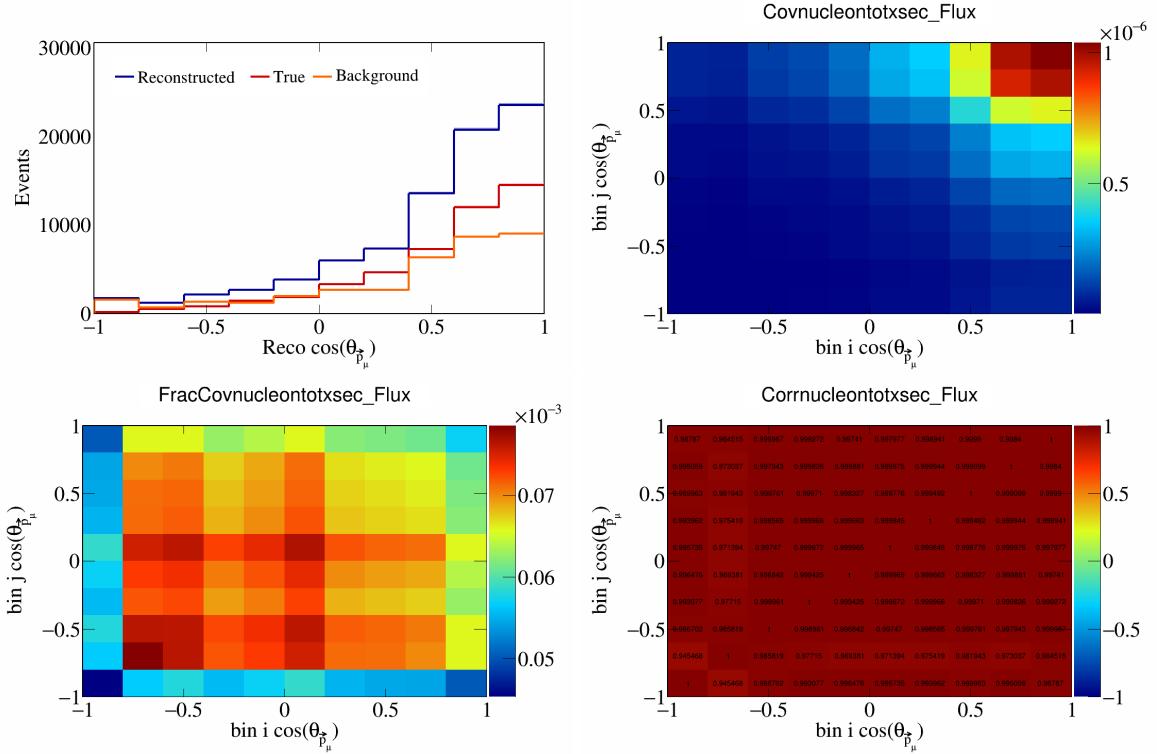


Figure 714: NucleonTotXSec variations for $\cos(\theta_{\vec{p}_\mu})$.

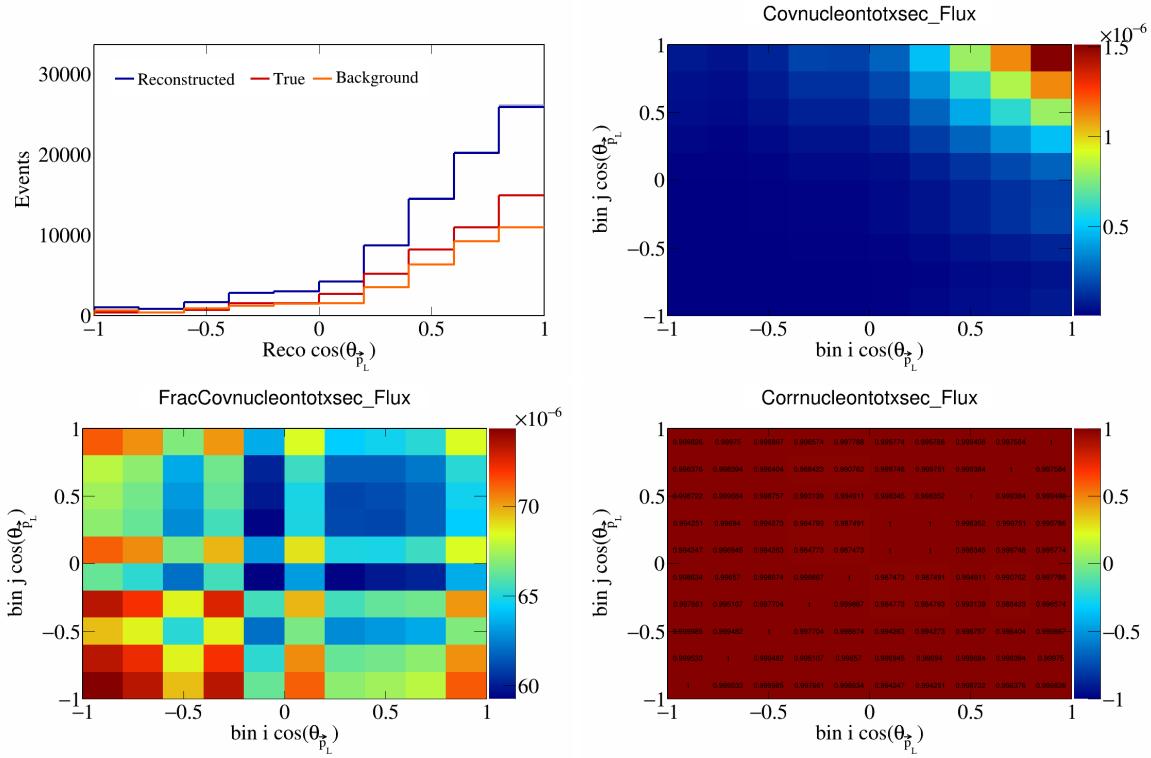


Figure 715: NucleonTotXSec variations for $\cos(\theta_{\vec{p}_L})$.

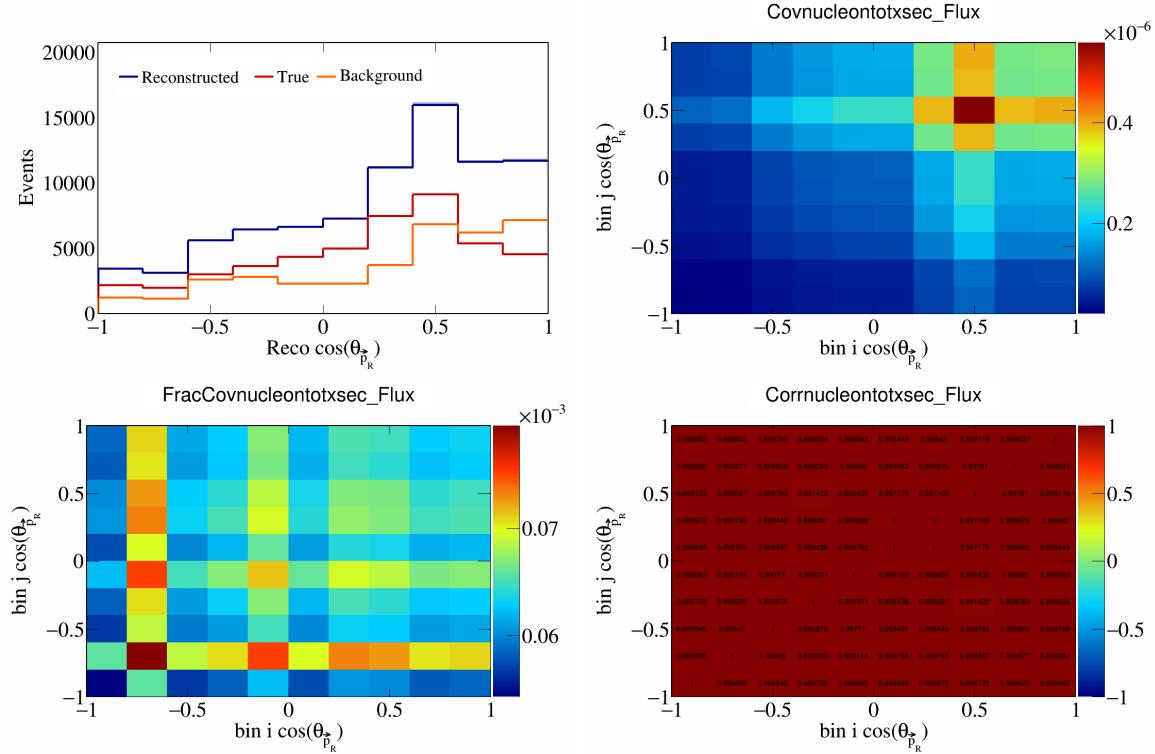


Figure 716: NucleonTotXSec variations for $\cos(\theta_{\vec{p}_R})$.

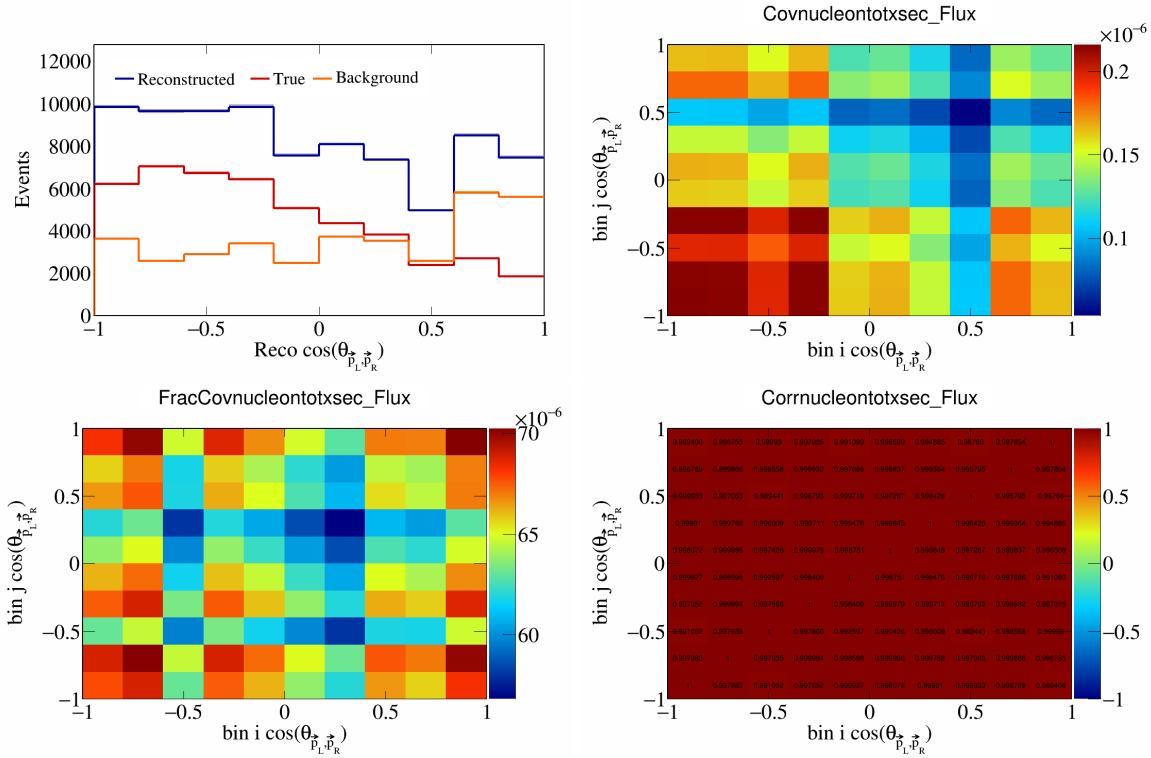


Figure 717: NucleonTotXSec variations for $\cos(\theta_{\vec{p}_L, \vec{p}_R})$.

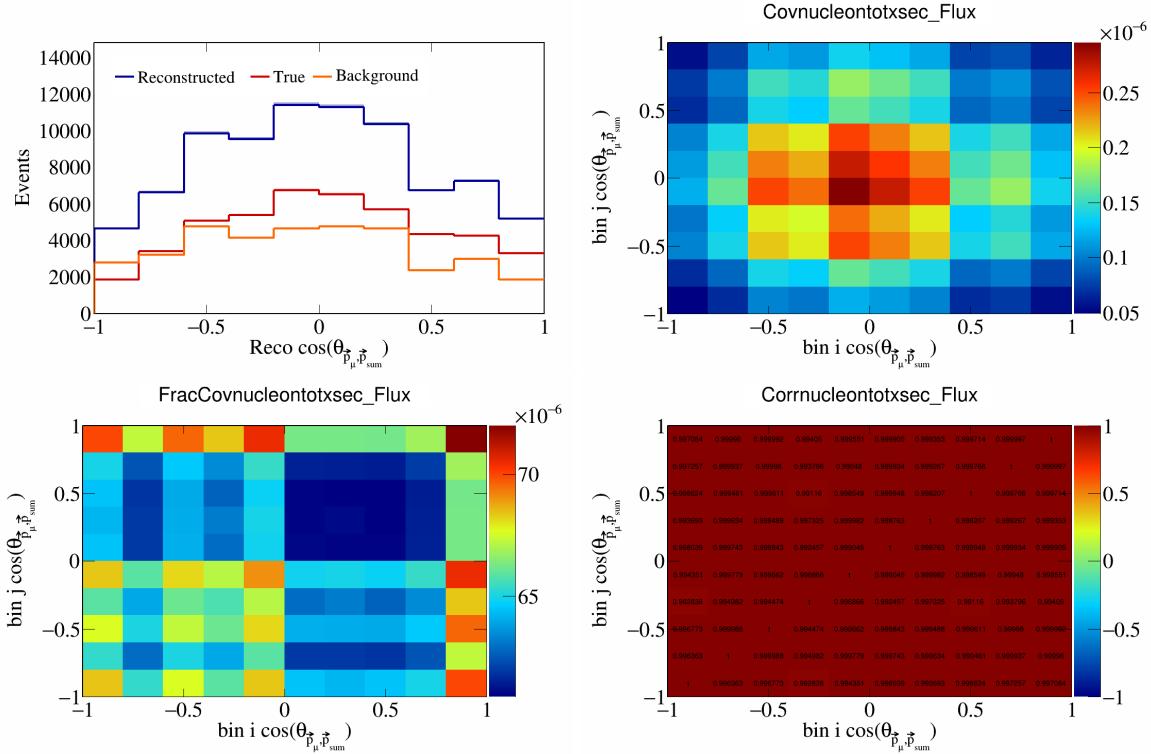


Figure 718: NucleonTotXSec variations for $\cos(\theta_{\vec{p}_\mu, \vec{p}_{\text{sum}}})$.

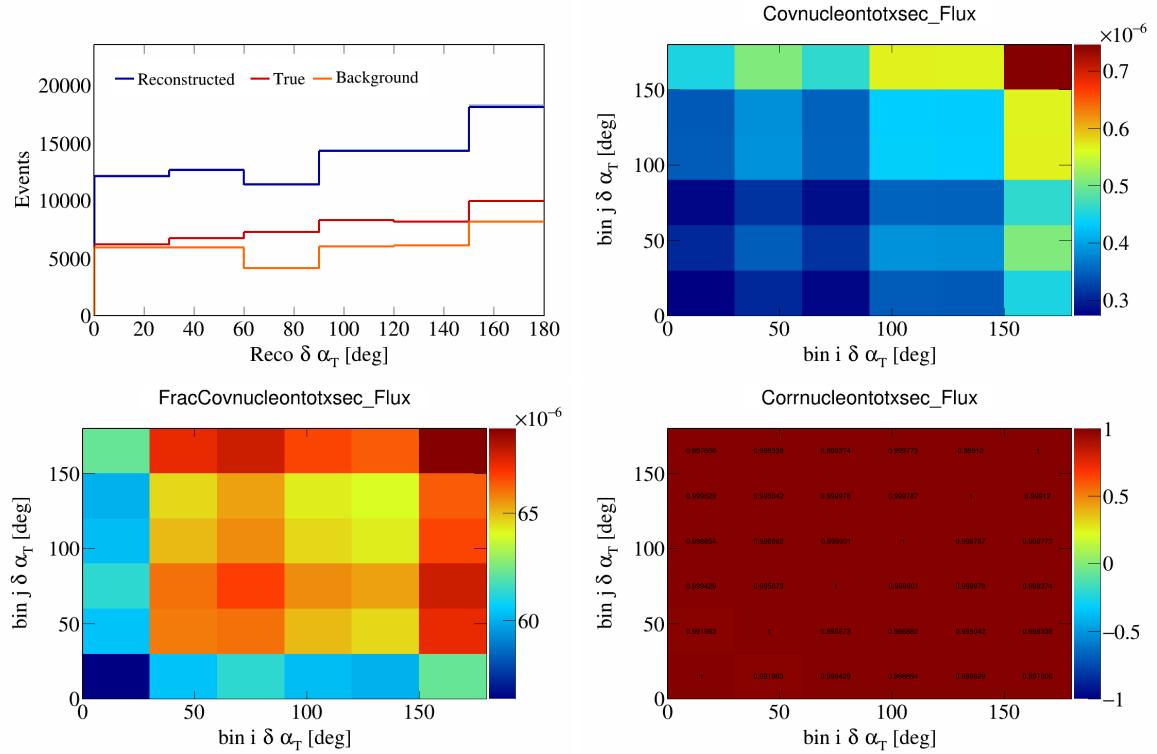


Figure 719: NucleonTotXSec variations for $\delta\alpha_T$.

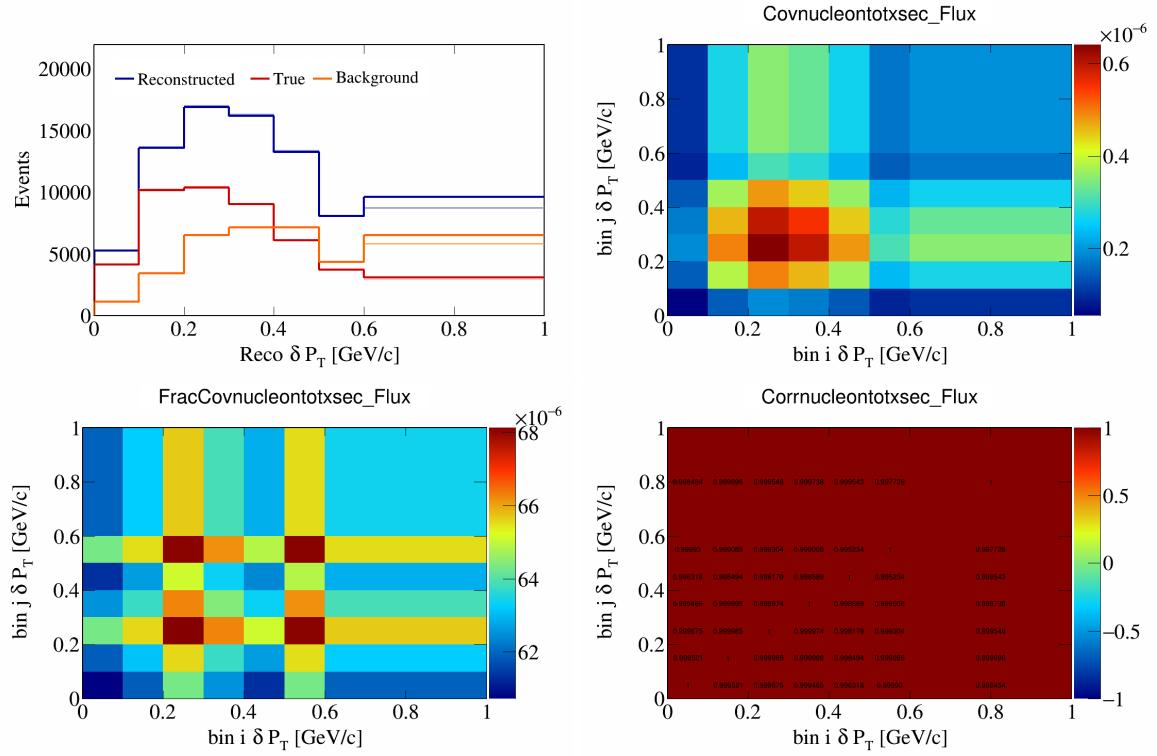


Figure 720: NucleonTotXSec variations for δP_T .

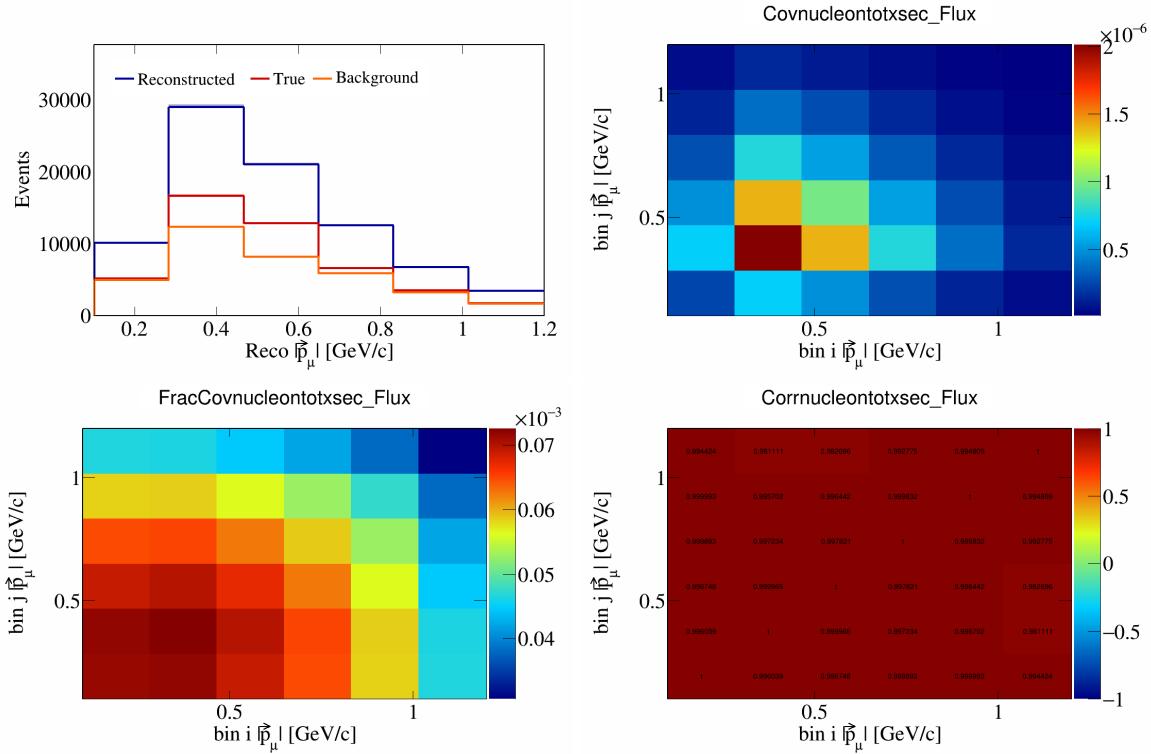


Figure 721: NucleonTotXSec variations for $|\vec{p}_\mu|$.

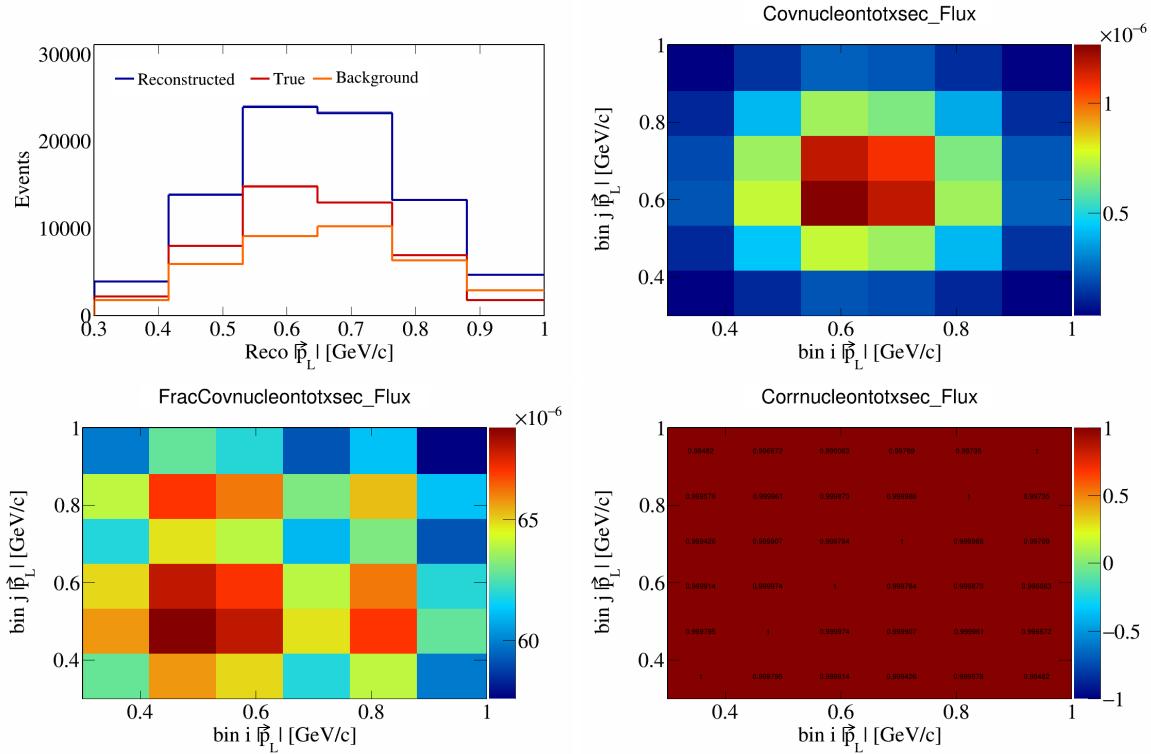


Figure 722: NucleonTotXSec variations for $|\vec{p}_L|$.

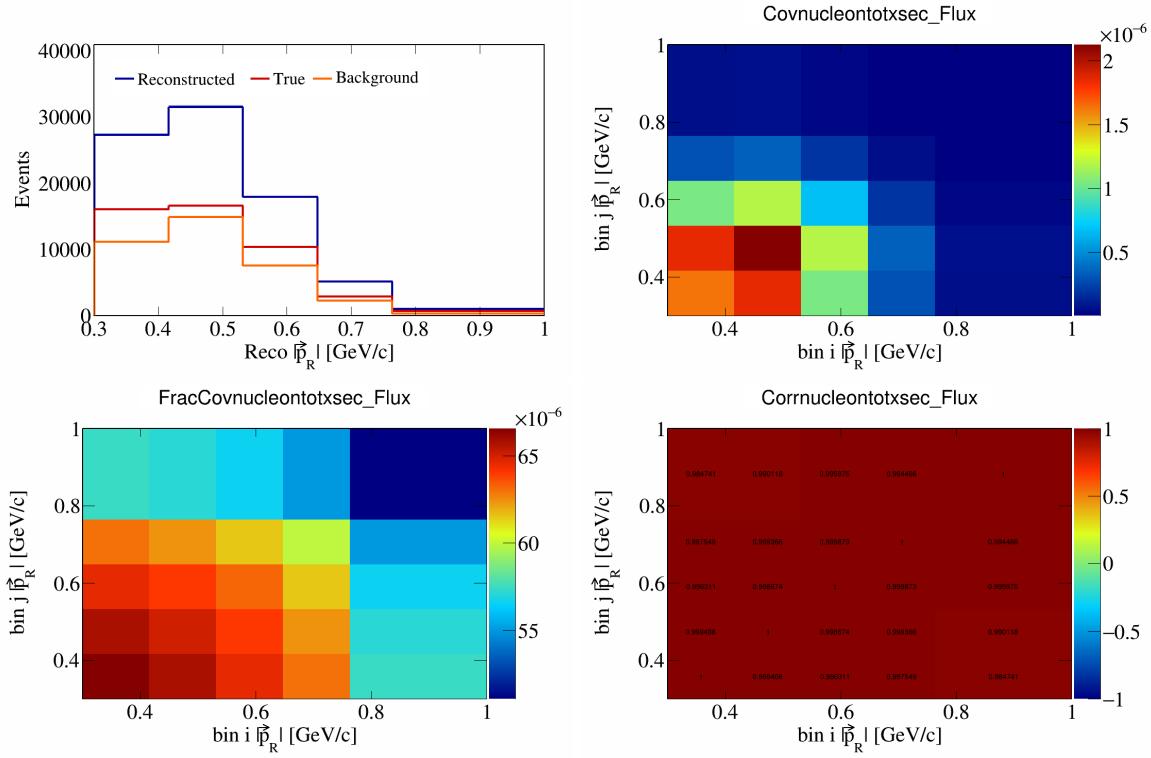


Figure 723: NucleonTotXSec variations for $|\vec{p}_R|$.

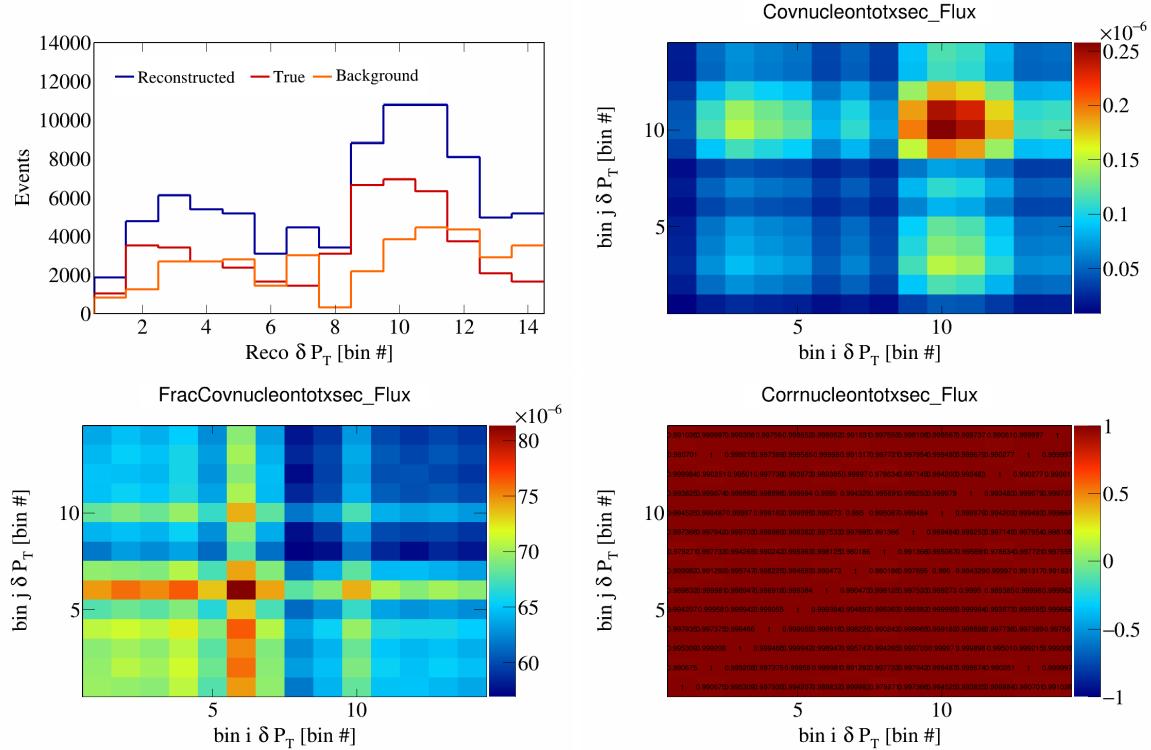


Figure 724: NucleonTotXSec variations for δP_T in $\cos(\theta_{\vec{p}_\mu})$.

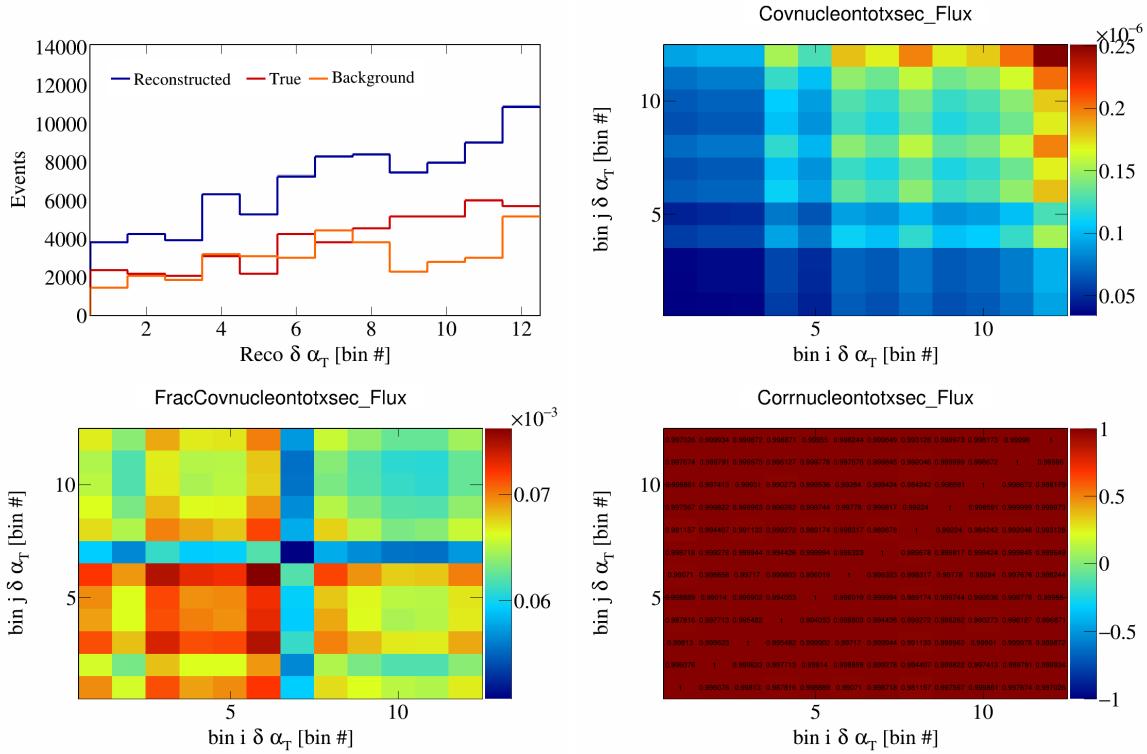


Figure 725: NucleonTotXSec variations for $\delta\alpha_T$ in $\cos(\theta_{\vec{p}_\mu})$.

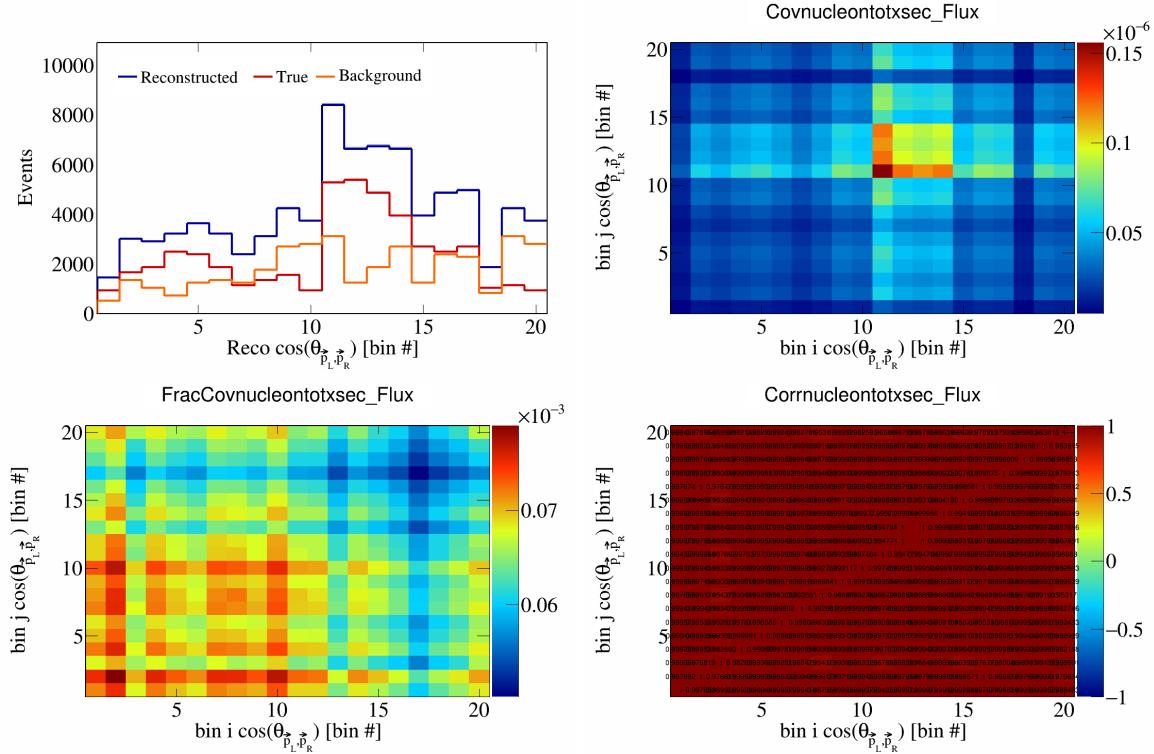


Figure 726: NucleonTotXSec variations for $\cos(\theta_{\vec{p}_L, \vec{p}_R})$ in $\cos(\theta_{\vec{p}_\mu})$.

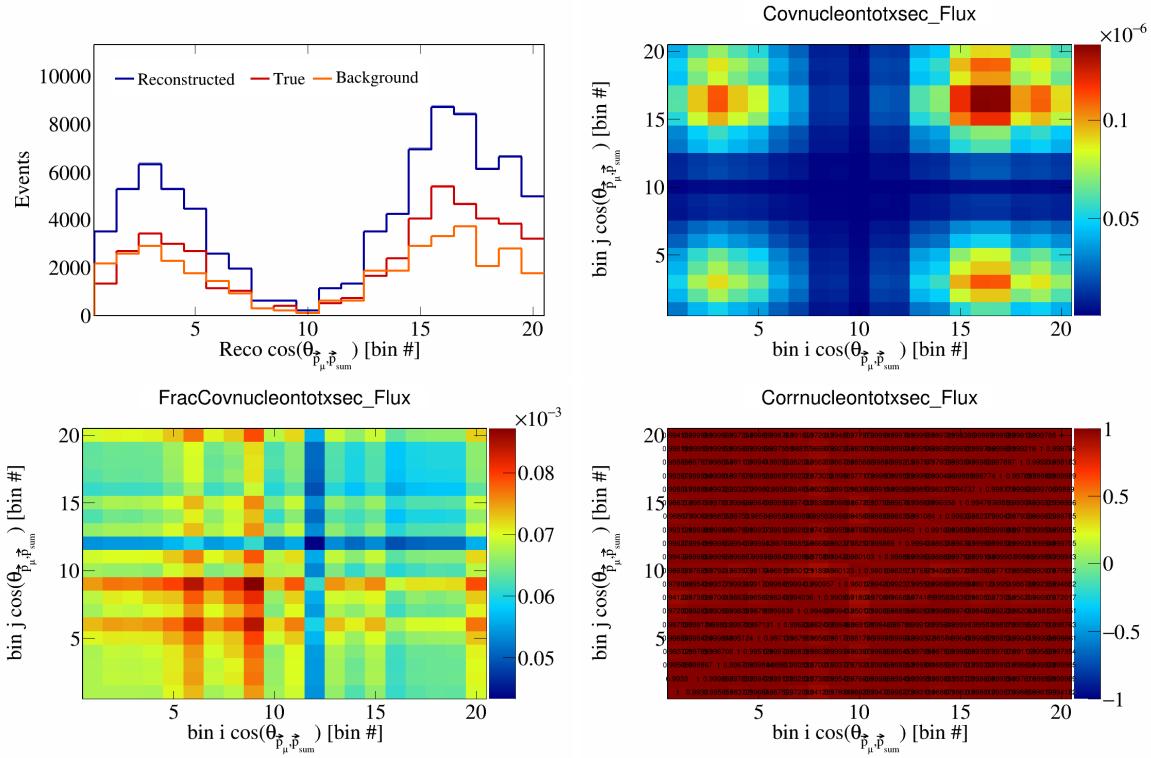


Figure 727: NucleonTotXSec variations for $\cos(\theta_{\vec{p}_\mu, \vec{p}_{\text{sum}}})$ in $\cos(\theta_{\vec{p}_\mu})$.

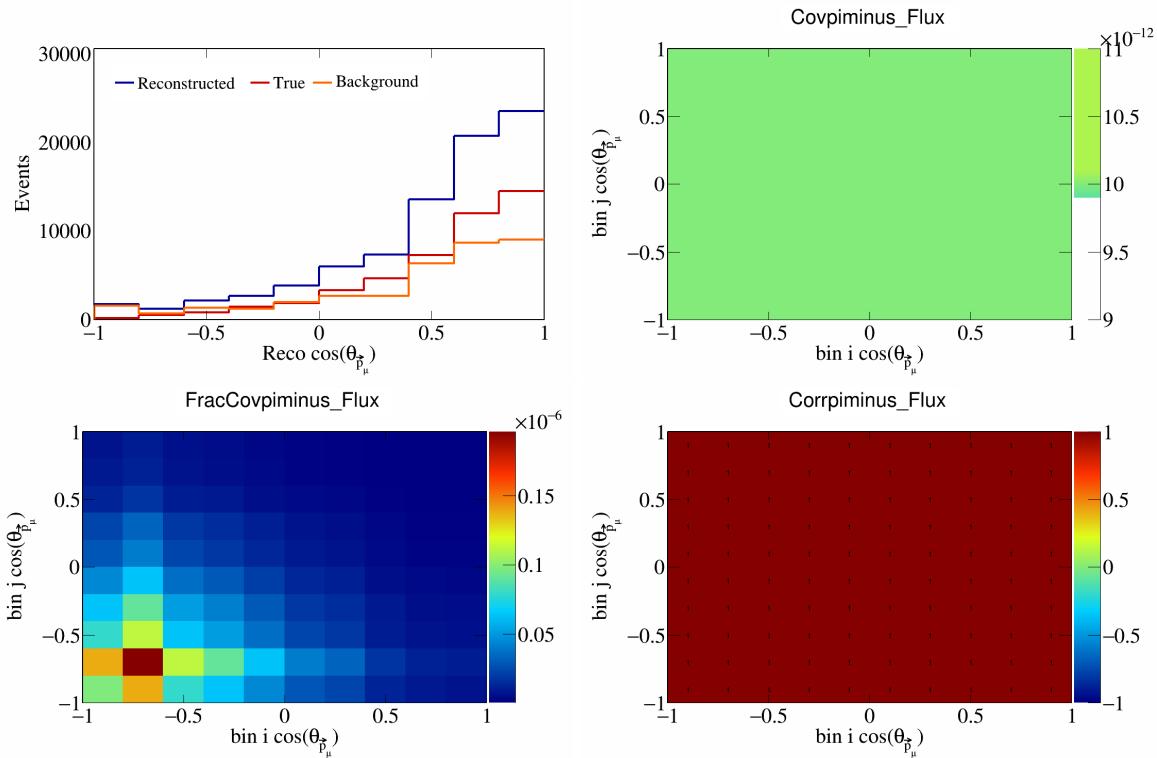


Figure 728: PiMinus variations for $\cos(\theta_{\vec{p}_\mu})$.

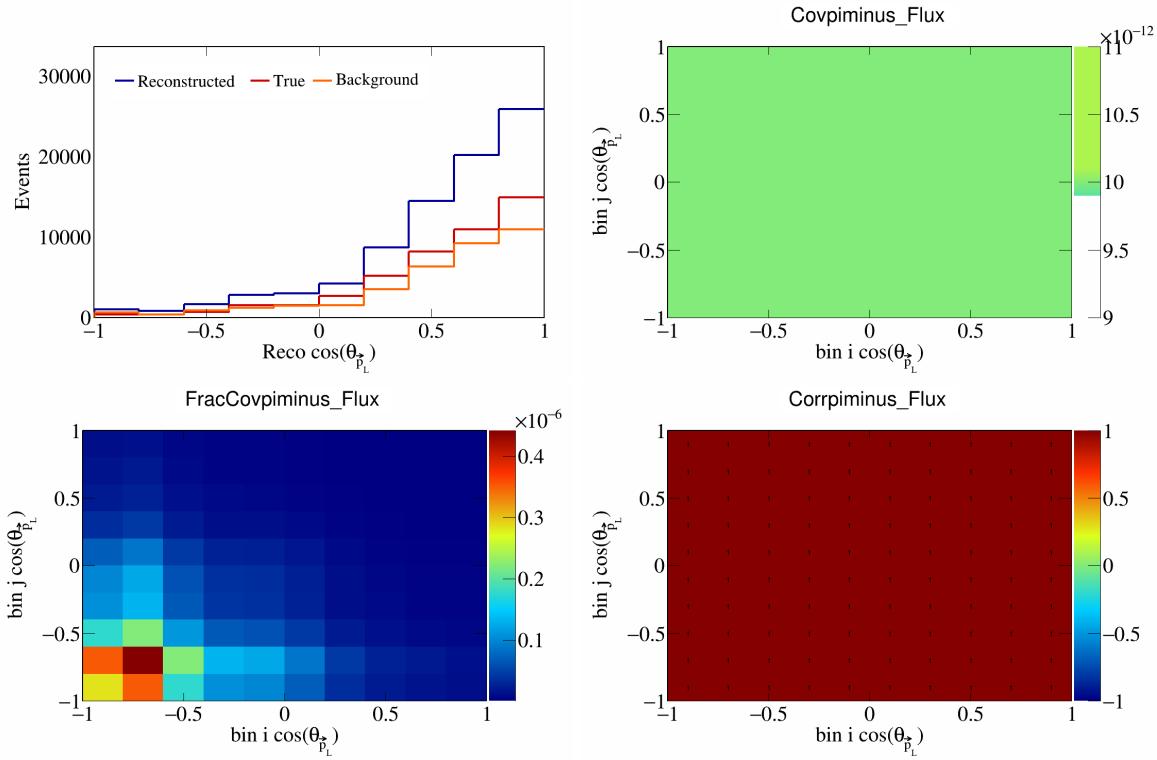


Figure 729: PiMinus variations for $\cos(\theta_{\vec{p}_L})$.

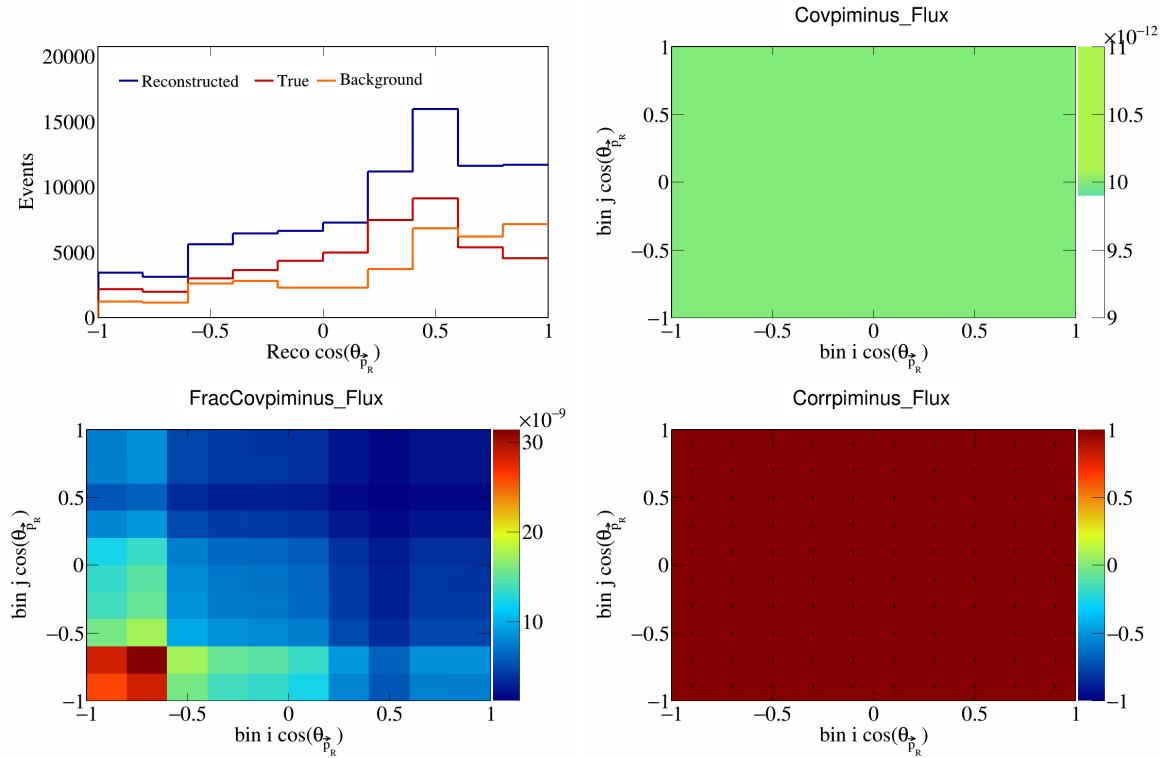


Figure 730: PiMinus variations for $\cos(\theta_{\vec{p}_R})$.

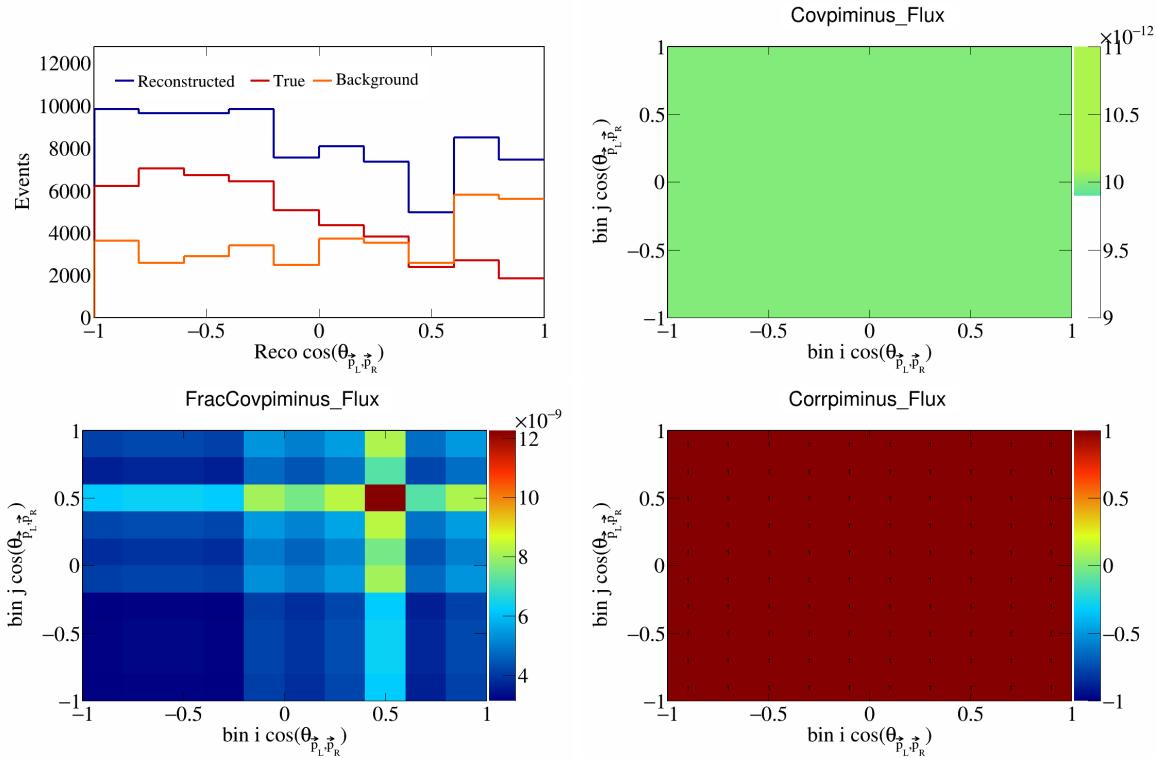


Figure 731: PiMinus variations for $\cos(\theta_{\vec{p}_L, \vec{p}_R})$.

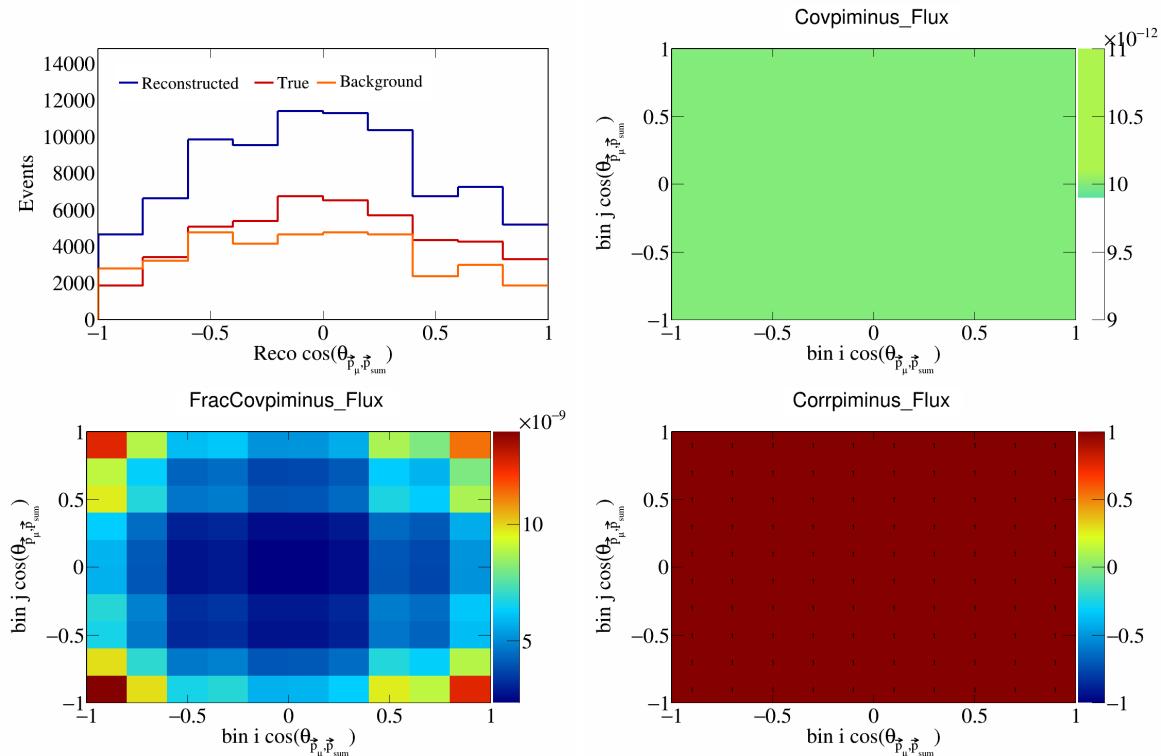


Figure 732: PiMinus variations for $\cos(\theta_{\vec{p}_\mu, \vec{p}_{\text{sum}}})$.

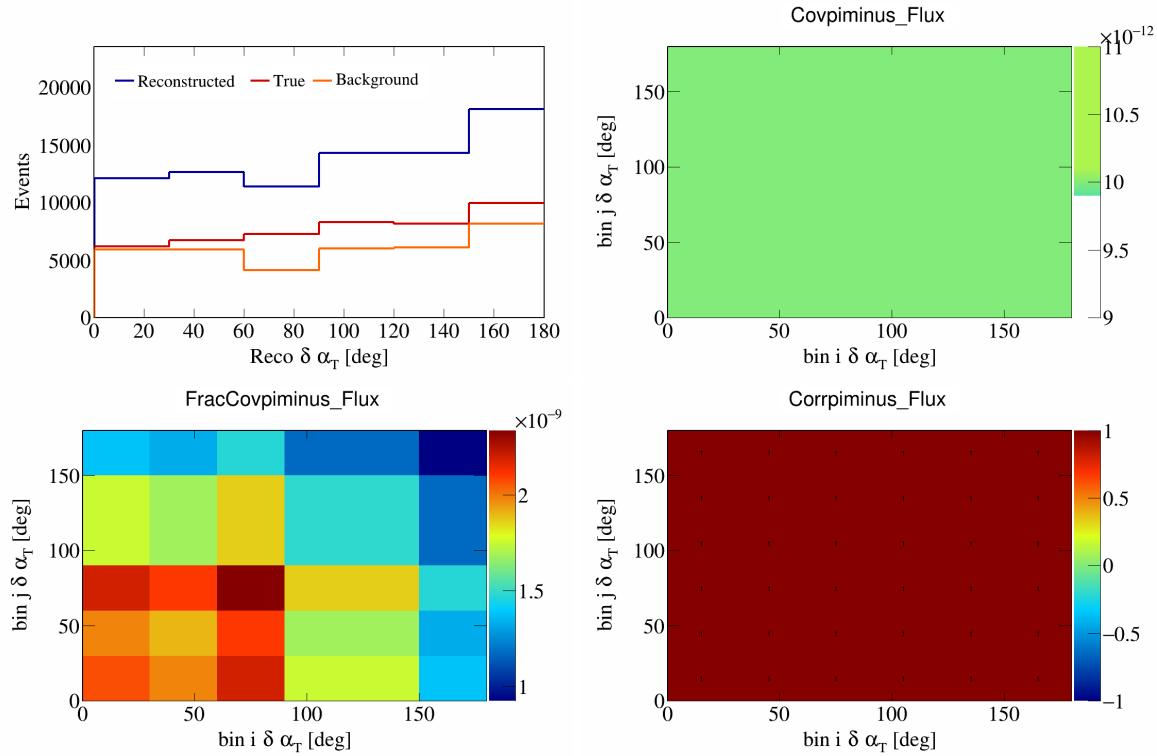


Figure 733: PiMinus variations for $\delta\alpha_T$.

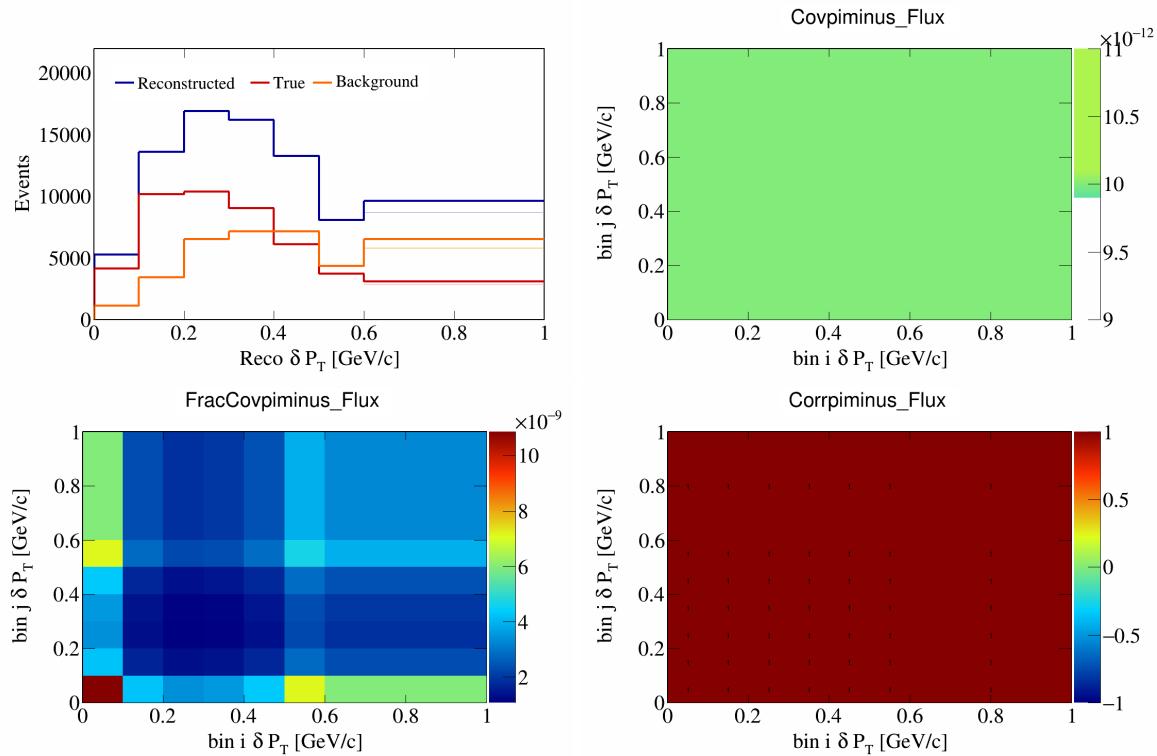


Figure 734: PiMinus variations for δP_T .

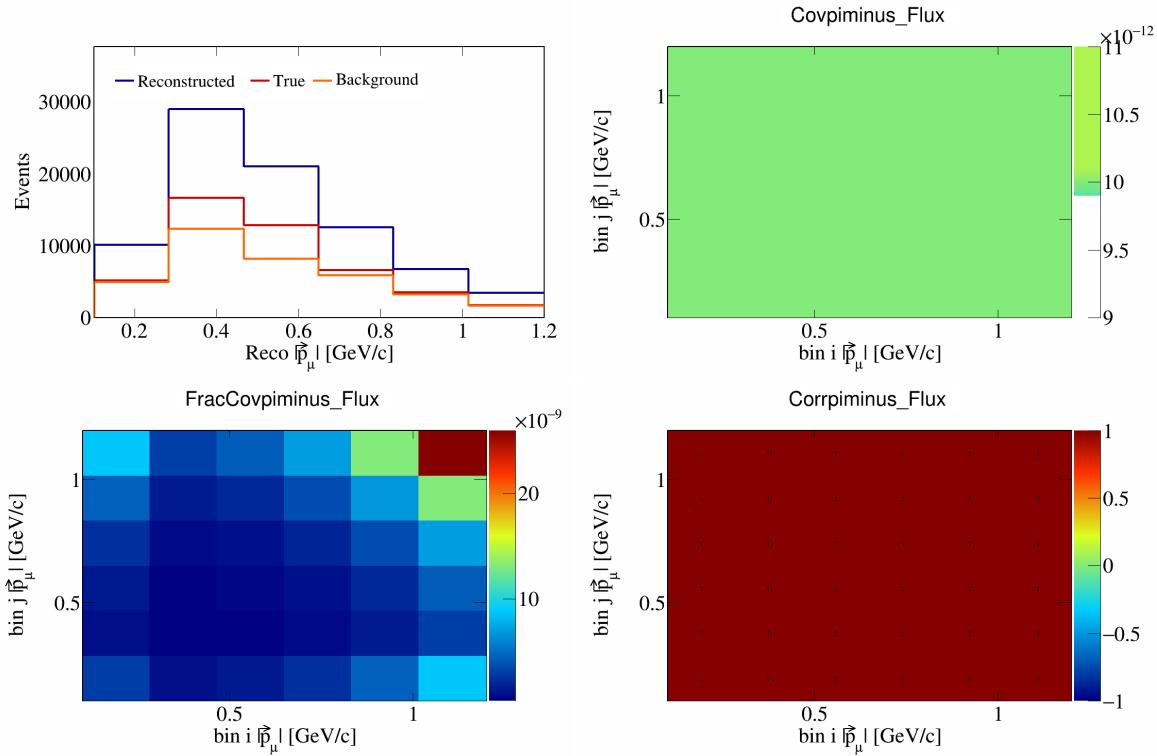


Figure 735: PiMinus variations for $|\vec{p}_\mu|$.

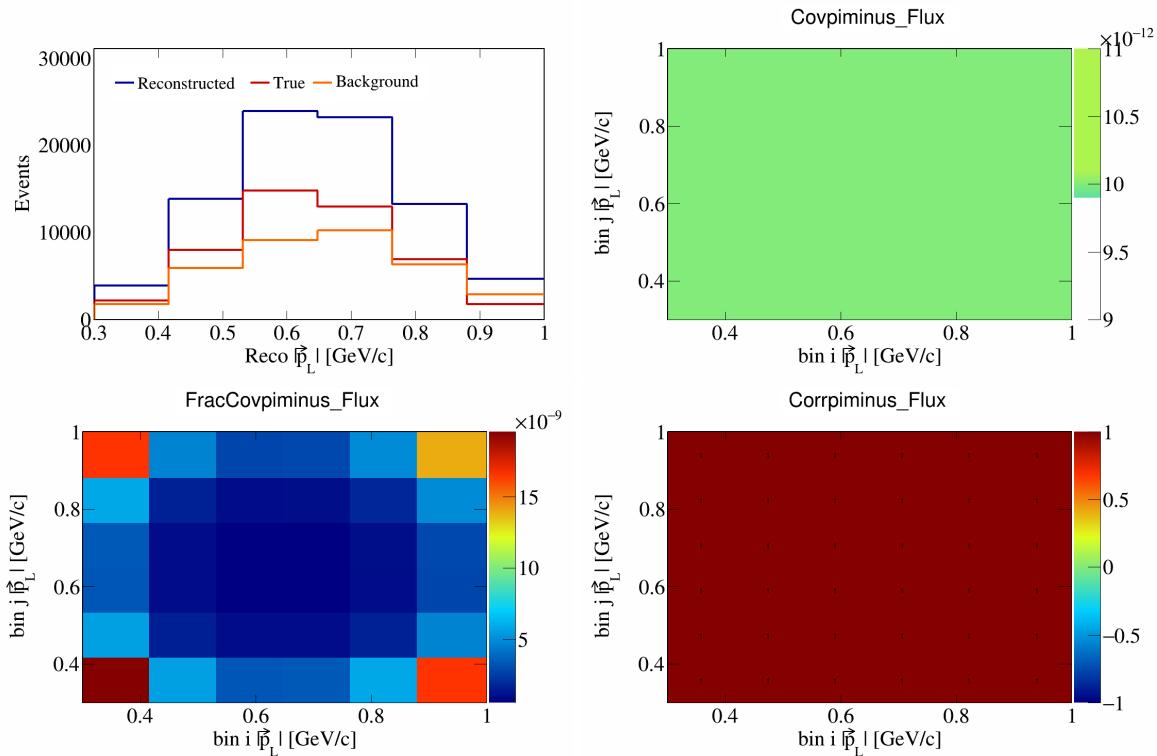


Figure 736: PiMinus variations for $|\vec{p}_L|$.

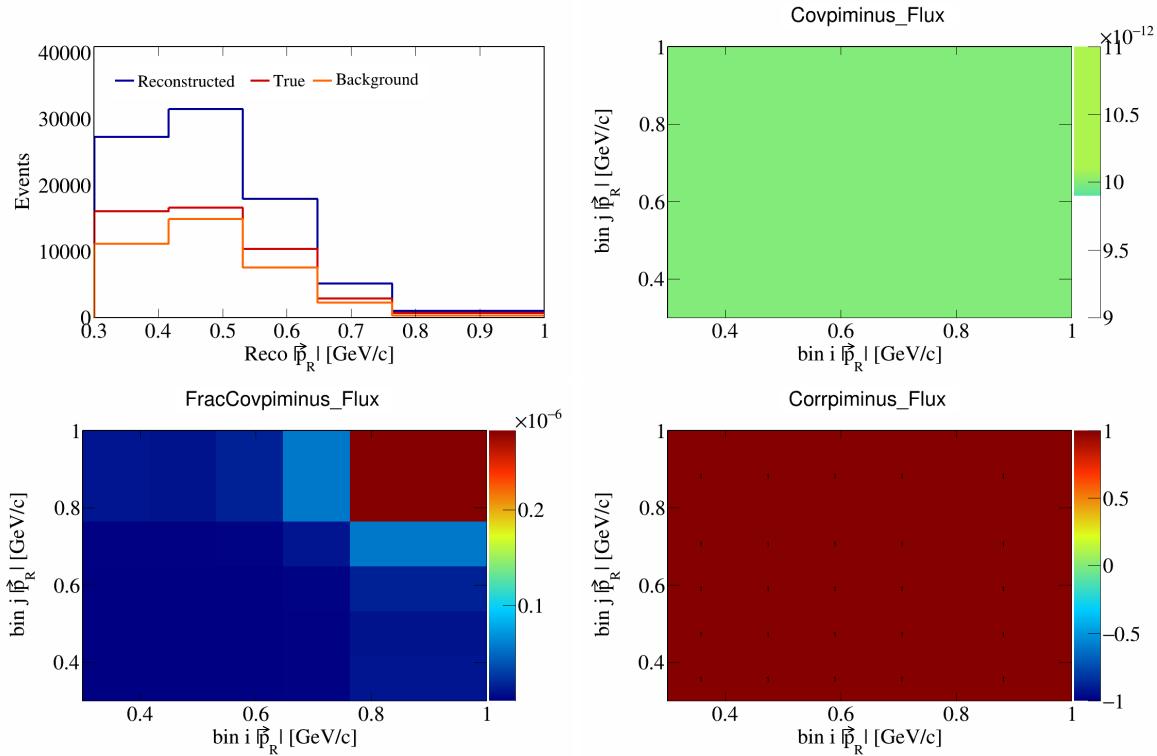


Figure 737: PiMinus variations for $|\vec{p}_R|$.

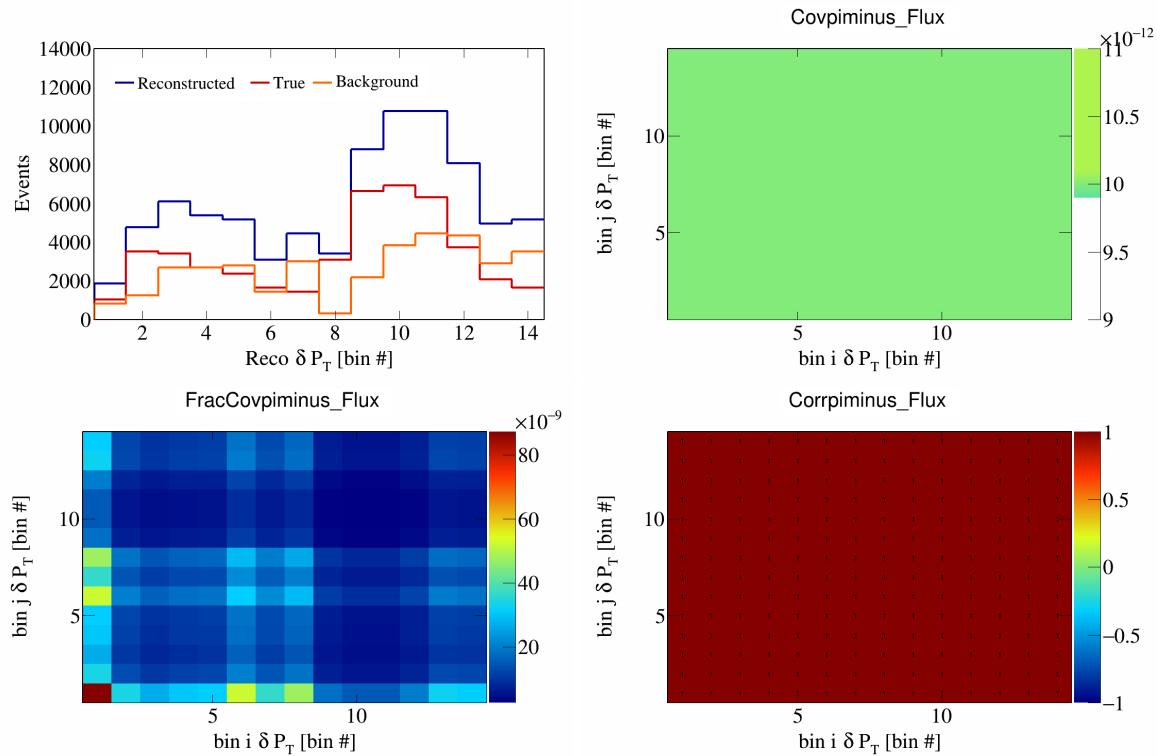


Figure 738: PiMinus variations for δP_T in $\cos(\theta_{\vec{p}_\mu})$.

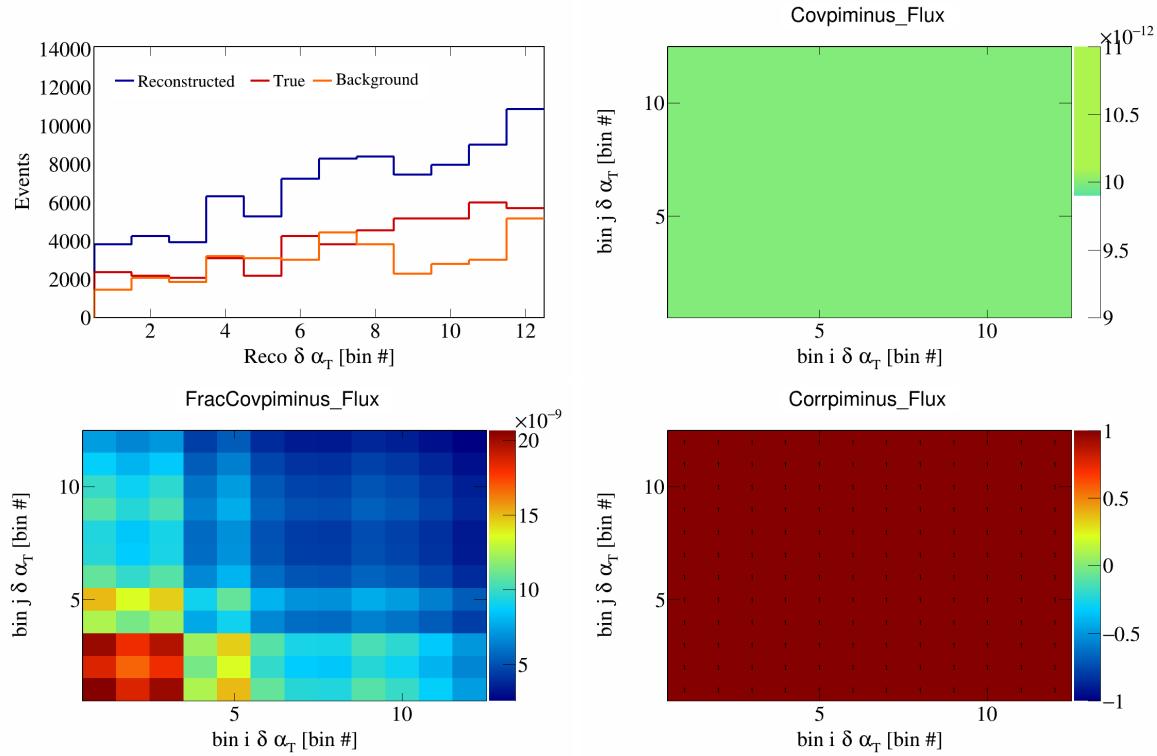


Figure 739: PiMinus variations for $\delta \alpha_T$ in $\cos(\theta_{\vec{p}_\mu})$.

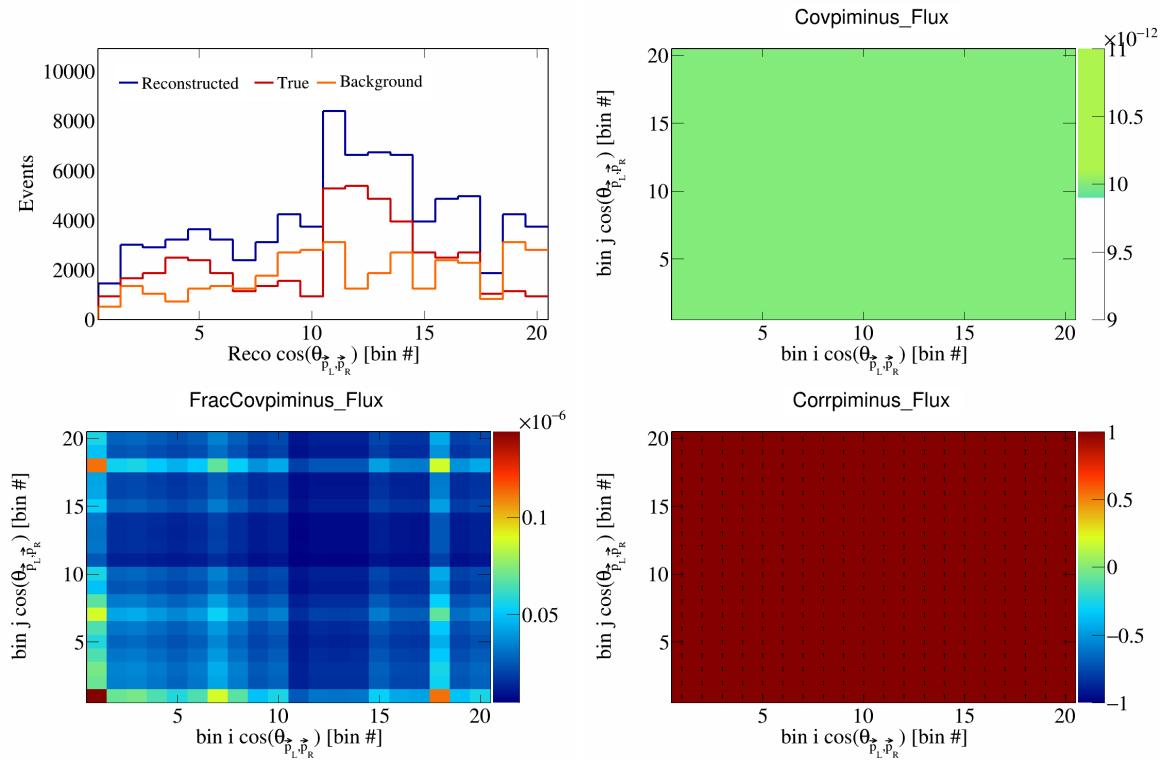


Figure 740: PiMinus variations for $\cos(\theta_{\vec{p}_L, \vec{p}_R})$ in $\cos(\theta_{\vec{p}_\mu})$.

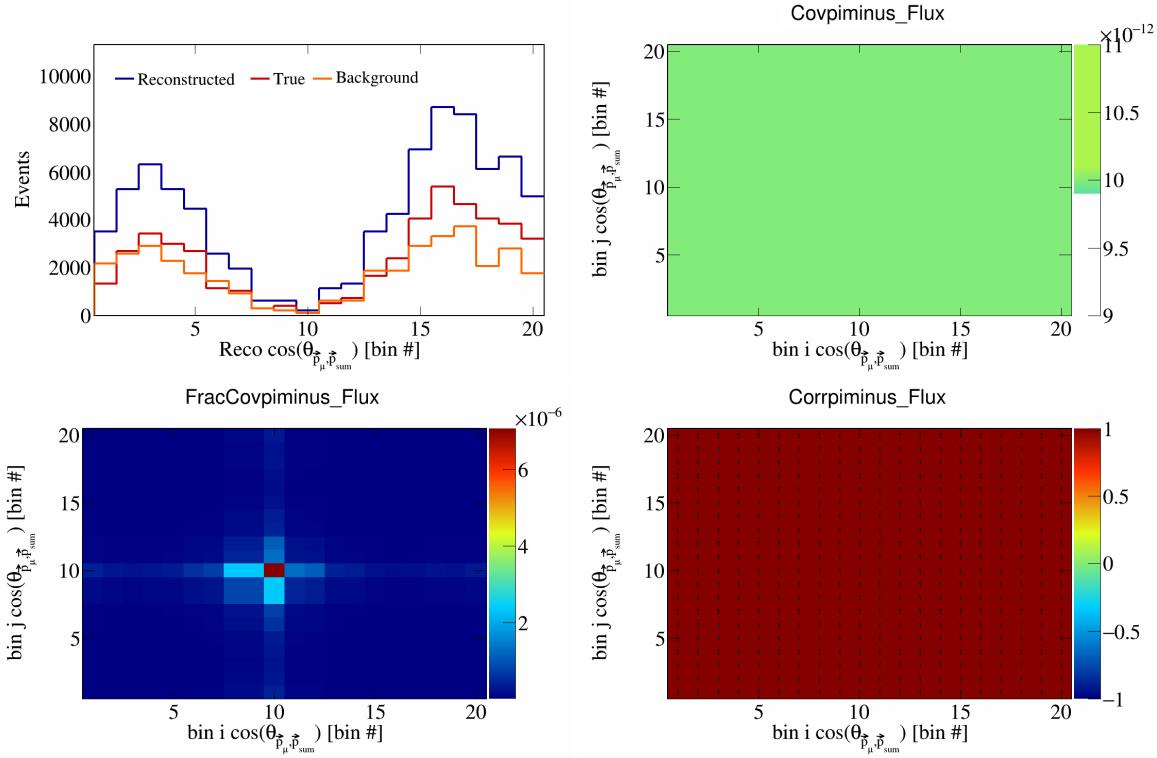


Figure 741: PiMinus variations for $\cos(\theta_{\vec{p}_\mu}, \vec{p}_{\text{sum}}^*)$ in $\cos(\theta_{\vec{p}_\mu}^*)$.

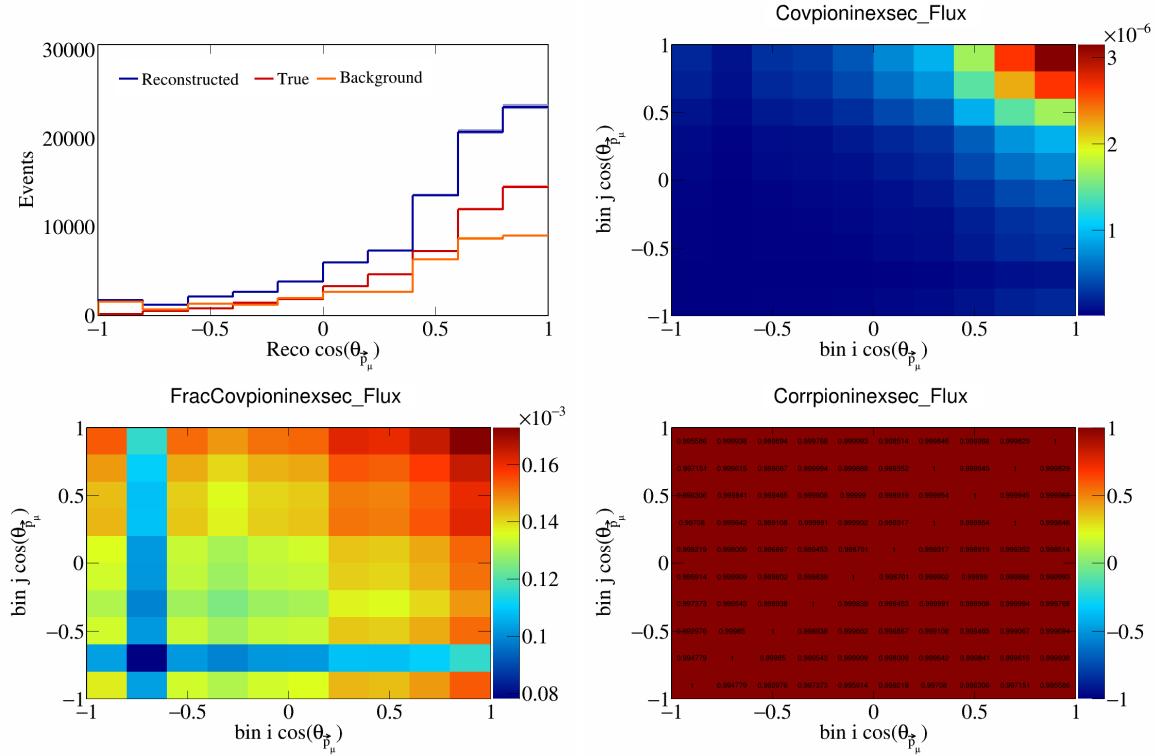


Figure 742: PionIneXSec variations for $\cos(\theta_{\vec{p}_\mu}^*)$.

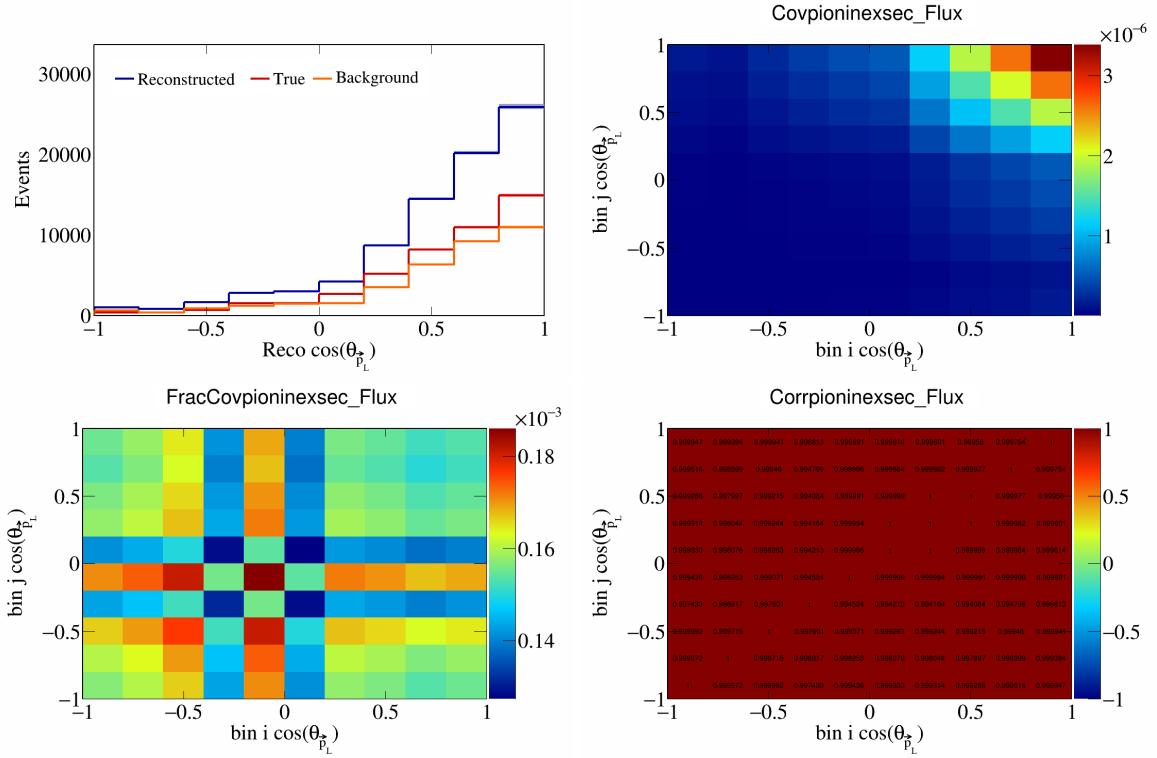


Figure 743: PionIneXSec variations for $\cos(\theta_{\vec{p}_L})$.

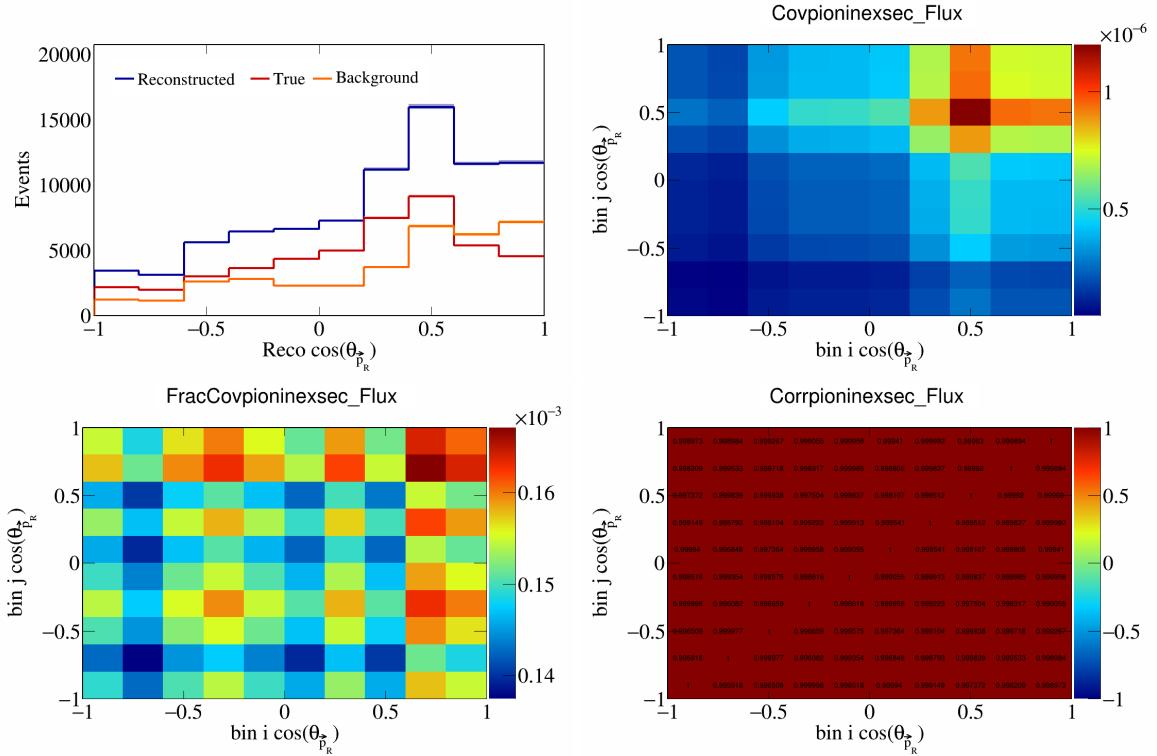


Figure 744: PionIneXSec variations for $\cos(\theta_{\vec{p}_R})$.

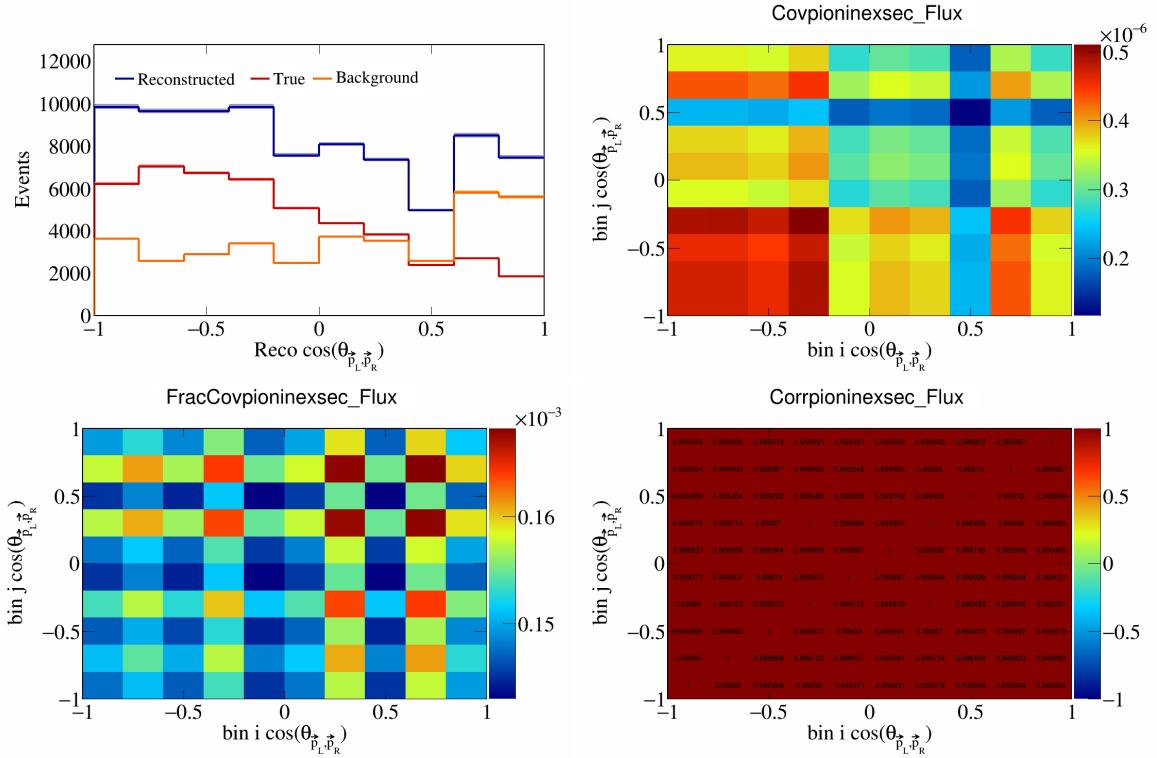


Figure 745: PionIneXSec variations for $\cos(\theta_{\vec{p}_L, \vec{p}_R})$.

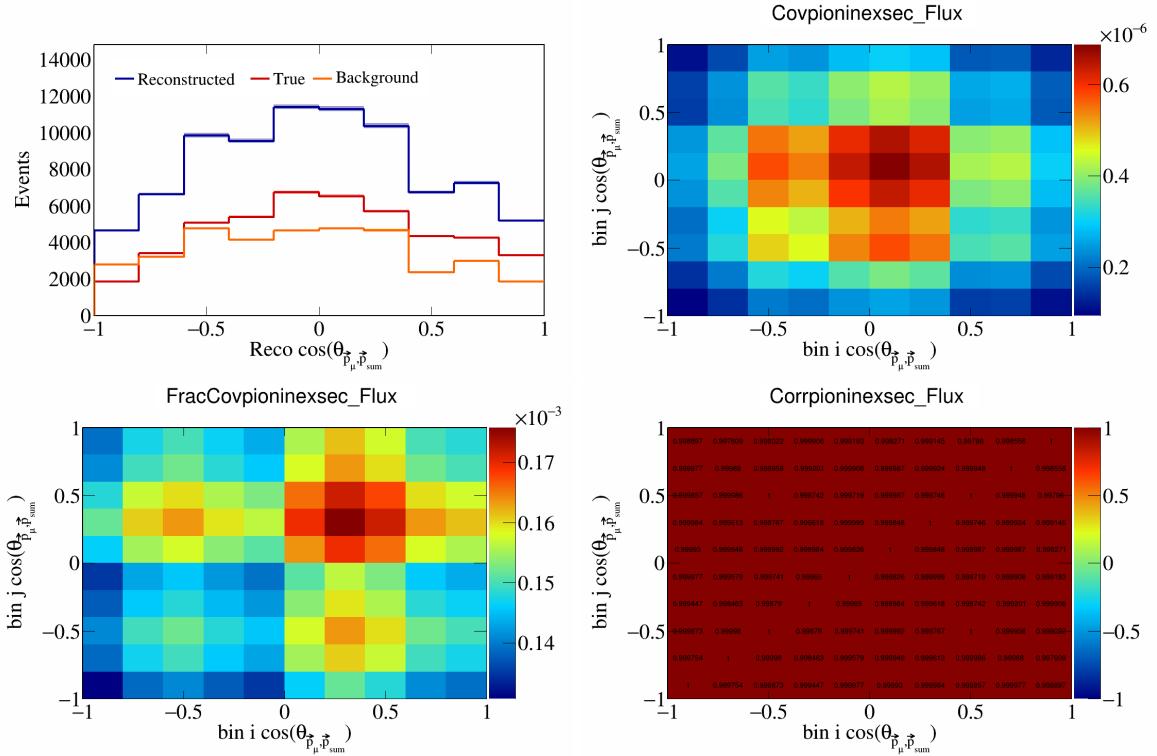


Figure 746: PionIneXSec variations for $\cos(\theta_{\vec{p}_\mu, \vec{p}_{\text{sum}}})$.

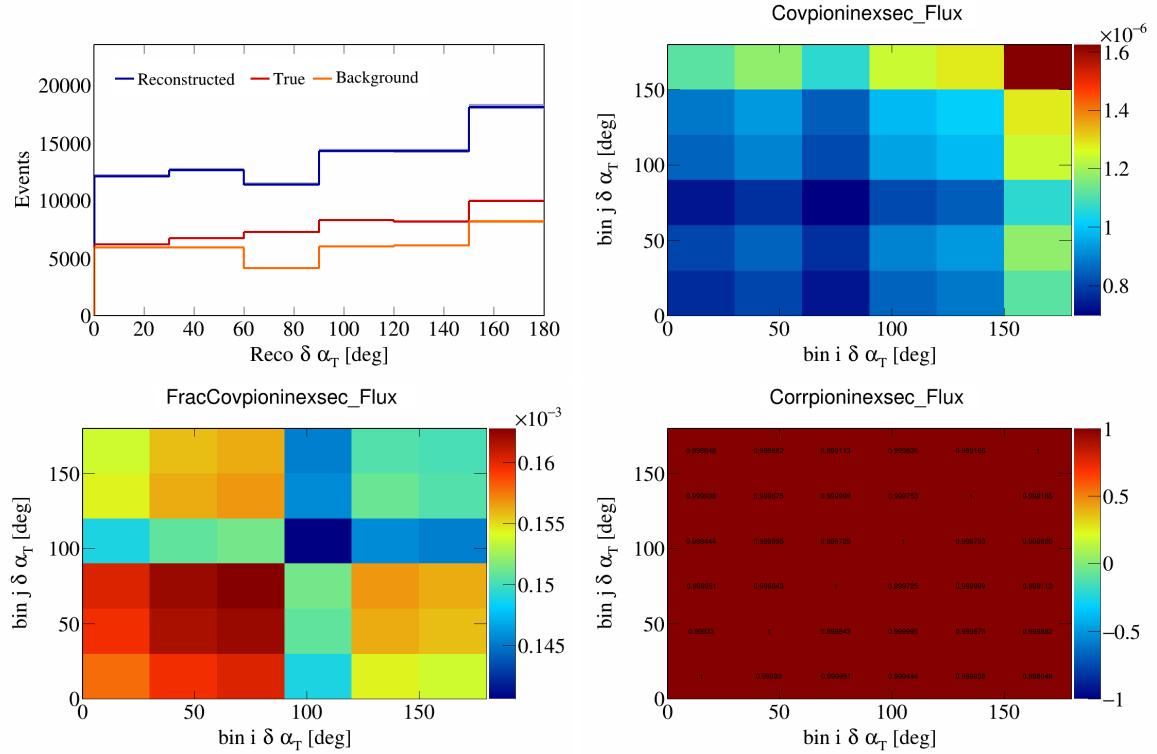


Figure 747: PionIneXSec variations for $\delta\alpha_T$.

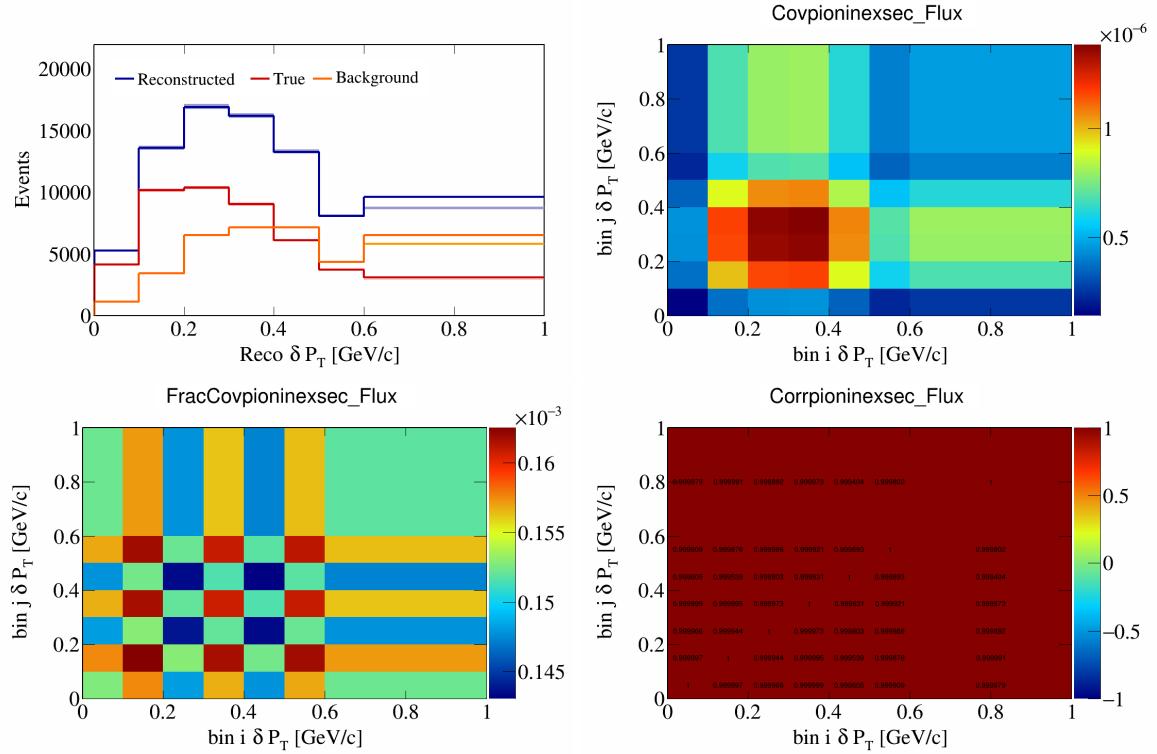


Figure 748: PionIneXSec variations for δP_T .

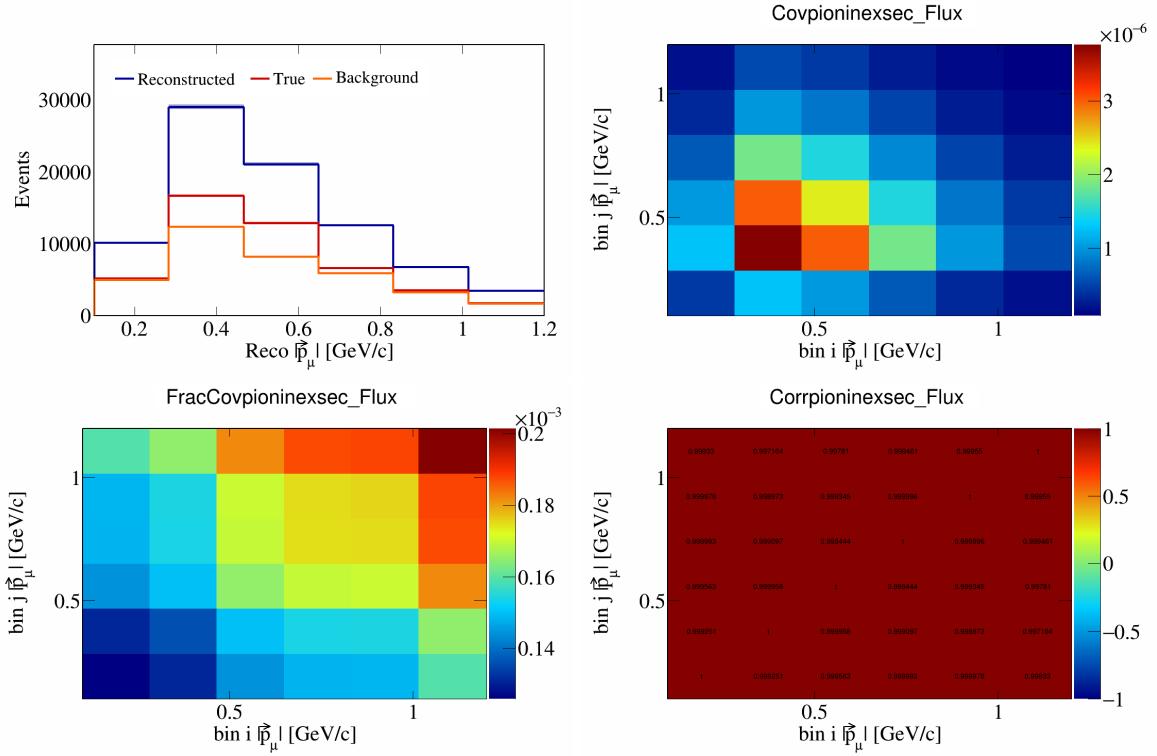


Figure 749: PionIneXSec variations for $|\vec{p}_\mu|$.

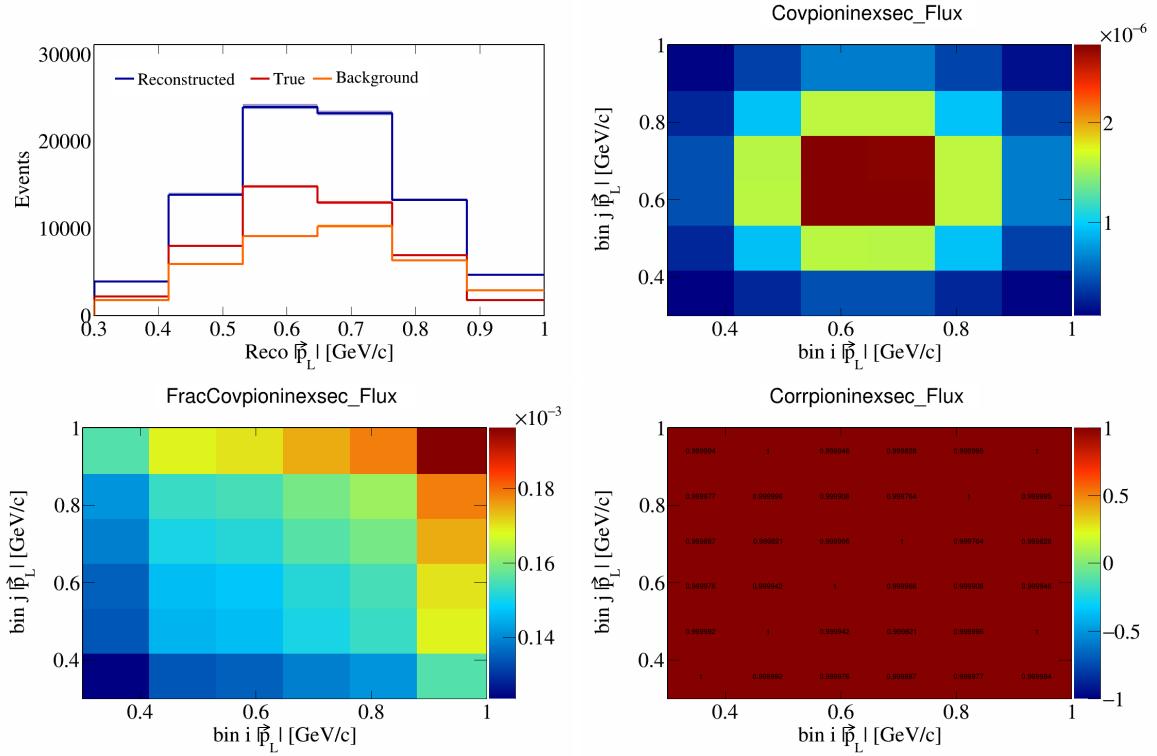


Figure 750: PionIneXSec variations for $|\vec{p}_L|$.

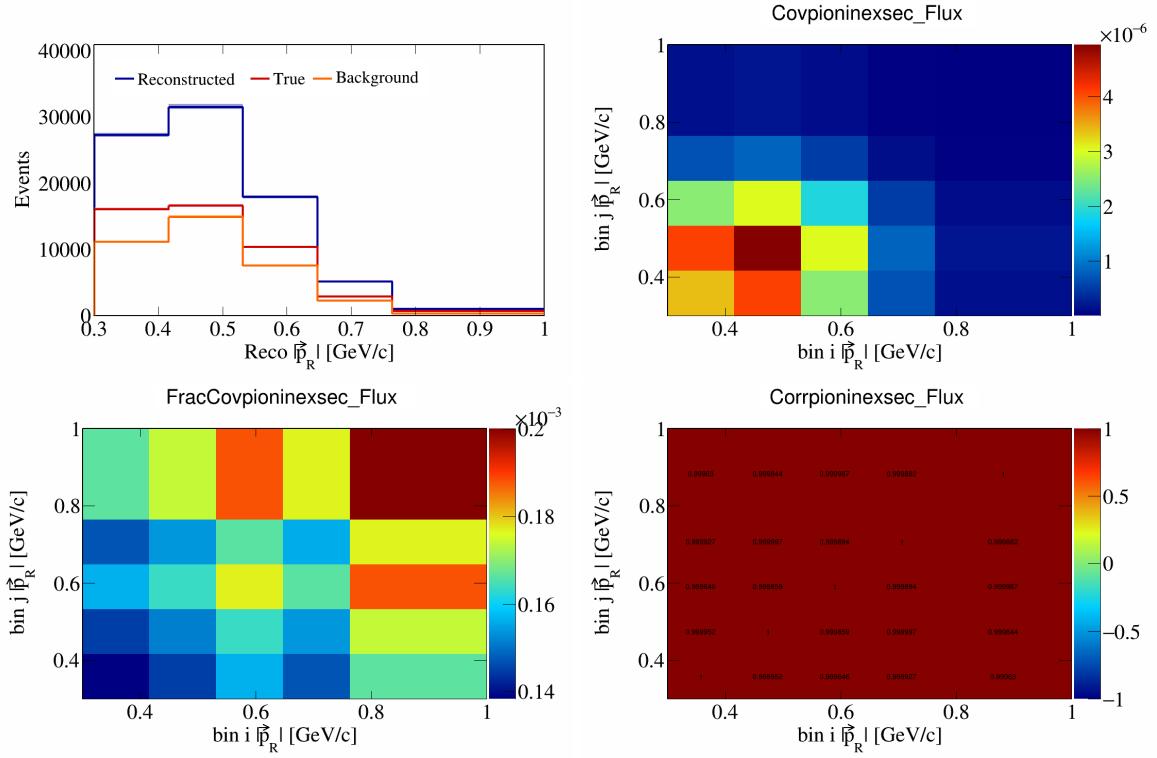


Figure 751: PionIneXSec variations for $|\vec{p}_R|$.

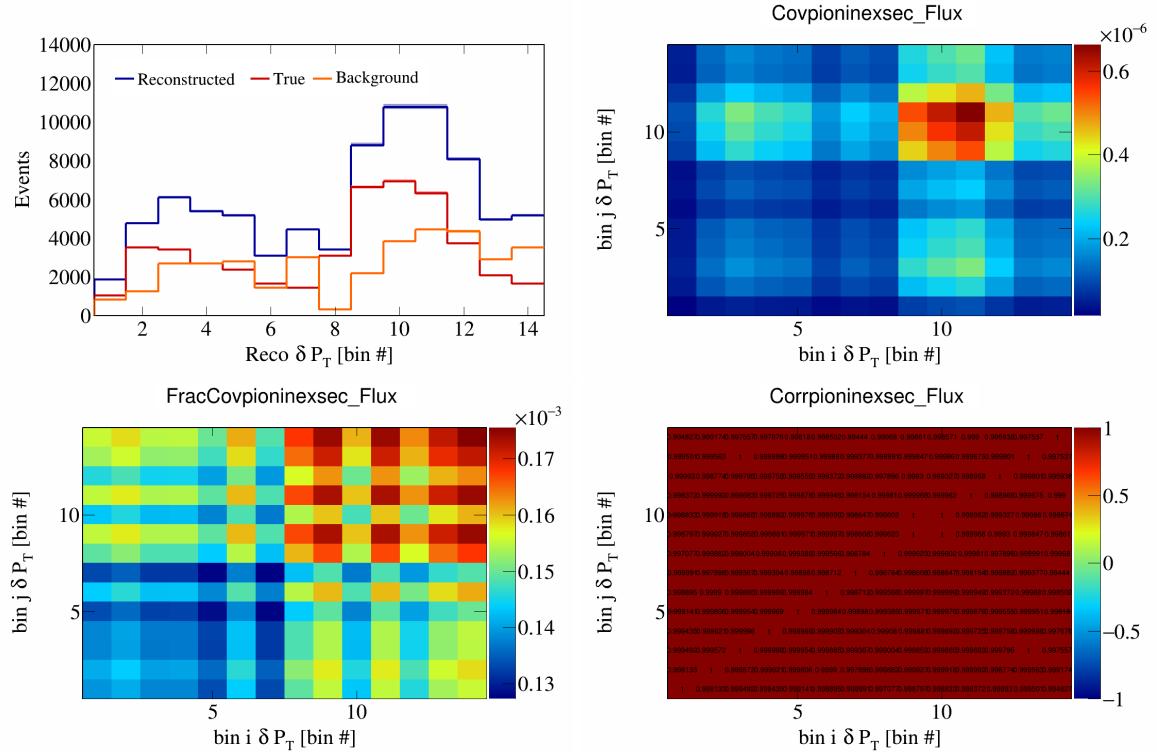


Figure 752: PionIneXSec variations for δP_T in $\cos(\theta_{\vec{p}_\mu})$.

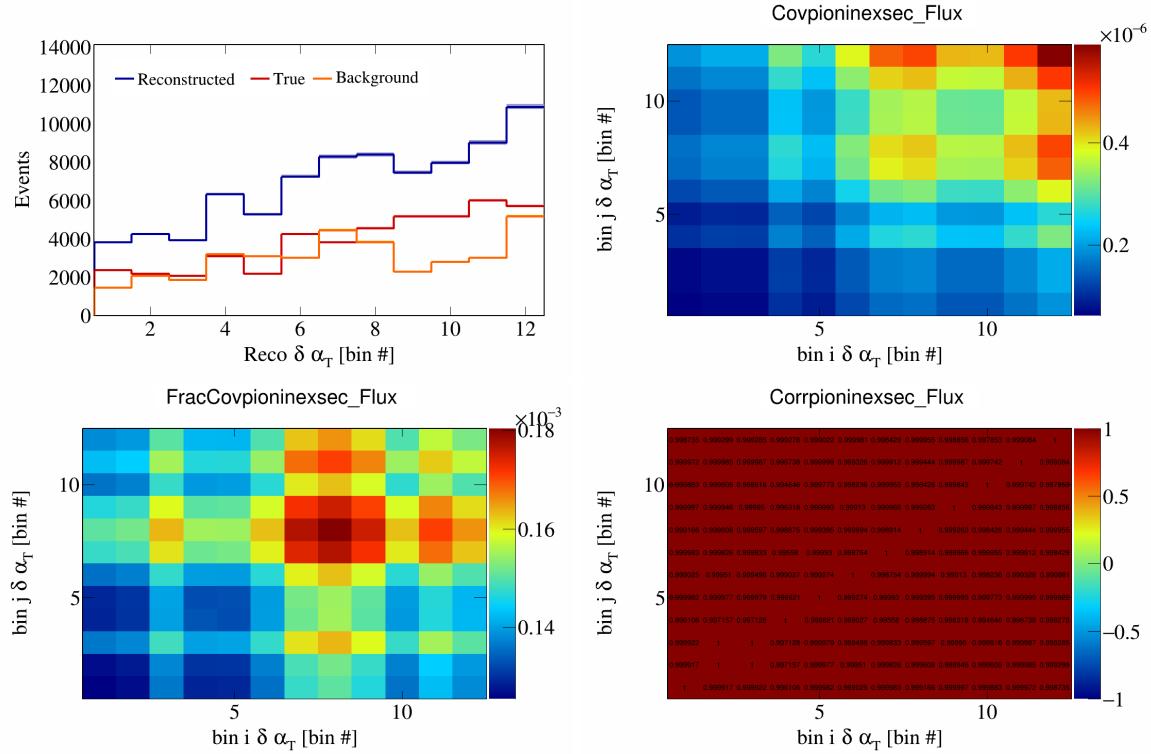


Figure 753: PionIneXSec variations for $\delta \alpha_T$ in $\cos(\theta_{\vec{p}_\mu})$.

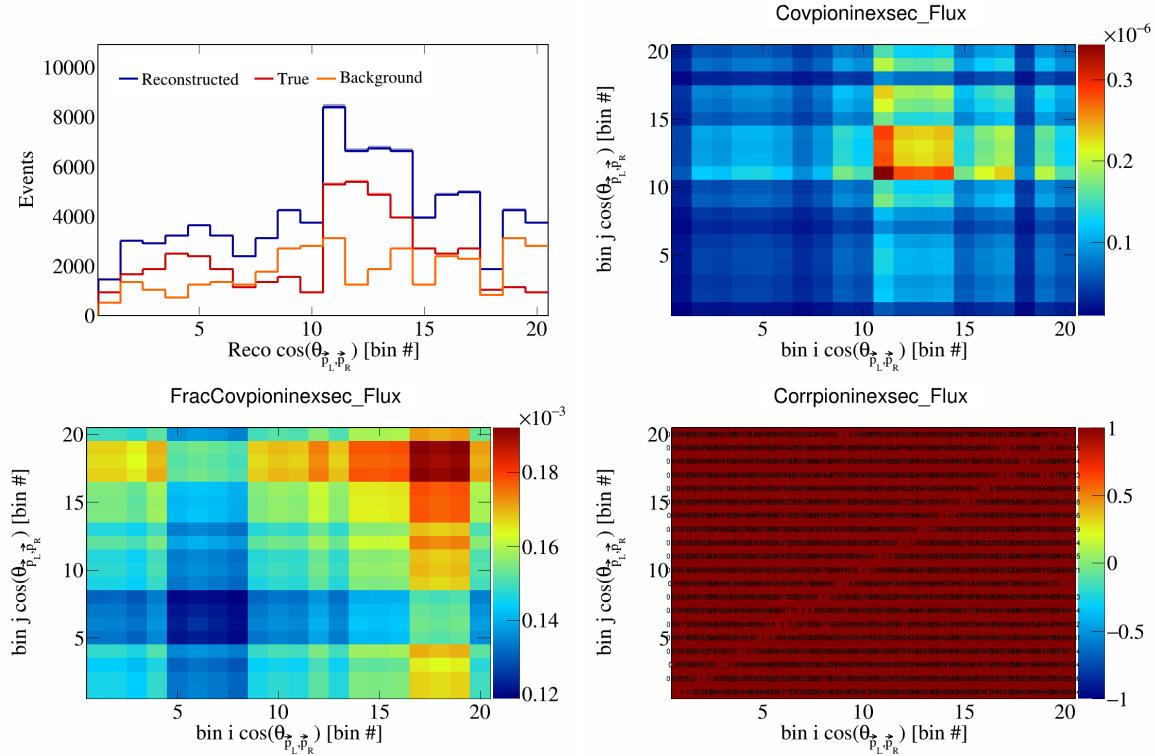


Figure 754: PionIneXSec variations for $\cos(\theta_{\vec{p}_L, \vec{p}_R})$ in $\cos(\theta_{\vec{p}_\mu})$.

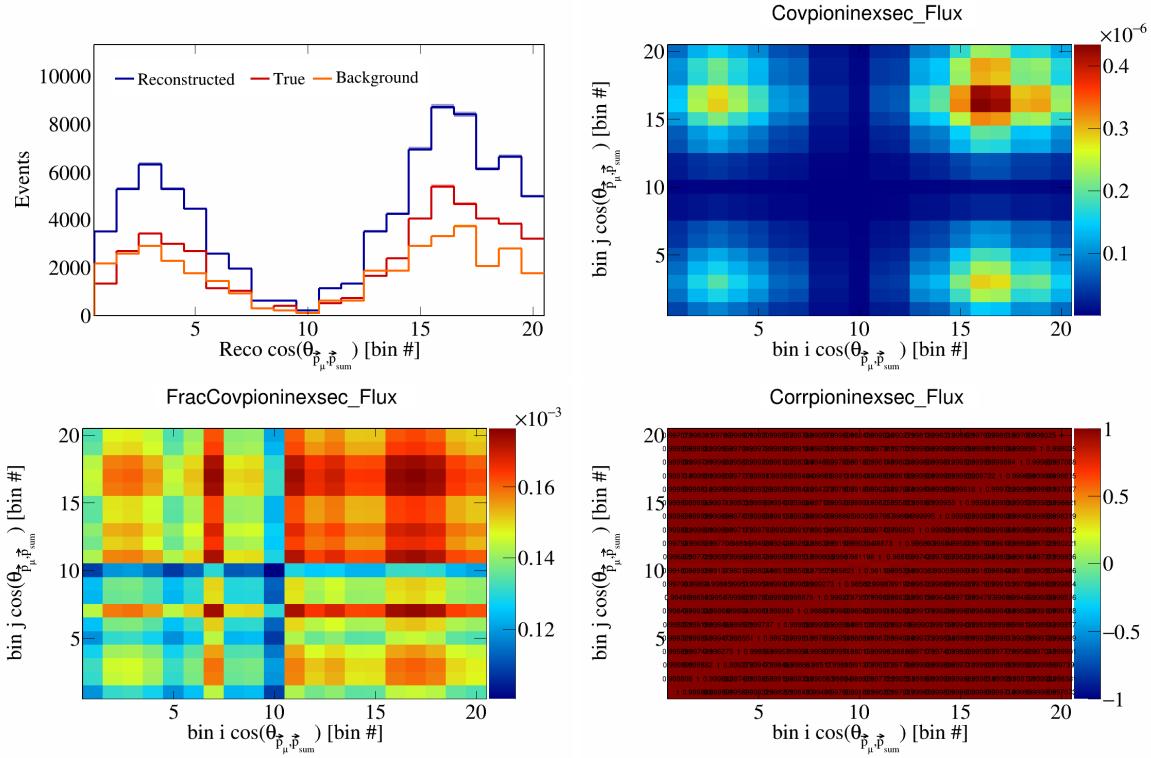


Figure 755: PionIneXSec variations for $\cos(\theta_{\vec{p}_\mu} \cdot \vec{p}_{\text{sum}})$ in $\cos(\theta_{\vec{p}_\mu})$.

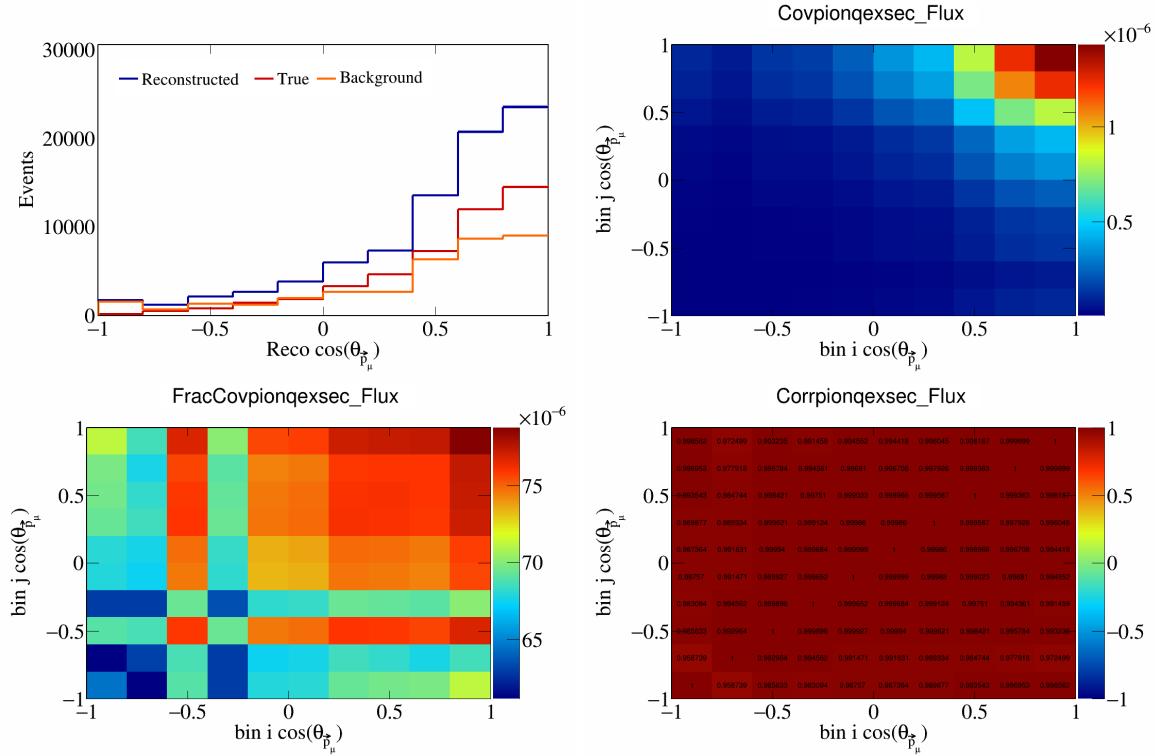


Figure 756: PionQeXSec variations for $\cos(\theta_{\vec{p}_\mu})$.

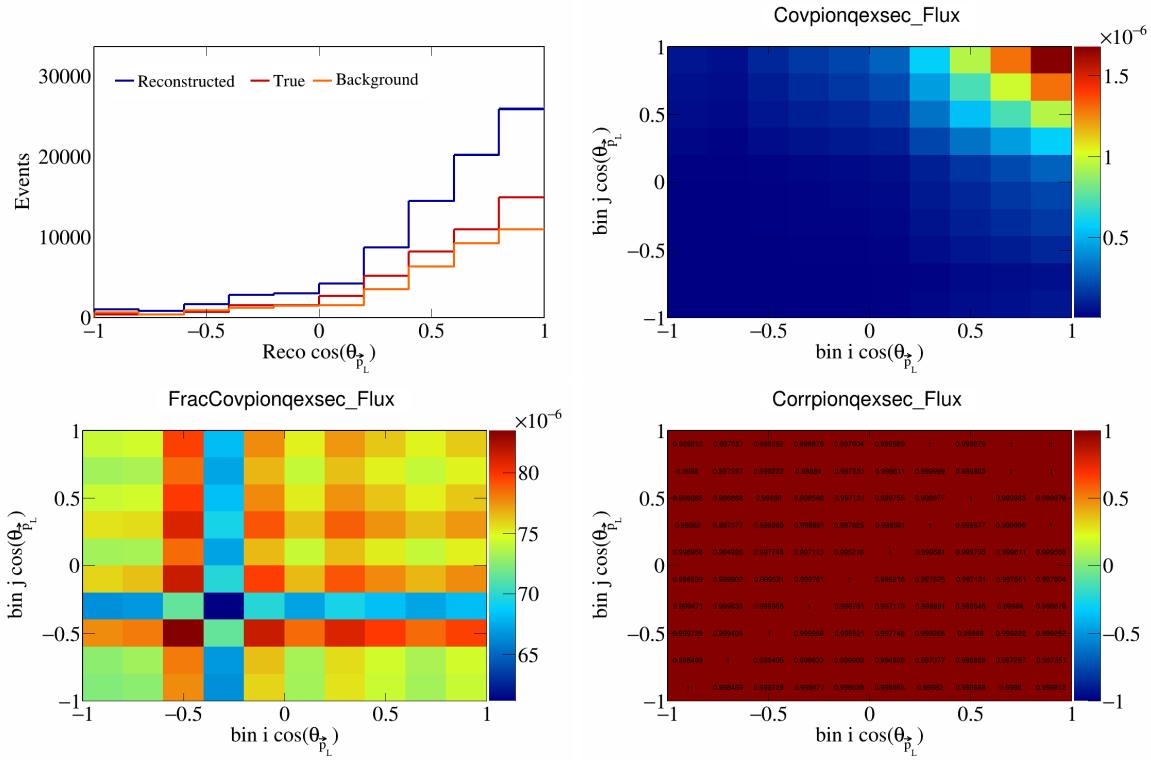


Figure 757: PionQeXSec variations for $\cos(\theta_{\vec{p}_L})$.

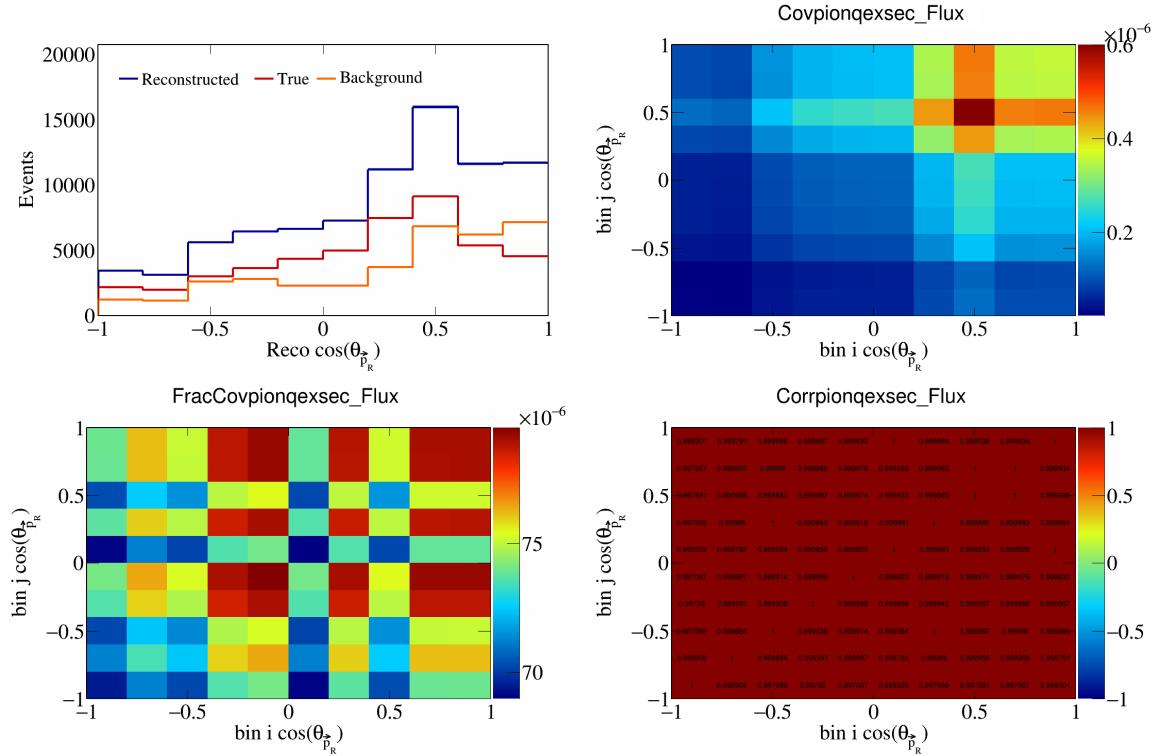


Figure 758: PionQeXSec variations for $\cos(\theta_{\vec{p}_R})$.

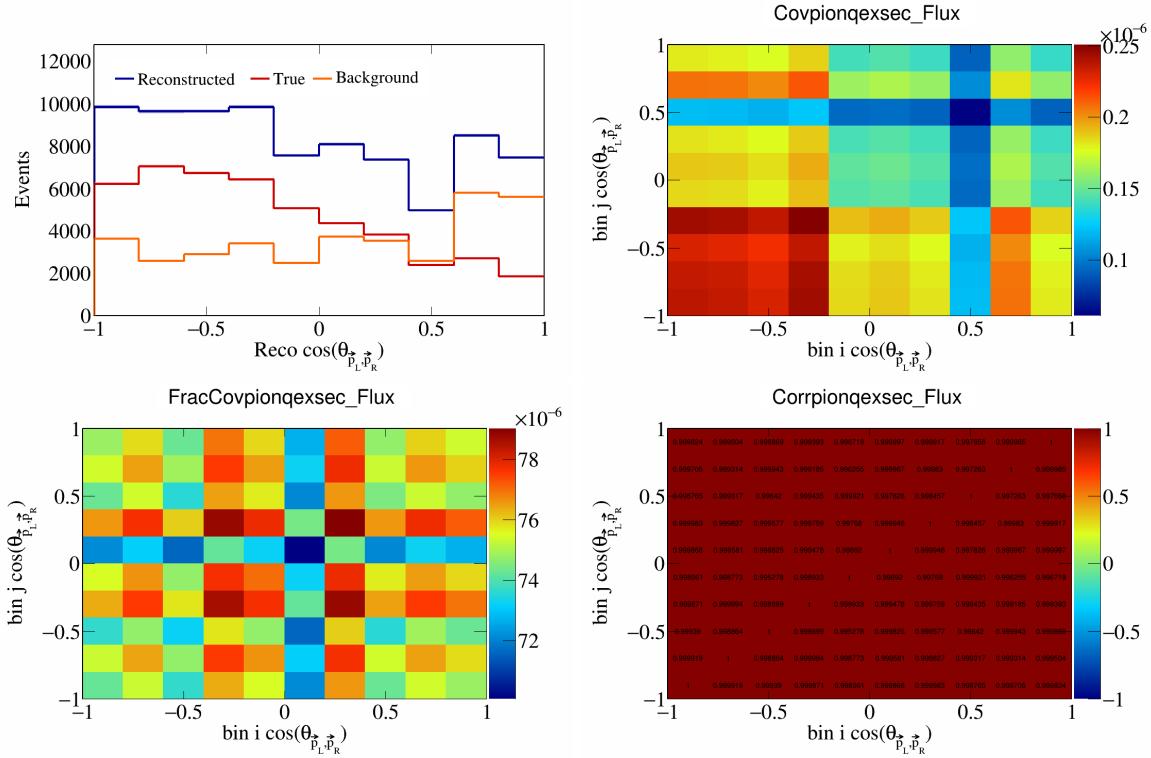


Figure 759: PionQeXSec variations for $\cos(\theta_{\vec{p}_L, \vec{p}_R})$.

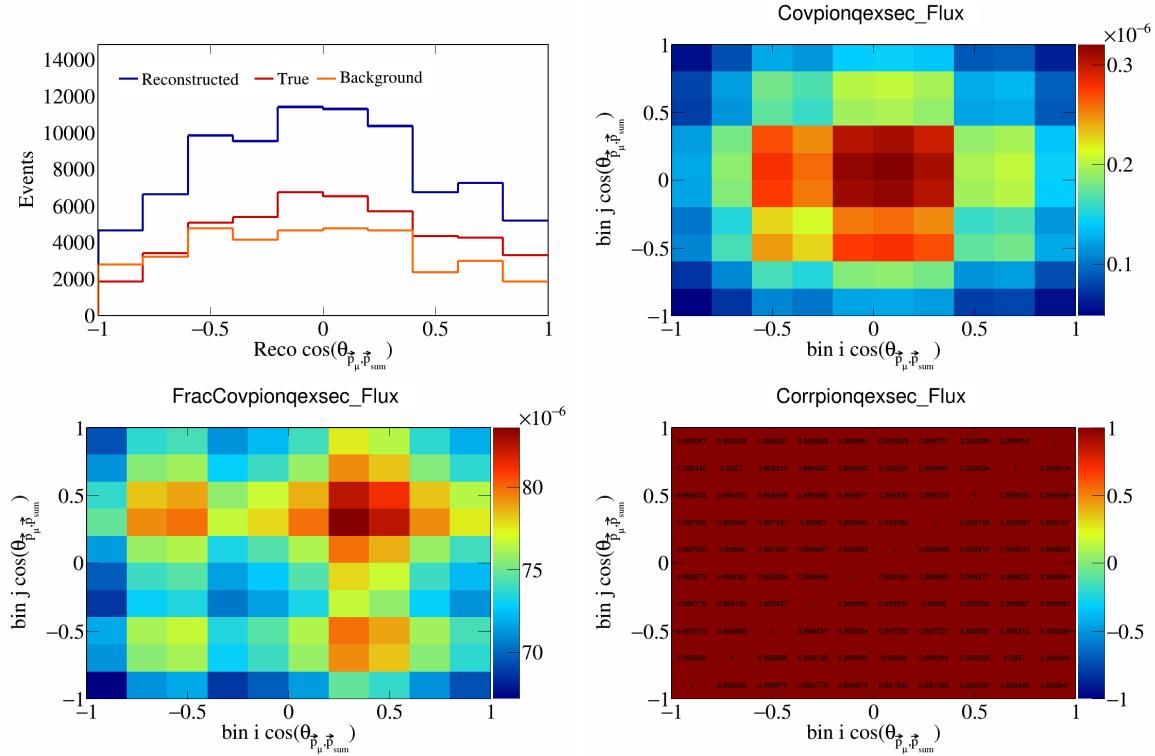


Figure 760: PionQeXSec variations for $\cos(\theta_{\vec{p}_\mu, \vec{p}_{\text{sum}}})$.

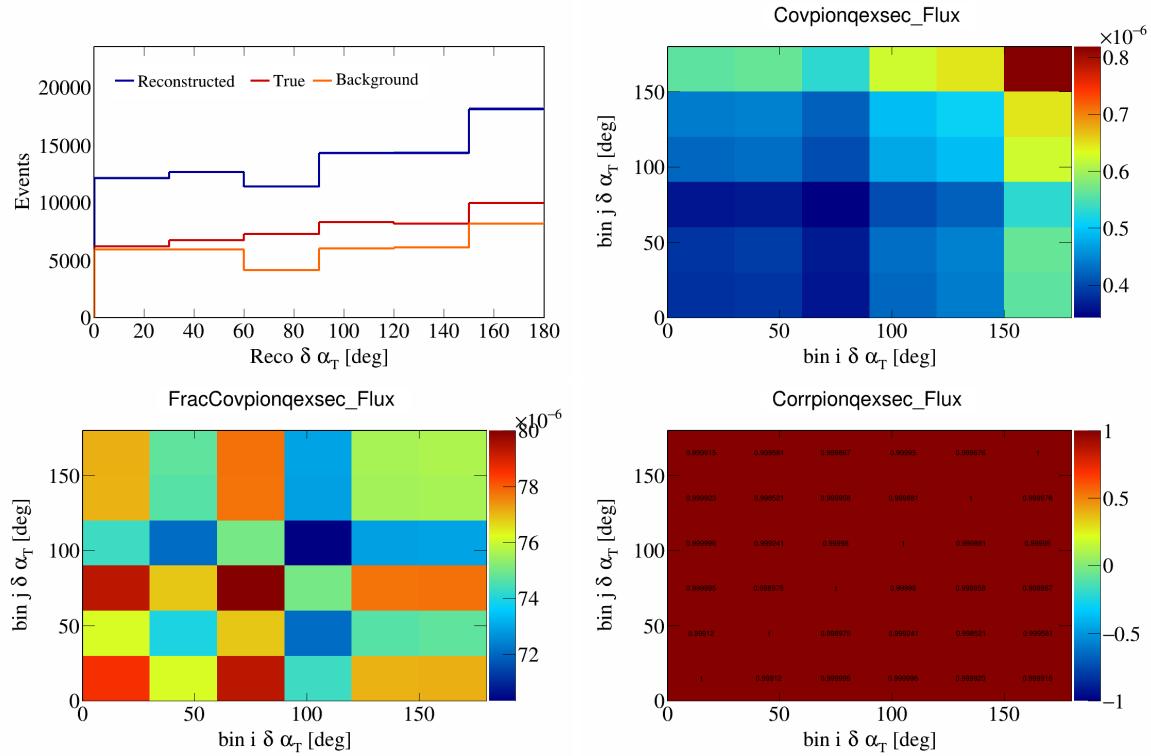


Figure 761: PionQeXSec variations for $\delta\alpha_T$.

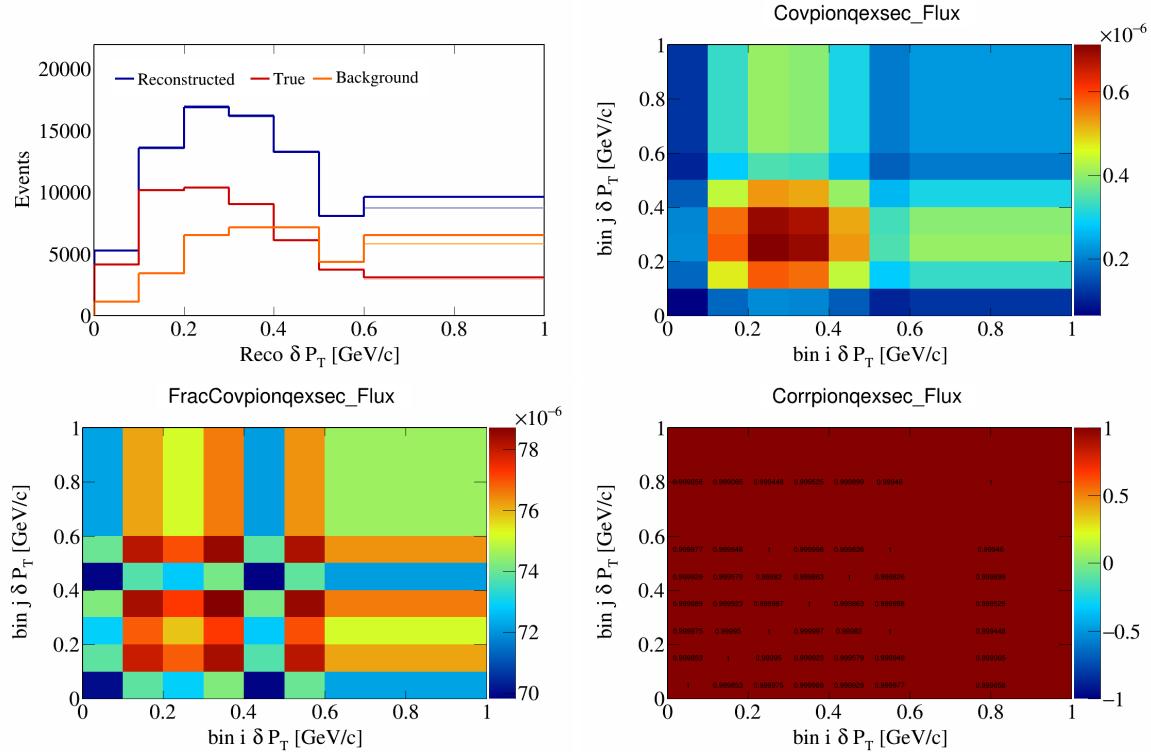


Figure 762: PionQeXSec variations for δP_T .

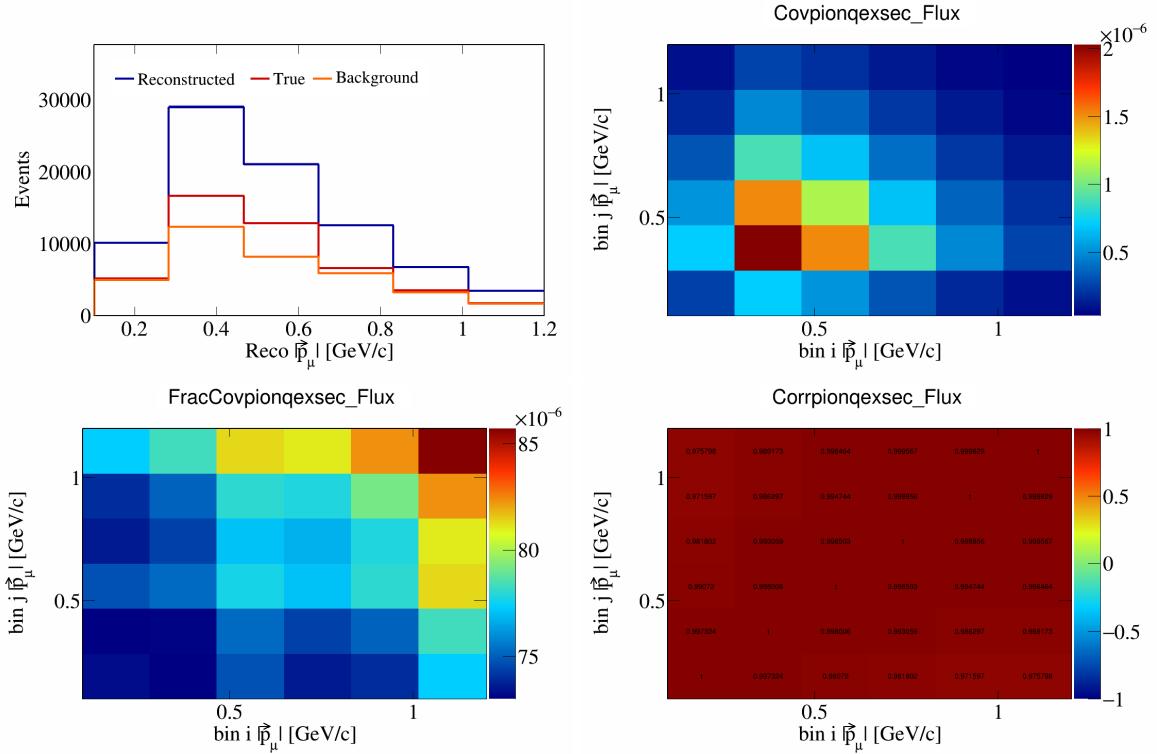


Figure 763: PionQeXSec variations for $|\vec{p}_\mu|$.

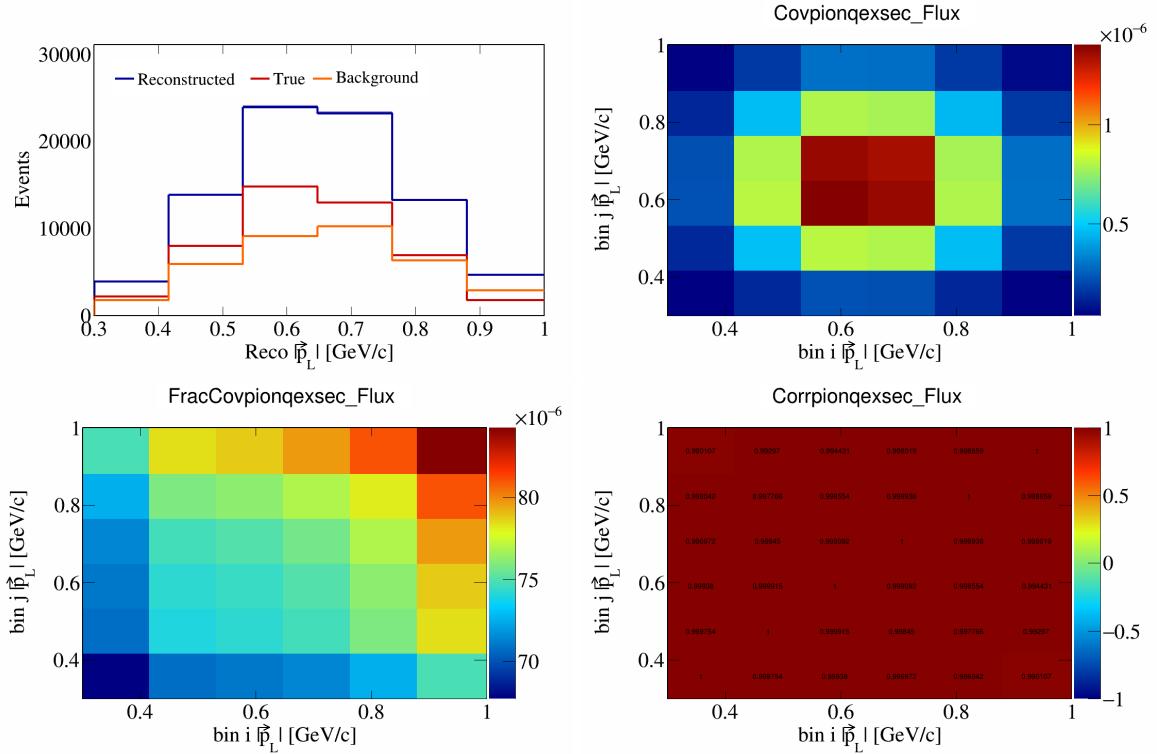


Figure 764: PionQeXSec variations for $|\vec{p}_L|$.

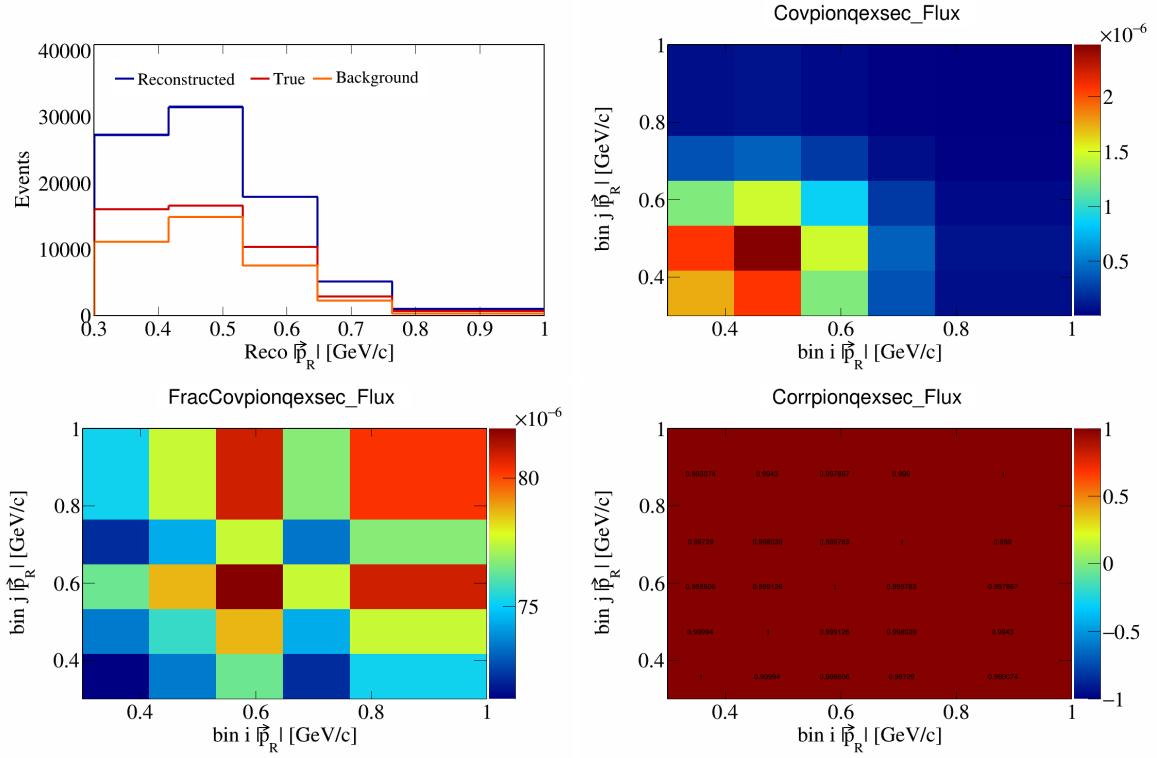


Figure 765: PionQeXSec variations for $|\vec{p}_R|$.

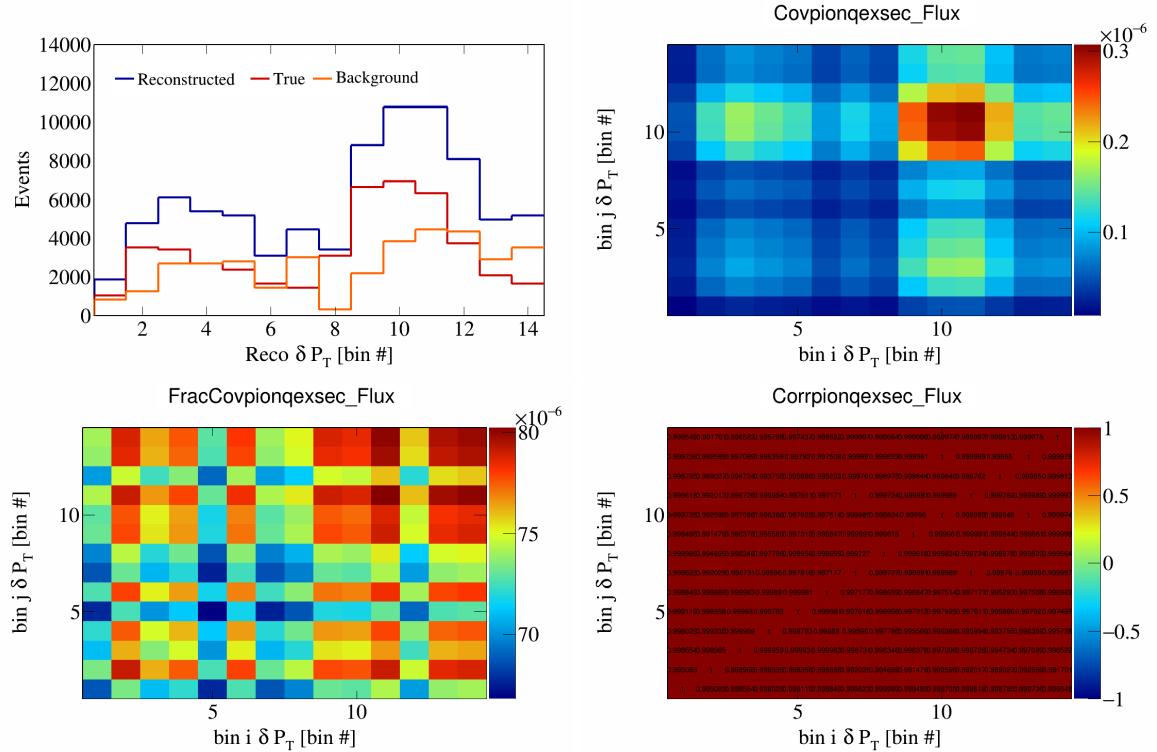


Figure 766: PionQeXSec variations for δP_T in $\cos(\theta_{\vec{p}_\mu})$.

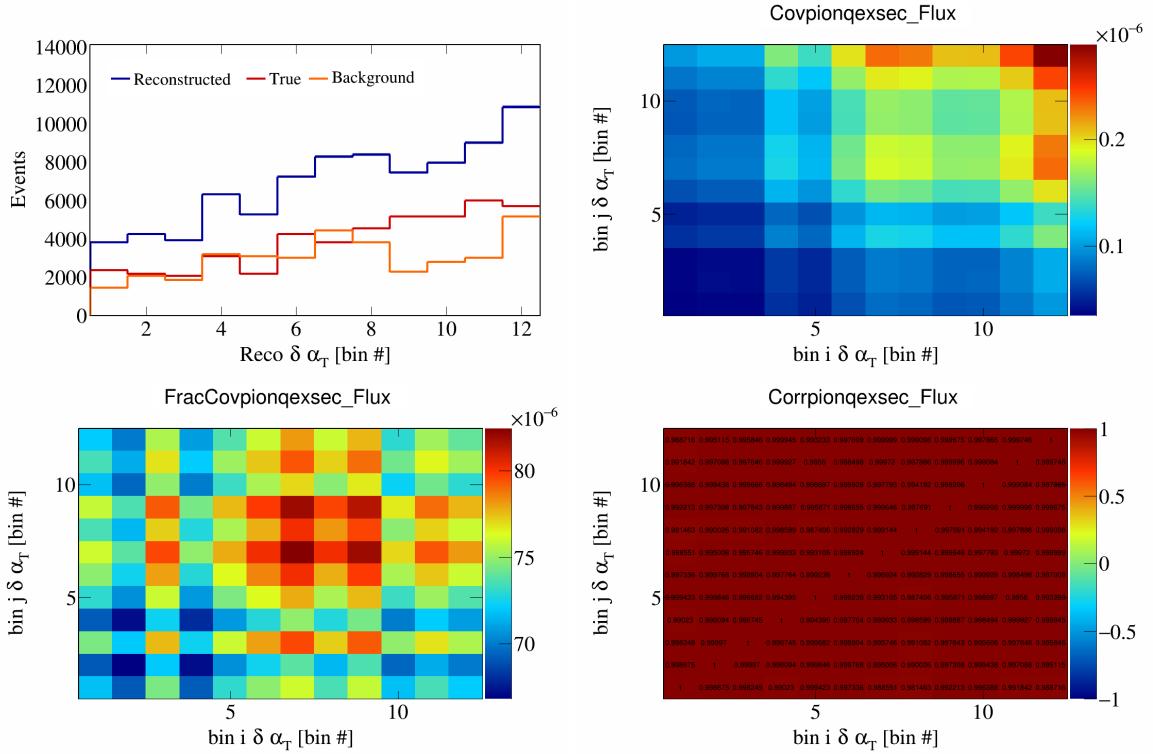


Figure 767: PionQeXSec variations for $\delta\alpha_T$ in $\cos(\theta_{\vec{p}_\mu})$.

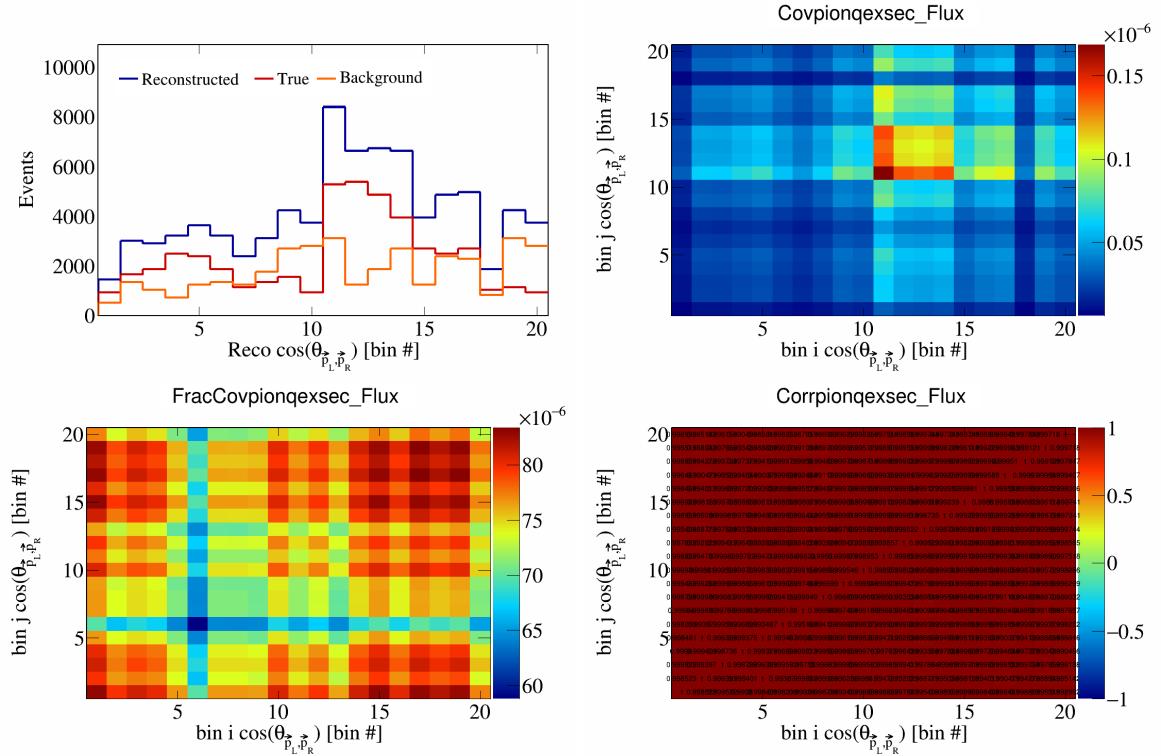


Figure 768: PionQeXSec variations for $\cos(\theta_{\vec{p}_L, \vec{p}_R})$ in $\cos(\theta_{\vec{p}_\mu})$.

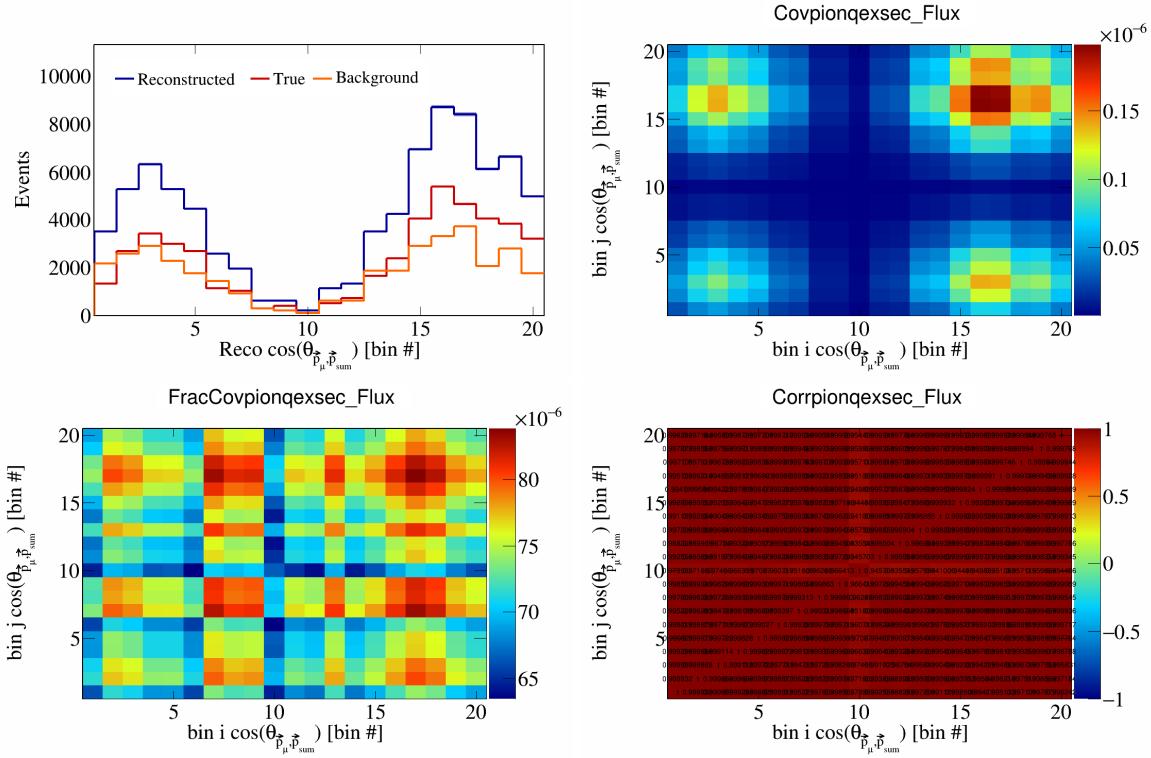


Figure 769: PionQeXSec variations for $\cos(\theta_{\vec{p}_\mu})$ in $\cos(\theta_{\vec{p}_\mu})$.

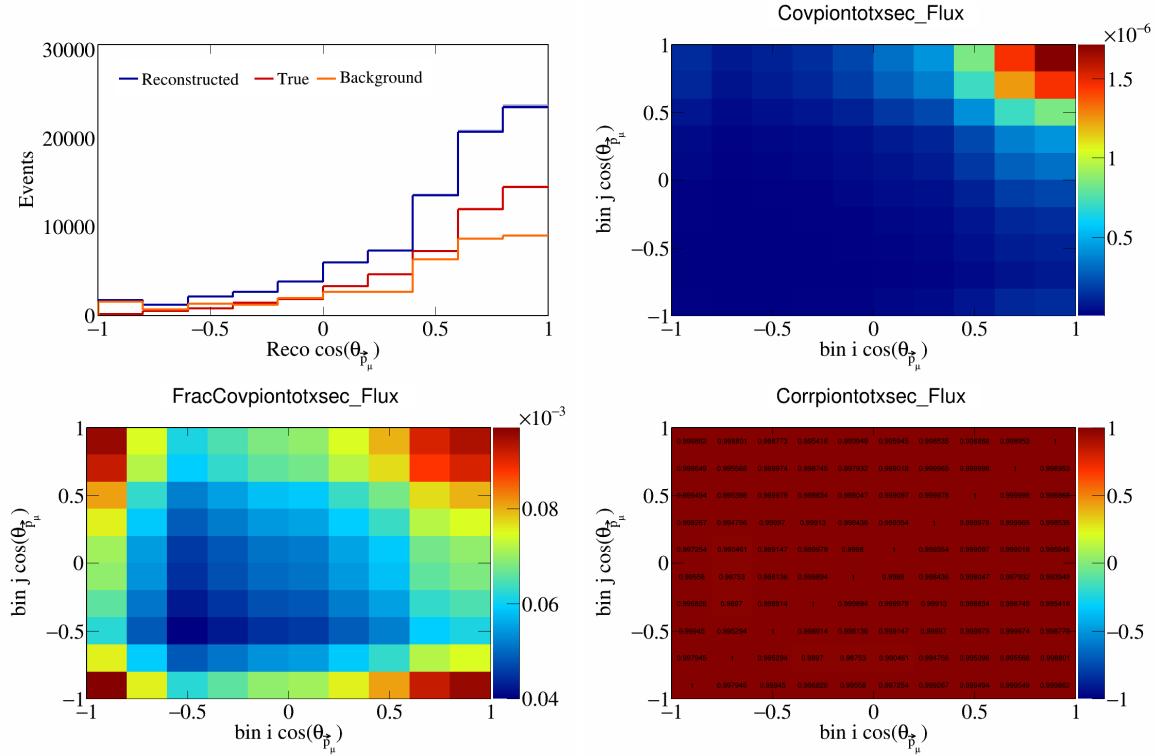


Figure 770: PionTotXSec variations for $\cos(\theta_{\vec{p}_\mu})$.

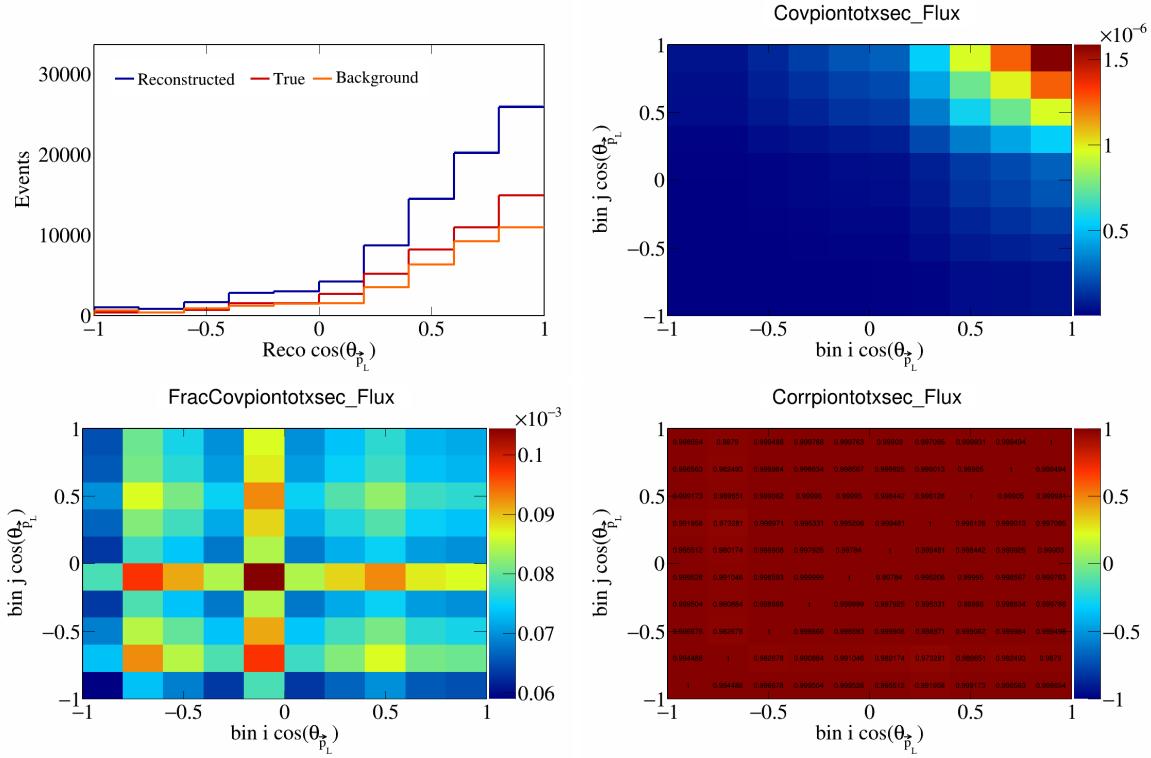


Figure 771: PionTotXSec variations for $\cos(\theta_{\vec{p}_L})$.

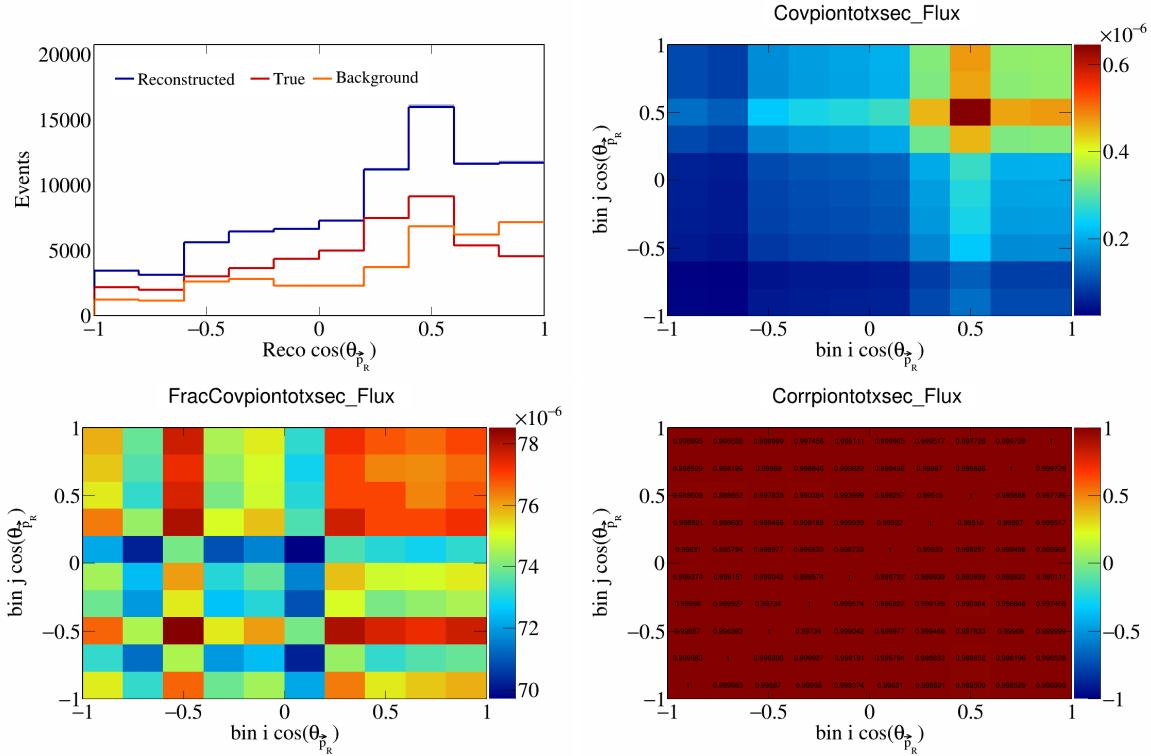


Figure 772: PionTotXSec variations for $\cos(\theta_{\vec{p}_R})$.

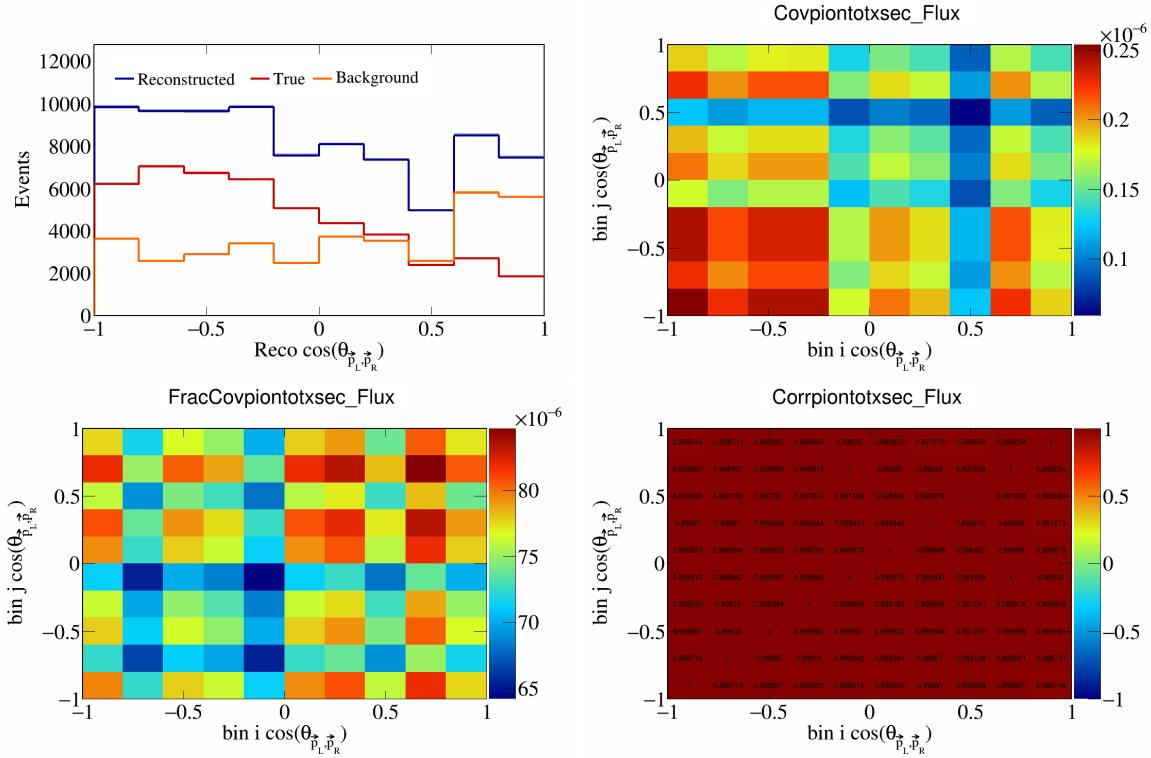


Figure 773: PionTotXSec variations for $\cos(\theta_{\vec{p}_L, \vec{p}_R})$.

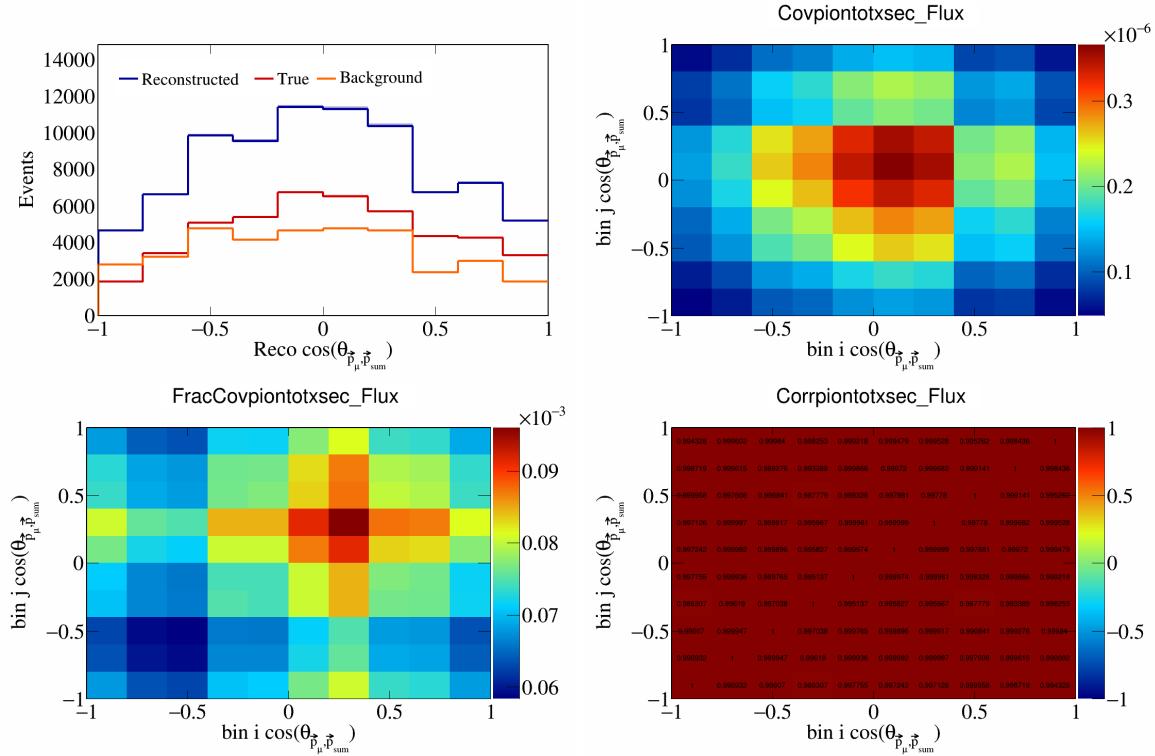


Figure 774: PionTotXSec variations for $\cos(\theta_{\vec{p}_\mu, \vec{p}_{\text{sum}}})$.

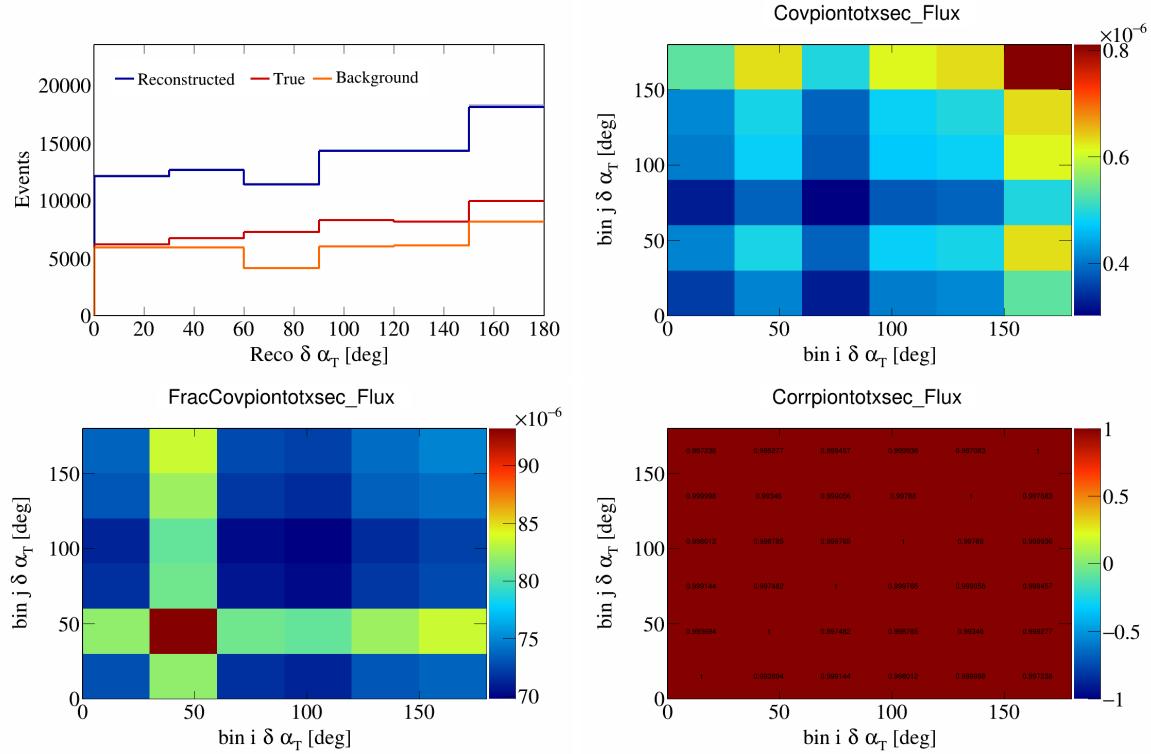


Figure 775: PionTotXSec variations for $\delta\alpha_T$.

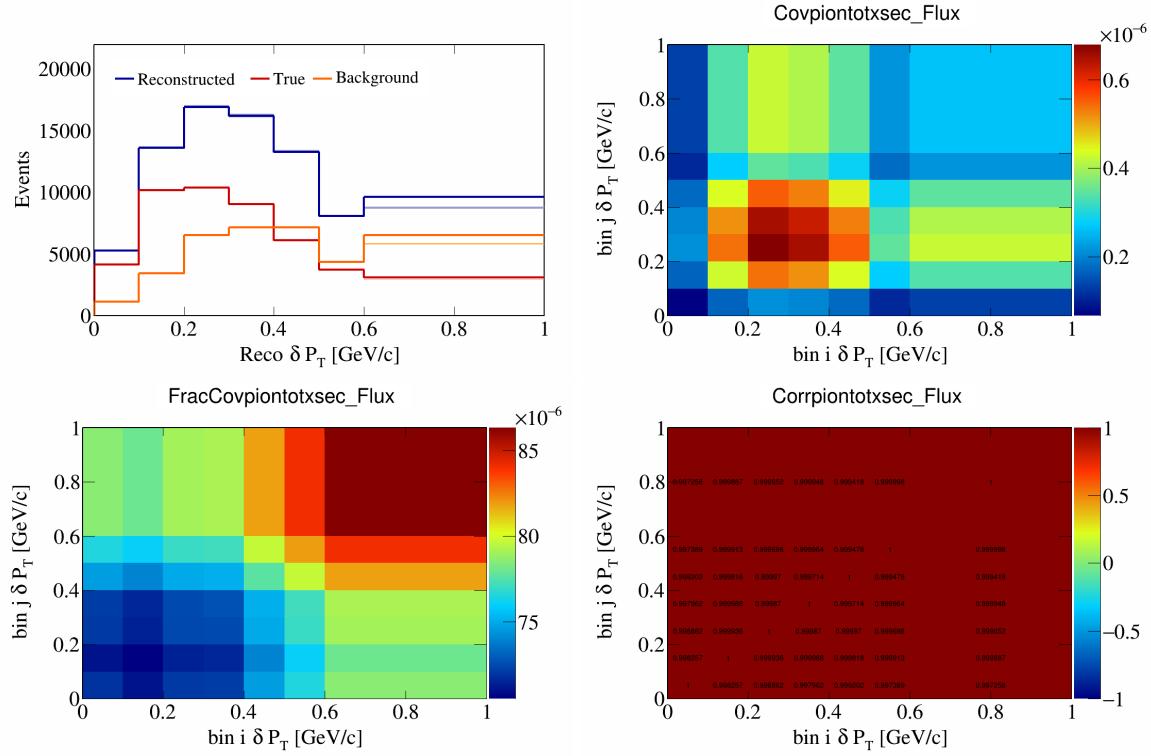


Figure 776: PionTotXSec variations for δP_T .

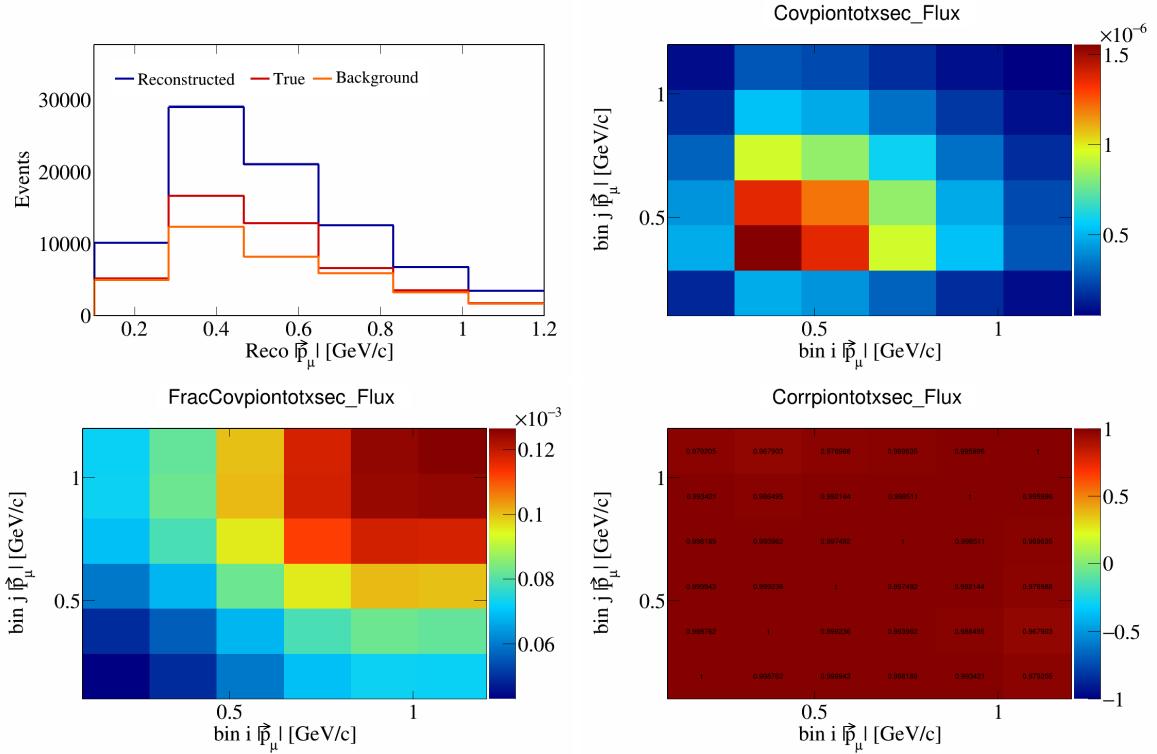


Figure 777: PionTotXSec variations for $|\vec{p}_\mu|$.

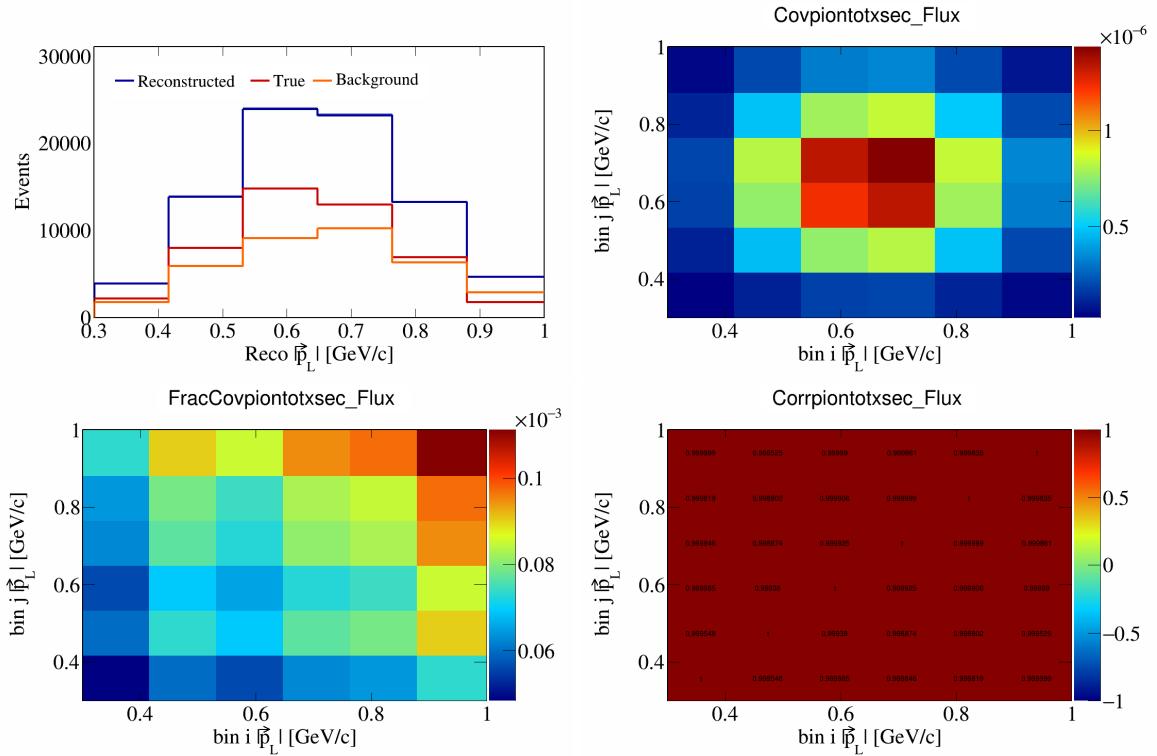


Figure 778: PionTotXSec variations for $|\vec{p}_L|$.

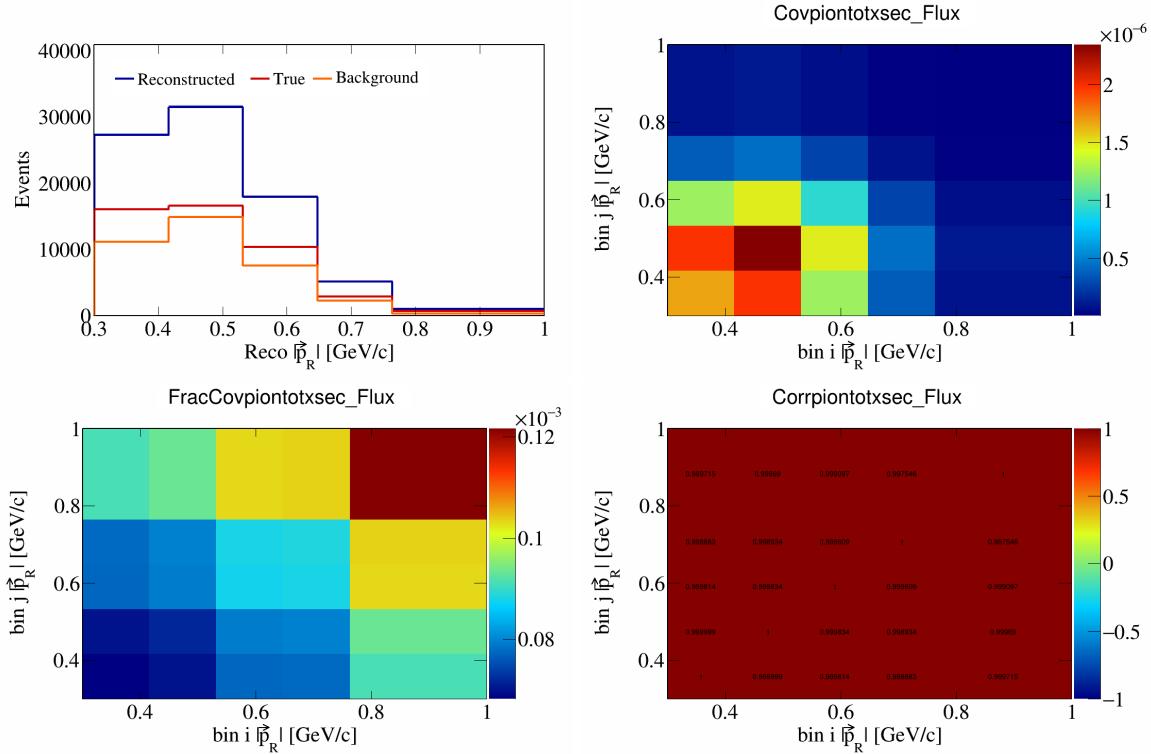


Figure 779: PionTotXSec variations for $|\vec{p}_R|$.

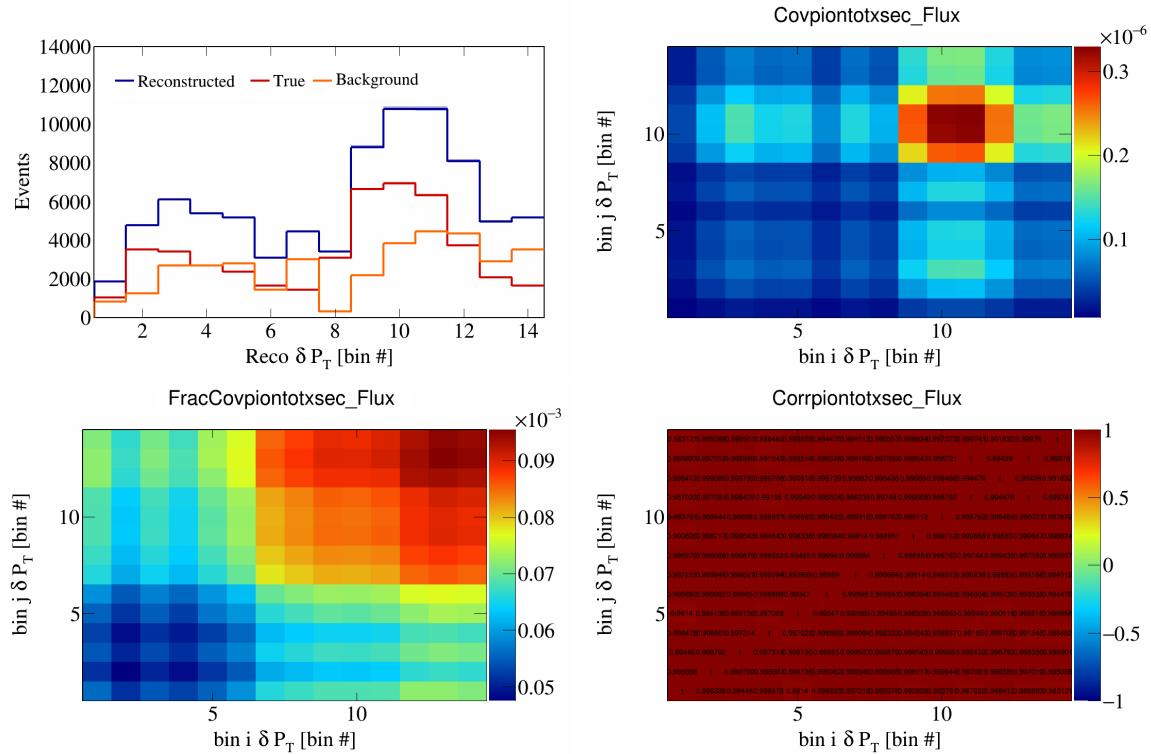


Figure 780: PionTotXSec variations for δP_T in $\cos(\theta_{\vec{p}_\mu})$.

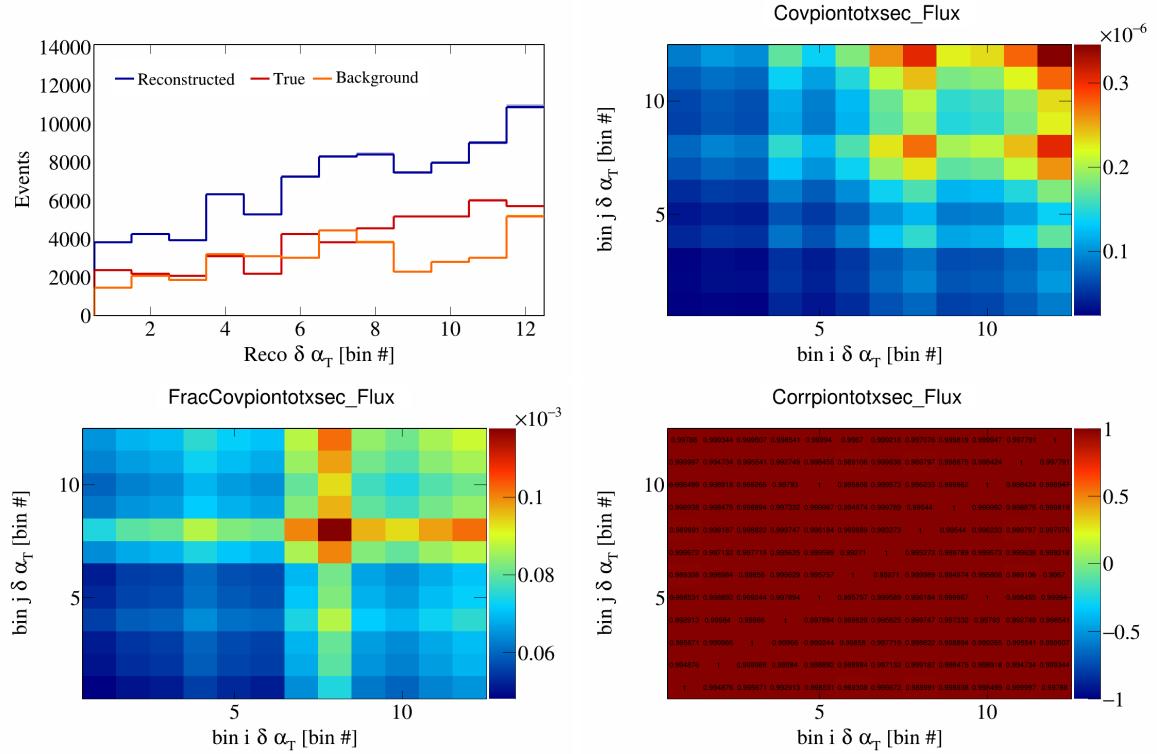


Figure 781: PionTotXSec variations for $\delta \alpha_T$ in $\cos(\theta_{\vec{p}_\mu})$.

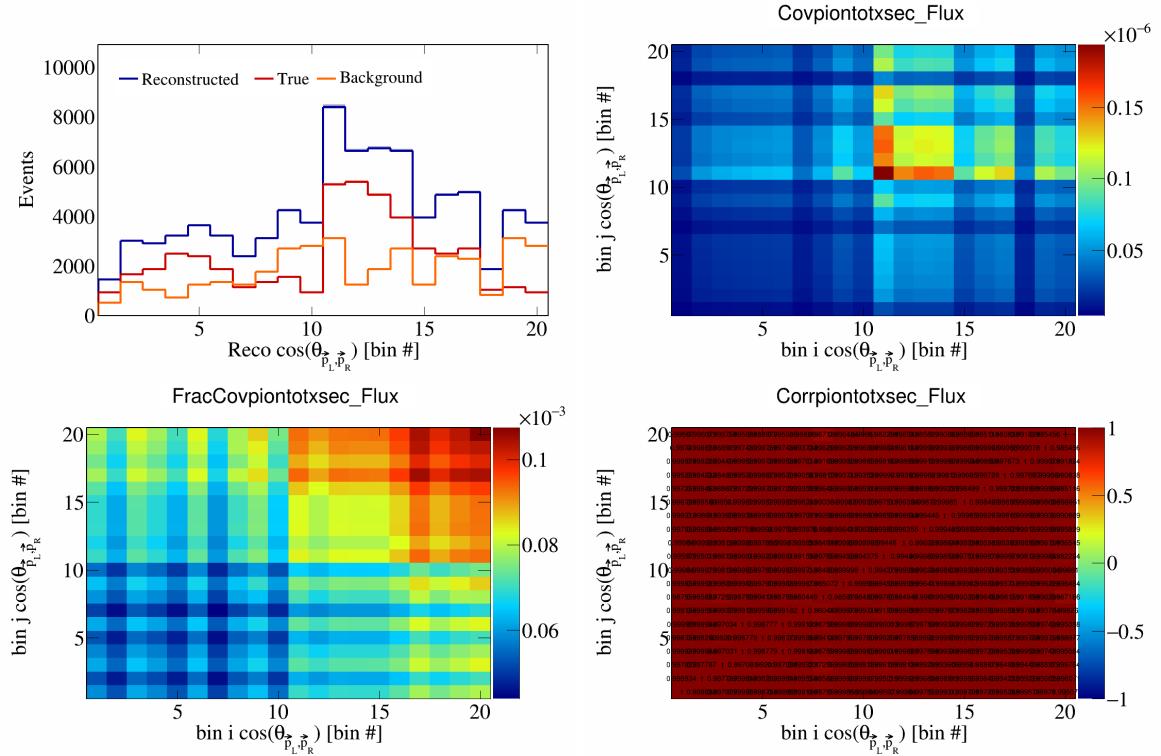


Figure 782: PionTotXSec variations for $\cos(\theta_{\vec{p}_L, \vec{p}_R})$ in $\cos(\theta_{\vec{p}_\mu})$.

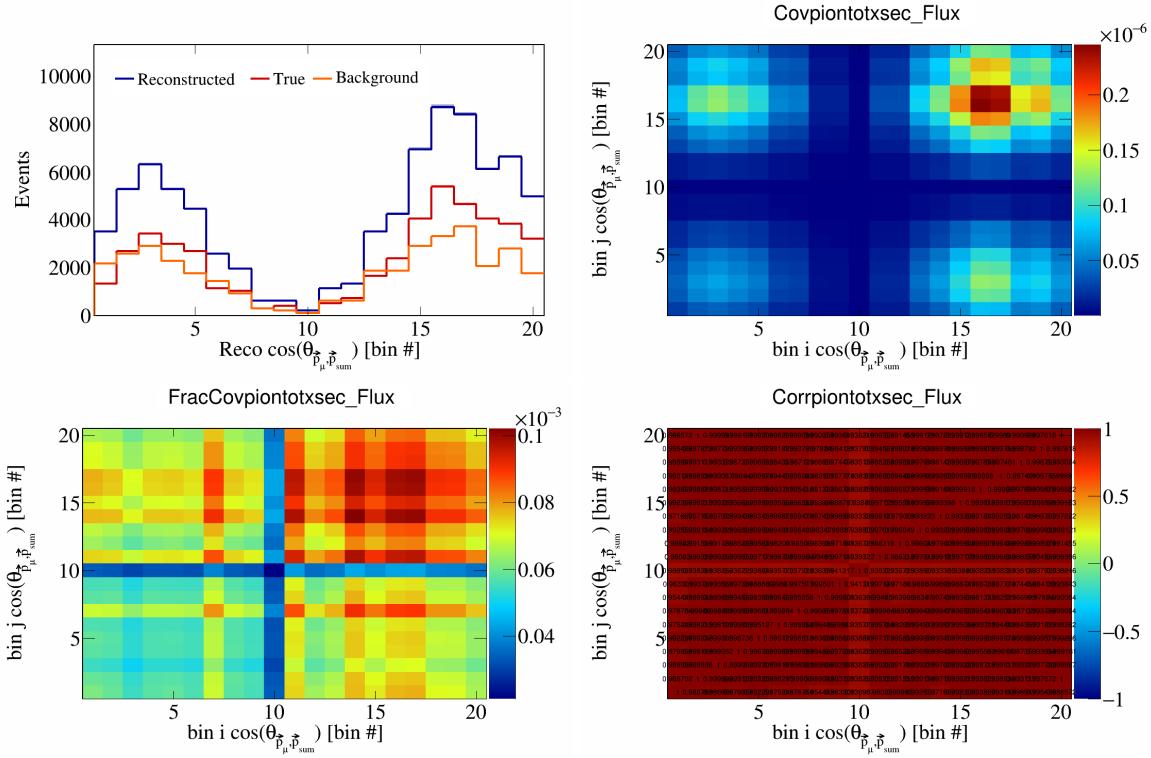


Figure 783: PionTotXSec variations for $\cos(\theta_{\vec{p}_\mu, \vec{p}_{\text{sum}}})$ in $\cos(\theta_{\vec{p}_\mu})$.

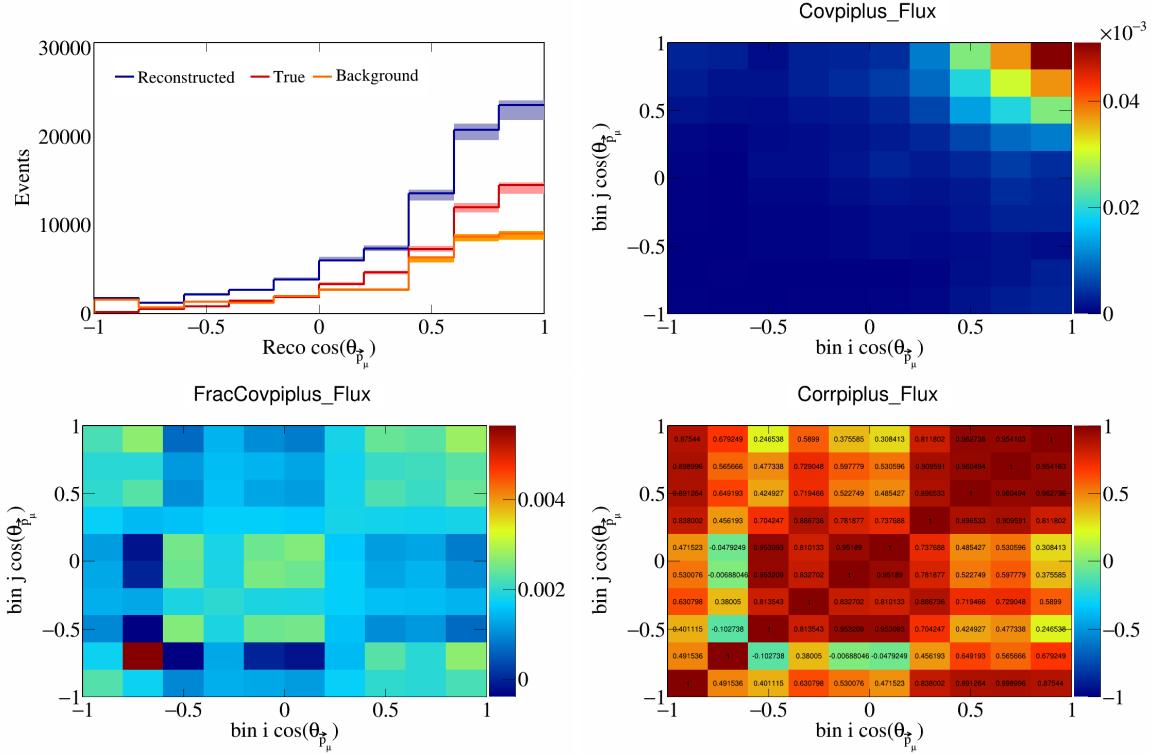


Figure 784: PiPlus variations for $\cos(\theta_{\vec{p}_\mu})$.

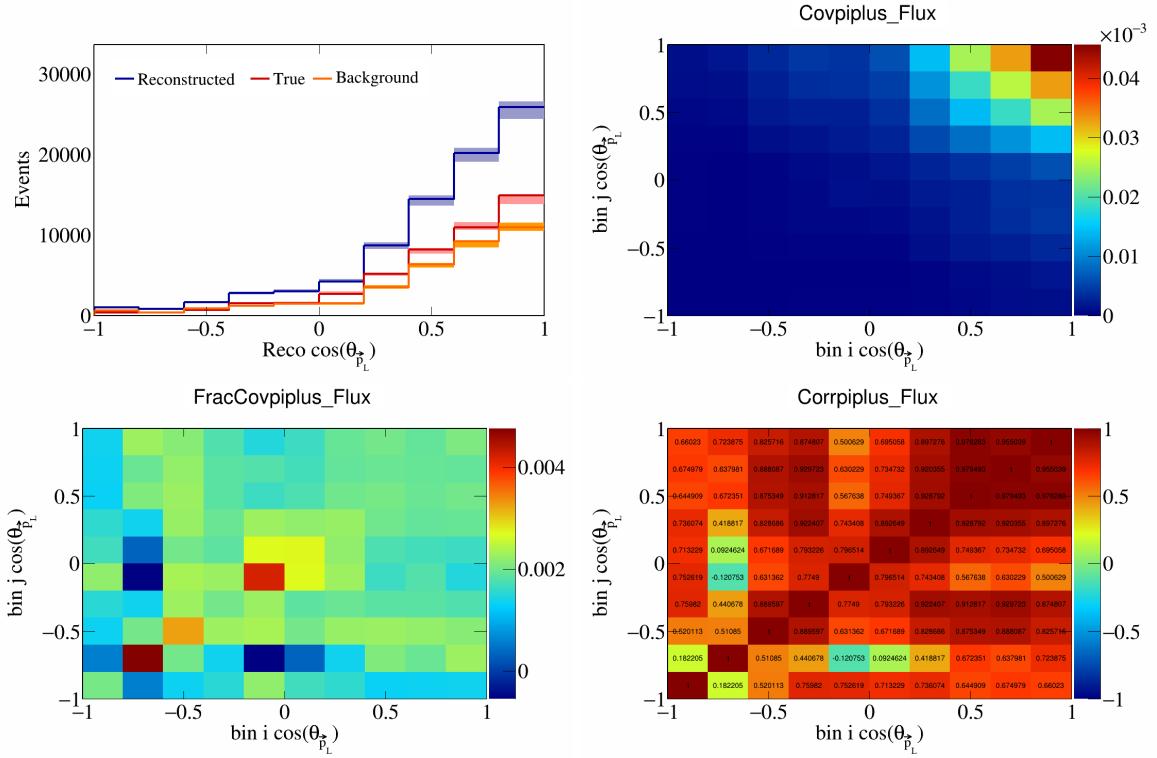


Figure 785: PiPlus variations for $\cos(\theta_{\vec{p}_L})$.

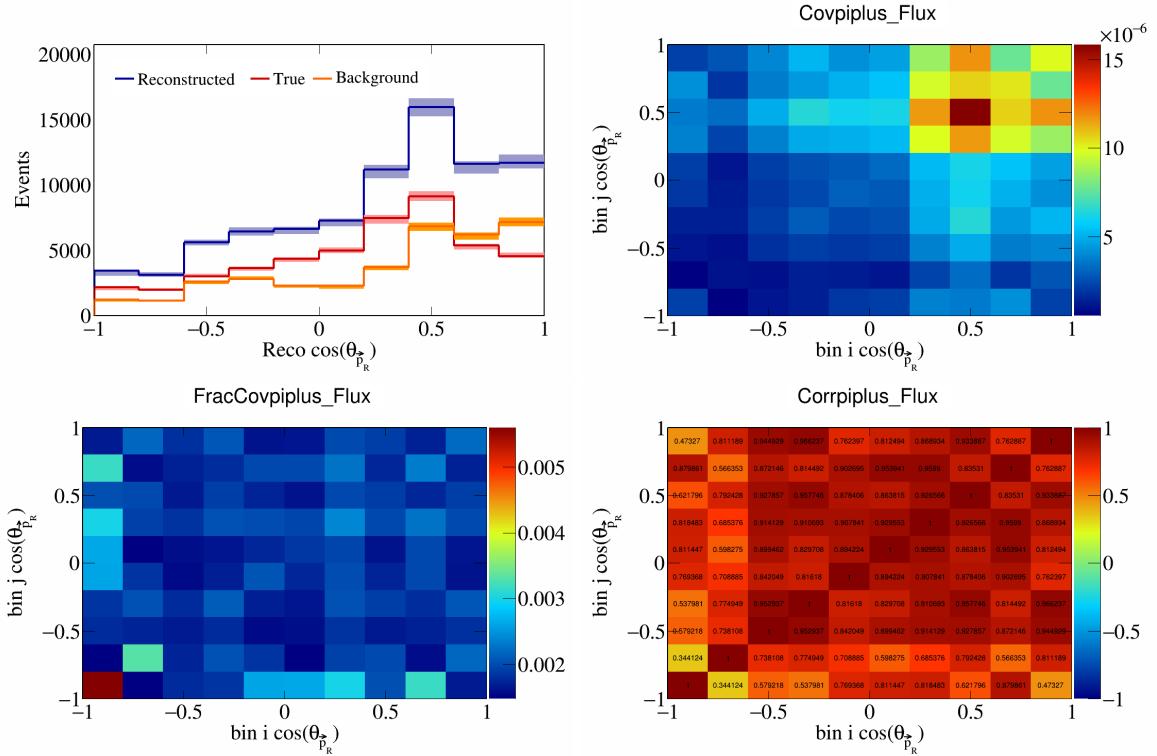


Figure 786: PiPlus variations for $\cos(\theta_{\vec{p}_R})$.

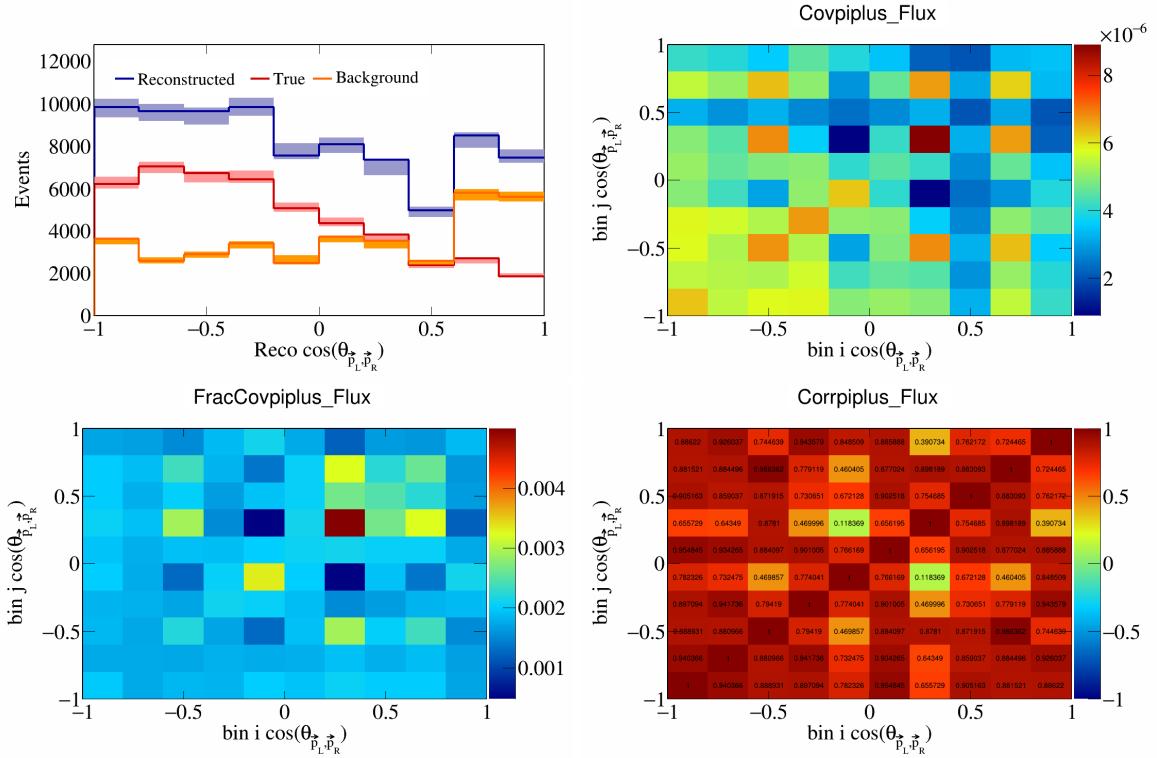


Figure 787: PiPlus variations for $\cos(\theta_{\vec{p}_L, \vec{p}_R})$.

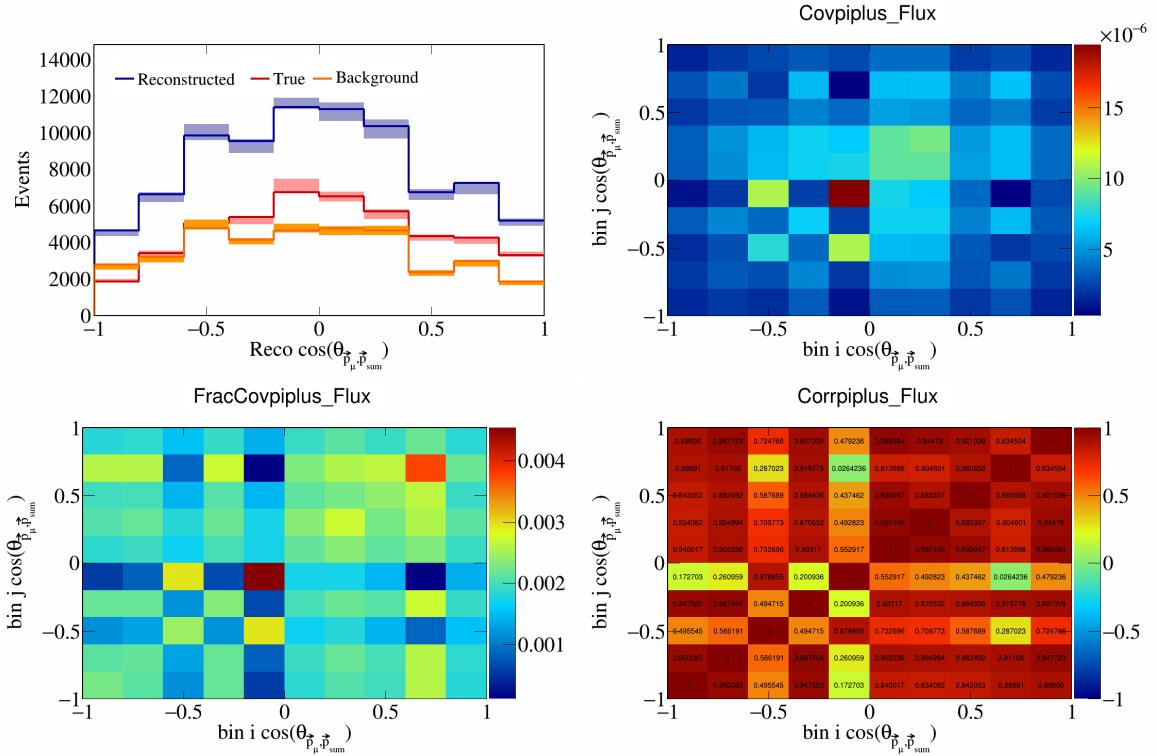


Figure 788: PiPlus variations for $\cos(\theta_{\vec{p}_\mu, \vec{p}_{\text{sum}}})$.

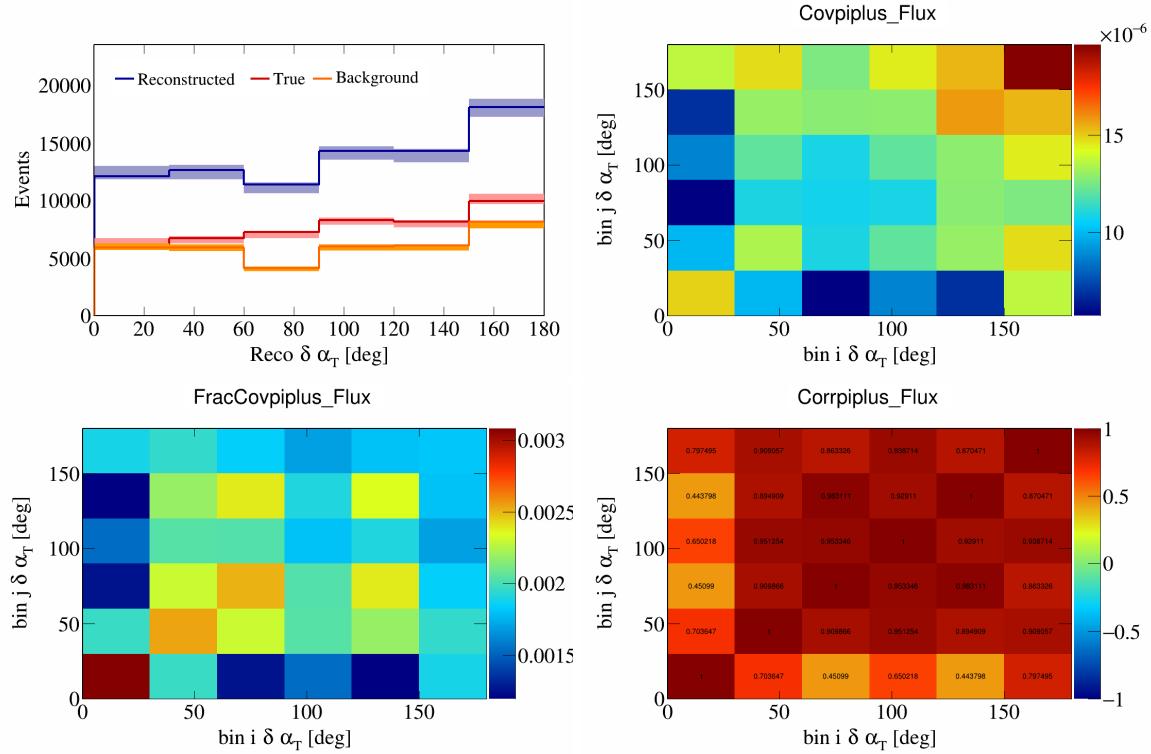


Figure 789: PiPlus variations for $\delta\alpha_T$.

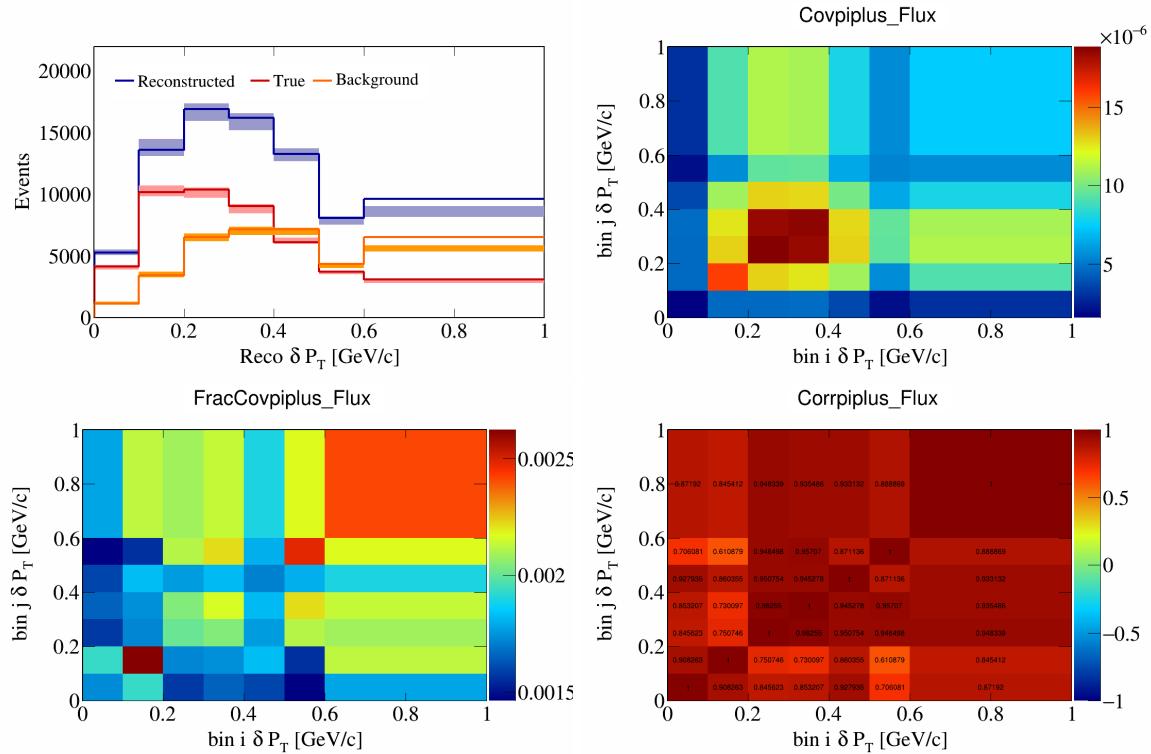


Figure 790: PiPlus variations for δP_T .

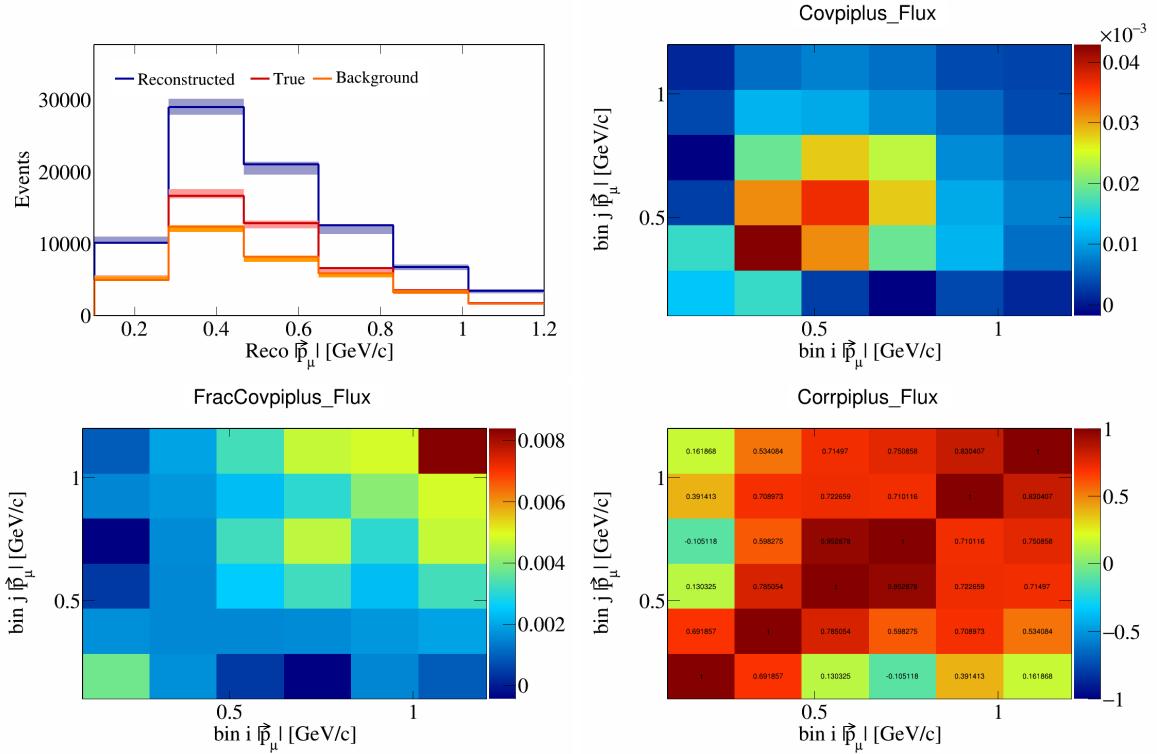


Figure 791: PiPlus variations for $|\vec{p}_\mu|$.

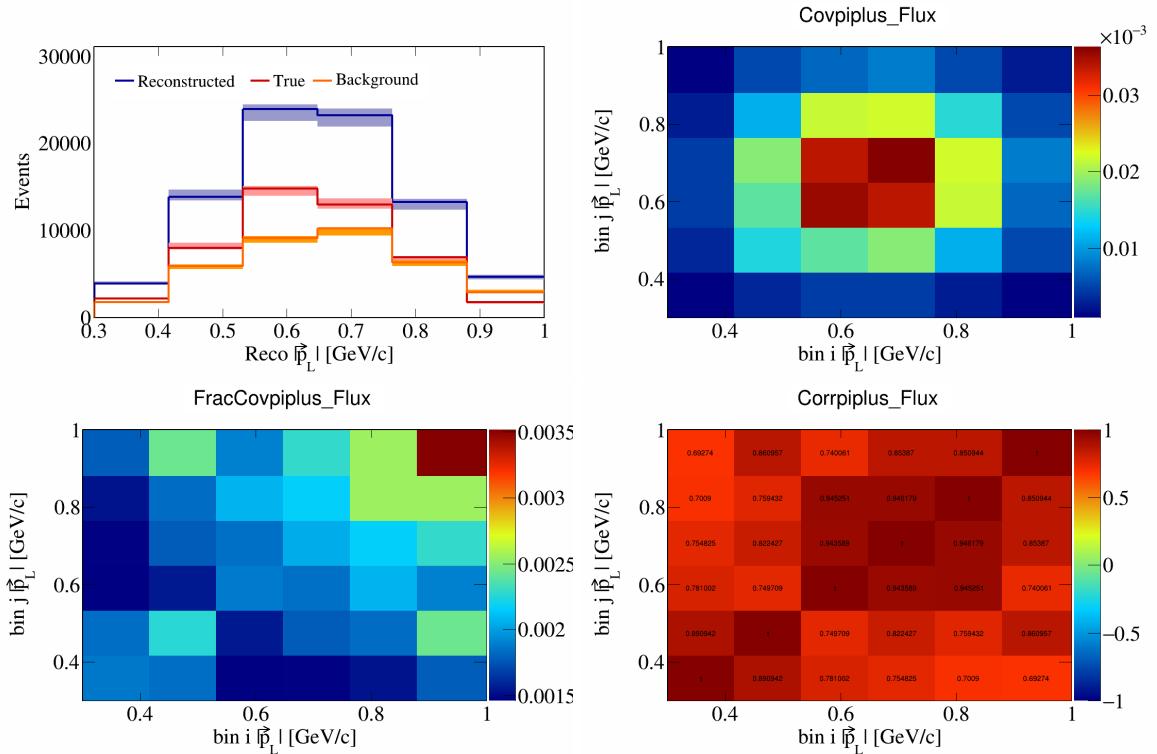


Figure 792: PiPlus variations for $|\vec{p}_L|$.

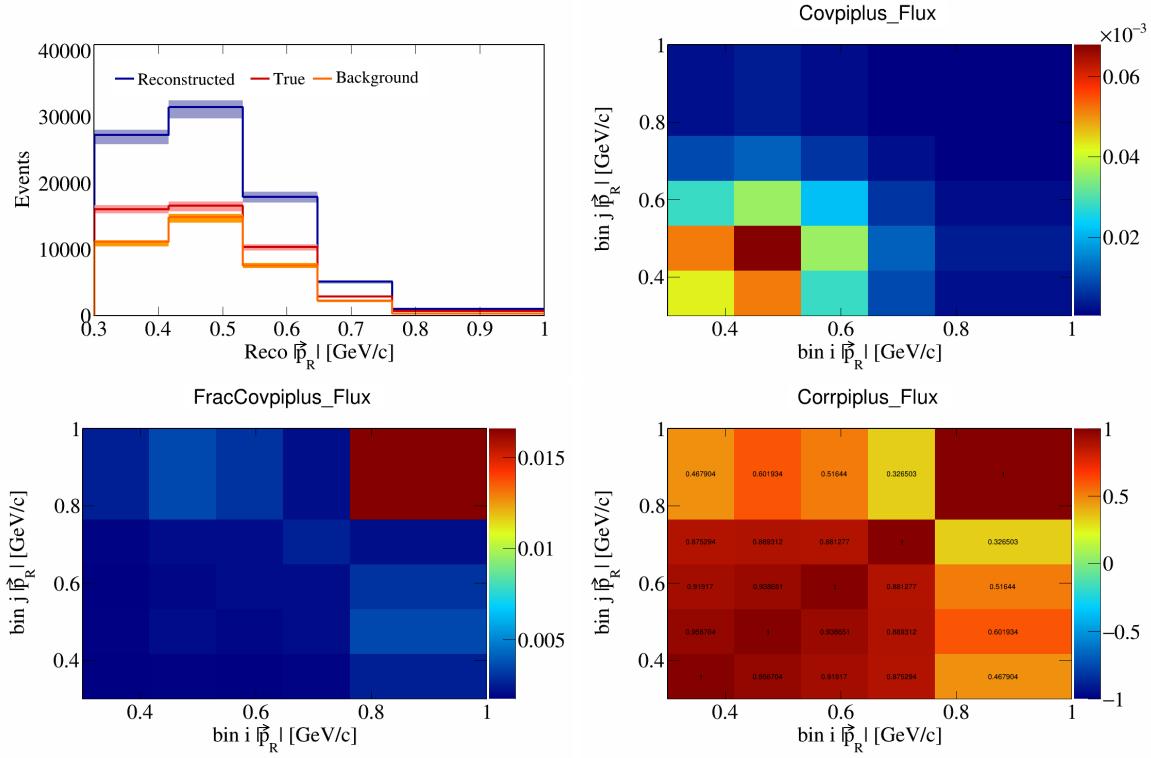


Figure 793: PiPlus variations for $|\vec{p}_R|$.

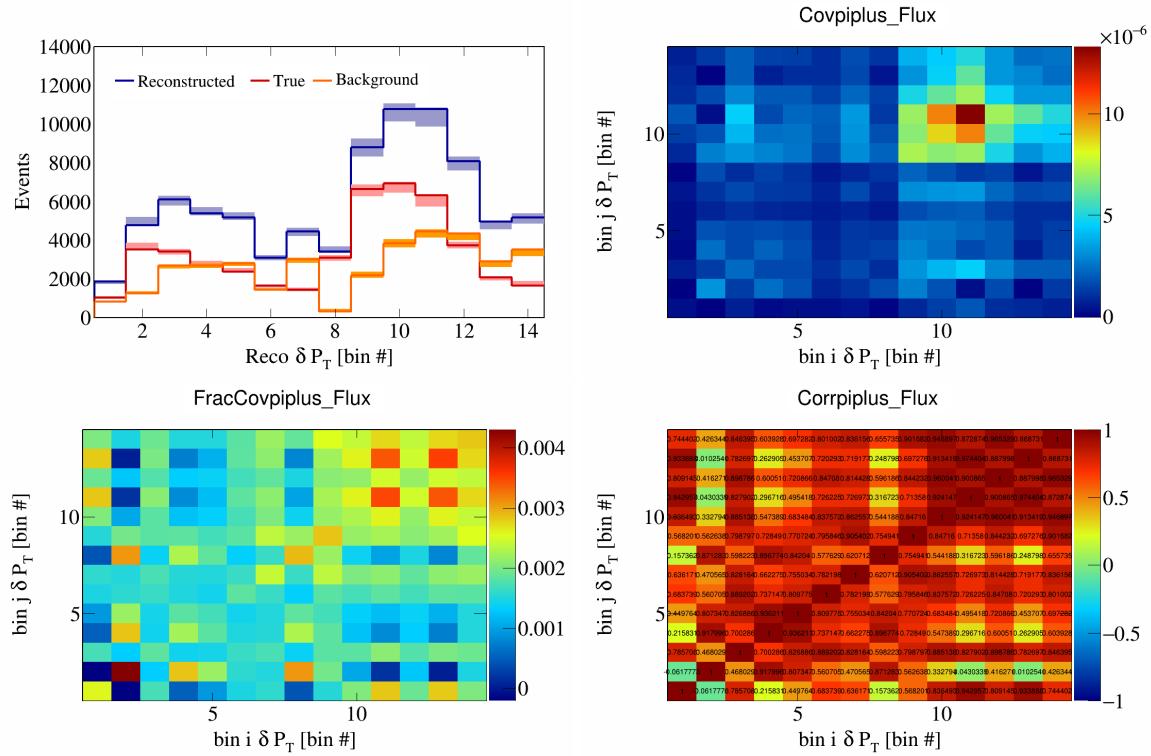


Figure 794: PiPlus variations for δP_T in $\cos(\theta_{\vec{p}_\mu})$.

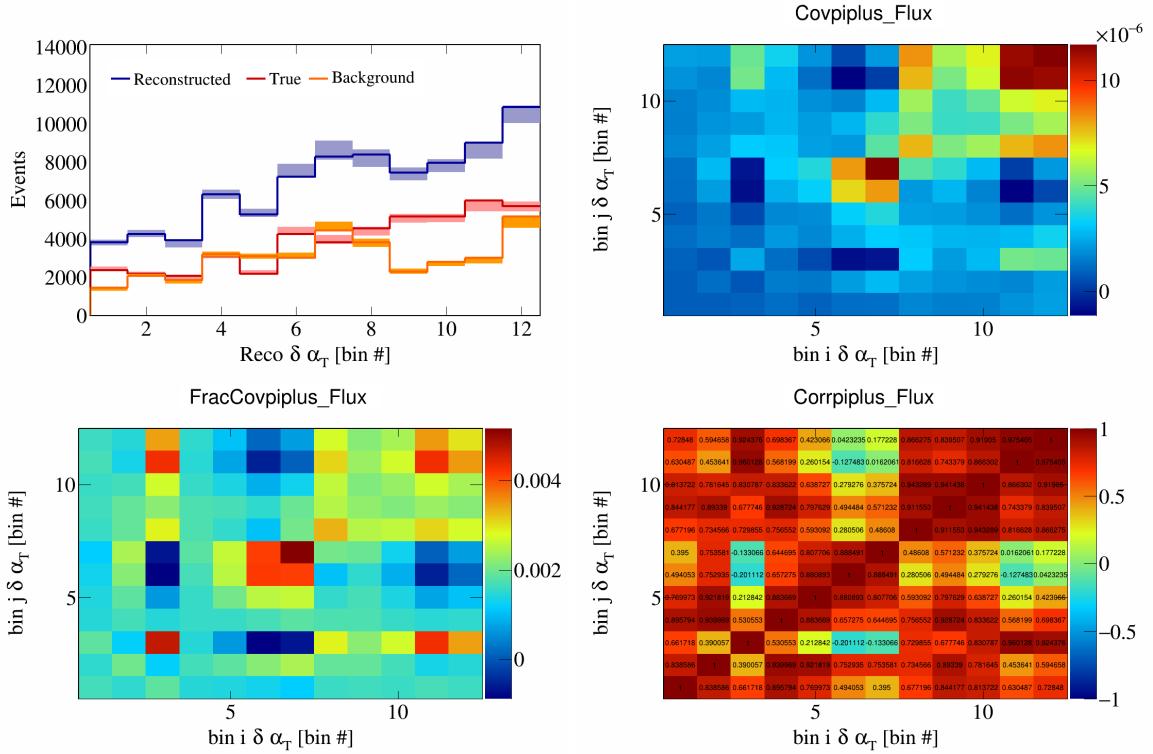


Figure 795: PiPlus variations for $\delta\alpha_T$ in $\cos(\theta_{\vec{p}_\mu})$.

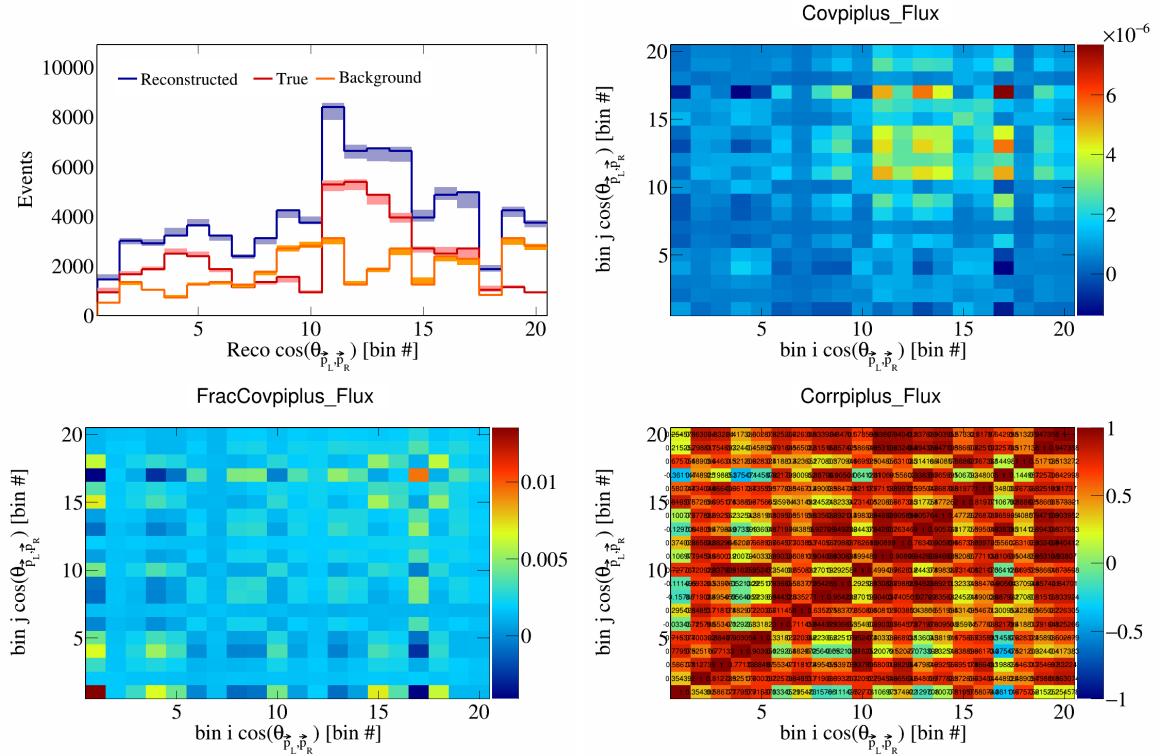


Figure 796: PiPlus variations for $\cos(\theta_{\vec{p}_L, \vec{p}_R})$ in $\cos(\theta_{\vec{p}_\mu})$.

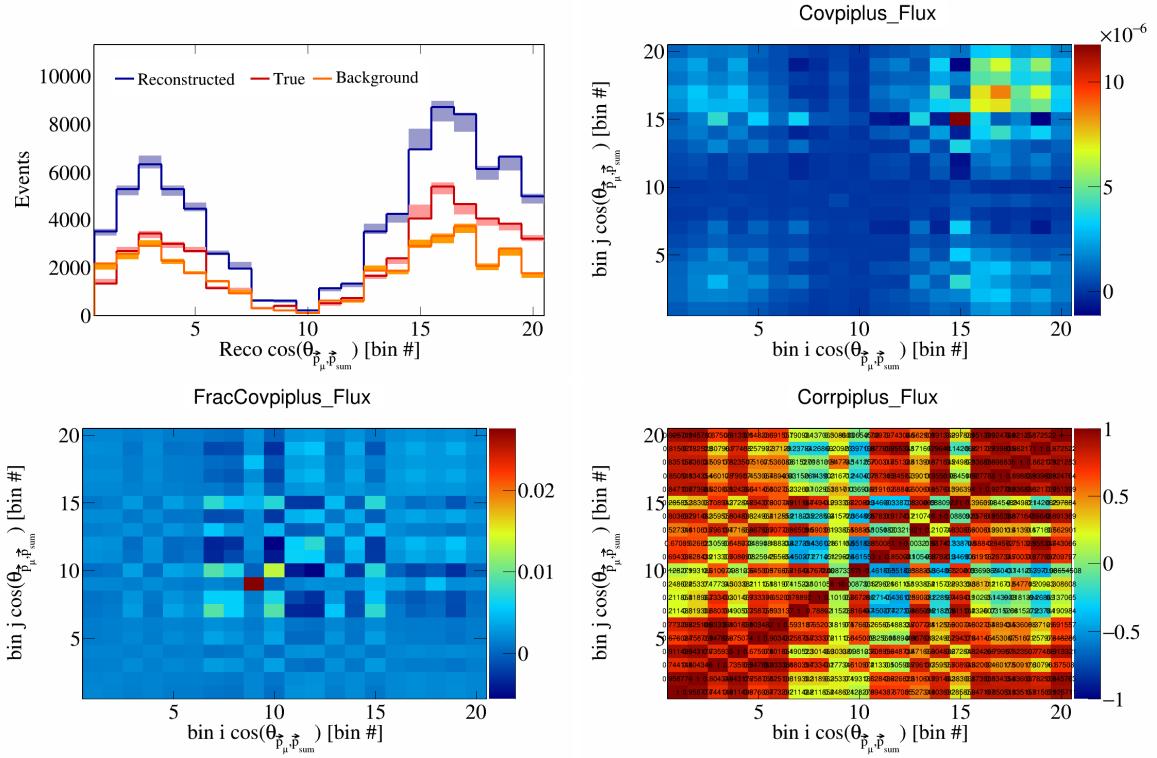


Figure 797: PiPlus variations for $\cos(\theta_{\vec{p}_\mu})$ in $\cos(\theta_{\vec{p}_\mu})$.

7.3 Statistical systematics

In this appendix, the covariance, fractional covariance, and correlation matrices for the statistical systematics are plotted.

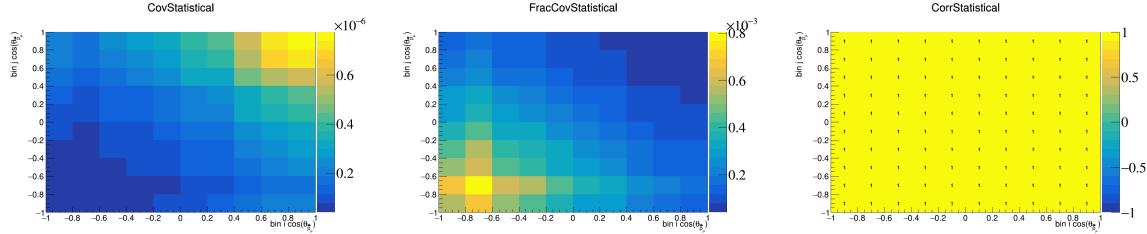


Figure 798: Statistical variations for $\cos(\theta_{\vec{p}_\mu})$.

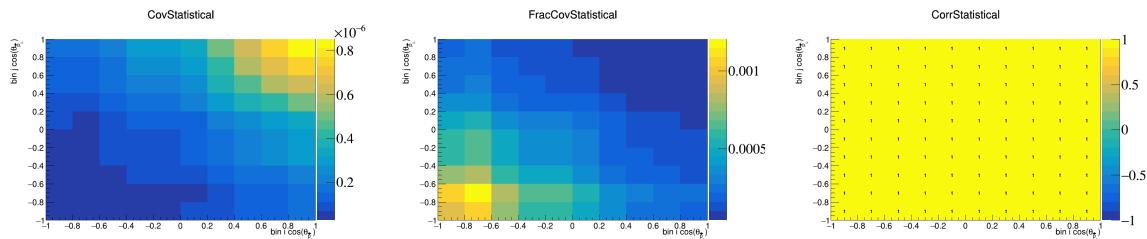


Figure 799: Statistical variations for $\cos(\theta_{\vec{p}_L})$.

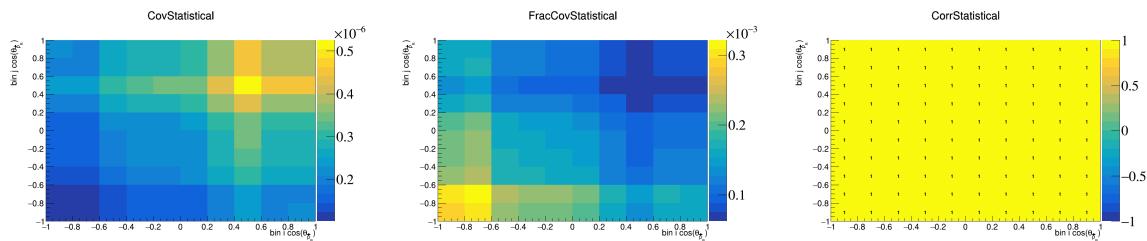


Figure 800: Statistical variations for $\cos(\theta_{\vec{p}_R})$.

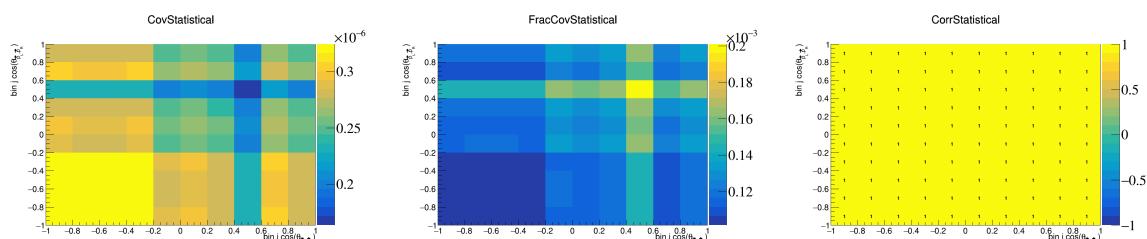


Figure 801: Statistical variations for $\cos(\theta_{\vec{p}_L, \vec{p}_R})$.

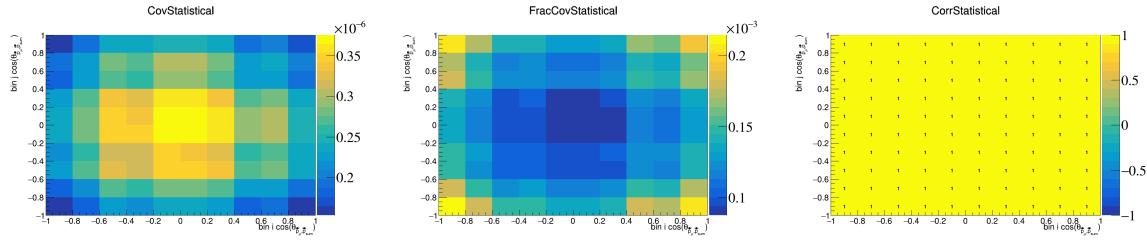


Figure 802: Statistical variations for $\cos(\theta_{\vec{p}_\mu, \vec{p}_{\text{sum}}})$.

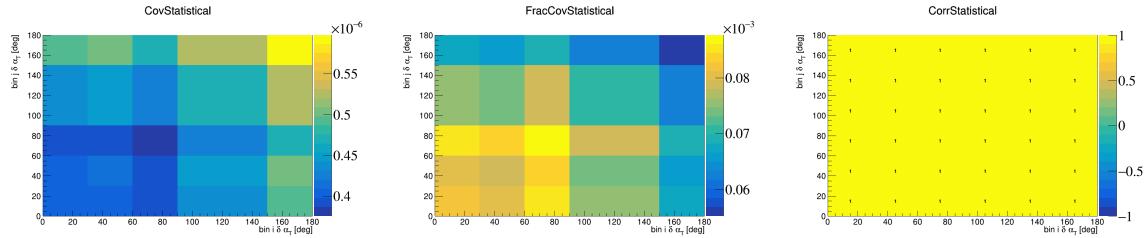


Figure 803: Statistical variations for $\delta \alpha_T$.

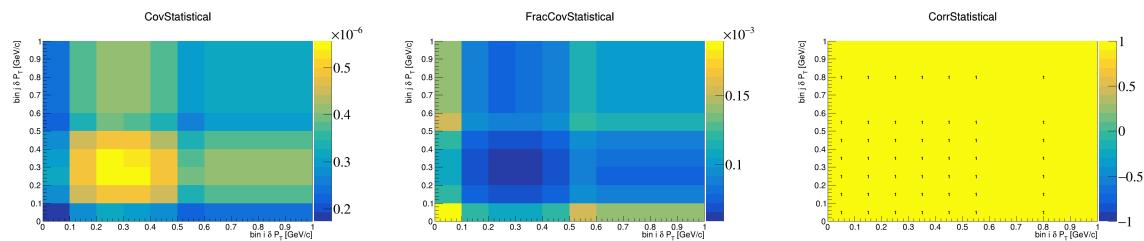


Figure 804: Statistical variations for δP_T .

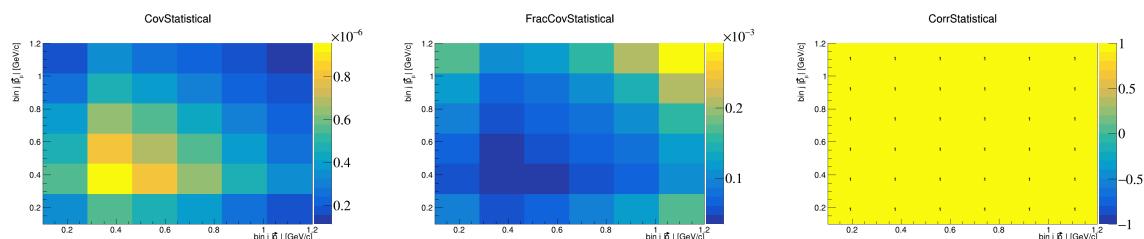


Figure 805: Statistical variations for $|\vec{p}_\mu|$.

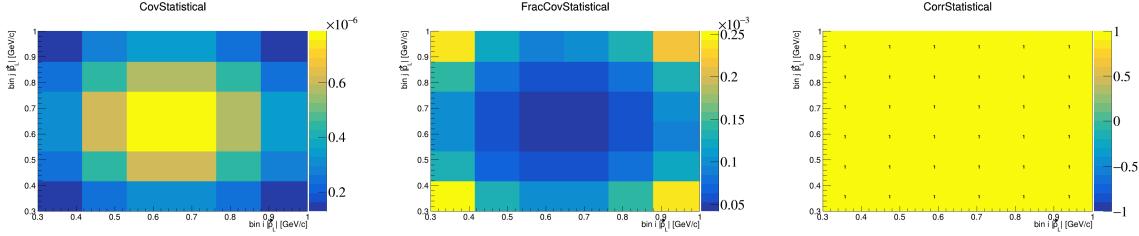


Figure 806: Statistical variations for $|\vec{p}_L|$.

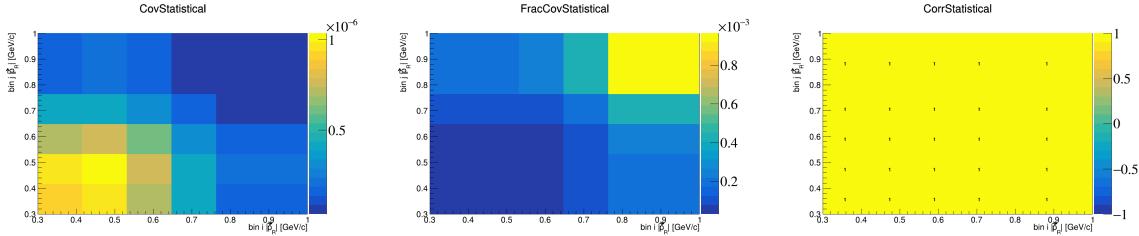


Figure 807: Statistical variations for $|\vec{p}_R|$.

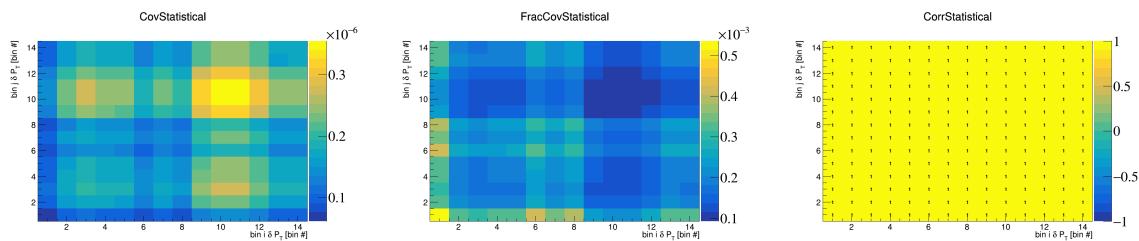


Figure 808: Statistical variations for δP_T in $\cos(\theta_{\vec{p}_\mu})$.

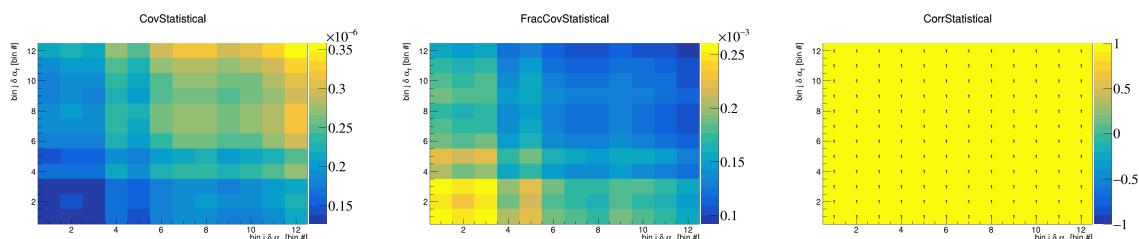


Figure 809: Statistical variations for $\delta \alpha_T$ in $\cos(\theta_{\vec{p}_\mu})$.

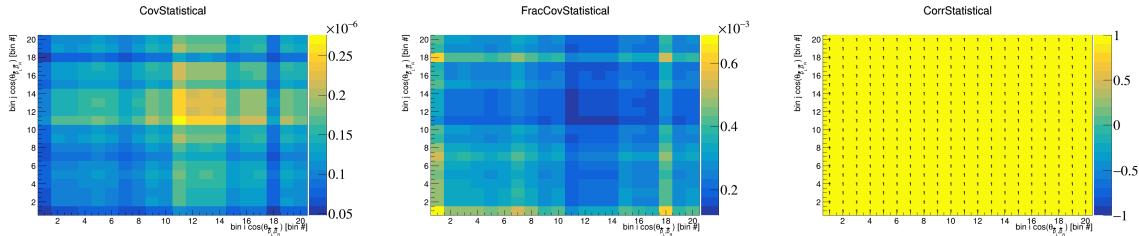


Figure 810: Statistical variations for $\cos(\theta_{\vec{p}_L, \vec{p}_R})$ in $\cos(\theta_{\vec{p}_\mu})$.

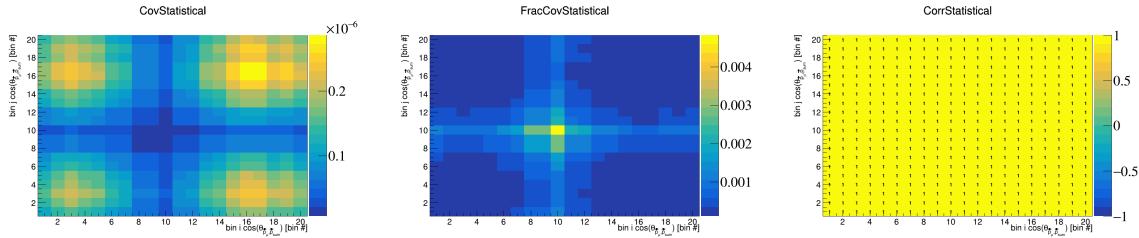


Figure 811: Statistical variations for $\cos(\theta_{\vec{p}_\mu, \vec{p}_{\text{sum}}})$ in $\cos(\theta_{\vec{p}_\mu})$.

316 7.4 POT

317 In this appendix, the covariance, fractional covariance, and correlation matrices for the POT systematics are
 318 plotted.

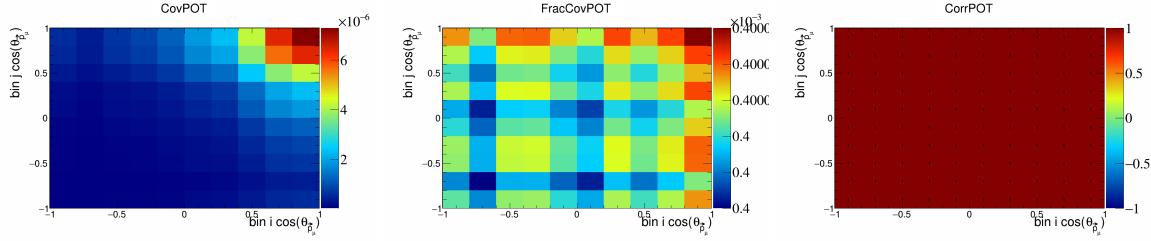


Figure 812: POT variations for $\cos(\theta_{\vec{p}_\mu})$.

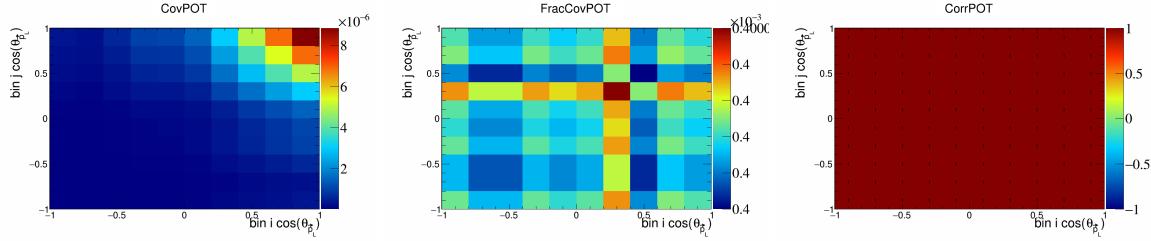


Figure 813: POT variations for $\cos(\theta_{\vec{p}_L})$.

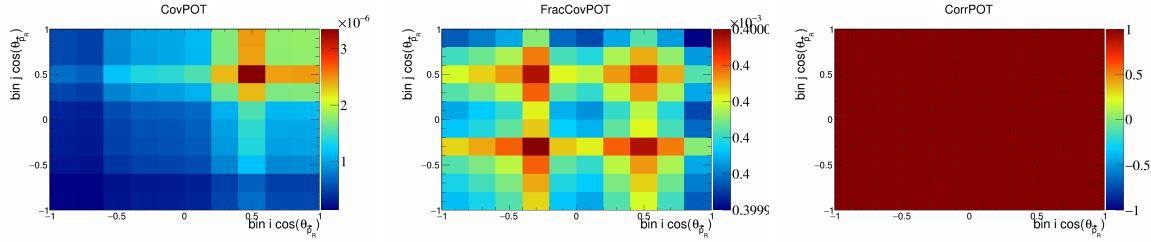


Figure 814: POT variations for $\cos(\theta_{\vec{p}_R})$.

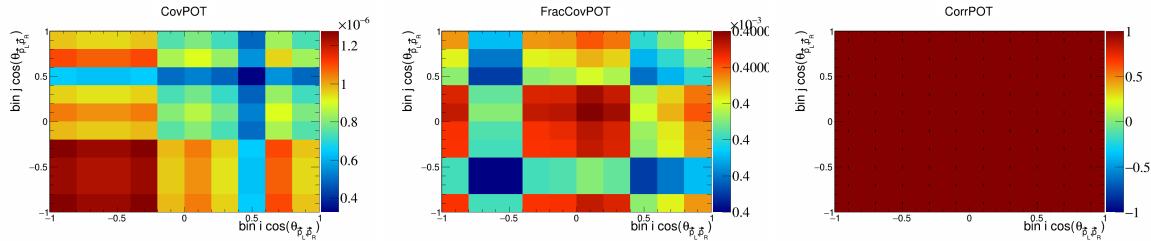


Figure 815: POT variations for $\cos(\theta_{\vec{p}_L, \vec{p}_R})$.

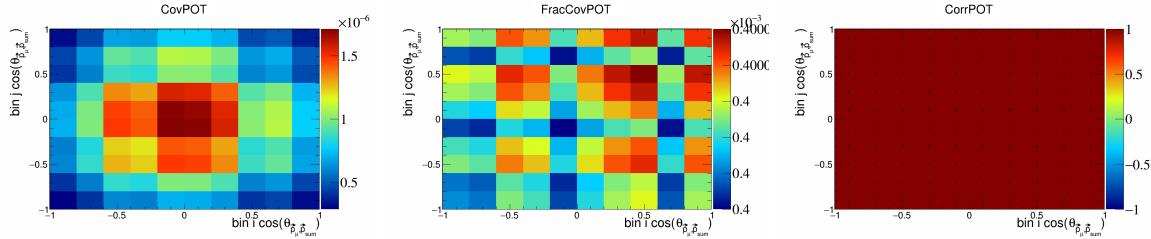


Figure 816: POT variations for $\cos(\theta_{\vec{p}_\mu}, \vec{p}_{\text{sum}})$.

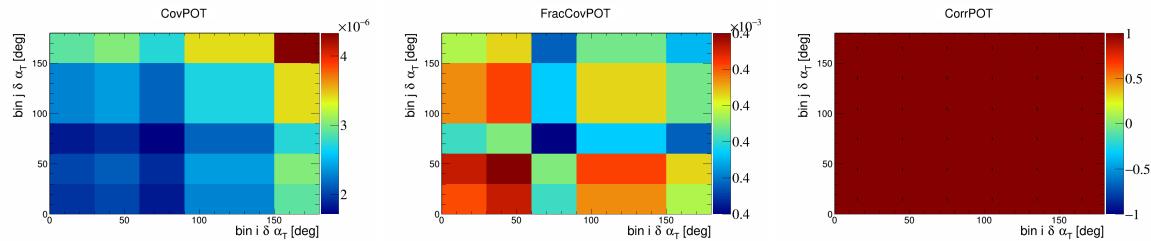


Figure 817: POT variations for $\delta\alpha_T$.

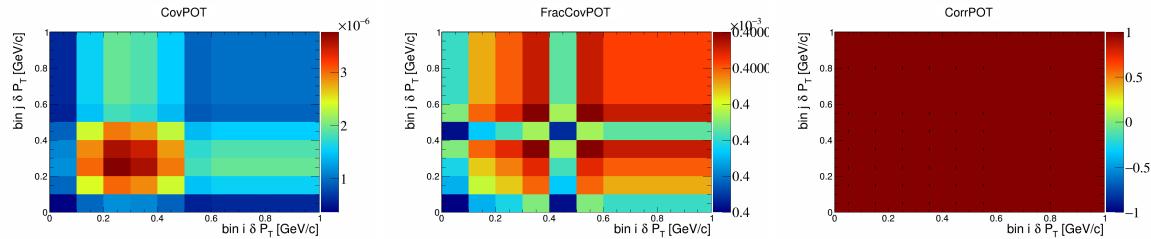


Figure 818: POT variations for δP_T .

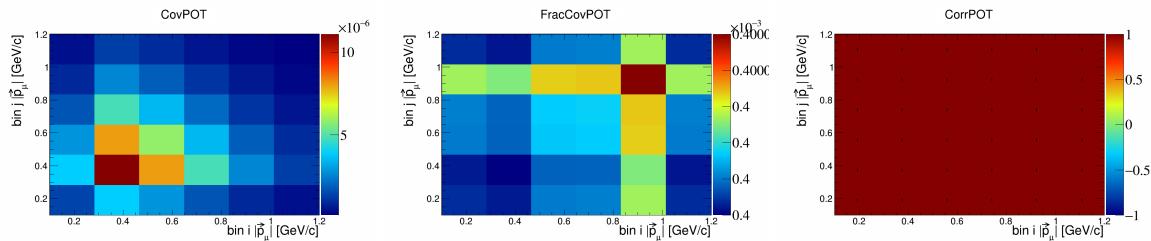


Figure 819: POT variations for $|\vec{p}_\mu|$.

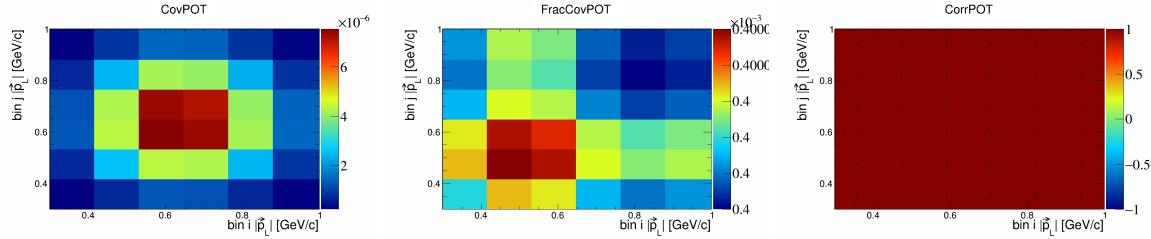


Figure 820: POT variations for $|\vec{p}_L|$.

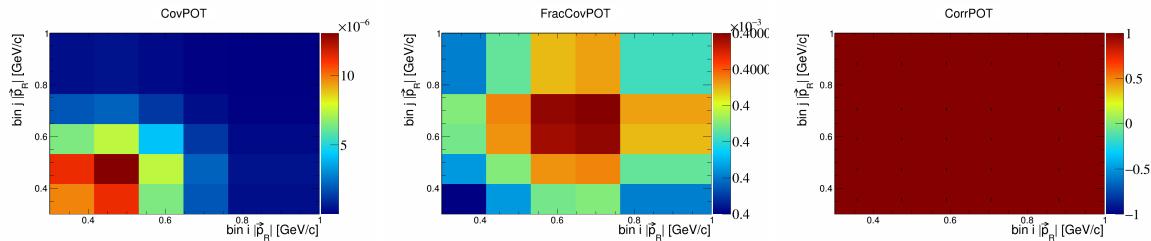


Figure 821: POT variations for $|\vec{p}_R|$.

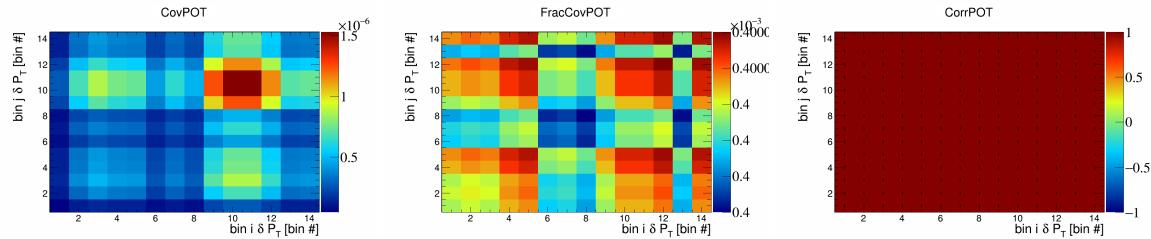


Figure 822: POT variations for δP_T in $\cos(\theta_{\vec{p}_\mu})$.

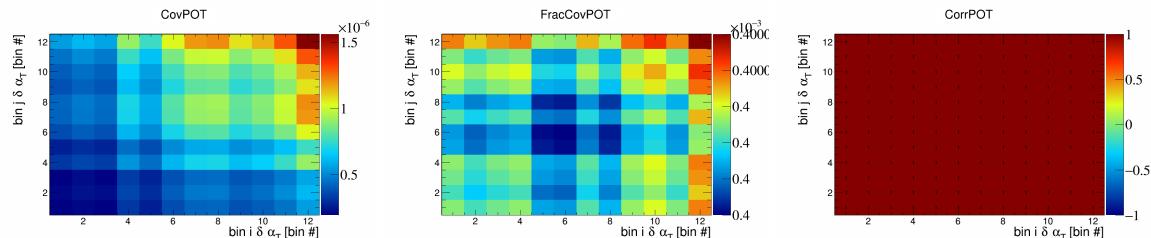


Figure 823: POT variations for $\delta \alpha_T$ in $\cos(\theta_{\vec{p}_\mu})$.

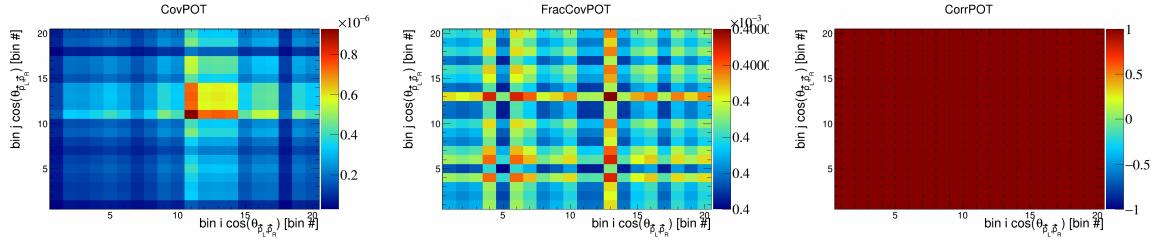


Figure 824: POT variations for $\cos(\theta_{\vec{p}_L, \vec{p}_R})$ in $\cos(\theta_{\vec{p}_\mu})$.

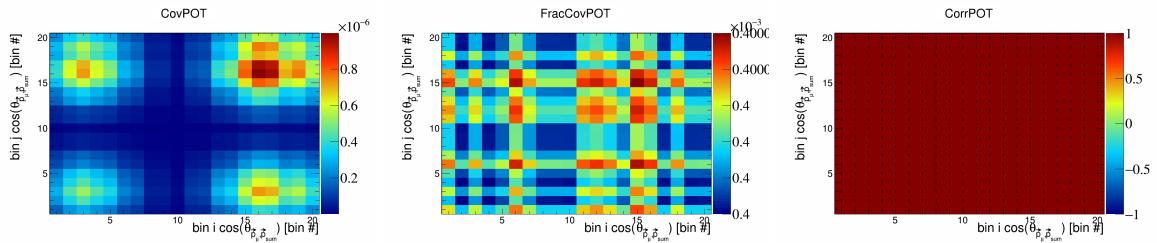


Figure 825: POT variations for $\cos(\theta_{\vec{p}_\mu, \vec{p}_{\text{sum}}})$ in $\cos(\theta_{\vec{p}_\mu})$.

319 7.5 Number of targets

320 In this appendix, the covariance, fractional covariance, and correlation matrices for the number of targets
 321 systematics are plotted.

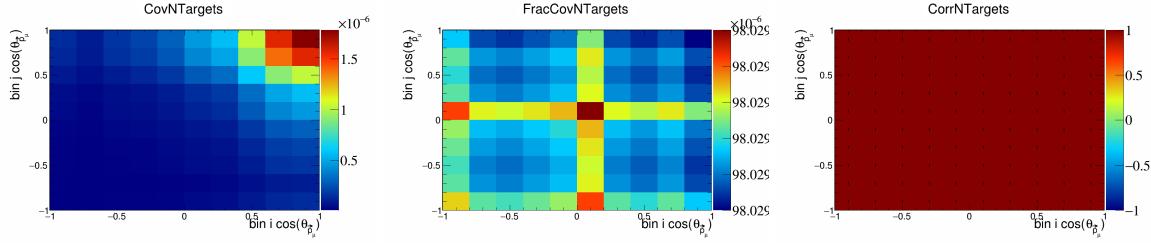


Figure 826: NTTargets variations for $\cos(\theta_{\vec{p}_\mu})$.

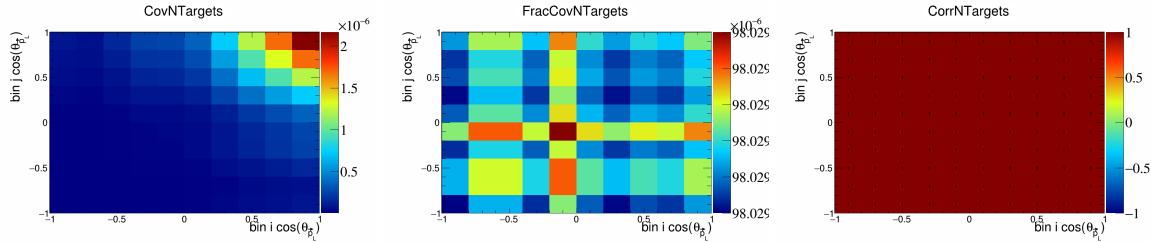


Figure 827: NTTargets variations for $\cos(\theta_{\vec{p}_L})$.

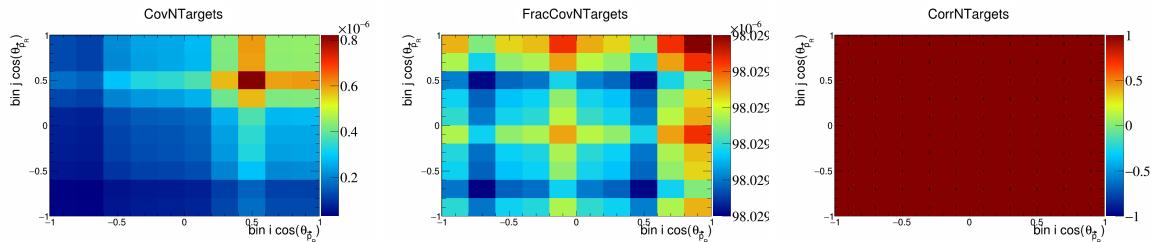


Figure 828: NTTargets variations for $\cos(\theta_{\vec{p}_R})$.

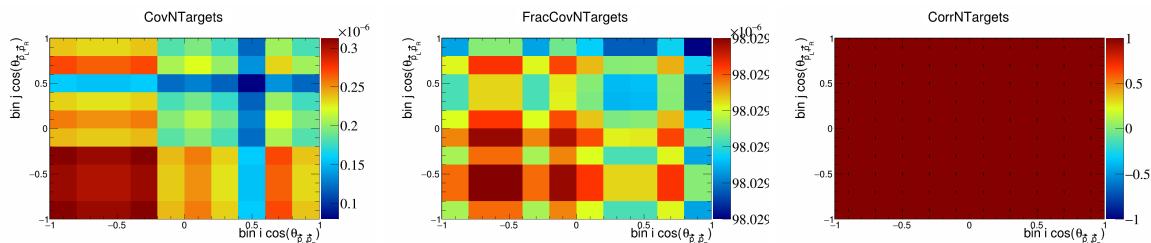


Figure 829: NTTargets variations for $\cos(\theta_{\vec{p}_L, \vec{p}_R})$.

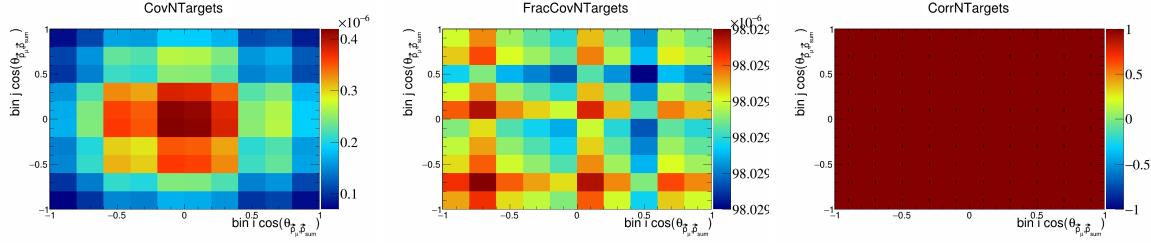


Figure 830: NTARGETS variations for $\cos(\theta_{\vec{p}_\mu, \vec{p}_{\text{sum}}})$.

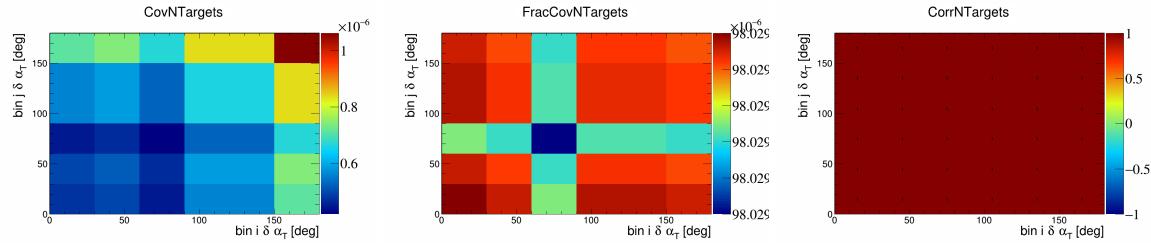


Figure 831: NTARGETS variations for $\delta \alpha_T$.

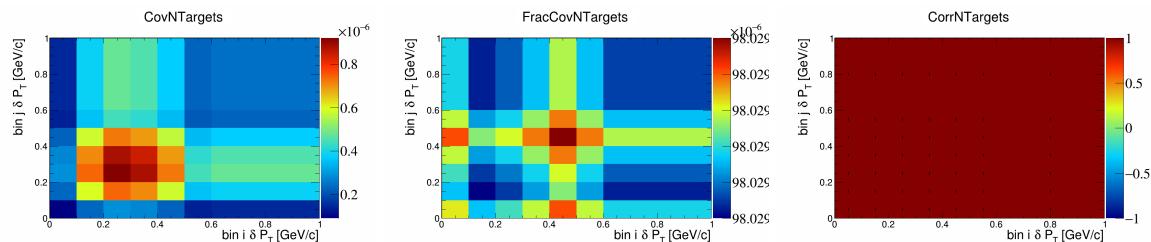


Figure 832: NTARGETS variations for δP_T .

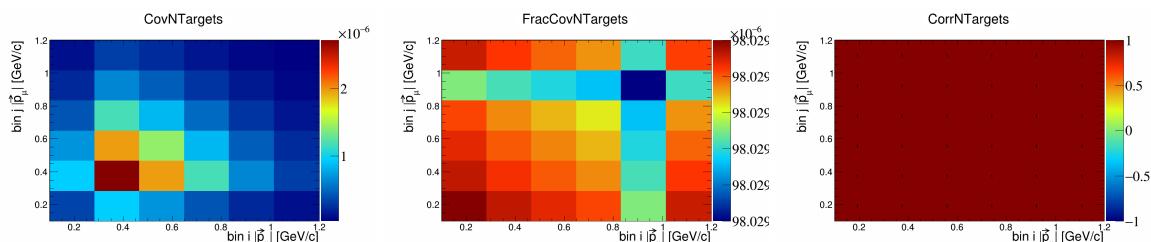


Figure 833: NTARGETS variations for $|\vec{p}_\mu|$.

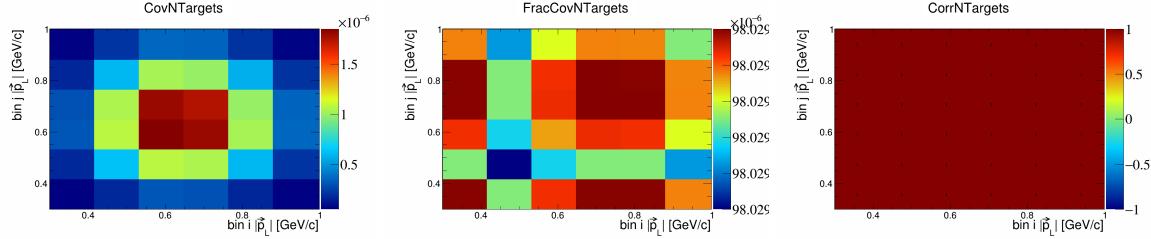


Figure 834: NTargets variations for $|\vec{p}_L|$.

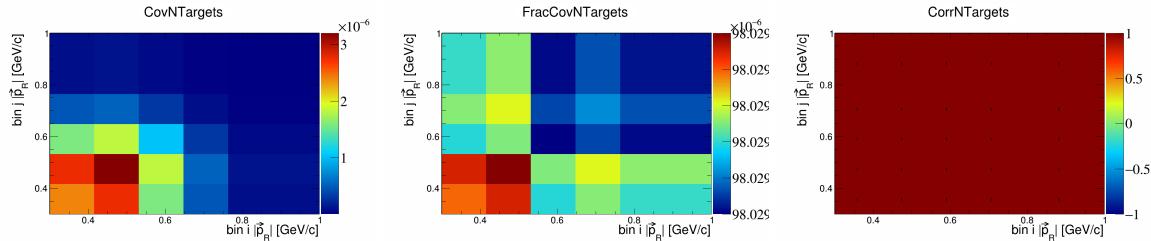


Figure 835: NTargets variations for $|\vec{p}_R|$.

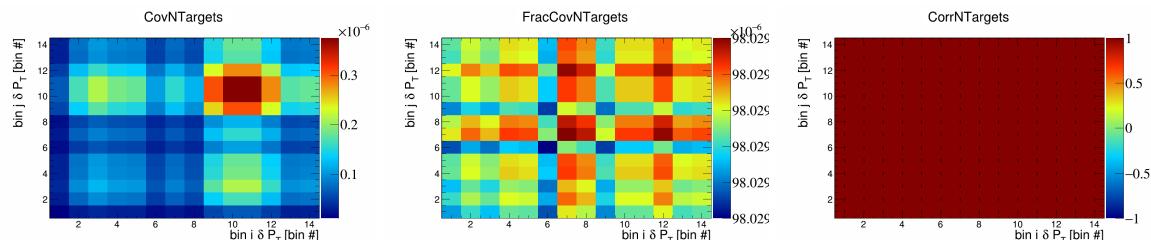


Figure 836: NTargets variations for δP_T in $\cos(\theta_{\vec{p}_\mu})$.

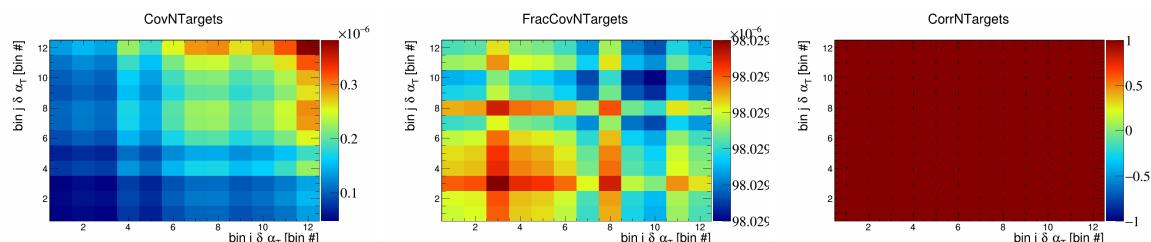


Figure 837: NTargets variations for $\delta \alpha_T$ in $\cos(\theta_{\vec{p}_\mu})$.

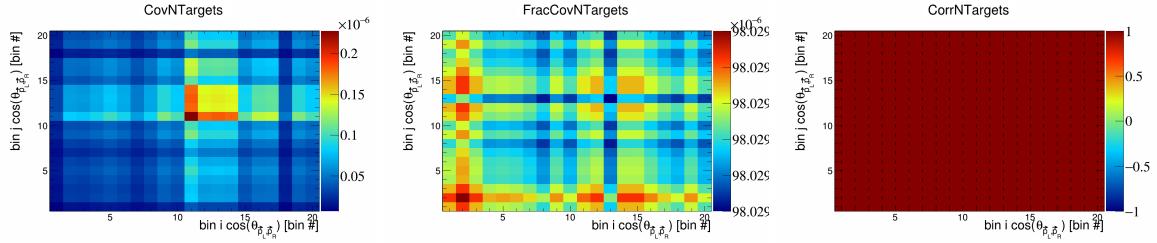


Figure 838: NTARGETS variations for $\cos(\theta_{\vec{p}_L, \vec{p}_R})$ in $\cos(\theta_{\vec{p}_\mu})$.

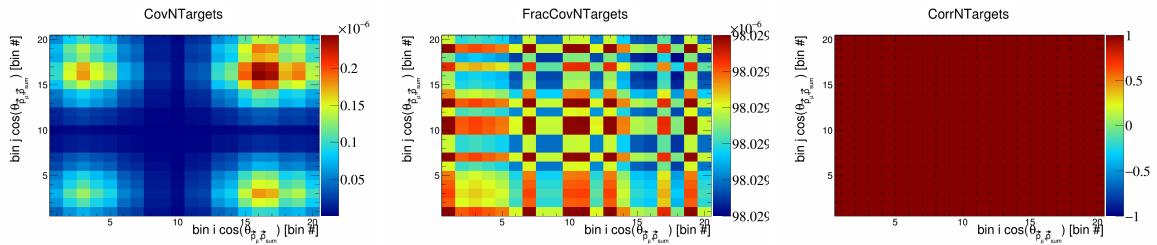


Figure 839: NTARGETS variations for $\cos(\theta_{\vec{p}_\mu, \vec{p}_{\text{sum}}})$ in $\cos(\theta_{\vec{p}_\mu})$.

7.6 Detector

In this appendix, the covariance, fractional covariance, and correlation matrices for the detector systematics are plotted.

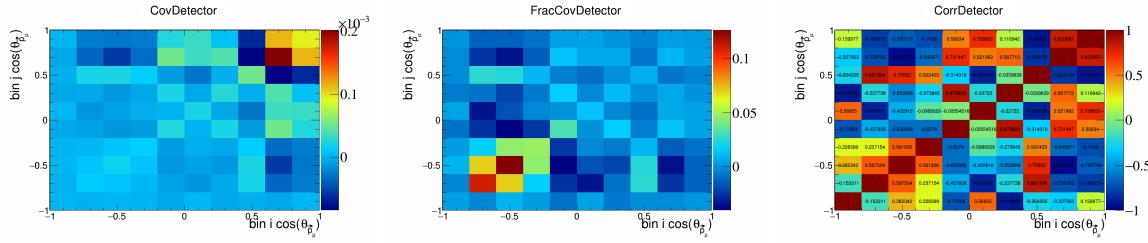


Figure 840: Detector variations for $\cos(\theta_{\vec{p}_\mu})$.

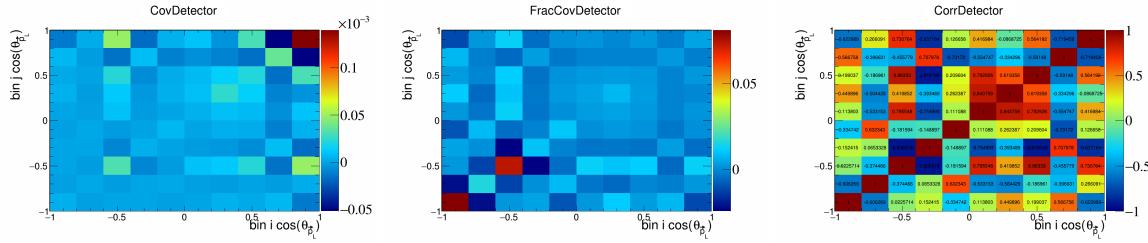


Figure 841: Detector variations for $\cos(\theta_{\vec{p}_L})$.

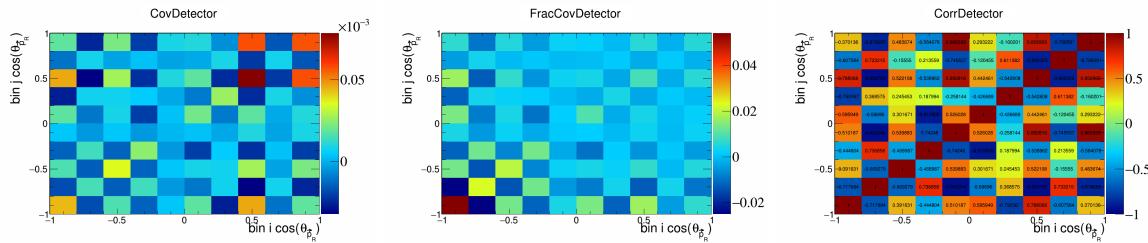


Figure 842: Detector variations for $\cos(\theta_{\vec{p}_R})$.

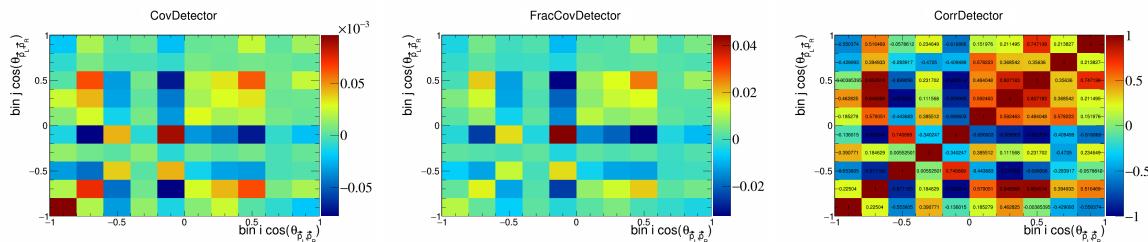


Figure 843: Detector variations for $\cos(\theta_{\vec{p}_L, \vec{p}_R})$.

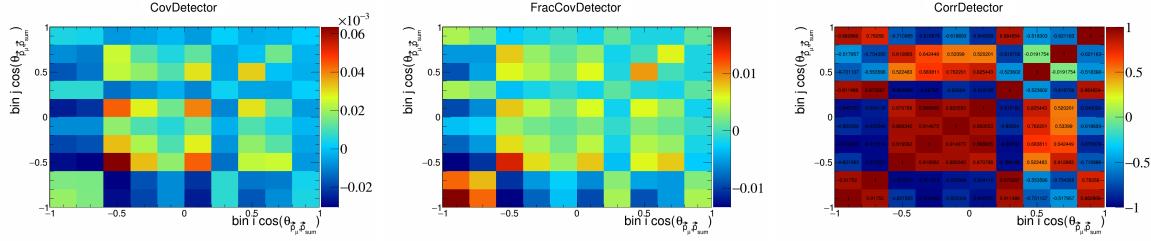


Figure 844: Detector variations for $\cos(\theta_{\vec{p}_\mu, \vec{p}_{\text{sum}}})$.

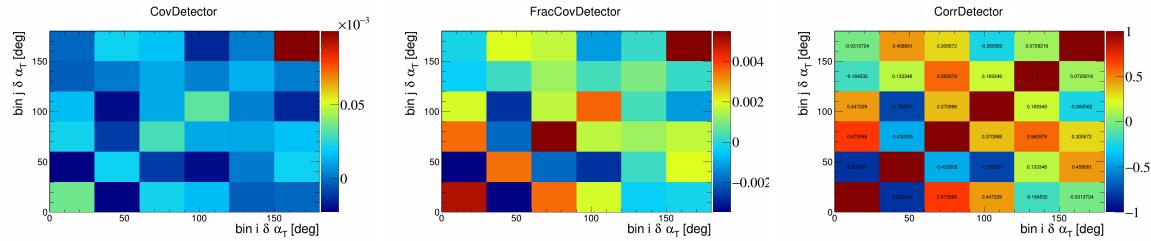


Figure 845: Detector variations for $\delta \alpha_T$.

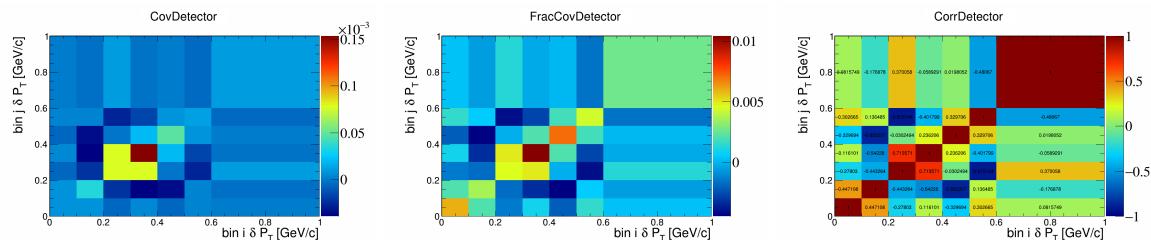


Figure 846: Detector variations for δP_T .

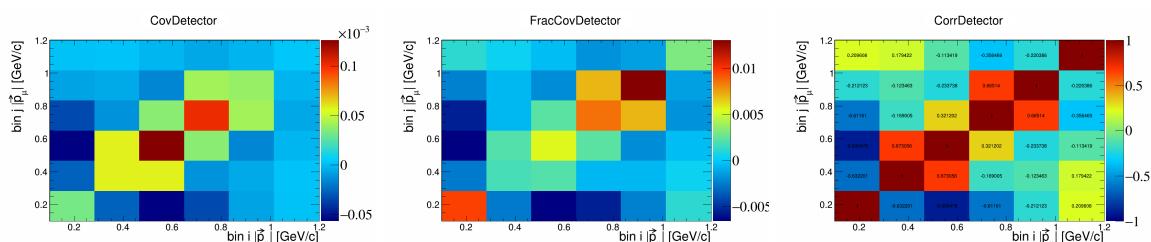


Figure 847: Detector variations for $|\vec{p}_\mu|$.

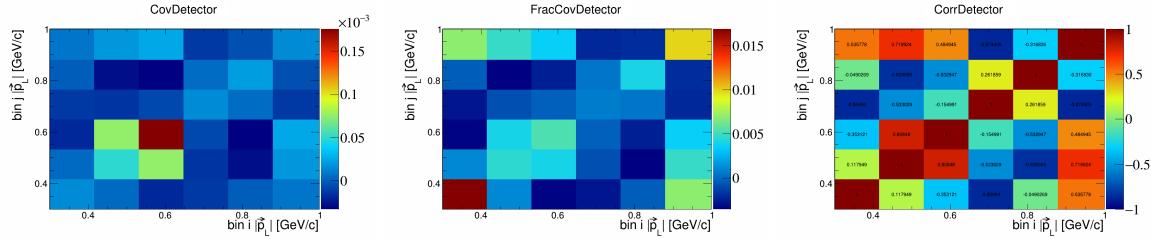


Figure 848: Detector variations for $|\vec{p}_L|$.

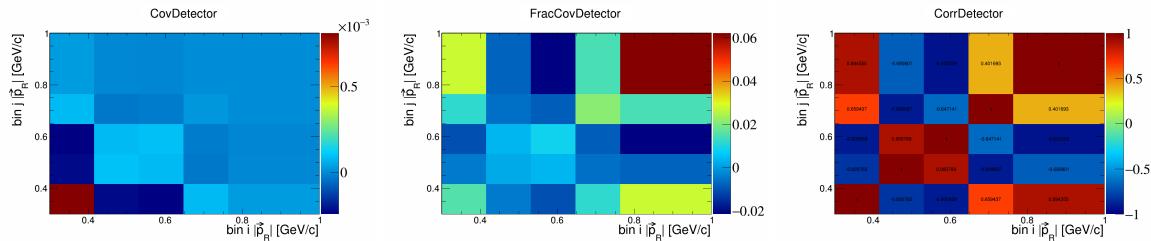


Figure 849: Detector variations for $|\vec{p}_R|$.

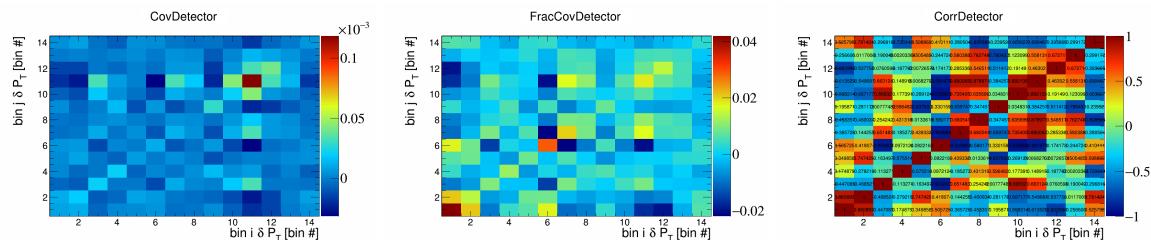


Figure 850: Detector variations for δP_T in $\cos(\theta_{\vec{p}_\mu})$.

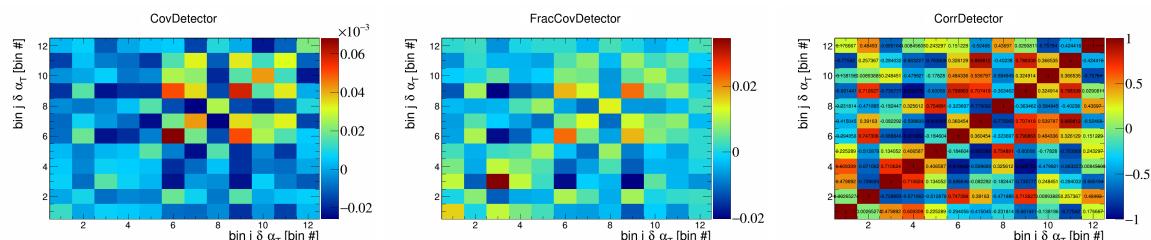


Figure 851: Detector variations for $\delta \alpha_T$ in $\cos(\theta_{\vec{p}_\mu})$.

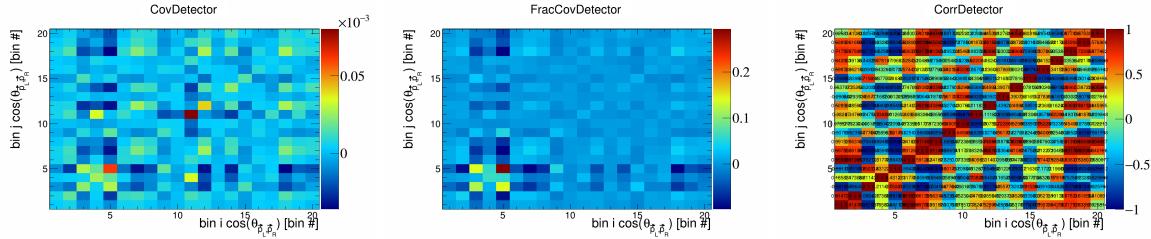


Figure 852: Detector variations for $\cos(\theta_{\vec{p}_L, \vec{p}_R})$ in $\cos(\theta_{\vec{p}_\mu})$.

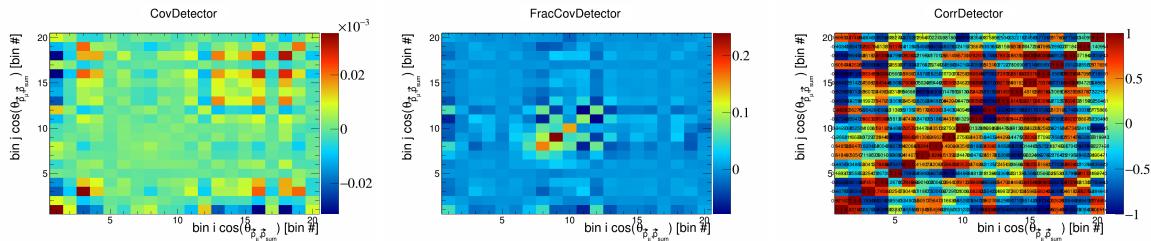


Figure 853: Detector variations for $\cos(\theta_{\vec{p}_\mu, \vec{p}_{\text{sum}}})$ in $\cos(\theta_{\vec{p}_\mu})$.

325 7.7 Reinteraction

326 In this appendix, the covariance, fractional covariance, and correlation matrices for the reinteraction sys-
 327 tematics are plotted.

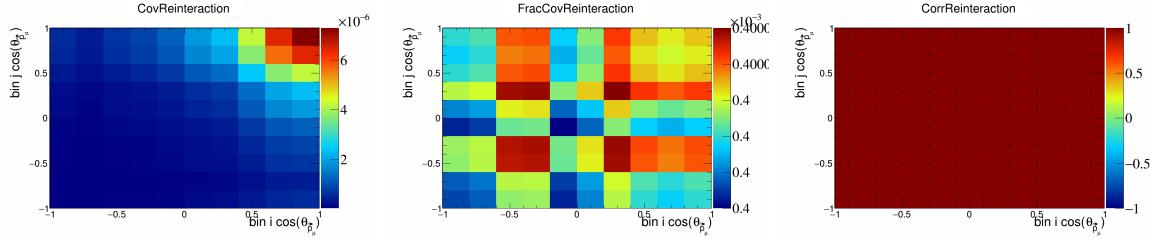


Figure 854: Reinteraction variations for $\cos(\theta_{\vec{p}_\mu})$.

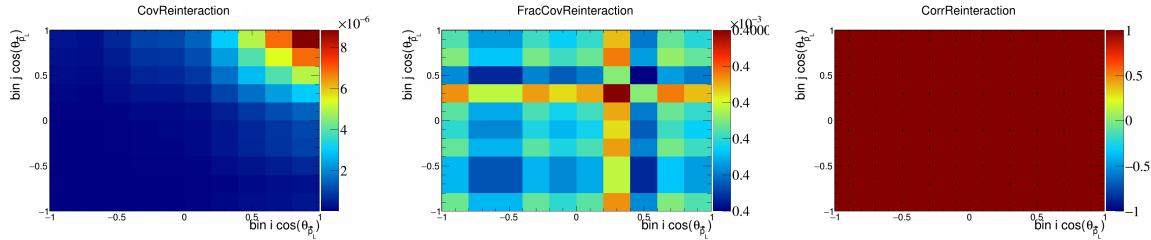


Figure 855: Reinteraction variations for $\cos(\theta_{\vec{p}_L})$.

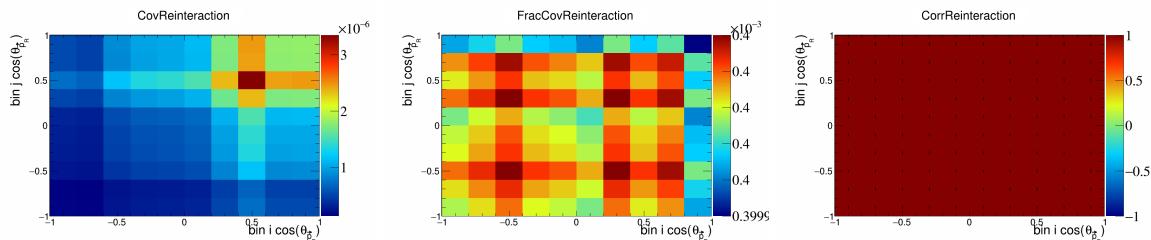


Figure 856: Reinteraction variations for $\cos(\theta_{\vec{p}_R})$.

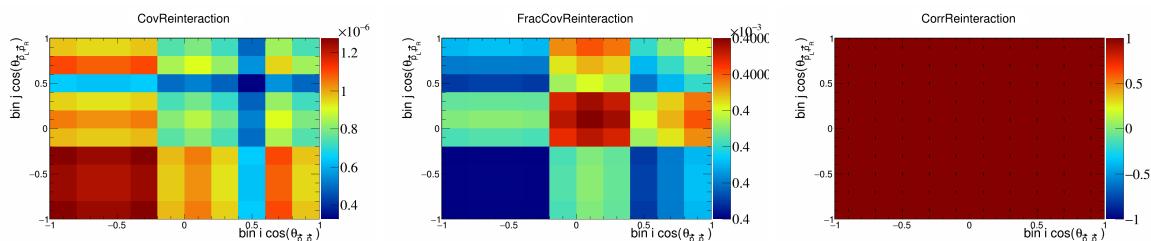


Figure 857: Reinteraction variations for $\cos(\theta_{\vec{p}_L, \vec{p}_R})$.

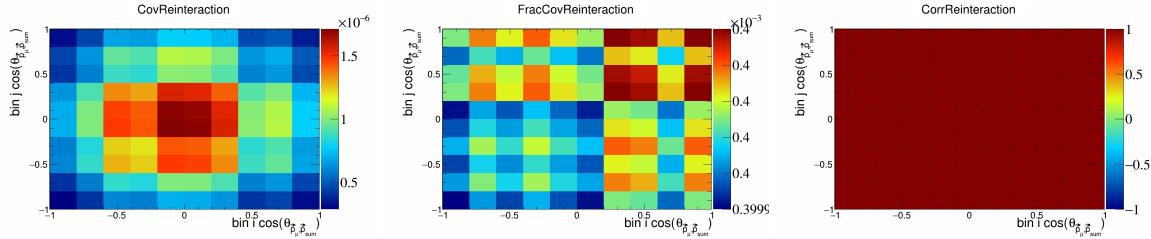


Figure 858: Reinteraction variations for $\cos(\theta_{\vec{p}_\mu, \vec{p}_{\text{sum}}})$.

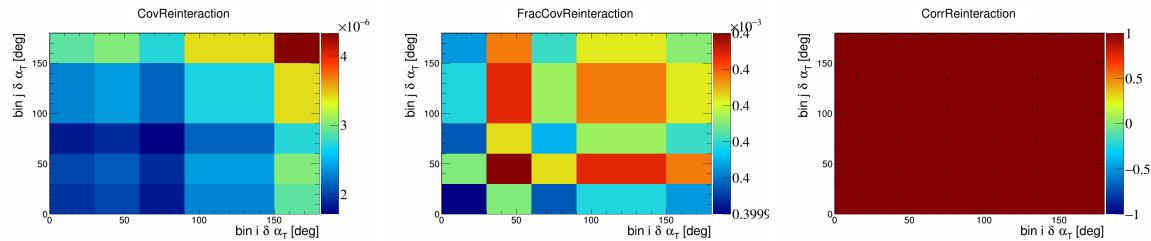


Figure 859: Reinteraction variations for $\delta \alpha_T$.

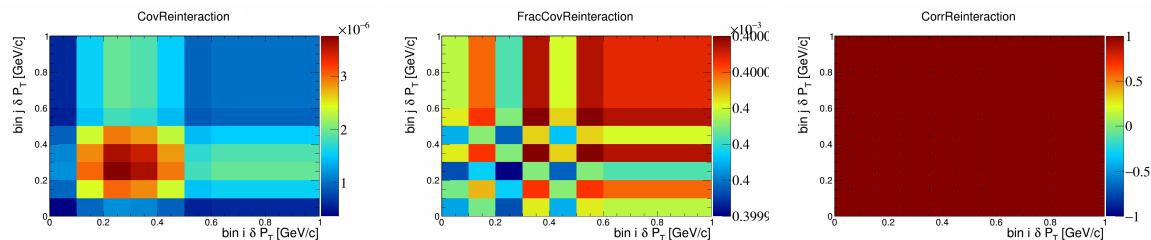


Figure 860: Reinteraction variations for δP_T .

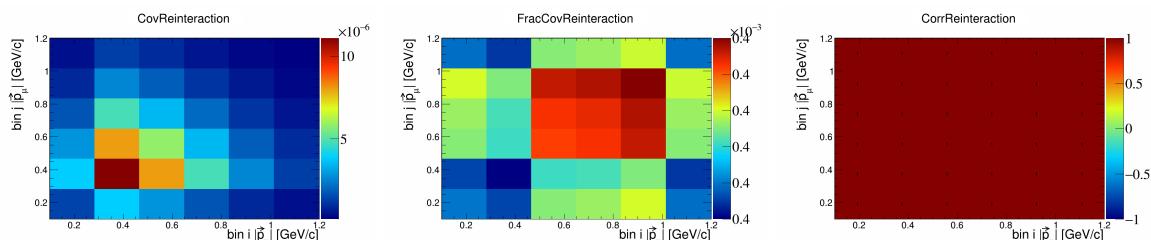


Figure 861: Reinteraction variations for $|\vec{p}_\mu|$.

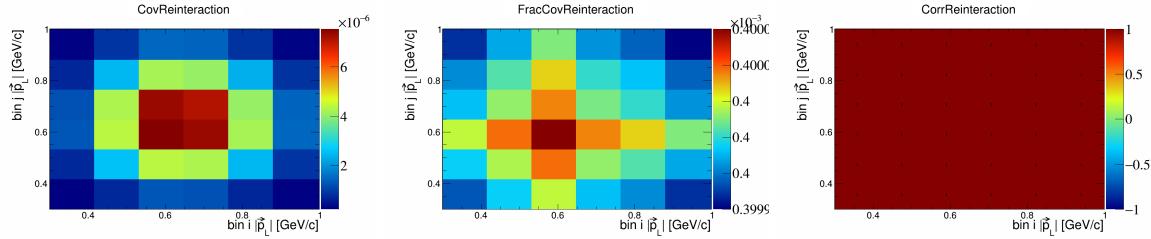


Figure 862: Reinteraction variations for $|\vec{p}_L|$.

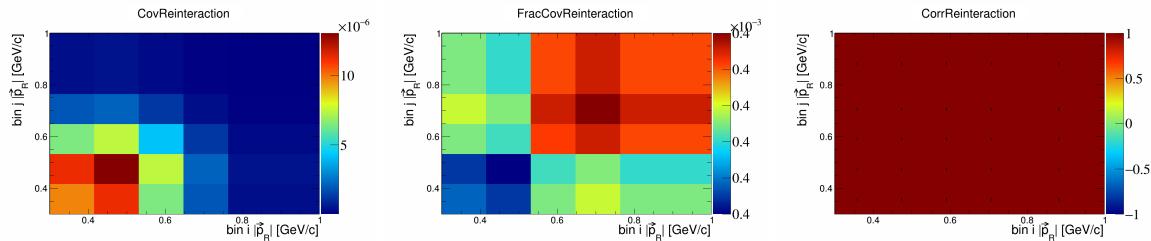


Figure 863: Reinteraction variations for $|\vec{p}_R|$.

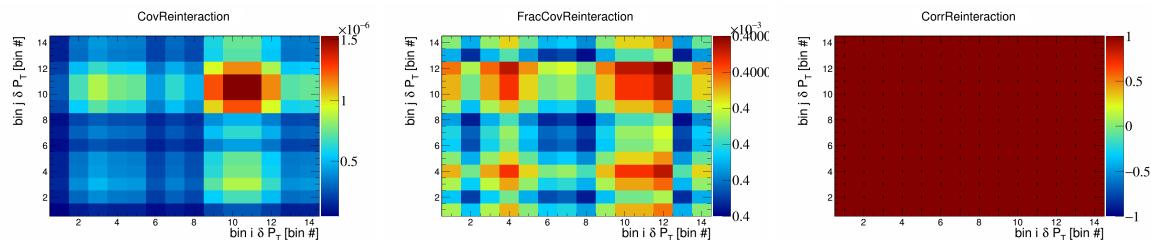


Figure 864: Reinteraction variations for δP_T in $\cos(\theta_{\vec{p}_\mu})$.

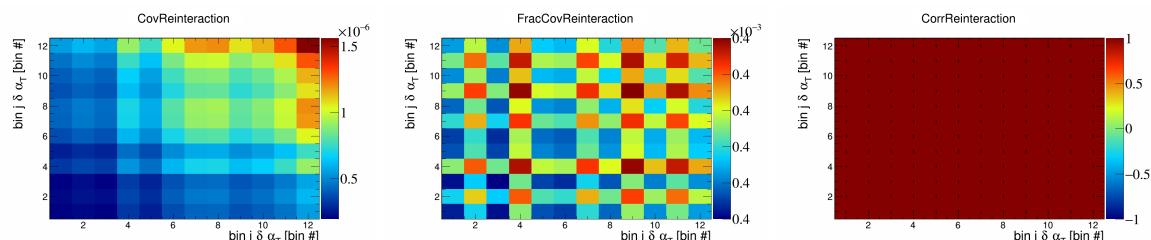


Figure 865: Reinteraction variations for $\delta \alpha_T$ in $\cos(\theta_{\vec{p}_\mu})$.

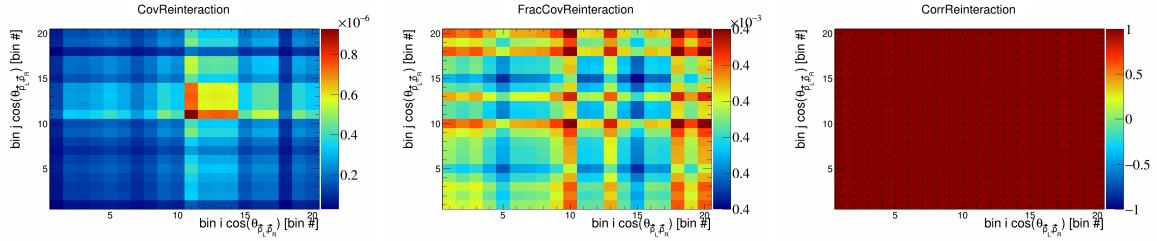


Figure 866: Reinteraction variations for $\cos(\theta_{\vec{p}_L, \vec{p}_R})$ in $\cos(\theta_{\vec{p}_\mu})$.

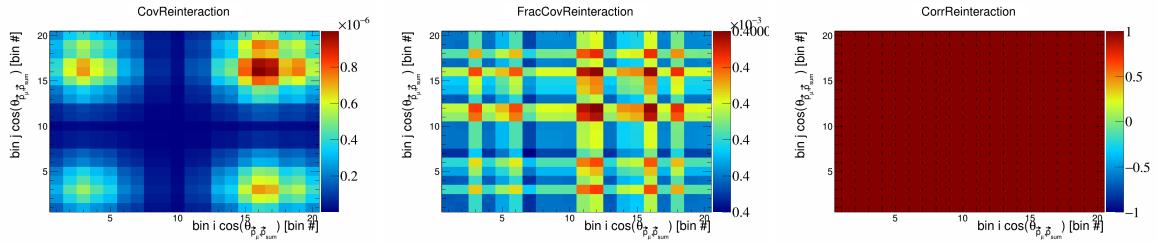


Figure 867: Reinteraction variations for $\cos(\theta_{\vec{p}_\mu, \vec{p}_{\text{sum}}})$ in $\cos(\theta_{\vec{p}_\mu})$.

328 **8 References**

- 329 [1] R. Acciarri, C. Adams, J. Asaadi, B. Baller, T. Bolton, C. Bromberg, F. Cavanna, E. Church, D. Edmunds, A. Ereditato, S. Farooq, B. Fleming, H. Greenlee, G. Horton-Smith, C. James, E. Klein, K. Lang, P. Laurens, R. Mehdiyev, B. Page, O. Palamara, K. Partyka, G. Rameika, B. Rebel, M. Soderberg, J. Spitz, A. M. Szelc, M. Weber, T. Yang, and G. P. Zeller. Detection of back-to-back proton pairs in charged-current neutrino interactions with the argoneut detector in the numi low energy beam line. *Phys. Rev. D*, 90:012008, Jul 2014.
- 330 [2] C. Andreopoulos, A. Bell, D. Bhattacharya, F. Cavanna, J. Dobson, S. Dytman, H. Gallagher, P. Guzowski, R. Hatcher, P. Kehayias, A. Meregaglia, D. Naples, G. Pearce, A. Rubbia, M. Whalley, and T. Yang. The genie neutrino monte carlo generator. *Nuclear Instruments and Methods in Physics Research Section A: Accelerators, Spectrometers, Detectors and Associated Equipment*, 614(1):87–104, 2010.
- 331 [3] Costas Andreopoulos, Christopher Barry, Steve Dytman, Hugh Gallagher, Tomasz Golan, Robert Hatcher, Gabriel Perdue, and Julia Yarba. The genie neutrino monte carlo generator: Physics and user manual, 2015.
- 332 [4] D. Ashery, I. Navon, G. Azuelos, H. K. Walter, H. J. Pfeiffer, and F. W. Schlepütz. True absorption and scattering of pions on nuclei. *Phys. Rev. C*, 23:2173–2185, May 1981.
- 333 [5] P. S. Auchincloss, R. Blair, C. Haber, E. Oltman, W. C. Leung, M. Ruiz, S. R. Mishra, P. Z. Quintas, F. J. Sciulli, M. H. Shaevitz, W. H. Smith, F. S. Merritt, M. Oreglia, P. Reutens, R. Coleman, H. E. Fisk, D. Levinthal, D. D. Yovanovitch, W. Marsh, P. A. Rapidis, H. B. White, A. Bodek, F. Borcherding, N. Giokaris, K. Lang, and I. E. Stockdale. Measurement of the inclusive charged-current cross section for neutrino and antineutrino scattering on isoscalar nucleons. *Zeitschrift für Physik C Particles and Fields*, 48(3):411–431, Sep 1990.
- 334 [6] Ch. Berger and L. M. Sehgal. Lepton mass effects in single pion production by neutrinos. *Phys. Rev. D*, 76:113004, Dec 2007.
- 335 [7] Ch. Berger and L. M. Sehgal. Partially conserved axial vector current and coherent pion production by low energy neutrinos. *Phys. Rev. D*, 79:053003, Mar 2009.
- 336 [8] B. Bourguille, J. Nieves, and F. Sánchez. Inclusive and exclusive neutrino-nucleus cross sections and the reconstruction of the interaction kinematics. *Journal of High Energy Physics*, 2021(4):4, Apr 2021.
- 337 [9] R.C. Carrasco and E. Oset. Interaction of real photons with nuclei from 100 to 500 mev. *Nuclear Physics A*, 536(3):445–508, 1992.
- 338 [10] R. Cruz-Torres, D. Lonardoni, R. Weiss, N. Barnea, D. W. Higinbotham, E. Piasetzky, A. Schmidt, L. B. Weinstein, R. B. Wiringa, and O. Hen. Many-body factorization and position-momentum equivalence of nuclear short-range correlations. *Nature Phys.*, 17(3):306–310, 2021.
- 339 [11] Jonathan Engel. Approximate treatment of lepton distortion in charged-current neutrino scattering from nuclei. *Phys. Rev. C*, 57:2004–2009, Apr 1998.
- 340 [12] T. Golan, J.T. Sobczyk, and J. Źmuda. Nuwro: the wrocław monte carlo generator of neutrino interactions. *Nuclear Physics B - Proceedings Supplements*, 229-232:499, 2012. Neutrino 2010.
- 341 [13] Krzysztof M. Graczyk and Jan T. Sobczyk. Form factors in the quark resonance model. *Phys. Rev. D*, 77:053001, Mar 2008.
- 342 [14] Yoshinari Hayato and Luke Pickering. The neut neutrino interaction simulation program library. *The European Physical Journal Special Topics*, 230(24):4469–4481, Dec 2021.
- 343 [15] Teppei Katori. Meson exchange current (MEC) models in neutrino interaction generators. *AIP Conference Proceedings*, 1663(1):030001, 05 2015.

- 372 [16] Konstantin S. Kuzmin, Vladimir V. Lyubushkin, and Vadim A. Naumov. Lepton polarization in neutrino–nucleon interactions. *Modern Physics Letters A*, 19(38):2815–2829, 2004.
- 373
- 374 [17] T. Leitner, L. Alvarez-Ruso, and U. Mosel. Charged current neutrino-nucleus interactions at intermediate energies. *Phys. Rev. C*, 73:065502, Jun 2006.
- 375
- 376 [18] C.H. Llewellyn Smith. Neutrino reactions at accelerator energies. *Physics Reports*, 3(5):261–379, 1972.
- 377 [19] Selection of numu charged current induced interactions with $N > 0$ protons and performance of events with $N = 2$ protons in the final state in the MicroBooNE detector from the BNB, Oct 2018.
- 378
- 379 [20] First Extraction of Single Differential Cross-Sections on Argon for CC1 μ 2p0 π Event Topologies in the MicroBooNE Detector. May 2022.
- 380
- 381 [21] Ulrich Mosel. Neutrino event generators: foundation, status and future. *Journal of Physics G: Nuclear and Particle Physics*, 46(11):113001, Sep 2019.
- 382
- 383 [22] J. Nieves, J. E. Amaro, and M. Valverde. Inclusive quasielastic charged-current neutrino-nucleus reactions. *Phys. Rev. C*, 70:055503, Nov 2004.
- 384
- 385 [23] J. Nieves, F. Sánchez, I. Ruiz Simo, and M. J. Vicente Vacas. Neutrino energy reconstruction and the shape of the charged current quasielastic-like total cross section. *Phys. Rev. D*, 85:113008, Jun 2012.
- 386
- 387 [24] J. Nieves, I. Ruiz Simo, and M. J. Vicente Vacas. Inclusive charged-current neutrino-nucleus reactions. *Phys. Rev. C*, 83:045501, Apr 2011.
- 388
- 389 [25] J. Schwehr, D. Cherdack, and R. Gran. Genie implementation of ific valencia model for qe-like 2p2h neutrino-nucleus cross section, 2017.
- 390
- 391 [26] Torbjörn Sjöstrand, Stephen Mrenna, and Peter Skands. Pythia 6.4 physics and manual. *Journal of High Energy Physics*, 2006(05):026, may 2006.
- 392
- 393 [27] W. Tang, X. Li, X. Qian, H. Wei, and C. Zhang. Data unfolding with wiener-svd method. *Journal of Instrumentation*, 12(10):P10002–P10002, October 2017.
- 394
- 395 [28] Júlia Tena-Vidal, Costas Andreopoulos, Adi Ashkenazi, Christopher Barry, Steve Dennis, Steve Dytman, Hugh Gallagher, Steven Gardiner, Walter Giele, Robert Hatcher, Or Hen, Libo Jiang, Igor D. Kakorin, Konstantin S. Kuzmin, Anselmo Meregaglia, Vadim A. Naumov, Afroditi Papadopoulou, Gabriel Perdue, Marco Roda, Vladyslav Syrotenko, and Jeremy Wolcott. Neutrino-nucleon cross-section model tuning in genie v3. *Phys. Rev. D*, 104:072009, Oct 2021.
- 396
- 397 [29] U. K. Yang and A. Bodek. Parton distributions, d/u , and higher twist effects at high x . *Phys. Rev. Lett.*, 82:2467–2470, Mar 1999.
- 398
- 399
- 400
- 401